Smoothed Finite Element Methods

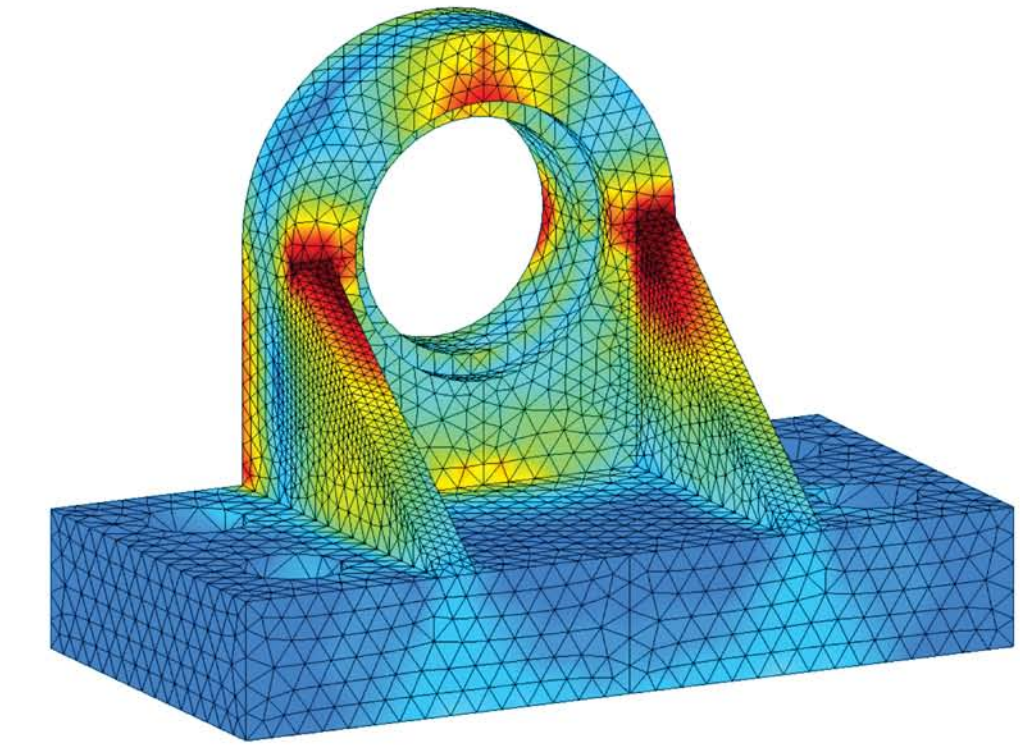

G.R. Liu and Nguyen Thoi Trung

CRC Press
Taylor & Francis Group

Smoothed Finite Element Methods

Smoothed Finite Element Methods

G.R. Liu
Nguyen Thoi Trung

CRC Press
Taylor & Francis Group
Boca Raton London New York

CRC Press is an imprint of the
Taylor & Francis Group, an **informa** business

CRC Press
Taylor & Francis Group
6000 Broken Sound Parkway NW, Suite 300
Boca Raton, FL 33487-2742

Printed in the United States of America on acid-free paper
10 9 8 7 6 5 4 3 2 1

International Standard Book Number-13: 978-1-4398-2028-5 (Ebook-PDF)

Visit the Taylor & Francis Web site at
http://www.taylorandfrancis.com

and the CRC Press Web site at
http://www.crcpress.com

To Zuona,Yun, Kun, Run, and my extended family for the time, support, and love they gave to me

—G. R. Liu

To my mother, my deceased father, my sisters (Thoi Minh—My Hanh), my daughter, (Minh Tu—Alpha) for the love, support, and inspiration they have given to me

—Nguyen Thoi Trung

Contents

Preface

Since the late 1950s, we have used the finite element method (FEM) as an essential and important tool for the modeling and simulation of practical problems with complex geometry. The first author (Dr. Liu) has been a user since 1979, when he wrote his first FEM code to solve a nonlinear mechanics problem for a frame structure as his university final-year project. Since then, FEM has been one of his major tools in dealing with many engineering and academic problems. Since the late 1980s, he has participated in and directed many engineering projects of very large scale with millions of degrees of freedom. In those projects, we have frequently encountered problems with mesh generation when using FEM software packages. For accuracy reasons, we want to use quality quadrilateral or hexahedron elements, but such a mesh is quite difficult to generate and requires a number of manual operations to cut the domain into proper pieces. The time spent on such operations has been very significant. To avoid this problem, we have tried to use triangular/tetrahedron elements. Mesh generation then becomes easier and can often be done automatically without much manual operations. However, the accuracy of the results is often quite poor, and most importantly the iteration may stop in the middle of the computation of nonlinear problems due to locking-related problems.

In searching for alternatives, the authors' group learned and developed mesh-free methods, and good progress has been made on that front. We can now safely say that by using proper mesh-free techniques, we can do pretty much what we want using only a background mesh of triangles/tetrahedrons. However, the operations in mesh-free methods are generally more complicated and can be quite costly in terms of computational effort and resources.

In examining FEM and mesh-free methods, we have found that a proper combination of these two can be advantageous. After a number of attempts in the past decades, we are finally satisfied with the so-called smooth finite element method (S-FEM). It is essentially a watered-down version of a family of mesh-free methods called smoothed point interpolation methods (S-PIMs) and hence is reasonably simple; however, it carries many key features of mesh-free methods. Most importantly, S-FEM needs only a triangular/tetrahedral mesh. Therefore, since 2005, we have been focusing on the establishment of the theoretical framework and the development of various S-FEM models. This book collects some of the major outcomes, providing a systematic description of S-FEM.

The authors will be happy to share, free of charge, some of the basic source codes of the S-FEM with the readers for academic research purposes and further developments. The authors, however, make no warranty whatsoever, expressed or implied, that the materials and codes given are free from errors. In no event shall the authors become liable to anyone for the use of the materials and codes. Under these conditions, interested readers may directly approach either author for these source codes. The authors appreciate very much a proper acknowledgment for the use of these materials and codes.

In preparing this book, a number of colleagues and students have supported and contributed to the writing. We express sincere thanks to all of them. Special thanks to K. Y. Dai, G. Y. Zhang, H. Nguyen-Xuan, L. Chen, N. Nourbakhshnia, Z. C. He, S. C. Wu, Z. Q. Zhang, X. Y. Cui, Q. Tang, and many others. Many of these individuals have contributed examples to this book in addition to their hard work in carrying out a number of projects related to the S-FEM covered in this book.

G. R. Liu
Nguyen Thoi Trung

Authors

G. R. Liu received his PhD from Tohoku University, Japan, in 1991. He was a postdoctoral fellow at Northwestern University, Illinois. He is currently the director of the Centre for Advanced Computations in Engineering Science (ACES), National University of Singapore. He is the president of the Association for Computational Mechanics (Singapore), and an executive council member of the International Association for Computational Mechanics. He is also a professor and deputy head of the department of mechanical engineering, National University of Singapore. He has provided consultation services to many national and international organizations. He has authored more than 500 technical publications, including more than 300 international journal papers and eight authored books, which include two bestsellers: *Meshfree Methods: Moving Beyond the Finite Element Method*, CRC, 2002 (1st edition); 2009 (2nd edition) and *Smoothed Particle Hydrodynamics: A Meshfree Particle Methods*, World Scientific, 2003. He is the editor-in-chief of the *International Journal of Computational Methods* and an editorial member of five other journals, including *IJNME*. He is the recipient of the Outstanding University Researchers Awards, the Defence Technology Prize (National award), the Silver Award at CrayQuest competition, the Excellent Teachers Awards, the Engineering Educator Awards, and the APACM Award for Computational Mechanics. His research interests include computational mechanics, mesh-free methods, nanoscale computation, microbiosystem computation, vibration and wave propagation in composites, mechanics of composites and smart materials, inverse problems, and numerical analysis.

Nguyen Thoi Trung (Nguyen-Thoi T) received his civil engineering degree from University of Technology, Hochiminh City, Vietnam in 1999 and his bachelor's degree in mathematics and computer science from University of Science, Hochiminh City, Vietnam in 2001. He then received his master's degree in applied mechanics from University of Science, Hochiminh City, Vietnam in 2003 and his European master's

degree in mechanics of constructions (EMMC) from University of Liege, Belgium in 2003. He received his PhD from National University of Singapore (NUS) in 2010. He is currently a lecturer at the department of mechanics, faculty of mathematics and computer science at the University of Science, Vietnam National University, HCM, Vietnam. He has authored more than 30 international journal papers related to S-FEM. He was the recipient of a silver medal on graduation from University of Technology, Hochiminh City, Vietnam, a master scholarship from University of Liege, Belgium, a PhD scholarship from NUS, and a president graduate fellowship from NUS. His research interests include computational mechanics, finite element methods, mesh-free methods, plasticity computation, mechanics of composites and smart materials, structural optimization, numerical analysis and multiphysics computation.

1

Introduction

In building an advanced engineering system or a product, engineers must undertake a very sophisticated process of modeling, simulation, designing, testing, and construction or fabrication. In such a process, a computer is routinely used as one of the most important tools. This book deals with topics related mainly to modeling and simulation, with a focus on numerical and computational methods. These topics play an increasingly important role in building advanced engineering systems in rapid and cost-effective ways, because modeling and simulation can be performed in a virtual environment on computers without physically building the system. Many computational methods and numerical techniques, such as the finite element method (FEM) [1–3], can be employed to deal with these topics. This book mainly focuses on the development of so-called smoothed finite element methods (S-FEM) that were proposed in the past few years, based on FEM and some mesh-free techniques.

This chapter first addresses *overall* issues related to numerical modeling and simulation and some important common terminologies used in the book. It then discusses major differences in key numerical techniques between S-FEM and the well-known and widely used FEM.

1.1 Physical Problems in Engineering

In reality, there are a large number of different physical phenomena in any practical engineering system. However, we can only deal with some of the major phenomena that significantly affect the performance of the system. These phenomena often need to be modeled and simulated to provide a necessary and sufficient in-depth understanding, in order to further improve or optimize the design of the system.

The physical problems covered in this book are

1. Mechanics for solids, structures, and piezoelectrics
2. Fracture mechanics
3. Heat transfer
4. Structural acoustics

The dimensions of these problems can be one dimensional (1D), two dimensional (2D), and three dimensional (3D), and the types of problems can be linear elastic, material nonlinear, geometric nonlinear, static, and dynamic (vibration and wave propagation).

Classical mathematical models have already been established for these problems, and governing equations in differential or partial differential equations (PDEs) have also been derived. Our focus will be mainly on the numerical modeling and simulation of these problems by solving these PDEs. These *differential forms* of PDEs are termed as *strong-form* governing equations that need to be satisfied, in theory, at any *point* inside the problem domain. These PDEs must have a proper set of boundary and initial conditions to complete the setting of a physically meaningful problem. For our numerical model to be meaningful, we naturally require the setting of the original physical problem to be *well-posed*.

Remark 1.1 Well-Posed Problems

The original mechanics problem setting (PDEs with boundary and initial conditions) must be *well-posed* in the *Hadamard* sense, by which we mean that there *exists* a *unique* solution that depends *continuously* on the data.

If the problem is not well-posed, there is nothing much a numerical method can do, except produce numerical numbers that are not certifiable or interpretable, or the numerical process simply breaks down, regardless of how good the method is. Note that some of the *ill-posed problems* in engineering are treatable using special techniques such as regularization (resetting, reformulating, adding in new information/assumptions, etc.), but it is beyond the scope of this book. Interested readers are referred to books dealing with ill-posed problems or inverse problems [4]. This book deals with only numerical or computational methods for solutions to well-posed problems. The currently well-established and often-used numerical tools include FEM [1–3], the finite difference method (FDM) [5], the finite volume method (FVM) [6], and recently various mesh-free methods [7–58]. The S-FEM discussed in this book represent a very powerful tool developed quite recently based on standard FEM settings, by incorporating some of the mesh-free techniques to modify or construct the strain field, so as to achieve more accurate solutions and solutions with special attractive properties that are useful in the analysis and hence the design of the system. S-FEM are thus methods in between the FEM and the mesh-free methods.

1.2 Numerical Techniques: Practical Solution Tools

In this section, we provide an overview of the numerical/computational methods/techniques for solutions to practical engineering problems. The

discussion is not meant to be rigorous, but to provide an overall picture of this quite complicated topic.

There are largely two categories of numerical methods for solving PDEs: the *direct* approach and the *indirect* approach. The direct approach, known as the *strong-form* method [such as the well-known FDM, collocation method (with regularization) [7,36,37], smoothed particle hydrodynamics (SPH) [59–63], and the gradient smoothing method (GSM) [53–56]], discretizes and solves the PDEs directly. The indirect approach, known as the *weak-form* method (such as FEM), first establishes an *alternative* weak-form equation that governs the same physical phenomena and then solves it. The typical and most widely used weak form is the Galerkin weak form. Weak-form equations are usually in an *integral form*, implying that they need to be satisfied only in an integral (averaged) sense: a weak requirement. Properly formulated weak-form methods are more general, and offer more efficient approximate solutions that are *stable* and *convergent* to the exact solution. Therefore, these methods are usually more accurate, reliable, robust, efficient, and of more practical importance. The FEM is such a typical Galerkin weak-form method.

Remark 1.2 On Stability

We just mentioned "stable solution," which requires some elaboration or clarification. The word "stable" is used very frequently in the literature on numerical and computational methods, and it is to a certain extent quite "abused." Rigorously, a numerical solution that is "stable" implies that for any admissible input data (forces, excitations, etc.), the solution (in a norm or a proper measure) can always be bounded by the input data (in a norm or a proper measure) for a physical problem. It relates essentially the uniqueness part of the well-posedness of a problem (Remark 1.1). A method that always produces such stable (accuracy aside) solutions is said to be a stable method. This rigorous definition essentially reflects two important aspects in producing a stable solution: the property of the numerical method and the property of input data. In other words, when we say a method is stable, we need to specify to what kind of input data. For some types of input data, we can formulate many stable numerical methods, but for some types of input data, one will never be able to find any stable numerical method in a specified norm measure. In this book, we *generally* consider only (unless otherwise specified) "real-life" inputs, meaning that we consider input data that are at least *square integrable* (in $\mathbb{L}^2$ space; see Chapter 3 for a more detailed definition). We do not usually consider mathematically idealized forces like "point force," which is not square integrable and never exists in reality. Under this general condition on input data, our definition of "stable" used in this book concerns only numerical methods or procedures. Essentially, it relates directly to the minimum eigenvalue of the numerical model, as will be frequently analyzed in the following chapters.

Remark 1.3 On Spatial Stability and Temporal Stability

There are two types of stability: *spatial* and *temporal*. The former refers to a numerical method for solving static problems, and the latter refers to a numerical method for solving dynamic problems. The spatial stability of a method involves only the formulation of the method based on finite spatial discretization of the model. When a method produces stable solutions for static problems, the method is said to be spatially stable. A temporally stable method produces stable solutions for dynamic problems, and hence involves proper formulations based on both spatial and temporal discretizations. When an unstable time-integration scheme is used to deal with the time variable, a spatially stable method will surely produce unstable solutions. However, even when a stable time-integration scheme is used, a spatially stable method is *not necessarily* stable when solving dynamic problems. In this book, we assume that the time-integration scheme used for dynamic problems is always stable (or can be made stable). Hence, temporal instability refers to methods that are unstable when a stable time-integration scheme is used. Essentially, temporal instability is observed as spurious unphysical modes (in free vibration) or oscillations (in transient vibration) in the solution to a dynamic problem. A temporally stable method should produce (1) *only* "legal" zero-energy modes that correspond to rigid body movements of the solid or structure and (2) all the nonzero energy modes must correspond to physical deformation of the system.

Remark 1.4 On Convergence

"Convergence" is in fact a rather involved terminology. The original meaning of convergence refers to the numerical solution of a discretized model as it approaches a *certain* value, when the discretization is properly refined to the *limit*. However, the "certain" value may or may not be the *exact* solution of the original physical problem. If a convergent solution is not to the exact solution, the meaningfulness of the solution and the usefulness of the numerical method can be in question, and hence special care may be required. Therefore, in this book, when we say a solution is convergent, we mean *by default* that it is convergent to the exact solution, unless otherwise specified. A numerical method is said to be convergent when it produces solutions that converge to the exact solution, as long as the numerical procedure is properly executed.

The notion of weakened weak (W^2) forms [28–30] has also been proposed based on the so-called $\mathbb{G}$ space theory [29–31]. The W^2 forms are very powerful and can also be written in the *form* of Galerkin for effective formulations of a wide class of computational methods based on finite element and mesh-free settings. It is much more general than the weak formulation, and the S-FEM models are a special case of the W^2 formulation. We will

not discuss $\mathbb{G}$ space theory and W^2 formulation in detail in this book. Instead, we will try to formulate our S-FEM models in the more familiar framework of standard weak formulations. Interested readers may refer to Refs. [28–31] for more details on $\mathbb{G}$ space theory and W^2 formulation.

In formulating the standard FEM model, we need three major steps: (1) construction of the shape function; (2) evaluation of the strain field; and (3) invoking a weak-form equation to create a discrete algebraic system of equations that can be solved routinely.

In formulating the S-FEM models, however, we need one additional step after the second step:

1. Construction of the shape function (for creating the displacement field or functions)
2. Evaluation of the strain field using the strain–displacement relation
3. Evaluation of the smoothed strain field
4. Invoking a weak-form equation (using the smoothed strain field) to create a discrete algebraic system of equations that can be solved routinely

1.3 Why S-FEM?

Once the displacement is properly assumed, the strain field is already available using simply the strain–displacement relation, known as the *compatible* strain field. A stable and convergent numerical method like FEM can be routinely formulated using the standard Galerkin formulation. Why do we want to modify or construct the strain field? The reasons are given below.

1.3.1 Overly Stiff Issues

In standard FEM settings, because the assumed displacement field is compatible over the entire problem domain, and the strain field is obtained using precisely the strain–displacement relation, the standard FEM model is said to be *fully compatible*. Such a fully compatible FEM model is *variationally consistent* and works well for many practical problems. However, there are three major issues associated with this type of fully compatible Galerkin formulation. The first issue is the well-known "overly stiff" phenomenon, leading to the so-called locking behavior for many problems. This overly stiff phenomenon can be observed for all standard finite elements, and is particularly critical for linear triangular elements. The S-FEM models can well resolve this issue, and can always produce models that are softer than FEM and even softer than the exact model.

1.3.2 Stress Accuracy Issues

The second issue with the standard FEM model is inaccuracy in stress solutions, especially when linear triangular and tetrahedral meshes are used. This issue is somewhat related to the overly stiff issue of the FEM model, but in fact has more to do with the element-based strain evaluation using the assumed piecewise continuous displacement field. Such a strain field becomes discontinuous on all the element interfaces. In the process of evaluating the stiffness of the system, such discontinuity is left untreated, leading to poor solutions in the stress field. The S-FEM models can offer ways of treating these discontinuities in the stage of formulation, and hence can improve both the displacement and the stress solution significantly. The ES-FEM model is a typical such model (see Chapter 7).

1.3.3 Mesh Distortion Issues

The third issue is the significant accuracy loss when the element mesh is heavily distorted, and hence the standard FEM strongly requires mesh quality. This issue is related to the mapping technique used in isoparametric elements where a so-called *Jacobian matrix* needs to be evaluated. When the shapes of the elements are distorted, the Jacobian matrix becomes badly conditioned, leading to deterioration in solution accuracy. Many of the S-FEM models can naturally overcome this problem, because no mapping is required in the formulation of all these models for all types of elements, and hence will have much less issues related to mesh distortion. Some of the S-FEM models, such as NS-FEM (Chapter 6), can work well for extremely distorted meshes.

1.3.4 Meshing Issues

It is well known that the standard FEM model requires quadrilateral elements (for 2D) and hexahedral elements (for 3D) and with good quality. Particularly, it does not like triangular and tetrahedral elements and often gives solutions of very poor accuracy, especially for stresses. We engineers, on the other hand, often prefer using triangular and tetrahedral meshes as they can be created much more easily, and even automatically, for complicated geometries. The saving on manpower in meshing using triangular and tetrahedral meshes is tremendous compared to any other type of element. In addition, when conducting adaptive analysis, automatic remeshing is required. Currently, only triangular and tetrahedral meshes can be remeshed automatically. It is widely believed that in future, we have no choice but to live with mainly triangular and tetrahedral meshes. Fortunately, it has already been found that some S-FEM models, such as the ES-FEM model (for 2D) and the FS-FEM model (for 3D), work

perfectly well with triangular and tetrahedral meshes, respectively. These models often produce solutions much better than the standard FEM using the same mesh and can even produce solutions better than the FEM using quadrilateral and hexahedral elements.

Note also that several efforts have been made to resolve the overly stiff phenomenon, especially in the area of hybrid or mixed FEM formulations based on three- or two-field principles. This book will not discuss those techniques. However, they can be very useful, and hence interested readers may refer to the related literature. To the authors, it is clear that more effective means, such as more innovative uses of the variational principles, out-of-the-box approaches beyond the standard variational principles, or work beyond the elements (bringing information from neighboring elements such as in the S-FEM models), are necessary.

1.3.5 Solution Certificate

The solution from a numerical method such as FEM contains modeling and numerical errors. Finding an approximate solution using the above-mentioned FEM procedure is important, but not sufficient, for advanced applications, and it becomes more and more important to obtain information about the quality of the solution. This not only makes the numerical result more applicable to practical engineering problems with certain confidence, but also guides us on how to further improve the solutions. However, the standard FEM can only give the lower bound solution, and therefore the solution error to the exact solution is unknown. Some of the S-FEM models such as NS-FEM, on the other hand, can produce upper bounds, providing a crucial *closure* for numerical solution bounds.

1.3.6 Computational Efficiency

We note that some of the issues mentioned above can be resolved using mesh-free methods [8]. However, it is well known that the mesh-free method is usually more expensive. It can be as much as 10 times slower than FEM (measured in displacement norm). Some of the recent mesh-free methods are even more efficient than the linear FEM model. For example, one of the most efficient mesh-free methods, ES-PIM-T6/3 [27], was found to be about two times faster (measured in displacement norm) than the linear FEM model using the same set of nodes [8]. However, there is still a lot of room for further improvement. It is clear to the authors that models that combine the FEM model with proper mesh-free techniques can be advantageous in terms of both simplicity and computational efficiency. The S-FEM models are such typical models, and can be viewed as one

of the most simplified mesh-free methods with the help of an element mesh.

1.3.7 Lower-Order Elements: A Preferred Choice

In solving practical engineering problems, we observed that lower-order elements (linear and bilinear) are most often used. There are a number of reasons for this. First, lower-order elements are simple and easy to use (for most analysts and engineers) in order to model problems with complicated geometries. Second, lower-order elements can be applied to a much wider range of engineering problems, because they require lower *regularity* of the solution. Third, it is easier to use lower-order elements for meshing and remeshing, which are needed in adaptive analyses. It is also very convenient to design contact algorithms for lower-order elements for nonlinear contact analysis. Moreover, it is easier to develop coupling procedures for lower elements for fluid–structural interaction problems. It is the authors' opinion that lower-order elements will always be the mainstream of elements used in solving practical complicated engineering problems. Therefore, several efforts have been made to make lower-order elements work effectively. S-FEM models are particularly good for lower-order elements. In fact, in this entire book, we use only lower-order elements for S-FEM models, although theoretically S-FEM models also work for higher-order elements. For special purposes, such as singularity near the crack tip, we can use proper local enrichments that can be done quite easily in S-FEM settings [64–66].

1.4 The Idea of S-FEM

The essential idea in S-FEM is to modify the compatible strain field, or construct a strain field using only the displacements, hoping that a Galerkin model using the modified/constructed strain field can deliver some good properties. Such a modification/construction can be performed within elements but more often *beyond* elements, bringing information from neighboring elements. Naturally, the strain field has to satisfy certain conditions, and the standard Galerkin weak form needs to be modified accordingly to ensure stability and convergence. In the formulation of S-FEM models in this book, we stick to the use of weak forms of "Galerkin type" to preserve the *symmetry* of the system and hence the efficiency of the model. Chapters 3 and 4 will discuss in great detail the standard Galerkin weak form and the smoothed Galerkin weak form, respectively.

Note that in many mesh-free settings, strain modification and construction are essential and the formulations are much more diversified. Interested readers are referred to Ref. [8] for more details.

1.5 Key Techniques Used in S-FEM

The major techniques used in S-FEM models may be summarized as follows:

1. Domain discretization using elements
2. The strain (gradient) smoothing technique
3. The smoothed Galerkin weak form
4. The point interpolation method (PIM)
5. Types of smoothing domains

It is clear that each of these technical ingredients is well known or seems to be quite plain. The combination of these seemingly plain techniques gives excellent properties to S-FEM models. It seems that the best parts of these technical ingredients are being put together so as to obtain models with desired properties. Domain discretization using elements has been practiced in FEM for more than half a century, and is still being practiced in all FEM modeling. Strain or gradient smoothing techniques have been used by many researchers as early as in the 1970s (see Chapter 4). The smoothed Galerkin weak form is an extension of the standard Galerkin weak form used in FEM, and can be derived from the standard variational principle. Understanding its stability conditions [29] opens a wide window for its use in various S-FEM models. The interpolation technique is probably one of the earliest numerical techniques, which has been widely used based on elements and, more generally, on mesh-free nodes [8]. It finds a very special place now in all S-FEM models for the formulation of general n-sided elements where we use "linear PIM" (Chapter 4), crack-tip elements (Chapter 10) where we use "enriched linear PIM" for simulating a singular stress field, and so on. The idea of using various types of smoothing domains has been recently used in meshfree techniques such as the PIM family [8]. This book extends this idea to FEM settings. It is, in fact, the single most important factor to determine the properties of an S-FEM model.

1.6 S-FEM Models and Properties

The S-FEM models developed so far are summarized in Table 1.1, together with their properties. It may be difficult to comprehend the contents of Table 1.1, but it can be a good reference when reading the later chapters.

TABLE 1.1

Versions of S-FEM Models and Properties

Abbreviation	Full Name	Formulation	Features/Properties
CS-FEM (2D) CS-FEM (3D)[a] (Chapters 4 and 5)	Cell-based smoothed finite element method using quadrilateral elements	Smoothed Galerkin Linear or enriched PIM[a] Quadrilateral cell-based smoothing domains	Linearly conforming Good accuracy Softer than FEM Superconvergence Conditionally stable
*n*CS-FEM (2D) *n*CS-FEM (3D)[a] (Chapters 4 and 5)	Cell-based smoothed finite element method using *n*-sided polygonal elements	Smoothed Galerkin Linear or enriched PIM[a] Triangular cell-based smoothing domains	Linearly conforming Good accuracy Superconvergence Spatially and temporally stable
NS-FEM (2D and 3D) (Chapters 4, 5, 10, and 14)	Node-based smoothed finite element method using *n*-sided polygonal elements (including T3 and T4)	Smoothed Galerkin Linear or enriched PIM Smoothing operation based on nodes	Linearly conforming Volumetric locking free Upper bound Strong superconvergence in energy norm Spatially stable, temporally instable
ES-FEM (2D) FS-FEM (3D) (Chapters 4, 7, 8, 10–15)	Edge-based (face-based) smoothed finite element method using *n*-sided polygonal elements (including T3 and T4)	Smoothed Galerkin Linear or enriched PIM Smoothing operation based on the edges (faces) of cells	Linearly conforming Ultra-accuracy Very efficient Strong superconvergence in displacement/energy norm Spatially and temporally stable
αFEM (2D) αFEM (3D) (Chapters 4 and 9)	Alpha finite element method using T3 and T4 elements	Smoothed and standard Galerkin Linear or enriched PIM[a] Smoothing operation based on the node and cells	Linearly conforming Nearly “exact” solution Strong superconvergence in displacement/energy norm Upper and lower bounds Spatially and temporally stable

[a] Yet to be developed.

1.7 Some Historical Notes

The first and typical S-FEM model is the cell-based smoothed FEM (CS-FEM, or originally called S-FEM) [67] formulated for general n-sided polygonal elements. Although the assumed displacement functions can still be viewed living in an $\mathbb{H}^1$ space, the expression for the compatible strain field is not generally available (it is also not necessary). The strain smoothing operation was used to construct the *smoothed strain* field. CS-FEM works very effectively for solid mechanics problems, including dynamic problems [68,69]. It can produce much more accurate stress solutions and solutions with attractive properties [67]. Because smoothed strains are obtained via line integrations along the smoothing domain boundary, and the derivatives of shape functions are not used in the formulation, a simple linear PIM can be applied to obtain the shape function values needed in the formulation; hence n-sided polygonal elements and a very heavily distorted mesh can be used [70]. Detailed theoretical aspects, including stability and convergence about CS-FEM, can be found in Ref. [69]. Since CS-FEM uses the smoothed Galerkin weak form, the assumed displacement functions can be viewed in an $\mathbb{H}^1$ space, and the smoothed strain field is orthogonal to the compatible strain field, CS-FEM models are variationally consistent.

The second S-FEM model is the node-based smoothed finite element method (NS-FEM) [71]. NS-FEM uses an FEM mesh that is further divided into a set of smoothing domains based on nodes. The element mesh and the smoothing domains are overlaid on each other. The modified strain field is constructed by using smoothing strain over the node-based smoothing domains, and linear PIM is used for constructing displacement function values (only on the boundary of the smoothing domain). NS-FEM can have different shapes of elements, including n-sided polygonal elements, using also linear PIM for computing the shape function values. Linear PIM was later enriched with proper terms for creating a singular stress field for fracture problems (see Chapter 10). It has the properties of upper bound, weak superconvergence, is insensitive to mesh distortion, and is overly soft. The overly soft behavior leads to spurious modes at higher energy levels for dynamic problems, and hence techniques are required for temporal stabilization. Note that when linear triangular and tetrahedral elements are used, NS-FEM produces the same results as the method of node-based uniform strain elements [72].

The third S-FEM model is the edge-based smoothed finite element method (ES-FEM) [73] for 2D and the face-based smoothed finite element method (FS-FEM) [74] for 3D. ES-FEM and FS-FEM are similar to NS-FEM, which uses an FEM mesh, and linear PIM for displacement function construction. Linear PIM can be enriched with proper terms for creating a

singular stress field for fracture problems (see Chapter 10). The difference is in the division of smoothing domains: based on edges (ES-FEM) or faces (FS-FEM) of the element mesh. The ES-FEM and FS-FEM models are weakly stiff and quite "close-to-exact," and hence have properties of strong superconvergence and ultra-accuracy. No spurious modes are found in ES-FEM and FS-FEM; hence they work very well for both static and dynamic problems.

Note that NS-FEM and ES-FEM/FS-FEM using linear elements are more like a mesh-free method, because their formulations are very different from FEM. The only thing that is in common is that the displacement functions used are still in an $\mathbb{H}^1$ space. The theory, interpolation procedure, integration, solution property, and the use of mesh depart quite a lot from the standard FEM procedure. They are in fact special cases of NS-PIMs [23,42] and ES-PIMs [27] based on the generalized smoothed Galerkin (GS-Galerkin) weak form [28,29].

An αFEM using triangular and tetrahedral elements for exact solutions to mechanics problems has also been proposed using a partially constructed strain field [75]. αFEM is essentially a combination of FEM and NS-FEM with an adjustable parameter α that can be tuned for solutions with desired properties. It was shown that the results of αFEM are much more accurate than those of FEM-T3 and even more accurate than those of FEM-Q4 when the same sets of nodes are used. αFEM can produce both lower and upper bounds to the exact solution in the energy norm for elasticity problems by properly choosing α. In addition, a preferable α approach has been devised for αFEM to produce nearly exact and superconvergent solutions for both displacement and energy norms. Furthermore, αFEM can make volumetric locking free. Intensive numerical studies have been conducted to confirm the theory and properties of αFEM. By further following this line of development, a superconvergent alpha finite element method (SαFEM) using triangular meshes was also proposed [76].

1.8 Outline of the Book

This book provides an introduction to S-FEM methods and their applications to solid mechanics, fracture mechanics, plates, piezoelectrics, heat transfer, and acoustics problems. Most of what is described in the book is the result of intensive research by G. R. Liu and his research team in the past decade. The works of other researchers are also introduced. The significance of this book is given below:

1. It is the only book available in the market that systematically describes newly developed S-FEM models that combine FEM and mesh-free techniques.

2. It presents techniques for *certified solutions* with both lower and upper bounds to elasticity problems of arbitrary complicated geometry, as long as a triangular or tetrahedral mesh can be built.
3. It presents techniques that produce superconvergent and nearly exact solutions in both displacement and energy error measures.
4. It covers all the basic theories, principles, formulations, techniques, and procedures of S-FEM models, including those for FEM that can be viewed as a special case of S-FEM.
5. A large number of examples for a wide range of engineering problems are provided with very thorough examinations using figures and tables: engineers will find the methods very reliable and easy to apply in their practical problems.

Current important general issues related to future computational methods are addressed. This can be beneficial to researchers, engineers, and students who are venturing into the development of novel computational methods. The book is written for senior (second year and above) university students, graduate students, researchers, and professionals in engineering and science. A knowledge of FEM is not required. Mechanical engineers, structural engineers, and practitioners will also find the book useful. The chapter-by-chapter description of the book is given below:

Chapter 1: Addresses the background, overall idea, essential techniques, general procedures, common preliminary issues, and terminologies.

Chapter 2: Provides the basic equations for the solid mechanics problem that is the default problem of this book. These equations will be used repetitively many times in the book.

Chapter 3: Presents an *abstracted* version of the widely used FEM in its standard form, with a discussion on important basic theorems and properties.

Chapter 4: Presents the overall modeling procedure, fundamental theories ensuring stability and convergence, error assessment matters, and necessary building blocks needed to construct useful S-FEM models.

Chapter 5: Introduces the *first* and closest S-FEM model to the FEM model: CS-FEM. Common techniques, such as shape function construction and selective formulation for handling volumetric locking, and so on, used in an S-FEM model, are covered in this chapter.

Chapter 6: The formulation of NS-FEM given in this chapter is presented for both 2D and 3D problems with emphasis on the *upper bound* solution, volumetric locking free property, and the superconvergent property in energy norm. In addition, an adaptive

analysis procedure using triangular elements is presented, with an automatic mesh refinement strategy and an error indicator based on the *computable* recovery strains.

Chapter 7: Introduces a very outstanding S-FEM model: ES-FEM, which is stable both spatially and temporally. ES-FEM is known as a "star" performer and is the best linear model found so far in terms of solution accuracy, stability, efficiency, and adaptation to complicated geometry. Static, dynamic, and nonlinear problems are dealt with in this chapter.

Chapter 8: Introduces FS-FEM, which is the 3D version of ES-FEM. It works very well with tetrahedron elements and is hence effective for 3D problems with complicated geometry. Both linear and nonlinear problems are examined.

Chapter 9: Presents a novel αFEM that uses a combined formulation of FEM and NS-FEM. This combined formulation makes the best use of the upper bound property of the NS-FEM and the lower bound property of the standard FEM. It is equipped with an α and is capable of producing a nearly exact solution in strain energy for any given linear elasticity problem that can be 2D or 3D.

Chapter 10: Extends the application of these S-FEM models for a particular class of problems: fracture mechanics. The emphasis is on the creation of the singular strain field near the crack tip, by the development of novel crack tip elements for S-FEM models using *enriched* PIM. The singular NS-FEM is capable of producing an upper bound solution and the singular ES-FEM is found to be ultra-accurate for fracture problems. They all use basic meshes of three-node triangular elements.

Chapter 11: Extends the ES-FEM and FS-FEM models to solve nonlinear mechanics problems of solids with viscoelastoplastic materials, for both 2D and 3D problems.

Chapter 12: Extends ES-FEM to static, free vibration and buckling analyses of plates, capitalizing these excellent features of ES-FEM found from the previous chapters. Our ES-FEM formulation is based on Reissner–Mindlin plates and is incorporated with the discrete shear gap (DSG) method. The ES-FEM-DSG3 method is free of shear locking and works well for both thin and thick plates.

Chapter 13: Applies the S-FEM formulation to solids of piezoelectric materials that are used for various "smart" devices.

Chapter 14: Applies the S-FEM formulation to heat transfer problems for solutions of special properties: upper bound and excellent accuracy.

Chapter 15: Applies the S-FEM formulation to acoustics problems. The emphasis is on the unique ability of ES-FEM to suppress the so-called *dispersion error* in wave propagation problems.

References

1. Zienkiewicz OC and Taylor RL. 2000. *The Finite Element Method*, 5th edition. Butterworth Heinemann, Oxford.
2. Hughes TJR. 1987. *The Finite Element Method: Linear Static and Dynamic Finite Element Analysis*. Prentice-Hall, Englewood Cliffs, NJ.
3. Liu GR and Quek SS. 2002. *The Finite Element Method: A Practical Course*. Butterworth Heinemann, Oxford.
4. Liu GR and Han X. 2003. *Computational Inverse Techniques in Nondestructive Evaluation*. CRC Press, Boca Raton, FL.
5. Kleiber M and Borkowski A. 1998. *Handbook of Computational Solid Mechanics*. Springer, Berlin.
6. LeVeque RJ. 2002. *Finite Volume Methods for Hyperbolic Problems*. Cambridge University Press, New York.
7. Liu GR and Gu YT. 2005. *An Introduction to Meshfree Method Methods and Their Programming*. Springer, Berlin.
8. Liu GR. 2009. *Meshfree Methods: Moving Beyond the Finite Element Method*, 2nd edition. Taylor & Francis/CRC Press, Boca Raton, FL.
9. Belytschko T, Krongauz Y, Organ D, Fleming M, and Krysl P. 1996. Meshless method: An overview and recent developments. *Computer Method in Applied Mechanics and Engineering*; 139: 3–47.
10. Atluri SN and Zhu T. 1998. A new meshless local Petrov–Galerkin (MLPG) approach in computational mechanics. *Computational Mechanics*; 22: 117–127.
11. Liu WK, Jun S, and Zhang YF. 1995. Reproducing kernel particle methods. *International Journal for Numerical Methods in Engineering*; 20: 1081–1106.
12. Belytschko T, Lu YY, and Gu L. 1994. Element-free Galerkin methods. *International Journal for Numerical Methods in Engineering*; 37: 229–256.
13. Liu WK and Chen Y. 1995. Wavelet and multiple scale reproducing kernel methods. *International Journal for Numerical Methods in Fluids*; 21: 901–931.
14. Liu WK, Adee J, and Jun S. 1993. Reproducing kernel and wavelet particle methods for elastic and plastic problems. In *Advanced Computational Methods for Material Modeling*, DJ Benson, Ed. 180/PVP 268 ASME, pp. 175–190.
15. Chen JS, Wu CT, Yoon S, and You Y. 2001. A stabilized conforming nodal integration for Galerkin meshfree method. *International Journal for Numerical Methods in Engineering*; 50: 435–466.
16. Armando DC and Oden JT. 1995. Hp clouds—a meshless method to solve boundary value problems. TICAM Report 95-05, University of Texas, Austin.
17. Babuska I and Melenk JM. 1995. The partition of unity finite element method. Technical report technical note BN-1185, Institute for Physical Science and Technology, University of Maryland.
18. Onate E, Idelsohn S, Zienkiewicz OC, and Taylor RL. 1996. A finite point method in computational mechanics applications to convective transport and fluid flow. *International Journal for Numerical Methods in Engineering*; 39: 3839–3866.
19. Liszka T and Orkisz J. 1980. The finite difference method at arbitrary irregular grids and its application in applied mechanics. *Computers and Structures*; 11: 83–95.

20. Jensen PS. 1980. Finite difference techniques for variable grids. *Computers and Structures*; 2: 17–29.
21. Liu GR and Gu YT. 1999. A point interpolation method. In *Proc. 4th Asia-Pacific Conference on Computational Mechanics*, December, Singapore, pp. 1009–1014.
22. Liu GR and Gu YT. 2001. A point interpolation method for two-dimensional solids. *International Journal for Numerical Methods in Engineering*; 50: 937–951.
23. Liu GR, Zhang GY, Dai KY, Wang YY, Zhong ZH, Li GY, and Han X. 2005. A linearly conforming point interpolation method (LC-PIM) for 2D solid mechanics problems. *International Journal of Computational Methods*; 2(4): 645–665.
24. Liu GR and Zhang GY. 2008. Upper bound solution to elasticity problems: A unique property of the linearly conforming point interpolation method (LC-PIM). *International Journal for Numerical Methods in Engineering*; 74: 1128–1161.
25. Li Y, Liu GR, Luan MT, Dai KY, Zhong ZH, Li GY, and Han X. 2007. Contact analysis for solids based on linearly conforming radial point interpolation method. *Computational Mechanics*; 39: 537–554.
26. Zhang GY, Liu GR, Nguyen-Thoi T, Song CX, Han X, Zhong ZH, and Li GY. 2007. The upper bound property for solid mechanics of the linearly conforming radial point interpolation method (LC-RPIM). *International Journal of Computational Methods*; 4(3): 521–541.
27. Liu GR and Zhang GY. 2008. Edge-based smoothed point interpolation methods. *International Journal of Computational Methods*; 5(4): 621–646.
28. Liu GR. 2009. A G space theory and weakened weak (W^2) form for a unified formulation of compatible and incompatible methods, Part I: Theory and Part II: Applications to solid mechanics problems. *International Journal for Numerical Methods in Engineering*; doi: 10.1002/nme.2719 and doi: 10.1002/nme.2720.
29. Liu GR. 2008. A generalized gradient smoothing technique and the smoothed bilinear form for Galerkin formulation of a wide class of computational methods. *International Journal of Computational Methods*; 5(2): 199–236.
30. Liu GR and Zhang GY. 2009. A normed G space and weakened weak (W^2) formulation of a cell-based Smoothed Point Interpolation Method. *International Journal of Computational Methods*; 6(1): 147–179.
31. Liu GR. 2009. On the G space theory. *International Journal of Computational Methods*; 6(2): 257–289.
32. Liu GR, Xu X, Zhang GR, and Gu YT. 2009. A point interpolation method with continuous strain field and superconvergence (PIM-CS) based on triangular mesh. *Computational Mechanics*; 43: 651–673.
33. Liu GR, Xu X, Zhang GR, and Nguyen-Thoi T. 2009. A superconvergence point interpolation method (SC-PIM) with piecewise linear strain field using triangular mesh. *International Journal for Numerical Methods in Engineering*; 77: 1439–1467.
34. Xu X, Liu GR, and Zhang GY. 2009. A point interpolation method with least square strain field (PIM-LSS) for solution bounds and ultra-accurate solutions using triangular mesh. *Computer Methods in Applied Mechanics and Engineering*; 198: 1486–1499.
35. Liu GR and Zhang GY. 2009. A strain-constructed point interpolation method (SC-PIM) and strain field construction schemes for mechanics problems of

solids and structures using triangular mesh. *International Journal for Numerical Methods in Engineering*; 1(1): 233–258.
36. Liu GR and Kee BBT. 2006. A stabilized least-squares radial point collocation method (LS-RPCM) for adaptive analysis. *Computer Method in Applied Mechanics and Engineering*; 195: 4843–4861.
37. Kee BBT, Liu GR, and Lu C. 2007. A regularized least-squares radial point collocation method (RLS-RPCM) for adaptive analysis. *Computational Mechanics*; 40: 837–853.
38. Liu GR. 2002. A point assembly method for stress analysis for two-dimensional solids. *International Journal of Solids and Structures*; 39: 261–276.
39. Liu GR, Zhang J, Li H, Lam KY, and Kee BBT. 2006. Radial point interpolation based finite difference method for mechanics problems. *International Journal for Numerical Methods in Engineering*; 68: 728–754.
40. Liu GR and Gu YT. 2001. A local point interpolation method for stress analysis of two-dimensional solids. *Structural Engineering and Mechanics*; 11(2): 221–236.
41. Liu GR and Gu YT. 2001. A local radial point interpolation method (LR-PIM) for free vibration analyses of 2-D solids. *Journal of Sound and Vibration*; 246(1): 29–46.
42. Liu GR, Li Y, Dai KY, Luan MT, and Xue W. 2006. A linearly conforming radial point interpolation method for solid mechanics problems. *International Journal of Computational Methods*; 3: 401–428.
43. Li Y, Liu GR, Luan MT, Dai KY, Zhong ZH, Li GY, and Han X. 2007. Contact analysis for solids based on linearly conforming radial point interpolation method. *Computational Mechanics*; 39: 537–554.
44. Zhang GY, Liu GR, Nguyen-Thoi T, Song CX, Han X, Zhong ZH, and Li GY. 2007. The upper bound property for solid mechanics of the linearly conforming radial point interpolation method (LC-RPIM). *International Journal of Computational Methods*; 4(3): 521–541.
45. Liu GR and Gu YT. 2000. Coupling of element free Galerkin method with boundary point interpolation method. In *Advances in Computational Engineering and Science*, SN Atluri, FW Brust, Eds. ICES'2K, Los Angeles, pp. 1427–1432.
46. Liu GR and Gu YT. 2000. Coupling of element free Galerkin and hybrid boundary element methods using modified variational formulation. *Computational Mechanics*; 26(2): 166–173.
47. Gu YT and Liu GR. 2001. A coupled element free Galerkin/boundary element method for stress analysis of two-dimensional solids. *Computer Methods in Applied Mechanics and Engineering*; 190: 4405–4419.
48. Gu YT and Liu GR. 2003. Hybrid boundary point interpolation methods and their coupling with the element free Galerkin method. *Engineering Analysis with Boundary Elements*; 27(9): 905–917.
49. Gu YT and Liu GR. 2002. A boundary point interpolation method for stress analysis of solids. *Computational Mechanics*; 28: 47–54.
50. Liu GR and Gu YT. 2004. Boundary meshfree methods based on the boundary point interpolation methods. *Engineering Analysis with Boundary Elements*; 28(5): 475–487.

51. Gu YT and Liu GR. 2003. A boundary radial point interpolation method (BRPIM) for 2-D structural analyses. *Structural Engineering and Mechanics*; 15(5): 535–550.
52. Gu YT and Liu GR. 2001. A boundary point interpolation method (BPIM) using radial function basis. In First MIT Conference on Computational Fluid and Solid Mechanics, MIT, pp. 1590–1592.
53. Liu GR and Xu XG. 2008. A gradient smoothing method (GSM) for fluid dynamics problems. *International Journal for Numerical Methods in Fluids*; 58: 1101–1133.
54. Xu GX, Liu GR, and Lee KH. 2009. Application of gradient smoothing method (GSM) for steady and unsteady incompressible flow problems using irregular triangles. *International Journal for Numerical Methods in Fluids*; submitted.
55. Xu GX, Liu GR, and Tani A. 2009. An adaptive gradient smoothing method (GSM) for fluid dynamics problems. *International Journal for Numerical Methods in Fluids*; 62: 499–529.
56. Liu GR, Zhang J, and Lam KY. 2008. A gradient smoothing method (GSM) with directional correction for solid mechanics problems. *Computational Mechanics*; 41: 457–472.
57. Liu GR and Gu YT. 2003. A meshfree method: Meshfree weak–strong (MWS) form method, for 2-D solids. *Computational Mechanics*; 33(1): 2–14.
58. Liu GR, Wu YL, and Ding H. 2004. Meshfree weak–strong (MWS) form method and its application to incompressible flow problems. *International Journal for Numerical Methods in Fluids*; 46: 1025–1047.
59. Lucy L. 1977. A numerical approach to testing the fission hypothesis. *The Astronomical Journal*; 82: 1013–1024.
60. Gingold RA and Monaghan JJ. 1977. Smooth particle hydrodynamics: Theory and applications to non-spherical stars. *Monthly Notices of the Royal Astronomical Society*; 181: 375–389.
61. Liu GR and Liu MB. 2003. *Smoothed Particle Hydrodynamics: A Meshfree Particle Method*. World Scientific, Hackensack, NJ.
62. Liu MB, Liu GR, and Zong Z. 2008. An overview on smoothed particle hydrodynamics. *International Journal of Computational Methods*; 5(1): 135–188.
63. Zhou CE, Liu GR, and Lou KY. 2007. Three-dimensional penetration simulation using smoothed particle hydrodynamics. *International Journal of Computational Methods*; 4(4): 671–691.
64. Liu GR, Nourbakhshnia N, and Zhang YW. 2009. A novel singular ES-FEM method for simulating singular stress fields near the crack-tips for linear fracture problems. *Engineering Fracture Mechanics*; accepted.
65. Liu GR, Nourbakhshnia N, Chen L, and Zhang YW. 2010. A novel general formation for singular stress field using the ES-FEM method for the analysis of mixed-mode cracks. *International Journal of Computational Methods*, 7(1): 191–214.
66. Liu GR, Chen L, Nguyen-Thoi T, and Zeng K. 2009. A novel singular node-based smoothed finite element method (NS-FEM) for upper bound solutions of fracture problems. *International Journal for Numerical Methods in Engineering*; accepted.
67. Liu GR, Dai KY, and Nguyen-Thoi T. 2007. A smoothed finite element method for mechanics problems. *Computational Mechanics*; 39: 859–877.

68. Dai KY and Liu GR. 2007. Free and forced vibration analysis using the smoothed finite element method (SFEM). *Journal of Sound and Vibration*; 301: 803–820.
69. Liu GR, Nguyen-Thoi T, Dai KY, and Lam KY. 2007. Theoretical aspects of the smoothed finite element method (SFEM). *International Journal for Numerical Methods in Engineering*; 71: 902–930.
70. Dai KY, Liu GR, and Nguyen-Thoi T. 2007. An *n*-sided polygonal smoothed finite element method (*n*SFEM) for solid mechanics. *Finite Elements in Analysis and Design*; 43: 847–860.
71. Liu GR, Nguyen-Thoi T, Nguyen-Xuan H, and Lam KY. 2009. A node-based smoothed finite element method (NS-FEM) for upper bound solutions to solid mechanics problems. *Computers and Structures*; 87: 14–26.
72. Dohrmann CR, Heinstein MW, Jung J, Key SW, and Witkowski WR. 2000. Node-based uniform strain elements for three-node triangular and four-node tetrahedral meshes. *International Journal for Numerical Methods in Engineering*; 47: 1549–1568.
73. Liu GR, Nguyen-Thoi T, and Lam KY. 2009. An edge-based smoothed finite element method (ES-FEM) for static, free and forced vibration analyses in solids. *Journal of Sound and Vibration*; 320: 1100–1130.
74. Nguyen-Thoi T, Liu GR, Lam KY, and Zhang GY. 2009. A face-based smoothed finite element method (FS-FEM) for 3D linear and nonlinear solid mechanics problems using 4-node tetrahedral elements. *International Journal for Numerical Methods in Engineering*; 78: 324–353.
75. Liu GR, Nguyen-Thoi T, and Lam KY. 2008. A novel alpha finite element method (αFEM) for exact solution to mechanics problems using triangular and tetrahedral elements. *Computer Methods in Applied Mechanics and Engineering*; 197: 3883–3897.
76. Liu GR, Nguyen-Xuan H, Nguyen-Thoi T, and Xu X. 2009. A novel weak form and a superconvergent alpha finite element method (SαFEM) for mechanics problems using triangular meshes. *Journal of Computational Physics*; 228: 4055–4087.

2

Basic Equations for Solid Mechanics

We now discuss a typical engineering problem: solid mechanics, which is *the default problem* studied in this book, because it is one of the most fundamental problems in all engineering systems wherever solid materials are used. The purpose of this chapter is to provide a set of basic equations for solids of linear elastic materials, which will be repeatedly used in later chapters. Our description will be abstract, sufficient for the use of later chapters and for a quick review and grasp of the major points in the formulation and setting of solid mechanics problems. For more detailed coverage on this topic, readers may refer to textbooks that are abundantly available in the open literature [1].

The *strong forms* for solid mechanics problems are the PDEs defined in the problem domain governing the equilibrium state at any point within a linear elastic solid, known as equilibrium equations. Figure 2.1 shows a general 3D solid. It is constrained on a part of the boundary and subjected to body forces distributed over the volume and surface forces on another part of the boundary. Figure 2.2 shows a 2D solid that is very thin in the z-direction. The forces are applied all within the x–y plane, and hence the stress components in the z-direction are all zero, known as the *plane stress* problem. Figure 2.3 shows a 2D solid that is very thick in the z-direction, such as a water dam with the z-axis representing the longitudinal direction. All the external forces and constraints are independent of z, resulting in zero strain components in the z-direction, known as the *plane strain* problem.

2.1 Equilibrium Equation: In Stresses

Consider, in general, a d-dimensional solid occupying a physical domain of $\Omega \in \mathbb{R}^d$ bounded by Γ. In this book, we speak of *open domain* by default, meaning that Ω does not include its boundary Γ. The static *equilibrium equation* governing the solid can be written in partial differential form in terms of stresses:

$$\frac{\partial \sigma_{ij}}{\partial x_j} + b_i = 0, \quad i, j = 1, \ldots, d \quad \text{in } \Omega, \tag{2.1}$$

where b_i is the given external body force and σ_{ij} is the (internal) stress that relates to the strains ε_{ij}.

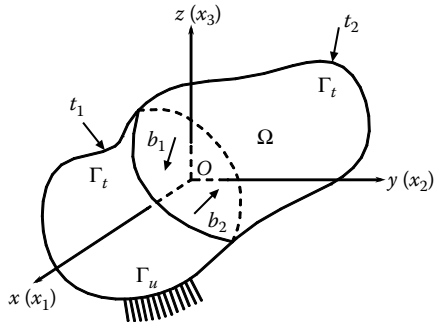

FIGURE 2.1 A constrained 3D solid subjected to external body and surface forces.

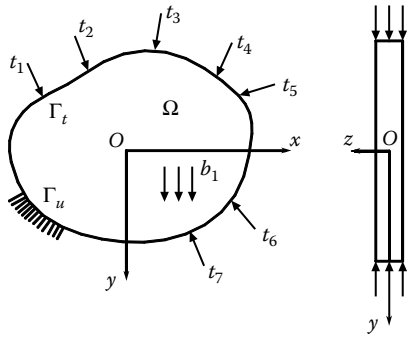

FIGURE 2.2 A 2D plane stress problem: a thin piece of flat solid subjected to only in-plane forces.

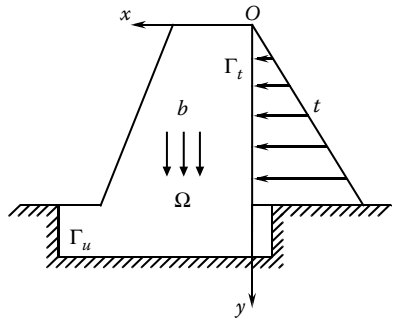

FIGURE 2.3 A typical 2D plane strain problem: cross section of a water dam.

2.2 Constitutive Equation

The stress and strains are related via the so-called *constitutive equation* or the generalized Hook's law:

$$\sigma_{ij} = C_{ijkl}\varepsilon_{kl}, \tag{2.2}$$

where C_{ijkl} is the elasticity tensor of the solid material that is symmetrical:

$$C_{ijkl} = C_{jikl} = C_{ijlk} = C_{klij}. \tag{2.3}$$

For isotropic Saint Venant Kirchhoff elastic materials, we have

$$C_{ijkl} = \lambda\delta_{ji}\delta_{kl} + \mu(\delta_{ik}\delta_{jl} + \delta_{il}\delta_{jk}), \tag{2.4}$$

where λ and μ are Lame's elastic constants.

2.3 Compatibility Equation

Under the small-displacement assumption, the strain tensor ε_{ij} relates to displacements by the so-called *compatibility equation* (also known as *kinematic equations* or strain–displacement relations):

$$\varepsilon_{ij} = \frac{1}{2}\left(\frac{\partial u_i}{\partial x_j} + \frac{\partial u_j}{\partial x_i}\right), \tag{2.5}$$

where u_i, $i = 1, \ldots, d$ is the displacement component in the x_i-direction at a point in Ω. When Equation 2.5 is satisfied, we say that the strains are *compatible* with the displacements, and such a strain field is said to be a compatible strain field.

2.4 Equilibrium Equation: In Displacements

Substituting Equations 2.2 and 2.5 into Equation 2.1, we have the equilibrium equation expressed in terms of displacements (that are small):

$$\frac{\partial}{\partial x_j}\left(C_{ijkl}\frac{\partial u_k}{\partial x_l}\right) + b_i = 0, \quad i, j = 1, \ldots, d \text{ in } \Omega. \tag{2.6}$$

The displacement $u_i, i = 1, \ldots, d$ now becomes the primary field variable. A method that solves Equation 2.6 primarily for the displacements is called a *displacement method*.

2.5 Equations in Matrix Form

For notation convenience, matrix forms of equations are often used in the book. The equilibrium equation 2.1 becomes

$$\mathbf{L}_d^T \boldsymbol{\sigma} + \mathbf{b} = \mathbf{0}, \tag{2.7}$$

where the body force vector is written as

$$\mathbf{b} = \begin{Bmatrix} b_1 \\ b_2 \end{Bmatrix} \quad \text{for 2D,} \quad \mathbf{b} = \begin{Bmatrix} b_1 \\ b_2 \\ b_3 \end{Bmatrix} \quad \text{for 3D.} \tag{2.8}$$

The matrix of differential operators $\mathbf{L}_d$ is given by

$$\mathbf{L}_d = \begin{bmatrix} \partial/\partial x_1 & 0 \\ 0 & \partial/\partial x_2 \\ \partial/\partial x_2 & \partial/\partial x_1 \end{bmatrix}_{3\times 2} \quad \text{for 2D,}$$

$$\mathbf{L}_d = \begin{bmatrix} \partial/\partial x_1 & 0 & 0 \\ 0 & \partial/\partial x_2 & 0 \\ 0 & 0 & \partial/\partial x_3 \\ 0 & \partial/\partial x_3 & \partial/\partial x_2 \\ \partial/\partial x_3 & 0 & \partial/\partial x_1 \\ \partial/\partial x_2 & \partial/\partial x_1 & 0 \end{bmatrix}_{6\times 3} \quad \text{for 3D.} \tag{2.9}$$

The compatibility equation 2.5 can also be written in matrix form as

$$\boldsymbol{\varepsilon} = \mathbf{L}_d \mathbf{u}. \tag{2.10}$$

The constitutive equation 2.2 becomes

$$\boldsymbol{\sigma} = \mathbf{c}\boldsymbol{\varepsilon}, \tag{2.11}$$

where $\boldsymbol{\sigma}$ is a vector that collects stress components in the form of

$$\boldsymbol{\sigma} = \begin{Bmatrix} \sigma_{11} \\ \sigma_{22} \\ \sigma_{12} \end{Bmatrix} \quad \text{for 2D,} \quad \boldsymbol{\sigma} = \begin{Bmatrix} \sigma_{11} \\ \sigma_{22} \\ \sigma_{33} \\ \sigma_{23} \\ \sigma_{13} \\ \sigma_{12} \end{Bmatrix} \quad \text{for 3D,} \tag{2.12}$$

and $\boldsymbol{\varepsilon}$ is a vector that collects strain components in the form of

$$\boldsymbol{\varepsilon} = \begin{Bmatrix} \varepsilon_{11} \\ \varepsilon_{22} \\ 2\varepsilon_{12} \end{Bmatrix} = \begin{Bmatrix} \varepsilon_{11} \\ \varepsilon_{22} \\ \gamma_{12} \end{Bmatrix} \quad \text{for 2D,} \quad \boldsymbol{\varepsilon} = \begin{Bmatrix} \varepsilon_{11} \\ \varepsilon_{22} \\ \varepsilon_{33} \\ 2\varepsilon_{23} \\ 2\varepsilon_{13} \\ 2\varepsilon_{12} \end{Bmatrix} = \begin{Bmatrix} \varepsilon_{11} \\ \varepsilon_{22} \\ \varepsilon_{33} \\ \gamma_{23} \\ \gamma_{13} \\ \gamma_{12} \end{Bmatrix} \quad \text{for 3D.} \tag{2.13}$$

The matrix of material *stiffness* constants $\mathbf{c}$ can be written explicitly in more familiar engineering notations as

$$\mathbf{c} = \begin{bmatrix} c_{11} & c_{12} & c_{13} & c_{14} & c_{15} & c_{16} \\ & c_{22} & c_{23} & c_{24} & c_{25} & c_{26} \\ & & c_{33} & c_{34} & c_{35} & c_{36} \\ & & & c_{44} & c_{45} & c_{46} \\ & \text{sy.} & & & c_{55} & c_{56} \\ & & & & & c_{66} \end{bmatrix}, \tag{2.14}$$

where "sy." stands for symmetry, meaning that $c_{ij} = c_{ji}$ for the symmetry property of the material. Thus, there are 21 independent material constants c_{ij}. For isotropic materials, $\mathbf{c}$ can be greatly reduced to

$$\mathbf{c} = \begin{bmatrix} c_{11} & c_{12} & c_{12} & 0 & 0 & 0 \\ & c_{11} & c_{12} & 0 & 0 & 0 \\ & & c_{11} & 0 & 0 & 0 \\ & & & \dfrac{c_{11}-c_{12}}{2} & 0 & 0 \\ & \text{sy.} & & & \dfrac{c_{11}-c_{12}}{2} & 0 \\ & & & & & \dfrac{c_{11}-c_{12}}{2} \end{bmatrix}, \tag{2.15}$$

where

$$c_{11} = \frac{E(1-\nu)}{(1-2\nu)(1+\nu)}, \quad c_{12} = \frac{E\nu}{(1-2\nu)(1+\nu)}, \quad \frac{c_{11}-c_{12}}{2} = \mu, \tag{2.16}$$

in which E, ν, and μ are, respectively, the well-known Young's modulus, Poisson's ratio, and shear modulus of the material. There are only two independent constants among these three constants, and the relationship

among these three constants is

$$\mu = \frac{E}{2(1+\nu)}. \tag{2.17}$$

Given any two of these three constants, the other can then be calculated using the above equation. For 2D plane stress problems, we further have

$$\mathbf{c} = \frac{E}{1-\nu^2}\begin{bmatrix} 1 & \nu & 0 \\ \nu & 1 & 0 \\ 0 & 0 & (1-\nu)/2 \end{bmatrix} \quad \text{(plane stress)}. \tag{2.18}$$

For 2D plane strain problems, the matrix of material stiffness constants $\mathbf{c}$ can be obtained by simply replacing E and ν, respectively, with $E/(1-\nu^2)$ and $\nu/(1-\nu)$, which leads to

$$\mathbf{c} = \frac{E(1-\nu)}{(1+\nu)(1-2\nu)}\begin{bmatrix} 1 & \frac{\nu}{1-\nu} & 0 \\ \frac{\nu}{1-\nu} & 1 & 0 \\ 0 & 0 & \frac{1-2\nu}{2(1-\nu)} \end{bmatrix} \quad \text{(plane strain)}. \tag{2.19}$$

The equilibrium equation in terms of the displacement vector becomes

$$\mathbf{L}_d^T \mathbf{c} \mathbf{L}_d \mathbf{u} + \mathbf{b} = \mathbf{0}, \tag{2.20}$$

where the vector of displacements is given as

$$\mathbf{u} = \begin{Bmatrix} u_1 \\ u_2 \end{Bmatrix} \quad \text{for 2D}, \quad \mathbf{u} = \begin{Bmatrix} u_1 \\ u_2 \\ u_3 \end{Bmatrix} \quad \text{for 3D}. \tag{2.21}$$

2.6 Boundary Conditions

The boundary conditions for a solid mechanics problem can usually be of two types: Dirichlet (essential, displacement) boundary condition and Neumann (natural, stress) boundary condition. Let Γ_u denote a part of Γ, on which the Dirichlet boundary condition is specified. We then have

$$u_i = u_{\Gamma i} \quad \text{on } \Gamma_u \in \Gamma, \tag{2.22}$$

where $u_{\Gamma i}$ is the specified displacement component on Γ_u. In this book, for simplicity we consider the homogeneous essential boundary condition by default:

$$u_i = 0 \quad \text{on } \Gamma_u \in \Gamma. \tag{2.23}$$

This type of problem is called the *force-driving* problem. For non-homogeneous essential boundary conditions, simple treatments in the standard FEM will be applied, and will be discussed on a case-by-case basis.

Let Γ_t denote a part of Γ, on which the Neumann boundary condition is satisfied,

$$\sigma_{ij} n_j = t_{\Gamma i} \quad \text{on } \Gamma_t \in \Gamma, \tag{2.24}$$

where n_j is the jth component of the unit outward normal and $t_{\Gamma i}$ is the specified boundary stress on Γ_t. The matrix form of Equation 2.24 is

$$\mathbf{L}_n^T \boldsymbol{\sigma} = \mathbf{t}_\Gamma \quad \text{on } \Gamma_t \in \Gamma, \tag{2.25}$$

where $\mathbf{L}_n$ is the matrix of the components of the unit outward normal arranged in the form of

$$\mathbf{L}_n = \begin{bmatrix} n_1 & 0 \\ 0 & n_2 \\ n_2 & n_1 \end{bmatrix}_{3\times 2} \quad \text{for 2D,} \quad \mathbf{L}_n = \begin{bmatrix} n_1 & 0 & 0 \\ 0 & n_2 & 0 \\ 0 & 0 & n_3 \\ 0 & n_3 & n_2 \\ n_3 & 0 & n_1 \\ n_2 & n_1 & 0 \end{bmatrix}_{6\times 3} \quad \text{for 3D.} \tag{2.26}$$

2.7 Some Standard Default Conventions and Notations

1. By default in this book, we speak of "open" domain. When a domain is denoted as Ω (bounded by Γ), Ω does not include the boundary Γ. When we refer to a "closed" domain, we will specifically use a frame: $\boxed{\Omega} = \Omega \cup \Gamma$. We also require, in general, that the domain is "Lipschitzian": it cannot be *singular*. For solids and structures with cracks and sharp corners, special treatments or considerations may be needed.

2. This book uses both matrix and indicial notations from time to time for more concise presentations. Therefore, we allow the vectors and matrix to have the following forms for easy conversion between these two notations whenever it is needed. For 3D problems, we have

Matrix notation	Indicial notation
$\mathbf{x} = \begin{Bmatrix} x_1 \\ x_2 \\ x_3 \end{Bmatrix} = \begin{Bmatrix} x \\ y \\ z \end{Bmatrix}, \quad \mathbf{u} = \begin{Bmatrix} u_1 \\ u_2 \\ u_3 \end{Bmatrix} = \begin{Bmatrix} u_x \\ u_y \\ u_z \end{Bmatrix} = \begin{Bmatrix} u \\ v \\ w \end{Bmatrix}$	$x_i, \quad i = 1,2,3$ $u_i, \quad i = 1,2,3$
$\mathbf{b} = \begin{Bmatrix} b_1 \\ b_2 \\ b_3 \end{Bmatrix} = \begin{Bmatrix} b_x \\ b_y \\ b_z \end{Bmatrix}, \quad \begin{Bmatrix} n_1 \\ n_2 \\ n_3 \end{Bmatrix} = \begin{Bmatrix} n_x \\ n_y \\ n_z \end{Bmatrix}$	$b_i, \quad i = 1,2,3$ $n_i, \quad i = 1,2,3$
$\boldsymbol{\sigma}^T = \{\sigma_{11} \quad \sigma_{22} \quad \sigma_{33} \quad \sigma_{23} \quad \sigma_{13} \quad \sigma_{12}\}$ $= \{\sigma_{xx} \quad \sigma_{yy} \quad \sigma_{zz} \quad \sigma_{yz} \quad \sigma_{xz} \quad \sigma_{xy}\}$	$\sigma_{ij}, \ i,j = 1,2,3$
$\boldsymbol{\varepsilon}^T = \{\varepsilon_{11} \quad \varepsilon_{22} \quad \varepsilon_{33} \quad 2\varepsilon_{23} \quad 2\varepsilon_{13} \quad 2\varepsilon_{12}\}$ $= \{\varepsilon_{xx} \quad \varepsilon_{yy} \quad \varepsilon_{zz} \quad \gamma_{yz} \quad \gamma_{xz} \quad \gamma_{xy}\}$	$\varepsilon_{ij}, \ i,j = 1,2,3$

(2.27)

The same is also applicable to 2D problems.

2.8 Remarks

We now conclude this chapter by summarizing the points made.

Remark 2.1 Stable Materials

In this book, unless specified, we consider solids and structures made of materials that are physically *stable*: meaning that any finite amount of strain will result in a finite amount of stress and hence a finite amount of positive strain energy. In other words, these material constants are positive definite or the matrix of material constants $\mathbf{c}$ is symmetric positive definite (SPD).

For stable solid materials, the stress–strain relation can also be written in the following reverse form:

$$\boldsymbol{\varepsilon} = \mathbf{s}\boldsymbol{\sigma}, \tag{2.28}$$

where $\mathbf{s}$ is a matrix of material *flexibility* constants that can be obtained from properly designed experiments. Because $\mathbf{c}$ is SPD, $\mathbf{s}$ must also be SPD, and hence both are invertible. We then have the simple relation

$$\mathbf{s} = \mathbf{c}^{-1} \quad \text{or} \quad \mathbf{c} = \mathbf{s}^{-1}. \tag{2.29}$$

Remark 2.2 Volumetric Locking: An Issue with Displacement Methods

The denominator 1–2ν in Equations 2.16 and 2.19 suggests a possible singularity problem when ν approaches 0.5, which can occur for so-called "incompressible" solid materials like rubber. This can have numerical implications when a displacement method is used to solve the problem, which is known as *volumetric locking*. Special techniques have been developed in the standard FEM to overcome this numerical problem. Techniques for S-FEM models that can deal with volumetric locking problems will be presented in Chapters 5 through 9.

Remark 2.3 Volumetric Locking Free: A Feature with Equilibrium Methods

Volumetric locking will not occur when an equilibrium model is used, where stress is used as the primary field variable. This is because when stress is treated as the primary field variable, strain is obtained using Equation 2.28 instead of Equation 2.16 or 2.19. Therefore, the term "$1 - 2\nu$" will not be in the denominator, leading to a volumetric locking free formulation. The NS-FEM model discussed in Chapter 6 has features similar to an equilibrium model, and is found to be volumetric locking free. Making use of such a nice property of the NS-FEM, all the S-FEM models are made volumetric locking free using the so-called selective formulation.

Remark 2.4 Strong Form

Equations 2.6 and 2.20 are the *strong-form* system of equations that govern the mechanics behavior of solids with displacement functions as the *primary* dependent field variables. The displacement functions are required to have at least the same order of *consistency* in the entire problem domain as *the order of differentiations* in the PDEs. Such a requirement on consistency for the displacement functions is said to be *strong*.

Solving strong-form equations directly is possible. Such methods are often called strong-form methods, and the so-called *collocation methods* are typical strong-form methods. However, care must be taken in using strong-form methods with local approximations because of stability issues [2,3]. This book will not discuss the strong-form methods but the weak-form methods: FEM and S-FEM, starting with the FEM method introduced in the next chapter.

References

1. Timoshenko SP and Goodier JN. 1970. *Theory of Elasticity*, 3rd edition. McGraw-Hill, New York.
2. Liu GR and Gu YT. 2005. *An Introduction to Meshfree Methods and Their Programming*, Chapters 5–7. Springer, Berlin.
3. Liu GR. 2009. *Meshfree Methods: Moving Beyond the Finite Element Method*, 2nd edition, Chapter 9. Taylor & Francis/CRC Press, Boca Raton, FL.

3

The Finite Element Method

In this chapter, we present an *abstracted* version of the widely used FEM in its standard form, because it is frequently used in this book and is the base for our S-FEM methods to be presented in later chapters. We will focus on some of the essential mathematical and numerical aspects and properties of FEM, but the mathematics language is kept as simple as possible with the objective of helping readers become familiar with the necessary terminologies, mathematics tools, and numerical treatments used in FEM and S-FEM. This also serves the purpose of easy reference in the later chapters of this book, when discussing the properties of our S-FEM models. Operational issues on the general procedure of FEM, discretization of the problem domain, shape function construction, weak-form statement, variational formulation, numerical integration, and formulation of the linear system of equations will be outlined. Theoretical issues on functional spaces, solution existence, uniqueness, error, convergence rate, and major properties of the FEM will also be presented in a concise and easy-to-understand fashion, but without details on the proofs. More complete and precise discussions on FEM and the detailed modeling techniques can be found in many dedicated books in the open literature, some of which are listed in, for example, Refs. [1–5].

FEM has a long history of development and hence has various advanced versions. The FEM introduced in this chapter is the "standard version" that is displacement based and fully compatible. We also focus on linear (or bilinear, trilinear) elements as they are most widely used in solving practical engineering problems, most adaptive to various types of practical engineering problems, in addition to the attractive simplicity, and easy for comprehension.

3.1 General Procedure of FEM

Consider static solid mechanics problems defined in a d-dimensional problem domain of $\Omega \in \mathbb{R}^d$ bounded by $\Gamma = \Gamma_u \cup \Gamma_t$, where Γ_u is the essential boundary and Γ_t is the natural boundary, as detailed in Chapter 2. A macro flowchart of the FEM procedure is schematically given in Figure 3.1.

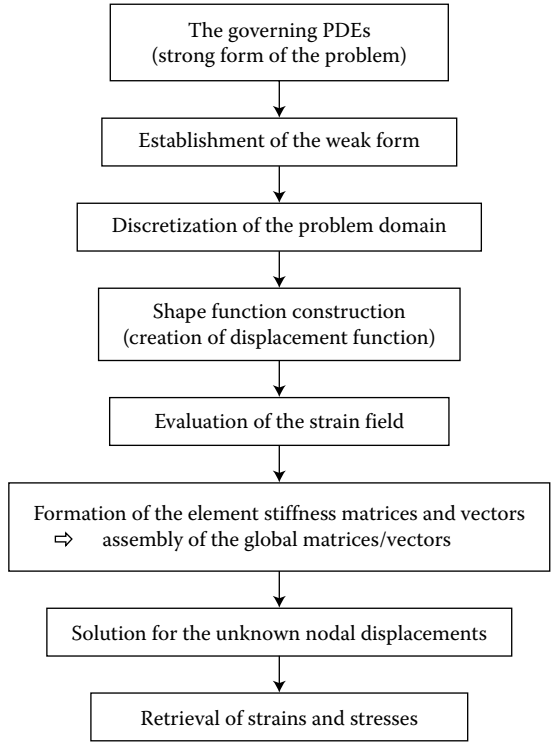

FIGURE 3.1 A macro flowchart of the basic FEM procedure.

The step-by-step procedure in FEM can be presented as follows.

Step (1): Establishment of the Weak Form

The governing PDEs given in Chapter 2 for solid mechanics problems are called the *strong* form, which requires strong continuity on the field variables (displacements), as stated in Remark 2.4. When solving such PDEs directly (known as strong-form methods), *trial* functions of field variables have to be differentiable up to the highest order of PDEs. Generally, it is impossible to find the exact analytical solution that satisfies these strong-form PDEs precisely, except for a few simple cases. Therefore, numerical methods are often used as practical means for approximated solutions. FEM uses weak formulation, which reduces the order of differentiation on trial functions. In mechanics, such a weak form is equivalent to the statement of the well-known *principle of minimum potential energy* to the engineering mechanics community. Note that the use of the weak-form instead of the original strong-form PDEs has changed the statement of the problem. In the continuous forms, both strong and weak statements are essentially equivalent. The weak form, however, becomes more general,

and offers a much more flexible way of creating numerical methods for stable and convergent solutions.

Step (2): Discretization of the Problem Domain

Once the weak form is established, the problem domain is discretized into a set of nonoverlapping and nongap subdomains called *elements*. This is to facilitate the easy creation of displacement functions. These elements are interconnected at the *nodes* located on element vertices (and boundaries for higher-order elements). The elements properly connected by these nodes constitute a *mesh*, and the domain discretization is often called meshing. The number, type, size, and arrangement of the elements have to be decided properly by the analyst. The elements should be small enough to capture the local variation of the displacements and hence to produce results of acceptable accuracy, but not too small for limited computational resources. For efficiency reasons, small elements are used where the results (such as displacement gradient) change rapidly, whereas larger elements can be used where the displacement field is relatively smooth.

Step (3): Shape Function Construction

Based on the elements, *shape functions* for creating the displacement field using nodal displacements are now constructed using polynomial basis functions (monomials). The shape function defines the "shape" of the variation of the displacements in the element, so that the variation displacement within the element can be fully determined, when the nodal displacements are given. Therefore, the nodal values of displacements become the (representative) unknowns in the discretized system of equations, and are known as *nodal* degrees of freedom (DOFs). Hence, it is often more convenient in the formulation to express these shape functions based on nodes (each node has one shape function for one displacement component formed by joining those obtained using the surrounding elements sharing this node), and they are called *nodal shape functions*. The nodal shape functions satisfy the following requirements.

i. *Local support*: The nodal shape function for a node has influence only on the first layer of the elements connected to the node, and is zero elsewhere. This property is ensured naturally in FEM, because these shape functions are constructed based on elements. This *local support* property of shape functions essentially ensures the sparse stiffness and mass matrices for an FEM model.
ii. *Linear independence*: All the nodal shape functions must be linearly independent. This is also naturally achieved by the nonoverlapping and nongap division of elements, and element-based shape function construction.

iii. *Consistency requirement*: The approximated displacements should be differentiable at least up to the rth order inside elements, where r is the order of the highest derivative appearing in the weak form. In FEM practices, this is ensured by the use of basic functions up to sufficiently high order. For solid mechanics problems governed by second-order PDEs, the first derivative of displacements is used in the weak form, and hence at least linear shape function should be used.

iv. *Compatibility requirement*: The approximated displacements should be differentiable at least up to the $(r-1)$th order on the interfaces of elements. A displacement function that satisfies this compatibility requirement is said to be a *compatible* displacement function. This is required by the continuity (or boundedness) of the weak form, and often special care must be taken to ensure this requirement. In FEM practices, proper mapping techniques are often used to ensure the compatibility. The compatibility is often referred to as continuity on the interfaces of elements.

v. *Partitions of unity*: The sum of all nodal shape functions at any point in the problem domain must be unity. This is needed to ensure the proper representation of a constant field or rigid motions of the solid, which is essential to any discrete numerical model in general. This is ensured by simple enclosure of the zero-order monomial (constant) in the basic terms for shape function construction [5].

vi. *Linear reproducibility*: This is the sufficient condition for the shape functions to be used to formulate an FEM model of second-order accuracy (meaning that the up to linear part of the displacement field function will be reproduced exactly, and error is only at second order and above). It is not a necessary requirement, if we do not demand second-order accuracy. Nevertheless, we require this condition, because it is not difficult to achieve in an FEM model when a polynomial basis is used. All one needs to do is to include the constant term and linear terms of the basis terms in the formulation of shape functions.

vii. *Completeness requirement*: Reproducibility of polynomials up to rth order. This can be viewed as a general expression of conditions (v) and (vi).

Step (4): Evaluation of Strain Field

Using the displacement functions created using the shape functions, the strain field can be evaluated via differentiation using simply the strain–displacement relation (or the compatibility equation) (Equation 2.10). Such a strain field is said to be a *compatible* strain field, because it satisfies the compatibility equation in terms of the strain–displacement relation.

Step (5): Formation of Element Stiffness Matrices and Vectors

The stiffness matrix and the load vector of an element can now be computed using the weak form established in step (1), the compatible displacement functions assumed using the shape functions created in step (3), and the compatible strain field obtained in step (4). Integration of the weak form can be performed effectively using numerical integration techniques, such as the popular Gauss quadrature technique with a sufficient number of Gauss points.

Step (6): Assembly of Global Matrices/Vectors

Since the whole problem domain is composed of finite elements, the individual elemental stiffness matrices and vectors computed in step (5) can now be "added" together by superposition based on nodes (called the *direct assembly*) to obtain the global equilibrium system of equations. Such a direct assembly is possible because the continuity or compatibility of the displacement field is ensured and no gaps occur anywhere in the domain.

Step (7): Solution for Unknown Nodal Displacements

The global stiffness matrix obtained from step (6) is symmetric but usually singular because of possible rigid body movements. To remove the singularity, we must impose proper boundary conditions to constrain all the rigid body movements, which leads to a modification of the stiffness matrix and/or the load vector. The modified stiffness matrix becomes SPD, as long as the original problem is well posed, and therefore the nodal displacements can be solved with ease using standard routines of linear algebraic equation systems. Once the solution of displacements at nodes is computed, the function of the displacement field for the whole problem domain can finally be determined.

Step (8): Retrieval of Element Strains and Stresses

From the computed nodal displacements, element strains can be computed using the strain–displacement relation, and then stresses using the constitutive relation. Some postprocessing techniques or recovery procedures can also be performed at this step to improve the accuracy of the strain and stress fields, which will often be performed in this book.

3.2 Proper Spaces

Finding an approximate solution using the above-mentioned FEM procedure is important but not sufficient for advanced analysis and

applications. It is becoming more and more important to obtain information about the *quality* of the solution. This will not only make the FEM result more applicable to practical engineering problems with certain confidence, but will also guide us on how to further improve the solutions. The knowledge of functional analysis is therefore necessary to achieve this goal.

For general problems, we are not able to obtain quantitative information about the *error* between exact and approximate solutions, since the exact solution is usually unknown. Instead, we can be satisfied with an *estimate* of such error with not only about the amount of the error but also the *rate of convergence* of a family of approximate solutions that converge to the exact solution. To perform such a convergence analysis in FEM, spaces of functions to which the solution belongs have to be defined properly and precisely. The spaces of functions used in FEM are generally *normed* spaces equipped with *inner product* induced norms to measure the "magnitude" of the functions or the derivatives of the functions in a certain manner. With the aid of such a norm, the procedure of obtaining an error estimate and the rate of convergence can be presented in rigorous forms.

This section introduces two types of spaces that are essential to the formulation and analysis of FEM: *Lebesgue* spaces and *Hilbert* spaces.

3.2.1 $\mathbb{L}^2$ Space: A Lebesgue Space

The $\mathbb{L}^2$ space of functions may be the most widely used space in functional analyses. It is defined as follows. Let Ω be a bounded domain in $\mathbb{R}^d$ ($d = 1, 2, 3$); the space $\mathbb{L}^2(\Omega; \mathbb{R}^1)$ of scalar functions $v \in \mathbb{R}^1$ on Ω is defined as

$$\mathbb{L}^2(\Omega; \mathbb{R}^1) = \left\{ v \in \mathbb{R}^1 | v \text{ is defined on } \Omega \in \mathbb{R}^d \text{ and } \int_\Omega v^2 \, \mathrm{d}\Omega < \infty \right\}, \quad (3.1)$$

which shows that any function $v \in \mathbb{R}^1$ in $\mathbb{L}^2(\Omega; \mathbb{R}^1)$ is square integrable* over Ω. Such a function can be continuous or discontinuous, but it has to be bounded in the *Lebesgue integral sense*, as defined in Equation 3.1. In other words, the function is at least piecewise continuous with "finite" discontinuities over the problem domain Ω.

Example 3.1: A Piecewise Linear and Continuous Function

The following function v,

$$v(x) = \begin{cases} 1 + x, & -1 \le x \le 0, \\ 1 - x, & 0 < x \le 1, \end{cases} \quad (3.2)$$

* Throughout the book, we speak of *open domains*, meaning that Ω does not include its boundary Γ, and we use the *Lebesgue* integration that allows *occasional omissions*.

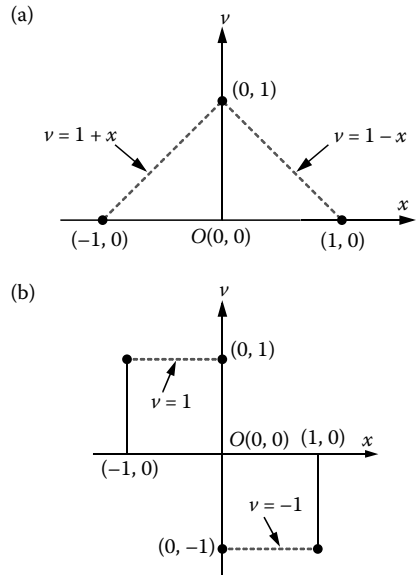

FIGURE 3.2 Examples of functions in $\mathbb{L}^2$ space: (a) piecewise continuous function; (b) Heaviside function (finite and discontinuous at one point).

is clearly piecewise linear and continuous on the finite 1D domain $\Omega = [-1,\ 1]$, as plotted in Figure 3.2a. It lives in $\mathbb{L}^2(\Omega; \mathbb{R}^1)$ space.

To show this, we examine the integration of v^2. Because this function has two pieces of linear function "hinged" at $x = 0$, the integration is broken into two pieces:

$$\int_{-1}^{1} v^2 \, dx = \int_{-1}^{0} (1+x)^2 \, dx + \lim_{\varepsilon \to 0+} \int_{0}^{1} (1-x)^2 \, dx$$

$$= \frac{2}{3} - \lim_{\varepsilon \to 0+} \left(\varepsilon - \varepsilon^2 + \frac{\varepsilon^3}{3} \right) = \frac{2}{3} < \infty, \tag{3.3}$$

which is finite (bounded). Hence the function v in Equation 3.2 belongs to $\mathbb{L}^2\ (\Omega; \mathbb{R}^1)$.

The function of a displacement component in a linear FEM model for 1D, 2D, and 3D problems is essentially a typical piecewise linear function but with multiple (finite number of) "hinge" points (lines and surfaces).

Example 3.2: Heaviside-Type Function

A Heaviside function defined as

$$v(x) = \begin{cases} 1, & -1 \le x \le 0 \\ -1, & 0 < x \le 1 \end{cases} \tag{3.4}$$

belongs to $\mathbb{L}^2(\Omega; \mathbb{R}^1)$ space.

To show this, we observe that the function has two continuous pieces and a finite discontinuous point at $x = 0$ in the domain $\Omega = [-1, 1]$, as plotted in Figure 3.2b. The integration of v^2 can be performed in two pieces $\Omega_1 = [-1, 0]$ and $\Omega_2 = [\varepsilon, 1]$, where ε is a positive infinitely small real number. We then have

$$\begin{aligned}\int_{-1}^{1} v^2 \, dx &= \int_{-1}^{0} 1^2 \, dx + \lim_{\varepsilon \to 0+} \int_{\varepsilon}^{1} (-1)^2 \, dx \\ &= 1 + \underbrace{\lim_{\varepsilon \to 0+} (1 - \varepsilon)}_{\to 1} = 1 + 1 = 2 < \infty, \end{aligned} \tag{3.5}$$

which shows clearly that the integration is finite. Therefore, the Heaviside function in Equation 3.4 belongs to $\mathbb{L}^2(\Omega; \mathbb{R}^1)$.

The function of a strain component field in a linear FEM model for 1D, 2D, and 3D problems is essentially a typical Heaviside function but with multiple discontinuous points (lines and surfaces). The strain component field in an FEM model is in $\mathbb{L}^2(\Omega; \mathbb{R}^1)$ space.

Example 3.3: A General Heaviside Function

A general Heaviside function is defined as

$$v(x) = \begin{cases} 1, & -1 \le x < 0, \\ c, & x = 0, \\ -1, & 0 < x \le 1, \end{cases} \tag{3.6}$$

where c is a *finite* real number. It lives also in $\mathbb{L}^2(\Omega; \mathbb{R}^1)$ space.

To show this, we observe that the function defined in Equation 3.6 has two continuous pieces and a discrete "jumping" point in domain $\Omega = [-1, 1]$, as plotted in Figure 3.2b. The integration of v^2 can be performed in three pieces as follows:

$$\begin{aligned}\int_{-1}^{1} v^2 \, dx &= \lim_{\varepsilon \to 0-} \int_{-1}^{\varepsilon} 1^2 \, dx + \lim_{\substack{\varepsilon \to 0- \\ \beta \to 0+}} \int_{\varepsilon}^{\beta} c^2 \, dx + \lim_{\beta \to 0+} \int_{\beta}^{1} (-1)^2 \, dx \\ &= \underbrace{\lim_{\varepsilon \to 0-} (\varepsilon + 1)}_{\to 1} + \underbrace{\lim_{\substack{\varepsilon \to 0- \\ \beta \to 0+}} \underbrace{c^2}_{\text{finite}} (\beta - \varepsilon)}_{=0} + \underbrace{\lim_{\beta \to 0+} (1 - \beta)}_{\to 1} = 1 + 1 = 2 < \infty, \end{aligned} \tag{3.7}$$

which is finite. Therefore, the general Heaviside function in Equation 3.6 belongs to $\mathbb{L}^2(\Omega; \mathbb{R}^1)$. We observed again that the function value at $x = 0$

can be omitted from the integral, regardless of the value of c, as long as it is finite.

Remark 3.1 Lebesgue Integration

The value of the integration will not change if we make *finite* changes to the *finite* value of the integrand only on a finite set of discrete points. Lebesgue integration is very forgiving of "occasional omissions." This is of fundamental importance to the FEM method, because it essentially allows us to use piecewise continuous displacement functions constructed using an element mesh. We can practically omit the discontinuity of the strain fields along these element interfaces, as long as our integration is performed based on elements, as we practice in the standard FEM models. Our integration over the entire problem can be changed to a summation of integrations over all the elements, and all the domains of integration are *open*: element interfaces can be omitted.

The space $\mathbb{L}^2(\Omega;\mathbb{R}^1)$ is associated with the scalar inner product

$$(v,w)_{\mathbb{L}^2(\Omega;\mathbb{R}^1)} = \int_\Omega v\,w\,\mathrm{d}\Omega \tag{3.8}$$

and equipped with the corresponding norm $\|\cdot\|_{\mathbb{L}^2(\Omega;\mathbb{R}^1)}$:

$$\|v\|_{\mathbb{L}^2(\Omega;\mathbb{R}^1)} = \left(\int_\Omega v^2\,\mathrm{d}\Omega\right)^{1/2} \equiv (v,v)^{1/2}. \tag{3.9}$$

For example, the norm $\|\cdot\|_{\mathbb{L}^2(\Omega;\mathbb{R}^1)}$ of the function v in Equation 3.2 is

$$\|v\|_{\mathbb{L}^2(\Omega;\mathbb{R}^1)} = \left(\int_{-1}^{1} v^2\,\mathrm{d}x\right)^{1/2} = \sqrt{\frac{2}{3}}. \tag{3.10}$$

Here we used the results of Example 3.1.

For example, the norm $\|\cdot\|_{\mathbb{L}^2(\Omega;\mathbb{R}^1)}$ of functions v in Equations 3.4 and 3.6 is

$$\|v\|_{\mathbb{L}^2(\Omega;\mathbb{R}^1)} = \left(\int_{-1}^{1} v^2\,\mathrm{d}x\right)^{1/2} = \sqrt{2}. \tag{3.11}$$

Here we used the results of Examples 3.2 and 3.3.

As the field variables of 2D and 3D solid mechanics problems are in vector form with d independent components, we denote more precisely the spaces as

$$\mathbb{L}^2(\Omega;\mathbb{R}^d) = \left\{ \mathbf{v} = (v_i,\ldots,v_d);\ v_i \in \mathbb{L}^2(\Omega;\mathbb{R}^1),\ i = 1,\ldots,d \right\}, \tag{3.12}$$

where $d = 2$ for 2D and $d = 3$ for 3D problems. Equation 3.12 means that each of the displacement components has to be square integrable over Ω, and the dimension of the space is expanded d times, because of the independence of the displacement components. Note that, in the general case, the number of components of field variables in the vector form can be different from d, for example in the beam, plate or shell problems.

The corresponding norm $\|\cdot\|_{\mathbb{L}^2(\Omega;\mathbb{R}^d)}$ becomes

$$\|\mathbf{v}\|_{\mathbb{L}^2(\Omega;\mathbb{R}^d)} = \left(\sum_{i=1}^{d} \|v_i\|^2_{\mathbb{L}^2(\Omega;\mathbb{R}^1)} \right)^{1/2}. \tag{3.13}$$

3.2.2 Hilbert Spaces

Hilbert spaces and their inequalities are essential for weak or variational formulations of the second-order boundary value mechanics problems presented in Chapter 2, and therefore will be discussed here. For a concise definition of Hilbert spaces, we first need to define the general notation of differentiations

$$D^\alpha v = \frac{\partial^{|\alpha|} v}{\partial x_1^{\alpha_1} \cdots \partial x_d^{\alpha_d}}, \tag{3.14}$$

where $\alpha = (\alpha_1,\ldots,\alpha_d)$ is a non-negative integer and $|\alpha| = \alpha_1 + \cdots + \alpha_d$.

For example, for a 2D problem ($d = 2$) with a partial derivative of order 2, $D^\alpha v$ is one of three second-order differentiations: $D^\alpha v = \partial^2 v/\partial x_1^2$ [with $\alpha = (\alpha_1,\alpha_2) = (2,0)$], $D^\alpha v = \partial^2 v/\partial x_1 \partial x_2$ [with $\alpha = (\alpha_1,\alpha_2) = (1,1)$], or $D^\alpha v = \partial^2 v/\partial x_2^2$ [with $\alpha = (\alpha_1,\alpha_2) = (0,2)$], all with $|\alpha| = 2$.

We are now ready to define Hilbert spaces $\mathbb{H}^m(\Omega;\mathbb{R}^1)$, where m is a non-negative integer, as

$$\mathbb{H}^m(\Omega;\mathbb{R}^1) = \left\{ v \in \mathbb{R}^1 \,\middle|\, D^\alpha v \in \mathbb{L}^2(\Omega;\mathbb{R}^1), \forall\, |\alpha| \le m \right\}, \tag{3.15}$$

which includes all functions whose derivatives up to mth order are all square integrable. Spaces $\mathbb{H}^m(\Omega;\mathbb{R}^1)$ are associated with the inner product

$$(v,w)_{\mathbb{H}^m(\Omega;\mathbb{R}^1)} = \sum_{|\alpha|\le m} \int_\Omega (D^\alpha v)(D^\alpha w)\, \mathrm{d}\Omega \tag{3.16}$$

and equipped with the induced (full) norm $\|\cdot\|_{\mathbb{H}^m(\Omega;\mathbb{R}^1)}$

$$\|v\|_{\mathbb{H}^m(\Omega;\mathbb{R}^1)} = \left(\sum_{|\alpha|\leq m} \int_\Omega \left|D^\alpha v\right|^2 \mathrm{d}\Omega \right)^{1/2} \tag{3.17}$$

as well as the seminorm $|\cdot|_{\mathbb{H}^m(\Omega;\mathbb{R}^1)}$

$$|v|_{\mathbb{H}^m(\Omega;\mathbb{R}^1)} = \left(\int_\Omega \left|D^m v\right|^2 \mathrm{d}\Omega \right)^{1/2} \tag{3.18}$$

that includes only the mth derivative. Note that $\mathbb{H}^m(\Omega;\mathbb{R}^1)$ is the Sobolev space $\mathbb{W}^{m,2}(\Omega;\mathbb{R}^1)$ [6], and in particular we note $\mathbb{H}^0(\Omega;\mathbb{R}^1) = \mathbb{L}^2(\Omega;\mathbb{R}^1)$. $\mathbb{H}^1(\Omega;\mathbb{R}^1)$ is the most relevant to the solid mechanics problem governed by equations given in Chapter 2:

$$\mathbb{H}^1(\Omega;\mathbb{R}^1) = \left\{ v \,|\, v \in \mathbb{L}^2(\Omega;\mathbb{R}^1), \frac{\partial v}{\partial x_i} \in \mathbb{L}^2(\Omega;\mathbb{R}^1),\ i = 1,\ldots,d \right\}, \tag{3.19}$$

with the scalar product $(\cdot,\cdot)_{\mathbb{H}^1(\Omega;\mathbb{R}^1)}$ defined by

$$(v,w)_{\mathbb{H}^1(\Omega;\mathbb{R}^1)} = \int_\Omega (vw + \nabla v \cdot \nabla w)\, \mathrm{d}\Omega, \tag{3.20}$$

where ∇v is the gradient of v defined by

$$\nabla v = \left\{ \frac{\partial v}{\partial x_1} \cdots \frac{\partial v}{\partial x_d} \right\}^T, \tag{3.21}$$

and the corresponding norm $\|\cdot\|_{\mathbb{H}^1(\Omega;\mathbb{R}^1)}$

$$\|v\|_{\mathbb{H}^1(\Omega;\mathbb{R}^1)} = \left[\int_\Omega (v^2 + |\nabla v|^2)\, \mathrm{d}\Omega \right]^{1/2} \tag{3.22}$$

and the seminorm $|\cdot|_{\mathbb{H}^1(\Omega;\mathbb{R}^1)}$

$$|v|_{\mathbb{H}^1(\Omega;\mathbb{R}^1)} = \left[\int_\Omega |\nabla v|^2\, \mathrm{d}\Omega \right]^{1/2}. \tag{3.23}$$

We further define the space $\mathbb{H}_0^1(\Omega;\mathbb{R}^1) = \left\{v \in \mathbb{H}^1(\Omega;\mathbb{R}^1) \,|\, v = 0 \text{ on } \Gamma_u\right\}$ to be the subset of $\mathbb{H}^1(\Omega;\mathbb{R}^1)$ with vanishing values on Γ_u, and $\mathbb{H}_0^1(\Omega;\mathbb{R}^1)$ is equipped with the same scalar product and norms as $\mathbb{H}^1(\Omega;\mathbb{R}^1)$.

Example 3.4: A Piecewise Linear and Continuous Function

The function v on the 1D domain $\Omega = [-1, 1]$ in Equation 3.2 belongs to $\mathbb{H}_0^1(\Omega;\mathbb{R}^1)$ because (1) the function v belongs to $\mathbb{L}^2(\Omega;\mathbb{R}^1)$ as shown in Example 3.1, (2) the derivative of the function

$$\frac{\partial v}{\partial x} = \begin{cases} 1, & -1 \le x \le 0 \\ -1, & 0 < x \le 1 \end{cases} \tag{3.24}$$

is a function of Heaviside type, and also belongs to $\mathbb{L}^2(\Omega;\mathbb{R}^1)$, as shown in Example 3.2, and (3) $v(-1) = 0$, $v(1) = 0$.

The $\mathbb{H}^1(\Omega;\mathbb{R}^1)$ norm of the function v in Example 3.1 is

$$\begin{aligned} \|v\|_{\mathbb{H}^1(\Omega;\mathbb{R}^1)} &= \left[\int_{-1}^{1} \left(v^2 + |\nabla v|^2\right) dx\right]^{1/2} \\ &= \left[\int_{-1}^{0} \left((1+x)^2 + 1^2\right) dx + \lim_{\varepsilon\to 0+} \int_{\varepsilon}^{1} \left((1-x)^2 + (-1)^2\right) dx\right]^{1/2} \\ &= \sqrt{\frac{8}{3} + \lim_{\varepsilon\to 0+} \left(2\varepsilon - \varepsilon^2 + \frac{\varepsilon^3}{3}\right)} = \sqrt{\frac{8}{3}}. \end{aligned} \tag{3.25}$$

The seminorm of the function v in Example 3.1 is

$$\begin{aligned} |v|_{\mathbb{H}^1(\Omega;\mathbb{R}^1)} &= \left[\int_{-1}^{1} |\nabla v|^2 \, dx\right]^{1/2} = \left[\int_{-1}^{0} 1^2 \, dx + \lim_{\varepsilon\to 0+} \int_{\varepsilon}^{1} |-1|^2 \, dx\right]^{1/2} \\ &= \sqrt{2 - \lim_{\varepsilon\to 0+} \varepsilon} = \sqrt{2}. \end{aligned} \tag{3.26}$$

The analysis given in Examples 3.1 and 3.4 shows that the function of a displacement component in a linear FEM model for 1D, 2D, and 3D problems lives generally in an $\mathbb{H}^1(\Omega;\mathbb{R}^1) \subset \mathbb{L}^2(\Omega;\mathbb{R}^1)$ space.

Example 3.5: A General Heaviside Function

The function v defined in Equation 3.6 over the 1D domain $\Omega = [-1, 1]$ does not belong to $\mathbb{H}^1(\Omega; \mathbb{R}^1)$.

To examine this, we first note that function v defined in Equation 3.6 belongs to $\mathbb{L}^2(\Omega; \mathbb{R}^1)$, as shown in Example 3.3. Next, let us examine whether $\partial v/\partial x$ belongs to $\mathbb{L}^2(\Omega; \mathbb{R}^1)$, using the following simple *intuitive* (may not be very rigorous) procedure. We know that $\partial v/\partial x$ for the function defined in Equation 3.6 does not even exist at $x = 0$, and hence it is difficult to examine it directly. Instead, we then construct a "milder" function (that is at least piecewise differentiable) in the following form:

$$v_m(x) = \begin{cases} 1, & -1 \le x < -\varepsilon, \\ \frac{-x}{\varepsilon}, & -\varepsilon \le x \le \varepsilon, \\ -1, & \varepsilon < x \le 1, \end{cases} \tag{3.27}$$

where ε is a positive infinitely small real number. This milder function is now continuous for any given ε, and should be smoother than the original function v defined in Equation 3.6 for any *arbitrary* small positive ε. We then examine the property of v_m defined in Equation 3.27. The derivative of v_m can be expressed as follows:

$$\frac{\partial v_m}{\partial x} = \begin{cases} 0, & -1 \le x < -\varepsilon, \\ \frac{-1}{\varepsilon}, & -\varepsilon \le x \le \varepsilon, \\ 0, & \varepsilon < x \le 1. \end{cases} \tag{3.28}$$

The integration of $(\partial v_m/\partial x)^2$ can be performed in three pieces, $\Omega_1 = [-1, -\varepsilon]$, $\Omega_2 = [-\varepsilon, \varepsilon]$, and $\Omega_3 = [\varepsilon, 1]$:

$$\begin{aligned} \int_{-1}^{1} \left(\frac{\partial v_m}{\partial x}\right)^2 \mathrm{d}x &= \int_{-1}^{-\varepsilon} 0^2 \,\mathrm{d}x + \int_{-\varepsilon}^{\varepsilon} \left(\frac{-1}{\varepsilon}\right)^2 \mathrm{d}x + \int_{\varepsilon}^{1} 0^2 \,\mathrm{d}x \\ &= 2\frac{1}{\varepsilon^2}\varepsilon = 2\frac{1}{\varepsilon}. \end{aligned} \tag{3.29}$$

It is easy to see that we cannot bound $\int_{-1}^{1} (\partial v_m/\partial x)^2 \mathrm{d}x$ at the limit of $\varepsilon \to 0$, and hence $\partial v_m/\partial x$ does not belong to $\mathbb{L}^2(\Omega; \mathbb{R}^1)$ at the limit of $\varepsilon \to 0$. Therefore, the function v_m defined in Equation 3.27 over the domain $\Omega = [-1, 1]$ does not belong to $\mathbb{H}^1(\Omega; \mathbb{R}^1)$ at the limit of $\varepsilon \to 0$. Hence, we can assert that the function v defined in Equation 3.6 over the domain $\Omega = [-1, 1]$ does not belong to $\mathbb{H}^1(\Omega; \mathbb{R}^1)$, because it is even less smoother than v_m defined in Equation 3.27, for any arbitrary small ε.

Example 3.5 is a typical example that discontinuous functions do not belong to $\mathbb{H}^1(\Omega; \mathbb{R}^1)$ space. Such functions cannot be directly used in an

FEM model. To make use of *some* types of discontinuous functions in constructing stable and convergent numerical models, we need to use the $\mathbb{G}$ space theory [7,8] that leads to weakened weak ($\mathbb{W}^2$) formulations [9,10]. Further discussion on this quite involved topic is beyond the scope of this book. In the formulation used in this book, we stick to the Hilbert space theory, and we now understand that the Heaviside functions defined in Equation 3.4 or 3.6 are not allowed in the FEM and S-FEM models as displacement functions.

When the domain Ω is bounded, there exists a constant C such that

$$\forall v \in \mathbb{H}_0^1(\Omega;\mathbb{R}^1), \quad \|v\|_{\mathbb{L}^2(\Omega;\mathbb{R}^1)} \leq C\,|v|_{\mathbb{H}^1(\Omega;\mathbb{R}^1)}\,, \tag{3.30}$$

which is known as Poincare–Friedrichs inequality [6]. In such a case, the seminorm $|\cdot|_{\mathbb{H}^1(\Omega;\mathbb{R}^1)}$ is a norm over the space $\mathbb{H}_0^1(\Omega;\mathbb{R}^1)$ equivalent to the norm $\|\cdot\|_{\mathbb{H}^1(\Omega;\mathbb{R}^1)}$. This implies that there exist positive real numbers C_1 and C_2 such that

$$C_1\,\|v\|_{\mathbb{H}^1(\Omega;\mathbb{R}^1)} \leq |v|_{\mathbb{H}^1(\Omega;\mathbb{R}^1)} \leq C_2\,\|v\|_{\mathbb{H}^1(\Omega;\mathbb{R}^1)}\,. \tag{3.31}$$

The Poincare–Friedrichs inequality is one of the most important inequalities in the weak formulation, because it ensures fundamentally the stability of the weak formulation.

Because vector field variables in 2D and 3D solid mechanics problems are in vector form with d components, we denote more precisely the spaces as

$$\mathbb{H}^1(\Omega;\mathbb{R}^d) = \left\{\mathbf{v} = (v_1,\ldots,v_d);\ v_i \in \mathbb{H}^1(\Omega;\mathbb{R}^1),\, i = 1,\ldots,d\right\}, \tag{3.32}$$

where $d = 2$ for 2D and $d = 3$ for 3D problems. The corresponding full norm $\|\cdot\|_{\mathbb{H}^1(\Omega;\mathbb{R}^d)}$ becomes

$$\|\mathbf{v}\|_{\mathbb{H}^1(\Omega;\mathbb{R}^d)} = \left(\sum_{i=1}^{d} \|v_i\|^2_{\mathbb{H}^1(\Omega;\mathbb{R}^1)}\right)^{1/2}, \tag{3.33}$$

and the seminorm $|\cdot|_{\mathbb{H}^1(\Omega;\mathbb{R}^d)}$ is

$$|\mathbf{v}|_{\mathbb{H}^1(\Omega;\mathbb{R}^d)} = \left(\sum_{i=1}^{d} |v_i|^2_{\mathbb{H}^1(\Omega;\mathbb{R}^1)}\right)^{1/2}. \tag{3.34}$$

Similarly, the space $\mathbb{H}_0^1(\Omega;\mathbb{R}^d) = \{\mathbf{v} \in \mathbb{H}^1(\Omega;\mathbb{R}^d) \,|\, \mathbf{v} = \mathbf{0} \text{ on } \Gamma_u\}$ is the subset of $\mathbb{H}^1(\Omega;\mathbb{R}^d)$ with vanishing values on Γ_u, and $\mathbb{H}_0^1(\Omega;\mathbb{R}^d)$ is equipped with the same scalar product and norms as $\mathbb{H}^1(\Omega;\mathbb{R}^d)$.

3.3 Weak Formulation and Properties of the Solution

3.3.1 Weak Formulation

We are now ready to derive the weak formulation for the solid mechanics problem in d-dimensions. To this end, we use the well-known weighted residual method. By multiplying Equation 2.7 with a test function $\mathbf{v} \in \mathbb{H}_0^1(\Omega; \mathbb{R}^d)$ and performing integration over the entire problem domain Ω, we have

$$\int_\Omega \mathbf{v}^T \mathbf{L}_d^T \boldsymbol{\sigma} \, d\Omega + \int_\Omega \mathbf{v}^T \mathbf{b} \, d\Omega = 0, \quad \forall \mathbf{v} \in \mathbb{H}_0^1(\Omega; \mathbb{R}^d). \tag{3.35}$$

Applying Green's divergence theorem, and using boundary conditions (Equations 2.23 and 2.24), we obtain

$$\underbrace{\int_\Omega (\mathbf{L}_d \mathbf{v})^T \, \mathbf{c} \, (\mathbf{L}_d \mathbf{u}) \, d\Omega}_{a(\mathbf{u},\mathbf{v})} = \underbrace{\int_\Omega \mathbf{v}^T \mathbf{b} \, d\Omega + \int_{\Gamma_t} \mathbf{v}^T \mathbf{t} \, d\Gamma}_{f(\mathbf{v})}, \quad \forall \mathbf{v} \in \mathbb{H}_0^1(\Omega; \mathbb{R}^d). \tag{3.36}$$

The d-dimensional solid mechanics problem governed by equilibrium (Equations 2.7) and boundary conditions 2.23 and 2.24 can be stated in the following well-known *weak statement*:

$$\text{Find } \mathbf{u} \in \mathbb{H}_0^1(\Omega; \mathbb{R}^d) \text{ such that } a(\mathbf{u}, \mathbf{v}) = f(\mathbf{v}), \quad \forall \mathbf{v} \in \mathbb{H}_0^1(\Omega; \mathbb{R}^d), \tag{3.37}$$

where $a(\mathbf{u}, \mathbf{v})$ is the bilinear form defined by

$$a(\mathbf{u}, \mathbf{v}) = \int_\Omega (\mathbf{L}_d \mathbf{u})^T \mathbf{c} (\mathbf{L}_d \mathbf{v}) d\Omega, \tag{3.38}$$

and $f(\mathbf{v})$ is the linear functional defined as

$$f(\mathbf{v}) = \int_\Omega \mathbf{v}^T \mathbf{b} \, d\Omega + \int_{\Gamma_t} \mathbf{v}^T \mathbf{t} \, d\Gamma. \tag{3.39}$$

The above weak formulation transforms the equilibrium system of Equations 2.7 and boundary conditions 2.23 and 2.24 into a single Equation 3.37 in which all of the features of the solution are presented. In Equation 3.37, we only need to perform the first derivatives for trial function $\mathbf{u}$. This is because part of the second-order derivatives on the trial function $\mathbf{u}$ has been "transferred" to the test function $\mathbf{v}$. As a result, the continuity requirement

on function $\mathbf{u}$ is one order *weakened* compared with the original requirement of second-order differentiable in the strong formulation in Equation 2.7. Therefore, formulation 3.37 is a *weak formulation* of the classical original *strong form* with equilibrium equations 2.7 and boundary conditions 2.23 and 2.24. Both functions $\mathbf{u}$ and $\mathbf{v}$ belong to the same space $\mathbb{H}_0^1(\Omega;\mathbb{R}^d)$, and hence it is a Galerkin weak form. We know that it is generally difficult to prove the existence of a solution of the strong form. However, using the weak form it is easy to prove the existence, uniqueness, and stability of the solution to Equation 3.37, as presented in Section 3.3.3.

3.3.2 Galerkin Weak Form

In the engineering community, most people are more familiar with the so-called Galerkin weak form that is often written as follows:

$$\int_\Omega \delta\boldsymbol{\varepsilon}^T \boldsymbol{c}\varepsilon \, d\Omega - \left(\int_\Omega \delta\mathbf{u}^T \mathbf{b} \, d\Omega + \int_{\Gamma_t} \delta\mathbf{u}^T \mathbf{t}_\Gamma \, d\Gamma \right) = 0, \tag{3.40}$$

where we use variational operator δ, and hence Equation 3.40 is called a variational statement. Using the displacement strain relation $\boldsymbol{\varepsilon} = \mathbf{L}_d\mathbf{u}$, Equation 3.40 can be further written explicitly in displacement as

$$\underbrace{\int_\Omega (\mathbf{L}_d\delta\mathbf{u})^T \mathbf{c}(\mathbf{L}_d\mathbf{u}) d\Omega}_{a(\mathbf{v},\mathbf{u})\equiv a(\delta\mathbf{u},\mathbf{u})} - \underbrace{\left(\int_\Omega \delta\mathbf{u}^T \mathbf{b} \, d\Omega + \int_{\Gamma_t} \delta\mathbf{u}^T \mathbf{t}_\Gamma \, d\Gamma \right)}_{f(\mathbf{v})\equiv f(\delta\mathbf{u})} = 0. \tag{3.41}$$

A numerical method based on the Galerkin weak form is therefore looking for a displacement field in $\mathbf{u} \in \mathbb{H}_0^1(\Omega;\mathbb{R}^d)$ that satisfies Equation 3.41 for any arbitrary function $\mathbf{v} \equiv \delta\mathbf{u} \in \mathbb{H}_0^1(\Omega;\mathbb{R}^d)$. Physically, such a displacement field makes the total potential energy in the entire system (solid or structure) minimum, and hence the solid/structure stays stable (in equilibrium) there. We now see clearly the relationship between the Galerkin weak form and the weak statement (Equation 3.37): they are essentially the same.

3.3.3 Existence, Uniqueness, and Stability of the Solution of Weak Form

From Equation 3.38, it is seen that $a(\mathbf{u},\mathbf{v})$ is a symmetric bilinear form on $\mathbb{H}_0^1(\Omega;\mathbb{R}^d)$. For stable materials (see Remark 2.1), using the well-known Cauchy–Schwarz inequality for the inner product induced norms, and the

equivalence of the full and seminorms of functions in an $\mathbb{H}_0^1(\Omega;\mathbb{R}^d)$ space, it is easy to prove that [6]

$$|a(\mathbf{u},\mathbf{v})| \leq C_3 \|\mathbf{u}\|_{\mathbb{H}^1(\Omega;\mathbb{R}^d)} \|\mathbf{v}\|_{\mathbb{H}^1(\Omega;\mathbb{R}^d)}, \tag{3.42}$$

where C_3 is a constant independent of $\mathbf{v},\mathbf{u} \in \mathbb{H}_0^1(\Omega;\mathbb{R}^d)$. The foregoing equation implies that $a(\mathbf{u},\mathbf{v})$ is continuous.

In addition, from Poincare's inequality,

$$\int_\Omega \mathbf{v}^T\mathbf{c}\mathbf{v}\,d\Omega \leq C_4 \int_\Omega (\mathbf{L}_d\mathbf{v})^T\mathbf{c}(\mathbf{L}_d\mathbf{v})d\Omega, \quad \forall \mathbf{v} \in \mathbb{H}_0^1(\Omega;\mathbb{R}^d), \tag{3.43}$$

where C_4 is an independent constant of $\mathbf{v} \in \mathbb{H}_0^1(\Omega;\mathbb{R}^d)$. We now have the following inequality:

$$a(\mathbf{v},\mathbf{v}) \geq \alpha \|\mathbf{v}\|^2_{\mathbb{H}^1(\Omega;\mathbb{R}^d)}, \tag{3.44}$$

where α is a constant independent of $\mathbf{v} \in \mathbb{H}_0^1(\Omega;\mathbb{R}^d)$, implying that $a(\mathbf{v},\mathbf{v})$ is $\mathbb{H}$-elliptic [3,6].

Next, we assume that $\mathbf{b} \in \mathbb{L}^2(\Omega;\mathbb{R}^d)$ and $\mathbf{t} \in \mathbb{L}^2(\Gamma_t;\mathbb{R}^d)$, so that $f(\mathbf{v})$ defined by Equation 3.39 is a continuous linear form.

Theorem 3.1: Existence, Uniqueness, and Stability [6]

Let $a(\cdot,\cdot)$: $\mathbb{H}_0^1(\Omega;\mathbb{R}^d) \times \mathbb{H}_0^1(\Omega;\mathbb{R}^d) \to \mathbb{R}$ be a continuous, $\mathbb{H}$-elliptic bilinear form on $\mathbb{H}_0^1(\Omega;\mathbb{R}^d)$. Furthermore, let $f(\mathbf{v})$: $\mathbb{H}_0^1(\Omega;\mathbb{R}^d) \to \mathbb{R}$ be a continuous linear functional on $\mathbb{H}_0^1(\Omega;\mathbb{R}^d)$. Then we have the following:

1. The weak form of finding $\mathbf{u} \in \mathbb{H}_0^1(\Omega;\mathbb{R}^d)$ that satisfies

$$a(\mathbf{u},\mathbf{v}) = f(\mathbf{v}), \quad \forall \mathbf{v} \in \mathbb{H}_0^1(\Omega;\mathbb{R}^d) \tag{3.45}$$

   has one and only one solution.

2. The solution depends continuously on the data, in the sense that

$$\|\mathbf{u}\|_{\mathbb{H}^1(\Omega;\mathbb{R}^d)} \leq \frac{1}{\alpha} \|f\|_{\mathbb{H}^{-1}(\Omega;\mathbb{R}^d)}, \tag{3.46}$$

   where

$$\|f\|_{\mathbb{H}^{-1}(\Omega;\mathbb{R}^d)} = \sup_{\substack{\mathbf{v}\in\mathbb{H}_0^1(\Omega;\mathbb{R}^d)\\ \mathbf{v}\neq\mathbf{0}}} \frac{|(f,\mathbf{v})|}{\|\mathbf{v}\|_{\mathbb{H}^1(\Omega;\mathbb{R}^d)}}. \tag{3.47}$$

Inequality 3.46 assures us that a small change in the linear functional $f(\mathbf{v})$ leads to a correspondingly small change in the solution $\mathbf{u} \in \mathbb{H}_0^1(\Omega;\mathbb{R}^d)$. In other words, the solution $\mathbf{u} \in \mathbb{H}_0^1(\Omega;\mathbb{R}^d)$ depends continuously on the data $f(\mathbf{v})$: our weak statement defines a well-posed problem with a stable solution.

3.4 Domain Discretization: Creation of Finite-Dimensional Space

In the weak statement given in Equation 3.37, $\mathbb{H}_0^1(\Omega;\mathbb{R}^d)$ is an infinite-dimensional space. It is generally impossible to solve the governing equations either in strong form (Equation 2.7) or in weak form (Equation 3.37) in analytical means for the *exact* solution. Fortunately, the weak formulation (Equation 3.37) can be naturally used to obtain *approximate* solutions. In the FEM formulation, this is conveniently done by creating a discrete solution space of finite dimension that is a subspace of the infinite-dimensional space, $\mathbb{H}_{0,h}^1(\Omega;\mathbb{R}^d) \subset \mathbb{H}_0^1(\Omega;\mathbb{R}^d)$, and an approximated solution $\tilde{\mathbf{u}} \in \mathbb{H}_{0,h}^1(\Omega;\mathbb{R}^d)$ is sought using the weak statement (Equation 3.37). Here h stands for finite dimension. At the limit of $h \to \mathbf{0}$, we expect $\mathbb{H}_{0,h}^1(\Omega;\mathbb{R}^d) \to \mathbb{H}_0^1(\Omega;\mathbb{R}^d)$, and $\tilde{\mathbf{u}} \to \mathbf{u}$. We can also find indications on how fast $\tilde{\mathbf{u}}$ approaches $\mathbf{u}$.

In our analysis process, we assume that there is no "geometric" error caused by the domain discretization, so that we can focus only on the error of approximation of weak formulation (Equation 3.37) induced by the use of finite-dimensional space $\mathbb{H}_{0,h}^1(\Omega;\mathbb{R}^d)$ that deviates from $\mathbb{H}_0^1(\Omega;\mathbb{R}^d)$. We assume also that the domain Ω in $\mathbb{R}^2$is polygonal. That is, boundary Γ of Ω is made of straight segments. Under these assumptions, it is easy to see that the whole domain can be covered exactly by polygonal elements. We are now ready to discretize the domain Ω into N_e of nonoverlapping and nongap elements with N_n nodes, such that $\Omega = \cup_{i=1}^{N_e} \Omega_i^e$ and $\Omega_i^e \cap \Omega_j^e = \emptyset$. $i \neq j$. We require that in the element mesh, there are no duplicated and hanging nodes.

3.5 Creation of Shape Functions

3.5.1 The General Procedure

Based on the element mesh, shape functions can be created based on each element using simply the interpolation procedure and the polynomial basis functions. The general procedure is as follows. Consider an element Ω_i^e

with n_n^e nodes; a component of displacement within the element is first expressed as

$$\tilde{u}(\mathbf{x}) = \sum_{j=1}^{n_n^e} p_j(\mathbf{x}) a_j = \mathbf{p}^T(\mathbf{x})\mathbf{a}, \tag{3.48}$$

where $\mathbf{x} = \{x_1 \cdots x_d\}$ is a vector of independent coordinate variables. For 2D domains, we often denote $\mathbf{x} = \{x \quad y\}$, and for 3D domains $\mathbf{x} = \{x \quad y \quad z\}$. $p_j(\mathbf{x})$ is the basic function of monomials, a_j is the coefficient for the monomial $p_j(\mathbf{x})$, and vector $\mathbf{a}$ has the form of

$$\mathbf{a} = \begin{Bmatrix} a_1 & a_2 & \cdots & a_{n_n^e} \end{Bmatrix}^T. \tag{3.49}$$

Clearly, the order of the consistency of the shape function depends on the polynomial basis functions used. For 1D problems, we use

$$\mathbf{p}^T(\mathbf{x}) = \mathbf{p}^T(x) = \{1 \quad x \quad x^2 \quad x^3 \quad x^4 \quad \cdots\}. \tag{3.50}$$

For 2D problems, we use

$$\mathbf{p}^T(\mathbf{x}) = \mathbf{p}^T(x,y) = \{1 \quad x \quad y \quad xy \quad x^2 \quad y^2 \quad \cdots\}. \tag{3.51}$$

For 3D problems, we use

$$\mathbf{p}^T(\mathbf{x}) = \mathbf{p}^T(x,y,z) = \{1 \quad x \quad y \quad z \quad xy \quad yz \quad zx \quad xyz \quad x^2 \quad y^2 \quad z^2 \quad \cdots\}. \tag{3.52}$$

For higher-order 2D and 3D elements, the choice of higher-order polynomial basis terms depends on the type of elements (order and node arrangement); it can be quite tricky and a number of formulations are available [5]. In this book we will focus only on lower-order elements that are most widely used in solving engineering problems. For three-node triangular elements (T3) and four-node tetrahedral elements (T4), we use

$$\mathbf{p}^T(\mathbf{x}) = \begin{cases} \{1 \quad x \quad y\} & \text{for T3,} \\ \{1 \quad x \quad y \quad z\} & \text{for T4.} \end{cases} \tag{3.53}$$

For four-node quadrilateral elements (Q4) and eight-node hexahedral elements (H8), we use

$$\mathbf{p}^T(\mathbf{x}) = \begin{cases} \{1 \quad x \quad y \quad xy\} & \text{for Q4,} \\ \{1 \quad x \quad y \quad z \quad xy \quad yz \quad zx \quad xyz\} & \text{for H8.} \end{cases} \tag{3.54}$$

Coefficients a_j in Equation 3.48 can be determined by enforcing that Equation 3.48 is satisfied at the n_n^e nodes of the element. At node j, we have

$$u_j = \mathbf{p}^T(\mathbf{x}_j)\mathbf{a}, \quad j = 1, 2, \ldots, n_n^e, \tag{3.55}$$

where u_j is the nodal value of u at $\mathbf{x} = \mathbf{x}_j$. Equation 3.55 can be rewritten in the following matrix form:

$$\mathbf{d}_e = \mathbf{P}_Q \mathbf{a}, \tag{3.56}$$

where $\mathbf{d}_e$ is the vector that collects the values of the field function at all the n_n^e nodes of the element,

$$\mathbf{d}_e = \begin{Bmatrix} u_1 & u_2 & \cdots & u_{n_n^e} \end{Bmatrix}^T, \tag{3.57}$$

and $\mathbf{P}_Q$ is called the *moment matrix* given by

$$\mathbf{P}_Q = \begin{bmatrix} \mathbf{p}^T(\mathbf{x}_1) \\ \mathbf{p}^T(\mathbf{x}_2) \\ \vdots \\ \mathbf{p}^T\left(\mathbf{x}_{n_n^e}\right) \end{bmatrix}. \tag{3.58}$$

The moment matrix $\mathbf{P}_Q$ is asymmetric. Assuming that the inverse of the moment matrix $\mathbf{P}_Q$ exists, and using Equation 3.56, we have

$$\mathbf{a} = \mathbf{P}_Q^{-1}\mathbf{d}_e. \tag{3.59}$$

Substituting Equation 3.59 into Equation 3.48, we obtain

$$\tilde{u}(\mathbf{x}) = \sum_{I=1}^{n_n^e} N_I^e(\mathbf{x}) u_I, \tag{3.60}$$

where N_I^e is the shape function for node I of the element. Equation 3.60 can be written in matrix form as

$$\tilde{u}(\mathbf{x}) = \mathbf{N}^e(\mathbf{x})\mathbf{d}_e, \tag{3.61}$$

where $\mathbf{N}^e(\mathbf{x})$ is a matrix of the shape functions for the element defined by

$$\mathbf{N}^e(\mathbf{x}) = \mathbf{p}^T(\mathbf{x})\mathbf{P}_Q^{-1} = \begin{bmatrix} N_1^e(\mathbf{x}) & N_2^e(\mathbf{x}) & \cdots & N_{n_n^e}^e(\mathbf{x}) \end{bmatrix}. \tag{3.62}$$

By simply joining together all the shape functions $N_I^e(\mathbf{x})$ of the first layer of elements sharing node I, we can obtain the nodal shape functions $N_I(\mathbf{x})$ for node I. In other words, $N_I^e(\mathbf{x})$ is a piece of $N_I(\mathbf{x})$. In actual implementation of FEM, $N_I^e(\mathbf{x})$ is often used, but in the formulation, $N_I(\mathbf{x})$ is much more convenient.

Using linear polynomial basis functions, linear shape functions can be easily created following the above-mentioned procedure. Figure 3.3 illustrates a typical nodal shape function $N_I(\mathbf{x})$ for the node at x_I for linear elements in a 1D problem domain. Figure 3.4 plots a typical nodal shape function $N_I(\mathbf{x})$ for the node at $\mathbf{x}_I$ for linear triangular elements in a 2D problem domain. These nodal shape functions are locally supported only by elements sharing the nodes, piecewise linear and continuous. They are all in $\mathbb{H}^1(\Omega;\mathbb{R}^d)$ space, as examined in Example 3.4, and can be used for the construction of FEM models.

Note that the moment matrix $\mathbf{P}_Q$ can be singular depending on the shape and nodal arrangement of the element. For often-used types of elements we know well how to prevent this from happening [5]. For any attempt to form new types of elements, care must be taken.

The above procedure gives shape functions for one component displacement function and for each element. The nodal shape function for a node can then be formed easily by simply joining the element shape functions

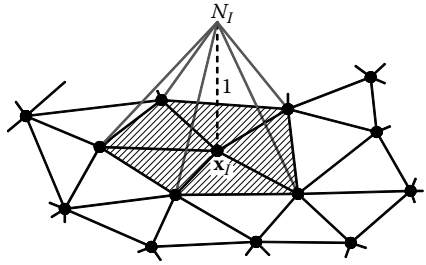

FIGURE 3.3 Nodal shape function N_I for the node at x_I for linear elements in a 1D domain.

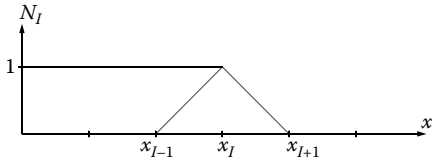

FIGURE 3.4 Nodal shape function N_I for the node at $\mathbf{x}_I$ for linear triangular elements in a 2D domain.

for all the elements surrounding the node. Note that in the standard FEM, we require the nodal shape function to be continuous, not only within the element but also on the interfaces of elements surrounding the node [in a proper $\mathbb{H}^1(\Omega;\mathbb{R}^d)$ space]. To ensure continuity (or compatibility), we perform coordination transformation or mapping to map for each element in the physical coordinate system into a so-called *natural* coordinate system, under which the element becomes a regular square (or cub). Therefore, under such a natural coordinate system the shape functions can be constructed with ease and the moment matrix will never be singular with the proper selection of polynomial basis terms. In addition, the continuity of the nodal shape function can now be ensured. Elements formulated using shape functions constructed in natural coordinates and using a coordinate mapping (using the same shape function) are so-called isoparametric elements. Detailed forms of such isoparametric Q4, H8 elements will be provided in separate sections later in this chapter.

Apart from the general procedure mentioned above, there are some "shortcut" approaches in developing shape functions for FEM elements. In such shortcut approaches we need to use the basic properties of shape functions.

3.5.2 Basic Conditions for Nodal Shape Functions

For node I, the nodal shape function $N_I(\mathbf{x})$ satisfies the following conditions given in precise mathematical definitions:

$$
\begin{aligned}
&N_I(\mathbf{x}) \in \mathbb{H}^1(\Omega;\mathbb{R}^1) \text{ (bounded and continuous in } \Omega),\\
&N_I(\mathbf{x}) \text{ is nonzero only within elements connected to node } I \\
&\quad \text{(compact support)},\\
&N_I(\mathbf{x}_J) = \delta_{IJ} \text{(Delta function property)},\\
&\sum_{I=1}^{n_n^e} N_I(\mathbf{x}) = 1 \text{ (partition of unity)},\\
&\sum_{I=1}^{n_n^e} N_I(\mathbf{x})\mathbf{x}_I = \mathbf{x} \text{ (linear consistency)},
\end{aligned}
\tag{3.63}
$$

where δ_{IJ} is the Kronecker Delta; n_n^e is the number of nodes of the element that hosts $\mathbf{x}$, and $\mathbf{x}_I$ is the coordinate of the Ith node of the element hosting $\mathbf{x}$.

3.6 Displacement Function Creation

We now need to create functions in $\mathbb{H}^1_{0,h}(\Omega;\mathbb{R}^d)$ for the construction of displacement fields. Because the nodal shape functions are linearly independent, it qualifies as a basis to form a space for an FEM model. An assumed displacement function for each displacement component can be expressed as a linear combination of the nodal shape functions with the nodal displacements as the coefficients. The finite element space $\mathbb{H}^1_{0,h}(\Omega;\mathbb{R}^d)$ can be spanned by the N_n independent nodal basis shape functions $\mathbf{N}_1, \mathbf{N}_2, \ldots, \mathbf{N}_{N_n}$:

$$\mathbb{H}^1_{0,h}(\Omega;\mathbb{R}^d) = \text{span}\{\mathbf{N}_I\}_{I=1}^{N_n}, \tag{3.64}$$

where $\mathbf{N}_I(\mathbf{x})$ is the matrix of shape functions. For example, for 2D problems, we have $\mathbf{N}_I(\mathbf{x}) = \begin{bmatrix} N_I(\mathbf{x}) & 0 \\ 0 & N_I(\mathbf{x}) \end{bmatrix}$, where each $N_I(\mathbf{x})$ is for one displacement component. The finite solution $\tilde{\mathbf{u}}$ should be in space $\mathbb{H}^1_{0,h}(\Omega;\mathbb{R}^d)$, and hence should have the form

$$\tilde{\mathbf{u}} = \sum_{I=1}^{N_n} \mathbf{N}_I(\mathbf{x})\tilde{\mathbf{d}}_I = \underbrace{\begin{bmatrix}\mathbf{N}_1(\mathbf{x}) & \mathbf{N}_2(\mathbf{x}) & \cdots & \mathbf{N}_{N_n}(\mathbf{x})\end{bmatrix}}_{\mathbf{N}(\mathbf{x})} \underbrace{\begin{Bmatrix}\tilde{\mathbf{d}}_1 \\ \tilde{\mathbf{d}}_2 \\ \vdots \\ \tilde{\mathbf{d}}_{N_n}\end{Bmatrix}}_{\tilde{\mathbf{d}}} = \mathbf{N}(\mathbf{x})\tilde{\mathbf{d}}, \tag{3.65}$$

where $\mathbf{x} = \{x_1 \ \cdots \ x_d\}^T$ and $\tilde{\mathbf{d}}_I = \tilde{\mathbf{u}}(\mathbf{x}_I)$, which is the nodal displacement vector at node I of the FEM solution.

Remark 3.2 Sparseness of the Shape Function Matrix

Because $\mathbf{N}_I(\mathbf{x})$ for node I is locally supported by elements sharing the node, it is zero beyond these elements. For any $\mathbf{x} \in \Omega_i^e \subset \Omega$, the ith element will have a very small number of nodes (e.g., 3 for T3 elements). Therefore, $\tilde{\mathbf{u}}(\mathbf{x})$ in Equation 3.65 relates only a small number of nodal shape functions, and hence the shape function matrix $\mathbf{N}(\mathbf{x})$ will be an extremely *sparse* matrix with lots of zeros for an actual model that usually has a large number of nodes.

The expression of $\tilde{\mathbf{u}}(\mathbf{x})$ in Equation 3.65 using all the field nodes is only for convenience in the expressions in FEM formulations; it needs only the nodes of the element hosting $\mathbf{x}$.

3.7 Strain Evaluation

Using Equation 3.65 and the strain–displacement relation (Equation 2.10), we obtain the (compatible) strains as

$$\tilde{\boldsymbol{\varepsilon}} = \mathbf{L}_d \tilde{\mathbf{u}} = \sum_{I=1}^{N_n} \underbrace{\mathbf{L}_d \mathbf{N}_I(\mathbf{x})}_{\tilde{\mathbf{B}}_I(\mathbf{x})} \tilde{\mathbf{d}}_I$$

$$= \underbrace{\begin{bmatrix} \tilde{\mathbf{B}}_1(\mathbf{x}) & \tilde{\mathbf{B}}_2(\mathbf{x}) & \cdots & \tilde{\mathbf{B}}_{N_n}(\mathbf{x}) \end{bmatrix}}_{\tilde{\mathbf{B}}(\mathbf{x})} \underbrace{\begin{Bmatrix} \tilde{\mathbf{d}}_1 \\ \tilde{\mathbf{d}}_2 \\ \vdots \\ \tilde{\mathbf{d}}_{N_n} \end{Bmatrix}}_{\tilde{\mathbf{d}}} = \tilde{\mathbf{B}}(\mathbf{x}) \tilde{\mathbf{d}}, \tag{3.66}$$

where $\tilde{\mathbf{B}}_I(\mathbf{x})$ is the "strain–displacement matrix" for node I, which is given by

$$\tilde{\mathbf{B}}_I(\mathbf{x}) = \mathbf{L}_d \mathbf{N}_I(\mathbf{x}) = \begin{cases} \begin{bmatrix} \partial N_I(\mathbf{x})/\partial x & 0 \\ 0 & \partial N_I(\mathbf{x})/\partial y \\ \partial N_I(\mathbf{x})/\partial y & \partial N_I(\mathbf{x})/\partial x \end{bmatrix} & \text{for 2D,} \\ \begin{bmatrix} \partial N_I(\mathbf{x})/\partial x & 0 & 0 \\ 0 & \partial N_I(\mathbf{x})/\partial y & 0 \\ 0 & 0 & \partial N_I(\mathbf{x})/\partial z \\ 0 & \partial N_I(\mathbf{x})/\partial z & \partial N_I(\mathbf{x})/\partial y \\ \partial N_I(\mathbf{x})/\partial z & 0 & \partial N_I(\mathbf{x})/\partial x \\ \partial N_I(\mathbf{x})/\partial y & \partial N_I(\mathbf{x})/\partial x & 0 \end{bmatrix} & \text{for 3D.} \end{cases} \tag{3.67}$$

Because the use of $\tilde{\mathbf{B}}_I(\mathbf{x})$ in Equation 3.66 and the nodal displacements gives the strains, $\tilde{\mathbf{B}}_I(\mathbf{x})$ is often called "strain matrix" for short. The global strain–displacement matrix can be given by

$$\tilde{\mathbf{B}}(\mathbf{x}) = \mathbf{L}_d \mathbf{N}(\mathbf{x}). \tag{3.68}$$

It is clear that because of the sparseness of the shape function matrix $\mathbf{N}(\mathbf{x})$, $\tilde{\mathbf{B}}(\mathbf{x})$ will also be very sparse.

3.8 Formulation of the Discretized System of Equations

Using Equation 3.37, the FEM weak statement for our discrete system becomes

$$\text{Find } \tilde{\mathbf{u}} \in \mathbb{H}^1_{0,h}(\Omega;\mathbb{R}^d) \text{ such that } a\left(\tilde{\mathbf{u}}, \mathbf{v}^h\right) = f(\mathbf{v}^h), \quad \forall \mathbf{v}^h \in \mathbb{H}^1_{0,h}(\Omega;\mathbb{R}^d). \tag{3.69}$$

Substituting Equation 3.65 as the trial function and setting $\mathbf{N}_I(\mathbf{x})$, $I = 1,\ldots,N_n$, as the test function $\mathbf{v}^h$ into Equation 3.69, we have the following system of N_n equations:

$$\sum_{J=1}^{N_n} a(\mathbf{N}_J, \mathbf{N}_I)\tilde{\mathbf{d}}_J = f(\mathbf{N}_I), \quad I = 1,\ldots,N_n, \tag{3.70}$$

which can be written as the standard matrix form of discretized algebraic equations:

$$\tilde{\mathbf{K}}\tilde{\mathbf{d}} = \tilde{\mathbf{f}}, \tag{3.71}$$

where $\tilde{\mathbf{d}}$ is the vector of nodal displacements for all the nodes in the entire problem domain, and $\tilde{\mathbf{K}}$ is the global stiffness matrix of the FEM model that can be expressed simply as

$$\tilde{\mathbf{K}} = \int_{\Omega} \tilde{\mathbf{B}}^T \mathbf{c} \tilde{\mathbf{B}} \, \mathrm{d}\Omega. \tag{3.72}$$

Because of the sparseness of $\tilde{\mathbf{B}}$, we will not actually use Equation 3.72 to compute $\tilde{\mathbf{K}}$. Instead, we evaluate the entries of $\tilde{\mathbf{K}}$ using

$$\tilde{\mathbf{K}}_{IJ} = \int_{\Omega} \tilde{\mathbf{B}}_I^T \mathbf{c} \tilde{\mathbf{B}}_J \, \mathrm{d}\Omega = \sum_{i=1}^{N_e} \underbrace{\int_{\Omega_i^e} \tilde{\mathbf{B}}_I^T \mathbf{c} \tilde{\mathbf{B}}_J \, \mathrm{d}\Omega}_{\tilde{\mathbf{K}}^e_{IJ,i}}. \tag{3.73}$$

This conversion of problem domain integration to the sum of elemental integrations is possible, because $\tilde{\mathbf{u}} \in \mathbb{H}^1_{0,h}(\Omega;\mathbb{R}^d)$ and because of the forgiving property of Lebesgue integration (see Remark 3.1). From Equation 3.73, it is seen that the actual evaluation of matrices $\tilde{\mathbf{K}}_{IJ}$ becomes the evaluation of matrices for each element. Condition (ii) in Equation 3.63 leads to $\tilde{\mathbf{K}}^e_{IJ,i} = 0$

for nodes I and J that are not attached to the same Ω_i^e, which means that the stiffness matrix will be sparse. The integration in Equation 3.73 can be performed effectively using the Gauss integration technique as presented in Section 3.15.

The vector $\tilde{\mathbf{f}}$ is the external force vector acting at all the nodes in the entire problem domain, with entries of

$$\begin{aligned}\tilde{\mathbf{f}}_I &= \int_{\Omega} \mathbf{N}_I^T(\mathbf{x})\mathbf{b}\,\mathrm{d}\Omega + \int_{\Gamma_t} \mathbf{N}_I^T(\mathbf{x})\mathbf{t}\,\mathrm{d}\Gamma \\ &= \sum_{i=1}^{N_e} \int_{\Omega_i^e} \mathbf{N}_I^T(\mathbf{x})\mathbf{b}\,\mathrm{d}\Omega + \sum_{i=1}^{N_e} \int_{\Gamma_{t,i}^e} \mathbf{N}_I^T(\mathbf{x})\mathbf{t}\,\mathrm{d}\Gamma, \end{aligned} \tag{3.74}$$

which can be evaluated in a similar way as for the stiffness matrix.

Once Equation 3.71 is obtained, the vector of nodal displacements $\tilde{\mathbf{d}}$ can be solved easily, as long as $\tilde{\mathbf{K}}$ is not singular. The strains and stresses in each element can be retrieved using the displacements obtained. Recovery procedures can also be performed to improve the accuracy of the strain and stress fields. However, such a recovery procedure will not improve the displacement solution.

As presented above, the formulation of FEM is in fact quite straightforward for solid mechanics problems. However, implementation of FEM to practical problems, formulations for mechanics of structures (beams, plates, shells, crack-tip elements, etc.), heat transfer and acoustic problems, issues related to actual modeling techniques, virtualization of computed numerical data, and application of FEM results to actual design problems can be quite intensive. This book will not pursue these issues any further. Readers may refer to the dedicated book [5] for more details.

We shall now address the following more theoretical and fundamental questions related to discrete FEM models:

- Can the FEM procedure ensure the *existence* and *uniqueness* of the solution ($\tilde{\mathbf{K}}$ is indeed not singular)?
- How does the solution depend on input data? Can we obtain solutions for any type of loading/forces?
- How does one *estimate* the error in the FEM solution?
- What is the *rate of convergence* of FEM solutions when the mesh is refined?

The following section provides answers to all these questions.

3.9 FEM Solution: Existence, Uniqueness, Error, and Convergence

Based on the theory of functional analysis [3,6], we now discuss some important properties, inequalities, and theorems for FEM.

Theorem 3.2: Existence, Uniqueness, and Stability

Let $\mathbb{H}^1_{0,h}(\Omega;\mathbb{R}^d)$ be a finite-dimensional subspace of the Hilbert space $\mathbb{H}^1_0(\Omega;\mathbb{R}^d)$, $a : \mathbb{H}^1_{0,h}(\Omega;\mathbb{R}^d) \times \mathbb{H}^1_{0,h}(\Omega;\mathbb{R}^d) \to \mathbb{R}$ a continuous, $\mathbb{H}$-elliptic bilinear form, and $f : \mathbb{H}^1_{0,h}(\Omega;\mathbb{R}^d) \to \mathbb{R}$ a bounded linear functional. Then there exists a unique function $\tilde{\mathbf{u}} \in \mathbb{H}^1_{0,h}(\Omega;\mathbb{R}^d)$ that satisfies the discrete weak statement 3.69. Furthermore, if $f(\tilde{\mathbf{u}})$ is of the form

$$f(\tilde{\mathbf{u}}) = \int_{\Omega} \tilde{\mathbf{u}}^T \mathbf{b}\, d\Omega + \int_{\Gamma_t} \tilde{\mathbf{u}}^T \mathbf{t}\, d\Gamma, \tag{3.75}$$

with $\mathbf{b} \in \mathbb{L}^2(\Omega;\mathbb{R}^d)$ and $\mathbf{t} \in \mathbb{L}^2(\Gamma_t;\mathbb{R}^d)$, then

$$\|\tilde{\mathbf{u}}\|_{\mathbb{H}^1(\Omega;\mathbb{R}^d)} \leq C_5 \left(\|\mathbf{b}\|_{\mathbb{L}^2(\Omega;\mathbb{R}^d)} + \|\mathbf{t}\|_{\mathbb{L}^2(\Gamma_t;\mathbb{R}^d)} \right), \tag{3.76}$$

where C_5 is a constant.

Theorem 3.2 provides the answer to the question of the existence and uniqueness of the FEM solution. In addition, the stability estimate (Equation 3.76) for the finite element solution, which is similar to the stability estimate (Equation 3.46) for continuous problems, reflects a very important property of FEM. It assures us that a small change in the linear functional $f(\tilde{\mathbf{u}})$ results correspondingly in only a "small" change in the solution $\tilde{\mathbf{u}} \in \mathbb{H}^1_{0,h}(\Omega;\mathbb{R}^d)$. In other words, the solution $\tilde{\mathbf{u}} \in \mathbb{H}^1_{0,h}(\Omega;\mathbb{R}^d)$ depends continuously on the data $f(\tilde{\mathbf{u}})$. This implies that our numerical problem is well posed, under conditions for both model creation and inputs (external forces) specified in Theorem 3.2.

Note that the continuity of the bilinear form a requires the original problem to be well posed physically: for solid mechanics problems, the material must be stable (see Remark 2.1). A detailed proof on this can be found in Ref. [11]. The $\mathbb{H}$-ellipticity of the bilinear form a also requires a stable material [11] and proper essential boundary conditions to at least constrain all the rigid movements.

We next proceed to examine the error $\mathbf{e} = \mathbf{u} - \tilde{\mathbf{u}}$, which is the difference between the exact and FEM solutions. We state the following theorem.

Theorem 3.3: "Best" Approximation

Let $\mathbf{u} \in \mathbb{H}_0^1(\Omega;\mathbb{R}^d)$ be the exact solution of the original problem governed by equilibrium equations 2.7 and boundary conditions 2.23 and 2.24, and $\tilde{\mathbf{u}} \in \mathbb{H}_{0,h}^1(\Omega;\mathbb{R}^d)$ be the finite element solution of the weak formulation (Equation 3.37), where $\mathbb{H}_{0,h}^1(\Omega;\mathbb{R}^d) \subset \mathbb{H}_0^1(\Omega;\mathbb{R}^d)$. Then

$$\left\|\mathbf{u}-\tilde{\mathbf{u}}\right\|_{\mathbb{H}^1(\Omega;\mathbb{R}^d)} \leq C_6 \left\|\mathbf{u}-\mathbf{v}^h\right\|_{\mathbb{H}^1(\Omega;\mathbb{R}^d)}, \quad \forall \mathbf{v}^h \in \mathbb{H}_{0,h}^1(\Omega;\mathbb{R}^d), \tag{3.77}$$

where C_6 is a constant independent of $\mathbf{v}^h$.

Theorem 3.3 implies that the approximation $\tilde{\mathbf{u}} \in \mathbb{H}_{0,h}^1(\Omega;\mathbb{R}^d)$ is the "best" possible approximation of the exact solution among all functions $\mathbf{v}^h \in \mathbb{H}_{0,h}^1(\Omega;\mathbb{R}^d)$, in the sense that $\|\mathbf{u}-\mathbf{v}^h\|_{\mathbb{H}^1(\Omega;\mathbb{R}^d)}$, $\forall \mathbf{v}^h \in \mathbb{H}_{0,h}^1(\Omega;\mathbb{R}^d)$, is always larger than or equal to $\|\mathbf{u}-\tilde{\mathbf{u}}\|_{\mathbb{H}^1(\Omega;\mathbb{R}^d)}$: the FEM solution $\tilde{\mathbf{u}}$ is the "best" possible function among all the functions in $\mathbb{H}_{0,h}^1(\Omega;\mathbb{R}^d)$, in the measure of norm $\|\cdot\|_{\mathbb{H}^1(\Omega;\mathbb{R}^d)}$.

In addition, this optimal feature of the FEM solution allows us to find a quantitative estimate of the bound of the solutions error in norm $\|\cdot\|_{\mathbb{H}^1(\Omega;\mathbb{R}^d)}$, by choosing a suitable function $\mathbf{v}^h \in \mathbb{H}_{0,h}^1(\Omega;\mathbb{R}^d)$ and estimating $\|\mathbf{u}-\mathbf{v}^h\|_{\mathbb{H}^1(\Omega;\mathbb{R}^d)}$. Usually, one chooses $\mathbf{v}^h = \mathcal{I}_h\mathbf{u}$, where $\mathcal{I}_h\mathbf{u} \in \mathbb{H}_{0,h}^1(\Omega;\mathbb{R}^d)$ is a suitable *interpolant* of $\mathbf{u} \in \mathbb{H}_0^1(\Omega;\mathbb{R}^d)$. This further leads to Theorem 3.4.

Remark 3.3 "Best" But There are Still Rooms

It may be noted that the "best" may be quite misleading. It is *only* the best in the form of Equation 3.77. First, the measure is in the norm $\|\cdot\|_{\mathbb{H}^1(\Omega;\mathbb{R}^d)}$, and if the norm of measure changes, the FEM solution $\tilde{\mathbf{u}}$ may not be still the best. Second, Equation 3.77 is with a constant C_6. Therefore, there are in fact a lot of "rooms" for other possible "bests." The S-FEM models explore these rooms.

Theorem 3.4: h-Dependence

Let $\mathbf{u}$ be the exact solution of the original problem governed by equilibrium equations 2.7 and boundary conditions 2.23 and 2.24. If Ω is a convex polygonal domain and $\tilde{\mathbf{u}} \in \mathbb{H}_{0,h}^1(\Omega;\mathbb{R}^d) \subset \mathbb{H}_0^1(\Omega;\mathbb{R}^d)$ is the finite element solution using interpolation with piecewise linear functions that satisfies the discrete weak statement (Equation 3.66), then there exist constants C_7, C_8 independent of $\mathbf{u}$ and h such that

$$\left\|\mathbf{u}-\tilde{\mathbf{u}}\right\|_{\mathbb{L}^2(\Omega;\mathbb{R}^d)} \leq C_7 h^2 \left|\mathbf{u}\right|_{\mathbb{H}^2(\Omega;\mathbb{R}^d)} \tag{3.78}$$

and

$$\left\|\mathbf{u}-\tilde{\mathbf{u}}\right\|_{\mathbb{H}^1(\Omega;\mathbb{R}^d)} \leq C_8 h \left|\mathbf{u}\right|_{\mathbb{H}^2(\Omega;\mathbb{R}^d)}, \tag{3.79}$$

where $|\mathbf{u}|_{\mathbb{H}^2(\Omega;\mathbb{R}^d)}$ is a seminorm. For 2D problems, it can be written explicitly from Equation 3.18 as

$$|\mathbf{u}|_{\mathbb{H}^2(\Omega;\mathbb{R}^d)} = \left[\int_\Omega \left(\left|\frac{\partial^2 \mathbf{u}}{\partial x^2}\right|^2 + 2\left|\frac{\partial^2 \mathbf{u}}{\partial x \partial y}\right| + \left|\frac{\partial^2 \mathbf{u}}{\partial y^2}\right|^2\right) \mathrm{d}\Omega\right]^{1/2}. \tag{3.80}$$

From Theorem 3.4, we have qualitative information that $\left\|\mathbf{u}-\tilde{\mathbf{u}}\right\|_{\mathbb{L}^2(\Omega;\mathbb{R}^d)}$ and $\left\|\mathbf{u}-\tilde{\mathbf{u}}\right\|_{\mathbb{H}^1(\Omega;\mathbb{R}^d)}$ approach zero when the size of element h approaches zero if the second-order derivative of the exact solution $\mathbf{u}$ is bounded on domain Ω. In addition, the power of h in Equations 3.78 and 3.79 also shows the theoretical convergence rate of finite element solutions in the corresponding norms. For problems of second-order PDEs as shown in Equation 2.7 with boundary conditions 2.23 and 2.24, the theoretical convergence rate of displacement $\tilde{\mathbf{u}}$ is 2 in the norm $\|\cdot\|_{\mathbb{L}^2(\Omega;\mathbb{R}^d)}$, and the theoretical convergence rate of the first derivative of $\tilde{\mathbf{u}}$ is 1 in the norm $\|\cdot\|_{\mathbb{H}^1(\Omega;\mathbb{R}^d)}$. In practice, these convergence rates also depend on the regularity of the exact solution $\mathbf{u}$, as shown in the right-hand sides of Equations 3.78 and 3.79. For example, for problems with singularities (at re-entrant and crack tips), the practical convergence rates may become smaller than the theoretical convergence rates [3,6]. We will see such cases in Chapter 10.

In the practical computation of solid mechanics, the norm $\left\|\mathbf{u}-\tilde{\mathbf{u}}\right\|_{\mathbb{H}^1(\Omega;\mathbb{R}^d)}$ is usually replaced by the seminorm $\left|\mathbf{u}-\tilde{\mathbf{u}}\right|_{\mathbb{H}^1(\Omega;\mathbb{R}^d)}$, which relates the total energy of the error between approximate and exact solutions over the whole domain; the norm $\left\|\mathbf{u}-\tilde{\mathbf{u}}\right\|_{\mathbb{L}^2(\Omega;\mathbb{R}^d)}$ represents the total error measured in norm $\|\cdot\|_{\mathbb{L}^2(\Omega;\mathbb{R}^d)}$ between the approximated and exact solutions in displacement. Generalization of the above theory of FEM for interpolation with polynomials of higher order can be found in Refs. [3,6], and hence will not be discussed in this book.

3.10 Some Other Properties of the FEM Solution

Property 3.1 Fully Compatible Property

An FEM model created strictly following the weak statement (Equation 3.69) is said to be fully compatible. Essentially a fully compatible FEM model is established using (1) compatible displacements: the approximated

displacements should be continuous on element interfaces and differentiable inside the elements; (2) compatible strain fields that are obtained using the strain–displacement relation; and (3) essential boundary conditions. In addition, we require, of course, that all the integrations in weak form have to be evaluated exactly. For discrete models, the integrations are usually evaluated using Gauss integration (see Section 3.15).

Remark 3.4 "Fully" or "Partially" Compatible: A Difference between FEM and S-FEM

Throughout this book, when an FEM model is used, it is by default fully compatible. Such an FEM model is also said to be *standard*. For convenience, when we say "a compatible FEM model" it means "a fully compatible FEM model." On the contrary, S-FEM models are only "partially" compatible: the displacement field in an S-FEM is compatible, but the strain field is not. This difference will be made clear and precise in later chapters.

Property 3.2 Lower Bound Property

The strain energy solution of a fully compatible FEM model of a force-driven problem is a lower bound of the exact strain energy

$$\tilde{E}\left(\tilde{\boldsymbol{\varepsilon}}\right) = \frac{1}{2}a\left(\tilde{\mathbf{u}},\tilde{\mathbf{u}}\right) \leq \frac{1}{2}a(\mathbf{u},\mathbf{u}) = E(\boldsymbol{\varepsilon}), \tag{3.81}$$

where $\tilde{\varepsilon} = \mathbf{L}_d\tilde{\mathbf{u}}$ is the strain obtained using FEM displacements $\tilde{\mathbf{u}} \in \mathbb{H}^1_{0,h}(\Omega;\mathbb{R}^d) \subset \mathbb{H}^1_0(\Omega;\mathbb{R}^d)$, $\boldsymbol{\varepsilon} = \mathbf{L}_d\mathbf{u}$ is the exact strain obtained using exact displacements $\mathbf{u} \in \mathbb{H}^1_0(\Omega;\mathbb{R}^d)$, and $E(\boldsymbol{\varepsilon})$ is the exact strain energy of the system defined as

$$E(\boldsymbol{\varepsilon}) = \frac{1}{2}\int_\Omega \boldsymbol{\varepsilon}^T\mathbf{c}\boldsymbol{\varepsilon}\,\mathrm{d}\Omega. \tag{3.82}$$

For the FEM model, strain energy can be evaluated using

$$\tilde{E}\left(\tilde{\boldsymbol{\varepsilon}}\right) = \frac{1}{2}\int_\Omega \tilde{\boldsymbol{\varepsilon}}^T\mathbf{c}\tilde{\boldsymbol{\varepsilon}}\,\mathrm{d}\Omega = \frac{1}{2}a\left(\tilde{\mathbf{u}},\tilde{\mathbf{u}}\right) = \frac{1}{2}\tilde{\mathbf{d}}^T\tilde{\mathbf{K}}\tilde{\mathbf{d}}, \tag{3.83}$$

and for the exact model we should have

$$E(\boldsymbol{\varepsilon}) = \frac{1}{2}\int_\Omega \boldsymbol{\varepsilon}^T\mathbf{c}\boldsymbol{\varepsilon}\,\mathrm{d}\Omega = \frac{1}{2}a(\mathbf{u},\mathbf{u}). \tag{3.84}$$

The proof of the lower bound property can be found in Refs. [2,12] in variational formulation. The lower bound property implies the well-known fact that the FEM solution underestimates the strain energy. This property of FEM provides a good global measure of the lower bound of the FEM solution with respect to the exact solution.

Property 3.3 Monotonic Convergence Property

For a given sequence of n_m *nested* element meshes $M_1, M_2, \ldots, M_{n_m}$, such that the corresponding solution spaces satisfy $\mathbb{H}^1_{0,M_1}(\Omega;\mathbb{R}^d) \subset \mathbb{H}^1_{0,M_2}(\Omega;\mathbb{R}^d) \cdots \subset \mathbb{H}^1_{0,M_{n_m}}(\Omega;\mathbb{R}^d) \subset \mathbb{H}^1_0(\Omega;\mathbb{R}^d)$, the strain energy solutions have the following inequalities:

$$\tilde{E}\left(\tilde{\boldsymbol{\varepsilon}}^{M_1}\right) \leq \tilde{E}\left(\tilde{\boldsymbol{\varepsilon}}^{M_2}\right) \leq \cdots \leq \tilde{E}\left(\tilde{\boldsymbol{\varepsilon}}^{M_{nm}}\right) \leq E(\boldsymbol{\varepsilon})\,, \tag{3.85}$$

where $\tilde{\boldsymbol{\varepsilon}}^{M_i}$ is the (fully) compatible FEM solution of strains obtained using mesh M_i. This property can be shown easily using the arguments given by Oliveira [13].

Property 3.4 Reproducibility of the Exact Solution

If the exact solution $\mathbf{u} \in \mathbb{H}^1_{0,h}(\Omega;\mathbb{R}^d) \subset \mathbb{H}^1_0(\Omega;\mathbb{R}^d)$, then the compatible FEM will reproduce the exact solution $\mathbf{u}$. This property can be easily proved [5,13].

In the following sections, we present the simplest but most popular finite elements that are widely used for practical engineering problems. These elements will also be used frequently throughout this book, and are the base for creating our S-FEM models.

3.11 Linear Triangular Element (T3)

The linear triangular element is the simplest element of all the FEM elements for 2D problems. It has three nodes and three edges and is often referred to as T3 element, as shown in Figure 3.5. In addition to its simplicity, the T3 element adapts very well to complicated geometries, and is the only 2D element that can be generated automatically for arbitrarily shaped domains without any manual intervention in the meshing process. Because of these excellent features, T3 elements are the most preferred elements to many engineering analysts, despite their shortcomings on poor accuracy in stresses. Our smoothed FEM models will be largely based on T3 elements for 2D problems, and are designed to overcome their poor stress accuracy and to have many additional properties. The following gives the details of the FEM formulation of T3 elements.

3.11.1 Shape Functions

Let $\tilde{\mathbf{u}}_i^e$ be the displacement at any point in a three-node triangular element Ω_i^e, as shown in Figure 3.5. Using the displacements at nodes and shape

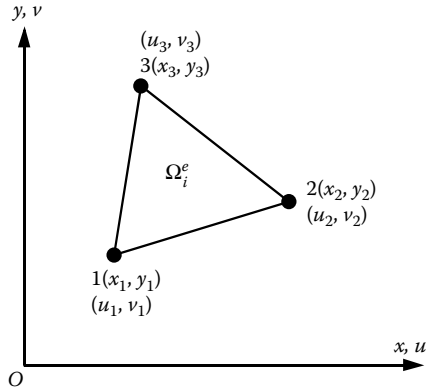

FIGURE 3.5 Three-node triangular elements in the physical Cartesian coordinate system Oxy.

functions, the displacement field within the element can be approximated using

$$\tilde{\mathbf{u}}_i^e = \mathbf{N}_i^e(\mathbf{x})\tilde{\mathbf{d}}_i^e, \tag{3.86}$$

where $\tilde{\mathbf{d}}_i^e$ is the vector of nodal displacements arranged in the order of

$$\tilde{\mathbf{d}}_i^e = \begin{Bmatrix} u_1 \\ v_1 \end{Bmatrix} \text{ displacements at node 1 of the element } \Omega_i^e$$
$$\begin{Bmatrix} u_2 \\ v_2 \end{Bmatrix} \text{ displacements at node 2 of the element } \Omega_i^e \quad , \tag{3.87}$$
$$\begin{Bmatrix} u_3 \\ v_3 \end{Bmatrix} \text{ displacements at node 3 of the element } \Omega_i^e$$

and the matrix of shape functions $\mathbf{N}_i^e(\mathbf{x})$ is arranged as

$$\mathbf{N}_i^e(\mathbf{x}) = \left[\underbrace{\begin{matrix} N_1 & 0 \\ 0 & N_1 \end{matrix}}_{\text{Node 1}} \quad \underbrace{\begin{matrix} N_2 & 0 \\ 0 & N_2 \end{matrix}}_{\text{Node 2}} \quad \underbrace{\begin{matrix} N_3 & 0 \\ 0 & N_3 \end{matrix}}_{\text{Node 3}} \right], \tag{3.88}$$

in which $N_j\,(j = 1, 2, 3)$ are three shape functions corresponding to three nodes of the triangular element as shown in Figure 3.4. Using directly the physical Cartesian coordinate system Oxy and following the procedure given in Section 3.5.1 or using the Delta function and partition of unity

properties of the shape functions given in Section 3.5.2, these three shape functions can be easily found as [5]

$$\begin{aligned} N_1 &= \frac{1}{2A_i^e}\left[\left(x_2y_3 - x_3y_2\right) + \left(y_2 - y_3\right)x + \left(x_3 - x_2\right)y\right], \\ N_2 &= \frac{1}{2A_i^e}\left[\left(x_3y_1 - x_1y_3\right) + \left(y_3 - y_1\right)x + \left(x_1 - x_3\right)y\right], \\ N_3 &= \frac{1}{2A_i^e}\left[\left(x_1y_2 - x_2y_1\right) + \left(y_1 - y_2\right)x + \left(x_2 - x_1\right)y\right], \end{aligned} \tag{3.89}$$

where x_j and y_j $(j = 1, 2, 3)$ are the coordinate values at the jth node as shown in Figure 3.5, and A_i^e is the area of the linear triangular element Ω_i^e that can be computed using

$$A_i^e = \frac{1}{2}\det\begin{bmatrix} 1 & x_1 & y_1 \\ 1 & x_2 & y_2 \\ 1 & x_3 & y_3 \end{bmatrix}. \tag{3.90}$$

In concise form, Equation 3.89 can be rewritten as

$$N_j = a_j + b_j x + c_j y \tag{3.91}$$

with

$$a_j = \frac{1}{2A_i^e}\left(x_k y_l - x_l y_k\right), \quad b_j = \frac{1}{2A_i^e}\left(y_k - y_l\right), \quad c_j = \frac{1}{2A_i^e}\left(x_l - x_k\right), \tag{3.92}$$

where subscript j varies from 1 to 3, and k and l are determined by cyclic permutation in the order of j, k, l. For example, if $j = 1$, then $k = 2$, $l = 3$; or if $j = 2$, then $k = 3$, $l = 1$.

Figure 3.4 shows a typical nodal shape function over surrounding elements. It is clear that the shape functions given in Equation 3.89 satisfy all the conditions listed in Section 3.5.2. We also note that the construction of shape functions for triangular elements will never fail, as long as the area of the element is not zero or these three nodes are not in-line. This means that the T3 elements are very robust.

3.11.2 Strain–Displacement Matrix

Using directly the physical Cartesian coordinate system Oxy and the strain–displacement relation (Equation 2.10), the strain–displacement matrix $\tilde{\mathbf{B}}_i^e$ for the linear triangular element Ω_i^e has the simple form of

$$\tilde{\mathbf{B}}_i^e = \begin{bmatrix} b_1 & 0 & b_2 & 0 & b_3 & 0 \\ 0 & c_1 & 0 & c_2 & 0 & c_3 \\ c_1 & b_1 & c_2 & b_2 & c_3 & b_3 \end{bmatrix}, \tag{3.93}$$

where b_j and c_j $(j = 1, 2, 3)$ are given in Equation 3.92 and are constants related only to the nodal coordinates of the element. It is thus clear that the strain–displacement matrix for the triangular element is a constant matrix, implying that the strains obtained using such an element will be constants within the element. Therefore, the T3 element is also often called a constant strain element.

3.11.3 Element Stiffness Matrix

The element stiffness matrix $\tilde{\mathbf{K}}_i^e$ for the linear triangular element Ω_i^e has the form of

$$\tilde{\mathbf{K}}_i^e = \int_{\Omega_i^e} \left(\tilde{\mathbf{B}}_i^e\right)^T \mathbf{c}\tilde{\mathbf{B}}_i^e \, \mathrm{d}\Omega = \left(\tilde{\mathbf{B}}_i^e\right)^T \mathbf{c}\tilde{\mathbf{B}}_i^e A_i^e. \tag{3.94}$$

Because the strain–displacement matrix $\tilde{\mathbf{B}}_i^e$ is constant, no numerical integration is needed to compute the stiffness matrix for a T3 element. Therefore, a T3 element is the only 2D element that needs no numerical integration. It is seen that the stiffness matrix for the three-node triangular element is indeed very simple. In fact, it is the simplest of all types of 2D elements.

3.12 Four-Node Quadrilateral Element (Q4)

The quadrilateral element has four nodes and four edges and is often referred to as Q4 element, as shown in Figure 3.6. It is probably as popular as the T3 element but for different reasons. It has a reasonably

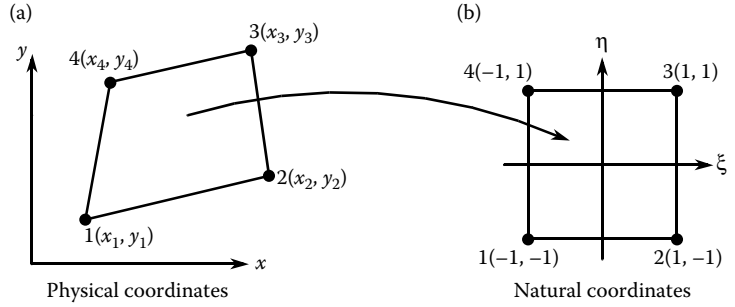

FIGURE 3.6 Coordinate mapping between physical coordinates and natural coordinates of the four-node quadrilateral element: (a) an arbitrary quadrilateral element in physical coordinates; (b) a square element in natural coordinates.

good adaptation to complicated geometries, because it does not require the inner angles to be right angles. The formulation of the Q4 element will be much more complicated, compared to the T3 element, due to the so-called mapping procedure. However, it is known to have a much more accurate stress solution, compared to the T3 elements using meshes of the same set of nodes. Therefore, Q4 elements are very popular and preferred by many. The biggest drawback for Q4 elements is the difficulty of generating the mesh for complicated geometries. Many efforts have been made in the automation of Q4 element mesh generation, but we still need some kind of manual intervention to create the Q4 element mesh. In addition, the loss of accuracy due to mesh distortion is often a big concern for Q4 elements. Our smoothed FEM models can also be created based on Q4 elements and they can have very good properties, as will be shown in later chapters. However, we offer these models only as an alternative and not the mainstream elements, simply because of the difficulty in mesh generation for practical engineering problems. The following gives the details of the FEM formulation of Q4 elements.

3.12.1 Shape Functions

The quadrilateral element has in general an arbitrary (to a certain degree) shape in the physical coordinate system, as shown in Figure 3.6a. When the general procedure given in Section 3.5.1 is used to create the shape functions for Q4 elements, we will have problems with the compatibility issue. The nodal shape functions so created will be discontinuous along the edges of the Q4 elements connected to the node. To prevent this from happening, a so-called coordinate mapping is performed. This essential idea for the mapping procedure is to map the Q4 element of general shape in the physical coordinate system (x, y) to a square element in the so-called natural coordinate system (ξ, η), as shown in Figure 3.6b. Due to the regular shape, the shape functions for the element in the natural coordinate system can be easily written out as follows:

$$\begin{aligned} N_1(\xi,\eta) &= \frac{1}{4}(1-\xi)(1-\eta), \quad N_2(\xi,\eta) = \frac{1}{4}(1+\xi)(1-\eta), \\ N_3(\xi,\eta) &= \frac{1}{4}(1+\xi)(1+\eta), \quad N_4(\xi,\eta) = \frac{1}{4}(1-\xi)(1+\eta). \end{aligned} \tag{3.95}$$

These nodal shape functions are linear with respect to both ξ and η, and hence they are often called bilinear shape functions. It is clear that this set of shape functions satisfies all the conditions listed in Section 3.5.2, and the nodal shape functions will be continuous along all edges of the element under the natural coordinate system. We then perform a proper coordinate transformation to ensure the correction correspondence of element edges

between the two coordination systems, and thus the compatibility of the nodal shape function for the Q4 element on all the edges can be preserved. Such a relationship between the physical and natural coordinate system is schematically shown in Figure 3.6. The mathematical formulation for such a mapping is given as follows:

$$x = \sum_{j=1}^{4} N_j(\xi, \eta)\, x_j, \quad y = \sum_{j=1}^{4} N_j(\xi, \eta)\, y_j, \tag{3.96}$$

where x_j and y_j ($j = 1, 2, 3, 4$) are the coordinate values at the jth node. Equation 3.96 defines clearly the relationship of the physical coordinates (x, y) and the natural coordinate (ξ, η). It is to confirm the correct edge correspondence of the element under these two coordination systems [5]. Because the mapping in Equation 3.96 uses the same bilinear shape functions given in Equation 3.95, this element is a typical isoparametric element.

3.12.2 Strain–Displacement Matrix

In order to evaluate the strain–displacement matrix $\tilde{\mathbf{B}}_i^e$ for the bilinear isoparametric element, it is first necessary to express the differentials in terms of the natural coordinates. Utilizing the chain rule for partial differentiation, we have

$$\frac{\partial N_j}{\partial \xi} = \frac{\partial N_j}{\partial x}\frac{\partial x}{\partial \xi} + \frac{\partial N_j}{\partial y}\frac{\partial y}{\partial \xi}, \quad \frac{\partial N_j}{\partial \eta} = \frac{\partial N_j}{\partial x}\frac{\partial x}{\partial \eta} + \frac{\partial N_j}{\partial y}\frac{\partial y}{\partial \eta}, \tag{3.97}$$

or in matrix form

$$\begin{bmatrix} \partial N_j/\partial \xi \\ \partial N_j/\partial \eta \end{bmatrix} = \mathbf{J} \begin{bmatrix} \partial N_j/\partial x \\ \partial N_j/\partial y \end{bmatrix}, \tag{3.98}$$

where $\mathbf{J}$ is the so-called *Jacobian matrix* defined by

$$\mathbf{J} = \begin{bmatrix} \partial x/\partial \xi & \partial y/\partial \xi \\ \partial x/\partial \eta & \partial y/\partial \eta \end{bmatrix}. \tag{3.99}$$

By substituting Equation 3.96 into Equation 3.99, we obtain

$$\mathbf{J} = \begin{bmatrix} \partial N_1/\partial \xi & \partial N_2/\partial \xi & \partial N_3/\partial \xi & \partial N_4/\partial \xi \\ \partial N_1/\partial \eta & \partial N_2/\partial \eta & \partial N_3/\partial \eta & \partial N_4/\partial \eta \end{bmatrix} \begin{bmatrix} x_1 & y_1 \\ x_2 & y_2 \\ x_3 & y_3 \\ x_4 & y_4 \end{bmatrix}. \tag{3.100}$$

If the Jacobian matrix is not singular or badly conditioned (the Q4 element is not heavily distorted), the differentials in terms of the physical coordinates can be expressed from Equation 3.98 as

$$\begin{bmatrix} \partial N_j/\partial x \\ \partial N_j/\partial y \end{bmatrix} = \mathbf{J}^{-1} \begin{bmatrix} \partial N_j/\partial \xi \\ \partial N_j/\partial \eta \end{bmatrix}. \tag{3.101}$$

We can now compute the strain–displacement matrix $\tilde{\mathbf{B}}_i^e$ for the bilinear isoparametric element by replacing all the differentials of the shape functions with respect to x and y with those with respect to ξ and η using Equation 3.101. This process needs to be performed numerically for Q4 elements, and cannot be given in explicit equations as we did for T3 elements. We note that the Jacobian matrix can however become singular or badly conditioned when the element is heavily distorted, implying that we need good-quality Q4 element mesh.

3.12.3 Element Stiffness Matrix

Once the strain–displacement matrix $\tilde{\mathbf{B}}_i^e$ has been obtained, the element stiffness matrix $\tilde{\mathbf{K}}_i^e$ for the bilinear isoparametric element Ω_i^e is computed (numerically) using

$$\tilde{\mathbf{K}}_i^e = \int_{\Omega_i^e} \left(\tilde{\mathbf{B}}_i^e\right)^T \mathbf{c} \tilde{\mathbf{B}}_i^e \, \mathrm{d}\Omega = \int_{-1}^{+1} \int_{-1}^{+1} \left(\tilde{\mathbf{B}}_i^e\right)^T \mathbf{c} \tilde{\mathbf{B}}_i^e \det|\mathbf{J}| \, \mathrm{d}\xi \, \mathrm{d}\eta, \tag{3.102}$$

where $\det|\mathbf{J}|$ is the determinant of the Jacobian matrix.

The integrand in Equation 3.102 is no longer constant. In fact, it is quite complicated and hence a numerical integration is generally needed. We often use the Gauss integration scheme that is briefly presented in Section 3.15.2.

3.13 Four-Node Tetrahedral Element (T4)

The four-node tetrahedral element is the analogue of the triangular element, but in 3D space, as shown in Figure 3.7. Naturally the formulation of T4 and T3 has a lot of similarities. Because of the 3D dimensionality, the geometry of the problem domain becomes even more complicated, and hence in practice T4 elements are more widely used for the simple reason of easy mesh generation. Our smoothed FEM models for 3D are mainly based on T4 elements. The following is the formulation procedure for the T4 element, which is quite similar to the T3 element for 2D problems.

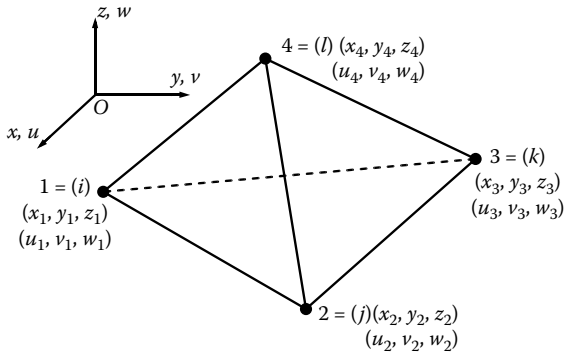

FIGURE 3.7 Four-node tetrahedral element in the physical Cartesian coordinate system *Oxyz*.

3.13.1 Shape Functions

For the four-node tetrahedral element Ω_i^e, the vector of nodal displacements $\tilde{\mathbf{d}}_i^e$ is arranged in the order of

$$\tilde{\mathbf{d}}_i^e = \begin{Bmatrix} u_1 \\ v_1 \\ w_1 \\ u_2 \\ v_2 \\ w_2 \\ u_3 \\ v_3 \\ w_3 \\ u_4 \\ v_4 \\ w_4 \end{Bmatrix} \begin{matrix} \left.\begin{matrix} \\ \\ \end{matrix}\right\} \text{displacements at node 1} \\ \left.\begin{matrix} \\ \\ \end{matrix}\right\} \text{displacements at node 2} \\ \left.\begin{matrix} \\ \\ \end{matrix}\right\} \text{displacements at node 3} \\ \left.\begin{matrix} \\ \\ \end{matrix}\right\} \text{displacements at node 4} \end{matrix} \tag{3.103}$$

and the matrix of shape functions $\mathbf{N}_i^e(\mathbf{x})$ is arranged accordingly as

$$\mathbf{N}_i^e(\mathbf{x}) = \begin{bmatrix} \underbrace{\begin{matrix} N_1 & 0 & 0 \\ 0 & N_1 & 0 \\ 0 & 0 & N_1 \end{matrix}}_{\text{Node 1}} & \underbrace{\begin{matrix} N_2 & 0 & 0 \\ 0 & N_2 & 0 \\ 0 & 0 & N_2 \end{matrix}}_{\text{Node 2}} & \underbrace{\begin{matrix} N_3 & 0 & 0 \\ 0 & N_3 & 0 \\ 0 & 0 & N_3 \end{matrix}}_{\text{Node 3}} & \underbrace{\begin{matrix} N_4 & 0 & 0 \\ 0 & N_4 & 0 \\ 0 & 0 & N_4 \end{matrix}}_{\text{Node 4}} \end{bmatrix}, \tag{3.104}$$

in which N_j $(j = 1, 2, 3, 4)$ are four shape functions corresponding to four nodes of the tetrahedral element.

Using directly the physical Cartesian coordinate system $Oxyz$, four shape functions have the following forms [5]:

$$N_j = \frac{1}{6V_i^e}\left(a_j + b_j x + c_j y + d_j z\right), \tag{3.105}$$

where

$$\begin{aligned} a_j &= \det\begin{bmatrix} x_k & y_k & z_k \\ x_l & y_l & z_l \\ x_m & y_m & z_m \end{bmatrix}, \qquad b_j = -\det\begin{bmatrix} 1 & y_k & z_k \\ 1 & y_l & z_l \\ 1 & y_m & z_m \end{bmatrix}, \\ c_j &= -\det\begin{bmatrix} y_k & 1 & z_k \\ y_l & 1 & z_l \\ y_m & 1 & z_m \end{bmatrix}, \qquad d_j = -\det\begin{bmatrix} y_k & z_k & 1 \\ y_l & z_l & 1 \\ y_m & z_m & 1 \end{bmatrix}, \end{aligned} \tag{3.106}$$

in which subscript j varies from 1 to 4, and k, l, and m are determined by cyclic permutation in the order of j, k, l, and m. For example, if $j = 1$, then $k = 2$, $l = 3$, and $m = 4$; if $j = 2$, then $k = 3$, $l = 4$, and $m = 1$. The volume of tetrahedron V_i^e of the tetrahedral element Ω_i^e is computed by

$$V_i^e = \frac{1}{6}\det\begin{bmatrix} 1 & x_j & y_j & z_j \\ 1 & x_k & y_k & z_k \\ 1 & x_l & y_l & z_l \\ 1 & x_m & y_m & z_m \end{bmatrix}. \tag{3.107}$$

3.13.2 Strain–Displacement Matrix

Using directly the physical Cartesian coordinate system $Oxyz$, the strain–displacement matrix $\tilde{\mathbf{B}}_i^e$ for the linear tetrahedral element Ω_i^e has the form

$$\tilde{\mathbf{B}}_i^e = \begin{bmatrix} b_1 & 0 & 0 & b_2 & 0 & 0 & b_3 & 0 & 0 & b_4 & 0 & 0 \\ 0 & c_1 & 0 & 0 & c_2 & 0 & 0 & c_3 & 0 & 0 & c_4 & 0 \\ 0 & 0 & d_1 & 0 & 0 & d_2 & 0 & 0 & d_3 & 0 & 0 & d_4 \\ c_1 & b_1 & 0 & c_2 & b_2 & 0 & c_3 & b_3 & 0 & c_4 & b_4 & 0 \\ 0 & d_1 & c_1 & 0 & d_2 & c_2 & 0 & d_3 & c_3 & 0 & d_4 & c_4 \\ d_1 & 0 & b_1 & d_2 & 0 & b_2 & d_3 & 0 & b_3 & d_4 & 0 & b_4 \end{bmatrix}, \tag{3.108}$$

where b_j, c_j, and d_j ($j = 1, 2, 3, 4$) are derived from Equation 3.106.

It is clear that the strain–displacement matrix $\tilde{\mathbf{B}}_i^e$ for the T4 element is a constant matrix, which implies that the strain obtained using such an element will be constant within the element. The T4 element is thus often called a constant strain element.

3.13.3 Element Stiffness Matrix

The element stiffness matrix $\tilde{\mathbf{K}}_i^e$ for the linear tetrahedral element Ω_i^e has the form

$$\tilde{\mathbf{K}}_i^e = \int_{\Omega_i^e} \left(\tilde{\mathbf{B}}_i^e\right)^T \mathbf{c}\tilde{\mathbf{B}}_i^e \, \mathrm{d}\Omega = \left(\tilde{\mathbf{B}}_i^e\right)^T \mathbf{c}\tilde{\mathbf{B}}_i^e V_i^e. \tag{3.109}$$

Similar to T3 elements, no numerical integration is needed for computing the stiffness matrix for T4 elements. It is also seen that the stiffness matrix for T4 elements is indeed very simple. In fact, it is the simplest of all types of 3D elements.

3.14 Eight-Node Hexahedral Element (H8)

The eight-node hexahedral element is the analogue of the Q4 element, but in 3D space, as shown in Figure 3.8a. Naturally the formulation of H8 and Q4 has a lot of similarities, such as it produces good results in stresses. Because of the 3D dimensionality, the geometry of the problem domain becomes even more complicated, and the creation of an H8 element mesh can be very difficult for practical problems with complicated geometries. Hence in practice, T4 elements are more widely used for the simple reason of easy mesh generation, especially when adaptive analysis is conducted. Theoretically, S-FEM models can also be built based on H8 elements, but in practice we do not, again because of mesh generation reasons and the good performance of the S-FEM model using T4 elements. We present the FEM H8 elements here because we will be using them in later chapters for comparison purposes.

3.14.1 Shape Functions

Similar to the Q4 elements for 2D problems, the formulation of H8 elements for 3D problems requires a similar mapping procedure. To cut the process short, the shape functions for the H8 element for 3D problems are defined in the natural coordinate system, as shown in Figure 3.8b:

$$N_1(\xi,\eta,\zeta) = \frac{1}{8}(1-\xi)(1-\eta)(1-\zeta), \quad N_2(\xi,\eta,\zeta) = \frac{1}{8}(1+\xi)(1-\eta)(1-\zeta),$$

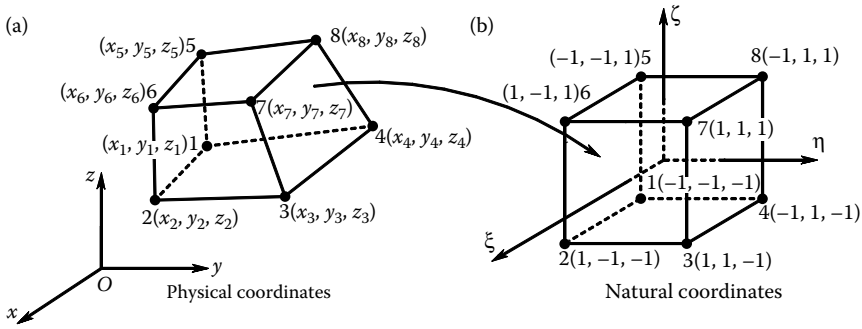

FIGURE 3.8 Coordinate mapping between physical coordinates and natural coordinates of the eight-node hexahedral element: (a) an arbitrary hexahedral element in physical coordinates; (b) a cubic element in natural coordinates.

$$N_3(\xi,\eta,\zeta) = \frac{1}{8}(1+\xi)(1+\eta)(1-\zeta), \quad N_4(\xi,\eta,\zeta) = \frac{1}{8}(1-\xi)(1+\eta)(1-\zeta),$$
$$N_5(\xi,\eta,\zeta) = \frac{1}{8}(1-\xi)(1-\eta)(1+\zeta), \quad N_6(\xi,\eta,\zeta) = \frac{1}{8}(1+\xi)(1-\eta)(1+\zeta),$$
$$N_7(\xi,\eta,\zeta) = \frac{1}{8}(1+\xi)(1+\eta)(1+\zeta), \quad N_8(\xi,\eta,\zeta) = \frac{1}{8}(1-\xi)(1+\eta)(1+\zeta). \tag{3.110}$$

These nodal shape functions are linear with respect to ξ, η, and ζ and the H8 element is called a trilinear element. It is clear that this set of shape functions satisfies all the conditions listed in Section 3.5.2. The relationship between the physical and natural coordinate system is schematically shown in Figure 3.8, and mathematically expressed as follows. The physical coordinates (x, y, z) are expressed explicitly in natural coordinates (ξ, η, ζ) as

$$x = \sum_{j=1}^{8} N_j(\xi,\eta,\zeta)\, x_j, \quad y = \sum_{j=1}^{8} N_j(\xi,\eta,\zeta)\, y_j, \quad z = \sum_{j=1}^{8} N_j(\xi,\eta,\zeta)\, z_j, \tag{3.111}$$

where x_j, y_j, z_j $(j = 1, 2, \ldots, 8)$ are the coordinate values at the jth node.

3.14.2 Strain–Displacement Matrix

To evaluate the strain–displacement matrix $\tilde{\mathbf{B}}_i^e$ for the eight-node isoparametric hexahedral element, it is first necessary to express the differentials in terms of natural coordinates. Utilizing the chain rule for partial

differentiation, we have

$$\begin{aligned}
\frac{\partial N_j}{\partial \xi} &= \frac{\partial N_j}{\partial x}\frac{\partial x}{\partial \xi} + \frac{\partial N_j}{\partial y}\frac{\partial y}{\partial \xi} + \frac{\partial N_j}{\partial z}\frac{\partial z}{\partial \xi}, \\
\frac{\partial N_j}{\partial \eta} &= \frac{\partial N_j}{\partial x}\frac{\partial x}{\partial \eta} + \frac{\partial N_j}{\partial y}\frac{\partial y}{\partial \eta} + \frac{\partial N_j}{\partial z}\frac{\partial z}{\partial \eta}, \\
\frac{\partial N_j}{\partial \zeta} &= \frac{\partial N_j}{\partial x}\frac{\partial x}{\partial \zeta} + \frac{\partial N_j}{\partial y}\frac{\partial y}{\partial \zeta} + \frac{\partial N_j}{\partial z}\frac{\partial z}{\partial \zeta},
\end{aligned} \tag{3.112}$$

or in the matrix form of

$$\begin{bmatrix} \partial N_j/\partial \xi \\ \partial N_j/\partial \eta \\ \partial N_j/\partial \zeta \end{bmatrix} = \mathbf{J} \begin{bmatrix} \partial N_j/\partial x \\ \partial N_j/\partial y \\ \partial N_j/\partial z \end{bmatrix}, \tag{3.113}$$

where $\mathbf{J}$ is the *Jacobian matrix* defined by

$$\mathbf{J} = \begin{bmatrix} \partial x/\partial \xi & \partial y/\partial \xi & \partial z/\partial \xi \\ \partial x/\partial \eta & \partial y/\partial \eta & \partial z/\partial \eta \\ \partial x/\partial \zeta & \partial y/\partial \zeta & \partial z/\partial \zeta \end{bmatrix}. \tag{3.114}$$

By substituting Equation 3.111 into Equation 3.114, we obtain

$$\mathbf{J} = \begin{bmatrix} \frac{\partial N_1}{\partial \xi} & \frac{\partial N_2}{\partial \xi} & \frac{\partial N_3}{\partial \xi} & \frac{\partial N_4}{\partial \xi} & \frac{\partial N_5}{\partial \xi} & \frac{\partial N_6}{\partial \xi} & \frac{\partial N_7}{\partial \xi} & \frac{\partial N_8}{\partial \xi} \\ \frac{\partial N_1}{\partial \eta} & \frac{\partial N_2}{\partial \eta} & \frac{\partial N_3}{\partial \eta} & \frac{\partial N_4}{\partial \eta} & \frac{\partial N_5}{\partial \eta} & \frac{\partial N_6}{\partial \eta} & \frac{\partial N_7}{\partial \eta} & \frac{\partial N_8}{\partial \eta} \\ \frac{\partial N_1}{\partial \zeta} & \frac{\partial N_2}{\partial \zeta} & \frac{\partial N_3}{\partial \zeta} & \frac{\partial N_4}{\partial \zeta} & \frac{\partial N_5}{\partial \zeta} & \frac{\partial N_6}{\partial \zeta} & \frac{\partial N_7}{\partial \zeta} & \frac{\partial N_8}{\partial \zeta} \end{bmatrix} \begin{bmatrix} x_1 & y_1 & z_1 \\ x_2 & y_2 & z_2 \\ x_3 & y_3 & z_3 \\ x_4 & y_4 & z_4 \\ x_5 & y_5 & z_5 \\ x_6 & y_6 & z_6 \\ x_7 & y_7 & z_7 \\ x_8 & y_8 & z_8 \end{bmatrix}. \tag{3.115}$$

If the Jacobian matrix is not singular, the differentials in terms of physical coordinates can be expressed from Equation 3.113 as

$$\begin{bmatrix} \partial N_j/\partial x \\ \partial N_j/\partial y \\ \partial N_j/\partial z \end{bmatrix} = \mathbf{J}^{-1} \begin{bmatrix} \partial N_j/\partial \xi \\ \partial N_j/\partial \eta \\ \partial N_j/\partial \zeta \end{bmatrix}. \tag{3.116}$$

We can now compute the strain–displacement matrix $\tilde{\mathbf{B}}_i^e$ for the eight-node isoparametric hexahedral element by replacing all the differentials of the shape functions with respect to x, y, and z with those with respect to ξ,

η, and ζ by Equation 3.116. This process needs to be performed numerically, and cannot be expressed explicitly as we do for T4 elements.

We note that the Jacobian matrix can however become singular or badly conditioned when the element is heavily distorted, implying that we need good-quality H8 element mesh.

3.14.3 Element Stiffness Matrix

Once the strain–displacement matrix $\tilde{\mathbf{B}}_i^e$ has been obtained, the element stiffness matrix $\tilde{\mathbf{K}}_i^e$ for the eight-node hexahedral element Ω_i^e is computed using

$$\tilde{\mathbf{K}}_i^e = \int_{\Omega_i^e} \left(\tilde{\mathbf{B}}_i^e\right)^T \mathbf{c}\tilde{\mathbf{B}}_i^e \mathrm{d}\Omega = \int_{-1}^{+1}\int_{-1}^{+1}\int_{-1}^{+1} \left(\tilde{\mathbf{B}}_i^e\right)^T \mathbf{c}\tilde{\mathbf{B}}_i^e \det|\mathbf{J}|\, \mathrm{d}\xi\, \mathrm{d}\eta\, \mathrm{d}\zeta, \tag{3.117}$$

where $\det|\mathbf{J}|$ is the determinant of the Jacobian matrix. The integrand in Equation 3.117 is no longer constant. In fact, it is quite complicated and hence a numerical integration is needed. We often use the Gauss integration scheme that is presented in Section 3.15.3.

3.15 Gauss Integration

The use of numerical integration is essential for the practical evaluation of integrals over domains. In practice, we usually divide the domain into smaller "quadrature domains" that can be elements (in FEM settings) or subcells obtained by further dividing the elements (in S-FEM settings) or smoothing domains (in S-FEM settings). We most often use *Gauss integration rules* or quadrature rules over each of these quadrature domains, because such rules use a minimal number of sample points to achieve a desired level of accuracy.

3.15.1 1D Rules

For integrations over 1D integration or quadrature domain $[-1, 1]$, Gauss integration is performed in the following simple summation form:

$$I = \int_{-1}^{1} f(\xi)\, \mathrm{d}\xi = \sum_{j=1}^{n_\xi^G} w_j f(\xi_j), \tag{3.118}$$

where n_ξ^G is the number of Gauss integration points in the ξ-axis, ξ_j is the sampling point, and w_j is the weight corresponding to these sampling points.

Gauss integration is very useful for the integration of polynomial functions. For a 1D integral, it can integrate exactly a polynomial function up to the order of $2n_\xi^G - 1$. Table 3.1 lists the locations of Gauss sampling points, corresponding weights, and accurate order of the polynomial function in a 1D integral.

3.15.2 2D Rules for the Square Domain

The simplest Gauss rules for 2D quadrature domains $[-1, 1] \times [-1, 1]$ are called *product rules*. They are derived by applying the 1D rules to each independent variable consecutively. Integration along the ξ-axis gives

$$I = \int_{-1}^{+1}\int_{-1}^{+1} f(\xi,\eta)\, d\xi\, d\eta = \int_{-1}^{1}\left(\int_{-1}^{1} f(\xi,\eta)d\xi\right) d\eta = \int_{-1}^{1}\left(\sum_{j=1}^{n_\xi^G} w_j f\left(\xi_j,\eta\right)\right) d\eta. \tag{3.119}$$

TABLE 3.1

Gauss Integration Points, Corresponding Weights, and Accurate Order of the Polynomial Function in a 1D Quadrature Domain of $[-1, 1]$

Number of Gauss Integration Points n_ξ^G	**ξ_j−Coordinate**	**Weights w_j**	**Order of Accuracy $2n_\xi^G - 1$**
1 point	0	2.0	1
2 points	$-1/\sqrt{3}$	1.0	3
	$1/\sqrt{3}$	1.0	
3 points	$-\sqrt{3/5}$	5/9	5
	0	8/9	
	$\sqrt{3/5}$	5/9	
4 points	−0.861136	0.347855	7
	−0.339981	0.652145	
	−0.339981	0.652145	
	−0.861136	0.347855	
5 points	−0.906180	0.236927	9
	−0.538469	0.478629	
	0	0.568889	
	−0.538469	0.478629	
	−0.906180	0.236927	
6 points	−0.932470	0.171324	11
	−0.661209	0.360762	
	−0.238619	0.467914	
	−0.238619	0.467914	
	−0.661209	0.360762	
	−0.932470	0.171324	

Integration next along the η-axis leads to

$$I = \int_{-1}^{+1}\int_{-1}^{+1} f(\xi,\eta)\,\mathrm{d}\xi\,\mathrm{d}\eta = \int_{-1}^{1}\left(\sum_{j=1}^{n_\xi^G} w_j f\left(\xi_j,\eta\right)\right)\mathrm{d}\eta = \sum_{k=1}^{n_\eta^G}\sum_{j=1}^{n_\xi^G} w_j w_k f\left(\xi_j,\eta_k\right), \tag{3.120}$$

where n_ξ^G and n_η^G are the number of Gauss integration points in the ξ and η axes, respectively; (ξ_j,η_k) are the sampling points and w_j, w_k are weights corresponding to these sampling points, respectively. In general, n_ξ^G and n_η^G do not have to be the same, but they are often chosen so. For the Q4 element, we just need 2×2 Gauss points to compute the element stiffness matrix by Equation 3.102. For higher-order elements, more Gauss points should be used along each direction following Table 3.1, based on the order of the integrand.

3.15.3 3D Rules for the Cubic Domain

Similarly to the 2D rules, the Gauss rules for the 3D domain can be simply written as

$$I = \int_{-1}^{+1}\int_{-1}^{+1}\int_{-1}^{+1} f\left(\xi,\eta,\zeta\right)\,\mathrm{d}\xi\,\mathrm{d}\eta\,\mathrm{d}\zeta = \sum_{j=1}^{n_\xi^G}\sum_{k=1}^{n_\eta^G}\sum_{l=1}^{n_\zeta^G} w_j w_k w_l f\left(\xi_j,\eta_k,\zeta_l\right), \tag{3.121}$$

where n_ξ^G, n_η^G, and n_ζ^G are the number of Gauss integration points in the ξ, η, and ζ axes, respectively; (ξ_j,η_k,ζ_l) are the sampling points and w_j, w_k, w_l are weights corresponding to these sampling points, respectively. For the H8 element, we just need $2\times 2\times 2$ Gauss points to compute the element stiffness matrix by Equation 3.108.

3.15.4 Gauss Integration over Triangular Quadrature Domains

Gauss integration is also used in evaluating isoparametric triangular elements of higher order. In addition, it is often used in the accurate computation of error norms between the exact solution (with high order) and numerical solutions. In all these cases, we need to perform integrations over triangular quadrature domains, and coordinate mapping as in the isoparametric elements, as shown in Figure 3.9, is needed. In the natural coordinate system, the shape functions have the forms

$$N_1 = 1-\xi-\eta,\quad N_2 = \xi,\quad N_3 = \eta \tag{3.122}$$

for the three nodes shown in Figure 3.9b.

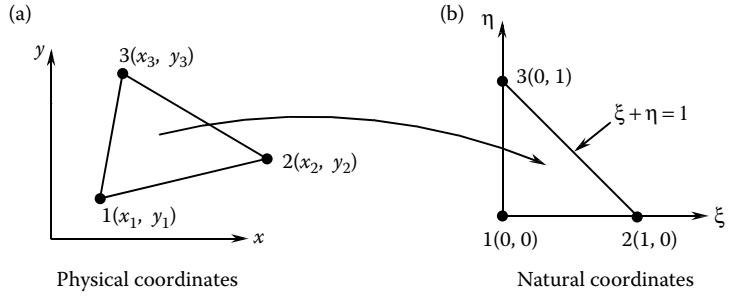

FIGURE 3.9 Coordinate mapping between physical coordinates and natural coordinates of the three-node triangular element: (a) an arbitrary triangular element in physical coordinates; (b) an isosceles right triangular element in natural coordinates.

Using the isoparametric formulation and the shape functions given in Equation 3.122, the procedure of evaluating the strain–displacement matrix $\tilde{\mathbf{B}}_i^e$ of three-node triangular elements can be done in a similar way as in the four-node quadrilateral elements, as presented in Section 3.12.2. The element stiffness matrix $\tilde{\mathbf{K}}_i^e$ for the three-node isoparametric triangular element is computed by

$$\tilde{\mathbf{K}}_i^e = \int_{\Omega_i^e} \left(\tilde{\mathbf{B}}_i^e\right)^T \mathbf{c}\tilde{\mathbf{B}}_i^e \, \mathrm{d}\Omega = \int_0^1 \int_0^{1-\xi} \left(\tilde{\mathbf{B}}_i^e\right)^T \mathbf{c}\tilde{\mathbf{B}}_i^e \det|\mathbf{J}| \, \mathrm{d}\eta \, \mathrm{d}\xi, \tag{3.123}$$

and Gauss integration over the triangular elements in the natural coordinate system is computed using

$$I = \int_0^1 \int_0^{1-\xi} f(\xi, \eta) \, \mathrm{d}\eta \, \mathrm{d}\xi = \sum_{j=1}^{n_{\xi\eta}^G} w_j f\left(\xi_j, \eta_j\right), \tag{3.124}$$

where $n_{\xi\eta}^G$ is the number of Gauss integration points in the natural coordinate system; (ξ_j, η_j) is the sampling point and w_j is the weight corresponding to the sampling point. For the T3 element, we just need one Gauss point to compute the element stiffness matrix, which will give the same results as that given in Equation 3.94. For higher-order integrands (such as higher-order elements and the evaluation of the solution errors), more Gauss points are needed based on the order of the integrand. Table 3.2 lists the locations of the Gauss sampling points, corresponding weights, and accurate order of the polynomial function for isosceles right triangular quadrature domain [14].

TABLE 3.2

Gauss Integration Points and Corresponding Weights for Isosceles Right Triangular Quadrature Domain

Number of Gauss Points $n_{\xi\eta}^{G}$	ξ_j-Coordinate	η_j-Coordinate	Weights w_j	Order of Accuracy
1 point	1/3	1/3	1/2	1
3 points	1/6, 4/6, 1/6	1/6, 1/6, 4/6	1/6, 1/6, 1/6	2
4 points	1/5, 3/5, 1/5, 1/3	1/5, 1/5, 3/5, 1/3	25/96, 25/96, 25/96, −9/32	3
6 points	0.0915762135098	0.0915762135098	0.05497587182766	4
	0.8168475729805	0.0915762135098	0.05497587182766	
	0.0915762135098	0.8168475729805	0.05497587182766	
	0.4459484909160	0.4459484909160	0.11169079483901	
	0.1081030181681	0.4459484909160	0.11169079483901	
	0.4459484909160	0.1081030181681	0.11169079483901	
7 points	0.1012865073235	0.1012865073235	0.06296959027240	5
	0.7974269853531	0.1012865073235	0.06296959027240	
	0.1012865073235	0.7974269853531	0.06296959027240	
	0.4701420641051	0.0597158717898	0.06619707639425	
	0.4701420641051	0.4701420641051	0.06619707639425	
	0.0597158717898	0.4701420641051	0.06619707639425	
	0.3333333333333	0.3333333333333	0.11250000000000	
12 points	0.06308901449150	0.06308901449150	0.02542245318510	6
	0.87382197101700	0.06308901449150	0.02542245318510	
	0.06308901449150	0.87382197101700	0.02542245318510	
	0.249286745170910	0.249286745170910	0.05839313786319	
	0.501426509658179	0.249286745170910	0.05839313786319	
	0.249286745170910	0.501426509658179	0.05839313786319	
	0.310352451033785	0.053145049844816	0.04142553780919	
	0.636502499121399	0.310352451033785	0.04142553780919	
	0.053145049844816	0.636502499121399	0.04142553780919	
	0.636502499121399	0.053145049844816	0.04142553780919	
	0.310352451033785	0.636502499121399	0.04142553780919	
	0.053145049844816	0.053145049844816	0.04142553780919	
13 points	0.06513010290220	0.06513010290220	0.02667361780440	7
	0.86973979419560	0.06513010290220	0.02667361780440	
	0.06513010290220	0.86973979419560	0.02667361780440	
	0.31286549600490	0.04869031542530	0.03855688044515	
	0.63844418856980	0.31286549600490	0.03855688044515	
	0.04869031542530	0.63844418856980	0.03855688044515	
	0.63844418856980	0.04869031542530	0.03855688044515	
	0.31286549600490	0.63844418856980	0.03855688044515	
	0.04869031542530	0.04869031542530	0.03855688044515	
	0.26034596607900	0.26034596607900	0.08780762871660	
	0.47930806784190	0.26034596607900	0.08780762871660	
	0.26034596607900	0.47930806784190	0.08780762871660	
	0.33333333333330	0.33333333333330	−0.07478502223385	

Source: Data from Dunavant DA. 1985. *International Journal for Numerical Methods in Engineering;* 21: 1129–1148.

3.15.5 Gauss Integration over Tetrahedral Quadrature Domains

Similarly to the isoparametric (T3) triangular element, Gauss integration is used in evaluating isoparametric tetrahedral elements of higher orders. In addition, it is often used in the accurate computation of error norms between the exact solution (with high order) and the numerical solutions for 3D problems. In all these cases, we need to perform integrations over tetrahedral quadrature domains, and coordinate mapping as in the isoparametric elements, as shown in Figure 3.10, is needed. In the natural coordinate system, the shape functions for T4 elements have the simple form of

$$N_1 = 1 - \xi - \eta - \zeta, \quad N_2 = \xi, \quad N_3 = \eta, \quad N_4 = \zeta \tag{3.125}$$

for the four nodes shown in Figure 3.10.

The procedure of evaluating the strain–displacement matrix $\tilde{\mathbf{B}}_i^e$ of four-node tetrahedral elements is therefore similar to that of eight-node hexahedral elements as presented in Section 3.14.2. The element stiffness matrix $\tilde{\mathbf{K}}_i^e$ for the four-node tetrahedral element Ω_i^e can be computed by

$$\tilde{\mathbf{K}}_i^e = \int_{\Omega_i^e} \left(\tilde{\mathbf{B}}_i^e\right)^T \mathbf{c}\tilde{\mathbf{B}}_i^e \mathrm{d}\Omega = \int_0^1 \int_0^{1-\xi} \int_0^{1-\eta-\xi} \left(\tilde{\mathbf{B}}_i^e\right)^T \mathbf{c}\tilde{\mathbf{B}}_i^e \det|\mathbf{J}|\, \mathrm{d}\zeta\, \mathrm{d}\eta\, \mathrm{d}\xi, \tag{3.126}$$

and Gauss integration over the isosceles right tetrahedral elements in the natural coordinate system is computed using

$$I = \int_0^1 \int_0^{1-\xi} \int_0^{1-\eta-\xi} f(\xi, \eta)\, \mathrm{d}\zeta\, \mathrm{d}\eta\, \mathrm{d}\xi = \sum_{j=1}^{n_{\xi\eta\zeta}^G} w_j f\left(\xi_j, \eta_j, \zeta_j\right), \tag{3.127}$$

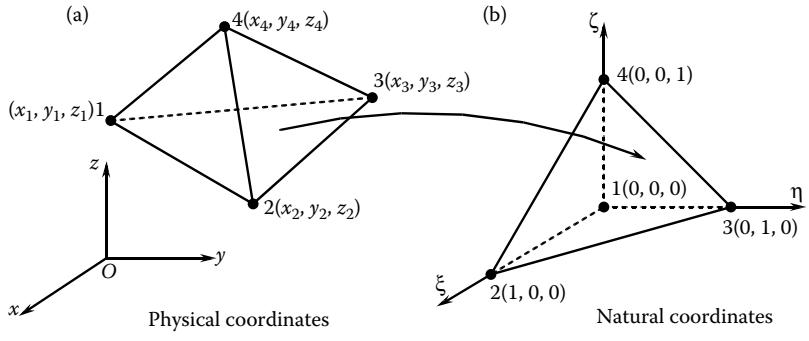

FIGURE 3.10 Coordinate mapping between physical coordinates and natural coordinates of the four-node tetrahedral element: (a) an arbitrary hexahedral element in physical coordinates; (b) an isosceles right hexahedral element in natural coordinates.

where $n_{\xi\eta\zeta}^{G}$ is the number of Gauss integration points in the natural coordinate system; (ξ_j, η_j, ζ_j) is the sampling point and w_j is the weight corresponding to the sampling point. For the T4 element, we just need one Gauss point to compute the element stiffness matrix, which will give the same results as using Equation 3.126. For higher-order integrands (such as higher-order elements and the evaluation of the solution errors), more Gauss points are needed based on the order of the integrand. Table 3.3 lists the locations of the Gauss sampling points, corresponding weights, and accurate order of the polynomial function for an isosceles right tetrahedral quadrature domain [15].

TABLE 3.3

Gauss Integration Points and Corresponding Weights in an Isosceles Right Tetrahedral Quadrature Domain

$n_{\xi\eta\zeta}^{G}$	ξ_j-Coordinate	η_j-Coordinate	ζ_j-Coordinate	Weights w_j	Order of Accuracy
1 point	1/4	1/4	1/4	1/6	1
4 points	a	b	b	1/24	2
	b	a	b	1/24	
	b	b	a	1/24	
	b	b	b	1/24	
where	$a = \left(5 + 3\sqrt{5}\right)/20 = 0.58541019662497$				
	$b = \left(5 - \sqrt{5}\right)/20 = 0.13819660112501$				
5 points	1/4	1/4	1/4	−2/15	3
	1/2	1/6	1/6	3/40	
	1/6	1/2	1/6	3/40	
	1/6	1/6	1/2	3/40	
	1/6	1/6	1/6	3/40	
11 points	1/4	1/4	1/4	−74/5625	4
	11/14	1/14	1/14	343/45,000	
	1/14	11/14	1/14	343/45,000	
	1/14	1/14	11/14	343/45,000	
	1/14	1/14	1/14	343/45,000	
	a	a	b	56/2250	
	a	b	a	56/2250	
	a	b	b	56/2250	
	b	a	a	56/2250	
	b	a	b	56/2250	
	b	b	a	56/2250	
where	$a = \left(1 + \sqrt{5/14}\right)/4 = 0.399403576166799$				
	$b = \left(1 - \sqrt{5/14}\right)/4 = 0.1005964238332008$				

Source: Data from Jinyun Y. 1984. *Computer Methods in Applied Mechanics and Engineering*; 43: 349–353.

Remark 3.5 Gauss Integration: Simple, Efficient, and Widely Used

The Gauss integration (quadrature) rule is a very simple tool for carrying out numerical integrations for piecewise continuous integrands. It is very efficient, with an order of $(2n_\xi^G - 1)$ accuracy (for square or cubic domains). It is widely used in FEM for evaluating the stiffness matrix, mass matrix, and force vectors. It is also frequently used in S-FEM for the evaluation of smoothed strains, mass matrices, and force vectors. It is indeed a very useful numerical tool.

3.16 Remarks

We conclude this chapter with these remarks.

Remark 3.6 Abstract Version of FEM

This chapter provides a very abstracted version of the standard FEM. For the purpose of using FEM and knowing the basic procedures and properties of FEM models, the materials given are largely sufficient. The materials, such as the formulation of linear elements and Gauss integration, presented in this chapter will be frequently referenced in later chapters.

Remark 3.7 FEM: Element-Based Operations

We have clearly seen a very distinct feature of an FEM model: numerical operations (such as interpolation, shape function construction, and integration) are based on elements. This feature is different from mesh-free methods, where numerical operations can be beyond elements/cells. More details on mesh-free methods can be found in Ref. [11]. In S-FEM models, numerical operations can also be beyond the elements. Therefore, S-FEM models have both features of standard FEM and mesh-free methods.

Remark 3.8 On Q4 and H8 Elements

Note that the Q4 element presented in Section 3.12 is not really a linear element. It is linear only along directions of the edges of the elements. It is in fact *quadratic* along any other direction. This is the major reason why the Q4 element performed much better than the linear T3 elements, and it is preferred by many in the current FEM practice. The only problem is the meshing of an arbitrarily complicated domain with Q4 elements. Our S-FEM models using T3 elements will be frequently compared against the FEM-Q4 elements.

The same situation can be observed with the H8 element. It is quadratic in any direction other than those along the element edges, and hence the

H8 element performed much better than the linear T4 elements. In the H8 element case, the problem is even more serious when coming to meshing. Currently, only the T4 element mesh can be created in a fairly automatic fashion for arbitrarily complicated domains. Our S-FEM models using T4 elements will be frequently compared against the FEM-H8 elements. If S-FEM-T3 and S-FEM-T4 can be made, respectively, comparable with FEM-Q4 and S-FEM-H8, we can then make important progress to develop a very practical and robust method for automatic meshing and remeshing for problems with arbitrarily complicated geometry. In addition, if S-FEM-T3 and S-FEM-T4 can also provide solution bounds to the same complicated problem, we can then progress further to have the numerical solution certified, and adaptive analysis can also be performed to our desired needs with minimum possible elements. The following chapters will present these important developments.

References

1. Bathe KJ. 1996. *Finite Element Procedures*. Prentice Hall, NJ.
2. Hughes TJR. 1987. *The Finite Element Method. Linear Static and Dynamic Finite Element Analysis*. Prentice Hall, NJ.
3. Johnson C. 1987. *Numerical Solution of Partial Differential Equations by the Finite Element Method*. Cambridge University Press, New York.
4. Zienkiewicz OC and Taylor RL. 2000. *The Finite Element Method*, 5th edition. Butterworth Heinemann, Oxford.
5. Liu GR and Quek SS. 2003. *The Finite Element Method: A Practical Course*. Butterworth Heinemann, Oxford.
6. Reddy BD. 1998. *Introductory Functional Analysis*. Springer, New York.
7. Liu GR. 2009. On the G space theory. *International Journal of Computational Methods*; 6(2): 257–289.
8. Liu GR. 2008. A generalized gradient smoothing technique and the smoothed bilinear form for Galerkin formulation of a wide class of computational methods. *International Journal of Computational Methods*; 5: 199–236.
9. Liu GR. 2009. A G space theory and weakened weak (W^2) form for a unified formulation of compatible and incompatible methods, Part I: Theory and Part II: Applications to solid mechanics problems. *International Journal for Numerical Methods in Engineering*, 81: 1093–1156.
10. Liu GR and Zhang GY. 2009. A normed G space and weakened weak (W^2) formulation of a cell-based smoothed point interpolation method. *International Journal of Computational Methods*; 6(1): 147–179.
11. Liu GR. 2009. *Meshfree Methods: Moving Beyond the Finite Element Method*, 2nd edition. CRC Press, Boca Raton, FL.
12. Veubeke BF. 1965. Displacement and equilibrium models in the finite element method. In *Stress Analysis*, OC Zienkiewicz and GS Holister, Eds. Wiley, London.

13. Oliveira Eduardo, R. and De Arantes E. 1968. Theoretical foundations of the finite element method. *International Journal of Solids and Structures*; 4: 929–952.
14. Dunavant DA. 1985. High degree efficient symmetrical Gaussian quadrature rules for the triangle. *International Journal for Numerical Methods in Engineering*; 21: 1129–1148.
15. Jinyun Y. 1984. Symmetric Gaussian quadrature formulae for tetrahedronal regions. *Computer Methods in Applied Mechanics and Engineering*; 43: 349–353.

4

Fundamental Theories for S-FEM

In a standard FEM model, we use directly the so-called compatible strain field that is obtained using the strain–displacement relation and the properly assumed displacement field, as shown in Chapter 3. The strain energy potential functional is evaluated using the compatible strain field. The Galerkin weak form is then used to establish the discrete system of equations. In other words, only the displacement field is assumed.

In an S-FEM model, however, after the displacement field assumption and the evaluation of the compatible strain field, we will modify the compatible strain field. Or we simply construct a strain field directly using the assumed displacement field, without evaluating the compatible strain field. The modified/constructed strain field is then used to evaluate the strain energy potential, and a proper energy weak form is used to construct the discretized model. Such a strain modification/construction must be done in a proper way to ensure stability and convergence and to obtain special properties for the S-FEM model established. In this book, we will use the strain smoothing technique to modify or construct the strain field. The so-called *smoothed Galerkin* weak form will then be used to establish the discrete linear system of equations for our S-FEM models.

This chapter presents the overall modeling procedure, fundamental theories, and necessary building blocks required to construct useful S-FEM models. Our discussion will focus on the creation of displacement field functions or shape function construction, strain modification, or construction, and most importantly the smoothed Galerkin weak form and related theorems with detailed proofs. Important and general features and properties of the S-FEM models will be analyzed, examined with proper proofs. We start with the general setting of S-FEM models.

Note that there are a number of different S-FEM models, because of the types of smoothing domains used, and these S-FEM models will have different features and properties. Four different smoothing domains created based on cells (elements), nodes, edges, and faces will be used to establish four different S-FEM models: cell-based S-FEM (CS-FEM), node-based S-FEM (NS-FEM), edge-based S-FEM (ES-FEM), and face-based S-FEM (FS-FEM). Each of the four S-FEM models will have different advantages and disadvantages. In addition, by a proper combination of NS-FEM and the standard FEM models with a scaling factor alpha (α), a numerical method, named αFEM that uses triangular and tetrahedral elements (αFEM-T3,

αFEM-T4), can also be formulated. αFEM can give nearly exact solutions at least in the strain energy solution.

We note that the theory presented in this chapter is applied, in general, to all these S-FEM models mentioned above, and will be used in later chapters when each of these S-FEM models is presented.

4.1 General Procedure for S-FEM Models

Consider a solid mechanics problem defined in a d-dimensional problem domain $\Omega \in \mathbb{R}^d$ bounded by $\Gamma = \Gamma_u \cup \Gamma_t$, where Γ_u is the essential boundary and Γ_t is the natural boundary, as detailed in Chapter 2. The general procedure of S-FEM models to solve a solid mechanics problem consists of largely the following steps:

1. Discretize the problem domain into elements. S-FEM uses in general n-sided polygonal elements, including triangular elements (T3) for 2D problems and tetrahedron elements (T4) for 3D problems. When T3 and T4 elements are used, meshing can be performed in the same way as in FEM, or simply using a triangulation algorithm such as the Delaunay triangulation algorithm that is widely available. When quadrilateral elements (Q4) are used, the meshing can be performed in exactly the same way as in the FEM. When n-sided elements are used, the procedures given in Section 4.2 may be followed.
2. Create a displacement field through the construction of shape functions. These shape functions constructed for S-FEM models are, in general, different from those used in the FEM model, except for the constant strain elements such as T3 and T4. They are more general, simple, and flexible than those for FEM.
3. Evaluate the compatible strain field in exactly the same way as in the FEM, if T3 or T4 elements are used. In general, for all types of S-FEM elements, S-FEM models can skip over this step.
4. Modify the compatible strain field if a T3 or T4 element is used, or construct the smoothed strain field using shape function values with the help of the gradient smoothing technique over local smoothing domains for all types of elements. The "smoothed strain field" is constructed via simple surface integration on the smoothing domain boundary without any need for coordinate mapping. The construction process of smoothed strain works for all S-FEM models, including those using T3 and T4 elements. FEM does not have this step.

5. Use the "smoothed Galerkin" weak form and the assumed displacement and smoothed strain fields to establish the discrete linear algebraic system of equations, instead of using the Galerkin weak form used in FEM. In this process, S-FEM requires only a simple summation over all the smoothing domains.
6. Impose essential boundary conditions, which are exactly the same as in FEM, because the nodal shape functions constructed in S-FEM always have the Delta function property, and then solve the algebraic system of equations to obtain the displacement solution.
7. Retrieval or recovery of the strain field may be performed, depending on the requirement of the analysis, which is similar to (but not the same as) the practices in FEM.
8. Results assessment that is the same as in FEM.

The following sections detail each of the major steps mentioned above.

4.2 Domain Discretization with Polygonal Elements

FEM does not in general use polygonal elements with more than four sides due mainly to the difficulty in creating shape functions. Therefore, not many techniques for generating such a mesh are available. One technique to discretize a problem domain into n-sided convex polygonal elements can be performed using the well-known Voronoi diagram, and the procedure can be described as follows [1].

The problem domain and its boundaries are first discretized by a set of properly scattered points $\mathbf{P} := \{p_1, p_2, \ldots, p_n\}$. Based on the given points, the domain is further decomposed into the same number of Voronoi cells $\mathbf{C} := \{C_1, C_2, \ldots, C_n\}$ according to the nearest-neighbor rule defined by

$$C_i = \left\{ \mathbf{x} \in \mathbb{R}^2 : d(\mathbf{x}, \mathbf{x}_i) < d\left(\mathbf{x}, \mathbf{x}_j\right), \forall j \neq i \right\}, \quad \forall i. \tag{4.1}$$

In the numerical implementation, as illustrated in Figure 4.1a, the so-generated Voronoi diagram has no cell vertices along the boundaries, and hence additional nodes along the boundary outside the domain need to be added to enclose the cells on the boundaries. With this, the boundary cells are then bounded, but these additional nodes of the cells do not fall *within* the problem domain as shown in Figure 4.1b. Next, these nodes are "shifted" inwards onto the boundaries as shown in Figure 4.1c. The final shape of these Voronoi cells is generally irregular but they are all convex polygons. The initial point p_i is regarded as the representative

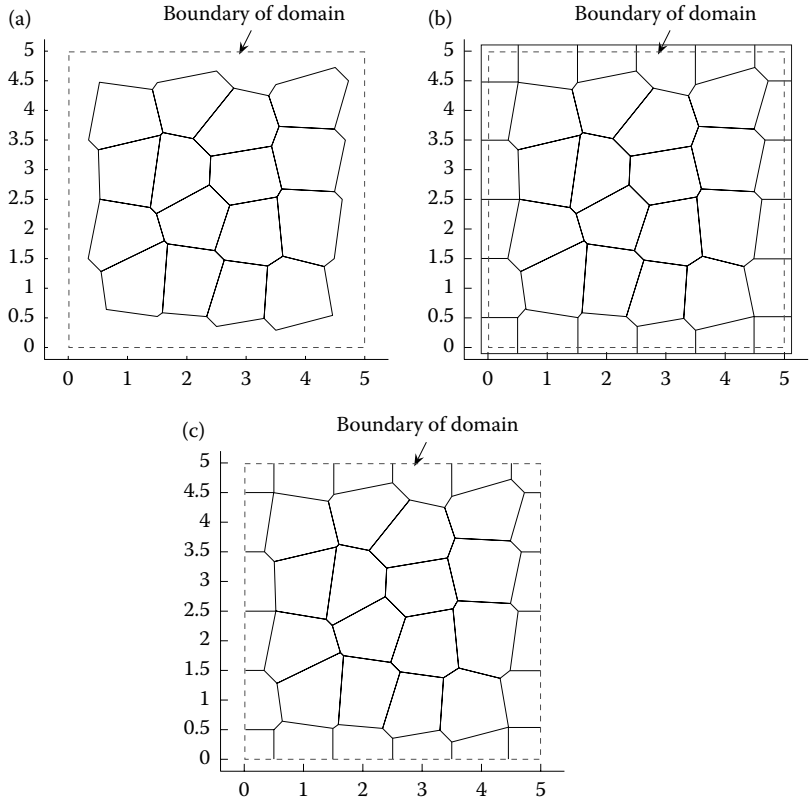

FIGURE 4.1 (a) Voronoi diagram without adding the nodes along the boundary outside the domain; (b) Voronoi diagram with the nodes added along the boundary outside the domain; and (c) final Voronoi diagram.

point of the *i*th element. Once we get the information of these Voronoi diagrams, a set of polygonal elements is then formed for our numerical analysis.

The following points need to be noted: (i) the original discrete points **P** only serve as numerical devices for domain discretization and are not used in the following numerical analysis; (ii) if we prefer more regular elements, such as rectangular elements and hexagonal elements, we need to arrange a special point pattern **P** before the generation of Voronoi diagrams; (iii) for demonstration purposes, we arrange the initial points in an arbitrary form in the following numerical examples without involving the computational cost. As a result, the number of element sides is generally changing from element to element, which is perfectly acceptable to S-FEM models.

4.3 Creating a Displacement Field: Shape Function Construction

S-FEM models create the displacement field functions based on a set of element mesh, through the construction of shape functions. Following exactly the same way as in the standard FEM (see Chapter 3), the problem domain is first discretized properly with N_e elements, N_{eg} edges (or N_{f} faces for 3D), and N_n nodes located at $\mathbf{x}_I$ ($I = 1, 2, \ldots, N_n$). Based on these elements, a set of N_n linearly independent nodal shape functions $\mathbf{N}_I(\mathbf{x}) \in \mathbb{H}^1_h(\Omega; \mathbb{R}^d)$ can be created. The solution of an S-FEM model in terms of a *continuous* displacement field function $\overline{\mathbf{u}} \in \mathbb{H}^1_{0,h}(\Omega; \mathbb{R}^d)$ is then assumed as

$$\overline{\mathbf{u}}(\mathbf{x}) = \sum_{I=1}^{N_n} \mathbf{N}_I(\mathbf{x})\, \overline{\mathbf{d}}_I = \underbrace{\left\{ \mathbf{N}_1(\mathbf{x}) \;\; \mathbf{N}_2(\mathbf{x}) \;\; \cdots \;\; \mathbf{N}_{N_n}(\mathbf{x}) \right\}}_{\mathbf{N}} \underbrace{\begin{Bmatrix} \overline{\mathbf{d}}_1 \\ \overline{\mathbf{d}}_2 \\ \vdots \\ \overline{\mathbf{d}}_{N_n} \end{Bmatrix}}_{\overline{\mathbf{d}}} = \mathbf{N}(\mathbf{x})\, \overline{\mathbf{d}}, \tag{4.2}$$

where $\mathbf{x} = \{x_1 \cdots x_d\}^T$ and $\overline{\mathbf{d}}_I = \overline{\mathbf{u}}(\mathbf{x}_I)$, which is the nodal displacement vector at node I in S-FEM models.

Note that the S-FEM models require only the shape function values to be evaluated at locations on the boundaries of smoothing domains, and no derivatives of the shape functions are needed. Essentially, all we need is to express the displacement value at any point on the smoothing domain boundary using the nodal displacements at surrounding nodes. This feature is significantly different from FEM, and will be used frequently in creating our S-FEM models. The shape function can be constructed in the following two ways: (1) using FEM shape functions (for models using T3 and T4 elements) and (2) using the simple "linear PIM," which is the simplest special case of the general "PIM" [2].

4.3.1 Linear Shape Functions

When three-node triangular (T3) elements or four-node tetrahedral (T4) elements are used, these linear shape functions can be easily obtained, as shown in Equations 3.89 and 3.105, respectively. The S-FEM models can use these shape functions directly.

4.3.2 Linear PIM: A General Approach

A simple linear PIM is now presented, as a general mean, for the construction of shape functions for all S-FEM models using any type of element.

Because the smoothed strain field can be computed using only the assumed displacement values at location on the smoothing domain boundaries, the S-FEM models work well for general n-sided polygonal elements. No derivatives of the assumed displacement field are required. Making use of this important feature, Dai et al. [3] devised a straightforward but important scheme that is now called linear PIM to compute the shape function values for general n-sided polygonal elements. The linear PIM method is now detailed as follows.

Consider an n-sided convex polygonal element Ω_i^e shown in Figure 4.2. We first divide the element into n nonoverlapping and nongap subtriangles $\Omega_{i,p}^e$ $(p = 1, 2, \ldots, n)$ by simply connecting n nodes with the central point O of the polygonal element, as shown in Figure 4.2. The coordinates of the central point O are calculated simply using the coordinates of the nodes:

$$x_O = \frac{1}{n}\sum_{p}^{n} x_p, \quad y_O = \frac{1}{n}\sum_{p}^{n} y_p, \tag{4.3}$$

where $\mathbf{x}_p = [x_p \; y_p]^T$ $(p = 1, 2, \ldots, n)$ are coordinates of the n nodes of the polygonal element.

We then assume that the displacement vector at the central point O, denoted as $\overline{\mathbf{d}}_O$, being the simple average of n displacement vectors $\overline{\mathbf{d}}_p$ $(p = 1, 2, \ldots, n)$ of n nodes of the element, is as follows:

$$\overline{\mathbf{d}}_O = \frac{1}{n}\sum_{p=1}^{n} \overline{\mathbf{d}}_p. \tag{4.4}$$

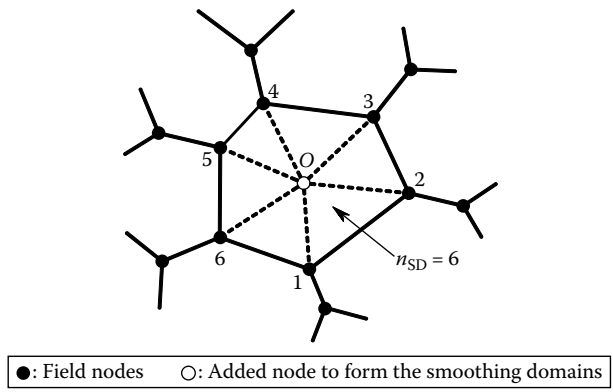

FIGURE 4.2 Division of a six-sided convex polygonal element into six subtriangles by connecting n field nodes with the central point O.

On the first triangular subtriangle $\Omega_{i,1}^e$ (triangle 1–2–O), we now construct a linear displacement field via linear interpolation:

$$\overline{\mathbf{u}}_{i,1}^e = \mathbf{N}_1\overline{\mathbf{d}}_1 + \mathbf{N}_2\overline{\mathbf{d}}_2 + \mathbf{N}_3\overline{\mathbf{d}}_O \quad \text{on } \Omega_{i,1}^e, \tag{4.5}$$

where $\mathbf{N}_j$ ($j = 1, 2, 3$) are the linear shape functions for the subtriangle constructed by three points, $1{-}2{-}O$, which is the same as the shape functions for triangular elements given in Equation 3.89. Substituting Equation 4.4 into Equation 4.5, we obtain

$$\begin{aligned}\overline{\mathbf{u}}_{i,1}^e = &\left(\mathbf{N}_1 + \frac{1}{n}\mathbf{N}_3\right)\overline{\mathbf{d}}_1 + \left(\mathbf{N}_2 + \frac{1}{n}\mathbf{N}_3\right)\overline{\mathbf{d}}_2 \\ &+ \frac{1}{n}\mathbf{N}_3\overline{\mathbf{d}}_3 + \cdots + \frac{1}{n}\mathbf{N}_3\overline{\mathbf{d}}_{n-1} + \frac{1}{n}\mathbf{N}_3\overline{\mathbf{d}}_n.\end{aligned} \tag{4.6}$$

The matrix of these shape functions for the subtriangle $\Omega_{i,1}^e \subset \Omega_i^e$ becomes

$$\mathbf{N}_{i,1}^e = \left\{\mathbf{N}_1 + \frac{1}{n}\mathbf{N}_3 \;\; \mathbf{N}_2 + \frac{1}{n}\mathbf{N}_3 \;\; \frac{1}{n}\mathbf{N}_3 \;\; \cdots \;\; \frac{1}{n}\mathbf{N}_3 \;\; \frac{1}{n}\mathbf{N}_3\right\}_{1\times n}. \tag{4.7}$$

Next, a linear displacement field on the second subtriangle $\Omega_{i,2}^e$ (triangle 2–3–O) is constructed, again via linear interpolation:

$$\overline{\mathbf{u}}_{i,2}^e = \mathbf{N}_1\overline{\mathbf{d}}_2 + \mathbf{N}_2\overline{\mathbf{d}}_3 + \mathbf{N}_3\overline{\mathbf{d}}_O \quad \text{on } \Omega_{i,2}^e, \tag{4.8}$$

which leads to

$$\begin{aligned}\overline{\mathbf{u}}_{i,2}^e = &\frac{1}{n}\mathbf{N}_3\overline{\mathbf{d}}_1 + \left(\mathbf{N}_1 + \frac{1}{n}\mathbf{N}_3\right)\overline{\mathbf{d}}_2 + \left(\mathbf{N}_2 + \frac{1}{n}\mathbf{N}_3\right)\overline{\mathbf{d}}_3 \\ &+ \frac{1}{n}\mathbf{N}_3\overline{\mathbf{d}}_4 + \cdots + \frac{1}{n}\mathbf{N}_3\overline{\mathbf{d}}_n.\end{aligned} \tag{4.9}$$

The matrix of these shape functions for the subtriangle $\Omega_{i,2}^e \subset \Omega_i^e$ becomes

$$\mathbf{N}_{i,2}^e = \left\{\frac{1}{n}\mathbf{N}_3 \;\; \mathbf{N}_1 + \frac{1}{n}\mathbf{N}_3 \;\; \mathbf{N}_2 + \frac{1}{n}\mathbf{N}_3 \;\; \frac{1}{n}\mathbf{N}_3 \;\; \cdots \;\; \frac{1}{n}\mathbf{N}_3\right\}_{1\times n}. \tag{4.10}$$

Following the same procedure, we can construct the matrices of these shape functions for all the remaining subtriangles, which gives $\mathbf{N}_{i,3}^e$ to $\mathbf{N}_{i,n}^e$. A piecewise linear displacement field can then be constructed as a union of all these linear pieces:

$$\overline{\mathbf{u}}_i^e(\mathbf{x}) = \bigcup_{p=1}^{n} \overline{\mathbf{u}}_{i,p}^e(\mathbf{x}). \tag{4.11}$$

Due to the linear variation feature of the displacement fields $\overline{\mathbf{u}}_{i,p}^e$ $(p = 1, 2, \ldots, n)$, the displacement field is obviously continuous along the interfaces of the subtriangles. The union of n linear displacement fields $\overline{\mathbf{u}}_{i,p}^e$ $(p = 1, 2, \ldots, n)$ creates a displacement field $\overline{\mathbf{u}}_i^e$ that is continuous and piecewise linear on the whole n-sided polygonal element Ω_i^e.

In addition, because the interpolation is linear, the displacements on the interfaces of all the polygonal elements will naturally be continuous; hence the displacement field over the entire problem domain Ω is compatible. Therefore, we have constructed a piecewise linear and continuous (compatible) displacement field function that lives in $\mathbb{H}_h^1(\Omega; \mathbb{R}^d)$ (see Example 3.4).

The union of shape function vectors $\mathbf{N}_{i,p}^e$ $(p = 1, 2, \ldots, n)$ also creates a shape function vector $\mathbf{N}_i^e$ (on the n-sided polygonal element Ω_i^e) that is linear within the subtriangles and continuous (compatible) along boundary segments of the subtriangles of the element. Hence

$$\mathbf{N}_i^e(\mathbf{x}) = \bigcup_{p=1}^{n} \mathbf{N}_{i,p}^e(\mathbf{x}), \tag{4.12}$$

which also lives in an $\mathbb{H}_h^1(\Omega; \mathbb{R}^d)$ space.

Remark 4.1 Properties of the Shape Functions for n-Sided Polygonal Elements

It is easy to verify the following properties of the shape function vector $\mathbf{N}_{i,p}^e = \underbrace{\left\{ \mathbf{N}_{i,p1}^e \;\; \mathbf{N}_{i,p2}^e \;\; \cdots \;\; \mathbf{N}_{i,pj}^e \;\; \cdots \;\; \mathbf{N}_{i,pn}^e \right\}}_{1 \times n}$ for any discrete point $\mathbf{x} \in \Omega_{i,p}^e \subset \Omega_i^e$ $(p = 1, 2, \ldots, n)$: (i) Kronecker Delta at nodes $\mathbf{x}_p$ and $\mathbf{x}_{p+1}$; (ii) partition of unity: $\sum_{j=1}^n \mathbf{N}_{i,pj}^e(\mathbf{x}) = 1$; (iii) linear consistency: $\sum_{j=1}^n \mathbf{N}_{i,pj}^e(\mathbf{x})\mathbf{x}_j = \mathbf{x}$; (iv) compatibility: continuous along the boundary segments of $\Omega_{i,p}^e$; and (v) $\mathbf{N}_{i,pj}^e(\mathbf{x}) \geq 0$.

Remark 4.2 Shape Function for the T3 Element

Note that for the three-node triangular elements, the above approach of creating shape functions will give exactly the linear shape function used in the triangular elements of the standard FEM. We therefore simply use the shape functions for the T3 element of the FEM given in Equation 3.89.

Remark 4.3 Shape Function for the T4 Element in 3D Problems

For the four-node tetrahedral elements, S-FEM models use the linear shape functions used in tetrahedral elements of the standard FEM given in Equation 3.105.

Remark 4.4 Shape Function by PIM

For all the elements used in S-FEM (T3, T4, Q4, n-sided polygonal), the linear PIM can always be used for evaluating the shape function values. Such a linear PIM can be enriched for special purposes (see Chapter 10). In more general mesh-free settings, the general PIM can be used for creating the shape functions for various smoothed PIMs or S-PIMs, which is beyond the scope of this book. Interested readers may refer to Ref. [2] for details.

Remark 4.5 Sparseness of the Shape Function Matrix

Because $\mathbf{N}_j(\mathbf{x})$ for node j is locally supported by elements sharing the node, it is zero beyond these elements. For any given $\mathbf{x} \in \Omega$, it will surely fall in one of the elements, say the ith element, and hence $\mathbf{x} \in \Omega_i^e \subset \Omega$. The ith element will have a very small number of nodes (e.g., three nodes for T3 elements). Therefore, $\overline{\mathbf{u}}(\mathbf{x})$ in Equation 4.2 relates only to three nodal shape functions, and the shape function matrix $\mathbf{N}(\mathbf{x})$ will be an extremely *sparse* matrix with lots of zeros for an actual model that usually has a large number of nodes, due to the locally supported feature of the nodal shape functions. The expression of $\overline{\mathbf{u}}(\mathbf{x})$ in Equation 4.2 using all the field nodes is only for convenience. In actual situations, we need only the nodes of the element hosting $\mathbf{x}$. This sparseness is largely the same as in FEM (see Remark 3.2).

4.4 Evaluation of the Compatible Strain Field

Following, again, exactly the same way as in the standard FEM (see Chapter 3), the compatible strain field can be evaluated using the strain–displacement relation. When the S-FEM solution in displacement is assumed in the form of Equation 4.2, we have

$$\tilde{\boldsymbol{\varepsilon}}(\mathbf{x}) = \mathbf{L}_d \overline{\mathbf{u}} = \mathbf{L}_d \left(\sum_{I=1}^{N_n} \mathbf{N}_I(\mathbf{x})\, \overline{\mathbf{d}}_I \right) = \sum_{I=1}^{N_n} \underbrace{\mathbf{L}_d \mathbf{N}_I(\mathbf{x})}_{\tilde{\mathbf{B}}_I} \overline{\mathbf{d}}_I = \sum_{I=1}^{N_n} \tilde{\mathbf{B}}_I \overline{\mathbf{d}}_I = \tilde{\mathbf{B}} \overline{\mathbf{d}}, \tag{4.13}$$

where

$$\tilde{\mathbf{B}}_I = \mathbf{L}_d \mathbf{N}_I(\mathbf{x}) \tag{4.14}$$

is the strain–displacement matrix, and

$$\tilde{\mathbf{B}} = \left[\underbrace{\tilde{\mathbf{B}}_1(\mathbf{x})}_{\mathbf{L}_d \mathbf{N}_1(\mathbf{x})} \quad \underbrace{\tilde{\mathbf{B}}_2(\mathbf{x})}_{\mathbf{L}_d \mathbf{N}_2(\mathbf{x})} \quad \cdots \quad \underbrace{\tilde{\mathbf{B}}_{N_n}(\mathbf{x})}_{\mathbf{L}_d \mathbf{N}_{N_n}(\mathbf{x})} \right] = \mathbf{L}_d \mathbf{N}(\mathbf{x}) \tag{4.15}$$

is the *global* strain–displacement matrix. It is clear that due to the sparseness of shape function matrix $\mathbf{N}$ (see Remark 4.5), $\tilde{\mathbf{B}}$ is also extremely sparse.

This step is usually skipped in S-FEM models. Only when T3 and T4 elements are used, the evaluation of compatible strain is (but does not have to be) performed for its simplicity. For other types of elements, it is difficult or tedious to evaluate the compatible strain field. The S-FEM models simply construct a "smoothed strain field," which is detailed in the following section.

4.5 Modify/Construct the Strain Field

A *smoothed* strain field can then be obtained via a proper modification of the compatible strain field when it is conveniently available, such as for T3 or T4 elements. Otherwise, a smoothed strain field can be constructed using directly the displacements, with the help of *smoothing* operation. Such a smoothing operation is performed based on a set of smoothing domains that are created on top of the element mesh.

4.5.1 Smoothing Domain Creation

In S-FEM models, a mesh of elements is required, which can be created in exactly the same manner as in the standard FEM using a commercially available software package or any proper in-house or open code. Consider now that a mesh of N_e elements with N_n nodes and N_{eg} edges (or N_{f} faces for 3D domains) has already been created.

On top of the element mesh, the problem domain Ω is then divided into a set of N_s "nonoverlap" and "no-gap" smoothing domains Ω_k^s such that $\Omega = \bigcup_{k=1}^{N_s} \Omega_k^s$ and $\Omega_i^s \cap \Omega_j^s = \emptyset, i \neq j$. In theory, such a division can be arbitrary when continuous shape functions are used.* In practice, however, it is usually performed based on element entities, such as cells residing in elements, or nodes, edges, or faces of the elements for easy formulation, numerical treatments, implementation, and efficient computation. To ensure the stability of S-FEM models, the number of smoothing domains created has to satisfy certain conditions, as will be discussed in detail in Section 4.6. Table 4.1 lists a number of types of smoothing domains and the corresponding S-FEM models.

In an S-FEM model, the smoothing domain usually consists of a number of (nonoverlapping and no-gap) subsmoothing domains: $\Omega_k^s = \bigcup_{q=1}^{n_s} \Omega_{k,q}^s$

* When discontinuous shape functions are used in general mesh-free settings, a so-called no-sharing rule needs to be observed [18].

TABLE 4.1

Typical Types of Smoothing Domains

Name	Method for Creation (Number of Smoothing Domains, N_s)	S-FEM Models	Problem Domain
Cell-based smoothing domain (CSD)	Based on elements ($N_s = N_e$ for single division) or cells formed by dividing further the elements ($N_s = N_c$ for multiple division)	CS-FEM (SFEM) [24,34,35]	1D, 2D, 3D
Node-based smoothing domain (NSD)	Based on each of the nodes of the mesh by connecting portions of the surrounding elements sharing the node ($N_s = N_n$)	NS-FEM [31]	1D, 2D, 3D
Edge-based smoothing domain (ESD)	Based on each edge of the mesh by connecting portions of the element sharing the edge ($N_s = N_{eg}$)	ES-FEM [36]	2D
Face-based smoothing domain (FSD)	Based on each face of the element mesh by connecting portions of the surrounding elements sharing the face ($N_s = N_f$)	FS-FEM [37]	3D

and $\Omega^s_{k,i} \cap \Omega^s_{k,j} = \emptyset, i \neq j$, where $\Omega^s_{k,q}$ is the qth subsmoothing domain and n_s is the number of subsmoothing domains that forms Ω^s_k, which is also the number of elements contributing to or "supporting" the smoothing domain.

4.5.1.1 CS-FEM

For CS-FEM, the number of smoothing domains N_s can be the same as the element number N_e, meaning one element is used as one smoothing domain, as shown in Figure 4.3. In this single division case, we have $N_s = N_e$. For stability reasons (see Section 4.6), it is more common to subdivide each element into SD $\in [1, \infty)$ number of smoothing domains, as shown in Figure 4.4. In this multidivision case, the number of smoothing domains should be the number of cells, N_c, and we have $N_s = N_c = \text{SD} \times N_e$ if the same SD is used for all the elements in the mesh.

4.5.1.2 NS-FEM

For NS-FEM using n-sided polygonal elements, the smoothing domain Ω^s_k associated with node k is created by connecting sequentially the mid-edge-point to the central points of the surrounding elements sharing node k as shown in Figure 4.5. In this case, a smoothing domain Ω^s_k consists of $n_s \geq 1$ subsmoothing domains $\Omega^s_{k,q}$, each of which is a part of the elements "supporting" the smoothing domain Ω^s_k. Thus n_s is in fact the number of elements sharing node k. These interfaces of the surrounding elements divide Ω^s_k into n_s subsmoothing domains $\Omega^s_{k,q}$ $(q = 1, \ldots, n_s)$, and hence also form the interfaces between these $\Omega^s_{k,q}$. Depending on the type of the mesh, and the location of the node in the mesh, n^s_k for each smoothing domain Ω^s_k will be different and, in general, $n_s \geq 1$.

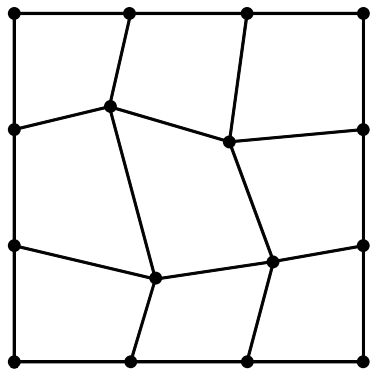

FIGURE 4.3 A simple example of an FEM mesh using four-node elements (Q4).

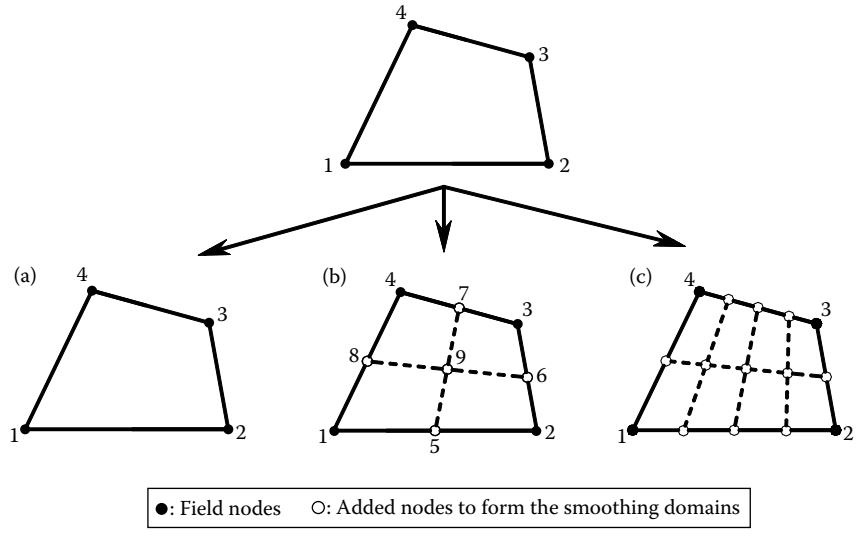

FIGURE 4.4 Division of a four-node quadrilateral element into the smoothing domains (SDs) in CS-FEM by connecting the mid-segment points of opposite segments of smoothing domains: (a) 1 SD; (b) 4 SDs; and (c) 8 SDs.

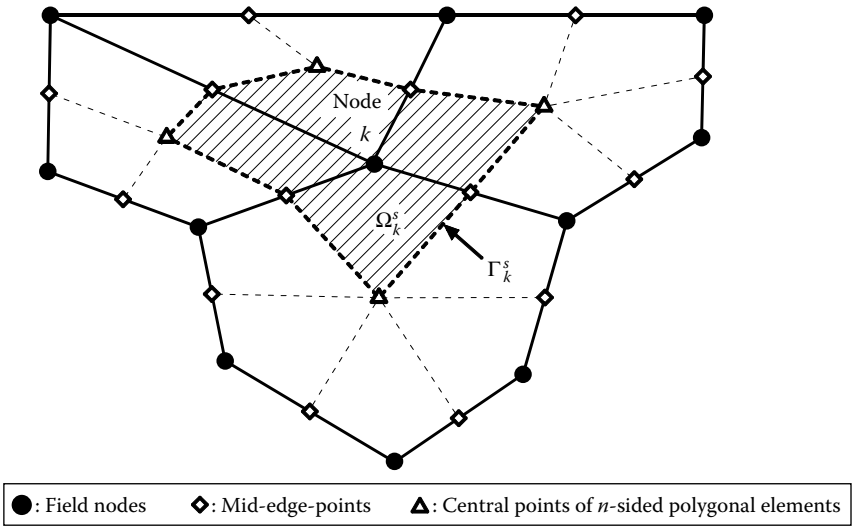

FIGURE 4.5 *n*-sided polygonal elements and the smoothing domain (shaded area) associated with node *k* in NS-FEM.

4.5.1.3 ES-FEM

For ES-FEM, the smoothing domain Ω_k^s is associated with the edge k of the elements, and hence $N_s = N_{\text{eg}}$ in this case. The edge-based smoothing domain is created by connecting two endpoints of the edge to central points of the adjacent elements as shown in Figures 4.6 and 4.7 (for a mesh of triangular elements). In this case, a smoothing domain Ω_k^s consists of n_s subsmoothing domains $\Omega_{k,q}^s$, each of which is a part of the elements supporting the smoothing domain Ω_k^s. Thus n_s is in fact the number of elements sharing edge k. The edge divides Ω_k^s into subsmoothing domains $\Omega_{k,q}^s$ $(q = 1, \ldots, n_s)$, and hence also forms the interfaces between these $\Omega_{k,q}^s$. For an *inner edge* (at least one of these two ending nodes of the edge is located inside the domain Ω), $n_s = 2$, and for a boundary edge (both ending nodes of the edge are located on Γ), $n_s = 1$.

4.5.1.4 FS-FEM

For FS-FEM, the smoothing domains are formed associated with faces of the elements in the mesh, and hence $N_s = N_{\text{f}}$ in this case. The smoothing

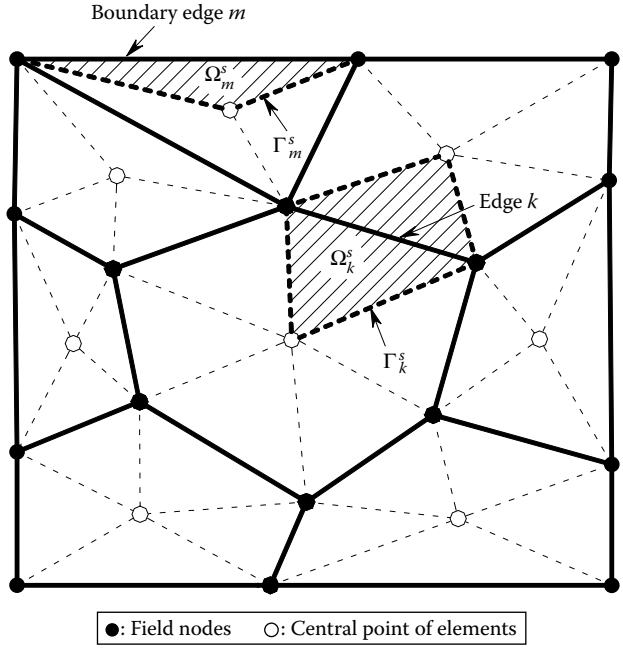

FIGURE 4.6 n-sided polygonal elements and the smoothing domains (shaded areas) associated with edges in ES-FEM.

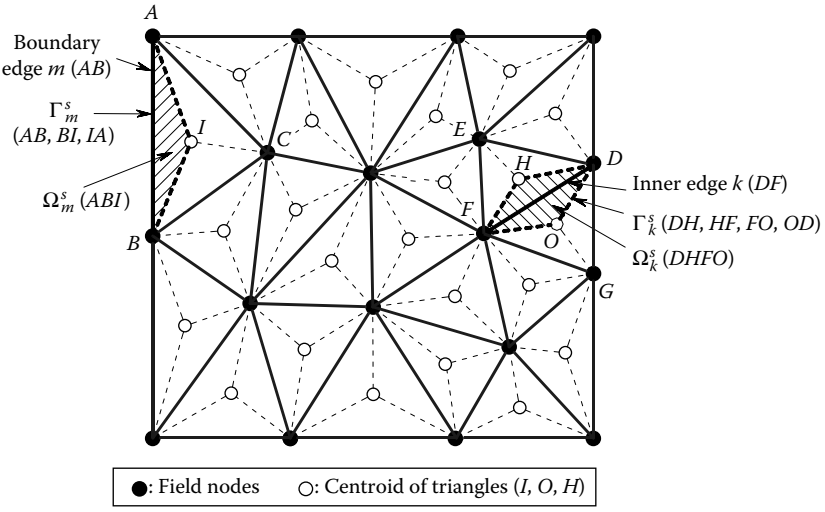

FIGURE 4.7 Triangular elements and the smoothing domains (shaded areas) associated with edges in ES-FEM.

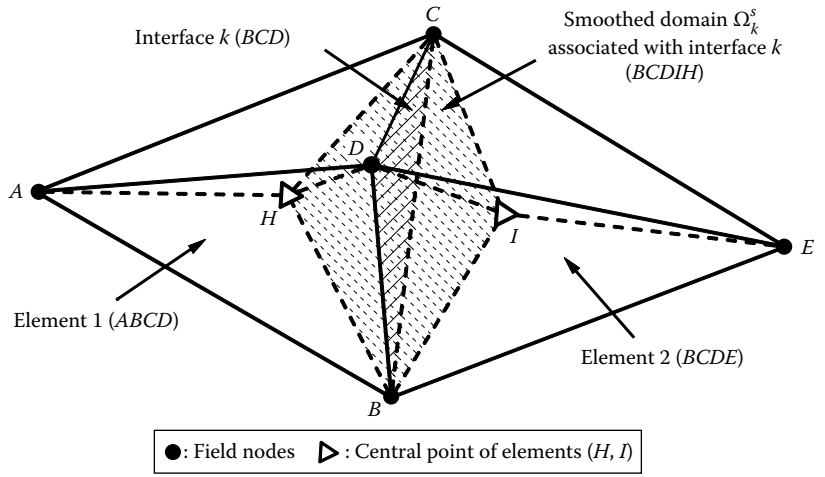

FIGURE 4.8 Two adjacent tetrahedral elements and the smoothing domain (shaded domain) formed based on their interface k in FS-FEM.

domain Ω_k^s associated with face k is created by connecting the nodes on the face to the centers of adjacent elements, as shown in Figure 4.8 for a mesh of tetrahedral elements. For an *inner face* (at least one of these nodes on the face is located inside the domain Ω), $n_s = 2$, and for a *boundary face* (all the nodes on the face are located on Γ), $n_s = 1$.

4.5.2 Smoothed Strain Field Creation

The strain/gradient smoothing technique is the simplest most frequently used approach to obtain a smoothed strain field for an S-FEM model. The approach uses two assumptions:

1. The strain at a location inside the smoothing domain is approximated by smoothing the compatible strain field or the displacement gradient in the smoothing domain, using the strain/gradient smoothing technique.
2. The smoothed strain field inside the entire smoothing domain is assumed to be constant and is the approximated strain obtained at step (1).

For the compatible strain field given in Equation 4.13, a smoothed strain field $\bar{\boldsymbol{\varepsilon}}$ at location $\mathbf{x}_k$ can be obtained using the integral approximation technique as follows [2,4–14]:

$$\bar{\boldsymbol{\varepsilon}}(\mathbf{x}_k) = \begin{cases} \int\limits_{\Omega_k^s} \tilde{\boldsymbol{\varepsilon}}(\mathbf{x})\, \widehat{W}(\mathbf{x}_k - \mathbf{x})\, \mathrm{d}\Omega & \text{when } \tilde{\boldsymbol{\varepsilon}}(\mathbf{x}) \text{ is easily available,} \\ \int\limits_{\Omega_k^s} \mathbf{L}_d \bar{\mathbf{u}}(\mathbf{x}) \widehat{W}(\mathbf{x}_k - \mathbf{x})\, \mathrm{d}\Omega & \text{in general,} \end{cases} \tag{4.16}$$

where $\tilde{\boldsymbol{\varepsilon}}(\mathbf{x})$ is the compatible strain field evaluated using an assumed displacement field, Ω_k^s is a smoothing domain defined in the local vicinity of $\mathbf{x}_k$, and $\widehat{W}(\mathbf{x}_k - \mathbf{x})$ is a smoothing or weight function associated with $\mathbf{x}_k$. To ensure a valid and efficient S-FEM model, the smoothing function has to satisfy certain basic conditions.

4.5.3 Basic Conditions for the Smoothing Function

The smoothing function should satisfy the following basic conditions [2,6]:

1. It should be "locally supported," meaning that it is nonzero only in the vicinity of $\mathbf{x}_k$
2. It should be positive over the local support domain
3. It should be centered at $\mathbf{x}_k$
4. It should satisfy the unity property

$$\int\limits_{\Omega_k^s} \widehat{W}(\mathbf{x}_k - \mathbf{x})\, \mathrm{d}\Omega = 1. \tag{4.17}$$

In this book, we use the following simplest form of the Heaviside-type smoothing function:

$$\widehat{W}(\mathbf{x}_k - \mathbf{x}) = \begin{cases} 1/A_k^s, & \mathbf{x} \in \boxed{\Omega}_k^s, \\ 0, & \mathbf{x} \notin \boxed{\Omega}_k^s, \end{cases} \tag{4.18}$$

where $A_k^s = \int_{\Omega_k^s} \mathrm{d}\Omega$ is the area of smoothing domain Ω_k^s. Here the frame for domain Ω_k^s stands for the *closed domain*: $\boxed{\Omega}_k^s = \Omega_k^s \cup \Gamma_k^s$. We require the smoothing function to vanish only out of $\boxed{\Omega}_k^s$ to ensure that $\widehat{W}(\mathbf{x}_k - \mathbf{x})$ is differentiable over Ω_k^s, which is important for the later application of Green's theorem.

4.5.4 Smoothed Strain by Smoothing the Compatible Strain

When the compatible strain field is easily available, using Equations 4.16 and 4.18 gives

$$\overline{\boldsymbol{\varepsilon}}(\mathbf{x}_k) = \frac{1}{A_k^s} \int_{\Omega_k^s} \tilde{\boldsymbol{\varepsilon}}(\mathbf{x})\, \mathrm{d}\Omega, \tag{4.19}$$

which means that the strain at $\mathbf{x}_k$ is approximated using the simple average of the compatible strain over the area of smoothing domain Ω_k^s. Note that our integration is over open domains, because we always use Lebesgue integration (see Remark 3.1): $\int_{\Omega_k^s} \tilde{\boldsymbol{\varepsilon}}(\mathbf{x})\, \mathrm{d}\Omega$ is the same as $\int_{\boxed{\Omega}_k^s} \tilde{\boldsymbol{\varepsilon}}(\mathbf{x})\, \mathrm{d}\Omega$.

In an S-FEM model, we further assume that the strain in the smoothing domain Ω_k^s is a constant and equals $\overline{\boldsymbol{\varepsilon}}(\mathbf{x}_k)$:

$$\overline{\boldsymbol{\varepsilon}}_k = \overline{\boldsymbol{\varepsilon}}_k(\mathbf{x}) = \overline{\boldsymbol{\varepsilon}}(\mathbf{x}_k) = \frac{1}{A_k^s} \int_{\Omega_k^s} \tilde{\boldsymbol{\varepsilon}}(\mathbf{x})\, \mathrm{d}\Omega, \quad \forall \mathbf{x} \in \Omega_k^s. \tag{4.20}$$

Therefore, the strain field in an S-FEM model is piecewise constant and lives in $\mathbb{L}^2(\Omega)$ space (see Example 3.2).

4.5.5 Smoothed Strain by Boundary Flux

In general, we assume that the compatible strain field is not easily available, and hence we shall work only with the displacement field. Because the assumed displacement field in an S-FEM model is *continuous* on Γ_k^s, and because $\widehat{W}(\mathbf{x}_k - \mathbf{x})$ defined in Equation 4.18 is differentiable over Ω_k^s, we

can then use Green's divergence theorem (or integration by parts), and Equation 4.16 becomes

$$\begin{aligned}\overline{\boldsymbol{\varepsilon}}(\mathbf{x}_k) &= \int_{\Omega_k^s} \hat{W}(\mathbf{x}_k - \mathbf{x})\, \mathbf{L}_d \overline{\mathbf{u}}(\mathbf{x})\, \mathrm{d}\Omega \\ &= -\int_{\Omega_k^s} \underbrace{\mathbf{L}_d \hat{W}(\mathbf{x}_k - \mathbf{x})}_{=\mathbf{0},\ \text{in } \Omega_k^s} \overline{\mathbf{u}}(\mathbf{x})\, \mathrm{d}\Omega + \frac{1}{A_k^s} \int_{\Gamma_k^s} \mathbf{L}_n(\mathbf{x}) \overline{\mathbf{u}}(\mathbf{x})\, \mathrm{d}\Gamma \\ &= \frac{1}{A_k^s} \int_{\Gamma_k^s} \mathbf{L}_n(\mathbf{x}) \overline{\mathbf{u}}(\mathbf{x})\, \mathrm{d}\Gamma, \end{aligned} \tag{4.21}$$

where $\mathbf{L}_n(\mathbf{x})$ is the matrix of components of the outward normal vector on boundary Γ_k^s and has the form of

$$\mathbf{L}_n(\mathbf{x}) = \begin{bmatrix} n_x & 0 \\ 0 & n_y \\ n_y & n_x \end{bmatrix}, \tag{4.22}$$

in which n_x and n_y are unit outward normal components in the x-axis and y-axis, respectively.

The integral on the right-hand side of Equation 4.21 is a line integration along the boundary of Ω_k^s denoted by Γ_k^s, meaning that the smoothed strain is obtained by the evaluation of flux on the boundary of the smoothing domain. In our S-FEM models, we further assume that the strain in the smoothing domain is constant and equals $\overline{\boldsymbol{\varepsilon}}(\mathbf{x}_k)$:

$$\overline{\boldsymbol{\varepsilon}}_k = \overline{\boldsymbol{\varepsilon}}_k(\mathbf{x}) = \overline{\boldsymbol{\varepsilon}}(\mathbf{x}_k) = \frac{1}{A_k^s} \int_{\Gamma_k^s} \mathbf{L}_n(\mathbf{x}) \overline{\mathbf{u}}(\mathbf{x})\, \mathrm{d}\Gamma, \quad \forall \mathbf{x} \in \Omega_k^s. \tag{4.23}$$

Note that as long as the displacement is continuous over Ω, Equation 4.23 is essentially the same as Equation 4.20. However, Equation 4.23 is much more general [2], and easier to apply for different types of elements and different S-FEM models. Therefore, for the general discussions of an S-FEM model in this book, we use Equation 4.23 as the default. We note the following.

Remark 4.6 Smoothed Strain Field: Using Only Displacements

The S-FEM model uses the smoothed strain field that is evaluated using only displacements on the boundary of the smoothing domains, ensuring the equivalence of strain in the smoothing domain and flux on the boundary of the smoothing domain. No derivatives of the displacements are needed.

4.5.6 An Analysis on Subdivision of Smoothing Domains

In an S-FEM model, the displacement is continuous over Ω. Each of the N_s smoothing domains Ω_k^s in general consist of $n_s \geq 1$ subsmoothing domain $\Omega_{k,q}^s$, each of which is a part of the elements sharing or "supporting" the smoothing domain Ω_k^s, as discussed in Section 4.5.1. These edges of the supporting elements divide Ω_k^s into $\Omega_{k,q}^s$ $(q = 1, \ldots, n_s)$ and hence form the interfaces between these $\Omega_{k,q}^s$. Therefore, the compatible strain field $\tilde{\boldsymbol{\varepsilon}}(\mathbf{x}) = \mathbf{L}_d \overline{\mathbf{u}}(\mathbf{x})$ (if obtained) is continuous (may not be constant) inside each of the subsmoothing domains $\Omega_{k,q}^s$, but can be discontinuous on the (inner) interfaces of domains $\Omega_{k,q}^s$. For example, for an ES-FEM model using three-node triangular elements of linear shape functions, as shown in Figure 4.9, a smoothing domain Ω_k^s associated with inner edge k will include $n_s = 2$ triangular subsmoothing domains $\Omega_{k,1}^s$ and $\Omega_{k,2}^s$ on both sides of the kth edge. The compatible strain field $\tilde{\boldsymbol{\varepsilon}}(\mathbf{x})$ is piecewise constant and discontinuous along edge k (or called the common inner boundary $\Gamma_{k,1-2(\text{inner})}^s$ of $\Omega_{k,1}^s$ and $\Omega_{k,2}^s$).

By using the piecewise constant smoothing function in Equation 4.18 and applying the divergence theorem on each subsmoothing cell $\Omega_{k,q}^s$ (note that our displacement function is continuous), the smoothed strain $\overline{\boldsymbol{\varepsilon}}_k$ of the smoothing domain Ω_k^s in Equation 4.16 can be evaluated as follows:

$$\overline{\boldsymbol{\varepsilon}}_k = \int_{\Omega_k^s} \mathbf{L}_d \overline{\mathbf{u}}(\mathbf{x}) \frac{1}{A_k^s} \, \mathrm{d}\Omega = \frac{1}{A_k^s} \sum_{q=1}^{n_s} \int_{\Omega_{k,q}^s} \mathbf{L}_d \overline{\mathbf{u}}(\mathbf{x}) \, \mathrm{d}\Omega = \frac{1}{A_k^s} \sum_{p=1}^{n_s} \int_{\Gamma_{k,q}^s} \mathbf{L}_n(\mathbf{x}) \overline{\mathbf{u}}(\mathbf{x}) \, \mathrm{d}\Gamma, \tag{4.24}$$

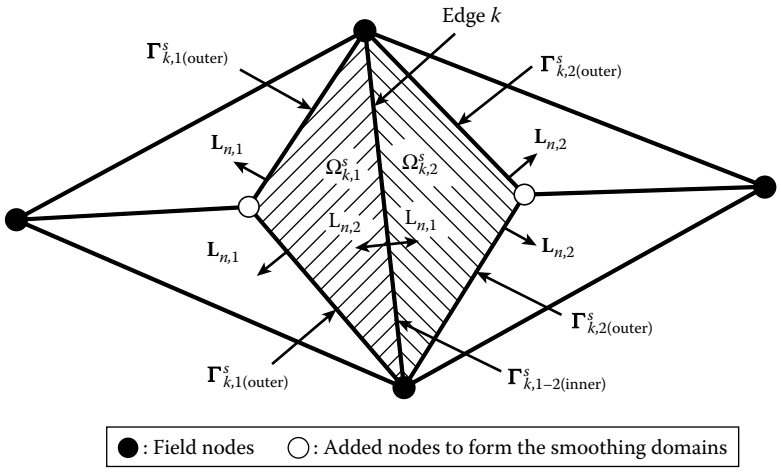

FIGURE 4.9 Division of the smoothing domain Ω_k^s associated with edge k into two adjacent subsmoothing domains $\Omega_{k,1}^s$ and $\Omega_{k,2}^s$ that have the common inner boundary $\Gamma_{k,1-2(\text{inner})}^s$.

where $\Gamma^s_{k,q}$ is the boundary of the smoothing cell $\Omega^s_{k,q}$ and $\mathbf{L}_n(\mathbf{x})$ is the matrix of the components of the outward normal vector on the boundary $\Gamma^s_{k,q}$.

The smoothing cell boundary segments $\Gamma^s_{k,q}$ are now categorized into two types: inner boundaries $\Gamma^s_{k,q(\text{inner})}$, which locate inside the smoothing domain Ω^s_k, and outer boundaries $\Gamma^s_{k,q(\text{outer})}$, which are on the boundary of the smoothing domain Ω^s_k. Because (again) the displacement field is *continuous*, we have the following results for two adjacent subsmoothing domains $\Omega^s_{k,1}$ and $\Omega^s_{k,2}$ that have the common inner boundary $\Gamma^s_{k,1-2(\text{inner})}$, as shown in Figure 4.9:

$$(\mathbf{L}_n(\mathbf{x})\overline{\mathbf{u}}(\mathbf{x}))\Big|_{\Gamma^s_{k,1(\text{inner})}} + (\mathbf{L}_n(\mathbf{x})\overline{\mathbf{u}}(\mathbf{x}))\Big|_{\Gamma^s_{k,2(\text{inner})}} = \mathbf{0} \quad \text{on } \Gamma^s_{k,1-2(\text{inner})}. \tag{4.25}$$

Equation 4.25 implies that when a *continuous* displacement field is used, the summation of two integrals $\sum_{q=1}^{2}\int_{\Gamma^s_{k,1-2(\text{inner})}} \mathbf{L}_n(\mathbf{x})\overline{\mathbf{u}}(\mathbf{x})\,\mathrm{d}\Gamma$ of two adjacent subsmoothing domains $\Omega^s_{k,1}$ and $\Omega^s_{k,2}$ on the inner boundaries $\Gamma^s_{k,1-2(\text{inner})}$ will vanish, due to the opposite sign of $\mathbf{L}_n$ for $\Gamma^s_{k,1(\text{inner})}$ and $\mathbf{L}_n$ for $\Gamma^s_{k,2(\text{inner})}$. Hence, the summation in Equation 4.24 for all inner boundaries $\Gamma^s_{k,q(\text{inner})}$ will vanish and Equation 4.24 is reduced into a much simpler form that keeps the summation over only these outer boundaries as follows:

$$\overline{\boldsymbol{\varepsilon}}_k = \frac{1}{A^s_k}\sum_{q=1}^{n_s}\int_{\Gamma^s_{k,q(\text{outer})}} \mathbf{L}_n(\mathbf{x})\overline{\mathbf{u}}(\mathbf{x})\,\mathrm{d}\Gamma = \frac{1}{A^s_k}\int_{\Gamma^s_k} \mathbf{L}_n(\mathbf{x})\overline{\mathbf{u}}(\mathbf{x})\,\mathrm{d}\Gamma, \tag{4.26}$$

where $\Gamma^s_k = \sum_{q=1}^{n_s}\Gamma^s_{k,q(\text{outer})}$ is the boundary of the smoothing domain Ω^s_k.

Note that Equation 4.26 is exactly Equation 4.23. The above derivation and analysis process shows that we can have an alternative procedure to evaluate the smoothed strain, by independently evaluating each portion of the subsmoothing domains of the smoothing domain and then adding together. This can sometimes make the numerical implementations easier, because we do not need to worry whether the smoothing domains are located on the boundary or located inside the problem domain. Equation 4.26 or 4.23 stands, as long as the assumed displacement field is continuous.

When the compatible strain field is easily available, Equation 4.19 for smoothing domains with multiple subsmoothing domains becomes

$$\overline{\boldsymbol{\varepsilon}}_k = \frac{1}{A^s_k}\int_{\Omega^s_k}\tilde{\boldsymbol{\varepsilon}}(\mathbf{x})\,\mathrm{d}\Omega = \frac{1}{A^s_k}\sum_{q=1}^{n_s} A^s_{k,q}\underbrace{\frac{1}{A^s_{k,q}}\int_{\Omega^s_{k,q}}\tilde{\boldsymbol{\varepsilon}}(\mathbf{x})\,\mathrm{d}\Omega}_{\overline{\boldsymbol{\varepsilon}}_{k,q}} = \frac{1}{A^s_k}\sum_{q=1}^{n_s} A^s_{k,q}\overline{\boldsymbol{\varepsilon}}_{k,q}, \tag{4.27}$$

which means that the smoothed strain in a smoothing domain is an area-weighted average of the smoothed strains in these subsmoothing domains. If the compatible strain in each subsmoothing domain is constant (such as in a T3 or T4 element), we further have

$$\bar{\boldsymbol{\varepsilon}}_k = \frac{1}{A_k^s} \sum_{q=1}^{n_s} A_{k,q}^s \tilde{\boldsymbol{\varepsilon}}_{k,q}, \tag{4.28}$$

where $\tilde{\boldsymbol{\varepsilon}}_{k,q}$ is the (constant) compatible strain of the qth subsmoothing domain of Ω_k^s.

4.5.7 Comments on Strain/Gradient Smoothing Techniques

Various smoothing techniques have been used for different purposes, including in nonlocal continuum mechanics [15] to introduce size effects, and in smoothed particle hydrodynamics [4–6] to approximate field functions and their derivatives. Gradient smoothing was in fact used in the well-known widely used FVM [7]. It was also used in formulating so-called quasiconforming elements [8] and for the discretization of differential operators based on nodes [9]. Strain smoothing was used to resolve material instabilities [10] and spatial instability in nodal integrated mesh-free methods [11]. It was also used in the so-called GSM to approximate the derivatives using various types of properly nested smoothing domains to construct strong-form models for solid mechanics problems [12], compressible fluids [13,14], and incompressible fluids [16]. It was found that as long as the smoothing operation is *strictly* used in all the gradient approximations in a *properly nested manner* and no interpolation is used, *stable* strong-form numerical models can be formulated [2]. The strain/gradient smoothing technique is indeed a very powerful piece of numerical technique. In this book, the strain smoothing operation defined in Equation 4.23 will be applied to construct the strain field in finite element settings using properly designed smoothing domains, leading to various S-FEM models.

The assumption given in Equations 4.20 and 4.23 simplifies to a great extent the numerical treatments in S-FEM models. It can be shown that the transformation from $\tilde{\boldsymbol{\varepsilon}}(\mathbf{x})$ to $\bar{\boldsymbol{\varepsilon}}(\mathbf{x})$ defined in Equations 4.20 and 4.23 is an orthogonal projection [2]. We will also show in Section 4.7 that the smoothed strain field satisfies the so-called orthogonal condition, which ensures the variational consistency of S-FEM models.

A generalized gradient smoothing technique has recently been proposed to allow the use of discontinuous displacement functions [17]. A so-called $\mathbb{G}$ space theory [18,19] and W^2 formulation of a wide class of computational methods (compatible and incompatible) under the FEM and mesh-free settings have also been established [17,18]. Detailed development in this direction can be found in Refs. [2–19].

4.5.8 Smoothed Strain–Displacement Matrix

Now, substituting Equation 4.2 into Equation 4.23, one obtains the smoothed strain as

$$\bar{\boldsymbol{\varepsilon}}(\mathbf{x}) = \sum_{I=1}^{N_n} \overline{\mathbf{B}}_I(\mathbf{x})\, \bar{\mathbf{d}}_I = \underbrace{\left[\, \overline{\mathbf{B}}_1(\mathbf{x}) \;\; \overline{\mathbf{B}}_2(\mathbf{x}) \;\; \cdots \;\; \overline{\mathbf{B}}_{N_n}(\mathbf{x}) \,\right]}_{\overline{\mathbf{B}}(\mathbf{x})} \bar{\mathbf{d}} = \overline{\mathbf{B}}(\mathbf{x})\, \bar{\mathbf{d}}, \tag{4.29}$$

where $\overline{\mathbf{B}}$ is the *global* "smoothed strain–displacement" matrix. It is clear that due to the sparseness of shape function matrix $\mathbf{N}$ (see Remark 4.5), $\overline{\mathbf{B}}$ is also extremely sparse, although it may be less sparse than the strain–displacement matrix $\tilde{\mathbf{B}}$ used in FEM. In an S-FEM model, $\overline{\mathbf{B}}_I(\mathbf{x})$ is nonzero only for the set of nodes "supporting" the smoothing domain Ω_k^s that hosts $\mathbf{x}$. This set of nodes consists of all the nodes of elements contributing to the smoothing domain Ω_k^s. For example, for ES-FEM using three-node triangular elements as shown in Figure 4.7, the sets of nodes are $\{A,\ B,\ C\}$ for the boundary edge m and $\{D,\ E,\ F,\ G\}$ for the inner edge k. The "smoothed" strain–displacement matrix $\overline{\mathbf{B}}_I$ is evaluated using

$$\overline{\mathbf{B}}_I = \frac{1}{A_k^s} \int_{\Gamma_k^s} \mathbf{L}_n(\mathbf{x}) \mathbf{N}_I(\mathbf{x})\, \mathrm{d}\Gamma = \begin{bmatrix} \bar{b}_{Ix} & 0 \\ 0 & \bar{b}_{Iy} \\ \bar{b}_{Iy} & \bar{b}_{Ix} \end{bmatrix} \tag{4.30}$$

with

$$\bar{b}_{Ih} = \frac{1}{A_k^s} \int_{\Gamma_k^s} n_h(\mathbf{x})\, N_I(\mathbf{x})\, \mathrm{d}\Gamma, \quad h = x, y. \tag{4.31}$$

The above line integration along Γ_k^s can be carried out using the Gauss quadrature technique (for the 1D domain in this case) given in Section 3.15.1. When a linearly compatible displacement field along the boundary Γ_k^s is used, one Gauss point is sufficient for the line integration along each segment $\Gamma_{k,p}^s$ of boundary Γ_k^s, and the above equation can be further simplified to a summation form

$$\bar{b}_{Ih} = \frac{1}{A_k^s} \sum_{p=1}^{n_\Gamma^s} n_{h,p}\, N_I\left(\mathbf{x}_p^{\mathrm{G}}\right) l_p, \quad h = x,\ y, \tag{4.32}$$

where n_Γ^s is the total number of boundary segments $\Gamma_{k,p}^s \in \Gamma_k^s$ and $\mathbf{x}_p^{\mathrm{G}}$ is the midpoint (Gauss point) of the boundary segment of $\Gamma_{k,p}^s$, whose length and outward unit normal are denoted as l_p and $n_{h,p}$, respectively.

When the created displacement function is continuous and the compatible strain–displacement $\tilde{\mathbf{B}}_I(\mathbf{x})$ is attainable, from the definition of the smoothed strain field $\bar{\boldsymbol{\varepsilon}}$ in Equation 4.23, it is easy to reveal the relationship between the smoothed strain–displacement matrix $\overline{\mathbf{B}}_I$ and the standard compatible strain–displacement matrix $\tilde{\mathbf{B}}_I(\mathbf{x})$ used in FEM:

$$\overline{\mathbf{B}}_I = \frac{1}{A_k^s}\int_{\Gamma_k^s} \mathbf{L}_n(\mathbf{x})\mathbf{N}_I(\mathbf{x})\mathrm{d}\Gamma = \frac{1}{A_k^s}\int_{\Omega_k^s} \mathbf{L}_d\mathbf{N}_I(\mathbf{x})\mathrm{d}\Omega = \frac{1}{A_k^s}\int_{\Omega_k^s} \tilde{\mathbf{B}}_I(\mathbf{x})\mathrm{d}\Omega, \quad (4.33)$$

which states that the smoothed strain–displacement matrix $\overline{\mathbf{B}}_I$ is the average of the standard compatible strain–displacement matrix $\tilde{\mathbf{B}}_I(\mathbf{x})$ over the smoothing domain Ω_k^s.

Note that the higher-order derivatives can be readily obtained by recursive application of Equation 4.23, as long as lower-order gradients can be interpolated from nodal values [3,20]. For example, the second order of the displacement gradients $\mathbf{D}^2(\overline{\mathbf{u}}(\mathbf{x}))$ can be obtained from the first order of the displacement gradients $\mathbf{D}^1(\overline{\mathbf{u}}(\mathbf{x}))$ in the same way:

$$\mathbf{D}^2(\overline{\mathbf{u}}(\mathbf{x})) = \int_{\Omega_k^s} \mathbf{L}_d\mathbf{D}^1(\overline{\mathbf{u}}(\mathbf{x}))\,\frac{1}{A_k^s}\,\mathrm{d}\Omega = \frac{1}{A_k^s}\int_{\Gamma_k^s} \mathbf{L}_n(\mathbf{x})\mathbf{D}^1(\overline{\mathbf{u}}(\mathbf{x}))\,\mathrm{d}\Gamma. \quad (4.34)$$

Note also that when we try to obtain the second derivative, the smoothing domains used for the first derivatives do not have to (and often it is better not to) be the same as those used for the second derivatives, as suggested in Refs. [13,14,16].

4.6 Minimum Number of Smoothing Domains: Essential to Stability

For an S-FEM model, the key to ensure the stability is the use of a sufficient number of smoothing domains that are linearly independent. The independence of smoothing domains is measured by the linear independence of the columns of the global smoothed strain–displacement matrix [17]. When the smoothing domains are created associated with element mesh entities (elements/cells, nodes, edges, or faces), and they do not overlap and do not have any gap, these smoothing domains are linearly independent. If, for example, a set of smoothing domains is created with different sizes, some of them covering more than one element, this set of smoothing domains can be dependent. To ensure the stability and hence the full rank of the (global) smoothed stiffness matrix, a minimum number of linearly

independent smoothing domains $N_s^{\min}$ must be used. Based on the study in Ref. [17], such a minimum number of smoothing domains should relate properly to the number of unprescribed nodal unknowns N_u, depending on the type of physical problems. The key consideration is to ensure that the independent energy equations sampled by all these smoothing domains are at least equal to the total number of unprescribed nodal unknowns N_u.

For 1D solid mechanics problem models with n_f nodes fixed, we immediately have $N_s^{\min} = N_u = N_n - n_f$. This is because one node carries only one unknown (displacement component in the x-direction), and one energy equation can be sampled from one (independent) smoothing domain.

For 2D solid mechanics problem models with n_t (unconstrained) nodes used for displacement field construction, the total number of unknowns in the model should be $N_u = 2n_t$, because one node carries two unknowns (displacement components in the x- and y-directions). On the other hand, the total number of energy equations that can be sampled from all the smoothing domains should be $3N_s$, because one smoothing domain gives three independent equations to measure the strain energy norm (each of three strain components produces strain energy independently). Therefore, we must have $N_s^{\min} = 2n_t/3$.

Exactly the same analysis can be done for 3D solid mechanics problem models. We now summarize the discussions in Table 4.2 for solid mechanics problems.

In general, it is found that among the four element mesh entities, elements, nodes, edges (for 2D problems), or faces (for 3D problems), the number of elements is usually least followed by the number of nodes. The number of edges and faces is always larger than that of nodes for any discretization. Therefore, S-FEM models using smoothing domains associated with edges (ES-FEM) or faces (FS-FEM) are always stable (spatially and temporally) because the number of smoothing domains N_s is always much larger than the minimum number of smoothing domains $N_s^{\min}$. This will be shown in more detail in Chapters 7 and 8. For the S-FEM model using smoothing domains associated with nodes (NS-FEM,

TABLE 4.2

Minimum Number of Smoothing Domains $N_s^{\min}$ for Solid Mechanics Problems with n_t (Unconstrained) Total Nodal Unknowns

Dimension of the Problem	Minimum Number of Smoothing Domains
1D	$N_s^{\min} = n_t$
2D	$N_s^{\min} = 2n_t/3$
3D	$N_s^{\min} = 3n_t/6 = n_t/2$

see Chapter 6), it satisfies exactly the minimum number of smoothing domains $N_s^{\min}$. An NS-FEM is spatially stable and hence works well for static problems, but is *temporally* instable (see Remark 1.3) and hence does not work well for dynamics problems without stabilization. For the S-FEM model using smoothing domains associated with elements (cells) (CS-FEM, see Chapter 5), the stability of the method is not ensured when the whole element is used as one smoothing domain because the minimum number of smoothing domains $N_s^{\min}$ may or may not be satisfied, depending on the setting of the problem. The element stiffness matrix can hence contain spurious zero energy modes, and the global stiffness matrix after imposing essential boundary conditions can be singular for some problems. Therefore, the stability of CS-FEM will only be ensured when more than one smoothing domain is used for each element. Details of the stability analyses of the methods will be presented in the following chapters.

Similar analysis can be done for heat transfer problems, for which each node carries only one unknown (the temperature). There are however one energy equation for 1D, two for 2D, and three for 3D problems. Table 4.3 lists the minimum number of smoothing domains $N_s^{\min}$ for heat transfer problems.

Remark 4.7 Convergence of the Smoothed Strain Field

Because the weight functions used in a smoothed model satisfy the conditions listed in Section 4.5.3, when $\Omega_k^s \to 0$, $\widehat{W}(\mathbf{x}_k - \mathbf{x}) \to \delta(\mathbf{x}_k - \mathbf{x})$. At such a limit, Equation 4.16 becomes

$$\lim_{\Omega_k^s \to 0} \overline{\boldsymbol{\varepsilon}}(\mathbf{x}_k) = \lim_{\Omega_k^s \to 0} \int_{\Omega_k^s} \tilde{\boldsymbol{\varepsilon}}(\mathbf{x})\, \delta(\mathbf{x}_k - \mathbf{x})\, \mathrm{d}\Omega = \tilde{\boldsymbol{\varepsilon}}(\mathbf{x}_k)\,. \tag{4.35}$$

This means that when the smoothing domain is refined, the smoothed strain field approaches the compatible strain field.

TABLE 4.3

Minimum Number of Smoothing Domains $N_s^{\min}$ for Heat Transfer Problems with n_t (Unconstrained) Total Nodal Unknowns

Dimension of the Problem	Minimum Number of Smoothing Domains
1D	$N_s^{\min} = n_t$
2D	$N_s^{\min} = n_t/2$
3D	$N_s^{\min} = n_t/3$

4.7 Smoothed Galerkin Weak Form

S-FEM uses the so-called smoothed Galerkin weak form that is defined as [2]

$$\sum_{k=1}^{N_s} A_k^s \underbrace{\left(\frac{1}{A_k^s}\int_{\Gamma_k^s} \mathbf{L}_n(\mathbf{x})\delta\overline{\mathbf{u}}(\mathbf{x})\mathrm{d}\Gamma\right)^T}_{\delta\bar{\boldsymbol{\varepsilon}}_k^{\mathrm{T}}} \mathbf{c} \underbrace{\left(\frac{1}{A_k^s}\int_{\Gamma_k^s} \mathbf{L}_n(\mathbf{x})\bar{\mathbf{u}}(\mathbf{x})\mathrm{d}\Gamma\right)}_{\bar{\boldsymbol{\varepsilon}}_k}$$

$$-\int_{\Omega} \delta\overline{\mathbf{u}}^T\mathbf{b}\,\mathrm{d}\Omega - \int_{\Gamma_t} \delta\overline{\mathbf{u}}^T\mathbf{t}\,\mathrm{d}\Gamma = 0 \tag{4.36}$$

or simply as

$$\sum_{k=1}^{N_s} A_k^s \delta\bar{\boldsymbol{\varepsilon}}_k^T \mathbf{c}\bar{\boldsymbol{\varepsilon}}_k - \int_{\Omega} \delta\overline{\mathbf{u}}^T\mathbf{b}\,\mathrm{d}\Omega - \int_{\Gamma_t} \delta\bar{\mathbf{u}}^T\mathbf{t}\,\mathrm{d}\Gamma = 0, \tag{4.37}$$

where N_s is the number of smoothed domains used for the entire problems domain, A_k^s is the area of the kth smoothing domain, $\overline{\mathbf{u}} \in \mathbb{H}^1_{0,h}(\Omega;\mathbb{R}^d)$, $\mathbf{b} \in \mathbb{L}^2(\Omega;\mathbb{R}^d)$ is the external body force applied over the problem domain, $\mathbf{t} \in \mathbb{L}^2(\Gamma_t;\mathbb{R}^d)$ is the external traction force applied on the natural boundary of the problem domain, and each of the components of strain $\bar{\boldsymbol{\varepsilon}}_k$ defined by Equation 4.23 lives in $\mathbb{L}^2(\Omega;\mathbb{R}^1)$ space.

Theorem 4.1: Smoothed Galerkin: Stability and Convergence to an Exact Solution

1. The S-FEM models formulated using the smoothed Galerkin weak form defined in Equation 4.36 are *variationally consistent*.
2. The smoothed Galerkin model is (spatially) stable, if at least the minimum number of independent smoothed domains defined in Table 4.2 is used in creating the model.
3. The solution of such a smoothed Galerkin model converges to the exact solution of a physically well-posed linear elasticity problem with stable material, when the mesh is refined.

Proof. We first examine item (1). We start with the following single-field Hellinger–Reissner weak form that is proved to be variationally

consistent [2,21,22]:

$$\int_{\Omega} \delta \left[-\frac{1}{2} \breve{\boldsymbol{\varepsilon}}^T(\overline{\mathbf{u}}) \mathbf{c} \breve{\boldsymbol{\varepsilon}}(\overline{\mathbf{u}}) + \breve{\boldsymbol{\varepsilon}}^T(\overline{\mathbf{u}}) \mathbf{c}(\mathbf{L}_d \overline{\mathbf{u}}) \right] \mathrm{d}\Omega - \int_{\Omega} \delta \overline{\mathbf{u}}^T \mathbf{b} \, \mathrm{d}\Omega + \int_{\Gamma_t} \delta \overline{\mathbf{u}}^T \mathbf{t}_\Gamma \mathrm{d}\Gamma = 0, \tag{4.38}$$

where $\overline{\mathbf{u}} \in \mathbb{H}^1_{0,h}(\Omega; \mathbb{R}^d)$ and $\breve{\boldsymbol{\varepsilon}}(\overline{\mathbf{u}})$ is the strain field that is "somehow" obtained using $\overline{\mathbf{u}}$. In our S-FEM models, we have

$$\breve{\boldsymbol{\varepsilon}}(\overline{\mathbf{u}}) = \overline{\boldsymbol{\varepsilon}}(\overline{\mathbf{u}}). \tag{4.39}$$

Equation 4.38 becomes

$$\int_{\Omega} \delta \left[-\frac{1}{2} \overline{\boldsymbol{\varepsilon}}^T(\overline{\mathbf{u}}) \mathbf{c} \overline{\boldsymbol{\varepsilon}}(\overline{\mathbf{u}}) + \overline{\boldsymbol{\varepsilon}}^T(\overline{\mathbf{u}}) \mathbf{c}(\mathbf{L}_d \overline{\mathbf{u}}) \right] \mathrm{d}\Omega - \int_{\Omega} \delta \overline{\mathbf{u}}^T \mathbf{b} \, \mathrm{d}\Omega + \int_{\Gamma_t} \delta \overline{\mathbf{u}}^T \mathbf{t}_\Gamma \mathrm{d}\Gamma = 0. \tag{4.40}$$

Because $\overline{\mathbf{u}} \in \mathbb{H}^1_{0,h}(\Omega; \mathbb{R}^d)$, $\mathbf{b} \in \mathbb{L}^2\left(\Omega; \mathbb{R}^d\right)$, $\mathbf{t} \in \mathbb{L}^2\left(\Gamma_t; \mathbb{R}^d\right)$, and $\bar{\varepsilon}_{ij} \in \mathbb{L}^2\left(\Omega; \mathbb{R}^1\right)$, all the energy terms in Equation 4.36 are bounded from above. We also note that the restrictions on force terms $\mathbf{b} \in \mathbb{L}^2\left(\Omega; \mathbb{R}^d\right)$ and $\mathbf{t} \in \mathbb{L}^2\left(\Gamma_t; \mathbb{R}^d\right)$ are sufficient (may be not necessary) for such a bound. This means that we do not consider forces such as point forces (that are not squarely integrable), although it may be included for some cases (e.g., point force in the 1D case).

Also, because of $\overline{\mathbf{u}} \in \mathbb{H}^1_{0,h}(\Omega; \mathbb{R}^1)$, $\bar{\varepsilon}_{ij} \in \mathbb{L}^2(\Omega; \mathbb{R}^1)$, and the occasional forgiving property of Lebesgue integration (see Remark 3.1), domain integration in the first term in the foregoing equation can be changed to a summation of integrals over all the smoothing domains that are nonoverlapping and no-gap. We thus have

$$\sum_{k=1}^{N_s} \delta \left[-\int_{\Omega_k^s} \frac{1}{2} \overline{\boldsymbol{\varepsilon}}_k^T(\overline{\mathbf{u}}) \mathbf{c} \overline{\boldsymbol{\varepsilon}}_k(\overline{\mathbf{u}}) \, \mathrm{d}\Omega + \int_{\Omega_k^s} \overline{\boldsymbol{\varepsilon}}_k^T(\overline{\mathbf{u}}) \mathbf{c}(\mathbf{L}_d \overline{\mathbf{u}}) \, \mathrm{d}\Omega \right]$$

$$- \int_{\Omega} \delta \overline{\mathbf{u}}^T \mathbf{b} \, \mathrm{d}\Omega + \int_{\Gamma_t} \delta \overline{\mathbf{u}}^T \mathbf{t}_\Gamma \mathrm{d}\Gamma = 0. \tag{4.41}$$

Using the fact that smoothed strain in our S-FEM model is assumed to be constant in the smoothing domain Ω_k^s, we immediately obtain

$$\int_{\Omega_k^s} \bar{\boldsymbol{\varepsilon}}_k^T(\overline{\mathbf{u}})\mathbf{c}\,(\mathbf{L}_d\overline{\mathbf{u}})\,\mathrm{d}\Omega = \bar{\boldsymbol{\varepsilon}}_k^T(\overline{\mathbf{u}})\mathbf{c}\underbrace{\int_{\Omega_k^s}(\mathbf{L}_d\overline{\mathbf{u}})\,\mathrm{d}\Omega}_{A_k^s\bar{\boldsymbol{\varepsilon}}_k} = A_k^s\bar{\boldsymbol{\varepsilon}}_k^T(\overline{\mathbf{u}})\mathbf{c}\bar{\boldsymbol{\varepsilon}}_k(\overline{\mathbf{u}})$$

$$= \int_{\Omega_k^s} \bar{\boldsymbol{\varepsilon}}_k^T(\overline{\mathbf{u}})\mathbf{c}\bar{\boldsymbol{\varepsilon}}_k(\overline{\mathbf{u}})\,\mathrm{d}\Omega, \tag{4.42}$$

which is the so-called local orthogonal condition for any of these smoothing domains [1,23]:

$$\int_{\Omega_k^s} \bar{\boldsymbol{\varepsilon}}_k^T(\overline{\mathbf{u}})\mathbf{c}\,(\mathbf{L}_d\overline{\mathbf{u}})\,\mathrm{d}\Omega = \int_{\Omega_k^s} \bar{\boldsymbol{\varepsilon}}_k^T(\overline{\mathbf{u}})\mathbf{c}\bar{\boldsymbol{\varepsilon}}_k(\overline{\mathbf{u}})\,\mathrm{d}\Omega. \tag{4.43}$$

Substituting the foregoing equation back to Equation 4.41 gives

$$\sum_{k=1}^{N_s}\delta\left[\int_{\Omega_k^s}\frac{1}{2}\bar{\boldsymbol{\varepsilon}}_k^T(\overline{\mathbf{u}})\mathbf{c}\bar{\boldsymbol{\varepsilon}}_k(\overline{\mathbf{u}})\,\mathrm{d}\Omega\right] - \int_{\Omega}\delta\bar{\mathbf{u}}^T\mathbf{b}\,\mathrm{d}\Omega + \int_{\Gamma_t}\delta\overline{\mathbf{u}}^T\mathbf{t}_\Gamma\,\mathrm{d}\Gamma = 0. \tag{4.44}$$

Moving the variation operator into the blanket, and using the fact that strain is constant in Ω_k^s, leads to Equation 4.37 or 4.36. Therefore, the smoothed Galerkin formulation is variationally consistent, and the solution will converge if the solution is stable.

Next, on item (2), we examine the stability of the solution. Because the smoothed domains created in the S-FEM models are independent and at least a minimum number of smoothed domains defined in Table 4.2 are used in creating the model, all the columns of the smoothed strain matrix will be linearly independent [18]. Therefore, the first term in Equation 4.36 will also be strictly larger than zero for any $\overline{\mathbf{u}} \in \mathbb{H}^1_{0,h}(\Omega;\mathbb{R}^d)$, and the stiffness matrix created will be SPD, as long as $\mathbf{c}$ is SPD. Therefore, the S-FEM models will be stable as long as the material is stable [18].

We piece together all these points and conclude that the solution of the smoothed Galerkin model is stable and convergent. Finally, on item (3), we examine the convergence of the solution. When the mesh is refined, the dimension of the elements approaches zero and the dimension of the smoothing domains also approaches zero. Based on Remark 4.7, the smoothed strain field will converge to the compatible strain field, and hence the smoothed Galerkin model approaches the standard Galerkin model.

Because the solution of a standard Galerkin model has already been proved to converge to the exact solution of a physically well-posed linear elasticity problem with stable material, the solution of the smoothed Galerkin model will also converge to the exact solution of the same problem. This completes the proof of the theorem. □

A proof on the variational consistency of S-FEM models based on matrix formulation can be found in Ref. [24].

For dynamic problems, all we need is to add in the inertial term. Therefore, the smoothed Galerkin weak form for dynamic problems can be written as [2]

$$\sum_{k=1}^{N_s} A_k^s \delta\bar{\boldsymbol{\varepsilon}}_k^T \mathbf{c} \bar{\boldsymbol{\varepsilon}}_k - \int_\Omega \delta\overline{\mathbf{u}}^T \mathbf{b}\, \mathrm{d}\Omega - \int_{\Gamma_t} \delta\overline{\mathbf{u}}^T \mathbf{t}\, \mathrm{d}\Gamma + \int_\Omega \rho\delta\overline{\mathbf{u}}^T \ddot{\overline{\mathbf{u}}}\, \mathrm{d}\Omega = 0. \tag{4.45}$$

Remark 4.8 W^2 Formulation

In using the standard weak formulation in FEM, we need to assume the displacement field and upon which we need to perform the differentiation to obtain the strain field to be fed into the Galerkin weak form. In our S-FEM models, however, we use the smoothed Galerkin weak form that uses the smoothed strain field. From Equation 4.36, we observe that in the smoothed Galerkin weak form, we need only the assumed displacement and no derivatives of the assumed displacement field are required. This means that the consistency requirement on the assumed displacement function is further weakened from the weak formulation. Therefore, S-FEM models are considered as a W^2 formulation, a term coined in Ref. [18] for general mesh-free settings.

4.8 Discretized Linear Algebraic System of Equations

Substituting Equations 4.2 and 4.29 into Equation 4.37, we have the standard discretized algebraic system of equations

$$\overline{\mathbf{K}}\,\overline{\mathbf{d}} = \tilde{\mathbf{f}}, \tag{4.46}$$

where $\overline{\mathbf{d}} \in \mathbb{R}_0^{dN_n}$ is the vector of nodal displacements for all the nodes in the S-FEM model, and $\overline{\mathbf{K}}$ is the *smoothed* stiffness matrix given in the general form of

$$\overline{\mathbf{K}} = \int_\Omega \overline{\mathbf{B}} \mathbf{c} \bar{\mathbf{B}}\, \mathrm{d}\Omega. \tag{4.47}$$

Because of the extreme sparseness of the $\overline{\mathbf{B}}$ matrix, we will not in practice use the foregoing equation to compute $\overline{\mathbf{K}}$. Instead, we compute only the following entries:

$$\overline{\mathbf{K}}_{IJ} = \int_{\Omega} \overline{\mathbf{B}}_I^T \mathbf{c} \overline{\mathbf{B}}_J \, \mathrm{d}\Omega = \sum_{k=1}^{N_s} \int_{\Omega_k^s} \overline{\mathbf{B}}_I^T \mathbf{c} \overline{\mathbf{B}}_J \, \mathrm{d}\Omega = \sum_{k=1}^{N_s} \overline{\mathbf{B}}_I^T \mathbf{c} \overline{\mathbf{B}}_J A_k^s, \tag{4.48}$$

which is the substiffness matrix for nodes I in relation to J, in a similar manner as in the standard FEM, except that the summation for S-FEM is performed over smoothing domains and not over elements. We now note the following:

1. In Equation 4.46, $\overline{\mathbf{K}}$ is SPD as long as the conditions given in Theorem 4.1 are satisfied.
2. The load vector $\tilde{\mathbf{f}}$ does not carry a bar-hat, because no smoothing function is applied to the linear functional in S-FEM models. The load vector is therefore computed in exactly the same way as in FEM.
3. In Equation 4.48, we see that in computing $\overline{\mathbf{K}}_{IJ}$ no numerical integration is needed.
4. Furthermore, $\overline{\mathbf{K}}_{IJ}$ needs to be computed only when nodes I and J share the same smoothing domain. Otherwise, it is zero. Hence, $\overline{\mathbf{K}}$ will be also sparse.

Hence, Equation 4.46 can be formed efficiently and solved with ease using standard routines because $\overline{\mathbf{K}}$ is SPD and sparse.

Also note that $\overline{\mathbf{K}}$ will be banded if the nodes are properly numbered, as that in FEM. For S-FEM models, the bandwidth of $\overline{\mathbf{K}}$ will be determined by the largest difference of node numbers of the nodes of the elements contributing to the smoothing domains. Specifically, when the smoothing domains are located inside the elements such as in CS-FEM, the bandwidth of $\overline{\mathbf{K}}$ will be the same as that of $\tilde{\mathbf{K}}$ in FEM. This is because the number of nodes related to the smoothing domains is identical to that related to the elements. However, when the smoothing domains cover parts of adjacent elements such as in NS-FEM, ES-FEM, or FS-FEM, the bandwidth of $\overline{\mathbf{K}}$ will be larger than that of $\tilde{\mathbf{K}}$ in FEM. This is because the number of nodes supporting the smoothing domains is larger than that of the elements.

From Equations 4.23, 4.30, and 4.32, it is seen that numerical integration on the domain Ω_k^s can now be transferred to integration on the boundary of the smoothing domain Γ_k^s. This is why no derivative of shape functions is involved in computing the field gradients and only shape function values at some Gauss points along the boundaries of smoothing domains are needed. This makes the computing procedure of the stiffness matrix in S-FEM models easier than that in the standard FEM. We directly use

the shape functions, and not the derivative of shape functions, to calculate the stiffness matrix via line integration along the boundaries of the smoothing domains. No mapping is needed. Finally, the line integrations can be performed easily using the Gaussian integration technique detailed in Section 3.15.

4.9 Solve the Algebraic System of Equations

Because the stiffness matrix $\overline{\mathbf{K}}$ of our S-FEM model will be SPD, we can then solve the algebraic system of Equations 4.46 for a unique solution for the nodal displacements. The procedure is exactly the same as in the standard FEM: using routinely available linear equation solvers. The solution will approach the exact solution of the original problem with square integrable external forces when the mesh is refined. After the nodal displacements are obtained, we can retrieve the displacement field using Equation 4.2, the smoothed strain field using Equation 4.29, and the stress field using the constitutive equation. Finally, the solution of the strain energy of the solid can be obtained via integration over the entire problem domain using the strain and stress solutions.

4.10 Error Assessment in S-FEM and FEM Models

To examine the accuracy and efficiency, the results of the S-FEM models will be compared with those of the standard FEM as well as the analytical or reference solutions. For quantitative study of the error and convergence rate of these numerical methods, two types of error norms are used in this book, that is, displacement norm and the so-called energy norm [25]. For meshes of the standard elements, T3, Q4, T4, and H8 (for FEM only), these error norms are evaluated based on elements, and hence applicable to both S-FEM and FEM models.

4.10.1 Displacement Norm

The displacement norm is defined as

$$e_d = \left\| \mathbf{u} - \breve{\mathbf{u}} \right\|_{\mathbf{L}^2(\Omega;\mathbb{R}^d)} = \left(\int_{\Omega} \left(\mathbf{u} - \breve{\mathbf{u}} \right)^T \left(\mathbf{u} - \breve{\mathbf{u}} \right) \mathrm{d}\Omega \right)^{1/2}$$
$$= \left(\sum_{i=1}^{N_e} \int_{\Omega_i^e} \left(\mathbf{u} - \breve{\mathbf{u}} \right)^T \left(\mathbf{u} - \breve{\mathbf{u}} \right) \mathrm{d}\Omega \right)^{1/2}, \tag{4.49}$$

where $\mathbf{u}$ is the exact (or analytical or reference) solution for the displacements and $\breve{\mathbf{u}}$ is the numerical solution for the displacements obtained using a numerical model.

The displacement norm defined in Equation 4.49 can be used for both S-FEM and FEM models; the comparison is fair and rigorous as long as the same mesh is used.

4.10.2 Energy Norm

The "energy norm" is defined by

$$e_e = \left[\int_{\Omega} \frac{1}{2} \left(\boldsymbol{\varepsilon} - \breve{\boldsymbol{\varepsilon}} \right)^T \mathbf{c} \left(\boldsymbol{\varepsilon} - \breve{\boldsymbol{\varepsilon}} \right) \right]^{1/2} = \left[\sum_{i=1}^{N_e} \int_{\Omega_i^e} \frac{1}{2} \left(\boldsymbol{\varepsilon} - \breve{\boldsymbol{\varepsilon}} \right)^T \mathbf{c} \left(\boldsymbol{\varepsilon} - \breve{\boldsymbol{\varepsilon}} \right) \right]^{1/2}, \quad (4.50)$$

where $\boldsymbol{\varepsilon}$ is the exact (or analytical or reference) solution for the strains and $\breve{\boldsymbol{\varepsilon}}$ is the numerical solution for the strains obtained using a numerical model. It is clear that the error defined by the "energy norm" physically measures the "energy caused by the distributed strain errors."

In order to evaluate the integrals in Equations 4.49 and 4.50 accurately, the mapping procedure using Gauss integration is performed on each element with a summation on all elements. In each element, a proper number of Gauss points, depending on the order of the integrand, will be used. For example, when a mesh of Q4 elements is used, and if the analytical strain $\boldsymbol{\varepsilon}$ is of the order of 2 leading to a fourth-order integrand in Equation 4.50, a set of 3×3 Gauss points is then used for each element. This is to ensure that there is no additional error introduced in the error assessment procedure.

4.10.3 Recovery Strain/Stress Field in S-FEM Models

In FEM, the strain (or stress) obtained in an element is continuous. Hence, the evaluation of integrals in Equation 4.50 using Gauss integration in each element in the FEM can be performed easily.

In S-FEM models, however, the strain (or stress) obtained is in general not continuous within an element. It is piecewise constant and discontinuous at the boundaries of smoothing domains located inside elements. Therefore in S-FEM models, it is necessary to create a continuous strain field in each element for easy evaluation of the integrals in Equation 4.50. In this book, we construct a "recovery" strain (or stress) field denoted as $\bar{\boldsymbol{\varepsilon}}^R$ using the "raw" strain values $\bar{\boldsymbol{\varepsilon}}$ at the nodes of the element. Such a recovery strain field $\bar{\boldsymbol{\varepsilon}}^R$ is continuous not only inside the element but also on the whole problem domain, and will usually be used as the final numerical results of the strain field of S-FEM models and in the error estimation using Equation 4.50. This

recovery strain field $\bar{\boldsymbol{\varepsilon}}^R$ improves the strain solution smoothness of S-FEM models, and also serves as a "reference" solution for establishing error indicators for adaptive analysis. Therefore, it is of importance.

For S-FEM models using the standard elements (T3, Q4 and T4), $\bar{\boldsymbol{\varepsilon}}^R$ is obtained for each element in the mesh using

$$\bar{\boldsymbol{\varepsilon}}^R = \sum_{j=1}^{n_n^e} N_j(\mathbf{x})\, \bar{\boldsymbol{\varepsilon}}(\mathbf{x}_j), \tag{4.51}$$

where n_n^e is the number of nodes of the element, $\bar{\boldsymbol{\varepsilon}}(\mathbf{x}_j)$ is the vector containing the strain components at nodes $\mathbf{x}_j$ of the element obtained using S-FEM models, and $N_j(\mathbf{x})$ is the matrix of the shape functions arranged properly for the element. The shape function is the same as that used in the standard FEM. For T3 elements, it is defined by Equation 3.89. For Q4 elements, it is defined by Equation 3.95, and for T4 elements, it is defined by Equation 3.105. The recovery strain solution defined in Equation 4.51 is termed as the linear (for T3 and T4) or bilinear (for Q4) recovery strain solution field.

4.10.4 Evaluation of Strain at Nodes in S-FEM Models

In the numerical implementation of S-FEM models (except for NS-FEM, which directly produces the strain values at nodes), the strains (or stresses) at node j will be the (area-weighted) averaged value of the "raw" strains (or stresses) of the smoothing domains Ω_k^s around node j, and are computed numerically by

$$\bar{\boldsymbol{\varepsilon}}(\mathbf{x}_j) = \frac{1}{A_j^{ns}} \sum_{k=1}^{n_s^j} \bar{\boldsymbol{\varepsilon}}_k\, A_k^s, \tag{4.52}$$

where n_s^j is the number of smoothing domains Ω_k^s around node j, $A_j^{ns} = \sum_{k=1}^{n_s^j} A_k^s$ is the total area/volume of all smoothing domains Ω_k^s around node j, $\bar{\boldsymbol{\varepsilon}}_k$ is the smoothing strain of the smoothing domain Ω_k^s, and A_k^s is the area/volume of the smoothing domain.

Figure 4.10 shows, for example, smoothing domains used to compute the strain (or stress) of nodes in ES-FEM using three-node triangular elements (T3).

4.10.5 Recovery Strain/Stress Field in FEM Models

To conduct a thorough examination of S-FEM solutions in the strain (stress) field, we need to assess the accuracy of the FEM solution in the strain (stress) field using the same set of nodes. For FEM models, because the strains (stresses) in the elements are already continuous, Equation 4.50 can be evaluated directly, and hence we do not have to compute a recovery

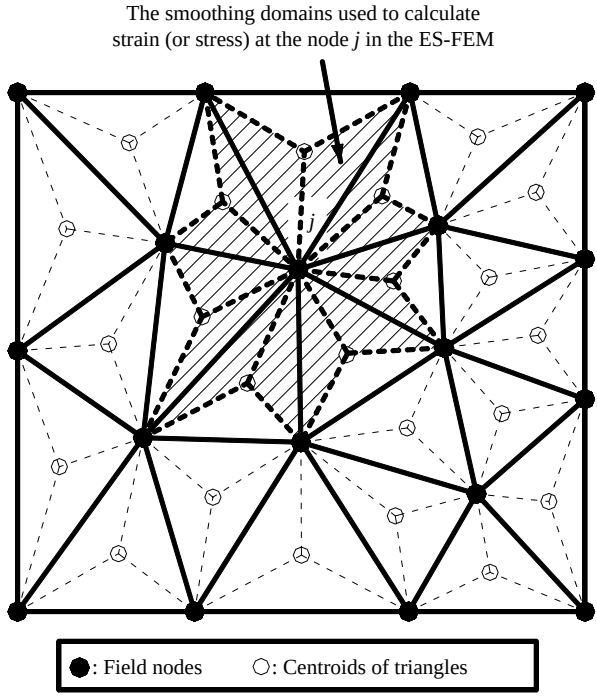

FIGURE 4.10 Smoothing domains used to compute the strain (or stress) of the nodes in ES-FEM using three-node triangular elements (T3).

strain solution field. However, we know that the recovery strain solution is much more accurate for FEM models, and we have the so-called super-convergence property [26,27]. To conduct "fairest" possible comparisons between S-FEM and FEM models, we will also often use the recovery strain solutions for FEM models. The recovery strain solution $\tilde{\boldsymbol{\varepsilon}}^R$ is obtained using

$$\tilde{\boldsymbol{\varepsilon}}^R = \sum_{j=1}^{n_n^e} N_j(\mathbf{x})\, \tilde{\boldsymbol{\varepsilon}}(\mathbf{x}_j). \tag{4.53}$$

It is clear that Equation 4.53 is exactly the same as Equation 4.51, except that $\tilde{\boldsymbol{\varepsilon}}(\mathbf{x}_j)$ is the vector containing compatible strain components at nodes $\mathbf{x}_j$ of the element obtained using the FEM model. However, obtaining the highly accurate nodal strain $\tilde{\boldsymbol{\varepsilon}}(\mathbf{x}_j)$ is quite complicated for Q4 and H8 elements, and is detailed in the following section.

4.10.6 Evaluation of Strains at Nodes in FEM Models

For T3 and T4 elements, the nodal $\tilde{\boldsymbol{\varepsilon}}(\mathbf{x}_j)$ strain at a node is obtained in a similar manner as in the S-FEM models: an area-weighted averaged strain

at the centroids of elements surrounding the node, that is,

$$\tilde{\boldsymbol{\varepsilon}}(\mathbf{x}_j) = \frac{1}{A_j^{ne}} \sum_{i=1}^{n_e^j} \tilde{\boldsymbol{\varepsilon}}_i(\mathbf{x}_c)\, A_i^e, \tag{4.54}$$

where n_e^j is the number of elements Ω_i^e around node j, $A_j^{ne} = \sum_{i=1}^{n_e^j} A_i^e$ is the total area of all the elements around node j, $\tilde{\boldsymbol{\varepsilon}}_i(\mathbf{x}_c)$ is the compatible strain evaluated at the centroid of the element, and A_i^e is the area of the element. Figure 4.11 shows, for example, the T3 elements used to compute the nodal strain (or stress) for node j, and the element strains (or stresses) located at the centroids of triangular elements in an FEM-T3 model.

For Q4 and H8 elements, the computation of nodal strain $\tilde{\boldsymbol{\varepsilon}}(\mathbf{x}_j)$ is much more involved, because the strain in the elements is not constant and is only computed at the Gauss integration points. An extrapolation from the strain

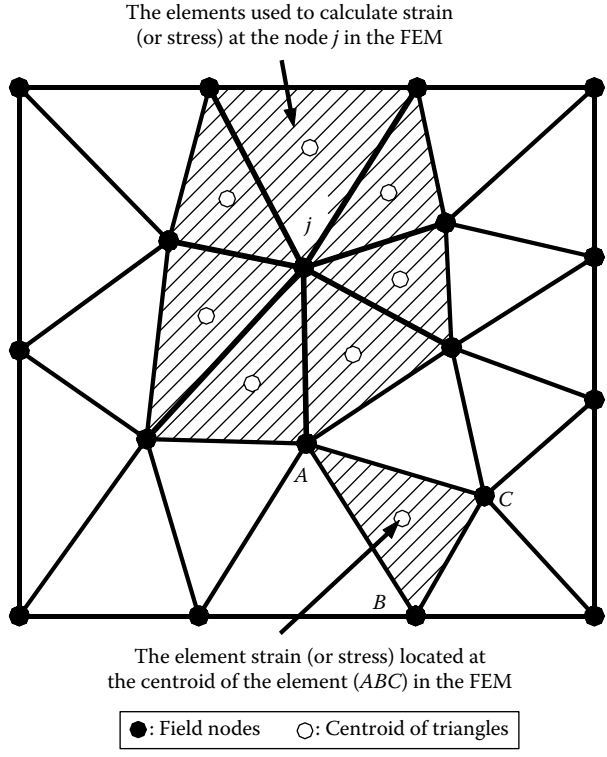

FIGURE 4.11 Elements used to compute the strain (or stress) of the node shared by all these elements, and the element strains (or stresses) located at the centroids of the triangular elements in an FEM-T3 model.

values at these Gauss points in the element onto the field (element) nodes of the element is therefore necessary [28]. In addition, it is expected that these strains extrapolated at the same nodal point from adjacent elements will not generally be the same, since the stresses are not continuous in an FEM model. Therefore, an area-weighted average (similar to Equation 4.55) of these extrapolated strains is computed for the node. In summary, we have the following three-step procedure to compute the nodal strain $\tilde{\boldsymbol{\varepsilon}}(\mathbf{x}_j)$ [28]:

1. Evaluate the strains at these Gauss points in the element
2. Extrapolate these strains to the nodes of the element
3. Average these strains computed for the same field node from the adjacent elements

The implementation of steps (1) and (3) is straightforward, and hence requires no further elaboration. It is, however, necessary to elaborate in more detail the extrapolation process in step (2), for which we choose a four-node bilinear (Q4) element as an example. As presented in Section 3.15.2, a set of 2×2 Gauss points is needed for a Q4 element to evaluate accurately the stiffness matrix. These Gauss points are marked as #1′, #2′, #3′, and #4′ in Figure 4.12a, in the same counterclockwise fashion as in the node numbering of the element. The coordinates of these Gauss points and field nodes in the natural coordinate system $O\xi\eta$ are listed in Table 4.4.

The "Gauss element" bounded by these four Gauss points is now considered as a "standard (natural) element," as shown in Figure 4.12b. The (natural) coordinates of the Gauss element, ξ' and η', and ξ and η, have the following simple relations,

$$\xi = \xi'/\sqrt{3}, \quad \eta = \eta'/\sqrt{3}, \quad \xi' = \xi\sqrt{3}, \quad \eta' = \eta\sqrt{3}, \tag{4.55}$$

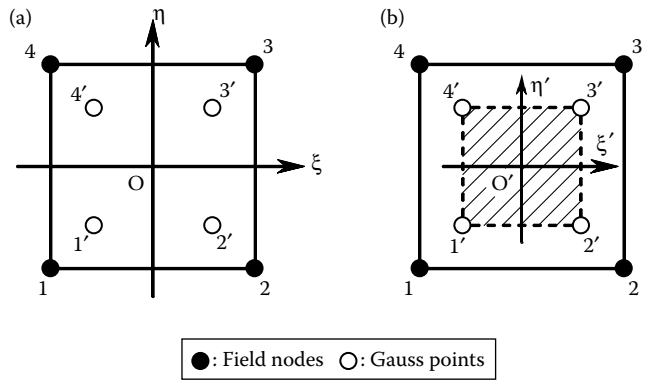

FIGURE 4.12 Extrapolation from Gauss integration points to field nodes: (a) natural coordinate system $O\xi\eta$; (b) coordinate system for the "Gauss element" $O'\xi'\eta'$.

TABLE 4.4

Coordinates of the Nodes and Gauss Points in the Natural Coordinate System $O\xi\eta$ for a Q4 Element

Field Nodes	#1	#2	#3	#4				
Gauss points					#1′	#2′	#3′	#4′
ξ	-1	1	1	-1	$-1/\sqrt{3}$	$1/\sqrt{3}$	$1/\sqrt{3}$	$1/\sqrt{3}$
η	-1	-1	1	1	$-1/\sqrt{3}$	$-1/\sqrt{3}$	$1/\sqrt{3}$	$-1/\sqrt{3}$

TABLE 4.5

Coordinates of the Field Nodes and Gauss Points in the Natural Coordinate System $O'\xi'\eta'$

Field Nodes	#1	#2	#3	#4				
Gauss points					#1′	#2′	#3′	#4′
ξ	$-\sqrt{3}$	$\sqrt{3}$	$\sqrt{3}$	$\sqrt{3}$	-1	1	1	-1
η	$-\sqrt{3}$	$-\sqrt{3}$	$\sqrt{3}$	$-\sqrt{3}$	-1	-1	1	1

and the coordinates of the Gauss points and field nodes in the coordinate system $O'\xi'\eta'$ of the Gauss element are listed in Table 4.5.

In an FEM-Q4 model, the strains at the Gauss points, $\tilde{\boldsymbol{\varepsilon}}_{j'}$ ($j' = 1', \ldots, 4'$), are known, and the strains $\tilde{\boldsymbol{\varepsilon}}(\xi', \eta')$ at point (ξ', η') can be extrapolated using the usual bilinear shape functions defined in the coordinates ξ' and η' as follows:

$$\tilde{\boldsymbol{\varepsilon}}(\xi', \eta') = \begin{bmatrix} \tilde{\boldsymbol{\varepsilon}}_{1'} & \tilde{\boldsymbol{\varepsilon}}_{2'} & \tilde{\boldsymbol{\varepsilon}}_{3'} & \tilde{\boldsymbol{\varepsilon}}_{4'} \end{bmatrix} \begin{bmatrix} N_1'(\xi', \eta') \\ N_2'(\xi', \eta') \\ N_3'(\xi', \eta') \\ N_4'(\xi', \eta') \end{bmatrix}, \tag{4.56}$$

where

$$\begin{aligned} N_1'(\xi', \eta') &= \frac{1}{4}(1 - \xi')(1 - \eta'), \\ N_2'(\xi', \eta') &= \frac{1}{4}(1 + \xi')(1 - \eta'), \\ N_3'(\xi', \eta') &= \frac{1}{4}(1 + \xi')(1 + \eta'), \\ N_4'(\xi', \eta') &= \frac{1}{4}(1 - \xi')(1 + \eta'). \end{aligned} \tag{4.57}$$

We can now extrapolate $\tilde{\boldsymbol{\varepsilon}}(\xi', \eta')$ to node #1 by letting $\xi' = \eta' = -\sqrt{3}$ in Equation 4.58. The same can be performed for the other three nodes #2, #3, and #4, and finally we obtain

$$\begin{bmatrix} \tilde{\boldsymbol{\varepsilon}}_1 \\ \tilde{\boldsymbol{\varepsilon}}_2 \\ \tilde{\boldsymbol{\varepsilon}}_3 \\ \tilde{\boldsymbol{\varepsilon}}_4 \end{bmatrix} = \begin{bmatrix} 1+\frac{1}{2}\sqrt{3} & -\frac{1}{2} & 1-\frac{1}{2}\sqrt{3} & -\frac{1}{2} \\ -\frac{1}{2} & 1+\frac{1}{2}\sqrt{3} & -\frac{1}{2} & 1-\frac{1}{2}\sqrt{3} \\ 1-\frac{1}{2}\sqrt{3} & -\frac{1}{2} & 1+\frac{1}{2}\sqrt{3} & -\frac{1}{2} \\ -\frac{1}{2} & 1-\frac{1}{2}\sqrt{3} & -\frac{1}{2} & 1+\frac{1}{2}\sqrt{3} \end{bmatrix} \begin{bmatrix} \tilde{\boldsymbol{\varepsilon}}_{1'} \\ \tilde{\boldsymbol{\varepsilon}}_{2'} \\ \tilde{\boldsymbol{\varepsilon}}_{3'} \\ \tilde{\boldsymbol{\varepsilon}}_{4'} \end{bmatrix}. \tag{4.58}$$

After going through this carefully designed three-step procedure, the recovery strain (stress) solution of an FEM-Q4 model will be very accurate and will have the so-called superconvergence property. Such a model is regarded as "optimal" and is denoted in this book as FEM-Q4-Re. It poses a serious challenge to the S-FEM models, in the comparison study based on the energy norm error measure. Note that a similar extrapolation procedure can be performed for the H8 element for 3D problems. In later chapters, we show that our S-FEM-T3 and S-FEM-T4 models will meet these challenges, using only triangular types of elements. Note also that such recovery operations used in FEM models help only the solution in the strain field and cannot help in any way the displacement solution. The S-FEM models, however, can improve solutions in both the displacement and strain fields, which is demonstrated in later chapters through a large number of examples.

4.10.7 Characteristic Length of the Sides of Elements

Note that in order to evaluate the convergence rates of the displacement and energy norms, it is necessary to define the "characteristic length" of the sides of the elements. Because the elements used in a mesh are different in dimension and of irregular shape, some kind of average is needed to determine the characteristic length. In this book, the characteristic length h is defined (by default) as follows. For T3 elements, h is evaluated by

$$h = \sqrt{\frac{2A_\Omega}{N_e}}, \tag{4.59}$$

where A_Ω is the area of the whole problem domain.

For Q4 and n-sided polygonal elements, h is evaluated by

$$h = \sqrt{\frac{A_\Omega}{N_e}}. \tag{4.60}$$

For four-node tetrahedral elements, h is evaluated by

$$h = \sqrt[3]{\frac{6V_\Omega}{N_e}}, \tag{4.61}$$

where V_Ω is the volume of the whole problem domain.

For eight-node hexahedral elements (just used for FEM), h is evaluated by

$$h = \sqrt[3]{\frac{V_\Omega}{N_e}}. \tag{4.62}$$

4.10.8 Error Assessment for *n*-Sided Polygonal Elements

When general n-sided polygonal elements (nCS-FEM, nNS-FEM, and nES-FEM) are used, it is very difficult to perform these integrations in Equations 4.49 and 4.50. In addition, the standard FEM cannot use these n-sided polygonal elements, and hence rigorous comparison is not needed. We, therefore, use the following simpler error norms.

The displacement norm for S-FEM models using n-sided polygonal elements is defined using nodal displacement values:

$$e_d = \frac{\sum_{i=1}^{N_{\text{dof}}} u_i - \bar{u}_i}{\sum_{i=1}^{N_{\text{dof}}} |u_i|} \times 100\%, \tag{4.63}$$

where u_i is the exact displacement at node $i, \bar{u}_i$ is the numerical displacement at node i, and N_{dof} is the total number of DOFs of the problem.

The energy norm for S-FEM models is defined as

$$e_e = \left(\frac{1}{2} \sum_{k=1}^{N_s} (\boldsymbol{\varepsilon} - \bar{\boldsymbol{\varepsilon}}_k)^T \, \mathbf{c} \, (\boldsymbol{\varepsilon} - \bar{\boldsymbol{\varepsilon}}_k) \, A_k^s \right)^{1/2}, \tag{4.64}$$

where $\bar{\boldsymbol{\varepsilon}}_k$ and A_k^s are smoothing strain and area of the smoothing domain Ω_k^s, respectively, $\boldsymbol{\varepsilon}$ is the analytical strain computed at nodes (for comparison with nNS-FEM), at edge-mid-points (for comparison with nES-FEM), or at central points of the smoothing domains Ω_k^s (for comparison with nCS-FEM), and N_s is the total number of smoothing domains.

4.10.9 Error in Strain Energy

When using Equation 4.50, there are difficulties in the numerical integration, depending on the problem. On the other hand, when using Equation 4.64, there can be comparability problems (see Section 4.10.10). Therefore, we use the following alternative error indicator for "errors in strain energy solution" or "strain energy error":

$$e_e = \sqrt{\frac{\left|E^{\text{ref}} - E^{\text{num}}\right|}{E^{\text{ref}}}}, \tag{4.65}$$

where E^{num} is the solution of strain energy obtained from a numerical model and E^{ref} is the reference solution of strain energy that can be the exact solution (if available) or obtained using a very fine mesh. These strain energies are evaluated using Equation 3.83 where integration over the entire problem domain is needed. Because E^{num} and E^{ref} are evaluated separately, these equations can be done easily based on either the elements or the smoothing domains. We can also use Equation 4.65 to study the convergence rate of a numerical model by changing the mesh density, but such a rate will be different from that obtained using Equation 4.50 for the same model, although they are "equivalent" in convergence (not the rate). More discussion is given in the following section.

4.10.10 On Different Norms

Note that compared to Equations 4.49 and 4.50, Equations 4.63 and 4.64 are much more convenient and cheap to use. It can be used essentially for all types of elements. Equation 4.63 should be equivalent to Equation 4.49 in terms of the convergence rate but not on the actual values. Because Equation 4.63 is equivalent to Equation 4.49, and it is very easy to evaluate, it is used in all S-FEM models using n-sided polygonal elements as well as in patch tests for all models and for all types of elements used in this book, where the comparison with FEM models is not on the agenda. Equation 4.49 is used for all FEM and S-FEM models using T3, Q4, T4, and H8 (for FEM only) elements, so that comparisons can be made in a common norm familiar to many.

Equations 4.50 and 4.64 will be different in both the actual values and the convergence rates. This is because the exact solutions are evaluated accurately in Equation 4.50 by using the Gauss integration rules, while the exact solutions in Equation 4.64 are only sampled at a point inside the smoothing domain. Equation 4.50 also has the same form as that of Equation 3.83 used for the standard FEM: it is the standard form used in FEM models. Equation 4.50 is used for all FEM and S-FEM models using

T3, Q4, T4, and H8 (for FEM only) elements, so that comparisons can be made in a common norm. Equation 4.64 is only used for measuring errors of n-sided polygonal elements, where the comparison with FEM is not on the agenda, because FEM does not use n-sided polygonal elements.

Note that comparisons are also often made in *strain energy error* defined in Equation 4.65, which is a global measure of the solution total strain energy in the system, and it should be fair to all the models involved in the comparison. It is mostly used to show the upper and lower bound properties of numerical models. In such a case, however, the rate of convergence *cannot* be checked against the theoretically predicted values given in Theorem 3.4, because of the difference in the norm measure. Therefore, care must be taken in interpreting such comparisons.

Remark 4.9 Norm Measure $\|\cdot\|_{\mathbb{G}^1(\Omega;\mathbb{R}^d)}$

Note that we can also use the so-called norm $\|\cdot\|_{\mathbb{G}^1(\Omega;\mathbb{R}^d)}$ to measure the solution error based on $\mathbb{G}$ space theory [17–19] (which is the same as that given in Equation 4.64 for S-FEM models). We choose not to use it whenever the comparison study is performed against the standard FEM model, because of the possible arguments on fairness. In this book, we use the norm $\|\cdot\|_{\mathbb{H}^1(\Omega;\mathbb{R}^d)}$ for all models when such a comparison is conducted.

4.11 Implementation Procedure for S-FEM Models

The numerical procedure for S-FEM models is outlined as follows:

1. Divide the problem domain into a set of elements and obtain information on node coordinates and element connectivity
2. Create the smoothing domains and determine the area/volume of the smoothing domains Ω_k^s and the information of the nodes of elements that support each of the smoothing domains
3. Loop over smoothing domains Ω_k^s
   a. Determine the outward unit normal of each boundary segment/area for the smoothing domain
   b. Compute the smoothed strain-displacement matrix $\overline{\mathbf{B}}_I$
   c. Evaluate the smoothed stiffness matrix $\overline{\mathbf{K}}_{IJ}$ and load vector of the current smoothing domain
   d. Assemble the contribution of the current smoothing domain to form global matrices and vectors
4. Implement essential boundary conditions

5. Solve the linear system of equations to obtain nodal displacements
6. Evaluate strains and stresses at locations of interest

Note that in our theoretical derivations, we require the assumed displacement solution $\overline{\mathbf{u}} \in \mathbb{H}^1_{0,h}(\Omega; \mathbb{R}^d)$, meaning that the essential boundary conditions are satisfied when the displacement field is assumed. In this way, the theoretical presentation can be nicely performed and the properties of the model can be examined conveniently. In the practical implementation and coding, however, the essential boundary conditions are imposed only after the system of equations is established. This is more convenient and is made possible because the shape functions constructed and used for creating the displacement field have the important Delta function properties (see Remark 4.1). This practical approach of treating the essential boundary conditions is exactly the same as in FEM: essentially by removing (or modifying) the rows and columns of the stiffness matrix [29].

4.12 General Properties of S-FEM Models

Property 4.1 Smoothed Strain Field: Incompatible

1. When the smoothing domain locates within the element such as in CS-FEM, the smoothed strains defined in Equation 4.23 will not be compatible in terms of strain–displacement relations (meaning that the strain–displacement relation is not satisfied) unless the assumed displacement field is linear.
2. When the smoothing domain covers parts of adjacent elements such as in NS-FEM, ES-FEM, or FS-FEM, the assumed smoothed strains defined in Equation 4.23 will not be compatible in terms of the strain–displacement relation for any assumed continuous displacement field.

We first examine item (1). When the smoothing domain locates within the element such as in CS-FEM, if the order of the assumed displacement field is higher than first order, the compatible strain produced by Equation 4.13 will not be constant. The constructed smoothing strains defined in Equation 4.23 are however constant in a smoothing domain. Hence the compatibility condition (the strain–displacement relation) is violated.

We then examine item (2). When the smoothing domain covers parts of adjacent elements such as in NS-FEM, ES-FEM, or FS-FEM, the smoothed strain given in Equation 4.23 is the area-weighted average of compatible strains over portions of the elements forming the smoothing domain.

Because the strains in these elements will in general be different, the average strain will be different from these element strains for any assumed continuous displacement field. Hence the compatibility condition is violated.

Property 4.1 (1) implies that the stress equilibrator in CS-FEM will destroy the compatibility in terms of the strain–displacement relation in smoothing domains for assumed displacement fields of bilinear or higher order. It also implies that when the linear displacement field is used (three-node triangular element), CS-FEM will be identical to the standard FEM, because the stress equilibrator is idle to a constant stress field derived from the linear displacement field. CS-FEM can therefore only be applied with significance to elements of higher order.

Property 4.1 (2) implies that the stress equilibrator in NS-FEM, ES-FEM, and FS-FEM will destroy the compatibility in terms of the strain–displacement relation in smoothing domains for any assumed continuous displacement field. Therefore, NS-FEM, ES-FEM, and FS-FEM will be quite different from FEM using any elements. Therefore, an S-FEM model is, in general, said to be partially compatible in comparison with the fully compatible FEM models (see Remark 3.4).

These violations of compatibility in terms of strain–displacement relations give S-FEM models very important softening effects and hence some important properties.

Property 4.2 Stress Equilibrium State within Smoothing Domains

The assumed smoothing strains defined in Equation 4.23 ensure a stress equilibrium state within the smoothing domain where there is no body force.

This can be observed easily based on the assumption made in Equation 4.23: the assumed smoothing strains become constants at any point in the smoothing domain. Therefore, the stresses obtained will also be constant in a smoothing domain. These constant stresses satisfy the equilibrium Equation 2.7 for free external loadings.

Property 4.2 is a simple but quite powerful statement: applying the strain smoothing technique to an smoothing domain in the problem domain results in a stress equilibrium status in the smoothing domain. We, therefore, call the smoothing operation a local *stress equilibrator*. Based on the minimum complementary principle [30], we know that if the stress field satisfies exactly the equilibrium equations and boundary conditions, we shall obtain an exact upper bound solution. Our S-FEM models will not satisfy the equilibrium equation for every point in the problem domain, but will in all satisfy the smoothed domains. When the smoothing domains are constructed properly to provide sufficient softening effects, we can expect an upper bound solution. This is often confirmed by the NS-FEM [31] that will be discussed in Chapter 6 in detail.

Property 4.3 Energy Consistency

S-FEM models are *energy consistent* when the assumed displacement is compatible (or the nodal shape functions are continuous) along the boundaries of smoothing domains.

This remark can be verified by observing a unique "complementary" situation for S-FEM models. On the one hand, equilibrium is ensured within each smoothing domain, as shown in Property 4.2, but compatibility is destroyed within the smoothing domain, as shown in Property 4.1. On the other hand, on the boundaries of the smoothing domains equilibrium and stress continuity are not guaranteed, but displacement continuity is ensured on the common boundaries of the smoothing domains due to the use of continuous nodal shape functions. It is this unique complementary satisfaction of *equilibrium* or *compatibility* conditions within the smoothing domains and on the boundaries of the smoothing domains that ensures no energy loss in any of the violation of equilibrium or compatibility conditions. We therefore state that S-FEM models are *energy consistent* when the assumed displacement is compatible or the nodal shape functions are continuous along the boundaries of smoothing domains.

Property 4.3 reveals the essential physical reason for why S-FEM models are variationally consistent: conservation of energy.

Theorem 4.2: Softening Effect [32]

For any given admissible (nonzero) displacement field $\mathbf{v} \in \mathbb{H}^1_{0,h}(\Omega;\mathbb{R}^d) \subset \mathbb{H}^1_0(\Omega;\mathbb{R}^d)$, the strain energy $\bar{E}(\mathbf{v})$ for an S-FEM model obtained from the smoothed strains is no larger than the strain energy $\tilde{E}(\mathbf{v})$ for an FEM model of the compatible displacement field:

$$\bar{E}(\mathbf{v}) \leq \tilde{E}(\mathbf{v}), \tag{4.66}$$

in which

$$\bar{E}(\mathbf{v}) = \frac{1}{2}\int_{\Omega} \bar{\boldsymbol{\varepsilon}}^T(\mathbf{v})\, \mathbf{c}\bar{\boldsymbol{\varepsilon}}(\mathbf{v})\, \mathrm{d}\Omega = \frac{1}{2}\sum_{k=1}^{N_s}\int_{\Omega_k^s} \bar{\boldsymbol{\varepsilon}}_k^T \mathbf{c}\bar{\boldsymbol{\varepsilon}}_k\, \mathrm{d}\Omega = \frac{1}{2}\sum_{k=1}^{N_s} \bar{\boldsymbol{\varepsilon}}_k^T \mathbf{c}\bar{\boldsymbol{\varepsilon}}_k A_k^s, \tag{4.67}$$

$$\tilde{E}(\mathbf{v}) = \frac{1}{2}\int_{\Omega} (\tilde{\boldsymbol{\varepsilon}}(\mathbf{v}))^T\, \mathbf{c}\tilde{\boldsymbol{\varepsilon}}(\mathbf{v})\, \mathrm{d}\Omega = \frac{1}{2}\sum_{k=1}^{N_s}\int_{\Omega_k^s} \tilde{\boldsymbol{\varepsilon}}^T \mathbf{c}\tilde{\boldsymbol{\varepsilon}}\, \mathrm{d}\Omega, \tag{4.68}$$

where $\bar{\boldsymbol{\varepsilon}} = \bar{\boldsymbol{\varepsilon}}(\mathbf{v})$ by Equation 4.23 is the smoothed strain in an S-FEM model and $\tilde{\boldsymbol{\varepsilon}} = \mathbf{L}_d\mathbf{v}$ is the compatible strain obtained in the FEM. The equality in Equation 4.66 is attained only when there is no smoothing effect in all the smoothing domains: $\bar{\boldsymbol{\varepsilon}}_k = \tilde{\boldsymbol{\varepsilon}}$ for all $\Omega_k^s (k = 1, 2, \ldots, N_s)$.

Proof. Examine the following equation on the smoothing domain Ω_k^s:

$$\int_{\Omega_k^s} (\overline{\boldsymbol{\varepsilon}}_k - \tilde{\boldsymbol{\varepsilon}})^T \mathbf{c} \, (\overline{\boldsymbol{\varepsilon}}_k - \tilde{\boldsymbol{\varepsilon}}) \, \mathrm{d}\Omega = \int_{\Omega_k^s} \overline{\boldsymbol{\varepsilon}}_k^T \mathbf{c} \tilde{\boldsymbol{\varepsilon}}_k \, \mathrm{d}\Omega - 2 \int_{\Omega_k^s} \overline{\boldsymbol{\varepsilon}}_k^T \mathbf{c} \tilde{\boldsymbol{\varepsilon}} \, \mathrm{d}\Omega + \int_{\Omega_k^s} \tilde{\boldsymbol{\varepsilon}}^T \mathbf{c} \tilde{\boldsymbol{\varepsilon}} \, \mathrm{d}\Omega. \tag{4.69}$$

Using orthogonal condition (4.43) and the fact that $\mathbf{c}$ is SPD, we have

$$\underbrace{\int_{\Omega_k^s} (\overline{\boldsymbol{\varepsilon}}_k - \tilde{\boldsymbol{\varepsilon}})^T \mathbf{c} (\overline{\boldsymbol{\varepsilon}}_k - \tilde{\boldsymbol{\varepsilon}}) \, \mathrm{d}\Omega}_{\geq 0} = \int_{\Omega_k^s} \tilde{\boldsymbol{\varepsilon}}^T \mathbf{c} \tilde{\boldsymbol{\varepsilon}} \, \mathrm{d}\Omega - \int_{\Omega_k^s} \overline{\boldsymbol{\varepsilon}}_k^T \mathbf{c} \overline{\boldsymbol{\varepsilon}}_k \, \mathrm{d}\Omega \geq 0, \tag{4.70}$$

which combines with Equations 4.67 and 4.68 to give Equation 4.66.

Now, on the equality, it is clear that when there is no smoothing effect in all the smoothing domains, $\overline{\boldsymbol{\varepsilon}}_k = \tilde{\boldsymbol{\varepsilon}}$ for all $\Omega_k^s (k = 1, 2, \ldots, N_s)$, the left-hand side of Equation 4.70 is strictly zero, and hence the equality in Equation 4.66 is attained. If there is at least one Ω_k^s where there is some smoothing effect and $\overline{\boldsymbol{\varepsilon}}_k \neq \tilde{\boldsymbol{\varepsilon}}$, the left-hand side of Equation 4.70 is strictly larger than zero, and will have

$$\overline{E} \, (\mathbf{v}) < \tilde{E} \, (\mathbf{v}) \, . \tag{4.71}$$

This completes our proof. □

Equation 4.66 can be expressed in a discrete form of arbitrary (but admissible) nodal displacement $\mathbf{h} \in \mathbb{R}_0^{dN_n}$ (where $\mathbb{R}_0^{dN_n}$ is a finite space of vectors of nodal displacement functions with a dimension of dN_n, and the essential boundary conditions are satisfied at all the essential boundary nodes) as

$$\underbrace{\frac{1}{2} \mathbf{h}^T \overline{\mathbf{K}} h}_{\overline{E}(\mathbf{h})} \leq \underbrace{\frac{1}{2} \mathbf{h}^T \tilde{\mathbf{K}} h}_{\tilde{E}(\mathbf{h})}, \tag{4.72}$$

where the equality holds only when there is no smoothing effect in all the smoothing domains: $\overline{\mathbf{K}} = \tilde{\mathbf{K}}$.

Theorem 4.3: Upper Bound to the FEM Solution [32]

For an elastic solid mechanics problem, when the same mesh is used, the strain energy obtained from the solution $\overline{\mathbf{d}} \in \mathbb{R}_0^{dN_n}$ of the S-FEM models is no less than that from the FEM solution $\tilde{\mathbf{d}} \in \mathbb{R}_0^{dN_n}$ based on the compatible displacement model:

$$\overline{E}(\overline{\mathbf{d}}) \geq \tilde{E}(\tilde{\mathbf{d}}), \tag{4.73}$$

where

$$\overline{E}(\overline{\mathbf{d}}) = \frac{1}{2}\overline{\mathbf{d}}^T\overline{\mathbf{K}}\overline{\mathbf{d}}, \tag{4.74}$$

$$\tilde{E}(\tilde{\mathbf{d}}) = \frac{1}{2}\tilde{\mathbf{d}}^T\tilde{\mathbf{K}}\tilde{\mathbf{d}}. \tag{4.75}$$

The equality in Equation 4.73 is attained only when there is no smoothing effect in all the smoothing domains: $\bar{\boldsymbol{\varepsilon}}_k = \tilde{\boldsymbol{\varepsilon}}$ for all $\Omega_k^s (k = 1, 2, \ldots, N_s)$.

Proof. In this proof, we assume first that there is at least one Ω_k^s where there is some smoothing effect resulting in $\bar{\boldsymbol{\varepsilon}}_k \neq \tilde{\boldsymbol{\varepsilon}}$. From Theorem 4.2, we have the stick inequality Equation 4.71. Therefore, we have, for any admissible and nonzero $\mathbf{h}$,

$$\underbrace{\frac{1}{2}\mathbf{h}^T\tilde{\mathbf{K}}\mathbf{h} - \frac{1}{2}\mathbf{h}^T\overline{\mathbf{K}}\mathbf{h}}_{>0} = \frac{1}{2}\mathbf{h}^T(\tilde{\mathbf{K}} - \overline{\mathbf{K}})\mathbf{h} > 0. \tag{4.76}$$

Equation 4.76 implies that matrix $(\tilde{\mathbf{K}} - \overline{\mathbf{K}})$ is SPD. In mechanics, it implies that $\tilde{\mathbf{K}}$ is "stiffer" than $\overline{\mathbf{K}}$. In addition, because of the SPD property of $\tilde{\mathbf{K}}$, the solution $\tilde{\mathbf{d}}$ of FEM can be expressed as

$$\tilde{\mathbf{d}} = \tilde{\mathbf{K}}^{-1}\tilde{\mathbf{f}}, \tag{4.77}$$

where $\tilde{\mathbf{f}}$ is the nodal force vector and is nonzero (or we will have only a trivial zero solution). Because of the SPD property of $\overline{\mathbf{K}}$, the solution $\bar{\mathbf{d}}$ of S-FEM models can be expressed as

$$\overline{\mathbf{d}} = \overline{\mathbf{K}}^{-1}\tilde{\mathbf{f}}. \tag{4.78}$$

The difference between the strain energies of FEM and of the solution of S-FEM models hence becomes

$$\begin{aligned}
\overline{E}(\overline{\mathbf{d}}) - \tilde{E}(\tilde{\mathbf{d}}) &= \frac{1}{2}(\overline{\mathbf{K}}^{-1}\tilde{\mathbf{f}})^T\overline{\mathbf{K}}(\overline{\mathbf{K}}^{-1}\tilde{\mathbf{f}}) - \frac{1}{2}(\tilde{\mathbf{K}}^{-1}\tilde{\mathbf{f}})^T\tilde{\mathbf{K}}(\tilde{\mathbf{K}}^{-1}\tilde{\mathbf{f}}) \\
&= \frac{1}{2}\tilde{\mathbf{f}}^T\overline{\mathbf{K}}^{-1}\tilde{\mathbf{f}} - \frac{1}{2}\tilde{\mathbf{f}}^T\tilde{\mathbf{K}}^{-1}\tilde{\mathbf{f}} \\
&= \frac{1}{2}\tilde{\mathbf{f}}^T\underbrace{(\overline{\mathbf{K}}^{-1} - \tilde{\mathbf{K}}^{-1})}_{\because \text{SPD}}\tilde{\mathbf{f}} > 0,
\end{aligned} \tag{4.79}$$

which gives Equation 4.73. Here we used the fact that $(\overline{\mathbf{K}}^{-1} - \tilde{\mathbf{K}}^{-1})$ is SPD.

Now, when there is no smoothing effect in all the smoothing domains, $\overline{\boldsymbol{\varepsilon}}_k = \tilde{\boldsymbol{\varepsilon}}$ for all $\Omega_k^s (k = 1, 2, \ldots, N_s)$, the smoothed Galerkin model is exactly the same as the Galerkin model. In this case, we will surely have the equality in Equation 4.73. This completes the proof of Theorem 4.3. □

Theorem 4.3 shows one very important property of S-FEM models. In mechanics, this means that the S-FEM models are "softer" than the FEM model. In other words, the common effect of the strain smoothing technique is the reduction of the overstiffness of the standard compatible FEM model. This effect is called the "softening effect," which contrasts with the "stiffening effect" caused by the assumed displacement field using the FEM shape functions in a conforming/fully compatible model. Due to the softening effect, the strain energy of the S-FEM models becomes larger than that of FEM.

Now, the following question naturally arises: How can we adjust the softening effect in the S-FEM models to ensure that the obtained solution gives an upper bound in the strain energy compared with the exact strain energy or gives a close-to-exact solution? All these questions will be addressed in the following chapters.

Theorem 4.4: Monotonic Convergence Property [17]

On a division of domain Ω into a set of N_s^{D1} smoothing domains $\Omega = \sum_{k=1}^{N_s^{D1}} \Omega_k^s$, if a new division N_s^{D2} is created in a nested fashion by subdividing the kth smoothing domain into n_s subsmoothing domains such that $\Omega_k^s = \sum_{p=1}^{n_s} \Omega_{k,p}^s$, $\Omega_{k,m}^s \cap \Omega_{k,n}^s = \emptyset, m \neq n$, then the following inequality stands:

$$\overline{E}_{D1}(\overline{\mathbf{u}}) \geq \overline{E}_{D2}(\overline{\mathbf{u}}), \tag{4.80}$$

where $\overline{E}_D(\overline{\mathbf{u}})$ is the strain energy solution obtained from an S-FEM model with a division of domain Ω into a set of D smoothing domains. The equality is attained only when all the nested subdivisions are idle.

This implies that the "softening" effect provided by the smoothing operation will be monotonically reduced with the increase of the number of smoothing domains constructed in a nested manner. A simple proof can be given using the triangle inequality of norms: the sum of the energy norm of functions is no less than the norm of the summed functions [17]. In addition, a specific proof for CS-FEM will also be conducted in Section 5.5.

Following Remark 4.7, we shall expect that when such a nested subdivision is performed intensively to all the smoothing domains so that $\Omega_{k,p}^s \to 0$ for all k and p, the model will approach the compatible model, which will

be discussed further in Theorem 4.5. Note also that this monotonic convergence property may not hold for problems with singularity, as will be shown in Chapter 10.

Theorem 4.5: Convergence Property

When $N_s \to \infty$, the solution $\overline{\mathbf{u}}$ of S-FEM models will approach the solution $\tilde{\mathbf{u}} \in \mathbb{H}^1_{0,h}(\Omega;\mathbb{R}^d) \subset \mathbb{H}^1_0(\Omega;\mathbb{R}^d)$ of the standard compatible displacement FEM model.

Proof. Assume that the problem has the solution $\tilde{\mathbf{u}} \in \mathbb{H}^1_{0,h}(\Omega;\mathbb{R}^d) \subset \mathbb{H}^1_0(\Omega;\mathbb{R}^d)$ of the standard compatible displacement FEM model. Now we consider finding the solution $\overline{\mathbf{u}}$ of S-FEM models for the same problem. In a given division N_s of domain Ω into a set of smoothing domains such that $\Omega = \sum_{k=1}^{N_s} \Omega_k^s$, when $N_s \to \infty$ and each smoothing domain Ω_k^s approaches zero, the smoothing function in Equation 4.18 approaches the Delta function. At such a limit $\overline{\boldsymbol{\varepsilon}} \to \tilde{\boldsymbol{\varepsilon}}$ (Remark 4.7), $\overline{\mathbf{B}} \to \tilde{\mathbf{B}}, \overline{\mathbf{K}} \to \tilde{\mathbf{K}}$, and the solution $\overline{\mathbf{u}}$ of the S-FEM models hence will approach the solution $\tilde{\mathbf{u}}$ of the standard compatible displacement FEM model. □

Theorem 4.5 also implies that in case the smoothing domain Ω_k^s is associated with the number of nodes N_n (NS-FEM), edges N_{eg} (ES-FEM), or faces N_{f} (FS-FEM) of FEM, the solution $\overline{\mathbf{u}}$ of S-FEM models will approach the exact solution, because the solution $\tilde{\mathbf{u}}$ of the standard compatible displacement FEM model also approaches the exact solution when N_n, N_{eg}, or N_{f} approaches infinity. This has already been discussed in the proof of Theorem 4.1.

4.13 Remarks

Finally, before concluding this chapter, we mention a few additional remarks for an S-FEM model for later references.

Remark 4.10 No Increase of DOFs

In S-FEM models, the unknowns of only the displacement are the same as that in the standard FEM model.

Remark 4.11 S-FEM Elements: Arbitrariness in Shape and Distortion

The domain discretization in an S-FEM model can be more flexible than that in the standard FEM. By constructing compatible shape functions based on physical coordinates, complicated elements such as arbitrary n-sided

convex polygonal elements can be used in the S-FEM models. Because no mapping is used in S-FEM, it is expected to be much more tolerant to element distortion.

Remark 4.12 Order and Enrichment of S-FEM Elements

In theory, S-FEM works for elements of any order, as long as at least the minimum number of independent smoothing domains is used to ensure the stability. For simplicity and effectiveness, we prefer using lower-order elements: linear or at most bilinear. For special purposes, however, we can always add in proper enrichment terms in the point interpolation procedure. A typical such case is represented by singular elements with a basic mesh of linear elements discussed in Chapter 10. The philosophy adopted in S-FEM is essentially for simplicity and robustness: to use the simplest mesh of basic linear elements with proper enrichments, when necessary, to suit special purposes.

Remark 4.13 The "Rooms" Explored by S-FEM Models: Better than the "Best"

S-FEM uses the smoothed Galerkin weak form. This *essentially* changed the bilinear form and hence the norm measures (see Remark 3.3), leading to the softening effects that push the S-FEM solution into the room between the FEM solution (lower bound, Property 3.2) and the exact solution. When this is achieved (as in ES-FEM), we obtain a solution (in strain energy) that will *always* be better than the FEM model using the same mesh. When this is "overdone" (as in NS-FEM), we obtain an upper bound solution. Either way, we achieve something that the standard FEM cannot offer: better than the best.

Remark 4.14 S-FEM: Beyond-Element Operations

We now see a very distinct feature of an S-FEM model compared to the FEM model: the numerical operations used in S-FEM are in general beyond the elements. Displacement interpolation (or shape function construction) is based on the element or nodes, but smoothed strain field construction is based on smoothing domains that are created beyond the element. In addition, the integration is also based on smoothing domains. Such a beyond-element operation allows bringing in information from surrounding elements, and hence improving the solution. It is clear that S-FEM models have features of both standard FEM and mesh-free methods.

Remark 4.15 On h-Dependence for S-FEM

The theory on the rate of convergence of S-FEM models is not discussed in detail in this book, because it requires a very lengthy derivation

and analysis. In addition, some of the theoretical issues related to rate convergence have not yet been fully resolved. Numerical examples will be presented in later chapters to show that (1) these S-FEM models will always pass the standard patch tests, implying at least second-order accuracy, and (2) the rates of convergence for various S-FEM models are often higher than the FEM counterparts using linear elements, especially in the displacement norm. These numerical rates found for S-FEM models obey at least Theorem 3.4, but much more thorough studies are required to prove this and to establish such a precise theorem for S-FEM models. A recent related study that led to a theorem for S-FEM similar to Theorem 3.3 is reported in Ref. [33]. This study showed that S-FEM will always work well, but precisely how well it works is still an open question. At this moment, we know that Theorem 3.4 should also hold for general S-FEM models at least when sufficiently smoothing domains are used, simply because of Theorem 4.5. The tricky part is that we do not want to use too many smoothing domains, so that we can have a better benefit. A theorem that can guide us on how to achieve that and how far we can really go is useful, but unfortunately it is not yet available.

Remark 4.16 S-FEM: Number of Smoothing Domains

The stability of S-FEM models can be ensured by using at least a minimum number of linearly independent smoothing domains, which is given in Tables 4.2 and 4.3.

Remark 4.17 S-FEM: Types of Smoothing Domains

S-FEM uses the strain smoothing technique to construct strain fields that are piecewise constant, and satisfies the orthogonal condition. It uses different types of smoothing domains that can be cell-, node-, edge-, and face-based, and these models are all softer than the FEM model using the same mesh. The following chapters will present S-FEM models using different types of smoothing domains, including the combined ones.

Remark 4.18 S-FEM Elements: Preference for Simplicity and Robustness

In general, we prefer to use T3 elements for 2D and T4 elements for 3D problems for the following reasons: (1) convenience in automatic mesh generation; (2) robustness for complicated geometries; (3) simplicity in formulation; (4) ease in implementation; and most importantly (5) S-FEM works well with these elements. The philosophy of S-FEM is clear: being simple and robust.

References

1. Okabe A, Boots B, and Sugihara K. 1992. *Spatial Tessellations: Concepts and Applications of Voronoi Diagrams*. Wiley, Chichester.
2. Liu GR. 2009. *Meshfree Methods: Moving Beyond the Finite Element Method*, 2nd Edition. Taylor & Francis/CRC Press, Boca Raton, FL.
3. Dai KY, Liu GR, and Nguyen-Thoi T. 2007. An *n*-sided polygonal smoothed finite element method (*n*SFEM) for solid mechanics. *Finite Elements in Analysis and Design*; 43: 847–860.
4. Lucy L. 1977. A numerical approach to testing the fission hypothesis. *The Astronomical Journal*; 82: 1013–1024.
5. Monaghan JJ. 1982. Why particle methods work. *SIAM Journal on Scientific and Statistical Computing*.; 3(4): 423–433.
6. Liu GR and Liu MB. 2003. Smoothed particle hydrodynamics—a meshfree practical method. World Scientific, Singapore.
7. LeVeque R.J. 2002. *Finite Volume Methods for Hyperbolic Problems*. Cambridge University Press, New York.
8. Tang LM, Chen WJ, and Liu Yingxi. 1984. Formulation of quasi-conforming element and Hu-Washizu principle. *Computers and Structures*; 19: 247–250.
9. Tang LM, Zhang YZ, Wu JX, Jie MY, Lu HX, and Chen WJ. 1973. On discretization of differential operator for solids (in Chinese). *J. Dalian Instit. Tech.*; 7–30.
10. Chen JS, Wu CT, and Belytschko T. 2000. Regularization of material instabilities by meshfree approximations with intrinsic length scales. *International Journal for Numerical Methods in Engineering*; 47: 1303–1322.
11. Chen JS, Wu CT, Yoon S, and You Y. 2001. A stabilized conforming nodal integration for Galerkin meshfree method. *International Journal for Numerical Methods in Engineering*; 50: 435–466.
12. Liu GR, Zhang J, and Lam KY. 2008. A gradient smoothing method (GSM) with directional correction for solid mechanics problems. *Computational Mechanics*; 41: 457–472.
13. Liu GR and Xu XG. 2008. A gradient smoothing method (GSM) for fluid dynamics problems. *International Journal for Numerical Methods in Fluids*; 58: 1101–1133.
14. Liu GR and Xu XG. 2009. An adaptive gradient smoothing method (GSM) for fluid dynamics problems. *International Journal for Numerical Methods in Fluids*; 62(5): 499–529.
15. Eringen. 1972. Nonlocal polar elastic continua. *International Journal of Engineering Science*; 10: 1.
16. Xu GX, Liu GR, and Lee KH. 2009. Application of gradient smoothing method (GSM) for steady and unsteady incompressible flow problems using irregular triangles. *International Journal for Numerical Methods in Fluids* (submitted).
17. Liu GR. 2008. A generalized gradient smoothing technique and the smoothed bilinear form for Galerkin formulation of a wide class of computational methods. *International Journal of Computational Methods*; 5: 199–236.

18. Liu GR. 2009. A G space theory and weakened weak (W^2) form for a unified formulation of compatible and incompatible methods: Part I Theory, Part II Application to solid mechanics problems. *International Journal for Numerical Methods in Engineering*; 81: 1093–1156.
19. Liu GR. 2009. On the G space theory. *International Journal of Computational Methods*; 5: 199–236.
20. Yoo JW, Moran B, and Chen JS. 2004. Stabilized conforming nodal integration in the natural-element method. *International Journal for Numerical Methods in Engineering*; 60: 861–890.
21. Hellinger E. 1914. Der allgermeine Ansatz der Mechanik der Kontinun. *Encycl. Math. Wiss.*; 4(4): 602.
22. Reissner E. 1950. On a variational theorem in elasticity. *Journal of Mathematical Physics*; 29: 90.
23. Simo JC and Hughes TJR. 1986. On the variational foundations of assumed strain methods. *Journal of Applied Mechanics*; 53: 51–54.
24. Liu GR, Nguyen-Thoi T, Dai KY, and Lam KY. 2007. Theoretical aspects of the smoothed finite element method (SFEM). *International Journal for Numerical Methods in Engineering*; 71: 902–930.
25. Zienkiewicz OC and Taylor RL. 2000. *The Finite Element Method*, 5th edition. Butterworth Heinemann, Oxford.
26. Zienkiewicz OC and Zhu JZ. 1992. The superconvergence patch recovery and a posteriori error estimates. Part 1: The recovery techniques. *International Journal for Numerical Methods in Engineering*; 33: 1331–1364.
27. Zienkiewicz OC and Zhu JZ. 1992. The superconvergence patch recovery and a posteriori error estimates. Part 2: Error estimates and adaptivity. *International Journal for Numerical Methods in Engineering*; 33: 1365–1382.
28. Felippa C. 2009. Introductions to Finite Element Methods (ASEN 5007), Chapter 28: Stress Recovery. http://www.colorado.edu/engineering/CAS/courses.d/IFEM.d/
29. Liu GR and Quek SS. 2003. *The Finite Element Method: A Practical Course*. Butterworth Heinemann, Oxford.
30. Fraeijs de Veubeke BM. 1965. Displacement and equilibrium models in the finite element method, In *Stress Analysis*, OC Zienkiewicz, Ed. Wiley, London.
31. Liu GR, Nguyen-Thoi T, Nguyen-Xuan H, and Lam KY. 2009. A node-based smoothed finite element method (NS-FEM) for upper bound solution to solid mechanics problems. *Computers and Structures*; 87: 14–26.
32. Liu GR and Zhang GY. 2008. Upper bound to elasticity problems using the linearly conforming point interpolation method (LC-PIM). *International Journal for Numerical Methods in Engineering*; 74: 1128–1161.
33. Liu GR, Nguyen-Xuan H, and Nguyen-Thoi T. 2009. A theoretical study on NS/ES-FEM: Properties, accuracy and convergence rates. *International Journal for Numerical Methods in Engineering*; (revised).
34. Liu GR, Dai KY, and Nguyen-Thoi T. 2007. A smoothed finite element method for mechanics problems. *Computational Mechanics*; 39: 859–877.
35. Liu GR, Nguyen-Thoi T, Nguyen-Xuan H, Dai KY, and Lam KY. 2009. On the essence and the evaluation of the shape functions for the smoothed finite element method (SFEM) (Letter to Editor). *International Journal for Numerical Methods in Engineering*; 77: 1863–1869.

36. Liu GR, Nguyen-Thoi T, and Lam KY. 2009. An edge-based smoothed finite element method (ES-FEM) for static, free and forced vibration analyses of solids. *Journal of Sound and Vibration*; 320: 1100–1130.
37. Nguyen-Thoi T, Liu GR, Lam KY, and Zhang GY. 2009. A face-based smoothed finite element method (FS-FEM) for 3D linear and nonlinear solid mechanics problems using 4-node tetrahedral elements. *International Journal for Numerical Methods in Engineering*; 78: 324–353.

5

Cell-Based Smoothed FEM

This chapter introduces the first S-FEM model: CS-FEM. It originated from Liu et al. [1–5] using the strain smoothing technique [6] based on finite element settings, and was initially termed S-FEM. It has been applied to solve many problems and extended to many other models. So far two distinct CS-FEM models have been developed: CS-FEM and *n*CS-FEM. CS-FEM uses bilinear quadrilateral (Q4) elements with *quadrilateral* smoothing domains created by further division of the Q4 elements. It is the original CS-FEM proposed in Refs. [1,2], and is the default model for all CS-FEM models. When we refer to a CS-FEM model, it implies that bilinear Q4 elements are used with quadrilateral smoothing domains. It may be the closest strain-modified method to the standard FEM briefed in Chapter 3 [7,8], in terms of shape functions used. In CS-FEM, the strain in an element is modified by smoothing the compatible strains over the quadrilateral smoothing domains, which gives important softening effects. CS-FEM can improve the accuracy and convergence rate of the FEM-Q4 model using the same mesh.

*n*CS-FEM originated in Ref. [4] as an extension from CS-FEM to the general *n*-sided polygonal elements, including triangular and quadrilateral elements. In *n*CS-FEM, the elements are divided into *triangular* smoothing domains. In theory, the *n*-sided polygonal elements can be concave [4]. In practice, however, we usually use convex polygonal elements, and hence our discussion in this chapter will assume that the elements are convex.

Any of the CS-FEM models follows the basic theory presented in Chapter 4, but it can have its own special features, due to cell-based smoothing operations. Special properties of these CS-FEM models will be presented and proved theoretically, and the stability analysis of CS-FEM and *n*CS-FEM is also conducted. Moreover, a selective CS-FEM is also formulated to overcome the volume-locking problems so that it can be applied for solids of incompressible materials. Numerical examples will be presented to confirm the theoretical properties of these CS-FEM models.

5.1 Cell-Based Smoothing Domain

5.1.1 Quadrilateral Smoothing Domains for CS-FEM

In CS-FEM, domain Ω is discretized into N_e quadrilateral elements as in the standard FEM-Q4, such that $\Omega = \cup_{i=1}^{N_e} \Omega_i^e$ and $\Omega_i^e \cap \Omega_j^e = \emptyset, i \neq j$. Each element Ω_i^e will be further subdivided into $n_e^s \in [1, \infty)$ *quadrilateral* smoothing domains in a nonoverlapping and no-gap manner such that $\Omega_i^e = \cup_{m=1}^{n_e^s} \Omega_{i,m}^s$, as shown in Figure 5.1. Therefore, the entire problem domain Ω is divided into a total of $N_s = N_e \times n_e^s$ smoothing domains that can be numbered in such a way that $\Omega = \cup_{k=1}^{N_s} \Omega_k^s$.

In using these quadrilateral cell-based smoothing domains, we expect that there could be cases where the number of smoothing domains does not satisfy the minimum number of smoothing domains given in Table 4.2 [9], when n_e^s is too small (e.g., in an extreme case: $n_e^s = 1$). Note also that the subdivision of each big smoothing domain into smaller smoothing domains is performed by connecting the mid-segment-points of opposite segments as shown in Figure 5.1. The summation required in the smoothed Galerkin weak form (Equation 4.37) and the strain smoothing operation (Equation 4.23) is performed over all these quadrilateral smoothing domains.

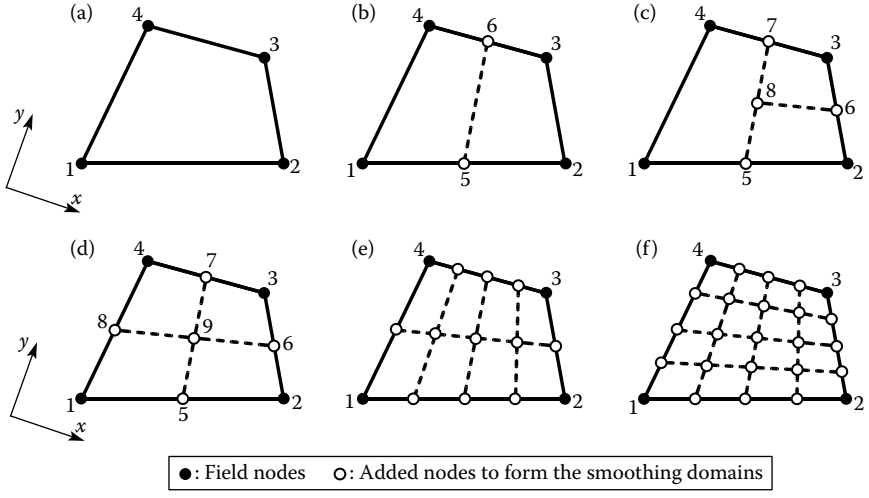

FIGURE 5.1 Division of a quadrilateral element into smoothing domains (SDs) in CS-FEM by connecting the mid-segment-points of opposite segments of smoothing domains: (a) 1 SD; (b) 2 SDs; (c) 3 SDs; (d) 4 SDs; (e) 8 SDs; and (f) 16 SDs.

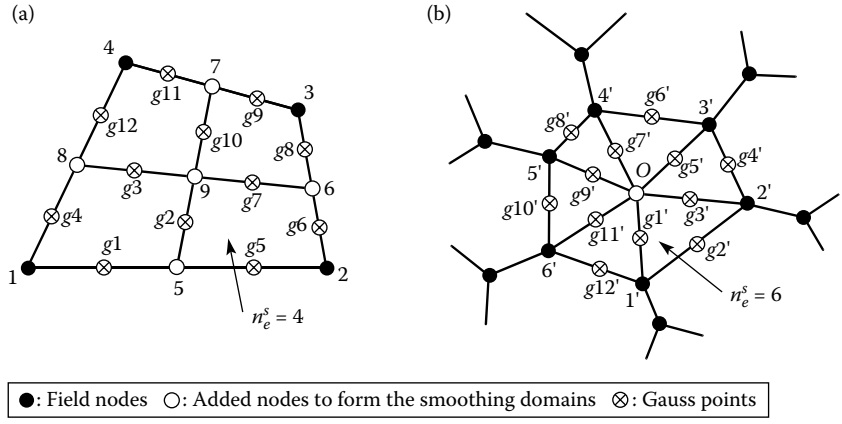

FIGURE 5.2 Positions of Gauss points at mid-segment-points on segments of smoothing domains: (a) four quadrilateral smoothing domains in a quadrilateral element and (b) six triangular smoothing domains in a six-sided convex polygonal element.

5.1.2 Triangular Smoothing Domains for *n*CS-FEM

In *n*CS-FEM, domain Ω is discretized into N_e n-sided polygonal elements, each of which has n nodes. The elements are not overlapping and there are no gaps between the elements: $\Omega = \cup_{i=1}^{N_e} \Omega_i^e$ and $\Omega_i^e \cap \Omega_j^e = \emptyset$, $i \neq j$. Each element is divided further into $n_e^s = n$ triangular smoothing domains in a nonoverlapping and no-gap manner such that $\Omega_i^e = \cup_{m=1}^{n_e^s} \Omega_{i,m}^s$. This is done by simply connecting the nodes of the elements to the centroids of the elements, as shown in Figure 5.2b. Therefore, the entire problem domain Ω is consequently divided into $N_S = \sum_{e=1}^{N_e} n_e^s$ smoothing domains that can be numbered in such a way that $\Omega = \cup_{k=1}^{N_s} \Omega_k^s$.

In using these triangular cell-based smoothing domains, the number of smoothing domains will always satisfy the minimum number of smoothing domains given in Table 4.2 [9]. This is because the number of smoothing domains is always no less than the number of nodes. The summation required in the smoothed Galerkin weak form (Equation 4.37) and the strain smoothing operation (Equation 4.23) is performed over all these triangular smoothing domains.

5.2 Discretized System of Equations

5.2.1 Formulation of CS-FEM

Consider now the solid mechanics problem defined in Chapter 2. Using the general formulation of the S-FEM models presented in Chapter 4, the

discretized linear system of equations for CS-FEM has the form

$$\overline{\mathbf{K}}^{\text{CS-FEM}}\bar{\mathbf{d}} = \tilde{\mathbf{f}}, \tag{5.1}$$

where $\bar{\mathbf{d}}$ is the vector of nodal displacements for all nodes, $\tilde{\mathbf{f}}$ is the vector of nodal forces applied on all the nodes in the problem domain, and $\overline{\mathbf{K}}^{\text{CS-FEM}}$ is the global *smoothed* stiffness matrix whose entries are given by

$$\begin{aligned}\overline{\mathbf{K}}_{IJ}^{\text{CS-FEM}} &= \sum_{i=1}^{N_e}\sum_{m=1}^{n_e^s}\int_{\Omega_{i,m}^s}\overline{\mathbf{B}}_I^T\mathbf{c}\underbrace{\overline{\mathbf{B}}_J}_{\text{constant in }\Omega_{i,m}^s}\mathrm{d}\Omega = \sum_{i=1}^{N_e}\sum_{m=1}^{n_e^s}\overline{\mathbf{B}}_I^T\mathbf{c}\overline{\mathbf{B}}_J A_{i,m}^s \\ &= \sum_{k=1}^{N_s}\overline{\mathbf{B}}_I^T\mathbf{c}\overline{\mathbf{B}}_J A_k^s,\end{aligned} \tag{5.2}$$

where $A_{i,m}^s = \int_{\Omega_{i,m}^e}\mathrm{d}\Omega$ is the area of quadrilateral smoothing domain $\Omega_{i,m}^s$, and the smoothed strain–displacement matrix $\overline{\mathbf{B}}_I$ is computed using Equation 4.30. All we need now is the assumed displacement function values on the boundaries of these smoothing domains, which can be evaluated using the shape functions created for the CS-FEM element using the procedures given in Section 5.3.

5.2.2 Formulation of *n*CS-FEM

Using the general formulation of the S-FEM models presented in Chapter 4, the linear algebraic system of equations of *n*CS-FEM has the form

$$\overline{\mathbf{K}}^{n\text{CS-FEM}}\bar{\mathbf{d}} = \tilde{\mathbf{f}}, \tag{5.3}$$

where $\bar{\mathbf{d}}$ is the vector of nodal displacements for all the nodes, $\tilde{\mathbf{f}}$ is the vector of nodal forces applied at all the nodes in the problem domain, and $\overline{\mathbf{K}}^{n\text{CS-FEM}}$ is the global smoothed stiffness matrix whose entries are given by

$$\overline{\mathbf{K}}_{IJ}^{n\text{CS-FEM}} = \sum_{i=1}^{N_e}\sum_{m=1}^{n_e^s}\int_{\Omega_{i,m}^e}\overline{\mathbf{B}}_I^T\mathbf{c}\overline{\mathbf{B}}_J\,\mathrm{d}\Omega = \sum_{i=1}^{N_e}\sum_{m=1}^{n_e^s}\overline{\mathbf{B}}_I^T\mathbf{c}\overline{\mathbf{B}}_J A_{i,m}^e = \sum_{k=1}^{N_s}\overline{\mathbf{B}}_I^T\mathbf{c}\overline{\mathbf{B}}_J A_k^s, \tag{5.4}$$

where $A_{i,m}^s = \int_{\Omega_{i,m}^e}\mathrm{d}\Omega$ is the area of triangular smoothing domain $\Omega_{i,m}^s$, and the smoothed strain–displacement matrix $\overline{\mathbf{B}}_I$ is computed using

Equation 4.30. Note again that the smoothed strain is constant within the smoothing domain, and hence no numerical integration is needed in computing $\overline{\mathbf{K}}_{IJ}^{n\text{CS-FEM}}$. In evaluating $\overline{\mathbf{B}}_I$, we need to use the shape functions created for the *n*CS-FEM element following the procedure given in the next section. Note that Equations 5.2 and 5.4 have exactly the same form, but the contents of these smoothing strain–displacement matrices are different. We repeat these formulae in order to avoid such confusion.

5.3 Shape Function Evaluation

As presented in Chapter 4, when a linear and continuous displacement field along the boundary of the smoothing domains is used, the smoothed strain–displacement matrix $\overline{\mathbf{B}}_I$ can be computed using only the shape function values at mid-segment-points (Gauss points) on each of the segments $\Gamma_{k,p}^s \in \Gamma_k^s$ of the smoothing domains Ω_k^s. No derivatives of the shape functions are needed. Therefore, many possible ways can be devised to compute these shape function values, and the most essential issue is to ensure the compatibility of the shape functions on all the interfaces of these smoothing domains. In our past practice, the shape function values at each Gauss point are evaluated by simple linear interpolation (or averaging) using two endpoints of the segment containing the Gauss point. For example, for the quadrilateral element subdivided into four quadrilateral smoothing domains as shown in Figure 5.2a, the shape function values at Gauss point $g1$ are evaluated by averaging those of nodes #1 and #5, and those at Gauss point $g2$ are the average of those of points #5 and #9. For the six-sided polygonal element subdivided into six triangular smoothing domains as shown in Figure 5.2b, the shape function values at Gauss point $g1'$ are the average of those of nodes #1′ and *O*, and those at Gauss point $g2'$ are the average of those of points #1′ and #2′. Therefore, in order to facilitate the evaluation of shape function values at Gauss points on the smoothing domain boundaries in CS-FEM and *n*CS-FEM, we need to first evaluate the shape function values at the endpoints of segments such as points #1, #2, . . . , #9 in Figure 5.2a and points #1′, #2′, . . . , #6′ and point *O* in Figure 5.2b.

5.3.1 Bilinear Shape Functions for CS-FEM

When quadrilateral elements (Q4) are used, we have two choices to create shape functions: (1) using bilinear shape functions that are the same as those for the bilinear Q4 element used in FEM and detailed in Section 3.12, and (2) treating the quadrilateral element as a four-sided

polygonal element, which will be detailed in Section 5.3.2 as a special case of an *n*-sided polygonal element. This section discusses the first option using bilinear Q4 elements in a CS-FEM model, which was an original formulation presented in Refs. [1,2].

In using bilinear Q4 elements, the element is divided into *quadrilateral* smoothing domains to preserve the bilinear feature. When needed, further subdivision of a big smoothing domain into smaller quadrilateral smoothing domains may also be performed. There are a number of ways to perform such a division, and the simplest one is by connecting the mid-segment-points of opposite segments as shown in Figure 5.1. Such a subdivision will ensure that shape function values on the boundaries of physical smoothing domains are linear and continuous on all the segments of the smoothing domains, which is essential to CS-FEM models using bilinear Q4 elements.

Note that in the standard FEM using bilinear Q4 elements, compatibility (continuity) on the element boundary is achieved by "mapping"; hence they are also called isoparametric elements because of the use of the same bilinear shape functions for both coordinate and displacement interpolation (see Chapter 3). In our CS-FEM models, this continuity is achieved in a simpler manner (linear interpolation or averaging), and no mapping is needed. The relation of the locations in a bilinear Q4 element for our CS-FEM model and that for the FEM-Q4 model are illustrated in Figure 5.3. Shape function values on lines 5-7, 6-8, 10-12, and 11-13 of the smoothing domains of a CS-FEM bilinear Q4 element correspond to mapped segments 5′-7′, 6′-8′, 10′-12′, and 11′-13′ on the isoparametric FEM-Q4 elements in the natural coordinate. This relation gives essentially the CS-FEM bilinear Q4

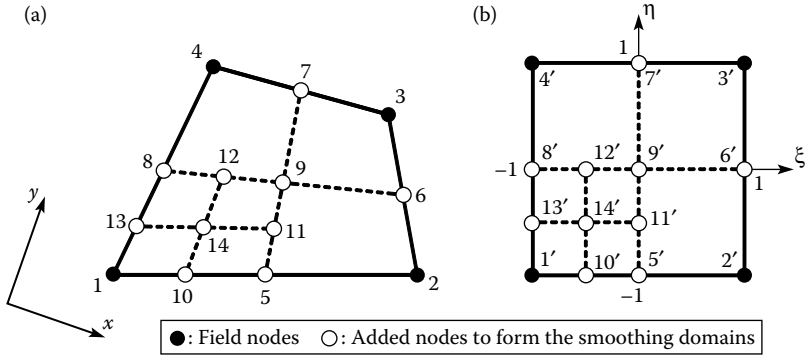

FIGURE 5.3 Division of an isoparametric element into quadrilateral smoothing domains. The lower-left quadrant is further divided into four smoothing domains by connecting the mid-segment-points of opposite segments: (a) quadrilateral smoothing domains of a CS-FEM element (no mapping is needed) and (b) element in the natural coordinate for the isoparametric FEM element (mapping is needed).

element a similar bilinear feature as that of the isoparametric FEM-Q4 element. Since no mapping is performed in CS-FEM, it is much less sensitive to element distortions, as will be demonstrated in the example section. A more general way of creating such a nonmapping shape function using the point interpolation method for mesh-free settings with cell-based smoothing can be found in Refs. [3,10].

In CS-FEM, a bilinear Q4 element can be, *in theory*, subdivided into some quadrilateral smoothing domains as shown in Figure 5.1. However, the numerical examples given in Section 5.8 will show that such a further division is often unnecessary and not preferable. A simple division of the element into four smoothing domains as shown in Figure 5.1d is one of the best choices for solid mechanics problems. The use of more than four smoothing domains gives no benefit in practical applications, although the model will still be stable and converge. Therefore, unless otherwise stated, the division of the element into four smoothing domains will be used as default in this section for convenience of discussion. Figure 5.2a and Table 5.1 present explicitly the shape function values at different points of a quadrilateral element divided into four quadrilateral smoothing domains. The number of support field nodes for the quadrilateral element is 4 (from #1 to #4). For the whole quadrilateral element, we have 12 line segments (1-5, 5-2, 2-6, 6-3, 3-7, 7-4, 4-8, 8-1, 5-9, 6-9, 7-9, 8-9). Each line segment needs only one Gauss point (due to linear interpolation). Therefore, there are a total of 12 Gauss points (from $g1$ to $g12$) used for all these smoothing domains in Ω_i^e, and the shape function values at all these 12 Gauss points are tabulated in Table 5.1 by simple inspection. This implies that the computation of shape function values in CS-FEM is simple, in addition to there being no need for the derivatives of shape functions.

5.3.2 Piecewise Linear Shape Functions for *n*CS-FEM

For *n*CS-FEM using *n*-sided polygonal elements including T3 and Q4 (but not the bilinear Q4 discussed in Section 5.3.1), smoothing domains are constructed by dividing the element into triangular smoothing domains, as shown in Figure 5.2b. Shape functions are constructed following the general procedure given in Section 4.3.2. It is clear that such shape functions are obviously compatible along the boundaries of triangular smoothing domains. Hence, the evaluation of shape function values at field nodes and central points such as points #1′, #2′, . . . , #6′ and point O in Figure 5.2b are very straightforward. In the actual implementation of an *n*CS-FEM model, the evaluation of shape function values is performed in the following very simple way. Figure 5.2b and Table 5.2 present explicitly the shape function values at different points of a six-sided polygonal element divided into six triangular smoothing domains. The number of support field nodes for this

TABLE 5.1

Values of Shape Functions at Different Points within a Quadrilateral Element (Figure 5.2a)

Point	Node 1	Node 2	Node 3	Node 4	Description
1	1.0	0	0	0	Field node
2	0	1.0	0	0	Field node
3	0	0	1.0	0	Field node
4	0	0	0	1.0	Field node
5	1/2	1/2	0	0	Side midpoint
6	0	1/2	1/2	0	Side midpoint
7	0	0	1/2	1/2	Side midpoint
8	1/2	0	0	1/2	Side midpoint
9	1/4	1/4	1/4	1/4	Intersection of two bimedians
$g1$	3/4	1/4	0	0	Gauss point (mid-segment-point of $\Gamma^s_{k,p}$)
$g2$	3/8	3/8	1/8	1/8	Gauss point (mid-segment-point of $\Gamma^s_{k,p}$)
$g3$	3/8	1/8	1/8	3/8	Gauss point (mid-segment-point of $\Gamma^s_{k,p}$)
$g4$	3/4	0	0	1/4	Gauss point (mid-segment-point of $\Gamma^s_{k,p}$)
$g5$	1/4	3/4	0	0	Gauss point (mid-segment-point of $\Gamma^s_{k,p}$)
$g6$	0	3/4	1/4	0	Gauss point (mid-segment-point of $\Gamma^s_{k,p}$)
$g7$	1/8	3/8	3/8	1/8	Gauss point (mid-segment-point of $\Gamma^s_{k,p}$)
$g8$	0	1/4	3/4	0	Gauss point (mid-segment-point of $\Gamma^s_{k,p}$)
$g9$	0	0	3/4	1/4	Gauss point (mid-segment-point of $\Gamma^s_{k,p}$)
$g10$	1/8	1/8	3/8	3/8	Gauss point (mid-segment-point of $\Gamma^s_{k,p}$)
$g11$	0	0	1/4	3/4	Gauss point (mid-segment-point of $\Gamma^s_{k,p}$)
$g12$	1/4	0	0	3/4	Gauss point (mid-segment-point of $\Gamma^s_{k,p}$)

six-sided element is 6 (from #1′ to #6′). We have a total of 12 segments (1′-2′, 2′-3′, 3′-4′, 4′-5′, 5′-6′, 6′-1′, 1′-*O*, 2′-*O*, 3′-*O*, 4′-*O*, 5′-*O*, 6′-*O*). Each segment needs only one Gauss point (due again to linear interpolation). Therefore, there are a total of 12 Gauss points (from $g1'$ to $g12'$) to be used for all the smoothing domains, and the shape function values at all these 12 Gauss points can be tabulated in Table 5.2 by, again, simple inspection.

It should be mentioned that the purpose of introducing interior points such as point #9 in Figure 5.2a or point *O* in Figure 5.2b and points on the edges such as #5, #6, #7, and #8 in Figure 5.2a is to facilitate the evaluation of the values of shape functions at some discrete points inside and on the segments of the interested element. There are no extra DOFs that are associated with these added points. In other words, these points carry no additional independent field variable. Therefore, the total DOFs of a

TABLE 5.2

Values of Shape Functions at Different Points within an n-sided Convex Polygonal Element (Figure 5.2b)

Point	Node 1′	Node 2′	Node 3′	Node 4′	Node 5′	Node 6′	Description
1′	1.0	0	0	0	0	0	Field node
2′	0	1.0	0	0	0	0	Field node
3′	0	0	1.0	0	0	0	Field node
4′	0	0	0	1.0	0	0	Field node
5′	0	0	0	0	1.0	0	Field node
6′	0	0	0	0	0	1.0	Field node
O	1/6	1/6	1/6	1/6	1/6	1/6	Centroid point
$g1'$	7/12	1/12	1/12	1/12	1/12	1/12	Gauss point (mid-segment-point of $\Gamma^s_{k,p}$)
$g2'$	1/2	1/2	0	0	0	0	Gauss point (mid-segment-point of $\Gamma^s_{k,p}$)
$g3'$	1/12	7/12	1/12	1/12	1/12	1/12	Gauss point (mid-segment-point of $\Gamma^s_{k,p}$)
$g4'$	0	1/2	1/2	0	0	0	Gauss point (mid-segment-point of $\Gamma^s_{k,p}$)
$g5'$	1/12	1/12	7/12	1/12	1/12	1/12	Gauss point (mid-segment-point of $\Gamma^s_{k,p}$)
$g6'$	0	0	1/2	1/2	0	0	Gauss point (mid-segment-point of $\Gamma^s_{k,p}$)
$g7'$	1/12	1/12	1/12	7/12	1/12	1/12	Gauss point (mid-segment-point of $\Gamma^s_{k,p}$)
$g8'$	0	0	0	1/2	1/2	0	Gauss point (mid-segment-point of $\Gamma^s_{k,p}$)
$g9'$	1/12	1/12	1/12	1/12	7/12	1/12	Gauss point (mid-segment-point of $\Gamma^s_{k,p}$)
$g10'$	0	0	0	0	1/2	1/2	Gauss point (mid-segment-point of $\Gamma^s_{k,p}$)
$g11'$	1/12	1/12	1/12	1/12	1/12	7/12	Gauss point (mid-segment-point of $\Gamma^s_{k,p}$)
$g12'$	1/2	0	0	0	0	1/2	Gauss point (mid-segment-point of $\Gamma^s_{k,p}$)

CS-FEM model will be exactly the same as the standard FEM using the same set of nodes.

We note now the following remark.

Remark 5.1 On the Shape of nCS-FEM Elements

It may be noted that *n*CS-FEM can have general *n*-sided polygonal elements with ease. This is because S-FEM models do not use the derivatives of the shape functions. The standard FEM, however, can only have T3 and (bilinear) Q4 elements. Any generalization to other types of FEM elements has to be very careful to ensure (1) a nonsingular moment matrix; (2) compatibility along the boundary of the elements; and (3) attainability of the derivatives of the shape functions, which can be quite difficult, when the shape of the elements becomes too complicated. Even when we use bilinear Q4 elements, we have to resort to quite a sophisticated "mapping" procedure.

5.4 Some Properties of CS-FEM

Remark 5.2 Single Smoothing Domain Versus Single Gauss Point

If only one single smoothing domain ($n_e^s = 1$) is used individually for each element in the problem domain, the solution of CS-FEM has similar properties with that of the standard FEM-Q4 using reduced integration (using one Gauss point) when the same mesh is used.

Remark 5.2 can be examined as follows. As shown in Equation 4.27, the smoothed strain–displacement matrix $\overline{\mathbf{B}}_I$ of CS-FEM is the average of the standard compatible strain–displacement matrix $\tilde{\mathbf{B}}_I(\mathbf{x})$ over the smoothing domain Ω_i^e, the physical element domain. However, for FEM-Q4 using reduced integration, $\tilde{\mathbf{B}}_I(\mathbf{x})$ is computed at the center of the isoparametric element, at $\xi = \eta = 0$. We thus have that $\tilde{\mathbf{B}}_I(\xi = 0, \eta = 0)$ in FEM-Q4 is also considered to be the average of $\tilde{\mathbf{B}}_I(\mathbf{x})$ over the isoparametric element. Therefore, it is clear that $\int_{\Omega_i^e} \overline{\mathbf{B}}_I^T \mathbf{c} \tilde{\mathbf{B}}_J \, d\Omega$ in CS-FEM is equivalent to $\int_{-1}^{1}\int_{-1}^{1} \tilde{\mathbf{B}}_I^T \mathbf{c} \tilde{\mathbf{B}}_J \mathbf{J} \, d\xi \, d\eta$ in FEM using reduced integration. The only difference is that $\tilde{\mathbf{B}}_I(\xi = 0, \eta = 0)$ in FEM is the average of $\tilde{\mathbf{B}}_I(\mathbf{x})$ over the isoparametric element and $\overline{\mathbf{B}}_I$ in CS-FEM is the average of $\tilde{\mathbf{B}}_I(\mathbf{x})$ over the element in physical coordinates. In case the elements are parallelograms, the results of CS-FEM and FEM will be identical.

Therefore, the solution of CS-FEM has similar properties with those of FEM using reduced integration. The element stiffness matrix can contain

spurious zero energy modes (known as hourglass modes) and thus may not be *spatially* stable. This is because the global stiffness matrix, even after imposing essential boundary conditions to remove rigid body motion, may still be singular depending on the setting of the problem [11].

Property 5.1 nCS-FEM-T3: Same as FEM-T3

When the same mesh of linear triangular elements (T3) is used, *n*CS-FEM is identical to FEM-T3.

When the same mesh of T3 is used in the *n*CS-FEM model, three triangular smoothing domains are used for each element. Because each element has only three nodes, the piecewise linear shape functions for each of these three triangular smoothing domains are in fact the same, because they are all determined by these same three nodes. Therefore, the smoothed strain fields in each of the triangular smoothing domains are all the same constant that is the compatible strain field in the T3 element. Therefore, FEM-T3 and *n*CS-FEM-T3 will be identical.

Can we use T3 elements to formulate a cell-based smoothed model that is different from the FEM-T3 model? The answer is "yes" and very accurate models can be formulated, but it requires the use of the general PIM. Interested readers may refer to recent work on the cell-based smoothed PIM [12].

Property 5.2 CS-FEM: Convergence to FEM-Q4

If each quadrilateral element is subdivided into n_e^s quadrilateral smoothing domains, and when $n_e^s \to \infty$ and the smoothing domain $\Omega_{i,m}^e \to 0$ for all the elements in the problem domain, the stiffness matrix $\overline{\mathbf{K}}_{IJ}^{\text{CS-FEM}}$ in Equation 5.2 will approach the stiffness matrix $\tilde{\mathbf{K}}_{IJ}^{\text{FEM}} = \int_\Omega \tilde{\mathbf{B}}_I^T(\mathbf{x})\mathbf{c}\tilde{\mathbf{B}}_J(\mathbf{x})\,\mathrm{d}\Omega$ of the standard FEM-Q4 with "full" (2×2) Gauss integration. At such a limit, the solution of CS-FEM will approach the solution of the standard compatible displacement FEM-Q4 model.

The proof of Property 5.2 can be found in Ref. [2], which is the same as the proof for Theorem 4.5.

Property 5.3 Monotonic Property

Consider a sequence of stable CS-FEM models using the bilinear Q4 element Ω_i^e that is divided *sequentially** into $n_e^s \geq 1$ quadrilateral smoothing domains. Let the strain energy of an element with $n_e^s = p$ smoothing

* The new division of $n_e^s = p + 1$ is obtained by further dividing any one of the smoothing domains in the current set of smoothing domains.

domains be

$$\overline{E}^{\text{CS-FEM}}_{n_e^s=p} = \sum_{m=1}^{p} \int_{\Omega^s_{i,m}} \bar{\boldsymbol{\varepsilon}}^T_{i,m} \mathbf{c} \bar{\boldsymbol{\varepsilon}}_{i,m} \, \mathrm{d}\Omega = \sum_{m=1}^{p} \bar{\boldsymbol{\varepsilon}}^T_{i,m} \mathbf{c} \bar{\boldsymbol{\varepsilon}}_{i,m} A^s_{i,m}. \tag{5.5}$$

We then have the following monotonic inequality:

$$\begin{aligned} \overline{E}^{\text{CS-FEM}}_{n_e^s=1} &< \overline{E}^{\text{CS-FEM}}_{n_e^s=2} < \cdots < \overline{E}^{\text{CS-FEM}}_{n_e^s=p-1} \\ &< \overline{E}^{\text{CS-FEM}}_{n_e^s=p} < \overline{E}^{\text{CS-FEM}}_{n_e^s=p+1} < \cdots < \overline{E}^{\text{CS-FEM}}_{n_e^s\to\infty} = \tilde{E}^{\text{FEM-Q4}}. \end{aligned} \tag{5.6}$$

Proof. Suppose that the domain Ω^e_i of the quadrilateral element has already been divided into $n_e^s = p \geq 1$ smoothing domains $\Omega^s_{i,m}$ such that $\Omega^e_i = \cup_{m=1}^{p} \Omega^s_{i,m}$. Let $\overline{E}^{\text{CS-FEM}}_{n_e^s=p}$ be the strain energy of the element when $n_e^s = p$. We now further divide the jth smoothing domain $\Omega^s_{i,j}$ into two smoothing domains $\Omega^s_{i,j1}$ and $\Omega^s_{i,j2}$ such that $\Omega^s_{i,j} = \Omega^s_{i,j1} \cup \Omega^s_{i,j2}$ and $\Omega^s_{i,j1} \cap \Omega^s_{i,j2} = \emptyset$, which results in a total of $n_e^s = p+1$ smoothing domains. Then, the strain energy of the element becomes $\overline{E}^{\text{CS-FEM}}_{n_e^s=p+1}$. Let $\tilde{\varepsilon}$ be the strain of the corresponding element of the standard displacement compatible FEM. We then have the following relationship for the smoothed strains:

$$\begin{aligned} \bar{\boldsymbol{\varepsilon}}_{\Omega^s_{i,j}} &= \frac{1}{A^s_{i,j}} \int_{\Omega^s_{i,j}} \tilde{\boldsymbol{\varepsilon}} \, \mathrm{d}\Omega = \frac{1}{A^s_{i,j}} \left[A^s_{i,j1} \int_{\Omega^s_{i,j1}} \frac{\tilde{\boldsymbol{\varepsilon}}}{A^s_{i,j1}} \mathrm{d}\Omega + A^s_{i,j2} \int_{\Omega^s_{i,j2}} \frac{\tilde{\boldsymbol{\varepsilon}}}{A^s_{i,j2}} \mathrm{d}\Omega \right] \\ &= \underbrace{\frac{A^s_{i,j1}}{A^s_{i,j}}}_{\alpha_1} \bar{\boldsymbol{\varepsilon}}_{\Omega^s_{i,j1}} + \underbrace{\frac{A^s_{i,j2}}{A^s_{i,j}}}_{\alpha_2} \bar{\boldsymbol{\varepsilon}}_{\Omega^s_{i,j2}} \\ &= \alpha_1 \bar{\boldsymbol{\varepsilon}}_{\Omega^s_{i,j1}} + \alpha_2 \bar{\boldsymbol{\varepsilon}}_{\Omega^s_{i,j2}}, \end{aligned} \tag{5.7}$$

where $\bar{\boldsymbol{\varepsilon}}_{\Omega^s_{i,j}}$ is the smoothed strain of domain $\Omega^s_{i,j}$ corresponding to $n_e^s = p$; $\bar{\boldsymbol{\varepsilon}}_{\Omega^s_{i,j1}}$ and $\bar{\boldsymbol{\varepsilon}}_{\Omega^s_{i,j2}}$ are the smoothed strains of domains $\Omega^s_{i,j1}$ and $\Omega^s_{i,j2}$ corresponding to $n_e^s = p+1$; $A^s_{i,j}$ is the area of domain $\Omega^s_{i,j}$ corresponding to $n_e^s = p$, $A^s_{i,j1}$ and $A^s_{i,j2}$ are the areas of domains $\Omega^s_{i,j1}$ and $\Omega^s_{i,j2}$ corresponding to $n_e^s = p+1$; $\alpha_1 = A^s_{i,j1}/A^s_{i,j} > 0$ and $\alpha_2 = A^s_{i,j2}/A^s_{i,j} > 0$. Note that we have the relationship

$$\alpha_1 + \alpha_2 = 1. \tag{5.8}$$

Considering the difference between $\overline{E}^{\text{CS-FEM}}_{n_e^s=p+1}$ and $\overline{E}^{\text{CS-FEM}}_{n_e^s=p}$, and using Equations 5.7 and 5.8, we obtain

$$
\begin{aligned}
&\overline{E}^{\text{CS-FEM}}_{n_e^s=p+1} - \overline{E}^{\text{CS-FEM}}_{n_e^s=p} \\
&\quad= \left(\bar{\boldsymbol{\varepsilon}}_{\Omega^s_{i,j1}}\right)^T \mathbf{c}\bar{\boldsymbol{\varepsilon}}_{\Omega^s_{i,j1}} A^s_{i,j1} + \left(\bar{\boldsymbol{\varepsilon}}_{\Omega^s_{i,j2}}\right)^T \mathbf{c}\bar{\boldsymbol{\varepsilon}}_{\Omega^s_{i,j2}} A^s_{i,j2} - \left(\bar{\boldsymbol{\varepsilon}}_{\Omega^s_{i,j}}\right)^T \mathbf{c}\bar{\boldsymbol{\varepsilon}}_{\Omega^s_{i,j}} A^s_{i,j} \\
&\quad= \left[\left(\bar{\boldsymbol{\varepsilon}}_{\Omega^s_{i,j1}}\right)^T \mathbf{c}\left(\bar{\boldsymbol{\varepsilon}}_{\Omega^s_{i,j1}}\right)\frac{A^s_{i,j1}}{A^s_{i,j}} + \left(\bar{\boldsymbol{\varepsilon}}_{\Omega^s_{i,j2}}\right)^h \mathbf{c}\left(\bar{\boldsymbol{\varepsilon}}_{\Omega^s_{i,j2}}\right)\frac{A^s_{i,j2}}{A^s_{i,j}}\right. \\
&\qquad\left. - \left(\bar{\boldsymbol{\varepsilon}}_{\Omega^s_{i,j}}\right)^h \mathbf{c}\left(\bar{\boldsymbol{\varepsilon}}_{\Omega^s_{i,j}}\right)\right] A^s_{i,j} \\
&\quad= \left[\alpha_1\left(\bar{\boldsymbol{\varepsilon}}_{\Omega^s_{i,j1}}\right)^T \mathbf{c}\bar{\boldsymbol{\varepsilon}}_{\Omega^s_{i,j1}} + \alpha_2\left(\bar{\boldsymbol{\varepsilon}}_{\Omega^s_{i,j2}}\right)^T \mathbf{c}\bar{\boldsymbol{\varepsilon}}_{\Omega^s_{i,j2}}\right. \\
&\qquad\left. - \left(\alpha_1\bar{\boldsymbol{\varepsilon}}_{\Omega^s_{i,j1}} + \alpha_2\bar{\boldsymbol{\varepsilon}}_{\Omega^s_{i,j2}}\right)^T \mathbf{c}\left(\alpha_1\bar{\boldsymbol{\varepsilon}}_{\Omega^s_{i,j1}} + \alpha_2\bar{\boldsymbol{\varepsilon}}_{\Omega^s_{i,j2}}\right)\right] A^s_{i,j} \\
&\quad= \left[\left(\alpha_1 - \alpha_1^2\right)\left(\bar{\boldsymbol{\varepsilon}}_{\Omega^s_{i,j1}}\right)^T \mathbf{c}\bar{\boldsymbol{\varepsilon}}_{\Omega^s_{i,j1}} + \left(\alpha_2 - \alpha_2^2\right)\left(\bar{\boldsymbol{\varepsilon}}_{\Omega^s_{i,j2}}\right)^T \mathbf{c}\bar{\boldsymbol{\varepsilon}}_{\Omega^s_{i,j2}}\right. \\
&\qquad\left. -\alpha_1\alpha_2\left(\left(\bar{\boldsymbol{\varepsilon}}_{\Omega^s_{i,j1}}\right)^T \mathbf{c}\bar{\boldsymbol{\varepsilon}}_{\Omega^s_{i,j2}} + \left(\bar{\boldsymbol{\varepsilon}}_{\Omega^s_{i,j2}}\right)^T \mathbf{c}\bar{\boldsymbol{\varepsilon}}_{\Omega^s_{i,j1}}\right)\right] A^s_{i,j} \\
&\quad= \left[\alpha_1\left(1-\alpha_1\right)\left(\bar{\boldsymbol{\varepsilon}}_{\Omega^s_{i,j1}}\right)^T \mathbf{c}\bar{\boldsymbol{\varepsilon}}_{\Omega^s_{i,j1}} + \alpha_2\left(1-\alpha_2\right)\left(\bar{\boldsymbol{\varepsilon}}_{\Omega^s_{i,j2}}\right)^T \mathbf{c}\bar{\boldsymbol{\varepsilon}}_{\Omega^s_{i,j2}}\right. \\
&\qquad\left. -\alpha_1\alpha_2\left(\left(\bar{\boldsymbol{\varepsilon}}_{\Omega^s_{i,j1}}\right)^T \mathbf{c}\bar{\boldsymbol{\varepsilon}}_{\Omega^s_{i,j2}} + \left(\bar{\boldsymbol{\varepsilon}}_{\Omega^s_{i,j2}}\right)^T \mathbf{c}\bar{\boldsymbol{\varepsilon}}_{\Omega^s_{i,j1}}\right)\right] A^s_{i,j} \\
&\quad= \left[\left(\bar{\boldsymbol{\varepsilon}}_{\Omega^s_{i,j1}}\right)^T \mathbf{c}\bar{\boldsymbol{\varepsilon}}_{\Omega^s_{i,j1}} + \left(\bar{\boldsymbol{\varepsilon}}_{\Omega^s_{i,j2}}\right)^T \mathbf{c}\bar{\boldsymbol{\varepsilon}}_{\Omega^s_{i,j2}} - \left(\left(\bar{\boldsymbol{\varepsilon}}_{\Omega^s_{i,j1}}\right)^T \mathbf{c}\bar{\boldsymbol{\varepsilon}}_{\Omega^s_{i,j2}}\right.\right. \\
&\qquad\left.\left. + \left(\bar{\boldsymbol{\varepsilon}}_{\Omega^s_{i,j2}}\right)^T \mathbf{c}\bar{\boldsymbol{\varepsilon}}_{\Omega^s_{i,j1}}\right)\right]\alpha_1\alpha_2 A^s_{i,j} \\
&\quad= \left(\bar{\boldsymbol{\varepsilon}}_{\Omega^s_{i,j1}} - \bar{\boldsymbol{\varepsilon}}_{\Omega^s_{i,j2}}\right)^T \mathbf{c}\left(\bar{\boldsymbol{\varepsilon}}_{\Omega^s_{i,j1}} - \bar{\boldsymbol{\varepsilon}}_{\Omega^s_{i,j2}}\right)\alpha_1\alpha_2 A^s_{i,j} > 0,
\end{aligned}
\tag{5.9}
$$

where we used the SPD property of the $\mathbf{c}$ matrix (assuming stable material).

By combining Equation 5.9 with Property 5.2, we obtain inequality 5.6. □

Monotonic inequality (Equation 5.6) is a powerful and useful statement resulting from the application of smoothing operations to functions in a positive definite quadratic functional. Inequality 5.6 also shows that with

the same displacement field, the strain energy of the element with $n_e^s = p+1$ domains is larger than that of the element with $n_e^s = p$ domains. In other words, the stiffness matrix of the element with $n_e^s = p+1$ smoothing domains is stiffer than that of the element with $n_e^s = p$ smoothing domains, which leads to the following remark.

Property 5.4 Softening Effects for CS-FEM: An Intuitive Statement

Let $\overline{\mathbf{K}}^{\text{CS-FEM}}_{n_e^s=p}$ be the stiffness matrix of the element with $n_e^s = p$ smoothing domains. We then have

$$\overline{\mathbf{K}}^{\text{CS-FEM}}_{n_e^s=1} \prec \overline{\mathbf{K}}^{\text{CS-FEM}}_{n_e^s=2} \prec \cdots \prec \overline{\mathbf{K}}^{\text{CS-FEM}}_{n_e^s=p-1} \prec \overline{\mathbf{K}}^{\text{CS-FEM}}_{n_e^s=p}$$

$$\prec \overline{\mathbf{K}}^{\text{CS-FEM}}_{n_e^s=p+1} \prec \cdots \prec \overline{\mathbf{K}}^{\text{CS-FEM}}_{n_e^s\to\infty} = \tilde{\mathbf{K}}^{\text{FEM-Q4}}, \tag{5.10}$$

where symbol "$\prec$" stands for an intuitive engineering term of *softer*. This implies that the use of larger smoothing domains provides more softening effects: the CS-FEM model is always softer than the FEM-Q4 counterpart, as shown in the general Theorem 4.2.

Property 5.4 shows that when the number of n_e^s in each element increases, the stiffness matrix $\overline{\mathbf{K}}^{\text{CS-FEM}}_{IJ}$ in Equation 5.2 will become "stiffer." The solution obtained will change monotonously from the solution of CS-FEM ($n_e^s = 1$) to that of the compatible displacement FEM-Q4 model ($n_e^s \to \infty$).

5.5 Stability of CS-FEM and *n*CS-FEM

As analyzed in Chapter 4, for any S-FEM model, the stability of the model should be checked carefully, and in theory we know that the minimum number of smoothing domains has to be used to ensure stability. In CS-FEM settings, it is possible that the minimum number of smoothing domains is not satisfied. In this section, an intensive eigenvalue analysis (see Remark 1.2) using quadrilateral elements is conducted to investigate numerically the stability properties of CS-FEM and *n*CS-FEM. The results of CS-FEM and *n*CS-FEM are compared with the standard FEM using the four-node isoparametric element (FEM-Q4) that is known for its stability. Line integration (with one GP for each line segment) is used for the smoothed strain evaluation in CS-FEM and *n*CS-FEM. Domain (element) integration using Gauss quadrature (1 GP and 2×2 GPs) is used for evaluating the stiffness matrix of FEM-Q4.

First, an eigenvalue analysis (or free vibration analysis) using the singular value decomposition technique is conducted for a square solid of

stable material ($E = 3.0 \times 10^7$, $v = 0.3$) meshed with a single quadrilateral element. The solid is left free from any constraint on the displacements. In CS-FEM, we divide each element into $n_e^s = 1$, 2, 4, 8, and 16 quadrilateral smoothing domains in the same way as shown in Figure 5.1. In *n*CS-FEM, we divide each quadrilateral element into $n_e^s = 4$ triangular smoothing domains.

The results for the eigenvalue analysis are listed in Table 5.3. It is shown that all these models have at least three zero eigenvalues. Because the free square solid should have three physical rigid body movements that need zero energy to move, it should have three zero-energy modes. Therefore, all these CS-FEM models with $n_e^s \geq 2$, *n*CS-FEM with $n_e^s = 4$, and FEM using full Gauss integration (2×2 GPs) have three legal zero eigenvalues. Once these three rigid movements are constrained, one needs some finite energy to move the solid: these models are all stable. In fact, the FEM with GP = 4 is well known for long being spatially and temporally stable (see Remark 1.3). We can now conclude that the solutions of CS-FEM using $n_e^s \geq 2$ quadrilateral smoothing domains and of *n*CS-FEM using $n_e^s = 4$ triangular smoothing domains will be stable at least for static problems. It is also very easy to verify that these CS-FEM models satisfy the condition of minimum number of smoothing domains given in Table 4.2.

For the CS-FEM using $n_e^s = 1$, we found five zero eigenvalues, which is similar (the same in this particular case) to the FEM using only one Gauss point (GP = 1), as stated in Remark 5.2. These two models have at least two illegal zero-energy modes that will not be physical but numerical, meaning that these two numerical models can be instable. In fact, the FEM with GP = 1 is well known for its instability. The element stiffness matrix contains spurious zero-energy modes, and the global stiffness matrix after imposing essential boundary conditions to remove the rigid motion can still be singular, unless two more additional proper DOFs are constrained.

TABLE 5.3

Eigenvalues of a Free Square Solid Meshed Using One Element ($E = 3.0 \times 10^7$, $v = 0.3$)

Eigen-	FEM-Q4		CS-FEM					*n*CS-FEM
Values	1 × 1 GP	2 × 2 GPs	$n_e^s = 1$	$n_e^s = 2$	$n_e^s = 4$	$n_e^s = 8$	$n_e^s = 16$	$n_e^s = 4$
8	4.286e+7	4.286e+7	4.286e+7	4.286e+7	4.286e+7	4.286e+7	4.286e+7	4.286e+7
7	2.308e+7	2.308e+7	2.308e+7	2.308e+7	2.308e+7	2.308e+7	2.308e+7	2.308e+7
6	2.308e+7	2.308e+7	2.308e+7	2.308e+7	2.308e+7	2.308e+7	2.308e+7	2.308e+7
5	0	1.484e+7	0	0.824e+7	1.113e+7	1.319e+7	1.391e+7	2.225e+7
4	0	1.484e+7	0	0.288e+7	1.113e+7	1.185e+7	1.391e+7	2.225e+7
3	0	0	0	0	0	0	0	0
2	0	0	0	0	0	0	0	0
1	0	0	0	0	0	0	0	0

Therefore, the solution can be instable. It is very easy to verify that CS-FEM with $n_e^s = 1$ does not satisfy the condition of the minimum number of smoothing domains given in Table 4.2.

Table 5.3 also shows that when n_e^s increases from 2 to 16, the lowest two nonzero eigenvalues (fourth and fifth modes) of CS-FEM will increase monotonously and approach those of FEM-Q4 using 2×2 GPs. These results are consistent with Properties 5.2 and 5.3, which show that when n_e^s monotonously approaches infinity, the CS-FEM solution will monotonously approach the solution of the standard displacement compatible FEM-Q4 model. In addition, from the nonzero eigenvalues of Table 5.3, it is seen that the CS-FEM model is softer than the (fully) compatible FEM-Q4 model, which is consistent with Property 5.4. Furthermore, we note from Table 5.3 that these two lowest nonzero eigenvalues (fourth and fifth modes) of *n*CS-FEM are, respectively, larger than those of the fully integrated FEM-Q4 model. This implies that the *n*CS-FEM model is stiffer than the compatible FEM-Q4 model.

Next, a comparison study is conducted for the same solid meshed with a single element, but with three DOFs fixed, and the results are listed in Table 5.4. We now observe two zero-energy modes for these two instable models (CS-FEM with $n_e^s = 1$ and FEM with GP = 1), even when all the rigid movements are constrained, which confirms that they will not be stable as discussed above. All the other models (CS-FEM models with $n_e^s \geq 2$, *n*CS-FEM with $n_e^s = 4$, and FEM with 2×2 GPs) have no more zero-energy models: they cannot move freely anymore, because the rigid body moments are constrained. They are stable.

Further, a study is conducted for the same free square solid meshed with 4×4 elements, and the results are listed in Table 5.5. It is found that the results are very similar to those given in Table 5.3, meaning that the instability of these two models (CS-FEM with $n_e^s = 1$ and FEM with GP = 1) will not change with the increase of elements.

TABLE 5.4

Eigenvalues of a Square Solid Meshed with One Element Fixed with Three DOFs ($E = 3.0 \times 10^7$, $v = 0.3$)

Eigen-	FEM-Q4		CS-FEM					*n*CS-FEM
Values	1 × 1 GP	2 × 2 GPs	$n_e^s = 1$	$n_e^s = 2$	$n_e^s = 4$	$n_e^s = 8$	$n_e^s = 16$	$n_e^s = 4$
8	2.935e+7	3.039e+7	2.935e+7	2.977e+7	2.997e+7	3.021e+7	3.029e+7	3.140e+7
7	1.474e+7	1.905e+7	1.474e+7	1.543e+7	1.925e+7	1.799e+7	1.863e+7	2.266e+7
6	1.154e+7	1.402e+7	1.154e+7	1.308e+7	1.378e+7	1.384e+7	1.392e+7	1.517e+7
5	1	0.843e+7	1	0.431e+7	0.568e+7	0.741e+7	0.798e+7	1.132e+7
4	1	0.229e+7	1	0.065e+7	0.220e+7	0.220e+7	0.220e+7	0.289e+7
3	1	1	1	1	1	1	1	1
2	0	1	0	1	1	1	1	1
1	0	1	0	1	1	1	1	1

TABLE 5.5

Eigenvalues of a Free Solid Meshed with 4×4 Elements ($E = 3.0 \times 10^7$, $v = 0.3$)

Eigen-	FEM-Q4		CS-FEM					*n*CS-FEM
Values	1 × 1 GP	2 × 2 GPs	$n_e^s = 1$	$n_e^s = 2$	$n_e^s = 4$	$n_e^s = 8$	$n_e^s = 16$	$n_e^s = 4$
8	2.770e+6	8.439e+6	2.770e+6	6.220e+6	8.291e+6	8.343e+y6	8.400e+6	8.823e+6
7	2.770e+6	6.182e+6	2.770e+6	5.748e+6	6.152e+6	6.163e+6	6.175e+6	6.226e+6
6	0	4.408e+6	0	3.576e+6	4.032e+6	4.177e+6	4.317e+6	5.053e+6
5	0	4.160e+6	0	3.508e+6	3.968e+6	4.063e+6	4.115e+6	4.478e+6
4	0	4.160e+6	0	3.320e+6	3.968e+6	4.024e+6	4.115e+6	4.478e+6
3	0	0	0	0	0	0	0	0
2	0	0	0	0	0	0	0	0
1	0	0	0	0	0	0	0	0

5.6 Standard Patch Test: Accuracy

Passing the standard patch test is a sufficient requirement for a stable numerical method based on the Galerkin weak form to converge and to demonstrate the second order accuracy. The standard patch is a quadrilateral domain with linear displacements imposed along the boundaries of the patch with at least one interior node arbitrarily located. Satisfaction of the standard patch test requires that the displacements at all the interior nodes follow "exactly" (to machine precision) the same displacement function imposed on the patch boundary.

The patch tests for CS-FEM are first conducted in great detail using as much as five patches, as shown in Figure 5.4 [3]. In these tests, a total of 25 test cases are created by rotating each of these five patches with $\theta = 0, \pi/6, \pi/4, \pi/3$, and $\pi/2$. Each four-node quadrilateral element is subdivided into smoothing domains in the fashion described in Section 5.1. In this particular case, we use $n_e^s = 1$, 2, 3, 4, 8, and 16 quadrilateral smoothing domains, as shown in Figure 5.1.

CS-FEM is used to solve the patch test problem for numerical solutions of displacements. The error in the displacement norm defined in Equation 4.63 is used to evaluate the error in the solutions.

The dimensionless parameters* are taken as $E = 100$ and $\nu = 0.3$ and the linear displacement field is specified on the boundary of the patches using

$$u = x, \qquad v = y. \tag{5.11}$$

* In this book, we often choose to use nondimensional parameters because the purpose of the examples is just to examine our numerical results, and no much physical implications. Any set of physical units is applicable to our results, as long as these units are consistent for all the inputs.

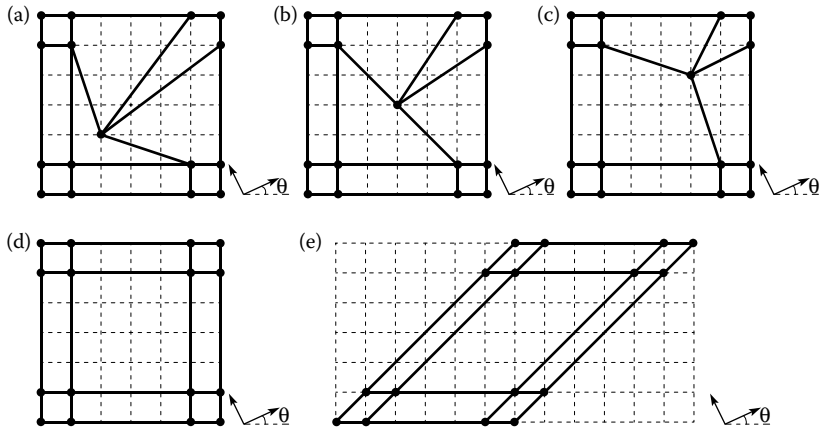

FIGURE 5.4 Meshes used for the patch test: (a) a mesh with a concave quadrilateral element; (b) a mesh with a quadrilateral element using three collinear points; (c) a mesh with general convex quadrilateral elements; (d) a mesh with rectangular elements; and (e) a mesh with parallelogram elements.

It is found that CS-FEM can pass all these standard patch tests within machine precision for all the above patch cases. Tables 5.6 and 5.7 show the results for the cases of $n_e^s = 1$ and $n_e^s = 4$, respectively.

Remark 5.3 On Standard Patch Tests

The results given in Table 5.6 show that even for the case of using $n_e^s = 1$ that has been found to be instable (see Section 5.5), the patch tests were all perfectly passed. This finding implies the following two important points:

1. An unstable S-FEM model can be stable for some settings of problems. In other words, it may not be always unstable. When the number of internal nodes is relatively small, and a large number of boundary nodes are constrained, an unstable S-FEM model can become stable, as shown in this patch test case where all the boundary nodes are fixed.
2. A model that passes the standard patch tests does not ensure stability, and hence convergence, for all types of problems, even if the problem is well posed. It shows the ability of the model in producing the linear field exactly (to machine accuracy): consistency. Only when the stability is ensured will the model converge. One can find many models that pass the standard patch tests but may not be stable and converge, as shown in Ref. [13].

TABLE 5.6

Displacement Norm of the Standard Patch Test e_d (%) for the Case of $n_e^s = 1$

	Patch (a)	**Patch (b)**	**Patch (c)**	**Patch (d)**	**Patch (e)**
$\theta = 0$	2.28e−14	8.07e−14	1.24e−13	1.27e−13	2.20e−13
$\theta = \pi/6$	5.05e−14	7.01e−14	8.04e−14	1.51e−13	3.45e−13
$\theta = \pi/4$	3.63e−14	4.46e−14	8.63e−14	8.48e−14	2.99e−13
$\theta = \pi/3$	3.45e−14	4.11e−14	6.48e−14	1.53e−13	1.43e−13
$\theta = \pi/2$	4.06e−14	5.09e−14	1.39e−13	1.55e−13	2.43e−13

The patch test for *n*CS-FEM is also conducted for a square patch using 36 *n*-sided polygonal elements, as shown in Figure 5.5. It is found again that *n*CS-FEM can pass the standard patch test within machine precision with a displacement error of $e_d = 1.83\,e - 13$ (%).

Property 5.5 CS-FEM: First-Order Consistency

CS-FEM and *n*CS-FEM have first-order consistency, meaning that they can produce a linear displacement field exactly. In other words, they are of second-order accuracy in the displacement solution: errors are at the second-order term or above.

Property 5.6 CS-FEM Solution: Stability and Convergence

Because of the stability confirmed in Section 5.5 and first-order consistency (Property 5.5), CS-FEM with $n_e^s \geq 2$ and *n*CS-FEM have a unique stable solution that converges to the exact solution of the original solid mechanics problem defined in Chapter 2. This confirms Theorem 4.1.

TABLE 5.7

Displacement Norm of the Standard Patch Test e_d (%) for the Case of $n_e^s = 4$

	Patch (a)	**Patch (b)**	**Patch (c)**	**Patch (d)**	**Patch (e)**
$\theta = 0$	1.11e−13	7.78e−14	5.69e−14	2.58e−13	9.51e−13
$\theta = \pi/6$	7.22e−14	1.38e−13	9.48e−14	3.05e−13	4.26e−13
$\theta = \pi/4$	5.78e−14	1.11e−13	1.85e−13	3.80e−13	7.72e−13
$\theta = \pi/3$	1.16e−13	8.28e−14	9.43e−14	2.09e−13	4.82e−13
$\theta = \pi/2$	1.31e−13	7.82e−14	1.03e−13	2.05e−13	6.93e−13

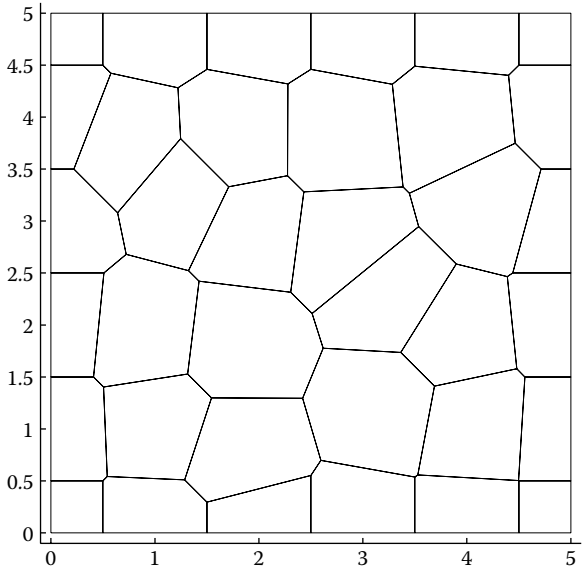

FIGURE 5.5 Domain discretization of a square patch using 36 n-sided polygonal elements.

5.7 Selective CS-FEM: Volumetric Locking Free [5]

Volumetric locking appears when the Poisson's ratio of the material approaches 0.5, as noted in Remark 2.2. The application of selective formulations in the standard FEM [7] has been found to effectively overcome such a locking; hence a similar idea is employed in this chapter to formulate a CS-FEM or nCS-FEM that is free from volumetric locking. In FEM, different quadrature orders are used for different material parts [7], while in CS-FEM we can simply vary the number of smoothing domains for these two different material "parts" (μ part and λ part). As presented in Remark 5.2, the solution of CS-FEM using only one smoothing domain ($n_e^s = 1$) for each quadrilateral element has the same properties as that of FEM using reduced integration (one Gauss point). We also know that the λ part is the culprit of volumetric locking. Therefore, in CS-FEM, we use $n_e^s = 1$ for each element for the λ part and $n_e^s = 4$ for the μ part. The details are given below.

The material property matrix $\mathbf{c}$ for isotropic materials is first decomposed into

$$\mathbf{c} = \mathbf{c}_1 + \mathbf{c}_2, \tag{5.12}$$

where $\mathbf{c}_1$ relates to the shearing modulus $\mu = E/[2(1+\nu)]$ and hence is termed the μ part of $\mathbf{c}$, and $\mathbf{c}_2$ relates to Lame's parameter $\lambda = 2\nu\mu/(1-2\nu)$

and hence is termed the λ part of $\mathbf{c}$. For plane strain cases, we have

$$\mathbf{c} = \begin{bmatrix} \lambda+2\mu & \lambda & 0 \\ \lambda & \lambda+2\mu & 0 \\ 0 & 0 & \mu \end{bmatrix} = \mu \begin{bmatrix} 2 & 0 & 0 \\ 0 & 2 & 0 \\ 0 & 0 & 1 \end{bmatrix} + \lambda \begin{bmatrix} 1 & 1 & 0 \\ 1 & 1 & 0 \\ 0 & 0 & 0 \end{bmatrix} = \mathbf{c}_1 + \mathbf{c}_2, \tag{5.13}$$

and for axisymmetric problems

$$\mathbf{c} = \mu \begin{bmatrix} 2 & 0 & 0 & 0 \\ 0 & 2 & 0 & 0 \\ 0 & 0 & 1 & 0 \\ 0 & 0 & 0 & 2 \end{bmatrix} + \lambda \begin{bmatrix} 1 & 1 & 0 & 1 \\ 1 & 1 & 0 & 1 \\ 0 & 0 & 0 & 0 \\ 1 & 1 & 0 & 1 \end{bmatrix} = \mathbf{c}_1 + \mathbf{c}_2. \tag{5.14}$$

The expression for computing the stiffness matrix can also be split into two parts accordingly. We then use $n_e^s = 1$ to calculate the stiffness matrix related to the λ part and $n_e^s = 4$ to calculate the one related to the μ part. The stiffness matrix of element Ω_i^e of the selective scheme becomes

$$\overline{\mathbf{K}}_i^e = \underbrace{\sum_{m=1}^{n_e^s} \left(\overline{\mathbf{B}}_{i,m}\right)^T \mathbf{c}_1 \overline{\mathbf{B}}_{i,m} A_{i,m}^s}_{\overline{\mathbf{K}}_1^{n_e^s=n}} + \underbrace{\left(\overline{\mathbf{B}}_i\right)^T \mathbf{c}_2 \overline{\mathbf{B}}_i A_i^s}_{\overline{\mathbf{K}}_2^{n_e^s=1}}, \tag{5.15}$$

where $\overline{\mathbf{B}}_i$ and A_i^s are the smoothed strain–displacement matrix and the area of the whole element Ω_i^e, respectively, and $\overline{\mathbf{B}}_{i,m}$ and $A_{i,m}^s$ are the smoothed strain–displacement matrix and the area of the smoothing domain $\Omega_{i,m}^s$, respectively.

It is clear that the selective CS-FEM is a little more expensive. However, it is volumetric locking free and hence very useful for solids with Poisson's rate close to 0.5.

Note also that the selective nCS-FEM can be implemented in exactly the same manner. In this case, we use $n_e^s = 1$ to calculate the stiffness matrix related to the λ part and $n_e^s = n$ (number of sides of the elements) to calculate the one related to the μ part.

5.8 Numerical Examples

To examine the accuracy and efficiency, the results of the CS-FEM methods (including CS-FEM and selective CS-FEM) will be compared with those of the standard FEM using quadrilateral elements (FEM-Q4) as well as the

analytical solution. Errors in the displacement and energy norms defined in Equations 4.49 and 4.50 are used in this analysis. In addition, for fair comparisons between FEM and CS-FEM, we also use the recovery strain field defined by Equation 4.53 as the final solution for FEM-Q4, and in such a case it is denoted as FEM-Q4-Re.

Example 5.8.1: A Rectangular Cantilever Loaded at the End

A rectangular cantilever with length L and height D is studied as a benchmark problem here. The cantilever is subjected to a parabolic traction at the free end, as shown in Figure 5.6. The beam is assumed to have a unit thickness so that the plane stress condition is valid. The analytical solution is available and can be found in Ref. [14]:

$$\begin{aligned} u_x &= \frac{Py}{6EI}\left[(6L-3x)x+(2+\nu)\left(y^2-\frac{D^2}{4}\right)\right], \\ u_y &= -\frac{P}{6EI}\left[3\nu y^2(L-x)+(4+5\nu)\frac{D^2x}{4}+(3L-x)x^2\right], \end{aligned} \tag{5.16}$$

where the moment of inertia I for a beam with rectangular cross section and unit thickness is given by $I = D^3/12$.

The stresses corresponding to the displacements (Equation 5.16) are

$$\sigma_{xx}(x,y) = \frac{P(L-x)y}{I}, \quad \sigma_{yy}(x,y) = 0, \quad \tau_{xy}(x,y) = -\frac{P}{2I}\left(\frac{D^2}{4}-y^2\right). \tag{5.17}$$

Related parameters are taken as $E = 3.0 \times 10^7\ \mathrm{N/m^2}$, $\nu = 0.3$, $D = 12\ \mathrm{m}$, $L = 48\ \mathrm{m}$, and $P = 1000\ \mathrm{N}$. The domain of the beam is discretized into two types of meshes using two different elements: four-node quadrilateral and n-sided polygonal elements are shown in Figure 5.7. In order to show the direction from which numerical displacements converge to the exact solution,

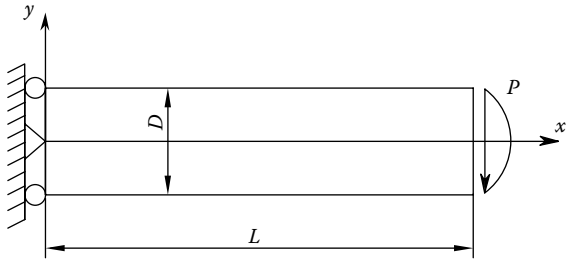

FIGURE 5.6 Cantilever loaded at the end.

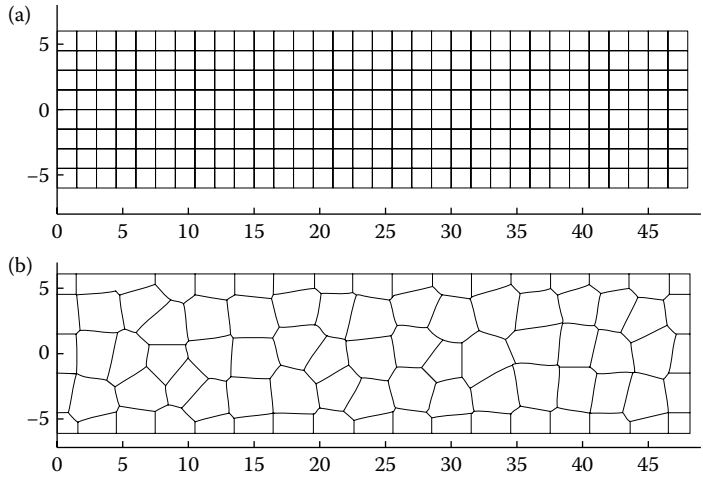

FIGURE 5.7 Domain discretization of the cantilever using (a) four-node quadrilateral elements and (b) n-sided polygonal elements.

the following sign function is used [2]:

$$e_{\text{sign}} = \text{sign}\left(\sum_{i=1}^{N_{\text{dof}}} \left(|\breve{u}_i| - |u_i|\right)\right), \tag{5.18}$$

where $\breve{u}_i$ is the numerical solution and u_i is the exact (or reference) solution. If $e_{\text{sign}} = 1$, the displacement of the numerical solutions converges to the exact solution from above, and $e_{\text{sign}} = -1$ indicates a convergence from below.

In the computation, the nodes on the left boundary are constrained using the exact displacements obtained from analytical formula 5.16 and the loading on the right boundary uses a parabolic distributed shear stress given in Equation 5.17. This is to remove the modeling error for the boundary conditions. The cantilever is analyzed using different numbers of elements and smoothing domains, $n_e^s = 1,\ 2,\ 3, 4,\ 8$, and 16, as shown in Figure 5.1. The exact solution for the strain energy of the problem can be easily computed and is found to be 4.4746 Nm.

Table 5.8 lists the tip displacements of the cantilever beam using different meshes and methods. Figure 5.8 shows the relative error in the displacement components v of the CS-FEM solution with respect to the analytical solution at $y = 0$, where a regular mesh of 32×8 is used. Figure 5.9 shows the strain energy solution for the entire beam obtained using models with different DOFs.

From Figures 5.8 and 5.9, we observe the following:

1. The results of CS-FEM ($n_e^s = 1$) and those of FEM-Q4 using reduced integration (one Gauss point) are identical. This is because the elements used are (regular) rectangles.

TABLE 5.8

Tip Displacements ($\times 10^{-3}$ m) of the Cantilever Beam Obtained Using Different Regular Elements (Analytical Solution $= 8.900 \times 10^{-3}$ m)

n_e^s	**Mesh (16 × 4)**	**Mesh (24 × 6)**	**Mesh (32 × 8)**	**Mesh (40 × 10)**	**Mesh (48 × 12)**
1	9.4542	9.1471	9.0319	8.9874	8.9581
2	9.2915	9.0699	8.9948	8.9604	8.9419
3	9.0574	8.9693	8.9389	8.9249	8.9172
4	8.8355	8.8711	8.8837	8.8896	8.8927
8	8.7978	8.8542	8.8741	8.8834	8.8885
16	8.6920	8.8061	8.8469	8.8659	8.8763
FEM (GP = 4)	8.6453	8.7847	8.8347	8.8581	8.8708

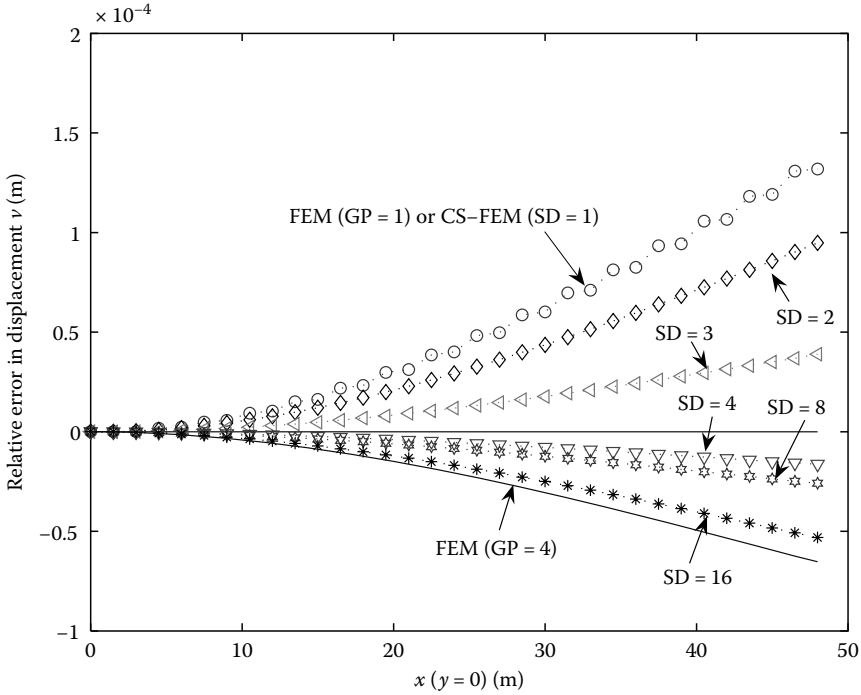

FIGURE 5.8 Comparison of the relative error in displacement v between CS-FEM and the analytical solution for the cantilever loaded at the end. The monotonic convergence behavior of the CS-FEM solution in displacement with respect to the number of smoothing domains is clearly shown for this problem.

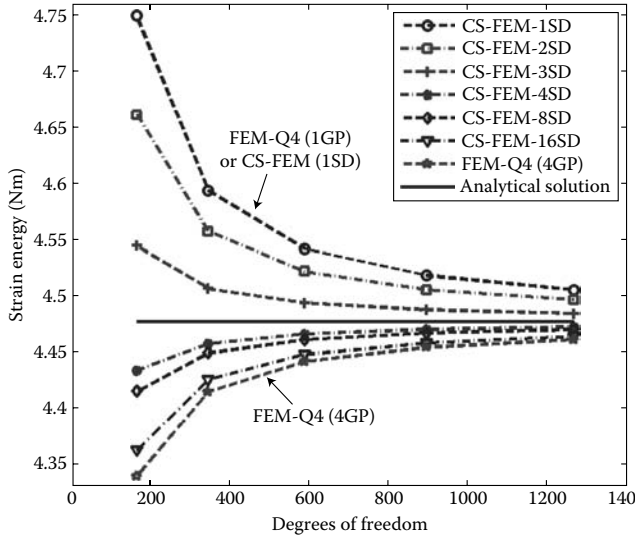

FIGURE 5.9 Convergence of the strain energy solutions of CS-FEM and FEM for the cantilever loaded at the end. The monotonic convergence behavior of the CS-FEM solution in strain energy with respect to both DOFs and the number of SDs is clearly shown.

2. The strain energy solution converges to the exact solution monotonically with the increase of DOFs, as shown in Figure 5.9. This confirms inequality 5.6.
3. The solutions change monotonically from the overestimated to the underestimated ones with the increase of n_e^s that is the number of smoothing domains per element, and then approach the result of FEM-Q4 using full integration (four Gauss points).
4. Figure 5.8 shows the monotonic convergence behavior of the CS-FEM solution in displacement for this problem, but this may not be true in general.
5. The use of $n_e^s = 4$ gives the best results as compared to the analytical ones for this problem.

Figure 5.10 shows that stresses computed at the center of the elements and at the nodes by CS-FEM agree very well with the analytical solutions. Figure 5.11 illustrates the second-order derivatives displacements obtained using CS-FEM and Equation 4.34. It is seen that the CS-FEM results agree well with the analytical solutions, even for the second-order derivatives. The gradients near the boundaries are generally less accurate when compared with those in the internal region because of the asymmetric smoothing domains used on the boundaries. This phenomenon has the same root as those observed in the SPH when a biased smoothing domain is used on the domain boundary [15]. This phenomenon is also reported in the nodal-natural element method by Yoo et al. [16].

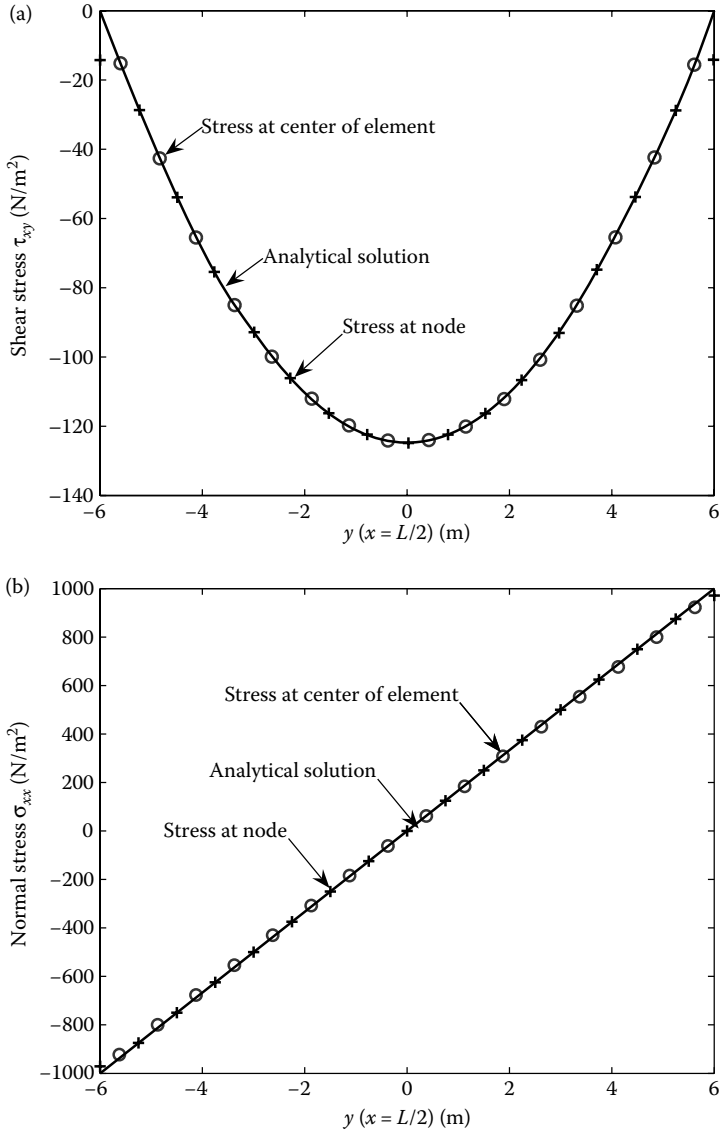

FIGURE 5.10 Comparison of the numerical results of CS-FEM with the analytical solutions for the cantilever loaded at the end: (a) shear stress τ_{xy} and (b) normal stress σ_{xx}.

Figure 5.12 shows the relative error in displacement v obtained using *n*CS-FEM together with the analytical solutions along $y = 6$. It is seen that the computed displacement using *n*CS-FEM is an underestimate and approaches the exact solution with the increase of DOFs, indicating that the *n*CS-FEM

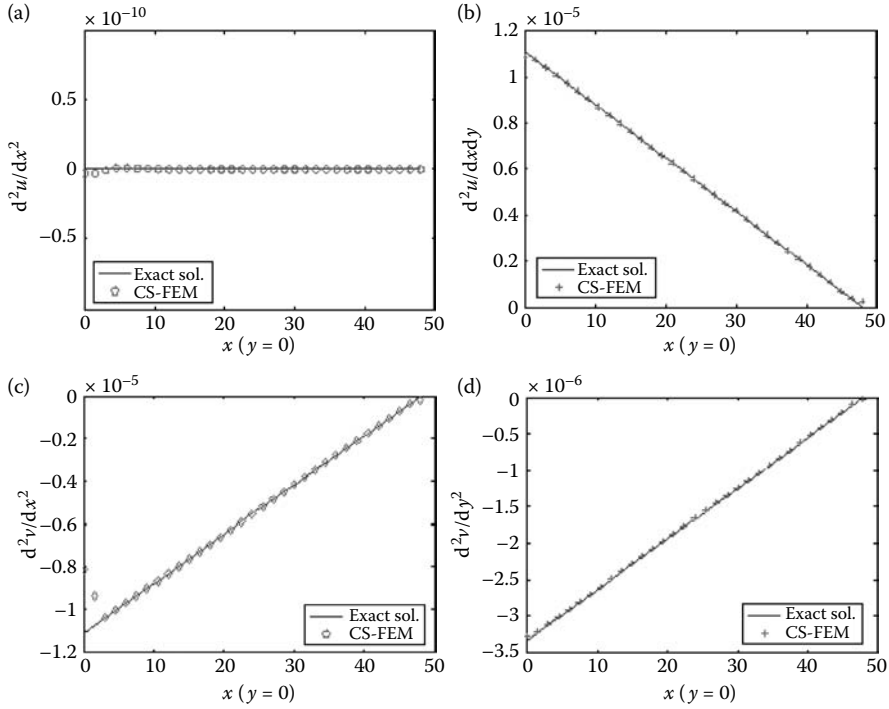

FIGURE 5.11 Second-order derivatives of displacements obtained using CS-FEM for the cantilever loaded at the end. (a) d^2u/dx^2; (b) $d^2u/dxdy$; (c) d^2v/dx^2; and (d) d^2v/dy^2.

model is still on the stiff side. Figure 5.13 shows the contour of the distribution of the relative error in displacement v between nCS-FEM and the analytical solution. Figures 5.14 and 5.15 plot the contours of stress distribution obtained using nCS-FEM in comparison with the analytical one. Good agreement has been observed.

The displacement and energy norms of the CS-FEM solution are compared with those of FEM-Q4 in Tables 5.9 and 5.10. The convergence rates are also plotted in Figures 5.16 and 5.17. It is again seen that both the error and convergence rate in the displacement and energy norms of the CS-FEM solution will approach those of FEM-Q4 when n_e^s (the number of smoothing domains in an element) increases. It is observed that CS-FEM-4SD ($n_e^s = 4$) performs the best among all these models and gives a much more accurate displacement solution than FEM-Q4, as shown in Figure 5.16. When the finest mesh ($h = 1$ m) is used, the error of CS-FEM-Q4 is about 1/4 that of FEM-Q4, as shown in Table 5.9. In terms of the convergence rates in the displacement norm, all these models have roughly the same value, approximately 2, which is the theoretical rate in the displacement norm for linear elements based on the standard Galerkin weak form (see Theorem 3.4). Although not very significant, the convergence rate of the CS-FEM solution is larger than that of FEM-Q4 in terms of displacements.

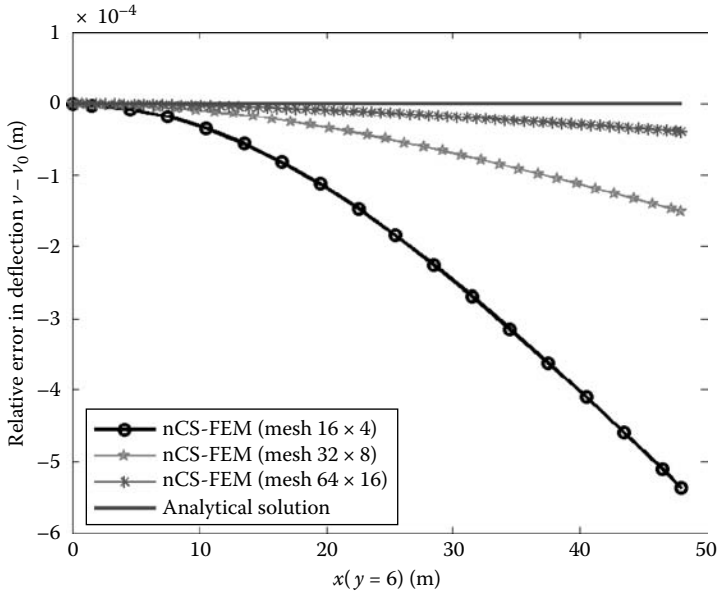

FIGURE 5.12 Relative error in deflection $v - v_0$ (m) along $y = 6$ computed using nCS-FEM and the analytical solution for the cantilever loaded at the end.

In terms of the error in the energy norm, the solution error of FEM-Q4-Re is the smallest, followed closely by that of CS-FEM-4SD, which is, in turn, much smaller than that of FEM-Q4, as shown in Figure 5.17. The convergence rate in the energy norm of the FEM-Q4 solution is approximately 1, which is the theoretical rate in the energy norm for linear elements based on the standard Galerkin weak form (see Theorem 3.4). The convergence rate for FEM-Q4-Re is, however, found to be 1.35, which shows that the FEM-Q4-Re solution is

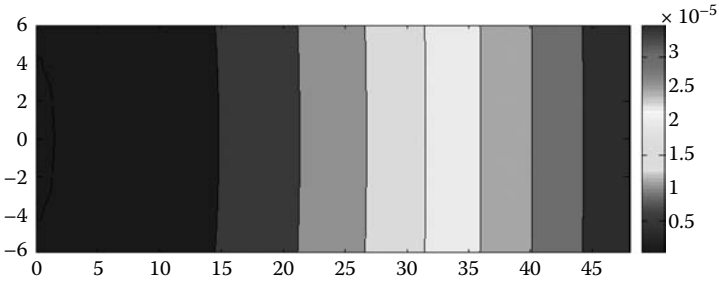

FIGURE 5.13 Contour of relative deflection errors (m) for the cantilever using nCS-FEM.

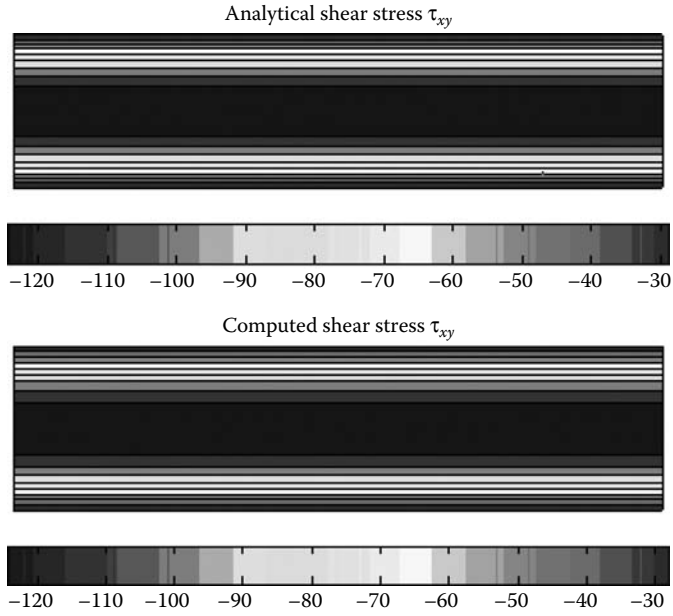

FIGURE 5.14 Contour of the analytical and computed shear stress τ_{xy} (N/m^2) for the cantilever using *n*CS-FEM.

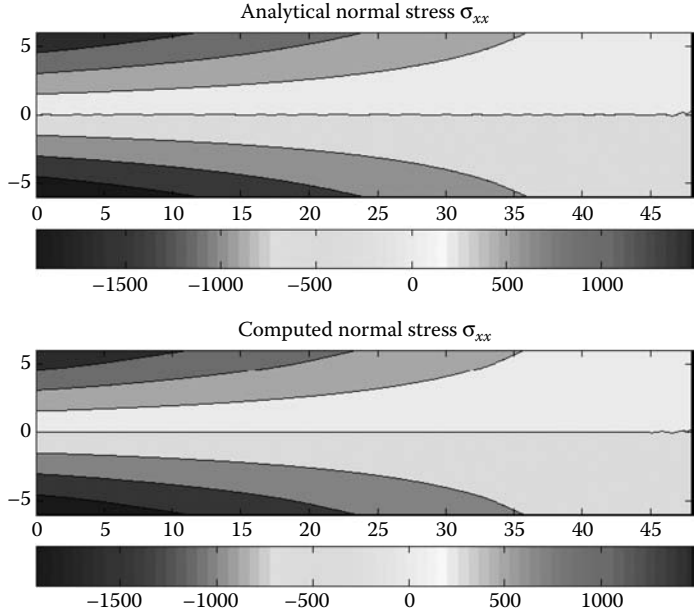

FIGURE 5.15 Contour of the analytical and computed normal stress σ_{xx} (N/m^2) for the cantilever using *n*CS-FEM.

TABLE 5.9

Displacement Norm ($\times 10^{-3}$) of the Cantilever Beam Obtained Using Different Element Sizes

Mesh	h	CS-FEM $n_e^s = 1$	CS-FEM $n_e^s = 2$	CS-FEM $n_e^s = 3$	CS-FEM $n_e^s = 4$	CS-FEM $n_e^s = 8$	CS-FEM $n_e^s = 16$	FEM-Q4 (GP = 4)
16×4	3.0	6.72	4.66	1.90	(−) 0.74	(−) 1.18	(−) 2.42	(−) 2.97
24×6	2	2.88	2.02	0.84	(−) 0.33	(−) 5.29	(−) 1.09	(−) 1.35
32×8	1.5	1.60	1.13	0.47	(−) 0.19	(−) 0.30	(−) 0.62	(−) 0.76
40×10	1.2	1.02	0.72	0.30	(−) 0.12	(−) 0.19	(−) 0.40	(−) 0.49
48×12	1	0.70	0.50	0.21	(−) 0.083	(−) 0.13	(−) 0.28	(−) 0.34

Note: Sign (−) shows that the solution is smaller than the exact solution; GP = 4 for FEM quadrilateral element is the minimum number for full integration.

"superconvergent."* The convergence rate for our CS-FEM solution is found to be 1.55, which is even higher than that of the FEM-Q4-Re solution. This shows clearly that the S-FEM models have strong superconvergence.

From the solution errors in both the displacement and energy norms, CS-FEM with $n_e^s = 4$ is the best choice for this example problem.

We note that the recovery operation used in FEM-Q4 has significantly improved the strain solution that is known to be superconvergent, and is the best possible solution that an FEM model can achieve. However, such a post-processing cannot improve the displacement solution of an FEM model. This particular example has clearly shown that although FEM-Q4-Re has performed slightly better than CS-FEM-4SD in terms of energy norm error (an indication

TABLE 5.10

Strain Energy ($\times 10^{-1}$ Nm) for the Cantilever Beam Obtained Using Different Element Sizes

Mesh	h	CS-FEM $n_e^s = 1$	CS-FEM $n_e^s = 2$	CS-FEM $n_e^s = 3$	CS-FEM $n_e^s = 4$	CS-FEM $n_e^s = 8$	CS-FEM $n_e^s = 16$	FEM-Q4 (GP=4)	FEM-Q4 Recovery (GP = 4)
16×4	3.0	2.96	3.29	2.84	2.38	2.45	2.63	3.71	2.06
24×6	2	1.75	1.88	1.59	1.30	1.33	1.41	2.49	1.14
32×8	1.5	1.19	1.26	1.04	0.85	0.86	0.90	1.88	0.75
40×10	1.2	0.87	0.92	0.75	0.60	0.61	0.64	1.50	0.54
48×12	1	0.68	0.71	0.58	0.46	0.47	0.48	1.25	0.41

* It is defined loosely in the book as the rate that is higher than the theoretical rate based on the standard weak formulation.

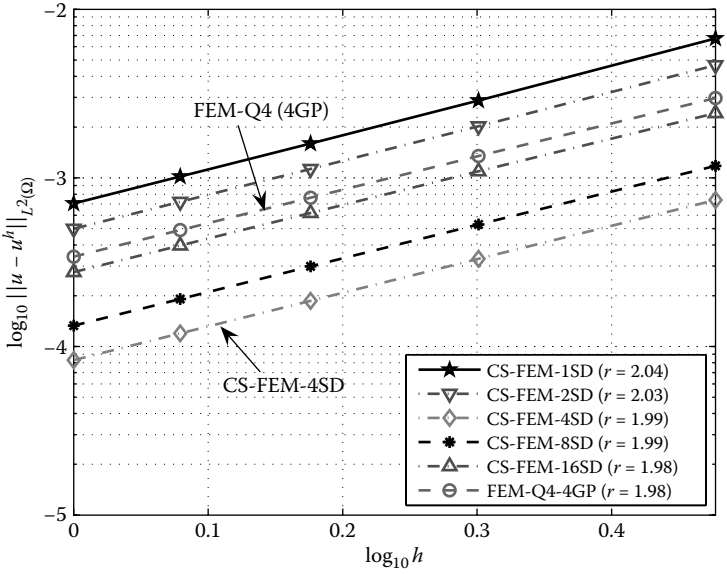

FIGURE 5.16 Error in the displacement norm of CS-FEM and FEM for the cantilever loaded at the end using the same meshes.

of strain error), CS-FEM-4SD performed much better than FEM-Q4 in the displacement solution. In addition, in terms of convergence rate, CS-FEM-4SD is higher than FEM-Q4-Re. CS-FEM-4SD shows strong superconvergence in the energy norm. In the displacement norm, we have also seen signs of superconvergence of the CS-FEM models: the rates for CS-FEM models with $n_e^s = 1$ and 2 did exceed the theoretical value of 2.0, although very marginal as shown in Figure 5.16. We will show in later chapters that some of the S-FEM models are also very strongly superconvergent in the displacement norm.

Note also that this numerical example confirms the bound properties of CS-FEM: it is always "softer" than FEM-Q4 using the same mesh, which confirms Theorem 4.2. In overall performance, CS-FEM-4SD outperforms FEM-Q4-Re for this example. We also note that the superiority of CS-FEM in terms of solution accuracy over FEM-Q4 is achieved with little additional computational effort: the setting of CS-FEM is almost the same as FEM-Q4; the difference is only in shape function evaluation and integration of the stiffness matrix.

Example 5.8.2: Infinite Plate with a Circular Hole

Figure 5.18 represents a plate with a central circular hole of radius $a = 1$ m, subjected to a unidirectional tensile load of 1.0 N/m at infinity in the x-direction.

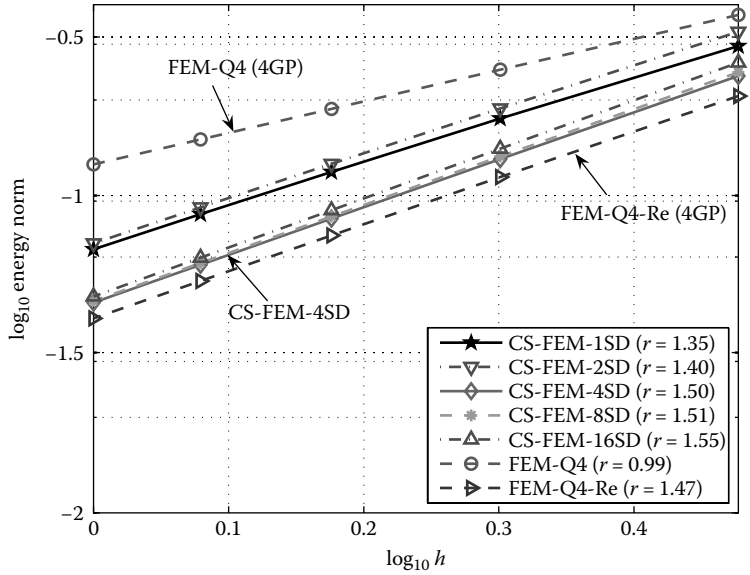

FIGURE 5.17 Error in the energy norm of CS-FEM and FEM for the cantilever loaded at the end using the same meshes.

Due to its symmetry, only the upper right quadrant of the plate is modeled. Figure 5.19 gives the discretization of the domain using quadrilateral and *n*-sided polygonal elements. The plane strain condition is considered, and $E = 1.0 \times 10^3$ N/m^2 and $\nu = 0.3$. Symmetric conditions are imposed on the left and bottom edges, and the inner boundary of the hole is traction free. The

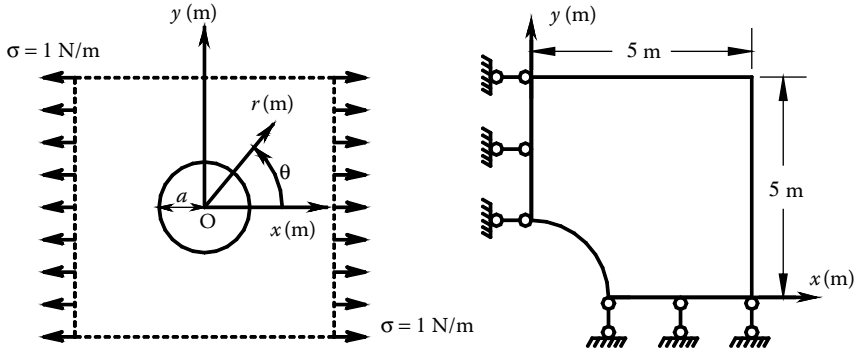

FIGURE 5.18 Infinite plate with a circular hole subjected to unidirectional tension and its quarter model with symmetric conditions imposed on the left and bottom edges.

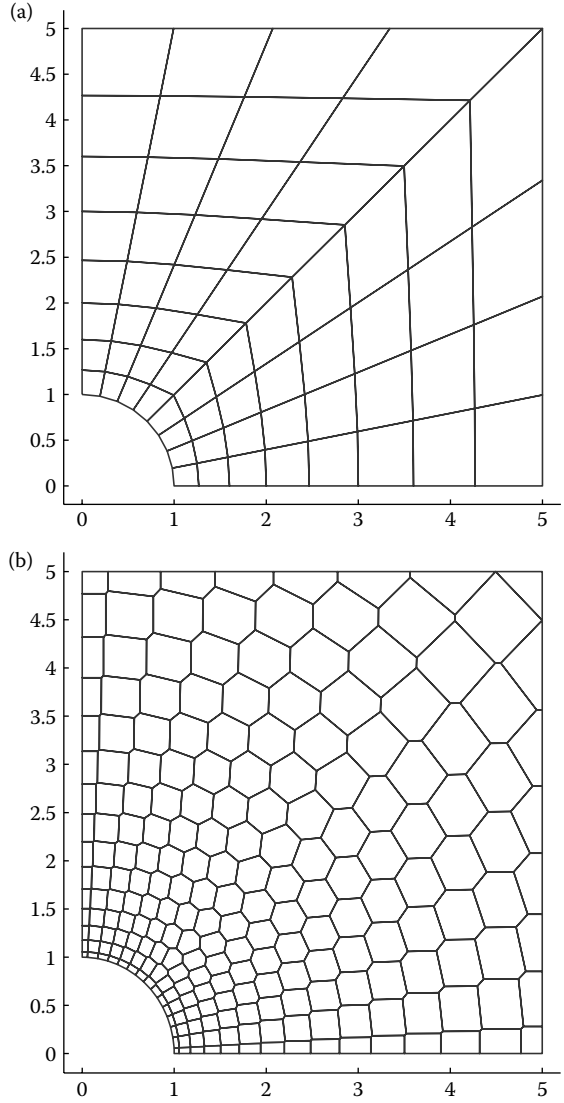

FIGURE 5.19 Domain discretization of the infinite plate with a circular hole using (a) four-node elements and (b) n-sided polygonal elements.

exact stresses for this problem are [14]

$$\sigma_{11} = 1 - \frac{a^2}{r^2}\left[\frac{3}{2}\cos 2\theta + \cos 4\theta\right] + \frac{3a^4}{2r^4}\cos 4\theta,$$

$$\sigma_{22} = -\frac{a^2}{r^2}\left[\frac{1}{2}\cos 2\theta - \cos 4\theta\right] - \frac{3a^4}{2r^4}\cos 4\theta, \tag{5.19}$$

$$\tau_{12} = -\frac{a^2}{r^2}\left[\frac{1}{2}\sin 2\theta + \sin 4\theta\right] + \frac{3a^4}{2r^4}\sin 4\theta,$$

where (r, θ) are the polar coordinates and θ is measured counterclockwise from the positive x-axis. Traction boundary conditions are imposed on the right ($x = 5$) and top ($y = 5$) edges based on the exact solution (Equation 5.19). The displacement components corresponding to the stresses are

$$u_1 = \frac{a}{8\mu}\left[\frac{r}{a}(\kappa + 1)\cos\theta + 2\frac{a}{r}((1+\kappa)\cos\theta + \cos 3\theta) - 2\frac{a^3}{r^3}\cos 3\theta\right],$$
$$u_2 = \frac{a}{8\mu}\left[\frac{r}{a}(\kappa - 3)\sin\theta + 2\frac{a}{r}((1-\kappa)\sin\theta + \sin 3\theta) - 2\frac{a^3}{r^3}\sin 3\theta\right], \tag{5.20}$$

where $\mu = E/(2(1+\nu))$ and κ is defined in terms of Poisson's ratio by $\kappa = 3 - 4\nu$ for plane strain cases.

Using CS-FEM, the domain is discretized using quadrilateral elements that are further divided into different numbers of smoothing domains, $n_e^s = 1$, 2, 3, 4, 8, and 16, as shown in Figure 5.1. From Figures 5.20 and 5.21, it

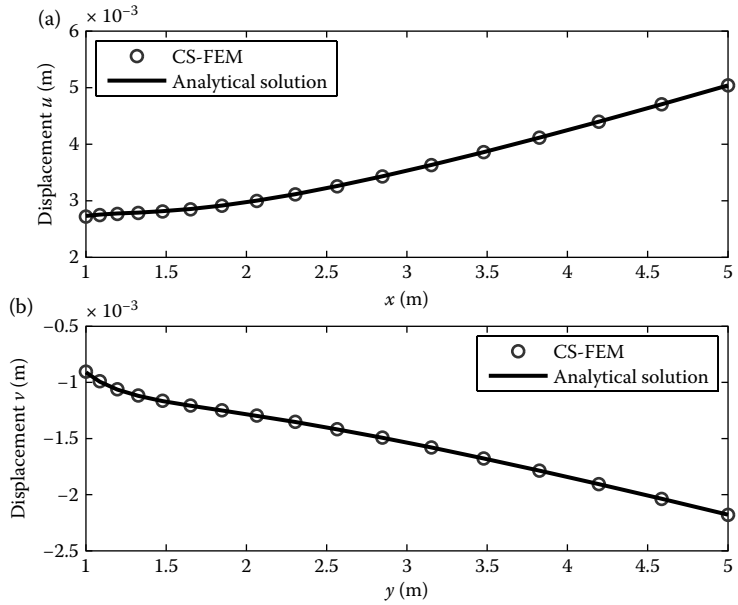

FIGURE 5.20 Numerical and exact displacements of the infinite plate with a hole using CS-FEM ($n_e^s = 4$): (a) displacement u and (b) displacement v.

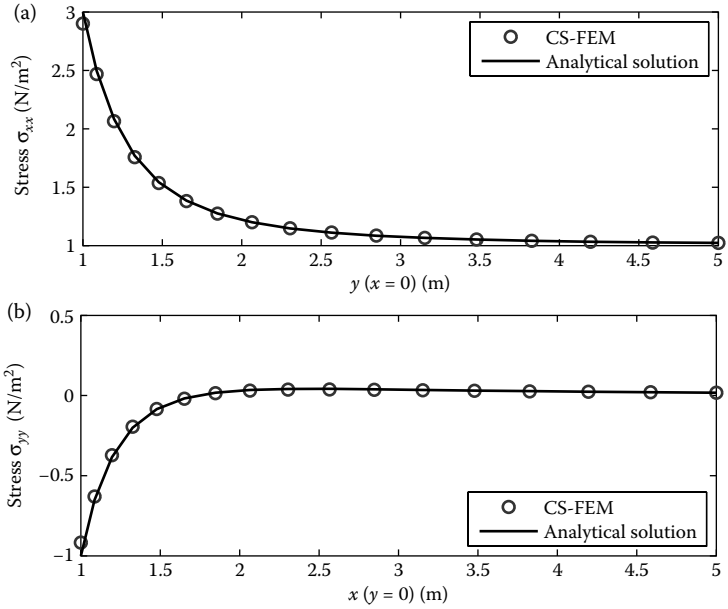

FIGURE 5.21 Numerical and exact stresses in the infinite plate with a hole using CS-FEM ($n_e^s = 4$): (a) σ_{xx} and (b) σ_{yy}.

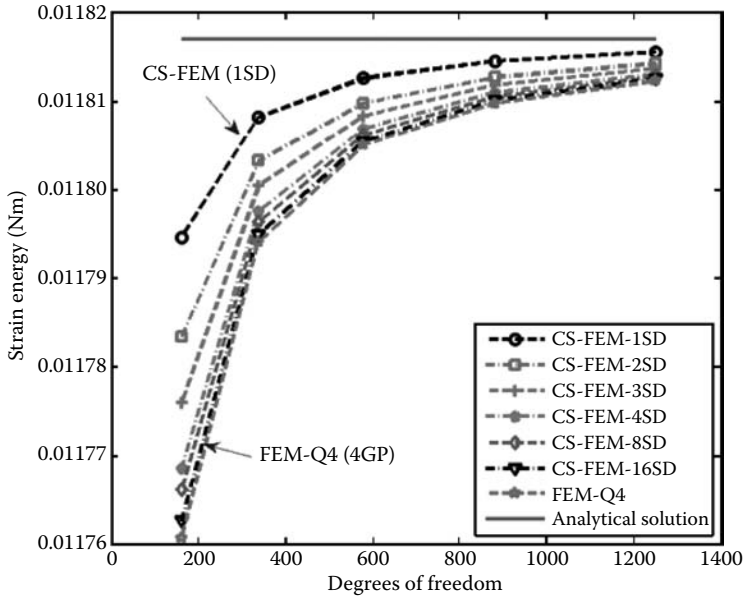

FIGURE 5.22 Convergence of the strain energy solutions of CS-FEM and FEM-Q4 for the infinite plate with a hole. The monotonic convergence behavior of the CS-FEM solution in strain energy with respect to the number of smoothing domains and DOFs is clearly shown.

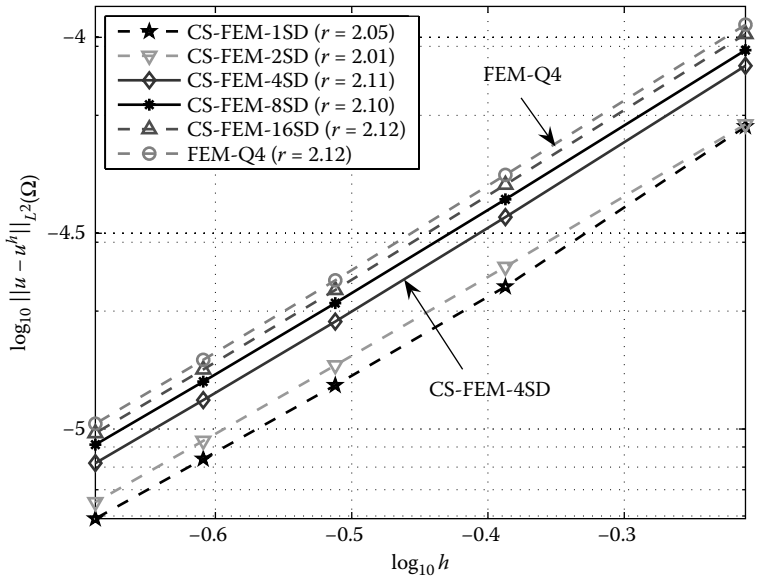

FIGURE 5.23 Convergence of error in the displacement norm of CS-FEM and FEM-Q4 in the infinite plate with a hole using the same meshes.

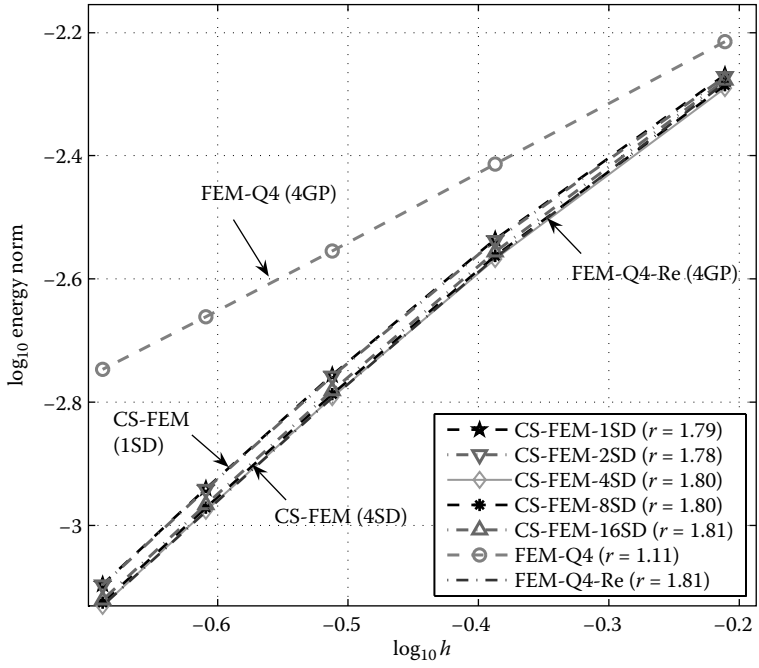

FIGURE 5.24 Convergence of error in the energy norm of solutions obtained using CS-FEM and FEM-Q4 in the infinite plate with a hole using the same meshes.

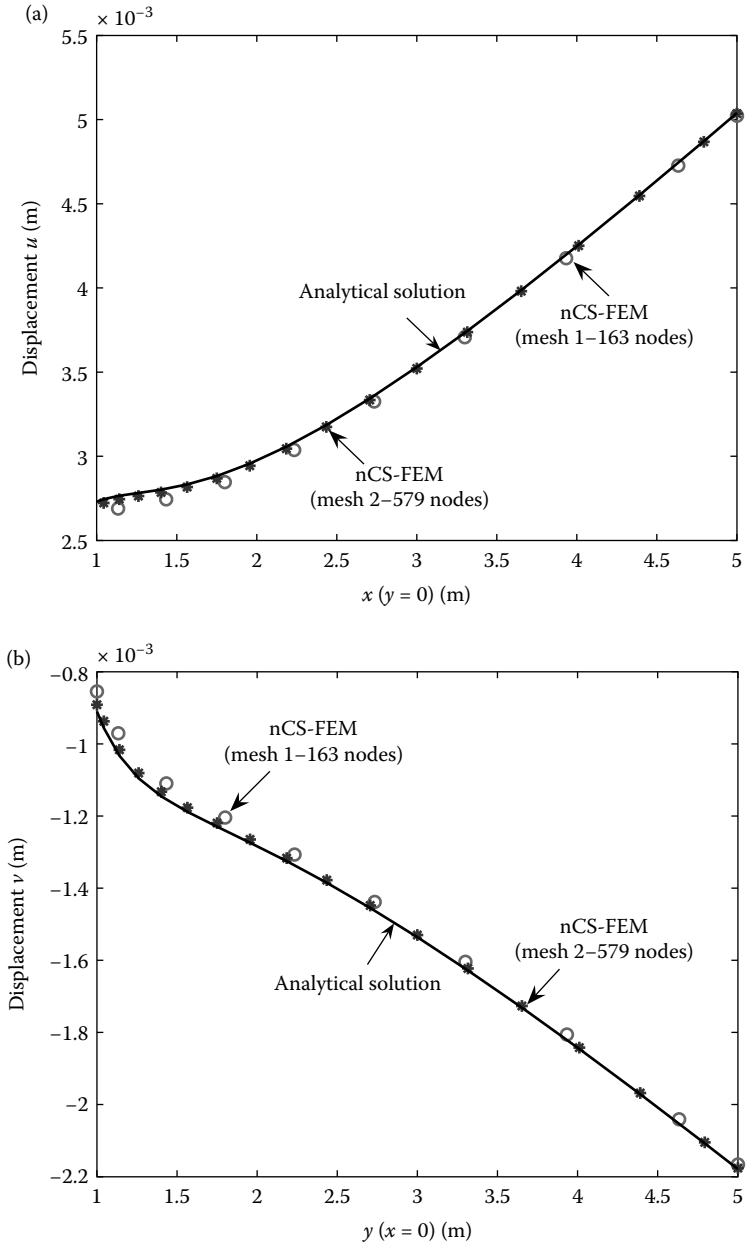

FIGURE 5.25 The exact displacement solution and the numerical solution computed using *n*CS-FEM for the infinite plate with a hole: (a) displacement u and (b) displacement v.

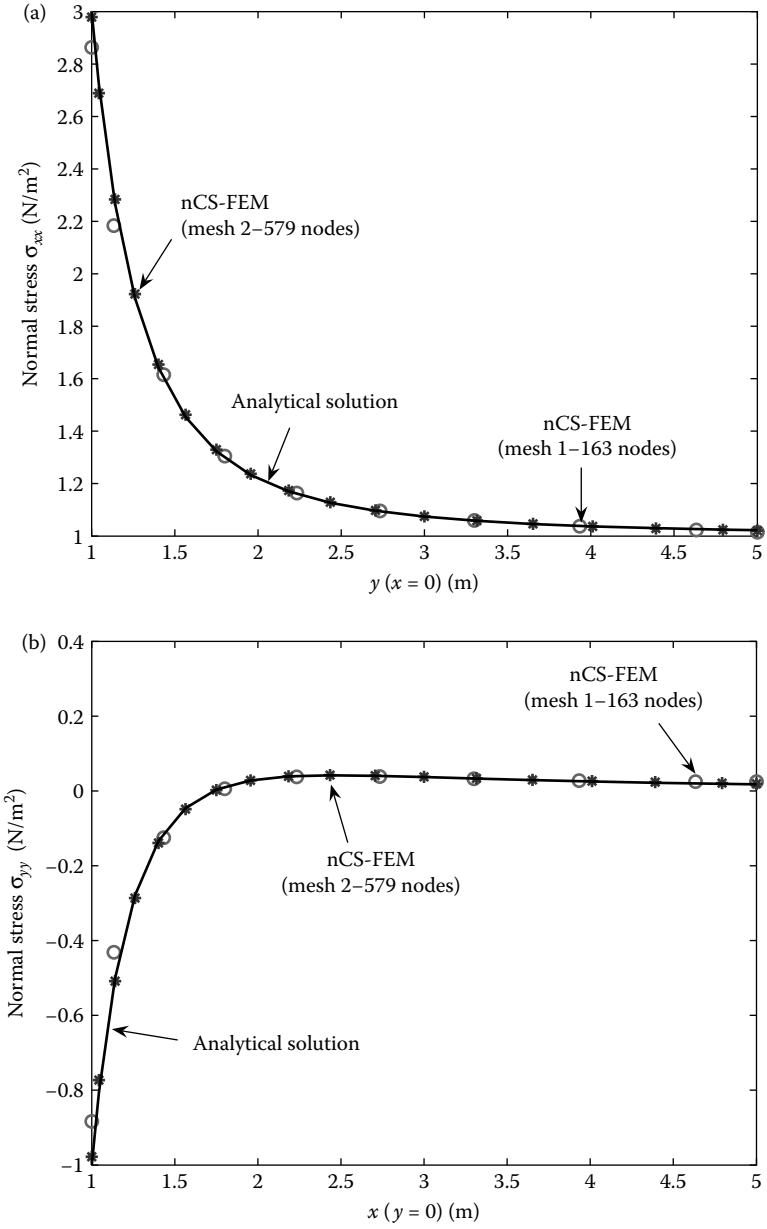

FIGURE 5.26 The exact solution of stresses and the numerical obtained using *n*CS-FEM for the infinite plate with a hole: (a) σ_{xx} and (b) σ_{yy}.

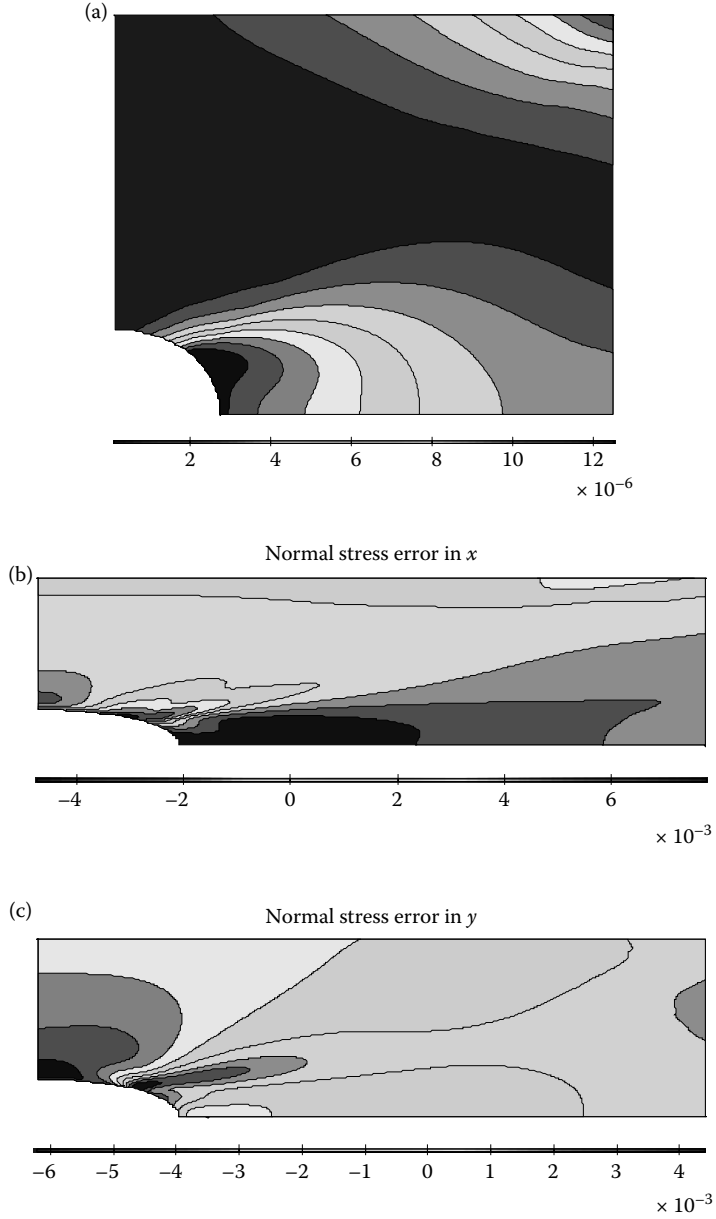

FIGURE 5.27 Contour plots of solutions for the infinite plate with a hole using *n*CS-FEM: (a) the error in displacement u; (b) the normal stress error in x-axis (N/m^2); and (c) the normal stress error in y-axis (N/m^2).

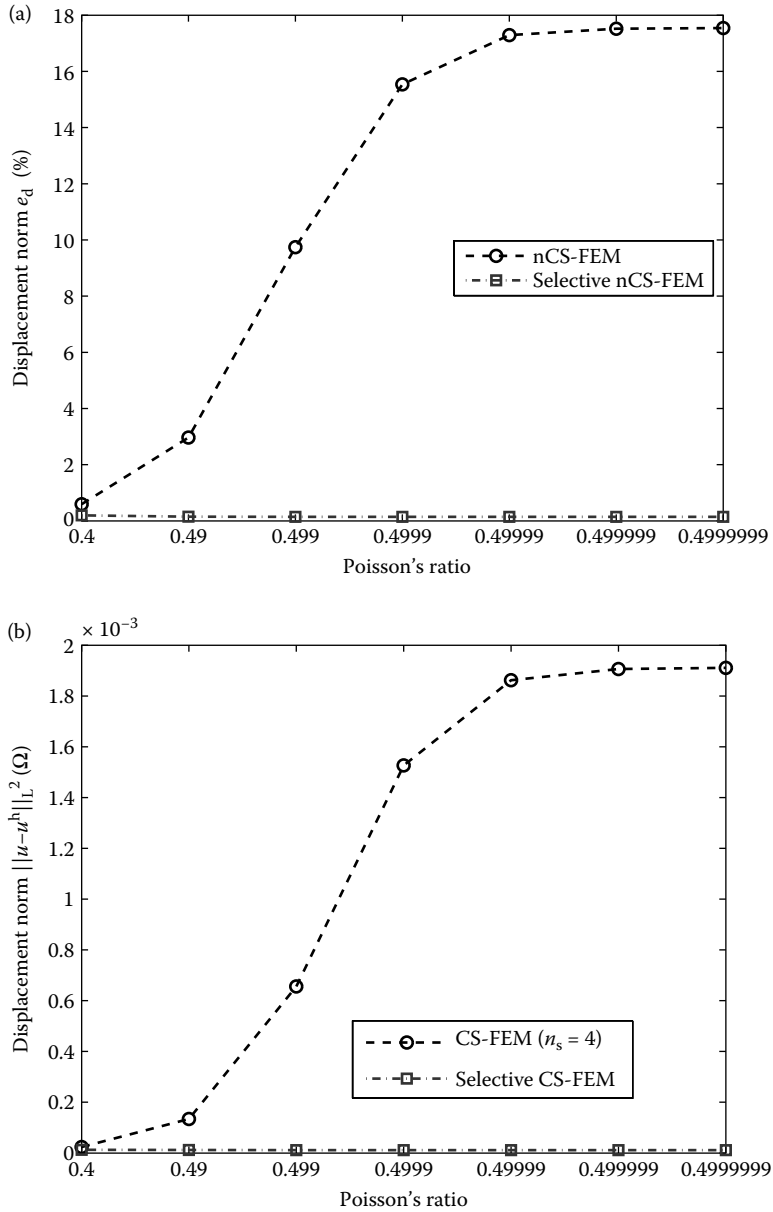

FIGURE 5.28 Error in the displacement norm versus different Poisson's ratios for the infinite plate with a hole: (a) *n*-sided polygonal elements (451 nodes) and (b) four-node quadrilateral elements (289 nodes).

is observed that all the computed displacements and stresses using CS-FEM ($n_e^s = 4$) are in good agreement with the analytical solutions.

Figure 5.22 shows the strain energy results of CS-FEM versus the DOFs used in the model, and Figure 5.23 plots the convergence of error in the displacement norm when the mesh is refined. It is shown clearly that the results of CS-FEM change monotonously from $n_e^s = 1$ to $n_e^s = 16$ and approach the result of FEM-Q4 using full integration (four Gauss points). This confirms Theorems 4.4 and 4.5.

Note that for this problem, the error in the displacement norm of CS-FEM is smallest when $n_e^s = 1$ is used, and all the computed strain energies are underestimates compared to the analytical solution. The bound property of the CS-FEM solution is again observed from this example: the CS-FEM model is always softer than the FEM-Q4 model, using the same mesh. Figure 5.23 clearly shows that CS-FEM-4SD outperforms FEM-Q4 in the displacement solution with roughly the same convergence rate.

Figure 5.24 shows the convergence of error in the energy norm of solutions obtained using CS-FEM for the infinite plate with a hole, together with those using FEM-Q4 and FEM-Q4-Re with the same meshes. The results again show that the error in the energy norm of the FEM-Q4-Re solution is very close to those of the CS-FEM models, which are all much smaller than that of FEM-Q4. FEM-Q4-Re and CS-FEM-4SD give almost the same accuracy in the energy norm. The convergence rate in the energy norm of FEM-Q4 is numerically about 1.1, whereas those of FEM-Q4-Re and CS-FEM are from 1.79 to 1.81, which are much higher than that of FEM-Q4. Also note that the error in the energy norm of the CS-FEM solution obtained using $n_e^s = 4$ is the best among all these CS-FEM models for this problem. In overall performance, CS-FEM-4SD again outperforms FEM-Re-Q4 for this example.

Using *n*CS-FEM, it is observed that all the computed displacements and stresses are in good agreement with the analytical solutions, as shown in Figures 5.25 and 5.26. With refinement of the mesh, the accuracy becomes better and approaches the exact solution. The contour plots of the error in displacement and stresses are shown in Figure 5.27. Accurate results are obtained.

Figure 5.28 plots the error in the displacement norm versus Poisson's ratio changing from 0.4 to 0.4999999 obtained using *n*CS-FEM and selective *n*CS-FEM with *n*-sided polygonal elements (451 nodes), and CS-FEM and selective CS-FEM with Q4 elements (289 nodes).

The results show that the selective CS-FEM presented in Section 5.7 is effective in overcoming volumetric locking for nearly incompressible materials, whereas CS-FEM ($n_e^s = 4$) and *n*CS-FEM are subjected to volumetric locking. We have also observed that locking starts as early as Poisson's ratio at 0.4.

5.9 Remarks

In this chapter, we presented CS-FEM models, including CS-FEM using Q4 elements and *n*CS-FEM using general *n*-sided polygonal elements.

Through the theoretical study, formulations and numerical examples, some remarks for CS-FEM and nCS-FEM can be made.

Remark 5.4 Shape Function Values

For CS-FEM and nCS-FEM, the evaluation of the shape function values at points on the smoothing domain boundaries can be done with ease, using the simple linear PIM. The compatibility of the displacement field on the smoothing domain boundaries can always be ensured using the linear PIM, as long as the interpolation is based on points on the smoothing domain boundaries.

Remark 5.5 Spatial Stability of CS-FEM Models

For CS-FEM using Q4 elements, when the number of smoothing domains $n_e^s = 1$, the solution of CS-FEM has similar properties with those of FEM-Q4 using reduced integration. The element stiffness matrix may contain spurious zero-energy modes, and the global stiffness matrix after imposing sufficient essential boundary conditions can still be singular depending on the setting of the problem. When n_e^s approaches infinity, the solution of CS-FEM will approach the solution of the standard compatible FEM-Q4 model. When n_e^s is a finite number larger than 1, the solutions of a stable CS-FEM in both displacement and strain energy will change monotonously from the solution of CS-FEM ($n_e^s = 1$) to that of FEM using full integration.

Remark 5.6 CS-FEM with $n_e^s = 4$: An Always Stable Model

In practical calculation, using $n_e^s = 4$ smoothing domains for each Q4 element in CS-FEM is advised for all problems. The numerical solution of CS-FEM ($n_e^s = 4$) is always stable, accurate, much better than its counterpart FEM-Q4, and often very close to the exact solution.

Remark 5.7 CS-FEM versus FEM-Q4

The errors in the energy norm of CS-FEM are much smaller than those of FEM-Q4. The convergence rates in the energy norm of CS-FEM are much higher than those of FEM-Q4. The errors and convergence rates in the displacement norm of CS-FEM will approach those of FEM-Q4 when the number of smoothing domains in elements increases. The error in the energy norm of the CS-FEM solution is a little higher than that of FEM-Q4-Re. The error in the displacement norm of the CS-FEM solution is much smaller than that of FEM-Q4. In overall performance, CS-FEM with $n_e^s = 4$ outperforms FEM-Q4-Re for the examples studied in this chapter.

Remark 5.8 On nCS-FEM: An Always Stable and Efficient Model

In *n*CS-FEM, *n*-sided polygonal elements using $n_e^s = n$ triangular smoothing cells can work and are always stable. *n*CS-FEM is found on the "stiff" side.

Remark 5.9 Selective CS-FEM and nCS-FEM: Volumetric Locking Free

The selective CS-FEM and *n*CS-FEM are simple and very effective in overcoming volumetric locking for problems of nearly incompressible materials.

CS-FEM has been studied further in theory [17] and extended for dynamic analyses [18], incompressible materials using selective integration [19], and plate and shell analyses [20–24]. It is also extended in combination with the extended finite element method (XFEM) to solve fracture mechanics problems in 2D continuum and plates [25].

Note that CS-FEM is indeed very similar to the standard FEM-Q4, and the numerical operations (interpolation, integration, etc.) are all based on elements. Switching from an FEM-Q4 code to a CS-FEM code is trivial requiring minimum alteration, and the major code structure can largely stay put. Such a simple switch is certainly justified for the benefits obtained. However, the use of Q4 elements is not preferable, due to the difficulty in fully automatic mesh generation. In the following chapters, we will introduce S-FEM models that work well with T3 elements (for 2D problems) and T4 elements (for 3D problems), which require accessing the information from neighboring elements for the smoothing operation to take effect we cannot and should not be confined by the element!

References

1. Liu GR, Dai KY, and Nguyen-Thoi T. 2007. A smoothed finite element method for mechanics problems. *Computational Mechanics*; 39: 859–877.
2. Liu GR, Nguyen-Thoi T, Dai KY, and Lam KY. 2007. Theoretical aspects of the smoothed finite element method (SFEM). *International Journal for Numerical Methods in Engineering*; 71: 902–930.
3. Liu GR, Nguyen-Thoi T, Nguyen-Xuan H, Dai KY, and Lam KY. 2009. On the essence and the evaluation of the shape functions for the smoothed finite element method (SFEM) (Letter to Editor). *International Journal for Numerical Methods in Engineering*; 77: 1863–1869.
4. Dai KY, Liu GR, and Nguyen-Thoi T. 2007. An *n*-sided polygonal smoothed finite element method (*n*SFEM) for solid mechanics. *Finite Elements in Analysis and Design*; 43: 847–860.
5. Nguyen-Thoi T, Liu GR, Dai KY, and Lam KY. 2007. Selective smoothed finite element method. *Tsinghua Science and Technology*; 12(5): 497–508.

6. Chen JS, Wu CT, Yoon S, and You Y. 2001. A stabilized conforming nodal integration for Galerkin meshfree method. *International Journal for Numerical Methods in Engineering*; 50: 435–466.
7. Hughes TJR. 1987. *The Finite Element Method: Linear Static and Dynamic Finite Element Analysis*. Prentice-Hall, Englewood Cliffs, NJ.
8. Liu GR and Quek SS. 2003. *The Finite Element Method: A Practical Course*. Butterworth Heinemann, Oxford.
9. Liu GR. 2008. A generalized gradient smoothing technique and the smoothed bilinear form for Galerkin formulation of a wide class of computational methods. *International Journal of Computational Methods*; 5(2): 199–236.
10. Liu GR and Zhang GY. 2009. A normed G space and a cell-based smoothed point interpolation method. *International Journal of Computational Methods*; 6(1): 147–179.
11. Kelly DW. 1980. Bounds on discretization error by special reduced integration of the Lagrange family of finite elements. *International Journal for Numerical Methods in Engineering*; 15: 1489–1506.
12. Liu GR, Zhang GY, and Zhang GR. 2009. A normed G space and weakened weak (W^2) formulation of a cell-based smoothed point interpolation method. *International Journal of Computational Methods*; 6(1): 147–179.
13. Liu GR and Gu YT. 2005. *An Introduction to Meshfree Methods and their Programming*. Springer, Berlin.
14. Timoshenko SP and Goodier JN. 1970. *Theory of Elasticity*, 3rd edition. McGraw-Hill, New York.
15. Liu GR and Liu MB. 2003. *Smoothed Particle Hydrodynamics—A Meshfree Particle Method*. World Scientific, Singapore.
16. Yoo JW, Moran B, and Chen JS. 2004. Stabilized conforming nodal integration in the natural-element method. *International Journal for Numerical Methods in Engineering*; 60: 861–890.
17. Hung N-X, Stéphane B, and Hung N-D. 2008. Smooth finite element methods: Convergence, accuracy and properties. *International Journal for Numerical Methods in Engineering*; 74: 175–208.
18. Dai KY and Liu GR. 2007. Free and forced analysis using the smoothed finite element method (SFEM). *Journal of Sound and Vibration*; 301: 803–820.
19. Nguyen-Xuan H, Bordas S, and Nguyen-Dang H. 2008. Addressing volumetric locking and instabilities by selective integration in smoothed finite elements. *Communications in Numerical Methods and Engineering*; 25: 19–34.
20. Nguyen-Xuan H and Nguyen-Thoi T. 2009. A stabilized smoothed finite element method for free vibration analysis of Mindlin–Reissner plates. *Communications in Numerical Methods in Engineering*; 25: 882–906.
21. Cui XY, Liu GR, Li GY, Zhao X, Nguyen-Thoi T, and Sun GY. 2008. A smoothed finite element method (SFEM) for linear and geometrically nonlinear analysis of plates and shells. *CMES-Computer Modeling in Engineering and Sciences*; 28(2): 109–125.
22. Nguyen-Thanh N, Rabczuk T, Nguyen-Xuan H, and Bordas S. 2008. A smoothed finite element method for shell analysis. *Computer Methods in Applied Mechanics and Engineering*; 198: 165–177.

23. Nguyen-Van H, Mai-Duy N, and Tran-Cong T. 2008. A smoothed four-node piezoelectric element for analysis of two-dimensional smart structures. *CMES-Computer Modeling in Engineering and Sciences*; 23(3): 209–222.
24. Nguyen-Xuan H, Rabczuk T, Bordas S, and Debongnie JF. 2008. A smoothed finite element method for plate analysis. *Computer Methods in Applied Mechanics and Engineering*; 197: 1184–1203.
25. Bordas S, Rabczuk T, Nguyen-Xuan H, Nguyen-Vinh P, Natarajan S, Bog T, Do-Minh Q, and Nguyen-Vinh H. 2009. Strain smoothing in FEM and XFEM. *Computers and Structures*; doi:10.1016/j.compstruc.2008.07.006.

6

Node-Based Smoothed FEM

6.1 Introduction

In order to determine the error in numerical solutions of complicated problems without knowing the exact solution or performing so-called duality in FEM analysis [1–3], it is practical to use two numerical models: one gives a lower bound and the other gives an upper bound of the unknown exact solution. This chapter discusses an S-FEM model that can be used for such a purpose. For convenience in discussion, we focus on the so-called force-driven solid mechanics problems: boundary value problems with homogeneous Dirichlet (or essential, or displacement) boundary conditions. The extension to other types of problems will be discussed in the remark section.

For the above-mentioned force-driven problems, the most popular model giving a lower bound in terms of strain energy is the fully compatible displacement FEM model (see Property 3.2), which is currently widely used in solving complicated engineering problems. Obtaining an upper bound solution is, on the other hand, usually much more difficult, and a great deal of effort has been made so far to overcome this difficulty. Currently, the model that can give an upper bound is one of the following model:

Model 1: the stress equilibrium FEM model [3]
Model 2: the recovery model using a statically admissible stress field from the displacement FEM solution [4–6]
Model 3: some hybrid equilibrium FEM model [7,8]
Model 4: the recently developed node-based S-FEM (or NS-FEM) model [9–13]

The first three models are known to have some disadvantages. For Model 1, there are three major drawbacks: (1) The equilibrium approach is mathematically much more complicated and hence difficult to implement and computationally more expensive; (2) Spurious modes often occur simply because the model is overly soft and tractions cannot be equilibrated by the approximated stress field; and (3) It is difficult to obtain the displacement field from the stress solutions because an integral equation has to be solved (i.e., essentially an inverse procedure). For Model 2, there are two

main drawbacks: (1) This procedure is complicated and computationally expensive, and (2) It is difficult to obtain desirable global errors because of the instability of the recovery upper bound solutions. For Model 3, there are three main drawbacks: (1) The procedure is complicated and computationally more expensive; (2) Additional DOFs are often required because of the use of both approximated displacement and stress variables; and (3) There exist spurious modes in the hybrid models. Because of these drawbacks, the three models are not yet widely used in practical applications to complicated engineering problems. They are still very much restricted to the area of academic research.

Model 4 is considered as the simplest, robust, and practical technique for obtaining upper bounds for problems of all dimensions and of arbitrary complexity as long as a triangular type of mesh can be created. Development in this new direction originated from the recent discovery that NS-PIM [12,13] can often produce upper bound solutions in strain energy for force-driven problems of arbitrary complexity as long as triangular background cells can be built. Similar properties were later also found in NS-FEM using different types of elements [9,10]. This chapter is therefore devoted to the NS-FEM that was initially proposed in Refs. [9,10] following the work of NS-PIM [12,13].

Apart from the important upper bound property, NS-FEM also possesses many other interesting properties that are similar to an equilibrium model, such as natural immunization from volumetric locking, ultra-accuracy, and superconvergence of the stress solution. In addition, NS-FEM works well for triangular types of elements that can be generated automatically for complicated geometries.

The formulation of NS-FEM given in this chapter is performed first for 2D problems using in general arbitrary n-sided polygonal elements, in particular triangular elements, and then for 3D problems using tetrahedral elements. In addition, an adaptive procedure for NS-FEM using triangular elements (NS-FEM-T3) with an error indicator based on the *computable* recovery strain is proposed [14]. Finally, numerical examples are presented to confirm the theory and to demonstrate the properties of the NS-FEM model.

6.2 Creation of Node-Based Smoothing Domains

In NS-FEM, the problem domain Ω is discretized using N_n elements with N_n nodes, such that $\Omega = \sum_{i=1}^{N_e} \Omega_i^e$ and $\Omega_i^e \cap \Omega_j^e = \emptyset$, $i \neq j$, as in FEM. The shape of the elements can be, in general, a polygon with an arbitrary number of sides. On top of the element mesh, a set of nonoverlapping no-gap smoothing domains is then created associated with nodes, such that $\Omega = \sum_{k=1}^{N_n} \Omega_k^s$ and $\Omega_i^s \cap \Omega_j^s = \emptyset$, $i \neq j$. In this case, the number of

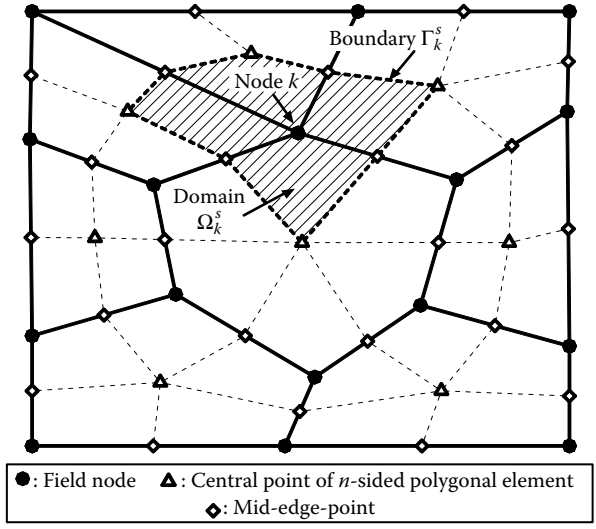

FIGURE 6.1 n-Sided polygonal elements and the smoothing domains associated with nodes.

smoothing domains is the same as the number of nodes: $N_s = N_n$, which satisfies the requirement of the minimum number of smoothing domains given in Table 4.2. This implies that NS-FEM should at least be spatially stable (see Theorem 4.1). The strain smoothing technique using the node-based smoothing domains [15] is used to create a strain field for the NS-FEM model where the assumed displacement field is constructed using an element mesh. For n-sided polygonal elements, the smoothing domain Ω_k^s associated with node k is created by sequentially connecting the mid-edge-point to the central points of the surrounding n-sided polygonal elements of node k, as shown in Figure 6.1. As a result, each n-sided polygonal element will be divided into n quadrilateral subdomains and each subdomain is attached to the nearest field node. The domain Ω_k^s associated with node k can also be viewed as the combination of the subdomains of all the elements surrounding node k.

6.3 Formulation of NS-FEM

6.3.1 General Formulation

Consider the solid mechanics problem defined in Chapter 2. Using the general formulation of the S-FEM models presented in Chapter 4, the linear system of equations of NS-FEM has the form

$$\overline{\mathbf{K}}^{\text{NS-FEM}}\,\overline{\mathbf{d}} = \tilde{\mathbf{f}}, \tag{6.1}$$

where $\overline{\mathbf{K}}^{\text{NS-FEM}}$ is the *smoothed* stiffness matrix whose entries are given by

$$\overline{\mathbf{K}}_{IJ}^{\text{NS-FEM}} = \int_{\Omega} \overline{\mathbf{B}}_I^T \mathbf{c} \overline{\mathbf{B}}_J \mathrm{d}\Omega = \sum_{k=1}^{N_n} \int_{\Omega_k^s} \overline{\mathbf{B}}_I^T \mathbf{c} \underbrace{\overline{\mathbf{B}}_J}_{\text{constant in } \Omega_k^s} \mathrm{d}\Omega = \sum_{k=1}^{N_n} \overline{\mathbf{B}}_I^T \mathbf{c} \overline{\mathbf{B}}_J A_k^s, \quad (6.2)$$

where $A_k^s = \int_{\Omega_k^s} \mathrm{d}\Omega$ is the area of node-based smoothing domain Ω_k^s, and the smoothed strain–displacement matrix $\overline{\mathbf{B}}_I$ is computed using Equation 4.30. It is clear that we need only the shape function values to obtain the smoothed strain–displacement matrix $\overline{\mathbf{B}}_I$. For general n-sided polygonal elements, shape function values are obtained following the same procedure given in Section 6.4.

6.3.2 NS-FEM-T3 for 2D problems

In particular, when linear triangular elements (T3) are used for 2D problems, Equation 4.30 can, of course, still be used. However, in such cases, we know that the compatible strains are constants in the T3 elements (see Section 3.11), and hence the formulation reduces to that given in Refs. [9,10]. The smoothed strain–displacement $\overline{\mathbf{B}}_I$ can be assembled simply using

$$\overline{\mathbf{B}}_I(\mathbf{x}_k) = \frac{1}{A_k^s} \sum_{j=1}^{n_k^e} \frac{1}{3} A_j^e \tilde{\mathbf{B}}_j^e, \quad (6.3)$$

where n_k^e is the number of elements around node k, A_j^e is the area of the jth element around node k, and matrix $\tilde{\mathbf{B}}_j^e = \sum_{I \in S_j^e} \tilde{\mathbf{B}}_I$ is the compatible strain–displacement matrix for the jth triangular element around node k. It is assembled from the compatible strain–displacement matrices $\tilde{\mathbf{B}}_I(\mathbf{x})$ of nodes in the set S_j^e containing three nodes of the jth triangular element. Matrix $\tilde{\mathbf{B}}_I(\mathbf{x})$ for node I is the strain–displacement matrix given by Equation 3.93 and A_k^s is the area of the kth smoothing domain computed using

$$A_k^s = \int_{\Omega_k^s} \mathrm{d}\Omega = \frac{1}{3} \sum_{j=1}^{n_k^e} A_j^e. \quad (6.4)$$

With this formulation, only the area and the usual "compatible" strain–displacement matrices $\tilde{\mathbf{B}}_j^e$ of the triangular elements are needed to calculate the system stiffness matrix for the NS-FEM-T3 model. The formulation is simple, but works only for triangular elements that use linear interpolation. For NS-FEM models using other elements, the smoothed

strain–displacement matrix $\overline{\mathbf{B}}_I$ has to be computed using the original Equation 4.30, and the shape functions have to be evaluated in the same way as given in Section 6.4.

6.3.3 NS-FEM-T4 for 3D Problems

The above formulation is quite straightforward to extend to 3D problems using four-node tetrahedral elements (T4). The smoothed strain–displacement matrix $\overline{\mathbf{B}}_I(\mathbf{x}_k)$ for an NS-FEM-T4 model is assembled using [9,10]

$$\overline{\mathbf{B}}_I(\mathbf{x}_k) = \frac{1}{V_k^s} \sum_{j=1}^{n_k^e} \frac{1}{4} V_j^e \tilde{\mathbf{B}}_j^e, \tag{6.5}$$

where V_j^e is the volume of the jth tetrahedral element around node k; V_k^s is the volume of the kth smoothing domain associated with node k, and is computed using

$$V_k^s = \int_{\Omega_k^s} \mathrm{d}\Omega = \frac{1}{4} \sum_{j=1}^{n_k^e} V_j^e. \tag{6.6}$$

In Equation 6.5, matrix $\tilde{\mathbf{B}}_j^e = \sum_{I \in S_j^e} \tilde{\mathbf{B}}_I$ is the compatible strain–displacement matrix for the jth tetrahedral element around node k. It is assembled from the compatible strain–displacement matrices $\tilde{\mathbf{B}}_I(\mathbf{x})$ of nodes in the set S_j^e containing four nodes of the jth tetrahedral element. Matrix $\tilde{\mathbf{B}}_I(\mathbf{x})$ for node I is the strain–displacement matrix given by Equation 3.108. With such a formulation, all we need is the volume and the usual "compatible" strain–displacement matrices $\tilde{\mathbf{B}}_j^e$ of the four-node tetrahedral elements to compute the system stiffness matrix for NS-FEM. The formulation is simple, but works only for tetrahedral elements that use linear interpolation. For other NS-FEM models, the smoothed strain–displacement matrix $\overline{\mathbf{B}}_I$ has to be computed using the original Equation 4.30 for S-FEM models, and the shape functions have to be evaluated in a similar way as given in the next section.

6.4 Evaluation of Shape Function Values

For NS-FEM using n-sided polygonal elements, the shape functions constructed in Section 4.3.2 can be used. When the displacement field along the boundary of the smoothing domains is continuous and linear, the

smoothed strain–displacement matrix $\overline{\mathbf{B}}_I$ can be computed using the shape function values at the mid-segment-points (Gauss points) along segments $\Gamma^s_{k,p} \in \Gamma^s_k$ of the smoothing domains. The shape function values at each Gauss point are evaluated by simple linear PIM, and they are essentially the average of those of two related endpoints of the segment containing the Gauss point. For example, the values of shape functions at point #*a* on segment $A - B$ shown in Figure 6.2 are evaluated as an average of those at two endpoints of the segment: points #*A* and #*B*. Therefore, in order to facilitate the evaluation of shape function values at Gauss points in NS-FEM, we first need to evaluate the shape function values at the endpoints of line segments of the smoothing domain boundary, such as mid-edge-points (#*A*, #*C*, #*E*, and #*G*) and central points (#*B*, #*D*, #*F*, and #*H*), as shown in Figure 6.2.

Figure 6.2 and Table 6.1 give explicitly the shape function values at different points of the smoothing domain associated with node *k*. The number of support nodes for the smoothing domain is 11, including node *k*, and we have a total of eight segments $\Gamma^s_{k,p}$ on $\Gamma^s_k(AB, BC, CD, DE, EF, FG, GH, HA)$. Each segment needs only one Gauss point (due to linear interpolation), and therefore there are a total of eight Gauss points (a, b, c, d, e, f, g, h) used for the entire smoothing domain Ω^s_k, and the shape function values at these eight Gauss points are tabulated in Table 6.1 by simple inspection.

It should be recalled that the purpose of introducing central points and mid-edge-points is to facilitate the evaluation of shape function values at

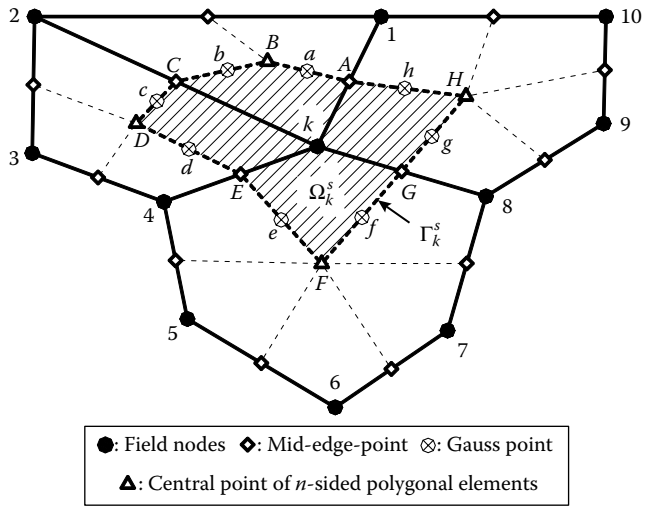

FIGURE 6.2 Position of Gauss points at mid-segment-points on the segments of smoothing domains associated with node *k* in a mesh of *n*-sided polygonal elements.

TABLE 6.1

Shape Function Values at Different Sites on the Smoothing Domain Boundary for Node k (cf. Figure 6.2)

Site	Node k	Node 1	Node 2	Node 3	Node 4	Node 5	Node 6	Node 7	Node 8	Node 9	Node 10	Description
k	1.0	0	0	0	0	0	0	0	0	0	0	Field node
1	0	1.0	0	0	0	0	0	0	0	0	0	Field node
2	0	0	1.0	0	0	0	0	0	0	0	0	Field node
3	0	0	0	1.0	0	0	0	0	0	0	0	Field node
4	0	0	0	0	1.0	0	0	0	0	0	0	Field node
5	0	0	0	0	0	1.0	0	0	0	0	0	Field node
6	0	0	0	0	0	0	1.0	0	0	0	0	Field node
7	0	0	0	0	0	0	0	1.0	0	0	0	Field node
8	0	0	0	0	0	0	0	0	1.0	0	0	Field node
9	0	0	0	0	0	0	0	0	0	1.0	0	Field node
10	0	0	0	0	0	0	0	0	0	0	1.0	Field node
A	1/2	1/2	0	0	0	0	0	0	0	0	0	Mid-edge-point
B	1/3	1/3	1/3	0	0	0	0	0	0	0	0	Centroid of element
C	1/2	0	1/2	0	0	0	0	0	0	0	0	Mid-edge-point
D	1/4	0	1/4	1/4	1/4	0	0	0	0	0	0	Centroid of element
E	1/2	0	0	0	1/2	0	0	0	0	0	0	Mid-edge-point
F	1/6	0	0	0	1/6	1/6	1/6	1/6	1/6	0	0	Centroid of element
G	1/2	0	0	0	0	0	0	0	1/2	0	0	Mid-edge-point
H	1/5	1/5	0	0	0	0	0	0	1/5	1/5	1/5	Centroid of element
a	**5/12**	**5/12**	**1/6**	**0**	**0**	**0**	**0**	**0**	**0**	**0**	**0**	**Mid-segment of** $\Gamma_{k,p}^s$
b	**5/12**	**1/6**	**5/12**	**0**	**0**	**0**	**0**	**0**	**0**	**0**	**0**	**Mid-segment of** $\Gamma_{k,p}^s$
c	**3/8**	**0**	**3/8**	**1/8**	**1/8**	**0**	**0**	**0**	**0**	**0**	**0**	**Mid-segment of** $\Gamma_{k,p}^s$
d	**3/8**	**0**	**1/8**	**1/8**	**3/8**	**0**	**0**	**0**	**0**	**0**	**0**	**Mid-segment of** $\Gamma_{k,p}^s$
e	**1/3**	**0**	**0**	**0**	**1/3**	**1/12**	**1/12**	**1/12**	**1/12**	**0**	**0**	**Mid-segment of** $\Gamma_{k,p}^s$
f	**1/3**	**0**	**0**	**0**	**1/12**	**1/12**	**1/12**	**1/12**	**1/3**	**0**	**0**	**Mid-segment of** $\Gamma_{k,p}^s$
g	**7/20**	**1/10**	**0**	**0**	**0**	**0**	**0**	**0**	**7/20**	**1/10**	**1/10**	**Mid-segment of** $\Gamma_{k,p}^s$
h	**7/10**	**7/10**	**0**	**0**	**0**	**0**	**0**	**0**	**1/10**	**1/10**	**1/10**	**Mid-segment of** $\Gamma_{k,p}^s$

these Gauss points. No extra DOFs are associated with these points. In other words, the DOFs of an NS-FEM are only these nodal DOFs, and no additional DOFs are introduced.

It is easy to see that the bilinear and linear shape functions for four-node quadrilateral (Q4) and triangular elements (T3) of the standard FEM are at least linear and satisfy naturally the continuity condition along the boundary of the smoothing domains. Hence, NS-FEM can be easily applied to the traditional four-node quadrilateral or triangular elements. For T3 elements, FEM shape functions given in Chapter 3 can be directly used and the results will be exactly the same as those following the procedure discussed in this section. For Q4 elements, shape function values are obtained using the procedure given in this section, which is exactly the same as the procedure given in Section 5.3.1. For the case of tetrahedral elements, the detailed formulation given in Section 6.3 should be followed.

6.5 Properties of NS-FEM

We now perform some analyses and tests to examine the properties of NS-FEM.

6.5.1 Essential Properties

NS-FEM possesses some of the interesting properties of equilibrium FEM models established based on the minimum complementary energy principle [16].

Property 6.1 Upper Bound Property of NS-FEM: To FEM

The total strain energy of numerical solution $\overline{E}_{\text{NS-FEM}}(\overline{\mathbf{d}})$ obtained from the NS-FEM solution is no less than that of FEM using the same mesh $\tilde{E}_{\text{FEM}}(\tilde{\mathbf{d}})$:

$$\overline{E}_{\text{NS-FEM}}(\overline{\mathbf{d}}) \geq \tilde{E}_{\text{FEM}}(\tilde{\mathbf{d}}), \tag{6.7}$$

where $\overline{\mathbf{d}}$ is the vector of nodal displacements computed using an NS-FEM model and $\tilde{\mathbf{d}}$ is that of the FEM model using the same mesh. The strain energy of the NS-FEM solution can be evaluated using

$$\overline{E}_{\text{NS-FEM}} = \frac{1}{2}\overline{\mathbf{d}}^T\overline{\mathbf{K}}^{\text{NS-FEM}}\overline{\mathbf{d}}, \tag{6.8}$$

where $\overline{\mathbf{K}}^{\text{NS-FEM}}$ is the system stiffness matrix of the NS-FEM model. The strain energy of the FEM solution can be evaluated using

$$\tilde{E}_{\text{FEM}}(\tilde{\mathbf{d}}) = \frac{1}{2}\tilde{\mathbf{d}}^T\tilde{\mathbf{K}}^{\text{FEM}}\tilde{\mathbf{d}}, \tag{6.9}$$

where $\tilde{\mathbf{K}}^{\text{FEM}}$ is the system stiffness matrix of the FEM model.

A detailed proof on the upper bound property, Equation 6.7, was given in Ref. [12], and is given in the proof of Theorem 4.3 in this book.

Property 6.2 Upper Bound Property of NS-FEM: To the Exact Solution

The numerical results demonstrated that when a reasonably fine mesh is used to ensure sufficient smoothing effects in the model, the strain energy of numerical solution $\overline{E}_{\text{NS-FEM}}(\overline{\mathbf{d}})$ obtained from the NS-FEM solution has the following relationship with the total strain energy of exact solution E_{exact}.

$$\overline{E}_{\text{NS-FEM}}(\overline{\mathbf{d}}) \geq E_{\text{exact}}(\mathbf{u}), \tag{6.10}$$

where $\mathbf{u}$ is the displacement of the exact solution of the same problem. The strain energy of the exact solution can be computed using

$$E_{\text{exact}} = \int_{\Omega}(\boldsymbol{\varepsilon}(\mathbf{u}))^T\mathbf{c}\boldsymbol{\varepsilon}(\mathbf{u})\mathrm{d}\Omega = \frac{1}{2}\sum_{i=1}^{N\text{e}}\int_{\Omega_i^e}(\boldsymbol{\varepsilon}_i^e)^T\mathbf{c}\boldsymbol{\varepsilon}_i^e\,\mathrm{d}\Omega, \tag{6.11}$$

where $\boldsymbol{\varepsilon}(\mathbf{u})$ is the exact strain field obtained using the exact displacement field $\mathbf{u}$ and $\boldsymbol{\varepsilon}_i^e$ is the exact strain solution of the ith element.

A detailed discussion on the upper bound property, Equation 6.10, and related conditions for the NS-PIM models can be found in Ref. [12].

Property 6.3 NS-FEM: Volumetric Locking Free

NS-FEM is naturally immune from volumetric locking, and no special treatments are needed for solids of nearly incompressible materials, when the softening effects are sufficient in the NS-FEM model. This is because the NS-FEM model is softer than the exact model, has the similar feature of an equilibrium model, and hence is volumetric locking free, when the mesh is sufficiently fine. The main reason why volume locking disappears in an equilibrium model is given in Remark 2.3.

Property 6.4 NS-FEM: Superconvergence in the Strain Energy Solution

The recovery strain/stress field constructed using the strains/stresses at nodes is very accurate and often superconvergent. This continuous

recovery strain/stress field obtained using NS-FEM can be used as a representation of the exact strain/stress field in adaptive analysis.

Property 6.5 NS-FEM: No Improvement in the Displacement Solution

The accuracy of displacement solutions in NS-FEM is not particularly high. It is, in general, at the same level as that of the standard FEM using the same mesh.

Note that $\overline{\mathbf{K}}^{\text{NS-FEM}}$ will also be banded if the nodes are properly numbered, as that in FEM. When linear triangular elements are used in an NS-FEM model, the bandwidth of $\overline{\mathbf{K}}^{\text{NS-FEM}}$ will be determined by the largest difference of node numbers of the nodes of all the first layer of triangular elements connected directly to the node. For 2D cases, a node-based smoothing domain used in the NS-FEM model is usually supported by 4–8 nodes. A triangular element used in the FEM model involves only three nodes. Therefore, it is clear that the bandwidth of an NS-FEM model will be about twice that of a linear FEM using the same triangular mesh. When a bandwidth solver is used to solve Equation 6.1, the complexity is proportional to the square of the bandwidth of the stiffness matrix $\overline{\mathbf{K}}^{\text{NS-FEM}}$. Therefore, we can expect that the solver time for NS-FEM will be about 4 times that of FEM using the same mesh.

The above analysis is quite rough but should be a good indicator. Of course, we have not yet taken solution accuracy and other properties into account. When a fairer comparison in terms of computational efficiency is made using properly defined error norm measures, the superiority of the NS-FEM model can be observed, as will be discussed in Section 6.7. We now note the following.

Property 6.6 NS-FEM: Increase in Bandwidth

The bandwidth of an NS-FEM model is about twice that of the FEM model, and the computational cost of an NS-FEM model is 4 times that of FEM using the same mesh, when a bandwidth solver is used. When a full-matrix solver is used, the complexity for solving the NS-FEM and FEM equations is the same for the same mesh.

6.5.2 Rank Test for the Stiffness Matrix: Stability Analysis

Property 6.7 NS-FEM: Spatially Stable

NS-FEM possesses only "legal" zero-energy modes that represent rigid motions, and there exists no spurious zero-energy mode. This means that NS-FEM is *spatially* stable.

As presented in Remark 5.2, a CS-FEM model can have spurious zero-energy modes when the entire element is used as one smoothing domain. This is because the total number of smoothing domains may not always satisfy the minimum number of smoothing domains $N_s^{\min}$ given in Table 4.2. The NS-FEM method possesses only "legal" zero-energy modes that represent rigid motions, and there exists no spurious zero-energy mode. This is ensured by the following:

1. NS-FEM satisfies the minimum number of smoothing domains $N_s^{\min}$ for problems of all dimensions required in Section 4.6. This can be easily verified because $N_s = N_n$.
2. Even at the individual element level, the numerical integration used to evaluate Equation 6.2 in NS-FEM satisfies the necessary condition given in Table 4.2, if the rigid motion is fixed (see also Section 6.1.3 in Ref. [17]). This is true for all possible NS-FEM models, as examined in detail in Table 6.2.
3. The shape functions used in NS-FEM are of partitions of unity, ensuring a proper representation of rigid movements.
4. Because each of the smoothing domains are created for different nodes, they are linearly independent, which ensures linearly independent columns in the smoothed strain–displacement matrix, and hence in the smoothed stiffness matrix. Hence the stiffness matrix in an NS-FEM model is SPD for stable materials, after rigid motion is fixed.

Therefore, NS-FEM will have the proper number of zero eigenmodes representing rigid body movements and will not have any spurious zero-energy modes. In other words, any deformation (except the rigid motions) will result in strain energy in an NS-FEM model, implying that it will be stable.

Note that although NS-FEM is spatially stable, this does not guarantee *temporal* stability (Remark 1.3). In fact, it can have non-zero-energy spurious modes and can be temporally unstable; hence special stabilization techniques are needed for NS-FEM to solve dynamic problems [18,19] and nonlinear problems [20]. In this book, however, we will not discuss this further. Interested readers may refer to Refs. [18–20]. An alternative and very efficient way of overcoming the temporal instability is to use ES-FEM, which will be discussed in more detail in Chapter 7.

Property 6.8 NS-FEM: Temporally Instable

NS-FEM is *temporally* instable and can have non-zero-energy spurious modes.

TABLE 6.2

Existence of Spurious Zero-Energy Modes in an Individual Element

Type of Element	NS-FEM	FEM with Reduced Integration
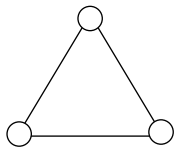 Triangle $N_R = 3$	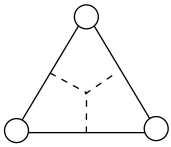 $n_Q = 3, N_Q = 3 \times n_Q = 9$ $n_t = 3, N_u = 2 \times n_t = 6$ $N_Q > N_u - N_R$ => spurious zero energy modes not possible	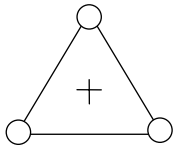 $n_Q = 1,\ N_Q = 3 \times n_Q = 3$ $n_t = 3, N_u = 2 \times n_t = 6$ $N_Q = N_u - N_R$ => spurious zero energy modes not possible
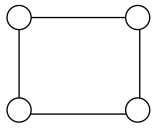 Quadrilateral $N_R = 3$	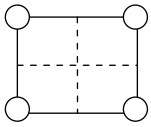 $n_Q = 4, N_Q = 3 \times n_Q = 12$ $n_t = 4, N_u = 2 \times n_t = 8$ $N_Q > N_u - N_R$ => spurious zero energy modes not possible	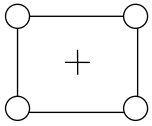 $n_Q = 1, N_Q = 3 \times n_Q = 3$ $n_t = 4, N_u = 2 \times n_t = 8$ $N_Q < N_u - N_R$ => spurious zero energy modes possible
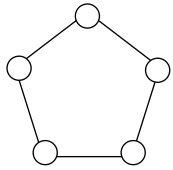 n-sided polygonal ($n > 4$) $N_R = 3$	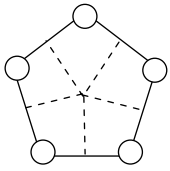 $n_Q = n, N_Q = 3 \times n_Q = 3n$ $n_t = n, N_u = 2 \times n_t = 2n$ $N_Q > N_u - N_R$ => spurious zero energy modes not possible	Not applicable

Notes: N_R, number of DOFs of rigid motion; n_Q, number of quadrature points/cells; N_Q, number of independent equations; n_t, number of nodes; and N_u, number of total DOFs.

6.5.3 Standard 2D Patch Tests: Accuracy

In this standard 2D patch test, we use a square patch. The patch is first discretized using 36 n-sided polygonal elements, as shown in Figure 5.5. We next create a set of smoothing domains following the procedure described

in Section 6.2. The linear displacement field is then specified on all the boundaries of the patch using Equation 5.11. NS-FEM is used to solve this patch test problem for numerical solutions. The error norm in displacements (Equation 4.63) is used to examine the computed results. The (dimensionless) material parameters are taken as $E = 100$ and $\nu = 0.3$. It is found that NS-FEM can pass the standard patch test within machine precision with an error norm in displacements of $e_d = 5.22\text{e} - 13(\%)$. This test verifies that the NS-FEM model has at least second-order accuracy, implying that the (displacement) error is at least on terms of second order and higher.

6.5.4 Standard 3D Patch Tests: Accuracy and Mesh Sensitivity

This 3D standard patch test is also known as the Irons first-order patch test. We perform this test in this section using a cubic patch, and it is conducted together with a mesh sensitivity analysis. The patch is first discretized with a number of tetrahedral elements with N_n nodes, in the same way as in FEM. Linear displacements are imposed along all the exterior boundaries of the cubic patch with at least one interior node. Similar to the 2D patch test, satisfaction of the patch test requires that the displacements of all the interior nodes follow "exactly" (to machine precision) the same linear function of the imposed displacements, and the constant strain/stress status in the 3D patch is reproduced.

The material parameters used in this patch test are $E = 6.895 \times 10^6$ kPa and $\nu = 0.25$, and the linear displacement field is specified by

$$\begin{aligned} u &= 0.001 * (2x + y + z)/2, \\ v &= 0.001 * (x + 2y + z)/2, \\ w &= 0.001 * (x + y + 2z)/2. \end{aligned} \tag{6.12}$$

The error norm in displacement (Equation 4.63) is used to examine the computed results. For this 3D patch test, we use the (absolute) "strain energy error" measure defined by

$$e_e = \left| \overline{E}_{\text{NS-FEM}} - E_{\text{exact}} \right|, \tag{6.13}$$

where the total strain energy of the exact solution E_{exact} is evaluated using

$$E_{\text{exact}} = \frac{1}{2} \boldsymbol{\varepsilon}^T \mathbf{c} \boldsymbol{\varepsilon} V_{\text{cubic}}, \tag{6.14}$$

in which the exact strains $\boldsymbol{\varepsilon}$ are used, and V_{cubic} is the volume of the cubic patch. The total strain energy of the numerical solution $\overline{E}_{\text{NS-FEM}}$ can be

evaluated using

$$\overline{E} = \frac{1}{2} \sum_{k=1}^{N_n} (\overline{\boldsymbol{\varepsilon}}_k)^T \, \mathbf{c} \overline{\boldsymbol{\varepsilon}}_k \, V_k^s, \tag{6.15}$$

where $\overline{\boldsymbol{\varepsilon}}_k$ is the strain for the kth node obtained using an NS-FEM model and V_k^s is the volume of the kth smoothing domain used in the patch.

Figure 6.3 shows the cubic patch with dimensions of 10 by 10 by 10. The patch is discretized using 29 four-node tetrahedral elements and 15 nodes (including eight nodes at the corners, six nodes at the center of six patch surfaces, and one interior node), as shown in Figure 6.3. In order to analyze the sensitivity of the results to mesh distortion, the interior node is moved randomly inside the cube from the center point in the following fashion:

$$\begin{aligned} x' &= x + \Delta x \cdot r_x \cdot \alpha_{\text{ir}}, \\ y' &= y + \Delta y \cdot r_y \cdot \alpha_{\text{ir}}, \\ z' &= z + \Delta z \cdot r_z \cdot \alpha_{\text{ir}}, \end{aligned} \tag{6.16}$$

where x, y, and z are the coordinates at the center point of the cubic patch; Δx, Δy, and Δz are the lengths of the cubic patch in the x-, y-, and z-directions, respectively. r_x, r_y, and r_z are computer-generated random numbers between -1.0 and 1.0 and α_{ir} is a prescribed irregularity factor chosen between 0.0 and 0.49. When $\alpha_{\text{ir}} = 0.0$, the interior node locates at the center point of the cubic patch, and when $\alpha_{\text{ir}} > 0.0$, the interior node

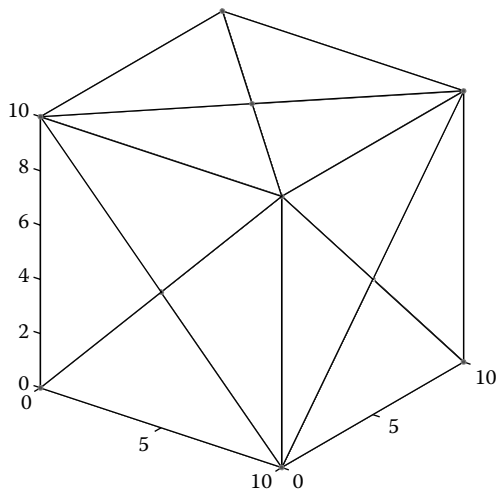

FIGURE 6.3 Domain discretization of a cubic patch with four-node tetrahedral elements.

TABLE 6.3

Error in Displacement Norm and Energy for the Patch Test

	$\alpha_{ir} = 0.0$	$\alpha_{ir} = 0.1$	$\alpha_{ir} = 0.2$	$\alpha_{ir} = 0.3$	$\alpha_{ir} = 0.4$	$\alpha_{ir} = 0.49$
Displacement norm e_d (%)	2.25e − 16	1.64e − 15	3.42e − 16	3.45e − 15	1.34e − 15	4.79e − 15
Energy error e_e	0.0	4.56e − 12	3.27e − 11	4.25e − 11	3.93e − 12	1.56e − 11

moves randomly inside the cubic patch. The larger the value of α_{ir}, the more irregular the shape of elements generated. At $\alpha_{ir} = 0.49$, the interior node is almost touching the surface of the cube.

It is found that NS-FEM-T4 using tetrahedral elements can pass the Irons first-order patch test within machine precision regardless of the value of α_{ir} used, as shown in Table 6.3. There is no accuracy loss due to the different choices of α_{ir} values: these errors are all within machine precision. This shows that NS-FEM-T4 can work well with severely distorted meshes.

Property 6.9 NS-FEM: First-order Consistency

NS-FEM has first-order consistency, meaning that it can produce a linear displacement field exactly. In other words, it is of second-order accuracy in displacement solution: errors are at second-order terms or above.

Property 6.10 NS-FEM Solution: Stability and Convergence

Because of the stability given in Property 6.7 and the first-order consistency given in Property 6.9, NS-FEM has a unique stable solution that converges to the exact solution of the original solid mechanics problem defined in Chapter 2. This confirms Theorem 4.1.

Property 6.11 NS-FEM is Insensitive to Mesh Distortion.

6.6 An Adaptive NS-FEM Using Triangular Elements

Since NS-FEM works very well with triangular elements that can be generated by automatic means and the results are not sensitive to mesh distortion, we are now ready to extend our NS-FEM-T3 for adaptive analyses [14]. An adaptive analysis technique is very important for the analysis of practical engineering problems. With such a technique analysts need not have to worry about mesh generation and mesh quality. In developing a good adaptive procedure, we need to devise two key techniques: a reasonably accurate error indicator and an appropriate refinement strategy. Because NS-FEM uses triangular elements, both techniques can be

developed with ease, as performed in Refs. [14,21]. In this chapter, an error indicator based on recovery strain is proposed for adaptive analyses. It is shown through intensive numerical experiments that the error indicator is "asymptotically" exact with the effectivity index close to unity. For mesh refinement, a simple and effective refinement strategy using newest node bisection is presented.

6.6.1 Error Indicators Using Recovery Strain

To devise an effective error indicator, we need to have a good understanding of errors in a numerical solution of the discrete model and a reasonably good tool for the assessment of solution errors. Unfortunately, assessing the error of numerical solutions is complicated, and can be more involved than obtaining the numerical solution. To minimize possible confusion and to conduct meaningful error analysis leading to a practical error indicator for our NS-FEM, we first define the following terminologies with detailed descriptions on the features of all the fields involved in solid mechanics problems.

$\mathbf{u}, \boldsymbol{\varepsilon}, \boldsymbol{\sigma}, \mathbf{d}$: "exact" solution of displacements, strains, stresses, and nodal displacements. Note that we express them all in vector form, meaning that there are a number of component field functions in the vector.

$\overline{\mathbf{u}}, \overline{\boldsymbol{\varepsilon}}, \overline{\boldsymbol{\sigma}}, \overline{\mathbf{d}}$: "raw" solution of an S-FEM model in terms of displacements, strains, stresses, and nodal displacements. Note that the strains (and stresses) are obtained using Equation 4.20 and the solutions of nodal displacements without any additional postprocess treatment (hence they are called "raw" solutions). Such a strain solution is constant in each of the smoothing domains, and hence they is piecewise constant over the problem domain. When we need to obtain the strains for an element, we perform a simple or an area-weighted average using all these strains in the different parts of the elements. In this case, we also call the strain the "averaged raw strain" in the element.

$\tilde{\mathbf{u}}, \tilde{\boldsymbol{\varepsilon}}, \tilde{\boldsymbol{\sigma}}, \tilde{\mathbf{d}}$: "raw" solution of an FEM model in displacements, strains, stresses, and nodal displacements. Note that when linear triangular elements are used, the strains (and stresses) are constant in each of the elements, and hence they are piecewise constant over the problem domain. When higher-order elements are used, they are continuous within elements and piecewise continuous over the problem domain. When we need to obtain the strains for a node, however, we perform a simple or area-weighted average using all these strains in the elements surrounding the node. In this case too, we call such a strain the "averaged raw strain" at the node.

Next, to evaluate the solution error in an element Ω_i^e, we define the following error indicator:

$$\eta_i(\boldsymbol{\varepsilon} - \overline{\boldsymbol{\varepsilon}}) = \|\boldsymbol{\varepsilon} - \overline{\boldsymbol{\varepsilon}}\|_{L^2(\Omega_i^e)}, \tag{6.17}$$

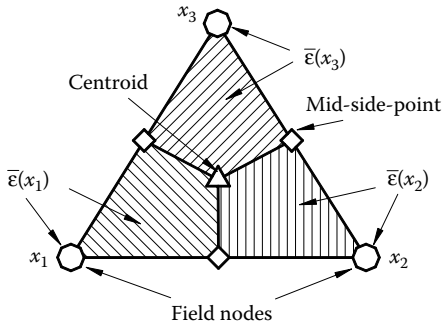

FIGURE 6.4 Strains (and stresses) at three field nodes and three quadrilateral subsmoothing domains within an element in an NS-FEM-T3 model.

where $\boldsymbol{\varepsilon} = \mathbf{L}_d\mathbf{u}$ is the exact strain and $\bar{\boldsymbol{\varepsilon}}$ is the raw strain solution in the element in NS-FEM-T3, as shown in Figure 6.4. However, the exact strain is usually unknown (or else we do not need any other forms of solutions). Thus we have to somehow find a good replacement of the exact solution, so that we can estimate the error indicator defined in Equation 6.17 without knowing the exact solution. Therefore, we construct a higher-order "recovery" strain solution $\bar{\boldsymbol{\varepsilon}}^R$ to replace $\mathbf{L}_d\mathbf{u}$. This means that $\bar{\boldsymbol{\varepsilon}}^R$ has to be more accurate than $\bar{\boldsymbol{\varepsilon}}$, meaning that

$$\left\| \mathbf{L}_d\mathbf{u} - \bar{\boldsymbol{\varepsilon}}^R \right\|_{L^2(\Omega_i^e)} \leq C_1 h^\alpha \left\| \mathbf{L}_d\mathbf{u} - \bar{\boldsymbol{\varepsilon}} \right\|_{L^2(\Omega_i^e)}, \quad \alpha > 0, \tag{6.18}$$

where C_1 is a general constant independent of $\mathbf{u}$, $\bar{\boldsymbol{\varepsilon}}$, and h. Equation 6.18 can be verified if the following effectivity index,

$$\gamma = \frac{\left\| \bar{\boldsymbol{\varepsilon}} - \bar{\boldsymbol{\varepsilon}}^R \right\|_{L^2(\Omega_i^e)}}{\left\| \bar{\boldsymbol{\varepsilon}} - \mathbf{L}_d\mathbf{u} \right\|_{L^2(\Omega_i^e)}}, \tag{6.19}$$

converges to unity when h approaches zero [22,23], meaning that $\left\| \bar{\boldsymbol{\varepsilon}} - \bar{\boldsymbol{\varepsilon}}^R \right\|_{L^2(\Omega_i^e)}$ is a good estimate of $\left\| \bar{\boldsymbol{\varepsilon}} - \mathbf{L}_d\mathbf{u} \right\|_{L^2(\Omega_i^e)}$. The verification process starts from

$$\left\| \bar{\boldsymbol{\varepsilon}} - \bar{\boldsymbol{\varepsilon}}^R \right\|_{L^2(\Omega_i^e)} = \left\| (\bar{\boldsymbol{\varepsilon}} - \mathbf{L}_d\mathbf{u}) - \left(\bar{\boldsymbol{\varepsilon}}^R - \mathbf{L}_d\mathbf{u} \right) \right\|_{L^2(\Omega_i^e)}. \tag{6.20}$$

Using triangle inequality, we have

$$\begin{aligned} \left\| \bar{\boldsymbol{\varepsilon}} - \mathbf{L}_d\mathbf{u} \right\|_{L^2(\Omega_i^e)} - \left\| \bar{\boldsymbol{\varepsilon}}^R - \mathbf{L}_d\mathbf{u} \right\|_{L^2(\Omega_i^e)} &\leq \left\| \bar{\boldsymbol{\varepsilon}} - \bar{\boldsymbol{\varepsilon}}^R \right\|_{L^2(\Omega_i^e)} \\ &\leq \left\| \bar{\boldsymbol{\varepsilon}} - \mathbf{L}_d\mathbf{u} \right\|_{L^2(\Omega_i^e)} + \left\| \bar{\boldsymbol{\varepsilon}}^R - \mathbf{L}_d\mathbf{u} \right\|_{L^2(\Omega_i^e).} \end{aligned} \tag{6.21}$$

Next, by dividing each term by $\|\overline{\boldsymbol{\varepsilon}} - \mathbf{L}_d\mathbf{u}\|_{L^2(\Omega_i^e)}$, we obtain

$$1 - \frac{\left\|\overline{\boldsymbol{\varepsilon}}^R - \mathbf{L}_d\mathbf{u}\right\|_{L^2(\Omega_i^e)}}{\|\overline{\boldsymbol{\varepsilon}} - \mathbf{L}_d\mathbf{u}\|_{L^2(\Omega_i^e)}} \leq \gamma \leq 1 + \frac{\left\|\overline{\boldsymbol{\varepsilon}}^R - \mathbf{L}_d\mathbf{u}\right\|_{L^2(\Omega_i^e)}}{\|\overline{\boldsymbol{\varepsilon}} - \mathbf{L}_d\mathbf{u}\|_{L^2(\Omega_i^e)}}. \tag{6.22}$$

Now, according to Zienkiewicz and Zhu in Refs. [22,23], Equation 6.18 is verified if a recovery solution $\overline{\boldsymbol{\varepsilon}}^R$ can be found such that it can converge to the exact strain at a higher rate with respect to h than the raw solution $\overline{\boldsymbol{\varepsilon}}$ in the element. In such cases, the effectivity index γ in Equation 6.22 will approach 1 as h approaches zero, and we shall have an "asymptotically" exact estimation: the error $\left\|\overline{\boldsymbol{\varepsilon}}^R - \overline{\boldsymbol{\varepsilon}}\right\|_{L^2(\Omega_i^e)}$ will approach $\|\mathbf{L}_d\mathbf{u} - \overline{\boldsymbol{\varepsilon}}\|_{L^2(\Omega_i^e)}$. Such a first-order recovery strain solution $\overline{\boldsymbol{\varepsilon}}^R$ used in NS-FEM can be constructed using Equation 4.51, using the "nodal" strain $\overline{\boldsymbol{\varepsilon}}(\mathbf{x}_j)$ defined in Equation 4.20 (see also Figure 6.4).

We argue intuitively that the recovery strain field $\overline{\boldsymbol{\varepsilon}}^R$ defined in Equation 4.51 over an element will converge at a higher rate to the exact strain field (i.e., smooth and hence high-order continuous) compared to the raw strain in the element. The argument goes as follows. We know that the raw strain field is constant in each nodal smoothing domain, and hence is piecewise constant over an element. On the other hand, the recovery strain field $\overline{\boldsymbol{\varepsilon}}^R$ defined in Equation 4.51 is linear (one order higher) over each of the elements, and hence the recovery field $\overline{\boldsymbol{\varepsilon}}^R$ is linearly continuous over the element. In addition, this continuous "surface" of the recovery field $\overline{\boldsymbol{\varepsilon}}^R$ passes through all these raw strains $\overline{\boldsymbol{\varepsilon}}$ at the three nodes of the element. If the (piecewise constant) raw strain field $\overline{\boldsymbol{\varepsilon}}$ converges to the exact strain field (which surely does, based on Theorem 4.1), the linearly continuous recovery field $\overline{\boldsymbol{\varepsilon}}^R$ should converge to the exact field at a higher rate when measured in the energy norm. This completes our intuitive argument.

Note that such an argument can be easily (at least for 1D cases) put into a rigorous mathematical derivation. We omit this, because we believe that an intuitive understanding can sometimes be more important than the mathematical derivation, and is sufficient for our analysis here.

Based on the above argument, we can now use

$$\eta_i(\overline{\boldsymbol{\varepsilon}}^R - \overline{\boldsymbol{\varepsilon}}) = \left\|\overline{\boldsymbol{\varepsilon}}^R - \overline{\boldsymbol{\varepsilon}}\right\|_{L^2(\Omega_i^e)} \tag{6.23}$$

as a practically usable error indicator for our NS-FEM settings. This type of error indicator is known as *a posteriori* error indicator that uses only *computable* numerical results to estimate the error in the solution.

Further, we will confirm Equation 6.23 via numerical experiments in Section 6.7. We shall show clearly the effectiveness and reliability of the error indicator (Equation 6.23) in replacing Equation 6.17. To accurately examine

the performance of the error indicator (Equation 6.23), the usual Gauss integration with the proper mapping procedure is performed for each of the three quadrilateral subdomains shown in Figure 6.4. The summation over these three quadrilateral subdomains is then performed for the element.

In summary, we have altogether three error indicators for strain solutions in energy norms for NS-FEM and FEM models.

Exact error in raw strain solution (E-raw error) (not computable in general):

$$\begin{aligned} \eta_i(\boldsymbol{\varepsilon} - \overline{\boldsymbol{\varepsilon}}) &= \|\boldsymbol{\varepsilon} - \overline{\boldsymbol{\varepsilon}}\|_{L^2(\Omega_i^e)} \quad \text{(NS-FEM models)}, \\ \eta_i(\boldsymbol{\varepsilon} - \tilde{\boldsymbol{\varepsilon}}) &= \|\boldsymbol{\varepsilon} - \tilde{\boldsymbol{\varepsilon}}\|_{L^2(\Omega_i^e)} \quad \text{(FEM models)}. \end{aligned} \tag{6.24}$$

Exact error in recovery strain solution (E-rec error) (not computable in general):

$$\begin{aligned} \eta_i(\boldsymbol{\varepsilon} - \overline{\boldsymbol{\varepsilon}}^R) &= \left\|\boldsymbol{\varepsilon} - \overline{\boldsymbol{\varepsilon}}^R\right\|_{L^2(\Omega_i^e)} \quad \text{(NS-FEM models)}, \\ \eta_i(\boldsymbol{\varepsilon} - \tilde{\boldsymbol{\varepsilon}}^R) &= \left\|\boldsymbol{\varepsilon} - \tilde{\boldsymbol{\varepsilon}}^R\right\|_{L^2(\Omega_i^e)} \quad \text{(FEM models)}. \end{aligned} \tag{6.25}$$

Recovery estimated error in raw strain solution (R-raw error) (computable):

$$\begin{aligned} \eta_i(\overline{\boldsymbol{\varepsilon}}^R - \overline{\boldsymbol{\varepsilon}}) &= \left\|\overline{\boldsymbol{\varepsilon}}^R - \overline{\boldsymbol{\varepsilon}}\right\|_{L^2(\Omega_i^e)} \quad \text{(NS-FEM models)}, \\ \eta_i(\tilde{\boldsymbol{\varepsilon}}^R - \tilde{\boldsymbol{\varepsilon}}) &= \left\|\tilde{\boldsymbol{\varepsilon}}^R - \tilde{\boldsymbol{\varepsilon}}\right\|_{L^2(\Omega_i^e)} \quad \text{(FEM models)}. \end{aligned} \tag{6.26}$$

Note that the E-raw and E-rec errors are not usually computable, unless we know the exact solution for the problem. The R-raw error, however, can always be obtained after the numerical solution of a model is obtained. The R-raw error is therefore a type of a posteriori error, very useful in the error estimation of a numerical model, convenient to use in an adaptive analysis, and frequently used in the following numerical examples. The E-raw and E-rec errors are useful in examining the R-raw error using benchmark problems to which the exact/reference solution is available.

6.6.2 Refinement Strategy

Let us first define the "marking" procedure using the error indicator (Equation 6.23). Let

$$\eta^2 = \sum_{i=1}^{N_e} (\eta_i^e)^2 \tag{6.27}$$

be a global error indicator with all the elemental contributions η_i^e associated with a triangle Ω_i^e. We will use the bulk marking process proposed by

Dorfler [24], in which set M contains the marked elements to be refined at a single step. Elements in set M should satisfy the following criteria:

$$\sum_{\Omega_i^e \in M} (\eta_i^e)^2 \geq \theta \eta^2 \quad \text{for some} \quad \theta \in (0,1). \tag{6.28}$$

A smaller θ will result in a larger set M and hence more refinement of triangles at one step; a larger θ will result in a smaller set M and hence a more optimal mesh but more refinement steps. Usually $\theta = 0.2 - 0.5$ is preferred, but it really depends on the need of the analyst.

Now a refinement strategy using newest node bisection is briefly presented [25]. First, a process of labeling is performed. From a triangulation Ψ of the problem domain Ω, for each triangle $\Omega_i^e \in \Psi$, one node of Ω_i^e is labeled as *peak* or *newest node*. The opposite edge of the peak is called *base* or *refinement edge*, as shown in Figure 6.5. Then the division of the refined triangle into two subtriangles using newest node bisection is conducted as follows:

i. The refined triangle is bisected into two new subtriangles by connecting the peak to the midpoint of the base, as shown in Figure 6.5.
ii. The new node created at the midpoint of the base is assigned to be the peak of both subtriangles, as shown in Figure 6.5.

Once the labeling is done for an initial triangulation, the decent triangulations inherit the label by rule (ii) such that the bisection process can proceed. The refinement strategy using newest node bisection will not lead to any degeneracy of mesh quality and is easy to implement because conforming is ensured in the marking step.

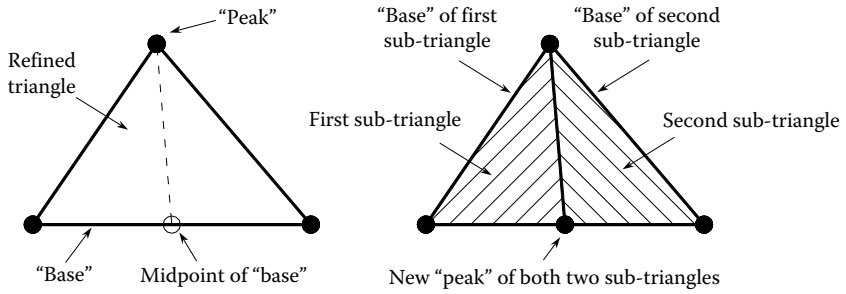

FIGURE 6.5 Division of the refined triangle into two subtriangles using newest node bisection.

6.7 Numerical Examples

Our NS-FEM uses the general n-sided polygonal elements, including triangular (T3) elements. When a triangular mesh is used, standard routines such as the Delaunay triangulation can be used. When a quadrilateral element mesh is used, commercial preprocessor FEM codes may be used for generating the mesh. Domain discretization with polygonal elements of the Voronoi diagram is performed in the same way as presented in Section 4.2. An NS-FEM code was developed based on the formulation stated above. In this section, some examples will be presented and analyzed to demonstrate numerically the properties of the NS-FEM method. For 2D problems, three kinds of elements are used: n-sided polygonal, four-node quadrilateral (Q4), and triangular elements (T3). For 3D problems, only tetrahedral elements (T4) are used for the simple reason of ease in mesh generation. In our discussions, the results of NS-FEM using n-sided polygonal elements (nNS-FEM) will be compared with those of cell-based S-FEM using n-sided polygonal elements (nCS-FEM), detailed in Chapter 5. The results of NS-FEM using four-node quadrilateral elements (NS-FEM-Q4) and triangular elements (NS-FEM-T3) will be compared with those of the standard FEM using quadrilateral elements (FEM-Q4), triangular elements (FEM-T3), and CS-FEM using four smoothing domains for each element (CS-FEM-Q4). The results of NS-FEM using tetrahedral elements (NS-FEM-T4) will be compared with those of the standard displacement FEM using four-node tetrahedral elements (FEM-T4) and eight-node hexahedral elements (FEM-H8).

For triangular and four-node quadrilateral elements, errors in both the displacement norm and the energy norm defined in Equations 4.49 and 4.50 are used in this analysis for the examination of numerical models. When the energy norm is used, we use the recovery strain solution for S-FEM models, and both raw and recovery strain solutions for FEM models.

For n-sided polygonal elements, errors in both the displacement norm and the energy norm defined in Equations 4.63 and 4.64 are used.

For these examples of adaptive analysis, to study the effectiveness of the present adaptive procedure, uniformly refined models of NS-FEM-T3 are also used. The results of NS-FEM-T3 will be compared with those of the standard linear FEM-T3 using both adaptive and uniformly refined models. For the adaptive procedure using FEM-T3, we use the same error indicator and the same refinement algorithm as that used in NS-FEM-T3. However in FEM-T3, the first-order recovery strain $\tilde{\boldsymbol{\varepsilon}}^R$ is obtained using Equation 4.53.

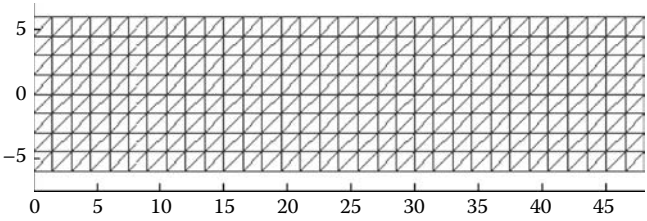

FIGURE 6.6 Domain discretization of the cantilever using triangular elements.

Example 6.7.1: A Rectangular Cantilever Loaded at the end

The rectangular cantilever loaded at the end described in Example 5.8.1 is used again in this examination. The geometry and boundary conditions of the cantilever are plotted in Figure 5.6. Problem domain discretizations with quadrilateral, *n*-sided polygonal, and triangular elements are shown in Figures 5.7 and 6.6.

Figure 6.7 shows that the stresses computed using NS-FEM-T3 and NS-FEM-Q4 agree well with the analytical solutions. Figure 6.8 shows the overall comparison of the stress distribution obtained using *n*NS-FEM and exact formulae. Very good agreement was observed. The numerical results of strain energy are presented in Tables 6.4 and 6.5, and are plotted in Figure 6.9 against the DOFs, revealing the convergence of the solution of all the models used. It can be found that the *n*NS-FEM, NS-FEM-Q4, and NS-FEM-T3 give upper bound

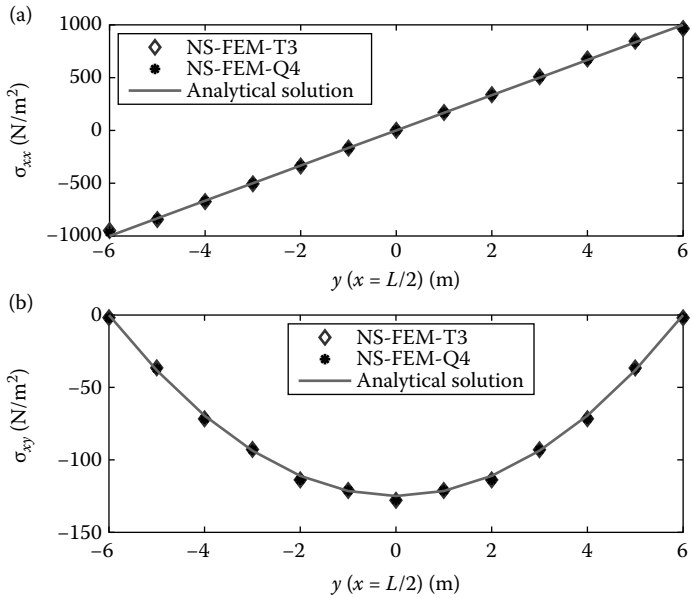

FIGURE 6.7 Comparison of the numerical results of NS-FEM models and analytical solutions for the cantilever loaded at the end: (a) normal stress σ_{xx} and (b) shear stress τ_{xy}.

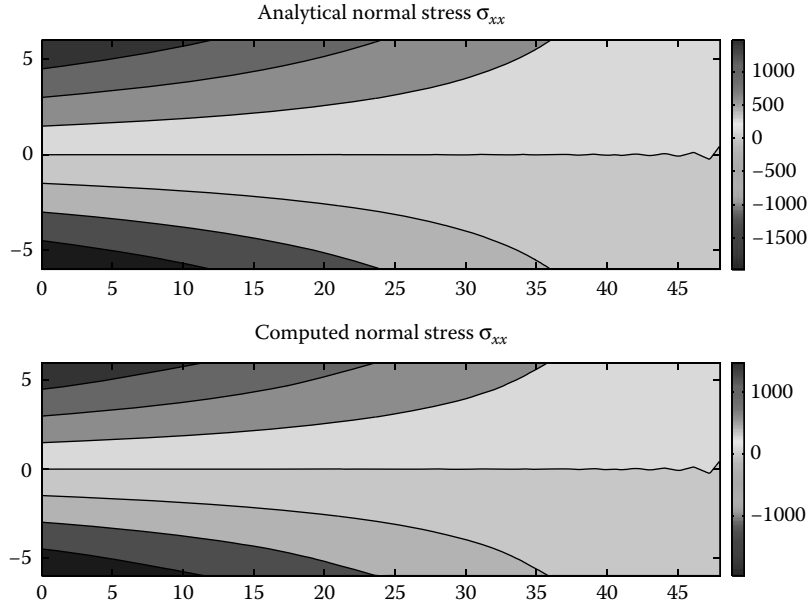

FIGURE 6.8 Contour of the analytical and the numerical normal stress σ_{xx} (N/m^2) for the cantilever obtained using *n*NS-FEM.

solutions in the strain energy, that is, the strain energies of *n*NS-FEM, NS-FEM-Q4, and NS-FEM-T3 are always larger than the exact one and converge to it with the increase of DOFs. In contrast, *n*CS-FEM, FEM-Q4, and FEM-T3 produce lower bound solutions in the strain energy. These results imply that we

TABLE 6.4

Strain Energy (Nm) Obtained Using Different Methods[a] for the Cantilever Problem Using the Same Set of Nodes

	Mesh (16 × 4)	**Mesh (24 × 6)**	**Mesh (32 × 8)**	**Mesh (40 × 10)**	**Mesh (48 × 12)**	**Analytical Solution**
DOFs	170	350	694	902	1274	
FEM-T3	3.7134	4.0973	4.2533	4.3301	4.3731	4.4747
FEM-Q4	4.3362	4.4118	4.4390	4.4518	4.4587	4.4747
CS-FEM-Q4	4.4310	4.4550	4.4635	4.4675	4.4697	4.4747
NS-FEM-T3	4.9785	4.7031	4.6051	4.5591	4.5338	4.4747
NS-FEM-Q4	4.7176	4.5898	4.5415	4.5183	4.5053	4.4747
ES-FEM-T3 [32]	4.4097	4.4539	4.4654	4.4697	4.4717	4.4747
αFEM-T3 [33] ($\alpha_{exact} = 0.6$)	4.4071	4.4566	4.4681	4.4719	4.4734	4.4747

[a] The numerical solutions of methods ES-FEM-T3 [32] and αFEM-T3 [33] presented in the following chapters are also provided in this table for easy reference.

TABLE 6.5

Strain Energy (Nm) Obtained Using Different Methods[a] for the Cantilever Problem Using the Same Polygonal Meshes

	Mesh 1	Mesh 2	Mesh 3	Mesh 4	Mesh 5	Analytical Solution
DOFs	344	704	1192	1808	2552	
*n*CS-FEM	4.1879	4.3347	4.3928	4.4218	4.4369	4.4747
*n*NS-FEM	4.6017	4.5397	4.5149	4.4999	4.4922	4.4747
*n*ES-FEM [34]	4.3800	4.4388	4.4532	4.4616	4.4657	4.4747

[a] The numerical solutions of the method *n*ES-FEM [34] presented in Chapter 7 are also provided in this table for easy reference.

now have a very simple procedure to determine the upper and lower bounds of the exact solution in a global error, by using NS-FEM together with CS-FEM or FEM and the same mesh.

Table 6.6 and Figure 6.10 compare solution errors in the displacement norm obtained using NS-FEM-T3 and NS-FEM-Q4, together with those of FEM and CS-FEM-Q4. When the finest mesh ($h = 1$ m) is used, the error of NS-FEM-T3 is about 0.6 times that of FEM-T3. The error of NS-FEM-Q4 is about 2 times that of FEM-Q4, but only 1/2 that of NS-FEM-T3. NS-FEM models performed in between FEM-T3 and FEM-Q4. In terms of convergence rate, all the models have a numerical rate slightly below the theoretical value of 2.0, and all the S-FEM models perform generally slightly better than the FEM counterparts.

Table 6.7 and Figure 6.11 compare the results of the energy norm of NS-FEM-T3 and NS-FEM-Q4 together with those of FEM and CS-FEM-Q4. It is seen that NS-FEM-T3 and NS-FEM-Q4 stand out clearly. When the finest mesh ($h = 1$ m) is used, the error of NS-FEM-T3 solution is about 1/8 that of FEM-T3, 1/3 that of FEM-Q4, and even better than FEM-Q4-Re. NS-FEM-Q4 performed better than NS-FEM-T3, but only by a small margin. In terms of convergence rate, all the S-FEM models performed much better than the FEM models, and all are significantly above 1.0, which is the theoretical value of the weak formulation. This shows that the S-FEM models are "superconvergent." NS-FEM-T3 has a rate of 1.2: a quite strong superconvergence.

Overall, CS-FEM-Q4 performed best for this problem. However, considering mesh generation issues and accuracy in stress (measured by the energy norm), NS-FEM-T3 is preferred, but uses only the triangular mesh. In addition, NS-FEM-T3 delivers an upper bound solution.

From this example we also note that NS-FEM-T3 and NS-FEM-Q4 possess three interesting properties similar to those of an equilibrium FEM model: (1) the strain energy is an upper bound of the exact solution; (2) the solution in the strain (stress) field is ultra-accurate and superconvergent; and (3) the displacement solutions are not so significantly more accurate but are still better than those of FEM-T3.

Note that the displacement solution in terms of convergence rate from an FEM model is quite difficult to improve, simply because it is already quite

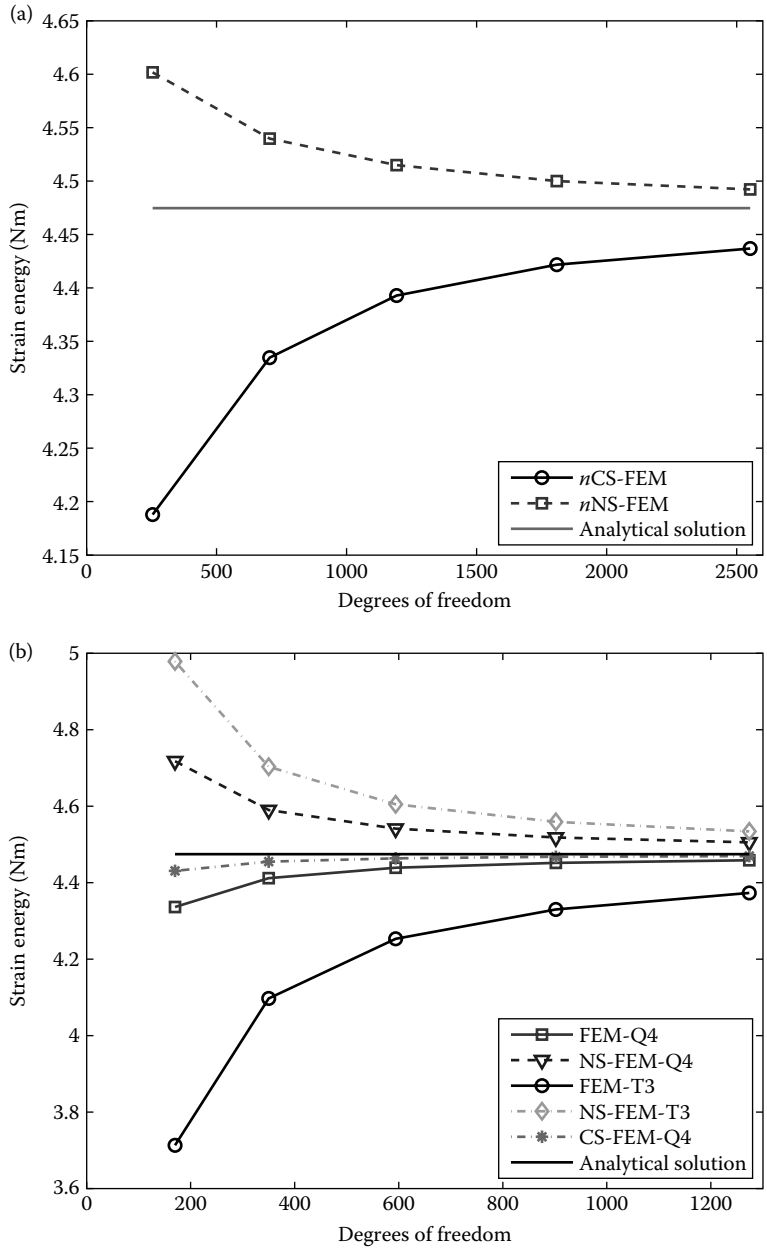

FIGURE 6.9 Convergence of the strain energy solution for the cantilever problem: (a) *n*-sided polygonal elements and (b) triangular and four-node elements.

TABLE 6.6

Error in Displacement Norm Obtained Using Different Methods[a] for the Cantilever Problem Using the Same Set of Nodes

	Mesh (16 × 4)	**Mesh (24 × 6)**	**Mesh (32 × 8)**	**Mesh (40 × 10)**	**Mesh (48 × 12)**
h (m)	4.0	2.0	1.5	1.2	1.0
FEM-T3	1.78e − 02	8.80e − 03	5.16e − 03	3.36e − 03	2.36e − 03
FEM-Q4	2.97e − 03	1.35e − 03	7.63e − 04	4.90e − 04	3.41e − 04
CS-FEM-Q4	7.40e − 04	3.31e − 04	1.87e − 04	1.20e − 04	8.31e − 05
NS-FEM-T3	1.23e − 02	5.60e − 03	3.20e − 03	2.07e − 03	1.45e − 03
NS-FEM-Q4	6.15e − 03	2.91e − 03	1.68e − 03	1.10e − 03	7.71e − 04
ES-FEM-T3 [32]	1.32e − 03	3.74e − 04	1.47e − 04	6.94e − 05	3.68e − 05
αFEM-T3 [33] ($\alpha_{exact} = 0.6$)	1.26e − 03	2.65e − 04	6.86e − 05	2.69e − 05	2.48e − 05

[a] The numerical solutions of methods ES-FEM-T3 [32] and αFEM-T3 [33] presented in the following chapters are also provided in this table for easy reference.

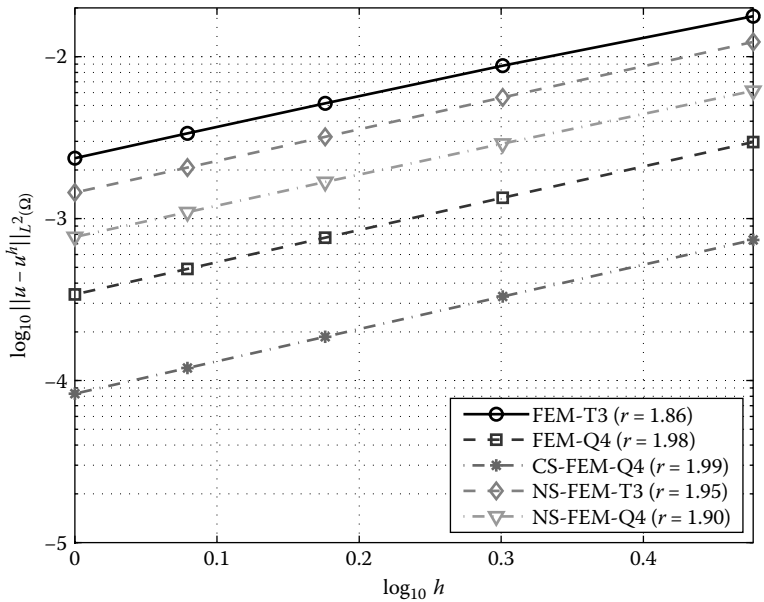

FIGURE 6.10 Error in the displacement norm for the NS-FEM solution in comparison with that of other methods for the cantilever problem using the same distribution of nodes.

"optimal" in the weak-form methods with displacement as the primary field variable. The rate of convergence in the displacement norm is already 2.0 for linear elements. Therefore, room for improvement is mainly in the energy norm or stress solution. We expect that the optimal rate for the energy norm should be

TABLE 6.7

Error in Energy Norm Obtained Using Different Methods[a] for the Cantilever Problem Using the Same Distribution of Nodes

	Mesh (16 × 4)	**Mesh (24 × 6)**	**Mesh (32 × 8)**	**Mesh (40 × 10)**	**Mesh (48 × 12)**
h (m)	4.0	2.0	1.5	1.2	1.0
FEM-T3	8.77e − 01	6.16e − 01	4.71e − 01	3.80e − 01	3.18e − 01
FEM-Q4	3.71e − 01	2.49e − 01	1.88e − 01	1.50e − 01	1.25e − 01
CS-FEM-Q4	2.38e − 01	1.30e − 01	8.46e − 02	6.05e − 02	4.60e − 02
NS-FEM-T3	1.44e − 01	9.45e − 02	6.71e − 02	5.06e − 02	3.99e − 02
NS-FEM-Q4	1.16e − 01	7.28e − 02	5.10e − 02	3.83e − 02	3.00e − 02
FEM-T3-Re	5.76e − 01	3.04e − 01	1.87e − 01	1.28e − 01	9.34e − 02
FEM-Q4-Re	2.06e − 01	1.14e − 01	7.49e − 02	5.38e − 02	4.10e − 02
ES-FEM-T3 [32]	2.96e − 01	1.58e − 01	1.02e − 01	7.28e − 02	5.53e − 02
αFEM-T3 [33] ($\alpha_{exact} = 0.6$)	2.93e − 01	1.54e − 01	9.86e − 02	7.00e − 02	5.31e − 02

[a] The numerical solutions of methods ES-FEM-T3 [32] and αFEM-T3 [33] presented in the following chapters are also provided in this table for easy reference.

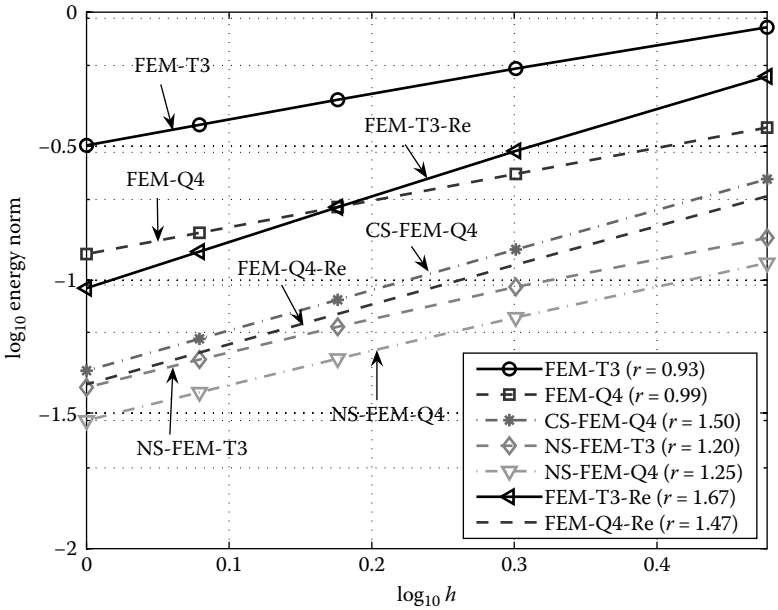

FIGURE 6.11 Error in the energy norm for the NS-FEM solution in comparison with that of other methods for the cantilever problem using the same distribution of nodes.

2.0, that is the optimal rate of the weak-form methods with stress as the primary field variable. NS-FEM-T3 is essentially a weak-form method with displacement as the primary field variable, but has achieved 1.2 for this problem, and hence is considered of quite strong superconvergence. These findings will be further confirmed by the following examples, and we will show that the S-FEM model can sometimes achieve the expected "optimal" rate of 2.0 in the energy norm.

Example 6.7.2: Infinite Plate With a Circular Hole

The infinite plate with a circular hole described in Example 5.8.2 is used again to examine the NS-FEM models. The geometry and boundary conditions of the problem are plotted in Figure 5.18. Figures 5.19 and 6.12 give the discretizations of the domain using four-node quadrilateral, *n*-sided polygonal, and triangular elements used in all the methods used for comparison.

The numerical results of strain energy are presented in Tables 6.8 and 6.9 and are plotted in Figure 6.13 against the DOFs, revealing the convergence of the solution of all the models used. It again shows the upper bound property on the strain energy of *n*NS-FEM, NS-FEM-Q4, and NS-FEM-T3, together with the lower bound property of the *n*CS-FEM, FEM-Q4, and FEM-T3. From Figures 6.14 and 6.15, all the computed displacements and stresses of *n*NS-FEM using *n*-sided polygonal elements are in very good agreement with the analytical solutions. With the refinement of the mesh, the accuracy is getting higher and higher.

Table 6.10 and Figure 6.16 compare the results of the displacement norm of NS-FEM-T3 and NS-FEM-Q4 with those of FEM and CS-FEM-Q4. It is again seen that CS-FEM-Q4 stands out clearly. When the finest mesh ($h = 0.1969$ m) is used, the error of CS-FEM-Q4 is about 1/5 that of FEM-T3 and

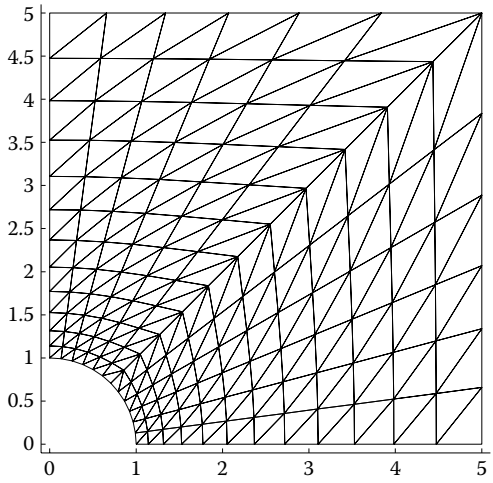

FIGURE 6.12 Domain discretization of the infinite plate with a circular hole using triangular elements.

TABLE 6.8

Strain Energy ($\times 10^{-2}$ Nm) Using Different Methods[a] for the Infinite Plate with a Circular Hole Using the Same Distribution of Nodes

	Mesh (12 x 12)	Mesh (16 x 16)	Mesh (20 x 20)	Mesh (24 x 24)	Analytical Solution
DOFs	338	578	882	1250	
FEM-T3	1.1762	1.1786	1.1797	1.1803	1.1817
FEM-Q4	1.1794	1.1805	1.1810	1.1812	1.1817
CS-FEM-Q4	1.1798	1.1807	1.1811	1.1813	1.1817
NS-FEM-T3	1.1848	1.1834	1.1827	1.1824	1.1817
NS-FEM-Q4	1.1850	1.1835	1.1827	1.1823	1.1817
ES-FEM-T3 [32]	1.1804	1.1811	1.1814	1.1815	1.1817

[a] The numerical solutions of the method ES-FEM-T3 [32] presented in the Chapter 7 are also provided in this table for easy reference.

TABLE 6.9

Strain Energy ($\times 10^{-2}$ Nm) Using Different Methods[a] for the Infinite Plate with a Circular Hole Using the Same for Polygonal Meshes

	Mesh 1	Mesh 2	Mesh 3	Mesh 4	Analytical Solution
DOFs	326	678	1158	1770	
*n*CS-FEM	1.1759	1.1791	1.1803	1.1808	1.1817
*n*NS-FEM	1.1820	1.1820	1.1820	1.1819	1.1817
*n*ES-FEM [34]	1.1785	1.1805	1.1812	1.1814	1.1817

[a] The numerical solutions of the method *n*ES-FEM [34] presented in Chapter 7 are also provided in this table for easy reference.

4/5 that of FEM-Q4. NS-FEM-T3 performed marginally better than FEM-T3. The error of NS-FEM-T3 is about 3.6 times that of FEM-Q4. In terms of convergence rate, except for FEM-T3, other models have a numerical rate slightly larger than the theoretical value of 2.0, with NS-FEM-T3 achieving the best rate of 2.15: a weak superconvergence in the displacement norm.

Table 6.11 and Figure 6.17 compare the results of the energy norm of NS-FEM-T3 and NS-FEM-Q4 with those of FEM and CS-FEM-Q4. It is again seen that NS-FEM-T3 and NS-FEM-Q4 stand out clearly. When the finest mesh ($h = 0.1969$ m) is used, the error of NS-FEM-T3 is about 1/9 that of FEM-T3, 1/5 that of FEM-Q4, 1/3.5 that of FEM-T3-Re, and even 1/2 that of FEM-Q4-Re. NS-FEM-Q4 performed better than NS-FEM-T3, but only by a small margin. In terms of convergence rate, all the S-FEM models performed much better than the FEM models, and all close to 2.0 and significantly above 1.0 that is the theoretical value of the weak formulation. This shows that the S-FEM models are super-convergent. NS-FEM-Q4 stands out clearly with a rate of 2.12: a very strong superconvergence.

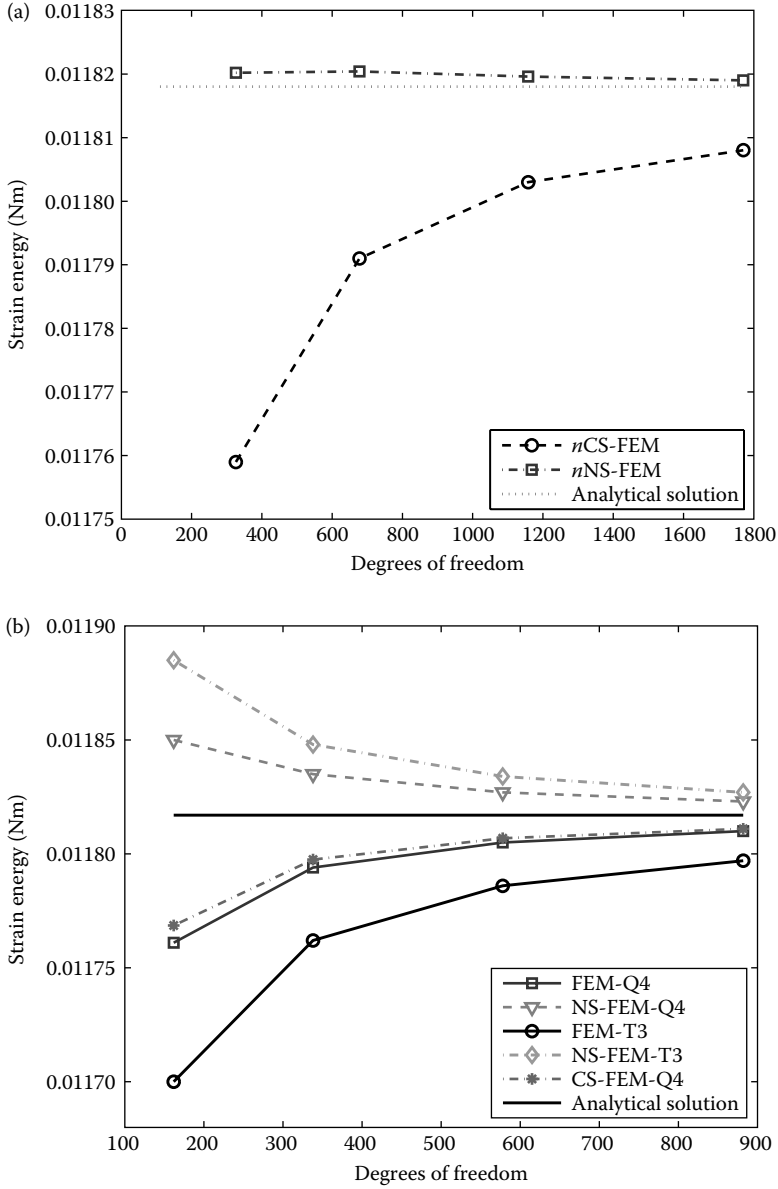

FIGURE 6.13 Convergence of the strain energy solution for the infinite plate with a circular hole: (a) *n*-sided polygonal elements and (b) triangular and four-node elements.

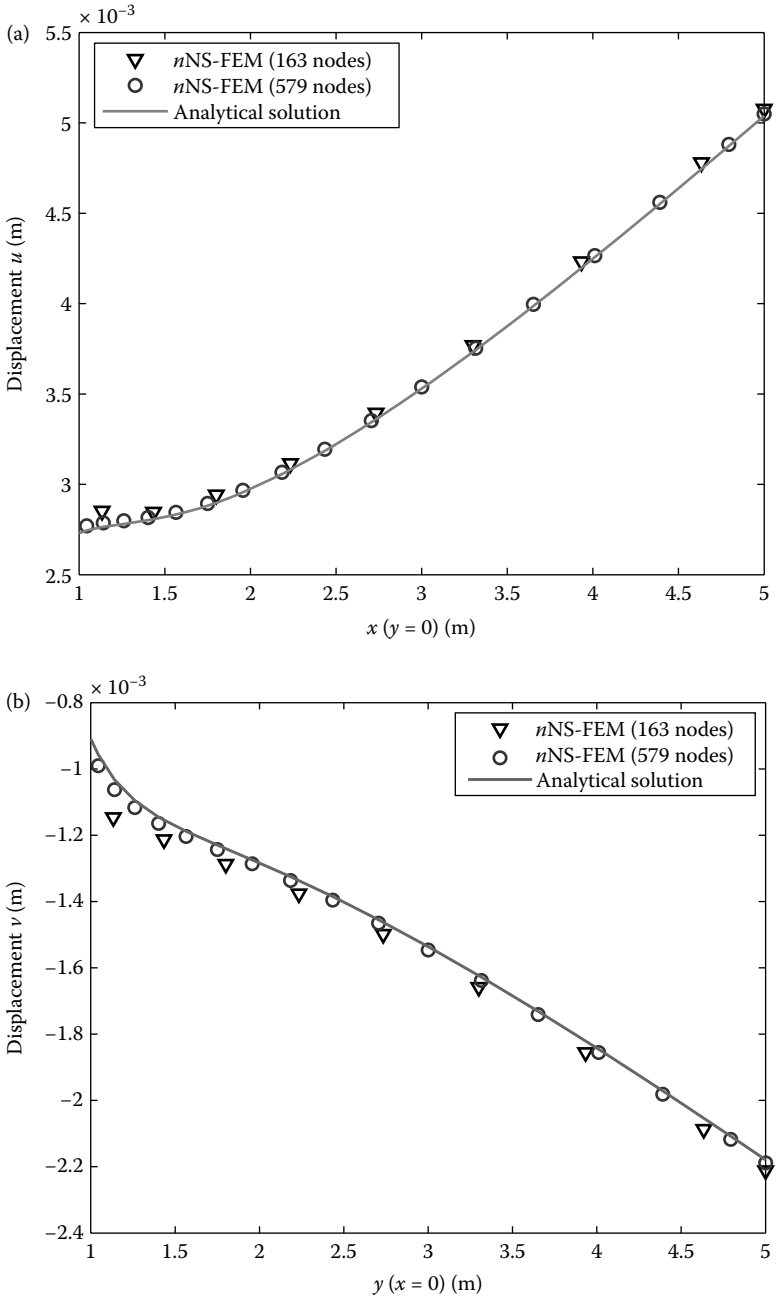

FIGURE 6.14 Exact and numerical displacements of *n*NS-FEM for the infinite plate with a circular hole: (a) displacement u(m) of nodes along the bottom side and (b) displacement v(m) of nodes along the left side.

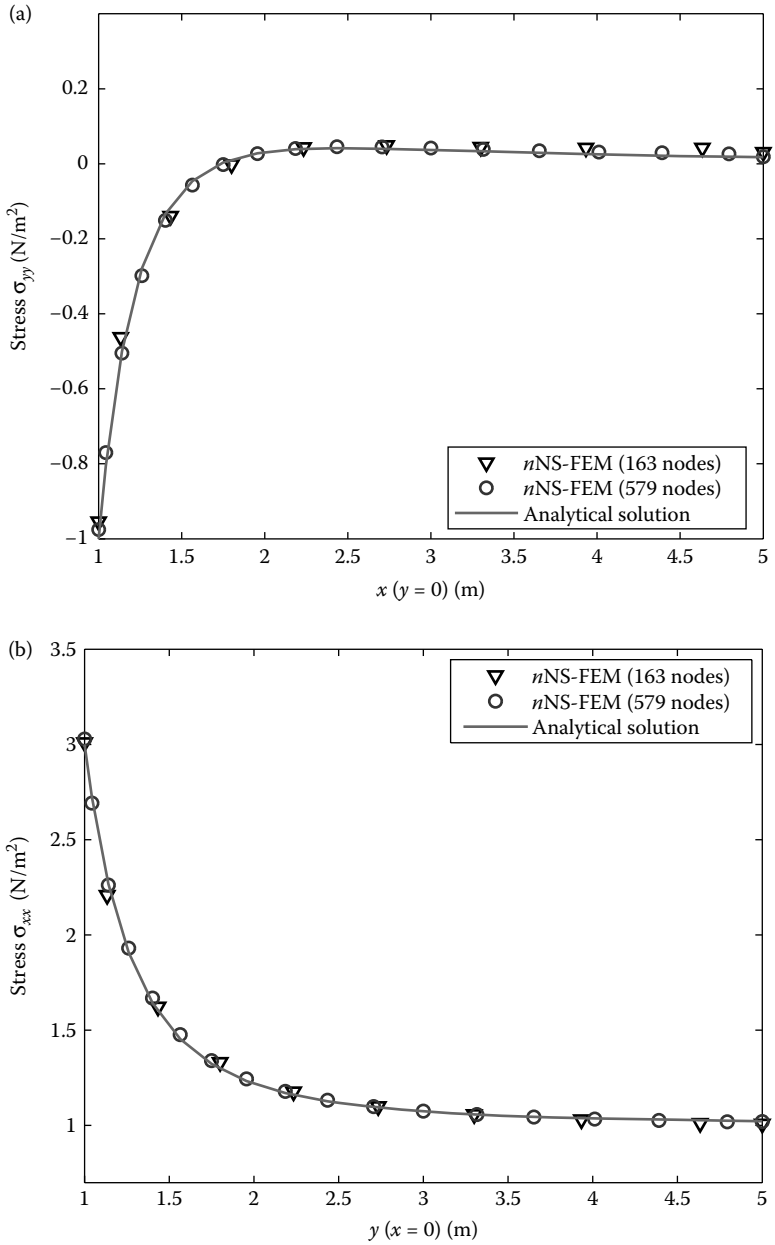

FIGURE 6.15 Exact and numerical stresses using nNS-FEM for the infinite plate with a circular hole: (a) stress σ_{yy} of nodes along the bottom side and (b) stress σ_{xx} of nodes along the left side.

TABLE 6.10

Error in Displacement Norm Obtained Using Different Methods[a] for the Infinite Plate with a Circular Hole Using the Same Distribution of Nodes

	Mesh 1	Mesh 2	Mesh 3	Mesh 4	Mesh 5
h (m)	0.5468	0.3786	0.2895	0.2343	0.1969
FEM-T3	2.80e − 04	1.42e − 04	8.45e − 05	5.61e − 05	4.01e − 05
FEM-Q4	1.08e − 04	4.46e − 05	2.40e − 05	1.50e − 05	1.03e − 05
CS-FEM-Q4	8.46e − 05	3.48e − 05	1.88e − 05	1.19e − 05	8.19e − 06
NS-FEM-T3	3.87e − 04	1.69e − 04	8.95e − 05	5.49e − 05	3.70e − 05
NS-FEM-Q4	2.73e − 04	1.29e − 04	7.04e − 05	4.35e − 05	2.94e − 05
ES-FEM-T3 [32]	8.03e − 05	2.95e − 05	1.63e − 05	1.06e − 05	7.46e − 06

[a] The numerical solutions of the method ES-FEM-T3 [32] presented in Chapter 7 are also provided in this table for easy reference.

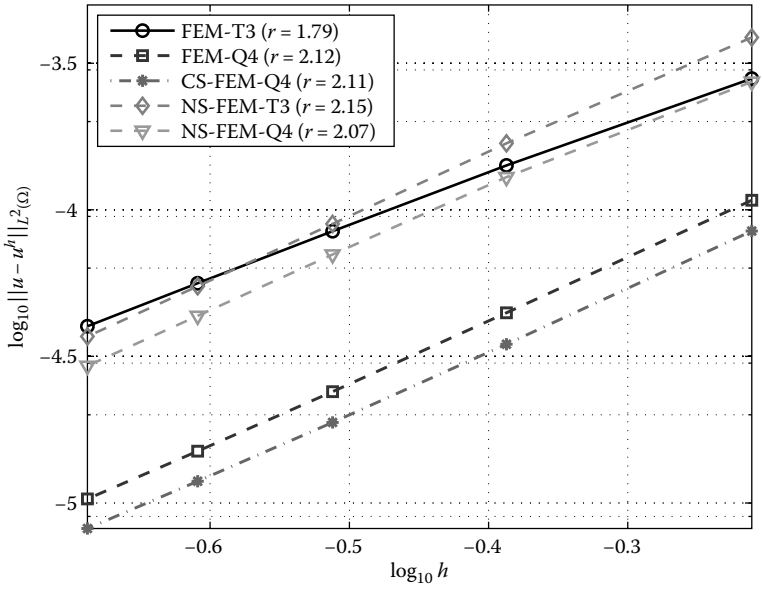

FIGURE 6.16 Error in the displacement norm for the NS-FEM solution in comparison with that of other methods for the infinite plate with a circular hole using the same distribution of nodes.

Figure 6.18 plots the error in solution in the displacement norm against Poisson's ratio changing from 0.4 to 0.4999999 obtained using FEM and NS-FEM models. Two types of element meshes are used in this study: n-sided polygonal elements (579 nodes) and four-node quadrilateral elements (mesh 16 × 16). The results show that nNS-FEM and NS-FEM-Q4 are naturally "immune"

TABLE 6.11

Error in Energy Norm Obtained Using Different Methods[a] for the Infinite Plate with a Circular Hole Using the Same Distribution of Nodes

	Mesh 1	**Mesh 2**	**Mesh 3**	**Mesh 4**	**Mesh 5**
h (m)	0.5468	0.3786	0.2895	0.2343	0.1969
FEM-T3	9.95e − 03	6.89e − 03	5.20e − 03	4.17e − 03	3.48e − 03
FEM-Q4	6.09e − 03	3.86e − 03	2.79e − 03	2.18e − 03	1.79e − 03
CS-FEM-Q4	5.12e − 03	2.70e − 03	1.61e − 03	1.06e − 03	7.41e − 04
NS-FEM-T3	3.08e − 03	1.50e − 03	8.52e − 04	5.39e − 04	3.68e − 04
NS-FEM-Q4	2.33e − 03	1.06e − 03	5.77e − 04	3.53e − 04	2.35e − 04
FEM-T3-Re	7.78e − 03	4.39e − 03	2.72e − 03	1.82e − 03	1.31e − 03
FEM-Q4-Re	5.22e − 03	2.72e − 03	1.61e − 03	1.05e − 03	7.41e − 04
ES-FEM-T3 [32]	5.27e − 03	2.69e − 03	1.59e − 03	1.04e − 03	7.29e − 04

[a] The numerical solutions of the method ES-FEM-T3 [32] presented in Chapter 7 are also provided in this table for easy reference.

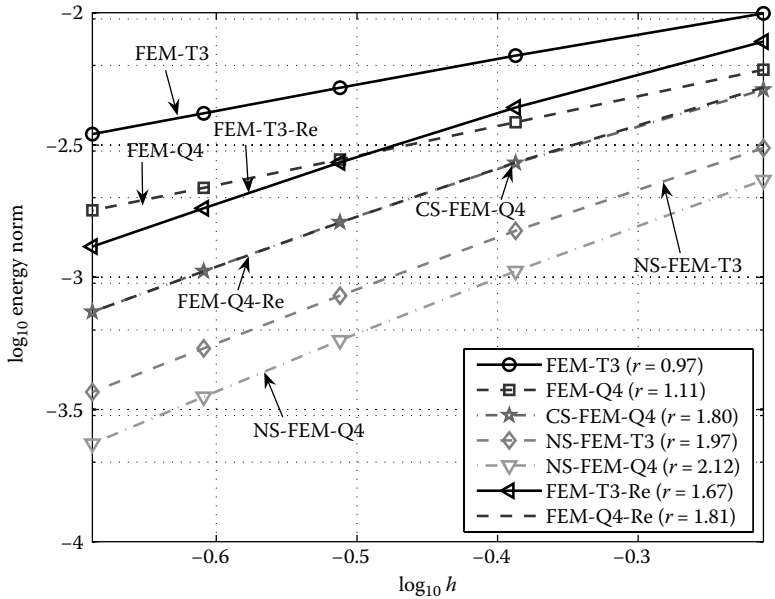

FIGURE 6.17 Error in the energy norm for the NS-FEM solution in comparison with that of other methods for the infinite plate with a circular hole using the same distribution of nodes.

from the volumetric locking: the error does not increase when Poisson's ratio approaches 0.5. *n*CS-FEM and FEM-Q4 are subjected to volumetric locking, resulting in a drastic accuracy loss in numerical solutions when Poisson's ratio approaches 0.5.

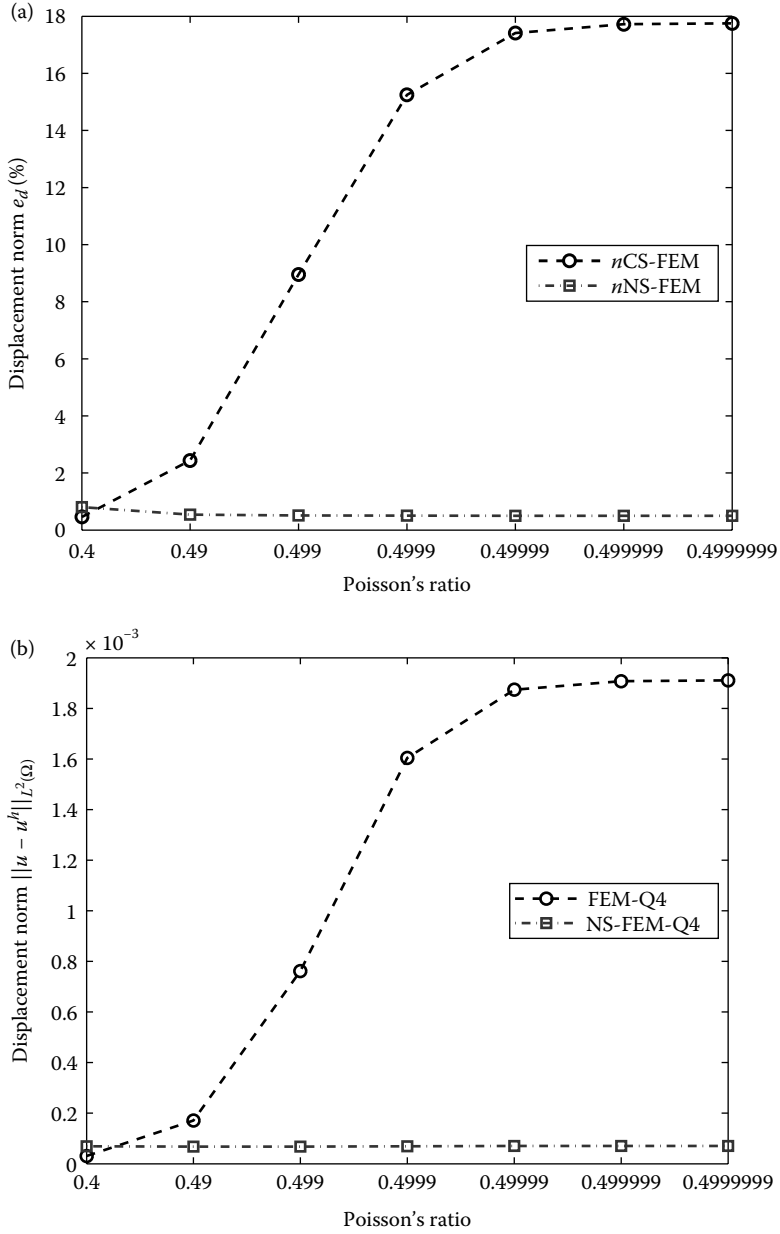

FIGURE 6.18 Error in the displacement norm versus Poisson's ratios close to 0.5 for the infinite plate with a circular hole: (a) *n*-sided polygonal elements (579 nodes) and (b) four-node quadrilateral elements (289 nodes).

Overall, it is again seen that NS-FEM models possess four interesting properties of an equilibrium FEM model: (1) the strain energy is an upper bound of the exact solution; (2) it is immune naturally from volumetric locking; (3) stress solutions are ultra-accurate and superconvergent; and (4) displacement solutions are at the same level as that of FEM-T3 using the same mesh.

For the adaptive analysis using NS-FEM-T3 and FEM-T3, we now examine the accuracy and convergence rate of energy norms as well as the effectivity index of error indicators. Three kinds of energy norms are used in the evaluation, the standard energy norm $\|\boldsymbol{\varepsilon} - \check{\boldsymbol{\varepsilon}}\|_{L^2}$ (E-raw error), the recovery energy norm $\left\|\boldsymbol{\varepsilon} - \check{\boldsymbol{\varepsilon}}^R\right\|_{L^2}$ (E-rec error), and *a posteriori* energy norm $\left\|\check{\boldsymbol{\varepsilon}}^R - \check{\boldsymbol{\varepsilon}}\right\|_{L^2}$ (R-raw error), where $\check{\boldsymbol{\varepsilon}}$ is the numerical result of the strain field obtained using any of NS-FEM-T3 and FEM-T3, $\mathbf{R}\check{\boldsymbol{\varepsilon}}$ is the first-order recovery strain field, and $\boldsymbol{\varepsilon}$ is the exact strain field.

Figure 6.19 shows the results of errors in various energy norms plotted together for two models: NS-FEM-T3 and FEM-T3. It is a quite busy plot, but gives very clear comparisons of all these error measures in the same picture. A careful comparison study from Figure 6.19 gives us the following major findings:

1. For NS-FEM-T3, the E-rec error $\left\|\boldsymbol{\varepsilon} - \bar{\boldsymbol{\varepsilon}}^R\right\|_{L^2}$ is much smaller than E-raw and R-raw errors. This implies that the recovery strain field $\bar{\boldsymbol{\varepsilon}}^R$ is much more accurate than the raw strain fields, and hence we shall use it as the final numerical solution. This finding is also true for the FEM-T3 model.
2. The errors in the NS-FEM-T3 solution in any of the three different error measures are much smaller than those of the FEM-T3 solution in the corresponding error measures.
3. The convergence rate of the norms in the NS-FEM-T3 solution in any of the three different error measures is consistently higher than that of the FEM-T3 solution in the corresponding error measures.
4. The E-rec errors of both NS-FEM-T3 and FEM-T3 are all superconvergent, but the convergence rate of NS-FEM-T3 ($r = 1.97$) is much higher than that of FEM-T3 ($r = 1.67$).
5. For the NS-FEM-T3 model, the R-raw error estimator $\left\|\bar{\boldsymbol{\varepsilon}}^R - \bar{\boldsymbol{\varepsilon}}\right\|_{L^2}$ is a very good alternative to the E-raw error $\|\boldsymbol{\varepsilon} - \bar{\boldsymbol{\varepsilon}}\|_{L^2}$, especially when a fine mesh is used. In other words, the recovery strain field is a very good representation of the exact strain field for the purpose of error estimation. The R-raw error $\left\|\bar{\boldsymbol{\varepsilon}}^R - \bar{\boldsymbol{\varepsilon}}\right\|_{L^2}$ is, however, an underestimated (not on the conservative side) E-raw error. This finding is also true for the FEM-T3 model.
6. A possible way of devising a conservative error estimate is to use the recovery strain field $\bar{\boldsymbol{\varepsilon}}^R$ as the final numerical strain field solution, but to use $\left\|\bar{\boldsymbol{\varepsilon}}^R - \bar{\boldsymbol{\varepsilon}}\right\|_{L^2}$ as the error bound of $\bar{\boldsymbol{\varepsilon}}^R$ to the exact solution. This is because we can expect

$$\left\|\boldsymbol{\varepsilon} - \bar{\boldsymbol{\varepsilon}}^R\right\|_{L^2} \leq \left\|\bar{\boldsymbol{\varepsilon}}^R - \bar{\boldsymbol{\varepsilon}}\right\|_{L^2}, \tag{6.29}$$

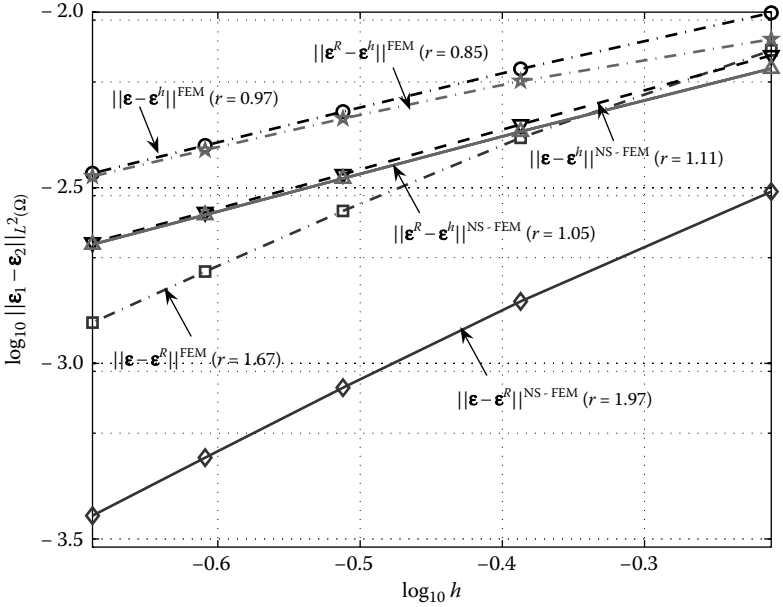

FIGURE 6.19 Errors in various energy norms for the solutions of NS-FEM-T3 and FEM-T3. The problem of the infinite plate with a circular hole ($\boldsymbol{\varepsilon}_1$ in the vertical axis stands for $\boldsymbol{\varepsilon}$ or $\mathbf{R}\boldsymbol{\varepsilon}^h$, and $\boldsymbol{\varepsilon}_2$ stands for $\boldsymbol{\varepsilon}^h$ or $\mathbf{R}\boldsymbol{\varepsilon}^h$, where $\boldsymbol{\varepsilon}^h$ stands the numerical solutions).

especially for fine meshes. Equation 6.29 can be easily understood intuitively. The left-hand side (LHS) of Equation 6.29 is the "distance" between a linear strain field and a higher-order continuous one, but the right-hand side (RHS) is the "distance" between a piecewise constant strain field and a linear one. The former has clearly a higher order of convergence than the latter and hence we shall have Equation 6.29 at least for fine meshes. This also can be observed from Figure 6.19.

Figure 6.20 plots the effectivity indexes θ for both NS-FEM-T3 and FEM-T3 models, which shows that

7. The effectivity indexes θ of both NS-FEM-T3 and FEM-T3 approach unity when the mesh is refined, but the results of NS-FEM-T3 are closer to unity than those of FEM-T3. The results of effectivity indexes θ in Figure 6.20 are echoed in Figure 6.19 and reconfirm item (5).

Now, we can conduct an adaptive analysis with the error indicators for the same problem of the infinite plate with a circular hole. The results of the strain energy obtained using NS-FEM-T3 and FEM-T3 with both uniform and adaptive models are shown in Figure 6.21. The solution error in the standard energy norm (E-raw error) obtained using NS-FEM-T3 and FEM-T3 with both uniform and adaptive models is shown in Figure 6.22. First, the results show that the adaptive models for both NS-FEM-T3 and FEM-T3 give a much higher convergence rate compared to the uniformly refined models. This demonstrates the effectiveness

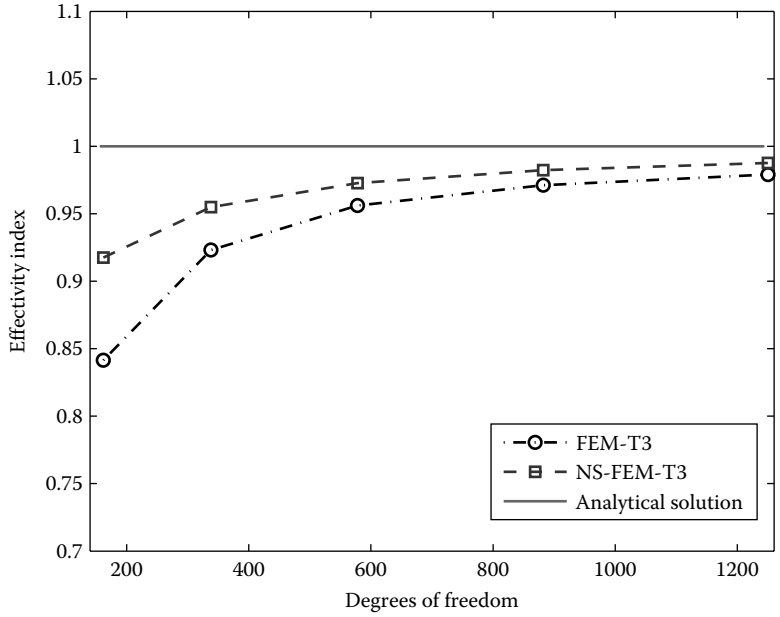

FIGURE 6.20 Effectivity index of the recovery error indicator for the solution of NS-FEM-T3 and FEM-T3 for the infinite plate with a circular hole.

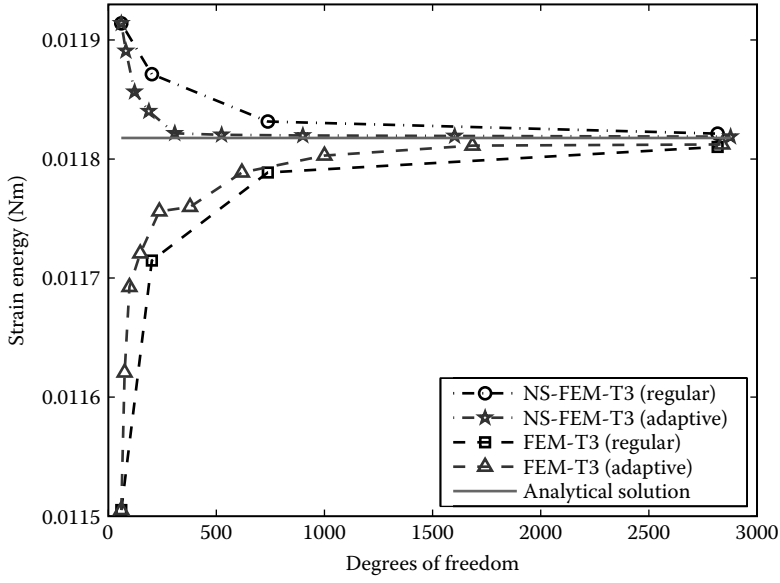

FIGURE 6.21 Convergence of the strain energy solution of NS-FEM-T3 and FEM-T3 for the infinite plate with a circular hole.

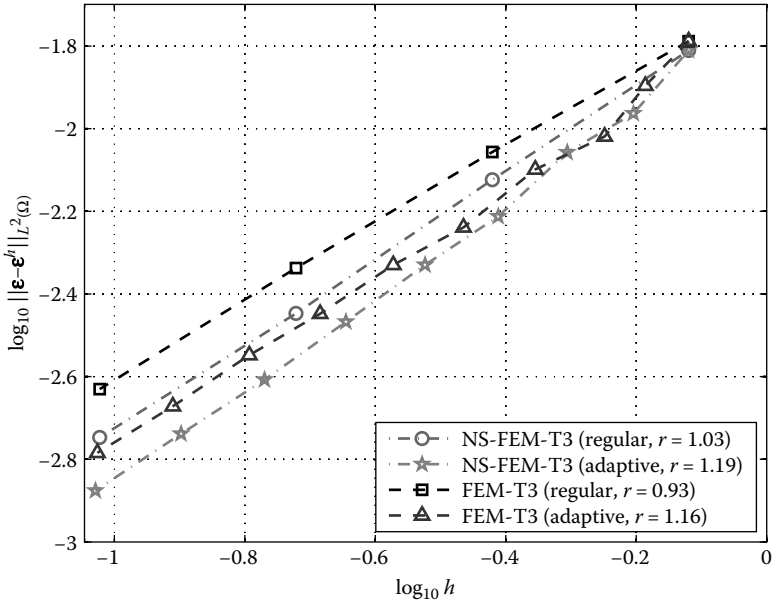

FIGURE 6.22 Error in the standard energy norms for solutions of NS-FEM-T3 and FEM-T3 for the infinite plate with a circular hole.

of the presented adaptive procedure. Second, compared with the linear FEM-T3, the NS-FEM-T3 achieves better accuracy and a higher convergence rate for both uniform and adaptive models. Third, the upper bound property in the strain energy of NS-FEM-T3 is always verified during the adaptive procedure.

Figure 6.23 compares the errors in the standard energy norms (E-raw error) and error estimators (Equation 6.23) (R-raw error) obtained using NS-FEM-T3 and FEM-T3. The results again show that the standard energy norms (E-raw errors) are very close to the error estimators (Equation 6.23) (R-raw errors) for both methods, but the results of NS-FEM-T3 are better and have a higher convergence rate than those of FEM-T3. Figure 6.24 again verifies the asymptotically exact property of the error estimator (Equation 6.23) in which the effectivity indexes of adaptive schemes for both methods converge to unity when the mesh is refined.

Figure 6.25 shows the sequence of meshes produced during the adaptive refinement steps using NS-FEM-T3. The results show that the refinement is most active in regions with significant stress concentration, as expected.

Example 6.7.3: L-Shaped 2D Solid Under Tension: Adaptive Analysis

Consider an L-shaped domain subject to unit tension. The dimensions and boundary conditions are shown in Figure 6.26. The thickness of the solid is $t = 1$ m, and a plane stress problem is considered. The material parameters of

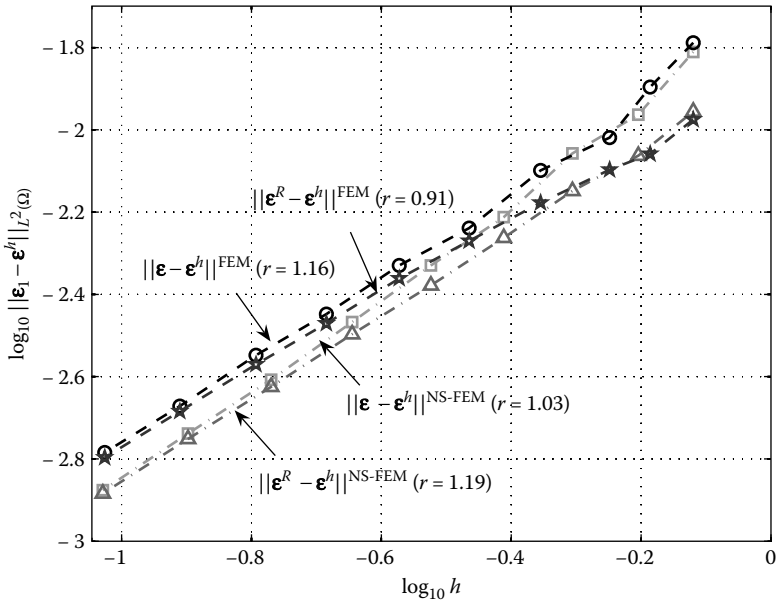

FIGURE 6.23 Error in the standard energy norms and a posteriori energy norms (or error estimators [Equation 6.23]) for solutions of NS-FEM-T3 and FEM-T3 for the infinite plate with a circular hole ($\boldsymbol{\varepsilon}_1$ in the vertical axis stands for $\boldsymbol{\varepsilon}$ or $\mathbf{R}\boldsymbol{\varepsilon}^h$).

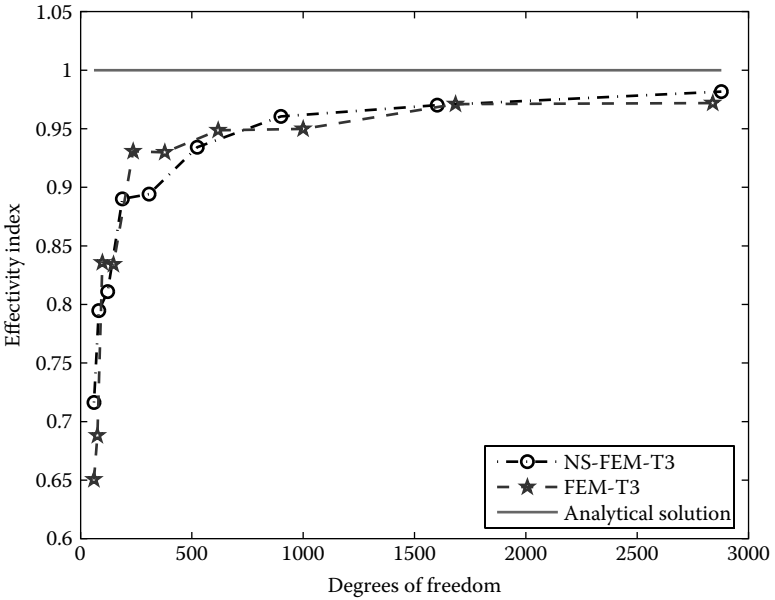

FIGURE 6.24 Effectivity index (adaptive scheme) of the recovery error indicator for solutions of NS-FEM-T3 and FEM-T3 for the infinite plate with a circular hole.

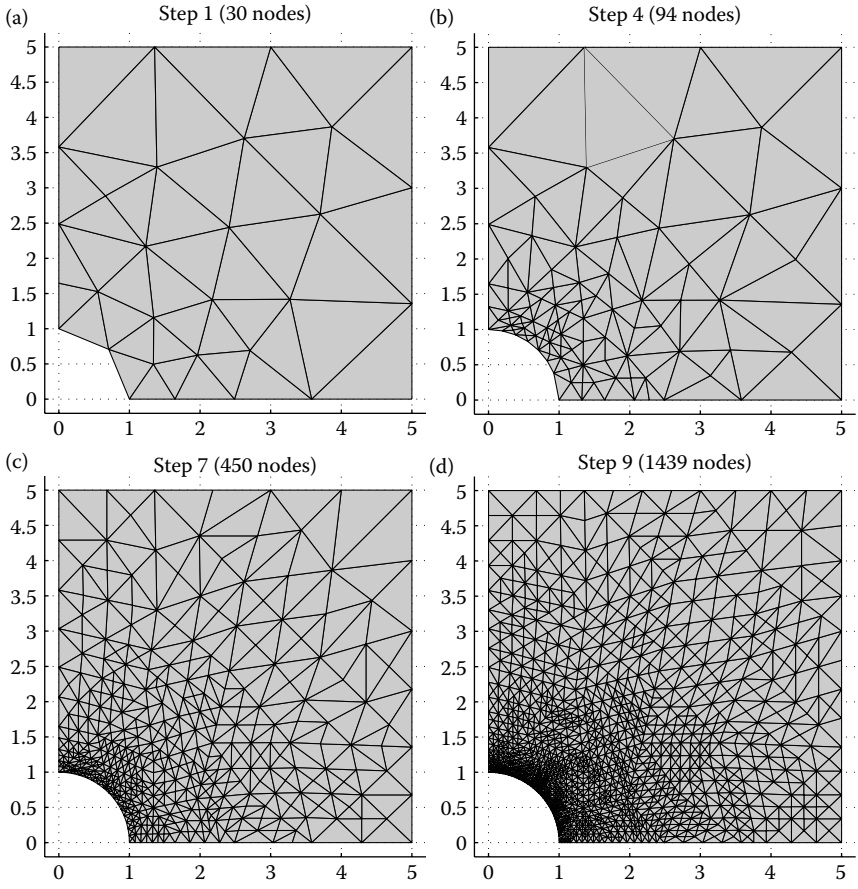

FIGURE 6.25 Sequence of adaptive refined meshes for the quarter plate using NS-FEM-T3. (a) Step 1 (30 nodes); (b) Step 4 (94 nodes); (c) Step 7 (450 nodes); and (d) Step 9 (1439 nodes).

the structure are $E = 1.0\,\text{N/m}^2$ and $\nu = 0.3$. In this example, stress singularity occurs at the re-entrant corner, and hence adaptive analysis is preferred for this type of problem.

The exact strain energy in this problem is not available. However, it can be estimated through the procedure of Richardson's extrapolation [26] from the solutions of displacement models and equilibrium models [16]. The estimated strain energy is the average of these two extrapolated strain energies. As given in Ref. [27], the reference strain energy is approximately 15,566 (Nm).

The error in energy norms for NS-FEM-T3 and FEM-T3 using both uniform and adaptive models is shown in Figure 6.27. Again, the results show that adaptive models using both NS-FEM-T3 and FEM-T3 give higher convergence rates compared to uniformly refined models. The results of NS-FEM-T3 are more accurate and converge faster than those of FEM-T3. For this problem, we have no analytical solution. Therefore we cannot show the superconvergence

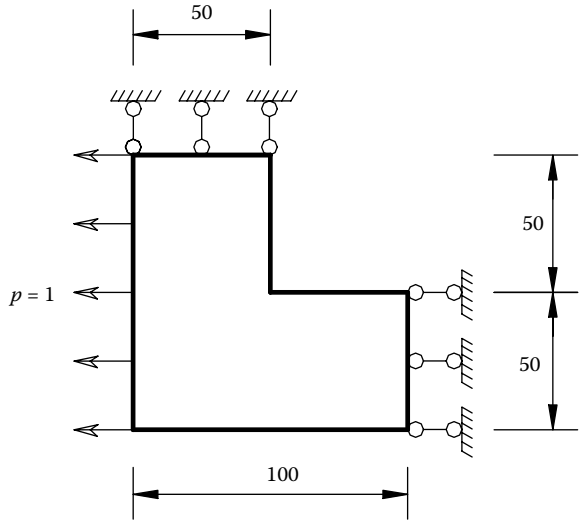

FIGURE 6.26 Problem setting for the L-shaped solid (length unit in m).

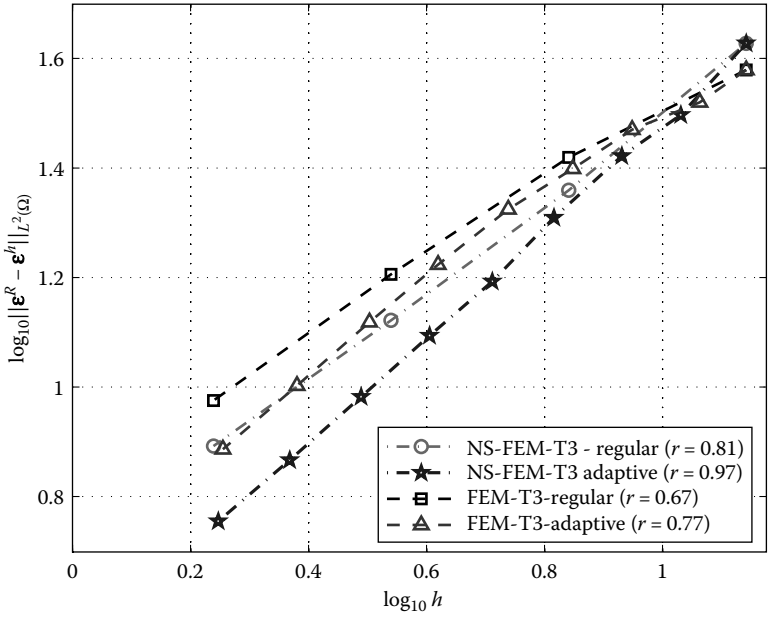

FIGURE 6.27 Error in a posteriori energy norms using the error indicator (Equation 6.23) for the solution of the L-shaped 2D solid problem.

of the errors measured in the recovery energy norm (E-rec error) between the analytical and recovery strains. However, based on the convergence rate of the errors in the a posteriori energy norm (R-raw error) of NS-FEM-T3 ($r = 0.97$), which is almost 1, we can see that the recovery strain is a reliable representation of the analytical strain and can produce efficiently an optimal convergence rate in the energy norm for this singular problem.

Figure 6.28 verifies the upper bound property in the strain energy of NS-FEM-T3 during the adaptive procedure. Figure 6.29 shows some steps of adaptive refinement models using NS-FEM-T3. The results show clearly that the refinement is focusing on the re-entrant corner where the stress is singular.

Example 6.7.4: Crack Problem in Linear Elasticity: Adaptive Analysis

Consider a crack problem in linear elasticity as shown in Figure 6.30. Data of the structure are $E = 1.0\,\text{N/m}^2$, $\nu = 0.3$, and $t = 1\,\text{m}$. Because of symmetry about the y-axis, only half the domain is modeled. By incorporating dual analysis [2] and the procedure of Richardson's extrapolation with very fine meshes, Beckers [27] proposed a good approximation of the exact strain energy as 8085 (Nm).

This crack problem has high singularity at the crack tip. As a result, the convergence rate of a posteriori energy norms (R-raw error) between the recovery and numerical strains using the uniformly refined models is low ($r = 0.35$

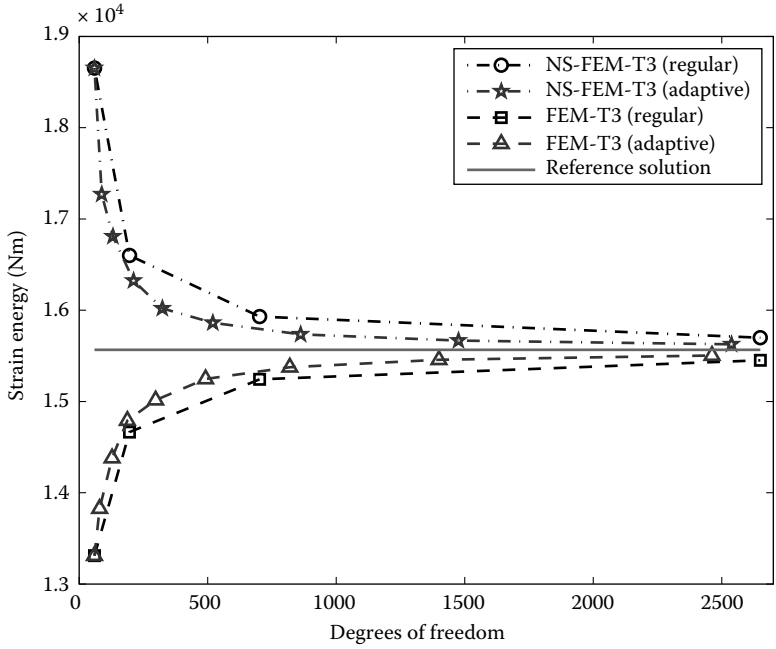

FIGURE 6.28 Convergence of the strain energy solution for the L-shaped 2D solid problem.

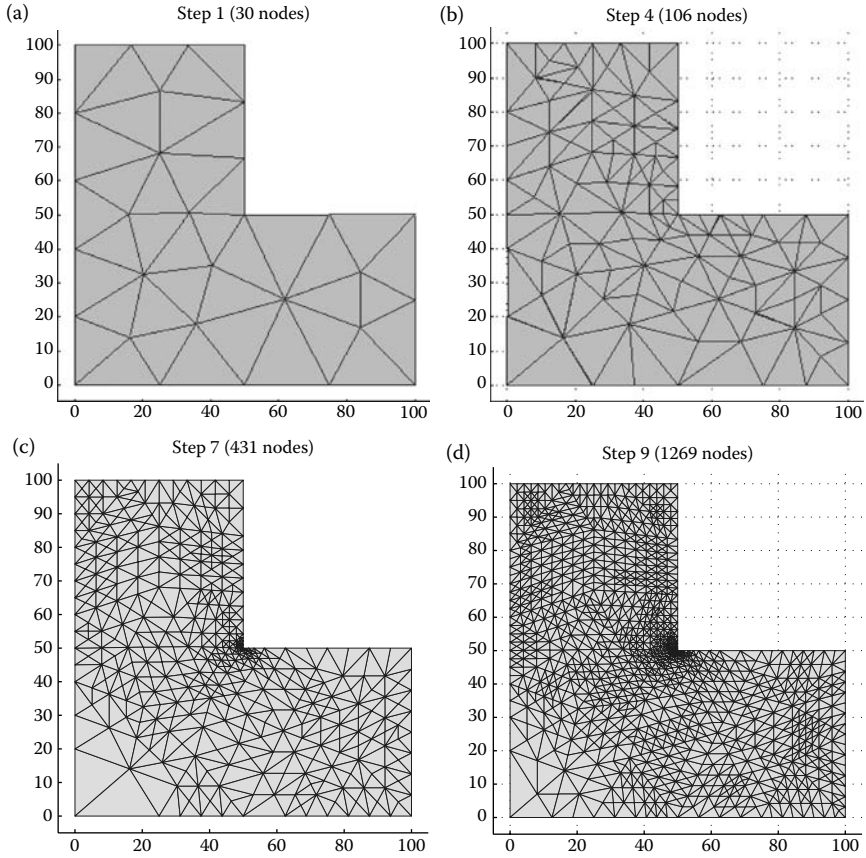

FIGURE 6.29 Sequence of adaptive refined meshes for the L-shaped 2D solid using NS-FEM-T3. (a) Step 1 (30 nodes); (b) Step 4 (106 nodes); (c) Step 7 (431 nodes); and (d) Step 9 (1269 nodes).

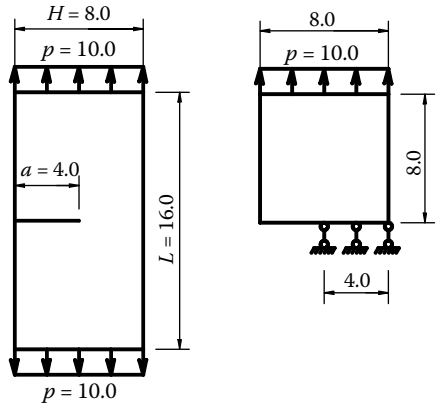

FIGURE 6.30 Crack problem setting and the half model.

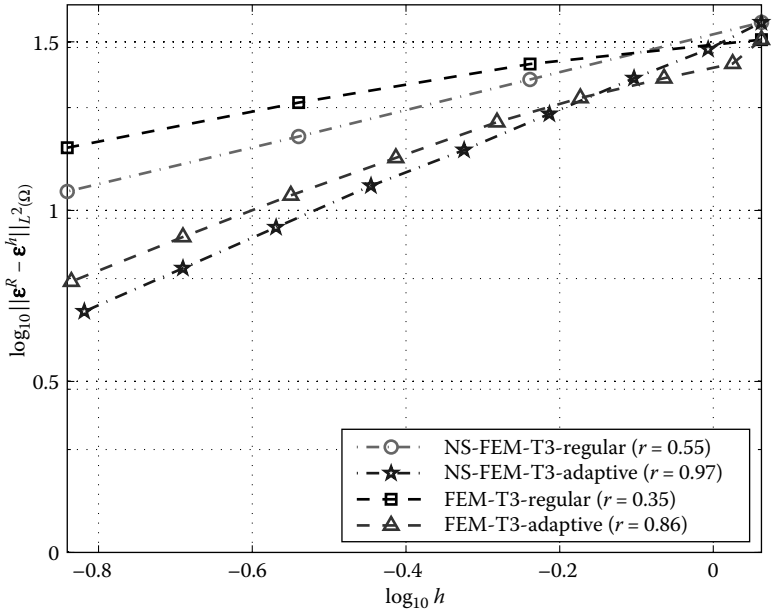

FIGURE 6.31 Error in a posteriori energy norms using the error indicator Equation 6.23 for the solution of the crack problem.

for FEM and $r = 0.55$ for NS-FEM), as shown in Figure 6.31. The adaptive schemes are therefore very necessary to improve the convergence rate. Figure 6.31 shows the energy norms of the adaptive models for both NS-FEM-T3 and FEM-T3. It is clearly shown that the adaptive models can obtain significantly higher (about double) convergence rates compared to the uniformly refined models. The results of NS-FEM-T3 are much better and give a higher convergence rate than those of FEM-T3. Without having the analytical solution, we cannot show the superconvergence of the error in the recovery energy norm (E-rec error) between the analytical and recovery strains. However, based on the convergence rate of the a posteriori energy norm (R-raw error) of NS-FEM-T3 ($r = 0.97$), which is almost 1, we can see that the recovery strain is a reliable representation of the analytical strain and can efficiently produce an optimal rate in the energy norm for this strongly singular case.

Figure 6.32 verifies the upper bound property in the strain energy of NS-FEM-T3 during the adaptive procedure. Figure 6.33 shows some steps of the adaptive refinement models using NS-FEM-T3. The results show clearly that the refinement is focused on the crack tip where the singularity is.

A more proper way of analyzing this type of problem with singularity is to use the singular S-FEM models, where the enriched linear PIM is used to create a proper singular stress field. The details are presented in Chapter 10.

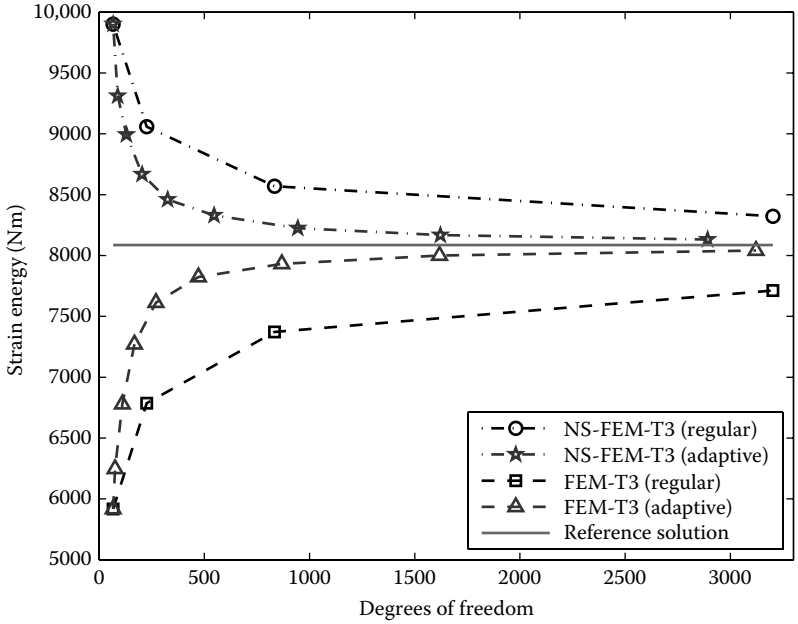

FIGURE 6.32 Convergence of the strain energy solution for the crack problem.

Example 6.7.5: 3D Lame Problem

The 3D Lame problem consists of a hollow sphere with inner radius $a = 1$ m, outer radius $b = 2$ m, and subjected to internal pressure $P = 100\,\text{N/m}^2$, as shown in Figure 6.34. For this benchmark problem, the analytical solution is available in the polar coordinate system [28]:

$$u_r = \frac{Pa^3 r}{E(b^3 - a^3)}\left[(1-2\nu) + (1+\nu)\frac{b^3}{2r^3}\right], \tag{6.30}$$

$$\sigma_r = \frac{Pa^3(b^3 - r^3)}{r^3(a^3 - b^3)}, \quad \sigma_\theta = \frac{Pa^3(b^3 + 2r^3)}{2r^3(b^3 - a^3)}, \tag{6.31}$$

where r is the radial distance from the centroid of the sphere to the point of interest in the sphere.

As the problem is spherically symmetrical, only one-eighth of the sphere model shown in Figure 6.34 is modeled, and symmetry conditions are imposed on the three mirror symmetric planes. The material parameters of the problem are $E = 10^3\,\text{N/m}^2$ and $\nu = 0.3$.

From Figure 6.35, it is observed that all the computed displacements and stresses of NS-FEM-T4 agree well with analytical solutions. Table 6.12 and Figure 6.36 show the upper bound property on the strain energy of NS-FEM-T4, while FEM-T4 and FEM-H8 give lower bounds.

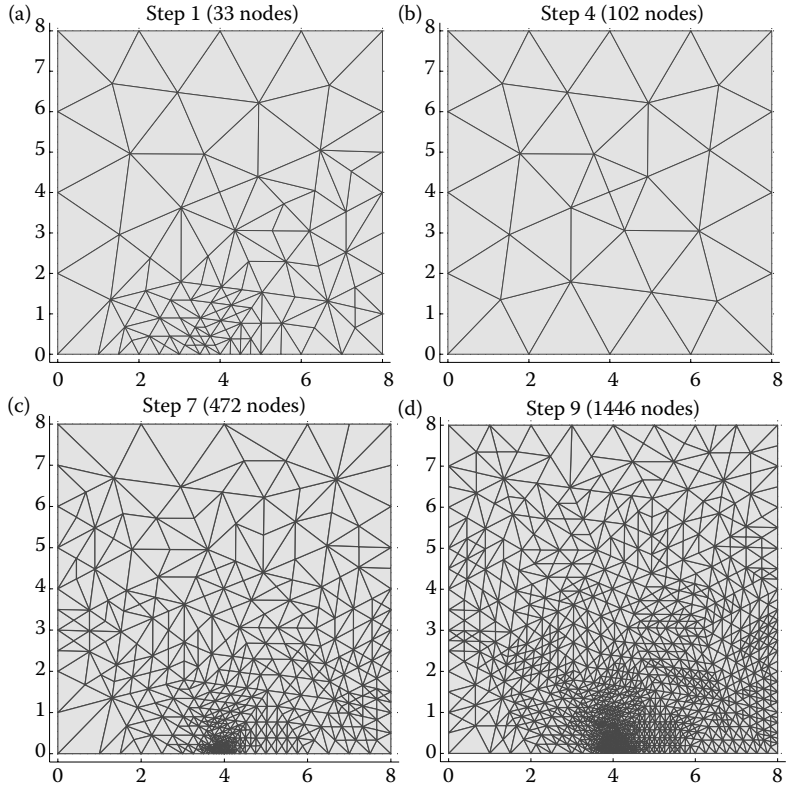

FIGURE 6.33 Sequence of adaptive refined meshes for the crack problem solved using NS-FEM-T3. (a) Step 1 (33 nodes); (b) Step 4 (102 nodes); (c) Step 7 (472 nodes); and (d) Step 9 (1446 nodes).

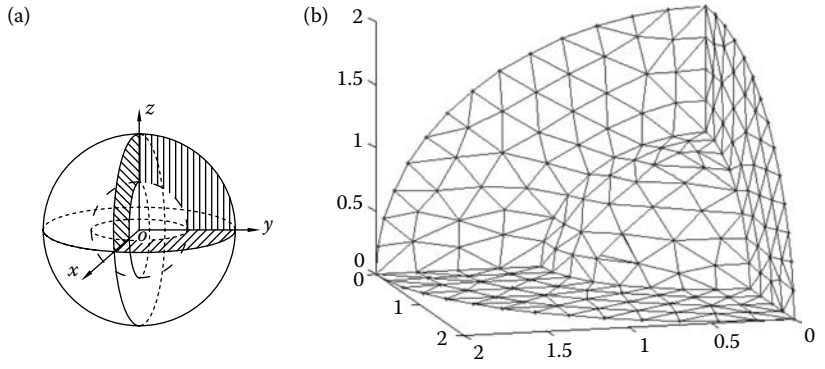

FIGURE 6.34 (a) Hollow sphere problem setting and (b) one-eighth model discretized using four-node tetrahedral elements.

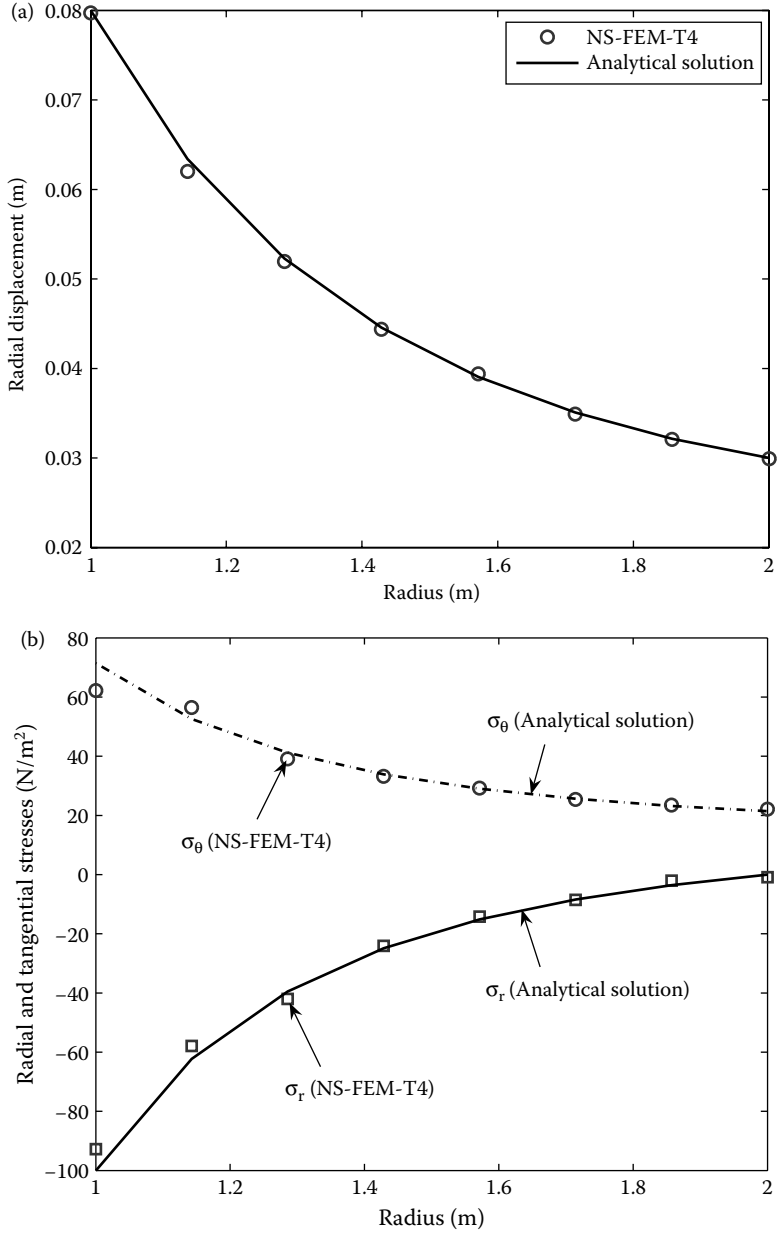

FIGURE 6.35 (a) Radial displacement v (m) and (b) radial and tangential stresses (N/m^2) for the hollow sphere subjected to inner pressure.

TABLE 6.12

Strain Energy ($\times 10^{-2}$ Nm) Obtained Using Different Methods[a] for the Hollow Sphere Subjected to Inner Pressure

	Mesh 1	Mesh 2	Mesh 3	Mesh 4	Solution Analytical
DOFs (T4)	1521	2337	3825	5814	
DOFs (H8)	1092	2535	3906	6951	
FEM-T4	5.9131	5.9986	6.0929	6.1387	6.3060
NS-FEM-T4	6.6227	5.5380	6.4580	6.4219	6.3060
FEM-H8	5.9827	6.1063	6.1668	6.2023	6.3060
FS-FEM-T4 [35]	6.0343	6.0955	6.1607	6.1906	6.3060
αFEM-T4 [33] ($\alpha_{exact} = 0.7$)	6.3081	6.3058	6.3059	6.3060	6.3060

[a] The numerical solutions of methods FS-FEM-T4 [35] and αFEM-T4 [33] presented in the following chapters are also provided in this table for easy reference.

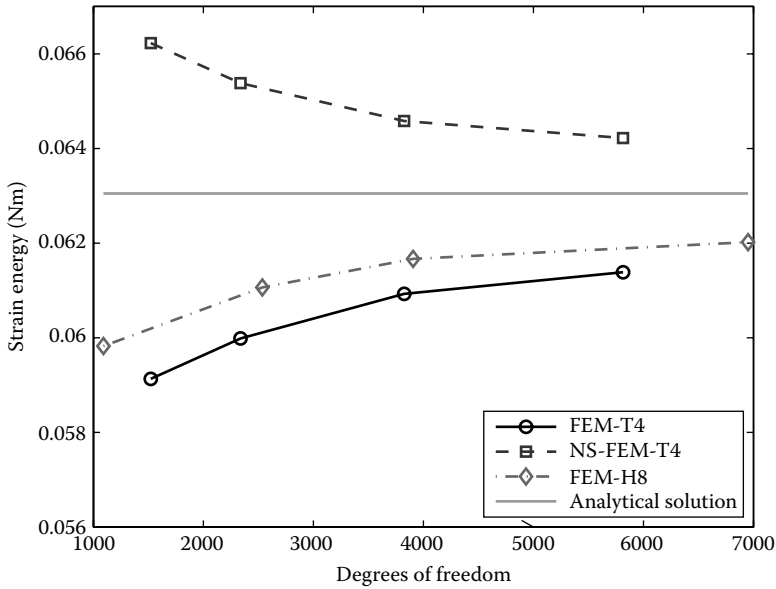

FIGURE 6.36 Convergence of the strain energy solution of NS-FEM-T4 in comparison with other methods for the hollow sphere subjected to inner pressure.

Table 6.13 and Figure 6.37 compare the solution error in the displacement norm obtained using NS-FEM-T4, together with those of FEM-T4 and FEM-H8. It is seen that FEM-H8 stands out clearly. When the third mesh ($h \approx 0.156$ m) is used, the error of FEM-H8 is about 1/3 that of NS-FEM-T4. NS-FEM-T4 performed better than FEM-T4, but only by a small margin. The performance of

TABLE 6.13

Error in Displacement Norm Obtained Using Different Methods[a] for the Hollow Sphere Subjected to Inner Pressure

	Mesh 1	**Mesh 2**	**Mesh 3**	**Mesh 4**
h (T4)	0.2193	0.1878	0.1565	0.1342
h (H8)	0.2535	0.1840	0.1563	0.1267
FEM-T4	4.06e − 03	3.12e − 03	2.07e − 03	1.58e − 03
NS-FEM-T4	3.68e − 03	2.76e − 03	1.88e − 03	1.48e − 03
FEM-H8	2.26e − 03	1.35e − 03	7.92e − 04	5.44e − 04
FS-FEM-T4 [35]	3.03e − 03	2.30e − 03	1.50e − 03	1.14e − 03
αFEM-T4 [33] ($\alpha_{\text{exact}} = 0.7$)	1.40e − 03	1.02e − 03	6.67e − 04	4.71e − 04

[a] The numerical solutions of methods FS-FEM-T4 [35] and αFEM-T4 [33] presented in the following chapters, are also provided in this table for easy reference.

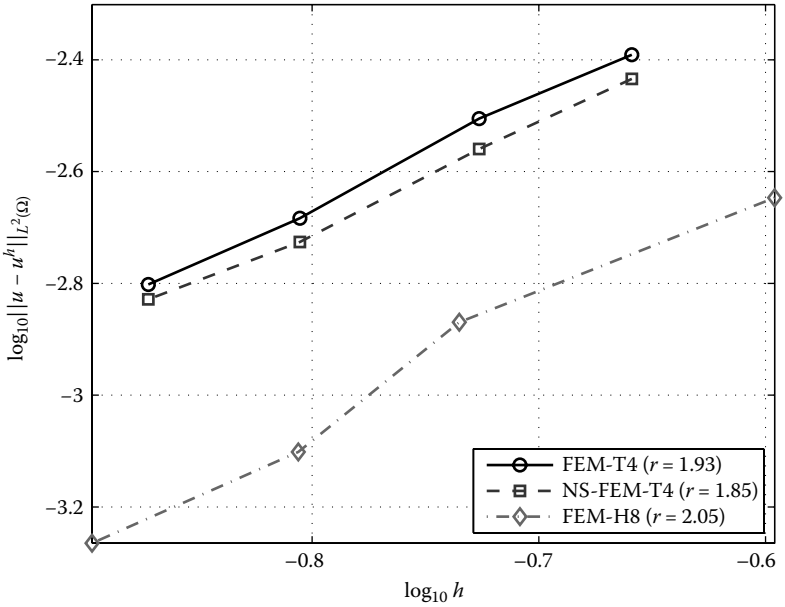

FIGURE 6.37 Error in the displacement norm for the NS-FEM-T4 solution in comparison with those of other methods for the hollow sphere subjected to inner pressure.

NS-FEM-T4 is in between FEM-T4 and FEM-H8: quite similar to the 2D cases. In terms of convergence rate, all the models have a numerical rate around the theoretical value of 2.0.

Table 6.14 and Figure 6.38 compare the results of the energy norm of NS-FEM-T4 with those of FEM-T4 and FEM-H8. It is again seen that NS-FEM-T4

TABLE 6.14

Error in Energy Norm Obtained Using Different Methods[a] for the Hollow Sphere Subjected to Inner Pressure

	Mesh 1	**Mesh 2**	**Mesh 3**	**Mesh 4**
h (T4)	0.2193	0.1878	0.1565	0.1342
h (H8)	0.2535	0.1840	0.1563	0.1267
FEM-T4	5.89e − 01	5.13e − 01	4.19e − 01	3.63e − 01
NS-FEM-T4	2.09e − 01	1.73e − 01	1.26e − 01	1.08e − 01
FEM-H8	5.51e − 01	4.22e − 01	3.42e − 01	2.85e − 01
FS-FEM-T4 [35]	3.75e − 01	3.03e − 01	2.24e − 01	1.86e − 01
FEM-T4-Re	4.20e − 01	3.39e − 01	2.51e − 01	2.08e − 01
FEM-H8-Re	4.90e − 01	3.31e − 01	2.56e − 01	1.98e − 01
αFEM-T4 [33] ($\alpha_{exact} = 0.7$)	2.83e − 01	2.30e − 01	1.71e − 01	1.44e − 01

[a] The numerical solutions of methods FS-FEM-T4 [35] and αFEM-T4 [33] presented in the following chapters are also provided in this table for easy reference.

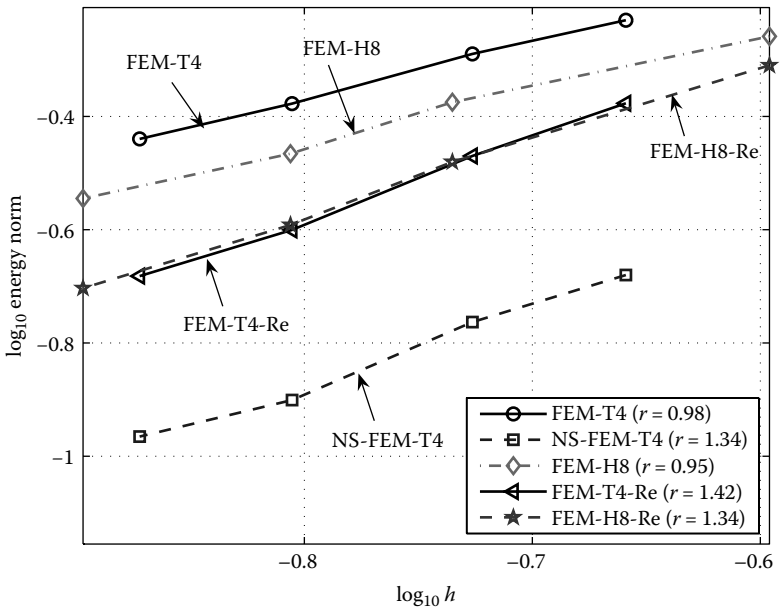

FIGURE 6.38 Error in the energy norm for the NS-FEM-T4 solution in comparison with those of other methods for the hollow sphere subjected to inner pressure.

stands out clearly. When the third mesh ($h \approx 0.156$ m) is used, the error of NS-FEM-T4 is about 2/7 that of FEM-T4, 2/5 that of FEM-H8, 1/2 that of FEM-T4-Re, and 1/2 that of FEM-H8-Re. In terms of convergence rate, NS-FEM-T4 stands out clearly with a rate of 1.34, while the rates of both FEM-T4 and FEM-H8 are slightly below the theoretical value of 1.0.

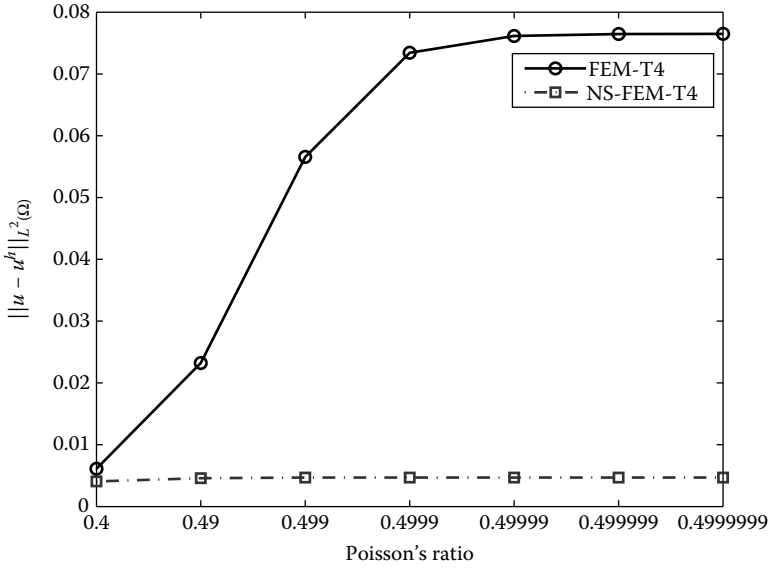

FIGURE 6.39 Displacement norm versus different Poisson's ratios for the hollow sphere subjected to inner pressure (507 nodes).

Figure 6.39 plots the error in the displacement norm against Poisson's ratio changing from 0.4 to 0.4999999 obtained using tetrahedral elements (507 nodes). The results show that NS-FEM-T4 is naturally immune from volumetric locking, while FEM-T4 is subjected to volumetric locking, resulting in a drastic accuracy loss in the numerical solutions.

Overall, it is again seen that NS-FEM-T4 models also possess four interesting properties that are similar to an equilibrium FEM model: (1) the strain energy is an upper bound of the exact solution; (2) it is immune naturally from volumetric locking; (3) the stress solutions are ultra-accurate and superconvergent; and (4) the displacement solutions are at about the same level as that of FEM-T4 using the same mesh.

Example 6.7.6: 3D Cubic Cantilever: Analysis for the Upper Bound

Consider a 3D cantilever of cubic shape, subjected to a uniform pressure on its upper face as shown in Figure 6.40. The exact solution of the problem is unknown. By incorporating the solutions of hexahedral superelement elements and the procedure of Richardson's extrapolation, Almeida Pereira [29] gave an approximation of the exact strain energy as 0.950930. In addition, using the commercial software ABAQUS with a very fine mesh including 30,204 nodes and 20,675 10-node tetrahedron elements, we computed another reference solution of the strain energy as 0.9486. Also from this reference, the deflection at point $A(1.0, 1.0, -0.5)$ is 3.3912.

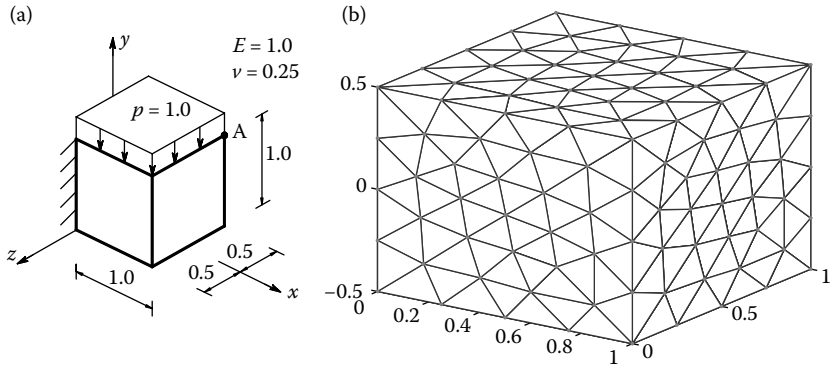

FIGURE 6.40 (a) A 3D cubic cantilever subjected to a uniform pressure on the top surface and (b) a mesh with four-node tetrahedral elements.

TABLE 6.15

Strain Energy Obtained Using Different Methods[a] for the 3D Cubic Cantilever Problem Subjected to a Uniform Pressure

	Mesh 1	Mesh 2	Mesh 3	Mesh 4	Mesh 5	Reference Solution [29]
DOFs (T4)	714	1221	2073	2856	4782	
DOFs (H8)	648	1029	1536	2187	3993	
FEM-T4	0.8572	0.8818	0.8978	0.9088	0.9190	0.9509
NS-FEM-T4	1.0059	0.9882	0.9808	0.9791	0.9704	0.9509
FEM-H8	0.8999	0.9116	0.9195	0.9251	0.9323	0.9509
FS-FEM-T4 [35]	0.8801	0.8989	0.9111	0.9206	0.9274	0.9509
αFEM-T4 [33] ($\alpha_{exact} = 0.62$)	0.9478	0.9478	0.9488	0.9518	0.9514	0.9509

[a] The numerical solutions of methods FS-FEM-T4 [35] and αFEM-T4 [33] presented in the following chapters are also provided in this table for easy reference.

Table 6.15 and Figure 6.41 confirm the upper bound property on the strain energy of NS-FEM-T4 and the lower bound property of FEM-T4 and FEM-H8 for this 3D problem. Table 6.16 and Figure 6.42 show the convergence of deflection at point $A(1.0, 1.0, -0.5)$. The results also show the upper bound property for the displacement solution of NS-FEM-T4 and the lower bound property of FEM-T4 and FEM-H8.

Example 6.7.7: A 3D L-Shaped Block: Analysis for the Upper Bound

Consider the 3D square block with a cubic hole subjected to surface traction q as shown in Figure 6.43. Due to the double symmetry of the problem, only a quarter of the domain is modeled, which becomes a 3D L-shaped block.

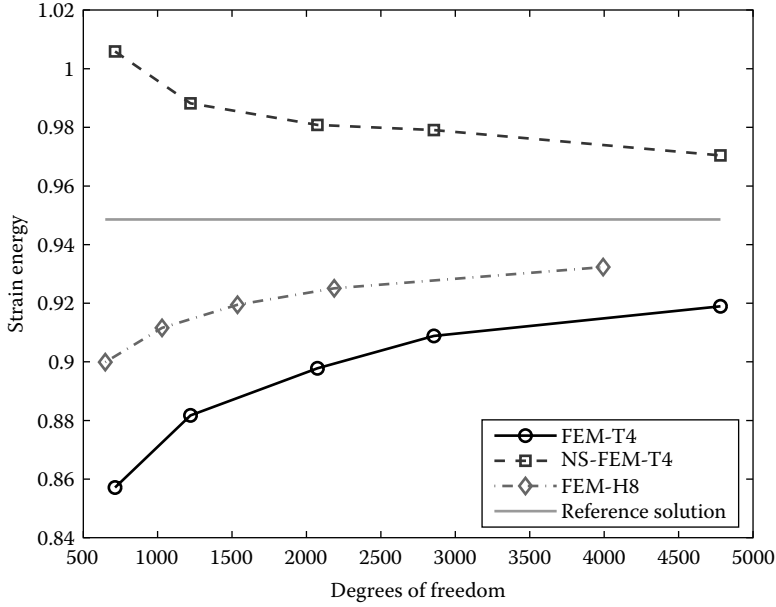

FIGURE 6.41 Convergence of the strain energy solution of NS-FEM-T4 in comparison with other methods of the 3D cubic cantilever problem subjected to a uniform pressure.

TABLE 6.16

Deflection at Point $A(1.0, 1.0, -0.5)$ Obtained Using Different Methods[a] for the 3D Cubic Cantilever Problem Subjected to a Uniform Pressure

	Mesh 1	Mesh 2	Mesh 3	Mesh 4	Mesh 5	Reference Solution
DOFs (T4)	714	1221	2073	2856	4782	
DOFs (H8)	648	1029	1536	2187	3993	
FEM-T4	3.0780	3.1752	3.2341	3.2732	3.3050	3.3912
NS-FEM-T4	3.5912	3.5418	3.4943	3.4818	3.4577	3.3912
FEM-H8	3.2523	3.2875	3.3107	3.3269	3.3474	3.3912
FS-FEM-T4 [35]	3.1669	3.2390	3.2800	3.3128	3.3324	3.3912
αFEM-T4 [33] ($\alpha_{exact} = 0.62$)	3.4064	3.4087	3.4031	3.4091	3.4053	3.3912

[a] The numerical solutions of methods FS-FEM-T4 [35] and αFEM-T4 [33] presented in the following chapters are also provided in this table for easy reference.

Analysis is performed using input data: $q = 1$, $a = 1$, $E = 1$, and $\nu = 0.3$. For this problem, the strain energy of 6.1999 given by Cugnon [30] is considered as the reference solution. In addition, using the commercial software ABAQUS with a very fine mesh including 33,641 nodes and 22,862 10-node

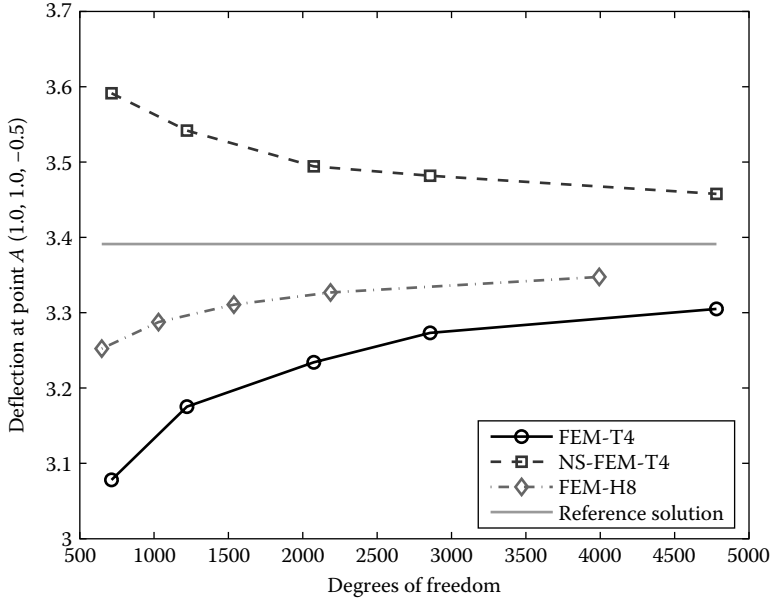

FIGURE 6.42 Convergence of the deflection solution at point $A(1.0, 1.0, -0.5)$ of NS-FEM-T4 in comparison with other methods of the cubic cantilever subjected to a uniform pressure.

tetrahedron elements, we computed another reference solution of the strain energy as 6.1916.

Again, Table 6.17 and Figure 6.44 confirm the upper bound property on the strain energy of NS-FEM-T4 and the lower bound property of the FEM-T4 for 3D problems.

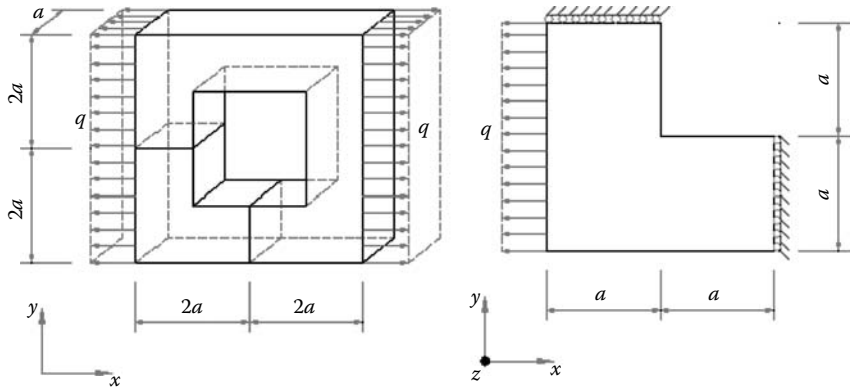

FIGURE 6.43 3D block and an L-shaped quarter model.

TABLE 6.17

Strain Energy Obtained Using Different Methods[a] for the 3D *L*-Shaped Block Problem

	Mesh 1	Mesh 2	Mesh 3	Mesh 4	Mesh 5	Reference Solution
DOFs	806	1284	2556	3834	4826	
FEM-T4	5.7164	5.8189	5.9524	6.0028	6.0305	6.1999
NSFEM-T4	6.6787	6.5454	6.4227	6.3897	6.3658	6.1999
FS-FEM-T4 [35]	5.8728	5.9532	6.0358	6.0731	6.0927	6.1999
αFEM-T4 [33] ($\alpha_{exact} = 0.7$)	6.1861	6.1824	6.1828	6.1808	6.1960	6.1999

[a] The numerical solutions of methods FS-FEM-T4 [35] and αFEM-T4 [33] presented in the following chapters are also provided in this table for easy reference.

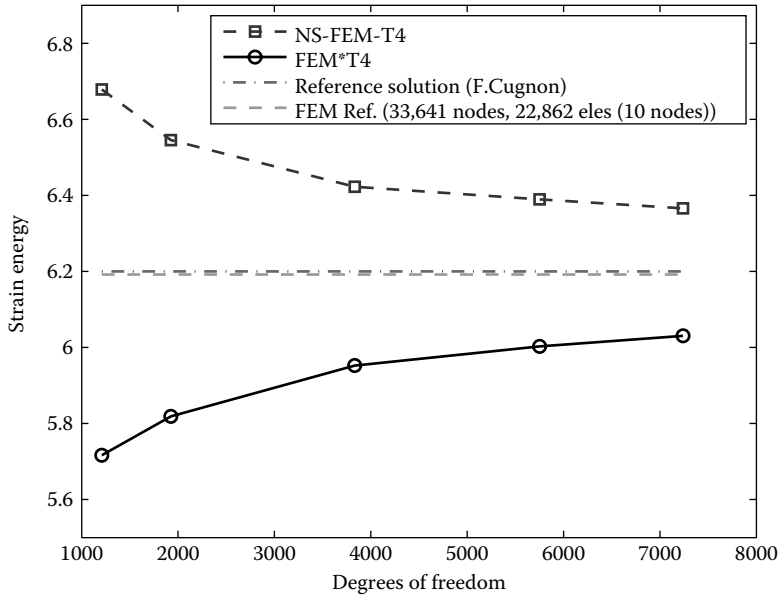

FIGURE 6.44 Convergence of the strain energy solution of the 3D L-shaped block problem.

6.8 Remarks

In this chapter, an NS-FEM for upper bound solutions to solid mechanics problems is proposed. Through the formulation, theoretical analyses, and numerical results, we finally summarize our discussions into the following remarks and close the chapter.

Remark 6.1 NS-FEM: Works for General Polygonal Elements

NS-FEM allows the use of general polygonal elements with an arbitrary number of sides. The method can be applied easily to traditional four-node quadrilateral or triangular elements. It works well with triangular elements for 2D problems and with tetrahedral elements for 3D problems.

Remark 6.2 PIM for Evaluating the Shape Function

In NS-FEM, smoothed strain fields are computed directly using only the shape functions at some particular points along segments of the boundary of the smoothing domains. Evaluation of the values of shape functions for discrete points can be performed in a trivial and simple manner for all types of meshes using the linear PIM. The numerical implementation of NS-FEM is straightforward and much simpler than those of equilibrium FEM models.

Remark 6.3 NS-FEM: Upper Bound, Volumetric Locking Free, and Superconvergence

NS-FEM is a displacement model using only displacements as unknowns. It, however, possesses interesting properties that are quite similar to those of an equilibrium FEM model such as the following: (1) the upper bound property of the strain energy, when a reasonably fine mesh is used for force-driven problems; (2) natural immunization from volumetric locking; (3) ultra-accuracy and superconvergence of stress solutions (measured in energy norm), and much more accurate than the FEM counterparts (with or without recovery); and (4) similar accuracy of displacement solutions compared to the standard linear FEM model that is already quite optimal.

In fact, at any point in all these smoothing domains, the equilibrium equations are satisfied in an NS-FEM model. It is, however, not an equilibrium model because the stresses right on these interfaces of the smoothing domains are not in equilibrium. Therefore, it is said to be a quasiequilibrium model. For *displacement-driven* problems (zero external forces but nonzero prescribed displacement on the essential boundary), we expect FEM and NS-FEM to swap their roles: NS-FEM gives the lower bound and FEM gives the upper bound. For general problems with mixed force and displacement boundary conditions, we can still expect these two models to bound the exact solution from both sides, although which model is on which side will be problem dependent.

Remark 6.4 NS-FEM and FEM: A General, Robust Mean for Solution Bounds

From the upper bound property of the strain energy of NS-FEM, a simple and practical approach is now available to determine both the upper and lower bounds in the strain energy, by combining *n*NS-FEM with *n*CS-FEM

(for n-sided polygonal elements) or with FEM (for triangular, four-node quadrilateral, or tetrahedral elements). This practical approach is also applicable to fracture problems (Chapter 10) and heat transfer problems (Chapter 14).

Remark 6.5 Recovery Error Indicator: Useful for Adaptive Analysis

An error indicator based on the recovery strain is proposed and shown to be asymptotically exact by numerical experiments. Together with the simple refinement strategy using newest node bisection, an adaptive procedure for NS-FEM using triangular elements is proposed. The numerical results of some benchmark problems show that the present adaptive procedure can accurately "catch" the stress concentration/singularity regions and perform the refinement properly. Compared to uniformly refined models, adaptive models achieve a very high convergence rate, and hence high efficiency. The 3D adaptive analyses using S-FEM (linear S-PIM) can be found in Ref. [31]. Chapter 10 presents a more proper simulation of the stress singular field using S-FEM models, where the linear PIM is enriched to produce the singular stress field.

Remark 6.6 NS-FEM Temporal Instability Remedies

NS-FEM is *temporally* instable and can have non-zero-energy spurious modes; hence special stabilization techniques are needed for NS-FEM to solve dynamic problems [18,19] and nonlinear problems [20]. An alternative and very efficient way of overcoming temporal instability is to use ES-FEM, which will be discussed in more detail in the next chapter.

Remark 6.7 NS-FEM: Upper Bounds for Dynamic and Nonlinear Problems

NS-FEM can be stabilized (temporally) to solve and obtain upper bounds for dynamic problems [18,19] and nonlinear problems [20]. The study on this important area is still ongoing to fully capitalize the unique upper bound property of NS-FEM for various types of problems. Interested readers may refer to Refs. [18–20] for latest developments.

References

1. Almeida JPM and Pereira OJBA. 2006. Upper bounds of the error in local quantities using equilibrated and compatible finite element solutions for linear elastic problems. *Computer Methods in Applied Mechanics and Engineering*; 195: 279–296.
2. Debongnie JF, Zhong HG, and Beckers P. 1995. Dual analysis with general boundary conditions. *Computer Methods in Applied Mechanics and Engineering*; 122: 183–192.

3. Veubeke BF. 1965. Displacement and equilibrium models in the finite element method. In *Stress Analysis*, OC Zienkiewicz and GS Holister, Eds. Wiley, London.
4. Coorevits P, Ladeveze P, and Pelle JP. 1995. An automatic procedure with a control of accuracy for finite element analysis in 2D elasticity. *Computer Methods in Applied Mechanics and Engineering*; 121: 91–121.
5. Ladeveze P, Coffignal G, and Pelle JP. 1986. Accuracy of elastoplastic and dynamic analysis. In *Accuracy Estimates and Adaptive Refinements in Finite Element Computations*, Chapter 11, I Babuska, OC Zienkiewicz, J Gago, and ER Oliveira, Eds. Wiley, New York.
6. Ladeveze P, Pelle JP, and Rougeot P. 1991. Error estimation and mesh optimisation for classical finite elements. *Engineering Computation*; 8: 69–80.
7. Almeida JPM and Freitas JAT. 1991. Alternative approach to the formulation of hybrid equilibrium finite elements. *Computers and Structures*; 40: 1043–1047.
8. Pereira OJBA, Almeida JPM, and Maunder EAW. 1999. Adaptive methods for hybrid equilibrium finite element models. *Computer Methods in Applied Mechanics and Engineering*; 176: 19–39.
9. Liu GR, Nguyen-Thoi T, Nguyen-Xuan H, and Lam KY. 2009. A node-based smoothed finite element method (NS-FEM) for upper bound solution to solid mechanics problems. *Computers and Structures*; 87: 14–26.
10. Nguyen-Thoi T, Liu GR, and Nguyen-Xuan H. 2009. Additional properties of the node-based smoothed finite element method (NS-FEM) for solid mechanics problems. *International Journal of Computational Methods*; 6(4): 633–666.
11. Liu GR, Nguyen-Xuan H, and Nguyen-Thoi T. 2009. A variationally consistent αFEM (VCαFEM) for solid mechanics problems. *International Journal for Numerical Methods in Engineering*; (revised).
12. Liu GR and Zhang GY. 2008. Upper bound solution to elasticity problems: A unique property of the linearly conforming point interpolation method (LC-PIM). *International Journal for Numerical Methods in Engineering*; 74: 1128–1161.
13. Liu GR, Zhang GY, Dai KY, Wang YY, Zhong ZH, Li GY, and Han X. 2005. A linearly conforming point interpolation method (LC-PIM) for 2D solid mechanics problems. *International Journal of Computational Methods*; 2(4): 645–665.
14. Nguyen-Thoi T, Liu GR, Nguyen-Xuan H, and Nguyen-Tran C. 2009. Adaptive analysis using the node-based smoothed finite element method (NS-FEM). *Communications in Numerical Methods in Engineering*; doi: 10.1002/cnm.1291.
15. Chen JS, Wu CT, Yoon S, and You Y. 2001. A stabilized conforming nodal integration for Galerkin meshfree method. *International Journal for Numerical Methods in Engineering*; 50: 435–466.
16. Fraeijs de Veubeke BM. 1965. Displacement and equilibrium models in the finite element method, In *Stress Analysis*, OC Zienkiewicz. Wiley, London.
17. Liu GR. 2002. *Meshfree Methods: Moving Beyond the Finite Element Method*. CRC Press, Boca Raton, FL.
18. Zhang ZQ and Liu GR. 2009. Temporal stabilization of the node-based smoothed finite element method (NS-FEM) and solution bound of linear elastostatics and vibration problems. *Computational Mechanics*; doi: 10.1007/s00466-009-0420-5.

19. Zhang ZQ and Liu GR. 2009. Upper and lower bounds for natural frequencies: a property of the smoothed finite element methods. *International Journal for Numerical Methods in Engineering*; (submitted).
20. Zhang ZQ and Liu GR. 2009. Solution bound and nearly exact solution to nonlinear elasticity using smoothed FEM models. *Computer Methods in Applied Mechanics and Engineering*; (revised).
21. Zhang GY, Liu GR, and Li Y. 2008. An efficient adaptive analysis procedure for certified solutions with exact bounds of strain energy for elasticity problems. *Finite Elements in Analysis and Design*; 44(14): 831–841.
22. Zienkiewicz OC and Zhu JZ. 1992. The superconvergence patch recovery and a posteriori error estimates. Part 1: The recovery techniques. *International Journal for Numerical Methods in Engineering*; 33: 1331–1364.
23. Zienkiewicz OC and Zhu JZ. 1992. The superconvergence patch recovery and a posteriori error estimates. Part 2: Error estimates and adaptivity. *International Journal for Numerical Methods in Engineering*; 33: 1365–1382.
24. Dorfler W. 1996. A convergent adaptive algorithm for Poisson's equation. *SIAM Journal on Numerical Analysis*; 33: 1106–1124.
25. Chen L and Zhang CS. 2006. AFEM@matlab: A Matlab package of adaptive finite element methods. Technique Report, Department of Mathematics, University of Maryland at College Park.
26. Richardson LF. 1910. The approximate arithmetical solution by finite differences of physical problems. *Transactions of the Royal Society (London)*; A210: 307–357.
27. Beckers P, Zhong HG, and Maunder E. 1993. Numerical comparison of several a posteriori error estimators for 2D stress analysis. *European Journal of Finite Element Method*; 1: 165–178.
28. Timoshenko SP and Goodier JN. 1970. *Theory of Elasticity*, 3rd edition. McGraw-Hill, New York.
29. Almeida Pereira OJB. 2008. Hybrid equilibrium hexahedral elements and super-elements. *Communications in Numerical Methods in Engineering*; 24(2): 157–165.
30. Cugnon F. 2000. Automatisation des calculs elements finis dans le cadre de la methode-p. PhD thesis, Universite de Lie.
31. Tang Q, Liu GR, Zhong ZH, and Zhang GY. 2000. A three-dimensional adaptive analysis using the node-based smoothed point interpolation method (NS-PIM), (submitted).
32. Liu GR, Nguyen-Thoi T, and Lam KY. 2009. An edge-based smoothed finite element method (ES-FEM) for static, free and forced vibration analyses in solids. *Journal of Sound and Vibration*; 320: 1100–1130.
33. Liu GR, Nguyen-Thoi T, and Lam KY. 2008. A novel alpha finite element method (αFEM) for exact solution to mechanics problems using triangular and tetrahedral elements. *Computer Methods in Applied Mechanics and Engineering*; 197: 3883–3897.
34. Nguyen-Thoi T, Liu GR, and Nguyen-Xuan H. 2009. An *n*-sided polygonal edge-based smoothed finite element method (*n*ES-FEM) for solid mechanics. *Communications in Numerical Methods in Engineering*; doi: 10.1002/cnm.1375.
35. Nguyen-Thoi T, Liu GR, Lam KY, and Zhang GY. 2009. A face-based smoothed finite element method (FS-FEM) for 3D linear and nonlinear solid mechanics problems using 4-node tetrahedral elements. *International Journal for Numerical Methods in Engineering*; 78: 324–353.

7

Edge-Based Smoothed FEM

7.1 Introduction

Chapter 6 has presented the NS-FEM [1], and it has proven via theoretical analysis and numerical examples that the NS-FEM is always spatially stable. In addition, the NS-FEM possesses interesting properties that are similar to those of an equilibrium FEM model. It is, however, found that the NS-FEM behaves "overly soft" resulting from overcorrection to the "overly stiff" behavior of the compatible FEM [1]. Such an overly soft behavior leads to the so-called temporal instability (see Remark 1.3) similar to those found in the equilibrium FEM models and in the nodal integration methods [2–4]. Temporal instability can be clearly observed when the NS-FEM is used for solving dynamic problems: (1) as spurious non-zero-energy modes in free vibration analyses, and (2) numerical instability in the time marching in forced vibration analyses.

In this chapter, we therefore present a very outstanding S-FEM model: the ES-FEM that is stable both spatially and temporally, and much more accurate compared with many existing FEMs. The ES-FEM was originated in Ref. [5] to create models with close-to-exact stiffness, so that it can produce ultra-accurate results for solving static problems, and stable and accurate results for dynamic problems. In the ES-FEM, the strain smoothing domains are associated with edges of the element mesh, and hence the integration of the weak form becomes a simple summation over these edge-based smoothing domains. The ES-FEM works well, in general for a mesh of arbitrarily n-sided polygonal elements [6], and in particular for linear triangular (T3) elements that can be generated for complicated geometry automatically [5]. In addition, a smoothing-domain-based selective ES/NS-FEM model has also been proposed that is immune from the volumetric locking, and works very well for solids of nearly incompressible materials [5,6].

For important mesh generation reasons, this chapter concentrates on the ES-FEM using linear triangular elements (ES-FEM-T3). In this case, the ES-FEM-T3 has been often found to possess the following excellent properties: (1) it has a very close-to-exact stiffness: it is much softer than

the "overly stiff" FEM and much stiffer than the "overly soft" NS-FEM model; (2) the results of the ES-FEM-T3 are often much more accurate than those of the FEM using the same linear triangular element mesh (FEM-T3) and often even more accurate than those of the FEM using quadrilateral elements (FEM-Q4) with the same sets of nodes. These results have been observed in static linear elastic problems and in nonlinear problems of large deformation; (3) no spurious non-zero-energy modes were found and hence the method is both spatially and temporally stable and hence works well for dynamic problems; (4) the implementation of the ES-FEM is straightforward: no additional DOF is used; (5) the ES-FEM can easily be extended to 3D problems using tetrahedral elements [7]; and (6) the computational efficiency of the ES-FEM-T3 is the most superior compared to that of numerical methods using the same sets of nodes.

7.2 Creation of Edge-Based Smoothing Domains

In the ES-FEM, the domain discretization is still based on general polygonal elements with an arbitrary number of sides, as in the NS-FEM presented in Chapter 6. Assume that the problem domain Ω is discretized using N_e elements, such that $\Omega = \sum_{i=1}^{N_e} \Omega_i^e$ and $\Omega_i^e \cap \Omega_j^e = \emptyset, i \neq j$. The element mesh shall have a total of N_n nodes and N_{eg} edges located in the entire problem domain. On top of the element mesh, the problem domain Ω is divided into $N_s = N_{\text{eg}}$ nonoverlap no-gap smoothing domains associated with the edges, such that $\Omega = \sum_{k=1}^{N_{\text{eg}}} \Omega_k^s$ and $\Omega_i^s \cap \Omega_j^s = \emptyset, i \neq j$. In this case, the number of smoothing domains is the same as the number of edges in the mesh: $N_s = N_{\text{eg}}$, which satisfies the requirement of minimum number of smoothing domains given in Table 4.2. This implies that the ES-FEM-T3 should be at least spatially stable (see Theorem 4.1).

For a mesh of n-sided polygonal elements, the smoothing domain Ω_k^s associated with the edge k is created by connecting two endpoints of the edge to central points of adjacent elements as shown in Figure 7.1. For a mesh of triangular elements, in particular, an ES-FEM-T3 setting is shown in Figure 7.2. The strain smoothing technique [8] is used to create a smoothed strain field that is constant in each of the smoothing domains. The summation required in the smoothed Galerkin weak form (Equation 4.37) is thus over all these edge-based smoothing domains.

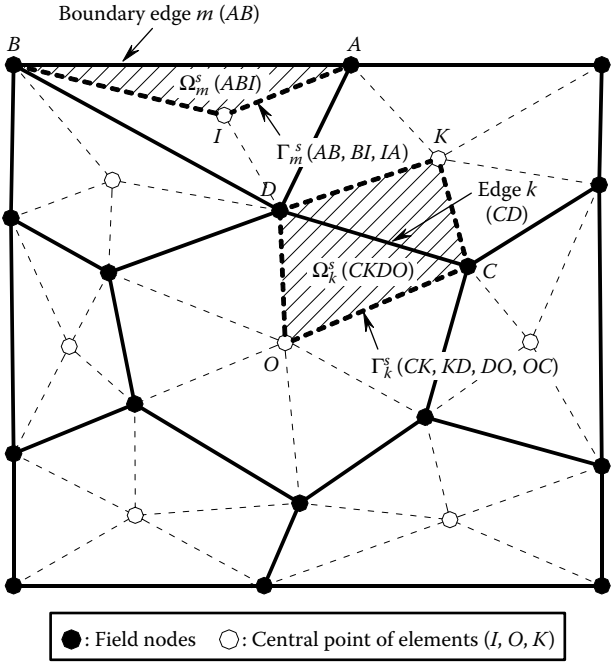

FIGURE 7.1 ES-FEM settings: domain discretization into arbitrary n-sided polygonal elements, and the smoothing domains created based on the edges of these elements.

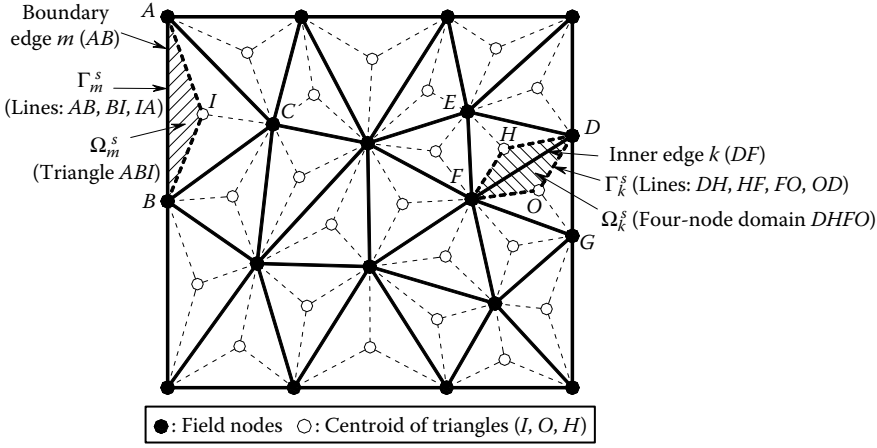

FIGURE 7.2 ES-FEM-T3 settings: triangular elements (solid lines) and the edge-based smoothing domains (shaded areas).

7.3 Formulation of the ES-FEM

7.3.1 Static Analyses

Considering the solid mechanic problem defined in Chapter 2, and using the general formulation for the static analysis of the S-FEM models presented in Chapter 4, the linear system of equations of the ES-FEM has the form of

$$\bar{\mathbf{K}}^{\text{ES-FEM}}\bar{\mathbf{d}} = \tilde{\mathbf{f}}, \tag{7.1}$$

where $\bar{\mathbf{K}}^{\text{ES-FEM}}$ is the *smoothed* stiffness matrix whose entries are given by

$$\bar{\mathbf{K}}_{IJ}^{\text{ES-FEM}} = \sum_{k=1}^{N_{\text{eg}}} \int_{\Omega_k^s} \bar{\mathbf{B}}_I^T \mathbf{c} \bar{\mathbf{B}}_J \, \mathrm{d}\Omega = \sum_{k=1}^{N_{\text{eg}}} \bar{\mathbf{B}}_I^T \mathbf{c} \bar{\mathbf{B}}_J A_k^s, \tag{7.2}$$

where $A_k^s = \int_{\Omega_k^s} \mathrm{d}\Omega$ is the area of the edge-based smoothing domain Ω_k^s, and the smoothed strain–displacement matrix $\bar{\mathbf{B}}_I$ is computed by Equation 4.30 using only shape function values on the boundaries of the edge-based smoothing domains.

In particular, when a mesh of linear triangular elements is used, the smoothed strain–displacement matrix $\bar{\mathbf{B}}_I$ can be assembled by the following simple equation:

$$\bar{\mathbf{B}}_I(\mathbf{x}_k) = \frac{1}{A_k^s} \sum_{j=1}^{n_k^e} \frac{1}{3} A_j^e \tilde{\mathbf{B}}_j^e, \tag{7.3}$$

where n_k^e is the number of elements around the edge k ($n_k^e = 1$ for the boundary edges and $n_k^e = 2$ for inner edges, as shown in Figure 7.2); A_j^e is the area of the jth element around the edge k; $\tilde{\mathbf{B}}_j^e$ is the compatible strain–displacement matrix of the jth element around the edge k and is computed similarly to that in Section 6.3.2; and A_k^s is the area of the smoothing domain of the kth edge computed using

$$A_k^s = \int_{\Omega_k^s} \mathrm{d}\Omega = \frac{1}{3} \sum_{j=1}^{n_k^e} A_j^e. \tag{7.4}$$

Note that with this formulation, only the area and the standard FEM compatible strain–displacement matrices $\tilde{\mathbf{B}}_j^e$ of triangular elements are needed to calculate the system stiffness matrix for the ES-FEM. The formulation

is simple, but works only for the type of triangular elements (T3) that uses linear interpolation over the element. For the ES-FEM models using other elements, the smoothed strain–displacement matrix $\bar{\mathbf{B}}_I$ has to be computed using the original Equation 4.30, and the shape functions have to be evaluated in the way given in Section 7.4.

The above formulation is quite straightforward and can be easily extended for the 3D problems using tetrahedral elements [7], which will be presented in Chapter 8.

7.3.2 Dynamic Analyses

Because the ES-FEM is both spatially and temporally stable [5] (this will be discussed further in Section 7.6.2), it suits well also for dynamic problems, such as free and forced vibrations analyses. If the inertial and damping forces are also considered in the dynamic equilibrium equations, the discretized system of equations in the ES-FEM can use the smoothed Galerkin weak form (Equation 4.45) and be expressed as a set of differential equations with respect to time:

$$\bar{\mathbf{K}}^{\text{ES-FEM}}\bar{\mathbf{d}} + \tilde{\mathbf{C}}\dot{\bar{\mathbf{d}}} + \tilde{\mathbf{M}}\ddot{\bar{\mathbf{d}}} = \tilde{\mathbf{f}}, \tag{7.5}$$

where $\tilde{\mathbf{M}}$ is the mass matrix

$$\tilde{\mathbf{M}} = \int_{\Omega} \mathbf{N}^T \rho \mathbf{N}\, \mathrm{d}\Omega, \tag{7.6}$$

in which ρ is the mass density. The damping matrix $\tilde{\mathbf{C}}$ is computed using

$$\tilde{\mathbf{C}} = \int_{\Omega} \mathbf{N}^T c \mathbf{N}\, \mathrm{d}\Omega, \tag{7.7}$$

where c is the damping coefficient.

For simplicity, the *Rayleigh damping* is used in this book, and the damping matrix $\tilde{\mathbf{C}}$ is assumed to be a linear combination of $\tilde{\mathbf{M}}$ and $\bar{\mathbf{K}}^{\text{ES-FEM}}$,

$$\tilde{\mathbf{C}} = \alpha\tilde{\mathbf{M}} + \beta\bar{\mathbf{K}}^{\text{ES-FEM}}, \tag{7.8}$$

where α and β are the Rayleigh damping coefficients.

Many existing standard schemes can be used to solve the second-order time-dependent problems, such as the Newmark method, the Crank–Nicholson method, and so on [9]. In this chapter, the Newmark method is used. When the current state at $t = t_0$ is known as $(\bar{\mathbf{d}}_0, \dot{\bar{\mathbf{d}}}_0, \ddot{\bar{\mathbf{d}}}_0)$, we aim

to find a new state $(\bar{\mathbf{d}}_1, \dot{\bar{\mathbf{d}}}_1, \ddot{\bar{\mathbf{d}}}_1)$ at $t_1 = t_0 + \theta\Delta t$ where $0.5 \leq \theta \leq 1$, using the following formulations:

$$\left[\left(\alpha + \frac{1}{\theta\Delta t}\right)\tilde{\mathbf{M}} + (\beta + \theta\Delta t)\,\bar{\mathbf{K}}^{\text{ES-FEM}}\right]\bar{\mathbf{d}}_1 = \theta\Delta t\tilde{\mathbf{f}}_1 + (1-\theta)\,\Delta t\tilde{\mathbf{f}}_0$$
$$+\left(\alpha + \frac{1}{\theta\Delta t}\right)\tilde{\mathbf{M}}\bar{\mathbf{d}}_0 + \frac{1}{\theta}\tilde{\mathbf{M}}\dot{\bar{\mathbf{d}}}_0 + [\beta - (1-\theta)\,\Delta t]\;\bar{\mathbf{K}}^{\text{ES-FEM}}\bar{\mathbf{d}}_0, \tag{7.9}$$

$$\dot{\bar{\mathbf{d}}}_1 = \frac{1}{\theta\Delta t}\left(\bar{\mathbf{d}}_1 - \bar{\mathbf{d}}_0\right) - \frac{1-\theta}{\theta}\dot{\bar{\mathbf{d}}}_0, \tag{7.10}$$

$$\ddot{\bar{\mathbf{d}}}_1 = \frac{1}{\theta\Delta t}\left(\dot{\bar{\mathbf{d}}}_1 - \dot{\bar{\mathbf{d}}}_0\right) - \frac{1-\theta}{\theta}\ddot{\bar{\mathbf{d}}}_0. \tag{7.11}$$

Without the damping and forcing terms, Equation 7.5 is reduced to a homogeneous differential equation:

$$\tilde{\mathbf{M}}\ddot{\bar{\mathbf{d}}} + \bar{\mathbf{K}}^{\text{ES-FEM}}\bar{\mathbf{d}} = \mathbf{0}. \tag{7.12}$$

A general solution of such a homogeneous equation can be written as

$$\bar{\mathbf{d}} = \bar{\mathbf{D}}\exp(i\omega t), \tag{7.13}$$

where t indicates time, $\bar{\mathbf{D}}$ is the amplitude of the sinusoidal displacements, and ω is the angular frequency. On its substitution into Equation 7.12, the *natural frequency* ω can be found by solving the following eigenvalue equation:

$$\left[\bar{\mathbf{K}}^{\text{ES-FEM}} - \omega^2\tilde{\mathbf{M}}\right]\bar{\mathbf{D}} = \mathbf{0}. \tag{7.14}$$

Finally, we note that the trial function used in an ES-FEM model is the same as that in the standard FEM. Therefore the force vector $\tilde{\mathbf{f}}$, mass matrix $\tilde{\mathbf{M}}$, and damping matrix $\tilde{\mathbf{C}}$ in the ES-FEM are also computed in exactly the same way as in the FEM. In other words, the ES-FEM changes only the stiffness matrix.

7.3.3 Lumped Mass Matrix

In dynamic analysis using the ES-FEM-T3, we can use the usual *consistent mass* matrix defined in Equation 7.6. For computational efficiency purposes, the well-known *lumped mass* matrix for the linear triangular elements Ω_i^e can also be used:

$$\tilde{\mathbf{M}}_i^e = \frac{\rho t A_i^e}{3}\mathbf{I}, \tag{7.15}$$

where $\mathbf{I}$ is the identity matrix of size 6 by 6, A_i^e is the area of the element, and ρ and t are the mass density and the thickness of the element, respectively. The diagonal form of the lumped mass matrix gives the superiority in terms of efficiency in computation over the consistent mass matrix in solving transient dynamics problems. Our past experience in studying the consistent and lumped mass matrices has led to the following remark.

Remark 7.1 On the Softening Effect of Lumping Mass

The use of lumped mass, in general, results in a "softer" model, meaning that the eigenvalues obtained will be smaller than those obtained using the consistent mass matrix for the same model.

Remark 7.1 has important implications in obtaining the bounds for dynamic problems. In this book, however, we will not discuss this any further. The interested reader may refer to Refs. [10,11].

7.3.4 Nonlinear Analysis of Large Deformation

The excellent stability and very close-to-exact stiffness feature of the ES-FEM make it an ideal candidate also for the analysis of nonlinear problems. Here, in this section, we consider the use of T3 elements in the ES-FEM model for large deformation nonlinear problems. In this case, the values of the smoothed strain–displacement matrices and stresses of the smoothing domains associated with edges become simply the average values of those of the adjacent elements around the edge, using Equation 7.3. All the other techniques developed and currently used in the FEM such as the total Lagrange formulation can be directly adopted. The ES-FEM-T3 model for nonlinear problems of large deformation based on the total Lagrange formulation [12,13] can be expressed as follows:

$$\left(\bar{\mathbf{K}}_L + \bar{\mathbf{K}}_{\mathrm{NL}}\right)\bar{\mathbf{d}} = \tilde{\mathbf{f}} - \bar{\mathbf{f}}_1, \tag{7.16}$$

where the stiffness matrix for the *linearized* portion can be written as

$$\bar{\mathbf{K}}_L = \sum_{k=1}^{N_{\mathrm{eg}}} \bar{\mathbf{B}}_L^T \mathbf{c} \bar{\mathbf{B}}_L A_k^s, \tag{7.17}$$

in which matrix $\bar{\mathbf{B}}_L$ is for the edge-based smoothing domains, and is computed using

$$\bar{\mathbf{B}}_L = \frac{1}{A_k^s} \sum_{j=1}^{n_k^e} \frac{1}{3} A_j^e \tilde{\mathbf{B}}_{L,j}^e. \tag{7.18}$$

In the foregoing equation, the matrix $\tilde{\mathbf{B}}_L^e$ for the elements sharing the edge is given by

$$\tilde{\mathbf{B}}_L^e = \begin{bmatrix} F_{11}N_{1,1} & F_{21}N_{1,1} & F_{11}N_{2,1} \\ F_{12}N_{1,2} & F_{22}N_{1,2} & F_{12}N_{2,2} \\ F_{11}N_{1,2}+F_{12}N_{1,1} & F_{21}N_{1,2}+F_{22}N_{1,1} & F_{11}N_{2,2}+F_{12}N_{2,1} \\ F_{21}N_{2,1} & F_{11}N_{3,1} & F_{21}N_{3,1} \\ F_{22}N_{2,2} & F_{12}N_{3,2} & F_{22}N_{3,2} \\ F_{21}N_{2,2}+F_{22}N_{2,1} & F_{11}N_{3,2}+F_{12}N_{3,1} & F_{21}N_{3,2}+F_{22}N_{3,1} \end{bmatrix}, \tag{7.19}$$

in which $N_{I,j} = \partial N_I / \partial X_j$ and F_{IJ} are entries of the deformation gradient tensor of the elements $\tilde{\mathbf{F}}^e$ that is computed using

$$\tilde{\mathbf{F}}^e = \begin{bmatrix} F_{11} & F_{12} \\ F_{21} & F_{22} \end{bmatrix} = \left(\frac{\partial \mathbf{x}}{\partial \mathbf{X}} \right)^T = \left(\mathbf{L}_d \bar{\mathbf{d}} + \mathbf{I} \right)^T. \tag{7.20}$$

The stiffness matrix for the nonlinear portion in Equation 7.16 can be written as

$$\bar{\mathbf{K}}_{\mathrm{NL}} = \sum_{k=1}^{N_{\mathrm{eg}}} \bar{\mathbf{B}}_{\mathrm{NL}}^T \bar{\mathbf{S}} \bar{\mathbf{B}}_{\mathrm{NL}} \, A_k^s, \tag{7.21}$$

where matrix $\bar{\mathbf{B}}_{\mathrm{NL}}$ is for the edge-based smoothing domains and is computed using

$$\bar{\mathbf{B}}_{\mathrm{NL}} = \frac{1}{A_k^s} \sum_{j=1}^{n_k^e} \frac{1}{3} A_j^e \tilde{\mathbf{B}}_{\mathrm{NL},j}^e. \tag{7.22}$$

In the foregoing equation, the matrix $\tilde{\mathbf{B}}_{\mathrm{NL}}^e$ is for the elements given by

$$\tilde{\mathbf{B}}_{\mathrm{NL}}^e = \begin{bmatrix} N_{1,1} & 0 & N_{2,1} & 0 & N_{3,1} & 0 \\ N_{1,2} & 0 & N_{2,2} & 0 & N_{3,2} & 0 \\ 0 & N_{1,1} & 0 & N_{2,1} & 0 & N_{3,1} \\ 0 & N_{1,2} & 0 & N_{2,2} & 0 & N_{3,2} \end{bmatrix}, \tag{7.23}$$

and matrix $\bar{\mathbf{S}}$ is for the edge-based smoothing domains, and is computed using

$$\bar{\mathbf{S}} = \frac{1}{A_k^s} \sum_{j=1}^{n_k^e} \frac{1}{3} A_j^e \tilde{\mathbf{S}}_j^e \quad \text{with} \quad \tilde{\mathbf{S}}^e = \begin{bmatrix} S_{11} & S_{12} & 0 & 0 \\ S_{12} & S_{22} & 0 & 0 \\ 0 & 0 & S_{11} & S_{12} \\ 0 & 0 & S_{12} & S_{22} \end{bmatrix}. \tag{7.24}$$

In the foregoing equation, the entries S_{IJ} of matrix $\tilde{\mathbf{S}}^e$ are derived from the second Piola–Kirchhoff stress tensor $\tilde{\boldsymbol{\Psi}}^e$ for the elements by

$$\tilde{\boldsymbol{\Psi}}^e = \begin{bmatrix} S_{11} \\ S_{22} \\ S_{12} \end{bmatrix} = \mathbf{c} \begin{bmatrix} E_{11} \\ E_{22} \\ 2E_{12} \end{bmatrix}. \tag{7.25}$$

The entries E_{IJ} in Equation 7.25 are derived from the entries of the Green–Lagrange strain tensor $\tilde{\mathbf{E}}^e$ of the elements as

$$\tilde{\mathbf{E}}^e = \begin{bmatrix} E_{11} & E_{12} \\ E_{21} & E_{22} \end{bmatrix} = \frac{1}{2}\left(\left(\tilde{\mathbf{F}}^e\right)^T \tilde{\mathbf{F}}^e - \mathbf{I}\right), \tag{7.26}$$

where $\mathbf{I}$ is the second-order unit matrix.

The "additional" force term caused by the nonlinearity in Equation 7.16 becomes

$$\bar{\mathbf{f}}_1 = \sum_{k=1}^{N_{\text{eg}}} \bar{\mathbf{B}}_L^T \bar{\boldsymbol{\Psi}} A_k^s, \tag{7.27}$$

where

$$\bar{\boldsymbol{\Psi}} = \frac{1}{A_k^s} \sum_{j=1}^{n_k^e} \frac{1}{3} A_j^e \tilde{\boldsymbol{\Psi}}_j^e. \tag{7.28}$$

7.4 Evaluation of the Shape Function Values in the ES-FEM

As presented generally in Chapter 4, when a compatible (continuous) displacement field along the boundary of the smoothing domains is used, the smoothed strain–displacement matrix $\bar{\mathbf{B}}_I$ can be in general computed using Equation 4.30 with only shape function values at mid-segment-points (Gauss points) along segments $\Gamma_{k,p}^s \in \Gamma_k^s$ of smoothing domains. The shape function value at each Gauss point is evaluated using the simple linear PIM using those of the two related endpoints that bound the segment containing that Gauss point. For example, the values of the shape functions at point #$g1$ on the segment 1-A shown in Figure 7.3 are evaluated by averaging the values of shape functions of two related nodes on the segment: points #1 and #A. Therefore, in order to facilitate the evaluation of shape function values at Gauss points in the ES-FEM, we first need to evaluate

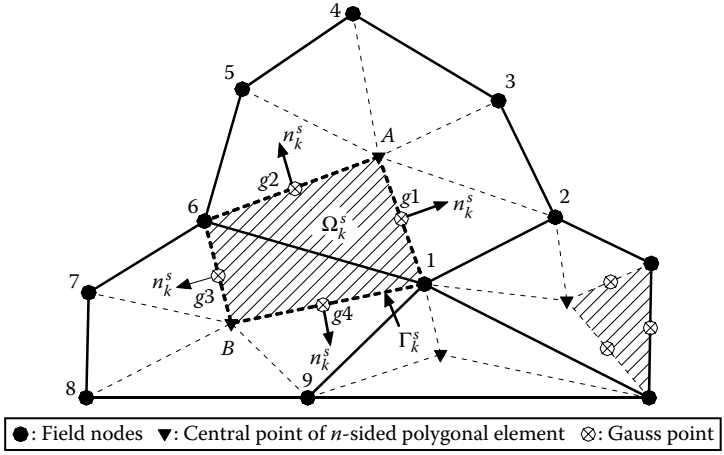

FIGURE 7.3 Gauss points of the smoothing domains associated with edges for n-sided polygonal elements in ES-FEM.

the shape function values at the endpoints of segments such as field nodes (#1, #6, etc.) and central points (#A, #B, etc.) shown in Figure 7.3.

For an ES-FEM model using n-sided polygonal elements, the shape functions constructed in Section 4.3.2 are used. These shape functions are obviously linear and compatible along the boundary of smoothing domains associated with edges. The evaluation of the shape function values at the endpoints of segments shown in Figure 7.3 is quite straightforward. Figure 7.3 and Table 7.1 give explicitly the shape function values at different points of the smoothing domain associated with the edge 1-6. The number of support nodes for the smoothing domain is 9 (from #1 to #9). We have four segments $\Gamma_{k,p}^s$ on Γ_k^s (1A, A6, 6B, B1). Each segment needs only one Gauss point and therefore there are a total of four Gauss points ($g1, g2, g3, g4$) used for the entire smoothing domain Ω_k^s associated with edge k(1-6), and the shape function values at these four Gauss points can be tabulated in Table 7.1 by simple inspection.

It may be mentioned again that no extra DOFs are associated with these points. In other words, these points are merely the locations for the linear interpolation, and carry no additional field variables. Only these nodes in the ES-FEM model carry field variables (displacements).

It is easy to see that the linear shape functions for triangular elements of the standard FEM satisfy naturally the linear compatible property along the boundary of the smoothing domains. Hence, the ES-FEM can be applied easily using the triangular elements without any modification of the shape functions. The smoothed strain–displacement matrix $\bar{\mathbf{B}}_I$ is given in Equation 7.3.

TABLE 7.1

Shape Function Values at Different Sites on the Smoothing Domain Boundary Associated with the Edge 1-6 in Figure 7.3

Site	Node 1	Node 2	Node 3	Node 4	Node 5	Node 6	Node 7	Node 8	Node 9	Description
1	1.0	0	0	0	0	0	0	0	0	Field node
2	0	1.0	0	0	0	0	0	0	0	Field node
3	0	0	1.0	0	0	0	0	0	0	Field node
4	0	0	0	1.0	0	0	0	0	0	Field node
5	0	0	0	0	1.0	0	0	0	0	Field node
6	0	0	0	0	0	1.0	0	0	0	Field node
7	0	0	0	0	0	0	1.0	0	0	Field node
8	0	0	0	0	0	0	0	1.0	0	Field node
9	0	0	0	0	0	0	0	0	1.0	Field node
A	1/6	1/6	1/6	1/6	1/6	1/6	0	0	0	Centroid of element
B	1/5	0	0	0	0	1/5	1/5	1/5	1/5	Centroid of element
$g1$	**7/12**	**1/12**	**1/12**	**1/12**	**1/12**	**1/12**	**0**	**0**	**0**	**Mid-segment-point of $\Gamma^s_{k,p}$**
$g2$	**1/12**	**1/12**	**1/12**	**1/12**	**1/12**	**7/12**	**0**	**0**	**0**	**Mid-segment-point of $\Gamma^s_{k,p}$**
$g3$	**1/10**	**0**	**0**	**0**	**0**	**6/10**	**1/10**	**1/10**	**1/10**	**Mid-segment-point of $\Gamma^s_{k,p}$**
$g4$	6/10	0	0	0	0	1/10	1/10	1/10	1/10	Mid-segment-point of $\Gamma^s_{k,p}$

7.5 A Smoothing-Domain-Based Selective ES/NS-FEM

The ES-FEM models formulated above are on the "stiff" side and are thus subjected to the volumetric locking (see Remark 2.2). Therefore, it cannot be used directly to solve problems with nearly incompressible materials with Poisson's ratio close to 0.5. On the other hand, we know that the NS-FEM formulated in Chapter 6 is naturally immune from the volume locking [1]. It is therefore making good sense to combine the NS- and ES-FEM formulations to construct the so-called smoothing-domain-based selective ES/NS-FEM that can overcome the volumetric locking problem and yet with good performance.

In this section, such a smoothing-domain-based selective scheme will be used in the combined formulation of ES/NS-FEM. We apply two different types of smoothing domains selectively for the two different material "parts" (μ part and λ part). Since the node-based smoothing domains used in the NS-FEM were found effective in overcoming volumetric locking, and the λ part is known as the "culprit" of the volumetric locking, we simply use the node-based domains for the λ part. Because the volumetric locking has nothing to do with the μ part, we use the edge-based domains (ES-FEM) for the μ part. Such a procedure is simple and easy to implement, and the stiffness matrix of the smoothing-domain-based selective ES/NS-FEM model can be simply written as

$$\bar{\mathbf{K}} = \underbrace{\sum_{i=1}^{N_{\text{eg}}} \left(\bar{\mathbf{B}}_{1,i}\right)^T \mathbf{c}_1 \bar{\mathbf{B}}_{1,i} A_{1,i}^s}_{\bar{\mathbf{K}}_1^{\text{ES-FEM}}} + \underbrace{\sum_{j=1}^{N_n} \left(\bar{\mathbf{B}}_{2,i}\right)^T \mathbf{c}_2 \bar{\mathbf{B}}_{2,j} A_{2,j}^s}_{\bar{\mathbf{K}}_2^{\text{NS-FEM}}}, \tag{7.29}$$

where $\bar{\mathbf{B}}_{1,i}$ and $A_{1,i}^s$ are the smoothed strain–displacement matrix and area of the smoothing domain $\Omega_{1,i}^s$ associated with edge i; $\bar{\mathbf{B}}_{2,j}$ and $A_{2,j}^s$ are the smoothed strain–displacement matrix and the area of the smoothing domain $\Omega_{2,j}^s$ associated with node j, respectively; $\mathbf{c}_1$ and $\mathbf{c}_2$ are the component material matrices decomposed from the material matrix $\mathbf{c}$ as presented by Equations 5.13 and 5.14; and N_{eg} and N_n are, respectively, the total number of edges and nodes located in the element mesh for the entire problem domain. The formulation of $\bar{\mathbf{K}}_1^{\text{ES-FEM}}$ follows simply Equation 7.2, and that of $\bar{\mathbf{K}}_2^{\text{NS-FEM}}$ following Equation 6.2.

7.6 Properties of the ES-FEM

We now perform some analysis and tests to examine the properties of the ES-FEM.

7.6.1 Rank Analysis for the ES-FEM Stiffness Matrix

Property 7.1 ES-FEM: Spatially Stable

The ES-FEM with n-sided polygonal elements possesses only "legal" zero-energy modes that represent the rigid motions, and there exists no spurious zero-energy mode. Therefore, it is spatially stable.

The spatial stability of the ES-FEM is ensured by the following key reasons:

i. The total number of edges is always bigger than that of nodes for any discretization. Therefore, the number of smoothing domains N_s is always much larger than the minimum number of smoothing domains $N_s^{\min}$ presented in Section 4.6.
ii. The edge-based smoothing domains are independent of each other and hence the strain smoothing operation ensures linearly independent columns (or rows) in the stiffness matrix [14]. This is true for all possible ES-FEM models, as examined in detail in Table 7.2.
iii. The shape functions used in the ES-FEM are of partition of unity, which ensures a proper representation of the rigid motions.

Due to the above-mentioned reasons, no deformed zero-energy mode will exist in an ES-FEM model. In other words, any finite deformation (except the rigid motions) will result in a finite amount of strain energy in an ES-FEM model (we assume, as always, that the material is stable).

Note also that for any type of element mesh, the number of edges are always larger than or equal to the number of nodes. Therefore, the ES-FEM model is always "stiffer" than the NS-FEM for the same element mesh, which explains partially why the ES-FEM is temporally stable (more discussion later) while the NS-FEM is not.

7.6.2 Temporal Stability of the ES-FEM-T3

Property 7.2 ES-FEM: Temporally Stable

There exist no spurious non-zero-energy modes in an ES-FEM-T3 model and thus it is temporally stable.

In the standard FEM-T3, the shape functions are (purely) linear and hence the compatible strain field in an element is constant. Therefore, only one Gauss point is needed to perform the domain integration for the weak form for each element. This implies that the number of Gauss points used in the entire problem domain equals the number of elements. Such an FEM-T3 model is known to be temporally stable in dynamic analysis and has no spurious non-zero-energy modes.

TABLE 7.2

Existence of Spurious Zero-Energy Modes in an Element

Type of Element	ES-FEM	FEM with Reduced Integration
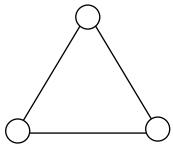 Triangle $N_R = 3$	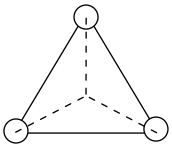 $n_Q = 3, \quad N_Q = 3 \times n_Q = 9$ $n_t = 3, \quad N_u = 2 \times n_t = 6$ $N_Q > N_u - N_R$ => Spurious zero-energy modes not possible	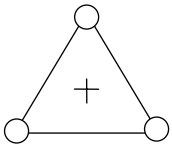 $n_Q = 1, \quad N_Q = 3 \times n_Q = 3$ $n_t = 3, \quad N_u = 2 \times n_t = 6$ $N_Q = N_u - N_R$ => Spurious zero-energy modes not possible
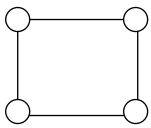 Quadrilateral $N_R = 3$	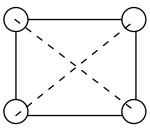 $n_Q = 4, \quad N_Q = 3 \times n_Q = 12$ $n_t = 4, \quad N_u = 2 \times n_t = 8$ $N_Q > N_u - N_R$ => Spurious zero-energy modes not possible	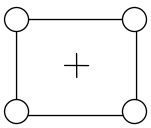 $n_Q = 1, \quad N_Q = 3 \times n_Q = 3$ $n_t = 4, \quad N_u = 2 \times n_t = 8$ $N_Q < N_u - N_R$ => Spurious zero-energy modes possible
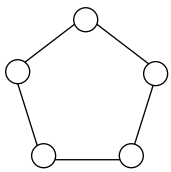 n-sided polygonal ($n > 4$) $N_R = 3$	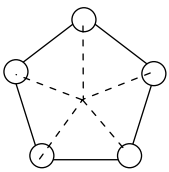 $n_Q = n, \quad N_Q = 3 \times n_Q = 3n$ $n_t = n, \quad N_u = 2 \times n_t = 2n$ $N_Q > N_u - N_R$ => Spurious zero-energy modes not possible	Not applicable

Notes: N_R, number of DOFs of rigid motion; n_Q, number of quadrature points/cells; N_Q, number of independent equations; n_t, number of nodes; and N_u, number of total DOFs.

In our ES-FEM using triangular meshes (ES-FEM-T3), the smoothing domains used are associated with edges of the elements and the strain (or stress) is constant over each smoothing domain. We know that the stability (both spatial and temporal) is directly related to the number

of "samplings" of the integrand in the weak form. Hence, for stability considerations, each smoothing domain can be viewed as equivalent to one Gauss point in terms of sampling the integrand in the weak form. Because the number of edges is always larger than the number of elements in any ES-FEM models, the number of samplings in an ES-FEM-T3 is, in fact, always larger than that in the standard FEM-T3. Therefore, the ES-FEM-T3 must be always stable temporally (also spatially), should have no spurious non-zero-energy modes, and is well suited for the dynamic analyses.

Note that, in the NS-FEM, smoothing domains associated with the node are employed to calculate the stiffness matrix. This works well for static problems. However, for vibration analysis, the NS-FEM is unstable because of the presence of spurious non-zero-energy modes [5]. This is because the number of nodes can be smaller than the number of elements and hence there is a chance of spurious modes appearing at a higher energy level. This phenomenon is quite similar to the underintegration of the weak form inherent in the nodal integration approach of mesh-free methods. The temporal instability, therefore, has been one of the main concerns of the NS-FEM and nodal integrated mesh-free methods [2–4]. The simplest and most effective solution is to use the edge-based smoothing domains: the ES-FEM. Based on the above discussions, we can further note the following.

Property 7.3 ES-FEM: Bound Property

The stiffness of an ES-FEM model is in between those of the FEM model and the NS-FEM model using the same mesh. Therefore, the strain energy solution of the ES-FEM will be in between those of the FEM and NS-FEM models using the same mesh. This also implies that the strain energy solution of ES-FEM will be better than either the FEM or the NS-FEM using the same mesh.

7.6.3 Standard Patch Tests

Standard patch tests are now performed for n-sided polygonal and triangular elements using our ES-FEM code. For the test using n-sided polygonal elements, a square patch is discretized with 36 n-sided polygonal elements as shown in Figure 5.5. For the test using triangular elements, the square patch is meshed with 32 irregular triangular elements, as shown in Figure 7.4.

The displacement norm (Equation 4.63) is used to examine the computed results. The material parameters are taken as $E = 100, \nu = 0.3$, and the linear displacement field is given by Equation 5.11. We state without showing detailed numbers that the ES-FEM can pass the standard patch test within machine precision. This test verifies that the ES-FEM model has at least

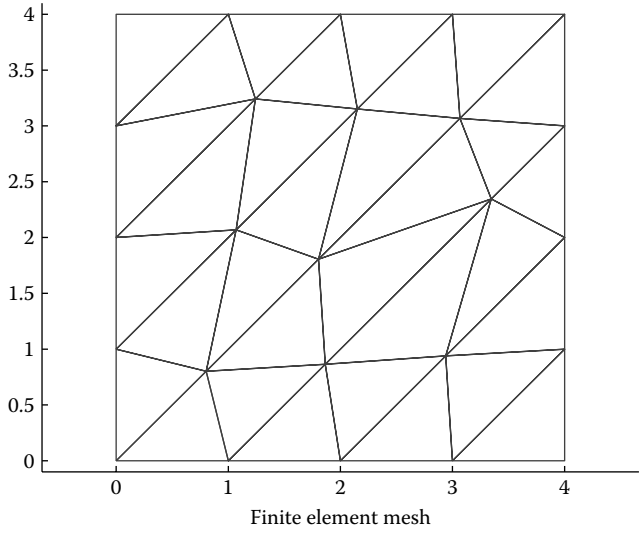

FIGURE 7.4 Mesh discretization using triangular elements for standard patch test.

second-order accuracy, implying that the displacement error is at least at the terms of second order or higher.

Property 7.4 ES-FEM: First Order Consistency

The ES-FEM has the first-order consistency, meaning that it can produce a linear displacement field exactly. In other words, it is of second-order accuracy in displacement solution: errors are at the terms of second order or above.

Property 7.5 ES-FEM Solution: Stability and Convergence

Due to the stability given in Property 7.1 and the first-order consistence given in Property 7.4, the ES-FEM has a unique stable solution that converges to the exact solution of the original solid mechanics problem defined in Chapter 2. This confirms Theorem 4.1.

7.7 Numerical Examples

In this section, some examples will be presented to demonstrate the properties of the ES-FEM models. For triangular elements, the ES-FEM-T3 results will be compared with those of NS-FEM-T3, FEM-T3, FEM-Q4, CS-FEM-Q4 ($n_e^s = 4$), and FEM using eight-node quadratic elements (FEM-Q8). For

the n-sided polygonal elements, the standard FEM model is not applicable and hence the nES-FEM results will be compared with those of nCS-FEM and nNS-FEM, using the same mesh.

For the triangular and four-node quadrilateral elements, the errors in both displacement norm and energy norm defined in Equations 4.49 and 4.50 are used for the examination of numerical models. When the energy norm is used, we use the recovery strain solution for S-FEM models, and both raw and recovery strain solutions for FEM models.

For n-sided polygonal elements, the errors in both displacement norm and energy norm defined in Equations 4.63 and 4.64 are used.

Example 7.7.1: A Rectangular Cantilever Loaded at the End: A Static Analysis

The benchmarking problem of a rectangular cantilever loaded at the end described in Example 5.8.1 is again used to examine the ES-FEM models. The geometry and boundary conditions of the cantilever are plotted in Figure 5.6. The domain discretizations with quadrilateral, n-sided polygonal and triangular elements are shown in Figures 5.7 and 6.6, respectively. The exact strain energy of the problem was found to be 4.4746 Nm.

Figures 7.5 and 7.6 compare the results of displacements and relative errors of the ES-FEM-T3 with FEM-T3, NS-FEM-T3, and FEM-Q4. It is shown that the FEM-T3 is very stiff, whereas the NS-FEM-T3 is very soft compared to the exact solution. The ES-FEM-T3 is stiffer than the NS-FEM-T3 and softer than the FEM-T3, and the ES-FEM-T3 solution is very close to the exact solution. Compared with all methods, the ES-FEM-T3 performs the best and even better than the FEM-Q4. Figure 7.7 shows that all the computed stresses using the ES-FEM-T3 agree excellently well with the analytical solutions.

The convergence of the strain energy is shown in Table 6.4 and plotted in Figure 7.8. It is seen that the FEM models behave in an overly stiff manner and hence give lower bounds, and the NS-FEM-T3 behaves in an overly soft manner and gives an upper bound. The solution of CS-FEM-Q4 is the most accurate. Although triangular elements are used, the ES-FEM-T3 result is as good as that of the CS-FEM-Q4 result.

The convergence of error in displacement norm is presented in Table 6.6 and plotted in Figure 7.9. It is seen that the ES-FEM-T3 stands out clearly. The error of displacement norm of the ES-FEM-T3 is the smallest among all the compared models when the fine meshes are used. When the finest mesh ($h = 1$ m) is used, the error of the ES-FEM-T3 is about 1/64 of FEM-T3, 1/9 of FEM-Q4, and even 2/5 of CS-FEM-Q4. In terms of convergence rate, the superconvergence is observed for the ES-FEM-T3 with a rate of 3.3 that is even much higher than the theoretical value of 2.0 for linear displacement models based on the weak formulation. We observe clearly now the "superconvergence" in terms of the displacement norm as well. Such a superconvergence is very much different from the usual superconvergence observed in the recovery FEM models, where

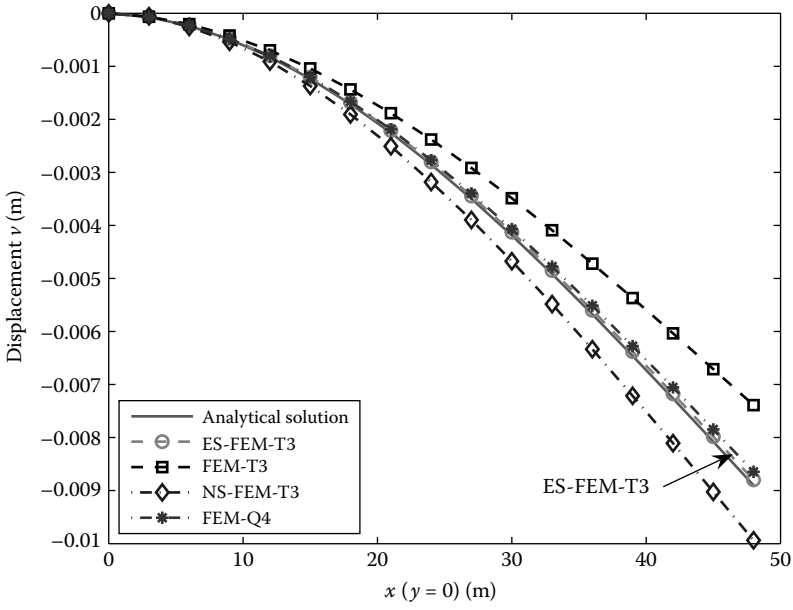

FIGURE 7.5 Distribution of displacement v along the horizontal middle axis of the cantilever subjected to a parabolic traction at the free end. The ES-FEM-T3 performs much better than FEM-T3 and even better than the FEM-Q4.

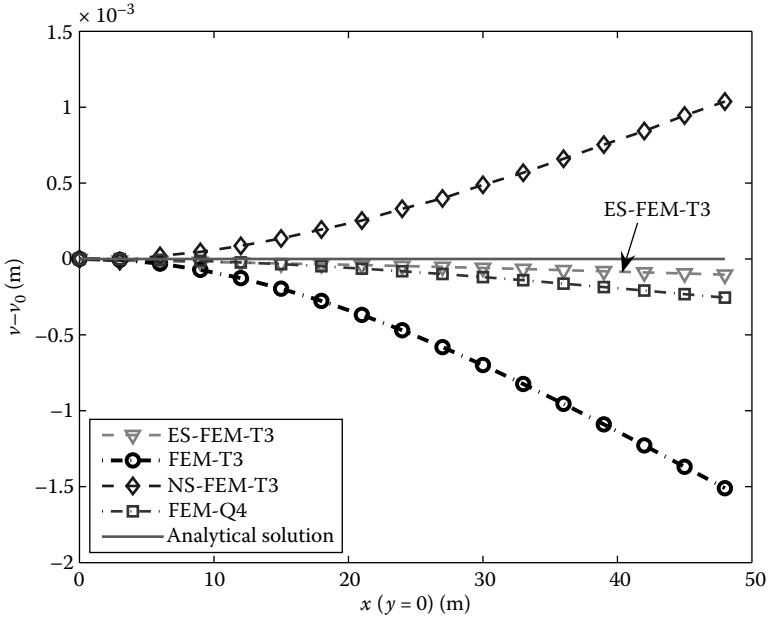

FIGURE 7.6 Relative error in displacement v along the horizontal middle axis of the cantilever subjected to a parabolic traction at the free end. The ES-FEM-T3 solution is very close to the exact one.

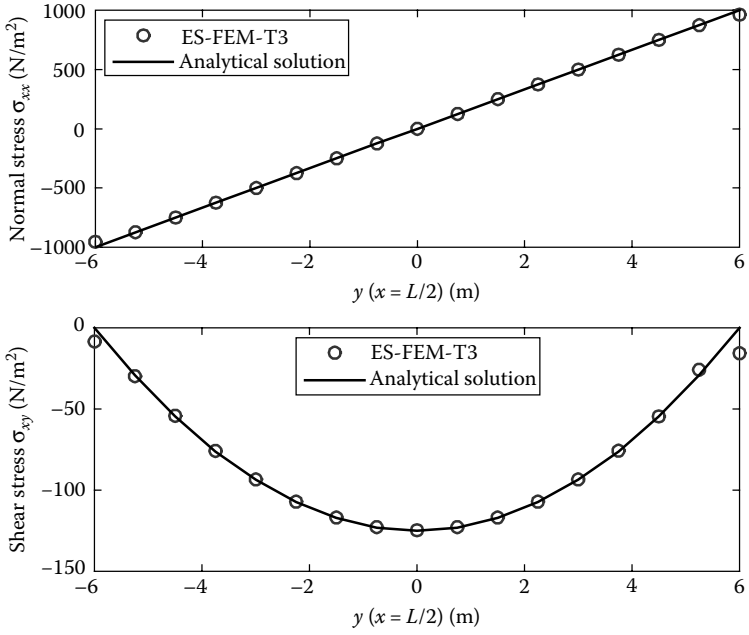

FIGURE 7.7 Normal stress σ_{xx} and shear stress σ_{xy} along the section of $x = L/2$ using the ES-FEM-T3 of the cantilever subjected to a parabolic traction at the free end.

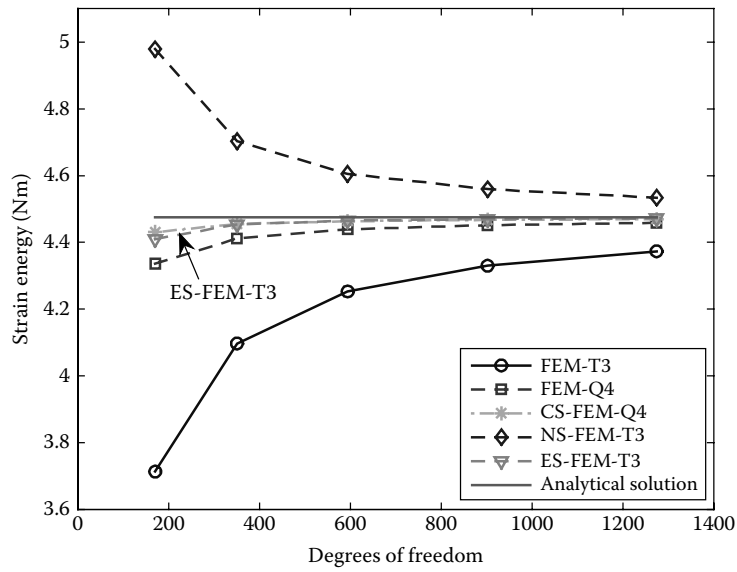

FIGURE 7.8 Convergence of the strain energy solution obtained using the ES-FEM-T3 in comparison with other methods for the cantilever subjected to a parabolic traction at the free end using the same distribution of nodes.

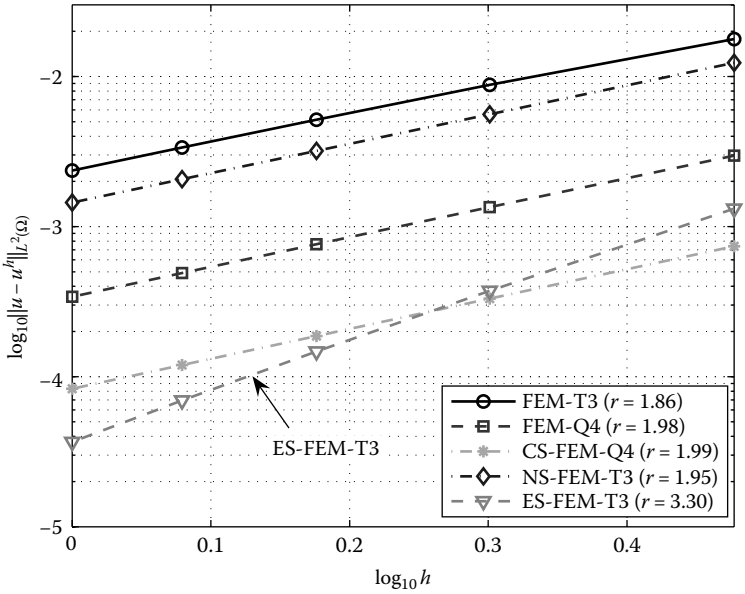

FIGURE 7.9 Error in displacement norm obtained using the ES-FEM-T3 in comparison with other methods for the cantilever subjected to a parabolic traction at the free end using the same set of nodes.

one can observe superconvergence only in energy norm and not in displacement norm. Such an excellent performance implies that the stiffness of the ES-FEM-T3 model is very "close to the exact stiffness" of the continuum solid. This unique feature of ES-FEM is very useful in dealing with various problems, especially dynamic problems including vibration and wave propagation (see Chapter 15).

The convergence of the error in energy norm is presented in Table 6.7 and plotted in Figure 7.10. It is seen again that these S-FEM-T3 models stand out clearly, and are compatible even with the FEM-Q4-Re. When the finest mesh ($h = 1$ m) is used, the solution accuracy of ES-FEM-T3 is not as good as those of CS-FEM-Q4, NS-FEM-T3, and FEM-Q4-Re, but it is still much better than that of FEM-T3, FEM-T3-Re, and FEM-Q4. The solution error of ES-FEM-T3 is about 1/6 of FEM-T3, 2/5 of FEM-Q4, 1/1.7 of FEM-T3-Re, and 1.3 times of FEM-Q4-Re. In terms of convergence rate, the superconvergence is observed for the ES-FEM-T3 with a rate of 1.52 that is much larger than the theoretical value of 1.0 for linear displacement models, and compatible with those of FEM-T3-Re (1.67) and FEM-Q4-Re (1.47).

Figure 7.11 compares the computation time of different methods using the same direct full-matrix solver. It is found that with the same sets of nodes, the computation time of the ES-FEM-T3 is only shorter than that of the NS-FEM-T3. However, when the efficiency of computation (CPU time for the same accuracy) in terms of both displacement and energy norms is considered, the ES-FEM-T3 model stands out clearly as a winner. Even though the ES-FEM-T3

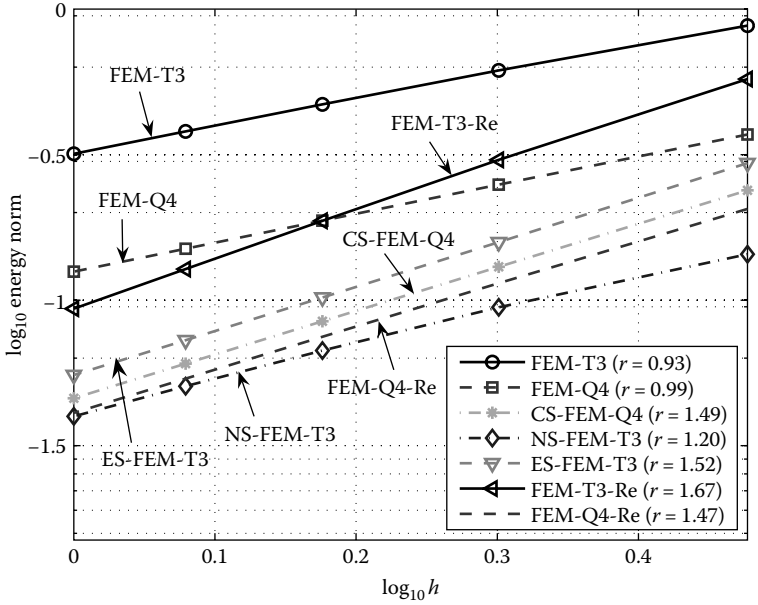

FIGURE 7.10 Error in energy norm obtained using the ES-FEM-T3 in comparison with other methods for the cantilever subjected to a parabolic traction at the free end using the same set of nodes.

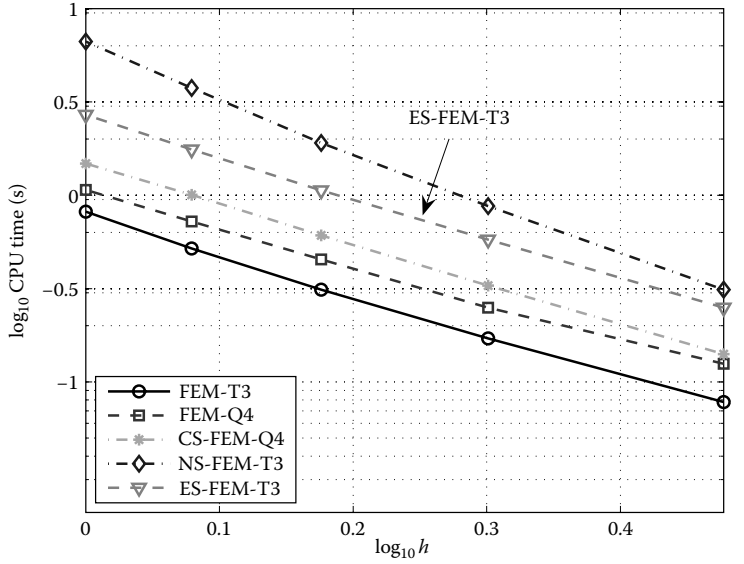

FIGURE 7.11 Comparison of the computation time of different methods for solving the cantilever subjected to a parabolic traction at the free end. For the same distribution of nodes, the FEM-T3 is the fastest to deliver the results.

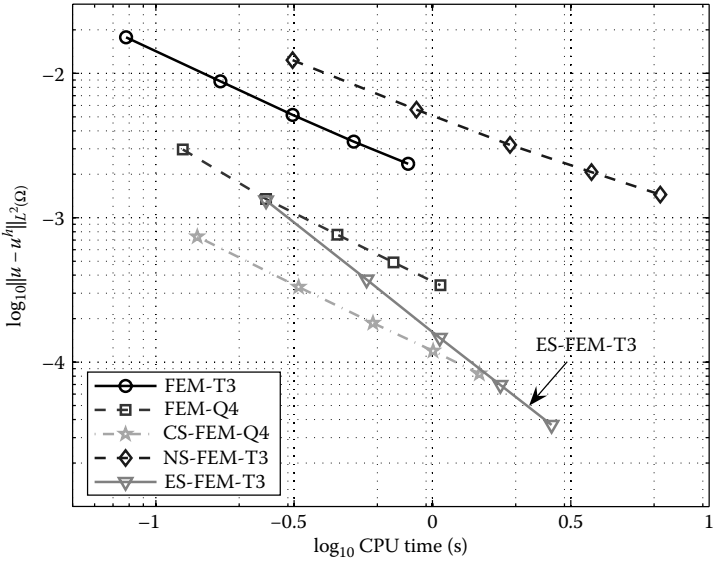

FIGURE 7.12 Comparison of the efficiency (computation time for the solutions of the same accuracy measured in displacement norm) for solving the cantilever subjected to a parabolic traction at the free end. The ES-FEM-T3 stands out clearly as a winner, even though it uses triangular elements. It wins by its superiority in convergence rate.

uses triangular elements, it wins by its superiority in convergence rate, as shown in Figure 7.12. One can therefore expect that when the finer mesh is used, the performance of ES-FEM-T3 will be even better. When the efficiency is measured in energy norm, the CS-FEM-Q4 is the most efficient, as shown in Figure 7.13. Among all the other models, the ES-FEM-T3 performs the best, even though it uses triangular elements. Because the ES-FEM-T3 works well with the triangular elements, which are very much preferred in automated mesh generation, it has a clear advantage over the FEM-Q4 and CS-FEM-Q4 models in the development of adaptive and automatic solution tools for domains of arbitrary complexity.

For the *n*-sided polygonal elements, Figure 7.14 shows that all the computed stresses using the *n*ES-FEM agree well with the analytical solutions. The convergence of the strain energy is shown in Table 6.5 and Figure 7.15. It is seen that the *n*ES-FEM has a very close-to-exact stiffness and hence is most accurate, while the *n*CS-FEM model behaves in an overly stiff manner and hence gives a lower bound, and *n*NS-FEM behaves in an overly soft manner and gives an upper bound.

The convergence of displacement norm is presented in Table 7.3 and plotted in Figure 7.16. It is seen that the *n*ES-FEM stands out clearly. The error of displacement norm of the *n*ES-FEM is the smallest among all the three models. When the finest mesh ($h = 1$ m) is used, the error of the *n*ES-FEM is about 1/4 of *n*CS-FEM and 1/2 of *n*NS-FEM. In terms of convergence rate, the *n*CS-FEM ($r = 1.85$) and *n*NS-FEM ($r = 1.71$) have a numerical rate smaller than the

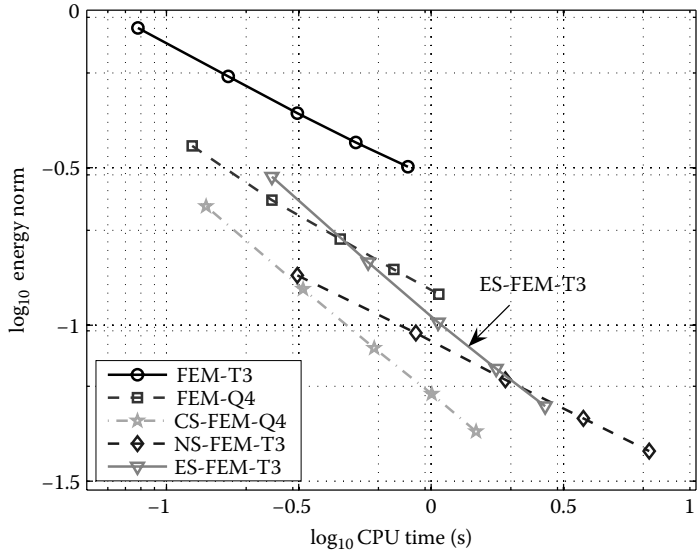

FIGURE 7.13 Comparison of the efficiency of computation time in terms of energy norm of the cantilever subjected to a parabolic traction at the free end. The CS-FEM-Q4 performed best, followed by the ES-FEM-T3 that uses triangular elements.

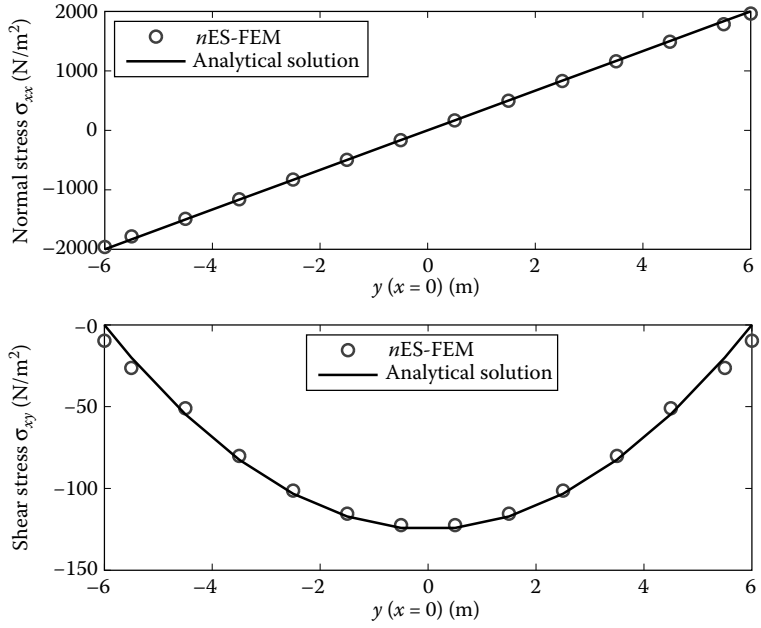

FIGURE 7.14 Normal stress σ_{xx} and shear stress σ_{xy} along the section of $x = 0$ using nES-FEM of the cantilever subjected to a parabolic traction at the free end.

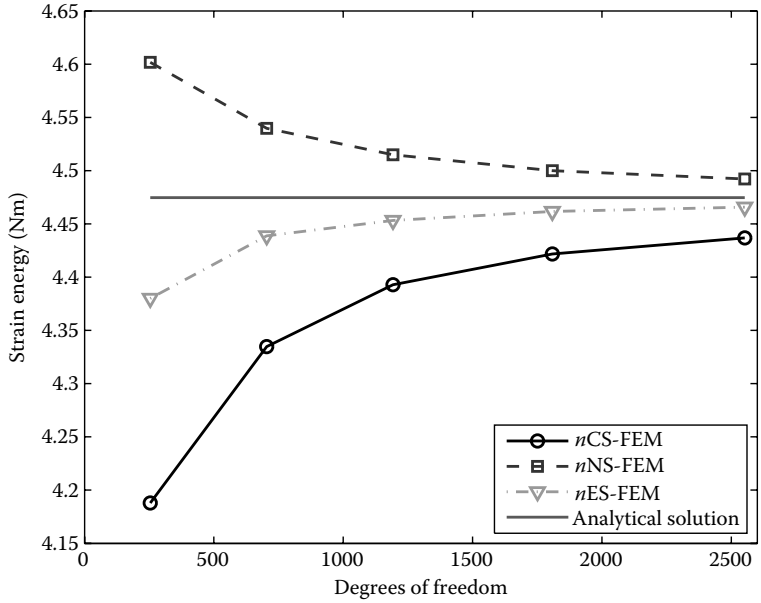

FIGURE 7.15 Convergence of the strain energy solution of *n*ES-FEM using *n*-sided polygonal elements in comparison with other methods for the cantilever subjected to a parabolic traction at the free end using the same meshes.

theoretical value of 2.0, while the rate of the *n*ES-FEM is $r = 2.16$, even larger than the theoretical value.

The convergence of the error in energy norm is presented in Table 7.4 and plotted in Figure 7.17. Again, it is seen that the *n*ES-FEM stands out clearly. The error of energy norm of the *n*ES-FEM is the smallest among the three models. When the finest mesh ($h = 1$ m) is used, the error of the *n*ES-FEM is about 2/5 of the *n*CS-FEM and 3/4 of the *n*NS-FEM. In terms of convergence rate, the *n*CS-FEM ($r = 0.93$) and *n*NS-FEM ($r = 0.94$) have a numerical rate smaller than the theoretical value of 1.0, while the rate of the *n*ES-FEM is larger with $r = 1.01$.

TABLE 7.3

Error in Displacement Norm (%) for Solutions Obtained Using Different Methods for the Cantilever Problem Using the Same Polygonal Meshes

	Mesh (16 × 4)	**Mesh (24 × 6)**	**Mesh (32 × 8)**	**Mesh (40 × 10)**	**Mesh (48 × 12)**
h (m)	4.0	2.0	1.5	1.2	1.0
*n*CS-FEM	6.21	3.01	1.76	1.13	0.81
*n*NS-FEM	3.06	1.55	0.98	0.60	0.44
*n*ES-FEM	2.10	0.77	0.46	0.27	0.19

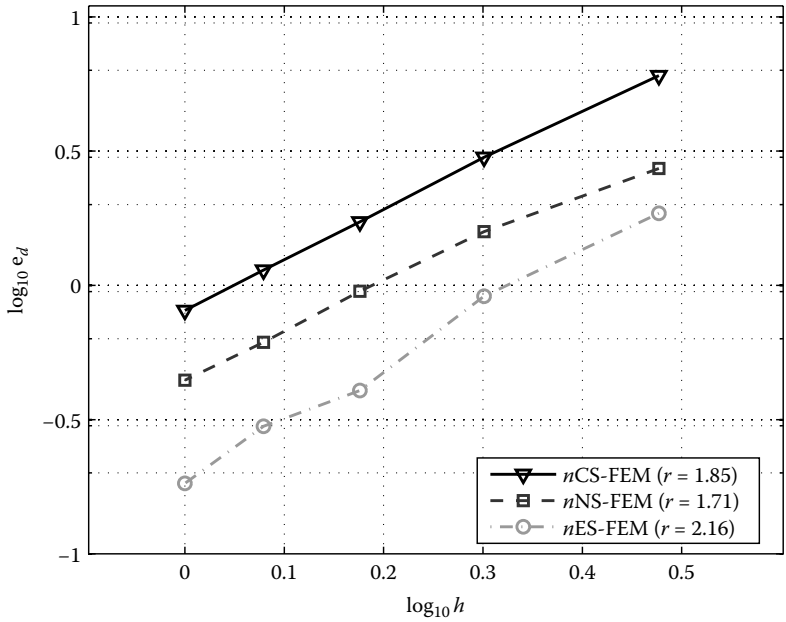

FIGURE 7.16 Error in displacement norm of *n*ES-FEM-T3 using *n*-sided polygonal elements in comparison with other methods for the cantilever subjected to a parabolic traction at the free end using the same meshes.

Example 7.7.2: Infinite Plate with a Circular Hole: A Static Analysis

The infinite plate with a circular hole described in Example 5.8.2 is used here to examine the ES-FEM models. The geometry and boundary conditions of the problem are plotted in Figure 5.18. Figures 5.19 and 6.12 give the discretization of the problem domain using four-node quadrilateral, *n*-sided polygonal and triangular elements, respectively.

Figures 7.18 and 7.19 show the comparison of displacements of the ES-FEM-T3 with the FEM-T3, NS-FEM-T3, and FEM-Q4. It is again found that the FEM-T3 model is very stiff, while the NS-FEM-T3 model is very soft compared

TABLE 7.4

Error in Energy Norm for Solutions Obtained Using Different Methods for the Cantilever Problem Using the Same Polygonal Meshes

	Mesh (16 × 4)	**Mesh (24 × 6)**	**Mesh (32 × 8)**	**Mesh (40 × 10)**	**Mesh (48 × 12)**
h (m)	4.0	2.0	1.5	1.2	1.0
*n*CS-FEM	0.4718	0.3326	0.2532	0.2025	0.1721
*n*NS-FEM	0.2588	0.1738	0.1296	0.1001	0.0897
*n*ES-FEM	0.1956	0.1413	0.1065	0.0782	0.0666

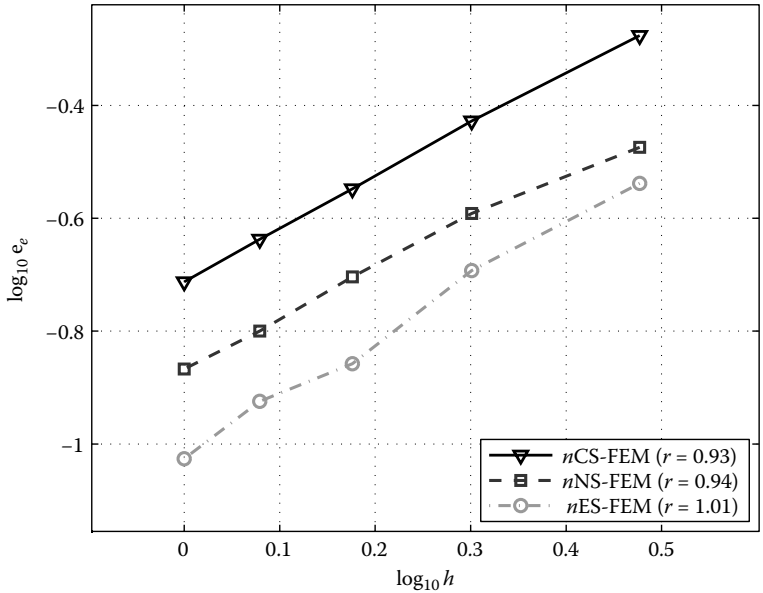

FIGURE 7.17 Error in energy norm of *n*ES-FEM-T3 using *n*-sided polygonal elements in comparison with other methods for the cantilever subjected to a parabolic traction at the free end using the same meshes.

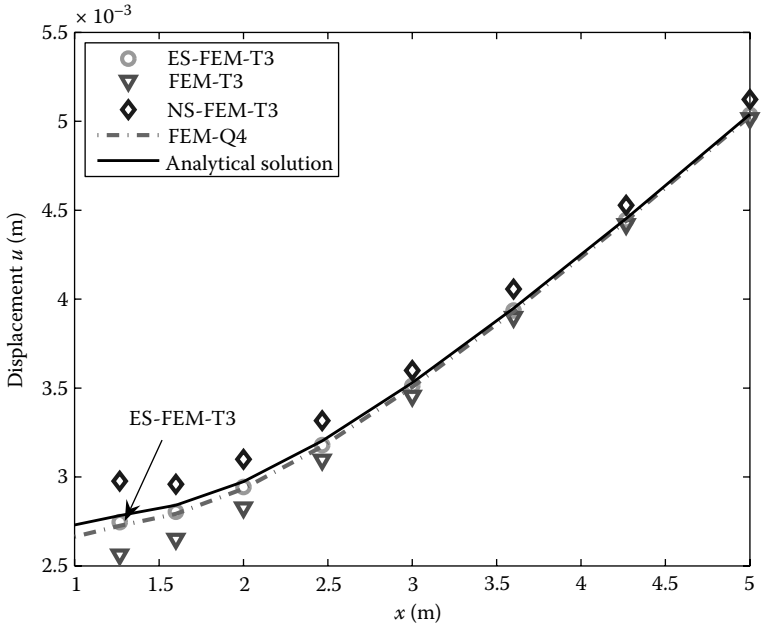

FIGURE 7.18 Distribution of displacement u along the bottom boundary of the infinite plate with a hole subjected to unidirectional tension.

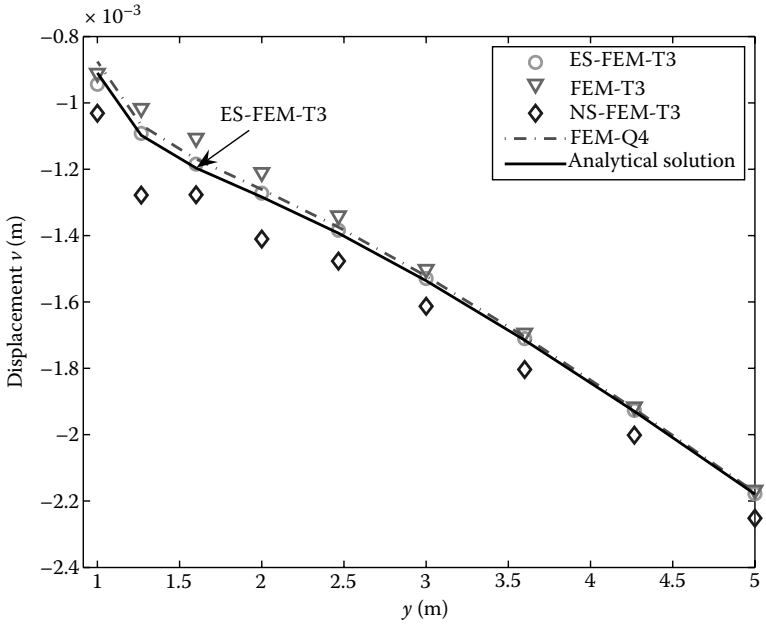

FIGURE 7.19 Distribution of displacement v along the left boundary of the infinite plate with a hole subjected to unidirectional tension.

to the exact model. The results of the ES-FEM-T3 are best and even better than those of the FEM-Q4. From Figure 7.20, it is observed that all the computed stresses using the ES-FEM-T3 agree well with the analytical solutions.

The convergence of the strain energy is shown in Table 6.8 and plotted in Figure 7.21. It is seen that the FEM models give lower bounds, the NS-FEM-T3 gives an upper bound, and the ES-FEM-T3 is the most accurate and even better than the CS-FEM-Q4.

The convergence of the error in displacement norm is shown in Table 6.10 and plotted in Figure 7.22. It is seen that the ES-FEM-T3 stands out clearly. The error of displacement norm of the ES-FEM-T3 is the smallest among all the compared models. When the finest mesh ($h = 0.1969$ m) is used, the error of the ES-FEM-T3 is about 1/5 of FEM-T3, 3/4 of FEM-Q4, and even a little smaller than that of CS-FEM-Q4. In terms of convergence rate, the rates of all methods, except the FEM-T3, are slightly larger than the theoretical value of 2.0 for linear displacement models.

The convergence of the error in energy norm is shown in Table 6.11 and is plotted in Figure 7.23. It is seen again that the S-FEM-T3 models stand out clearly together with the FEM-Q4-Re. When the finest mesh ($h = 0.1969$ m) is used, the error of the ES-FEM-T3 is only worse than that of the NS-FEM-T3. This error is almost equal to that of CS-FEM-Q4 and FEM-Q4-Re, and is much better than that of FEM-T3, FEM-T3-Re, and FEM-Q4. It is about 1/5 of FEM-T3, 2/5 of FEM-Q4, 0.56 times of FEM-T3-Re, and slightly better than FEM-Q4-Re.

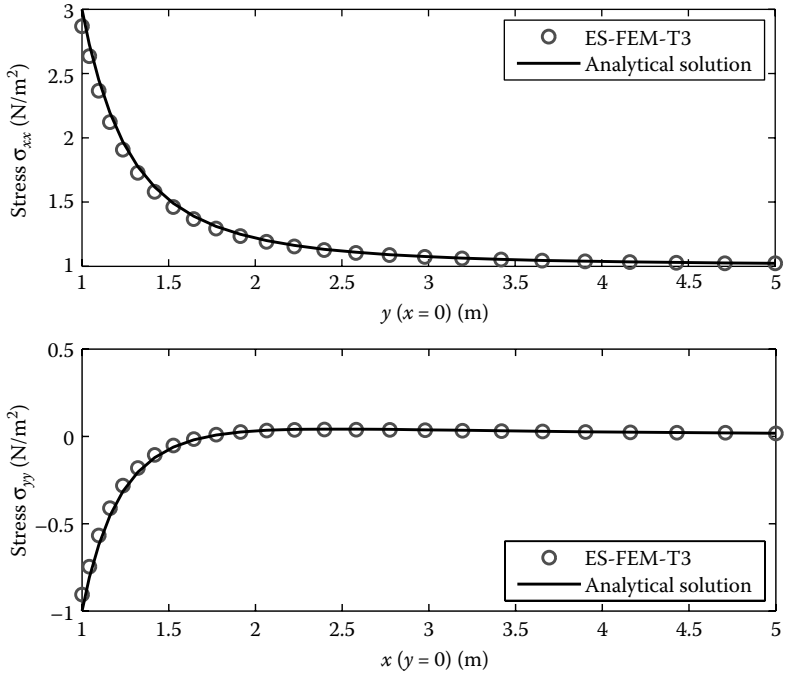

FIGURE 7.20 Stress σ_{xx} along the left boundary ($x = 0$) and stress σ_{yy} along the bottom boundary ($y = 0$) using ES-FEM-T3 of the infinite plate with a hole subjected to unidirectional tension.

In terms of convergence rate, the superconvergence is again observed for ES-FEM-T3 with a rate of 1.83 that is quite close to the optimal rate of 2.0 for the equilibrium model, much larger than the theoretical value of 1.0 for linear displacement models based on weak formulations, and higher than those of FEM-T3-Re (1.67) and FEM-Q4-Re (1.81).

Figures 7.24 and 7.25 plot the results obtained using *n*-sided polygonal elements. It is observed that all the computed displacements and stresses agree well with the analytical solutions. The convergence of the strain energy is shown in Table 6.9 and Figure 7.26. Again the *n*ES-FEM is found most accurate, while the *n*CS-FEM model gives a lower bound and *n*NS-FEM gives an upper bound.

The error in displacement norm is shown in Table 7.5 and plotted in Figure 7.27. In terms of accuracy, it is seen that the *n*ES-FEM stands out clearly. The error of displacement norm of the *n*ES-FEM is the smallest among the three models. When the finest mesh ($h = 0.1969$ m) is used, the error of the *n*ES-FEM is about 1/8 of *n*NS-FEM and 1/2 of *n*CS-FEM. In terms of convergence rate, the *n*ES-FEM ($r = 1.69$) is less than that of *n*CS-FEM ($r = 2.04$) but still larger than that of *n*NS-FEM ($r = 1.32$).

The convergence of the error in energy norm is presented in Table 7.6 and plotted in Figure 7.28. Again, it is seen that the *n*ES-FEM stands out clearly.

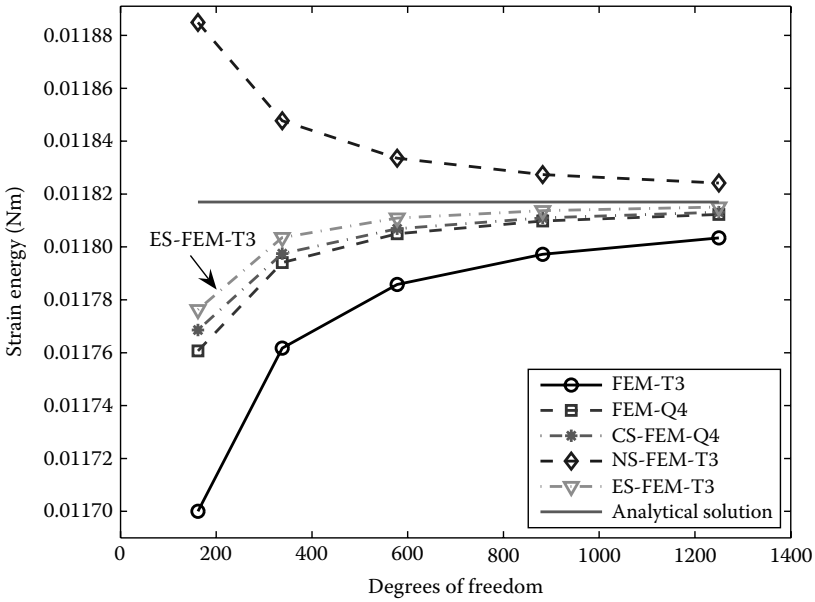

FIGURE 7.21 Convergence of the strain energy solution of ES-FEM-T3 in comparison with other methods for the infinite plate with a hole subjected to unidirectional tension using the same distribution of nodes.

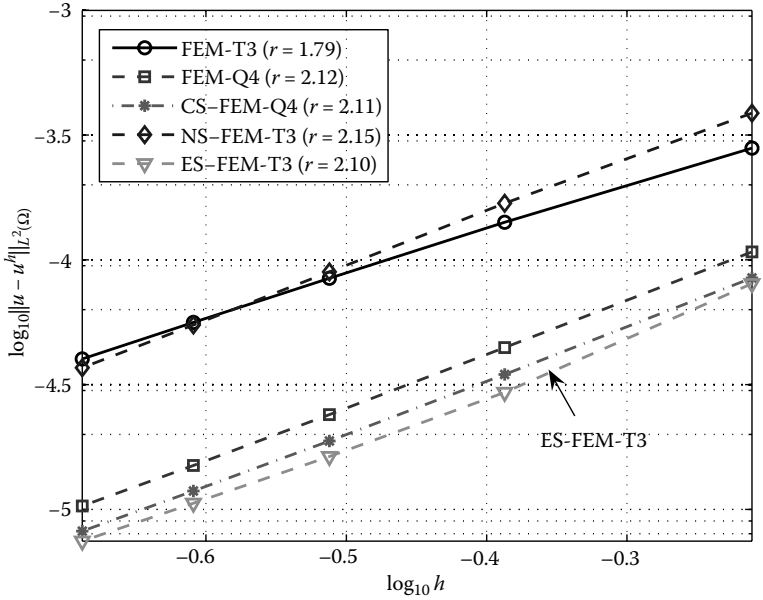

FIGURE 7.22 Error in displacement norm of the ES-FEM-T3 solution in comparison with other methods for the infinite plate with a hole subjected to unidirectional tension using the same distribution of nodes.

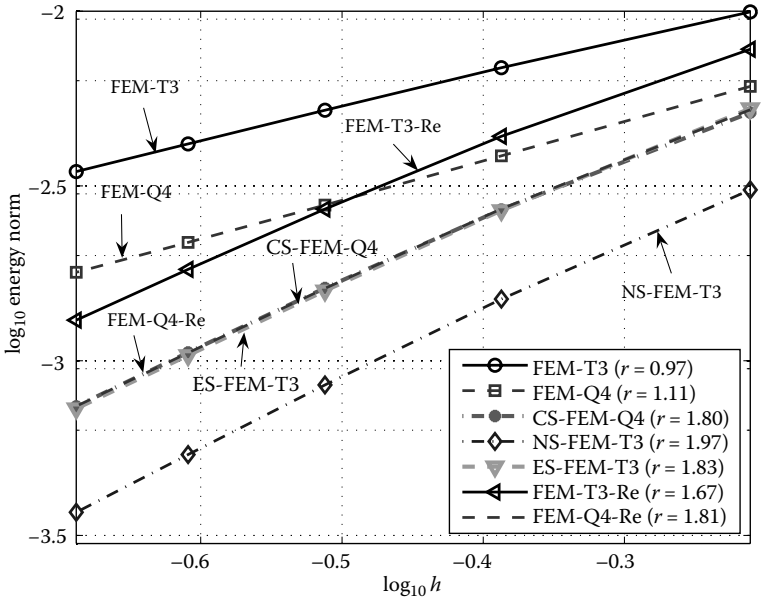

FIGURE 7.23 Error in energy norm of the ES-FEM-T3 solution in comparison with other methods for the infinite plate with a hole subjected to unidirectional tension using the same distribution of nodes.

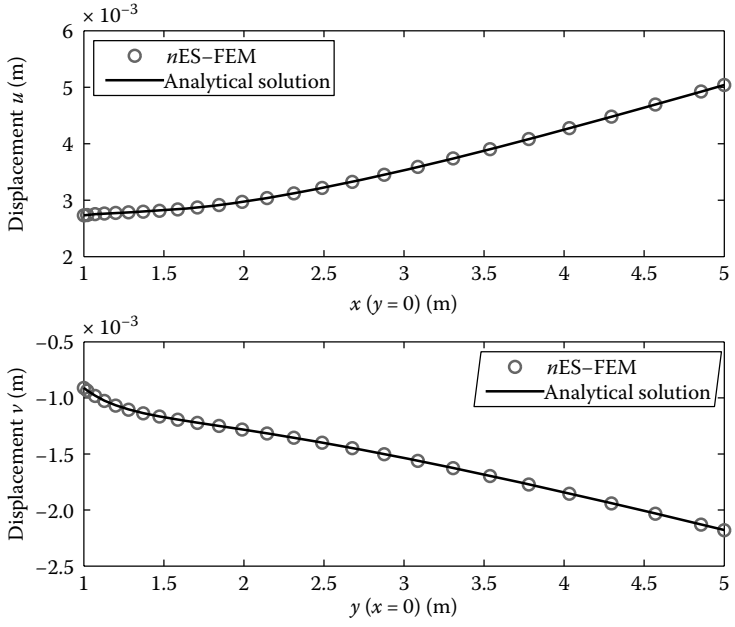

FIGURE 7.24 Displacement u along the bottom boundary and displacement v along the left boundary using nES-FEM of the infinite plate with a hole subjected to unidirectional tension.

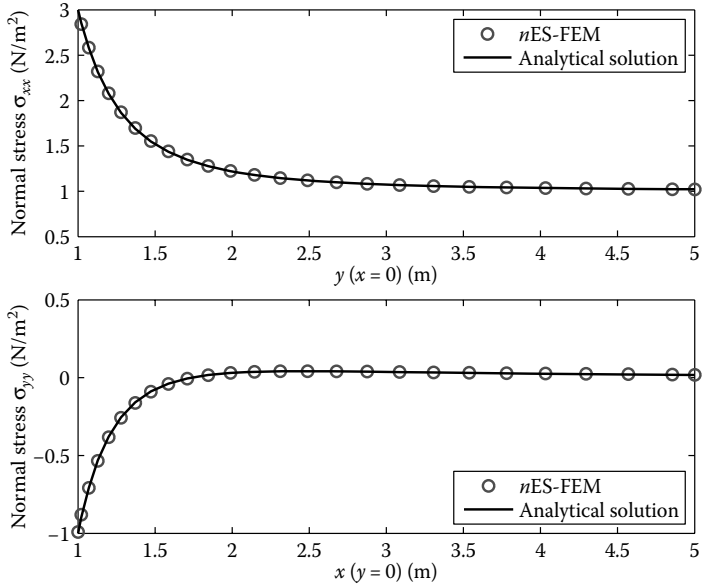

FIGURE 7.25 Stress σ_{xx} along the left boundary ($x = 0$) and stress σ_{yy} along the bottom boundary ($y = 0$) using *n*ES-FEM of the infinite plate with a hole subjected to unidirectional tension.

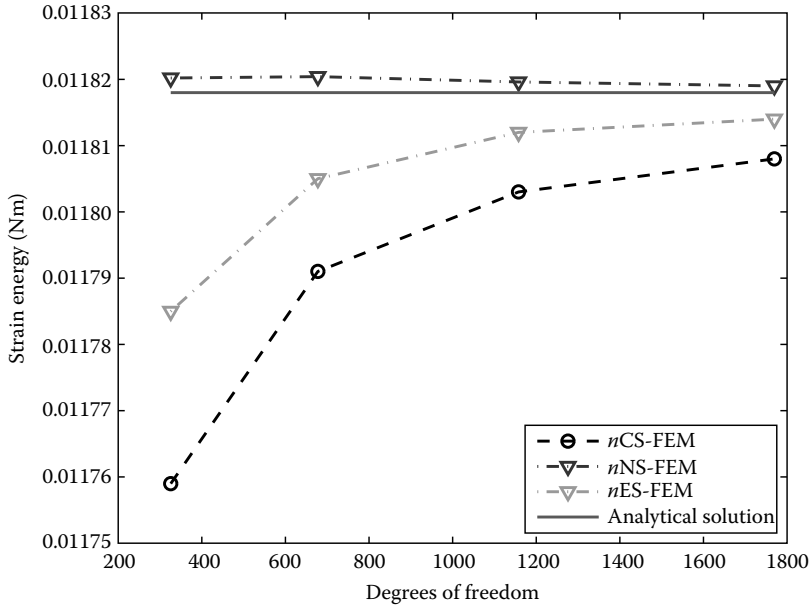

FIGURE 7.26 Convergence of the strain energy solution of *n*ES-FEM using *n*-sided polygonal elements in comparison with other methods for the infinite plate with a hole subjected to unidirectional tension using the same meshes.

TABLE 7.5

Error in Displacement Norm (%) in Solutions Obtained Using Different Methods for the Infinite Plate with a Hole Using the Same Polygonal Meshes

	Mesh 1	**Mesh 2**	**Mesh 3**	**Mesh 4**	**Mesh 5**
h (m)	0.5468	0.3786	0.2895	0.2343	0.1969
*n*CS-FEM	1.2895	0.6299	0.3638	0.2335	0.1628
*n*NS-FEM	2.2983	1.3538	0.9439	0.7201	0.5840
*n*ES-FEM	0.5015	0.2494	0.1537	0.1039	0.0744

The error of energy norm of the *n*ES-FEM is the smallest among the three models. When the finest mesh ($h = 0.1969$ m) is used, the error of the *n*ES-FEM is about 1/4 of *n*CS-FEM and 1/3 of *n*NS-FEM. In terms of convergence rate, the superconvergence is again observed for the *n*ES-FEM with a rate of 1.98 that is almost the optimal rate of 2.0 for the equilibrium model, and twice of the theoretical value of 1.0 for linear displacement models based on weak formulations.

Figure 7.29 shows the displacement norm against Poisson's ratio changing from 0.4 to 0.4999999. The results show that the smoothing-domain-based

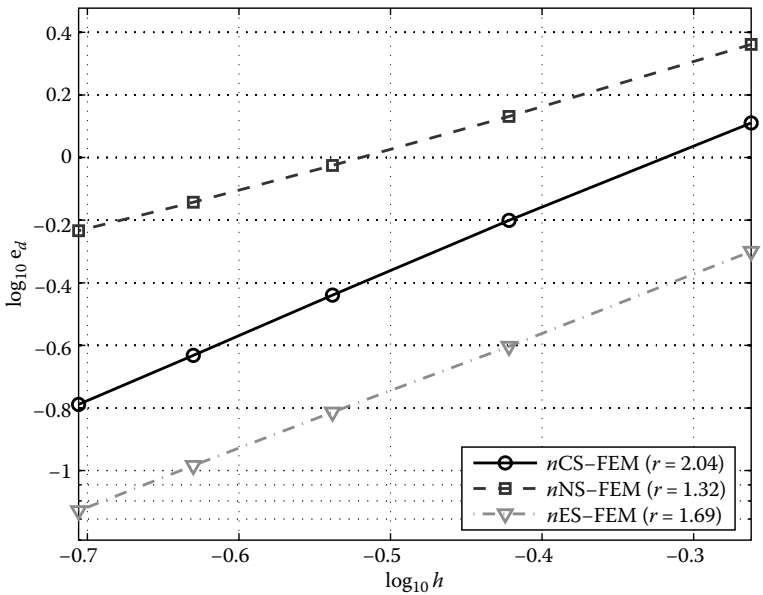

FIGURE 7.27 Error in displacement norm of *n*ES-FEM-T3 using *n*-sided polygonal elements in comparison with other methods for the infinite plate with a hole subjected to unidirectional tension using the same meshes.

TABLE 7.6

Error in Energy Norm ($\times 10^{-3}$) in Solutions Obtained Using Different Methods for the Infinite Plate with a Hole Using the Same Polygonal Meshes

	Mesh 1	**Mesh 2**	**Mesh 3**	**Mesh 4**	**Mesh 5**
h (m)	0.5468	0.3786	0.2895	0.2343	0.1969
*n*CS-FEM	5.0119	3.4427	2.5880	2.0613	1.7091
*n*NS-FEM	4.5090	2.9545	2.1723	1.7047	1.3964
*n*ES-FEM	3.2525	1.6328	0.9604	0.6242	0.4368

selective *n*ES/NS-FEM and ES-/NS-FEM-T3 models detailed in Section 7.5 can overcome the volumetric locking for nearly incompressible materials. Although the *n*NS-FEM and NS-FEM-T3 models are also immune from the volumetric locking, the smoothing-domain-based selective *n*ES/NS-FEM and ES-/NS-FEM-T3 models give much better results than those of *n*NS-FEM and NS-FEM-T3, owing to the contribution from the edge-based smoothing in the *n*ES-FEM and ES-FEM-T3 formulations.

Compared to the results given in Figure 6.18, it is observed that the ES-FEM model locks at the Poisson's ratio of 0.49, while the FEM model locks at a

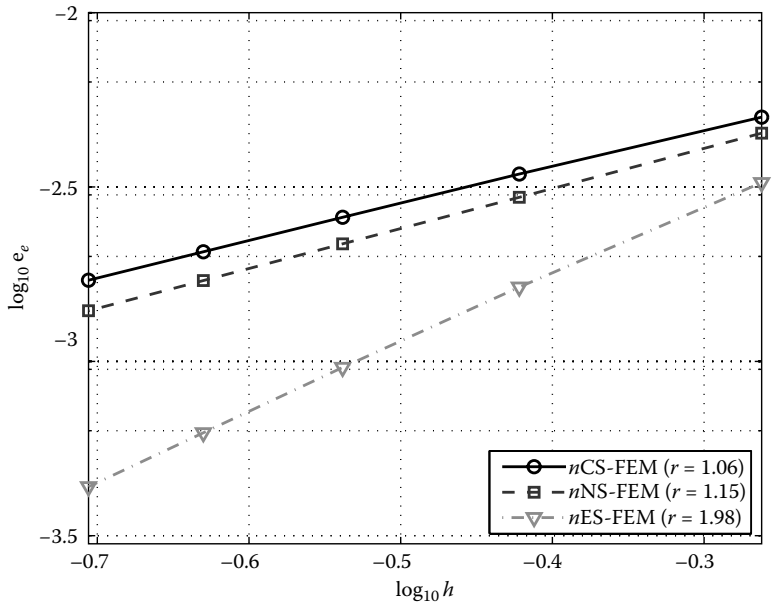

FIGURE 7.28 Error in energy norm of *n*ES-FEM-T3 using *n*-sided polygonal elements in comparison with other methods for the infinite plate with a hole subjected to unidirectional tension using the same meshes.

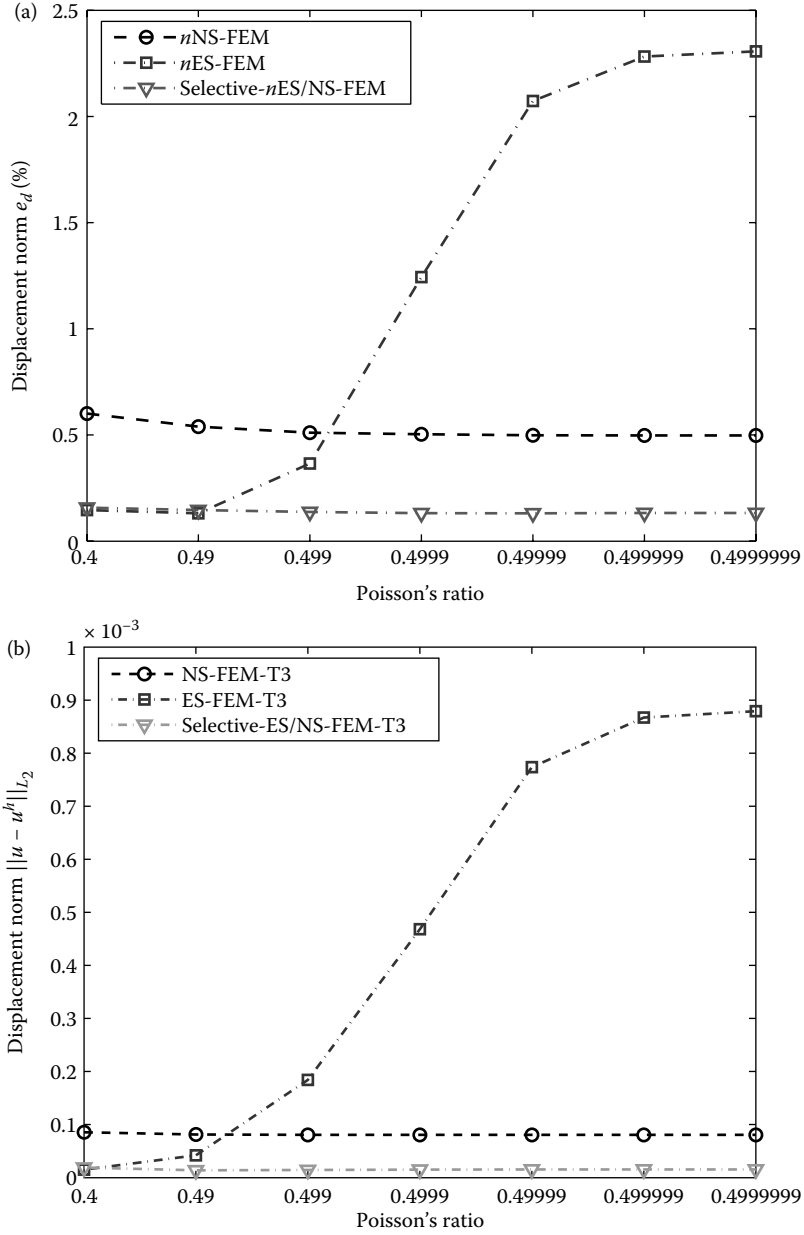

FIGURE 7.29 Displacement norm with different Poisson's ratios. (a) *n*-sided polygonal elements (579 nodes); (b) triangular elements (289 nodes).

Poisson's ratio of 0.4. This shows that the smoothing operation used in the ES-FEM helps to reduce quite significantly the degree of volumetric locking. To avoid the volumetric locking entirely, the selective ES/NS-FEM models should be used.

Example 7.7.3: Free Vibration Analysis of a Rectangular Cantilever Beam

In this example, a rectangular cantilever beam is studied. The parameters used are length $L = 100\,\text{mm}$, height $H = 10\,\text{mm}$, thickness $t = 1.0\,\text{mm}$, Young's modulus $= E = 2.1 \times 10^4\,\text{kgf/mm}^2$, Poisson's ratio $\nu = 0.3$, and mass density $\rho = 8.0 \times 10^{-10}\,\text{kgf s}^2/\text{mm}^4$. A plane stress problem is considered. This problem has also been investigated in Ref. [15]. Using the Euler–Bernoulli beam theory we obtain the fundamental frequency $f_1 = 0.08276 \times 10^4\,\text{Hz}$ that can serve as a reference. Three kinds of regular meshes are used in the analysis using the FEM-T3, NS-FEM-T3, FEM-Q4, and ES-FEM-T3 for comparison purpose. Because the exact solution is not available, numerical results using the FEM-Q4 with a very fine mesh (100×10) for the same problem are computed and used as the reference solutions.

Table 7.7 lists the first 12 natural frequencies of the beam, and the first 12 modes using the NS-FEM-T3 and ES-FEM-T3 are plotted in Figure 7.30. It is observed that (1) the ES-FEM-T3 does not have any spurious non-zero-energy and all the modes obtained correspond to physical modes; (2) the NS-FEM-T3 has non-physical spurious non-zero-energy modes due to its being overly soft; (3) the natural frequencies obtained using the ES-FEM-T3 are much larger than those of FEM-T3 that is known to be overly stiff; and (4) the ES-FEM-T3 results are generally the closest to the reference solution, and they converge faster than even FEM-Q4 with the same sets of nodes. Because the natural frequencies can be used as a good indicator for assessing the stiffness of a model, the above findings confirm again that the ES-FEM-T3 model has a very close-to-exact stiffness.

Example 7.7.4: Free Vibration Analysis of a Shear Wall

In this example, a shear wall with four square openings (see Figure 7.31) is analyzed, which has been solved using the BEM by Brebbia et al. [16]. The bottom edge of the wall is fully clamped. The plane stress case is considered with $E = 10,000$, $\nu = 0.2$, $t = 1.0$, and $\rho = 1.0$.* Two types of meshes of triangular and quadrilateral elements are used as shown in Figure 7.32. Numerical results using the FEM-Q8 with 6104 nodes and 1922 elements for the same problem

* In this book, we often choose to use nondimensional parameters because the purpose of the examples is just to examine our numerical results, and no much about physical implications. Any set of physical units is applicable to our results, as long as these units are consistent for all the inputs and outputs.

TABLE 7.7

First 12 Natural Frequencies ($\times 10^4$ Hz) of a Cantilever Beam

Model	NS-FEM-T3	ES-FEM-T3	FEM-T3	FEM-Q4	Reference (FEM-Q4) (100 x 10)
Mesh: 10 × 1	0.058	0.105	0.169	0.099	0.082
Nodes: 22	0.324	0.602	0.916	0.579	0.494
Elements: 10	0.744	1.283	1.287	1.283	1.282
quadrilateral	0.988	1.518	2.184	1.483	1.302
elements or 20	1.011[a]	2.636	3.594	2.618	2.366
triangles	1.135	3.772	3.834	3.814	3.609
	1.278[a]	3.856	5.034	3.882	3.844
	1.571	5.035	6.242	5.192	4.967
	2.370	6.083	6.415	6.235	6.396
	3.269	6.152	7.594	6.485	6.402
	3.706[a]	7.052	8.479	7.704	7.885
	3.864[a]	7.721	8.703	8.463	8.929
Mesh: 20 × 2	0.068	0.085	0.112	0.087	0.082
Nodes: 63	0.403	0.508	0.654	0.520	0.494
Elements: 40	1.052	1.283	1.284	1.283	1.282
quadrilateral	1.281	1.325	1.675	1.364	1.302
elements or 80	1.647[a]	2.378	2.955	2.469	2.366
triangles	1.879	3.578	3.842	3.748	3.609
	2.782[a]	3.830	4.387	3.838	3.844
	3.093	4.853	5.884	5.132	4.967
	3.678	6.153	6.375	6.359	6.396
	3.809	6.318	7.405	6.573	6.402
	4.054[a]	7.442	8.821	8.034	7.885
	4.161[a]	8.678	8.941	8.819	8.929
Mesh: 40 × 4	0.078	0.083	0.091	0.084	0.082
Nodes: 205	0.465	0.495	0.541	0.500	0.494
Elements: 160	1.220	1.283	1.283	1.283	1.282
quadrilateral	1.282	1.301	1.416	1.317	1.302
elements or 320	1.669[a]	2.355	2.557	2.393	2.366
triangles	2.201	3.578	3.843	3.646	3.609
	3.252[a]	3.841	3.879	3.843	3.844
	3.327	4.903	5.309	5.015	4.967
	3.834	6.287	6.394	6.388	6.396
	4.525	6.377	6.809	6.456	6.402
	4.641[a]	7.699	8.347	7.940	7.885
	5.328[a]	8.875	8.918	8.906	8.929

[a] Spurious non-zero-energy modes.

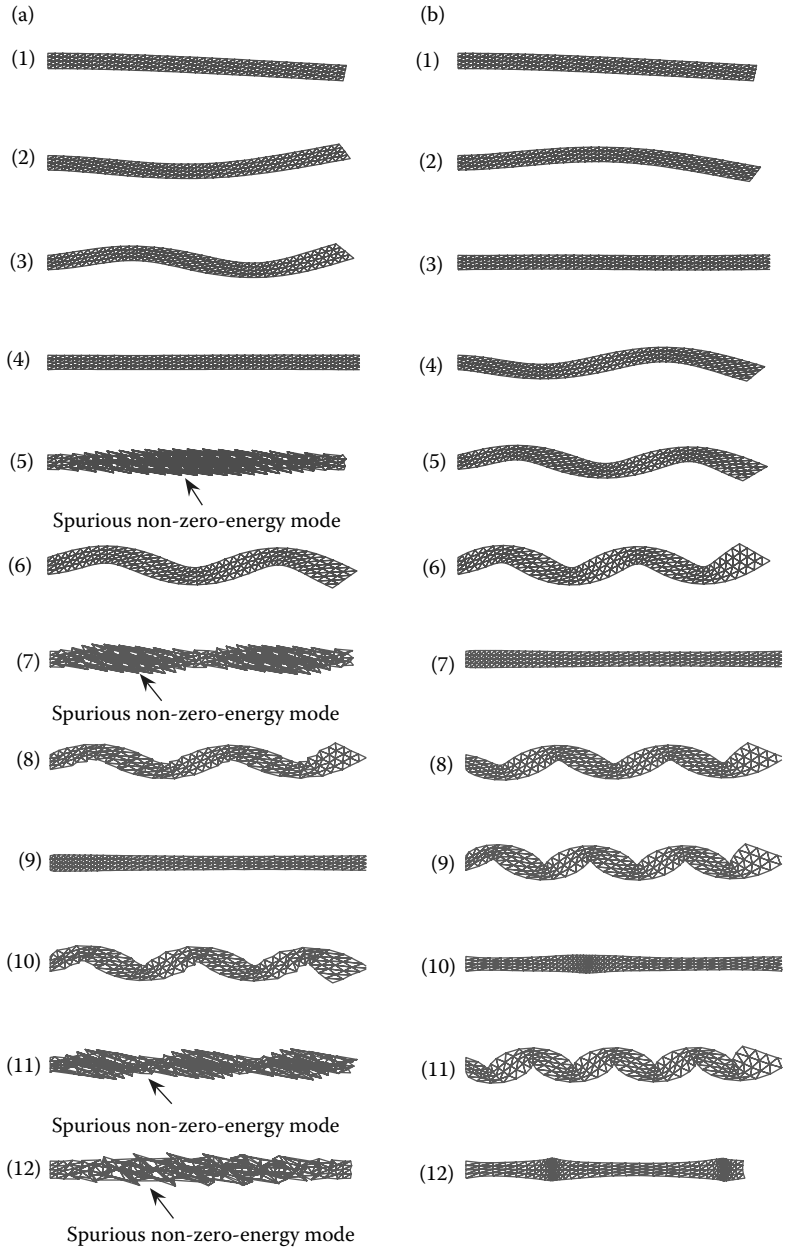

FIGURE 7.30 First 12 modes of the cantilever beam by (a) NS-FEM-T3 and (b) ES-FEM-T3.

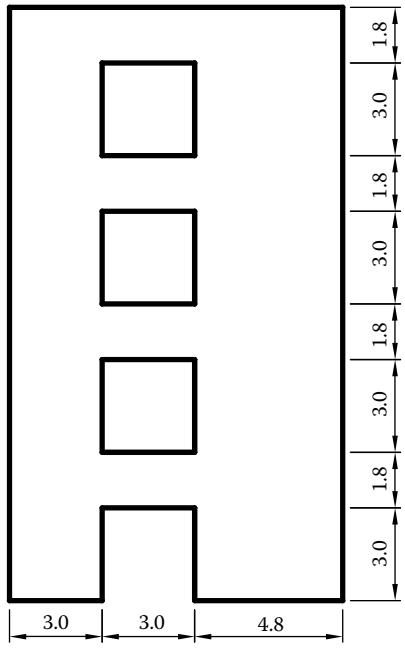

FIGURE 7.31 A shear wall with four square openings.

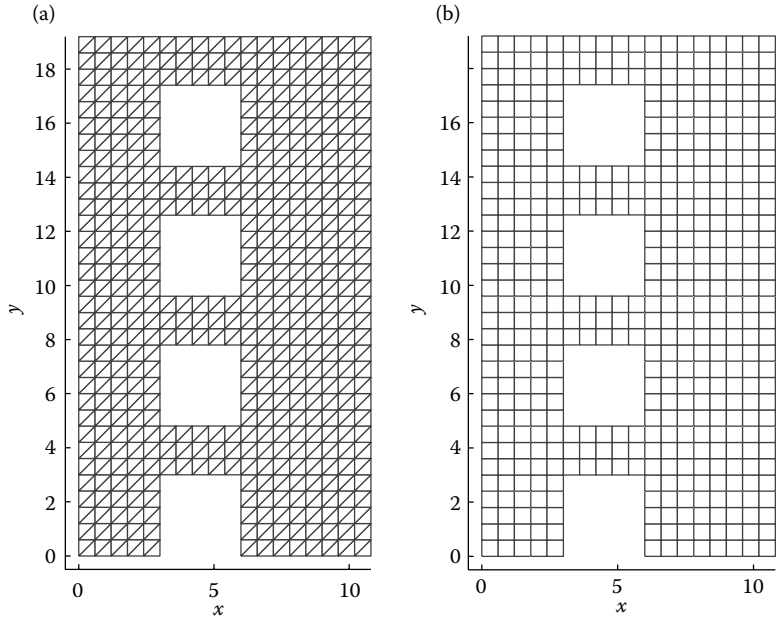

FIGURE 7.32 Domain discretization using triangular and four-node quadrilateral elements of the shear wall with four openings: (a) triangular mesh; (b) quadrilateral mesh.

are computed and used as reference solutions, in place of the unavailable exact solutions.

Table 7.8 lists the first 12 natural frequencies, and the first 12 modes using NS-FEM-T3 and ES-FEM-T3 are plotted in Figures 7.33 and 7.34. It is again observed that (1) the ES-FEM-T3 does not have any spurious non-zero-energy modes and all modes are physical; (2) the NS-FEM-T3 produces nonphysical spurious modes at high energy level; (3) the natural frequencies obtained using the ES-FEM-T3 is much larger than those of the FEM-T3 that is known to be overly stiff; and (4) the ES-FEM-T3 results are the closest to the reference solution, and they converge faster than even FEM-Q4 with the same sets of nodes used. This example confirms again that the ES-FEM-T3 model possesses a very close-to-exact stiffness.

Example 7.7.5: Free Vibration Analysis of a Connecting Rod

A free vibration analysis of a connecting rod shown in Figure 7.35 is performed. The plane stress problem is considered with material parameters of $E = 10 \times 10^9$ N/m^2, $\nu = 0.3$, and $\rho = 7.8 \times 10^3$ kg/m^3. The nodes on the left inner circumference are fixed in two directions. Two types of meshes of triangular and quadrilateral elements are used, as shown in Figure 7.36. Numerical results using FEM-Q4 and FEM-Q8 for the same problem are computed and used as reference solutions for comparison purposes.

The results are listed in Table 7.9. It is observed that the ES-FEM-T3 gives comparable results as FEM-Q4 using more nodes than ES-FEM-T3. Again, Figures 7.37 and 7.38 show that the ES-FEM-T3 does not have any spurious non-zero-energy modes, while the NS-FEM-T3 has. This example reconfirms the fact that the ES-FEM-T3 model is temporally stable, has a very close-to-exact stiffness, and is expected to perform well in transient vibration analysis.

Example 7.7.6: Transient Vibration Analysis of a Cantilever Beam

A benchmark problem of a cantilever beam is investigated using the ES-FEM-T3 model with the Newmark method for time stepping. The beam is subjected to a tip harmonic loading $f(t) = \cos \omega_f t$ in the y-direction. The plane strain problem is considered with nondimensional parameters as $L = 4.0$, $H = 1.0$, $t = 1.0$, $E = 1.0$, $\nu = 0.3$, $\rho = 1.0$, $\alpha = 0.005$, $\beta = 0.272$, $\omega_f = 0.05$, and $\theta = 0.5$. The domain of the beam is represented with 10×4 elements. Three FEM models of FEM-T3, FEM-Q4, and FEM-Q8 are also used in the analysis for comparison purposes. The time step for time integration is set at $\Delta t = 1.57$. From the dynamic responses shown in Figure 7.39, it is seen that the amplitude of ES-FEM-T3 is closer to that of FEM-Q8 as compared to FEM-Q4. This shows that ES-FEM-T3 using triangular elements can be applied to transient vibration analysis to deliver results of excellent accuracy. This is partially due to the fact that the ES-FEM-T3 model has very close-to-exact stiffness, which we have observed in all these free vibration examples.

TABLE 7.8

First 12 Natural Frequencies ω (rad/s) of a Shear Wall

Model	NS-FEM-T3	ES-FEM-T3	FEM-T3	FEM-Q4	Reference (FEM-Q8) (6104 Nodes, 1922 Elements)	Reference (Brebbia et al. [16])
Nodes: 559	1.827	2.050	2.144	2.073	2.011	2.079
Elements: 476	6.511	7.038	7.319	7.096	6.952	7.181
quadrilateral	7.515	7.620	7.651	7.625	7.600	7.644
elements or 952	10.183	11.743	12.554	11.938	11.471	11.833
triangles	13.733	15.143	15.943	15.341	14.972	15.947
	14.709[a]	18.214	18.763	18.345	18.066	18.644
	17.032	19.714	20.382	19.876	19.581	20.268
	17.104[a]	21.994	22.676	22.210	21.872	22.765
	18.360	22.778	23.640	23.001	22.636	
	18.890[a]	23.349	24.126	23.552	23.293	
	19.450[a]	25.052	25.534	25.175	25.018	
	19.538[a]	25.837	26.845	26.071	25.877	
Nodes: 2072	1.935	2.022	2.063	2.032	2.011	2.079
Elements: 1904	6.776	6.976	7.087	6.999	6.952	7.181
quadrilateral	7.566	7.606	7.620	7.609	7.600	7.644
elements or 3808	10.895	11.551	11.880	11.625	11.471	11.833
triangles	14.468	15.019	15.322	15.092	14.972	15.947
	15.324[a]	18.108	18.317	18.158	18.066	18.644
	17.553	19.619	19.862	19.677	19.581	20.268
	17.834[a]	21.908	22.197	21.987	21.872	22.765
	19.152	22.681	23.000	22.759	22.636	
	20.511[a]	23.308	23.569	23.380	23.293	
	21.027[a]	25.030	25.206	25.073	25.018	
	21.303[a]	25.875	26.216	25.956	25.877	

[a] Spurious non-zero-energy modes.

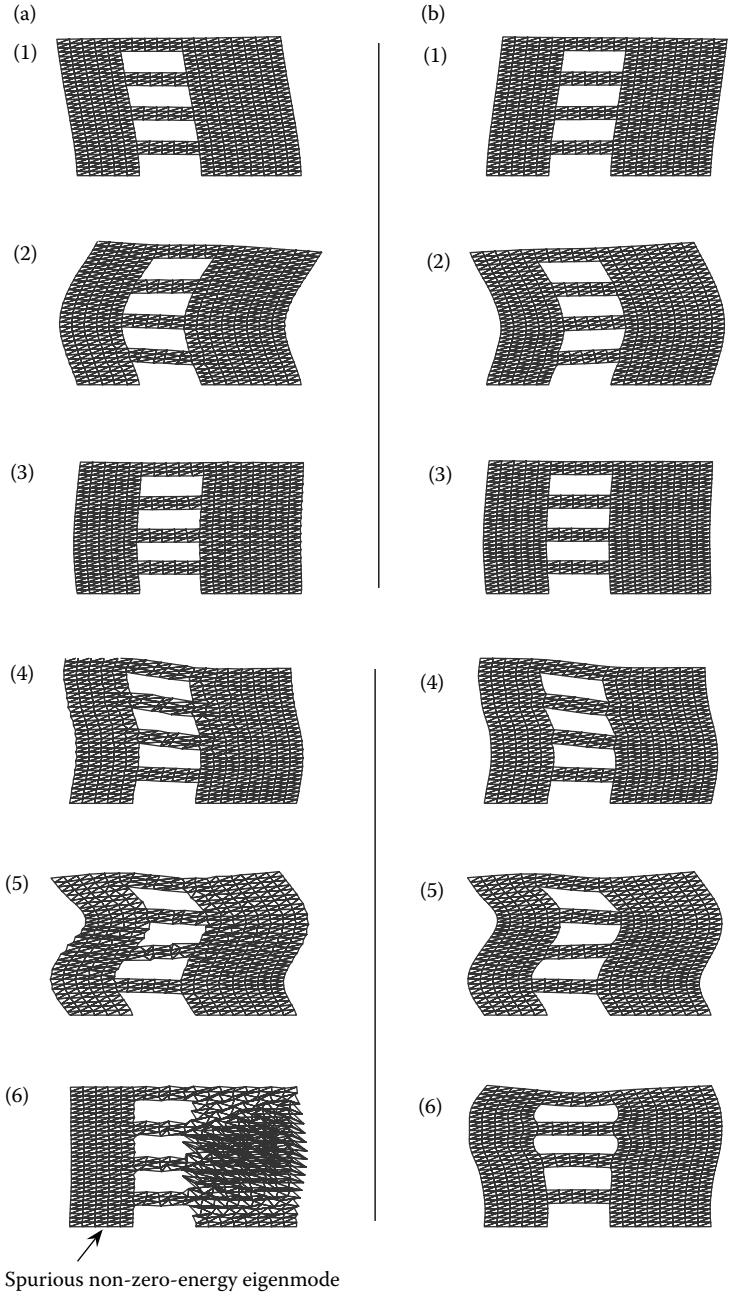

FIGURE 7.33 First to sixth modes of the shear wall by (a) NS-FEM-T3 and (b) ES-FEM-T3.

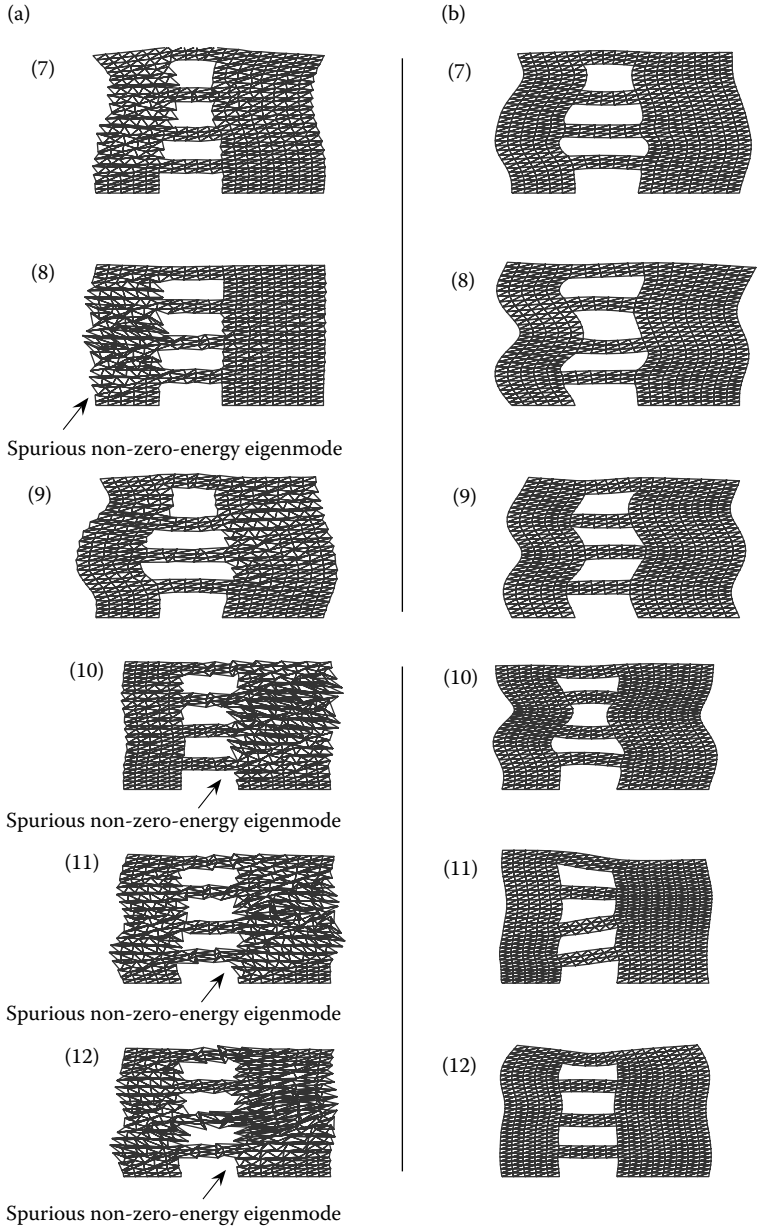

FIGURE 7.34 Seventh to 12th modes of the shear wall by (a) NS-FEM-T3 and (b) ES-FEM-T3.

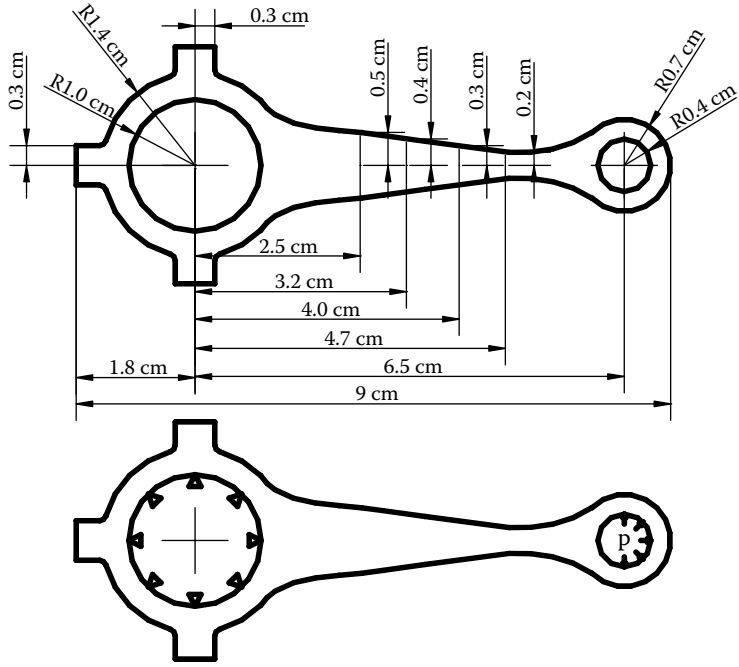

FIGURE 7.35 Geometric model, loading, and boundary conditions of an automobile connecting bar.

Example 7.7.7: Transient Vibration Analysis of a Spherical Shell

As shown in Figure 7.40, a spherical shell is studied that is subjected to a concentrated time-dependent loading at its apex. Due to the symmetry, only half of the spherical shell is modeled, as shown in Figure 7.41. Two types of meshes of triangular and quadrilateral elements are created for the half model. For the model of triangular elements, we deliberately made it asymmetric. Nondimensional numerical parameters are used: $R = 12$, $t = 0.1$, $\phi = 10.9°$, $\theta = 0.5$, $E = 1.0$, $\nu = 0.3$, and $\rho = 1.0$.

The time-dependence of the loading is first specified in the harmonic form of $f(t) = \cos \omega_f t$ and its dynamic responses are plotted in Figure 7.42 for the case of $\omega_f = 0.05$ and time step $\Delta t = 5$. No damping effect is included in this case. Again, it is seen that the amplitude of the ES-FEM-T3 is much more accurate than that of the FEM-T3 model and is comparable to that of the FEM-Q4 model with the same set of nodes.

Next, a Heaviside step load $f(t) = 1$ is added at the apex since $t = 0$. Without damping, it is seen from Figure 7.43 that the deflection at the apex approaches, in an oscillatory fashion, a constant value with increase in time. With the inclusion of damping ($\alpha = 0.005$, $\beta = 0.272$), the response is damped out with time as expected.

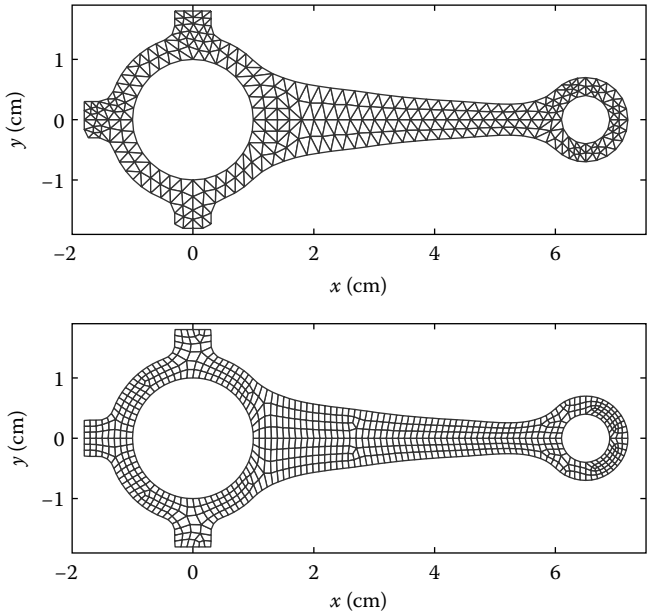

FIGURE 7.36 Domain discretization using triangular and four-node quadrilateral elements of the automobile connecting bar.

Example 7.7.8: Cantilever Beam Undergoing a Large Deformation

The use of ES-FEM-T3 for large deformation analysis of a cantilever beam subjected to a concentrated tip load is now examined in this example. The size of the beam is (10 cm × 2 cm) and the beam is initially discretized using a mesh of 20 × 4. The related parameters are taken as $E = 3.0 \times 10^7$ N/cm^2 and $\nu = 0.3$. The analysis based on the total Lagrange formulation under the plane strain condition is carried out using 20 increment steps ($n = 20$) with $\Delta F = 10$ KN applied at each step.

Figure 7.44 plots the initial and final configurations after 20 steps of increment of the deformation using the ES-FEM-T3. Table 7.10 and Figure 7.45 show the relation between the tip deflection versus the load step. The simulation converges in a very rapid pace and in each load increment the iteration is performed less than five times. It can be seen that (1) with the same set of nodes, the FEM-T3 behaves much stiffer than the FEM-Q4; (2) the nonlinear effect makes the cantilever beam behave much stiffer compared to the linear solution; and (3) the results of the ES-FEM-T3 are quite close to that of the FEM-Q4. This shows that the ES-FEM-T3 works well for nonlinear analysis even compared to the FEM-Q4.

TABLE 7.9

First 12 Natural Frequencies (Hz) of a Connecting Bar

Model	NS-FEM-T3	ES-FEM-T3	FEM-T3	Reference (FEM-Q4) (537 Nodes, 429 Elements)	Reference (FEM-Q4) (1455 Nodes, 1256 Elements)	Reference (FEM-Q8) (10,002 Nodes, 3125 Elements)
Nodes: 373	4.94	5.14	5.32	5.14		5.12
Elements: 574	20.81	22.06	22.94	22.05		21.84
triangles	48.39	49.38	49.70	49.30		49.12
	48.49	52.04	54.06	52.23		51.40
	84.93	92.72	96.86	93.61		91.79
	97.68	109.59	114.31	108.59		106.15
	114.03	132.68	142.45	134.64		130.14
	123.32[a]	158.24	163.97	159.45		156.14
	143.64[a]	158.95	169.28	160.59		157.70
	144.66[a]	201.38	204.58	203.52		200.06
	151.43	204.84	210.12	208.68		204.41
	161.95[a]	209.28	210.74	209.02		204.99
Nodes: 1321	5.05	5.12	5.21		5.12	5.12
Elements: 2296	21.49	21.88	22.27		21.91	21.84
triangles	48.88	49.17	49.35		49.21	49.12
	50.40	51.52	52.49		51.66	51.40
	89.61	91.93	93.84		92.39	91.79
	92.65[a]	106.85	109.28		107.51	106.15
	103.44	130.55	134.58		131.48	130.14
	125.65	156.35	159.74		157.51	156.14
	151.62[a]	157.85	159.97		158.69	157.70
	152.01[a]	200.90	203.35		201.69	200.06
	155.54	204.26	207.50		206.04	204.41
	188.59[a]	206.53	209.18		209.92	204.99

[a] Spurious non-zero-energy modes.

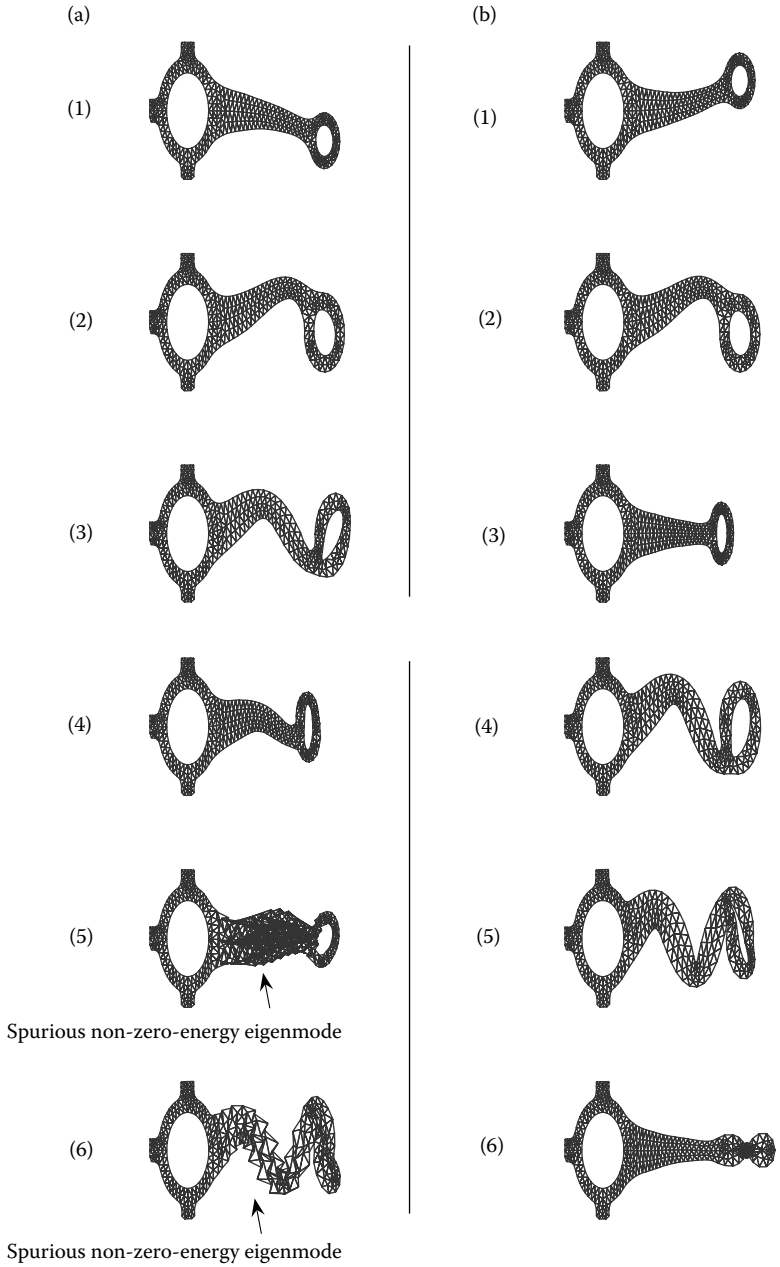

FIGURE 7.37 First to sixth modes of the connecting bar by (a) NS-FEM-T3 and (b) ES-FEM-T3.

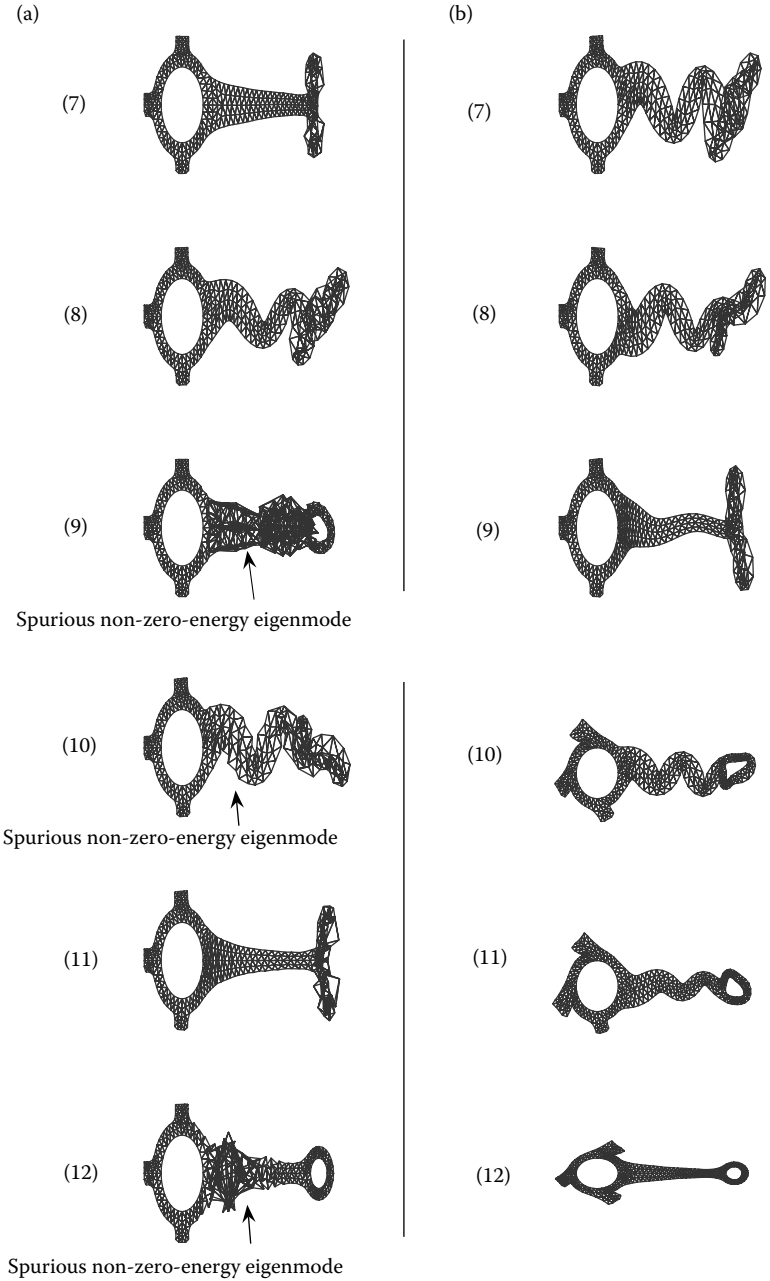

FIGURE 7.38 Seventh to 12th modes of the connecting bar by (a) NS-FEM-T3 and (b) ES-FEM-T3.

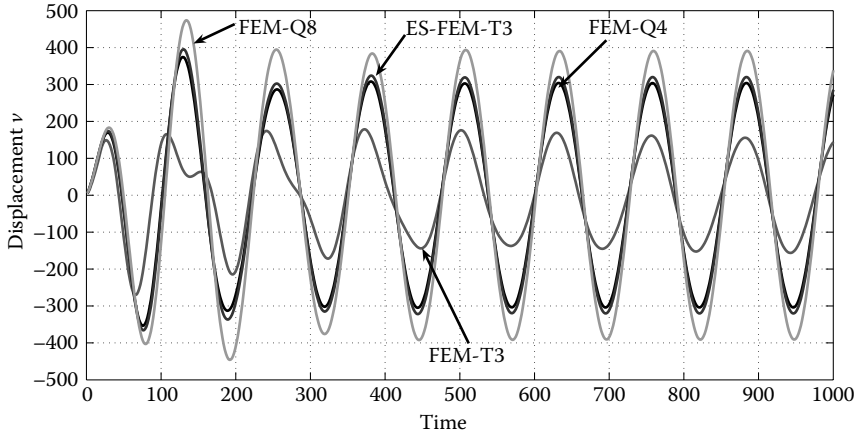

FIGURE 7.39 Transient responses for the cantilever beam subjected to a harmonic loading.

7.8 Remarks

In this chapter, an ES-FEM is presented for stable and accurate solutions to static, dynamic, linear, and nonlinear problems of 2D solids. Through the theoretical analyses, formulation, and numerical examples, we finally mention the following remarks:

Remark 7.2 ES-FEM: Works Well with General Polygonal Elements

The ES-FEM can use general n-sided polygonal elements including triangular elements, and is spatially stable. The extension of the method for 3D problems using tetrahedral elements is also straightforward, and will be done in the next chapter.

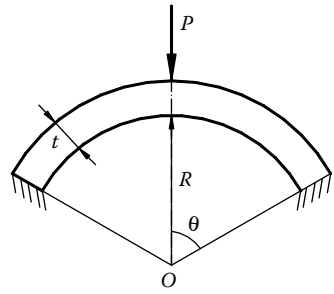

FIGURE 7.40 A spherical shell subjected to a concentrated loading at its apex.

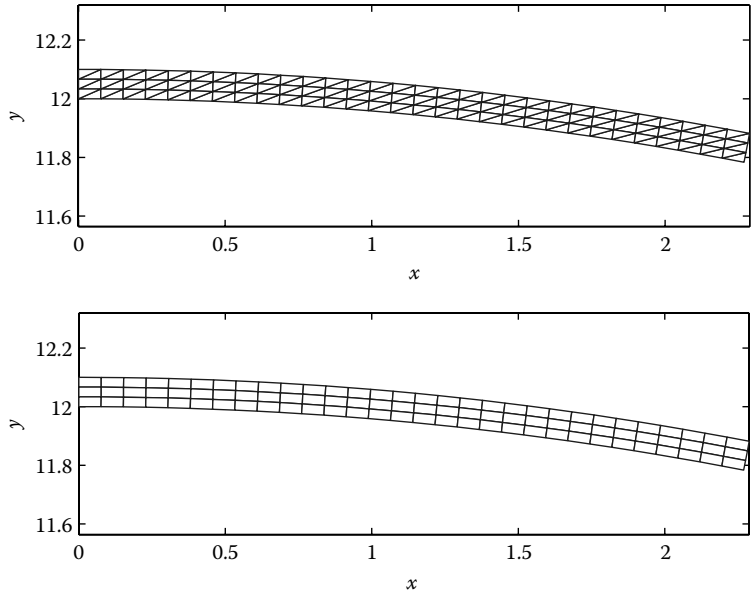

FIGURE 7.41 Domain discretization of half of the spherical shell using triangular and four-node quadrilateral elements.

Remark 7.3 ES-FEM: Linear PIM for Shape Function Evaluation

In the ES-FEM using n-sided polygonal elements, field gradients are computed directly using only shape functions themselves at some particular points along segments of the boundary of the smoothing domains. The

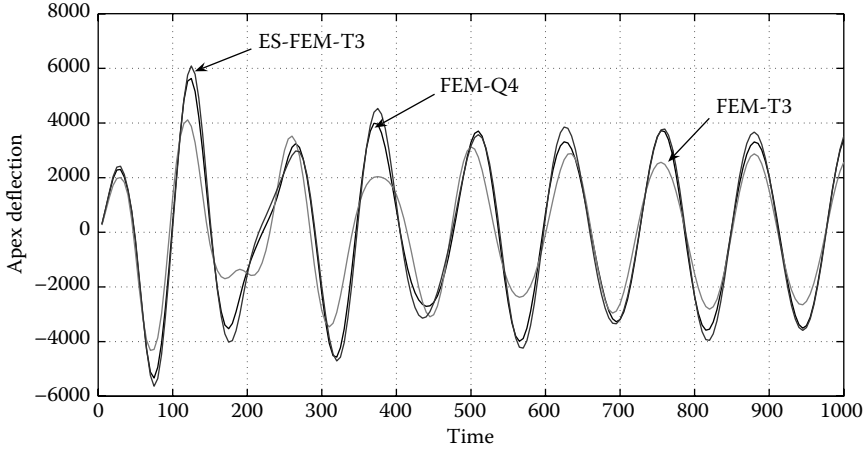

FIGURE 7.42 Transient responses for the spherical shell subjected to a harmonic loading.

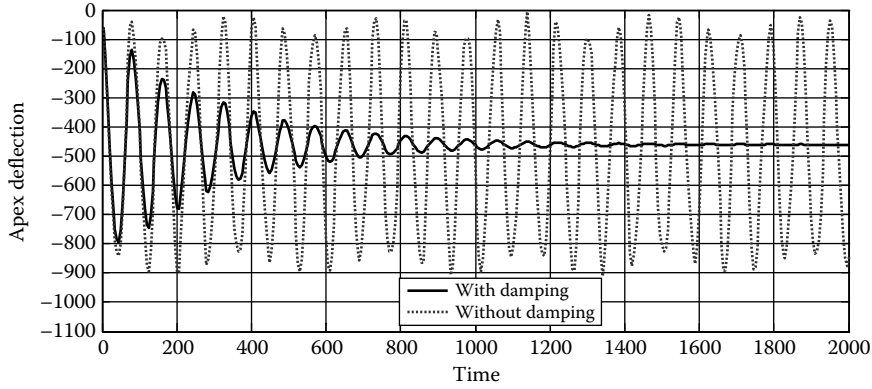

FIGURE 7.43 Transient responses obtained using the ES-FEM-T3 for the spherical shell subjected to a Heaviside step loading.

values of shape functions for the discrete points of an n-sided polygonal element are determined using a simple linear PIM.

Remark 7.4 ES-FEM: Easy to Implement and no Increase of DOFs

The ES-FEM formulation is straightforward and the implementation is almost as easy as the FEM, without the increase of DOFs.

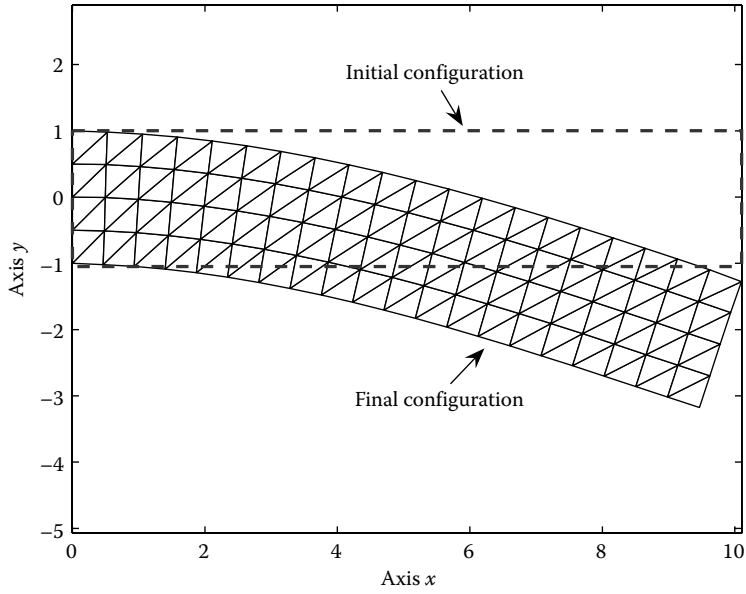

FIGURE 7.44 Initial and final deformed configurations for the 2D cantilever beam subjected to a concentrated tip load.

TABLE 7.10

Tip Deflection (cm) versus the Load Step of the Cantilever Beam Subjected to a Concentrated Tip Load

Load Step	FEM-T3 (Linear)	FEM-T3 (Nonlinear)	FEM-Q4 (Linear)	FEM-Q4 (Nonlinear)	ES-FEM-T3 (Linear)	ES-FEM-T3 (Nonlinear)
$n = 2$	0.25	0.24 (3)[a]	0.30	0.28 (3)	0.31	0.29 (3)
$n = 4$	0.50	0.46 (3)	0.60	0.52 (3)	0.61	0.53 (3)
$n = 6$	0.76	0.65 (3)	0.90	0.74 (3)	0.92	0.75 (3)
$n = 8$	1.01	0.83 (3)	1.20	0.95 (4)	1.22	0.97 (4)
$n = 10$	1.26	1.01 (4)	1.49	1.16 (4)	1.53	1.18 (4)
$n = 12$	1.51	1.18 (4)	1.79	1.37 (4)	1.83	1.39 (4)
$n = 14$	1.76	1.36 (4)	2.09	1.58 (4)	2.14	1.60 (4)
$n = 16$	2.01	1.53 (4)	2.39	1.78 (4)	2.44	1.81 (5)
$n = 18$	2.27	1.71 (4)	2.69	1.98 (5)	2.75	2.02 (5)
$n = 20$	2.52	1.88 (5)	2.99	2.19 (5)	3.05	2.23 (5)

[a] The number in brackets shows the number of iterations.

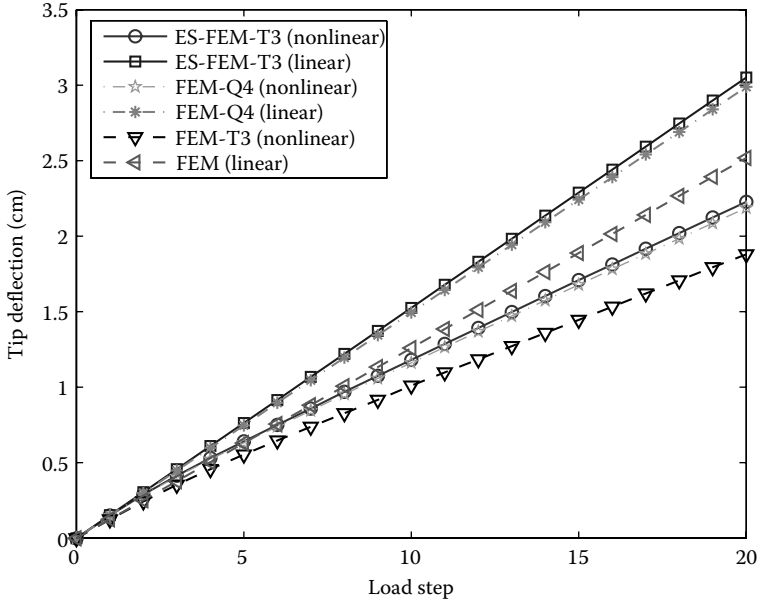

FIGURE 7.45 Tip deflection (cm) versus the load step for the cantilever beam subjected to a concentrated tip load.

Remark 7.5 ES-FEM: Spatially and Temporally Stable

The ES-FEM is both spatially and temporally stable, and hence works well for static, dynamic, linear, and nonlinear problems.

Remark 7.6 ES-FEM: Superconvergence and Ultra-Accuracy

The ES-FEM often shows superconvergence in both displacement norm and energy norm. The ES-FEM-T3 solution is found to be "ultra-accurate": the numerical results of the ES-FEM-T3 using triangular elements are found to be much more accurate than FEM-T3 and FEM-T3-Re in both displacement and energy norms, often even more accurate in both displacement and energy norms than the FEM using quadrilateral elements with the same sets of nodes.

Remark 7.7 ES-FEM-T3: Very Close-to-Exact Stiffness

The ES-FEM-T3 often produces models with stiffness very close-to-exact stiffness. This can be observed from the accuracy of the eigenvalues (natural frequencies) produced by the ES-FEM-T3 model. We have not yet found any linear model that produces better results in terms of "stiffness" than the ES-FEM-T3 (except the αFEM with a tunable parameter). This unique

property of ES-FEM-T3 is very important for dynamic problems including vibration and wave propagation (see Chapter 15).

Remark 7.8 ES-FEM-T3: Efficient

With the same sets of nodes and the same direct solver, the computation time of the ES-FEM-T3 is longer than that of the FEM-T3. However, when the computational efficiency (computation time for the same accuracy) and convergence rates in both displacement and energy norms are considered, the ES-FEM-T3 is the most superior. Because the rates of convergence of the solution of the ES-FEM models are higher than the FEM counterparts, the computational efficiency of the ES-FEM becomes more significant when the mesh is refined.

Remark 7.9 ES/NS-FEM-T3: Volumetric Locking Free

A smoothing-domain-based selective ES/NS-FEM-T3 is effective in overcoming the volumetric locking for problems of nearly incompressible materials.

Remark 7.10 ES-FEM-T3: Excellent in Vibration Analysis

For the free vibration analysis, the ES-FEM-T3 using triangular elements gives more accurate results and higher convergence rate than the FEM-Q4. No spurious non-zero-energy modes were found in vibration analysis and hence the ES-FEM-T3 is found to be stable temporally for all the examples studied. For the forced vibration analysis, the vibration period obtained using the ES-FEM-T3 is more accurate compared to the FEM-Q4, and the vibration amplitude is closer to that of the higher-order FEM-Q8.

Remark 7.11 ES-FEM-T3: Excellent in Nonlinear Analysis

For nonlinear problems of large deformation, the numerical results of the ES-FEM-T3 using triangular elements are even more accurate than FEM using quadrilateral elements with the same sets of nodes.

Remark 7.12 ES-FEM: Other Applications

The ES-FEM has been developed for 2D piezoelectric [17], 2D viscoelastoplastic [18], plate [19], and primal-dual shakedown analyses [20]. Clearly, the ES-FEM is applicable to many other types of problems in different areas. More general models based on mesh-free settings, such as the ES-PIM, can be found in Ref. [21].

Due to the excellent performance of the ES-FEM-T3, it is regarded as a "star" performer for 2D problems, and will be used for various types of problems in this book in later chapters. It would be quite a challenge to find a better linear model than the ES-FEM-T3 in terms of (1) adaptation

to complicated geometry; (2) suitability for automatically meshing [22]; (3) stability; (4) solution accuracy; and (5) computational efficiency. The authors' group has tried and is still trying quite hard on this during the past few years but without much progress.

References

1. Liu GR, Nguyen-Thoi T, Nguyen-Xuan H, and Lam KY. 2009. A node-based smoothed finite element method (NS-FEM) for upper bound solution to solid mechanics problems. *Computers and Structures*; 87: 14–26.
2. Nagashima T. 1999. Node-by-node meshless approach and its applications to structural analyses. *International Journal for Numerical Methods in Engineering*; 46: 341–385.
3. Puso MA, Chen JS, Zywicz E, and Elmer W. 2008. Meshfree and finite element nodal integration methods. *International Journal for Numerical Methods in Engineering*; 74: 416–446.
4. Puso MA and Solberg J. 2006. A stabilized nodally integrated tetrahedral. *International Journal for Numerical Methods in Engineering*; 67: 841–867.
5. Liu GR, Nguyen-Thoi T, and Lam KY. 2009. An edge-based smoothed finite element method (ES-FEM) for static, free and forced vibration analyses in solids. *Journal of Sound and Vibration*; 320: 1100–1130.
6. Nguyen-Thoi T, Liu GR, and Nguyen-Xuan H. 2009. An *n*-sided polygonal edge-based smoothed finite element method (nES-FEM) for solid mechanics. *Communications in Numerical Methods in Engineering*; doi:10.1002/cnm.1375.
7. Nguyen-Thoi T, Liu GR, Lam KY, and Zhang GY. 2009. A face-based smoothed finite element method (FS-FEM) for 3D linear and nonlinear solid mechanics problems using 4-node tetrahedral elements. *International Journal for Numerical Methods in Engineering*; 78: 324–353.
8. Chen JS, Wu CT, Yoon S, and You Y. 2001. A stabilized conforming nodal integration for Galerkin meshfree method. *International Journal for Numerical Methods in Engineering*; 50: 435–466.
9. Smith IM and Griffiths DV. 1998. *Programming the Finite Element Method*, 3rd edition. Wiley, New York.
10. Zhang ZQ and Liu GR. 2009. Temporal stabilization of the node-based smoothed finite element method (NS-FEM) and solution bound of linear elastostatics and vibration problems. *Computational Mechanics*; doi: 10.1007/s00466-009-0420-5.
11. Zhang ZQ and Liu GR. 2009. Upper and lower bounds for natural frequencies: A property of the smoothed finite element methods. *International Journal for Numerical Methods in Engineering*; (submitted).
12. Bathe KJ. 1996. *Finite Element Procedures*. Prentice-Hall, Massachusetts (MIT), NJ.
13. Reddy JN. 2004. *An Introduction to Nonlinear Finite Element Analysis*. Oxford University Press, Oxford.

14. Liu GR. 2009. A G space theory and weakened weak (W^2) form for a unified formulation of compatible and incompatible methods: Part I: Theory, Part II: Application to solid mechanics problems. *International Journal for Numerical Methods in Engineering*; 81: 1093–1156.
15. Dai KY and Liu GR. 2007. Free and forced analysis using the smoothed finite element method (SFEM). *Journal of Sound and Vibration*; 301: 803–820.
16. Brebbia CA, Telles JC, and Wrobel LC. 1984. *Boundary Element Techniques*. Springer, Berlin.
17. Nguyen-Xuan H, Liu GR, Nguyen-Thoi T, and Nguyen-Tran C. 2009. An edge-based smoothed finite element method (ES-FEM) for analysis of two-dimensional piezoelectric structures. *Smart Materials and Structures*; 18: 065015 (12pp.).
18. Nguyen-Thoi T, Liu GR, Vu-Do HC, and Nguyen-Xuan H. 2009. An edge-based smoothed finite element method (ES-FEM) for visco-elastoplastic analyses of 2D solids using triangular mesh. *Computational Mechanics*; 45: 23–44.
19. Nguyen-Xuan H, Liu GR, Thai-Hoang C, and Nguyen-Thoi T. 2009. An edge-based smoothed finite element method with stabilized discrete shear gap technique for analysis of Reissner–Mindlin plates. *Computer Methods in Applied Mechanics and Engineering*; 199: 471–489.
20. Tran Thanh Ngoc, Liu GR, Nguyen-Xuan H, and Nguyen-Thoi T. 2009. An edge-based smoothed finite element method for primal-dual shakedown analysis of structures. *International Journal for Numerical Methods in Engineering*; doi: 10.1002/nme.2804.
21. Liu GR and Zhang GR. 2008. Edge-based smoothed point interpolation methods. *International Journal of Computational Methods*; 5(4): 621–646.
22. Cheng L and Liu GR. 2008. Adaptive analysis using the edge-based smoothed finite element method; (submitted).

8

Face-Based Smoothed FEM

8.1 Introduction

Solving 3D problems is usually much more difficult due mainly to the complexity of the geometry. When the FEM is used, meshing a complicated 3D domain with quality elements can be quite a daunting task to any analyst. The four-node tetrahedral element (T4) is often used for 3D problems, because of its simplicity in formulation and implementation: piecewise linear approximation of displacement field and constant strain field. Most commercially available FEM codes use tetrahedral elements for adaptive analyses of 3D problems, due to the simple fact that tetrahedral meshes can be most automatically generated and refined for complicated geometrical domains. The FEM-T4 is thus clearly superior at least for two counts: simplicity and adaptation.

However, the FEM-T4 also possesses some crucial shortcomings for problems of solid mechanics. Three such shortcomings are the well-known overly stiff behavior, poor stress solution, and volumetric locking in the nearly incompressible cases. In order to overcome these disadvantages, some new finite elements were proposed. Dohrmann et al. [1] presented a weighted least-squares approach in which a linear displacement field is fitted to an element's nodal displacements. The method is claimed to be computationally efficient and free from the volumetric locking. However, more nodes are required on the element boundary to obtain a least-square-fitted linear displacement field. Dohrmann et al. [2] also proposed a nodal integration FEM in which each element is associated with a single node and the linear interpolation functions of the original mesh are used. The method can avoid the volumetric locking and performs better than the FEM-T4 in terms of stress solution for static problems. The nodal integration FEM can be viewed as a special linear case of the NS-FEM presented in Chapter 6, and the linear case of NS-PIM [3,4] formulated using the generalized gradient smoothing technique [5] and the point interpolation shape functions [6]. However, for dynamic problems, these types of node-based smoothed methods are known to be "overly soft" and *temporally unstable* due to the presence of spurious modes at higher energy levels, as we have seen in Chapter 7. Therefore, stabilization schemes [7–9] are required for dynamic problems.

In this chapter, in order to overcome the above-mentioned disadvantages of the FEM-T4 and the NS-FEM-T4 presented in Chapter 6, we extend the idea of ES-FEM-T3 for 3D problems, and both linear and geometrically nonlinear problems are considered. Instead of using the edge-based smoothing domains in 2D problems, we will now use the face-based smoothing domains for smoothed strain field construction. It is therefore termed as FS-FEM using T4 elements. In FS-FEM-T4, the system stiffness matrix is computed using smoothed strains, and hence the FS-FEM-T4 model is found softer than that of FEM-T4 using the same mesh. Some numerical results will be presented to demonstrate the efficiency and properties of FS-FEM-T4 for both linear and geometrically nonlinear 3D problems. It will be shown that the implementation of FS-FEM-T4 is straightforward and no additional DOFs are used, and the results are much better than those of FEM-T4, without much increase in computational efforts. It will be both spatially and temporally stable.

In addition, a smoothing-domain-based selective FS/NS-FEM-T4 model is also formulated using combined face-based and node-based smoothing operations. The selective FS/NS-FEM-T4 is found to be "immune" from volumetric locking and works well naturally for 3D problems of nearly incompressible materials, due to the volumetric locking-free property inherited from the NS-FEM.

8.2 Face-Based Smoothing Domain Creation

In FS-FEM-T4, the 3D problem domain is meshed into tetrahedral elements in the same way as in the standard FEM-T4. Since we only use T4 elements, the mesh generation can be done with ease for complicated geometries. The existing preprocessors for the FEM code or the standard Delaunay triangulation algorithms can be used.

Consider now a 3D domain Ω discretized with N_e tetrahedral elements and N_n nodes, such that $\Omega = \sum_{i=1}^{N_e} \Omega_i^e$ and $\Omega_i^e \cap \Omega_j^e \neq \emptyset$, $i \neq j$. The T4 element mesh shall have a total of N_f faces. On top of the element mesh we now further create a set of 3D smoothing domains based on the N_f faces of the element mesh, such that $\Omega = \sum_{k=1}^{N_f} \Omega_k^s$ and $\Omega_i^s \cap \Omega_j^s \neq \emptyset$, $i \neq j$. In this case, the number of smoothing domains is the same as the number of faces in the mesh: $N_s = N_f$, which satisfies the requirement of minimum number of smoothing domains given in Table 4.2. This implies that the FS-FEM-T4 should be at least spatially stable (see Theorem 4.1). The smoothing domain Ω_k^s associated with the face k is created by simply connecting three nodes of the face to the centers of the adjacent elements as shown in Figure 8.1. The procedure is simple, and can always be performed for a given T4 element

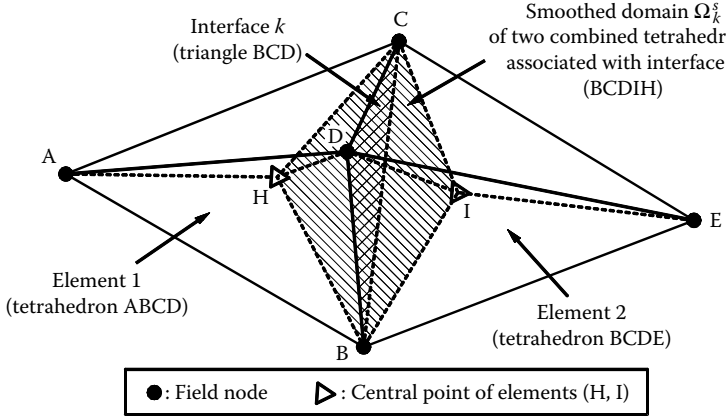

FIGURE 8.1 Two adjacent tetrahedral elements and the smoothing domain Ω_k^s (shaded domain) formed based on their interface k in FS-FEM-T4.

mesh without any technical difficulty. Strain smoothing operations [10] are then performed over these smoothing domains for creating a piecewise constant strain field, which is then used to establish the discretized linear algebraic system of equations.

8.3 Formulation of FS-FEM-T4

8.3.1 Static Analysis

Consider the solid mechanics problems defined in Chapter 2. Using the general formulation of S-FEM presented in Chapter 4, a linear system of equations of FS-FEM-T4 for the static analysis has the form of

$$\overline{\mathbf{K}}^{\text{FS-FEM}}\overline{\mathbf{d}} = \tilde{\mathbf{f}}, \tag{8.1}$$

where $\overline{\mathbf{K}}^{\text{FS-FEM}}$ is the *smoothed* stiffness matrix whose entries are given by

$$\overline{\mathbf{K}}_{IJ}^{\text{FS-FEM}} = \int_{\Omega} \overline{\mathbf{B}}_I^T \mathbf{c} \overline{\mathbf{B}}_J \, \mathrm{d}\Omega = \sum_{k=1}^{N_f} \int_{\Omega_k^s} \overline{\mathbf{B}}_I^T \mathbf{c} \overline{\mathbf{B}}_J \, \mathrm{d}\Omega = \sum_{k=1}^{N_f} \overline{\mathbf{B}}_I^T \mathbf{c} \overline{\mathbf{B}}_J V_k^s, \tag{8.2}$$

where V_k^s is the volume of the face-based smoothing domain Ω_k^s and is computed by a local summation of

$$V_k^s = \int_{\Omega_k^s} \mathrm{d}\Omega = \frac{1}{4} \sum_{j=1}^{n_k^e} V_j^e, \tag{8.3}$$

where n_k^e is the number of elements attached to the face k ($n_k^e = 1$ for the boundary faces and $n_k^e = 2$ for inner faces) and V_j^e is the volume of the jth element attached to the face k. Due to the use of tetrahedral elements with the linear shape functions, the entries of matrix $\tilde{\mathbf{B}}_j$ are constants over each element, and hence the smoothed strain–displacement matrix $\overline{\mathbf{B}}_I$ on the domain Ω_k^s is computed numerically simply by an local *assembly* process similarly as in the FEM:

$$\overline{\mathbf{B}}_I = \frac{1}{V_k^s} \sum_{j=1}^{n_k^e} \frac{1}{4} V_j^e \tilde{\mathbf{B}}_j, \tag{8.4}$$

where $\tilde{\mathbf{B}}_j$ is the strain–displacement matrix of the jth element attached to the face k and computed similarly to that in Section 6.3.3.

From Equation 8.4, it is clear that the entries of matrix $\overline{\mathbf{B}}_I$ are constants over each smoothing domain. With this formulation, only the volume and the usual compatible strain–displacement matrices $\tilde{\mathbf{B}}_j$ of the FEM-T4 element are needed to compute the system stiffness matrix for FS-FEM-T4. The alteration to the standard FEM code is therefore very little.

The above formulation is simple, but works only for T4 elements that use linear interpolation. In theory, FS-FEM works also for other types of elements, as long as a continuous displacement field on the smoothing domain surface can be created. For these general FS-FEM models, the smoothed strain–displacement matrix $\overline{\mathbf{B}}_I$ has to be computed using the original Equation 4.30.

8.3.2 Nonlinear Analysis of Large Deformation

The extension of our FS-FEM-T4 to geometrically nonlinear problems of large deformation is straightforward, and a similar procedure to that used in the standard FEM can be adopted with minor changes. For isotropic linear elastic solids, the values of strain gradient matrices and stresses at the face-based smoothing domains become the volume-weighted average values of those of the adjacent elements attached to the face. The formulation of FS-FEM-T4 for geometrically nonlinear problems of large deformation

based on the total Lagrange formulation [11,12] and the discrete system of equations can be expressed as follows:

$$\left(\overline{\mathbf{K}}_L^{\text{FS-FEM}} + \overline{\mathbf{K}}_{\text{NL}}^{\text{FS-FEM}}\right)\overline{\mathbf{d}} = \tilde{\mathbf{f}} - \bar{\mathbf{f}}_1, \tag{8.5}$$

where the stiffness matrix for the linearized portion can be written as

$$\overline{\mathbf{K}}_L^{\text{FS-FEM}} = \sum_{k=1}^{N_f} \overline{\mathbf{B}}_L^T \mathbf{c} \overline{\mathbf{B}}_L V_k^s, \tag{8.6}$$

in which matrix $\overline{\mathbf{B}}_L$ is for the face-based smoothing domains, and is computed using

$$\overline{\mathbf{B}}_L = \frac{1}{V_k^s} \sum_{j=1}^{n_k^e} \frac{1}{4} V_j^e \tilde{\mathbf{B}}_{L,j}^e. \tag{8.7}$$

In the foregoing equation, matrix $\tilde{\mathbf{B}}_L^e$ for an element is given by

$$\tilde{\mathbf{B}}_L^e = \begin{bmatrix} F_{11}N_{1,1} & F_{21}N_{1,1} & F_{31}N_{1,1} \\ F_{12}N_{1,2} & F_{22}N_{1,2} & F_{32}N_{1,2} \\ F_{13}N_{1,3} & F_{23}N_{1,3} & F_{33}N_{1,3} \\ F_{11}N_{1,2} + F_{12}N_{1,1} & F_{21}N_{1,2} + F_{22}N_{1,1} & F_{31}N_{1,2} + F_{32}N_{1,1} \\ F_{12}N_{1,3} + F_{13}N_{1,2} & F_{22}N_{1,3} + F_{23}N_{1,2} & F_{32}N_{1,3} + F_{33}N_{1,2} \\ F_{11}N_{1,3} + F_{13}N_{1,1} & F_{21}N_{1,3} + F_{23}N_{1,1} & F_{31}N_{1,3} + F_{33}N_{1,1} \end{bmatrix}$$

$$\begin{bmatrix} F_{11}N_{2,1} & \cdots & F_{31}N_{4,1} \\ F_{12}N_{2,2} & \cdots & F_{32}N_{4,2} \\ F_{13}N_{2,3} & \cdots & F_{33}N_{4,3} \\ F_{11}N_{2,2} + F_{12}N_{2,1} & \cdots & F_{31}N_{4,2} + F_{32}N_{4,1} \\ F_{12}N_{2,3} + F_{13}N_{2,2} & \cdots & F_{32}N_{4,3} + F_{33}N_{4,2} \\ F_{11}N_{2,3} + F_{13}N_{2,1} & \cdots & F_{31}N_{4,3} + F_{33}N_{4,1} \end{bmatrix}, \tag{8.8}$$

in which $N_{I,j} = \partial N_I / \partial X_j$ and F_{IJ} are the entries of the deformation gradient tensor for the element $\tilde{\mathbf{F}}^e$ that is computed by

$$\tilde{\mathbf{F}}^e = \begin{bmatrix} F_{11} & F_{12} & F_{13} \\ F_{21} & F_{22} & F_{23} \\ F_{31} & F_{32} & F_{33} \end{bmatrix} = \left(\frac{\partial \mathbf{x}}{\partial \mathbf{X}}\right)^T = \left(\mathbf{L}_d \overline{\mathbf{d}} + \mathbf{I}\right)^T. \tag{8.9}$$

The stiffness matrix for the nonlinear portion in Equation 8.5 can be written as

$$\overline{\mathbf{K}}_{\mathrm{NL}}^{\text{FS-FEM}} = \sum_{k=1}^{N_f} \overline{\mathbf{B}}_{\mathrm{NL}}^{T} \overline{\mathbf{S}\mathbf{B}}_{\mathrm{NL}} V_k^s, \tag{8.10}$$

where matrix $\overline{\mathbf{B}}_{\mathrm{NL}}$ is for the face-based smoothing domains, and is computed using

$$\overline{\mathbf{B}}_{\mathrm{NL}} = \frac{1}{V_k^s} \sum_{j=1}^{n_k^e} \frac{1}{4} V_j^e \tilde{\mathbf{B}}_{\mathrm{NL},j}^e. \tag{8.11}$$

In the foregoing equation, matrix $\tilde{\mathbf{B}}_{\mathrm{NL}}^e$ is for the elements, and is given by

$$\tilde{\mathbf{B}}_{\mathrm{NL}}^e = \begin{bmatrix} N_{1,1} & 0 & 0 & N_{2,1} & \cdots & 0 \\ N_{1,2} & 0 & 0 & N_{2,2} & \cdots & 0 \\ N_{1,3} & 0 & 0 & N_{2,3} & \cdots & 0 \\ 0 & N_{1,1} & 0 & 0 & \cdots & 0 \\ 0 & N_{1,2} & 0 & 0 & \cdots & 0 \\ 0 & N_{1,3} & 0 & 0 & \cdots & 0 \\ 0 & 0 & N_{1,1} & 0 & \cdots & N_{4,1} \\ 0 & 0 & N_{1,2} & 0 & \cdots & N_{4,2} \\ 0 & 0 & N_{1,3} & 0 & \cdots & N_{4,3} \end{bmatrix}, \tag{8.12}$$

and matrix $\overline{\mathbf{S}}$ is for the face-based smoothing domains, and is computed using

$$\overline{\mathbf{S}} = \frac{1}{V_k^s} \sum_{j=1}^{n_k^e} \frac{1}{4} V_j^e \tilde{\mathbf{S}}_j^e \quad \text{with}$$

$$\tilde{\mathbf{S}}^e = \begin{bmatrix} S_{11} & S_{12} & S_{13} & 0 & 0 & 0 & 0 & 0 & 0 \\ S_{12} & S_{22} & S_{23} & 0 & 0 & 0 & 0 & 0 & 0 \\ S_{13} & S_{23} & S_{33} & 0 & 0 & 0 & 0 & 0 & 0 \\ 0 & 0 & 0 & S_{11} & S_{12} & S_{13} & 0 & 0 & 0 \\ 0 & 0 & 0 & S_{12} & S_{22} & S_{23} & 0 & 0 & 0 \\ 0 & 0 & 0 & S_{13} & S_{23} & S_{33} & 0 & 0 & 0 \\ 0 & 0 & 0 & 0 & 0 & 0 & S_{11} & S_{12} & S_{13} \\ 0 & 0 & 0 & 0 & 0 & 0 & S_{12} & S_{22} & S_{23} \\ 0 & 0 & 0 & 0 & 0 & 0 & S_{13} & S_{23} & S_{33} \end{bmatrix}, \tag{8.13}$$

in which the entries S_{IJ} of matrix $\tilde{\mathbf{S}}^e$ are derived from the second Piola–Kirchhoff stress tensor $\tilde{\boldsymbol{\Psi}}^e$ for the element by

$$\tilde{\boldsymbol{\Psi}}^e = \begin{bmatrix} S_{11} \\ S_{22} \\ S_{33} \\ S_{12} \\ S_{23} \\ S_{31} \end{bmatrix} = \mathbf{c} \begin{bmatrix} E_{11} \\ E_{22} \\ E_{33} \\ 2E_{12} \\ 2E_{23} \\ 2E_{31} \end{bmatrix}. \tag{8.14}$$

The entries E_{IJ} in Equation 8.14 are derived from the entries of the Green–Lagrange strain tensor $\tilde{\mathbf{E}}^e$ for the elements as

$$\tilde{\mathbf{E}}^e = \begin{bmatrix} E_{11} & E_{12} & E_{13} \\ E_{21} & E_{22} & E_{23} \\ E_{31} & E_{32} & E_{33} \end{bmatrix} = \frac{1}{2}\left(\left(\tilde{\mathbf{F}}^e\right)^T \tilde{\mathbf{F}}^e - \mathbf{I}\right), \tag{8.15}$$

where $\mathbf{I}$ is the 3×3 unity matrix.

The "additional" force term caused by the nonlinearity in Equation 8.5 becomes

$$\bar{\mathbf{f}}_1 = \sum_{k=1}^{N_f} \overline{\mathbf{B}}_L^T \overline{\boldsymbol{\Psi}} V_k^s, \tag{8.16}$$

where

$$\overline{\boldsymbol{\Psi}} = \frac{1}{V_k^s} \sum_{j=1}^{n_k^e} \frac{1}{4} V_j^e \tilde{\boldsymbol{\Psi}}_{1,j}^e. \tag{8.17}$$

8.4 A Smoothing-Domain-Based Selective FS/NS-FEM-T4 Model

Similar to the ES/NS-FEM-T3 given in Section 7.5, this section presents a smoothing-domain-based selective FS/NS-FEM-T4 for 3D solids of incompressible materials. We use two different types of smoothing domains selectively for two different material "parts" (μ part and λ part). This scheme comes from the realization of two facts: (1) the node-based smoothing domains used in NS-FEM-T4 were found effective in overcoming the volumetric locking [13], and (2) the λ part is known as the "culprit" of the volumetric locking. We therefore use the node-based smoothing domains

for the λ part and face-based smoothing domains for the μ part. The stiffness matrix of the smoothing-domain-based selective FS/NS-FEM-T4 model becomes

$$\overline{\mathbf{K}} = \underbrace{\sum_{i=1}^{N_f} \left(\overline{\mathbf{B}}_{1,i}\right)^T \mathbf{c}_1 \overline{\mathbf{B}}_{1,i} V_{1,i}}_{\overline{\mathbf{K}}_1^{\text{FS-FEM}}} + \underbrace{\sum_{j=1}^{N_n} \left(\overline{\mathbf{B}}_{2,j}\right)^T \mathbf{c}_2 \overline{\mathbf{B}}_{2,j} V_{2,j}}_{\overline{\mathbf{K}}_2^{\text{NS-FEM}}}, \tag{8.18}$$

where $\overline{\mathbf{B}}_{1,i}$ and $V_{1,i}$ are the smoothed strain–displacement matrix and the volume of the smoothing domain associated with face i; $\overline{\mathbf{B}}_{2,j}$ and $V_{2,j}$ are the smoothed strain–displacement matrix and the volume of the smoothing domain associated with node j; N_n is the total number of nodes in the entire problem domain; and matrices $\mathbf{c}_1$ and $\mathbf{c}_2$ are derived from the material constant matrix $\mathbf{c}$ for the 3D cases as follows:

$$\mathbf{c} = \underbrace{\mu \begin{bmatrix} 2 & 0 & 0 & 0 & 0 & 0 \\ 0 & 2 & 0 & 0 & 0 & 0 \\ 0 & 0 & 2 & 0 & 0 & 0 \\ 0 & 0 & 0 & 1 & 0 & 0 \\ 0 & 0 & 0 & 0 & 1 & 0 \\ 0 & 0 & 0 & 0 & 0 & 1 \end{bmatrix}}_{\mathbf{c}_1} + \underbrace{\lambda \begin{bmatrix} 1 & 1 & 1 & 0 & 0 & 0 \\ 1 & 1 & 1 & 0 & 0 & 0 \\ 1 & 1 & 1 & 0 & 0 & 0 \\ 0 & 0 & 0 & 0 & 0 & 0 \\ 0 & 0 & 0 & 0 & 0 & 0 \\ 0 & 0 & 0 & 0 & 0 & 0 \end{bmatrix}}_{\mathbf{c}_2} = \mathbf{c}_1 + \mathbf{c}_2. \tag{8.19}$$

8.5 Stability, Accuracy, and Mesh Sensitivity

8.5.1 Stability of FS-FEM-T4

Property 8.1 FS-FEM: Both Spatially and Temporally Stable

FS-FEM-T4 possesses only "legal" zero-energy modes that represent the rigid motions and hence FS-FEM-T4 is *spatially stable*. There exist no spurious non-zero-energy modes and thus FS-FEM-T4 is also *temporally stable*.

To examine (intuitively) this property, we first note that both the FEM-T4 and ES-FEM-T4 models are variationally consistent (see Theorem 4.1). Therefore, the stability of the model will be of concern only to the numerical integration in the weak forms. In the standard FEM-T4 using linear shape functions, the integration of the weak form is based on elements. For each element, only one Gauss point is needed for the exact evaluation of the integrals. This implies that the number of Gauss points used in the integration of the weak form equals the number of elements used in the problem domain. Such an FEM-T4 model is well known to be stable both

spatially and temporally and hence is widely used for dynamics analysis and has no spurious non-zero-energy modes. In fact, it is known to be too stiff.

In FS-FEM-T4, the smoothing domains used are associated with the faces, and the strain (or stress) on each smoothing domain is constant. Therefore, each smoothing domain can be considered equivalent to one Gauss sampling point in evaluating the integration of the weak form [5]. Because the number of faces is always larger than the number of elements in any T4 element mesh, the number of sampling points for the evaluation of the weak form in the FS-FEM-T4 is always larger than that in the FEM-T4. Therefore, the FS-FEM-T4 should be more stable than the FEM-T4 model, has no spurious non-zero-energy modes, and is well suited for the dynamic analysis. This property of FS-FEM-T4 is quite similar to that of ES-FEM-T3 for dynamics analyses of 2D solid mechanics problems [14].

Note that in NS-FEM [13] the smoothing domains used are associated with the nodes. NS-FEM has been proven to be spatially stable, works well for static problems, and can produce upper bound solutions. However, for vibration analysis, NS-FEM is unstable due to the presence of spurious non-zero-energy modes. This is because the number of nodes in a T4 element mesh can be much smaller than the number of elements. This situation is similar to the underintegration of the weak form inherent in the nodal integration approach of mesh-free methods. The temporal instability, therefore, is one of the main concerns of NS-FEM and mesh-free methods, and special stabilization techniques are required for solving dynamic problems [7,15,16].

8.5.2 Patch Test and Mesh Sensitivity

The Irons first-order patch test presented in Section 6.5.4 is performed again for our FS-FEM-T4. The errors in displacement norm (Equation 4.63) and in the (absolute) strain energy error (Equation 6.13) are used to examine quantitatively the computed results. An analysis of the sensitivity of the solution against highly distorted meshes similar to that in Section 6.5.4 is also considered.

The results of the patch test are listed in Table 8.1 for meshes of different irregularities. It is found that FS-FEM-T4 can pass the Irons first-order patch test within machine precision regardless of the irregularity factor α_{ir} used. There is no accuracy loss due to the different choices of α_{ir} value. This shows that FS-FEM-T4 can produce the linear field exactly and hence has at least a second-order accuracy (the displacement error is only in the terms of second order and/or above). Together with the stability, the FS-FEM solution will always converge to the exact solution. This patch test also shows that FS-FEM-T4 can work well with the severely distorted meshes. We now note:

TABLE 8.1

Solution Error in Displacement and Strain Energy Error for the Patch Test

	$\alpha_{ir} = 0.0$	$\alpha_{ir} = 0.1$	$\alpha_{ir} = 0.2$	$\alpha_{ir} = 0.3$	$\alpha_{ir} = 0.4$	$\alpha_{ir} = 0.49$
Displacement e_d (%)	3.95e − 16	1.16e − 15	7.73e − 16	1.00e − 15	1.53e − 15	2.21e − 15
Strain energy e_e	0.0	7.28e − 12	1.82e − 11	1.09e − 11	7.28e − 12	2.12e − 11

Property 8.2 FS-FEM-T4: First-Order Consistency

FS-FEM-T4 has the first-order consistency, meaning that it can produce a linear displacement field exactly. In other words, they are of second-order accuracy in displacement solution: errors are at terms of second order or above.

Property 8.3 FS-FEM-T4 Solution: Stability and Convergence

Due to the stability given in Property 8.1 and the first-order consistence given in Property 8.2, FS-FEM-T4 has a unique stable solution that converges to the exact solution of the original solid mechanics problem defined in Chapter 2. This confirms Theorem 4.1.

Property 8.4 FS-FEM-T4 is Less Sensitive Compared to FEM-T4.

8.6 Numerical Examples

In this section, examples will be presented to demonstrate the properties of the FS-FEM-T4 method. To show advantages of FS-FEM-T4, the results of the present method will be compared with those of FEM using tetrahedral elements (FEM-T4), eight-node hexahedral elements (FEM-H8), and NS-FEM using tetrahedral elements (NS-FEM-T4) [13].

The errors in both displacement norm and energy norm defined in Equations 4.49 and 4.50 are used in this analysis for the examination of numerical models. When the energy norm is used, we use the recovery strain solution for S-FEM models, and both raw and recovery strain solutions for FEM models.

Example 8.6.1: The 3D Lame Problem

The 3D Lame problem described in Example 6.7.5 is used again in the examination of our FS-FEM-T4. Only one-eighth of the sphere model is considered and

discretized, as shown in Figure 6.34, and the symmetry conditions are imposed properly on these three mirror symmetric planes. The exact strain energy of the problem is known as $E_{\text{exact}} = 6.306 \times 10^{-2}$ Nm.

Figures 8.2 and 8.3 plot the distribution of the displacements and stresses obtained using FS-FEM-T4, together with the analytical solution. It can be seen clearly that the FS-FEM-T4 results agree very well with the analytical solution. Table 6.12 and Figure 8.4 show the convergence of the strain energy solution. It is seen that the results of NS-FEM-T4 are an upper bound solution, and that of FS-FEM-T4 is a lower bound solution, all with respect to the exact solution. The results of FS-FEM-T4 are almost the same as those of FEM-H8 and much more accurate than those of FEM-T4.

Table 6.13 and Figure 8.5 give the solution error in displacement norm obtained using FS-FEM-T4, together with those of other methods using the same meshes. It is found that the result of FS-FEM-T4 is less accurate than that of FEM-H8 but is more accurate than those of NS-FEM-T4 and FEM-T4. When the third mesh ($h \approx 0.156$ m) is used, the error of FS-FEM-T4 is about 3/4 of FEM-T4 and NS-FEM-T4. In terms of convergence rate, the rate for FS-FEM-T4 ($r = 1.99$) is also larger than those of FEM-T4 ($r = 1.93$) and NS-FEM-T4 ($r = 1.85$).

Table 6.14 and Figure 8.6 show the solution error in energy norm obtained using FS-FEM-T4, together with those of other methods using the same meshes. It is found that the results of FS-FEM-T4 are only less accurate than those of

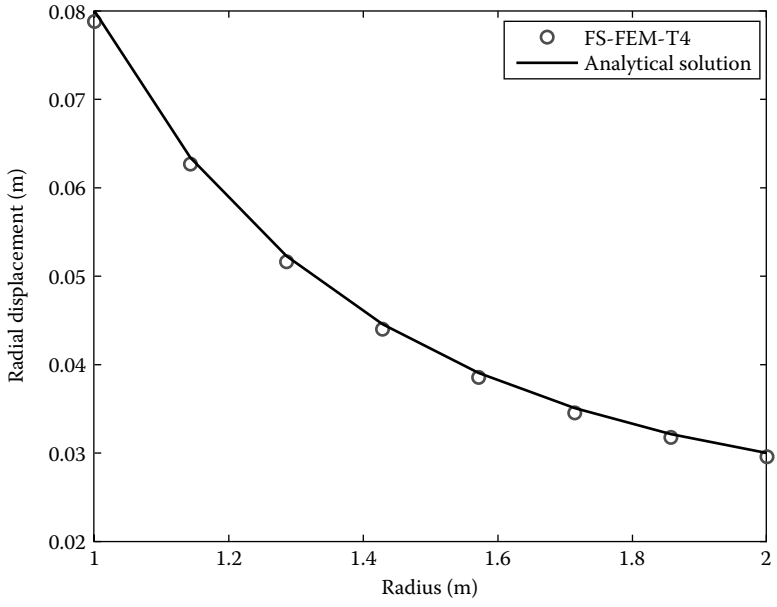

FIGURE 8.2 Distribution of the radial displacement in the hollow sphere subjected to an inner pressure.

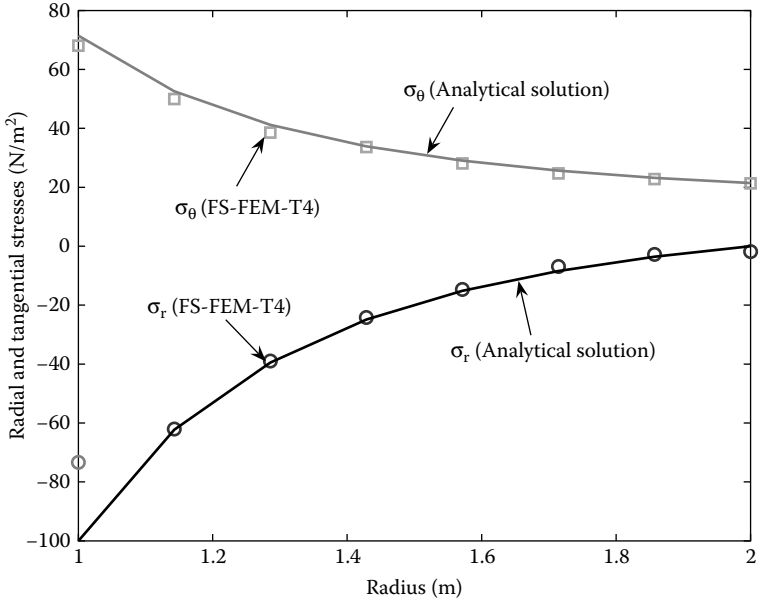

FIGURE 8.3 Distribution of the radial and tangential stresses in the hollow sphere subjected to an inner pressure.

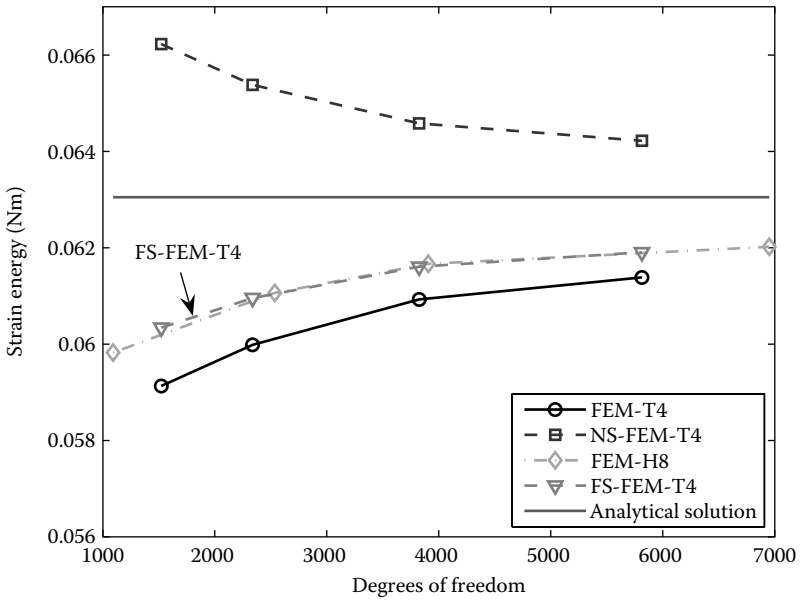

FIGURE 8.4 Convergence of strain energy solution of FS-FEM-T4 in comparison with other methods for the hollow sphere subjected to an inner pressure.

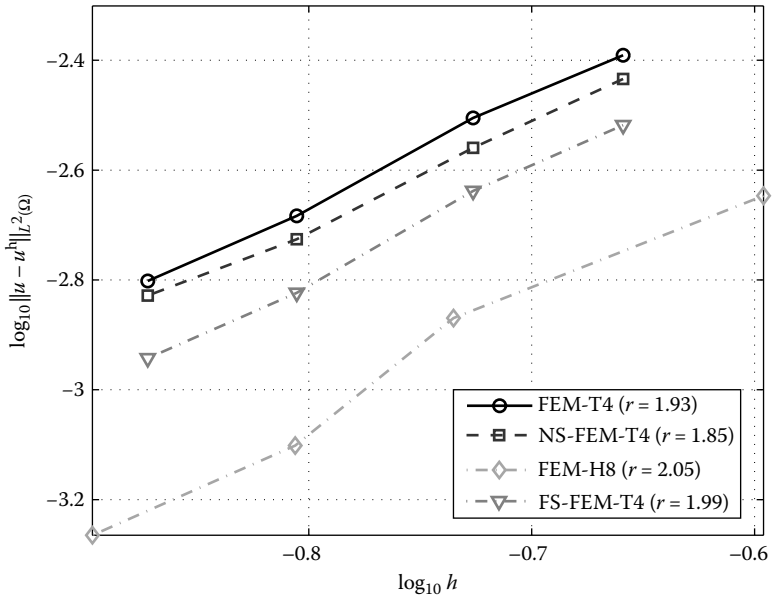

FIGURE 8.5 Error in displacement norm of FS-FEM-T4 in comparison with other methods for the hollow sphere subjected to an inner pressure.

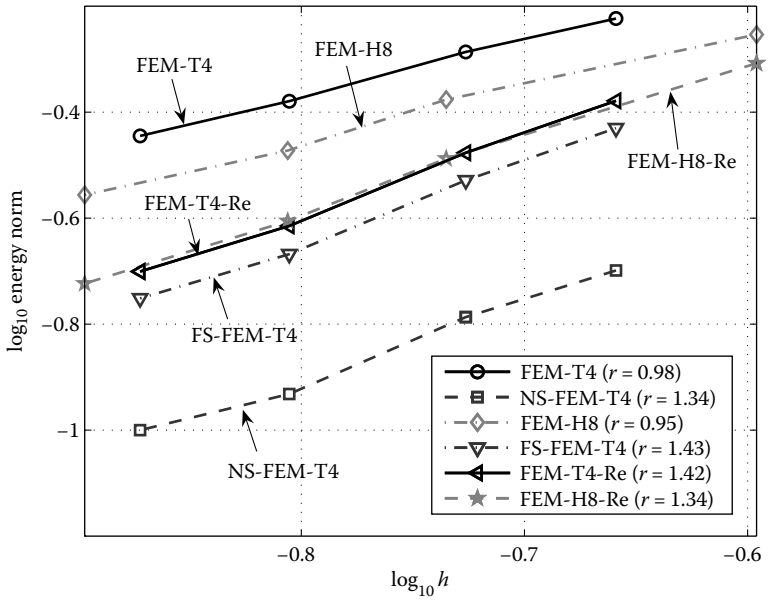

FIGURE 8.6 Error in energy norm of FS-FEM-T4 in comparison with other methods for the hollow sphere subjected to an inner pressure.

NS-FEM-T4 but are more accurate than those of FEM-T4, FEM-H8, and even FEM-T4-Re and FEM-H8-Re. When the third mesh ($h \approx 0.156$ m) is used, the error of FS-FEM-T4 is about 1/1.9 of FEM-T4, 1/1.5 of FEM-H8, and 1/1.1 of FEM-T4-Re or FEM-H8-Re. In terms of convergence rate, FS-FEM-T4 stands out clearly with a rate of $r = 1.43$, which is much larger than the theoretical value of 1.0, much higher than the FEM-H8, and compatible with FEM-T4-Re and FEM-H8-Re. All the above results show that FS-FEM-T4 is significantly more accurate than FEM-T4 and FEM-H8, and even better than FEM-T4-Re and FEM-H8-Re for 3D linear problems.

Figure 8.7 shows the solution error in displacement norm using the smoothing-domain-based selective FS/NS-FEM-T4 for nearly incompressible material when Poisson's ratio varies from 0.4 to 0.4999999. The results show that the smoothing-domain-based selective FS/NS-FEM-T4 model can overcome naturally the volumetric locking for solids of nearly incompressible materials, without any additional treatments. This is due to the volumetric looking-free feature of NS-FEM models discussed in Chapter 6.

Example 8.6.2: A 3D Cubic Cantilever

The 3D cantilever of cubic shape subjected to a uniform pressure on its upper face described in Example 6.7.6 is again studied, but using FS-FEM-T4. The discretization of the 3D cubic cantilever using tetrahedral elements is shown

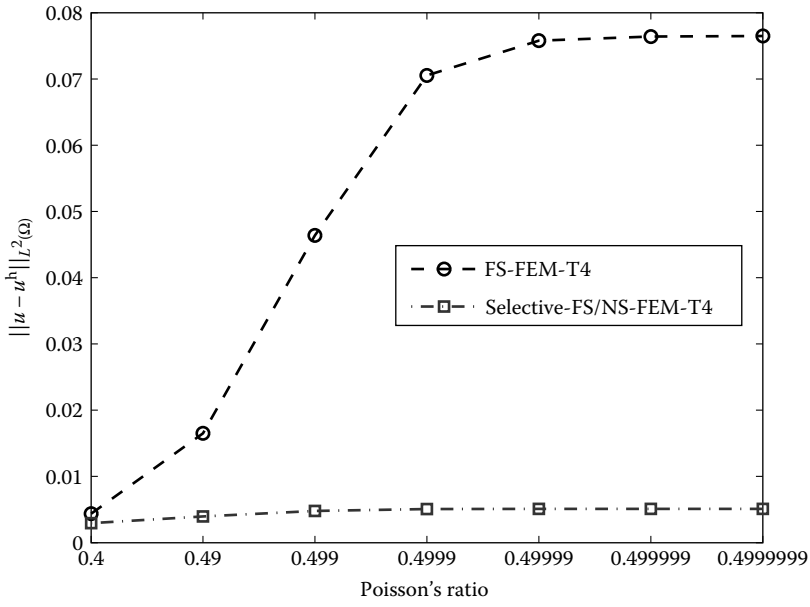

FIGURE 8.7 Error in displacement norm versus different Poisson's ratios of the hollow sphere subjected to an inner pressure.

in Figure 6.40. The reference solutions for this problem are obtained using the standard FEM with a very fine mesh of 30,204 nodes and 20,675 10-node tetrahedron elements. The reference solutions of strain energy and deflection at point $A(1.0, 1.0, -0.5)$ are found to be 0.9486 and 3.3912, respectively.

Table 6.15 and Figure 8.8 show the convergence of the strain energy solution obtained using FS-FEM-T4, together with those obtained using other methods. Table 6.16 and Figure 8.9 show the convergence curves of the deflection at point A obtained using FS-FEM-T4, together with other methods. It is found that the results of FS-FEM-T4 are less accurate than those of FEM-H8, but much more accurate than those of FEM-T4 for this problem. These results again show that FS-FEM-T4 is significantly more accurate than FEM-T4 for 3D linear elasticity problems.

Example 8.6.3: A 3D Cantilever Beam: A Geometrically Nonlinear Analysis

This example examines the use of FS-FEM-T4 for the geometrically nonlinear analysis of large deformation for 3D solids. A 3D cantilever beam subjected to a uniformly distributed load is considered. The size of the beam is (10 cm × 2 cm × 2 cm) and is discretized using a mesh including 1322 nodes and 5802 tetrahedral elements as shown in Figure 8.10. The material parameters are taken as $E = 3.0 \times 10^7$ KN/cm^2, $\nu = 0.3$.

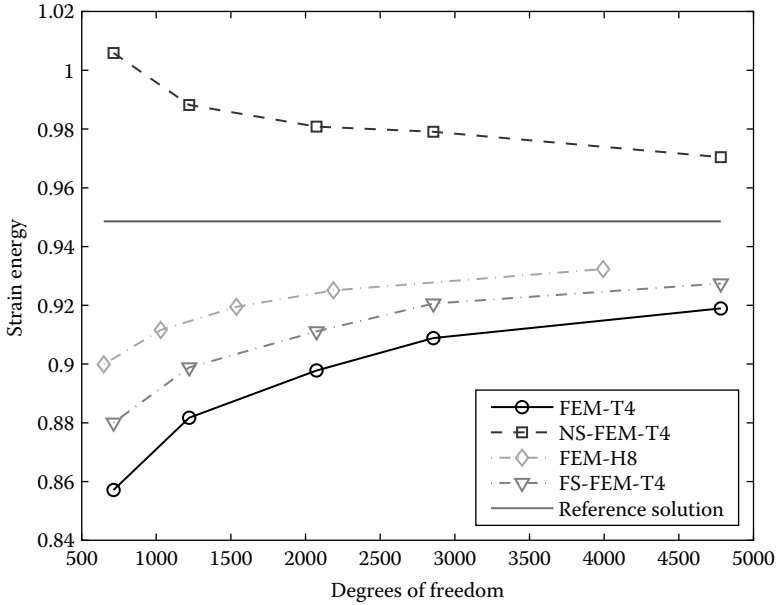

FIGURE 8.8 Convergence of the strain energy solution of FS-FEM-T4 in comparison with other methods for the cubic cantilever subjected to a uniform pressure on the top surface.

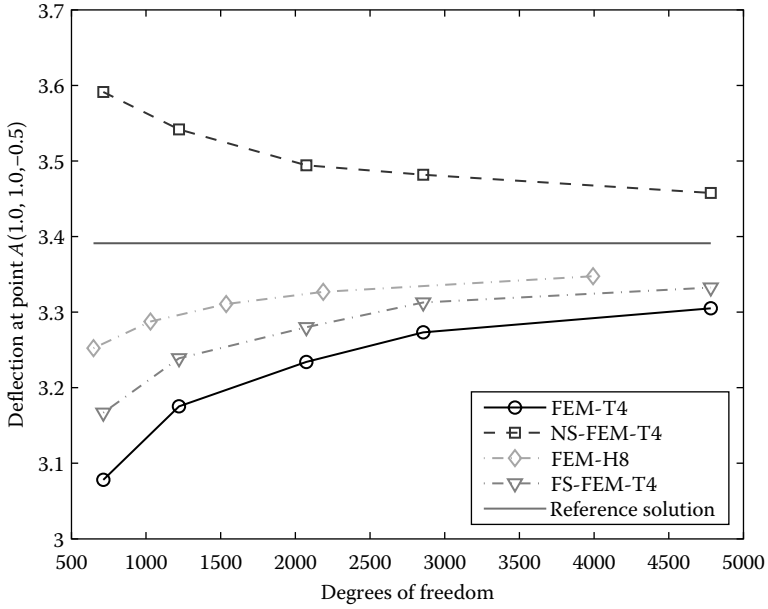

FIGURE 8.9 Convergence of the deflection at point $A(1.0, 1.0, -0.5)$ of FS-FEM-T4 in comparison with other methods for the cubic cantilever subjected to a uniform pressure.

First, a mesh sensitivity analysis is performed for the linear problem using FS-FEM-T4 and FEM-T4 in a similar way as in the Iron first-order patch test. To create distorted meshes, the interior nodes are intentionally moved randomly inside the cantilever beam from the original regular positions. The moved coordinates are computed using Equation 6.16. In addition, the interior nodes of boundary faces are also moved randomly inside their original faces. Only the nodes located on the boundary sides of the cantilever beam are kept unchanged. Table 8.2 shows the relation between the tip deflection versus the prescribed irregularity factor α_{ir} chosen between 0.0 and 0.4, and Figure 8.11 plots a severely distorted mesh with $\alpha_{ir} = 0.4$. The results are computed using both FS-FEM-T4 and FEM-T4 models with exactly the same meshes, and listed in Table 8.2. For easy analysis, we use the result of the tip deflection $d = 2.5292$ obtained using FEM-H8 with 2304 nodes as a reference solution. Table 8.2 shows that FS-FEM-T4 produces more accurate results and is less sensitive to the mesh distortion than those of FEM-T4. This finding implies that FS-FEM-T4 is much more suitable than FEM-T4 for geometrically nonlinear analysis of large deformation, where heavy mesh distortions are generally expected.

Geometrically nonlinear analyses based on the total Lagrange formulation (that are often used in the FEM) are carried out using 10 increment steps ($n = 10$) with $\Delta f = 4\,\text{KN/cm}^2$ in each step, using FS-FEM-T4, FEM-T4, and FEM-H8. Figure 8.10 plots the initial and final configurations after 10 steps of increments of the deformation using FS-FEM-T4. Table 8.3 and Figure 8.12 show the relation between the tip deflection and the load steps obtained using different

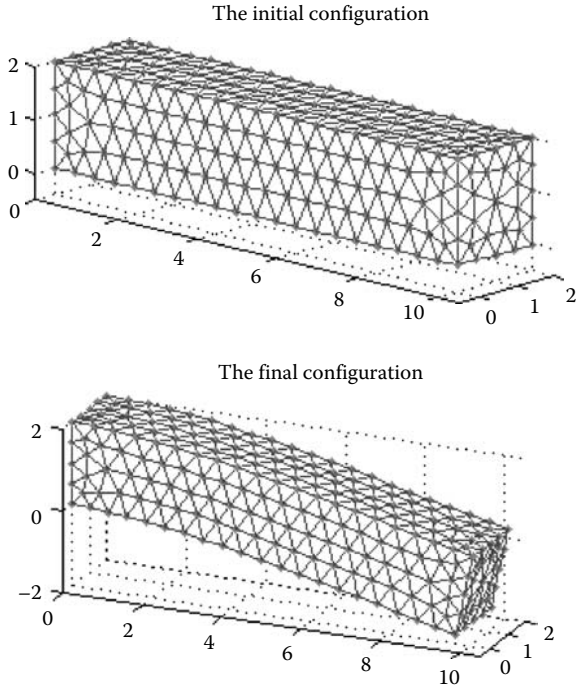

FIGURE 8.10 Initial and final configurations of the 3D cantilever beam subjected to a uniformly distributed load using the FS-FEM-T4 in the geometrically nonlinear analysis.

methods. The simulation result converges very rapidly in each load increment: only less than five iterations are needed. The results show that the nonlinear effects make the cantilever beam to behave stiffer compared to the linear solutions. In the geometrically nonlinear analysis, the results of FS-FEM-T4 are softer than those of FEM-T4 but stiffer than those of FEM-H8 using 1323 nodes.

TABLE 8.2

Tip Deflection (cm) versus the Irregularity Factor α_{ir} for the 3D Cantilever Beam Subjected to a Uniformly Distributed Load

	$\alpha_{ir} = 0.0$	$\alpha_{ir} = 0.1$	$\alpha_{ir} = 0.2$	$\alpha_{ir} = 0.3$	$\alpha_{ir} = 0.4$
FS-FEM-T4	2.4429	2.4373	2.4218	2.3888	2.3418
(1322 nodes)		(0.23%)[a]	(0.86%)	(2.21%)	(4.14%)
FEM-T4	2.3639	2.3559	2.3349	2.2933	2.2141
(1322 nodes)		(0.34%)	(1.23%)	(2.99%)	(6.34%)

Note: Reference solution: 2.5292.

[a] The number in parentheses shows the relative error (%) between the numerical results at $\alpha_{ir} > 0$ and the numerical results at $\alpha_{ir} = 0.0$.

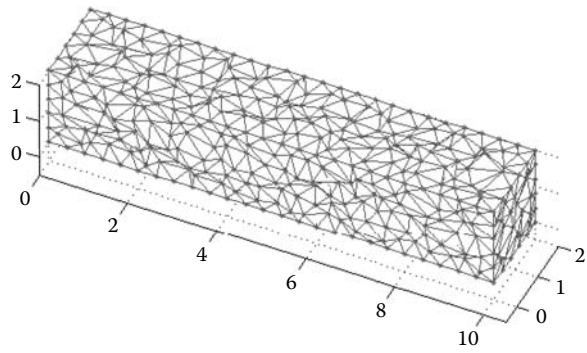

FIGURE 8.11 Domain discretization of the 3D cantilever beam subjected to a uniformly distributed load using severely distorted tetrahedral elements.

All these results suggest that FS-FEM-T4 performs more accurately than FEM-T4 for 3D geometrically nonlinear analysis of large deformation.

Example 8.6.4: An Axletree Base: Linear and Geometrically Nonlinear Analyses

In this example of the practical problem, both linear and geometrically nonlinear analyses of an axletree base are studied using the FS-FEM-T4 method. Figure 8.13 shows the model of the axletree base, which is symmetric about the y–z plane. A whole model with 8882 nodes and 40,409 elements is used for linear analysis, and a half model with 1342 nodes and 5124 tetrahedral elements is then created for nonlinear analysis. The axletree base is subjected

TABLE 8.3

Tip Deflection (cm) at the Load Steps for the 3D Cantilever Beam Subjected to a Uniformly Distributed Load

Load Step	FEM-T4 (Linear) (1322 Nodes)	FEM-T4 (Nonlinear) (1322 Nodes)	FEM-H8 (Nonlinear) (1323 Nodes)	FS-FEM-T4 (Nonlinear) (1322 Nodes)
$n = 1$	0.2364	0.2295 (3)[a]	0.2421 (3)	0.2365 (3)
$n = 2$	0.4728	0.4314 (3)	0.4522 (3)	0.4430 (3)
$n = 3$	0.7092	0.6119 (3)	0.6405 (3)	0.6277 (3)
$n = 4$	0.9456	0.7831 (3)	0.8205 (3)	0.8038 (3)
$n = 5$	1.1819	0.9511 (3)	1.0022 (4)	0.9818 (4)
$n = 6$	1.4183	1.1210 (4)	1.1762 (4)	1.1516 (4)
$n = 7$	1.6547	1.2847 (4)	1.3495 (4)	1.3206 (4)
$n = 8$	1.8911	1.4479 (4)	1.5222 (4)	1.4891 (4)
$n = 9$	2.1275	1.6104 (4)	1.6943 (4)	1.6569 (4)
$n = 10$	2.3639	1.7724 (4)	1.8656 (4)	1.8242 (4)

[a] The number in parentheses shows the number of iterations.

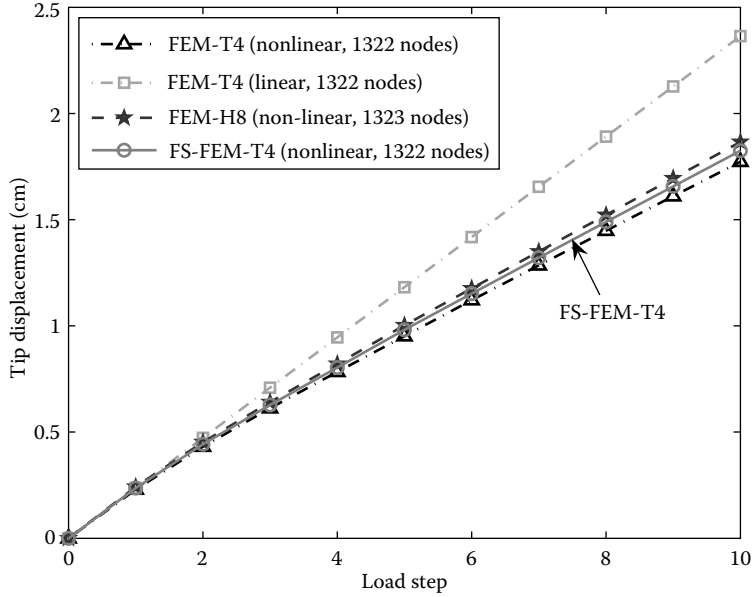

FIGURE 8.12 Tip deflection (cm) versus the load step of the 3D cantilever beam subjected to a uniformly distributed load in the geometrically nonlinear analysis.

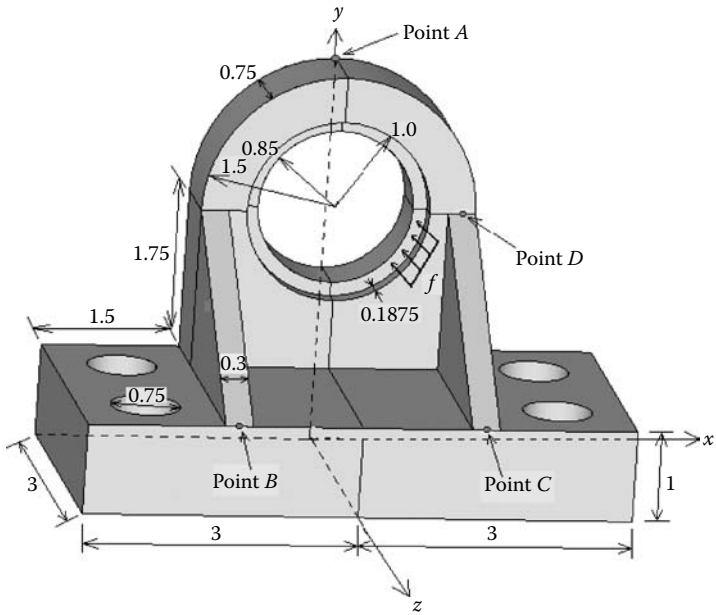

FIGURE 8.13 The axletree base model.

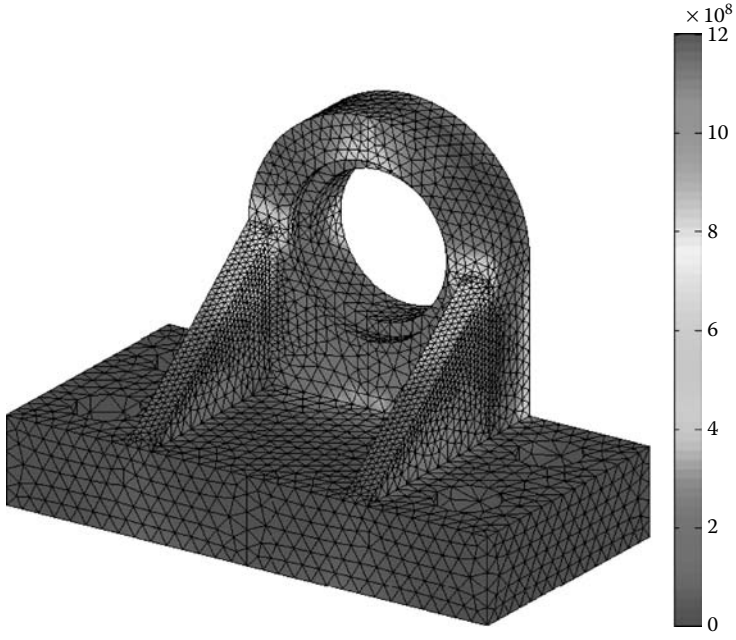

FIGURE 8.14 Distribution of the von-Mises stress in the linear analysis of small deformation using FS-FEM-T4.

to a uniformly distributed force f on the concave annulus in the z-direction and is fixed at the locations of four lower cylindrical holes and on the bottom plane. The related parameters are taken as $E = 3.0 \times 10^7\ \mathrm{N/cm^2}$, $\nu = 0.3$.

We first assumed that the problem is linear and conducted a linear static analysis with a loading of $f = 4000\,\mathrm{KN/cm^2}$. Figure 8.14 plots the distribution of the von-Mises stress σ_v in the axletree base computed using FS-FEM-T4. The von-Mises stress is computed using the stress components in the form of

$$\sigma_v = \sqrt{\frac{1}{2}\Big[(\sigma_{11}-\sigma_{22})^2 + (\sigma_{22}-\sigma_{33})^2 + (\sigma_{33}-\sigma_{11})^2 + 6\left(\sigma_{12}^2+\sigma_{23}^2+\sigma_{13}^2\right)\Big]}. \tag{8.20}$$

It can be observed from Figure 8.14 that stress concentrations are registered at the upper connecting zones of these two supporting "ribs," where the problem domain is concave, as expected.

We next consider the large deformation that results in geometric nonlinearity. The analysis based on the total Lagrange formulation is carried out using 10 increment steps ($n = 10$) with $\Delta f = 400\,\mathrm{KN/cm^2}$ at each step. Figure 8.15 shows the initial and final configurations viewed from the top of the 3D axletree base after 10 steps of simulation using FS-FEM-T4. Table 8.4 and Figure 8.16 show the relation between the tip displacement (point A) in the z-direction versus the load steps obtained using different methods. The simulation converges in

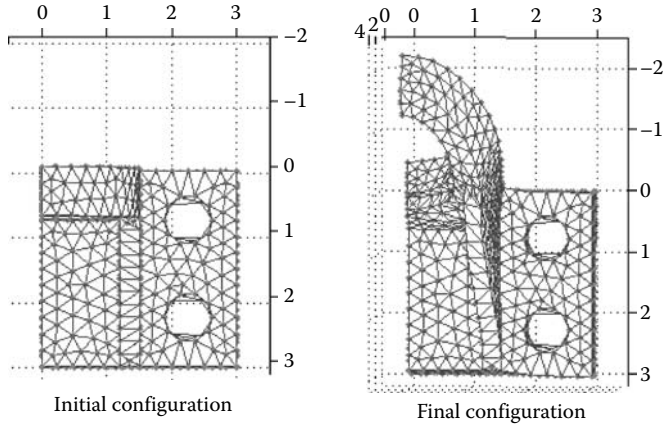

FIGURE 8.15 Initial and final configurations viewed from the top of a 3D axletree base using four-node tetrahedral elements in the geometrically nonlinear analysis.

a rapid speed in each load increment; only less than nine iterations are needed. It can be seen that the nonlinear effects make the axletree base behave stiffer compared to the linear solutions. In this geometrically nonlinear analysis, the results of FS-FEM-T4 are found softer than those of FEM-T4 and almost similar to that of FEM-T4 using 2520 nodes.

Note that for this problem, a discretization using eight-node hexahedral elements is very difficult if it is not impossible due to the complexity of the geometry of the problem, especially for areas near points *B*, *C*, and *D* shown in Figure 8.13. All these results again show that FS-FEM-T4 performs more accurately than FEM-T4 for 3D linear and nonlinear problems with complicated geometry.

TABLE 8.4

Tip Displacement (Point *A*) (cm) in the *z*-Direction at Load Steps for the 3D Axletree Base Using Four-Node Tetrahedral Elements for the Geometrically Nonlinear Analysis

Load Step	FEM-T4 (Linear) (1342 Nodes)	FEM-T4 (Nonlinear) (1342 Nodes)	FEM-T4 (Nonlinear) (2520 Nodes)	FS-FEM-T4 (Nonlinear) (1342 Nodes)
$n = 1$	0.3534	0.3104 (3)[a]	0.3260 (3)	0.3274 (3)
$n = 2$	0.7068	0.5700 (4)	0.5990 (4)	0.6017 (4)
$n = 3$	1.0601	0.8120 (5)	0.8538 (5)	0.8577 (5)
$n = 4$	1.4135	1.0419 (5)	1.0963 (5)	1.1012 (5)
$n = 5$	1.7669	1.2568 (6)	1.3210 (6)	1.3268 (6)
$n = 6$	2.1203	1.4650 (6)	1.5393 (6)	1.5460 (6)
$n = 7$	2.4737	1.6652 (7)	1.7360 (7)	1.7434 (7)
$n = 8$	2.8271	1.8436 (7)	1.9340 (7)	1.9421 (7)
$n = 9$	3.1804	2.0269 (8)	2.1074 (8)	2.1161 (8)
$N = 10$	3.5338	2.1855 (8)	2.2901 (8)	2.2996 (8)

[a] The number in parentheses shows the number of iterations.

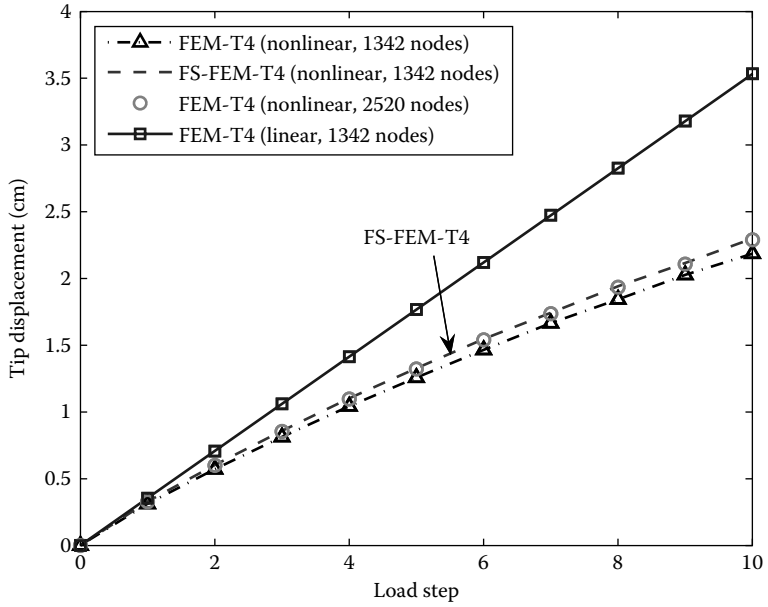

FIGURE 8.16 Tip displacement (point A) in the z-direction versus the load step of a 3D axletree base using four-node tetrahedral elements in the geometrically nonlinear analysis.

Example 8.6.5: Bonded Nearly Incompressible Rubber Block: Material and Geometrically Nonlinear Analyses

In this final example, we present the result of a generally nonlinear analysis by considering both material and geometrical nonlinearities. We analyze a bonded rubber cube of $L = 0.1$ m plotted in Figure 8.17. Although the initial geometry is very simple, it becomes extremely complicated after the large deformation.

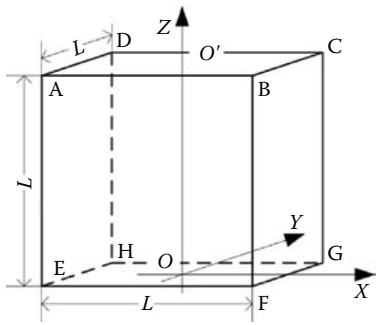

FIGURE 8.17 A bonded cube made of nearly incompressible rubber.

The total Lagrange formulation is used in the selective FS/NS-FEM-T4 setting, as detailed in Ref. [17]. The nearly incompressible Mooney–Rivlin hyperelastic material model is used with parameters of $A_{10} = 20\,\text{MPa}$, $A_{01} = 1\,\text{MPa}$, $\kappa = 1000\,\text{MPa}$, and density $\rho_0 = 2000\,\text{kg/m}^3$. The boundary conditions are as follows. On the top area A-B-C-D, the velocity in the vertical direction is set to zero: $\hat{v}_z^n|_{\text{top}} = 0$, and a torsion velocity is applied on the top surface in the form of

$$v_\theta^n|_{\text{top}} = \begin{cases} 5 \times 10^4 \pi t^n & 5 \times 10^4 \pi t^n < 100\pi \\ 100\pi & 5 \times 10^4 \pi t^n < 100\pi \end{cases} (\text{rad/s}). \tag{8.21}$$

On the bottom surface E-F-G-H, we set velocity $\hat{v}_z^n|_{\text{bot}} = 0$ and $v_\theta^n|_{\text{bot}} = -v_\theta^n|_{\text{top}}$.

The initial conditions are $\mathbf{v}^0 = \mathbf{0}$ and $\mathbf{u}^0 = \mathbf{0}$, meaning that the cube stays still initially.

The selective FS/NS-FEM-T4 with 65,224 elements and 12,197 nodes is adopted in the analysis. The analysis procedure automatically stops when $J = \det(\mathbf{F}) \leq 0$, indicating unphysical results due to the element distortion. Figure 8.18 shows the deformed configurations at different loading levels. In this example, the selective FS/NS-FEM-T4 can work up to an applied torsion angle

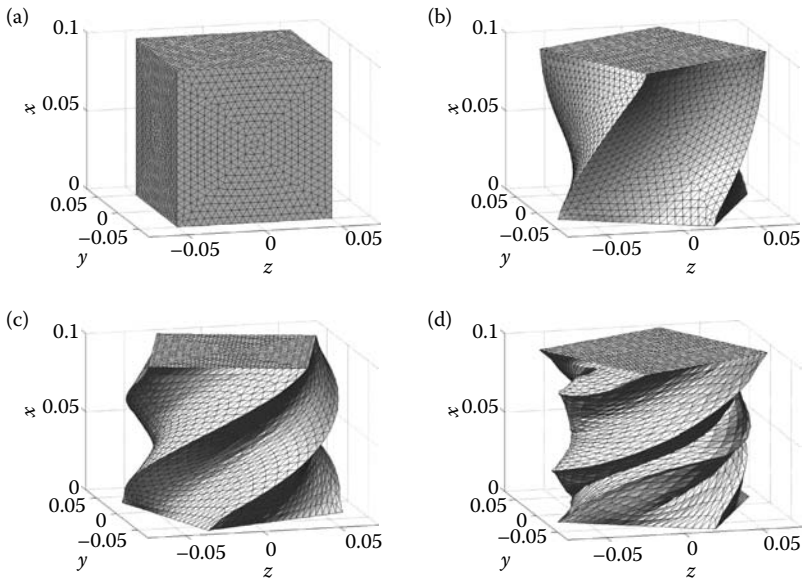

FIGURE 8.18 The bonded rubber cube under torsion solved using the selective FS/NS-FEM-T4 with 65,224 elements: (a) Initial configuration, (b) $\theta = 1.65\pi$, (c) $\theta = 1.9\pi$, and (d) $\theta = 2.15\pi$.

of $\theta = 2.15\pi$, which is much larger than that of an FEM model using 10-node triangular elements that can only reach $\theta = 1.80\pi$, due to the element distortion [17]. This shows that the selective FS/NS-FEM is much less sensitive to element distortion. In addition, no volumetric locking is observed in this example because of the use of selective FS/NS-FEM that is free from such a locking.

8.7 Remarks

In this chapter, an FS-FEM (FS-FEM-T4) is formulated and applied to solve 3D solid mechanics problems. Both linear and geometrically nonlinear problems are considered, using four-node tetrahedral elements that can be generated automatically for complicated domains. In FS-FEM-T4, the system stiffness matrix is computed using the smoothed strains over the smoothing domains associated with the faces of tetrahedral elements. Through the theoretical analyses, formulations, and numerical examples presented, we note the following remarks.

Remark 8.1 FS-FEM: Works Well with 3D T4 Elements

FS-FEM works well with tetrahedral elements and produces accurate solutions for problems with complicated geometry. FS-FEM-T4 is significantly more accurate than FEM-T4 using tetrahedral elements and is comparable to FEM-H8 and FEM-H8-Re for both linear and nonlinear analyses.

Remark 8.2 FS-FEM-T4: Easy to Implement in the Standard FEM Codes

The formulation of FS-FEM-T4 is straightforward and no additional DOFs are used in the model. It can be implemented easily to the standard FEM codes.

Remark 8.3 FS/NS-FEM-T4: Free from Volumetric Locking

The smoothing-domain-based selective FS/NS-FEM-T4 model is immune from volumetric locking and hence it works well for solids of nearly incompressible materials, in addition to showing less sensitivity to element distortion.

Remark 8.4 FS-FEM-T4: the Best Linear Model for 3D Problems

So far the author's group has not been able to find any linear model (except the αFEM with a tunable parameter) that works better than the FS-FEM-T4 for 3D problems, in terms of (1) adaptation to complicated geometry; (2) suitability for automatically meshing [18]; (3) stability; (4) solution accuracy; (5) computational efficiency; and (6) free from locking.

Remark 8.5 FS-FEM-T4: Less Effective than ES-FEM-T3

We note that the benefit from the face-based smoothing operations for 3D problems is not as significant as that from the "start" performer ES-FEM-T3 for 2D problems. The reasons are not yet clear to the authors, but we believe that the "relatively" large number of elements in a 3D tetrahedron mesh may be a major reason. In the 2D case, a quadrilateral element can be typically divided into two triangular elements (T3) without change in the number of nodes, but in the 3D case a hexahedral element can be typically divided into five or six tetrahedral elements (T4) [19]. The large number of elements affects the results in two folders. First, compared to the fact that the T3 element mesh is much stiffer compared to the Q4 mesh, the T4 element mesh is not too much stiffer compared to the H8 mesh. As a result, the performance of FEM-T4 is less stiff compared to FEM-T3, and the solution is not always that bad when recovery is performed, as can be seen from Example 8.6.1 where the results of FEM-T4-Re and FEM-H8-Re are almost the same. What happened is that the FEM-T4 loses in lower-order interpolation, but gains in the number of elements. Therefore, the room for improvement of the solution accuracy from FS-FEM-T4 to FEM-T4 becomes smaller. Second, the large number of elements results in the large number of faces in a T4 mesh, which results in the use of too many smoothing domains and reduces the softening effects and hence the benefits that it brings. Note that because of the fully compatible formulation in FEM-T4, it is naturally too stiff and unavoidably suffers from volumetric locking, as shown in Example 8.6.1 where the solution locks when the Poisson's ratio is larger than 0.4. The locking behavior limits significantly the use of FEM-T4 elements. FS/NS-FEM-T4 resolves this problem very effectively.

Finding a practical and more efficient way of properly reducing the number of smoothing domains for 3D S-FEM models can lead to a model that is better than FS-FEM-T4. Such a number should be in between the NS- and FS-FEM models. At this point of time, we got an idea for an alternative way of controlling the smoothing effects: αFEM-T4, which will be detailed in the next chapter.

References

1. Dohrmann CR, Key SW, Heinstein MW, and Jung J. 1998. A least squares approach for uniform strain triangular and tetrahedral finite elements. *International Journal for Numerical Methods in Engineering*; 42: 1181–1197.
2. Dohrmann CR, Heinstein MW, Jung J, Key SW, and Witkowski WR 2000. Node-based uniform strain elements for three-node triangular and four-node tetrahedral meshes. *International Journal for Numerical Methods in Engineering*; 47: 1549–1568.

3. Liu GR, Zhang GY, Dai KY, Wang YY, Zhong ZH, Li GY, and Han X. 2005. A linearly conforming point interpolation method (LC-PIM) for 2D solid mechanics problems. *International Journal of Computational Methods*; 2(4): 645–665.
4. Zhang GY, Liu GR, Wang YY, Huang HT, Zhong ZH, Li GY, and Han X. 2007. A linearly conforming point interpolation method (LC-PIM) for three-dimensional elasticity problems. *International Journal for Numerical Methods in Engineering*; 72: 1524–1543.
5. Liu GR. 2008. A generalized gradient smoothing technique and the smoothed bilinear form for Galerkin formulation of a wide class of computational methods. *International Journal of Computational Methods*; 5(2): 199–236.
6. Liu GR. 2002. *Meshfree Methods: Moving Beyond the Finite Element Method*. CRC Press, Boca Raton, FL.
7. Puso MA and Solberg J. 2006. A formulation and analysis of a stabilized nodally integrated tetrahedral. *International Journal for Numerical Methods in Engineering*; 67: 841–867.
8. Zhang ZQ and Liu GR. 2009. Temporal stabilization of the node-based smoothed finite element method (NS-FEM) and solution bound of linear elastostatics and vibration problems. *Computational Mechanics*; doi: 10.1007/s00466-009-0420-5.
9. Zhang ZQ and Liu GR. 2009. Upper and lower bounds for natural frequencies: A property of the smoothed finite element methods. *International Journal for Numerical Methods in Engineering*; (submitted).
10. Chen JS, Wu CT, Yoon S, and You Y. 2001. A stabilized conforming nodal integration for Galerkin meshfree method. *International Journal for Numerical Methods in Engineering*; 50: 435–466.
11. Bathe KJ. 1996. *Finite Element Procedures*. MIT Press/Prentice Hall, Cambridge, MA/Englewood Cliffs, NJ.
12. Reddy JN. 2004. *An Introduction to Nonlinear Finite Element Analysis*. Oxford University Press, Oxford.
13. Liu GR, Nguyen-Thoi T, Nguyen-Xuan H, and Lam KY. 2009. A node-based smoothed finite element method (NS-FEM) for upper bound solution to solid mechanics problems. *Computers and Structures*; 87: 14–26.
14. Liu GR, Nguyen-Thoi T, and Lam KY. 2009. An edge-based smoothed finite element method (ES-FEM) for static, free and forced vibration analyses of solids. *Journal of Sound and Vibration*; 320: 1100–1130.
15. Nagashima T. 1999. Node-by-node meshless approach and its applications to structural analyses. *International Journal for Numerical Methods in Engineering*; 46: 341–385.
16. Puso MA, Chen JS, Zywicz E, and Elmer W. 2008. Meshfree and finite element nodal integration methods. *International Journal for Numerical Methods in Engineering*; 74: 416–446.
17. Zhang ZQ and Liu GR. 2009. Explicit dynamics smoothed finite element methods for large deformation of nonlinear solids using triangle and tetrahedron. *Computational Mechanics*; (submitted).
18. Tang Q and Liu GR. 2009. Adaptive analysis for 3D problems using FS-FEM; (submitted).
19. Liu GR and Quek SS. 2003. *The Finite Element Method: A Practical Course*. Butterworth Heinemann, Oxford.

9

The αFEM

9.1 Introduction

As discussed in Chapter 3, the standard displacement FEM has a lot of good properties but shows some shortcomings, including the stress accuracy issues [1,2]. Therefore, efforts have been made to overcome these shortcomings and to improve the accuracy of the solution, including the S-FEM models presented in the previous chapters and the mixed FEM models [3–9] based on the mixed variational principles. All these efforts mainly focus on solution accuracy improvements. Obtaining the exact solution (at least in a norm) using a discrete numerical method is, however, a much more fascinating and attractive idea in the area of computational methods. Some interesting efforts have been made recently in Liu's group aiming at obtaining the exact solution in a norm using discrete models [1,2,10]. The so-called alpha finite element method using four-node quadrilateral elements (αFEM-Q4) has been developed for the purpose of finding a nearly exact solution in strain energy using coarse meshes [1]. The αFEM-Q4 gives a novel idea that works in the framework of FEM-Q4, by simply scaling the gradient of strains using a factor $\alpha \in [0, 1]$. Because the change needed is minor, the coding of αFEM-Q4 is almost exactly the same as the standard FEM-Q4. In addition, the resultant strain energy function for the αFEM-Q4 model has a very simple polynomial form in terms of α. Based on such a simple function of strain energy curves, a general procedure of αFEM-Q4 has been suggested to obtain nearly exact or best possible solutions, using meshes with the same aspect ratio. An exact-α approach is devised for overestimation problems and a zero-α approach for underestimation problems. The αFEM-Q4 has clearly opened a new window of opportunity to obtain numerical solutions that are exact at least in a norm. However, the original αFEM-Q4 based on quadrilateral elements cannot provide the exact solution to all elasticity problems. Furthermore, the αFEM-Q4 requires a quadrilateral mesh that cannot be generated in a fully automated manner for complicated domains.

Making use of the upper bound property of NS-FEM (see Chapter 6), the lower bound property of the standard FEM in strain energy, and

the important idea of αFEM-Q4, we introduce now a novel alpha finite element method using three-node triangular (αFEM-T3) elements for 2D problems and four-node tetrahedral elements (αFEM-T4) for 3D problems, which were originally presented in Ref. [2]. The essential idea of the method is to introduce a scale factor $\alpha \in [0, 1]$ to establish a continuous function of strain energy that contains contributions from both the standard FEM and NS-FEM. Our formulation ensures the variational consistence and compatibility of the displacement field and hence guarantees reproducing the linear field exactly. Based on the facts that the standard FEM of triangular and tetrahedral elements is spatially stable (no spurious zero-energy modes) and that the NS-FEM is also spatially stable as proved by Liu et al. [10], our αFEM-T3 and αFEM-T4 will always be spatially stable. This stability together with the linear consistence ensures convergence of the solution. This novel, combined formulation of FEM and NS-FEM makes best use of the upper bound property of the NS-FEM and the lower bound property of the standard FEM, and is equipped with a free parameter for tuning for special properties. Using meshes with the same aspect ratio, a unified approach has been proposed to obtain the nearly exact solution in strain energy for any given linear elasticity problem. The αFEM-T3 and αFEM-T4 are also applied to nonlinear problems of large deformation. In such cases, the exact solution is usually difficult to obtain, but the accuracy of the solution can be significantly improved. As will be shown, the numerical results for 2D (using αFEM-T3) and 3D (using αFEM-T4) problems confirm that the present method gives excellent performance compared to both the standard FEM and NS-FEM. The αFEM-T3 and αFEM-T4 are very easy to implement and apply to practical problems of complicated geometry, and the existing linear FEM code can largely be utilized.

Note that αFEM-T3 and αFEM-T4 [2] are very much different from αFEM-Q4 for quadrilateral elements [1] in terms of both formulation procedures and the approach. First, the numerical treatments in αFEM-Q4 are still element-based, but those in αFEM-T3 and αFEM-T4 are both element- and node-based. Second, in the case of αFEM-Q4, the strain field in an element is (bi)linear (with respect to the coordinates), which allows us to scale the gradient of the strain field by simply introducing a scaling factor α. In αFEM-T3 and αFEM-T4, however, the strain field in an element is constant, and hence it is not possible to scale the gradient of the strain field in the element because it is zero, if the numerical operations are still element-based. Therefore, a new technique has to be devised to bring in the information from the surrounding elements to create a desirable strain field. Third, αFEM-Q4 can only give a nearly exact solution in strain energy for a class of overestimation problems [1], whereas

αFEM-T3 and αFEM-T4 can provide a nearly exact solution in strain energy for all linear elasticity problems without using any postprocessing techniques.

9.2 Idea of αFEM-T3 and αFEM-T4

9.2.1 αFEM-T3 for 2D Problems

αFEM-T3 combines both NS-FEM-T3 and standard FEM-T3 by using the scale factor $\alpha \in [0, 1]$. As presented in Chapter 6, in NS-FEM-T3, the domain Ω_i^e of each triangular element is divided into three quadrilateral subdomains of equal area, and each quadrilateral subdomain contributes to the stiffness matrix of the node attached, as shown in Figure 9.1. In αFEM-T3, the domain Ω_i^e of the triangular element is divided into four subdomains with a scale factor α as shown in Figure 9.1: three quadrilateral subdomains at the three corners are scaled down by $(1 - \alpha^2)$ and are all having an equal area of $(1 - \alpha^2)A_i^e/3$. The remaining Y-shaped subdomain in the middle of the element has an area of $\alpha^2 A_i^e$. The same procedure in NS-FEM-T3 is then used to compute the stiffness contributions of the three quadrilateral subdomains at the three corners, while the usual procedure of FEM-T3 is used to compute the stiffness contribution for the Y-shaped subdomain. The entries in submatrices of the system stiffness matrix $\hat{\mathbf{K}}^{\alpha\text{FEM-T3}}$ will be assembled from the entries of those of NS-FEM-T3 and FEM-T3. The detailed formulation becomes

$$\hat{\mathbf{K}}_{IJ}^{\alpha\text{FEM-T3}} = \sum_{k=1}^{N_n} \overline{\mathbf{K}}_{IJ,k}^{\text{NS-FEM-T3}} + \sum_{i=1}^{N_e} \tilde{\mathbf{K}}_{IJ,i}^{\text{FEM}}, \tag{9.1}$$

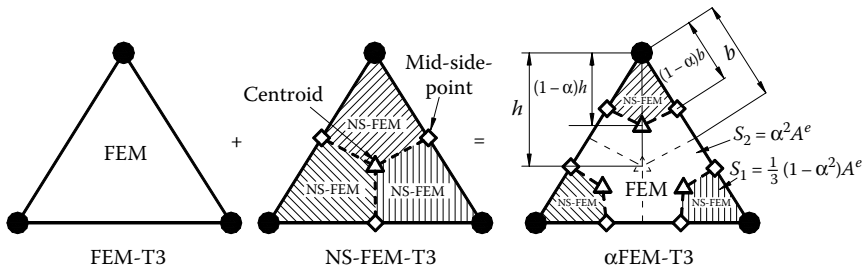

FIGURE 9.1 An αFEM-T3 element: a combination of the triangular elements of FEM and NS-FEM. The NS-FEM is used for three quadrilaterals, and the FEM is used for the Y-shaped domain in the center.

where N_n is the total number of nodes, N_e is the total number of elements in the entire problem domain, and

$$\overline{\mathbf{K}}_{IJ,k}^{\text{NS-FEM-T3}} = \int_{\Omega_{k,\alpha}^s} \left(\overline{\mathbf{B}}_I^{\alpha}(\mathbf{x}_k)\right)^T \mathbf{c}\overline{\mathbf{B}}_J^{\alpha}(\mathbf{x}_k)\, \mathrm{d}\Omega, \tag{9.2}$$

$$\tilde{\mathbf{K}}_{IJ,i}^{\text{FEM}} = \int_{\Omega_{i,\alpha}^e} \tilde{\mathbf{B}}_I^T \mathbf{c}\tilde{\mathbf{B}}_J\, \mathrm{d}\Omega = \tilde{\mathbf{B}}_I^T \mathbf{c}\tilde{\mathbf{B}}_J \alpha^2 A_i^e, \tag{9.3}$$

in which $\Omega_{i,\alpha}^e$ is the Y-shaped subdomain in the triangular element; $\Omega_{k,\alpha}^s$ is the smoothing domain associated with node k and bounded by $\Gamma_{k,\alpha}^s$, as shown in Figure 9.2. The smoothed strain–displacement matrix $\overline{\mathbf{B}}_I^{\alpha}(\mathbf{x}_k)$ for $\Omega_{k,\alpha}^s$ is computed using

$$\overline{\mathbf{B}}_I^{\alpha}(\mathbf{x}_k) = \frac{1}{A_{k,\alpha}^s} \sum_{j=1}^{n_k^e} \frac{1}{3}(1-\alpha^2) A_j^e \tilde{\mathbf{B}}_{I,j} = \frac{1}{A_k^s} \sum_{j=1}^{n_k^e} \frac{1}{3} A_j^e \tilde{\mathbf{B}}_{I,j} = \overline{\mathbf{B}}_I(\mathbf{x}_k), \tag{9.4}$$

which implies that we can use the matrix $\overline{\mathbf{B}}_I(\mathbf{x}_k)$ defined in Equation 6.3 for domain Ω_k^s instead of the matrix $\overline{\mathbf{B}}_I^{\alpha}(\mathbf{x}_k)$ for domain $\Omega_{k,\alpha}^s$ in the computation. Note that to obtain Equation 9.4, the following relation between the area

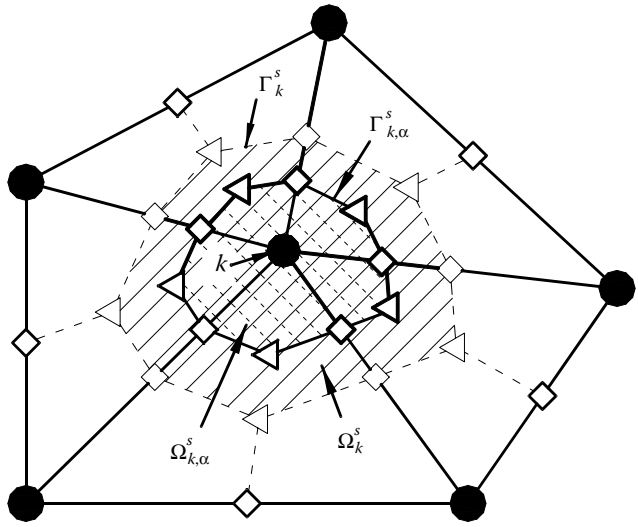

FIGURE 9.2 Smoothing domain associated with nodes for triangular elements in an αFEM-T3 model.

$A^s_{k,\alpha}$ of the domain $\Omega^s_{k,\alpha}$ and the area A^s_k defined in Equation 6.4 of the domain Ω^s_k is used:

$$A^s_{k,\alpha} = \int\limits_{\Omega^s_{k,\alpha}} \mathrm{d}\Omega = \sum_{j=1}^{n^e_k} \frac{1}{3}(1-\alpha^2)A^e_j = (1-\alpha^2)A^s_k, \tag{9.5}$$

where n^e_k is the number of elements around node k; A^e_j is the whole area of the jth element around node k.

Using Equations 9.4 and 9.5, Equation 9.2 can now be written as

$$\overline{\mathbf{K}}^{\text{NS-FEM-T3}}_{IJ,k} = (1-\alpha^2)\overline{\mathbf{B}}^T_I \mathbf{c}\overline{\mathbf{B}}_J A^s_k, \tag{9.6}$$

which implies that we can simplify the procedure of coding of αFEM-T3 by using the original NS-FEM-T3. Each triangular element is divided into three quadrilaterals of equal area to compute the contributions to the stiffness matrix with a scaling down of $(1-\alpha^2)$.

To compute Equation 9.3, the standard FEM using triangular elements (FEM-T3) is used to compute the contributions to the stiffness matrix with a simple scaling down with a factor of α^2.

The αFEM-T3 model is now equipped with a scaling factor α that acts as a "knob" controlling the contributions from portions of NS-FEM-T3 and FEM-T3. Since both NS-FEM-T3 and FEM-T3 models are spatially stable and convergent, when the factor α is "turned" from 0 to 1, a continuous function of solution in a norm can be expected from the solution of NS-FEM-T3 to that of FEM-T3.

This is the basic idea of αFEM-T3: it is very simple as shown and very powerful as will be shown.

9.2.2 αFEM-T4 for 3D Problems

The extension from αFEM-T3 to αFEM-T4 is straightforward. Following the same idea and concept of αFEM-T3 presented above, we can easily develop an αFEM-T4 model for 3D problems using tetrahedral elements. In this case, the (volumetric) domain Ω^e_i of each tetrahedral element will be divided into five subdomains using a similar scaling factor α: four subdomains at four corners will have an equal volume of $(1-\alpha^3)/4\ V^e_i$. The remaining domain in the middle of the element will have a volume of $\alpha^3 V^e_i$. The NS-FEM-T4 is then used to compute for four corner subdomains of equal volumes, while FEM-T4 is used to compute for the remaining subdomain in the middle. The system stiffness matrix $\hat{\mathbf{K}}^{\text{αFEM-T4}}$ is computed using

$$\hat{\mathbf{K}}^{\text{αFEM-T4}}_{IJ} = \sum_{k=1}^{N_n} \overline{\mathbf{K}}^{\text{NS-FEM-T4}}_{IJ,k} + \sum_{i=1}^{N_e} \tilde{\mathbf{K}}^{\text{FEM-T4}}_{IJ,i}, \tag{9.7}$$

with the matrices $\overline{\mathbf{K}}_{IJ,k}^{\text{NS-FEM-T4}}$ and $\tilde{\mathbf{K}}_{IJ,i}^{\text{FEM-T4}}$ computed as follows:

$$\overline{\mathbf{K}}_{IJ,k}^{\text{NS-FEM-T4}} = (1-\alpha^3)\overline{\mathbf{B}}_I^T \mathbf{c}\overline{\mathbf{B}}_J V_k^s, \tag{9.8}$$

$$\tilde{\mathbf{K}}_{IJ,i}^{\text{FEM-T4}} = \int_{\Omega_{i,\alpha}^e} \tilde{\mathbf{B}}_I^T \mathbf{c}\tilde{\mathbf{B}}_J \, \mathrm{d}\Omega = \tilde{\mathbf{B}}_I^T \mathbf{c}\tilde{\mathbf{B}}_J \alpha^3 V_i^e, \tag{9.9}$$

in which $\Omega_{i,\alpha}^e$ is the remaining domain in the middle of the T4 element; the smoothed strain–displacement matrix $\overline{\mathbf{B}}_I$ is computed using Equation 6.5, V_k^s is computed using Equation 6.6, and the compatible strain–displacement matrix $\tilde{\mathbf{B}}_I$ is computed using Equation 3.108.

9.2.3 Properties of αFEM-T3 and αFEM-T4

We now discuss the properties of αFEM-T3 and αFEM-T4 models. We consider linear elasticity problems with homogeneous essential boundary conditions. First, we note the following:

Property 9.1 Displacement Compatibility

The assumed displacement field is compatible (piecewise-linear and continuous throughout the domain) in the αFEM-T3 and αFEM-T4 models.

This property can be clearly seen from the αFEM-T3 and αFEM-T4 formulation procedure: linear interpolation for displacement is used in all the elements in the entire problem domain. αFEM-T3 and αFEM-T4 do not change in any way the assumed displacement field. This property (together with the spatial stability) ensures that αFEM-T3 and αFEM-T4 with any $\alpha \in [0, 1]$ will be able to reproduce exactly the linear field. This will be further confirmed numerically in the patch tests given in Section 9.4.2.

Property 9.2 Variational Consistence and Stability

αFEM-T3 (or αFEM-T4) is variationally consistent and stable.

Property 9.2 can be understood intuitively in a very simple argument: because both FEM-T3 and NS-FEM-T3 are variationally consistent, the linear (area-weighted) combination of them must also be variationally consistent. It can be rigorously proven using the modified or the single field Hellinger–Reissner principle or the orthogonal conditions; one such proof can be found in Ref. [2]. By the same argument, because both FEM-T3 and NS-FEM-T3 are spatially stable, the area-weighted linear combination of them must also be spatially stable. Because FEM-T3 is also known to be temporally stable, the temporal stability of αFEM-T3 depends on the contributions from NS-FEM-T3. In any case, αFEM-T3 should be more stable than NS-FEM-T3, as long as there is some amount of contribution from

FEM-T3 ($\alpha > 0.0$). Our recent study has shown that a very small α can make αFEM-T3 temporally stable [11]. Other stabilization techniques are also possible [12].

Property 9.3 Lower Bound Property

When $\alpha = 1.0$, αFEM-T3 and αFEM-T4 become the standard FEM. The strain energy $\hat{E}(\alpha = 1)$ is an underestimation of the exact strain energy.

Property 9.4 Upper Bound Property

When $\alpha = 0.0$, αFEM-T3 and αFEM-T4 become the NS-FEM. The strain energy $\hat{E}(\alpha = 0)$ is an overestimation of the linear FEM model and can be an overestimation of the exact strain energy for sufficiently fine models with sufficient smoothing effects.

A proof and arguments that show the same upper bound properties of LC-PIM can be found in Ref. [13]. An intuitive explanation as to why NS-FEM can always produce an upper bound solution was also presented in Ref. [10]. The numerical examples in Section 9.5 will confirm the property.

Property 9.5 Solution Continuity Property

When α changes from 0.0 to 1.0, the solutions of αFEM-T3 and αFEM-T4 are continuous functions of α from the solution of NS-FEM and that of standard FEM.

This is because both NS-FEM and standard FEM are spatially stable and can converge, and the introduction of α is via a partitions-of-unity interpolation form using these two models.

Property 9.6 Exact Solution Property

The exact solution in strain energy exactly falls in the range of the solutions of αFEM-T3 and αFEM-T4 with $\alpha \in [0, 1]$, as long as the corresponding NS-FEM model has sufficient smoothing effects. This means that the exact solution in strain energy can be obtained using αFEM-T3 and αFEM-T4 with an $\alpha_{\text{exact}} \in [0, 1]$.

This property is a natural outcome of Properties 9.3 through 9.5. Based on Property 9.6, one can now devise the following procedure to compute a nearly exact solution in strain energy, by finding an approximate $\alpha_{\text{exact}} \in [0, 1]$.

We know that such an α can depend on the problem and also on the mesh, and therefore a universally workable α will not be easy to find. This is as expected, as finding the exact solution using a finite discrete model will never be easy. Our numerical study has shown that using meshes of elements with the same aspect ratio, the strain energy curves

$\hat{E}(\alpha)$ corresponding to these meshes will intersect approximately at a common point $(\alpha_{\text{exact}}, E_{\text{exact}})$, which gives the nearly exact strain energy of the problem. Note that the solution that is the "best" in strain energy usually leads to a "very good" solution in displacement norm, because of the relation between the strain energy and displacement solution: $\hat{E}(\alpha) = 1/2\ \hat{\mathbf{d}}^T \hat{\mathbf{K}}^{\alpha\text{FEM}} \hat{\mathbf{d}}$.

In the following analysis, the meshes with the same aspect ratio are defined in two ways: regular and irregular. Regular meshes are used only for regular domains, and the ratio of the numbers of element divisions along the coordinate directions has to be kept identical, when the mesh is refined. For example, for the rectangular 2D meshes, the three meshes (16×4), (32×8), and (64×16) have the same aspect ratio of 4. Irregular meshes can be used for any domain; the meshes with the same aspect ratio are obtained by dividing, in a nested manner, each element of the initial coarse mesh into $2^2, 3^2, 4^2$, and so on equal elements for triangular elements and into $2^3, 3^3, 4^3$, and so on equal elements for tetrahedral elements. Such a refinement is available in many automatic programs creating three-node triangular and four-node tetrahedral elements, and hence it can be done without any technical difficulty. Note that we do not require the elements in a mesh to have the same aspect ratio. We require only the elements in two consequent meshes to have the same aspect ratio.

Property 9.7 αFEM: No DOF Increase

The stiffness matrix of αFEM-T3 and αFEM-T4 has the same dimension as the corresponding standard FEM using the same mesh. The unknowns of the αFEM-T3 and αFEM-T4 models are only the displacements, and the number of unknowns is the same as that of the standard FEM using the same mesh.

Property 9.8 αFEM: Volumetric Locking Free

For the nearly incompressible materials (Poisson's ratio ν approaches 0.5), the volumetric locking can be avoided by using $\alpha = 0$ or a very small $\alpha = 0.5 - \nu$ for the αFEM-T3 (or αFEM-T4) model, where ν is the Poisson's ratio, which is smaller than but very close to 0.5. Note that, for this kind of problems, we have to give up obtaining the "exact" solution and only focus on solving the volumetric locking issue, because we have only one "knob" in an αFEM model.

From the above formulation of αFEM-T3, it is clear that only the area and the usual compatible strain–displacement matrices $\breve{\mathbf{B}}_I$ of triangular elements (and the factor α) are needed to compute the system stiffness matrix. Therefore, in the actual programming, the standard FEM (Chapter 3) and NS-FEM-T3 (Chapter 6) formulae are used directly to compute the entries of the stiffness matrices with scaling by α^2 and $(1 - \alpha^2)$, respectively,

as shown in Equations 9.3 and 9.6 for αFEM-T3. The same applies to αFEM-T4, and the scaling should be α^3 and $(1-\alpha^3)$, respectively, as shown in Equations 9.8 and 9.9.

9.3 αFEM-T3 and αFEM-T4 for Nonlinear Problems

For nonlinear problems of large deformation, the values of the strain–displacement matrices and stresses at the nodes become simply the average values of those of the adjacent elements surrounding the node, and all the other techniques developed and currently used in the standard FEM such as the total Lagrange formulation [14,15] can be directly adopted. The αFEM-T3 model for nonlinear problems of large deformation based on the total Lagrange formulation can be expressed as follows:

$$\left(\hat{\mathbf{K}}_L^{\alpha\text{FEM}} + \hat{\mathbf{K}}_{\text{NL}}^{\alpha\text{FEM}}\right)\hat{\mathbf{d}} = \tilde{\mathbf{f}} - \hat{\mathbf{f}}_1, \tag{9.10}$$

where the stiffness matrix for the linearized portion can be written as

$$\hat{\mathbf{K}}_L^{\alpha\text{FEM}} = \sum_{k=1}^{N_n}(1-\alpha^2)\overline{\mathbf{B}}_L^T\mathbf{c}\overline{\mathbf{B}}_L A_k^s + \sum_{i=1}^{N_e}\alpha^2\tilde{\mathbf{B}}_L^T\mathbf{c}\tilde{\mathbf{B}}_L A_i^e, \tag{9.11}$$

in which the matrix $\overline{\mathbf{B}}_L$ relates to the node-based smoothing domains, and is computed using

$$\overline{\mathbf{B}}_L = \frac{1}{A_k^s}\sum_{j=1}^{n_k^e}\frac{1}{3}A_j^e\tilde{\mathbf{B}}_{L,j}^e, \tag{9.12}$$

and matrix $\tilde{\mathbf{B}}_L^e$ corresponding to the elements is given by

$$\tilde{\mathbf{B}}_L^e = \begin{bmatrix} F_{11}N_{1,1} & F_{21}N_{1,1} & F_{11}N_{2,1} \\ F_{12}N_{1,2} & F_{22}N_{1,2} & F_{12}N_{2,2} \\ F_{11}N_{1,2}+F_{12}N_{1,1} & F_{21}N_{1,2}+F_{22}N_{1,1} & F_{11}N_{2,2}+F_{12}N_{2,1} \end{bmatrix}$$

$$\begin{bmatrix} F_{21}N_{2,1} & F_{11}N_{3,1} & F_{21}N_{3,1} \\ F_{22}N_{2,2} & F_{12}N_{3,2} & F_{22}N_{3,2} \\ F_{21}N_{2,2}+F_{22}N_{2,1} & F_{11}N_{3,2}+F_{12}N_{3,1} & F_{21}N_{3,2}+F_{22}N_{3,1} \end{bmatrix}, \tag{9.13}$$

in which $N_{I,j} = \partial N_I / \partial X_j$ and F_{IJ} are entries of the deformation gradient tensor of the elements $\tilde{\mathbf{F}}^e$ that is computed by

$$\tilde{\mathbf{F}}^e = \begin{bmatrix} F_{11} & F_{12} \\ F_{21} & F_{22} \end{bmatrix} = \left(\frac{\partial \mathbf{x}}{\partial \mathbf{X}} \right)^T = (\mathbf{L}_d \hat{\mathbf{d}} + \mathbf{I})^T. \tag{9.14}$$

The stiffness matrix for the nonlinear portion in Equation 9.10 can be written as

$$\hat{\mathbf{K}}_{\mathrm{NL}}^{\alpha\mathrm{FEM}} = \sum_{k=1}^{N_n} (1-\alpha^2) \overline{\mathbf{B}}_{\mathrm{NL}}^T \overline{\mathbf{S}\mathbf{B}}_{\mathrm{NL}} A_k^s + \sum_{i=1}^{N_e} \alpha^2 \left(\tilde{\mathbf{B}}_{\mathrm{NL}}^e \right)^T \tilde{\mathbf{S}}_i^e \tilde{\mathbf{B}}_{\mathrm{NL}}^e A_i^e, \tag{9.15}$$

where matrix $\overline{\mathbf{B}}_{\mathrm{NL}}$ is for the node-based smoothing domain and is computed using

$$\overline{\mathbf{B}}_{\mathrm{NL}} = \frac{1}{A_k^s} \sum_{j=1}^{n_k^e} \frac{1}{3} A_j^e \tilde{\mathbf{B}}_{\mathrm{NL},j}^e, \tag{9.16}$$

with matrix $\tilde{\mathbf{B}}_{\mathrm{NL}}^e$ associated with the elements given by

$$\tilde{\mathbf{B}}_{\mathrm{NL}}^e = \begin{bmatrix} N_{1,1} & 0 & N_{2,1} & 0 & N_{3,1} & 0 \\ N_{1,2} & 0 & N_{2,2} & 0 & N_{3,2} & 0 \\ 0 & N_{1,1} & 0 & N_{2,1} & 0 & N_{3,1} \\ 0 & N_{1,2} & 0 & N_{2,2} & 0 & N_{3,2} \end{bmatrix}, \tag{9.17}$$

and matrix $\overline{\mathbf{S}}$ is for the node-based smoothing domains, and is computed using

$$\overline{\mathbf{S}} = \frac{1}{A_k^s} \sum_{j=1}^{n_k^e} \frac{1}{3} A_j^e \tilde{\mathbf{S}}_j^e \quad \text{with} \quad \tilde{\mathbf{S}}^e = \begin{bmatrix} S_{11} & S_{12} & 0 & 0 \\ S_{12} & S_{22} & 0 & 0 \\ 0 & 0 & S_{11} & S_{12} \\ 0 & 0 & S_{12} & S_{22} \end{bmatrix}. \tag{9.18}$$

In the foregoing equation, the entries S_{IJ} of matrix $\tilde{\mathbf{S}}^e$ are derived from the second Piola–Kirchhoff stress tensor $\tilde{\boldsymbol{\Psi}}^e$ for the elements by

$$\tilde{\boldsymbol{\Psi}}^e = \begin{bmatrix} S_{11} \\ S_{22} \\ S_{12} \end{bmatrix} = \mathbf{c} \begin{bmatrix} E_{11} \\ E_{22} \\ 2E_{12} \end{bmatrix}. \tag{9.19}$$

The entries E_{IJ} in Equation 9.19 are derived from the entries of the Green–Lagrange strain tensor $\tilde{\mathbf{E}}^e$ for the elements as

$$\tilde{\mathbf{E}}^e = \begin{bmatrix} E_{11} & E_{12} \\ E_{21} & E_{22} \end{bmatrix} = \frac{1}{2}\left(\left(\tilde{\mathbf{F}}^e\right)^T \tilde{\mathbf{F}}^e - \mathbf{I}\right), \tag{9.20}$$

where $\mathbf{I}$ is the second-order identity matrix.

The "additional" force term caused by the nonlinearity in Equation 9.10 becomes

$$\hat{\mathbf{f}}_1 = \sum_{k=1}^{N_n} (1-\alpha^2)\overline{\mathbf{B}}_L^T \overline{\boldsymbol{\Psi}} A_k^s + \sum_{i=1}^{N_e} \alpha^2 \left(\tilde{\mathbf{B}}_L^e\right)^T \tilde{\boldsymbol{\Psi}}_i^e A_i^e, \tag{9.21}$$

with

$$\overline{\boldsymbol{\Psi}} = \frac{1}{A_k^s} \sum_{j=1}^{n_k^e} \frac{1}{3} A_j^e \tilde{\boldsymbol{\Psi}}_j^e. \tag{9.22}$$

The formulation presented above can be easily extended to αFEM-T4 for 3D problems using tetrahedral elements. Numerical examples of large deformation nonlinear problems will be presented in Section 9.5.

9.4 Implementation and Patch Tests

9.4.1 Exact Solution for Linear Elastic Problems

A numerical procedure for computing a nearly exact solution for a linear elastic problem using αFEM-T3 (or αFEM-T4) can be summarized as follows:

1. Discretize the domain Ω into two sets of coarse mesh of triangular elements (or tetrahedral elements for 3D problems) with the same aspect ratio
2. Choose one array of $\alpha \in \overline{0:1}$, for example $\alpha = [0.0 \quad 0.2 \quad \cdots \quad 0.8 \quad 1.0]^T$
3. Loop over two sets of mesh created in step 1
4. Loop over the array of $\alpha \in \overline{0:1}$
5. Loop over all the elements using the standard FEM:
   - Compute and save the strain–displacement matrix $\tilde{\mathbf{B}}$ for the elements

- Evaluate the stiffness matrix and force vector for the elements
- Multiply the stiffness matrix of the element with α^2 for triangular elements by Equation 9.3 (or with α^3 for tetrahedral elements by Equation 9.9) and then assemble into the global stiffness matrix
- Assemble the force vector into the global force vector

6. End the loop over all the elements
7. Loop over all the nodes using the NS-FEM:
   - Use strain–displacement matrices $\tilde{\mathbf{B}}$ of the element saved in step 5 to compute the smoothed strain–displacement matrix $\overline{\mathbf{B}}$ of the node by Equation 6.3 for triangular elements or by Equation 6.5 for tetrahedral elements
   - Evaluate the stiffness matrix of the node by Equation 6.2
   - Multiply the stiffness matrix of the node with $(1-\alpha^2)$ for triangular elements by Equation 9.6 (or $(1-\alpha^3)$ for tetrahedral elements by Equation 9.8) and then assemble into the global stiffness matrix
8. End the loop over all the nodes
9. Implement essential boundary conditions
10. Solve the system of equations for the nodal displacements
11. Evaluate strain, stress, and save the global strain energy
12. End the loop over the array containing $\alpha \in \overline{0:1}$
13. End the loop over two sets of coarse meshes
14. Interpolate the exact strain energy at α_{exact} from two arrays containing the strain energies saved at step 11
15. Use α_{exact} and a finer mesh with the same aspect ratio as the two coarse meshes to compute the final solution through steps 5–11.

As seen from the above-mentioned procedure, obtaining α_{exact} requires additional effort, and hence we may want to avoid it. Based on the theory presented, we know that in any case, the accuracy (in the strain energy or displacement norm) of a combined model is always better than either FEM or NS-FEM for any $\alpha \in (0,\ 1)$. This guarantees that we can get a better solution only using any $\alpha \in (0,\ 1)$. Therefore, if we only need to improve the accuracy of the solution, we may simply use directly an $\alpha \in \overline{0.45:0.65}$ in 2D problems and $\alpha \in \overline{0.60:0.80}$ in 3D problems for any meshes without searching for the α_{exact}. This range of α is found preferable by numerical "experiments" on different linear problems using αFEM-T3 and αFEM-T4. By this method, the α chosen will not be optimal and the solution may not

be very close to the exact one, but the accuracy of the solution is often much better than the FEM using the same mesh.

For nonlinear problems of large deformation, it is generally difficult to obtain the "exact" solution for all loading stages. Our aim is thus to improve the accuracy of the solution. Similarly to linear problems, we recommend using an $\alpha \in \overline{0.45 : 0.65}$ (in 2D problems) and $\alpha \in \overline{0.60 : 0.80}$ (in 3D problems) for nonlinear analyses. The tested examples have so far shown that for such an α, the accuracy of the solution is often much better than the FEM. Alternatively, we can also use the optimal value α found from a linearized problem using the procedures given in Section 9.4.1 and apply it for all the loading stages of the large deformation problem. The α chosen in this manner is not optimal for the nonlinear problem and we will not obtain a nearly exact solution, but it is still much better than the standard FEM solution using the same mesh.

9.4.2 Standard Patch Tests

9.4.2.1 Standard Patch Test for 2D Problems

An irregular domain discretization of a square patch using 58 three-node triangular elements is shown in Figure 9.3. The displacement norm (Equation 4.63) is used to examine the results computed. The parameters are taken as $E = 100$, $\nu = 0.3$ and the linear displacement field is given by Equation 5.11.

It is found that αFEM-T3 can pass the standard patch test within machine precision regardless of the value of $\alpha \in [0, 1]$ used, as shown in Table 9.1.

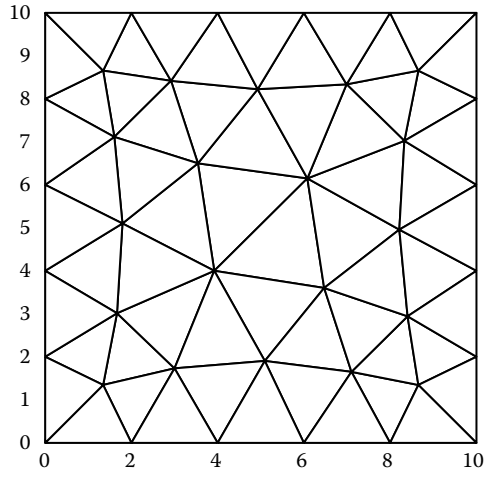

FIGURE 9.3 Domain discretization of a square patch using three-node triangular elements.

TABLE 9.1

Error in Displacement Norm e_d (%) for the Standard 2D Patch Test

$\alpha = 0.0$ (NS-FEM-T3)	$\alpha = 0.2$	$\alpha = 0.4105$[a]	$\alpha = 0.6038$[a]	$\alpha = 0.8$	$\alpha = 1.0$ (FEM-T3)
0.2757e-12	1.6029e-12	1.4327e-12	2.1737e-12	0.7946e-12	1.6499e-12

[a] Arbitrarily generated number.

This example confirms Property 1 for 2D problems: αFEM-T3 is displacement compatible, linearly conforming (capable of producing exactly any linear displacement field for any $\alpha \in [0, 1]$). Therefore, αFEM-T3 is at least of second-order accuracy in displacement solution. Together with the proven stability, αFEM-T3 will always converge to any exact solution that can be approximated via a piecewise linear interpolation, and the convergence rate will be at least 2 for the displacement solution.

9.4.2.2 The Irons First-Order Patch Test for 3D Problems

The Irons first-order patch test as presented in Section 6.5.4 is again used here, but in this case for testing αFEM-T4. The displacement norm (Equation 4.63) is used to quantitatively examine the computed results, and the energy error is defined by

$$e_e(\alpha) = \left| \hat{E}(\alpha) - E_{\text{exact}} \right|, \tag{9.23}$$

where the total strain energy of the αFEM-T4 solution $\hat{E}(\alpha)$ is computed using

$$\begin{aligned} \hat{E}(\alpha) &= \tilde{E}^{\text{FEM}}(\alpha) + \overline{E}^{\text{NS-FEM}}(\alpha) \\ &= \frac{1}{2} \sum_{i=1}^{N_e} \left(\tilde{\boldsymbol{\varepsilon}}_i\right)^T \mathbf{c} \tilde{\boldsymbol{\varepsilon}}_i \alpha^3 V_i^e + \frac{1}{2} \sum_{k=1}^{N_n} \left(\overline{\boldsymbol{\varepsilon}}_k\right)^T \mathbf{c} \overline{\boldsymbol{\varepsilon}}_k (1 - \alpha^3) V_k^s, \end{aligned} \tag{9.24}$$

where N_e is the total number of elements used in the problem domain, N_n is the total number of nodes of the model, $\tilde{\boldsymbol{\varepsilon}}_i$ is the strain of the numerical solution of the ith element, and $\overline{\boldsymbol{\varepsilon}}_k$ is the smoothed strain of the numerical solution for the kth node.

It is found that αFEM-T4 can pass the standard first-order patch test within machine precision regardless of the value of $\alpha \in [0, 1]$, as shown in Tables 9.2 and 9.3. There is no accuracy loss due to the different choices of α values. This example confirms Property 1 for 3D problems.

TABLE 9.2

Error in Displacement Norm e_d (%) for Irons First-Order 3D Patch Test

α = 0.0 (NS-FEM-T4, Tetrahedral Element)	**α = 0.2**	**α = 0.4083[a]**	**α = 0.6149[a]**	**α = 0.8**	**α = 1.0 (FEM-T4)**
0.08e-12	0.23e-12	0.82e-12	1.46e-12	13.06e-12	0.06e-12

[a] Arbitrarily generated number.

TABLE 9.3

Strain Energy Error e_e for the Irons First-Order 3D Patch Test

α = 0.0 (NS-FEM-T4, Tetrahedral Element)	**α = 0.2**	**α = 0.4083[a]**	**α = 0.6149[a]**	**α = 0.8**	**(FEM-T4)**
2.55e-11	2.55e-11	2.55e-11	2.55e-11	2.55e-11	2.55e-11

[a] Arbitrarily generated number.

Property 9.9 FEM: First-Order Consistency

αFEM-T4 has first-order consistency, meaning that it can produce a linear displacement field exactly. In other words, they are of second-order accuracy in displacement solution: errors are at the terms of second order or above.

Property 9.10 αFEM-T4 Solution: Stability and Convergence

Owing to the stability given in Property 9.2 and the first-order consistence given in Property 9.9, αFEM-T4 has a unique stable solution that converges to the exact solution of the original solid mechanics problem defined in Chapter 2. This confirms Theorem 4.1.

9.5 Numerical Examples

The errors in both displacement norm and energy norm defined in Equations 4.49 and 4.50 are used in this analysis for the examination of numerical models. When the energy norm is used, we use the recovery strain solution for the S-FEM and αFEM models, and both raw and recovery strain solutions for FEM models. Note that the strains at nodes $\hat{\boldsymbol{\varepsilon}}(\mathbf{x}_j)$ for αFEM-T3 and αFEM-T4 are computed in the same way as those of NS-FEM-T3 and NS-FEM-T4, respectively.

Example 9.5.1: Cantilever Beam Subjected to a Tip Load: A Convergence Study

The cantilever loaded at the end, which was described in Example 5.8.1, is tested again but using the αFEM-T3, in comparison with a number of other methods. The geometry and boundary conditions of the cantilever are plotted in Figure 5.6. The mesh of quadrilateral and triangular elements is shown in Figures 5.7a and 6.6, respectively. The exact strain energy of the problem is known as 4.4746 Nm.

Following the procedures given in Section 9.4.1, we found that $\alpha_{\text{exact}} = 0.6$ at the intersection of two strain energy curves using two meshes with the same aspect ratio (32×8 and 40×10), as shown in Figure 9.4.

Table 6.6 and Figure 9.5 compare the solution errors in displacement norm obtained using αFEM-T3 (at $\alpha_{\text{exact}} = 0.6$), together with other methods. It is seen that αFEM-T3 stands out clearly. When the mesh with $h = 1.2$ m is used, the error of αFEM-T3 is about 1/125 of FEM-T3, 1/18 of FEM-Q4, and 2/9 of CS-FEM-Q4. In terms of convergence rate, the rate of αFEM-T3 stands out clearly with $r = 4.2$, which is much larger than the theoretical value of 2.0: a very strong superconvergence in displacement norm.

Table 6.7 and Figure 9.6 compare the solution errors in energy norm obtained using αFEM-T3 (at $\alpha_{\text{exact}} = 0.6$) with other methods. It is seen that the results of αFEM-T3 are much more accurate than FEM-T3, FEM-T3-Re, and FEM-Q4, and are slightly more accurate than those of the "star" performer ES-FEM-T3. It is, however, less accurate than NS-FEM-T3, FEM-Q4-Re, and CS-FEM-Q4. When the mesh with $h = 1.2$ m is used, the error in energy norm of αFEM-T3 is about 1/5.4 of FEM-T3, 1/2 of FEM-Q4, and 1/2 of FEM-T3-Re, but 1.3 times FEM-Q4-Re and the best performer NS-FEM-T3. In terms of convergence rate,

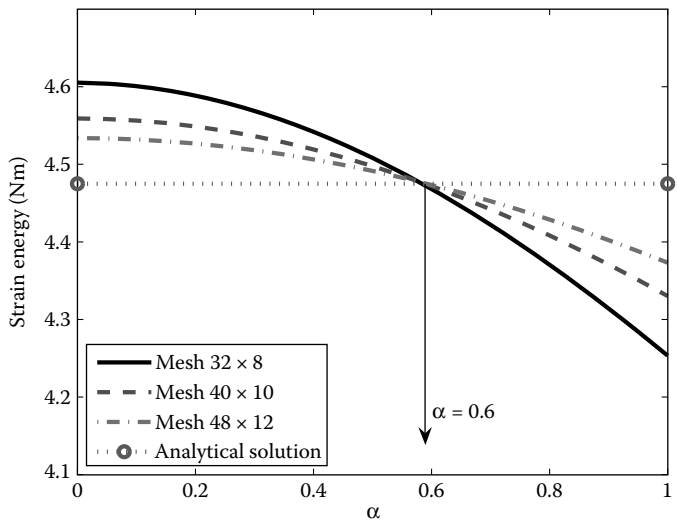

FIGURE 9.4 The strain energy curves of three meshes with the same aspect ratios intersect at $\alpha_{\text{exact}} = 0.6$ for the cantilever loaded at the end.

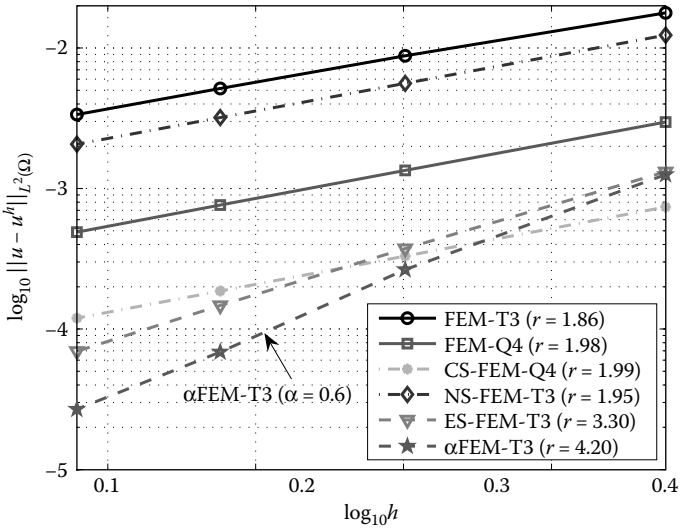

FIGURE 9.5 Error in displacement norm of αFEM-T3 ($\alpha_{exact} = 0.6$) in comparison with other methods for the cantilever loaded at the end using the same set of nodes.

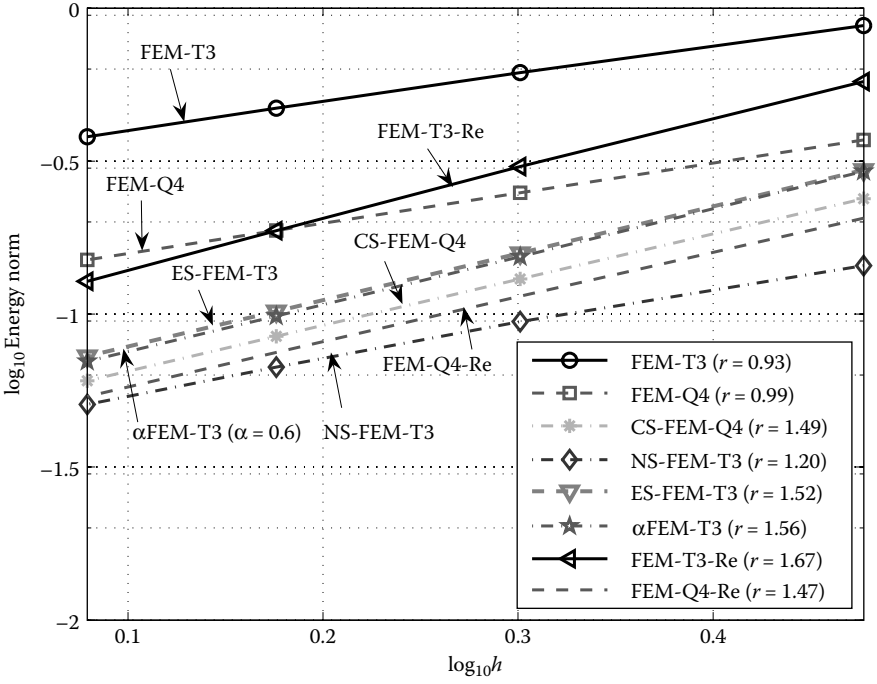

FIGURE 9.6 Error in energy norm of αFEM-T3 ($\alpha_{exact} = 0.6$) in comparison with other methods for the cantilever loaded at the end using the same set of nodes.

the rate of the αFEM-T3 also stands out clearly with $r = 1.56$, which is much larger than the theoretical value of 1.0: a very strong superconvergence also in energy norm. This example clearly shows the outstanding performance of α FEM using the triangular element mesh.

Example 9.5.2: Cook's Membrane: Test for Membrane Elements

The Cook's membrane problem [16] is also a widely used benchmark problem for numerical methods. It is a clamped tapered panel subjected to an in-plane shearing load resulting in deformation dominated by a bending response, as shown in Figure 9.7. The material parameters used are Young's modulus $E = 1$

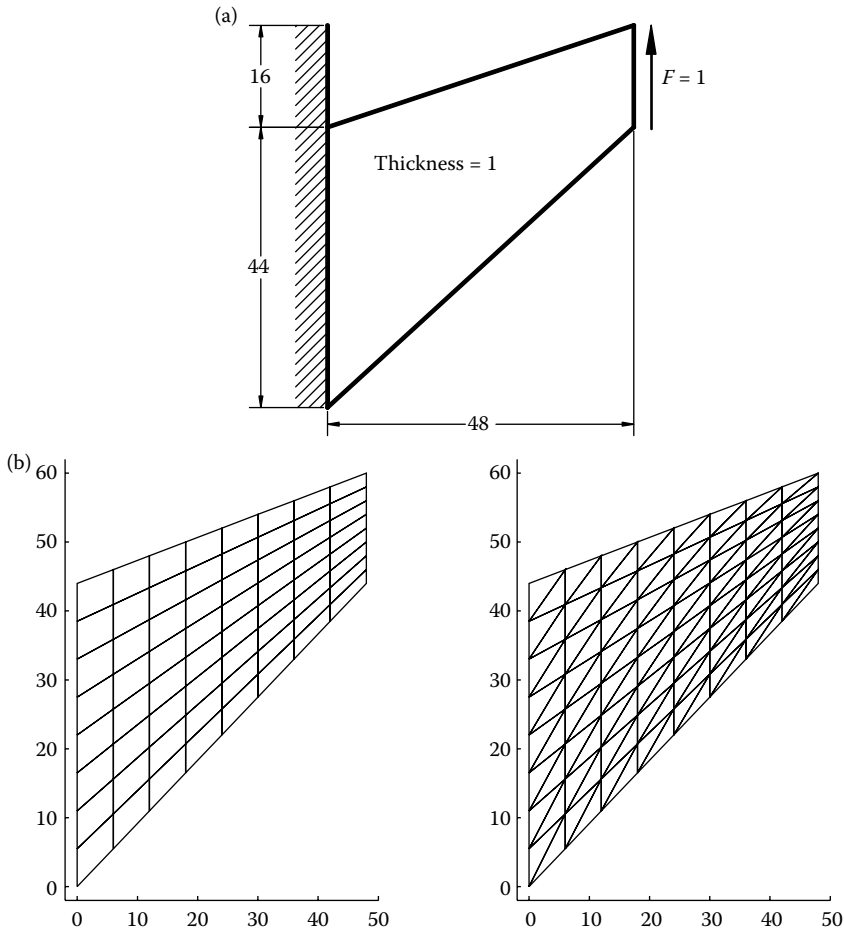

FIGURE 9.7 (a) Cook's membrane problem and (b) its discretization using four-node quadrilateral and three-node triangular elements.

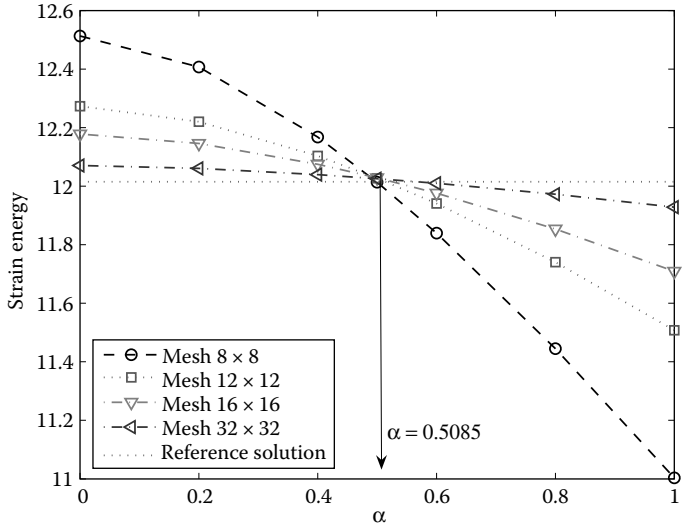

FIGURE 9.8 The strain energy curves of four meshes with the same aspect ratios intersect at $\alpha_{\text{exact}} = 0.5085$ for Cook's membrane problem.

and Poisson's ratio $\nu = 1/3$. Two discretizations of Cook's membrane problem using four-node quadrilateral and three-node triangular elements are also shown in Figure 9.7. The exact solution of the problem is unknown. Under the plane stress condition, the reference value of the vertical displacement at the tip center is found to be 23.9642 [17] and the reference value of the strain energy is 12.015 [16].

Using αFEM-T3 and following the procedures given in Section 9.4.1, we found that $\alpha_{\text{exact}} = 0.5085$ at the intersection of strain energy curves using meshes with the same aspect ratio as plotted in Figure 9.8. Table 9.4 and Figure 9.9 compare the result of the displacement at the tip center obtained

TABLE 9.4

Results of Tip Displacement Obtained from Different Methods for Cook's Problem

Mesh	**4 × 4**	**8 × 8**	**16 × 16**	**32 × 32**
FEM-Q4	18.3086	22.0710	23.4370	23.8204
Qm6 [18]	23.0056	23.7006	23.8923	23.9402
FB [19]	22.0950	23.4370	23.8204	23.9163
QBI [20]	20.4654	22.9098	23.6766	23.8923
KF [21]	19.8903	22.6941	23.6047	23.8683
Qnew [17]	23.0775	23.7006	23.8923	23.9402
αFEM-T3 ($\alpha_{\text{exact}} = 0.5085$)	23.7006	24.0322	24.0053	23.9777
Reference value	23.9642	23.9642	23.9642	23.9642

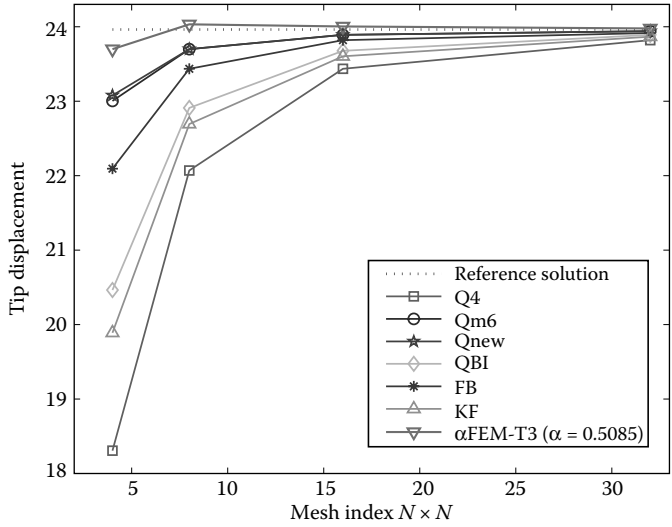

FIGURE 9.9 Convergence of tip displacement of αFEM-T3 ($\alpha = 0.5085$) in comparison with other methods for Cook's membrane using the same set of nodes.

using αFEM-T3, with six published four-node quadrilateral elements: FEM-Q4, Qm6-modified Wilson element [18], FB-one Gauss point with hourglass stabilization [19], QBI-quintessential bending/incompressible element [20], KF-one Gauss point with hourglass control [21], and Qnew—an improved stabilization technique for the one-point quadrature integration method [17]. It can be seen that the αFEM-T3 with $\alpha_{\text{exact}} = 0.5085$ clearly outperforms all these methods.

In addition to the results shown in Figure 9.9, we make a more detailed comparison of αFEM-T3 with other elements for coarse meshes, and the results in numbers are listed in Table 9.5. It is again found that αFEM-T3 at $\alpha_{\text{exact}} = 0.5085$ gives excellent performance compared to all the other methods.

Example 9.5.3: Semi-Infinite Plane: A Convergence Study

The semi-infinite plane subjected to a uniform pressure within a finite range ($-a \le x \le a$) shown in Figure 9.10 is studied. The plane strain condition is considered. The analytical stresses are given by [22]

$$\begin{aligned}
\sigma_{11} &= \frac{p}{2\pi}\left[2(\theta_1 - \theta_2) - \sin 2\theta_1 + \sin 2\theta_2\right], \\
\sigma_{22} &= \frac{p}{2\pi}\left[2(\theta_1 - \theta_2) + \sin 2\theta_1 - \sin 2\theta_2\right], \\
\tau_{12} &= \frac{p}{2\pi}\left[\cos 2\theta_1 - \cos 2\theta_2\right].
\end{aligned} \tag{9.25}$$

TABLE 9.5

Results of Tip Displacement and Strain Energy Obtained from Different Methods for Cook's Problem

	Tip Displacement			Strain Energy		
	2 × 2	**4 × 4**	**8 × 8**	**2 × 2**	**4 × 4**	**8 × 8**
AT	19.67 (27)[a]	22.41 (75)	23.45 (243)	9.84	11.22	11.75
P-S	21.13 (18)	23.02 (50)	23.69 (162)	10.50	11.51	11.85
CH(0–1)	23.01 (18)	23.48 (50)	23.81 (162)	11.47	11.75	11.91
ECQ4/LQ6	23.05 (18)	23.48 (50)	23.81 (162)	11.48	11.75	11.91
HMQ/HQ4	21.35 (18)	23.04 (50)	23.69 (162)	10.61	11.52	11.85
FEMIXHB	22.81 (35)	23.52 (135)	23.92 (527)	11.27	11.79	11.97
AGQ6-I	23.07	23.68	23.87	—	—	—
AGQ6-II	25.92	24.37	24.04	—	—	—
QACM4	20.74	22.99	23.69	—	—	—
QACII6	25.92	24.37	24.04	—	—	—
αFEM-T3 ($\alpha_{exact} = 0.5085$)	—	23.56 (50)	23.99 (162)	—	11.77	12.00
Reference value	23.9642	23.9642	23.9642	12.015	12.015	12.015

[a] Number of DOFs denoted in parentheses.

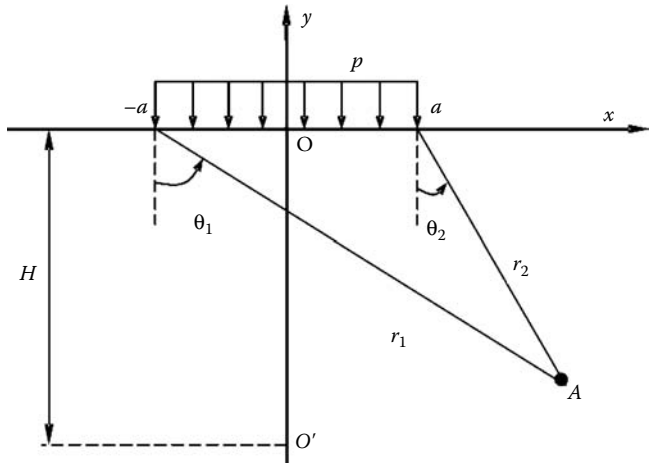

FIGURE 9.10 Semi-infinite plane subjected to a uniform pressure.

The directions of θ_1 and θ_2 are indicated in Figure 9.10. The corresponding displacements can be expressed as

$$u_1 = \frac{p(1-\nu^2)}{\pi E}\left[\frac{1-2\nu}{1-\nu}\left[(x+a)\theta_1 - (x-a)\theta_2\right] + 2y\ln\frac{r_1}{r_2}\right],$$

$$u_2 = \frac{p(1-\nu^2)}{\pi E}\left[\frac{1-2\nu}{1-\nu}\left[y(\theta_1-\theta_2)+2H\arctan\frac{1}{c}\right]+2(x-a)\ln r_2\right.$$
$$\left.-2(x+a)\ln r_1+4a\ln a+2a\ln(1+c^2)\right], \tag{9.26}$$

where $H = ca$ is the distance from the origin to point O', and c is a given coefficient.

Due to the symmetry about the y-axis, the problem is modeled with a $5a \times 5a$ square with $a = 0.2$ m, The parameters used in the problem are Young's modulus $E = 10^5$ N/m^2, Poisson's ratio $\nu = 0.3$, $c = 100$, and $p = 1 \times 10^4$ N/m^2. The symmetry boundary condition is imposed on the left side, and the bottom side is constrained using the exact displacements given by Equation 9.26, The right side is subjected to tractions computed from Equation 9.25. Figure 9.11 gives the discretization of the domain using four-node quadrilateral and triangular elements, respectively. The exact strain energy of the problem is known as 45.585 Nm.

Following the procedures given in Section 9.4.1, we found that $\alpha_{\text{exact}} = 0.48$ at the intersection of strain energy curves using meshes with the same aspect ratio as shown in Figure 9.12.

Table 9.6 and Figure 9.13 show the convergence of strain energy of αFEM-T3 (at $\alpha_{\text{exact}} = 0.48$) in comparison with different methods. It is seen that the results of αFEM-T3 are almost identical with the analytical solution, even with the coarse meshes. From Figures 9.14 and 9.15, it is observed that all the computed displacements and stresses using αFEM-T3 (at $\alpha_{\text{exact}} = 0.48$) agree well with the analytical solutions.

Table 9.7 and Figure 9.16 compare the solution error in displacement norm obtained using the αFEM-T3 (at $\alpha_{\text{exact}} = 0.48$) with other methods. In terms

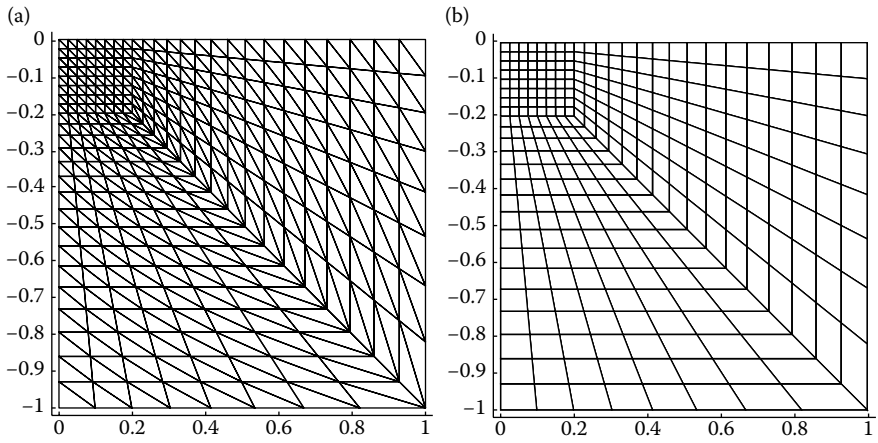

FIGURE 9.11 Domain discretization of the semi-infinite plane using: (a) three-node triangular elements and (b) four-node quadrilateral elements.

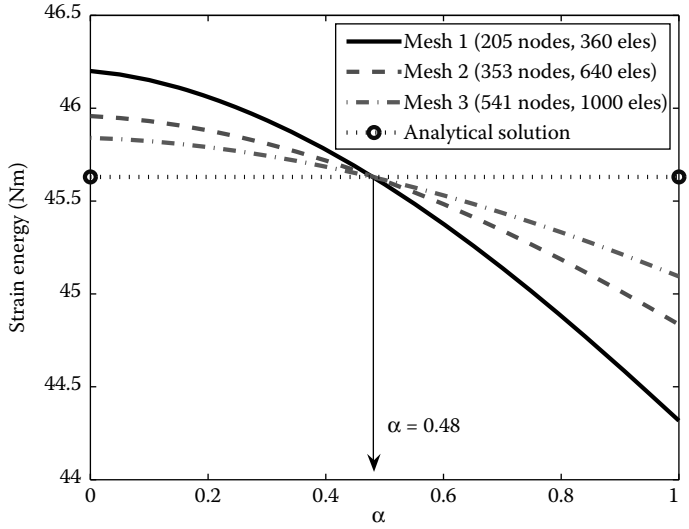

FIGURE 9.12 The strain energy curves of three meshes with the same aspect ratios intersect at $\alpha_{exact} = 0.48$ for the semi-infinite plane subjected to a uniform pressure.

of accuracy, the αFEM-T3 and the start performer ES-FEM-T3 stand out clearly. When the finest mesh ($h = 0.0373$ m) is used, the error of the αFEM-T3 is about 1/3.6 of FEM-T3 and 1/1.4 of FEM-Q4. In terms of convergence rate, the rate of αFEM-T3 is also larger than that of FEM-T3.

Table 9.8 and Figure 9.17 give the solution error in energy norm obtained using the αFEM-T3 (at $\alpha_{exact} = 0.48$), together with those obtained using other methods. In terms of accuracy, the results of αFEM-T3 stand out clearly together with NS-FEM-T3. When the finest mesh ($h = 0.0373$ m) is used, the error of αFEM-T3 is about 1/3.8 of FEM-T3, 1/2.3 of FEM-Q4, 1/1.6 of FEM-T3-Re, and

TABLE 9.6

Strain Energy (Nm) Obtained Using Different Methods for the Semi-Infinite Plane Subjected to a Uniform Pressure Using the Same Distribution of Nodes

	Mesh 1	**Mesh 2**	**Mesh 3**	**Mesh 4**	**Mesh 5**	**Analytical Solution**
DOFs	194	410	706	1082	1538	
FEM-T3	43.0502	44.3177	44.8352	45.0938	45.2411	45.5850
FEM-Q4	44.6815	45.1768	45.3586	45.4452	45.4932	45.5850
CS-FEM-Q4	44.8423	45.2543	45.4043	45.4753	45.5146	45.5850
NS-FEM-T3	46.8508	46.2003	45.9577	45.8401	45.7739	45.5850
ES-FEM-T3	45.1151	45.4122	45.5056	45.5458	45.5665	45.5850
αFEM-T3 ($\alpha_{exact} = 0.48$)	45.5744	45.6290	45.6322	45.6291	45.6258	45.5850

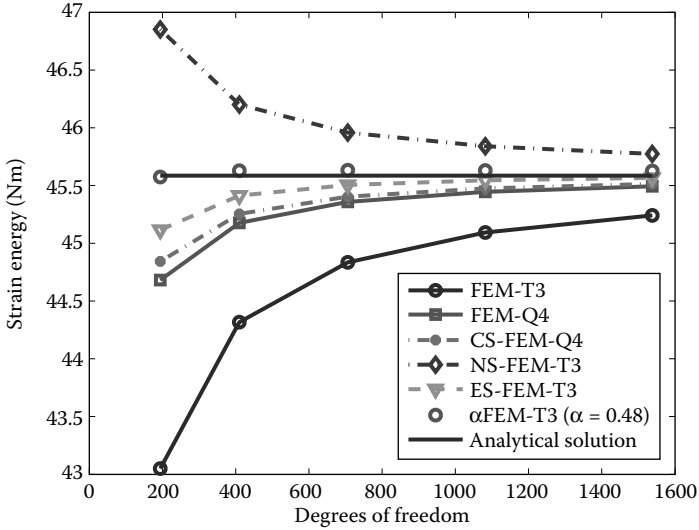

FIGURE 9.13 Convergence of strain energy of αFEM-T3 ($\alpha_{exact} = 0.48$) in comparison with other methods for the semi-infinite plane subjected to a uniform pressure.

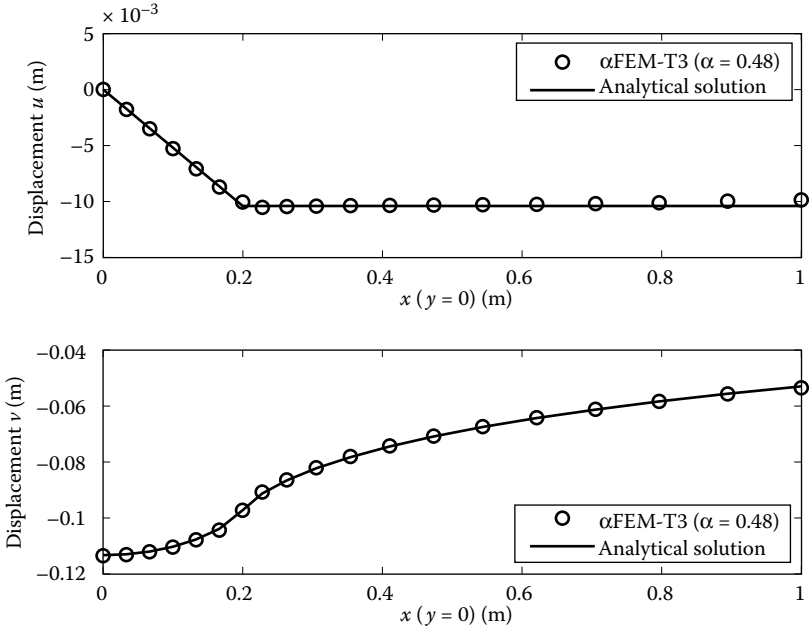

FIGURE 9.14 Computed and exact displacements of the semi-infinite plane subjected to a uniform pressure using the αFEM-T3 ($\alpha_{exact} = 0.48$).

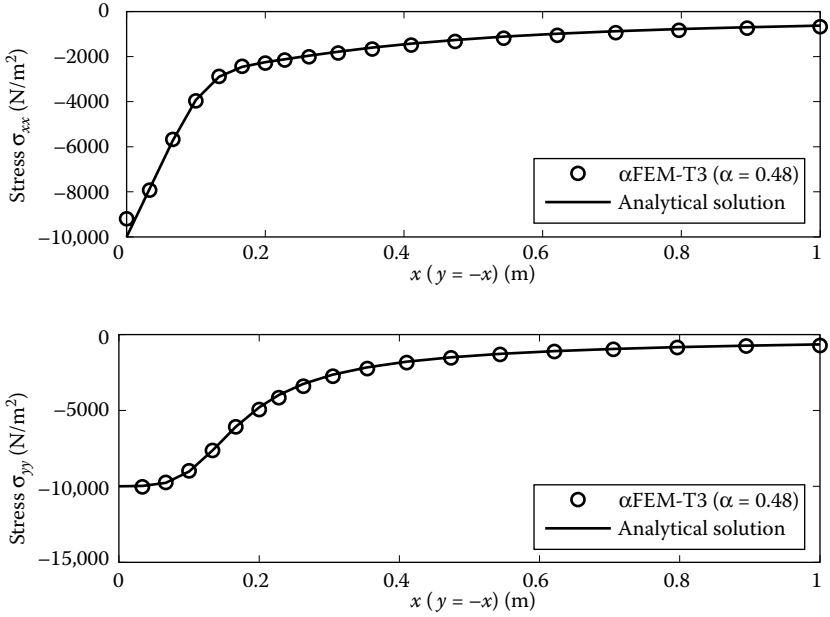

FIGURE 9.15 Computed and exact stresses of the semi-infinite plane subjected to a uniform pressure using the αFEM-T3 ($\alpha_{\text{exact}} = 0.48$).

even 1/12 of FEM-Q4-Re. In terms of convergence rate, the superconvergence is observed for αFEM-T3 with a rate of 1.21 that is much larger than the theoretical value of 1.0.

Next, we test αFEM-T3 for volumetric locking by varying the Poisson's ratio from 0.4 to 0.4999999. As presented in Property 9.8, it is recommended to use $\alpha = 0$ or a very small $\alpha = 0.5 - \nu$. Table 9.9 and Figure 9.18 show the displacement norm versus different Poisson's ratios for αFEM-T3, FEM-T3, and

TABLE 9.7

Error in Displacement Norm Obtained Using Different Methods for the Semi-Infinite Plane Subjected to a Uniform Pressure Using the Same Set of Nodes

	Mesh 1	**Mesh 2**	**Mesh 3**	**Mesh 4**	**Mesh 5**
h (m)	0.1118	0.0745	0.0559	0.0447	0.0373
FEM-T3	7.94e-04	4.07e-04	2.46e-04	1.64e-04	1.17e-04
FEM-Q4	3.77e-04	1.76e-04	1.01e-04	6.56e-05	4.60e-05
CS-FEM-Q4	3.53e-04	1.63e-04	9.36e-05	6.06e-05	4.24e-05
NS-FEM-T3	4.92e-04	2.19e-04	1.24e-04	7.95e-05	5.54e-05
ES-FEM-T3	2.84e-04	1.25e-04	6.95e-05	4.40e-05	3.03e-05
αFEM-T3 ($\alpha_{\text{exact}} = 0.48$)	2.53e-04	1.20e-04	7.00e-05	4.57e-05	3.21e-05

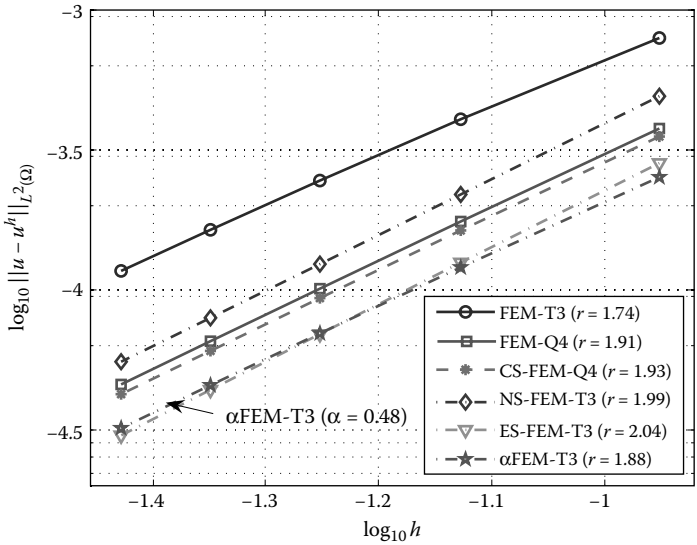

FIGURE 9.16 Error in displacement norm of αFEM-T3 ($\alpha_{\text{exact}} = 0.48$) in comparison with other methods for the semi-infinite plane subjected to a uniform pressure using the same set of nodes.

FEM-Q4 (the mesh with 353 nodes and $h = 0.0559$ m is used). The results show that the αFEM-T3 can avoid the volumetric locking, while FEM-T3 and FEM-Q4 clearly suffered from volumetric locking. The results of αFEM-T3 using $\alpha = 0.5 - \nu$ are a little better than those obtained by simply using $\alpha = 0$, and hence $\alpha = 0.5 - \nu$ is recommended. Note also that using $\alpha = 0.5 - \nu$ can also help to stabilize the solution for dynamic problems.

TABLE 9.8

Error in Energy Norm Obtained Using Different Methods for the Semi-Infinite Plane Subjected to a Uniform Pressure Using the Same Set of Nodes

	Mesh 1	**Mesh 2**	**Mesh 3**	**Mesh 4**	**Mesh 5**
h (m)	0.1118	0.0745	0.0559	0.0447	0.0373
FEM-T3	1.3498	0.9540	0.7372	0.6012	0.5081
FEM-Q4	0.8772	0.5946	0.4515	0.3648	0.3066
CS-FEM-Q4	0.6138	0.3631	0.2529	0.1924	0.1547
NS-FEM-T3	0.4284	0.2627	0.1883	0.1466	0.1200
ES-FEM-T3	0.5976	0.3585	0.2527	0.1941	0.1572
FEM-T3-Re	0.9009	0.5326	0.3662	0.2755	0.2196
FEM-Q4-Re	0.6337	0.3744	0.2604	0.1982	0.1596
αFEM-T3 ($\alpha_{\text{exact}} = 0.48$)	0.5052	0.3035	0.2143	0.1649	0.1338

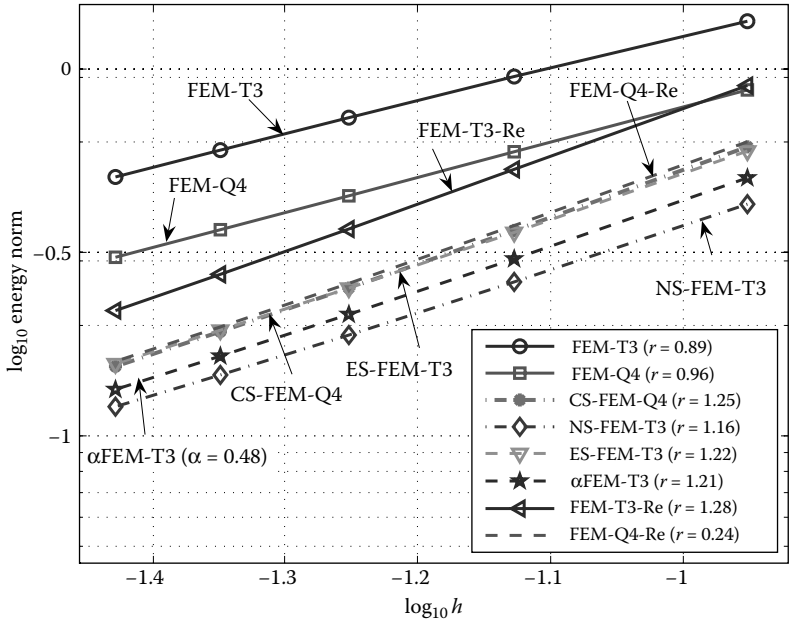

FIGURE 9.17 Error in energy norm of αFEM-T3 ($\alpha_{exact} = 0.48$) in comparison with other methods for the semi-infinite plane subjected to a uniform pressure using the same set of nodes.

Example 9.5.4: Cantilever Beam Subjected to a Tip Load: A Large Deformation

The use of αFEM-T3 for large deformation analysis of a cantilever beam subjected to a concentrated tip load is now examined. The size of the beam is

TABLE 9.9

Error in Displacement Norm versus Different Poisson's Ratios for the Semi-Infinite Plane Subjected to a Uniform Pressure ($\times 10^{-4}$)

Mesh	Poisson's Ratios	αFEM-T3 $\alpha = 0$	αFEM-T3 $\alpha = 0.5 - \nu$	FEM-T3	FEM-Q4
12 × 12	$\nu = 0.4$	1.24		3.34	1.12
12 × 12	$\nu = 0.49$	1.25	1.21	14.28	4.43
12 × 12	$\nu = 0.499$	1.29	1.28	33.09	19.62
12 × 12	$\nu = 0.4999$	1.30	1.29	42.44	41.86
12 × 12	$\nu = 0.49999$	1.30	1.30	45.78	54.65
12 × 12	$\nu = 0.499999$	1.30	1.30	47.18	62.10
12 × 12	$\nu = 0.4999999$	1.30	1.30	47.42	64.10

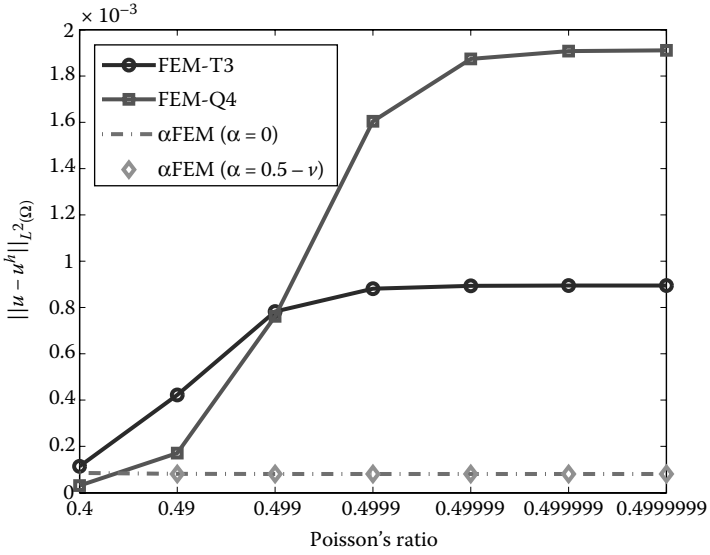

FIGURE 9.18 Error in displacement norm versus different Poisson's ratios of the material for the semi-infinite plane subjected to a uniform pressure (the mesh with 353 nodes and $h = 0.0559$ is used).

(10 cm × 2 cm) and is initially discretized using a mesh of 20 × 4. The related parameters are taken as $E = 3.0 \times 10^7$ N/cm^2 and $\nu = 0.3$. The analysis based on the total Lagrange formulation under the plane strain condition is carried out using 20 increment steps ($n = 20$) with $\Delta F = 10$ KN in each step.

Figure 9.19 plots the initial and final configurations after 20 steps of increment of the deformation using αFEM-T3 with $\alpha = 0.6$. Table 9.10 and Figure 9.20 show the relation between the tip deflection and the load step. The simulation converges in a very rapid speed and, in each load increment, less than five iterations are performed. It can be seen that, with the same set of nodes, the FEM-T3 model behaves much stiffer than FEM-Q4. The results show that the nonlinear effect makes the cantilever beam to behave much stiffer, compared to the linear solutions with the increase of loading. The results of FEM-Q4 are bounded by those of αFEM-T3 using $\alpha = 0.45$ and $\alpha = 0.65$ in a very small range. When $\alpha = 0.60$ or $\alpha = 0.65$ is used, the αFEM-T3 solution is quite close to that of FEM-Q4. This shows that αFEM-T3 with $\alpha \in \overline{0.45 : 0.65}$ also works well in the 2D nonlinear analysis compared to the solution of FEM-Q4.

Example 9.5.5: The 3D Lame Problem: A Convergence Study

The 3D Lame problem described in Example 6.7.5 is used again in this examination, but in this case for testing αFEM-T4. As the problem is spherically

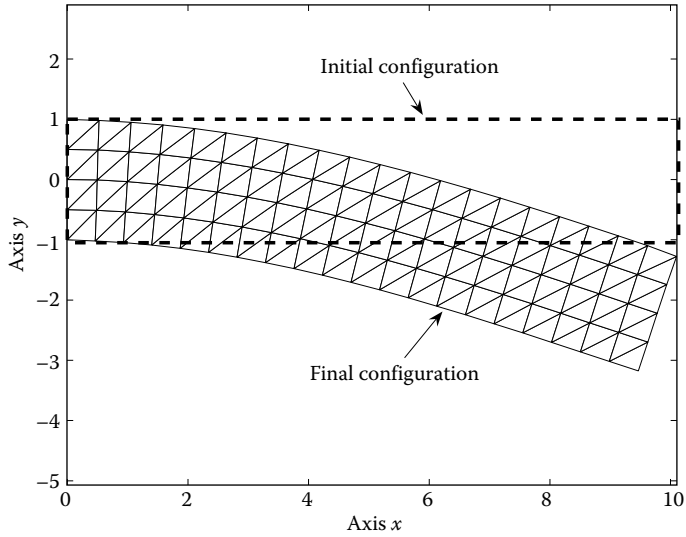

FIGURE 9.19 Initial and final configurations of the cantilever beam subjected to a tip load.

symmetrical, only one-eighth of the sphere model is used as shown in Figure 6.34 and symmetry conditions are imposed on the three mirror symmetric planes. Following the procedures given in Section 9.4.1, we first compute the strain energy curves using different meshes of elements of the same aspect ratio, and the results are plotted in Figure 9.21. It is found that the strain energy curves

TABLE 9.10

Tip Deflection (cm) at the Loading Steps for the Cantilever Beam Subjected to a Concentrated Tip Load

Load Step	FEM-T3 (Linear)	FEM-T3 (Nonlinear)	FEM-Q4 (Linear)	FEM-Q4 (Nonlinear)	αFEM-T3 ($\alpha = 0.45$) (Nonlinear)	αFEM-T3 ($\alpha = 0.60$) (Nonlinear)	αFEM-T3 ($\alpha = 0.65$) (Nonlinear)
$n = 2$	0.2518	0.2440 (3)[a]	0.2989	0.2841 (3)	0.3015 (3)	0.2879 (3)	0.2828 (3)
$n = 4$	0.5037	0.4569 (3)	0.5977	0.5225 (3)	0.5511 (3)	0.5286 (3)	0.5204 (3)
$n = 6$	0.7555	0.6467 (3)	0.8966	0.7387 (3)	0.7803 (3)	0.7475 (3)	0.7356 (3)
$n = 8$	1.0074	0.8272 (3)	1.1955	0.9541 (4)	1.009 (4)	0.9657 (4)	0.9501 (4)
$n = 10$	1.2592	1.0101 (4)	1.4943	1.1614 (4)	1.2310 (4)	1.1761 (4)	1.1563 (4)
$n = 12$	1.5111	1.1847 (4)	1.7932	1.3684 (4)	1.4531 (4)	1.3864 (4)	1.3623 (4)
$n = 14$	1.7629	1.3589 (4)	2.0921	1.5754 (4)	1.6751 (4)	1.5966 (4)	1.5682 (4)
$n = 16$	2.0148	1.5330 (4)	2.3909	1.7821 (4)	1.8932 (5)	1.8047 (5)	1.7740 (4)
$n = 18$	2.2666	1.7069 (4)	2.6898	1.9844 (5)	2.1111 (5)	2.0114 (5)	1.9753 (5)
$n = 20$	2.5185	1.8795 (5)	2.9886	2.1872 (5)	2.3280 (5)	2.2173 (5)	2.1772 (5)

[a] The number in parentheses shows the number of iterations.

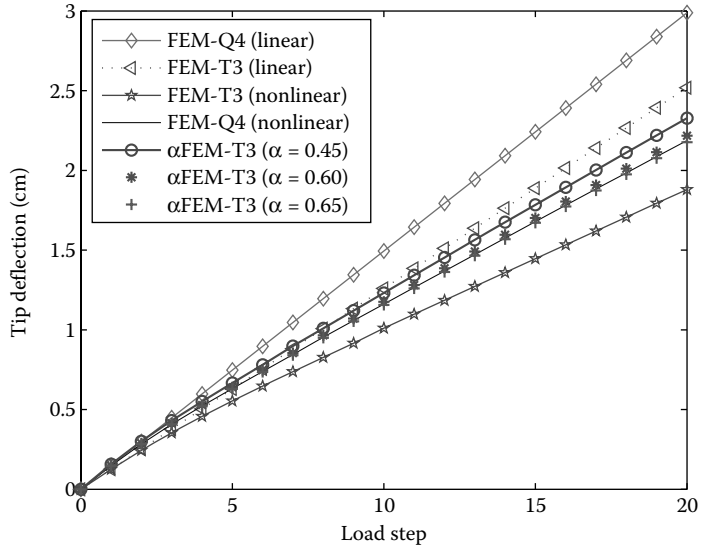

FIGURE 9.20 Tip deflection (cm) versus the loading steps of the cantilever beam subjected to a tip load.

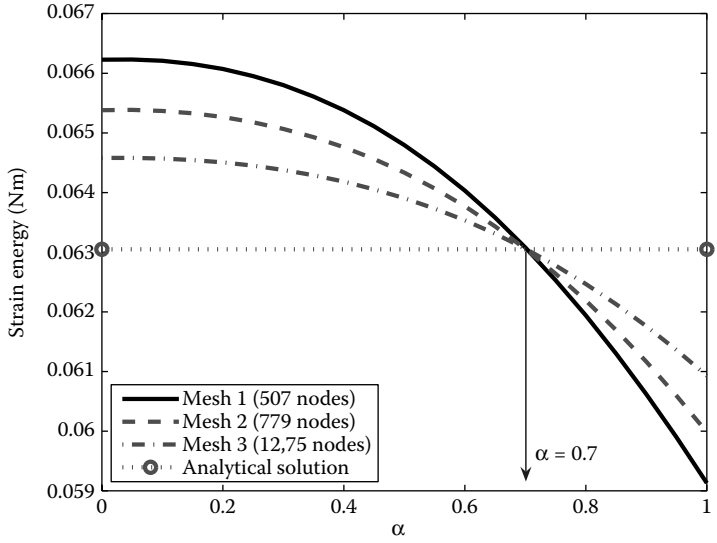

FIGURE 9.21 Strain energy curves of meshes with the same aspect ratios intersect at $\alpha_{exact} = 0.7$ for the hollow sphere subjected to inner pressure.

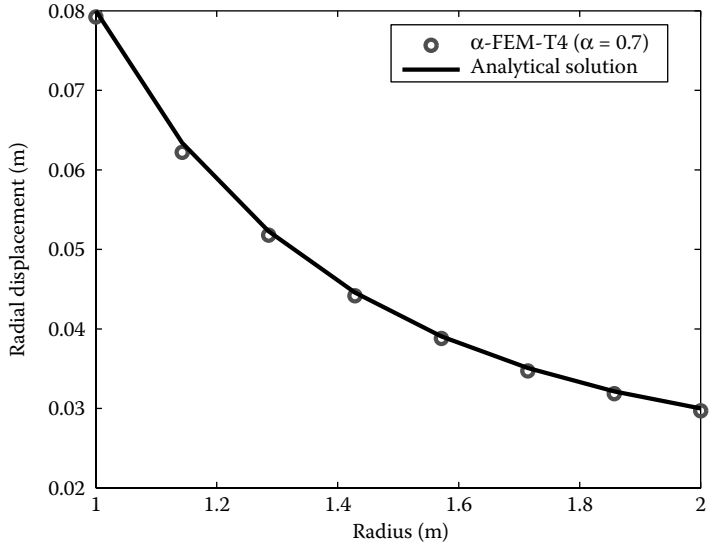

FIGURE 9.22 Distribution of the radial displacement of the hollow sphere subjected to inner pressure using αFEM-T4 ($\alpha_{\text{exact}} = 0.7$).

versus $\alpha \in [0,\ 1]$ using three meshes intersect each other at $\alpha_{\text{exact}} = 0.7$. Figures 9.22 and 9.23 show that the distribution of the displacement and stresses using αFEM-T4 (at $\alpha_{\text{exact}} = 0.7$) agree very well with the analytical solution. Compared to the $\alpha_{\text{exact}} = 0.6$ found for the 2D cantilever, we observed that for 3D problems, we need smaller node-based smoothing operation to reduce the softening effects because FEM-T4 is less stiff than FEM-T3, as discussed in Remark 8.5.

Table 6.12 and Figure 9.24 show the convergence of strain energy of αFEM-T4 (at $\alpha_{\text{exact}} = 0.7$) in comparison with other methods. It is again seen that the strain energies obtained using the αFEM-T4 are almost identical to the analytical solution ($E_{\text{exact}} = 6.305 \times 10^{-2}$) even when very coarse meshes are used.

Table 6.13 and Figure 9.25 provide the solution error in displacement norm obtained using the αFEM-T4 (at $\alpha_{\text{exact}} = 0.7$), together with other methods. It is seen that the αFEM-T4 stands out clearly. When the third mesh ($h \approx 0.156$ m) is used, the error of the αFEM-T4 is about 3/10 of FEM-T4, and even 9/10 of FEM-H8. In terms of convergence rate, the αFEM-T4 stands out clearly with a rate of $r = 2.22$, which is much larger than the theoretical value of 2.0 and much higher than even the FEM-H8 ($r = 2.05$): a quite strong superconvergence in displacement norm.

Table 6.14 and Figure 9.26 compare the solution error in energy norm obtained using the αFEM-T4 (at $\alpha_{\text{exact}} = 0.7$) with those of other methods. It is found that the results of αFEM-T4 are only less accurate than those of NS-FEM-T4 but more accurate than those of FEM-H8 and FEM-T4. When the third mesh ($h \approx 0.156$ m) is used, the error of the αFEM-T4 solution is about 1/2.5 of FEM-T4, 1/2 of the FEM-H8 solution, 1/1.4 of the FEM-T4-Re solution,

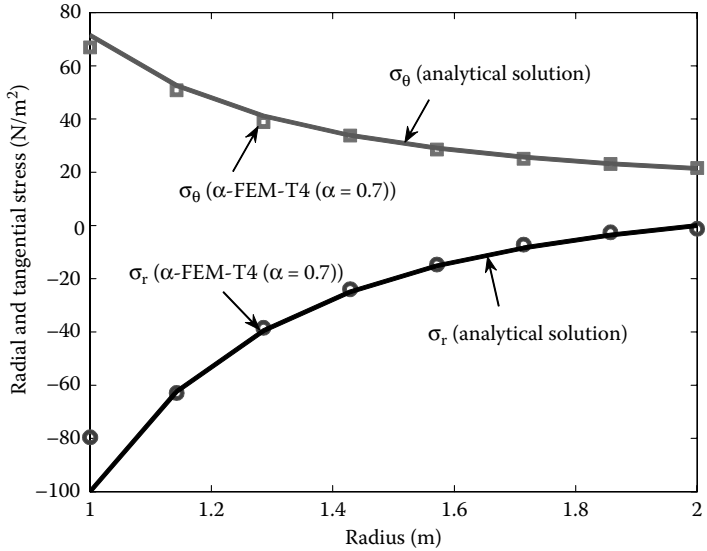

FIGURE 9.23 Distribution of the radial and tangential stresses in the hollow sphere subjected to inner pressure using αFEM-T4 ($\alpha_{exact} = 0.7$).

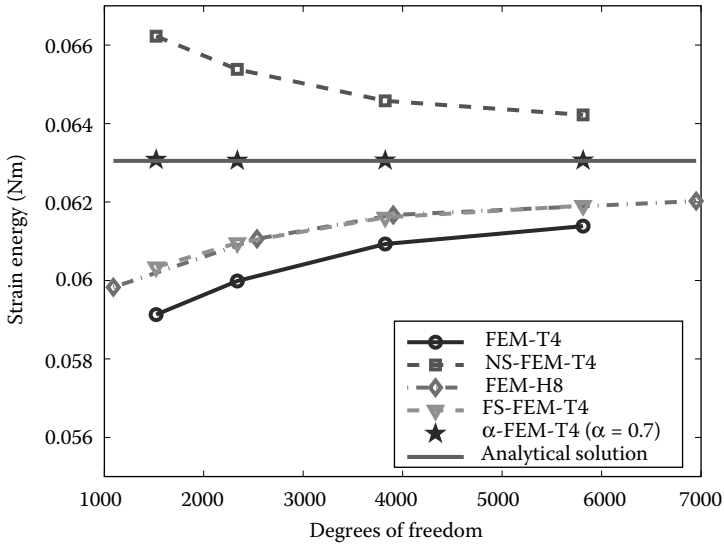

FIGURE 9.24 Convergence of strain energy solution of the αFEM-T4 ($\alpha_{exact} = 0.7$) in comparison with other methods for the hollow sphere subjected to inner pressure.

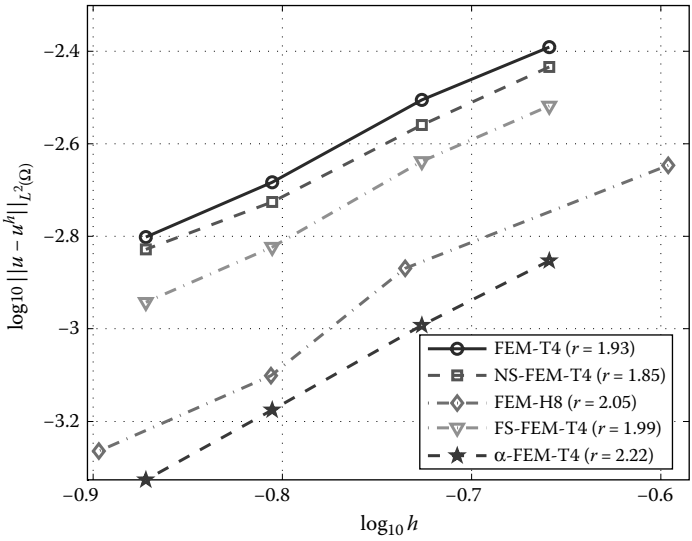

FIGURE 9.25 Error in displacement norm of αFEM-T4 ($\alpha_{\text{exact}} = 0.7$) in comparison with other methods for the hollow sphere subjected to inner pressure.

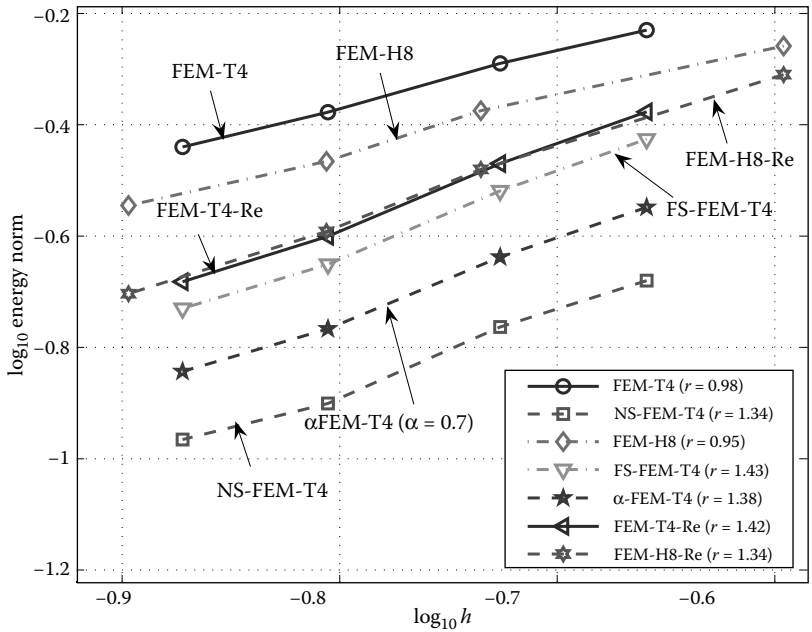

FIGURE 9.26 Error in energy norm of the solution obtained using αFEM-T4 ($\alpha_{\text{exact}} = 0.7$) in comparison with other methods for the hollow sphere subjected to inner pressure.

or 1/1.4 of the FEM-H8-Re solution. In terms of convergence rate, the rate of αFEM-T4 also stands out clearly, $r = 1.38$, which is much larger than the theoretical value of 1.0 and much higher than even the FEM-H8 ($r = 0.95$): a strong superconvergence.

Example 9.5.6: The 3D Cubic Cantilever: Accuracy Study

The 3D cantilever of cubic shape subjected to a uniform pressure on its upper face described in Example 6.7.6 is again considered. A discretization of the 3D cubic cantilever using tetrahedral elements is shown in Figure 6.40. The exact solution of the problem is unknown. By incorporating the solutions of hexahedral superelement elements and the procedure of Richardson's extrapolation, Almeida Pereira [23] has given an approximately "exact" solution in strain energy of 0.950930. In addition, using the standard FEM and a very fine mesh with 30,204 nodes and 20,675 ten-node tetrahedron elements, another reference solution of the strain energy is found to be $E = 0.9486$. This fine FEM model also gives a reference solution of 3.3912 for the deflection at point A located at (1.0, 1.0, −0.5).

From Figure 9.27, it is found that the strain energy curves using three meshes with the same aspect ratio versus $\alpha \in [0, 1]$ intersect at $\alpha_{\text{exact}} = 0.62$. Table 6.15 and Figure 9.28 show the convergence of strain energy of αFEM-T4 ($\alpha_{\text{exact}} = 0.62$) in comparison with four different methods. It is again seen that the strain energies obtained using αFEM-T4 are very close to the reference solution ($E_{\text{ref}} = 0.950930$), even when coarse meshes are used.

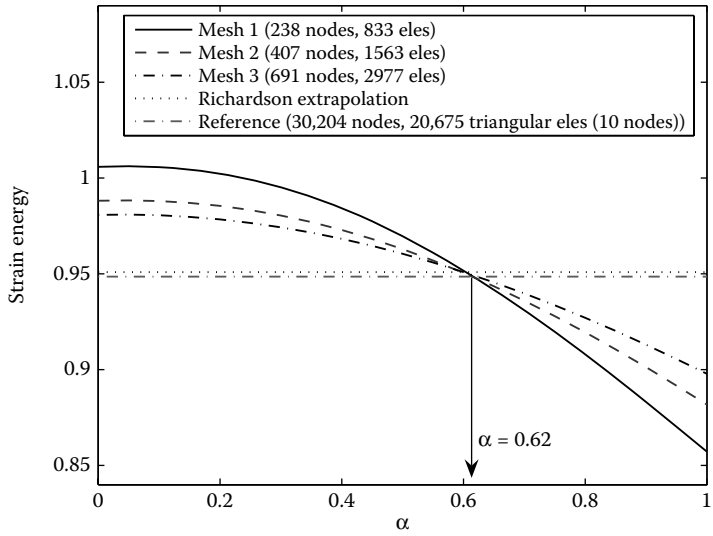

FIGURE 9.27 The strain energy curves of three meshes with the same aspect ratios to find $\alpha_{\text{exact}} = 0.62$ for the cubic cantilever.

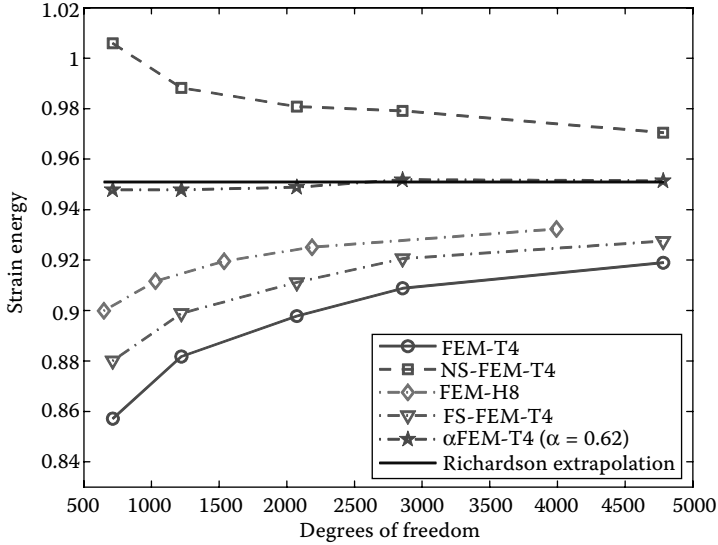

FIGURE 9.28 Convergence of the strain energy solutions of αFEM-T4 ($\alpha_{\text{exact}} = 0.62$) in comparison with other methods for the cubic cantilever subjected to a uniform pressure on the top surface.

Table 6.16 and Figure 9.29 show the convergence of the tip deflection at point $A(1, 1, -0.5)$ obtained using the αFEM-T4 (at $\alpha_{\text{exact}} = 0.62$), together with other different methods for comparison. It is again seen that the deflection solutions of αFEM-T4 are very close to the reference solution (3.3912) even when using the coarse meshes.

Example 9.5.7: The 3D L-shaped Block: Accuracy Study

The 3D cubic block with a smaller cubic hole subjected to a surface traction q described in Example 6.7.7 is again considered. Due to the double mirror symmetry of the problem, only a quarter of the domain is modeled, which becomes a 3D L-shaped block as shown in Figure 6.43. The analysis is performed using dimensionless input data: $q = 1$, $a = 1$, $E = 1$, and $\nu = 0.3$. For this problem, the strain energy of 6.1999 given by Cugnon [24] is considered as the reference solution. In addition, using standard FEM and a very fine mesh with 33,641 nodes and 22,862 ten-node tetrahedron elements, another reference solution of the strain energy has been found to be 6.1916.

From Figure 9.30, it is found that the strain energy curves using three meshes with the same aspect ratio versus $\alpha \in [0,\ 1]$ intersect at $\alpha_{\text{exact}} = 0.7$. Table 6.17 and Figure 9.31 show the convergence of strain energy of αFEM-T4 ($\alpha_{exact} = 0.7$) in comparison with three different methods. It is again seen that the strain energies obtained using αFEM-T4 are very close to the reference solution, even when the coarse meshes are used.

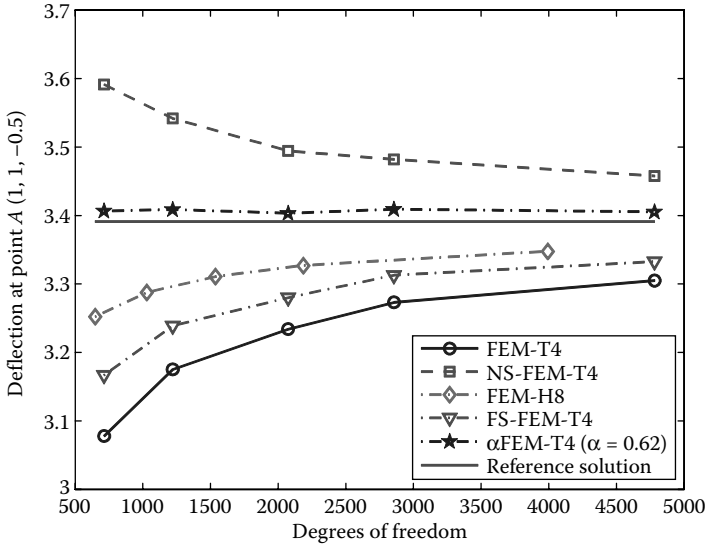

FIGURE 9.29 Convergence of the deflection at point $A(1.0, 1.0, -0.5)$ of αFEM-T4 ($\alpha_{\text{exact}} = 0.62$) in comparison with other methods for the cubic cantilever subjected to a uniform pressure on the top surface.

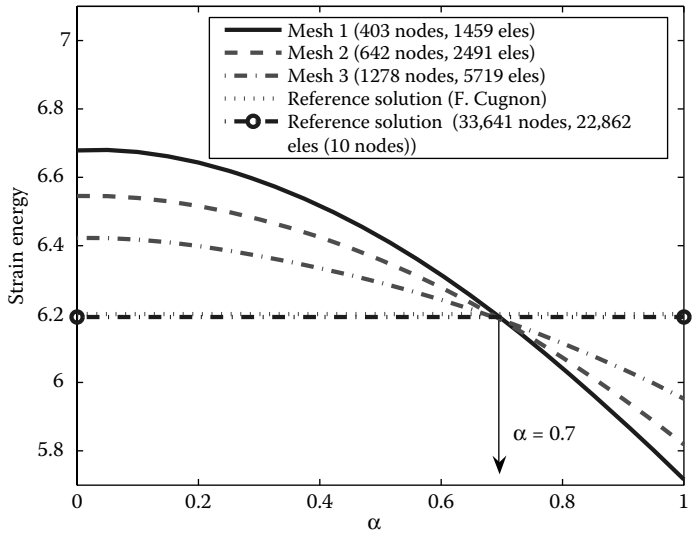

FIGURE 9.30 The strain energy curves of three meshes with the same aspect ratios to find $\alpha_{\text{exact}} = 0.7$ for the L-shaped 3D problem.

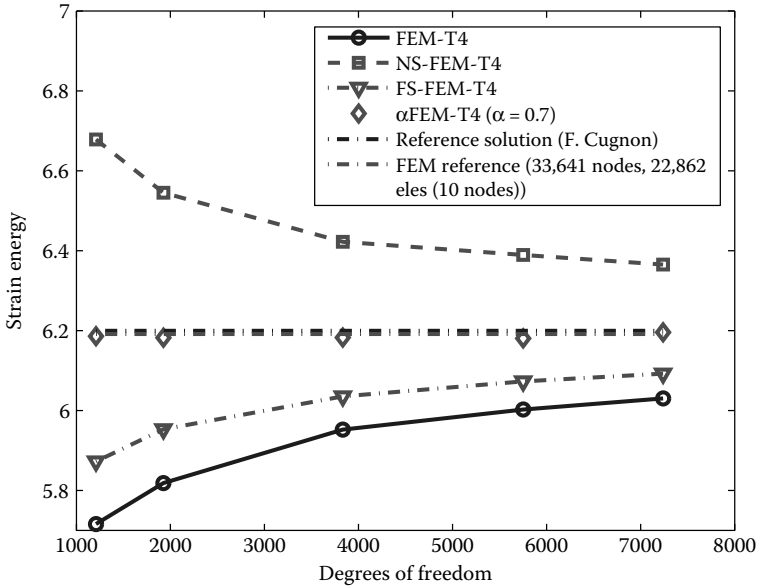

FIGURE 9.31 Convergence of the strain energy solutions of αFEM-T4 ($\alpha_{\text{exact}} = 0.7$) in comparison with other methods for the L-shaped 3D problem.

Example 9.5.8: The 3D Cantilever Beam: A Large Deformation Analysis

This example examines the αFEM-T4 for large deformation analysis of 3D solids. The 3D cantilever beam with the size (10 cm×2 cm×2 cm) subjected to a uniformly distributed load as presented in Example 8.6.3 is considered. The cantilever beam is discretized using a mesh including 1322 nodes and 5802 tetrahedral elements. The related parameters are taken as $E = 3.0 \times 10^7$ N/cm^2 and $\nu = 0.3$. The analysis is based on the total Lagrange formulation, and is carried out using 10 increment steps ($n = 10$) with an increment of $\Delta f = 4$ KN/cm^2 at each step.

Figure 9.32 displays the initial and final configurations of the 3D beam after 10 steps of loadings using αFEM-T4 with $\alpha = 0.7 \in \overline{0.60 : 0.80}$. Table 9.11 and Figure 9.33 show the tip deflections of the beam at various load steps obtained using different methods. The simulation converges in a very rapid speed, and in each load increment, only less than five iterations are performed. It can be observed that the nonlinear effects make the cantilever beam behave stiffer compared to the linear solutions. In the nonlinear analysis, when $\alpha = 0.7$ is used, the results of αFEM-T4 are softer than those of FEM-T4, and are very close to those of FEM using eight-node hexahedral element (FEM-H8) using a much finer mesh with 2304 nodes. The results of αFEM-T4 are found to be even

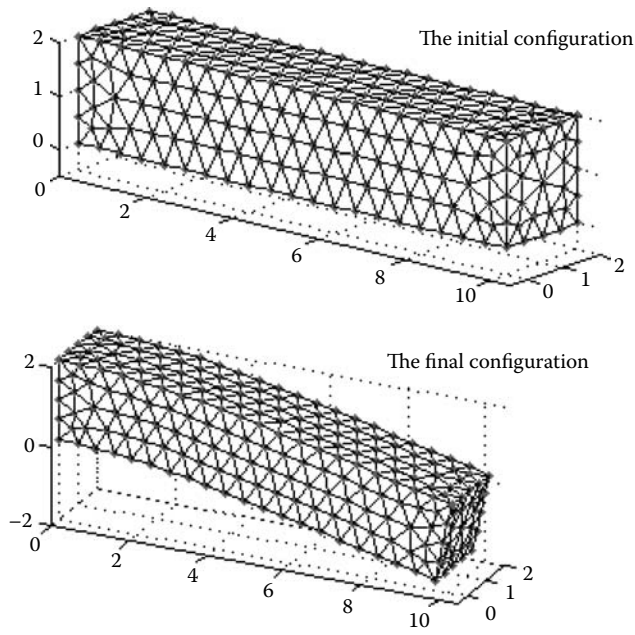

FIGURE 9.32 Initial and final configurations of the 3D cantilever beam subjected to the regular distributed load using four-node tetrahedral elements.

TABLE 9.11

Tip Deflection (cm) at the Loading Steps for the 3D Cantilever Beam Subjected to a Regular Distributed Load

Load Step	FEM-T4 (Linear) (1322 Nodes)	FEM-T4 (Nonlinear) (1322 Nodes)	FS-FEM-T4 (1322 Nodes)	FEM-H8 (Nonlinear) (2304 Nodes)	αFEM-T4 (α = 0.7) (Nonlinear) (1322 Nodes)
$n = 1$	0.2364	0.2295 (3)[a]	0.2365 (3)	0.2441 (3)	0.2472 (3)
$n = 2$	0.4728	0.4314 (3)	0.4430 (3)	0.4556 (3)	0.4606 (3)
$n = 3$	0.7092	0.6119 (3)	0.6277 (3)	0.6451 (3)	0.6521 (3)
$n = 4$	0.9456	0.7831 (3)	0.8038 (3)	0.8266 (3)	0.8358 (3)
$n = 5$	1.1819	0.9511 (3)	0.9818 (4)	1.0097 (4)	1.0211 (4)
$n = 6$	1.4183	1.1210 (4)	1.1516 (4)	1.1853 (4)	1.1990 (4)
$n = 7$	1.6547	1.2847 (4)	1.3206 (4)	1.3602 (4)	1.3763 (4)
$n = 8$	1.8911	1.4479 (4)	1.4891 (4)	1.5344 (4)	1.5529 (4)
$n = 9$	2.1275	1.6104 (4)	1.6569 (4)	1.7080 (4)	1.7289 (4)
$n = 10$	2.3639	1.7724 (4)	1.8242 (4)	1.8809 (4)	1.9041 (4)

[a] The number in parentheses shows the number of iterations.

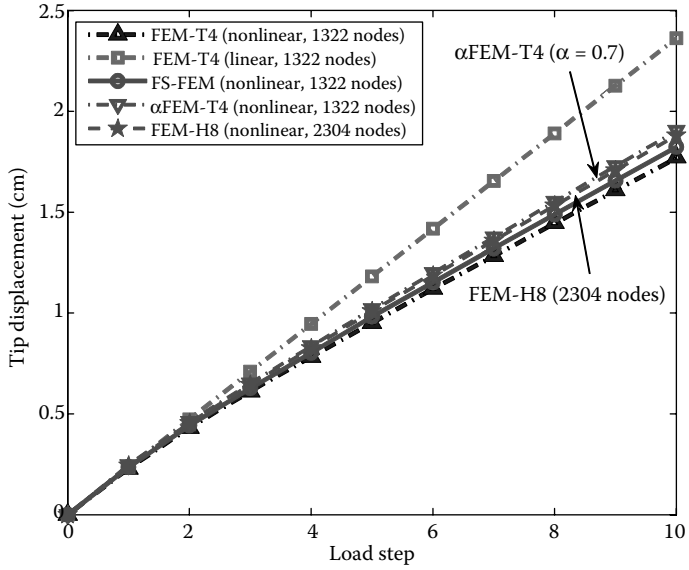

FIGURE 9.33 Tip deflection (cm) versus the loading steps of the 3D cantilever beam subjected to a uniformly distributed load.

more accurate than that of FS-FEM-T4, in relation to the reference solution. This shows that αFEM-T4 ($\alpha \in \overline{0.60 : 0.80}$) also works effectively for 3D nonlinear large deformation analysis.

9.6 Remarks

In this chapter, an αFEM with a scale factor α using three-node triangular elements (αFEM-T3) for 2D and four-node tetrahedral elements (αFEM-T4) for 3D is presented. Through the theoretical study and numerical examples in this chapter, the following remarks may be made.

Remark 9.1 αFEM: Stable, Variationally Consistent, and of Second-Order Accuracy

αFEM-T3 and αFEM-T4 are stable, variationally consistent, and of at least second-order accuracy. It uses compatible displacement field, and hence can reproduce linear field exactly for any $\alpha \in [0,\ 1]$.

Remark 9.2 αFEM: Delivers Both Upper and Lower Bounds

αFEM-T3 and αFEM-T4 are equipped with a scaling factor α that controls the contributions from NS-FEM and FEM models. When the factor α varies

from 0 to 1, a continuous function of solutions from the solution of the NS-FEM model to that of the FEM can be obtained. When $\alpha = 0$, αFEM-T3 and αFEM-T4 become the NS-FEM, and the strain energy $\hat{E}(\alpha = 0)$ is an upper bound solution in terms of the exact strain energy, when the model has sufficient smoothing effects. When $\alpha = 1$, αFEM-T3 and αFEM-T4 become the standard FEM, and the strain energy $\hat{E}(\alpha = 1)$ is a lower bound of the exact strain energy.

Remark 9.3 αFEM: For Nearly Exact Solutions

A unique approach has been proposed for αFEM-T3 and αFEM-T4 to obtain the nearly exact solution in strain energy for linear elasticity problems. This approach uses two coarse meshes with the same aspect ratio to search for an approximate α_{exact}. αFEM-T3 and αFEM-T4 with such an α_{exact} are capable of providing a "nearly exact" solution in strain energy using a discrete model with very coarse meshes.

Remark 9.4 αFEM: Easy to Implement and No Numerical Integration

The implementation of αFEM-T3 (or αFEM-T4) in practical applications is relatively easy and quite similar to the standard FEM because (1) automatic refinement from an initial coarse mesh to obtain the meshes of T3 and T4 elements with the same aspect ratio is readily available in many existing programs; (2) αFEM-T3 (or αFEM-T4) uses the strain–displacement matrices $\tilde{\boldsymbol{B}}$ of the standard FEM and area (or volume) of elements to compute the system stiffness matrix; and (3) no new numerical integration is necessary. The αFEM-T3 (or αFEM-T4) is found very promising and can be easily incorporated into the existing commercial software packages with a little modification.

Remark 9.5 αFEM: Volumetric Locking Free

For plane strain problems with nearly incompressible materials, we recommend the use of $\alpha = 0$ or a very small $\alpha = 0.5 - \nu$ to solve the volumetric locking problem.

Remark 9.6 αFEM: Works Well for Nonlinear Problems

αFEM-T3 and αFEM-T4 can be used to obtain accurate solutions for nonlinear problems of large deformation.

Remark 9.7 αFEM: Works Well with Triangular Types of Elements and Hence Suits Well for Adaptive Analysis

The αFEM-T3 (or αFEM-T4) is suitable also for adaptive analysis as it uses only triangular and tetrahedral elements that can be automatically generated for complicated domains.

Remark 9.8 Efficient Search for α_{exact}: An Open Topic

Searching efficiently for a good approximation of α_{exact} is still an open topic. If a more efficient scheme can be devised, αFEM-T3 and αFEM-T4 can find even much wider applications, simply because we can tune the model as we wish. An $\alpha \in \overline{0.45 : 0.65}$ (for 2D) and $\alpha \in \overline{0.60 : 0.80}$ (for 3D) are recommended for usual engineering problems. In general, if the solid is heavily constrained, the α should be smaller, and vice versa.

Remark 9.9 Efficiency: Larger Bandwidth

The αFEM has the same bandwidth as the NS-FEM-T3 (or NS-FEM-T4) that is much larger than ES-FEM-T3 (or FS-FEM-T4), and hence the efficiency will be affected. If the α_{exact} can be efficiently found, it is not a problem, because producing the nearly exact solution can make it an ultimate winner. Otherwise, ES-FEM-T3 and FS-FEM-T4 can still be good competitors.

Finally, we note that there is still very big room for improvement of αFEM, and some improvised methods can be developed along this line in future.

References

1. Liu GR, Nguyen-Thoi T, and Lam KY. 2009. A novel FEM by scaling the gradient of strains with factor α (αFEM). *Computational Mechanics*; 43: 369–391.
2. Liu GR, Nguyen-Thoi T, and Lam KY. 2008. A novel alpha finite element method (αFEM) for exact solution to mechanics problems using triangular and tetrahedral elements. *Computer Methods in Applied Mechanics and Engineering*; 197: 3883–3897.
3. Arnold DN. 1990. Mixed finite element methods for elliptic problems. *Computer Methods in Applied Mechanics and Engineering*; 82: 281–300.
4. Mijuca D and Berkovic M. 1998. On the Efficiency of the Primal-Mixed Finite Element Scheme. *Advances in Computational Structured Mechanics*, Civil-Comp Press, Kippen Stirling, UK, pp. 61–69.
5. Rong TY and Lu AQ. 2001. Generalized mixed variational principles and solutions for ill-conditioned problems in computational mechanics: Part I. Volumetric locking. *Computer Methods in Applied Mechanics and Engineering*; 191: 407–422.
6. Rong TY and Lu AQ. 2003. Generalized mixed variational principles and solutions for ill-conditioned problems in computational mechanics: Part II. Shear locking. *Computer Methods in Applied Mechanics and Engineering*; 192: 4981–5000.
7. Pian THH and Sumihara K. 1984. Rational approach for assumed stress finite elements. *International Journal for Numerical Methods in Engineering*; 20: 1685–1695.
8. Pian THH and Wu CC. 2006. *Hybrid and Incompatible Finite Element Methods*. CRC Press, Boca Raton, FL.

9. Zhou T and Nie Y. 2001. A combined hybrid approach to finite element schemes of high performance. *International Journal for Numerical Methods in Engineering*; 51: 181–202.
10. Liu GR, Nguyen-Thoi T, Nguyen-Xuan H, and Lam KY. 2009. A node-based smoothed finite element method (NS-FEM) for upper bound solution to solid mechanics problems. *Computers and Structures*; 87: 14–26.
11. Zhang ZQ and Liu GR. 2009. Solution bound and nearly exact solution to nonlinear elasticity using smoothed FEM models. *Computer Methods in Applied Mechanics and Engineering*; doi:10.1007/s00466-009-0420-5.
12. Zhang ZQ and Liu GR. 2009. Temporal stabilization of the node-based smoothed finite element method (NS-FEM) and solution bound of linear elastostatics and vibration problems. *Computational Mechanics*; (revised).
13. Liu GR and Zhang GY. 2008. Upper bound solution to elasticity problems: A unique property of the linearly conforming point interpolation method (LC-PIM). *International Journal for Numerical Methods in Engineering*; 74: 1128–1161.
14. Bathe KJ. 1996. *Finite Element Procedures*. Prentice-Hall, Massachusetts (MIT).
15. Reddy JN. 2004. *An Introduction to Nonlinear Finite Element Analysis*. Oxford University Press, Oxford.
16. Cook R. 1974. Improved two-dimensional finite element. *Journal of the Structural Division, ASCE 100*; ST6: 1851–1863.
17. Fredriksson M and Ottosen NS. 2004. Fast and accurate 4-node quadrilateral. *International Journal for Numerical Methods in Engineering*; 61: 1809–1834.
18. Taylor RL, Beresford PJ, and Wilson EL. 1976. A non-conforming element for stress analysis. *International Journal for Numerical Methods in Engineering*; 10: 1211–1219.
19. Flanagan DP and Belytschko T. 1981. A uniform strain hexahedron and quadrilateral with orthogonal hourglass control. *International Journal for Numerical Methods in Engineering*; 17: 679–706.
20. Belytschko T and Bachrach E. 1986. Efficient implementation of quadrilaterals with high coarse-mesh accuracy. *Computer Methods in Applied Mechanics and Engineering*; 54: 279–301.
21. Kosloff D and Frazier GA. 1978. Treatment of hourglass patterns in low order finite element codes. *International Journal for Numerical and Analytical Methods in Geomechanics*; 2: 57–72.
22. Timoshenko SP and Goodier JN. 1970. *Theory of Elasticity*, 3rd edition. McGraw-Hill, New York.
23. Almeida Pereira OJB. 2008. Hybrid equilibrium hexahedral elements and super-elements. *Communications in Numerical Methods in Engineering*; 24(2): 157–165.
24. Cugnon F. 2000. Automatisation des calculs elements finis dans le cadre de la methode-p. PhD thesis, Universite de Lie.

10

S-FEM for Fracture Mechanics

10.1 Introduction

In previous chapters, we have introduced a number of S-FEM models and demonstrated the excellent properties and performance of these models for general problems of solid mechanics defined (by default) in a *Lipschitzian* domain (i.e., not *singular*). This chapter aims to extend the application of these S-FEM models for a particular class of problems: fracture mechanics [1] where there are singularities caused by *non-Lipschitzian* domains such as domains containing cracks and re-entrants. We consider in this chapter only "sharp" cracks whose two surfaces are in-line. We will deal with the most essential and important aspects of fracture mechanics: creation of the singular stress field at the crack-tip. Such fracture problems have been well studied using FEM [1–3] making use of the so-called quadratic singular elements (T6 or Q8), and many of these theories and techniques will be used in this chapter. S-FEM models for fracture problems were devised and advanced recently in Refs. [4–7] by using a basic mesh of three-node linear triangular (T3) elements, and these works will be closely followed in this chapter.

As shown in previous chapters, in all these S-FEM formulations, one needs only the values (not the derivatives) of the assumed displacement functions on the boundaries of the smoothing domains. Making use of this important feature, a new technique called the "enriched linear PIM" for constructing shape functions was suggested [4] to formulate a special "crack-tip element" that can produce a proper order of stress singularity near the crack-tip and yet be compatible with the surrounding linear T3 elements. Singular ES-FEM (sES-FEM) [4,5,7] and singular NS-FEM (sNS-FEM) [6] were then formulated for computing the J-integral (or energy release rate) and stress intensity factors (SIFs) of fracture problems of mode I, mode II, mixed mode, and interfacial mode. One of the distinct features of these works is that they use a basic mesh of T3 elements that can be generated automatically for problems with complicated geometry. The system stiffness matrix is then computed using the smoothed strains over the smoothing domains associated with the edges or nodes of the triangular elements. The procedure for regular elements not directly connected to

the crack-tip is exactly the same as that in previous chapters. For crack-tip elements connected directly to the crack-tip, further division of smoothing domains may be required to better capture the singular feature of the strain field at the crack-tip. The SIFs for mode I, mode II, mixed mode, and the interfacial mode have been calculated based on the area-path integrals looping around the crack-tip, based on the interaction integral method. A number of examples with all these fracture modes have been presented. The results have demonstrated that (1) the sNS-FEM-T3 can produce upper bound solutions for fracture problems, and (2) the sES-FEM-T3 produces ultra-accurate solutions that are much more accurate than the FEM-T3 and even more accurate than the singular quadratic FEM-T6 models.

10.2 Singular Stress Field Creation at the Crack-Tip

The singular S-FEMs (sES-FEM and sNS-FEM) formulated in this chapter use a basic mesh of three-node linear T3 elements that can be generated automatically for problems with complicated geometry. Linear interpolation for the displacement field is used for the entire problem domain, except for one layer of five-node triangular (T5) crack-tip elements specially designed to simulate the strain (and hence the stress) singularity near the crack-tip. The creation of such a singular stress field consists of two steps: displacement interpolation along the crack-tip edge of the T5 elements using the enriched linear PIM and the displacement field creation within the T5 crack-tip elements.

10.2.1 Enriched Linear PIM for Interpolation along the Crack-Tip Edge

The most fundamental issue in modeling linear fracture mechanics problems using the FEM or any other numerical methods including the S-FEM is to simulate properly the singularity stress field near the crack-tip while maintaining a certain order of consistency. When the polynomial basis functions are used in the conventional finite elements, consistency can be easily achieved, but strain field singularity at the crack-tip cannot be produced, for which we have to resort to the so-called singular elements. Currently, the most widely used singular element in the standard FEM setting is the quadratic crack-tip element with the mid-edge nodes being shifted on the element edge by a quarter edge length toward the crack-tip. The singularity is then achieved nicely by the well-known isoparametric mapping procedure [2,3]. There are two types of such crack-tip elements widely used in fracture mechanics problems: eight-noded quadrilateral

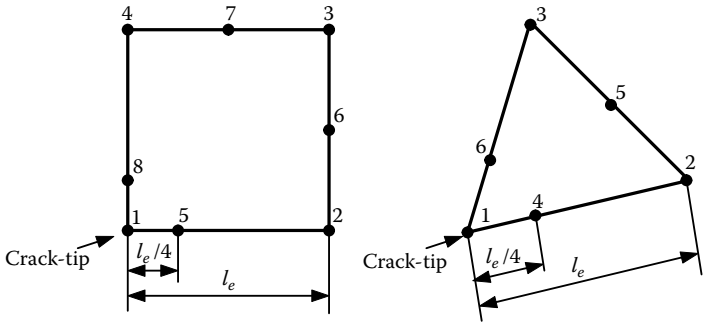

FIGURE 10.1 The schematic of the quadratic eight-node quadrilateral (Q8) and six-node triangular (T6) crack-tip elements widely used in the FEM. The stress singularity is achieved by shifting the regular middle edge node by a quarter-length of the element toward the crack-tip.

(Q8) and six-noded triangular (T6) elements, as shown in Figure 10.1. When these types of elements are used, the entire element mesh has to be, in principle, quadratic elements of the same type. Otherwise, proper additional measures have to be used to ensure compatibility of the displacement field.

In our singular S-FEM (sS-FEM) models [4–7], however, no mapping is used, and the stress singularity is created by a simple PIM with extra basis functions of proper fractional order polynomials. The basic mesh used in an S-FEM consists of linear T3 elements with a layer of specially designed crack-tip T5 elements. Figure 10.2a shows a typical layer of special crack-tip elements used in an S-FEM model for fracture problems with a crack, where the crack-tip is located at node 1 and the surface of the crack is defined by the free edges of the triangular elements. Because we use three-node triangular mesh, such a meshing and nodal arrangement can always be done without any technical difficulty.

In the sS-FEM, we add in a node on each edge of the triangular elements that is connected to the crack-tip node (called the crack-tip edge), as shown in Figure 10.2a. The location of the added intermediate node can be in general at any point within the crack-tip edge, as shown in Figure 10.2b. Therefore, the crack-tip element has a total of five nodes, and is termed as T5 elements. Based on such an S-FEM setting, the displacement field, for example the component u, at any point of interest on a crack-tip edge of length l_e (>0) can be approximated using the following "enriched linear PIM":

$$u^h = c_0 + c_1 r + c_2 \sqrt{r}, \tag{10.1}$$

where r is the radial coordinate originated at the crack-tip (node 1), and c_i ($i = 0, 1, 2$) are the three constants that are yet to be determined.

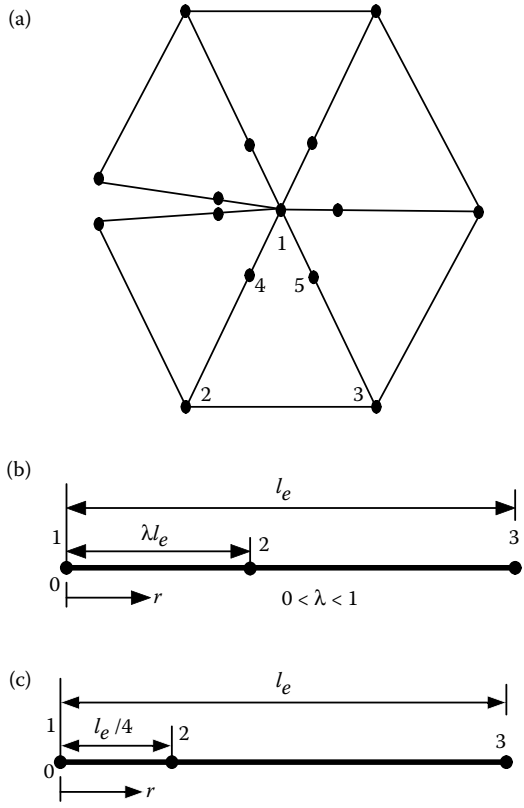

FIGURE 10.2 Crack-tip configuration for S-FEM models using a basic mesh of triangular elements. (a) One layer of five-node triangular (T5) crack-tip elements with one additional node is added on each edge leading to the crack-tip (called the crack-tip edge); (b) interpolation on a crack-tip edge with three nodes (node 2 can be in general anywhere on the edge); (c) a special case when node 2 is located at one-quarter edge length (similar to the FEM).

Clearly, the assumed displacement using Equation 10.1 is at least linearly complete with respect to the radial coordinate. Using Equation 10.1, the displacements at nodes 1, 2, and 3 can now be expressed as follows.

At node 1 where $r = 0$, we have

$$u_1 = c_0. \tag{10.2}$$

At node 2 where $r = \lambda l_e$:

$$u_2 = c_0 + c_1 \lambda l_e + c_2 \sqrt{\lambda l_e}. \tag{10.3}$$

At node 3 where $r = l_e$:

$$u_3 = c_0 + c_1 l_e + c_2 \sqrt{l_e}, \tag{10.4}$$

where u_i $(i = 1, 2, 3)$ are the three nodal displacements, and the parameter $\lambda \in (0, 1)$ controls the location of node 2. Solving this simultaneous system of three Equations 10.2 through 10.4 for constants c_i, we can easily obtain

$$\begin{aligned} c_0 &= u_1, \\ c_1 &= \frac{1}{\lambda l_e}\left[\left(-1 + \frac{(1-\lambda)\sqrt{\lambda l_e}}{\sqrt{\lambda l_e} - \lambda\sqrt{l_e}}\right)u_1 + \left(1 - \frac{\sqrt{\lambda l_e}}{\sqrt{\lambda l_e} - \lambda\sqrt{l_e}}\right)u_2 \right. \\ &\quad \left. + \frac{\lambda\sqrt{\lambda l_e}}{\sqrt{\lambda l_e} - \lambda\sqrt{l_e}}u_3\right], \\ c_2 &= \frac{1}{\sqrt{\lambda l_e} - \lambda\sqrt{l_e}}[(\lambda - 1)u_1 + u_2 - \lambda u_3]. \end{aligned} \tag{10.5}$$

We will always have a solution for c_i as long as $l_e \neq 0$ and $\lambda \in (0, 1)$. After substituting c_i $(i = 1, 2, 3)$ back to Equation 10.1, we arrive at

$$u^h = \left\{ \begin{array}{c} \underbrace{1 + \frac{r}{\lambda l_e}\left(-1 + \frac{(1-\lambda)\sqrt{\lambda l_e}}{\sqrt{\lambda l_e} - \lambda\sqrt{l_e}}\right) + \frac{\sqrt{r}}{\sqrt{\lambda l_e} - \lambda\sqrt{l_e}}(\lambda - 1)}_{\phi_1} \\ \underbrace{\frac{r}{\lambda l_e}\left(1 - \frac{\sqrt{\lambda l_e}}{\sqrt{\lambda l_e} - \lambda\sqrt{l_e}}\right) + \frac{\sqrt{r}}{\sqrt{\lambda l_e} - \lambda\sqrt{l_e}}}_{\phi_2} \\ \underbrace{\frac{r}{\lambda l_e}\left(\frac{\lambda\sqrt{\lambda l_e}}{\sqrt{\lambda l_e} - \lambda\sqrt{l_e}}\right) - \frac{\lambda\sqrt{r}}{\sqrt{\lambda l_e} - \lambda\sqrt{l_e}}}_{\phi_3} \end{array} \right\}^T \left\{ \begin{array}{c} u_1 \\ u_2 \\ u_3 \end{array} \right\}, \tag{10.6}$$

where ϕ_i $(i = 1, 2, 3)$ are called the "basic" nodal shape functions for these three nodes on the crack-tip edge that can be written in the following

row-matrix form:

$$\Phi = \left\{ \begin{array}{l} \underbrace{1+\dfrac{r}{\lambda l_e}\left(-1+\dfrac{(1-\lambda)\sqrt{\lambda l_e}}{\sqrt{\lambda l_e}-\lambda\sqrt{l_e}}\right)+\dfrac{\sqrt{r}}{\sqrt{\lambda l_e}-\lambda\sqrt{l_e}}(\lambda-1)}_{\phi_1} \\ \underbrace{\dfrac{r}{\lambda l_e}\left(1-\dfrac{\sqrt{\lambda l_e}}{\sqrt{\lambda l_e}-\lambda\sqrt{l_e}}\right)+\dfrac{\sqrt{r}}{\sqrt{\lambda l_e}-\lambda\sqrt{l_e}}}_{\phi_2} \\ \underbrace{\dfrac{r}{\lambda l_e}\left(\dfrac{\lambda\sqrt{\lambda l_e}}{\sqrt{\lambda l_e}-\lambda\sqrt{l_e}}\right)-\dfrac{\lambda\sqrt{r}}{\sqrt{\lambda l_e}-\lambda\sqrt{l_e}}}_{\phi_3} \end{array} \right\}^T$$

$$= [\,\phi_1 \quad \phi_2 \quad \phi_3\,], \tag{10.7}$$

where

$$\begin{aligned} \phi_1 &= 1+\frac{r}{\lambda l_e}\left(-1+\frac{(1-\lambda)\sqrt{\lambda l_e}}{\sqrt{\lambda l_e}-\lambda\sqrt{l_e}}\right)+\frac{\sqrt{r}}{\sqrt{\lambda l_e}-\lambda\sqrt{l_e}}(\lambda-1), \\ \phi_2 &= \frac{r}{\lambda l_e}\left(1-\frac{\sqrt{\lambda l_e}}{\sqrt{\lambda l_e}-\lambda\sqrt{l_e}}\right)+\frac{\sqrt{r}}{\sqrt{\lambda l_e}-\lambda\sqrt{l_e}}, \\ \phi_3 &= \frac{r}{\lambda l_e}\left(\frac{\lambda\sqrt{\lambda l_e}}{\sqrt{\lambda l_e}-\lambda\sqrt{l_e}}\right)-\frac{\lambda\sqrt{r}}{\sqrt{\lambda l_e}-\lambda\sqrt{l_e}}. \end{aligned} \tag{10.8}$$

Equation 10.6 can simply be written as

$$u^h = \begin{bmatrix}\phi_1 & \phi_2 & \phi_3\end{bmatrix} \begin{Bmatrix} u_1 \\ u_2 \\ u_3 \end{Bmatrix}. \tag{10.9}$$

It is clear that these three nodal shape functions are (complete) linear in r and "enriched" with a special basis $\sqrt{r}$ that is capable of producing the very much needed strain (hence stress) singularity field of the order of $\frac{1}{2}$ near the crack-tip. This can be easily verified by differentiation of the assumed displacements. Note also that, in this formulation, the intermediate edge node 2 can be at any location on the edge controlled by factor λ. Therefore, this formulation is very general and different from the usual FEM crack-tip elements where the intermediate nodes *must* be located at quarter lengths to the crack-tip. Another difference is that the usual FEM crack-tip element achieves singularity by coordinate mapping, while the sES-FEM achieves singularity via a very simple procedure of direct PIM

with a proper fractional order basis term $\sqrt{r}$ and no mapping is needed. This approach used in the sS-FEM is thus much more direct and straightforward. This is because the same order singular strain field can be obtained near the crack-tip, regardless of the location of node 2, as shown in the direct interpolation formulation given above. In the numerical examples section, we will show numerically that the location of the immediate node is indeed not essential, and therefore we often chose to place the intermediate edge nodes at a quarter length position, as we have already used in the FEM crack-tip elements.

When the location of the added node is at the one quarter length of the edge or $\lambda = 1/4$, as shown in Figure 10.2c, we shall have

$$u = \left[\underbrace{1 + 2\frac{r}{l_e} - 3\sqrt{\frac{r}{l_e}}}_{\phi_1} \quad \underbrace{-4\frac{r}{l_e} + 4\sqrt{\frac{r}{l_e}}}_{\phi_2} \quad \underbrace{\frac{2r}{l_e} - \sqrt{\frac{r}{l_e}}}_{\phi_3} \right] \begin{Bmatrix} u_1 \\ u_2 \\ u_3 \end{Bmatrix}, \tag{10.10}$$

where

$$\begin{aligned} \phi_1 &= 1 + 2\frac{r}{l_e} - 3\sqrt{\frac{r}{l_e}}, \\ \phi_2 &= -4\frac{r}{l_e} + 4\sqrt{\frac{r}{l_e}}, \\ \phi_3 &= \frac{2r}{l_e} - \sqrt{\frac{r}{l_e}}. \end{aligned} \tag{10.11}$$

Note again that in our formulation for S-FEM methods, placing the intermediate edge nodes at a quarter length position is not a must, but merely one choice that mimics the standard FEM crack-tip elements.

10.2.2 Displacement Interpolation within a Five-Node Crack-Tip Element

In our sS-FEM, we use linear T3 elements for areas without singularity, and one layer of the specially designed singular T5 crack-tip elements to produce the stress singularity behavior at the crack-tip. In three of the crack-tip elements shown in Figure 10.3, we assume that

1. In the radial direction, the displacement varies with r via the enriched form of Equation 10.9
2. In the tangential direction, the displacement varies linearly

We consider now only the element in the middle, element 1-4-2-3-5, as shown in Figure 10.3. For the convenience of interpolation, we introduce

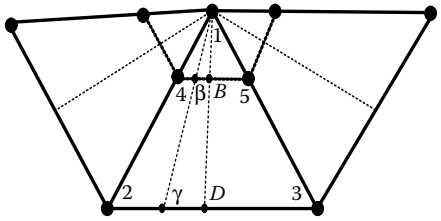

FIGURE 10.3 Displacement interpolation within a five-node crack-tip element (1-2-3-4-5): Three T5 elements connected to the crack-tip node 1. The T5 crack-tip elements are varied with r via Equation 10.9 in the radial direction (e.g., the direction along the lines 1-4-2; 1-β-γ; 1-*B*-*D*; 1-5-3) and linear in the tangential direction (e.g., the direction along the lines 4-5; 2-3).

two points D and B that are, respectively, the midpoints of lines 2-3 and 4-5 (see Figure 10.3). The displacements can be evaluated using the simple linear PIM (averaging) as follows:

$$u_B = \frac{1}{2}(u_4 + u_5), \tag{10.12}$$

$$u_D = \frac{1}{2}(u_2 + u_3), \tag{10.13}$$

where u_i $(i = 1, 2, \ldots, 5)$ are, respectively, the nodal displacements at nodes of the crack-tip element.

For any point on the straight line 1-*B*-*D*, displacement is then interpolated using Equation 10.9, but for line 1-*B*-*D*,

$$u = u_1\phi_1 + u_B\phi_2 + u_D\phi_3. \tag{10.14}$$

Substituting Equations 10.12 and 10.13 into the foregoing equation, we have

$$u = u_1\phi_1 + \frac{1}{2}(u_4 + u_5)\phi_2 + \frac{1}{2}(u_2 + u_3)\phi_3. \tag{10.15}$$

Rearranging, the interpolation at any point on the line 1-*B*-*D* can be written as follows:

$$u = u_1\phi_1 + \frac{1}{2}\phi_3 u_2 + \frac{1}{2}\phi_3 u_3 + \frac{1}{2}\phi_2 u_4 + \frac{1}{2}\phi_2 u_5. \tag{10.16}$$

Similarly, for any point on an arbitrary straight line originated from the crack-tip node, 1-β-γ, where the position of β is on the line 4-5 and that of γ is on the line 2-3 as shown in Figure 10.3, the displacement is evaluated again using Equation 10.9, whereas for line 1-β-γ, the displacement is evaluated using

$$u = u_1\phi_1 + u_\beta\phi_2 + u_\gamma\phi_3. \tag{10.17}$$

The displacements at β and γ can be evaluated using the following linear interpolation:

$$u_\beta = \left(1 - \frac{l_{\beta-4}}{l_{4-5}}\right) u_4 + \frac{l_{\beta-4}}{l_{4-5}} u_5, \tag{10.18}$$

$$u_\gamma = \left(1 - \frac{l_{\gamma-2}}{l_{2-3}}\right) u_2 + \frac{l_{\gamma-2}}{l_{2-3}} u_3, \tag{10.19}$$

where l_{i-j} is the distance between two points i and j. Invoking the simple fact that

$$\frac{l_{\beta-4}}{l_{4-5}} = \frac{l_{\gamma-2}}{l_{2-3}} = \alpha, \tag{10.20}$$

we finally arrive at

$$u = \underbrace{\phi_1}_{N_1} u_1 + \underbrace{(1-\alpha)\phi_3}_{N_2} u_2 + \underbrace{\alpha\phi_3}_{N_3} u_3 + \underbrace{(1-\alpha)\phi_2}_{N_4} u_4 + \underbrace{\alpha\phi_2}_{N_5} u_5. \tag{10.21}$$

This is the general formulation for displacement interpolation within a crack-tip element. The general form of shape functions for the five-node crack-tip element can be written as

$$\begin{aligned} N_1 &= \phi_1, \\ N_2 &= (1-\alpha)\phi_3, \\ N_3 &= \alpha\phi_3, \\ N_4 &= (1-\alpha)\phi_2, \\ N_5 &= \alpha\phi_2. \end{aligned} \tag{10.22}$$

Because in our sS-FEM we do not need the derivatives of shape functions, Equations 10.21 and 10.22 are all we need to compute the stiffness matrix and create the numerical model for our sS-FEM, as we did in previous chapters.

10.3 Possible sS-FEM Methods

Once a proper singular stress field is created, we can then create sS-FEM models for linear fracture problems using various types of smoothing domains. If cell-based smoothing domains (see Chapter 5) are used, we

have a singular CS-FEM (sCS-FEM) model. If node-based smoothing domains are used (see Chapter 6), we have an sNS-FEM model. Similarly, we shall have an sES-FEM model (see Chapter 7), and an sFS-FEM model (see Chapter 8). If partially node-based smoothing domains (see Chapter 9) are used, we even have a singular αFEM model. Because the differences in all these models are mainly in the smoothing domains, this chapter discusses only two sS-FEM models: sES-FEM and sNS-FEM, which have distinct properties. The sNS-FEM can produce upper bound solutions, and the sES-FEM can produce ultra-accurate solutions. Other types of models can also be created with ease, by changing the types of properly formed smoothing domains with proper numerical implementations.

10.4 sNS-FEM Models

As discussed in Chapter 6, the NS-FEM model uses smoothing domains created based on nodes. Figure 10.4 shows schematically the construction of node-based strain smoothing domains for sNS-FEM. For all the nodes other than the crack-tip node, the treatments for the smoothing domains are exactly the same as in the NS-FEM discussed in Chapter 6. For the crack-tip node smoothing domain, however, special treatments are required to better

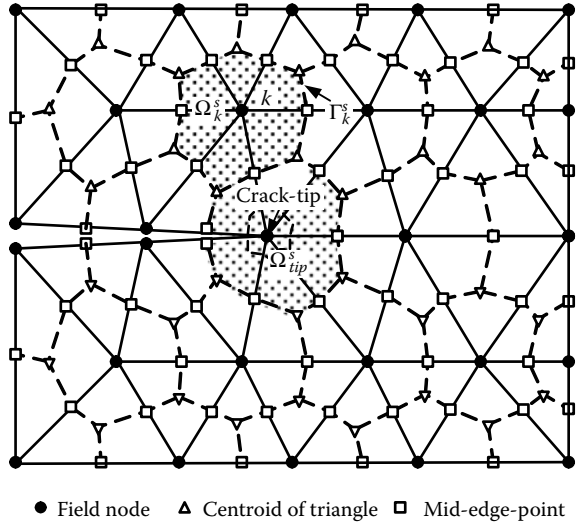

FIGURE 10.4 An sNS-FEM model. Basic mesh: linear T3 elements (solid lines). Node-based smoothing domains are bounded by dashed lines. One layer of six T5 crack-tip elements is used. Subdivisions for the smoothing domain of the crack-tip node may be needed.

capture the singularity near the crack-tip. The following are four schemes for the construction of subsmoothing domains (S-SDs) for the crack-tip node smoothing domain.

10.4.1 Scheme 1: One-Layer Edge-Based Subdivision: sNS-FEM-T3(1)

Figure 10.5 shows the Scheme 1 for the subdivision of the smoothing domain for the crack-tip node. It is clear that Scheme 1 divides the crack-tip node smoothing domain into one layer of smoothing domains based on the crack-tip element edges leading to the crack-tip node. In the particular case shown in Figure 10.5, we have seven subdivisions corresponding to the seven element edges connecting the crack-tip node. For the crack-tip edge on the boundary (crack surface), the sub-smoothing domain is a half of that in the element on the boundary. The boundary S-SD is created by connecting sequentially the following points: the crack-tip node, the mid-edge-point, the centroid of the singular element on the edge, and then returning to the crack-tip. For example, the S-SD$^{(1)}$ shown in Figure 10.5 is created by connecting sequentially points #*A*, #*B*, #*C*, and #*A*.

For the inner crack-tip edge, the subsmoothing domain consists of two halves of two elements sharing the edge. It is created by connecting sequentially the following points: the crack-tip node, the centroid of one adjacent singular element on the edge, the mid-edge-point, the centroid of another adjacent singular element, and then returning to the crack-tip. For example,

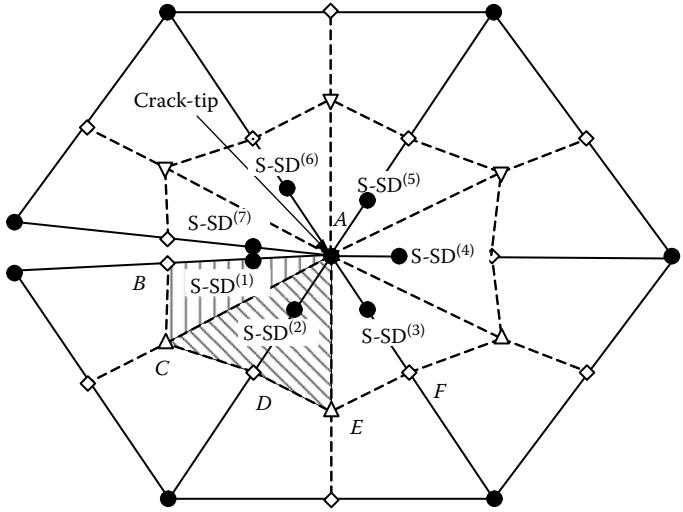

FIGURE 10.5 Subdivision of the smoothing domain for the crack-tip node: Scheme 1: one-layer edge-based subdivision. In this particular case, we have seven subdivisions corresponding to the seven element edges connecting the crack-tip node (7 S-SDs).

the S-SD$^{(2)}$ shown in Figure 10.5 is created by connecting sequentially points #*A*, #*C*, #*D*, #*E*, and #*A*.

The sNS-FEM using T3 elements and Scheme 1 is noted as sNS-FEM-T3(1).

10.4.2 Scheme 2: Two-Layer Edge-Based Subdivision: sNS-FEM-T3(2)

Figure 10.6 shows schematically Scheme 2 for the subdivision of the crack-tip nodal smoothing domain. It is exactly the same as Scheme 1, but with two layers. In this case we have a total of 14 subsmoothing domains (14 S-SDs): the outer layer has S-SD$^{(1)}$ to S-SD$^{(7)}$, and the inner layer has S-SD$^{(8)}$ to S-SD$^{(14)}$. The dimension in the radial direction of the inner subsmoothing domains is set at 1/8 of the element length in that direction. For example, for the subsmoothing domains in the outer layer, the S-SD$^{(1)}$ shown in Figure 10.6 is created by connecting sequentially #*B*, #*C*, #*C*″, #*B*″, and #*B*, where the positions of points #*B*″ and #*C*″ are defined from points #*A*, #*B*′, and #*C*′ with offset distances of $\overline{AB}'' = (\overline{AB'}/8)$ and $\overline{AC''} = (\overline{AC'}/8)$. S-SD$^{(2)}$ is created by connecting sequentially #*C*, #*D*, #*E*, #*E*″, #*D*″, #*C*″, and #*C*, where the positions of points #*E*″ and #*D*″ are defined from points #*A*, #*E*′, and #*D*′ with offset distances of $\overline{AE''} = (\overline{AE'}/8)$ and $\overline{AD''} = (\overline{AD'}/8)$. For the subsmoothing domains in the inner layer, S-SD$^{(8)}$ is constructed by connecting sequentially #*A*, #*B*″, #*C*″, and #*A*, and S-SD$^{(9)}$ is constructed by connecting sequentially #*A*, #*C*″, #*D*″, #*E*″, and #*A*.

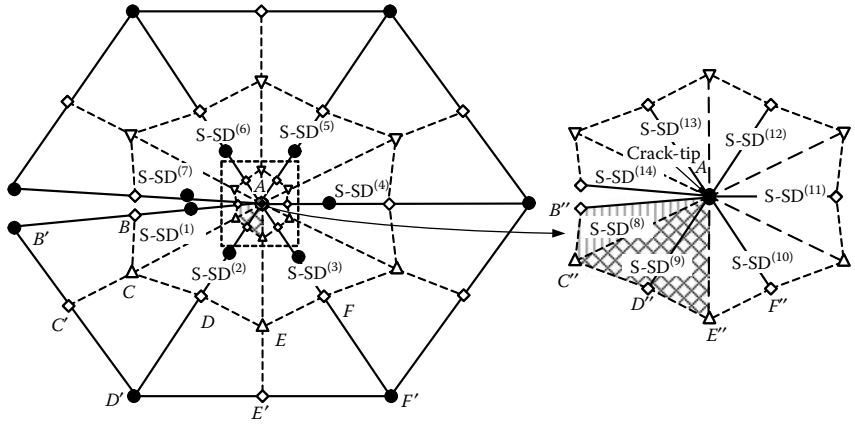

FIGURE 10.6 Subdivision of the smoothing domain for the crack-tip node: Scheme 2, two-layer edge-based subdivision. The division is similar to Scheme 1, but has two layers. In this particular case, we have 14 subdivisions (14 S-SDs), seven S-SDs for each layer.

The sNS-FEM using T3 elements and Scheme 2 is noted as sNS-FEM-T3(2).

10.4.3 Scheme 3: One-Layer Cell-Based Subdivision: sNS-FEM-T3(3)

Figure 10.7 shows Scheme 3 for the subdivision of the smoothing domain of the crack-tip node: one-layer cell-based subdivision. The division is similar to Scheme 1, but it is based on cells (i.e., the 1/3) of the singular element connected to the crack-tip. Since there are six elements in this case, we have six subdivisions. For example, the S-SD$^{(2)}$ is formed by connecting points #*A*, #*D*, #*E*, and #*F*.

The sNS-FEM using T3 elements and Scheme 3 is noted as sNS-FEM-T3(3).

10.4.4 Scheme 4: Two-Layer Cell-Based Subdivision: sNS-FEM-T3(4)

Figure 10.8 shows Scheme 4 for the subdivision of the smoothing domain of the crack-tip node: two-layer cell-based subdivision. Scheme 4 is similar to Scheme 3, but with two layers. In this particular case, we have a total of 12 subdivisions, six S-SDs for each layer. The dimension in the radial

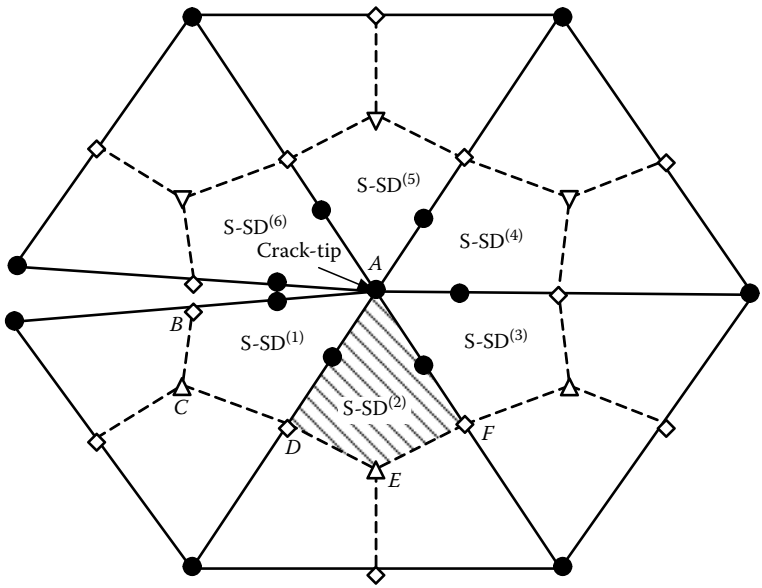

FIGURE 10.7 Scheme 3, one-layer cell-based subdivision. The division is similar to Scheme 1, but it is based on cells (i.e., the 1/3) of the element connected to the crack-tip. There are six elements in this case; hence we have six subdivisions (6 S-SDs).

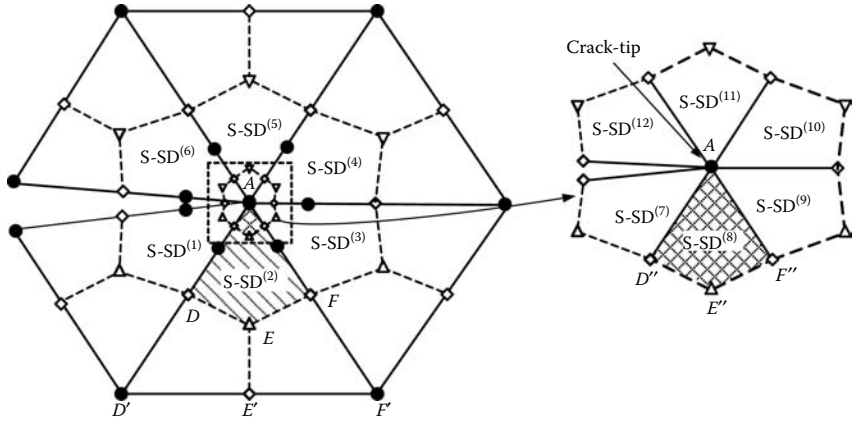

FIGURE 10.8 Scheme 4: two-layer cell-based subdivision. The division is similar to Scheme 3, but with two layers. In this particular case, we have a total of 12 subdivisions, six S-SDs for each layer.

direction of the inner subsmoothing domains is set at 1/8 of the element length in that direction. For example, for the subsmoothing domains in the outer layer, the S-SD$^{(2)}$ shown in Figure 10.8 is created by connecting sequentially #D'', #D, #E, #F, F'', E'', and D'', where the positions of points #D'', #E'', and #F'' are defined from points #A, #E', #D', and #F' with offset distances of $\overline{AD''} = (\overline{AD'}/8)$, $\overline{AE''} = (\overline{AE'}/8)$, and $\overline{AF''} = (\overline{AF'}/8)$. For the subsmoothing domains in the inner layer, S-SD$^{(8)}$ is constructed by connecting sequentially #A, #D'', #E'', F'', and #A.

The sNS-FEM using T3 elements and Scheme 4 is noted as sNS-FEM-T3(4).

10.5 sES-FEM Models

As discussed in Chapter 7, the ES-FEM model uses smoothing domains created based on the edges of the element mesh, and it is found to be a "star" performer. It is thus chosen for fracture problems in this section. Figure 10.9 shows schematically the construction of edge-based strain smoothing domains for sES-FEM models with one layer of six five-node crack-tip elements with the intermediate nodes at the $\frac{1}{4}$ edge length. For all the edges other than those connected to the crack-tip node, the treatments for the smoothing domains are exactly the same as in the ES-FEM discussed in Chapter 7. For the smoothing domains of crack-tip edges leading to the crack-tip node, however, special treatments are required to better capture

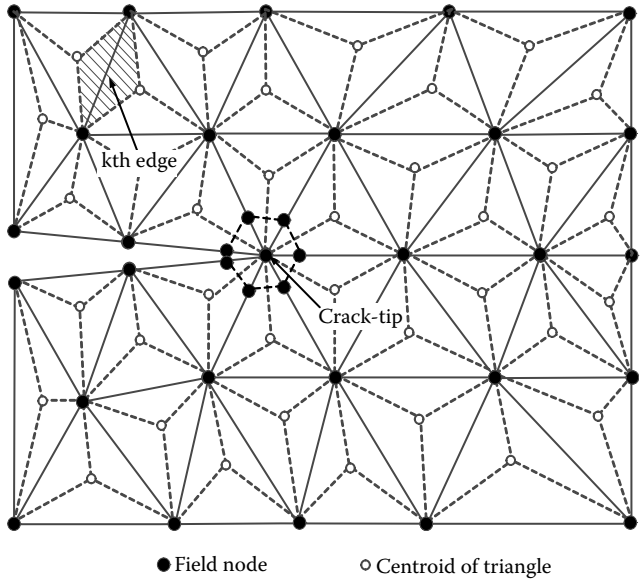

FIGURE 10.9 An sES-FEM model. Basic mesh: linear T3 elements (solid lines). Edge-based smoothing domains are bounded by dashed lines. One layer of six T5 crack-tip elements. Subdivisions for smoothing domains for crack-tip edges connected to the crack-tip node may be needed.

the singularity near the crack-tip. The following are the three schemes for the construction of subsmoothing domains for these smoothing domains of crack-tip edges.

10.5.1 Scheme 1: One Smoothing Domain per Edge

Consider the smoothing domain for edge 1-2 (where node 1 is at the crack-tip) shared by two crack-tip elements (1-4-2-3-5 and 1-7-6-2-4) as shown in Figure 10.10. In this case, only one smoothing domain (S-SD=1) for the crack-tip edge 1-2 is used. The smoothing domain is constructed in the same way as in the standard ES-FEM by connecting 1-C_2-2-C_1-1, where C_1 is the centroid of element 1-4-2-3-5, and C_2 is the centroid of the neighboring element 1-7-6-2-4 sharing the same edge 1-2.

10.5.2 Scheme 2: Two Subsmoothing Domains per Edge

Figure 10.11 shows Scheme 2 for the subdivision of the edge-based smoothing domain of the crack-tip edge 1-2. Two subsmoothing domains are used for the crack-tip edge. S-SD1 is formed by connecting 4-B_2-C_2-2-C_1-B_1-4,

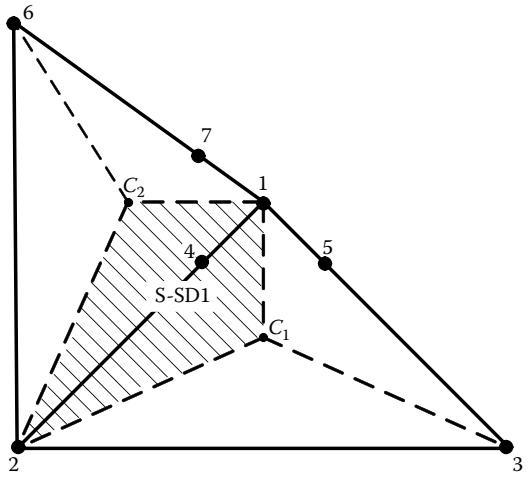

FIGURE 10.10 Scheme 1: One subsmoothing domain (S-SD=1) is used for the crack-tip edge 1-2 (the crack-tip node 1). The smoothing domain for edge 1-2 shared by two elements (1-4-2-3-5 and 1-7-6-2-4) is constructed in the same way as in the ES-FEM by connecting 1-C_2-2-C_1-1.

and S-SD2 is formed by connecting 1-B_2-4-B_1-1, where B_1 is the cross point of the two lines 1-C_1 and 4-5 for element 1-4-2-3-5, B_2 is the cross point of the two lines 1-C_2 and 4-7 for the neighboring element 1-7-6-2-4 sharing the same edge 1-2.

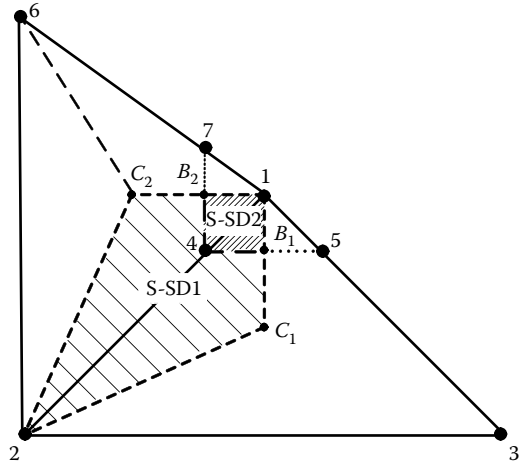

FIGURE 10.11 Scheme 2: Two subsmoothing domains (S-SD=2) are used for the crack-tip edge 1-2 (the crack-tip node 1). S-SD1 is formed by connecting 4-B_2-C_2-2-C_1-B_1-4 and S-SD2 is formed by connecting 1-B_2-4-B_1-1.

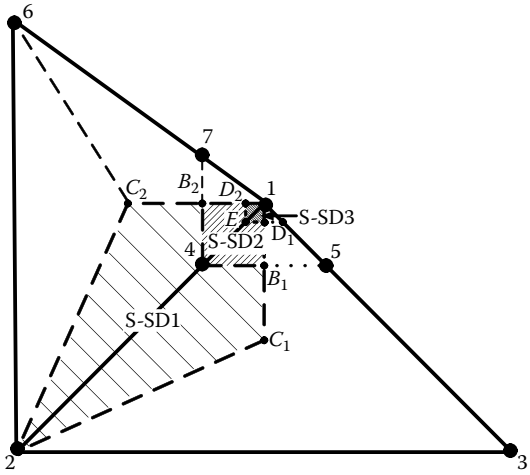

FIGURE 10.12 Scheme 3: Three subsmoothing domains (S-SD=3) are used for the crack-tip edge 1-2 (the crack-tip node 1). S-SD1 is formed by connecting 4-B_2-C_2-2-C_1-B_1-4; S-SD2 is formed by connecting E-D_2-B_2-4-B_1-D_1-E, and S-SD3 is formed by connecting 1-D_2-E-D_1-1.

10.5.3 Scheme 3: Three Subsmoothing Domains per Edge

Figure 10.12 shows Scheme 3 for the subdivision of the edge-based smoothing domain of the crack-tip edge 1-2. These three subsmoothing cells are as follows: S-SD1 is formed by connecting 4-B_2-C_2-2-C_1-B_1-4; S-SD2 is formed by connecting E-D_2-B_2-4-B_1-D_1-E, and S-SD3 is formed by connecting 1-D_2-E-D_1-1, where the positions of points #D_1, #E, and #D_2 are defined from points #1, #B_1, #4, and #B_2 with offset distances of $\overline{1-D_1} = (\overline{1-B_1}/4)$, $\overline{1-E} = (\overline{1-4}/4)$, and $\overline{1-D_2} = (\overline{1-B_2}/4)$.

10.6 Stiffness Matrix Evaluation

Based on the S-FEM procedure, the stiffness matrix of the whole model is the summation of the submatrices of these stiffness matrices associated with all the strain smoothing domains. The procedure is exactly the same as those given in Chapter 6 for NS-FEM models and Chapter 7 for ES-FEM models. The only differences are the following: (1) for the crack-tip area, more smoothing domains are used (each S-SD is treated as one independent smoothing domain), and (2) more Gauss points are needed along some of the boundary segments of these S-SDs to compute the smoothed strains for the S-SDs. Therefore, we will not repeat the detailed procedures here.

Instead, we will focus our discussions on the evolution of the physics of the fracture mechanics problems using S-FEM models.

10.7 *J*-Integral and SIF Evaluation

10.7.1 Line-Path for the *J*-Integral

Based on the linear elasticity, the general form of the J-integral value is identical to the energy release rate G of the potential energy. For a 2D crack the J-integral or G can be written as [8]

$$J = G = -\frac{\mathrm{d}}{\mathrm{d}a}\prod(\mathbf{u}) = -\int_{\Gamma_J}\left(\sigma_{ij}\frac{\partial u_i}{\partial x_1} - W(u_i)\delta_{1j}\right)n_j\,\mathrm{d}\Gamma,$$

$$i = 1 \text{ or } 2, \quad j = 1 \text{ or } 2, \tag{10.23}$$

where a is the crack length, Γ_J is an arbitrary line-path for the integration that encloses the crack-tip located at the origin of the coordinate system, as shown in Figure 10.13, n_j is the outward unit normal on Γ_J, σ_{ij} is the stress, and u_i is the ith displacement component.

In Equation 10.23, Π is the potential energy for the crack to grow and W is the strain potential energy (density) for the whole model:

$$W = \frac{1}{2}\sigma_{ij}c_{ijkl}\varepsilon_{kl}. \tag{10.24}$$

10.7.2 Area-Path for *J*-Integral

Theoretically, we know that the J value is integration path independent. Numerically however, we surely observe some path dependence, owing

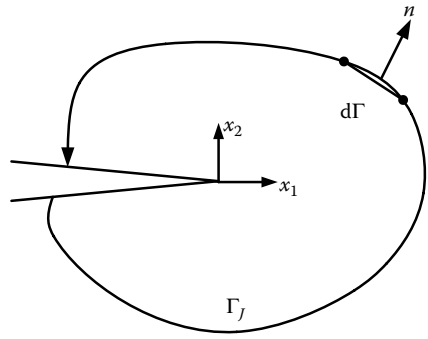

FIGURE 10.13 Line-path for the J-integral that encloses the crack-tip.

to numerical errors. To achieve better "numerical" path independence for the J value, we often use a so-called area-path in lieu of the line-path for the integration [9–11]. The J-integral can then be defined in the form of

$$J = \int_{A_J} \left(\sigma_{ij} \frac{\partial u_i}{\partial x_1} - W \delta_{1j} \right) \frac{\partial q}{\partial x_j} \, \mathrm{d}A, \tag{10.25}$$

where A_J is area-path enclosed by the union of these line segments Γ_{J1}, Γ_-, Γ_{J2}, and Γ_+, as shown in Figure 10.14. The segments Γ_- and Γ_+ are, respectively, the boundaries of the lower and upper crack faces. q is a sufficiently smooth weight function defined over A_J. We will discuss in Sections 10.8.3 and 10.8.4 how A_J and q should be constructed for our sS-FEM models. With such a construction, we will then show a simple proof of the identity of the area-path equation 10.25 and the line-path equation 10.23.

10.7.3 Mixed Mode and *J*-Integral

For the general fracture problems of mixed mode in an isotropic material, the relationship between the value of the J-integral and the two SIFs can be given as

$$J = \frac{K_{\mathrm{I}}^2 + K_{\mathrm{II}}^2}{E'}, \tag{10.26}$$

where K_{I} is the SIF value for the pure opening mode I, K_{II} is the SIF value for the pure shearing mode II, and E' is the material constant related to

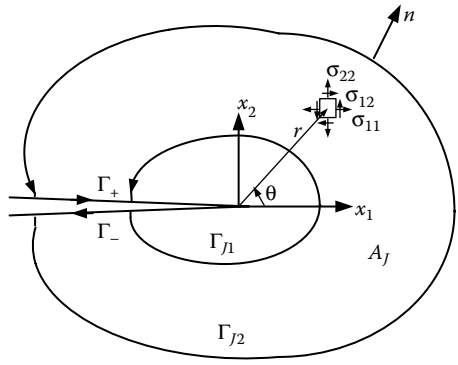

FIGURE 10.14 Area-path for the J-integral that encloses the crack-tip.

Young's modulus E and Poisson's ratio ν in the form of

$$E' = \begin{cases} E & \text{(plane stress)}, \\ \dfrac{E}{1-\nu^2} & \text{(plane strain)}. \end{cases} \tag{10.27}$$

For the cases of pure mode I, Equation 10.26 is reduced to

$$J = \frac{K_{\mathrm{I}}^2}{E'}. \tag{10.28}$$

Similarly, for pure mode II, we shall have

$$J = \frac{K_{\mathrm{II}}^2}{E'}. \tag{10.29}$$

Therefore, once J is found, we can easily obtain the value of K_{I} and K_{II}, as long as the fracture mode is purely either mode I or mode II. However, for the mixed mode problems, simply using one J-integral value is not sufficient to obtain two SIF values, because the J value relates both SIFs in a coupled manner for mixed mode in the form of Equation 10.26. We need to establish two states of the cracked body to extract these two values of K_{I} and K_{II}, which leads to the so-called interaction integral method [9–11].

10.8 Interaction Integral Method for Mixed Mode

10.8.1 Mixed Mode

In the interaction integral method, two states of a cracked body are used to evaluate these two SIFs in the coupled field. State 1 with field variables $(\sigma_{ij}^{(1)}, \varepsilon_{ij}^{(1)}, u_i^{(1)})$ corresponds to the coupled state of the mixed mode, and state 2 with field variables $(\sigma_{ij}^{(2)}, \varepsilon_{ij}^{(2)}, u_i^{(2)})$ is an *auxiliary* state. The asymptotic fields for mode I or II are chosen as an auxiliary state 2. The following two conditions exist for these SIFs for the auxiliary fields:

$$\begin{aligned} &K_{\mathrm{I}}^{(2)} = 1 \ \text{ and } \ K_{\mathrm{II}}^{(2)} = 0 \quad \text{when pure mode I is chosen as state 2,} \\ &K_{\mathrm{I}}^{(2)} = 0 \ \text{ and } \ K_{\mathrm{II}}^{(2)} = 1 \quad \text{when pure mode II is chosen as state 2.} \end{aligned} \tag{10.30}$$

The parameters of $\sigma_{ij}^{(2)}, \varepsilon_{ij}^{(2)}, u_i^{(2)}$, $(i, j = 1, 2)$ for the auxiliary state can be evaluated from the following relations [12].

For pure mode I, the stresses and displacements can be calculated as

$$\begin{aligned}
\sigma_{11}^{(2)} &= \frac{K_{\mathrm{I}}^{(2)}}{\sqrt{2\pi r}} \cos\frac{\theta}{2}\left(1-\sin\frac{\theta}{2}\sin\frac{3\theta}{2}\right),\\
\sigma_{22}^{(2)} &= \frac{K_{\mathrm{I}}^{(2)}}{\sqrt{2\pi r}} \cos\frac{\theta}{2}\left(1+\sin\frac{\theta}{2}\sin\frac{3\theta}{2}\right),\\
\sigma_{12}^{(2)} &= \frac{K_{\mathrm{I}}^{(2)}}{\sqrt{2\pi r}} \cos\frac{\theta}{2}\sin\frac{\theta}{2}\cos\frac{3\theta}{2},\\
\sigma_{12}^{(2)} &= \sigma_{21}^{(2)},\\
u_1^{(2)} &= \frac{K_{\mathrm{I}}^{(2)}(1+\nu)\sqrt{r}}{E\sqrt{2\pi}} \cos\frac{\theta}{2}(\kappa-\cos\theta),\\
u_2^{(2)} &= \frac{K_{\mathrm{I}}^{(2)}(1+\nu)\sqrt{r}}{E\sqrt{2\pi}} \sin\frac{\theta}{2}(\kappa-\cos\theta),
\end{aligned} \tag{10.31}$$

where r and θ are polar coordinates that are measured from the origin at the crack-tip node, and κ is defined as

$$\kappa = \begin{cases} \dfrac{3-\nu}{1+\nu} & \text{(plane stress)},\\ 3-4\nu & \text{(plane strain)}. \end{cases} \tag{10.32}$$

For pure mode II, we shall have

$$\begin{aligned}
\sigma_{11}^{(2)} &= \frac{-K_{\mathrm{II}}^{(2)}}{\sqrt{2\pi r}} \sin\frac{\theta}{2}\left(2+\cos\frac{\theta}{2}\cos\frac{3\theta}{2}\right),\\
\sigma_{22}^{(2)} &= \frac{K_{\mathrm{II}}^{(2)}}{\sqrt{2\pi r}} \cos\frac{\theta}{2}\sin\frac{\theta}{2}\cos\frac{3\theta}{2},\\
\sigma_{12}^{(2)} &= \frac{K_{\mathrm{II}}^{(2)}}{\sqrt{2\pi r}} \cos\frac{\theta}{2}\left(1-\sin\frac{\theta}{2}\sin\frac{3\theta}{2}\right),\\
\sigma_{12}^{(2)} &= \sigma_{21}^{(2)},\\
u_1^{(2)} &= \frac{K_{\mathrm{II}}^{(2)}(1+\nu)\sqrt{r}}{E\sqrt{2\pi}} \sin\frac{\theta}{2}(\kappa+2+\cos\theta),\\
u_2^{(2)} &= \frac{-K_{\mathrm{II}}^{(2)}(1+\nu)\sqrt{r}}{E\sqrt{2\pi}} \cos\frac{\theta}{2}(\kappa-2+\cos\theta).
\end{aligned} \tag{10.33}$$

With the given displacement field, the strain can be calculated using

$$\varepsilon_{ij}^{(2)} = \frac{1}{2}\left(u_{i,j}^{(2)} + u_{j,i}^{(2)}\right). \tag{10.34}$$

In linear elastic fracture mechanics, the superimposition of fields can be performed and hence we shall have

$$\begin{aligned}\sigma_{ij}^{(1+2)} &= \sigma_{ij}^{(1)} + \sigma_{ij}^{(2)},\\ \varepsilon_{ij}^{(1+2)} &= \varepsilon_{ij}^{(1)} + \varepsilon_{ij}^{(2)},\\ u_i^{(1+2)} &= u_i^{(1)} + u_i^{(2)}.\end{aligned} \tag{10.35}$$

Similarly, for SIFs, we shall also have

$$\begin{aligned}K_{\mathrm{I}}^{(1+2)} &= K_{\mathrm{I}}^{(1)} + K_{\mathrm{I}}^{(2)},\\ K_{\mathrm{II}}^{(1+2)} &= K_{\mathrm{II}}^{(1)} + K_{\mathrm{II}}^{(2)}.\end{aligned} \tag{10.36}$$

Then the J-integral value for the combined states 1 and 2 will be derived using Equations 10.23 and 10.35 as

$$\begin{aligned}J^{(1+2)} = \int_{\Gamma_J} \Bigg[&\frac{1}{2}\left(\sigma_{ij}^{(1)} + \sigma_{ij}^{(2)}\right)\left(\varepsilon_{ij}^{(1)} + \varepsilon_{ij}^{(2)}\right)\delta_{1j}\\ &- \left(\sigma_{ij}^{(1)} + \sigma_{ij}^{(2)}\right)\frac{\partial\left(u_i^{(1)} + u_i^{(2)}\right)}{\partial x_1}\Bigg] n_j \,\mathrm{d}\Gamma.\end{aligned} \tag{10.37}$$

After expanding and rearranging terms, the above equation becomes

$$J^{(1+2)} = J^{(1)} + J^{(2)} + I^{(1,2)}, \tag{10.38}$$

where $I^{(1,2)}$ is called the "interaction integral" representing the interaction between states 1 and 2, and is expressed as

$$I^{(1,2)} = \int_{\Gamma_J} \left[W^{(1,2)}\delta_{1j} - \sigma_{ij}^{(1)}\frac{\partial u_i^{(2)}}{\partial x_1} - \sigma_{ij}^{(2)}\frac{\partial u_i^{(1)}}{\partial x_1}\right] n_j \,\mathrm{d}\Gamma, \tag{10.39}$$

in which $W^{(1,2)}$ is the interaction strain energy defined as

$$W^{(1,2)} = \sigma_{ij}^{(1)}\varepsilon_{ij}^{(2)} = \sigma_{ij}^{(2)}\varepsilon_{ij}^{(1)}. \tag{10.40}$$

On the other hand, based on Equation 10.26, the J-integral for the sum of states 1 and 2 relates to these SIFs in the form of

$$J^{(1+2)} = \frac{\left(K_{\mathrm{I}}^{(1+2)}\right)^2}{E'} + \frac{\left(K_{\mathrm{II}}^{(1+2)}\right)^2}{E'}. \tag{10.41}$$

Using Equation 10.36, we arrive at

$$J^{(1+2)} = J^{(1)} + J^{(2)} + \frac{2}{E'}\left(K_{\mathrm{I}}^{(1)}K_{\mathrm{I}}^{(2)} + K_{\mathrm{II}}^{(1)}K_{\mathrm{II}}^{(2)}\right). \tag{10.42}$$

Comparison between Equations 10.38 and 10.42 gives

$$I^{(1,2)} = \frac{2}{E'}\left(K_{\mathrm{I}}^{(1)}K_{\mathrm{I}}^{(2)} + K_{\mathrm{II}}^{(1)}K_{\mathrm{II}}^{(2)}\right). \tag{10.43}$$

Finally, by choosing an asymptotic field (for state 2) as either the field for the pure mode I or the pure mode II, the SIFs at each chosen mode can be computed using

$$\begin{aligned} K_{\mathrm{I}} &= K_{\mathrm{I}}^{(1)} = \frac{2}{E'} I^{(1,\text{Mode I})}, \\ K_{\mathrm{II}} &= K_{\mathrm{II}}^{(1)} = \frac{2}{E'} I^{(1,\text{Mode II})}. \end{aligned} \tag{10.44}$$

In summary, for evaluating SIFs in a mixed-mode problem, the interaction integral in Equation 10.39 can be evaluated first. SIFs for the mixed mode can then be easily calculated using Equation 10.44 for a chosen state 2. For better path-independent numerical results, we will also use an area-path integral form of the interaction integral [9–11]:

$$I^{(1,2)} = -\int_{A_J}\left[w^{(1,2)}\delta_{1j} - \sigma_{ij}^{(1)}\frac{\partial u_i^{(2)}}{\partial x_1} - \sigma_{ij}^{(2)}\frac{\partial u_i^{(1)}}{\partial x_1}\right]\frac{\partial q}{\partial x_j}\,\mathrm{d}A. \tag{10.45}$$

This area-path interaction integral will be used in our work to compute $I^{(1,\text{Mode I})}$ and $I^{(1,\text{Mode II})}$, and then the SIFs will be calculated using Equation 10.44. We will discuss in Sections 10.8.3 and 10.8.4 how A_J and q should be constructed for our sS-FEM models. With such a construction, we will then show a simple proof that Equation 10.45 is identical to the original line-path integral defined in Equation 10.39.

10.8.2 Interface Cracks

For cracks located along the interface between two materials, the problem become more complicated, and the complex SIF $K_C = K_{\mathrm{I}} + iK_{\mathrm{II}}$ should be used. The in-plane tractions at a distance r ahead of the crack-tip are given by [13]

$$(\sigma_{22} + i\tau_{12})_{\theta=0} = \frac{K_C r^{i\varepsilon}}{\sqrt{2\pi r}}, \tag{10.46}$$

where $i = \sqrt{-1}$, and ε is the bimaterial constant given by

$$\varepsilon = \frac{1}{2\pi} \log\left(\frac{1-\beta}{1+\beta}\right), \tag{10.47}$$

in which β is the second Dundurs parameter defined as [14]

$$\beta = \frac{\mu_1(\kappa_2 - 1) - \mu_2(\kappa_1 - 1)}{\mu_1(\kappa_2 + 1) + \mu_2(\kappa_1 + 1)}, \tag{10.48}$$

with

$$\kappa_i = \begin{cases} \dfrac{3 - v_i}{1 + v_i} & \text{(plane stress)} \\ 3 - 4v_i & \text{(plane strain)} \end{cases}, \quad (i = 1, 2). \tag{10.49}$$

The material constants μ_i, v_i, and κ_i $(i = 1, 2)$ are, respectively, the shear modulus, Poisson's ratio, and the Kolosov constant. The J-integral value or the energy release rate G relates to the SIF amplitude for the interface crack as follows [13,15]:

$$J = G = \frac{1}{E^*} \frac{|K_{\mathrm{C}}|^2}{\cosh^2(\pi\varepsilon)}, \quad |K_{\mathrm{C}}|^2 = K_{\mathrm{C}}\bar{K}_{\mathrm{C}} = K_{\mathrm{I}}^2 + K_{\mathrm{II}}^2, \tag{10.50}$$

where

$$\frac{2}{E^*} = \frac{1}{E_1'} + \frac{1}{E_2'}, \qquad E_i' = \begin{cases} E_i & \text{(plane stress),} \\ \dfrac{E_i}{1 - v_i^2} & \text{(plane strain).} \end{cases} \tag{10.51}$$

Using a similar procedure as that for the mixed mode given in Section 10.8 for the interface crack, we shall have

$$I^{(1,2)} = \frac{2}{E^*} \frac{K_{\mathrm{I}}^{(1)} K_{\mathrm{I}}^{(2)} + K_{\mathrm{II}}^{(1)} K_{\mathrm{II}}^{(2)}}{\cosh^2(\pi\varepsilon)} \quad \text{(interface crack).} \tag{10.52}$$

Choosing an auxiliary state 2 as the pure mode I asymptotic fields, we shall have $K_{\mathrm{I}}^{(2)} = 1$, $K_{\mathrm{II}}^{(2)} = 0$, and K_{I} can then be computed using

$$K_{\mathrm{I}} = K_{\mathrm{I}}^{(1)} = \frac{E^* \cosh^2(\pi\varepsilon)}{2} I^{(1,\text{Mode I})} \quad \text{(interface crack).} \tag{10.53}$$

Choosing next an auxiliary state 2 as the pure mode II asymptotic fields, we have $K_{\mathrm{II}}^{(2)} = 1$, $K_{\mathrm{I}}^{(2)} = 0$, and K_{II} can now be computed using

$$K_{\mathrm{II}} = K_{\mathrm{II}}^{(1)} = \frac{E^* \cosh^2(\pi\varepsilon)}{2} I^{(1,\text{Mode II})} \quad \text{(interface crack).} \tag{10.54}$$

We now need to determine the area-path for the interaction integral.

10.8.3 Determination of Area-Path

Because our sS-FEM model uses a basic mesh of linear T3 elements, a simple scheme can be devised to determine the area-path A_J shown in Figure 10.15. First, a set of elements having at least one node within a circle of radius r_d is found, and this element set is denoted as S_e. If all the nodes of an element e are all inside the circle, it belongs to the element set S_e^{in}. The area occupied by the element set S_e^{in} is noted as A_e^{in}, and the outer boundary of area A_e^{in} gives the line-path Γ_{J1} (see Figure 10.14). The intersection of sets S_e and S_e^{in} forms element set: $S_e^A = S_e \cap S_e^{\text{in}}$. The element set S_e^A then forms the area-path A_J, and the outer boundary of S_e^A forms the line-path Γ_{J2} (see Figures 10.14 and 10.15). Because three-node elements are used in our sS-FEM, any circle will naturally always select a layer of elements that form A_J.

10.8.4 Determination of Function *q*

The weighting function q used in the area-path interaction integral (Equation 10.45) is then chosen as a piecewise linear function passing through the

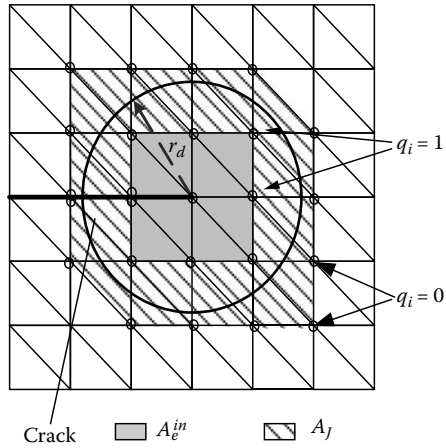

FIGURE 10.15 Determination of area-path for the interaction integral and weight function q.

nodal values at all the nodes belonging to all the elements in S_e. If a node n_i belonging to any element $e \in S_e$ lies outside the circle, then the nodal value of the weighting function is set to zero: $q_i = 0$ (see Figure 10.15); if a node n_i lies inside the circle, the weighting function is then set to unity $q_i = 1$. A function form via linear interpolation using all these nodal values q_i is differentiable in any of these elements, and hence is "sufficiently" smooth, because Equation 10.45 requires only the first differentiation (in a piecewise manner). Since the elements set S_e^{in} has all the nodes inside the circle as shown in Figure 10.15, the weight function will be a constant (unit) within all these elements in set S_e^{in}. Because the gradient of q is used in Equation 10.45, the element set S_e^{in} will contribute nothing to the area-path interaction integral. This is precisely the reason why the area-path A_J does not include the area occupied by all these elements in set S_e^{in}, and only elements in set S_e^A are included.

The function of $q(\mathbf{x})$ at any point $\mathbf{x}$ inside A_J can be found using a simple interpolation using the nodal values q_i:

$$q(\mathbf{x}) = \sum_{i=1}^{n_n^e} N_i(\mathbf{x}) q_i, \tag{10.55}$$

where n_n^e is the number of nodes of the element hosting $\mathbf{x}$, and $N_i(\mathbf{x})$ is the shape function for that element.

With $q(\mathbf{x})$ being clearly defined in Equation 10.55, integration given in Equation 10.45 can be evaluated easily via the usual Gauss integration technique.

10.8.5 A Simple Proof of Equivalence of the Line-Path and Area-Path Integrals

Note that using the A_J and $q(\mathbf{x})$ defined above, we have essentially made the value of $q(\mathbf{x})$ at all the nodes located on Γ_{J2} to be zero, and on Γ_{J1} to be 1. Because we use linear interpolations, $q(\mathbf{x})$ will be zero everywhere on Γ_{J2}, and unity everywhere on Γ_{J1}. We can now easily show the following identity:

$$\begin{aligned} J &= -\int_{A_J} \left(W\delta_{1j} - \sigma_{ij} \frac{\partial u_i}{\partial x_1} \right) \frac{\partial q}{\partial x_j} \, \mathrm{d}A \\ &= -\int_{\Gamma_A} \underbrace{\left[\left(W\delta_{1j} - \sigma_{ij} \frac{\partial u_i}{\partial x_1} \right) \right]}_{g} q n_j \, \mathrm{d}\Gamma \quad \text{(Green's theorem)} \end{aligned}$$

$$= -\underbrace{\int_{\Gamma_{J2}} gqn_j \, d\Gamma}_{\therefore q=0, \therefore =0} - \underbrace{\int_{\Gamma_+} gqn_j \, d\Gamma}_{\substack{\therefore \text{ free traction} \\ \text{on } \Gamma_+, \therefore =0}} + \int_{\Gamma_{J1}} gqn_j \, d\Gamma - \underbrace{\int_{\Gamma_-} gqn_j \, d\Gamma}_{\substack{\therefore \text{ free traction} \\ \text{on } \Gamma_+, \therefore =0}}$$

$$= \underbrace{\int_{\Gamma_{J1}} \left[\left(W\delta_{1j} - \sigma_{ij} \frac{\partial u_i}{\partial x_1} \right) \right] n_j \, d\Gamma}_{\substack{J\text{-integral in the original} \\ \text{form of line path}}} \quad (\therefore q = 1 \text{ on } \Gamma_{J1}). \tag{10.56}$$

In the second line of the above derivation, we used Green's theorem of divergence and $\Gamma_A = \Gamma_{J2} \cup (-\Gamma_{J1}) \cup \Gamma_- \cup \Gamma_+$ is the line-path that encloses the area-path A_J, as shown in Figure 10.14. We also use the fact that [16,17]

$$\frac{\partial}{\partial x_j} \left(\sigma_{ij} \frac{\partial u_i}{\partial x_1} - w\delta_{1j} \right) = 0. \tag{10.57}$$

This proves that the area-path integration given in Equation 10.25 is identical to the original line-path integral defined in Equation 10.23 along the line-path J_1.

A similar procedure can be used to show the same identity for the following interaction integrals:

$$I^{(1,2)} = -\int_{A_J} \left[W^{(1,2)}\delta_{1j} - \sigma_{ij}^{(1)} \frac{\partial u_i^{(2)}}{\partial x_1} - \sigma_{ij}^{(2)} \frac{\partial u_i^{(1)}}{\partial x_1} \right] \frac{\partial q}{\partial x_j} dA$$

$$= -\int_{\Gamma_J} \underbrace{\left[W^{(1,2)}\delta_{1j} - \sigma_{ij}^{(1)} \frac{\partial u_i^{(2)}}{\partial x_1} - \sigma_{ij}^{(2)} \frac{\partial u_i^{(1)}}{\partial x_1} \right]}_{g} qn_j \, d\Gamma \text{ (Green's theorem)}$$

$$= -\underbrace{\int_{\Gamma_{J2}} gqn_j \, d\Gamma}_{\therefore q=0 \text{ on } \Gamma_{J2}, \therefore =0} - \underbrace{\int_{\Gamma_+} gqn_j \, d\Gamma}_{\substack{\therefore \text{free traction} \\ \text{on } \Gamma_+, \therefore =0}} + \int_{\Gamma_{J1}} gqn_j \, d\Gamma - \underbrace{\int_{\Gamma_-} gqn_j \, d\Gamma}_{\substack{\therefore \text{ free traction} \\ \text{on } \Gamma_+, \therefore =0}}$$

$$= \underbrace{\int_{\Gamma_{J1}} \left[W^{(1,2)}\delta_{1j} - \sigma_{ij}^{(1)} \frac{\partial u_i^{(2)}}{\partial x_1} - \sigma_{ij}^{(2)} \frac{\partial u_i^{(1)}}{\partial x_1} \right] n_j \, d\Gamma}_{I^{(1,2)} \text{ the original line-path integral}} \ (\therefore q = 1 \text{ on } \Gamma_{J1}).$$

(10.58)

This proves that the area-path integration given in Equation 10.45 is identical to the original line-path integral defined in Equation 10.39 along the line-path J_1.

In all the example problems presented in this chapter, we always use the area-path integrals for numerical results of better path independence.

10.9 Numerical Examples Solved Using sES-FEM-T3

In this section, examples are presented to demonstrate the accuracy of sES-FEM using triangular elements (sES-FEM-T3) for solution outputs of the strain energy, the SIFs, as well as the displacements. Fracture problems of mode I, mode II, and mixed mode will be considered. For comparison purposes, all the problems are also solved using FEM-T3 and standard ES-FEM-T3 and sES-FEM-T3 using the same basic mesh of linear T3 elements. The effects of different values of λ that change the intermediate node locations on the crack-tip edges connecting to the crack-tip node are first investigated in detail. The effect of the number of subsmoothing domains and the number of Gauss points on the sES-FEM-T3 solution outputs will then be examined.

To study the accuracy of the solutions quantitatively, the relative error is defined as

$$e_s = \frac{s^{\text{numerical}} - s^{\text{exact}}}{s^{\text{exact}}} \times 100\%, \tag{10.59}$$

where s denotes a solution output (K_{I} or K_{II} or J), the superscript "exact" denotes the exact or analytical solution, and the superscript "numerical" denotes a numerical solution obtained using a numerical method. From Equation 10.59, it is clear that a negative relative error indicates that the numerical solution is smaller than the exact one, and vice versa.

Example 10.9.1: A Plate with a Central Crack Subjected to Tension (Mode I)

We first consider the simplest fracture problem: a rectangular plate (2D solid) of homogeneous isotropic material containing a horizontal central crack. The plate is subjected to a tension load in the vertical direction, as shown in Figure 10.16. Under this setting, the fracture problem is of pure mode I. The parameters used in this analysis are plate width $w = 10.0$ cm, plate length $L = 25.0$ cm, crack length $a = 4$ cm, and unit tension force $\sigma = 1$ N/cm^2. The material constants are $E = 3 \times 10^7$ N/cm^2 and $\nu = 0.25$. The analytical solution of SIFs for

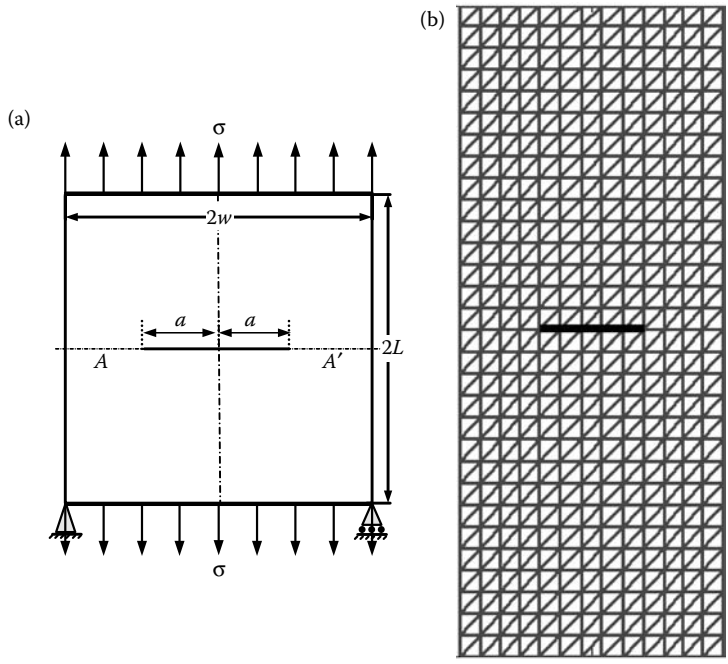

FIGURE 10.16 (a) A rectangular plate with a central crack subject to tension (pure mode I) and (b) a typical mesh with 904 DOFs used for the rectangular plate with a central crack subjected to tension.

such a structure is given by Tada et al. [12]:

$$K_{\mathrm{I}} = \sigma\sqrt{\pi a}\left[1 - 0.025\left(\frac{a}{w}\right)^2 - 0.06\left(\frac{a}{w}\right)^4\right]\left(\sec\left(\frac{\pi a}{2w}\right)\right)^{0.5}. \qquad (10.60)$$

Based on this formula the analytical value of the SIF for this plate is found as $K_{\mathrm{I}} = 3.9315\ \mathrm{Ncm}^{-3/2}$. The problem is then solved using sES-FEM-T3, together with FEM-T3 and ES-FEM-T3 for comparison and examination purposes.

EFFECTS OF THE POSITION OF THE INTERMEDIATE NODE (λ VALUE)

Using the sES-FEM-T3 with two subsmoothing domains (S-SD = 2) for the layer of crack-tip elements (see Figure 10.9), the effects of the intermediate node positions on the crack-tip edges have been examined by choosing different values of λ. The results in terms of the strain energy have been tabulated in Table 10.1 for models with different numbers of DOFs. The results are obtained

TABLE 10.1

Results in Strain Energy ($\times 10^{-5}$) for the Plate with Horizontal Central Crack Obtained Using sES-FEM-T3 with Two Subsmoothing Domains (S-SD=2) for the Crack-Tip Elements with Different Locations for the Mid-Edge Nodes

DOFs	904	1588	2268	8340
sES-FEM ($\lambda = 1/4$)	1.72204905	1.72497385	1.72548221	1.72632994
sES-FEM ($\lambda = 1/32$)	1.72406262	1.72573576	1.72657777	1.72714066
sES-FEM ($\lambda = 1/16$)	1.72406087	1.72573426	1.72657649	1.72713992
sES-FEM ($\lambda = 1/8$)	1.72406077	1.72573432	1.72657661	1.72713998
sES-FEM ($\lambda = 1/5$)	1.72406155	1.72573522	1.72657748	1.72714048
sES-FEM ($\lambda = 1/4$)	1.72406223	1.72574492	1.72657820	1.72714090
sES-FEM ($\lambda = 2/5$)	1.72406470	1.72573870	1.72658082	1.72714240
sES-FEM ($\lambda = 1/2$)	1.72406664	1.72574085	1.72658287	1.72714359
sES-FEM ($\lambda = 2/3$)	1.72407033	1.72574492	1.72658678	1.72714583

using a basically "uniform" mesh, a typical example of which is shown in Figure 10.16b. From Table 10.1 we note the following:

1. The strain energy results of the sES-FEM converge very fast, even though a uniform mesh is used without special zooming into the crack-tip. This is because the correct singular field at the crack-tip is properly simulated for any λ chosen between 0 and 1.
2. For any given set of nodes, the sES-FEM solution in terms of strain energy does not change significantly with the λ value, as shown in Table 10.1. When λ changes from 1/32 to 2/3, at least five significant digits in the solution data are not changed. This confirms our theoretical prediction that we can locate the intermediate node at any location on the crack-tip edge.

Due to these findings, we will use $\lambda = 1/4$ as a default for our sS-FEM models, just to be the same as what we do in the standard FEM singular elements. Note that, in contrast, the position of the intermediate node for a singular FEM element *has to* be fixed at $\lambda = 1/4$ at all times. In the following examples, $\lambda = 1/4$ is used for all the sS-FEM models, unless specified otherwise.

TABLE 10.2A

Comparison of Results in Strain Energy ($\times 10^{-5}$) for the Plate with a Horizontal Central Crack Obtained Using Different Methods Using Models of Different Nodal Density

DOFs	904	1588	2268	8340
FEM-T3	1.67057367	1.68487968	1.69090244	1.70843735
ES-FEM-T3	1.69587814	1.70545384	1.70903205	1.71841662
sES-FEM-T3 (S-SD=1, $\lambda = 1/4$)	1.72204905	1.72497385	1.72548221	1.72632994
sES-FEM-T3 (S-SD=2, $\lambda = 1/4$)	1.72406223	1.72574492	1.72657820	1.72714090

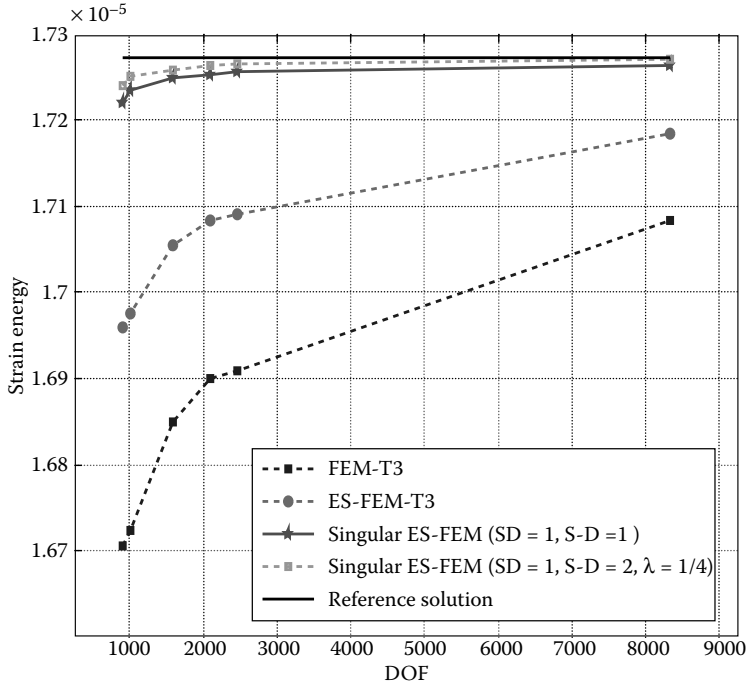

FIGURE 10.17 Strain energy results for the rectangular plate subjected to tension (mode I).

TABLE 10.2B

Comparison of the Strain Energy Error for the Plate with a Horizontal Central Crack Obtained Using Different Methods Using Models of Different Nodal Density

DOFs	**904**	**1588**	**2100**	**8340**
Number of elements	780	1428	1920	8000
h	1.132277034	0.836827409	0.721687836	0.353553390
FEM-T3	0.1810664063	0.1565320102	0.1468373569	0.1042259337
ES-FEM-T3	0.1346642869	0.1122070068	0.1043910483	0.0713115079
sFEM-T6	0.0674012351	0.0549345012	0.0493278031	0.0295496372
sES-FEM-T3 SIN(S-SD=2)	0.0546765192	0.0405327608	0.0388421147	0.0225298149

COMPARISON OF STRAIN ENERGY SOLUTIONS OF DIFFERENT MODELS

Figure 10.17 plots the comparison of results in strain energy for the plate with a horizontal central crack obtained using different methods and meshes with different numbers of nodes. These results are also tabulated in Table 10.2. From Figure 10.17 and Table 10.2, we note the following:

1. The strain energy results of all these models converge to the exact solution from below. This shows that these models all produce lower bound solution in terms of strain energy.
2. For any given set of nodes, the strain energy of the FEM-T3 is the lowest and that of the sES-FEM-T3 with S-SD=2 is the highest. This implies that the FEM-T3 model is the most "stiff," and the sES-FEM-T3 with S-SD=2 is the most "soft" among all these models compared. Because we know that all these solutions are lower bounds, we can conclude that the solution of sES-FEM-T3 with S-SD=2 is the most accurate, and the FEM-T3 is the worst. The accuracy (in terms of strain energy) ranking of these models would be sES-FEM-T3 with S-SD=2; sES-FEM-T3 with S-SD=1; ES-FEM-T3; and FEM-T3. The improvement of ES-FEM-T3 from FEM-T3 is very significant, showing clearly the benefit of the edge-based strain smoothing operations. The further improvement of sES-FEM-T3 from ES-FEM-T3 is also quite remarkable, showing the significance of the singular field approximation. Therefore, compared with FEM-T3, the sES-FEM-T3 has double significant improvement.
3. We also noticed that the results of sES-FEM-T3 with S-SD=1 and S-SD=2 are very close. For this particular example the first three digits in the results are exact. In general, this is also largely true. There will be cases where the results using S-SD=2 are noticeably better. Therefore, in many cases, we simply use sES-FEM-T3 with S-SD=1 for fracture problems, as this is much simpler and has almost not changed from the standard ES-FEM (except for the interpolation for the crack-tip elements). To be on the safer side, we can always use S-SD=2. The use of S-SD=3 or above can also further improve the solution, but not very significantly. A more detailed study on this issue can be found in Ref. [4], and some examples will also be shown later. In this chapter we will use either S-SD=1 or S-SD=2 for all sES-FEM-T3 models.
4. The ranking of the "stiffness" of all these models is FEM-T3, ES-FEM-T3, sES-FEM-T3 with S-SD=1, and sES-FEM-T3 with S-SD=2. This ranking can be well explained based on the theories of S-FEM models. We know already from Chapter 4 that ES-FEM will be softer than the FEM using the same mesh. By introducing the intermediate nodes to the crack-tip elements, we have much better simulated the displacement field for the areas near the crack-tip. This makes the

sES-FEM model softer than the ES-FEM. A similar argument was first put forward in Ref. [18].

5. Based on the monotonic convergence property (see Theorem 4.4), we expect (in the nonsingular cases) that when the number of smoothing domains is increased in a nested manner, the S-FEM models will become stiffer. Therefore, the strain energy solution should become smaller. This example, however, shows the opposite. In our opinion, this is because of the singularity of the field for our fracture problems. Although the use of more smoothing domains makes the model stiffer, at the same time it can also capture much better the singularity feature of the model, making the model softer. Because the singularity capturing is more significant to the solution, the increase of S-SDs in the crack-tip elements can result in a softer ES-FEM model that is a lower bound, as shown in this case.

In the following studies, we use sES-FEM-T3 with S-SD=1 as a default sES-FEM-T3 model. By sES-FEM-T3, we mean sES-FEM-T3 with S-SD=1. When S-SD=2 is used, we will specify it explicitly.

STRAIN ENERGY SOLUTION: CONVERGENCE RATE

Figure 10.18 plots the comparison of the strain energy error defined in Equation 4.65 for the plate with a horizontal central crack obtained using different models and meshes with different numbers of nodes. The element "length" is computed using

$$h = \sqrt{\frac{A_\Omega}{N_e}}, \tag{4.60}$$

where A_Ω is the area of the whole problem domain. These results are also tabulated in Table 10.2. From Table 10.2 and Figure 10.18, we note the following:

1. The convergence rate for FEM-T3 is reduced to below 0.5, which is much lower than the theoretical rate of 1.0 (using H^1 norm measure). This is because the problem is not *Lipschitzian* and has a "consequence" on the convergence rate of the numerical solutions.
2. The convergence rate for ES-FEM-T3 is reduced to below 0.55, which is much lower than the theoretical rate of 1.0, but quite higher than that of FEM-T3 (0.47). This shows the edge-based smoothing effects, mitigating some of the "consequences."
3. The convergence rate for sES-FEM-T3 is registered at 0.76. Although it is still lower than the theoretical rate of 1.0, it is much higher than that the convergence rate for FEM-T3 (0.47). It is even higher than that for FEM-T6 (0.71) with FEM crack-tip elements. The sES-FEM-T3 performs the best among all these models, in terms of both convergence rate and accuracy.

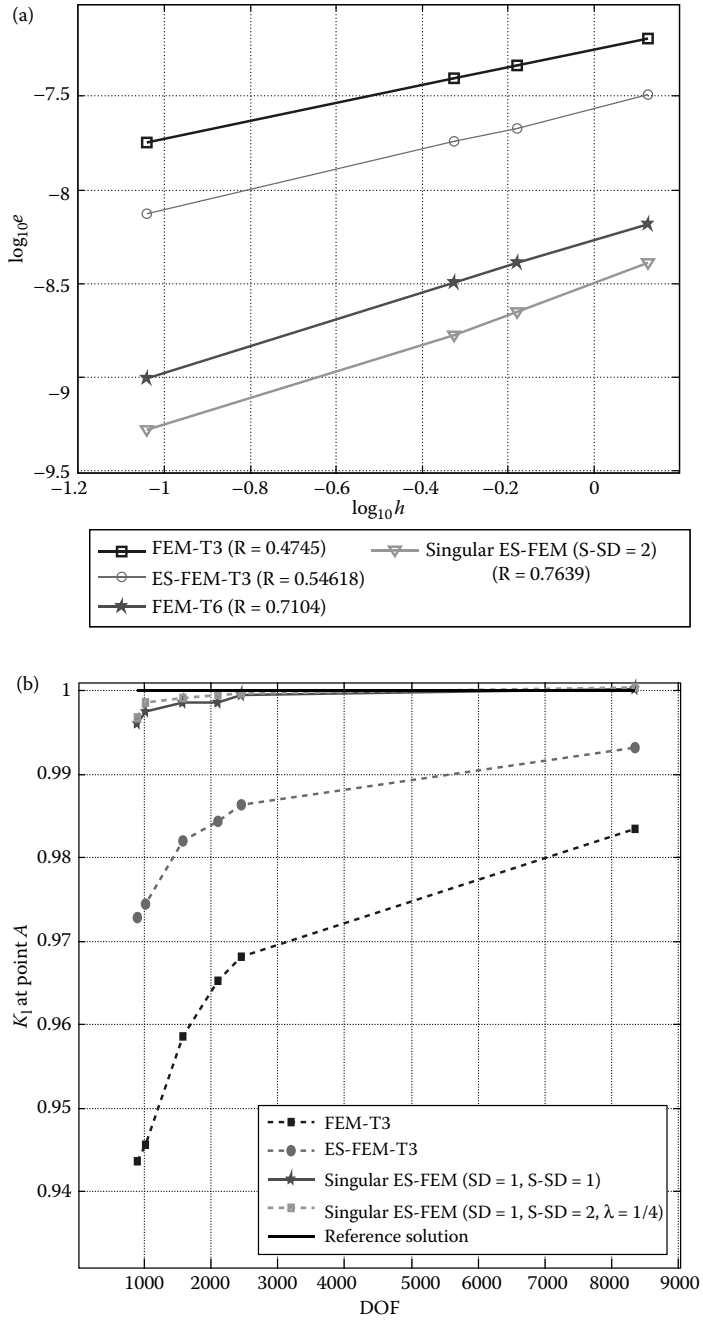

FIGURE 10.18 (a) Convergence rates in strain energy solution for the rectangular plate subjected to tension (mode I). Comparison with different models. (b) Normalized SIF at crack-tip A for the rectangular plate with a central crack subjected to tension (mode I).

SIF SOLUTIONS

Table 10.3 lists the K_{I} values computed numerically using FEM-T3, ES-FEM-T3, and sES-FEM-T3 (default model with S-SD=1, $\lambda = 1/4$), respectively, for two crack-tips A and A'. The error is computed against the analytical solution: $K_{\mathrm{I}} = 3.9315\ \mathrm{Ncm}^{-3/2}$. Figure 10.18 plots the K_{I} values computed numerically using FEM-T3, ES-FEM-T3, sES-FEM-T3, and sES-FEM-T3 with S-SD=2 for crack-tip A. From these figures and Table 10.3, we note the following key points:

1. It is clear from Table 10.3 that the SIF values obtained numerically at two crack-tips A and A' are very close to each other and identical at least to four significant digits. This result confirms that our method works well numerically and can predict the symmetry feature of the field variables. It shows that the sES-FEM-T3 can work well also for the domains with multiple crack-tips.
2. Figure 10.18 shows that the SIF results of all these models converge, and converge from below, which is similar to the results for strain energy. This shows that these models all produce lower bound SIF solutions for this problem.
3. The accuracy in terms of SIF ranking of these models would be sES-FEM-T3, ES-FEM-T3, and FEM-T3. We observe again that compared with FEM-T3, sES-FEM-T3 has double significant improvement. With only 904 DOFs, the sES-FEM-T3 produces results with less than 0.4% error in K_{I} value, as shown in Table 10.3. Further improvement can be made by using S-SD=2, but it is quite marginal for this case, as shown in Figure 10.18.

TABLE 10.3

SIF Solution: K_{I} (Evaluated Numerically for Two Points A and A', and Normalized with the Analytical Value of $K_I = 3.9315\,\mathrm{Ncm}^{-3/2}$)

	DOFs	**904 (e_s%)**	**1588 (e_s%)**	**2464 (e_s%)**	**8340 (e_s%)**
Point A	FEM-T3	0.9436	0.9586	0.9681	0.9834
		(−5.6434)	(−4.1437)	(−3.1901)	(−1.6589)
	ES-FEM-T3	0.9729	0.9820	0.9863	0.9931
		(−2.7122)	(−1.8016)	(−1.3702)	(−0.6896)
	sES-FEM-T3	0.9961	0.9985	0.9995	1.0002
		(−0.3859)	(−0.1503)	(−0.0524)	(−0.0158)
Point A'	FEM-T3	0.9436	0.9586	0.9681	0.9834
		(−5.6442)	(−4.1447)	(−3.1909)	(−1.6594)
	ES-FEM-T3	0.9729	0.9820	0.9863	0.9931
		(−2.7132)	(−1.8021)	(−1.3707)	(−0.6898)
	sES-FEM-T3	0.9961	0.9985	0.9995	1.0002
		(−0.3864)	(−0.1506)	(−0.0524)	(0.0155)

Example 10.9.2: Plate with a Central Crack Subject to Shear (Mode II)

In this example, we study a square plate subjected to shear force $\tau = 1$ N/mm^2 that gives a pure mode II state, as shown in Figure 10.19. In our numerical model, the plate dimensions have been fixed at $w = 200$ mm, and the crack length is $a = 10$ mm. Since w/a is as large as 20, the solution for the infinite plate can be employed as a good reference solution. The analytical solution (when the plate dimensions go to infinity) can be found simply as $K_{\text{II}} = \tau\sqrt{\pi a} = 5.6050\ \text{Nmm}^{-3/2}$. The material properties used is the same as those in Example 10.9.1. For this problem, we use an irregular mesh with fine zoning near the crack-tip. ABAQUS® CAE is used for mesh generation, and a typical mesh with 360 DOFs is plotted in Figure 10.20. The problem is solved numerically using different methods including FEM-T3, ES-FEM, and sES-FEM.

We first checked again on the effects of using S-SD=1 and 2 on the solution, and it is found that these results are very close, although S-SD=2 can give a little better solution.

STRAIN ENERGY SOLUTIONS

The results in terms of both strain energy values are tabulated in Table 10.4 and plotted in Figure 10.21. From Figure 10.21 and Table 10.4, we observe that the improvement of ES-FEM-T3 from FEM-T3 is very significant, showing clearly the benefit of the strain smoothing operations. The further improvement of sES-FEM-T3 from ES-FEM-T3 is also quite remarkable, showing the significance of the singular field approximation. Therefore, compared with FEM-T3, sES-FEM-T3 has double significant improvement. This finding is largely in line with those found in the previous mode I case.

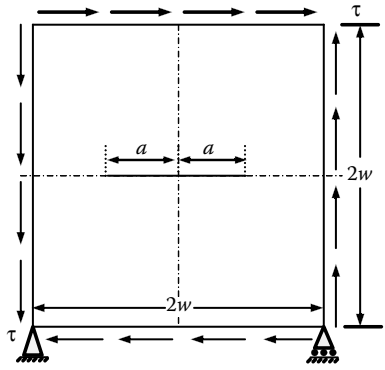

FIGURE 10.19 Square plate with a central crack subjected to shear (pure mode II).

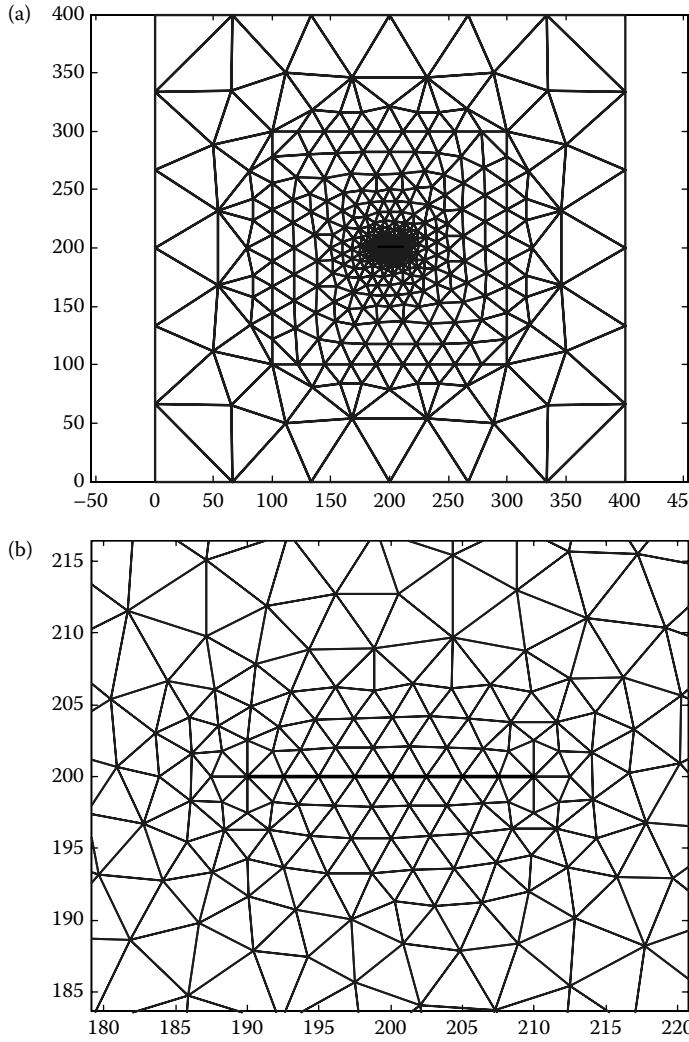

FIGURE 10.20 (a) A typical mesh with 360 DOFs for the square plate with a central crack subjected to shear (pure mode II); and (b) zooming near the crack.

SIF SOLUTIONS

We conducted a check again on the symmetry of the numerical SIF values, by computing the results for both crack-tips, and it is found again for this case that the results for these two tips are very close. In the following analysis, we discuss only the results obtained for the left crack-tip.

TABLE 10.4

Comparison of Results in Strain Energy for the Square Plate with Horizontal Central Crack Subjected to Shear Obtained Using Different Methods with Different DOFs

DOFs	360	504	704	2206	5382
FEM-T3	976.2515	976.2868	976.3033	976.3235	976.3471
ES-FEM-T3	976.4103	976.4345	976.4362	976.4364	976.4384
sES-FEM-T3	976.5364	976.5650	976.5660	976.5667	976.5735

The results in SIF values are tabulated in Table 10.5 and plotted in Figure 10.22. Similar to the previous example, the sES-FEM-T3 solution is much more (about 5–60 times) accurate than the FEM-T3 using the same basic mesh. The improvement is more significant for the finer mesh, owing to both the higher convergence rate of the S-FEM model and better capturing of the singular field.

This mode II example confirms largely the findings for the previous mode I example.

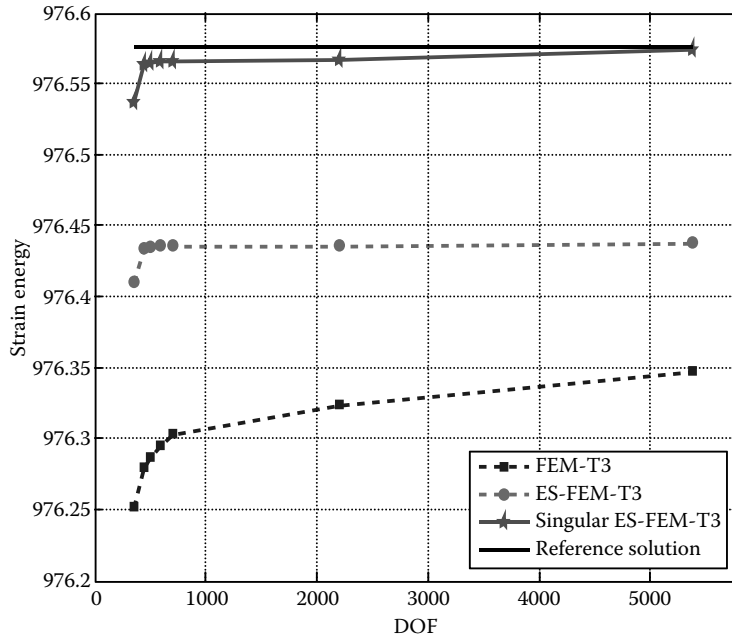

FIGURE 10.21 Strain energy results for the infinite plate under mode II.

TABLE 10.5

K_{II} Solution for the Square Plate with Horizontal Central Crack Subjected to Shear Obtained Using Different Methods with Different DOFs (Normalized with the Analytical Values of $K_{\text{II}}^{\text{exact}} = 5.6050\ \text{Nmm}^{-3/2}$, Evaluated Numerically for Point A)

DOFs	**360 (e_s%)**	**504 (e_s%)**	**704 (e_s%)**	**2206 (e_s%)**	**5382 (e_s%)**
FEM-T3	0.9509	0.9649	0.9710	0.9856	0.9880
	(−4.9083)	(−3.5083)	(−2.9042)	(−1.4402)	(−1.2036)
ES-FEM-T3	0.9847	0.9894	0.9933	0.9937	0.9937
	(−1.5301)	(−1.0580)	(−0.6701)	(−0.6287)	(−0.6287)
sES-FEM-T3	0.9888	0.9948	0.9982	0.9989	0.9998
	(−1.1155)	(−0.5160)	(−0.1824)	(−0.1060)	(−0.0211)

Example 10.9.3: Plate with Double Edge Cracks (Mode I)

We consider now a rectangular plate of isotropic material with symmetric double edge cracks subjected to tension, as shown in Figure 10.23. The plate is subjected to a "remote" tensile stress σ at the top edge and fixed at the bottom edge, which gives a mode I state. The analytical formula of the SIF for such a

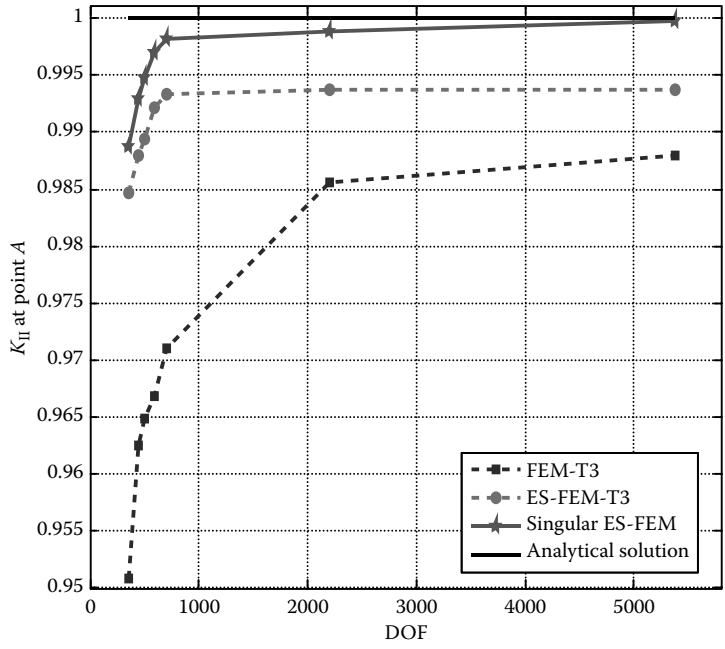

FIGURE 10.22 Normalized SIF at point A for the square plate subjected to shear (mode II).

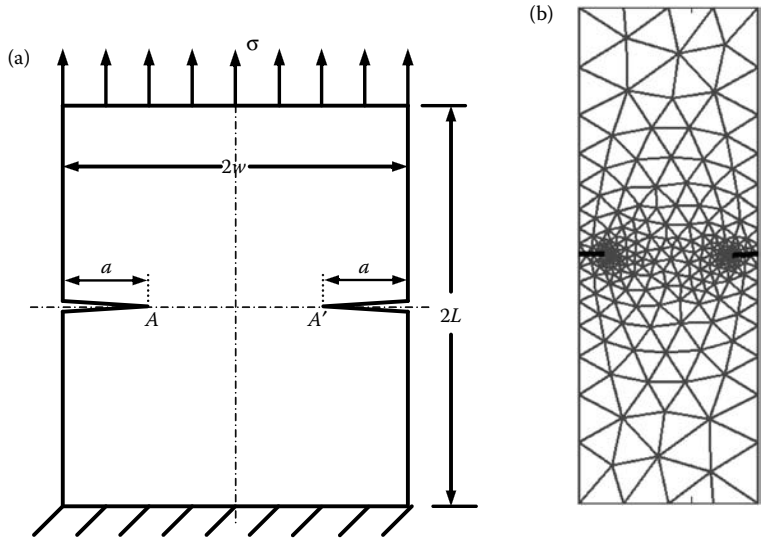

FIGURE 10.23 (a) A rectangular plate with symmetric double edge cracks subjected to tension and (b) a typical mesh with 530 DOFs.

specimen is given in Ref. [12]:

$$K_{\mathrm{I}} = \sigma\sqrt{\pi a}\left[1.122 - 0.561\left(\frac{a}{w}\right) - 0.205\left(\frac{a}{w}\right)^2 + 0.471\left(\frac{a}{w}\right)^3 - 0.910\left(\frac{a}{w}\right)^4\right] \Big/ \left(1 - \frac{a}{w}\right)^{0.5}. \tag{10.61}$$

In numerical analysis, the parameters used are $w = 4.0$ cm, $L = 11.0$ cm, $a = 1.2$ cm, and $\sigma = 1$ N/cm^2. The material constants are $E = 3 \times 10^7$ N/cm^2 and $\nu = 0.25$. With this set of data, the analytical solution is found to be $K_{\mathrm{I}} = 2.1964$ Ncm$^{-3/2}$. Irregular meshes with the finer mesh near the crack-tips are used in this example, and a typical mesh is plotted in Figure 10.23b.

STRAIN ENERGY SOLUTIONS

The results in terms of both strain energy values are tabulated in Table 10.6 and plotted in Figure 10.24. From Figure 10.24 and Table 10.6, we observe that the improvement of ES-FEM-T3 from FEM-T3 is most significant, showing clearly the benefit of the strain smoothing operations. The further improvement of sES-FEM-T3 from ES-FEM-T3 is also quite significant, showing the significance of the singular field approximation. Therefore, compared with FEM-T3, sES-FEM-T3 has double significant improvement. This finding is largely in line with those found in the previous examples for both mode I and mode II cases.

TABLE 10.6

Comparison of Results in Strain Energy ($\times 10^{-4}$) for the Plate with Double Edge Cracks Obtained Using Different Methods Using Different Number of Nodes

DOFs	336	530	948	1286	1780
FEM-T3	2.8552	2.8756	2.8823	2.8860	2.8880
ES-FEM-T3	2.8862	2.8952	2.8960	2.8975	2.8979
sES-FEM-T3 (S-SD=1)	2.8930	2.9022	2.9028	2.9043	2.9047
sES-FEM-T3 (S-SD=2)	2.8953	2.9046	2.9053	2.9068	2.9072
sES-FEM-T3 (S-SD=3)	2.8953	2.9047	2.9054	2.9068	2.9073

In this example, however, we found that the use of S-SD=2 in the sES-FEM-T3 has quite noticeable improvement compared to the use of S-SD=1. This finding suggests that the use of S-SD=2 in the sES-FEM-T3 is more robust. Further, we used S-SD=3 in this example, and it is found that the use of S-SD=3 can further improve the solution for this case, but improvement is only at the fifth digit or beyond. Therefore, it may be recommended that for cases for which we are not very sure, we shall use S-SD=2 in the sES-FEM-T3. This increases only slightly the complexity in the computation, as it affects only the crack-tip elements.

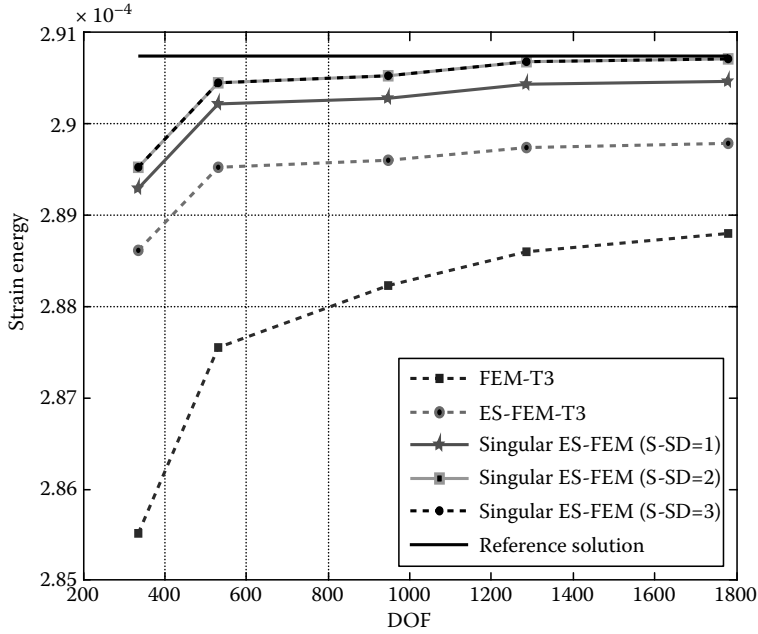

FIGURE 10.24 Strain energy results for the plate with double edge crack.

SIF SOLUTIONS

The SIF results (for crack-tip *A*) have been tabulated in Table 10.7 and depicted in Figure 10.25. Similar to the previous example, the solution of sES-FEM-T3 with S-SD=2 is much more (about 4–40 times for this example) accurate than the FEM-T3 using the same basic mesh. The solution of sES-FEM-T3 with S-SD=1 is about 3–16 times more accurate than the FEM-T3 for this example. The improvement is more significant for finer meshes, due to both the higher convergence rate of the S-FEM model and better capturing of the singular field. The results of ES-FEM-T3 are about twice more accurate than those of FEM-T3, both models ignoring the singularity of stress field. It is also found that the use of S-SD=3 can further improve the solution for SIF value, but the improvement is marginal also for this example.

This mode I example confirms largely the findings for the previous modes I and II examples, except the outstanding performance of sES-FEM-T3 with S-SD=2.

Example 10.9.4: A Plate with an Edge Crack (Mixed Mode)

We next examine the sES-FEM for a fracture problem of mixed mode: a rectangular plate of isotropic material with an edge crack subjected to shear load, as shown in Figure 10.26. The problem is considered as a plane strain problem, and the dimensions of the problem domain are $w = 7.0$ cm, $L = 8.0$ cm, and $a = 3.5$ cm. The plate is fully fixed on the bottom edge and a unit shear load of $\tau = 1$ N/cm^2 is applied on the top edge. Under this setting, the problem becomes a mixed-mode fracture problem. The Young's modulus and Poisson's ratio of the material are $E = 3 \times 10^7$ N/cm^2 and $\nu = 0.25$, respectively.

TABLE 10.7

K_{I} Solution for the Plate with Double Edge Cracks Obtained Using Different Methods Using Different Numbers of Nodes (Relative to the Analytical Solution of $K_{\mathrm{I}} = 2.1964$ Ncm$^{-3/2}$; Evaluated Numerically for Point *A*)

DOFs	**336 (e_s%)**	**530 (e_s%)**	**948 (e_s%)**	**1286 (e_s%)**	**1780 (e_s%)**
FEM-T3	0.9249	0.9582	0.9691	0.9722	0.9752
	(−7.5073)	(−4.1825)	(−3.0897)	(−2.7782)	(−2.4750)
ES-FEM-T3	0.9725	0.9840	0.9843	0.9848	0.9843
	(−2.7469)	(−1.5971)	(−1.5716)	(−1.5176)	(−1.5675)
sES-FEM-T3 (S-SD=1)	0.9772	0.9890	0.9924	0.9941	0.9985
	(−2.2839)	(−1.1035)	(−0.7596)	(−0.5863)	(−0.1498)
sES-FEM-T3 (S-SD=2)	0.9796	0.9916	0.9933	0.9951	0.9994
	(−2.0376)	(−0.8378)	(−0.6873)	(−0.4854)	(−0.0564)
sES-FEM-T3 (S-SD=3)	0.9797	0.9916	0.9934	0.9951	0.9995
	(−2.0288)	(−0.8356)	(−0.6600)	(−0.4898)	(−0.0465)

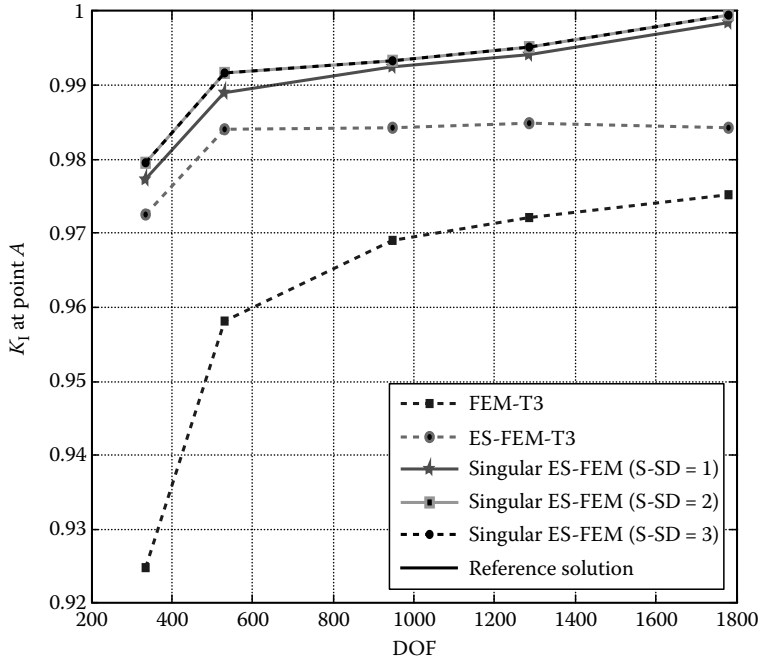

FIGURE 10.25 Normalized K_I at point A for the double edge crack specimen.

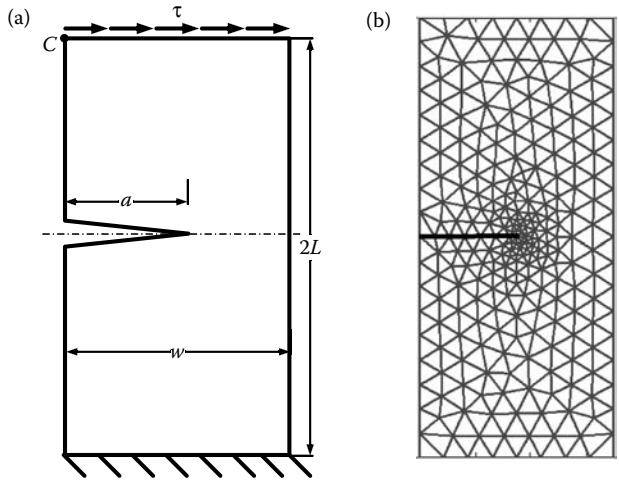

FIGURE 10.26 (a) A rectangular plate with an edge crack subjected to shear force (mixed mode) and (b) a typical mesh with 566 DOFs.

In these example problems of mixed mode, we will investigate in detail the effects on various solution of (1) the number of subsmoothing domains (S-SD=1, 2, and 3), and (2) the number of Gauss points used in the integration of boundary segments (along the radial directions) of the subsmoothing domains. We will look at the solution outputs in terms of strain energy, displacements, and SIF values.

STRAIN ENERGY SOLUTIONS

The results in terms of strain energy have been computed using different methods including FEM-T3, ES-FEM-T3, and sES-FEM with different numbers of S-SDs. These results are plotted in Figure 10.27 and tabulated in Table 10.8. In performing the line integration for computing the smoothed strains along the line segments in the radial direction for the crack-tip edges, we need to use more than one Gauss point. This is to capture the rapid variation of the singular field. Our study has shown that at least five Gauss points are needed for these line segments. In Figure 10.27 and Table 10.8, we provide the results obtained using five and seven Gauss points for the cases of S-SD=1 and 2. It is shown that the use of five Gauss points is sufficient, because it gives results very close to those obtained using seven Gauss points, and the difference is only at the fifth

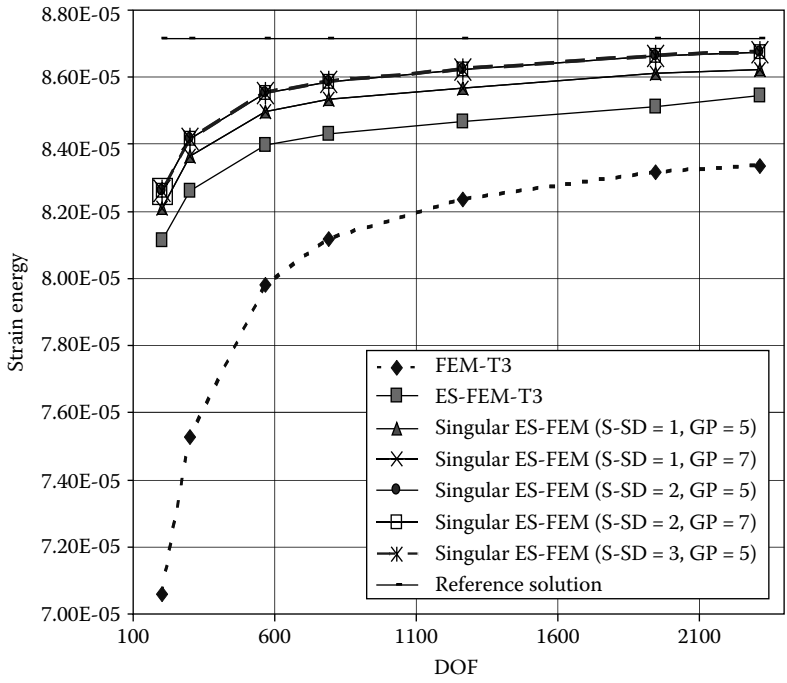

FIGURE 10.27 Strain energy solution for the rectangular plate with an edge crack subjected to shear (mixed mode).

TABLE 10.8

Comparison of Results in Strain Energy ($\times 10^{-5}$) for the Plate an Edge Crack Obtained Using Different Methods Using Different Mesh Density

DOFs	202	566	790	1264	1946	2316
FEM-T3	7.059816	7.981250	8.118690	8.234273	8.318031	8.336030
ES-FEM-T3	8.113270	8.396488	8.432329	8.469624	8.512212	8.544447
sES-FEM-T3 (S-SD=1, GP=5)	8.209445	8.499314	8.533056	8.569464	8.611947	8.623414
sES-FEM-T3 (S-SD=1, GP=7)	8.209355	8.499217	8.532960	8.569370	8.611852	8.623320
sES-FEM-T3 (S-SD=2, GP=5)	8.259971	8.551294	8.585696	8.6212151	8.664186	8.675881
sES-FEM-T3 (S-SD=2, GP=7)	8.259871	8.551282	8.585681	8.621212	8.664106	8.675880
sES-FEM-T3 (S-SD=3, GP=5)	8.259992	8.551305	8.585699	8.621296	8.664192	8.675890

digit and beyond. This is true for both S-SD=1 and 2, and should be certainly true for S-SD=3 because finer subdivision should demand less for the number of Gauss points. Therefore, in all our examples and discussions we use five Gauss points as default.

From Figure 10.27, it is also seen that the solution obtained using S-SD=2 is quite noticeably more accurate than that obtained using S-SD=1. When S-SD=3 is used, the further improvement becomes very marginal, and the difference is only at the sixth digit and beyond, as shown in Table 10.8. This example suggests the use of S-SD=2.

We note that the improvement of ES-FEM-T3 from FEM-T3 is very significant, due to the benefit of the strain smoothing operations. The further improvement of sES-FEM-T3 from ES-FEM-T3 is quite remarkable, showing the significance of the singular field approximation.

DISPLACEMENT SOLUTIONS

The results in terms of displacement in the x-direction at the left-top corner are plotted in Figure 10.28 and tabulated in Table 10.9. Similar findings for the strain energy solution can be largely observed for the displacement solution. Hence, we will not repeat the detailed discussions. We state, without showing further figures and tables, that a similar finding is observed also for the displacement component in the y-direction (Table 10.10).

SIF SOLUTIONS

Figure 10.29 and Table 10.11 and Figure 10.30 and Table 10.12 provide the results, respectively, for SIFs K_{I} and K_{II} for this mixed-mode problem. The exact

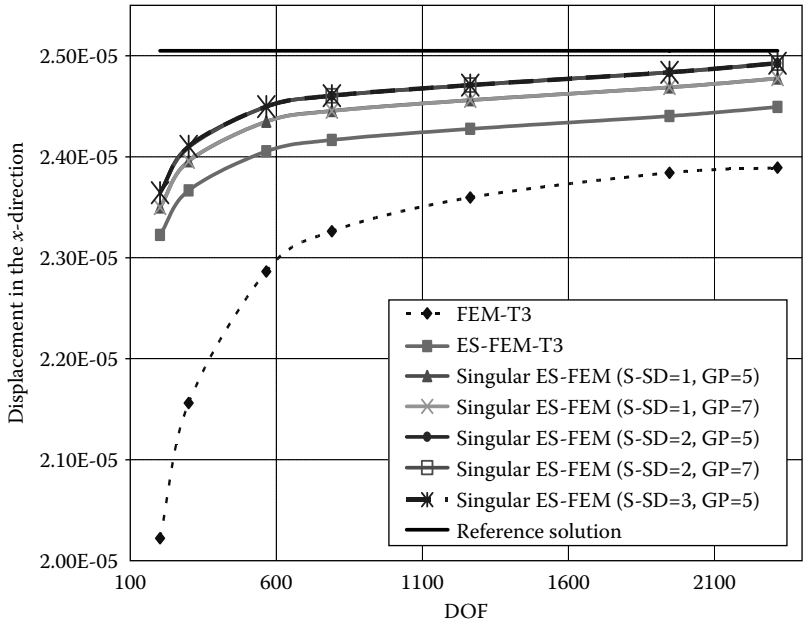

FIGURE 10.28 Displacement in the x-direction at point C of the plate with an edge crack subjected to shear load (mixed mode).

SIF for such a problem is available and has been given by [12]

$$\begin{aligned} K_{\mathrm{I}} &= 34.0, \\ K_{\mathrm{II}} &= 4.55. \end{aligned} \tag{10.62}$$

Similar findings as those for the strain energy solution can be observed largely for the SIF solutions, except that the sES-FEM-T3 gives upper bound solutions

TABLE 10.9

Comparison of Results in the Displacement ($\times 10^{-5}$ cm) in the x-Direction at the Left-Top Corner of the Plate an Edge Cracks Obtained Using Different Methods Using Different Mesh Density

DOFs	**202**	**566**	**790**	**1264**	**1946**	**2316**
FEM-T3	2.02224	2.28643	2.32621	2.35970	2.38415	2.38927
ES-FEM-T3	2.32254	2.40550	2.41665	2.42774	2.44036	2.44947
sES-FEM-T3 (S-SD=1, GP=5)	2.35001	2.43484	2.44547	2.45623	2.46885	2.47762
sES-FEM-T3 (S-SD=1, GP=7)	2.35000	2.43481	2.44536	2.45620	2.46882	2.47761
sES-FEM-T3 (S-SD=2, GP=5)	2.36449	2.44975	2.46041	2.47104	2.48371	2.49264
sES-FEM-T3 (S-SD=2, GP=7)	2.36443	2.44969	2.46040	2.47101	2.48368	2.49261
sES-FEM-T3 (S-SD=3, GP=5)	2.36445	2.44969	2.46045	2.47109	2.48370	2.49268

TABLE 10.10

Comparison of Results in the Displacement ($\times 10^{-5}$) in the y-Direction at the Left-Top Corner of the Plate an Edge Cracks Obtained Using Different Methods Using Different Mesh Density

DOFs	202	566	790	1264	1946	2316
FEM-T3	0.925	1.05	1.07	1.09	1.09	1.09
sES-FEM-T3	1.09	1.12	1.12	1.12	1.12	1.12
sES-FEM-T3 (S-SD=1, GP=5)	1.11	1.14	1.14	1.14	1.14	1.14
sES-FEM-T3 (S-SD=1, GP=7)	1.11	1.14	1.14	1.14	1.14	1.14
sES-FEM-T3 (S-SD=2, GP=5)	1.12	1.15	1.15	1.15	1.15	1.15
sES-FEM-T3 (S-SD=2, GP=7)	1.12	1.15	1.15	1.15	1.15	1.15

in terms of SIF solution when the mesh is refined as shown in Figures 10.29 and 10.30 and the shaded numbers in Tables 10.11 and 10.12.

PATH INDEPENDENCE OF THE SIFs

It is known that the path independence is one of the most significant features of the *J*-integral and the interaction integrals. We shall now examine such path

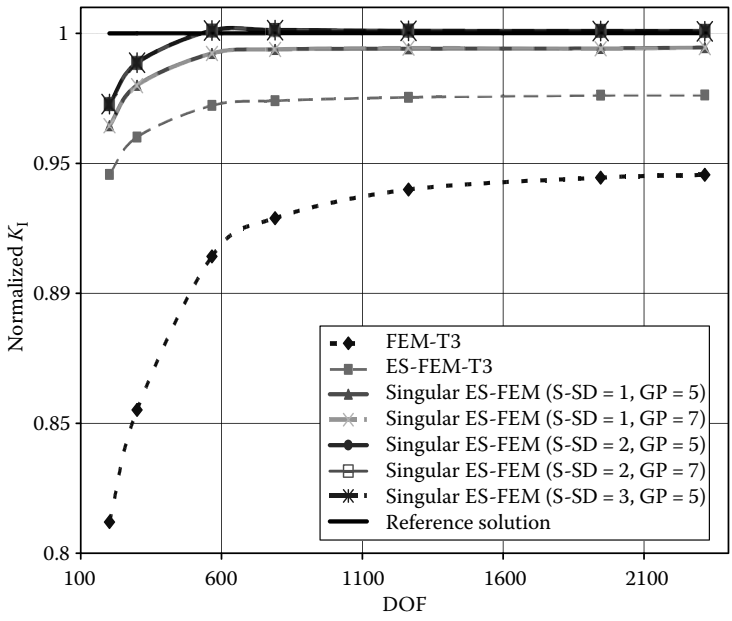

FIGURE 10.29 Normalized SIF of the first mode calculated by different methods.

TABLE 10.11

Comparison of Results in Normalized K_I at the Left-Top Corner of the Plate and Edge Cracks Obtained Using Different Methods Using Different Mesh Densities

DOFs	202 (e_s%)	566 (e_s%)	790 (e_s%)	1264 (e_s%)	1946 (e_s%)	2316 (e_s%)
FEM-T3	0.8120	0.9142	0.9289	0.9399	0.9445	0.9456
	(−18.8)	(−8.58)	(−7.11)	(−6.01)	(−5.55)	(−5.44)
ES-FEM-T3	0.9457	0.9723	0.9741	0.9754	0.9762	0.9763
	(−5.43)	(−2.77)	(−2.59)	(−2.46)	(−2.38)	(−2.37)
sES-FEM-T3	0.9645	0.9923	0.9938	0.9941	0.9942	0.9945
(S-SD=1, GP=5)	(−3.55)	(−0.769)	(−0.620)	(−0.589)	(−0.576)	(−0.547)
sES-FEM-T3	0.9645	0.9923	0.9938	0.9941	0.9943	0.9945
(S-SD=1, GP=7)	(−3.55)	(−0.769)	(−0.620)	(−0.586)	(−0.568)	(−0.547)
sES-FEM-T3	0.9727	1.0011	1.0013	1.0010	1.0009	1.0009
(S-SD=2, GP=5)	(−2.73)	(0.110)	(0.134)	(0.101)	(0.090)	(0.090)
sES-FEM-T3	0.9728	1.0010	1.0012	1.0010	1.0009	1.0009
(S-SD=2, GP=7)	(−2.72)	(0.101)	(0.123)	(0.101)	(0.090)	(0.090)
sES-FEM-T3	0.9728	1.0011	1.0012	1.0010	1.0009	1.0008
(S-SD=3, GP=5)	(−2.72)	(0.110)	(0.114)	(0.103)	(0.088)	(0.0834)

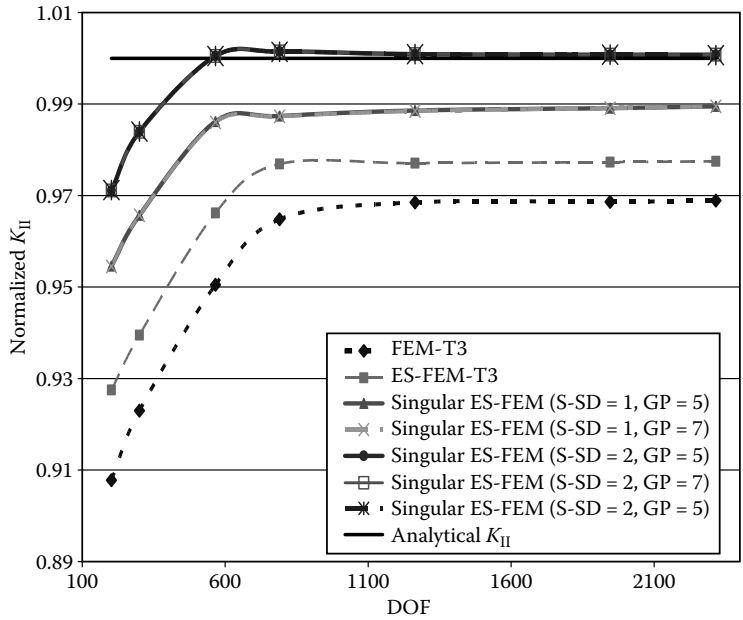

FIGURE 10.30 Normalized SIF of the second mode calculated by different methods.

TABLE 10.12

Comparison of Results in Normalized K_{II} at the Left-Top Corner of the Plate and Edge Cracks Obtained Using Different Methods Using Different Mesh Densities

DOFs	**202**	**566**	**790**	**1264**	**1946**	**2316**
FEM-T3	0.9078	0.9505	0.9648	0.9685	0.9686	0.9689
	(−9.22)	(−4.95)	(−3.52)	(−3.15)	(−3.14)	(−3.11)
ES-FEM	0.9275	0.9662	0.9769	0.9771	0.9773	0.9775
	(−7.25)	(−3.38)	(−2.31)	(−2.29)	(−2.27)	(−2.25)
sES-FEM	0.9546	0.9862	0.9874	0.9886	0.9891	0.9895
(S-SD=1, GP=5)	(−4.54)	(−1.38)	(−1.26)	(−1.14)	(−1.09)	(−1.05)
sES-FEM	0.9545	0.9860	0.9873	0.9885	0.9891	0.9895
(S-SD=1, GP=7)	(−4.55)	(−1.40)	(−1.27)	(−1.15)	(−1.10)	(−1.05)
sES-FEM	0.9711	1.0005	1.0015	1.0009	1.0008	1.0008
(S-SD=2, GP=5)	(−2.89)	(0.0511)	(0.150)	(0.0942)	(0.0815)	(0.0796)
sES-FEM	0.9710	1.0005	1.0014	1.0009	1.0008	1.0008
(S-SD=2, GP=7)	(−2.90)	(0.0507)	(0.140)	(0.911)	(0.0802)	(0.0796)
sES-FEM	0.9712	1.0005	1.0014	1.0009	1.0008	1.0007
(S-SD=3, GP=5)	(−2.88)	(0.0511)	(0.0544)	(0.0941)	(0.0821)	(0.0710)

independence using numerical examples, by choosing various area-paths with different dimensions for the computation of SIF values.

Example 10.9.5: A Plate with an Edge Crack (Mixed Mode)

Example 10.9.5 is chosen for this study. The area-path integration domain is determined using a closed circle with a radius r_d around the crack-tip, as shown in Figure 10.31. The procedure to determine the area-path is given in Section 10.8.3 and that for determining the weight function is given in Section 10.8.4.

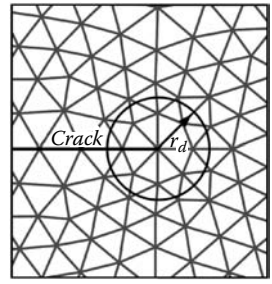

FIGURE 10.31 Circle used to determine the area-path for the interaction integrals for SIF calculations.

TABLE 10.13

Normalized SIF Value Computed Using Different Area-Path Sizes

SIFs	Path Sizes r_d	FEM-T3	ES-FEM-T3	sES-FEM (S-SD=1)
K_{I}	0.1[a]	0.89590	0.88903	0.24523
	0.3	0.96184	0.98930	1.00191
	0.5	0.95860	0.98716	0.99614
	0.7	0.95675	0.98721	0.99618
	0.9	0.95629	0.98721	0.99617
K_{II}	0.1[a]	0.86272	0.88056	0.63693
	0.3	0.97170	0.98193	0.98839
	0.5	0.97560	0.98290	0.98663
	0.7	0.97493	0.98256	0.98629
	0.9	0.97561	0.98334	0.98706

[a] The dimension of the crack-tip element is $h = 0.2$, so the region within $r_d = 0.1$ is inside the crack-tip element.

The results of both SIFs K_{I} and K_{II} are tabulated in Table 10.13 for different radii ranging from the crack-tip element size to about seven times the crack-tip element size. It is found that (1) the results are not good when the circle is inside the layer of the crack-tip element; (2) when $r_d \geq 0.3$ (three times the crack-tip element size), the area-path independence is clearly observed; and (3) ES-FEM-T3 and sES-FEM-T3 give better area-path independence than FEM-T3.

Example 10.9.6: A Plate with a Central Inclined Crack (Mixed Mode)

We now study another mixed-mode problem. A rectangular plate with an inclined crack subjected to a unit tension load shown in Figure 10.32 is considered. In this example, we have $w = 20$ mm, a $= \sqrt{2}$ mm, and $\varphi = \pi/4$. The analytical solution for this setting is available as

$$\begin{aligned} K_{\mathrm{I}} &= \sigma\sqrt{\pi a}\sin^2\,\varphi, \\ K_{\mathrm{II}} &= \sigma\sqrt{\pi a}\,\sin\,\varphi\,\cos\,\varphi. \end{aligned} \tag{10.63}$$

For the case of fixed $\varphi = \pi/4$, we shall have the normalized SIF values:

$$\begin{aligned} \frac{K_{\mathrm{I}}}{\sigma\sqrt{\pi a}} &= 0.5, \\ \frac{K_{\mathrm{II}}}{\sigma\sqrt{\pi a}} &= 0.5. \end{aligned} \tag{10.64}$$

The results of both SIFs K_{I} and K_{II} for both crack-tips are tabulated in Table 10.14. It is observed that (1) when $r_d \geq 0.4$ (two times the crack-tip

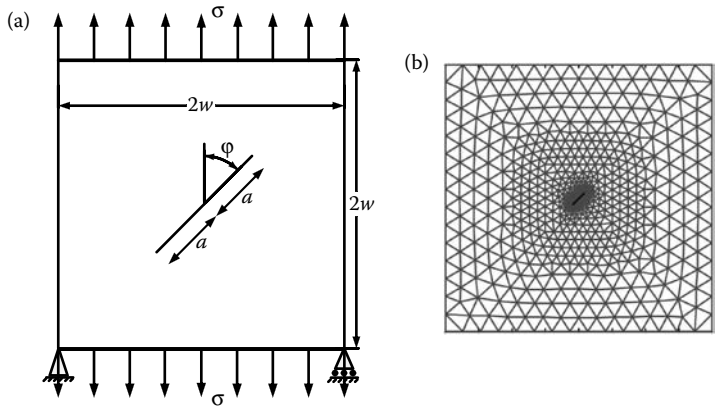

FIGURE 10.32 (a) Square plate with an inclined central crack subjected to tension and (b) mesh used in the computation.

TABLE 10.14

Normalized SIF Values Obtained Using sES-FEM-T3 (S-SD=1) for the Square Plate with an Inclined Crack (the Dimension of the Crack-Tip Element is $h = 0.2$)

Crack-tip	SIFs	$r_d = 0.4$ (e_s %)	$r_d = 0.6$ (e_s %)	$r_d = 0.7$ (e_s %)	$r_d = 0.9$ (e_s %)	$r_d = 1$ (e_s %)
A	$K_{\mathrm{I}}/\sigma\sqrt{\pi a}$	0.4991	0.4997	0.4996	0.5001	0.5002
		(−0.0867)	(−0.0269)	(−0.0359)	(0.0127)	(0.0203)
	$K_{\mathrm{II}}/\sigma\sqrt{\pi a}$	0.4962	0.5017	0.5018	0.5060	0.5010
		(−0.380)	(0.169)	(0.180)	(0.597)	(0.105)
A'	$K_{\mathrm{I}}/\sigma\sqrt{\pi a}$	0.4985	0.4985	0.4987	0.4981	0.4989
		(−0.147)	(−0.153)	(−0.128)	(−0.186)	(−0.110)
	$K_{\mathrm{II}}/\sigma\sqrt{\pi a}$	0.4963	0.5022	0.5022	0.5062	0.5023
		(−0.365)	(0.224)	(0.224)	(0.623)	(0.232)

element size), the area-path independence is well observed; (2) the results for both crack-tips are very close, and the difference is at the third digit and beyond; and (3) the results for K_{I} are 2–5 times more accurate than those for K_{II}.

10.10 Numerical Examples Solved Using sNS-FEM-T3

In this section, examples are presented to demonstrate the property of the sNS-FEM using meshes of triangular elements (sNS-FEM-T3) for computing the solution outputs in terms of strain energy and SIFs. Fracture problems of mode I, mode II, and mixed mode will be considered with a

focus on the upper bound solutions as well as the accuracy of the solution. For comparison purposes, all the problems are also solved using FEM-T3, singular FEM-T6 (sFEM-T6) [2,3], standard NS-FEM-T3, standard ES-FEM-T3, and sES-FEM-T3, using the same basic mesh of linear T3 elements. The effect of the number of subsmoothing domains used in the sNS-FEM on these solution outputs will also be examined.

Example 10.10.1: A Plate with an Edge Crack Subjected to Tension (Mode I)

A rectangular plate with an edge-crack of isotropic material subjected to tension, as shown in Figure 10.33, is first considered with plane strain assumption. The material parameters used are Young's modulus $E = 3 \times 10^7$ and Poisson's ratio $\nu = 0.3$. The dimensions of the plate are $w = 1.0$, $L = 2.0$, and $a = 0.3$, and it is loaded on the top edge with unit traction $\sigma = 1.0$. The displacement components in the y-direction are fixed on the bottom edge, and both the displacement components are fixed at the bottom left corner. In SIF analysis, the problem is essentially the same as in Example 10.9.3, and the exact solution of K_I can be computed using Equation 10.61 [1,12]: $K_I = 1.6118$.

Five "uniform" meshes with 231, 861, 1891, 3321, and 5151 nodes are used in the computation. A typical mesh of $a/h = 8.0$ (3321 nodes in total), where h is the mesh spacing, in the vicinity of the crack-tip, is shown in Figure 10.33b. Because the singularity is properly modeled, we can practically use

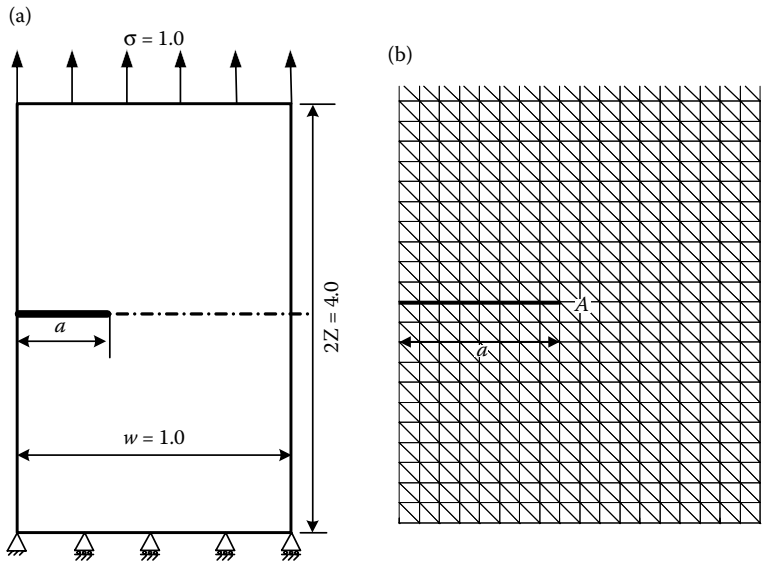

FIGURE 10.33 (a) Rectangular plate with an edge crack subjected to tension and (b) typical meshes in the vicinity of the crack ($a/h = 8.0$).

uniform meshes for fracture problems without local zoning-in at the crack-tip. In computing the interaction integral values, the domain radius of $r_d = r_k h$ with $r_k = 3.0$ is set for defining the area-path for the integration.

The problem is analyzed using sNS-FEM-T3, together with other models using the same meshes. The reference or "exact" solution of the strain energy is calculated using the sFEM-T6 with a very fine mesh (23,488 nodes), and the solutions are found to be strain energy=1.164×10^{-8}.

BOUND PROPERTY IN STRAIN ENERGY SOLUTIONS

Figure 10.34 shows the convergence of the strain energy with an increase of DOF. From Figure 10.34, we observe the following:

1. *Bound property*: The computed strain energy solutions using the FEM and the sFEM-T6 models are always smaller than the "exact" reference solutions, owing to the lower bound property of the FEM models. On the contrary, the solutions obtained using the NS-FEM and sNS-FEM models are always bigger than the reference solutions. The results suggest that the sNS-FEM provides upper bound solutions in strain energy. It is also

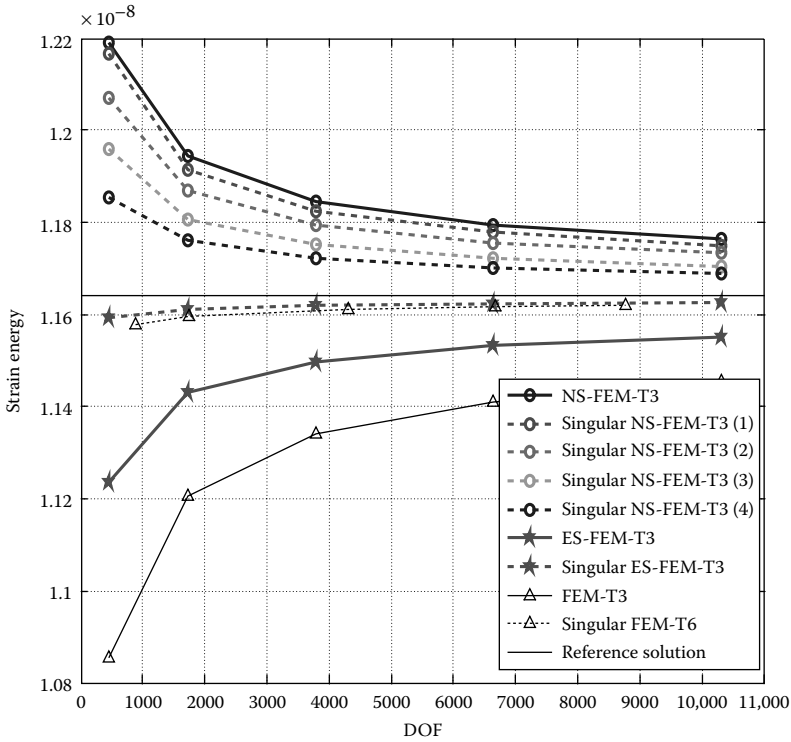

FIGURE 10.34 Convergence of the strain energy for the problem of a plate with an edge crack subjected to tension.

observed that with the increase of DOFs, the strain energy solutions of the sFEM models converge to the reference solutions from below, while the strain energy solutions of the sNS-FEM models converge from above. This finding is very important, because we can now bound the exact solution from both sides, in terms of strain energy solution.

2. *Softening effects*: The NS-FEM model without using the singular element is the most soft, which gives the loosest upper bound. For all the four sNS-FEM models, Scheme 1 (one-layer edge-based subdivisions) is the most soft, giving the loosest upper bound, followed by Scheme 2 (two-layer edge-based subdivisions). Scheme 4 (two-layer cell-based subdivisions) is the least soft, giving the tightest upper bound, followed by Scheme 3 (one-layer cell-based subdivisions). Therefore, Scheme 4 gives the best upper bound solution.
3. *Ultra-accuracy*: The sES-FEM-T3 is found as giving the most accurate solution, and the accuracy is much better than the FEM-T3 as seen in many earlier examples and even better than the sFEM-T6 using a basic mesh of quadrilateral elements for the same DOFs. This supports the ultra-accuracy property of the sES-FEM-T3 models also for fracture problems.

We note that with the use of one-layer T5 singular elements, the S-FEM-T3 models work very well for fracture problems, with sNS-FEM-T3 giving upper bounds and sES-FEM-T3 giving ultra-accurate solutions.

BOUND PROPERTY IN SIF SOLUTIONS

Figure 10.35 shows the convergence of the K_I solution with an increase of DOFs. It can be clearly observed that the findings for the strain energy solution are largely true for the K_I solution. The computed K_I values of the FEM and sFEM-T6 models are always smaller than the "exact" reference solutions. On the contrary, the computed K_I values using the NS-FEM and sNS-FEM models are always bigger than the reference solutions. The results show that the sNS-FEM provides upper bound solutions also in terms of K_I values. It is also observed that with the increase of DOFs, the K_I values obtained using these FEM models and these NS-FEM models converge to the exact solution, respectively, from below and above. We now can bound the exact solution from both sides, also in terms of the K_I solution, at least for this case. We are not sure whether this finding for K_I solution can hold in general. We have not yet found any exception for all the example problems studied, but could not prove this theoretically. It remains, for now, an open question.

EFFECT OF THE NUMBER OF SUBSMOOTHING DOMAINS ON STRAIN ENERGY

The strain energy solution obtained using the standard NS-FEM and the sNS-FEM with four different schemes of smoothing domains around the crack-tip given in Section 10.4 is plotted in Figure 10.34. It is seen that the results of the sNS-FEM using four schemes are much closer to the reference value, compared

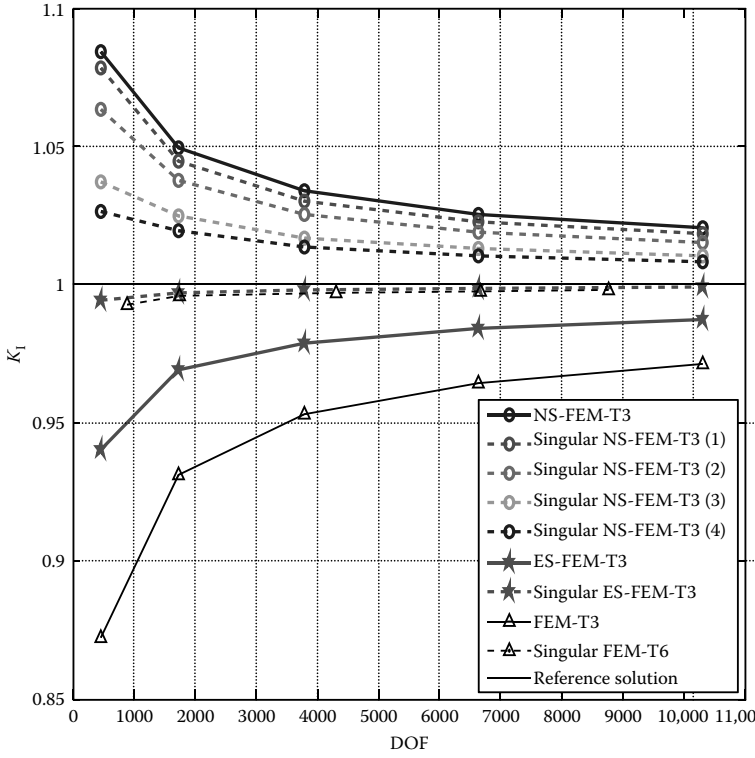

FIGURE 10.35 Convergence of the K_I for the problem of a plate with an edge crack subjected to tension.

to those of the standard NS-FEM without considering the singularity of the field. It is also found that the sNS-FEM using Scheme 4 (two-layer cell-based subdivision), denoted as sNS-FEM(4) or sNS-FEM(4), provides the best accuracy in the SIFs, compared to other schemes of smoothing domains. We observed in general that the schemes of cell-based subsmoothing domain divisions performed better than the edge-based ones. This is because the NS-FEM model is too soft, and cell-based smoothing helps to reduce the softness.

EFFECT OF THE SCHEMES OF SMOOTHING DOMAINS ON SIF SOLUTION

The SIF solution obtained using the standard NS-FEM and the sNS-FEM with four different schemes of subsmoothing domains around the crack-tip given in Section 10.4 is plotted in Figure 10.35. Very similar findings for strain energy solution are found here for the SIF solutions as well: (1) sNS-FEM(4) performed the best, and (2) the schemes of cell-based subsmoothing domain divisions performed better than the edge-based ones. Based on these findings for both strain energy and SIF values, sNS-FEM(4) will be used as default in the following studies, unless stated otherwise.

TABLE 10.15

Area-Path Independence for the Mode I Fracture Problem Solved Using sNS-FEM-T3(4)

Mesh Size	Area-Path Dimension (r_k)	K_I/K_I^{exact} (e_s %)
$a/h = 4.0$ (a = 1.0, h = 0.25)	2	1.0243 (2.4)
	3	1.0248 (2.5)
	4	1.0251 (2.5)
$a/h = 8.0$ (a = 1.0, h = 0.125)	2	1.0126 (1.2)
	3	1.0129 (1.3)
	4	1.0130 (1.3)
	5	1.0130 (1.3)

Note that although sNS-FEM(4) gives a better solution in terms of accuracy, there could be cases where it may not provide upper bound solutions. For such cases (if any), we may need to use the sNS-FEM(1) or even NS-FEM with sufficiently fine mesh for upper bound solutions.

AREA-PATH INDEPENDENCE

In this area-path independence study, we consider several different area-paths for the interaction integrals described in Section 10.8.3. The results computed using sNS-FEM-T3 are listed in Table 10.15. It is found that (1) the differences caused by the area-path differences for all these cases are beyond the third digit for both meshes, and (2) the effects of the mesh size is larger than that of the area-path size. We may conclude that the SIF value is area-path-independent for these cases studied.

Example 10.10.2: A Plate with an Edge Crack Subjected to Shear (Mixed Mode)

A rectangular plate with an edge-crack of isotropic material subjected to shear, as shown in Figure 10.36, is next considered with plane strain conditions. The material parameters used are Young's modulus $E = 3 \times 10^7$ and Poisson's ratio $\nu = 0.3$. The dimensions of the plate are $w = 7.0$, $L = 8.0$, and $a = 3.5$, and the plate is subjected a shear force in the y-direction on the top edge with a unit traction of $\tau = 1.0$. The displacement components in the y-direction are fixed on the bottom edge, and both the displacement components are fixed at the bottom left corner. In SIF analysis, the problem is essentially the same as in Example 10.9.4, and the exact solutions [1,12] of K_{I} and K_{II} can be computed using Equation 10.62. All the other settings and meshes used are exactly the same as in Example 10.10.1.

Five "uniform" meshes with 435, 703, 1653, 3003, and 4753 nodes are used in the computation. The reference or "exact" solution of the strain energy

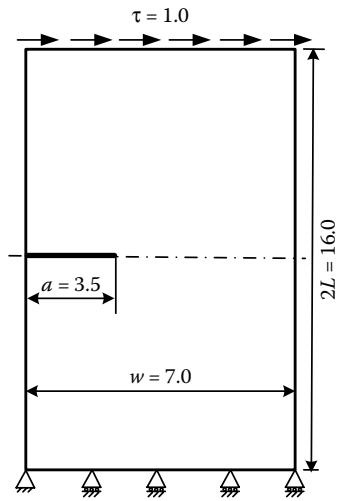

FIGURE 10.36 Rectangular plate with an edge crack subjected to shear.

is calculated using the sFEM with a very fine mesh (53,561 nodes), and the solution in strain energy is found to be 8.7903×10^{-5}.

BOUND PROPERTY OF SOLUTIONS

The strain energy, K_{I} and K_{II} solutions were obtained using various FEM, sES-FEM, and sNS-FEM models for this mixed-mode fracture problem, and the results are plotted, respectively, in Figures 10.37 and 10.38. It is observed that the SIF values obtained using the FEM models are lower bounds, and those obtained using the sNS-FEM models are upper bounds. Together they bound the exact solutions from both sides. These findings reconfirm what we have found in Example 10.10.1. In addition, we observed from Figure 10.38 the significance of using the singular elements on the accuracy of the K_{II} solution: the sNS-FEM models using a layer of T5 singular elements are much more accurate than the NS-FEM model. This implies that the use of singular T5 elements is particularly more important for K_{II} solution that is a much weaker mode in the mixed-mode problem.

EFFECT OF THE SCHEMES OF SUBSMOOTHING DOMAINS

From Figures 10.37 through 10.39, it is seen that the numerical solutions (strain energy, K_{I} and K_{II}) of the sNS-FEM using four schemes are much closer to the exact solutions, compared to those of the standard NS-FEM. It is also noted that the sNS-FEM(4) provides the best accuracy in all these numerical solutions. In addition, we also observed that for the K_{II} solution, the sNS-FEM models are significantly better than the NS-FEM.

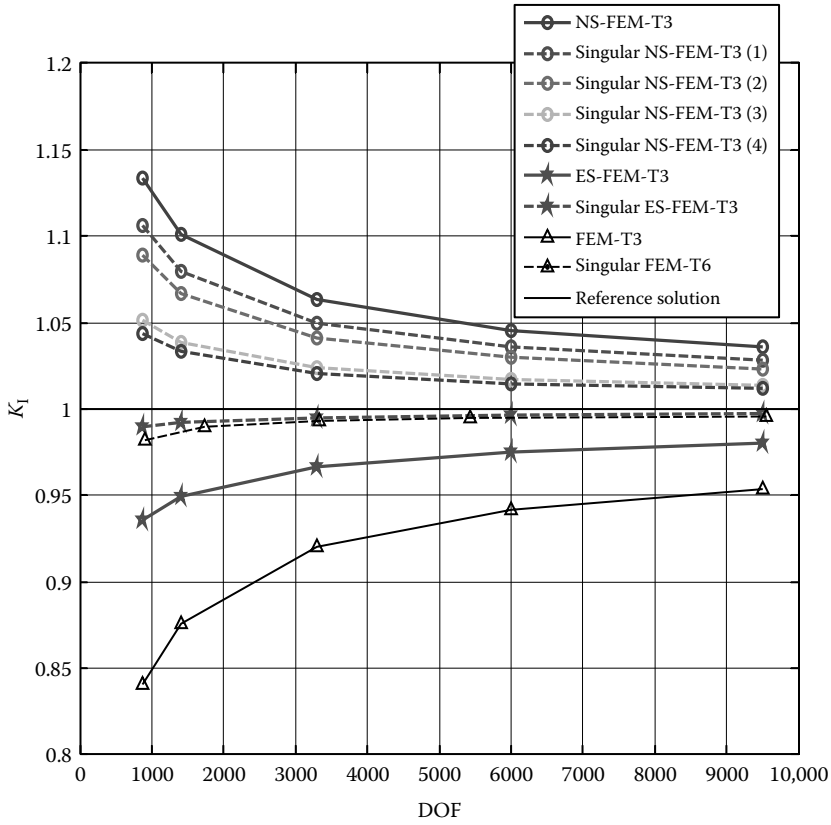

FIGURE 10.37 Convergence of the K_I for the problem of a plate with an edge crack subjected to shearing.

AREA-PATH INDEPENDENCE

For the mixed-mode problem, we studied also the area-path independence. The results computed using sNS-FEM-T3 (Scheme 4) are listed in Table 10.16. It is found that (1) the differences caused by the different area-paths for all these cases are beyond the third digit for both K_I and K_{II} and for both meshes, and (2) the effects of the mesh size are larger than that of the area-path size.

Example 10.10.3: Bimaterial Plate with a Center-Crack (Interfacial Mixed Mode)

We consider now a fracture problem of an interface crack located in between two different elastic semi-infinite planes. Plane strain conditions are assumed. The exact solution to this problem for a remote traction of $\mathbf{t} = \sigma_{22}^{\infty} + i\tau_{12}^{\infty}$ was obtained by Rice and Sih [19]. The solution for K_I and K_{II} at the right crack-tip

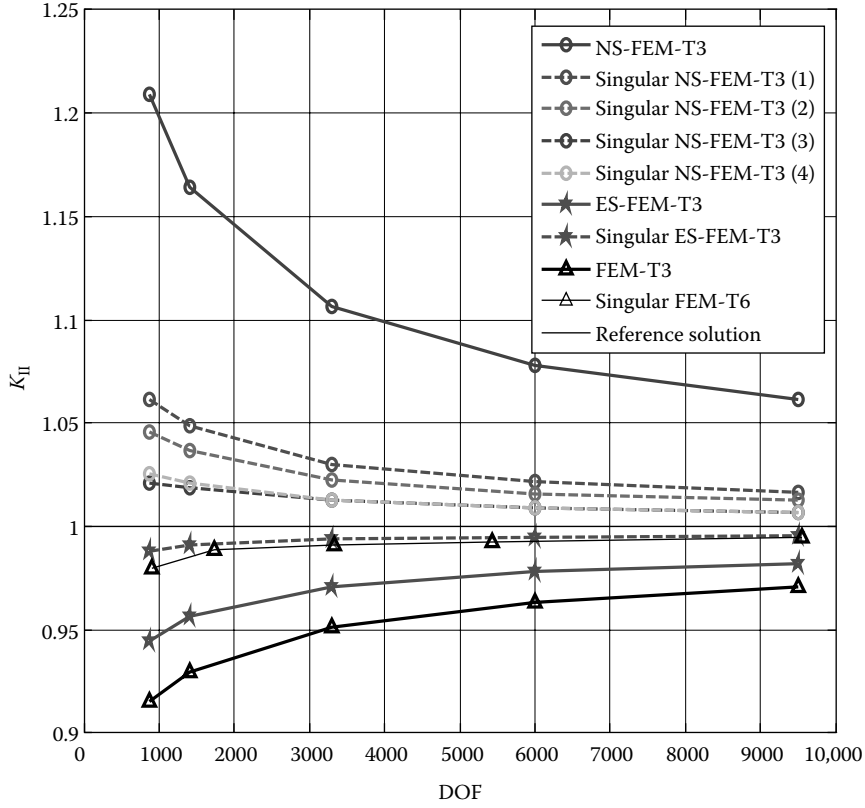

FIGURE 10.38 Convergence of the K_{II} for the problem of a plate with an edge crack subjected to shearing.

is given by [19,20]

$$K_C = K_I + iK_{II} = (\sigma_{22}^{\infty} + i\tau_{12}^{\infty})(1 + 2i\varepsilon)\sqrt{\pi a}(2a)^{-i\varepsilon}. \tag{10.65}$$

Here we consider only the case of pure tension load, and in this case, the problem is symmetric. Therefore, only half of the domain needs to be considered with the appropriate displacement constraints on the plane of symmetry, as shown in Figure 10.40. To remove the edge singularity, the right edge is also constrained in the x-direction [19]. The factors K_0 and J_0 defined in the following equation are used to normalize the solution of SIFs and J-integral, respectively.

$$K_0 = \sigma_{22}^{\infty}\sqrt{\pi a}, \qquad J_0 = \frac{(\sigma_{22}^{\infty})^2 \pi a}{E_1}, \tag{10.66}$$

where $2a$ is the (whole) crack length. The material constants used in the numerical computation are $E_1 = 1.0 \times 10^3$ Pa, $E_2/E_1 = 22$, $\nu_1 = 0.3$, and

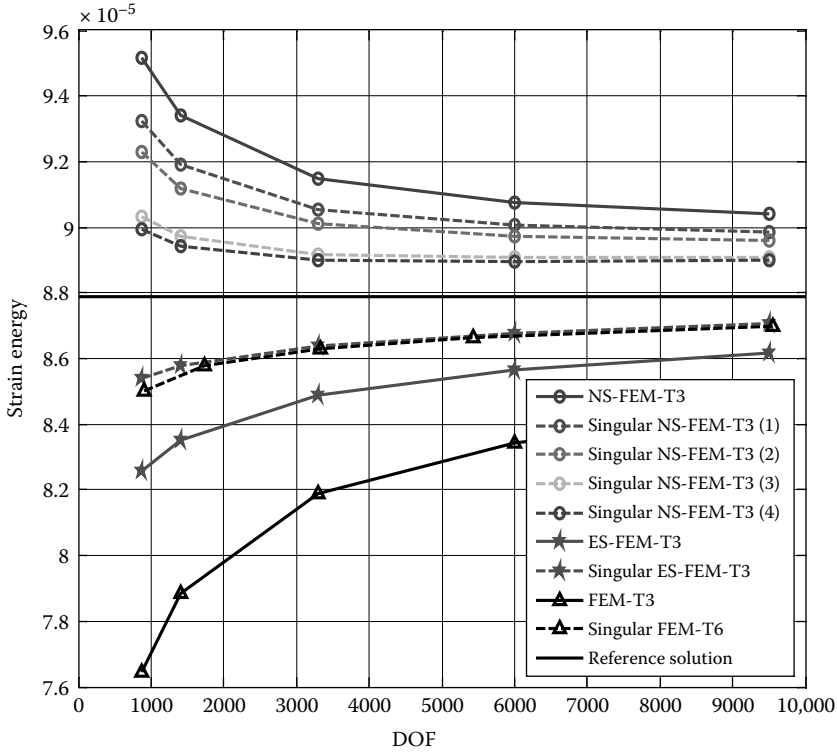

FIGURE 10.39 Convergence of the strain energy for the problem of a plate with an edge crack subjected to shearing.

TABLE 10.16

Area-Path Independence for the Mixed-Mode Fracture Problem Solved Using sNS-FEM-T3(4)

Mesh Size	Area-Path Dimension (r_k)	$K_{\mathrm{I}}/K_{\mathrm{I}}^{\mathrm{exact}}$ (% Error)	$K_{\mathrm{II}}/K_{\mathrm{II}}^{\mathrm{exact}}$ (% Error)
$a/h = 4.0$ ($a = 1.0, h = 0.25$)	2	1.0385 (3.8)	1.0217 (2.17)
	3	1.0389 (3.9)	1.0167 (1.67)
	4	1.0390 (3.9)	1.0190 (1.90)
$a/h = 8.0$ ($a = 1.0, h = 0.125$)	2	1.0171 (1.7)	1.0116 (1.16)
	3	1.0175 (1.8)	1.0068 (0.68)
	4	1.0175 (1.8)	1.0084 (0.84)
	5	1.0175 (1.8)	1.0087 (0.87)

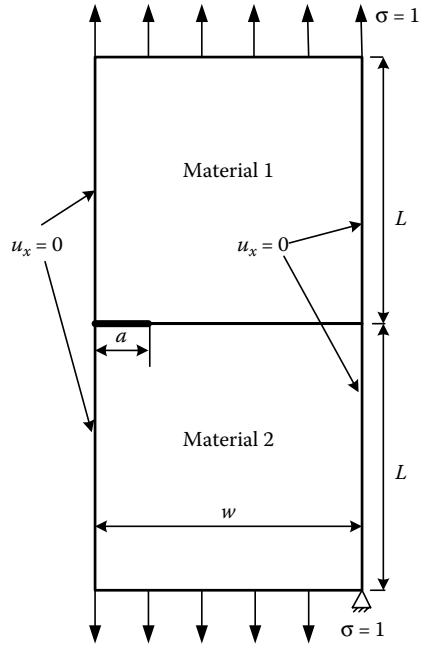

FIGURE 10.40 Plate made of bimaterials with a center-crack subjected to tension. Only half of the domain is modeled due to symmetry.

$\nu_2 = 0.2571$. The exact solutions found from Equation 10.65 are as follows:

$$\frac{K_{\mathrm{I}}}{K_0} = 1.008, \quad \frac{K_{\mathrm{II}}}{K_0} = 0.1097, \quad \frac{J}{J_0} = 1.4358. \tag{10.67}$$

In our numerical computation, we can only model a finite domain. To avoid the effect of finite size, so that we can compare the numerical results with the exact solution, "large" models are built with $w/a = 10$ (where the crack length is fixed at $a = 1$). Four "uniform" meshes with 681, 1891, 3321, and 5151 nodes are used in the computation, and $r_k = 5$ is used to create the area-path for the interaction integral evaluation for this example problem.

ACCURACY IN SOLUTION OUTPUTS

Table 10.17 shows the comparison of the solutions in terms of SIFs and the energy release rate using different numerical methods [FEM-T3, sFEM-T6, NS-FEM-T3, and sNS-FEM-T3(4)]. These solution outputs of K_{I}, K_{II}, and J are also plotted in Figures 10.41 through 10.43 for easy observation. From Table 10.17 and these figures, it can be found that when singular elements are used, the solution becomes much more accurate. This is true for any methods and for any solution outputs, and it reinforces the importance of the enrichment in the crack-tip field.

TABLE 10.17

Plate of Bimaterials with a Center-Crack Subjected to Tension: Comparison of the SIFs and Energy Release Rate Obtained Using Different Methods (Exact Solutions: $K_I/K_0 = 1.008$; $K_{II}/K_0 = 0.1097$; $J/J_0 = 1.4358$)

	DOFs	1722 (e_s%)	3782 (e_s%)	6642 (e_s%)	10,302 (e_s%)
K_I/K_0	NS-FEM-T3	1.0252 (1.7)	1.0205 (1.2)	1.0189 (1.0)	1.0179 (0.9)
	sNS-FEM-T3	1.0166 (0.8)	1.0127 (0.4)	1.0116 (0.3)	1.0105 (0.2)
	ES-FEM-T3	0.9989 (−0.9)	1.0020 (−0.6)	1.0033 (−0.5)	1.0041 (−0.4)
	sES-FEM-T3	1.0051 (−0.3)	1.0060 (−0.2)	1.0061 (−0.2)	1.0063 (−0.2)
	FEM-T3	0.9834 (−2.4)	0.9903 (−1.8)	0.9939 (−1.4)	0.9959 (−1.2)
	sFEM-T6	1.0046 (−0.4)	1.0057 (−0.3)	1.0059 (−0.2)	1.0062 (−0.2)
K_{II}/K_0	NS-FEM-T3	0.0801 (−27.0)	0.0924 (−15.8)	0.0979 (−10.8)	0.1023 (−6.7)
	sNS-FEM-T3	0.0912 (−16.9)	0.0981 (−10.6)	0.1037 (−5.5)	0.1086 (−1.0)
	ES-FEM-T3	0.1134 (3.4)	0.1118 (1.0)	0.1108 (1.0)	0.1104 (0.6)
	sES-FEM-T3	0.1106 (0.9)	0.1105 (0.9)	0.1101 (0.3)	0.1099 (0.2)
	FEM-T3	0.1192 (8.6)	0.1141(4.6)	0.1122 (2.3)	0.1111 (1.3)
	sFEM-T6	0.1104 (0.7)	0.1103 (0.6)	0.1100 (0.3)	0.1099 (0.2)
J/J_0	NS-FEM-T3	1.4765 (2.8)	1.4659 (2.1)	1.4627 (1.8)	1.4611 (1.7)
	sNS-FEM-T3	1.4546 (1.3)	1.4453 (0.7)	1.4438 (0.5)	1.4421 (0.4)
	ES-FEM-T3	1.4109 (−1.7)	1.4188 (−1.2)	1.4223 (−0.9)	1.4244 (−0.8)
	sES-FEM-T3	1.4273 (−0.6)	1.4296 (−0.4)	1.4301 (−0.4)	1.4306 (−0.3)
	FEM-T3	1.3699 (−4.6)	1.3872 (−3.4)	1.3964 (−2.7)	1.4018 (−2.4)
	sFEM-T6	1.4240 (−0.8)	1.4283 (−0.5)	1.4296 (−0.4)	1.4301 (−0.4)

Note: Shaded, upper bounds.

BOUND PROPERTY OF SOLUTIONS

From Table 10.17 and these figures, it can be found that the K_I and J obtained using the sFEM models are smaller than the exact solutions (the negative relative error) and converge from below. On the contrary, the K_I and J values obtained using the sNS-FEM models are larger than the exact ones (the positive relative error, shaded) and converge from above.

However, the opposite is found for the K_{II} solution: the FEM results converge from above, and the sNS-FEM results converge from below, as shown in Figure 10.42. This finding implies that for solution in terms of SIFs, it is not always guaranteed that NS-FEM produces upper bound and FEM produces lower bound. What seems always to be true is that these computed values of the FEM and the NS-FEM models will stay opposite sides. These solutions will converge to the exact solution from different sides. This is important because we can always bound the exact solutions from two sides. This is, in fact, all we need in practical applications.

AREA-PATH INDEPENDENCE

The area-path independence is also conducted for this interfacial crack case, and the results for different paths are listed in Table 10.18. For K_I and J values,

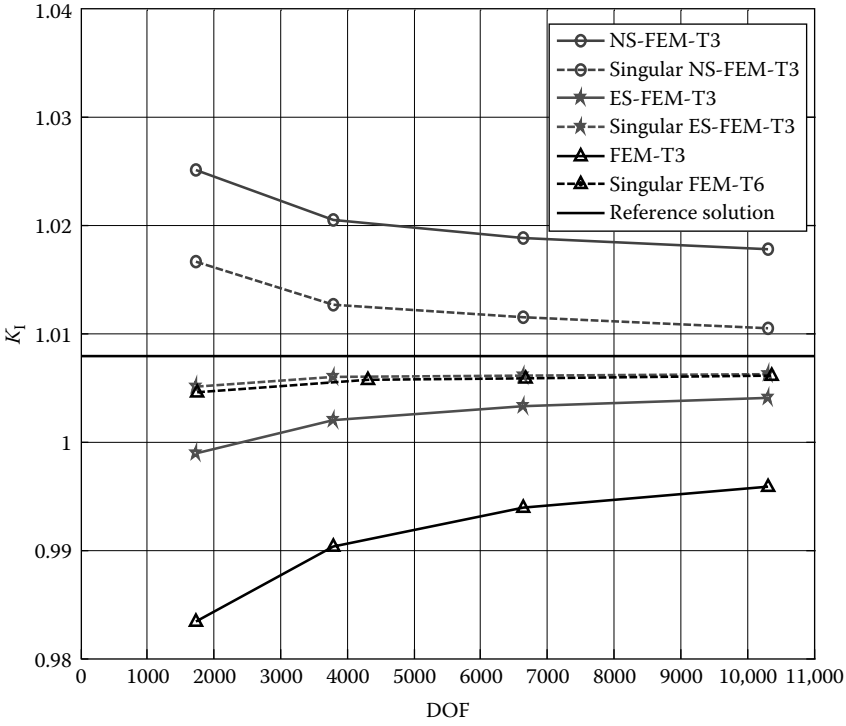

FIGURE 10.41 Convergence of the K_I for the plate of bimaterials with a center-crack subjected to tension.

we have the similar finding that the differences caused by different area-paths used for all these cases are beyond the third digit for both meshes. Different from the previous examples, however, we found from this interfacial crack example that K_{II} showed quite strong area-path dependence numerically. Area-path with $r_k = 4$ seems to be the best for this case. Therefore, for interfacial crack, care must be taken in numerical analysis, and further studies on this issue are required.

Example 10.10.4: Interfacial Crack in a Film/Substrate System

PROBLEM SETTINGS

The final example of this chapter considers a practical problem of a thin-film/substrate system with an interfacial crack subject to four-point bending. Owing to symmetry, only one-half of the domain is modeled in this analysis. The dimensions of the domain and crack and the displacement boundary conditions are given in Figure 10.44. The thickness of film is denoted by h_f and that of the substrate by h_s. The total thickness is denoted by $h_t = h_f + h_s$. E_f and v_f are the Young's modulus and Poisson's ratio of the film, and E_s and v_s are those

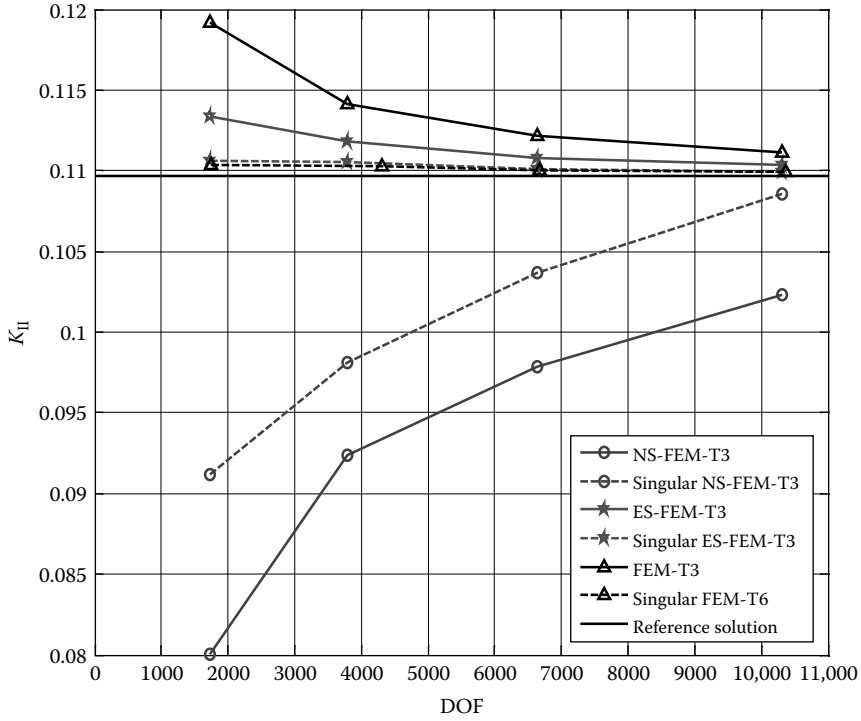

FIGURE 10.42 Convergence of the K_{II} for the plate of bimaterials with a center-crack subjected to tension.

for the substrate. The objective of this analysis is to evaluate the energy release rate G for the interfacial crack.

When the interface crack length is significantly larger than the thickness of the film, a steady-state condition is reached and the energy release rate stabilizes at a constant value, G_{ss}, which is known as the *steady-state* energy that can be calculated using [21]

$$G_{ss} = \frac{3(1-\nu_s^2)P^2L^2}{2E_s b^2 h_t^3} \times \left\{ \left(\frac{h_t}{h_s}\right)^3 - \lambda_m \left[\left(\frac{h_f}{h_t}\right)^3 + \lambda_m \left(\frac{h_s}{h_t}\right)^3 + 3\lambda_m \frac{h_f h_s}{h_t^2} \left(\frac{h_f}{h_t} + \lambda \frac{h_s}{h_t}\right) \right] \right\}, \tag{10.68}$$

where b is the depth (into the paper) of the film/substrate system and λ_m relates to the ratio of the properties of the two materials:

$$\lambda_m = \frac{E_s(1-\nu_f^2)}{E_f(1-\nu_s^2)}, \tag{10.69}$$

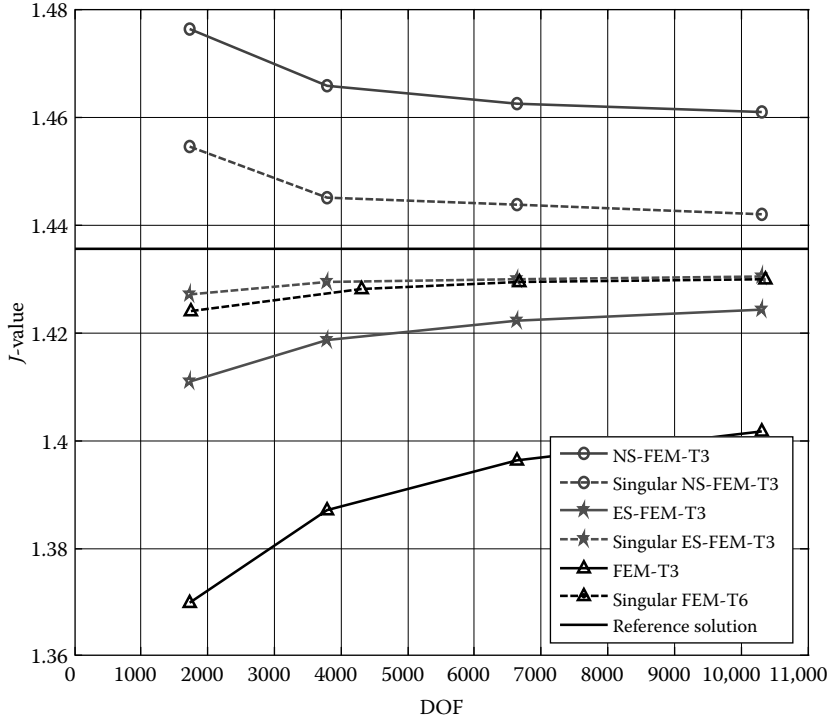

FIGURE 10.43 Convergence of the *J*-integral for the plate of bimaterials with a center-crack subjected to tension.

TABLE 10.18

Area-Path Independence of the sNS-FEM-T3 Solutions for Plate of Bimaterials with a Center-Crack Subjected to Remote Tension

Mesh Size	Area-Path Dimension (r_k)	J/J_0 (e_s %)	K_I/K_0 (e_s %)	K_{II}/K_0 (e_s %)
$a/h = 6.0$	3	1.4445 (0.6)	1.0097 (0.2)	0.1230 (12.1)
	4	1.4470 (0.8)	1.0124 (0.4)	0.1070 (−2.5)
	5	1.4453 (0.6)	1.0127 (0.5)	0.0981 (−10.6)
	6	1.4451 (0.6)	1.0129 (0.5)	0.0952 (−13.1)
$a/h = 8.0$	3	1.4413 (0.4)	1.0073 (−0.1)	0.1328 (21.1)
	4	1.4437 (0.5)	1.0106 (0.3)	0.1126 (2.5)
	5	1.4438 (0.6)	1.0116 (0.4)	0.1037 (−5.5)
	6	1.4444 (0.6)	1.0121 (0.4)	0.1010 (−7.9)

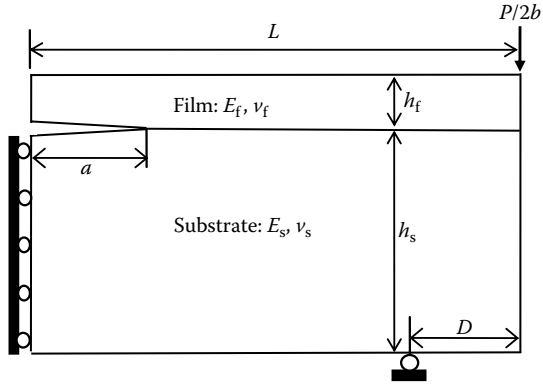

FIGURE 10.44 A thin-film/substrate system with an interfacial crack subjected to four-point bending. Only half of the domain is modeled.

For interfacial cracks, the phase angle ψ is an important parameter in the characterization of interfacial fracture toughness. It measures the relative proportion of shear-to-normal tractions at a characteristic distance l ahead of the crack-tip, and is defined as [19]

$$\mathbf{K}l^{i\varepsilon} = |\mathbf{K}|\, \mathrm{e}^{i\psi}. \tag{10.70}$$

The characteristic length l given in Equation 10.70 is taken as the total thickness of the film/substrate system h_t, and ψ can be obtained using

$$\psi = \tan^{-1}\left(\frac{\mathrm{Im}[\mathbf{K}h_t^{i\varepsilon}]}{\mathrm{Re}[\mathbf{K}h_t^{i\varepsilon}]}\right). \tag{10.71}$$

We now define reference parameters K_0 and G_0 as

$$K_0 = \frac{PL}{bh_t^{3/2}}, \quad G_0 = \frac{(1-\nu_s^2)P^2L^2}{E_s b^2 h_t^3}, \tag{10.72}$$

which are used to normalize the solution outputs of SIFs and the energy release rate G (that equals the J-integral value), as shown in Equation 10.23.

In our numerical models, the geometric parameters are set as

$a = 30, \quad b = 1;$

$h_f = 1, \quad h_t = 10,$ which gives $h_f/h_t = 0.1;$

$L = 125, \quad D = 50,$ which gives $L/D = 2.5; D/h_t = 5$ and $a/h_t = 3$

The material parameters used are $E_s = 1.0 \times 10^3$, $E_f/E_s = 10$, and $\nu_f = \nu_s = 0.3$. The plate is subjected to a unit loading of $P = 1$. The mesh with

$h_f/h = 6.0$ (3156 nodes) and the domain radius parameter $r_k = 5$ are used for the interaction integral. Based on this setting, the exact steady-state energy release rate is found from Equation 10.68: $G_{ss} = 1.3632$, $K_0 = 1.5811$, and $G_0 = 2.2750 \times 10^{-4}$.

NUMERICAL SOLUTIONS: ACCURACY AND BOUND PROPERTY

Table 10.19 lists the solution of energy release rates obtained by FEM, sFEM, ES-FEM, sES-FEM, NS-FEM and sNS-FEM, together with solutions of K_I, K_{II}, and ψ. In terms of energy release rate, we first note that (1) the solution accuracy of FEM-T3 and NS-FEM-T3 is of about the same level, and (2) the sES-FEM-T3 solutions are the most accurate, followed closely by the higher-order sFEM-T6. Most importantly, we observe again that the NS-FEM models produce upper bound solutions in energy release rate, while the FEM models produce lower bounds. The exact solution of $G_{ss} = 1.3632$ fails indeed in between 1.3531 (a lower bound by sFEM-T6) and 1.3779 (an upper bound by sNS-FEM-T3).

Now, with the total thickness fixed at $h_t = 10$, we vary the thickness of the film to achieve the thickness ratio h_f/h_t varying in the range of [0.1, 0.5]. We then compute two quite extreme cases of bimaterial combinations: $E_f/E_s = 0.1$ and 10. Table 10.20 lists the solution of steady-state energy release rates for different thickness ratios and different bimaterial combinations. We first notice that for all these cases, the numerical solutions are very accurate for the quite coarse mesh used. This implies that our singular models are very robust for interfacial crack problems, and this is made possible by the enrichment of displacement field near the crack-tip. In terms of energy release rate, we observe that (1) the sES-FEM-T3 is of about the same accuracy as the higher-order sFEM-T6, and they are about twice more accurate than that of the (basically) linear sNS-FEM-T3, and (2) most importantly, the sFEM-T6 bounds the solution from below and the sNS-FEM-T3 bounds from above, which provides a very important and practical mean to bound the exact solution from both sides for the interfacial crack problems.

TABLE 10.19

Numerical Solutions Obtained Using Various Methods for the Film/Substrate System Subjected to Four-Point Bending (the Exact $G_{ss} = 1.3632$; Mesh Size $h = h_f/6$)

Method	J/J_0 (e_s %)	K_I/K_0	K_{II}/K_0	ψ
FEM-T3	1.3142 (−3.6)	0.9386	1.2832	43.81
sFEM-T6	1.3502 (−0.9)	0.9564	1.2965	43.54
ES-FEM-T3	1.3423 (−1.5)	0.9517	1.2946	43.68
sES-FEM-T3	1.3511 (−0.8)	0.9572	1.2970	43.57
NS-FEM-T3	1.4123 (3.5)	0.9970	1.3123	42.77
sNS-FEM-T3	1.3779 (1.1)	0.9882	1.3061	42.89

TABLE 10.20

Effect of Elastic Modulus Ratio and Thickness Ratio on the Numerical Solutions Obtained Using Various Methods for the Film/Substrate System Subjected to Four-Point Bending

		sFEM-T6	sES-FEM-T3		sNS-FEM-T3	
E_f/E_s	h_f/h_t	J/J_0 (e_s %)	J/J_0 (e_s %)	Exact J/J_0	J/J_0 (e_s %)	ψ
10	0.1	1.3507 (−0.9)	1.3511 (−0.8)	1.3632	1.3779 (1.1)	42.89
	0.2	2.2618 (−0.8)	2.2626 (−0.7)	2.2793	2.3234 (1.9)	42.00
	0.3	3.6964 (−0.7)	3.6969 (−0.7)	3.7254	3.7875 (1.7)	38.85
	0.4	6.2749 (−0.8)	6.2754 (−0.8)	6.3249	6.4264 (1.6)	35.34
	0.5	11.3450 (−0.9)	11.3451 (−0.9)	11.4523	11.6746 (1.9)	32.32
0.1	0.1	0.0802 (−0.8)	0.0801 (−0.9)	0.0807	0.0822 (1.8)	61.98
	0.2	0.3019 (−0.8)	0.3022 (−0.7)	0.3043	0.3112 (2.2)	55.72
	0.3	0.8957 (−0.5)	0.8959 (−0.5)	0.9010	0.9290 (2.5)	51.14
	0.4	2.4519 (−0.5)	2.4518 (−0.5)	2.4655	2.4976 (1.3)	47.43
	0.5	6.4698 (−0.9)	6.4706 (−0.8)	6.5228	6.6522 (1.8)	44.70

10.11 Remarks

In this chapter, we formulated the sS-FEMs with a focus on the sNS-FEM and sES-FEM, using a basic mesh of three-node triangular (T3) elements. A general five-node triangular (T5) crack-tip element is presented with an additional node on each of the two crack-tip edges. Only one layer of singular T5 elements is used around the crack-tip to provide the crucial capacity to produce the important singularity field. Intensive numerical studies have been conducted to examine these sNS-FEM-T3 and sES-FEM-T3 models. The following remarks should be mentioned before concluding this chapter.

Remark 10.1 T5 Crack-Tip Element: Simple, Unique, and Effective

For the T5 singular crack-tip elements, the mid-edge node can be located at any point within the crack-tip edge. One quarter-length away from the crack-tip is recommended, just to be the same as what we used to do in the standard FEM. The use of T5 elements is simple, unique, and effective to improve the solutions for fracture problems.

Remark 10.2 sES-FEM-T3 with S-SD=2: Ultra-Accurate, Best Linear Model

For sES-FEM-T3, S-SD=2 is recommended. The sES-FEM-T3 produces an ultra-accurate solution that is as much as 50 times more accurate than

the FEM-T3 and even more accurate than the higher-order sFEM-T6. The sES-FEM-T3 usually produces lower bound solution for strain energy for force-driving problems, but it can also give upper bound depending on the setting of the problem. Because the sES-FEM-T3 mode has a very close-to-exact stiffness, the solution is often quite close to the exact one and hence can be on both sides. The sES-FEM-T3 may be a "star" performer and probably the best linear model so far found for fracture problems. It can be very challenging to find a linear model that performs better than the sES-FEM-T3 for fracture problems.

Remark 10.3 sNS-FEM-T3 with Scheme 4: Upper Bound Solutions

For sNS-FEM-T3, Scheme 4 for subsmoothing domain division is recommended. The sNS-FEM-T3 solution accuracy is, by large, at the same level as the FEM-T3 solution accuracy. However, it has a very important upper bound property: it produces upper bound solutions in strain energy (or the strain energy release rate or the J-integral value) for force-driving problems, in contrast to the FEM that produces lower bounds. Using sES-FEM-T3 together with sFEM-T6 (or FEM-T3), we can now bound the solution for fracture problems from both sides.

Remark 10.4 sS-FEM Solutions: Area-Path Independent

The area-path independence is generally observed via numerical examples for both sES-FEM-T3 and sNS-FEM-T3 models.

Remark 10.5 sS-FEM: High Convergence Rate

The convergence rate for sES-FEM-T3 is found to be much higher than that of FEM-T3 and even higher than that of the sFEM-T6. It is, however, still a little lower than the theoretical rate for convex domains.

Remark 10.6 sS-FEM Formulation: Other Extensions

Note that a similar idea can be used for creating the S-FEM model for problems with different orders of singularity. This is because S-FEM does not need the derivatives of field functions for constructing the stiffness matrix. If a proper interpolation can be done to create the desired field, an efficient model can then be created. In addition, the sS-FEM can be extended for crack propagation problems [7]. More general methods can be created based on the mesh-free settings [22].

References

1. Anderson TL. 1995. *Fracture Mechanics: Fundamentals and Applications*. CRC Press, Boston.
2. Zienkiewicz OC and Taylor RL. 2000. *The Finite Element Method*, 5th edition. Butterworth Heinemann, Oxford.
3. Liu GR and Quek SS. 2003. *Finite Element Method: A Practical Course*. Butterworth Heinemann, Burlington, MA.
4. Liu GR, Nourbakhshnia N, and Zhang YW. 2009. A novel singular ES-FEM method for simulating singular stress fields near the crack-tips for linear fracture problems. *Engineering Fracture Mechanics*; accepted.
5. Liu GR, Nourbakhshnia N, Chen L, and Zhang YW. 2009. A general construction of singular stress field in the ES-FEM method for analysis of fracture problems of mixed-mode cracks. *International Journal for Computational Methods*, 191–214.
6. Liu GR, Chen L, Nguyen-Thoi T, and Zeng K. 2009. A novel singular node-based smoothed finite element method (NS-FEM) for upper bound solutions of fracture problems. *International Journal for Numerical Methods in Engineering*; accepted.
7. Nourbakhshnia N, Liu GR, Chen L, and Zhang YW. 2010. A singular ES-FEM method for crack propagation problems, *Computer Methods in Applied Mechanics and Engineering*; revised.
8. Moran B and Shih CF. 1987. Crack-tip and associated domain integrals from momentum and energy balance. *Engineering Fracture Mechanics*; 27(6): 615–641.
9. Li FZ, Shih CF, and Needleman A. 1985. A comparison of methods for calculating energy release rates. *Engineering Fracture Mechanics*; 1(2): 405–421.
10. Belytschko T and Black T. 1999. Elastic crack growth in finite elements with minimal remeshing. *International Journal for Numerical Methods in Engineering*; 45(5): 601–620.
11. Moes N, Dolbow J, and Belytschko T. 1999. A finite element method for crack growth without remeshing. *International Journal for Numerical Methods in Engineering*; 46(1): 131–150.
12. Tada H, Paris PC, and Irwin GR. 2000. *The Stress Analysis of Cracks Handbook*. ASME Press, New York.
13. Shih CF. 1988. Cracks on bi-material interfaces: Elasticity and plasticity aspects. *Materials Science and Engineering A*; 143: 77–90.
14. Dundurs J. 1969. Edge-bonded dissimilar orthogonal elastic wedges. *Journal of Applied Mechanics*; 36: 650–652.
15. Shih CF and Asaro RJ. 1988. Elastic–plastic analysis of cracks on bi-material interfaces: Part I-small scale yielding. *Journal of Applied Mechanics*; 55: 299–316.
16. Eshelby JD. 1956. The continuum theory of lattice defects. In *Solid State Physics*, F Seitz and D Turnbull, Eds. Academic Press; New York, Vol. 3, pp. 79–144.
17. Eshelby JD. 1970. The energy momentum tensor in continuum mechanics. In *Inelastic Behavior of Solids*, MF Kanninen et al., Eds. McGraw-Hill, New York, pp. 77–114.

18. Liu GR and Zhang GY. 2008. Upper bound solution to elasticity problems: A unique property of the linearly conforming point interpolation method (LC-PIM). *International Journal for Numerical Methods in Engineering*; 74: 1128–1161.
19. Rice JR. 1988. Elastic fracture mechanics concepts for interfacial cracks. *Journal of Applied Mechanics*; 55: 98–103.
20. Rice JR and Sih GC. 1965. Plane problems of cracks in dissimilar media. *Journal of Applied Mechanics*; 32: 418–423.
21. Charalambides PG, Lund J, Evans AG, and McMeeking RM. 1989. A test specimen for determining the fracture resistance of bi-material interfaces. *Journal of Applied Mechanics*; 56: 77–82.
22. Liu GR. 2009. *Meshfree Methods: Moving Beyond the Finite Element Method*, 2nd edition. Taylor & Francis/CRC Press, Boca Raton, FL.

11

S-FEM for Viscoelastoplasticity

11.1 Introduction

In practical engineering systems, various other types of materials are used apart from the most often used linear elastic materials. One example of such a type of materials is the so-called viscoelastoplastic materials [1]. Currently, mechanics problems for solids of viscoelastoplastic materials can be modeled using the FEM, based on the so-called *dual* formulation or *primal* formulation. In the dual formulation [2], the displacement and stress approximations are computed simultaneously with *yield functions* and *flow rules* written in terms of *admissible stresses*. In the primal formulation [2], the strains are treated as the primary variables and a discretization is required for simultaneous approximations of both the displacement and plastic strain fields.

In this chapter, we aim to extend the S-FEM models to solve mechanics problems of solids with viscoelastoplastic materials, and both 2D and 3D problems will be considered. In particular, the ES-FEM-T3 (Chapter 7) will be used for 2D problems and FS-FEM-T4 (Chapter 8) will be used for 3D problems, using types of triangular and tetrahedral elements. ES-FEM-T3 and FS-FEM-T4 are chosen because of their excellent performance and stability both spatially and temporally as earlier studies have shown [3,4]. Our formulation is based on the dual formulation, and the ES-FEM-T3 and FS-FEM-T4 procedures are combined with the formulation of Carstensen and Klose [1] that was used in the standard FEM. The material behavior, including perfect viscoelastoplasticity and viscoelastoplasticity with isotropic and linear kinematic hardening, is modeled with the von-Mises conditions and the Prandtl–Reuss flow rule. In the present dual formulation, both displacements and stresses are first treated as primary variables. We then eliminate the stress variables at a later stage and convert the problem to be only displacement dependent, so that it can be much easier to solve. Therefore, the approach used in this chapter is *eventually* still a displacement method.

Examples will be presented to examine the present ES-FEM-T3 and FS-FEM-T4 formulations, and the numerical results and a posteriori error estimations demonstrate some superior properties of ES-FEM-T3 and

FS-FEM-T4 compared to standard FEM counterparts in solving viscoelasto-plasticity problems.

11.2 Strong Formulation for Viscoelastoplasticity

11.2.1 Equilibrium Equation

The strong form of the governing equation for a viscoelastoplastic solid that deforms in the "pseudo" time interval $t \in [0, T]$ is expressed in the form of equilibrium equation defined in the problem domain Ω bounded by Γ. At any given time, we shall have

$$\mathbf{L}_d \boldsymbol{\sigma} + \mathbf{b} = \mathbf{0} \quad \text{in } \Omega, \tag{11.1}$$

where all these terms are defined in Chapter 2.

11.2.2 Boundary Conditions

The boundary conditions on the Dirichlet boundary Γ_u is defined at any given time instance as

$$\mathbf{u} = \mathbf{w}_0 \quad \text{on } \Gamma_u \tag{11.2}$$

We note that the Dirichlet boundary condition considered here is in general nonhomogeneous. The Neumann boundary condition can be expressed as

$$\boldsymbol{\sigma}^T \mathbf{n} = \mathbf{t} \quad \text{on } \Gamma_t, \tag{11.3}$$

which is also nonhomogeneous in general and should be enforced at all times.

11.2.3 Constitution Equation, Yield Function, and Flow Rule

For viscoelastoplasticity problems, the constitutive equations, yield function, and flow rule must be properly defined and enforced at all times. In the context of small strain, the total strain $\boldsymbol{\varepsilon}(\mathbf{u})$ is separated into two parts:

$$\boldsymbol{\varepsilon}(\mathbf{u}) = \mathbf{e}(\boldsymbol{\sigma}) + \mathbf{p}(\boldsymbol{\xi}), \tag{11.4}$$

where $\mathbf{e}(\boldsymbol{\sigma}) = \mathbf{c}^{-1}\boldsymbol{\sigma}$ is the elastic strain vector and $\mathbf{p}(\boldsymbol{\xi})$ is the irreversible plastic strain vector with $\boldsymbol{\xi}$ being an internal variable.

To properly describe the evolution process for the plastic strain, it is required to define *admissible stresses*, a *yield function*, and an *associated flow rule*. In this work, we use the von-Mises yield function and the Prandtl–Reuss flow rule, and the evolution process is modeled in the following procedure.

Let $\mathbf{p}$ and $\boldsymbol{\xi}$ be the kinematic variables of the generalized strain $\mathbf{P} = (\mathbf{p}, \boldsymbol{\xi})$, and let $\Sigma = (\boldsymbol{\sigma}, \boldsymbol{\alpha})$ be the corresponding generalized stress, where $\boldsymbol{\alpha}$ is the hardening parameter describing internal stresses. We define Υ as the admissible stresses set, which is a closed, convex set, containing $\mathbf{0}$ and defined by

$$\Upsilon = \{\Sigma : \Phi(\Sigma) \leq 0\}, \tag{11.5}$$

where Φ is the von-Mises yield function that is presented specifically for different viscoelastoplasticity cases as follows:

Case a: Perfect viscoelastoplasticity
In this case, there is no hardening and the internal variables $\boldsymbol{\xi}, \boldsymbol{\alpha}$ are absent. The von-Mises yield function can be simply given as

$$\Phi(\boldsymbol{\sigma}) = \|\text{dev}(\boldsymbol{\sigma})\| - \sigma_Y, \tag{11.6}$$

where σ_Y is the yield stress; $\|\mathbf{x}\|$ is the norm of a vector $\mathbf{x} = \{x_1 \quad x_2 \quad \cdots \quad x_n\}^T$ and computed by $\|\mathbf{x}\| = \sqrt{\sum_{i=1}^{n} x_i^2}$; $\text{dev}(\mathbf{x})$ is the deviator vector of a vector $\mathbf{x}$ and computed using

$$\text{dev}(\mathbf{x}) = \mathbf{x} - \frac{\text{tr}(\mathbf{x})}{d}\mathbf{I}, \tag{11.7}$$

in which d is the dimension of the problem ($d = 2$ for 2D and $d = 3$ for 3D); $\mathbf{I} = \{1 \quad 1 \quad 0\}^T$ for 2D problems and $\mathbf{I} = \{1 \quad 1 \quad 1 \quad 0 \quad 0 \quad 0\}^T$ for 3D problems; and $\text{tr}(\mathbf{x})$ is the trace operator defined by

$$\text{tr}(\mathbf{x}) = \sum_{i=1}^{d} \mathbf{x}_i. \tag{11.8}$$

The Prandtl–Reuss flow rule has the form of

$$\dot{\mathbf{p}} = \begin{cases} \frac{1}{v}\left(\|\text{dev}(\boldsymbol{\sigma})\| - \sigma_Y\right) & \text{if } \|\text{dev}(\boldsymbol{\sigma})\| > \sigma_Y, \\ 0 & \text{if } \|\text{dev}(\boldsymbol{\sigma})\| \leq \sigma_Y, \end{cases} \tag{11.9}$$

where v is the viscosity parameter and $v > 0$, and $\dot{\mathbf{p}}$ is the velocity of plasticity strain.

Case b: Viscoelastoplasticity with isotropic hardening
In the case of isotropic hardening, the material behavior is characterized by a modulus of hardening $H \geq 0$, and $\boldsymbol{\alpha} \equiv \alpha^{\mathrm{I}} \geq 0$ (I stands for isotropic) becomes a scalar hardening parameter that relates to the scalar internal strain variable ξ in the form of

$$\alpha^{\mathrm{I}} = -H_1 \xi, \tag{11.10}$$

where H_1 is a positive hardening parameter.

The von-Mises yield function can then be written as

$$\Phi(\boldsymbol{\sigma}, \alpha^{\mathrm{I}}) = \|\mathrm{dev}(\boldsymbol{\sigma})\| - \sigma_Y(1 + H\alpha^{\mathrm{I}}). \tag{11.11}$$

For the viscosity parameter $v > 0$, the Prandtl–Reuss flow rule becomes

$$\begin{pmatrix} \dot{\mathbf{p}} \\ \dot{\xi} \end{pmatrix} = \begin{cases} \dfrac{1}{v} \dfrac{1}{\left(1 + H^2 \sigma_Y^2\right)} \begin{pmatrix} \|\mathrm{dev}(\boldsymbol{\sigma})\| - \left(1 + \alpha^{\mathrm{I}} H\right) \sigma_Y \\ -H\sigma_Y \left(\|\mathrm{dev}(\boldsymbol{\sigma})\| - \left(1 + \alpha^{\mathrm{I}} H\right) \sigma_Y\right) \end{pmatrix} & \\ \qquad\qquad \text{if } \|\mathrm{dev}(\boldsymbol{\sigma})\| > \left(1 + \alpha^{\mathrm{I}} H\right) \sigma_Y, & \\ \begin{pmatrix} 0 \\ 0 \end{pmatrix} \qquad \text{if } \|\mathrm{dev}(\boldsymbol{\sigma})\| \leq \left(1 + \alpha^{\mathrm{I}} H\right) \sigma_Y, & \end{cases} \tag{11.12}$$

where $\dot{\xi}$ is the velocity of the scalar internal strain variable.

Case c: Viscoelastoplasticity with linear kinematic hardening
In the case of linear kinematic hardening, the internal stress $\boldsymbol{\alpha} \equiv \boldsymbol{\alpha}^{\mathrm{K}}$ (K stands for kinematic) relates to the internal strain $\boldsymbol{\xi}$ in the following simple form of

$$\boldsymbol{\alpha}^{\mathrm{K}} = -k_1 \boldsymbol{\xi}, \tag{11.13}$$

where k_1 is a positive parameter.

The von-Mises yield function is now written as

$$\boldsymbol{\Phi}\left(\boldsymbol{\sigma}, \boldsymbol{\alpha}^{\mathrm{K}}\right) = \left\|\mathrm{dev}(\boldsymbol{\sigma}) - \mathrm{dev}\left(\boldsymbol{\alpha}^{\mathrm{K}}\right)\right\| - \sigma_Y. \tag{11.14}$$

For the viscosity parameter $v > 0$, the Prandtl–Reuss flow rule has the form of

$$\begin{pmatrix} \dot{\mathbf{p}} \\ \dot{\boldsymbol{\xi}} \end{pmatrix} = \begin{cases} \dfrac{1}{2v} \begin{pmatrix} \left\|\mathrm{dev}\left(\boldsymbol{\sigma} - \boldsymbol{\alpha}^{\mathrm{K}}\right)\right\| - \sigma_Y \\ -\left(\left\|\mathrm{dev}\left(\boldsymbol{\sigma} - \boldsymbol{\alpha}^{\mathrm{K}}\right)\right\| - \sigma_Y\right) \end{pmatrix} & \text{if } \left\|\mathrm{dev}\left(\boldsymbol{\sigma} - \boldsymbol{\alpha}^{\mathrm{K}}\right)\right\| > \sigma_Y, \\ \begin{pmatrix} 0 \\ 0 \end{pmatrix} & \text{if } \left\|\mathrm{dev}\left(\boldsymbol{\sigma} - \boldsymbol{\alpha}^{\mathrm{K}}\right)\right\| \leq \sigma_Y. \end{cases} \tag{11.15}$$

The Prandtl–Reuss flow rule can be written in the following general form [1]:

$$\begin{bmatrix} \dot{\mathbf{p}} \\ \dot{\boldsymbol{\xi}} \end{bmatrix} = \frac{1}{v} \begin{bmatrix} \boldsymbol{\sigma} - \Pi\boldsymbol{\sigma} \\ \boldsymbol{\alpha} - \Pi\boldsymbol{\alpha} \end{bmatrix}, \tag{11.16}$$

where the viscosity parameter $v > 0$, and $\Pi\boldsymbol{\sigma}$ and $\Pi\boldsymbol{\alpha}$ are defined as the projections of $(\boldsymbol{\sigma}, \boldsymbol{\alpha})$ into the admissible stresses set Υ.

11.3 FEM for Viscoelastoplasticity: A Dual Formulation

11.3.1 Galerkin Weak Form

The viscoelastoplasticity problem defined in Section 11.2 can now be stated in a weak formulation [1]: Seek $\mathbf{u} \in \mathbb{H}^1(\Omega; \mathrm{R}^d)$ such that $\mathbf{u} = \mathbf{w}_0$ on Γ_{D}, and for all $\mathbf{v} \in \mathbb{H}^1_0(\Omega; \mathrm{R}^d) = \{\mathbf{v} \in \mathbb{H}^1(\Omega; \mathrm{R}^d) : \mathbf{v} = \mathbf{0} \text{ on } \Gamma_{\mathrm{D}}\}$, the following equations are satisfied:

$$\int_{\Omega} (\boldsymbol{\sigma}(\mathbf{u}))^T \, \boldsymbol{\varepsilon}(\mathbf{v}) \, \mathrm{d}\Omega = \int_{\Omega} \mathbf{v}^T \mathbf{b} \, \mathrm{d}\Omega + \int_{\Gamma_t} \mathbf{v}^T \mathbf{t} \, \mathrm{d}\Gamma \tag{11.17}$$

and

$$\begin{bmatrix} \dot{\mathbf{p}} \\ \dot{\boldsymbol{\xi}} \end{bmatrix} = \begin{bmatrix} \boldsymbol{\varepsilon}(\dot{\mathbf{u}}) - \mathbf{c}^{-1}\dot{\boldsymbol{\sigma}} \\ \boldsymbol{\xi}(\dot{\boldsymbol{\alpha}}) \end{bmatrix} = \frac{1}{v} \begin{bmatrix} \boldsymbol{\sigma} - \Pi\boldsymbol{\sigma} \\ \boldsymbol{\alpha} - \Pi\boldsymbol{\alpha} \end{bmatrix}. \tag{11.18}$$

Equation 11.17 is the standard Galerkin weak form for the mechanics problem of solids of viscoelastoplastic materials, which is subjected to the constraint Equation 11.18.

11.3.2 Time Discretization Scheme

Equations 11.17 and 11.18 are formulated as a sort of time-dependent problem for the "time" $t \in [0, T]$. The generalized midpoint rule [1] is used here as the time-discretization scheme. At each time step, with given variables $(\mathbf{u}(t), \boldsymbol{\sigma}(t), \boldsymbol{\alpha}(t))$ at time t_0 denoted as $(\mathbf{u}_0, \boldsymbol{\sigma}_0, \boldsymbol{\alpha}_0)$, a spatial problem needs to be solved for unknowns at time $t_1 = t_0 + \Delta t$ denoted as $(\mathbf{u}_1, \boldsymbol{\sigma}_1, \boldsymbol{\alpha}_1)$. Time derivatives are then substituted by the backward difference quotients. For instance, $\dot{\mathbf{u}}$ is substituted by $(\mathbf{u}_\vartheta - \mathbf{u}_0)/\vartheta\Delta t$ where $\mathbf{u}_\vartheta = (1 - \vartheta)\mathbf{u}_0 + \vartheta\mathbf{u}_1$

with $1/2 \leq \vartheta \leq 1$. The weak statement for the time-discrete problem now becomes: Seek $\mathbf{u}_\vartheta \in \mathbb{H}^1(\Omega; \mathrm{R}^d)$ such that $\mathbf{u}_\vartheta = \mathbf{w}_0$ on Γ_D, and

$$\int_\Omega (\boldsymbol{\sigma}(\mathbf{u}_\vartheta))^T \boldsymbol{\varepsilon}(\mathbf{v})\, \mathrm{d}\Omega = \int_\Omega \mathbf{v}^T \mathbf{b}_\vartheta \Omega + \int_{\Gamma_t} \mathbf{v}^T \mathbf{t}_\vartheta\, \mathrm{d}\Gamma, \quad \forall \mathbf{v} \in \mathbb{H}_0^1(\Omega; \mathrm{R}^d) \tag{11.19}$$

and

$$\frac{1}{\vartheta \Delta t} \begin{bmatrix} \boldsymbol{\varepsilon}(\mathbf{u}_\vartheta - \mathbf{u}_0) - \mathbf{c}^{-1}(\boldsymbol{\sigma}_\vartheta - \boldsymbol{\sigma}_0) \\ \boldsymbol{\xi}(\boldsymbol{\alpha}_\vartheta - \boldsymbol{\alpha}_0) \end{bmatrix} = \frac{1}{v} \begin{bmatrix} \boldsymbol{\sigma}_\vartheta - \Pi \boldsymbol{\sigma}_\vartheta \\ \boldsymbol{\alpha}_\vartheta - \Pi \boldsymbol{\alpha}_\vartheta \end{bmatrix} \begin{matrix} \text{(a)} \\ \text{(b)} \end{matrix} \tag{11.20}$$

where $\mathbf{t}_\vartheta = (1-\vartheta)\mathbf{t}_0 + \vartheta \mathbf{t}_1$, $\mathbf{b}_\vartheta = (1-\vartheta)\mathbf{b}_0 + \vartheta \mathbf{b}_1$ in which $\mathbf{b}_0$, $\mathbf{t}_0$, $\mathbf{b}_1$, and $\mathbf{t}_1$ are the body forces and surface forces at time t_0, t_1, respectively.

In the plastic phase, it is easy to define $\boldsymbol{\alpha}_\vartheta$ from the Equation 11.20b. Therefore, the time discretization problem will reduce into solving Equations 11.19 and 11.20a which are in fact a dual formulation containing both stress and displacement as field variables. To solve the system of Equations 11.19 and 11.20a efficiently, we need to eliminate one variable. This can be done by first expressing explicitly the stress $\boldsymbol{\sigma}_\vartheta$ in the form of displacement $\mathbf{u}_\vartheta$ using Equation 11.20a, and then substituting it into Equation 11.19. The problem will then become only displacement dependent, and we need to solve the resultant form of Equation 11.19, to which our ES- and FS-FEM can be utilized. This solution process is briefly summarized for different cases of viscoelastoplastic materials in the following subsections.

11.3.3 Analytic Expression of the Stress Tensor

The Equation 11.20a, or the flow law, can be rewritten as

$$\mathbf{A} - \frac{\mathbf{c}^{-1}\boldsymbol{\sigma}_\vartheta}{\vartheta \Delta t} = \frac{1}{v}(\mathbf{I} - \Pi)\boldsymbol{\sigma}_\vartheta, \tag{11.21}$$

where $\mathbf{A} = \boldsymbol{\varepsilon}(\mathbf{u}_\vartheta - \mathbf{u}_0)/(\vartheta \Delta t) + \mathbf{c}^{-1}\boldsymbol{\sigma}_0/(\vartheta \Delta t)$. Using the stress–strain (constitutive) relation in elasticity, we obtain the expression of the elastic strain vector in the form of

$$\mathbf{e}_\vartheta = \mathbf{c}^{-1}\boldsymbol{\sigma}_\vartheta = \frac{1}{\mathrm{d}^2\lambda + 2\mathrm{d}\mu} \mathrm{tr}\boldsymbol{\sigma}_\vartheta \mathbf{I} + \frac{1}{2\mu} \mathrm{dev}\boldsymbol{\sigma}_\vartheta, \tag{11.22}$$

where μ and λ are Lame's constants.

By solving Equations 11.21 and 11.20b with the flow rule given in Equation 11.9, or 11.12 or 11.15, the explicit expressions for the stress vector $\boldsymbol{\sigma}_\vartheta$

for viscoelastoplasticity problems can be derived for the corresponding three cases [1]:

In the elastic phase, for all cases we have

$$\boldsymbol{\sigma}_{\vartheta} = C_1 \mathrm{tr}(\vartheta \Delta t \mathbf{A})\mathbf{I} + 2\mu \mathrm{dev}(\vartheta \Delta t \mathbf{A}). \tag{11.23}$$

In the plastic phase,

Case a: Perfect viscoelastoplasticity
The plastic occurs when $\|\mathrm{dev}(\vartheta \Delta t \mathbf{A})\| > \beta \sigma_Y$ and

$$\boldsymbol{\sigma}_{\vartheta} = C_1 \mathrm{tr}(\vartheta \Delta t \mathbf{A})\mathbf{I} + \left(C_2 + \frac{C_3}{\|\mathrm{dev}\,(\vartheta \Delta t \mathbf{A})\|} \right) \mathrm{dev}(\vartheta \Delta t \mathbf{A}), \tag{11.24}$$

where

$$C_1 = \lambda + \frac{2\mu}{d}, \quad C_2 = \frac{v}{(\beta v + \vartheta \Delta t)}, \quad C_3 = \frac{\vartheta \Delta t \sigma_Y}{(\beta v + \vartheta \Delta t)}, \tag{11.25}$$

in which $\beta = 1/(2\mu)$.

Case b: Viscoelastoplasticity with isotropic hardening
The plastic occurs when $\|\mathrm{dev}(\vartheta \Delta t \mathbf{A})\| > \beta(1 + \alpha_0^{\mathrm{I}} H)\sigma_Y$ and we have

$$\boldsymbol{\sigma}_{\vartheta} = C_1 \mathrm{tr}(\vartheta \Delta t \mathbf{A})\mathbf{I} + \left(\frac{C_3}{(C_2 \|\mathrm{dev}\,(\vartheta \Delta t \mathbf{A})\|)} + \frac{C_4}{C_2} \right) \mathrm{dev}(\vartheta \Delta t \mathbf{A}), \tag{11.26}$$

where

$$\begin{aligned} &C_1 = \lambda + \frac{2\mu}{d}, \quad C_2 = \beta v \left(1 + H^2 \sigma_Y^2\right) + \vartheta \Delta t \left(1 + \beta H_1 H^2 \sigma_Y^2\right) \\ &C_3 = \vartheta \Delta t \sigma_Y \left(1 + \alpha_0^{\mathrm{I}} H\right), \quad C_4 = H_1 H^2 \vartheta \Delta t \sigma_Y^2 + v \left(1 + H^2 \sigma_Y^2\right), \end{aligned} \tag{11.27}$$

in which α_0^I is the initial scalar hardening parameter.

Case c: Viscoelastoplasticity with linear kinematic hardening
The plastic occurs when $\|\mathrm{dev}(\vartheta \Delta t \mathbf{A} - \beta \boldsymbol{\alpha}_0^{\mathrm{K}})\| > \beta \sigma_Y$ and we obtain

$$\begin{aligned} \boldsymbol{\sigma}_{\vartheta} = C_1 \mathrm{tr}(\vartheta \Delta t \mathbf{A})\mathbf{I} + &\left(C_2 + \frac{C_3}{\left\|\mathrm{dev}\left(\vartheta \Delta t \mathbf{A} - \beta \boldsymbol{\alpha}_0^{\mathrm{K}}\right)\right\|} \right) \mathrm{dev}\left(\vartheta \Delta t \mathbf{A} - \beta \boldsymbol{\alpha}_0^{\mathrm{K}}\right) \\ &+ \mathrm{dev}\left(\boldsymbol{\alpha}_0^{\mathrm{K}}\right), \end{aligned} \tag{11.28}$$

where $\boldsymbol{\alpha}_0^{\mathrm{K}}$ is the initial hardening parameter, and

$$C_1 = \lambda + \frac{2\mu}{d}, \quad C_2 = \frac{\vartheta \Delta t k_1 + 2v}{\vartheta \Delta t + \beta \vartheta \Delta t k_1 + v/\mu}, \quad C_3 = \frac{\vartheta \Delta t \sigma_Y}{\vartheta \Delta t + \beta \vartheta \Delta t k_1 + v/\mu}. \tag{11.29}$$

By substituting the stress $\boldsymbol{\sigma}_\vartheta$ described explicitly in Equation 11.24 or 11.26 or 11.28 into Equation 11.19, we obtain a set of equations that depends only on the displacement field, which can be solved using a numerical method with a proper spatial discretization. In this chapter, we use ES-FEM for 2D problems and FS-FEM for 3D problems.

11.3.4 Discretization in Space using FEM-T3/FEM-T4

Using a triangulation procedure, the domain Ω can be discretized into N_e elements and N_n nodes such that $\Omega = \bigcup_{i=1}^{N_e} \Omega_i^e$ and $\Omega_i^e \cap \Omega_j^e = \emptyset, i \neq j$. In the discretized version of Equation 11.19, the spaces $\mathbb{H}^1(\Omega; \mathrm{R}^d)$ and $\mathbb{H}_0^1(\Omega; \mathrm{R}^d)$ are replaced by finite dimensional subspaces $\mathbb{H}_h^1(\Omega; \mathrm{R}^d) \subset \mathbb{H}^1(\Omega; \mathrm{R}^d)$ and $\mathbb{H}_{0,h}^1(\Omega; \mathrm{R}^d) \subset \mathbb{H}_0^1(\Omega; \mathrm{R}^d)$, respectively, as in the standard FEM procedures. The discretized weak form becomes: Seek $\tilde{\mathbf{u}}_\vartheta \in \mathbb{H}_h^1(\Omega; \mathrm{R}^d)$ such that $\tilde{\mathbf{u}}_\vartheta = \mathbf{w}_0$ on Γ_{D} and

$$\int_\Omega \left(\tilde{\boldsymbol{\sigma}}_\vartheta \left(\tilde{\boldsymbol{\varepsilon}} \left(\tilde{\mathbf{u}}_\vartheta - \mathbf{u}_0 \right) + \mathbf{c}^{-1} \boldsymbol{\sigma}_0 \right) \right)^T \tilde{\varepsilon}(\tilde{\mathbf{v}}) \, \mathrm{d}\Omega = \int_\Omega \tilde{\mathbf{v}}^T \mathbf{b}_\vartheta \, \mathrm{d}x + \int_{\Gamma_t} \tilde{\mathbf{v}}^T \mathbf{t}_\vartheta \, \mathrm{d}\Gamma,$$

$$\forall \tilde{\mathbf{v}} \in \mathbb{H}_{0,h}^1(\Omega; \mathrm{R}^d). \tag{11.30}$$

Let $(\varphi_1, \ldots, \varphi_{N_n d})$ be the nodal basis of the finite dimensional space $\mathbb{H}_h^1(\Omega; \mathrm{R}^d)$, where φ_j is the independent scalar shape function on the jth node satisfying the Kronecker condition $\varphi_j(j) = 1$ and $\varphi_j(l) = 0$, $j \neq l$; the discretized weak form now becomes: Seek $\tilde{\mathbf{u}}_\vartheta \in \mathbb{H}_h^1(\Omega; \mathrm{R}^d)$ such that $\tilde{\mathbf{u}}_\vartheta = \mathbf{w}_0$ on Γ_{D} and

$$\tilde{\mathbf{F}}_j = \int_\Omega \left(\tilde{\boldsymbol{\sigma}}_\vartheta \left(\tilde{\boldsymbol{\varepsilon}} \left(\tilde{\mathbf{u}}_\vartheta - \mathbf{u}_0 \right) + \mathbf{c}^{-1} \boldsymbol{\sigma}_0 \right) \right)^T \tilde{\boldsymbol{\varepsilon}}(\varphi_j) \, \mathrm{d}\Omega - \int_\Omega \varphi_j \mathbf{b}_\vartheta \, \mathrm{d}\Omega - \int_{\Gamma_t} \varphi_j \mathbf{t}_\vartheta \, \mathrm{d}\Gamma = 0 \tag{11.31}$$

for $j = 1, \ldots, N_n d$, which produces a set of $N_n d$ equations. $\tilde{\mathbf{F}}_j$ in Equation 11.31 can be written as the sum of two parts:

$$\tilde{\mathbf{F}}_j \left(\tilde{\mathbf{u}}_\vartheta \right) = \tilde{\mathbf{Q}}_j \left(\tilde{\mathbf{u}}_\vartheta \right) - \tilde{\mathbf{P}}_j, \tag{11.32}$$

where part $\tilde{\mathbf{Q}}_j$ depends on $\tilde{\mathbf{u}}_\vartheta$ and is given by

$$\tilde{\mathbf{Q}}_j\left(\tilde{\mathbf{u}}_\vartheta\right) = \tilde{\mathbf{Q}}_j = \int_\Omega \left(\tilde{\boldsymbol{\sigma}}_\vartheta\left(\tilde{\boldsymbol{\varepsilon}}\left(\tilde{\mathbf{u}}_\vartheta - \mathbf{u}_0\right) + \mathbf{c}^{-1}\boldsymbol{\sigma}_0\right)\right)^T \tilde{\boldsymbol{\varepsilon}}(\varphi_j)\,\mathrm{d}\Omega, \tag{11.33}$$

and part $\tilde{\mathbf{P}}_j$ that is independent of $\tilde{\mathbf{u}}_\vartheta$:

$$\tilde{\mathbf{P}}_j = \int_\Omega \varphi_j \mathbf{b}_\vartheta\,\mathrm{d}\Omega + \int_{\Gamma_t} \varphi_j \mathbf{t}_\vartheta\,\mathrm{d}\Gamma. \tag{11.34}$$

11.3.5 Iterative Solution

It is clear that Equation 11.31 is nonlinear in nature. In order to solve Equation 11.31, the widely used Newton–Raphson method is used. At each step of the Newton iterations, the discrete displacement vector $\tilde{\mathbf{u}}_\vartheta^p$ at the pth iteration (i.e., expressed in the nodal basis by $\tilde{\mathbf{u}}_\vartheta^p = \sum_{j=1}^{N_n d} \varphi_j \tilde{u}_j$) is determined from the iterative solution process:

$$\widetilde{D\mathbf{F}}\left(\tilde{\mathbf{u}}_\vartheta^p\right)\tilde{\mathbf{u}}_\vartheta^{p+1} = \widetilde{D\mathbf{F}}\left(\tilde{\mathbf{u}}_\vartheta^p\right)\tilde{\mathbf{u}}_\vartheta^p - \tilde{\mathbf{F}}\left(\tilde{\mathbf{u}}_\vartheta^p\right), \tag{11.35}$$

where $\widetilde{D\mathbf{F}}(\tilde{\mathbf{u}}_\vartheta^p)$ is in fact the system stiffness matrix whose entries are defined as

$$\left(\widetilde{D\mathbf{F}}\left(\tilde{u}_{\vartheta,1}^p, \ldots, \tilde{u}_{\vartheta,N_n d}^p\right)\right)_{rw} = \frac{\partial \tilde{\mathbf{F}}_r\left(\tilde{u}_{\vartheta,1}^p, \ldots, \tilde{u}_{\vartheta,N_n d}^p\right)}{\partial \tilde{u}_{\vartheta,w}^p}, \tag{11.36}$$

where $r, w \in \Psi^{\mathrm{dof}}$ is the set containing DOFs of whole problem domain.

In the numerical performance for the FEM-T3/FEM-T4, the system stiffness matrix $D\mathbf{F}(\tilde{\mathbf{u}}_\vartheta^p)$ as well as the vector $\tilde{\mathbf{F}}(\tilde{\mathbf{u}}_\vartheta)$ in Equation 11.31 are expressed as a sum over all elements $\Omega_i^e \in \Omega$. The entries of the local stiffness matrix $\widetilde{D\mathbf{F}}^i$ for element Ω_i^e are now defined by

$$\begin{aligned}
\widetilde{D\mathbf{F}}_{rw}^i &= \frac{\partial \tilde{\mathbf{F}}_r^i}{\partial \tilde{u}_{\vartheta,w}^p} = \frac{\partial \tilde{\mathbf{Q}}_r^i}{\partial \tilde{u}_{\vartheta,w}^p} \\
&= \frac{\partial}{\partial \tilde{u}_{\vartheta,w}^p}\left(\int_{\Omega_i^e} \tilde{\boldsymbol{\sigma}}_\vartheta\left(\tilde{\boldsymbol{\varepsilon}}\left(\sum_{l\in\tilde{\Psi}^{\mathrm{dof}}} \tilde{u}_{\vartheta,l}^p \varphi_l - \mathbf{u}_0\right) + \mathbf{c}^{-1}\boldsymbol{\sigma}_0\right)^T \tilde{\boldsymbol{\varepsilon}}(\varphi_r)\,\mathrm{d}\Omega\right),
\end{aligned} \tag{11.37}$$

where $r, w \in \tilde{\Psi}^{\text{dof}}$ is the set containing DOFs of element Ω_i^e, and

$$\tilde{\mathbf{Q}}_r^i = \int_{\Omega_i^e} \left(\tilde{\boldsymbol{\sigma}}_\vartheta \left(\tilde{\boldsymbol{\varepsilon}}\left(\tilde{\mathbf{u}}_\vartheta - \mathbf{u}_0\right) + \mathbf{c}^{-1}\boldsymbol{\sigma}_0\right)\right)^T \tilde{\boldsymbol{\varepsilon}}(\varphi_r)\, \mathrm{d}\Omega. \tag{11.38}$$

Now, by substituting the expression $\tilde{\boldsymbol{\sigma}}_\vartheta \left(\tilde{\boldsymbol{\varepsilon}}\left(\tilde{\mathbf{u}}_\vartheta - \mathbf{u}_0\right) + \mathbf{c}^{-1}\boldsymbol{\sigma}_0\right)$ in Equations 11.37 and 11.38 by explicit forms of Equations 11.23, 11.24, 11.26, and 11.28 for different cases of viscoelastoplasticity problems, we have

Case a: Perfect viscoelastoplasticity

$$\tilde{\mathbf{Q}}_r^i = S_i^e \left(C_1 \mathrm{tr}(\tilde{\mathbf{v}})\mathrm{tr}\left(\tilde{\boldsymbol{\varepsilon}}(\varphi_r)\right) + C_4 \left(\mathrm{dev}(\tilde{\mathbf{v}})\right)^T \tilde{\boldsymbol{\varepsilon}}(\varphi_r)\right), \tag{11.39}$$

$$\begin{aligned}\widetilde{D\mathbf{F}}_{rw}^i = S_i^e \Big(&C_1 \mathrm{tr}\left(\tilde{\boldsymbol{\varepsilon}}(\varphi_r)\right) \mathrm{tr}\left(\tilde{\boldsymbol{\varepsilon}}(\varphi_w)\right) + C_4 \left(\mathrm{dev}\left(\tilde{\boldsymbol{\varepsilon}}(\varphi_r)\right)\right)^T \tilde{\boldsymbol{\varepsilon}}(\varphi_w) \\ &-(C_5)_r \left(\mathrm{dev}(\tilde{\mathbf{v}})\right)^T \tilde{\boldsymbol{\varepsilon}}(\varphi_w)\Big),\end{aligned} \tag{11.40}$$

where $S_i^e = A_i^e$ for the FEM-T3 and $S_i^e = V_i^e$ for the FEM-T4; $\tilde{\mathbf{v}} = \tilde{\boldsymbol{\varepsilon}}\left(\tilde{\mathbf{u}}_\vartheta - \mathbf{u}_0\right) + \mathbf{c}^{-1}\boldsymbol{\sigma}_0$; and

$$C_4 = \begin{cases} C_2 + C_3 / \left\|\mathrm{dev}(\tilde{\mathbf{v}})\right\| & \text{if } \left\|\mathrm{dev}(\tilde{\mathbf{v}})\right\| - \beta\sigma_Y > 0, \\ 2\mu & \text{else,} \end{cases}$$

$$C_5 = \begin{cases} C_3 / \left\|\mathrm{dev}\left(\tilde{\mathbf{v}}\right)\right\|^3 \left[\left(\mathrm{dev}\left(\tilde{\boldsymbol{\varepsilon}}\left(\varphi_r\right)\right)\right)^T \mathrm{dev}\left(\tilde{\mathbf{v}}\right)\right]_{r=1}^{n_n^e d} & \text{if } \left\|\mathrm{dev}\left(\tilde{\mathbf{v}}\right)\right\| - \beta\sigma_Y > 0, \\ \underbrace{\left\{\begin{array}{ccc} 0 & \cdots & 0 \end{array}\right\}^T}_{\text{size of } 1\times n_n^e d} & \text{else,} \end{cases} \tag{11.41}$$

in which n_n^e is the number of nodes of an element ($n_n^e = 3$ for FEM-T3, $n_n^e = 4$ for FEM-T4); and C_1, C_2, C_3 are given in Equation 11.25.

Case b: Viscoelastoplasticity with isotropic hardening

$$\tilde{\mathbf{Q}}_r^i = S_i^e \left(C_1 \mathrm{tr}(\tilde{\mathbf{v}})\mathrm{tr}\left(\tilde{\boldsymbol{\varepsilon}}(\varphi_r)\right) + C_5 \left(\mathrm{dev}(\tilde{\mathbf{v}})\right)^T \tilde{\boldsymbol{\varepsilon}}(\varphi_r)\right), \tag{11.42}$$

$$\begin{aligned}\widetilde{D\mathbf{F}}_{rw}^i = S_i^e \Big(&C_1 \mathrm{tr}\left(\tilde{\boldsymbol{\varepsilon}}(\varphi_r)\right) \mathrm{tr}\left(\tilde{\boldsymbol{\varepsilon}}(\varphi_w)\right) + C_5 \left(\mathrm{dev}\left(\tilde{\boldsymbol{\varepsilon}}(\varphi_r)\right)\right)^T \tilde{\boldsymbol{\varepsilon}}(\varphi_w) \\ &-(C_6)_r \left(\mathrm{dev}(\tilde{\mathbf{v}})\right)^T \tilde{\boldsymbol{\varepsilon}}(\varphi_w)\Big),\end{aligned} \tag{11.43}$$

with

$$C_5 = \begin{cases} C_3/\left(C_2 \left\|\mathrm{dev}(\tilde{\mathbf{v}})\right\|\right) + C_4/C_2 & \text{if } \left\|\mathrm{dev}(\tilde{\mathbf{v}})\right\| - \beta\left(1+\alpha_0^{\mathrm{I}}H\right)\sigma_Y > 0, \\ 2\mu & \text{else,} \end{cases}$$

$$C_6 = \begin{cases} C_3/\left(C_2 \left\|\mathrm{dev}(\tilde{\mathbf{v}})\right\|^3\right)\left[\left(\mathrm{dev}\left(\tilde{\boldsymbol{\varepsilon}}(\varphi_r)\right)\right)^T \mathrm{dev}(\tilde{\mathbf{v}})\right]_{r=1}^{n_n^e d} & \\ & \text{if } \left\|\mathrm{dev}(\tilde{\mathbf{v}})\right\| - \beta\left(1+\alpha_0^{\mathrm{I}}H\right)\sigma_Y > 0, \\ \underbrace{\{0 \quad \cdots \quad 0\}}_{\text{size of } 1\times n_n^e d}^T & \text{else,} \end{cases} \tag{11.44}$$

where C_1, C_2, C_3, C_4 are determined by Equation 11.27.

Case c: Viscoelastoplasticity with linear kinematic hardening

$$\overline{\mathbf{Q}}_r^i = S_i^e\Big(\left(C_1\mathrm{tr}(\tilde{\mathbf{v}})\mathrm{tr}\left(\tilde{\boldsymbol{\varepsilon}}(\varphi_r)\right)\right) + C_4\left(\mathrm{dev}(\tilde{\mathbf{v}})\right)^T \tilde{\boldsymbol{\varepsilon}}(\varphi_r) + c\left(\mathrm{dev}\left(\boldsymbol{\alpha}_0^{\mathrm{K}}\right)\right)^T \tilde{\boldsymbol{\varepsilon}}(\varphi_r)\Big). \tag{11.45}$$

$$\widetilde{D\mathbf{F}}_{rw}^i = S_i^e\left(C_1\mathrm{tr}\left(\tilde{\boldsymbol{\varepsilon}}(\varphi_r)\right)\mathrm{tr}\left(\tilde{\boldsymbol{\varepsilon}}(\varphi_w)\right) + C_4\left(\mathrm{dev}\left(\tilde{\boldsymbol{\varepsilon}}(\varphi_r)\right)\right)^T \tilde{\boldsymbol{\varepsilon}}(\varphi_w) - (C_5)_r\left(\mathrm{dev}(\tilde{\mathbf{v}})\right)^T \tilde{\boldsymbol{\varepsilon}}(\varphi_w)\right), \tag{11.46}$$

where

$$C_4 = \begin{cases} C_3/\left\|\mathrm{dev}\left(\tilde{\mathbf{v}}\right)\right\| + C_2 & \text{if } \left\|\mathrm{dev}\left(\tilde{\mathbf{v}} - \beta\boldsymbol{\alpha}_0^{\mathrm{K}}\right)\right\| - \beta\sigma_Y > 0, \\ 2\mu & \text{else,} \end{cases}$$

$$C_5 = \begin{cases} C_3/\left\|\mathrm{dev}\left(\tilde{\mathbf{v}}\right)\right\|^3\left[\left(\mathrm{dev}\left(\tilde{\boldsymbol{\varepsilon}}(\varphi_r)\right)\right)^T \mathrm{dev}\left(\tilde{\mathbf{v}}\right)\right]_{r=1}^{n_n^e d} & \\ & \text{if } \left\|\mathrm{dev}\left(\tilde{\mathbf{v}} - \beta\boldsymbol{\alpha}_0^{\mathrm{K}}\right)\right\| - \beta\sigma_Y > 0, \\ \underbrace{\left\{0 \quad \cdots \quad 0\right\}}_{\text{size of } 1\times n_n^e d}^T & \text{else,} \end{cases} \tag{11.47}$$

$$c = \begin{cases} 1 & \text{if } \left\|\mathrm{dev}\left(\tilde{\mathbf{v}} - \beta\boldsymbol{\alpha}_0^{\mathrm{K}}\right)\right\| - \beta\sigma_Y > 0, \\ 0 & \text{else,} \end{cases}$$

in which C_1, C_2, C_3 are determined by Equation 11.29.

To properly apply the nonhomogeneous Dirichlet boundary conditions for our nonlinear problem, we use the approach of Lagrange multipliers. Combining the Newton iteration (Equation 11.35) and the set of boundary conditions imposed through Lagrange multipliers $\boldsymbol{\lambda}$, the extended system of equations is obtained:

$$\begin{pmatrix} \widetilde{D\mathbf{F}}\left(\tilde{\mathbf{u}}_{\vartheta}^{p}\right) & \mathbf{G}^{T} \\ \mathbf{G} & \mathbf{0} \end{pmatrix} \begin{pmatrix} \tilde{\mathbf{u}}_{\vartheta}^{p+1} \\ \mathbf{l} \end{pmatrix} = \begin{pmatrix} \tilde{\mathbf{b}} \\ \mathbf{w}_0 \end{pmatrix}, \tag{11.48}$$

where $\tilde{\mathbf{f}} = \widetilde{D\mathbf{F}}\left(\tilde{\mathbf{u}}_{\vartheta}^{p}\right)\tilde{\mathbf{u}}_{\vartheta}^{p} - \tilde{\mathbf{F}}\left(\tilde{\mathbf{u}}_{\vartheta}^{p}\right)$ and $\mathbf{G}$ is a matrix created from the given Dirichlet boundary conditions such that $\mathbf{G}\tilde{\mathbf{u}}_{\vartheta}^{p+1} = \mathbf{w}_0$.

The extended system of Equation 11.48 can now be solved for $\tilde{\mathbf{u}}_{\vartheta}^{p+1}$ and $\boldsymbol{\lambda}$ at each time step. The solving process is iterated until the relative residual $\tilde{\mathbf{F}}\left(\tilde{u}_{\vartheta,z_1}^{p+1}, \ldots, \tilde{u}_{\vartheta,z_m}^{p+1}\right)$ for the m free nodes $(z_1, \ldots, z_m) \in \Xi$ (where Ξ is the set of free nodes) is smaller than a given tolerance or the maximum number of iterations is larger than a prescribed number.

11.4 S-FEM for Viscoelastoplasticity: A Dual Formulation

In establishing our S-FEM models, we use the same mesh as the FEM models. On top of the element mesh, we will create a set of different types of smoothing domains, and we could have a CS-FEM model (see Chapter 5), an NS-FEM model (see Chapter 6), an ES-FEM model (see Chapter 7), or an FS-FEM model (see Chapter 8), and even an αFEM model (see Chapter 9). Based on any type of smoothing domain, we can establish the smoothed Galerkin weak form for the viscoelastoplasticity problems.

11.4.1 Smoothed Galerkin Weak Form

Following the same procedure as that given in Chapter 4, the viscoelastoplasticity problem defined in Section 11.2 can now be stated in a smoothed Galerkin weak formulation:

Seek $\overline{\mathbf{u}}_{\vartheta} \in \mathbb{H}_h^1(\Omega; \mathrm{R}^d)$ such that $\overline{\mathbf{u}}_{\vartheta} = \mathbf{w}_0$ on Γ_D and

$$\sum_{k=1}^{N_s} S_k^s \left(\overline{\boldsymbol{\sigma}}_{\vartheta}\left(\overline{\boldsymbol{\varepsilon}}_k\left(\overline{\mathbf{u}}_{\vartheta} - \mathbf{u}_0\right) + \mathbf{c}^{-1}\boldsymbol{\sigma}_0\right)\right)^{T} \overline{\boldsymbol{\varepsilon}}_k(\overline{\mathbf{v}}) = \int_{\Omega} \overline{\mathbf{v}}^{T}\mathbf{b}_{\vartheta}\,\mathrm{d}x + \int_{\Gamma_t} \overline{\mathbf{v}}^{T}\mathbf{t}_{\vartheta}\,\mathrm{d}\Gamma, \quad \forall \overline{\mathbf{v}} \in \mathbb{H}_{0,h}^1(\Omega; \mathrm{R}^d), \tag{11.49}$$

where $S_k^s = A_k^s$ for the ES-FEM-T3 and $S_k^s = V_k^s$ for the FS-FEM-T4, and for all smoothing domains we shall have

$$\frac{1}{\vartheta \Delta t}\begin{bmatrix} \overline{\boldsymbol{\varepsilon}}\left(\overline{\mathbf{u}}_\vartheta - \mathbf{u}_0\right) - \mathbf{c}^{-1}\left(\overline{\boldsymbol{\sigma}}_\vartheta - \boldsymbol{\sigma}_0\right) \\ \overline{\boldsymbol{\xi}}\left(\overline{\boldsymbol{\alpha}}, t_\vartheta\right) - \overline{\boldsymbol{\xi}}\left(\overline{\boldsymbol{\alpha}}, t_0\right) \end{bmatrix} = \frac{1}{v}\begin{bmatrix} \overline{\boldsymbol{\sigma}}_\vartheta - \Pi\overline{\boldsymbol{\sigma}}_\vartheta \\ \overline{\boldsymbol{\alpha}}_\vartheta - \Pi\overline{\boldsymbol{\alpha}}_\vartheta \end{bmatrix}, \tag{11.50}$$

where $\mathbf{t}_\vartheta = (1-\vartheta)\mathbf{t}_0 + \vartheta\mathbf{t}_1$, $\mathbf{b}_\vartheta = (1-\vartheta)\mathbf{b}_0 + \vartheta\mathbf{b}_1$ in which $\mathbf{b}_0$, $\mathbf{t}_0$, $\mathbf{b}_1$, and $\mathbf{t}_1$ are the body forces and surface forces at time t_0, t_1, respectively.

Equation 11.49 is the smoothed Galerkin weak form for mechanics problem of solids of viscoelastoplastic materials, which is subjected to the constraint Equation 11.50. Note that the time discretization and the iteration procedure used in the S-FEM are exactly the same as those used in the FEM. In the following section, we discuss two particular S-FEM models: ES-FEM-T3 and FS-FEM-T4 for viscoelastoplasticity for, respectively, 2D and 3D problems, owing to their outstanding performance and stability both spatially and temporally, as our earlier studies have shown [5,6]. Both ES-FEM-T3 and FS-FEM-T4 were found to be the best linear model for static and dynamic linear problems, geometric nonlinear problems, and fracture mechanics problems. We now examine their performance for material nonlinear problems.

11.4.2 ES-FEM-T3/FS-FEM-T4 for Viscoelastoplasticity

Using Equation 4.20, we can evaluate the smoothing strains for the smoothing domain Ω_k^s associated with the edge/face k by

$$\begin{aligned} \overline{\boldsymbol{\varepsilon}}_k &= \frac{1}{A_k^s}\sum_{j=1}^{n_k^e}\frac{1}{3}A_j^e\tilde{\boldsymbol{\varepsilon}}_j \quad \text{for the ES-FEM-T3,} \\ \overline{\boldsymbol{\varepsilon}}_k &= \frac{1}{V_k^s}\sum_{j=1}^{n_k^e}\frac{1}{4}V_j^e\tilde{\boldsymbol{\varepsilon}}_j \quad \text{for the FS-FEM-T4,} \end{aligned} \tag{11.51}$$

where $\tilde{\boldsymbol{\varepsilon}}_j$ is the compatible total strain used in the same FEM model for the jth element sharing the edge/face k.

The discretized version of weak form for the viscoelastoplasticity problems using the ES-FEM-T3/FS-FEM-T4 follows Equations 11.49 and 11.50. The iteration form of the discretized weak form now becomes: Seek

$\overline{\mathbf{u}}_\vartheta \in \mathbb{H}_h^1(\Omega;\mathrm{R}^d)$ such that $\overline{\mathbf{u}}_\vartheta = \mathbf{w}_0$ on Γ_D and

$$\overline{\mathbf{F}}_j = \sum_{k=1}^{N_s} S_k^s \left(\overline{\boldsymbol{\sigma}}_\vartheta \left(\overline{\boldsymbol{\varepsilon}}_k(\overline{\mathbf{u}}_\vartheta - \mathbf{u}_0) + \mathbf{c}^{-1}\boldsymbol{\sigma}_0 \right) \right)^T \overline{\boldsymbol{\varepsilon}}_k(\varphi_j) - \int_\Omega \varphi_j \mathbf{b}_\vartheta \, \mathrm{d}\Omega - \int_{\Gamma_t} \varphi_j \mathbf{t}_\vartheta \, \mathrm{d}\Gamma = 0, \tag{11.52}$$

for $j = 1, \ldots, N_n d$, and the entries of the system stiffness matrix $\overline{D\mathbf{F}}_{rw}$ become

$$\left(\overline{D\mathbf{F}} \left(\overline{u}^p_{\vartheta,1}, \ldots, \overline{u}^p_{\vartheta,N_n d} \right) \right)^s_{rw} = \frac{\partial \overline{\mathbf{F}}_r \left(\overline{u}^p_{\vartheta,1}, \ldots, \overline{u}^p_{\vartheta,N_n d} \right)}{\partial \overline{u}^p_{\vartheta,w}}. \tag{11.53}$$

In ES-FEM-T3/FS-FEM-T4, the system stiffness matrix $\overline{D\mathbf{F}}(\overline{\mathbf{u}}^p_\vartheta)$ as well as the vector $\overline{\mathbf{F}}_j(\overline{\mathbf{u}}_\vartheta)$ are expressed as a sum over all the smoothing domains Ω_k^s. The local stiffness matrix $\overline{D\mathbf{F}}^s_{rw}$ for the smoothing domain Ω_k^s is now defined by

$$\begin{aligned} \overline{D\mathbf{F}}^k_{rw} &= \frac{\partial \overline{\mathbf{F}}^k_r}{\partial \overline{u}^p_{\vartheta,w}} = \frac{\partial \overline{\mathbf{Q}}^k_r}{\partial \overline{u}^p_{\vartheta,w}} \\ &= \frac{\partial}{\partial \overline{u}^p_{\vartheta,w}} \left(\int_{\Omega_k^s} \overline{\boldsymbol{\sigma}}_\vartheta \left(\overline{\boldsymbol{\varepsilon}}_k \left(\sum_{l \in \overline{\Psi}_k^{\mathrm{dof}}} \overline{u}^p_{\vartheta,l} \varphi_l - \mathbf{u}_0 \right) + \mathbf{c}^{-1}\boldsymbol{\sigma}_0 \right)^T \overline{\boldsymbol{\varepsilon}}_k(\varphi_r) \, \mathrm{d}\Omega \right), \end{aligned} \tag{11.54}$$

where

$$\overline{\mathbf{Q}}^k_r = \int_{\Omega_k^s} \left(\overline{\boldsymbol{\sigma}}_\vartheta \left(\overline{\boldsymbol{\varepsilon}}_k \left(\overline{\mathbf{u}}_\vartheta - \mathbf{u}_0 \right) + \mathbf{c}^{-1}\boldsymbol{\sigma}_0 \right) \right)^T \overline{\boldsymbol{\varepsilon}}_k \left(\varphi_r \right) \mathrm{d}\Omega, \tag{11.55}$$

and $r, w \in \overline{\Psi}_k^{\mathrm{dof}}$ is the set containing DOFs of the elements attached to the common edge/face k. For example in ES-FEM-T3, for the boundary edge m shown in Figure 7.2, $\overline{\Psi}_k^{\mathrm{dof}}$ is the set containing DOFs of nodes $\{A,\ B,\ C\}$ and the total number of DOFs for the kth smoothing domain is $\overline{N}_k^{\mathrm{dof}} = 3d$; for the inner edge k presented in Figure 7.2, $\overline{\Psi}_k^{\mathrm{dof}}$ is the set containing DOFs of nodes $\{D,\ E,\ F,\ G\}$ and the total number of DOFs $\overline{N}_k^{\mathrm{dof}} = 4d$. In FS-FEM-T4, for the face k as shown in Figure 8.1, $\overline{\Psi}_k^{\mathrm{dof}}$ is the set containing DOFs of

nodes $\{A, B, C, D, E\}$ and the total number of DOFs for this kth smoothing domain is $\overline{N}_k^{\text{dof}} = 5d$.

Note that the bandwidth of the stiffness matrix for the ES-FEM-T3/FS-FEM-T4 is larger than that of the FEM counterparts, because the number of nodes related to the smoothing domains associated with inner edges/faces is four and five, respectively, which is one larger than that related to the element in the FEM model. The computational *cost* of ES-FEM-T3/FS-FEM-T4 is therefore larger than that of FEM counterparts for the same meshes. Only when the solution accuracy is taken into account, the computational *efficiency* of of ES-FEM-T3/FS-FEM-T4 can be much higher than that of FEM counterparts.

Now, substituting the expression $\overline{\boldsymbol{\sigma}}_\vartheta \left(\overline{\boldsymbol{\varepsilon}}_k \left(\overline{\mathbf{u}}_\vartheta - \mathbf{u}_0\right) + \mathbf{c}^{-1}\boldsymbol{\sigma}_0\right)$ in Equations 11.54 and 11.55 using these explicit forms of Equations 11.23, 11.24, 11.26, and 11.28 for different cases of plasticity materials, and by just replacing $\boldsymbol{\varepsilon}$ by $\overline{\boldsymbol{\varepsilon}}_k$ in all these equations, we have

Case a: Perfect viscoelastoplasticity

$$\overline{\mathbf{Q}}_r^k = S_k^s \left(C_1 \text{tr}\left(\overline{\mathbf{v}}_k\right) \text{tr}\left(\overline{\boldsymbol{\varepsilon}}_k(\varphi_r)\right) + C_4 \left(\text{dev}\left(\overline{\mathbf{v}}_k\right)\right)^T \overline{\boldsymbol{\varepsilon}}_k(\varphi_r)\right), \tag{11.56}$$

$$\begin{aligned}\overline{D\mathbf{F}}_{rw}^k = S_k^s \Big(&C_1 \text{tr}\left(\overline{\boldsymbol{\varepsilon}}_k(\varphi_r)\right) \text{tr}\left(\overline{\boldsymbol{\varepsilon}}_k(\varphi_w)\right) + C_4 \left(\text{dev}\left(\overline{\boldsymbol{\varepsilon}}_k(\varphi_r)\right)\right)^T \overline{\boldsymbol{\varepsilon}}_k(\varphi_w) \\ &-(C_5)_r \left(\text{dev}\left(\overline{\mathbf{v}}_k\right)\right)^T \overline{\boldsymbol{\varepsilon}}_k(\varphi_w)\Big),\end{aligned} \tag{11.57}$$

where $\overline{\mathbf{v}}_k = \overline{\boldsymbol{\varepsilon}}_k \left(\overline{\mathbf{u}}_\vartheta - \mathbf{u}_0\right) + \mathbf{c}^{-1}\boldsymbol{\sigma}_0$; and

$$C_4 = \begin{cases} C_2 + C_3/\|\text{dev}\left(\overline{\mathbf{v}}_k\right)\| & \text{if } \|\text{dev}\left(\overline{\mathbf{v}}_k\right)\| - \beta\sigma_Y > 0, \\ 2\mu & \text{else,} \end{cases}$$

$$C_5 = \begin{cases} C_3/\|\text{dev}\left(\overline{\mathbf{v}}_k\right)\|^3 \left[\left(\text{dev}\left(\overline{\boldsymbol{\varepsilon}}_k(\varphi_r)\right)\right)^T \text{dev}\left(\overline{\mathbf{v}}_k\right)\right]_{r=1}^{\overline{N}_k^{\text{dof}}} & \\ \qquad\qquad \text{if } \|\text{dev}\left(\overline{\mathbf{v}}_k\right)\| - \beta\sigma_Y > 0, & \\ \underbrace{\{0 \quad \cdots \quad 0\}}_{\text{size of } 1\times\overline{N}_k^{\text{dof}}}^T \qquad \text{else,} & \end{cases} \tag{11.58}$$

in which parameters C_1, C_2, C_3 are given by Equation 11.25.

Case b: Viscoelastoplasticity with isotropic hardening

$$\overline{\mathbf{Q}}_r^k = S_k^s \left(C_1 \mathrm{tr}(\overline{\mathbf{v}}_k) \mathrm{tr}\left(\overline{\boldsymbol{\varepsilon}}_k(\varphi_r)\right) + C_5 \left(\mathrm{dev}(\overline{\mathbf{v}}_k)\right)^T \overline{\boldsymbol{\varepsilon}}_k(\varphi_r) \right), \tag{11.59}$$

$$\overline{D\mathbf{F}}_{rw}^k = S_k^s \Big(C_1 \mathrm{tr}\left(\overline{\boldsymbol{\varepsilon}}_k(\varphi_r)\right) \mathrm{tr}\left(\overline{\boldsymbol{\varepsilon}}_k(\varphi_w)\right) + C_5 \left(\mathrm{dev}\left(\overline{\boldsymbol{\varepsilon}}_k(\varphi_r)\right)\right)^T \overline{\boldsymbol{\varepsilon}}_k(\varphi_w) - (C_6)_r \left(\mathrm{dev}(\overline{\mathbf{v}}_k)\right)^T \overline{\boldsymbol{\varepsilon}}_k(\varphi_w) \Big), \tag{11.60}$$

where

$$C_5 = \begin{cases} C_3/(C_2 \|\mathrm{dev}(\overline{\mathbf{v}}_k)\|) + C_4/C_2 & \text{if } \|\mathrm{dev}\left(\overline{\mathbf{v}}_k\right)\| - \beta\left(1 + \alpha_0^{\mathrm{I}} H\right)\sigma_Y > 0, \\ 2\mu & \text{else,} \end{cases}$$

$$C_6 = \begin{cases} C_3/\left(C_2 \|\mathrm{dev}(\overline{\mathbf{v}}_k)\|^3\right) \left[\left(\mathrm{dev}\left(\overline{\boldsymbol{\varepsilon}}_k(\varphi_r)\right)\right)^T \mathrm{dev}(\overline{\mathbf{v}}_k) \right]_{r=1}^{\overline{N}_k^{\mathrm{dof}}} & \text{if } \|\mathrm{dev}(\overline{\mathbf{v}}_k)\| - \beta(1 + \alpha_0^{\mathrm{I}} H)\sigma_Y > 0, \\ \underbrace{\{0 \quad \cdots \quad 0\}}_{\text{size of } 1\times\overline{N}_k^{\mathrm{dof}}}^T & \text{else,} \end{cases} \tag{11.61}$$

in which C_1, C_2, C_3, C_4 are defined in Equation 11.27.

Case c: Viscoelastoplasticity with linear kinematic hardening

$$\overline{\mathbf{Q}}_r^k = S_k^s \Big(\left(C_1 \mathrm{tr}\left(\overline{\mathbf{v}}_k\right) \mathrm{tr}\left(\overline{\boldsymbol{\varepsilon}}_k\left(\varphi_r\right)\right)\right) + C_4 \left(\mathrm{dev}\left(\overline{\mathbf{v}}_k\right)\right)^T \overline{\boldsymbol{\varepsilon}}_k\left(\varphi_r\right) + c \left(\mathrm{dev}\left(\boldsymbol{\alpha}_0^{\mathrm{K}}\right)\right)^T \overline{\boldsymbol{\varepsilon}}_k(\varphi_r) \Big), \tag{11.62}$$

$$\overline{D\mathbf{F}}_{rw}^k = S_k^s \Big(C_1 \mathrm{tr}\left(\overline{\boldsymbol{\varepsilon}}_k\left(\varphi_r\right)\right) \mathrm{tr}\left(\overline{\boldsymbol{\varepsilon}}_k\left(\varphi_w\right)\right) + C_4 \left(\mathrm{dev}\left(\overline{\boldsymbol{\varepsilon}}_k\left(\varphi_r\right)\right)\right)^T \overline{\boldsymbol{\varepsilon}}_k\left(\varphi_w\right) - (C_5)_r \left(\mathrm{dev}(\overline{\mathbf{v}}_k)\right)^T \overline{\boldsymbol{\varepsilon}}_k(\varphi_w) \Big), \tag{11.63}$$

where

$$C_4 = \begin{cases} C_3/\|\mathrm{dev}(\overline{\mathbf{v}}_k)\| + C_2 & \text{if } \left\|\mathrm{dev}\left(\overline{\mathbf{v}}_k - \beta\boldsymbol{\alpha}_0^{\mathrm{K}}\right)\right\| - \beta\sigma_Y > 0, \\ 2\mu & \text{else,} \end{cases}$$

$$C_5 = \begin{cases} C_3/\|\mathrm{dev}(\overline{\mathbf{v}}_k)\|^3 \left[\left(\mathrm{dev}\left(\overline{\boldsymbol{\varepsilon}}_k(\varphi_r)\right)\right)^T \mathrm{dev}\left(\overline{\mathbf{v}}_k\right) \right]_{r=1}^{\overline{N}_k^{\mathrm{dof}}} & \text{if } \left\|\mathrm{dev}\left(\overline{\mathbf{v}}_k - \beta\boldsymbol{\alpha}_0^{\mathrm{K}}\right)\right\| - \beta\sigma_Y > 0, \\ \underbrace{\{0 \quad \cdots \quad 0\}}_{\text{size of } 1\times\overline{N}_k^{\mathrm{dof}} d}^T & \text{else,} \end{cases}$$

$$c = \begin{cases} 1 & \text{if } \left\| \operatorname{dev}\left(\overline{\mathbf{v}}_k - \beta \boldsymbol{\alpha}_0^{\mathrm{K}}\right) \right\| - \beta \sigma_Y > 0, \\ 0 & \text{else,} \end{cases} \tag{11.64}$$

in which C_1, C_2, C_3 are given in Equation 11.29.

Similar to the FEM models, to properly apply the nonhomogeneous Dirichlet boundary conditions for our nonlinear problem, we use the approach of Lagrange multipliers, which gives the extended system of equations:

$$\begin{pmatrix} \overline{D\mathbf{F}}\left(\overline{\mathbf{u}}_\vartheta^p\right) & \mathbf{G}^T \\ \mathbf{G} & \mathbf{0} \end{pmatrix} \begin{pmatrix} \overline{\mathbf{u}}_\vartheta^{p+1} \\ \overline{\boldsymbol{\lambda}} \end{pmatrix} = \begin{pmatrix} \overline{\mathbf{b}} \\ \mathbf{w}_0 \end{pmatrix}, \tag{11.65}$$

where $\overline{\boldsymbol{\lambda}}$ is the vector of Lagrange multipliers for our ES-FEM-T3/FS-FEM-T4 models, $\overline{\mathbf{f}} = \overline{D\mathbf{F}}\left(\overline{\mathbf{u}}_\vartheta^p\right) - \overline{\mathbf{F}}\left(\overline{\mathbf{u}}_\vartheta^p\right)$ and $\mathbf{G}$ is a matrix created from the given Dirichlet boundary conditions such that $\mathbf{G}\overline{\mathbf{u}}_\vartheta^{p+1} = \mathbf{w}_0$.

The extended system of Equations 11.65 can now be solved for $\overline{\mathbf{u}}_\vartheta^{p+1}$ and $\overline{\boldsymbol{\lambda}}$ at each time step. The solving process is iterated in exactly the same way as that in the FEM model.

We note that the shape functions for elements in the ES-FEM-T3/FS-FEM-T4 is the same as that in the standard FEM and therefore the force vector $\tilde{\mathbf{P}}_j$ in the ES-FEM-T3/FS-FEM-T4 is computed in exactly the same way as in the FEM. In other words, the ES-FEM-T3/FS-FEM-T4 changes only the stiffness matrix and the terms related to the stiffness matrix. Figures 11.1 through 11.3 present the macro flowchart to solve the viscoelastoplasticity problems using the ES-FEM-T3/FS-FEM-T4.

11.5 *A Posteriori* Error Estimation

In order to estimate the accuracy of the solution of ES-FEM-T3/FS-FEM-T4, in comparison with that of FEM for the viscoelastoplasticity problems, a quantitative, fair, and accurate assessment of the numerical solutions is needed. In this assessment for viscoelastoplasticity material, we use the following efficient *a posteriori* error estimation to measure the error in stress solution [1,7]:

$$\eta^h = \frac{\left\| \breve{\boldsymbol{\sigma}}^R - \breve{\boldsymbol{\sigma}} \right\|_{L^2(\Omega)}}{\left\| \breve{\boldsymbol{\sigma}} \right\|_{L^2(\Omega)}} = \frac{\left(\sum_{i=1}^{N_e} \int_{\Omega_i^e} (\breve{\boldsymbol{\sigma}}^R - \breve{\boldsymbol{\sigma}})^T (\breve{\boldsymbol{\sigma}}^R - \breve{\boldsymbol{\sigma}}) \, \mathrm{d}\Omega \right)^{1/2}}{\left(\sum_{i=1}^{N_e} \int_{\Omega_i^e} \breve{\boldsymbol{\sigma}}^T \breve{\boldsymbol{\sigma}} \, \mathrm{d}\Omega \right)^{1/2}}, \tag{11.66}$$

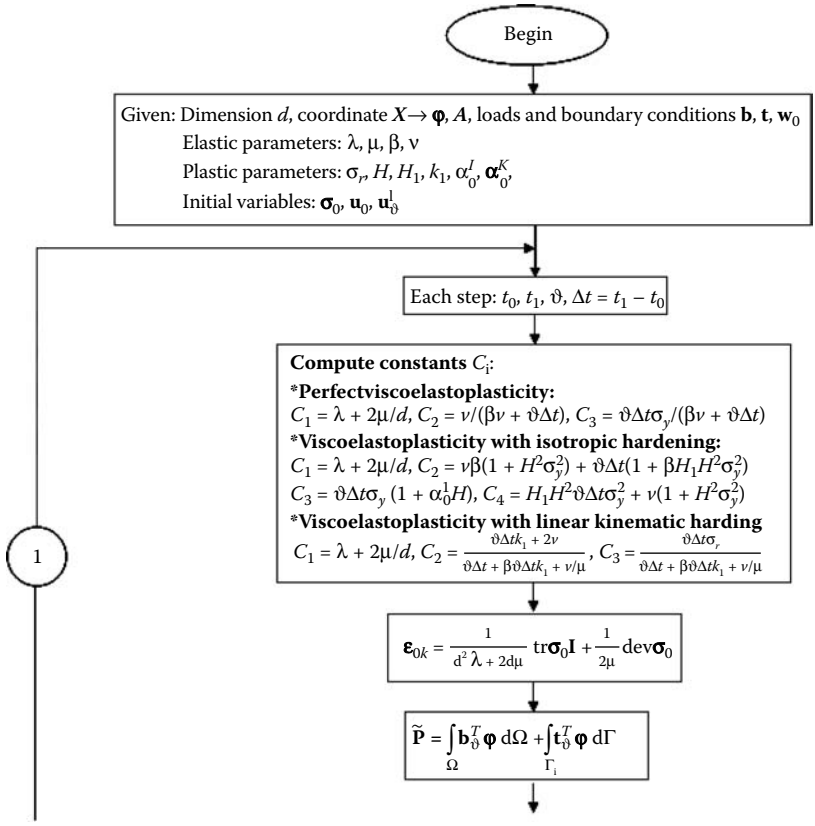

FIGURE 11.1 Flowchart to solve the elastoviscoplasticity problems using ES-FEM-T3/FS-FEM-T4: part 1.

where $\breve{\boldsymbol{\sigma}}$ is the "raw" results of stress in an element, and $\breve{\boldsymbol{\sigma}}^R$ is the recovery stress in an element defined by

$$\begin{aligned}\breve{\boldsymbol{\sigma}}^R &= \sum_{j=1}^{3} N_j(\mathbf{x})\breve{\boldsymbol{\sigma}}(\mathbf{x}_j) \quad \text{for triangular elements,}\\ \breve{\boldsymbol{\sigma}}^R &= \sum_{j=1}^{4} N_j(\mathbf{x})\breve{\boldsymbol{\sigma}}(\mathbf{x}_j) \quad \text{for tetrahedral elements,}\end{aligned} \tag{11.67}$$

where $N_j(\mathbf{x})$ are the linear shape functions of triangles/tetrahedrons used in the standard FEM, and $\breve{\boldsymbol{\sigma}}(\mathbf{x}_j)$ are stress values at nodes of the element of any numerical methods.

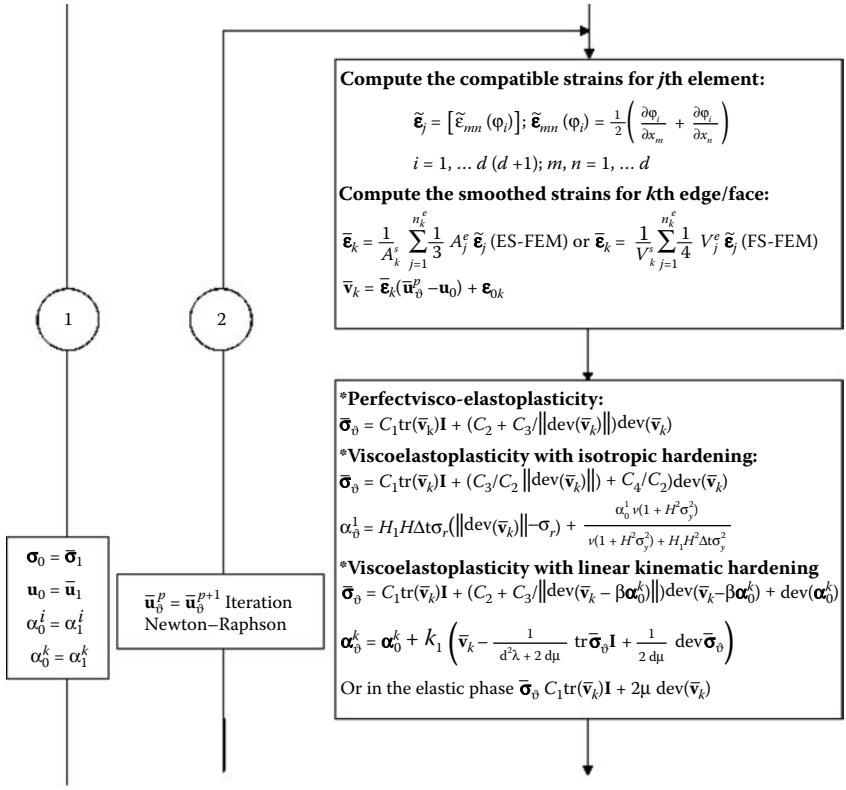

FIGURE 11.2 Flowchart to solve the elastoviscoplasticity problems using ES-FEM-T3/FS-FEM-T4: part 2.

Recall from Section 4.10.4 that for the S-FEM models, when computing the stresses $\breve{\boldsymbol{\sigma}}(\mathbf{x}_j)$ at a node $\mathbf{x}_j$, we simply average (area-weighted) the stresses of smoothing domains associated with the node, as shown in Figure 4.10 for the ES-FEM-T3.

Similarly (see Section 4.10.6), for FEM-T3/FEM-T4 the stresses $\breve{\boldsymbol{\sigma}}(\mathbf{x}_j)$ at a node $\mathbf{x}_j$ are the area-weighted averaged stresses of those of the elements surrounding the node, as shown in Figure 4.11 for the FEM-T3.

In evaluating the integrals in Equation 11.66 for triangular/tetrahedral elements, the Gauss integration rule in Sections 3.15.4 and 3.15.5 with a proper mapping procedure is used for each element, respectively, and then with a summation on all elements. In each element, a proper number of Gauss points depending on the order of the recovery solution $\breve{\boldsymbol{\sigma}}^R$ will be used to ensure accurate integration.

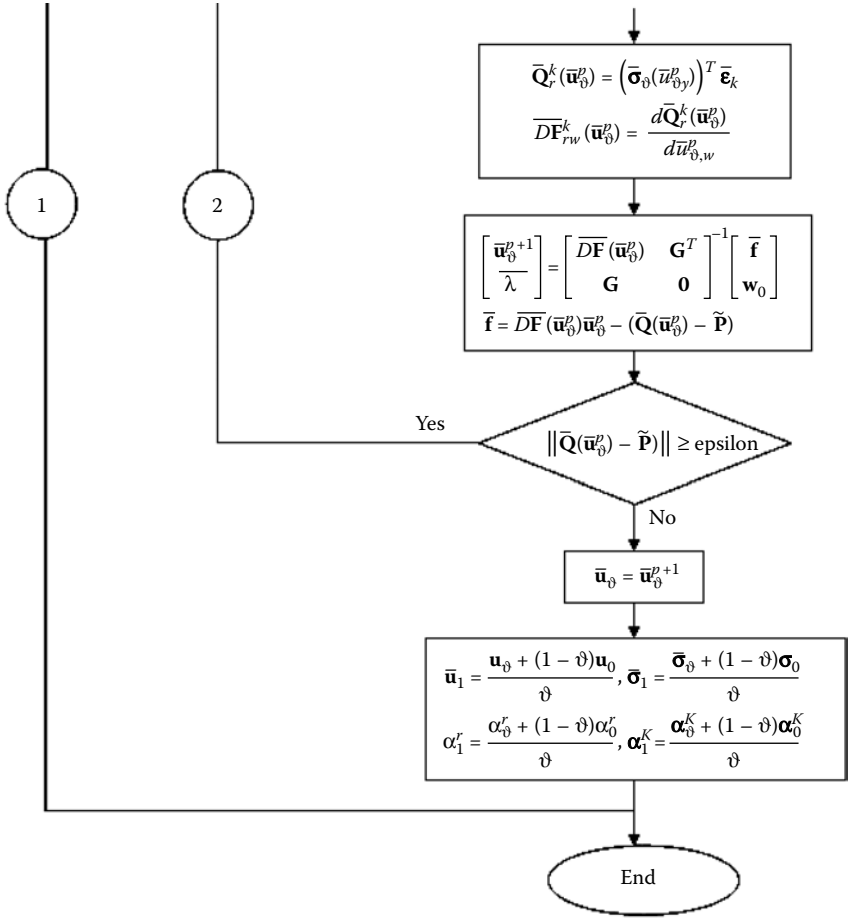

FIGURE 11.3 Flowchart to solve the elastoviscoplasticity problems using ES-FEM-T3/FS-FEM-T4: part 3.

11.6 Numerical Examples

Codes of ES-FEM-T3 and FS-FEM-T4 have been developed based on the formulations given above, respectively, for 2D and 3D problems. In this section, three numerical examples of 2D problems and four numerical examples of 3D problems will be solved using these codes, and the results will be presented to demonstrate the accuracy and properties of ES-FEM-T3/FS-FEM-T4 for viscoelastoplasticity analyses. To demonstrate convincingly the superior properties of ES-FEM-T3/FS-FEM-T4

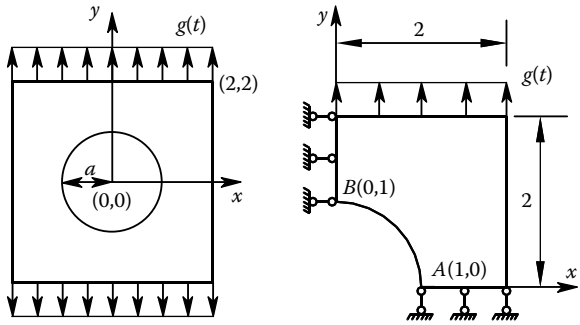

FIGURE 11.4 A plate with a circular hole subjected to time-dependent surface forces $g(t)$ and its quarter model with symmetric conditions imposed on the left and bottom edges.

methods, the results will be compared to those of the standard FEM counterparts [1].

Example 11.6.1: Plate with a Circular Hole: 2D Perfect Viscoelastoplasticity

Figure 11.4 represents a 2D solid of a square domain of $\Omega = [-2, 2] \times [-2, 2]$ with a central circular hole of radius $a = 1$, subjected to time-dependent uniformly distributed surface forces $g(t) = 500\,t$ to outer normal at the top and bottom edges. The rest of the boundary is set free at all times. Due to the symmetry, only the upper right quadrant of the 2D solid is modeled. Symmetric conditions are imposed on the left and bottom edges of the quarter model, and the inner boundary of the hole is traction free. Figure 11.5 shows a mesh of the domain using 561 nodes and 1024 triangular elements. Assuming that the material is of perfect viscoelastoplasticity with Young's modulus $E = 206,900$, Poisson's ratio $\nu = 0.29$, yield stress $\sigma_Y = 450$, and the initial data for the stress vector $\boldsymbol{\sigma}_0$ are set to zero.

The solution is computed in the time interval from $t = 0$ to $t = 0.3$ in 10 uniform time steps of $\Delta t = 0.03$. Using the mesh shown in Figure 11.5, numerical results are obtained and listed in Table 11.1. It is found that the material remains elastic in the first six steps, between $t = 0$ and $t = 0.18$ for both ES-FEM-T3 and FEM-T3, because the number of iterations at these times is one. Table 11.1 also shows that after the materials undergo plastic deformation, the number of iterations in Newton's method required in both ES-FEM-T3 and FEM-T3 is almost the same. The estimated errors η^h (using Equation 11.66) for ES-FEM-T3 are more than two times less than those of FEM-T3 using the same mesh. In addition, Figure 11.6 compares the computational cost and efficiency between FEM-T3 and ES-FEM-T3 for a range of meshes at $t = 0.3$. It is seen that with the same mesh, the computational cost of ES-FEM-T3 is larger than that of FEM-T3, as shown in Figure 11.6a. However, when the efficiency of computation in terms of the solution error versus computational cost for a range of meshes is

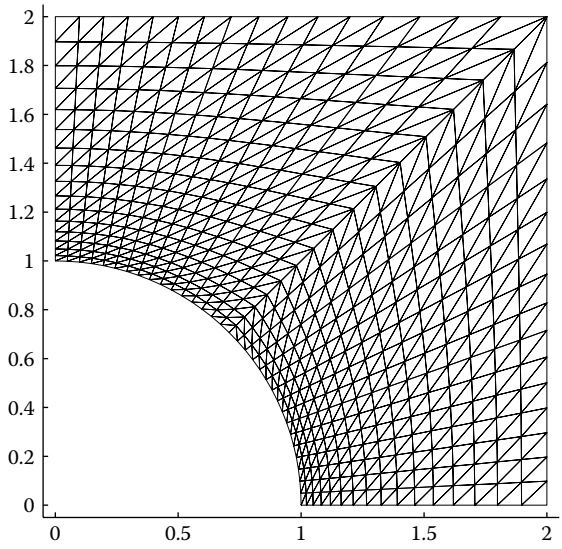

FIGURE 11.5 A domain discretization using 561 nodes and 1024 triangular elements for the 2D solid with a circular hole subjected to time-dependent surface forces $g(t)$.

considered, the ES-FEM-T3 is found more efficient than the FEM-T3, as shown in Figure 11.6b.

Figure 11.7 shows the elastic shear energy density $\|\text{dev}(\breve{\boldsymbol{\sigma}}^R)\|^2/(4\mu)$ obtained using FEM-T3 and ES-FEM-T3 at $t = 0.3$. The plasticity domain first appears at

TABLE 11.1

Number of Iterations and the Estimated Error Using FEM-T3 and ES-FEM-T3 at Various Time Steps for the 2D Solid with a Circular Hole

	FEM-T3		ES-FEM-T3	
Step	**Iterations**	$\eta^h = \dfrac{\left\|\breve{\sigma}^R - \breve{\sigma}\right\|_{L^2(\Omega)}}{\left\|\breve{\sigma}\right\|_{L^2(\Omega)}}$	**Iterations**	$\eta^h = \dfrac{\left\|\breve{\sigma}^R - \breve{\sigma}\right\|_{L^2(\Omega)}}{\left\|\breve{\sigma}\right\|_{L^2(\Omega)}}$
1	1	0.1	1	0.0475
2	1	0.1	1	0.0475
3	1	0.1	1	0.0475
4	1	0.1	1	0.0475
5	1	0.1	1	0.0475
6	1	0.1	1	0.0475
7	3	0.1	3	0.0475
8	4	0.101	4	0.0476
9	4	0.103	4	0.0480
10	4	0.106	4	0.0486

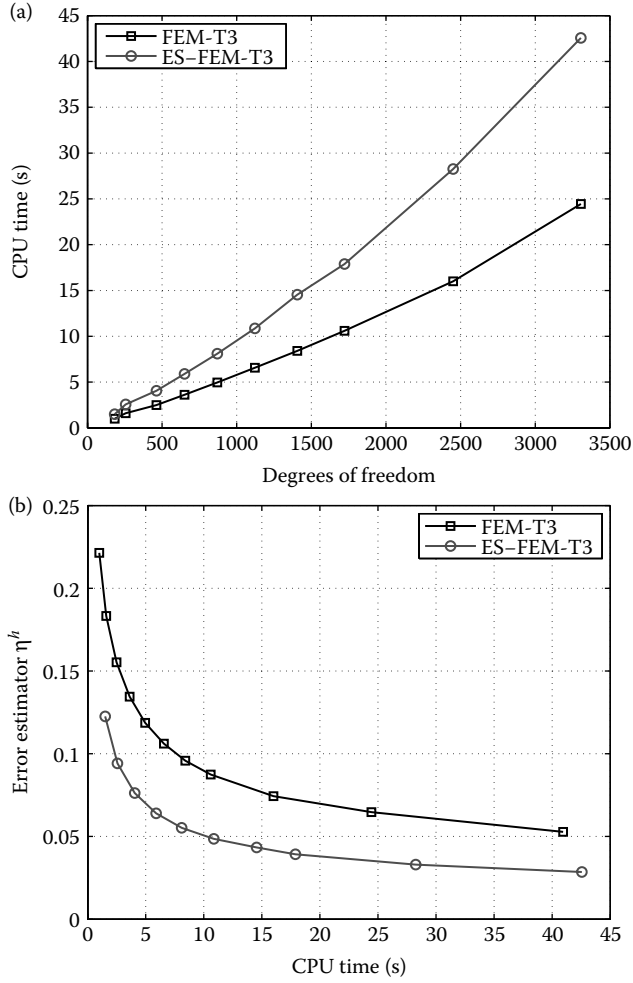

FIGURE 11.6 Comparison of the computational cost and efficiency between FEM-T3 and ES-FEM-T3 for a range of meshes at $t = 0.3$ for the plate with a hole: (a) CPU time using the same mesh and (b) computational efficiency.

the corner starting from point $A(1, 0)$ and then at the other corner starting from point $B(0,1)$. The evolution process of the elastic shear energy density $\|\text{dev}(\tilde{\boldsymbol{\sigma}}^R)\|^2/(4\mu)$ can be clearly observed from the ES-FEM-T3 results at some different time steps (see Figure 11.8).

Table 11.2 compares the solution of the displacements of points $A(1, 0)$ and $B(0, 1)$ using FEM-T3 and ES-FEM-T3 at different times. The results show that the displacements of ES-FEM-T3 are larger than those of FEM-T3. This implies that the ES-FEM-T3 model can reduce the overstiffness of the standard FEM-T3

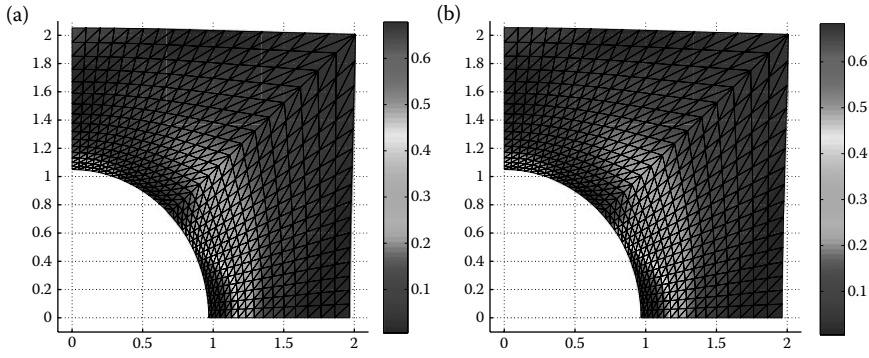

FIGURE 11.7 Elastic shear energy density $\|\text{dev}(\breve{\boldsymbol{\sigma}}^R)\|^2/(4\mu)$ for the plate with a hole using (a) FEM-T3 and (b) ES-FEM-T3 at $t = 0.3$ (mesh with 561 nodes and 1024 elements).

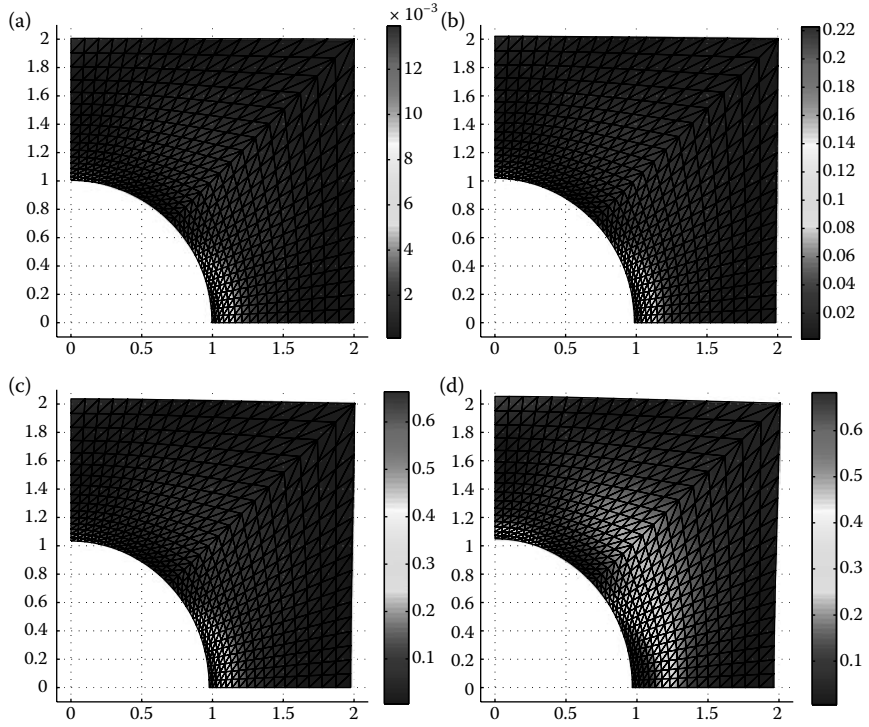

FIGURE 11.8 Evolution of the elastic shear energy density $\|\text{dev}(\breve{\boldsymbol{\sigma}}^R)\|^2/(4\mu)$ obtained using ES-FEM-T3 at different time steps for the plate with a hole: (a) $t = 0.12$; (b) $t = 0.18$; (c) $t = 0.24$; and (d) $t = 0.3$.

TABLE 11.2

Horizontal Displacement u_A at point $A(1,0)$ and Vertical Displacement v_B at point $B(0,1)$ using FEM-T3 and ES-FEM-T3 at Various Time Steps for the 2D Solid with a Circular Hole

Number of	FEM-T3		ES-FEM-T3	
Time Steps	$u_A(\times 10^{-3})$	$v_B(\times 10^{-3})$	$u_A(\times 10^{-3})$	$v_B(\times 10^{-3})$
1	−0.312	0.4862	−0.316	0.4921
2	−0.624	0.9724	−0.632	0.9842
3	−0.936	1.4586	−0.949	1.4763
4	−1.248	1.9448	−1.265	1.9684
5	−1.560	2.4311	−1.581	2.4605
6	−1.871	2.9173	−1.897	2.9526
7	−2.184	3.4038	−2.214	3.4450
8	−2.503	3.9016	−2.536	3.9530
9	−2.823	4.4286	−2.861	4.4947
10	−3.159	4.9956	−3.183	5.0833

model using triangular elements. This property was found earlier for linear elastic problems by Liu et al. [3].

Figure 11.9 shows the convergence of the elastic strain energy $E = \int_\Omega (\breve{\boldsymbol{\sigma}}_\vartheta)^T \breve{\mathbf{e}}_\vartheta \, d\Omega$ when the mesh is refined using both FEM-T3 and ES-FEM-T3 at a fixed time $t = 0.3$. The solution of ES-FEM-T3 using a very fine mesh with

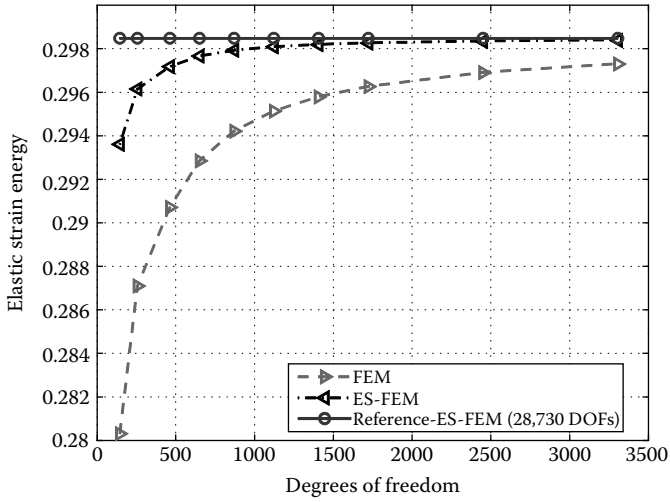

FIGURE 11.9 Convergence of the solution in elastic strain energy $E = \int_\Omega (\breve{\boldsymbol{\sigma}}_\vartheta)^T \breve{\mathbf{e}}_\vartheta \, d\Omega$ obtained using FEM-T3 and ES-FEM-T3 at for the 2D solid with a circular hole.

28,730 DOFs is used as the reference solution for comparison purpose. The results show clearly that the ES-FEM-T3 model is much softer and gives more accurate results than the FEM-T3 model using the same mesh of triangular elements, especially for the coarse meshes.

Example 11.6.2: Cook's Membrane: Viscoelastoplasticity with Isotropic Hardening

The widely used 2D Cook's membrane problem is used here for viscoelastoplastic analysis. This benchmark problem, shown in Figure 11.10, refers to a clamped airplane-wing-shaped panel subjected to an in-plane shearing load $g(t) = e^{3t}/40$ on the opposite end ($x = 48$) with vanishing volume force f. The domain is meshed with 289 nodes and 512 triangular elements, as shown in Figure 11.10. Assume that the material has viscoelastoplasticity with isotropic hardening with Young's modulus $E = 2900$, Poisson's ratio $v = 0.4$, yield stress $\sigma_Y = 0.1$, $H = 1000$, $H_1 = 1$, and the initial data for the stress vector $\boldsymbol{\sigma}_0$ and the scalar hardening parameter α_0^{I} are set to zero.

The solution is computed in the time interval from $t = 0$ to $t = 0.25$ with 10 uniform time steps of $\Delta t = 0.025$, using the mesh shown in Figure 11.10. It is found that the material remains elastic at the first two steps, between $t = 0$ and $t = 0.05$ for both ES-FEM-T3 and FEM-T3, as shown in Table 11.3. We also found that the number of iterations in Newton's method of both ES-FEM-T3 and FEM-T3 is almost the same (see Table 11.3). The estimated errors η^h using Equation 11.66 for ES-FEM-T3 are about three times less than those of FEM-T3. In addition, Figure 11.11 compares the computational cost and efficiency between FEM-T3 and ES-FEM-T3 for a range of meshes at $t = 0.25$. It is seen

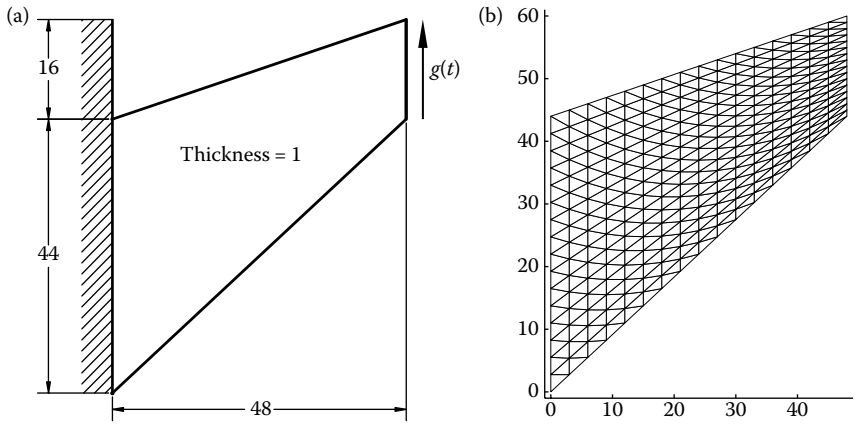

FIGURE 11.10 Cook's membrane problem. (a) Model together applied load and boundary condition and (b) mesh with 289 nodes and 512 triangular elements.

TABLE 11.3

Number of Iterations and the Estimated Error Using FEM-T3 and ES-FEM-T3 at Various Times for the Cook's Membrane Problem

	FEM-T3		ES-FEM-T3	
Number of Time Steps	**Iterations**	$\eta^h = \dfrac{\left\|\breve{\boldsymbol{\sigma}}^R - \breve{\boldsymbol{\sigma}}\right\|_{L^2(\Omega)}}{\left\|\breve{\boldsymbol{\sigma}}\right\|_{L^2(\Omega)}}$	**Iterations**	$\eta^h = \dfrac{\left\|\breve{\boldsymbol{\sigma}}^R - \breve{\boldsymbol{\sigma}}\right\|_{L^2(\Omega)}}{\left\|\breve{\boldsymbol{\sigma}}\right\|_{L^2(\Omega)}}$
1	1	0.197645	1	0.076465
2	1	0.197645	1	0.076465
3	3	0.197646	3	0.076469
4	3	0.197650	3	0.076469
5	3	0.197652	3	0.076466
6	3	0.197654	3	0.076453
7	3	0.197656	3	0.076431
8	4	0.197660	4	0.076402
9	4	0.197671	4	0.076366
10	4	0.197690	4	0.076325

that with the same mesh, the computational cost of ES-FEM-T3 is larger than that of FEM-T3, as shown in Figure 11.11a. However, when the efficiency of computation (computation time for the same accuracy) in terms of the solution error versus computational cost for a range of meshes is considered, the ES-FEM-T3 is more efficient than the FEM-T3, as shown in Figure 11.11b.

Figure 11.12 shows the elastic shear energy density $\|\text{dev}(\breve{\boldsymbol{\sigma}}^R)\|^2/(4\mu)$ using FEM-T3 and ES-FEM-T3 at $t = 0.25$ for the mesh as shown in Figure 11.10. The evolution process of the elastic shear energy density is demonstrated using the ES-FEM-T3 at four different time instances as shown in Figure 11.13.

Table 11.4 compares the solution of the displacements of point $A(48,60)$ using the FEM-T3 and ES-FEM-T3 at different time instances. The results show that the displacements of ES-FEM-T3 are larger than those of FEM-T3. This again verifies the fact that the ES-FEM-T3 model can reduce the overstiffness of the standard FEM-T3 model using triangular elements.

Figure 11.14 shows the convergence of the elastic strain energy $E = \int_\Omega (\breve{\boldsymbol{\sigma}}_\vartheta)^T \breve{\mathbf{e}}_\vartheta \, d\Omega$ when the mesh is refined using both FEM-T3 and ES-FEM-T3 at $t = 0.25$. The solution of ES-FEM-T3 using a very fine mesh with as much as 26,041 DOFs is used as reference solution for comparison. The results again show clearly the finding that the ES-FEM-T3 model is much softer and gives more accurate results than the FEM-T3 model using triangular elements, especially for the coarse meshes.

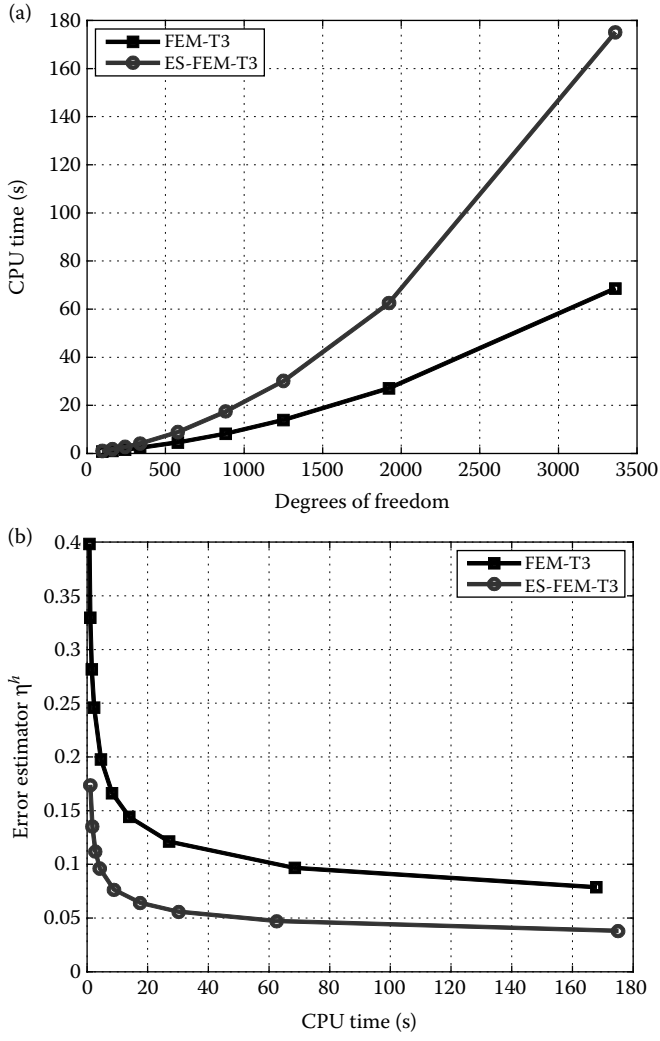

FIGURE 11.11 Comparison of the computational cost and efficiency between FEM-T3 and ES-FEM-T3 for a range of meshes at $t = 0.25$ for the Cook's membrane problem: (a) CPU time using the same mesh and (b) computational efficiency.

Example 11.6.3: Axisymmetric Ring: Viscoelastoplasticity with Linear Kinematic Hardening

Figure 11.15 shows a thick axisymmetric ring, with an internal radius $a = 1$ and an external radius $b = 2$. The ring is subjected to time-dependent surface forces $g_1(r, \varphi, t) = te_r$ on the inner circumference and $g_2(r, \varphi, t) = -te_r/4$ on the outer circumference with $e_r = \begin{bmatrix} \cos\varphi & \sin\varphi \end{bmatrix}^T$. There is no body force.

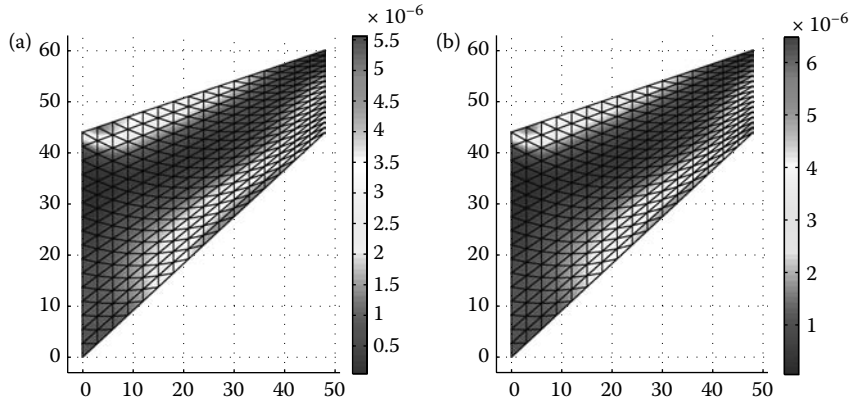

FIGURE 11.12 Distribution of the elastic shear energy density $\|\text{dev}(\overset{\smile}{\boldsymbol{\sigma}}^{R})\|^2/(4\mu)$ for the Cook's membrane problem using (a) FEM-T3 and (b) ES-FEM-T3 at $t = 0.25$ (mesh with 289 nodes and 512 elements).

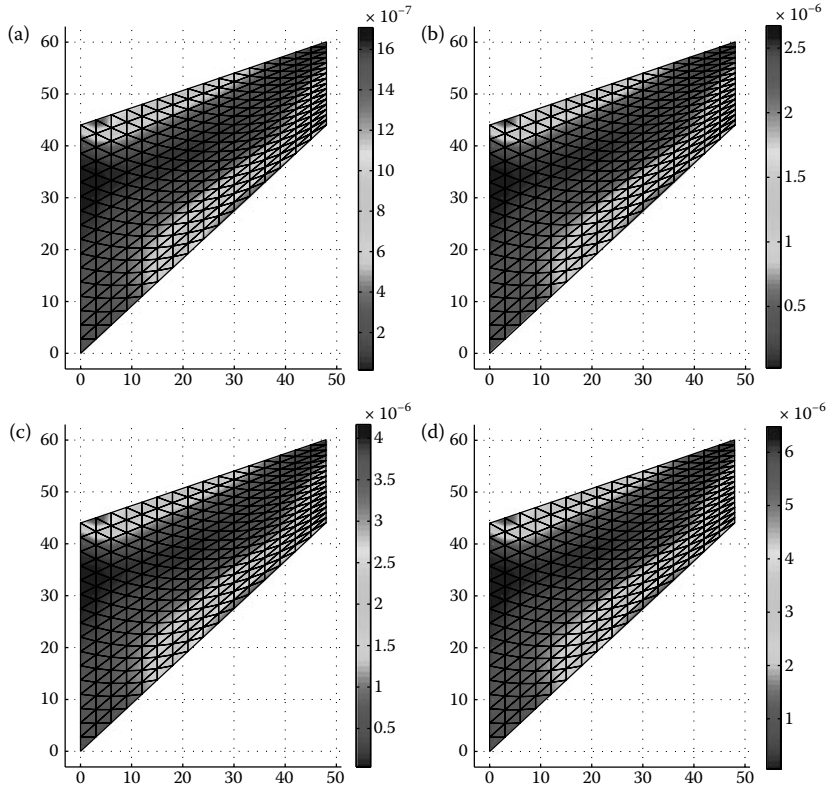

FIGURE 11.13 Evolution of the distribution of the elastic shear energy density $\|\text{dev}(\overset{\smile}{\boldsymbol{\sigma}}^{R})\|^2/(4\mu)$ using ES-FEM-T3 at four different times for the Cook's membrane problem: (a) $t = 0.025$; (b) $t = 0.10$; (c) $t = 0.175$; and (d) $t = 0.25$.

TABLE 11.4

Displacement at point $A(48, 60)$ using FEM-T3 and ES-FEM-T3 at Various Time Steps for the Cook's Membrane Problem

	FEM-T3		ES-FEM-T3	
Step	u_A	v_B	u_A	v_B
1	−0.0022	0.0031	−0.0023	0.0032
2	−0.0024	0.0033	−0.0025	0.0034
3	−0.0026	0.0035	−0.0027	0.0037
4	−0.0028	0.0038	−0.0029	0.0040
5	−0.0030	0.0041	−0.0031	0.0043
6	−0.0032	0.0044	−0.0034	0.0046
7	−0.0035	0.0048	−0.0036	0.0049
8	−0.0037	0.0052	−0.0039	0.0053
9	−0.0040	0.0056	−0.0042	0.0057
10	−0.0043	0.0060	−0.0045	0.0062

For this problem, the exact solution is available: [1]

$$u(r, \varphi, t) = u_r(r, t) e_r,$$

$$\sigma(r, \varphi, t) = \sigma_r(r, t) e_r \otimes e_r + \sigma_\varphi e_\varphi \otimes e_\varphi$$

$$= \sigma_r(r, t) \begin{bmatrix} \cos^2 \varphi \\ \sin^2 \varphi \\ 2 \cos \varphi \sin \varphi \end{bmatrix} + \sigma_\varphi \begin{bmatrix} \sin^2 \varphi \\ \cos^2 \varphi \\ -2 \cos \varphi \sin \varphi \end{bmatrix}, \tag{11.68}$$

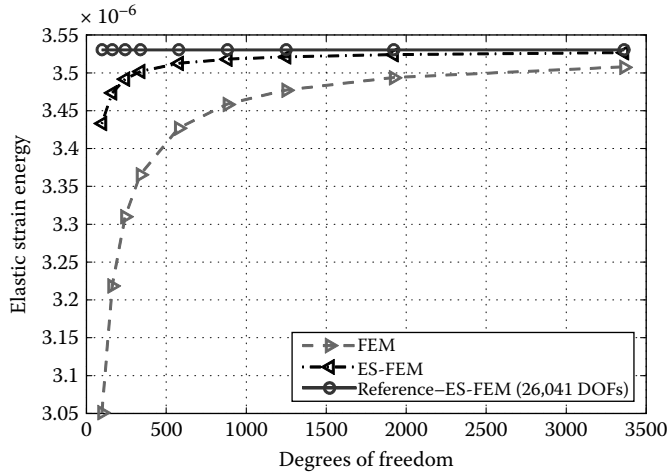

FIGURE 11.14 Convergence of the elastic strain energy $E = \int_\Omega (\breve{\boldsymbol{\sigma}}_\vartheta)^T \breve{\mathbf{e}}_\vartheta \, d\Omega$ versus the number of DOFs using FEM-T3 and ES-FEM-T3 at $t = 0.25$ for the Cook's membrane problem.

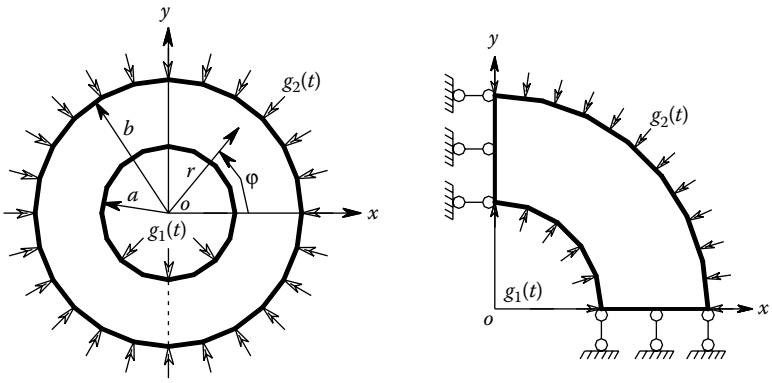

FIGURE 11.15 The axis symmetric ring subjected to time-dependent surface forces $g_1(t)$ on the inner circumference and $g_2(t)$ on the outer circumference, and its quarter model with symmetric conditions imposed on the left and bottom edges.

$$p(r,\varphi,t) = P_r(r,t)(e_r \otimes e_r - e_\varphi \otimes e_\varphi) = P_r(r,t)\begin{bmatrix}\cos^2\varphi - \sin^2\varphi \\ \sin^2\varphi - \cos^2\varphi \\ 4\cos\varphi\sin\varphi\end{bmatrix},$$

where $e_\varphi = \begin{bmatrix}-\sin\varphi & \cos\varphi\end{bmatrix}^T$ and

$$u_r(r,t) = \begin{cases} \dfrac{t}{2\mu r} - \dfrac{1}{3}\psi I(R(t))\left(r + \dfrac{4a}{\mu r}\right) & \text{for } r \geq R(t), \\ \dfrac{t}{2\mu r} - \dfrac{1}{3}\psi I(R(t))\left(4r + \dfrac{4a}{\mu r}\right) + \psi I(r) r & \text{for } r < R(t), \end{cases} \tag{11.69}$$

$$\sigma_r(r,t) = \begin{cases} -\dfrac{t}{r^2} - \dfrac{8}{3}a\psi I\,(R(t))\left(\dfrac{1}{4} - \dfrac{1}{r^2}\right) & \text{for } r \geq R(t), \\ -\dfrac{t}{r^2} - \dfrac{8}{3}a\psi I\,(R(t))\left(1 - \dfrac{1}{r^2}\right) + 2a\psi I(r) & \text{for } r < R(t), \end{cases} \tag{11.70}$$

$$\sigma_\varphi(r,t) = \frac{\partial\,(r\sigma_r)}{\partial r}, \tag{11.71}$$

$$P_r(r,t) = \begin{cases} 0 & \text{for } r \geq R(t), \\ \dfrac{\sigma_Y}{\sqrt{2}\,(a\psi + k_1)}\left(1 - \dfrac{R^2}{r^2}\right) & \text{for } r < R(t), \end{cases} \tag{11.72}$$

$$I(r) = \frac{\sigma_Y}{\sqrt{2}(a\psi + k_1)}\left(\ln r + \frac{1}{2}\left(\frac{R^2}{r^2} - R^2\right)\right), \tag{11.73}$$

and $a = \mu + \lambda$, $\psi = 2\mu/(2\mu + \lambda)$. With $\alpha = 4a\psi/[3(a\psi + k_1)]$, the radius of the plastic boundary $R(t)$ is the positive root of the following equation:

$$f(R) = -2\alpha \ln R + (\alpha - 1)R^2 - \alpha + \frac{\sqrt{2}}{\sigma_Y}t. \tag{11.74}$$

Because of the axisymmetric characteristic of the problem, we only need to model one-quarter of the ring, as shown in Figure 11.15, with symmetric conditions imposed on the left and bottom edges. The quarter domain is meshed with 561 nodes and 1024 triangular elements, as shown in Figure 11.16. Assume that the material has viscoelastoplasticity with linear kinematic hardening with Young's modulus $E = 70,000$, Poisson's ratio $\nu = 0.33$, yield stress $\sigma_Y = 0.2$, the hardening parameter $k_1 = 1$, and the initial data for the displacement $\mathbf{u}_0$, the stress vector σ_0 and the hardening parameter $\boldsymbol{\alpha}_0^K$ are set to zero.

Using the mesh as shown in Figure 11.16, the solution is computed in the time interval from $t = 0$ to $t = 0.22$ with 11 uniform time steps of $\Delta t = 0.02$. It is found that the material remains elastic at the first seven steps (when no iterations are needed) that correspond to time intervals from $t = 0$ to $t = 0.14$, as shown in Table 11.5. The material becomes plastic at $t = 0.16$, as predicted by both ES-FEM-T3 and FEM-T3. Table 11.5 shows the exact error e and the estimated error η^h for the stress solution at different times together with the number of iterations used in Newton's method. The results show that the ratio e/η^h almost equals 1 for all the iterations, which implies that the estimated error η^h using Equation 11.66 can be considered as a very accurate error estimator. This example therefore asserts the reliability and accuracy of the estimated error η^h by Equation 11.66. In addition, the results also show that the number of iterations in Newton's method of both ES-FEM-T3 and FEM-T3 is almost the same, but the estimated errors η^h using Equation 11.66 for ES-FEM-T3 are about 3 times less than those of FEM-T3. Furthermore, Figure 11.17 compares the computational cost and efficiency between FEM-T3 and ES-FEM-T3 for a range of meshes at $t = 0.22$. It is seen that with the same mesh, the computational cost of ES-FEM-T3 is larger than that of FEM-T3 as shown in Figure 11.17a. However, when the efficiency of computation in terms of the solution error

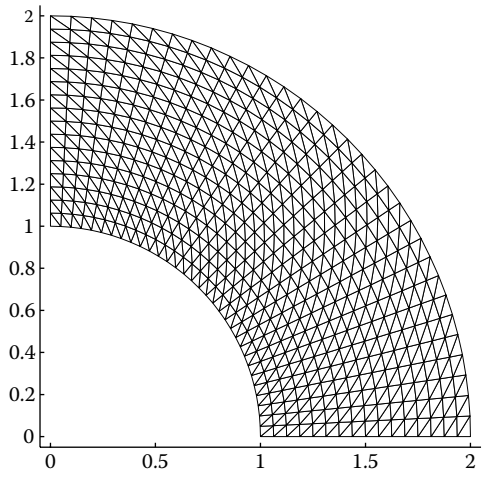

FIGURE 11.16 Domain discretization of one-quarter of the axisymmetric ring using 561 nodes and 1024 triangular elements.

TABLE 11.5

Number of Iterations and the Estimated Error in the Stress Solution Obtained using FEM-T3 and ES-FEM-T3 at Various Times for the Axisymmetric Ring Problem

Number of Time Steps	FEM-T3				ES-FEM-T3			
	Iterations	$e=\frac{\left\|\sigma-\breve{\sigma}\right\|_{L^2}}{\left\|\breve{\sigma}\right\|_{L^2}}$	$\eta^h=\frac{\left\|\breve{\sigma}^R-\breve{\sigma}\right\|_{L^2}}{\left\|\breve{\sigma}\right\|_{L^2}}$	$\frac{e}{\eta_h}$	Iterations	$e=\frac{\left\|\sigma-\breve{\sigma}\right\|_{L^2}}{\left\|\breve{\sigma}\right\|_{L^2}}$	$\eta^h=\frac{\left\|\breve{\sigma}^R-\breve{\sigma}\right\|_{L^2}}{\left\|\breve{\sigma}\right\|_{L^2}}$	$\frac{e}{\eta_h}$
1	1	0.079725	0.0792	1.01	1	0.03342	0.0328	1.02
2	1	0.079725	0.0792	1.01	1	0.03342	0.0328	1.02
3	1	0.079725	0.0792	1.01	1	0.03342	0.0328	1.02
4	1	0.079725	0.0792	1.01	1	0.03342	0.0328	1.02
5	1	0.079725	0.0792	1.01	1	0.03342	0.0328	1.02
6	1	0.079725	0.0792	1.01	1	0.03342	0.0328	1.02
7	1	0.079725	0.0792	1.01	1	0.03342	0.0328	1.02
8	3	0.083988	0.0816	1.03	4	0.03376	0.0331	1.02
9	4	0.089265	0.0874	1.02	4	0.03372	0.0340	0.99
10	5	0.095374	0.0933	1.02	4	0.03269	0.0330	0.99
11	5	0.102883	0.1004	1.02	5	0.03206	0.0324	0.99

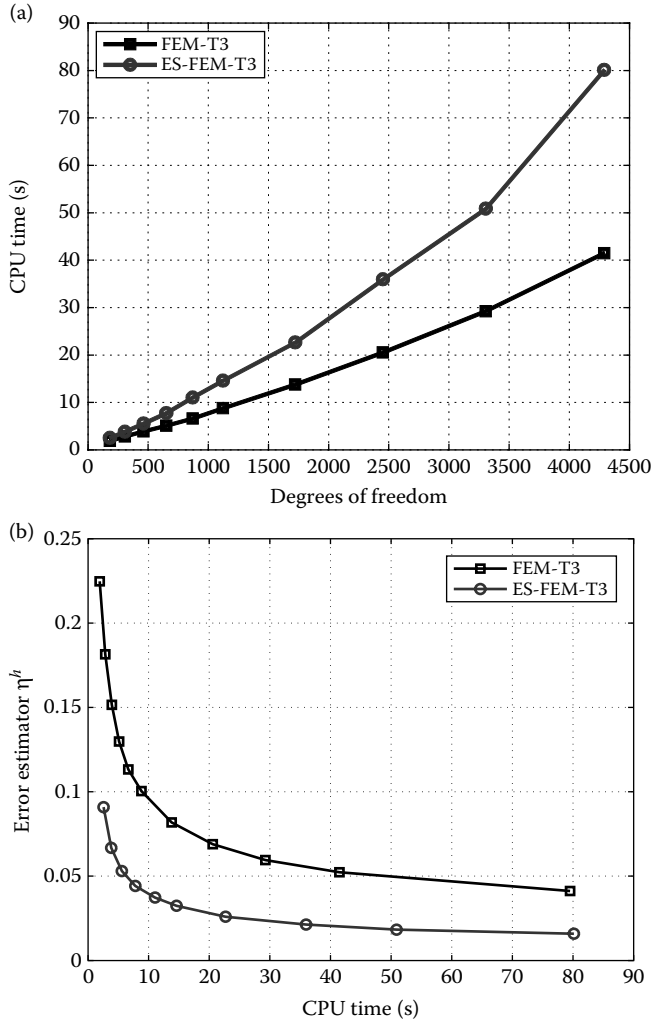

FIGURE 11.17 Comparison of the computational cost and efficiency between FEM-T3 and ES-FEM-T3 for a range of meshes at $t = 0.22$ for the axisymmetric ring problem: (a) CPU time using the same mesh and (b) computational efficiency.

versus computational cost for a range of meshes is considered, the ES-FEM-T3 is more efficient than the FEM-T3 as shown in Figure 11.17b.

Figure 11.18 shows the solution in terms of elastic shear energy density $\|\text{dev}(\breve{\boldsymbol{\sigma}}^R)\|^2/(4\mu)$ obtained using both FEM-T3 and ES-FEM-T3 at $t = 0.22$. It is shown that the plastic domain first appears at the inner circumference and extends toward the outer circumference. The development of the elastic shear energy density $\|\text{dev}(\breve{\boldsymbol{\sigma}}^R)\|^2/(4\mu)$ is demonstrated using the ES-FEM-T3 solution at different time instances as shown in Figure 11.19.

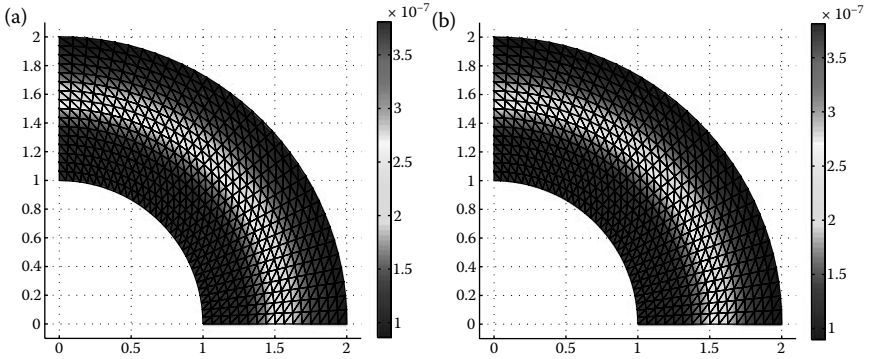

FIGURE 11.18 Elastic shear energy density $\|\text{dev}(\overset{\smile}{\boldsymbol{\sigma}}^{R})\|^2/(4\mu)$ for the axis-symmetric ring problem using (a) FEM-T3 and (b) ES-FEM-T3 at $t = 0.22$ (mesh with 561 nodes and 1024 triangular elements).

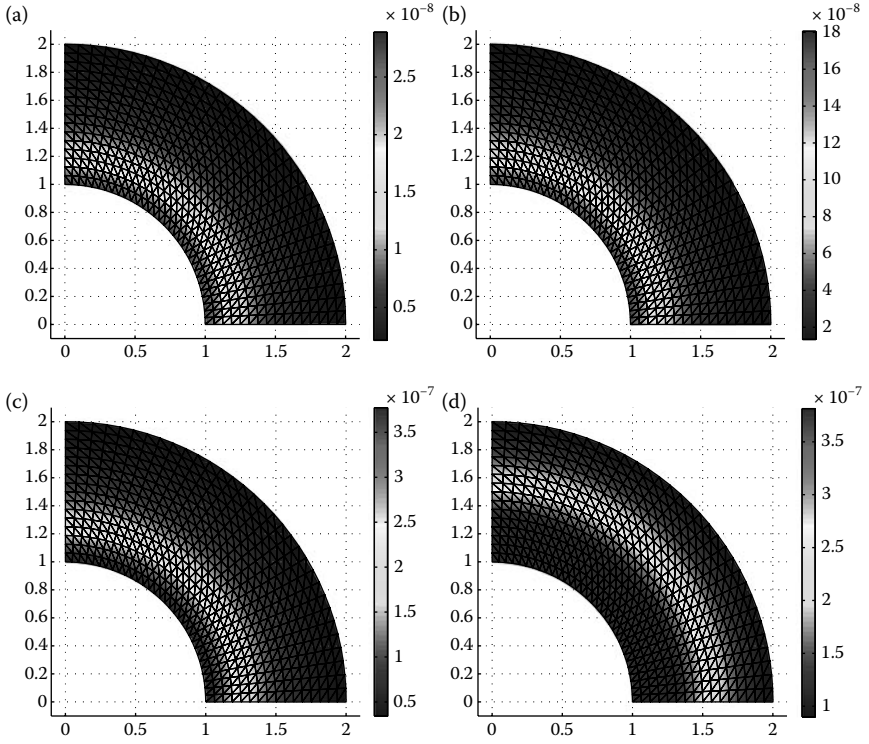

FIGURE 11.19 Evolution of the elastic shear energy density $\|\text{dev}(\overset{\smile}{\boldsymbol{\sigma}}^{R})\|^2/(4\mu)$ using ES-FEM-T3 at some different time steps for the axis-symmetric ring problem: (a) $t = 0.04$; (b) $t = 0.1$; (c) $t = 0.16$; and (d) $t = 0.22$.

TABLE 11.6

Horizontal Displacement at point $A(1,0)$ and Vertical Displacement at point $B(0,1)$ using FEM-T3 and ES-FEM-T3 at Various Times for the Axisymmetric Ring Problem

	FEM-T3				ES-FEM-T3			
Time	**Iterations**	u_A	v_B	u_A/v_B	**Iterations**	u_A	v_B	u_A/v_B
1	1	0.0376	0.0381	0.9866	1	0.0379	0.0380	0.9979
2	1	0.0752	0.0763	0.9866	1	0.0759	0.0760	0.9979
3	1	0.1129	0.1144	0.9866	1	0.1138	0.1141	0.9979
4	1	0.1505	0.1525	0.9866	1	0.1518	0.1521	0.9979
5	1	0.1881	0.1907	0.9866	1	0.1897	0.1901	0.9979
6	1	0.2257	0.2288	0.9866	1	0.2276	0.2281	0.9979
7	1	0.2634	0.2669	0.9866	1	0.2656	0.2662	0.9979
8	3	0.3049	0.3097	0.9845	3	0.3077	0.3091	0.9955
9	4	0.3586	0.3653	0.9817	4	0.3620	0.3642	0.9941
10	5	0.4305	0.4385	0.9819	4	0.4356	0.4386	0.9931
11	5	0.5336	0.5386	0.9906	4	0.5382	0.5422	0.9927

Table 11.6 shows the solution in terms of the ratio of radial displacements between points $A(1,0)$ and $B(0,1)$ using FEM-T3 and ES-FEM-T3 at various time instances. Because our problem is axial-symmetric, such a ratio should be unity. It is found that the results obtained using the ES-FEM-T3 is more symmetric than those of the FEM-T3. This finding is also supported by the solution of the elastic shear energy density $\|\text{dev}(\breve{\boldsymbol{\sigma}}^R)\|^2/(4\mu)$ shown as a contour plot in Figure 11.20 obtained using a coarse mesh with 45 nodes and 64 triangular elements.

Figure 11.21 shows the convergence of the elastic strain energy $E = \int_\Omega (\breve{\boldsymbol{\sigma}}_\vartheta)^T \breve{\mathbf{e}}_\vartheta \, d\Omega$ when the mesh is refined using both FEM-T3 and ES-FEM-T3 at a fixed time $t = 0.22$. The results again verify the finding that the ES-FEM-T3 model is much softer and gives much more accurate results than the FEM-T3 model using the same triangular elements.

Example 11.6.4: A 3D Solid with a Cylindrical Hole: Perfect Viscoelastoplasticity

Figure 11.22 shows a thick "plate" with the dimensions in the *xOy* plane as $[-2,2] \times [-2,2]$ and the thickness in the z-direction as $[-0.5, 0.5]$. Because of the bulky geometry, the "plate" is treated as a 3D solid. The 3D solid has a central cylindrical hole in the z-direction with a radius of $a = 1$ and is subjected to time-dependent forces $g(t) = 100t$ in the y-direction on the two outer surfaces. Because of its symmetry, only the upper right quadrant of the solid is modeled. Symmetric conditions are imposed on the symmetric planes, and the inner boundary of the hole is traction free. Figure 11.23 shows the mesh

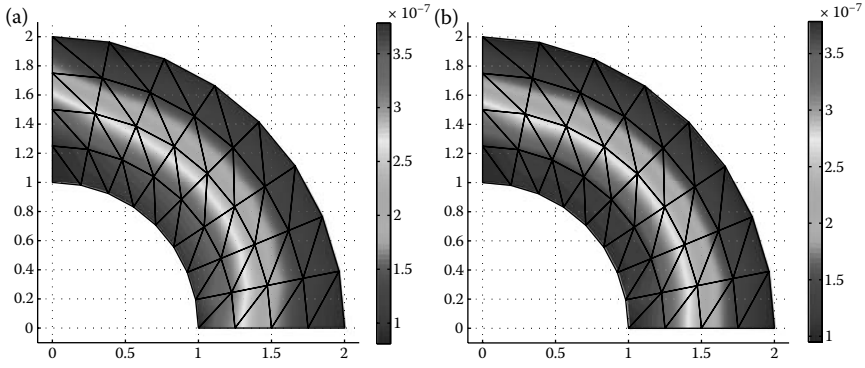

FIGURE 11.20 Distribution of the elastic shear energy density $\|\mathrm{dev}(\breve{\boldsymbol{\sigma}}^{R})\|^2/(4\mu)$ for the axis-symmetric ring problem using (a) FEM-T3; and (b) ES-FEM-T3 at $t = 0.22$ (mesh with 45 nodes and 64 triangular elements).

for the model with 2007 nodes (6021 DOFs) and 8998 tetrahedral elements. Assume that the material has perfect viscoelastoplasticity with Young's modulus $E = 206,900$, Poisson's ratio $\nu = 0.29$, yield stress $\sigma_Y = 550$, and the initial data for the stress vector $\boldsymbol{\sigma}_0$ are set to zero.

Using the mesh as shown in Figure 11.23, the solution is computed in the time interval from $t = 0$ to $t = 1.0$ with 10 uniform time steps of $\Delta t = 0.1$.

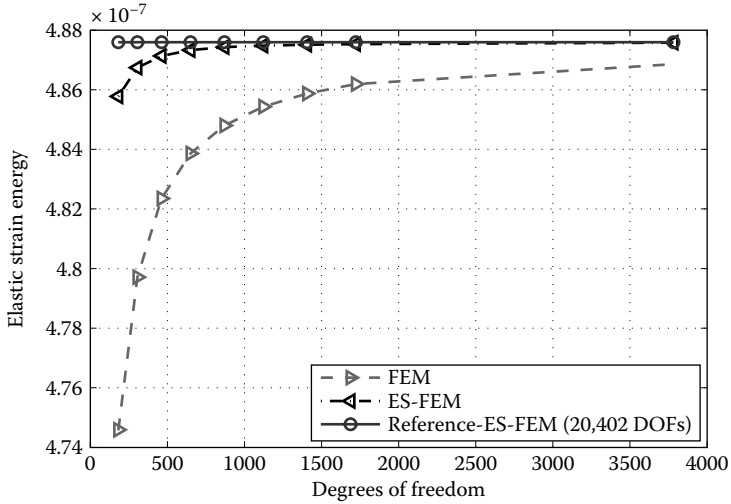

FIGURE 11.21 Convergence of the elastic strain energy $E = \int_\Omega (\breve{\boldsymbol{\sigma}}_\vartheta)^T \breve{\mathbf{e}}_\vartheta \, \mathrm{d}\Omega$ versus the number of DOFs using FEM-T3 and ES-FEM-T3 at $t = 0.22$ for the axis-symmetric ring problem.

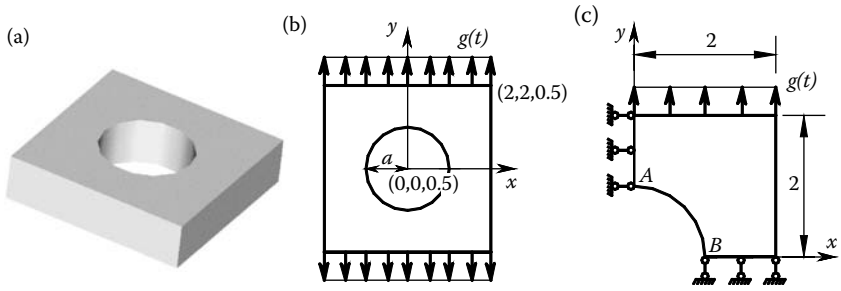

FIGURE 11.22 A 3D solid block with a cylindrical hole subjected to time-dependent surface forces: (a) 3D full geometric model; (b) model with forces viewed from the positive direction of the z-axis; and (c) one-eighth of the model with forces and symmetric boundary conditions.

It is found that the material remains elastic in the first seven steps (where no iterations are needed), between $t = 0$ and $t = 0.7$ for both FS-FEM-T4 and FEM-T4, as shown in Table 11.7. The number of iterations used in Newton's method of both FS-FEM-T4 and FEM-T4 is almost the same (see Table 11.7). The estimated errors η^h using Equation 11.66 for FS-FEM-T4 are about 30% less than those of FEM-T4. In addition, Figure 11.24 compares the computational cost and efficiency between FEM-T4 and FS-FEM-T4 for a range of meshes at $t = 1$. It is seen that with the same mesh, the computational cost of FS-FEM-T4 is larger than that of FEM-T4 as shown in Figure 11.24a. However, when the efficiency of computation in terms of the solution error versus computational cost for a range of meshes is considered, the FS-FEM-T4 is more efficient than the FEM-T4 as shown in Figure 11.24b.

Figure 11.25 shows the distribution of the elastic shear energy density $\|\text{dev}(\breve{\boldsymbol{\sigma}}^R)\|^2/(4\mu)$ at $t = 1.0$ obtained using both FEM-T4 and FS-FEM-T4.

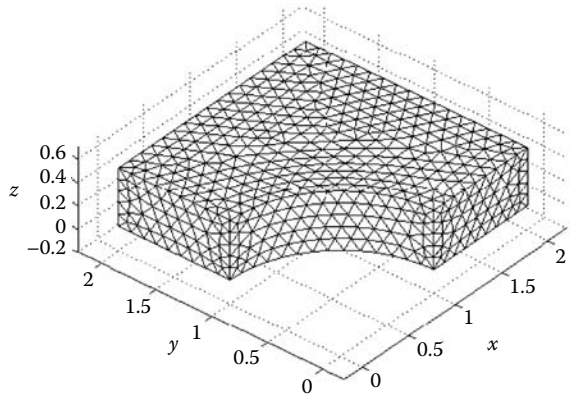

FIGURE 11.23 Mesh with 2007 nodes and 8998 tetrahedral elements for the 3D solid block with a cylindrical hole subjected to time-dependent surface forces $g(t)$.

TABLE 11.7

Number of Iterations and the Estimated Error using FEM-T4 and FS-FEM-T4 at Various Times for the 3D Solid with a Cylindrical Hole

Number of Time Steps	FEM-T4		FS-FEM-T4	
	Iterations	$\eta^h = \frac{\left\|\breve{\sigma}^R - \breve{\sigma}\right\|_{L^2}}{\left\|\breve{\sigma}\right\|_{L^2}}$	Iterations	$\eta^h = \frac{\left\|\breve{\sigma}^R - \breve{\sigma}\right\|_{L^2}}{\left\|\breve{\sigma}\right\|_{L^2}}$
1	1	0.1260	1	0.0853
2	1	0.1260	1	0.0853
3	1	0.1260	1	0.0853
4	1	0.1260	1	0.0853
5	1	0.1260	1	0.0853
6	1	0.1260	1	0.0853
7	1	0.1260	1	0.0853
8	4	0.1256	3	0.0849
9	4	0.1255	4	0.0845
10	4	0.1264	4	0.0848

The evolution process of the elastic shear energy density $\|\text{dev}(\breve{\boldsymbol{\sigma}}^R)\|^2/(4\mu)$ is demonstrated using the FS-FEM-T4 at four different time instances in Figure 11.26. It is shown that the plasticity domain first appears at the corner starting from point $A(0, 1, 0.5)$ and then at the other corner starting from point $B(1, 0, 0.5)$.

Figures 11.27 and 11.28 show, respectively, the convergence of displacements at points A, B and the elastic strain energy $E = \int_\Omega (\breve{\boldsymbol{\sigma}}_\vartheta)^T \breve{\mathbf{e}}_\vartheta \, d\Omega$ when the mesh is refined at a fixed time $t = 1$. The results from both FEM-T4 and FS-FEM-T4 models are plotted. The solution of the FS-FEM-T4 using a very fine mesh with 17,991 DOFs and 29,543 elements is used as the reference solution for comparison. The results show clearly that the FS-FEM-T4 model is softer and gives more accurate results than the FEM-T4 model using the same mesh of tetrahedral elements.

Example 11.6.5: A 3D L-shaped Block: Perfect Viscoelastoplasticity

Consider the 3D square block with a cubic hole subjected to the outer surface traction q as shown in Figure 11.29a. Due to the symmetric property of the problem, only one-eighth of the domain is modeled, which becomes a 3D L-shaped block with the length of $2a$ for the long edge, a for the short edge, and $a/2$ for the thickness as shown in Figure 11.29b. The symmetric conditions are imposed on the cutting boundary planes. Figure 11.30 gives a discretization of the domain using 2327 nodes and 10,584 tetrahedral elements. The 3D L-shaped block is subjected to time-dependent outer pressures $q(t) = 120t$ in the x-direction and the data of length $a = 1$. Assume that the material has perfect viscoelastoplasticity with Young's modulus $E = 206,900$, Poisson's ratio

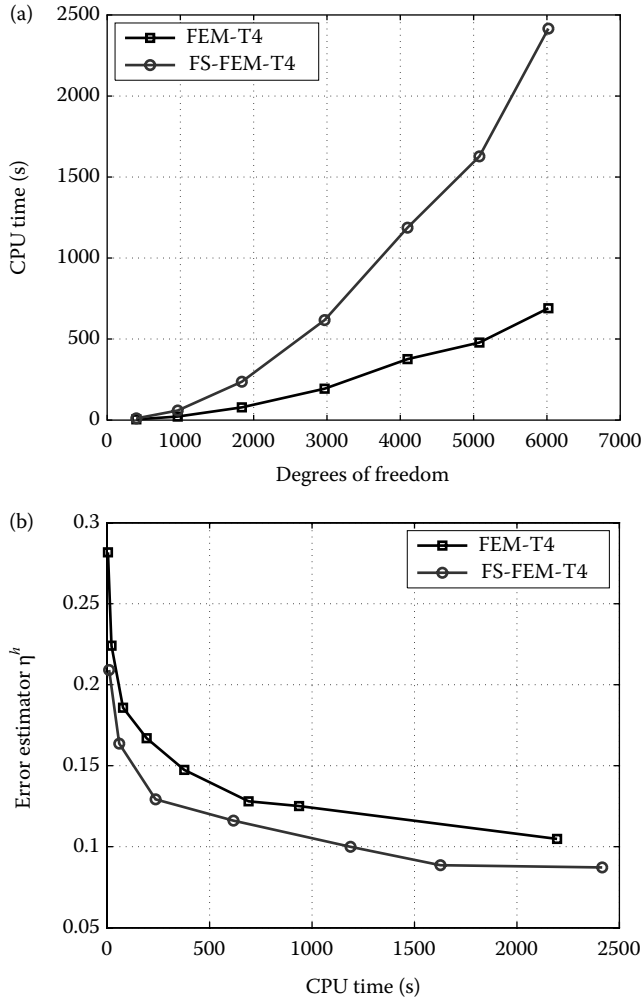

FIGURE 11.24 Comparison of the computational cost and efficiency between FEM-T4 and FS-FEM-T4 for a range of meshes at $t = 1$ for the thick plate with a cylindrical hole: (a) CPU time using the same mesh and (b) computational efficiency.

$\nu = 0.29$, yield stress $\sigma_Y = 500$, and the initial data for the stress vector $\boldsymbol{\sigma}_0$ are set to zero.

The solution is calculated in the time interval from $t = 0$ to $t = 1.0$ in 10 equal steps of $\Delta t = 0.1$. Using the mesh as shown in Figure 11.30, the material remains elastic in four first steps, between $t = 0$ and $t = 0.4$ for both FS-FEM-T4 and FEM-T4 as shown in Table 11.8. Table 11.8 also shows that the number of iterations in Newton's method of both FS-FEM-T4 and FEM-T4 is the same, but the estimated errors η^h using Equation 11.66 of FS-FEM-T4 are about 30% less

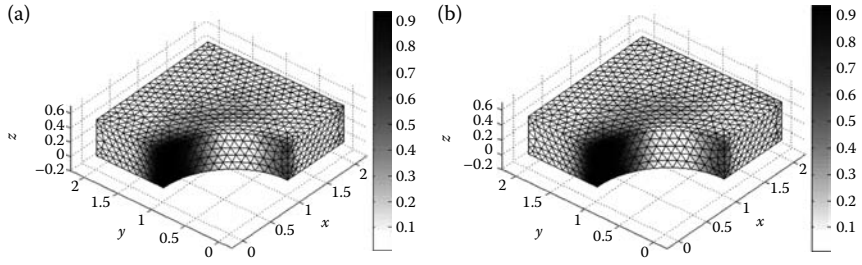

FIGURE 11.25 Distribution of the elastic shear energy density $\|\text{dev}(\breve{\boldsymbol{\sigma}}^{R})\|^2/(4\mu)$ (the gray stone) of the 3D solid block with a cylindrical hole at $t = 1.0$ (mesh with 2007 nodes and 8998 tetrahedral elements); (a) FEM-T4 and (b) FS-FEM-T4.

than those of FEM-T4. In addition, Figure 11.31 compares the computational cost and efficiency between FEM-T4 and FS-FEM-T4 for a range of meshes at $t = 1$. It is seen that with the same mesh, the computational cost of FS-FEM-T4 is larger than that of FEM-T4 as shown in Figure 11.31a. However, when the efficiency of computation in terms of the solution error versus computational

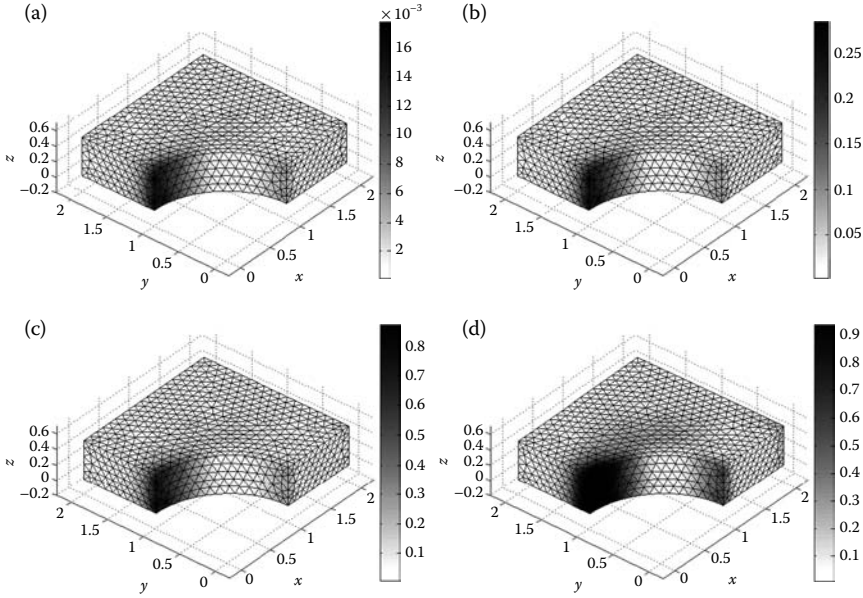

FIGURE 11.26 Evolution of the elastic shear energy density $\|\text{dev}(\breve{\boldsymbol{\sigma}}^{R})\|^2/(4\mu)$ using FS-FEM-T4 at four different time instances for the thick plate with a cylindrical hole: (a) $t = 0.1$; (b) $t = 0.4$; (c) $t = 0.7$; and (d) $t = 1.0$.

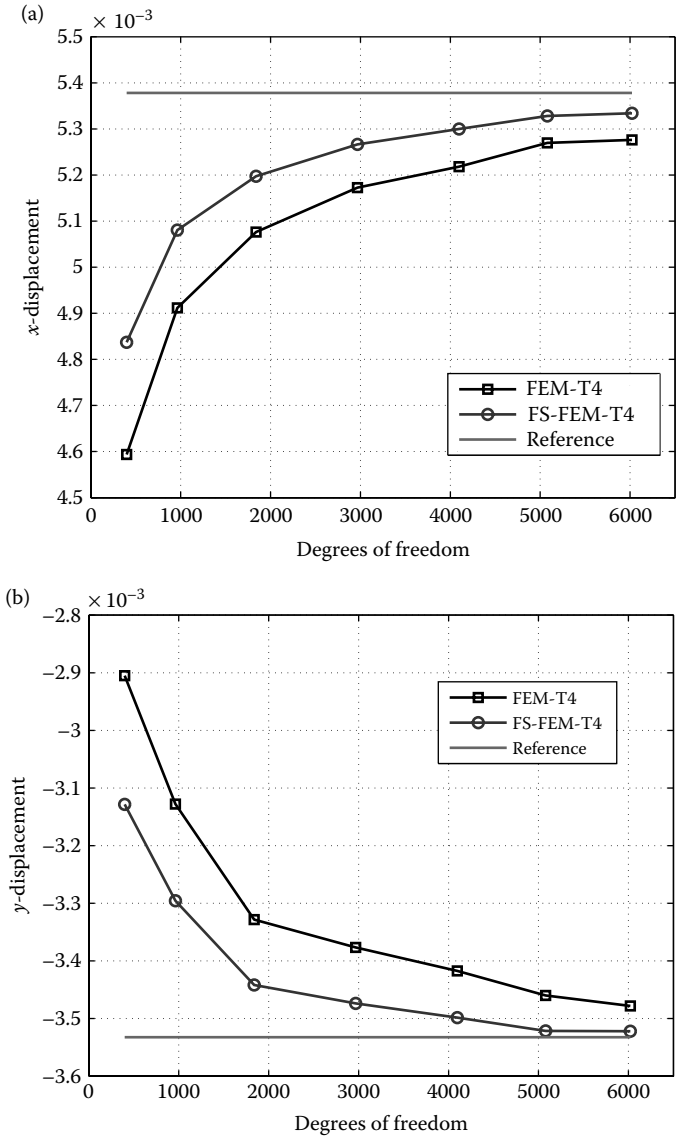

FIGURE 11.27 Displacements at points A and B versus the number of DOFs used in FS-FEM-T4 and FEM-T4 for the 3D solid block with a cylindrical hole: (a) x-displacement of node A and (b) y-displacement of node B.

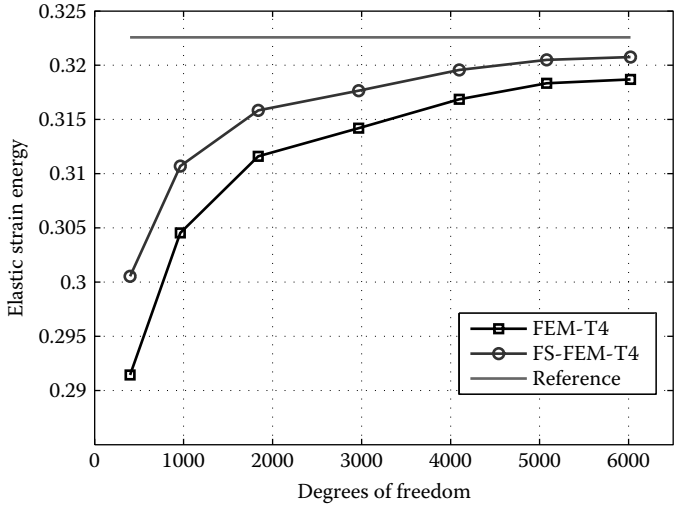

FIGURE 11.28 Convergence of the elastic strain energy $E = \int_\Omega (\breve{\boldsymbol{\sigma}}_\vartheta)^T \breve{\mathbf{e}}_\vartheta \, \mathrm{d}\Omega$ freedom at a fixed time $t = 1$ of the 3D solid block with a cylindrical hole.

cost for a range of meshes is considered, the FS-FEM-T4 is more efficient than the FEM-T4 as shown in Figure 11.31b.

Figure 11.32 shows the elastic shear energy density $\|\mathrm{dev}(\breve{\boldsymbol{\sigma}}^R)\|^2/(4\mu)$ at $t = 1.0$, which is also almost the same for FEM-T4 and FS-FEM-T4. The evolution of the elastic shear energy density $\|\mathrm{dev}(\breve{\boldsymbol{\sigma}}^R)\|^2/(4\mu)$ is demonstrated by using

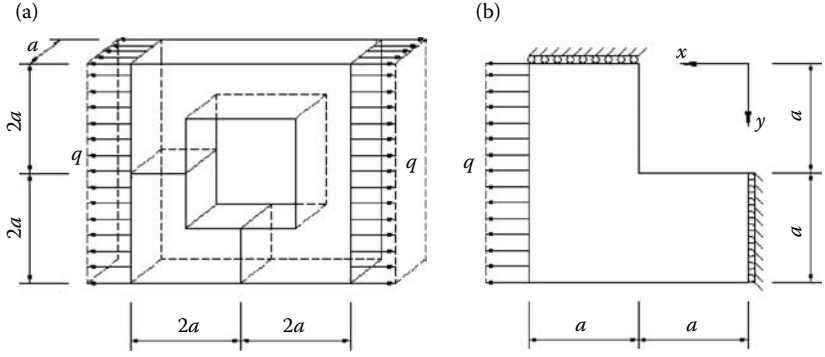

FIGURE 11.29 (a) A 3D block with a cubic hole subjected to surface traction q and (b) the 3D L-shaped problem modeled from one-eighth of the 3D block with a cubic hole (the length of the long edge is $2a$, that of the short edge is a, and the thickness is $a/2$ and symmetric conditions are imposed on the cutting boundary planes).

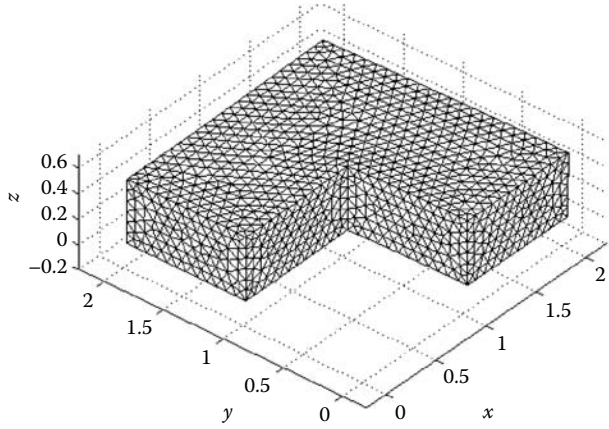

FIGURE 11.30 A domain discretization using 2327 nodes and 10,584 tetrahedral elements for the 3D L-shaped problem.

FS-FEM-T4 at different time steps as shown in Figure 11.33 in which the plastic domain first appears at the re-entrant corner.

Figure 11.34 shows the convergence of the elastic strain energy $E = \int_\Omega (\breve{\boldsymbol{\sigma}}_\vartheta)^T \breve{\mathbf{e}}_\vartheta \, d\Omega$ versus the number of DOFs using FEM-T4 and FS-FEM-T4 at $t = 1.0$. The solution of FS-FEM-T4 using a very fine mesh including 15,390 DOFs and 24,777 elements is used as the reference solution. The results again verify that the FS-FEM-T4 model is softer and gives more accurate results than the FEM-T4 model using tetrahedral elements.

TABLE 11.8

Number of Iterations and the Estimated Error Using FEM and FS-FEM at Various Time Steps for the 3D L-Shaped Problem

	FEM		FS-FEM	
Step	**Iterations**	$\eta^h = \dfrac{\left\|\breve{\boldsymbol{\sigma}}^R - \breve{\boldsymbol{\sigma}}\right\|_{L^2}}{\left\|\breve{\boldsymbol{\sigma}}\right\|_{L^2}}$	**Iterations**	$\eta^h = \dfrac{\left\|\breve{\boldsymbol{\sigma}}^R - \breve{\boldsymbol{\sigma}}\right\|_{L^2}}{\left\|\breve{\boldsymbol{\sigma}}\right\|_{L^2}}$
1	1	0.1343	1	0.0951
2	1	0.1343	1	0.0951
3	1	0.1343	1	0.0951
4	1	0.1343	1	0.0951
5	2	0.1343	2	0.0951
6	3	0.1344	3	0.0952
7	4	0.1351	4	0.0955
8	4	0.1358	4	0.0953
9	4	0.1365	4	0.0949
10	5	0.1385	5	0.0950

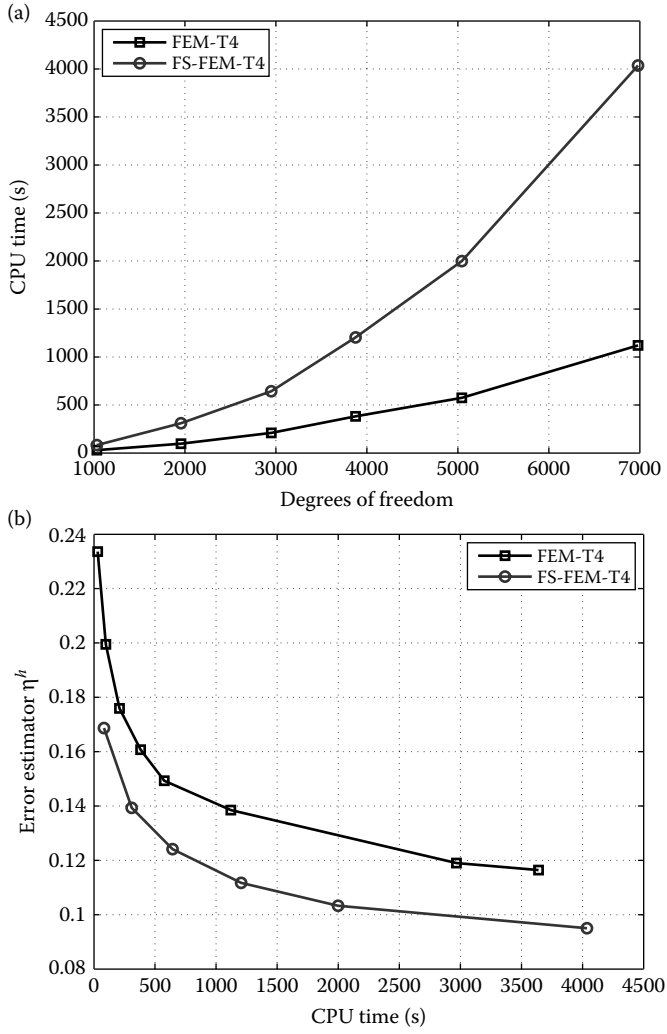

FIGURE 11.31 Comparison of the computational cost and efficiency between FEM and FS-FEM for a range of meshes at $t = 1$ for the 3D L-shaped problem: (a) CPU time using the same mesh and (b) computational efficiency.

Example 11.6.6: Hollow Sphere: 3D Viscoelastoplasticity with Isotropic Hardening

The domain of the hollow sphere is defined as $\Omega = B(0, 2)/B(0, 1.3)$ [the origin $O(0, 0, 0)$, inner radius $a = 1.3$, and outer radius $b = 2.0$]. The hollow sphere is subjected to a uniform pressure $g(r, \varphi, t) = 50te_r$ on the inner spherical surface with $e_r = \begin{bmatrix}\cos\varphi & \sin\varphi\end{bmatrix}^T$. Because of the symmetric characteristics

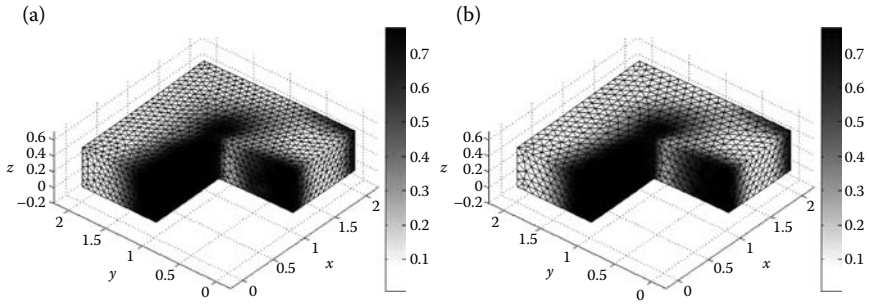

FIGURE 11.32 Elastic shear energy density $\|\text{dev}(\overset{\smile}{\boldsymbol{\sigma}}^{R})\|^2/(4\mu)$ (the gray stone) of the 3D L-shaped problem at $t = 1.0$ (mesh with 2327 nodes and 10,584 tetrahedral elements). (a) FEM and (b) FS-FEM.

of the problem, only one-eighth of hollow sphere needs to be modeled as shown in Figure 11.35, and symmetric conditions are imposed on the symmetric planes. Assuming that the material has viscoelastoplasticity with isotropic hardening with Young's modulus $E = 40,000$, Poisson's ratio $\nu = 0.25$, yield stress $\sigma_Y = 100$, hardening parameter $H = 3$, $H_1 = 1$; and the initial stress vector $\boldsymbol{\sigma}_0$ and the scalar hardening parameter α_0^I are set to zero.

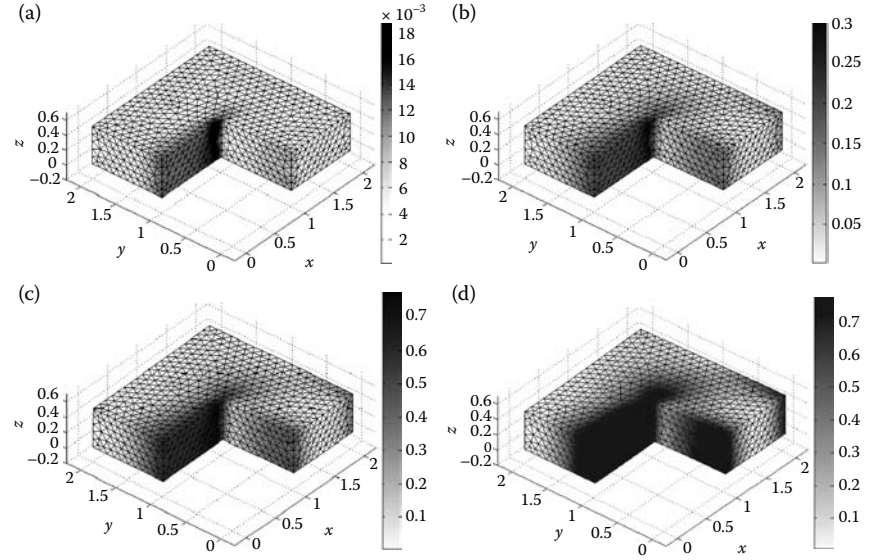

FIGURE 11.33 Evolution of the elastic shear energy density $\|\text{dev}(\overset{\smile}{\boldsymbol{\sigma}}^{R})\|^2/(4\mu)$ using FS-FEM at different time steps for the 3D L-shaped problem: (a) $t = 0.1$; (b) $t = 0.4$; (c) $t = 0.7$; and (d) $t = 1.0$.

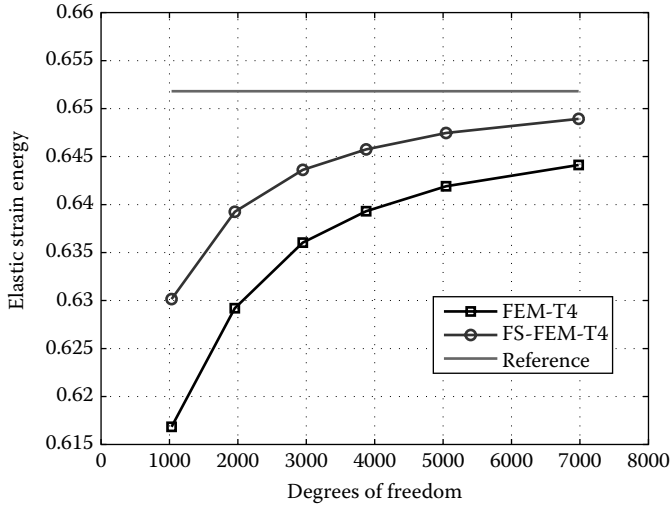

FIGURE 11.34 Convergence of the elastic strain energy $E = \int_\Omega (\breve{\boldsymbol{\sigma}}_\vartheta)^T \breve{\mathbf{e}}_\vartheta \, d\Omega$ versus the number of DOFs at $t = 1$ of the 3D L-shaped problem.

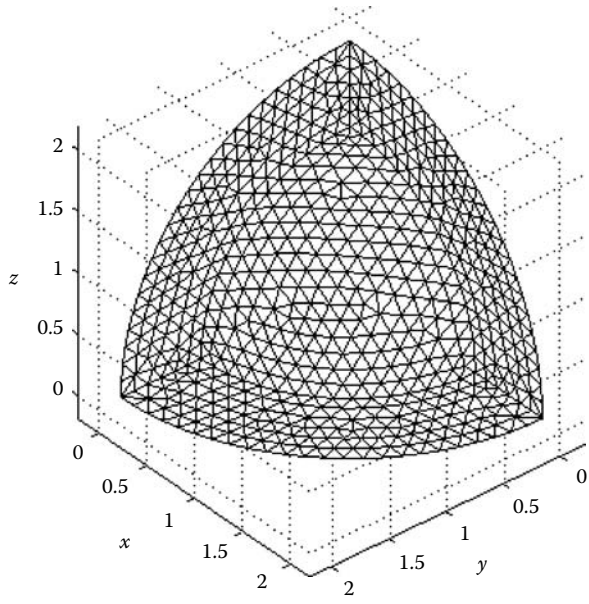

FIGURE 11.35 One-eighth of the hollow sphere discretized by 2234 nodes and 10,385 tetrahedral elements.

TABLE 11.9

Number of Iterations and the Estimated Error Using FEM-T4 and FS-FEM-T4 at Various Time Steps for Hollow Sphere Problem

	FEM-T4		FS-FEM-T4	
Step	**Iterations**	$\eta^h = \frac{\left\|\breve{\sigma}^R - \breve{\sigma}\right\|_{L^2}}{\left\|\breve{\sigma}\right\|_{L^2}}$	**Iterations**	$\eta^h = \frac{\left\|\breve{\sigma}^R - \breve{\sigma}\right\|_{L^2}}{\left\|\breve{\sigma}\right\|_{L^2}}$
1	1	0.1053	1	0.0745
2	1	0.1053	1	0.0745
3	1	0.1053	1	0.0745
4	1	0.1053	1	0.0745
5	1	0.1053	1	0.0745
6	1	0.1053	1	0.0745
7	1	0.1053	1	0.0745
8	2	0.1053	2	0.0745
9	3	0.1053	3	0.0744
10	3	0.1053	3	0.0744

Using the mesh as shown in Figure 11.35, the solution is computed using both FS-FEM-T4 and FEM-T4 for the time interval from $t = 0$ to $t = 1.0$ with 10 uniform time steps of $\Delta t = 0.1$. It is found that the material remains elastic in the first seven steps from $t = 0$ to $t = 0.7$ as shown in Table 11.9. The number of iterations used in Newton's method for both FS-FEM-T4 and FEM-T4 is almost the same. The estimated errors η^h using Equation 11.66 of FS-FEM-T4 are about 30% less than those of FEM-T4. In addition, Figure 11.36 compares the computational cost and efficiency between FEM-T4 and FS-FEM-T4 for a range of meshes at $t = 1$. It is seen that with the same mesh, the computational cost of FS-FEM-T4 is larger than that of FEM-T4 as shown in Figure 11.36a. However, when the efficiency of computation in terms of the solution error versus computational cost for a range of meshes is considered, FS-FEM-T4 is more efficient than FEM-T4 as shown in Figure 11.36b.

Figure 11.37 shows the distribution of the elastic shear energy density $\|\text{dev}(\breve{\boldsymbol{\sigma}}^R)\|^2/(4\mu)$ at $t = 1.0$ obtained using both FEM-T4 and FS-FEM-T4. The evolution process of the elastic shear energy density $\|\text{dev}(\breve{\boldsymbol{\sigma}}^R)\|^2/(4\mu)$ is shown using the FS-FEM-T4 results at four different times in Figure 11.38. It is found that the plastic domain first appears at the inner circumference and extends outward.

Table 11.10 shows the results in terms of the differences of the radial displacement components between points $A(1.3, 0, 0)$ and $B(0, 1.3, 0)$ using FEM-T4 and FS-FEM-T4 at various times. Because our problem is axial-symmetric, such differences should be zero. It is seen from Table 11.10 that for this symmetric problem, the results of FS-FEM-T4 produce more symmetric results than those of FEM-T4.

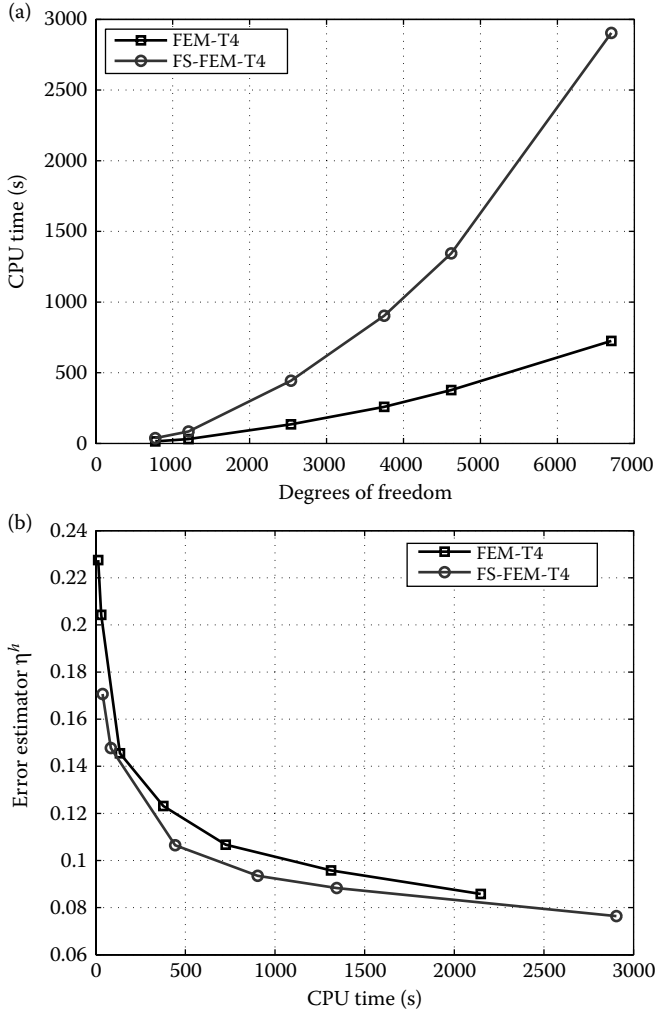

FIGURE 11.36 Comparison of the computational cost and efficiency between FEM-T4 and FS-FEM-T4 for a range of meshes at $t = 1$ for the hollow sphere problem: (a) CPU time using the same mesh and (b) computational efficiency.

Figure 11.39 shows the convergence of the elastic strain energy $E = \int_\Omega (\breve{\boldsymbol{\sigma}}_\vartheta)^T \breve{\mathbf{e}}_\vartheta \, d\Omega$ when the mesh is refined using both FEM-T4 and FS-FEM-T4 at a fixed time $t = 1.0$. The solution of FS-FEM-T4 using a very fine mesh with 17,988 DOFs and 30,168 elements is used as the reference solution for comparison. The results again confirm that the FS-FEM-T4 model is softer and gives more accurate results than the FEM-T4 model using the same mesh of tetrahedral elements.

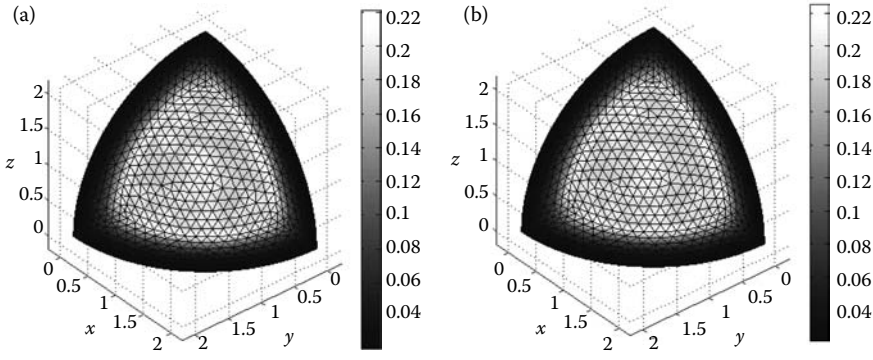

FIGURE 11.37 Distribution of the elastic shear energy density $\|\text{dev}(\overset{\smile}{\boldsymbol{\sigma}}^R)\|^2/(4\mu)$ for the hollow sphere problem using (a) FEM-T4 and (b) FS-FEM-T4 at $t = 1.0$ (mesh with 2234 nodes and 10,385 elements).

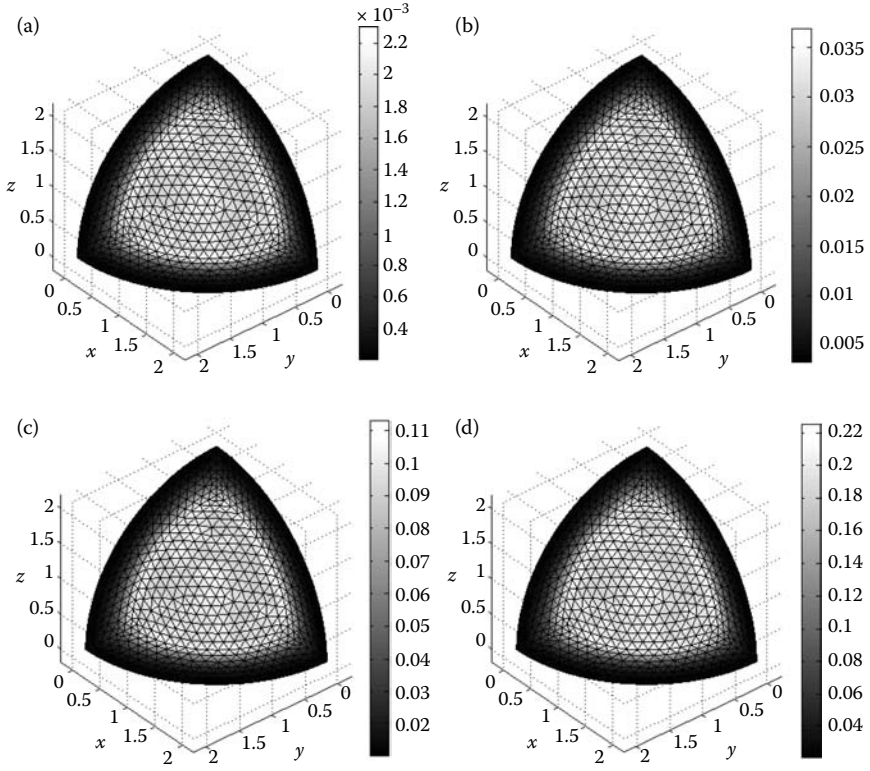

FIGURE 11.38 Evolution of the elastic shear energy density $\|\text{dev}(\overset{\smile}{\boldsymbol{\sigma}}^R)\|^2/(4\mu)$ using FS-FEM-T4 at different time steps for the hollow sphere problem: (a) $t = 0.1$; (b) $t = 0.4$; (c) $t = 0.7$; and (d) $t = 1.0$.

TABLE 11.10

Radial Displacements at points $A(1.3, 0, 0)$ and $B(0, 1.3, 0)$ Obtained using FEM-T4 and FS-FEM-T4 at Various Times for the Hollow Sphere Problem

Number of	FEM-T4			FS-FEM-T4		
Time Step	u_A	v_B	$\lvert u_A - v_B \rvert$	u_A	v_B	$\lvert u_A - v_B \rvert$
1	0.0001664	0.0001658	6.45119E-07	0.0001682	0.0001680	1.87086E-07
2	0.0003328	0.0003315	1.29024E-06	0.0003364	0.0003364	0
3	0.0004992	0.0004973	1.93536E-06	0.0005046	0.0005040	5.61257E-07
4	0.0006656	0.0006630	2.58047E-06	0.0006728	0.0006720	7.48343E-07
5	0.0008320	0.0008288	3.22559E-06	0.0008410	0.0008400	9.35429E-07
6	0.0009984	0.0009945	3.87071E-06	0.0010092	0.0010081	1.12251E-06
7	0.0011648	0.0011603	4.51583E-06	0.0011774	0.0011761	1.3096E-06
8	0.0013312	0.0013260	5.15844E-06	0.0013456	0.0013441	1.49466E-06
9	0.0014980	0.0014922	5.80887E-06	0.0015142	0.00151251	1.6819E-06
10	0.0016667	0.0016603	6.46026E-06	0.0016850	0.00168311	1.84285E-06

Example 11.6.7: 3D Cook's Membrane: Viscoelastoplasticity with Linear Kinematic Hardening

The final example for this chapter is a 3D Cook's membrane shown in Figure 11.40. The 3D solid is meshed with 2317 nodes and 9583 tetrahedral elements. At the right end of the membrane, there is a time-dependent shear force $g = 90t$

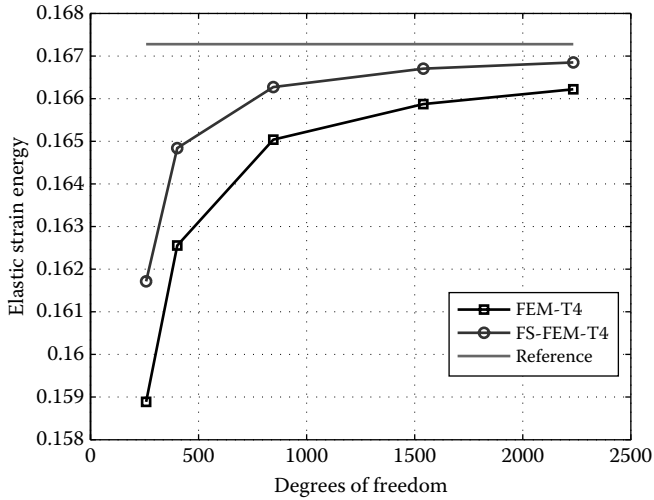

FIGURE 11.39 Convergence of the elastic strain energy $E = \int_\Omega (\breve{\boldsymbol{\sigma}}_\vartheta)^T \breve{\mathbf{e}}_\vartheta \, d\Omega$ versus the number of DOFs at $t = 1$ of the hollow sphere problem.

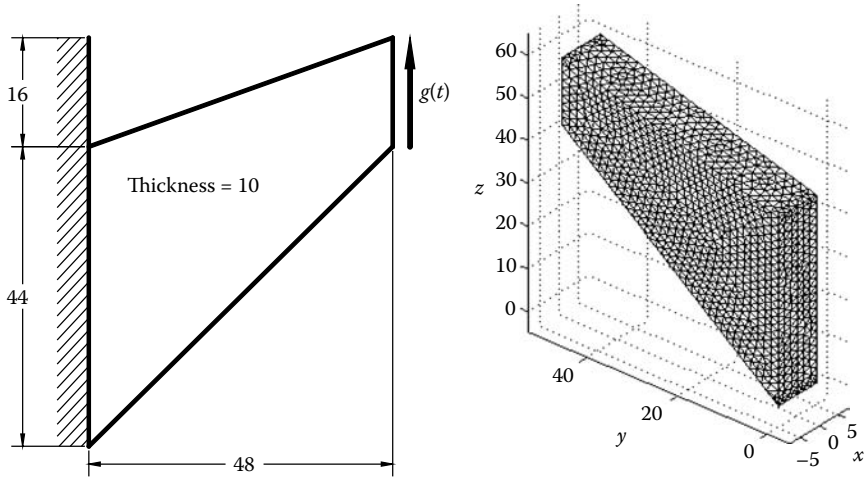

FIGURE 11.40 The 3D Cook's membrane subjected to a time-dependent shear force and its discretization using 2317 nodes and 9583 tetrahedral elements.

and the other end is fixed. Assume that the material has viscoelastoplasticity with linear kinematic hardening with Young's modulus $E = 70,000$, Poisson's ratio $\nu = 0.3$, yield stress $\sigma_Y = 400$, and hardening parameter $k_1 = 2$. The initial data for the displacement $\boldsymbol{u}_0$, the stress vector $\boldsymbol{\sigma}_0$, and the hardening parameter $\boldsymbol{\alpha}_0^K$ are set to zero.

TABLE 11.11

Number of Iterations and the Estimated Error using FEM-T4 and FS-FEM-T4 at Various Time Steps for the 3D Cook's Membrane Problem

	FEM-T4		FS-FEM-T4	
Step	**Iterations**	$\eta^h = \frac{\left\|\breve{\sigma}^R - \breve{\sigma}\right\|_{L^2}}{\left\|\breve{\sigma}\right\|_{L^2}}$	**Iterations**	$\eta^h = \frac{\left\|\breve{\sigma}^R - \breve{\sigma}\right\|_{L^2}}{\left\|\breve{\sigma}\right\|_{L^2}}$
1	1	0.1087	1	0.0735
2	1	0.1087	1	0.0735
3	1	0.1087	1	0.0735
4	1	0.1087	1	0.0735
5	1	0.1087	1	0.0735
6	3	0.1087	3	0.0735
7	3	0.1088	3	0.0735
8	3	0.1092	4	0.0738
9	4	0.1101	4	0.0745
10	4	0.1118	4	0.0755

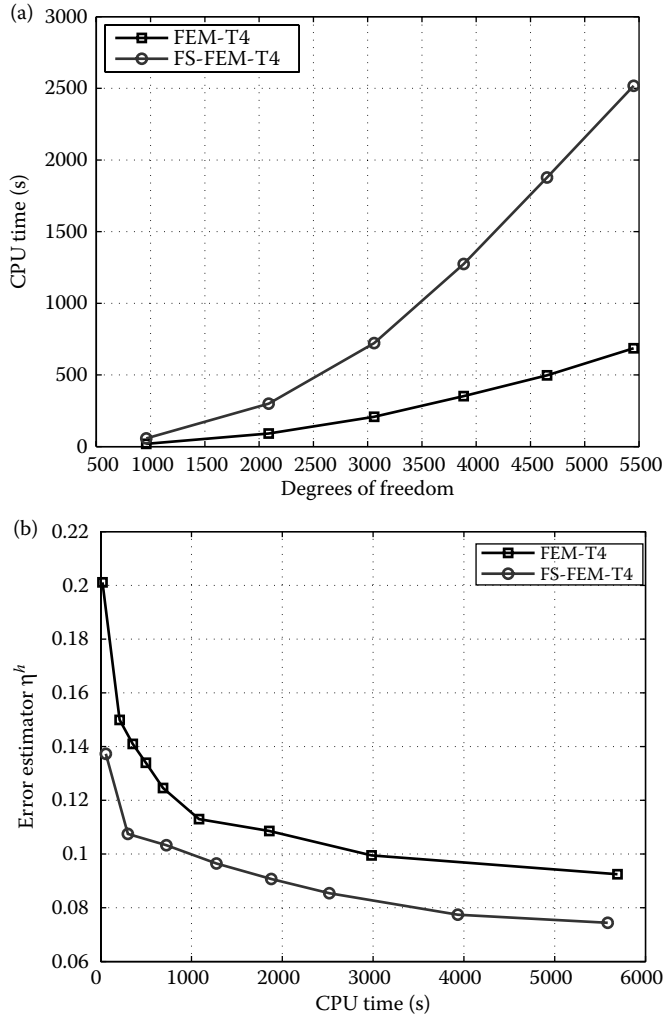

FIGURE 11.41 Comparison of the computational cost and efficiency between FEM-T4 and FS-FEM-T4 for a range of meshes at $t = 1$ for the 3D Cook's membrane problem: (a) CPU time using the same mesh and (b) computational efficiency.

Using the mesh as shown in Figure 11.40, the solution is computed using both FS-FEM-T4 and FEM-T4 models for the time interval from $t = 0$ to $t = 1.0$ with 10 uniform time steps of $\Delta t = 0.1$. It is found that the material remains elastic in the first five steps from $t = 0$ to $t = 0.5$ as shown in Table 11.11. The number of iterations used in Newton's method for both FS-FEM-T4 and FEM-T4 is almost the same. The estimated errors η^h using Equation 11.66 of FS-FEM-T4 are about 30% less than those of FEM-T4. In addition, Figure 11.41 compares the

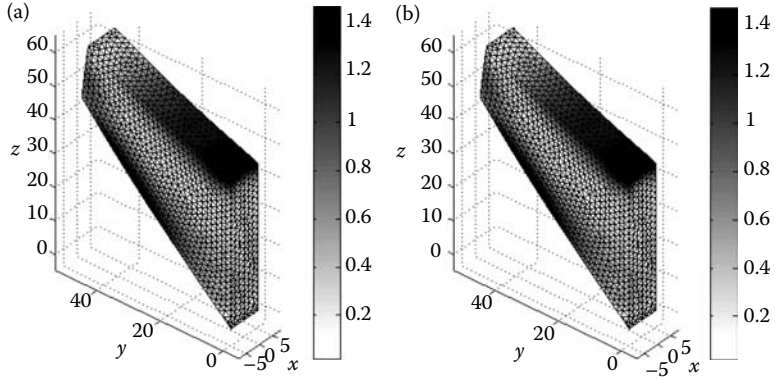

FIGURE 11.42 Distribution of the elastic shear energy density $\|\text{dev}(\breve{\boldsymbol{\sigma}}^R)\|^2/(4\mu)$ for the 3D Cook's membrane problem using FEM-T4 and FS-FEM-T4 at $t = 1.0$ (mesh with 2317 nodes and 9583 tetrahedral elements). (a) FEM-T4 and (b) FS-FEM-T4.

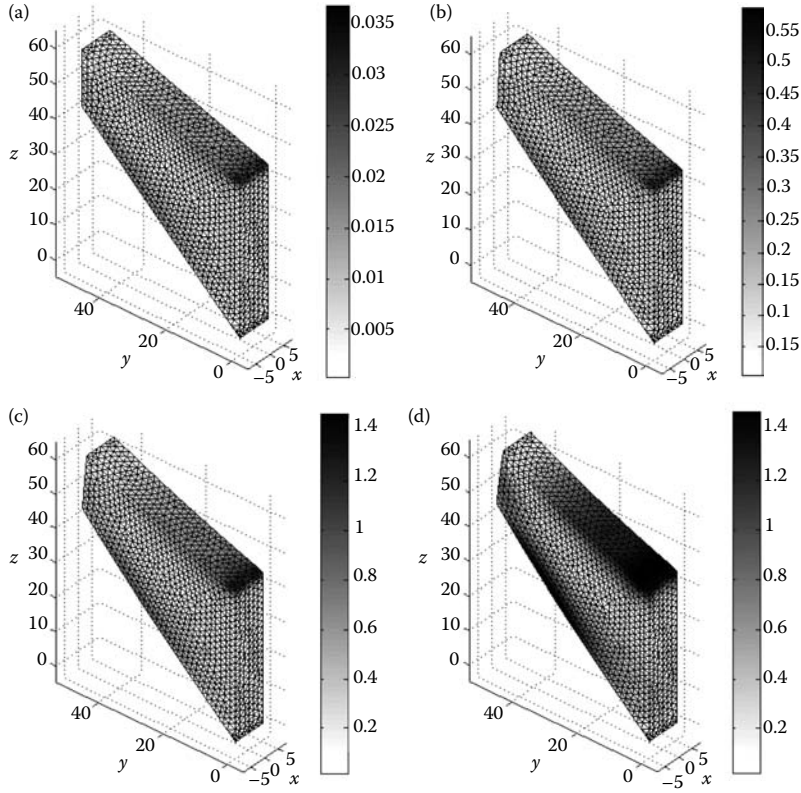

FIGURE 11.43 Evolution of the elastic shear energy density $\|\text{dev}(\breve{\boldsymbol{\sigma}}^R)\|^2/(4\mu)$ obtained using FS-FEM-T4 at four different time instances for the 3D Cook's membrane problem: (a) $t = 0.1$; (b) $t = 0.4$; (c) $t = 0.7$; and (d) $t = 1.0$.

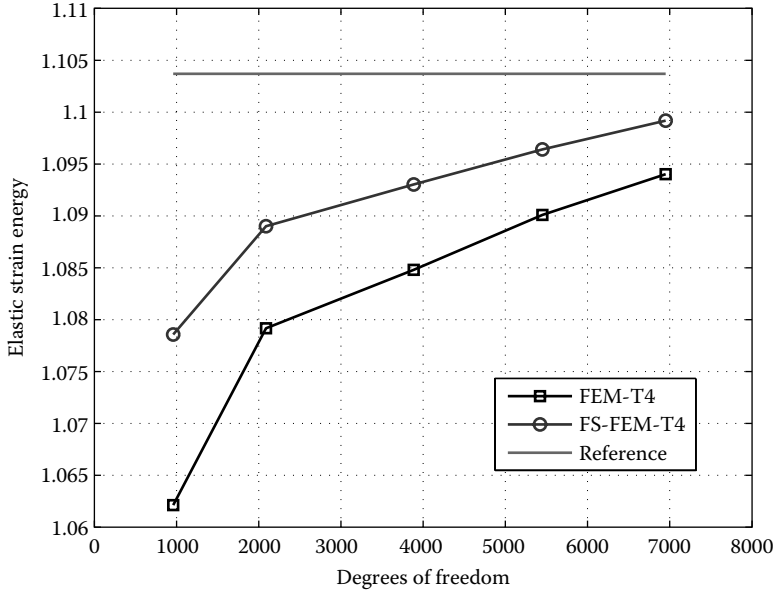

FIGURE 11.44 Convergence of the elastic strain energy $E = \int_\Omega (\breve{\boldsymbol{\sigma}}_\vartheta)^T \breve{\mathbf{e}}_\vartheta \, d\Omega$ versus the number of DOFs at $t = 1$ for the 3D Cook's membrane problem.

computational cost and efficiency between FEM-T4 and FS-FEM-T4 for a range of meshes at $t = 1$. It is seen that with the same mesh, the computational cost of FS-FEM-T4 is larger than that of FEM-T4 as shown in Figure 11.41a. However, when the efficiency of computation (computation time for the same accuracy) in terms of the solution error versus computational cost for a range of meshes is considered, the FS-FEM-T4 is more efficient than the FEM-T4 as shown in Figure 11.41b.

Figure 11.42 shows the distribution of the elastic shear energy density $\|\text{dev}(\breve{\boldsymbol{\sigma}}^R)\|^2/(4\mu)$ at $t = 1.0$ obtained using both FEM-T4 and FS-FEM-T4. The evolution of the elastic shear energy density $\|\text{dev}(\breve{\boldsymbol{\sigma}}^R)\|^2/(4\mu)$ is shown using the FS-FEM-T4 results at four different time instances, and is shown in Figure 11.43. It is observed that the plastic domain first appears at the fixed upper corner and then moves to the middle part of the lower boundary face.

Figure 11.44 shows the convergence of the elastic strain energy $E = \int_\Omega (\breve{\boldsymbol{\sigma}}_\vartheta)^T \breve{\mathbf{e}}_\vartheta \, d\Omega$ using both FEM-T4 and FS-FEM-T4 at $t = 1.0$. The solution of FS-FEM-T4 using a very fine mesh with 17,307 DOFs and 26,084 elements is used as the reference solution. The results again verify that the FS-FEM-T4 model is softer and gives more accurate results than the FEM-T4 model using the same mesh of tetrahedral elements.

11.7 Concluding Remarks

In this chapter, we presented dual formulations for viscoelastoplasticity problems. Both the standard Galerkin weak form and the smoothed Galerkin weak forms are derived. A general formulation for S-FEM models is also given by combining the model of Carstensen and Klose [1] with the von-Mises conditions and the Prandtl–Reuss flow rule. In particular, ES-FEM-T3 and FS-FEM-T4 are coded for solving the complicated nonlinear problems for 2D and 3D viscoelastoplasticity solids. The material behavior considered includes perfect viscoelastoplasticity and viscoelastoplasticity with isotropic and linear kinematic hardening in a dual model, with displacements and the stresses as the main variables. In our numerical procedure, however, we eliminate the stress variables and the problem eventually becomes only displacement dependent, and hence the problem can easily be solved using ES-FEM-T3 and FS-FEM-T4. The numerical results of ES-FEM-T3 and FS-FEM-T4 using triangular and tetrahedral elements lead to the following remarks:

1. The displacement results of ES-FEM-T3/FS-FEM-T4 are larger than those of FEM-T3/FEM-T4. These results reconfirm clearly that ES-FEM-T3/FS-FEM-T4 models are softer than their FEM counterparts.
2. The elastic strain energies of ES-FEM-T3/FS-FEM-T4 are much more accurate than those of FEM-T3/FEM-T4, which is largely the same finding as we found for linear elastic problems.
3. The a posteriori estimated error η^h used in this work is shown to be reliable in estimating the error in the stress solution in ES-FEM-T3, FS-FEM-T4, FEM-T3, and FEM-T4. For 2D problems, the a posteriori estimated error η^h of ES-FEM-T3 is about 2–3 times smaller than those of FEM-T3. For 3D problems, the a posteriori estimated error η^h of FS-FEM-T4 is about 30% smaller than those of FEM-T4.
4. The bandwidth of the stiffness matrix of ES-FEM-T3 (FS-FEM-T4) is about 4/3 (5/4) times larger than that of FEM counterparts, and hence the computational cost of ES-FEM-T3/FS-FEM-T4 in numerical examples is larger than that of FEM for the same mesh. However, when the efficiency of computation (computation time for the same accuracy) is considered, the ES-FEM-T3 (FS-FEM-T4) is in fact more efficient than FEM-T3 (FEM-T4).
5. For the coarse meshes, the results of ES-FEM-T3 are much more accurate than those of FEM-T3.
6. For the axis-symmetric problems, the results of ES-FEM-T3/FS-FEM-T4 are more symmetric than those of FEM-T3/FEM-T4.

These examples have shown that the "star" quality of ES-FEM-T3 and FS-FEM-T4 models has also been found for material nonlinear problems. They are likely the best linear models for nonlinear problems in terms of (1) adaptation to complicated geometry; (2) suitability for automatically meshing; (3) stability; (4) solution accuracy; and (5) computational efficiency.

References

1. Carstensen C and Klose R. 2002. Elastoviscoplastic Finite Element Analysis in 100 lines of Matlab. *Journal of Numerical Mathematics*; 10: 157–192.
2. Han W and Reddy BD. 1995. Computational plasticity: The variational basis and numerical analysis. *Computational Mechanics Advances*; 2(283): 400.
3. Liu GR, Nguyen-Thoi T, and Lam KY. 2009. An edge-based smoothed finite element method (ES-FEM) for static, free and forced vibration analyses of solids. *Journal of Sound and Vibration*; 320: 1100–1130.
4. Nguyen-Thoi T, Liu GR, Lam KY, and Zhang GY. 2009. A face-based smoothed finite element method (FS-FEM) for 3D linear and nonlinear solid mechanics problems using 4-node tetrahedral elements. *International Journal for Numerical Methods in Engineering*; 78: 324–353.
5. Nguyen-Thoi T, Liu GR, Vu-Do HC, and Nguyen-Xuan H. 2009. An edge-based smoothed finite element method (ES-FEM) for visco-elastoplastic analyses in 2D solids using triangular mesh. *Computational Mechanics*; 45: 23–44.
6. Nguyen-Thoi T, Liu GR, Vu-Do HC, and Nguyen-Xuan H. 2009. A face-based smoothed finite element method (FS-FEM) for visco-elastoplastic analyses of 3D solids using tetrahedral mesh. *Computer Methods in Applied Mechanics and Engineering*; 198: 3479–3498.
7. Carstensen C and Funken SA. 2001. Averaging technique for FE—a posteriori error control in elasticity. Part 1: Conforming FEM. *Computer Methods in Applied Mechanics and Engineering*; 190: 2483–2498.

12

ES-FEM for Plates

12.1 Introduction

The numerical analysis of a plate using the FEM has played an important role in engineering applications in structural engineering [1], because (1) the plate is one of the most widely used essential structural components, and (2) the FEM is so far one of the most important and robust numerical methods. In recent years, mesh-free methods have also been developed and applied to various problems for different types of plates [2]. In practical engineering applications, lower-order Reissner–Mindlin plate elements are preferred due to its simplicity, efficiency and applicability to "thick" plates. However, when applied to thin plates, these low-order plate elements often suffer from the so-called *shear locking*. In order to eliminate shear locking, many attempts have been made and the selective reduced integration scheme was proposed [3–6]. The idea of the selective reduced integration scheme is to split the strain energy into two parts: the bending-related term and the shear-related one. Two different integration rules are then used, respectively, for the bending strain energy and the shear strain energy. For example, for four-node quadrilateral elements with bilinear shape functions, the reduced integration (using a single Gauss point) is used to compute shear strain energy, while the full Gauss integration (using 2×2 Gauss points) is used for the bending strain energy. Such a selective reduced integration scheme is very simple, easy to apply, and works well for many cases. Unfortunately, the reduced integration often leads to rank deficiency in the stiffness matrix, which can be observed as zero-energy modes. Various improvements have also been made in the formulation, and many numerical techniques have been developed to overcome the shear locking problem, aiming to increase the accuracy and to ensure the stability of the solution, such as the mixed formulation or hybrid elements [7–17], enhanced assumed strain (EAS) methods [18–22], and assumed natural strain (ANS) methods [23–32]. Recently, the so-called DSG method [33] was proposed to overcome the shear locking problem. The DSG is somewhat similar to the ANS methods in the aspect of modifying the strains within the element, but is different in the aspect of removing collocation points. The DSG method is found to work well for elements of different orders and shapes [33].

This chapter aims to extend the "star" performer ES-FEM-T3 to static, free vibration and buckling analyses of plates, capitalizing on these excellent features of the ES-FEM found from the previous chapters. The ES-FEM formulation will be based on the Reissner–Mindlin plates, and uses (again) only triangular meshes for the excellent geometric adaptation. In order to avoid the transverse shear locking and to improve the accuracy, the ES-FEM-T3 is incorporated with the DSG method [33] together with a stabilization technique [34]. The method was termed as ES-FEM-T3 with the stabilized DSG method or ES-FEM-DSG3 for short. The numerical examples will show that the ES-FEM-DSG3 method is free of shear locking and is a strong competitor to other existing elements found in the literature. The ES-FEM-DSG3 works well for both thin and thick plates for various problems: static, free vibration and buckling, as will be demonstrated in this chapter.

12.2 Weak Form for the Reissner–Mindlin Plate

Consider a plate under bending deformation. The middle (neutral) surface of plate is chosen as the reference plane that occupies a domain $\Omega \subset R^2$ as shown in Figure 12.1a. Let w be the transverse displacement (deflection), and $\boldsymbol{\beta}^T = \begin{bmatrix} \beta_x & \beta_y \end{bmatrix}$ be the vector of rotations, in which β_x, β_y are the rotations of the middle plane around the y-axis and x-axis, respectively, with the positive directions defined as shown in Figure 12.1b. The unknown vector of three independent field variables at any point in the problem domain of the Reissner–Mindlin plates can be written as

$$\mathbf{u}^T = \begin{bmatrix} w & \beta_x & \beta_y \end{bmatrix}. \tag{12.1}$$

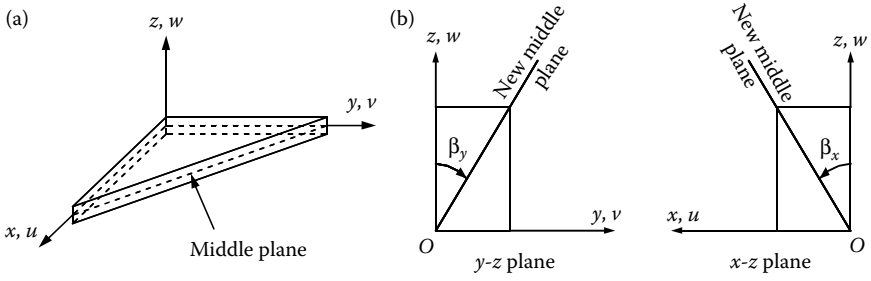

FIGURE 12.1 Three-node triangular plate element and field variables for the Reissner–Mindlin plates: (a) positive directions of displacement u, v, and w; and (b) positive directions of β_x and β_y.

The curvature of the deflected plate is defined as

$$\boldsymbol{\kappa} = \mathbf{L}_d \boldsymbol{\beta} \tag{12.2}$$

and the shear strains are defined as

$$\boldsymbol{\gamma} = \nabla w + \boldsymbol{\beta}, \tag{12.3}$$

where $\nabla = \begin{bmatrix} \partial/\partial x & \partial/\partial y \end{bmatrix}^T$ is the gradient operator.

The standard Galerkin weak form of the static equilibrium equations for the Reissner–Mindlin plate can now be written as [1]

$$\int_\Omega \delta\boldsymbol{\kappa}^T \mathbf{D}^b \boldsymbol{\kappa}\, \mathrm{d}\Omega + \int_\Omega \delta\boldsymbol{\gamma}^T \mathbf{D}^s \boldsymbol{\gamma}\, \mathrm{d}\Omega = \int_\Omega \delta\mathbf{u}^T \mathbf{b}\, \mathrm{d}\Omega, \tag{12.4}$$

where $\mathbf{b} = \begin{bmatrix} b(x,y) & 0 & 0 \end{bmatrix}^T$ is the distributed load applied on the plate. The matrix $\mathbf{D}^b$ is the material matrix related to the bending deformation, and is given by

$$\mathbf{D}^b = \frac{Et^3}{12\left(1-\nu^2\right)} \begin{bmatrix} 1 & \nu & 0 \\ \nu & 1 & 0 \\ 0 & 0 & (1-\nu)/2 \end{bmatrix}, \tag{12.5}$$

with E being the Young's modulus and t the thickness of the plate. The matrix $\mathbf{D}^s$ is the material matrix related to shear deformation, and has the form of

$$\mathbf{D}^s = kt \begin{bmatrix} \mu & 0 \\ 0 & \mu \end{bmatrix}, \tag{12.6}$$

with the shear modulus μ and the shear correction factor $k = 5/6$.

For the free vibration analysis of the Reissner–Mindlin plates, the standard Galerkin weak form can be derived from the dynamic form of the energy principle [1,2]:

$$\int_\Omega \delta\boldsymbol{\kappa}^T \mathbf{D}^b \boldsymbol{\kappa}\, \mathrm{d}\Omega + \int_\Omega \delta\boldsymbol{\gamma}^T \mathbf{D}^s \boldsymbol{\gamma}\, \mathrm{d}\Omega + \int_\Omega \delta\mathbf{u}^T \rho\, \ddot{\mathbf{u}}\, \mathrm{d}\Omega = 0, \tag{12.7}$$

where ρ is the mass density of the material of the plate.

For buckling analyses, nonlinear strain resulting from the in-plane prebuckling stresses $\hat{\boldsymbol{\sigma}}_0$ must be considered. The standard Galerkin weak form becomes [2,35]

$$\int_\Omega \delta\boldsymbol{\kappa}^T \mathbf{D}^b \boldsymbol{\kappa}\, \mathrm{d}\Omega + \int_\Omega \delta\boldsymbol{\gamma}^T \mathbf{D}^s \boldsymbol{\gamma}\, \mathrm{d}\Omega + t\int_\Omega \nabla^T \delta w\, \hat{\boldsymbol{\sigma}}_0\, \nabla w\, \mathrm{d}\Omega + \frac{t^3}{12}\int_\Omega \begin{bmatrix} \nabla^T \delta\beta_x & \nabla^T \delta\beta_y \end{bmatrix} \begin{bmatrix} \hat{\boldsymbol{\sigma}}_0 & \mathbf{0} \\ \mathbf{0} & \hat{\boldsymbol{\sigma}}_0 \end{bmatrix} \begin{bmatrix} \nabla\beta_x \\ \nabla\beta_y \end{bmatrix} \mathrm{d}\Omega = 0, \tag{12.8}$$

where

$$\hat{\boldsymbol{\sigma}}_0 = \begin{bmatrix} \sigma_x^0 & \sigma_{xy}^0 \\ \sigma_{xy}^0 & \sigma_y^0 \end{bmatrix}. \tag{12.9}$$

Equation 12.8 can be rewritten in a concise form of

$$\int_\Omega \delta\boldsymbol{\kappa}^T \mathbf{D}^b \boldsymbol{\kappa}\, \mathrm{d}\Omega + \int_\Omega \delta\boldsymbol{\gamma}^T \mathbf{D}^s \boldsymbol{\gamma}\, \mathrm{d}\Omega + \int_\Omega \left(\delta\boldsymbol{\varepsilon}^{\mathrm{g}}\right)^T \boldsymbol{\tau}\, \boldsymbol{\varepsilon}^{\mathrm{g}}\, \mathrm{d}\Omega = 0, \tag{12.10}$$

where

$$\boldsymbol{\tau} = \begin{bmatrix} t\hat{\boldsymbol{\sigma}}_0 & \mathbf{0} & \mathbf{0} \\ \mathbf{0} & \dfrac{t^3}{12}\hat{\boldsymbol{\sigma}}_0 & \mathbf{0} \\ \mathbf{0} & \mathbf{0} & \dfrac{t^3}{12}\hat{\boldsymbol{\sigma}}_0 \end{bmatrix} = \begin{bmatrix} t\sigma_x^0 & t\sigma_{xy}^0 & 0 & 0 & 0 & 0 \\ t\sigma_{xy}^0 & t\sigma_y^0 & 0 & 0 & 0 & 0 \\ 0 & 0 & \dfrac{t^3}{12}\sigma_x^0 & \dfrac{t^3}{12}\sigma_{xy}^0 & 0 & 0 \\ 0 & 0 & \dfrac{t^3}{12}\sigma_{xy}^0 & \dfrac{t^3}{12}\sigma_y^0 & 0 & 0 \\ 0 & 0 & 0 & 0 & \dfrac{t^3}{12}\sigma_x^0 & \dfrac{t^3}{12}\sigma_{xy}^0 \\ 0 & 0 & 0 & 0 & \dfrac{t^3}{12}\sigma_{xy}^0 & \dfrac{t^3}{12}\sigma_y^0 \end{bmatrix}, \tag{12.11}$$

and $\boldsymbol{\varepsilon}^{\mathrm{g}}$ is known as the geometrical strains:

$$\boldsymbol{\varepsilon}^{\mathrm{g}} = \begin{bmatrix} \partial w/\partial x & 0 & 0 \\ \partial w/\partial y & 0 & 0 \\ 0 & \partial\beta_x/\partial x & 0 \\ 0 & \partial\beta_x/\partial y & 0 \\ 0 & 0 & \partial\beta_y/\partial x \\ 0 & 0 & \partial\beta_y/\partial y \end{bmatrix}. \tag{12.12}$$

12.3 FEM Formulation for the Reissner–Mindlin Plate

In the FEM, the problem domain Ω for the middle (neutral) plane is meshed with N_e finite elements such that $\Omega = \bigcup_{i=1}^{N_e} \Omega_i^e$ and $\Omega_i^e \cap \Omega_j^e \neq \emptyset, i \neq j$. The finite element solution $\tilde{\mathbf{u}} = \begin{bmatrix} w & \beta_x & \beta_y \end{bmatrix}^T$ of a displacement model for the Reissner–Mindlin plate can then be expressed as

$$\tilde{\mathbf{u}} = \sum_{I=1}^{N_n} \underbrace{\begin{bmatrix} N_I(\mathbf{x}) & 0 & 0 \\ 0 & N_I(\mathbf{x}) & 0 \\ 0 & 0 & N_I(\mathbf{x}) \end{bmatrix}}_{\mathbf{N}_I(\mathbf{x})} \tilde{\mathbf{d}}_I, \tag{12.13}$$

where N_n is the total number of nodes in the discretized model; $N_I(\mathbf{x})$ and $\tilde{\mathbf{d}}_I = \begin{bmatrix} w_I & \beta_{xI} & \beta_{yI} \end{bmatrix}^T$ are, respectively, the shape function and the nodal DOFs for node I.

The curvature, shear strains, and geometrical strains are approximated as

$$\begin{aligned} \tilde{\boldsymbol{\kappa}} &= \sum_I \tilde{\mathbf{B}}_I^b \tilde{\mathbf{d}}_I, \\ \tilde{\boldsymbol{\gamma}}^s &= \sum_I \tilde{\mathbf{B}}_I^s \tilde{\mathbf{d}}_I, \\ \tilde{\boldsymbol{\varepsilon}}^g &= \sum_I \tilde{\mathbf{B}}_I^g \tilde{\mathbf{d}}_I, \end{aligned} \tag{12.14}$$

where

$$\tilde{\mathbf{B}}_I^b = \begin{bmatrix} 0 & \partial N_I/\partial x & 0 \\ 0 & 0 & \partial N_I/\partial y \\ 0 & \partial N_I/\partial y & \partial N_I/\partial x \end{bmatrix}, \tag{12.15a}$$

$$\tilde{\mathbf{B}}_I^s = \begin{bmatrix} \partial N_I/\partial x & N_I & 0 \\ \partial N_I/\partial y & 0 & N_I \end{bmatrix}, \tag{12.15b}$$

$$\tilde{\mathbf{B}}_I^g = \begin{bmatrix} \partial N_I/\partial x & 0 & 0 \\ \partial N_I/\partial y & 0 & 0 \\ 0 & \partial N_I/\partial x & 0 \\ 0 & \partial N_I/\partial y & 0 \\ 0 & 0 & \partial N_I/\partial x \\ 0 & 0 & \partial N_I/\partial y \end{bmatrix}. \tag{12.15c}$$

The discretized system of equations of the Reissner–Mindlin plate using the FEM for static analysis can then be expressed as

$$\tilde{\mathbf{K}}\tilde{\mathbf{d}} = \tilde{\mathbf{f}}, \tag{12.16}$$

where

$$\begin{aligned}\tilde{\mathbf{K}} &= \int_{\Omega} \left(\tilde{\mathbf{B}}^b\right)^T \mathbf{D}^b \tilde{\mathbf{B}}^b \, \mathrm{d}\Omega + \int_{\Omega} \left(\tilde{\mathbf{B}}^s\right)^T \mathbf{D}^s \tilde{\mathbf{B}}^s \, \mathrm{d}\Omega \\ &= \sum_{i=1}^{N_e} \int_{\Omega_i^e} \left(\tilde{\mathbf{B}}^b\right)^T \mathbf{D}^b \tilde{\mathbf{B}}^b \, \mathrm{d}\Omega + \sum_{i=1}^{N_e} \int_{\Omega_i^e} \left(\tilde{\mathbf{B}}^s\right)^T \mathbf{D}^s \tilde{\mathbf{B}}^s \, \mathrm{d}\Omega \end{aligned} \tag{12.17}$$

is the global stiffness matrix, and the (global) load vector becomes

$$\tilde{\mathbf{f}} = \int_{\Omega} \mathbf{N}^T \mathbf{b} \, \mathrm{d}\Omega + \tilde{\mathbf{f}}^b = \sum_{i=1}^{N_e} \int_{\Omega_i^e} \mathbf{N}^T \mathbf{b} \, \mathrm{d}\Omega + \tilde{\mathbf{f}}^b, \tag{12.18}$$

in which $\mathbf{f}^b$ relates to the prescribed boundary loads.

For the free vibration, the force term vanishes, and we shall have

$$(\tilde{\mathbf{K}} - \omega^2 \tilde{\mathbf{M}})\tilde{\mathbf{d}} = \mathbf{0}, \tag{12.19}$$

where ω is the natural frequency of the free vibration, and $\tilde{\mathbf{M}}$ is the global "mass" matrix

$$\tilde{\mathbf{M}} = \int_{\Omega} \mathbf{N}^T \mathbf{m} \mathbf{N}^T \, \mathrm{d}\Omega = \sum_{i=1}^{N_e} \int_{\Omega_i^e} \mathbf{N}^T \mathbf{m} \mathbf{N}^T \, \mathrm{d}\Omega \quad \text{with} \quad \mathbf{m} = \rho \begin{bmatrix} t & 0 & 0 \\ 0 & \dfrac{t^3}{12} & 0 \\ 0 & 0 & \dfrac{t^3}{12} \end{bmatrix} \tag{12.20}$$

For buckling analyses, we have

$$(\tilde{\mathbf{K}} - \lambda_{\mathrm{cr}} \tilde{\mathbf{G}})\tilde{\mathbf{d}} = \mathbf{0}, \tag{12.21}$$

where λ_{cr} is the so-called critical buckling load, and

$$\tilde{\mathbf{G}} = \int_{\Omega} \left(\tilde{\mathbf{B}}^{\mathrm{g}}\right)^T \boldsymbol{\tau} \, \tilde{\mathbf{B}}^{\mathrm{g}} \, \mathrm{d}\Omega \tag{12.22}$$

is the geometrical stiffness matrix.

12.4 ES-FEM-DSG3 for the Reissner–Mindlin Plate

This section formulates an ES-FEM with the stabilized DSG technique using triangular element (ES-FEM-DSG3) for the Reissner–Mindlin plates [36]. The formulation consists of the following ingredients:

1. The ES-FEM [37] using triangular elements for 2D solids
2. The shear-locking-free triangular finite element (DSG3) for the Reissner–Mindlin plate proposed by Bletzinger et al. [33]
3. A stabilization technique proposed by Lyly et al. [34] to further improve the stability and accuracy of the original DSG method.

With these key ingredients in place working nicely together, we can expect our ES-FEM-DSG3 model to be stable, accurate, and work well for both thin and thick plates. The following provides details of these technical ingredients.

12.4.1 The DSG3 Formulation

Using a mesh of triangular elements, the approximation $\tilde{\mathbf{u}} = \begin{bmatrix} \tilde{w} & \tilde{\beta}_x & \tilde{\beta}_y \end{bmatrix}^T$ for a three-node triangular element Ω_i^e shown in Figure 12.2 for the Reissner–Mindlin plate can be written, at the element level, as

$$\tilde{\mathbf{u}} = \sum_{I=1}^{3} \begin{bmatrix} N_I(\mathbf{x}) & 0 & 0 \\ 0 & N_I(\mathbf{x}) & 0 \\ 0 & 0 & N_I(\mathbf{x}) \end{bmatrix} \tilde{\mathbf{d}}_I^e, \tag{12.23}$$

where $\tilde{\mathbf{d}}_I^e = \begin{bmatrix} \tilde{w}_I & \tilde{\beta}_{xI} & \tilde{\beta}_{yI} \end{bmatrix}^T$ is the "displacement" vector of the nodal DOFs of $\tilde{\mathbf{u}}$ associated with node I, and $N_I(\mathbf{x})$ is linear shape function

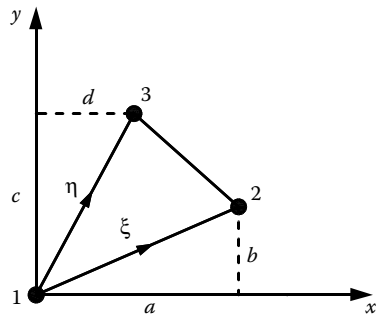

FIGURE 12.2 Three-node triangular plate element and local coordinates.

defined, in natural coordinates (see Figure 3.9b), by

$$N_1 = 1 - \xi - \eta, \quad N_2 = \xi, \quad N_3 = \eta. \tag{12.24}$$

The curvatures of the deflection in the element are then obtained by

$$\tilde{\boldsymbol{\kappa}} = \tilde{\mathbf{B}}^b \tilde{\mathbf{d}}^e, \tag{12.25}$$

where $\tilde{\mathbf{d}}^e$ is the nodal displacement vector of the element and $\tilde{\mathbf{B}}^b$ contains the derivatives of the shape functions that are constants:

$$\tilde{\mathbf{B}}^b = \frac{1}{2A_i^e}\begin{bmatrix} 0 & b-c & 0 & 0 & c & 0 & 0 & -b & 0 \\ 0 & 0 & d-a & 0 & 0 & -d & 0 & 0 & a \\ 0 & d-a & b-c & 0 & -d & c & 0 & a & -b \end{bmatrix}, \tag{12.26}$$

with $a = x_2 - x_1$, $b = y_2 - y_1$, $c = y_3 - y_1$, $d = x_3 - x_1$, and A_i^e is the area of the triangular element.

The geometrical strains are written as

$$\tilde{\boldsymbol{\varepsilon}}^{\mathrm{g}} = \tilde{\mathbf{B}}^{\mathrm{g}} \tilde{\mathbf{d}}^e, \tag{12.27}$$

where

$$\tilde{\mathbf{B}}^{\mathrm{g}} = \frac{1}{2A_i^e}\begin{bmatrix} b-c & 0 & 0 & c & 0 & 0 & -b & 0 & 0 \\ d-a & 0 & 0 & -d & 0 & 0 & a & 0 & 0 \\ 0 & b-c & 0 & 0 & c & 0 & 0 & -b & 0 \\ 0 & d-a & 0 & 0 & -d & 0 & 0 & a & 0 \\ 0 & 0 & b-c & 0 & 0 & c & 0 & 0 & -b \\ 0 & 0 & d-a & 0 & 0 & -d & 0 & 0 & a \end{bmatrix}. \tag{12.28}$$

As reported in many previous publications on the Reissner–Mindlin elements, the shear locking often occurs when the thickness plate becomes small, where the pure bending dominates the plate deformation. This is because, based on the Reissner–Mindlin theory (using Equation 12.15b to evaluate the shear strains), the transverse shear strains do not vanish under the pure bending conditions. Such a conflict of the bending and shearing strain fields under thin plate situations leads to the shear locking problem. In order to overcome this conflict, Bletzinger et al. [33] have proposed the DSG method to alter the shear strain field. The altered shear strains are in the form of

$$\tilde{\boldsymbol{\gamma}} = \tilde{\mathbf{B}}^s \tilde{\mathbf{d}}^e, \tag{12.29}$$

where

$$\tilde{\mathbf{B}}^s = \frac{1}{2A_i^e}\begin{bmatrix} b-c & A_i^e & 0 & c & \frac{ac}{2} & \frac{bc}{2} & -b & -\frac{bd}{2} & -\frac{bc}{2} \\ d-a & 0 & A_i^e & -d & -\frac{ad}{2} & -\frac{bd}{2} & a & \frac{ad}{2} & \frac{ac}{2} \end{bmatrix}. \tag{12.30}$$

Equation 12.30 is now used in place of Equation 12.15_{b} for evaluating the shear strains. Substituting Equations 12.26 and 12.30 into Equation 12.17, the global stiffness matrix now becomes

$$\tilde{\mathbf{K}}^{\mathrm{DSG3}} = \sum_{i=1}^{N_e} \tilde{\mathbf{K}}_i^{e\mathrm{DSG3}}, \tag{12.31}$$

where the element stiffness matrix $\tilde{\mathbf{K}}_i^{e\mathrm{DSG3}}$ for the DSG3 element becomes

$$\begin{aligned} \tilde{\mathbf{K}}_i^{e\mathrm{DSG3}} &= \int_{\Omega_i^e} \left(\tilde{\mathbf{B}}^b\right)^T \mathbf{D}^b \tilde{\mathbf{B}}^b \,\mathrm{d}\Omega + \int_{\Omega_i^e} \left(\tilde{\mathbf{B}}^s\right)^T \mathbf{D}^s \tilde{\mathbf{B}}^s \,\mathrm{d}\Omega \\ &= \left(\tilde{\mathbf{B}}^b\right)^T \mathbf{D}^b \tilde{\mathbf{B}}^b A_i^e + \left(\tilde{\mathbf{B}}^s\right)^T \mathbf{D}^s \tilde{\mathbf{B}}^s A_i^e. \end{aligned} \tag{12.32}$$

Substituting Equation 12.28 into Equation 12.22, the global geometrical stiffness matrix $\tilde{\mathbf{G}}^{\mathrm{DSG3}}$ becomes

$$\tilde{\mathbf{G}}^{\mathrm{DSG3}} = \sum_{i=1}^{N_e} \tilde{\mathbf{G}}_i^{e\mathrm{DSG3}}, \tag{12.33}$$

where the element geometrical stiffness matrix $\tilde{\mathbf{G}}_i^{e\mathrm{DSG3}}$ is given as

$$\tilde{\mathbf{G}}_i^{e\mathrm{DSG3}} = \int_{\Omega_i^e} \left(\tilde{\mathbf{B}}^{\mathrm{g}}\right)^T \boldsymbol{\tau} \tilde{\mathbf{B}}^{\mathrm{g}} \,\mathrm{d}\Omega = \left(\tilde{\mathbf{B}}^{\mathrm{g}}\right)^T \boldsymbol{\tau} \tilde{\mathbf{B}}^{\mathrm{g}} A_i^e. \tag{12.34}$$

12.4.2 Improved Stability

It was suggested [34] that a stabilization term needs to be added to the original DSG3 element to further improve the accuracy of approximate

solutions and to stabilize shear force oscillations. Such a modification is achieved by simply replacing $\mathbf{D}^s$ in Equation 12.32 by $\hat{\mathbf{D}}^s$ as follows:

$$\begin{aligned}\tilde{\mathbf{K}}_i^{e\text{DSG3}} &= \int_{\Omega_i^e} \left(\tilde{\mathbf{B}}^b\right)^T \mathbf{D}^b \tilde{\mathbf{B}}^b \, \mathrm{d}\Omega + \int_{\Omega_i^e} \left(\tilde{\mathbf{B}}^s\right)^T \hat{\mathbf{D}}^s \tilde{\mathbf{B}}^s \, \mathrm{d}\Omega \\ &= \left(\tilde{\mathbf{B}}^b\right)^T \mathbf{D}^b \tilde{\mathbf{B}}^b A_i^e + \left(\tilde{\mathbf{B}}^s\right)^T \hat{\mathbf{D}}^s \tilde{\mathbf{B}}^s A_i^e, \end{aligned} \tag{12.35}$$

where

$$\hat{\mathbf{D}}^s = \frac{kt^3}{t^2 + \alpha h_e^2} \begin{bmatrix} 1 & 0 \\ 0 & 1 \end{bmatrix}, \tag{12.36}$$

in which h_e is the length of the longest edges of the element and α is a stabilization parameter that is a prespecified positive constant. In this chapter, it is fixed at 0.05 for static problems and 0.1 for dynamics problems as suggested in Ref. [34]. More details of the stabilization of the original DSG3 element can be found in Ref. [38].

12.4.3 Smoothing Operations for the Reissner–Mindlin Plates

In this section, the ES-FEM [37] is now formulated for the Reissner–Mindlin plates with the stabilized DSG technique (DSG3) [34,38]. The formulated ES-FEM-DSG3 will be stable and works well for both thin and thick plates using only triangular elements.

Using the edge-based smoothing operation as in the ES-FEM, we obtain the smoothed curvature, shear strain, and geometrical strain over the smoothing domain Ω_k^s associated with the kth edge:

$$\begin{aligned} \bar{\boldsymbol{\kappa}}_k &= \frac{1}{A_k^s} \int_{\Omega_k^s} \tilde{\boldsymbol{\kappa}}(\mathbf{x}) \, \mathrm{d}\Omega, \\ \bar{\boldsymbol{\gamma}}_k &= \frac{1}{A_k^s} \int_{\Omega_k^s} \tilde{\boldsymbol{\gamma}}(\mathbf{x}) \, \mathrm{d}\Omega, \\ \bar{\boldsymbol{\varepsilon}}_k^{\mathrm{g}} &= \frac{1}{A_k^s} \int_{\Omega_k^s} \tilde{\boldsymbol{\varepsilon}}^{\mathrm{g}}(\mathbf{x}) \, \mathrm{d}\Omega, \end{aligned} \tag{12.37}$$

where A_k^s is the area of the smoothing domain Ω_k^s and is computed by Equation 7.4.

Substituting Equations 12.25, 12.29, and 12.27 into Equation 12.37, the smoothed strains for the smoothing domains of edge k can be expressed in the following forms:

$$\begin{aligned}
\overline{\boldsymbol{\kappa}}_k &= \sum_{I=1}^{n_k^e} \overline{\mathbf{B}}_I^b(\mathbf{x}_k)\overline{\mathbf{d}}_I, \\
\overline{\boldsymbol{\gamma}}_k &= \sum_{I=1}^{n_k^e} \overline{\mathbf{B}}_I^s(\mathbf{x}_k)\overline{\mathbf{d}}_I, \\
\overline{\boldsymbol{\varepsilon}}_k^{\mathrm{g}} &= \sum_{I=1}^{n_k^e} \overline{\mathbf{B}}_I^{\mathrm{g}}(\mathbf{x}_k)\overline{\mathbf{d}}_I,
\end{aligned} \tag{12.38}$$

where n_k^e is the number of elements attached to edge k as detailed in Section 7.3.1; $\overline{\mathbf{B}}_I^b(\mathbf{x}_k)$, $\overline{\mathbf{B}}_I^s(\mathbf{x}_k)$, and $\overline{\mathbf{B}}_I^{\mathrm{g}}(\mathbf{x}_k)$ are the smoothing gradient matrices corresponding to the smoothing domain Ω_k^s and are given, respectively, by

$$\begin{aligned}
\overline{\mathbf{B}}_I^b(\mathbf{x}_k) &= \frac{1}{A_k^s}\sum_{j=1}^{n_k^e}\frac{1}{3}A_j^e\tilde{\mathbf{B}}_j^b, \\
\overline{\mathbf{B}}_I^s(\mathbf{x}_k) &= \frac{1}{A_k^s}\sum_{j=1}^{n_k^e}\frac{1}{3}A_j^e\tilde{\mathbf{B}}_j^s, \\
\overline{\mathbf{B}}_I^{\mathrm{g}}(\mathbf{x}_k) &= \frac{1}{A_k^s}\sum_{j=1}^{n_k^e}\frac{1}{3}A_j^e\tilde{\mathbf{B}}_j^{\mathrm{g}},
\end{aligned} \tag{12.39}$$

where the compatible gradient matrices $\tilde{\mathbf{B}}_j^b$ (of 3×3 dimensions), $\tilde{\mathbf{B}}_j^s$ (of 2×3 dimensions), and $\tilde{\mathbf{B}}_j^{\mathrm{g}}$ (of 6×3 dimensions) are obtained using matrices given in Equations 12.26, 12.30, and 12.28, respectively.

12.4.4 Smoothed Galerkin Weak Forms for Reissner–Mindlin Plates

For the free vibration analysis of Reissner–Mindlin plates, the smoothed Galerkin weak form can be written as [2]

$$\sum_{k=1}^{N_s} A_k^s \delta\overline{\boldsymbol{\kappa}}^T \mathbf{D}^b \overline{\boldsymbol{\kappa}} + \sum_{k=1}^{N_s} A_k^s \delta\overline{\boldsymbol{\gamma}}^T \mathbf{D}^s \overline{\boldsymbol{\gamma}} + \int_\Omega \delta\mathbf{u}^T \rho\ddot{\mathbf{u}}\,\mathrm{d}\Omega = 0, \tag{12.40}$$

where N_s is the number of smoothing domains. In our ES-FEM, it is the number of edges in the element mesh $N_s = N_{\text{eg}}$. For static problems, we simply drop the dynamic term in the foregoing equation.

For buckling analyses, the smoothed Galerkin weak form becomes

$$\sum_{k=1}^{N_s} A_k^s \delta\overline{\boldsymbol{\kappa}}^T \mathbf{D}^b \overline{\boldsymbol{\kappa}} + \sum_{k=1}^{N_s} A_k^s \delta\overline{\boldsymbol{\gamma}}^T \mathbf{D}^s \overline{\boldsymbol{\gamma}} + \sum_{k=1}^{N_s} A_k^s \left(\delta\overline{\boldsymbol{\varepsilon}}^{\text{g}}\right)^T \boldsymbol{\tau}\overline{\boldsymbol{\varepsilon}}^{\text{g}} = 0. \tag{12.41}$$

Note that the foregoing smoothed Galerkin weak form is applicable to formulate other S-FEM models using corresponding smoothing domains properly constructed.

12.4.5 Discretized System of Equations for ES-FEM-DSG3

The discretized system of equations of the ES-FEM-DSG3 method for dynamic problems can be obtained using Equation 12.40:

$$\overline{\mathbf{K}}\,\overline{\mathbf{d}} + \tilde{\mathbf{M}}\ddot{\overline{\mathbf{d}}} = \tilde{\mathbf{f}}. \tag{12.42}$$

We note that the smoothed operations change only the stiffness matrix. For static problems, we simply remove the dynamic term. For the free vibration, the force term vanishes, and we thus set the external forces to zero, leading to

$$\left(\overline{\mathbf{K}} - \omega^2\tilde{\mathbf{M}}\right)\overline{\mathbf{d}} = \mathbf{0}. \tag{12.43}$$

For the buckling analysis, we use Equation 12.41, which gives

$$\left(\overline{\mathbf{K}} - \lambda_{\text{cr}}\overline{\mathbf{G}}\right)\overline{\mathbf{d}} = \mathbf{0}. \tag{12.44}$$

The global stiffness and geometrical stiffness matrices of the ES-FEM-DSG3 method are assembled based on edge-based smoothed domains using

$$\overline{\mathbf{K}} = \sum_{k=1}^{N_{\text{eg}}} \overline{\mathbf{K}}_k^s, \tag{12.45}$$

$$\overline{\mathbf{G}} = \sum_{k=1}^{N_{\text{eg}}} \overline{\mathbf{G}}_k^s, \tag{12.46}$$

where the stiffness matrix $\overline{\mathbf{K}}_k^s$ and the geometrical stiffness matrix $\overline{\mathbf{G}}_k^s$ associated with the edge-based smoothing domain Ω_k^s are given by

$$\overline{\mathbf{K}}_k^s = \left(\overline{\mathbf{B}}^b\right)^T \mathbf{D}^b \overline{\mathbf{B}}^b A_k^s + \left(\overline{\mathbf{B}}^s\right)^T \hat{\mathbf{D}}^s \overline{\mathbf{B}}^s A_k^s, \tag{12.47}$$

$$\overline{\mathbf{G}}_k^s = \overline{\mathbf{B}}^{gT} \boldsymbol{\tau} \overline{\mathbf{B}}^g A_k^s. \tag{12.48}$$

It is seen from Equations 12.47 and 12.48 that the stiffness matrices in our ES-FEM-DSG3 method require no numerical integration, but a simple summation over all the edge-based smoothing domains. Note that the rank of the ES-FEM-DSG3 model is similar to that of the DSG3 model. This is because of the similarity in ranks of FEM-T3 and ES-FEM-T3, as examined in Chapter 7. Therefore, the stability of an ES-FEM-DSG3 model is ensured.

12.5 Numerical Examples: Patch Test

Based on the formulation presented above, an ES-FEM-DSG3 code has been developed. A series of tests are now conducted to examine the method, starting from the usual patch test. The patch test for plate problems was introduced to examine the convergence of finite elements, and it is used here to examine our ES-FEM-DSG3 models. A rectangular patch shown in Figure 12.3 is used, and it is meshed with four triangular elements with one arbitrarily located interior node (the fifth node). The deflection on the patch boundary is assumed to be a second-order polynomial:

$$w = \left(1 + x + 2y + x^2 + xy + y^2\right)/2. \tag{12.49}$$

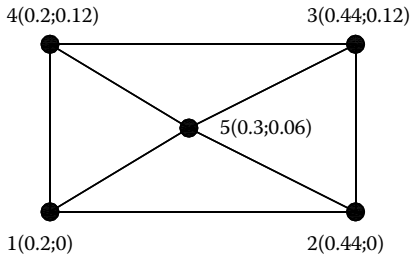

FIGURE 12.3 Rectangular plate patch used in the patch test. The patch is meshed with four elements with an arbitrarily located interior node.

TABLE 12.1

Patch Test Results for Fifth Node in Figure 12.3 Using ES-FEM-DSG3

Methods	w_5	β_{x5}	β_{y5}	m_{x5}	m_{y5}	m_{xy5}
DSG3	0.6422	1.1300	−0.6400	−0.0111	−0.0111	−0.0033
ES-FEM-DSG3	0.6422	1.1300	−0.6400	−0.0111	−0.0111	−0.0033
Exact	0.6422	1.1300	−0.6400	−0.0111	−0.0111	−0.0033

The ES-FEM-DSG3 code is then used to compute "displacement" (deflection and rotation) and "stress" (moments) fields. The patch test results for the fifth node are listed in Table 12.1. It is shown that the ES-FEM-DSG3 model produces the correct fields within machine precision for the arbitrarily located interior node, implying that the ES-FEM-DSG3 passes the patch test successfully.

12.6 Numerical Examples: Static Analysis

Example 12.6.1: Square Plates

We now use the ES-FEM-DSG3 code to solve the simple static problem of a square plate. Figure 12.4a and b describes the models of the square plate with length a and thickness t. The plate is subjected to a uniform load of $b(x, y) = 1$, and is given for both clamped and simply supported boundary conditions. The material parameters used are Young's modulus $E = 1.092 \times 10^6$ and Poisson's ratio $\nu = 0.3$. Due to its symmetry, only the upper right quadrant of the square plate is modeled. Symmetric conditions are imposed on the left and bottom edges of the quarter model. Uniform meshes of $N \times N$ four-node quadrilateral plate elements shown in Figure 12.4c and $2 \times N \times N$ three-node triangular plate elements shown in Figure 12.4d, with $N = 2, 4, 8, 16$, and 32, are used in the computation.

For the clamped plate, the convergence of the normalized deflection and the normalized moment at the center point of the plate is computed, and the results are plotted against the mesh density in terms of number of elements per edge N, as shown in Figure 12.5. From the deflection results shown in Figure 12.5a, it is seen that the ES-FEM-DSG3 model achieves the higher accuracy compared to those using FEM-DSG3 (short for DSG3) and MIN3 [31] elements. For very coarse meshes, the ES-FEM-DSG3 results are less accurate than that of the four-node MITC4 plate element [23]. However, the ES-FEM-DSG3 results become more accurate than that of the MITC4 element when the mesh gets finer, as shown in Figure 12.5a. For the moment results shown in Figure 12.5b, the ES-FEM-DSG3 model achieves higher accuracy compared to all these models for all the meshes of different densities.

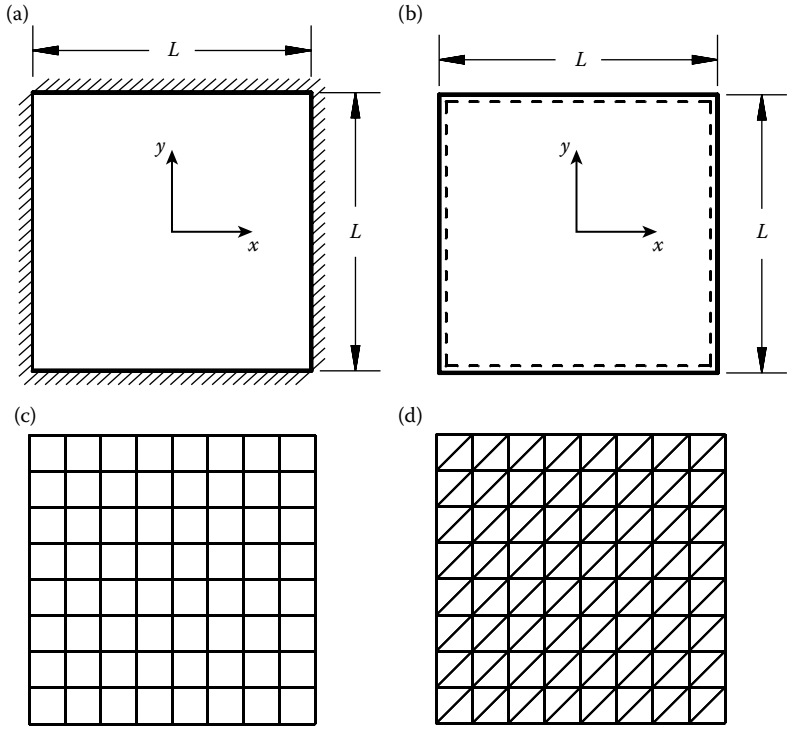

FIGURE 12.4 Two square plate models and the representative meshes: (a) clamped plate; (b) simply supported plate; (c) regular mesh using four-node quadrilateral plate elements; and (d) regular mesh using three-node triangular elements.

Note that the plate used in Figure 12.5 is very thin with an aspect ratio of $t/L = 0.001$. The results obtained using our ES-FEM-DSG3 model converge to the exact solution when the meshes used become finer, as shown in Figure 12.5a and b. This confirms that our ES-FEM-DSG3 method is free of shear locking.

In terms of the relative strain energy error for the same thin plate at $t/L = 0.001$, ES-FEM-DSG3 performs the best among all these models compared as shown in Figure 12.6, where the relative strain energy error is defined as

$$e_E = \frac{|E_{\text{num}} - E_{\text{exact}}|}{E_{\text{exact}}} \times 100\%, \tag{12.50}$$

with the strain energies defined by

$$E_{\text{num}} = \frac{1}{2}\breve{\mathbf{d}}_{\text{num}}^T \breve{\mathbf{K}}_{\text{num}} \breve{\mathbf{d}}_{\text{num}} \quad \text{and} \quad E_{\text{exact}} = \frac{1}{2}\int_\Omega \delta\boldsymbol{\kappa}^T \mathbf{D}^b \boldsymbol{\kappa}\, \mathrm{d}\Omega + \frac{1}{2}\int_\Omega \delta\boldsymbol{\gamma}^T \mathbf{D}^s \boldsymbol{\gamma}\, \mathrm{d}\Omega, \tag{12.51}$$

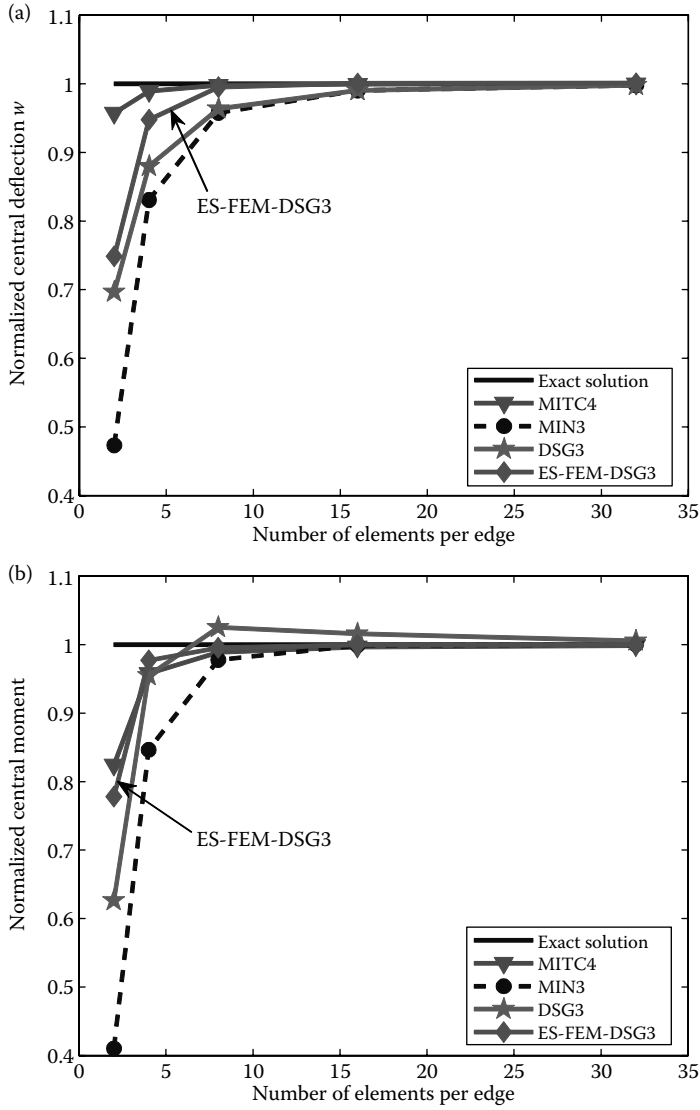

FIGURE 12.5 Results obtained using the ES-FEM-DSG3 method in comparison with other methods for the clamped square plate. The plate is very thin with $t/L = 0.001$: (a) central deflection and (b) central moment.

in which $\breve{\mathbf{d}}$ is the vector of the nodal "displacement" vector computed using any numerical model; $\breve{\mathbf{K}}_{\text{num}}$ is the system stiffness matrix of the corresponding numerical model; $\boldsymbol{\kappa}$ and $\boldsymbol{\gamma}$ are the curvature and shear strain of the exact solution of the same problem.

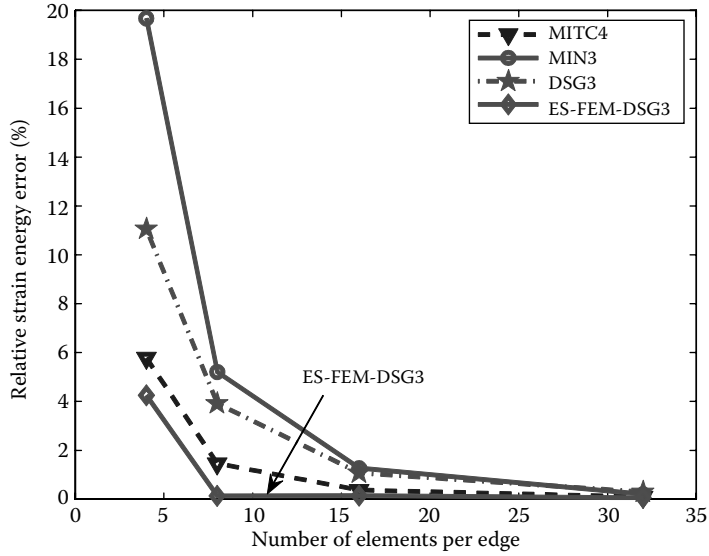

FIGURE 12.6 Relative error in strain energy obtained using the ES-FEM-DSG3 method in comparison with other methods for the clamped square plate.

For the simply supported plate, Figure 12.7 plots the convergence of the normalized deflection and the normalized moment at the center of the plate. In this case, we chose a thick plate with $t/L = 0.01$. It is seen that the ES-FEM-DSG3 method is still superior to the DSG3 and MIN3 elements. In terms of the deflection solution, the MITC4 element performed better than the ES-FEM-DSG3 method. In terms of the moment solution, the ES-FEM-DSG3 method is slightly more accurate than the next performer of MITC4 elements and, hence, is the best among all these methods.

The relative strain energy error for the same thick plate with $t/L = 0.01$ is given in Figure 12.8. It is seen that the ES-FEM-DSG3 method performed the best. It is less accurate than that obtained using the MITC4 elements for coarse mesh but more accurate for finer meshes. The ES-FEM-DSG3 method performs much better than the other two models that use triangular elements.

Example 12.6.2: Skew Plate Subjected to a Uniform Load

Let us now consider a rhombic plate studied by Morley and provide a very accurate reference solution for comparison [39]. The plate is subjected to a uniform load $b(x, y) = 1$, and the dimensions of the plate and boundary conditions are specified in Figure 12.9. The geometry and material parameters used are length $L = 100$, thickness $t = 0.1$, Young's modulus $E = 10.92$, and Poisson's ratio $\nu = 0.3$. The aspect ratio of this plate is $t/L = 0.001$ and, hence, is a very thin plate under practical engineering considerations.

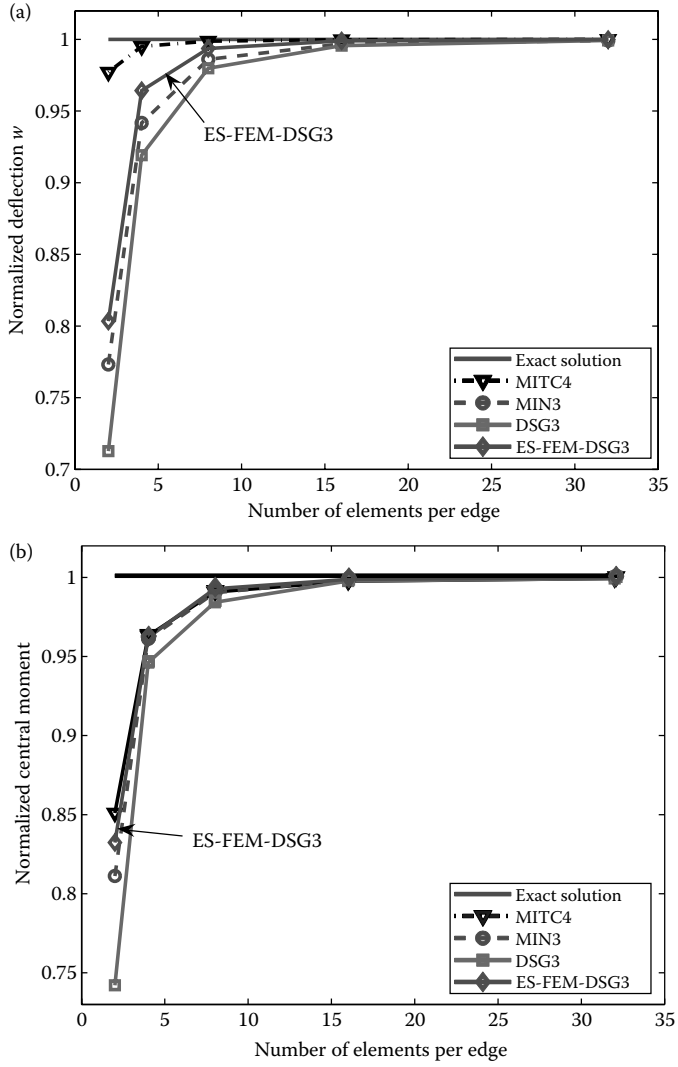

FIGURE 12.7 Results obtained using the ES-FEM-DSG3 method in comparison with other methods for the simply supported thick square plate ($t/L = 0.01$): (a) central deflection and (b) central moment.

The convergence of the solution in the deflection and principal moments at the central point is plotted in Figure 12.10, in which the principal moments are obtained by solving

$$|\mathbf{m} - \lambda \mathbf{I}| = \begin{vmatrix} m_{11} - \lambda & m_{12} \\ m_{12} & m_{22} - \lambda \end{vmatrix} = (m_{11} - \lambda)(m_{22} - \lambda) - m_{12}^2 = 0$$

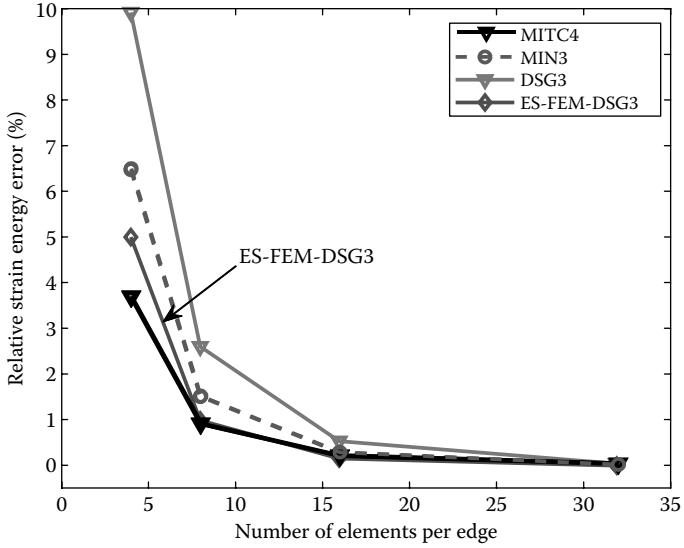

FIGURE 12.8 Relative error in strain energy solution of the ES-FEM-DSG3 method in comparison with other methods for the simply supported thick square plate ($t/L = 0.01$).

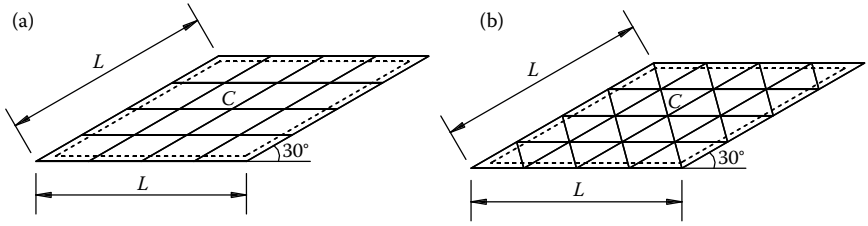

FIGURE 12.9 A simply supported rhombic plate: (a) mesh with four-node quadrilateral plate elements and (b) mesh with three-node triangular plate elements.

or

$$\lambda^2 - (m_{11} + m_{22})\lambda + m_{11}m_{22} - m_{12}^2 = 0, \tag{12.52}$$

which gives the maximum and minimum principle moments:

$$m_{\max} = \lambda_1 = \frac{(m_{11} + m_{22}) + \Delta}{2}, \quad m_{\min} = \lambda_2 = \frac{(m_{11} + m_{22}) - \Delta}{2}, \tag{12.53}$$

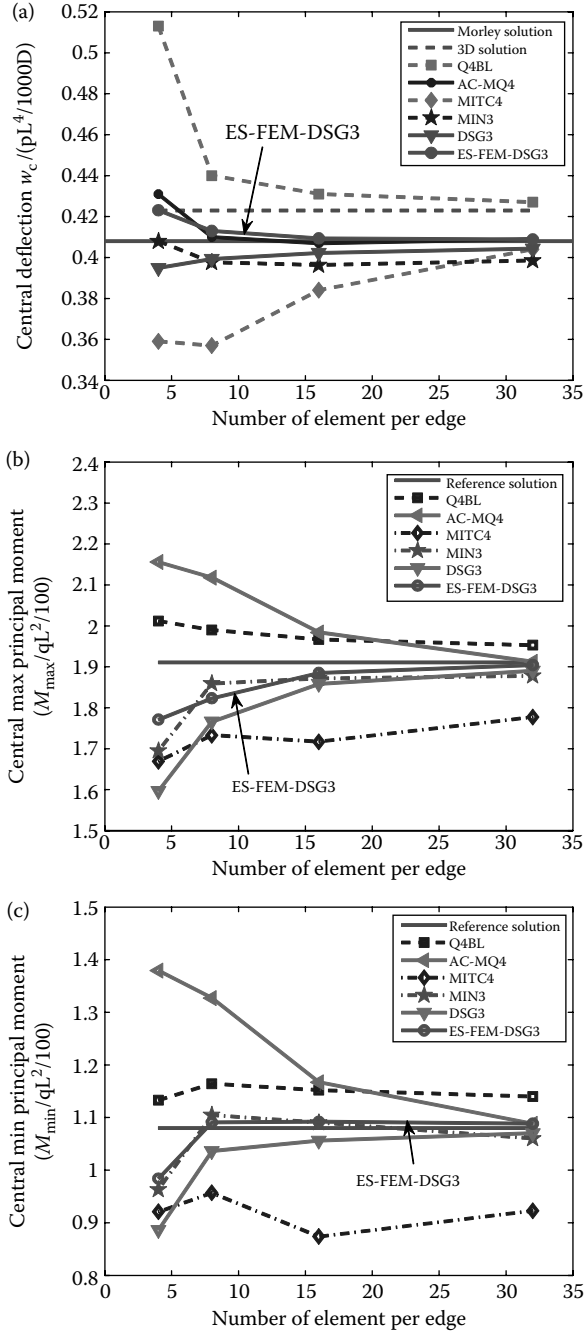

FIGURE 12.10 Results of the ES-FEM-DSG3 method in comparison with other methods for the rhombic plate: (a) central deflection; (b) central maximum principal moment; and (c) central minimum principal moment.

where m_{11}, m_{22}, and m_{12} are moments obtained in the Descartes coordinate system and

$$\Delta = (m_{11} + m_{22})^2 - 4(m_{11}m_{22} - m_{12}^2). \tag{12.54}$$

It is seen again that the ES-FEM-DSG3 method shows, in general, superior performance compared to all the models found in Ref. [40], including those using quadrilateral elements such as the MITC4 and AC-MQ4. Figure 12.10a shows the results for the central deflection; the ES-FEM-DSG3 method gives the best solution together with the AC-MQ4 model using quadrilateral elements. Even the competitor MITC4 found in the previous square plate example is now much less accurate than the ES-FEM-DSG3 method. This is because the elements used in this rhombic plate are quite skewed, and quadrilateral elements are usually quite sensitive to mesh distortion. Although the AC-MQ4 becomes now the competitor of the ES-FEM-DSG3 method in terms of the deflection, when we look at the solution in moments, the ES-FEM-DSG3 method will give a much more accurate solution, as shown in Figure 12.10b and c. This example has clearly shown that the ES-FEM-DSG3 method performed the best and is far better that all the other models in overall performance.

Figure 12.10 also shows clearly the edge-based smoothing effect that can be observed from the difference of the two curves by the ES-FEM-DSG3 method and the DSG3 method.

12.7 Numerical Examples: Free Vibration of Plates

In this section, we investigate the accuracy and efficiency of the ES-FEM-DSG3 method used for computing the natural frequencies of plates. The plate may have a combined boundary condition (BC) with free (F), simply (S) supported, or clamped (C) edges. For convenience in discussion, we use the usual notation convention for these boundary conditions. The symbol, CFSF, for instance, represents a boundary condition for a plate whose four edges are clamped, free, simply supported and free. To examine the accuracy of the solution precisely, the results of the ES-FEM-DSG3 method are then compared to analytical solutions, together with some other numerical results that are available in the literature.

Example 12.7.1: Square Plates

We consider square plates of length L and thickness t shown in Figure 12.4. The material parameters are Young's modulus $E = 2.0 \times 10^{11}$, Poisson's ratio $\nu = 0.3$, and the density mass $\rho = 8000$. The square plate is modeled with uniform meshes of 4, 8, 16, and 22 elements per side. The solutions of natural frequencies are all nondimensionalized by $\varpi = \left(\omega^2 \rho L^4 t/D\right)^{1/4}$, where $D = Et^3/\left(12\left(1-\nu^2\right)\right)$ is the flexural rigidity of the plate.

TABLE 12.2

A Nondimensional Frequency Parameter ϖ of a Square Plate with SSSS Supports

		Mode Number					
t/L	**Methods**	**1**	**2**	**3**	**4**	**5**	**6**
0.005	DSG3	5.5626	8.8148	11.8281	13.4126	18.1948	19.2897
		4.7327	7.4926	8.2237	10.2755	11.6968	12.4915
		4.5131	7.1502	7.3169	9.3628	10.3772	10.4461
		4.4781	7.0905	7.1718	9.1455	10.1643	10.1814
	ES-FEM-DSG3	4.9168	8.1996	9.4593	11.5035	14.2016	15.0164
		4.5376	7.2981	7.4659	9.6486	10.8937	11.0280
		4.4641	7.0870	7.1193	9.0582	10.1444	10.1489
		4.4537	7.0565	7.0729	8.9731	10.0410	10.0422
	Exact [41]	4.443	7.025	7.025	8.886	9.935	9.935
0.1	DSG3	4.9970	8.1490	9.4311	11.3540	14.1290	14.9353
		4.4891	7.0697	7.2530	9.1263	10.2195	10.3361
		4.3943	6.8227	6.8587	8.5447	9.4557	9.4616
		4.3809	6.7854	6.8037	8.4543	9.3441	9.3457
	ES-FEM-DSG3	4.7376	7.6580	8.4524	10.1882	12.1227	12.7533
		4.4433	6.9495	7.0727	8.8487	9.8575	9.9221
		4.3846	6.7922	6.8196	8.4744	9.3666	9.3698
		4.3759	6.7692	6.7834	8.4173	9.2968	9.2976
	Exact [41]	4.37	6.74	6.74	8.35	9.22	9.22

The first problem studied is thin ($t/L = 0.005$) and thick ($t/L = 0.1$) plates with SSSS supports. Table 12.2 lists the six lowest modes obtained using meshes of 4×4, 8×8, 16×16, and 22×22 rectangular elements as shown in Figure 12.4c, and meshes of $2 \times 4 \times 4$, $2 \times 8 \times 8$, $2 \times 16 \times 16$, and $2 \times 22 \times 22$ triangular elements as shown in Figure 12.4d. It is observed that the results obtained using the ES-FEM-DSG3 method agree well with the analytical results [41] and are more accurate than those of the DSG3 element for both thin and thick plates.

The second problem is a CCCC square plate shown in Figure 12.4a. The meshes used are the same as those for the SSSS plate case. Table 12.3 shows the six lowest modes of the CCCC plate. It is found again that the results of the ES-FEM-DSG3 are better than those of the DSG3.

The convergence of computed frequencies ($\varpi^h/\varpi_{\text{exact}}$) of SSSS and CCCC plates is plotted in Figure 12.11. It is seen that the results obtained using the ES-FEM-DSG3 methods are much more accurate and converge much faster than those obtained using DSG3. The edge-based smoothing effect is clearly observable from the difference between the two curves by the ES-FEM-DSG3 method and the DSG3 method.

The eight shape modes of free vibration of the CCCC square plate using the ES-FEM-DSG3 method are plotted in Figure 12.12. We also note that no spurious energy modes are found for the ES-FEM-DSG3 method.

TABLE 12.3

A Nondimensional Frequency Parameter ϖ of a CCCC Square Plate

		Mode Sequence Number					
t/L	**Methods**	**1**	**2**	**3**	**4**	**5**	**6**
0.005	DSG3	8.4197	12.7720	14.9652	17.2579	21.3890	21.7600
		6.7161	9.7867	10.5673	12.9981	14.5306	15.3143
		6.1786	8.8759	9.0680	11.2452	12.2182	12.2992
		6.0889	8.7239	8.8202	10.8567	11.8519	11.8845
	ES-FEM-DSG3	6.9741	10.1934	11.4756	13.0548	15.4035	15.9360
		6.1982	9.0117	9.2894	11.5616	12.7950	13.0357
		6.0355	8.6535	8.7081	10.6584	11.7430	11.7720
		6.0158	8.6075	8.6353	10.5252	11.6032	11.6293
	Exact [55]	5.999	8.568	8.568	10.407	11.472	11.498
0.1	DSG3	6.8748	9.8938	11.0847	12.6362	15.1032	15.6402
		5.9547	8.3618	8.6293	10.2985	11.3415	11.5397
		5.7616	7.9935	8.0525	9.5772	10.4153	10.4697
		5.7337	7.9381	7.9686	9.4589	10.2758	10.3246
	ES-FEM-DSG3	6.2662	8.7952	9.6625	10.9112	12.6101	13.1360
		5.8068	8.0861	8.2701	9.8397	10.7600	10.8960
		5.7250	7.9211	7.9627	9.4499	10.2631	10.3126
		5.7141	7.8990	7.9206	9.3896	10.1935	10.2411
	Exact [55]	5.71	7.88	7.88	9.33	10.13	10.18

We compute further five sets of various boundary conditions for the square plate: SSSF, SFSF, CCCF, CFCF, and CFSF. In these cases, regular meshes using 20×20 rectangular elements and $2 \times 20 \times 20$ triangular elements are used, and the first four lowest frequencies are computed and listed in Table 12.4. The results obtained using the ES-FEM-DSG3 are mostly more accurate than those of the DSG3, in comparison with the exact solution [42].

Example 12.7.2: Skew Plates

Let us consider the thin and thick cantilever rhombic plates with CFFF supports. The geometry of the plate is illustrated in Figure 12.13 with a skew angle of $\alpha = 60°$. The material parameters are Young's modulus $E = 2.0 \times 10^{11}$, Poisson's ratio $\nu = 0.3$, and density mass $\rho = 8000$. The total number of DOFs used in this example is 1323 DOFs. Table 12.5 shows the six lowest modes of the CFFF rhombic plate. The solution of the ES-FEM-DSG3 method is often found be closer to that of the semianalytical method using the pb-2 Ritz method [43], compared to the DSG3 element.

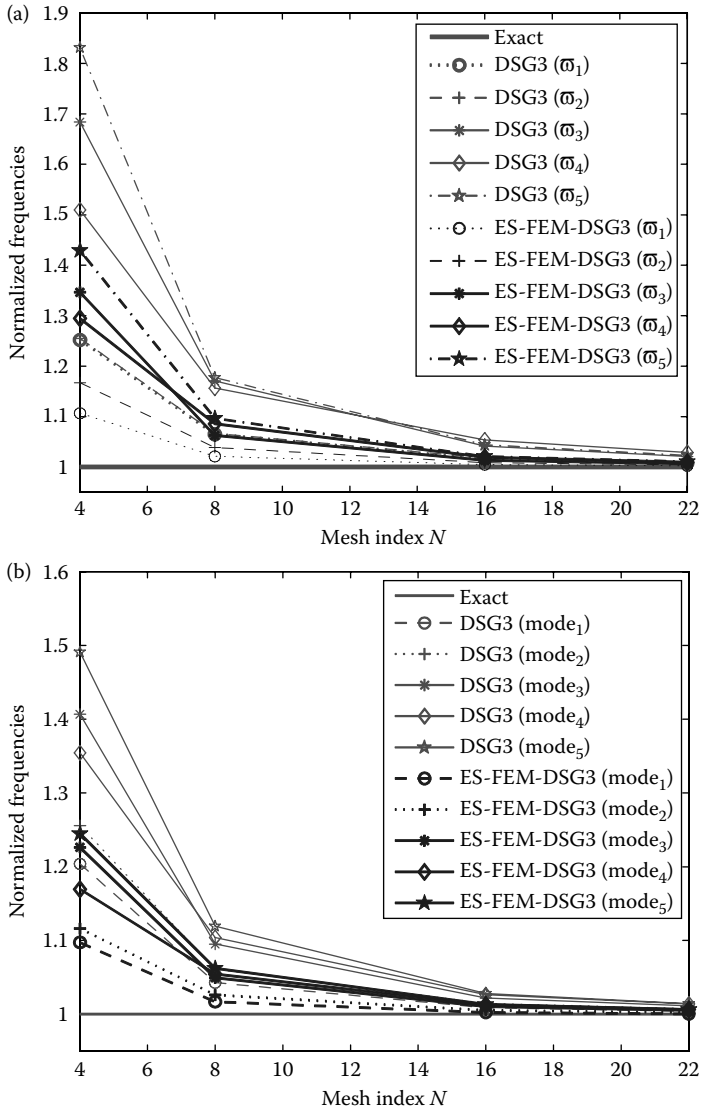

FIGURE 12.11 Convergence of normalized frequency $\varpi^h/\varpi_{\text{exact}}$ for thin plates with $t/L = 0.005$ obtained using ES-FEM-DSG3 and DSG3: (a) SSSS plate and (b) CCCC plate.

Example 12.7.3: Circle Plates

In this example, a circular plate with the clamped boundary shown in Figure 12.14 is studied. The material parameters are Young's modulus $E = 2.0 \times 10^{11}$, Poisson's ratio $\nu = 0.3$, radius $R = 5$, and density mass

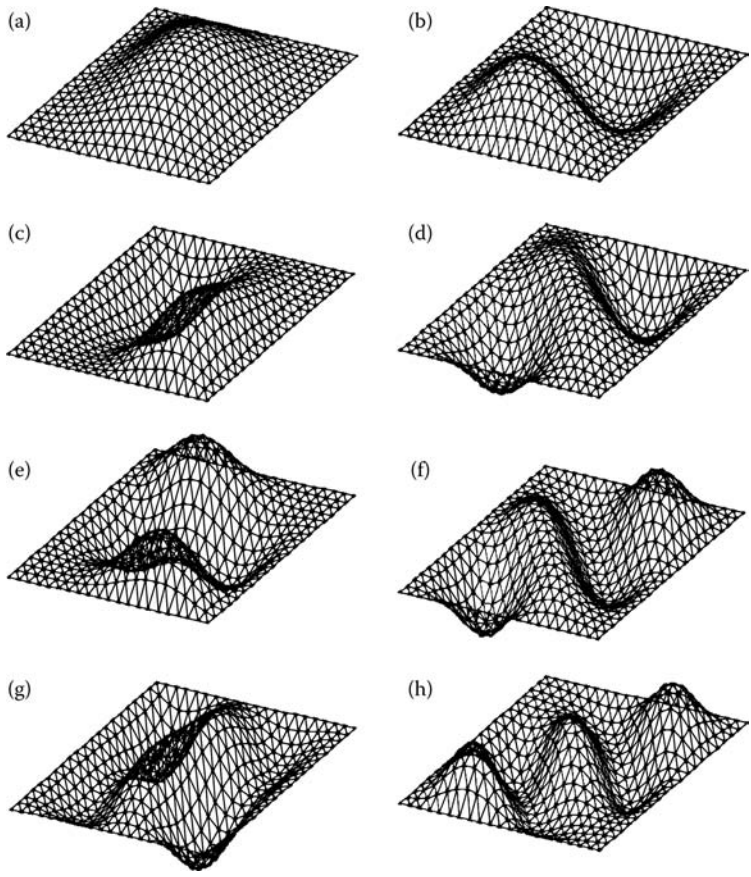

FIGURE 12.12 The first eight shape modes of the CCCC plate using ES-FEM-DSG3 with $t/L = 0.005$. (a)–(h) 1 to 8 shape modes.

$\rho = 8000$. The plate is meshed with 848 triangular elements with 460 nodes. Two aspect ratios, $h/2^*R = 0.01$ and 0.1, are considered. Table 12.6 lists the results for a thin plate of $h/2^*R = 0.01$. It is seen that the frequencies obtained from the ES-FEM-DSG3 method are closer to analytical solutions given in Refs. [42,44], compared to those of the DSG3 model. The ES-FEM-DSG3 method is a good competitor to quadrilateral plate elements such as the ANS solutions (ANS4) [45] and the higher-order ANS solutions (ANS9) [46]. Table 12.7 lists the results for the thick plate of $h/2^*R = 0.1$. It is shown again that the ES-FEM-DSG3 results are very accurate in comparison to the ANS4 element that used 432 quadrilateral elements (or 864 triangular elements). The first 16 shape modes of the circular plate using the ES-FEM-DSG3 are plotted in Figure 12.15. It is evident that no spurious zero-energy modes are observed.

TABLE 12.4

A Nondimensional Frequency Parameter $\varpi = \omega L^2\sqrt{\rho t/D}$ of a Square Plate ($t/L = 0.005$) with Various Boundary Conditions

		Mode Number			
BC Type	**Methods**	**1**	**2**	**3**	**4**
SSSF	DSG3	11.7720	28.3759	41.9628	61.5092
	ES-FEM-DSG3	11.6831	27.8382	41.4312	59.6720
	Exact [42]	11.685	27.756	41.197	59.066
SFSF	DSG3	9.6673	16.3522	37.6792	39.5026
	ES-FEM-DSG3	9.6425	16.1239	36.9054	39.2167
	Exact [42]	9.631	16.135	36.726	38.945
CCCF	DSG3	24.2848	41.7698	65.0068	80.9461
	ES-FEM-DSG3	23.8947	40.1998	63.5127	77.8776
	Exact [42]	24.020	40.039	63.493	76.761
CFCF	DSG3	22.3437	27.1814	45.8829	62.5225
	ES-FEM-DSG3	22.1715	26.4259	43.9273	62.9466
	Exact [42]	22.272	26.529	43.664	64.466
CFSF	DSG3	15.2788	21.0199	41.1975	50.3328
	ES-FEM-DSG3	15.2035	20.5856	39.9697	49.7767
	Exact [42]	15.285	20.673	39.882	49.500

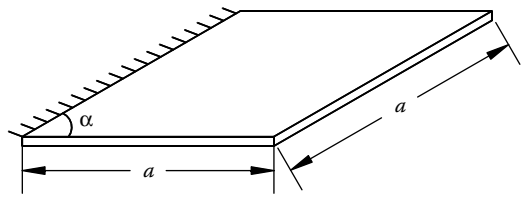

FIGURE 12.13 Cantilever CFFF skew plate.

Example 12.7.4: Triangular Plates

Let us consider cantilever clamped-free-free (CFF) triangular plates with various shapes, as shown in Figure 12.16a and b. The material parameters are Young's modulus $E = 2.0 \times 10^{11}$, Poisson's ratio $\nu = 0.3$, and density mass $\rho = 8000$. Nondimensional frequency parameter $\varpi = \varpi a^2(\rho t/D)^{1/2}/\pi^2$ of these triangular square plates with aspect ratios $t/a = 0.001$ and 0.2 are calculated. The mesh of 744 triangular elements with 423 nodes is used to compute the modes for various skew angles: $\alpha = 0,\ 15,\ 30,\ 45$, and 60. Table 12.8 gives the six lowest modes of the thin triangular plate ($t/a = 0.001$). The first four frequencies obtained using the ES-FEM-DSG3 method are shown in Figure 12.17, together

TABLE 12.5

A Nondimensional Frequency Parameter $\varpi = \left(\omega a^2/\pi^2\right)\sqrt{\rho t/D}$ of a CFFF Rhombic Plate

		Mode Number					
t/a	**Methods**	**1**	**2**	**3**	**4**	**5**	**6**
0.001	DSG3	0.3988	0.9580	2.5996	2.6562	4.2551	5.2267
	ES-FEM-DSG3	0.3976	0.9532	2.5785	2.6400	4.2209	5.1825
	Ref. [43]	0.398	0.954	2.564	2.627	4.189	5.131
0.2	DSG3	0.3785	0.8262	2.0109	2.1918	3.1631	3.8302
	ES-FEM-DSG3	0.3772	0.8192	1.9933	2.1785	3.1296	3.7937
	Ref. [43]	0.377	0.817	1.981	2.166	3.104	3.760

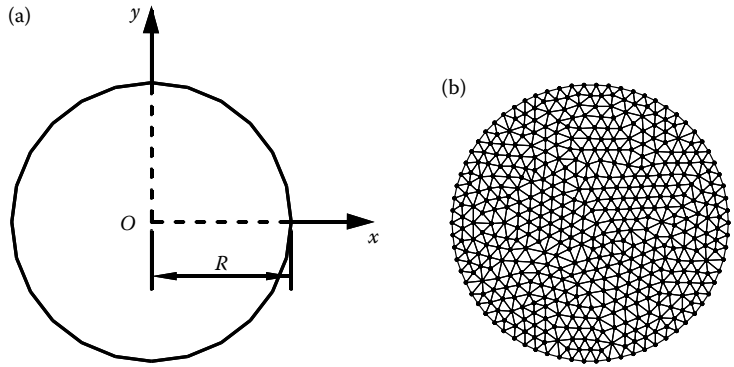

FIGURE 12.14 (a) The circle plate and (b) an initial mesh using three-node triangular elements.

with the results obtained using the MITC4 finite element formulation [45] [the ANS method (ANS4) using a mesh of 398 four-node quadrilateral elements or 796 triangular elements], and those obtained using two other numerical methods such as the Rayleigh–Ritz method [47] and the pb-2 Ritz method [48]. From the results given in Table 12.8 and Figure 12.17, we found that the frequencies of the ES-FEM-DSG3 are often bounded by the solutions of the Rayleigh–Ritz and the pb-2 Ritz models. The results for thick plates are provided in Table 12.9. It is found that the ES-FEM-DSG3 works well also for thick plates.

Figure 12.18 plots the first 12 shape modes of free vibration of cantilever triangular square plate obtained using the ES-FEM-DSG3: no spurious modes are found. We note that our method using three-node triangular elements worked naturally well for plates with irregular shapes. Therefore, the ES-FEM-DSG3 is a very effective and robust numerical model for plates of complicated geometries.

TABLE 12.6

The Parameterized Natural Frequencies $\varpi = \left(\omega R^2\right)\sqrt{\rho t/D}$ of a Clamped Circular Plate with $t/2{*}R = 0.01$

Mode	DSG3	ES-FEM-DSG3	ANS4 [45]	ANS9 [46]	Exact [42]	Exact [44]
1	10.2941	10.2402	10.2572	10.2129	10.2158	10.216
2	21.6504	21.3966	21.4981	21.2311	21.2600	21.260
3	21.6599	21.4096	21.4981	21.2311	21.2600	21.260
4	35.9885	35.3012	35.3941	34.7816	34.8800	34.877
5	35.9981	35.3277	35.5173	34.7915	34.8800	34.877
6	41.1864	40.3671	40.8975	39.6766	39.7710	39.771
7	53.4374	52.0138	52.2054	50.8348	51.0400	51.030
8	53.5173	52.1013	52.2054	50.8348	51.0400	51.030
9	64.2317	62.3053	63.2397	60.6761	60.8200	60.829
10	64.4073	62.4665	63.2397	60.6761	60.8200	60.829
11	74.2254	71.6554	71.7426	69.3028	69.6659	69.666
12	74.3270	71.7269	72.0375	69.3379	69.6659	69.666
13	91.4366	87.7019	88.1498	84.2999	84.5800	84.583
14	91.5328	87.7861	89.3007	84.3835	84.5800	84.583

TABLE 12.7

The Parameterized Natural Frequencies $\varpi = \left(\omega R^2\right)\sqrt{\rho t/D}$ of a Clamped Circular Plate with $t/2{*}R = 0.1$

Mode	DSG3	ES-FEM-DSG3	Exact [44]	ANS4 [45]^1	ANS4 [45]^2
1	9.3012	9.2527	9.240	9.2605	9.2277
2	18.0038	17.8372	17.834	17.9469	17.8010
3	18.0098	17.8428	17.834	17.9469	17.8010
4	27.6010	27.2344	27.214	27.0345	26.6801
5	27.6082	27.2391	27.214	27.6566	27.2246
6	30.9865	30.5173	30.211	30.3221	29.8562
7	37.9464	37.2817	37.109	37.2579	36.3966
8	37.9817	37.3128	37.109	37.2579	36.3966
9	43.9528	43.0626	42.409	43.2702	42.1089
10	44.0324	43.1328	42.409	43.2702	42.1089
11	48.9624	47.8823	47.340	47.7074	46.0596
12	48.9793	47.8976	47.340	47.8028	46.0985
13	57.2487	55.7747	54.557	56.0625	53.9332
14	57.2776	55.8052	54.557	57.1311	54.7720

Note: The alternative form of MITC4 [45]^1 using a consistent mass; the alternative form of MITC4 [45]^2 using a lumped mass.

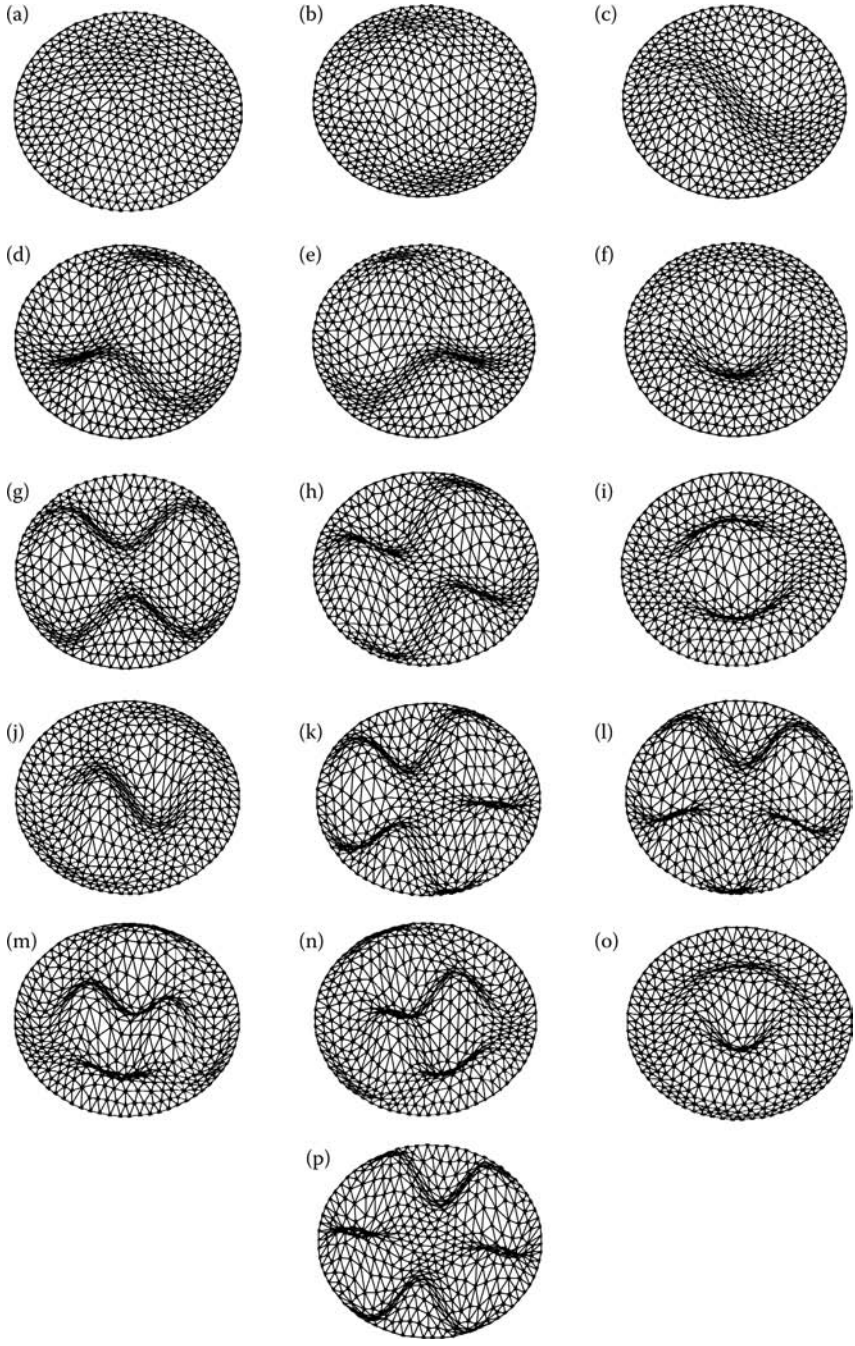

FIGURE 12.15 The first 16 shape modes of a clamped circle plate using the ES-FEM-DSG3. (a)–(p) 1 to 16 shape modes.

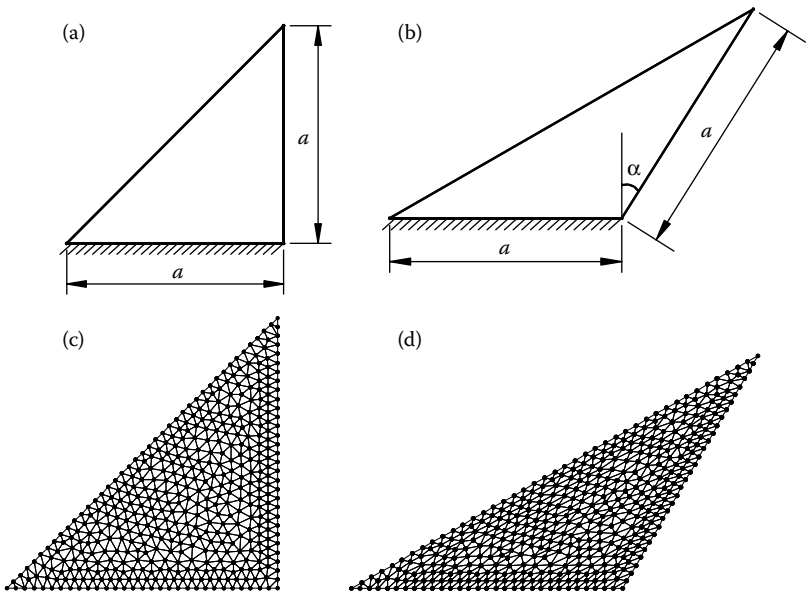

FIGURE 12.16 Triangular cantilever plates and meshes: (a) square triangular plate, (b) rhombic triangular plate, (c) a mesh of square triangular plates using three-node triangular elements; and (d) a mesh of rhombic triangular plates using three-node triangular elements.

12.8 Numerical Examples: Buckling of Plates

In the following examples, we analyze the buckling of plates. The factor of buckling load is defined as $K = \lambda_{cr} b^2/(\pi^2 D)$, where b is the edge width of the plate and λ_{cr} is the critical buckling load. The material parameters are Young's modulus $E = 2.0 \times 10^{11}$ and Poisson's ratio $\nu = 0.3$.

Example 12.8.1: Rectangular Plates Subjected to Uniaxial Compression

We first consider a plate with length a, width b, and thickness t subjected to a uniaxial compression. Simply supported (SSSS) and clamped (CCCC) boundary conditions are used. The geometry and regular mesh of the plate are shown in Figure 12.19. Table 12.10 gives the results of the buckling load factor obtained using meshes of 4×4, 8×8, 12×12, 16×16, and 20×20 rectangular elements. Figure 12.20 plots the normalized buckling load K^h/K_{exact} of a square plate with the thickness ratio $t/b = 0.01$, where K^h is the buckling load of the numerical methods and K_{exact} is the buckling load of the analytical solution [49]. It is evident that the ES-FEM-DSG3 method gives a much more accurate

TABLE 12.8

The Parameterized Natural Frequencies $\varpi = \left(\omega a^2/\pi^2\right)\sqrt{\rho t/D}$ of Triangular Plates with $t/a = 0.001$

		Mode Number					
α°	**Methods**	**1**	**2**	**3**	**4**	**5**	**6**
0	DSG3	0.6252	2.3890	3.3404	5.7589	7.8723	10.3026
	ES-FEM-DSG3	0.6242	2.3789	3.3159	5.7124	7.7919	10.1547
	Rayleigh–Ritz [47]	0.624	2.377	3.308	5.689	7.743	—
	Pb2 Rayleigh–Ritz [48]	0.625	2.377	3.310	5.689	7.743	—
	Experimental [56]	0.588	2.318	3.239	5.540	7.518	—
	ANS4 [45]	0.624	2.379	3.317	5.724	7.794	10.200
15	DSG3	0.5855	2.1926	3.4528	5.3481	7.3996	10.2498
	ES-FEM-DSG3	0.5840	2.1833	3.4163	5.3020	7.3112	10.0779
	Rayleigh–Ritz [47]	0.584	2.181	3.409	5.280	7.264	—
	Pb2 Rayleigh–Ritz [48]	0.586	2.182	3.412	5.279	7.263	—
	ANS4 [45]	0.583	2.181	3.413	5.303	7.289	10.095
30	DSG3	0.5798	2.1880	3.7157	5.5983	7.2814	10.7753
	ES-FEM-DSG3	0.5766	2.1778	3.6539	5.5361	7.1628	10.5108
	Rayleigh–Ritz [47]	0.576	2.174	3.639	5.511	7.108	—
	Pb2 Rayleigh–Ritz [48]	0.578	2.178	3.657	5.518	7.109	—
	ANS4 [45]	0.575	2.174	3.638	5.534	7.139	10.477
45	DSG3	0.6006	2.3564	4.2795	6.5930	7.8615	11.7850
	ES-FEM-DSG3	0.5923	2.3359	4.1699	6.4424	7.6658	11.3496
	Rayleigh–Ritz [47]	0.590	2.329	4.137	6.381	7.602	—
	Pb2 Rayleigh–Ritz [48]	0.593	2.335	4.222	6.487	7.609	—
	ANS4 [45]	0.588	2.324	4.126	6.381	7.614	11.224
60	DSG3	0.6497	2.7022	5.6491	8.3505	10.7757	14.6003
	ES-FEM-DSG3	0.6261	2.6101	5.4283	7.7333	10.3756	13.3296
	Rayleigh–Ritz [47]	0.617	2.576	5.376	7.524	10.285	—
	Pb2 Rayleigh–Ritz [48]	0.636	2.618	5.521	8.254	10.395	—
	ANS4 [45]	0.613	2.564	5.353	7.460	10.306	12.942

solution that converges to the exact solution much faster than the DSG3 element. The performance of the ES-FEM-DSG3 method is also compared with several other methods in the literature. Table 12.11 shows the factor values K_b obtained using the ES-FEM-DSG3 method and $2 \times 16 \times 16$ triangular elements, together with other methods. The relative errors compared with exact results are given in parentheses. It is found that the ES-FEM-DSG3 results agree well with the analytical solution [49], spline finite strip methods [50,51], and the radial point interpolation mesh-free method [35], and are much more accurate than those of the DSG3 method.

The results of buckling load factors of SSSS, CCCC, and FCFC plates with thickness-to-width ratios $t/b = 0.05$ and 0.1 are listed in Table 12.12. The

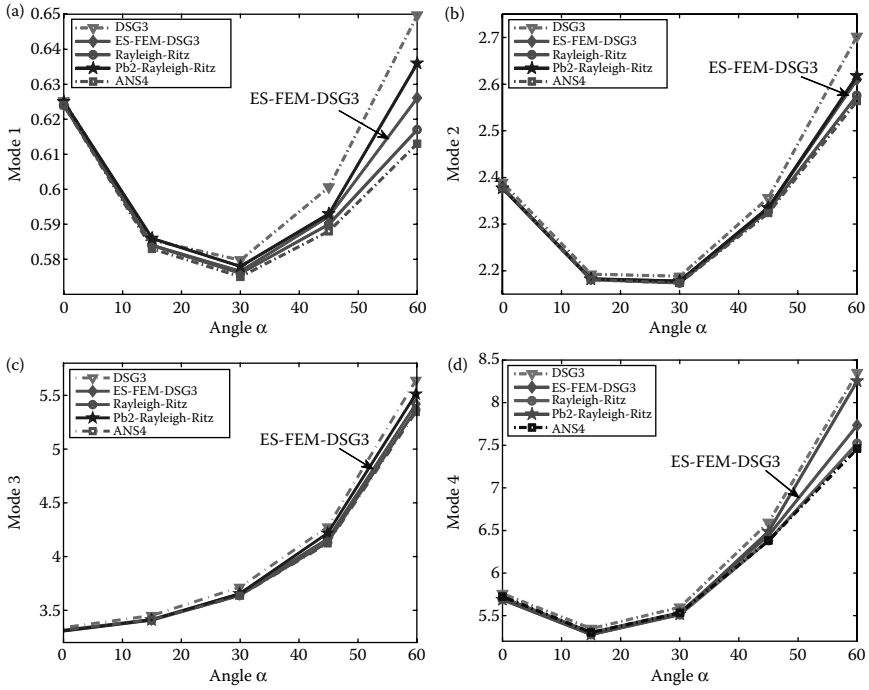

FIGURE 12.17 The first four frequencies of ES-FEM-DSG3 in comparison with other methods for the triangular plate with $t/a = 0.001$: (a) mode 1; (b) mode 2; (c) mode 3; and (d) mode 4.

results obtained using the ES-FEM-DSG3 method are compared with those of the DSG3 method, the radial point interpolation mesh-free method [35], and the pb-2 Ritz method [52].

Simply supported rectangular plates with various thickness-to-width ratios $t/b = 0.05$, 0.1, and 0.2 and length-to-width ratios $a/b = 0.5$, 1.0, 1.5, 2.0, and 2.5 are analyzed. Table 12.13 and Figure 12.21 give the results of buckling factors using the regular mesh of 16×16 rectangular elements. The DSG3 and ES-FEM-DSG3 results are also compared to the pb-2 Ritz and the mesh-free method [53]. It is seen that the ES-FEM-DSG3 results are in good agreement with the mesh-free method and the pb-2 Ritz method [52]. Figure 12.22 plots the axial buckling modes obtained using the ES-FEM-DSG3 method for simply supported rectangular plates with the thickness-to-width ratio $t/b = 0.01$ and various length-to-width ratios $a/b = 1.0$, 1.5, 2.0, and 2.5. No spurious buckling modes are observed.

Example 12.8.2: Square Plates Subjected to Biaxial Compression

Buckling of a square plate subjected to biaxial compression is considered. The geometry of the plates is shown in Figure 12.19b, and a mesh of $2 \times 16 \times 16$

TABLE 12.9

The Parameterized Natural Frequencies $\varpi = \left(\omega a^2/\pi^2\right)\sqrt{\rho t/D}$ of Triangular Plates with the Aspect Ratio $a/b = 1$ and $t/b = 0.2$

		Mode Number					
α°	Methods	1	2	3	4	5	6
0	DSG3	0.5830	1.9101	2.4176	3.9772	5.0265	5.9521
	ES-FEM-DSG3	0.5823	1.9040	2.4083	3.9559	4.9954	5.8994
	Pb2 Rayleigh–Ritz [48]	0.582	1.900	2.408	3.936	—	—
	FEM [57]	0.581	1.901	2.410	—	—	—
	ANS4 [45]	0.582	1.915	2.428	3.984	5.018	5.944
15	DSG3	0.5449	1.7803	2.3959	3.6668	4.8504	5.6057
	ES-FEM-DSG3	0.5441	1.7749	2.3854	3.6467	4.8208	5.5385
	Pb2 Rayleigh–Ritz [48]	0.544	1.771	2.386	3.628	—	—
	FEM [57]	0.543	1.770	2.388	—	—	—
	ANS4 [45]	0.545	1.764	2.420	3.608	4.820	5.431
30	DSG3	0.5339	1.7815	2.4356	3.6085	4.7829	5.4532
	ES-FEM-DSG3	0.5328	1.7754	2.4206	3.5842	4.7444	5.3377
	Pb2 Rayleigh–Ritz [48]	0.533	1.772	2.419	3.565	—	—
	FEM [57]	0.532	1.769	2.419	—	—	—
	ANS4 [45]	0.532	1.773	2.437	3.591	4.765	5.323
45	DSG3	0.5412	1.8977	2.5304	3.7518	4.8188	5.4304
	ES-FEM-DSG3	0.5391	1.8882	2.5004	3.7035	4.6800	5.2256
	Pb2 Rayleigh–Ritz [48]	0.540	1.885	2.489	3.674	—	—
	FEM [57]	0.538	1.881	2.482	—	—	—
	ANS4 [45]	0.541	1.884	2.518	3.748	4.740	5.292
60	DSG3	0.5634	2.0837	2.5355	4.0862	4.6612	5.9782
	ES-FEM-DSG3	0.5588	2.0623	2.4356	3.8009	4.3393	5.5835
	Pb2 Rayleigh–Ritz [48]	0.559	2.059	2.396	3.590	—	—
	FEM [57]	0.555	2.047	2.386	—	—	—
	ANS4 [45]	0.559	2.095	2.483	3.910	4.517	5.763

triangular elements is used. Table 12.14 gives the buckling factor of the square plate subjected to biaxial compression with three essential boundary conditions (SSSS, CCCC, and SCSC). It can be seen that the ES-FEM-DSG3 results agree well with the analytical solution [49] and the spline finite strip methods [50,51].

Example 12.8.3: Rectangular Plates Subjected to In-Plane Pure Shear

Consider first a simply supported plate subjected to in-plane shear as shown in Figure 12.19c. The factors K of shear buckling loads of this plate are computed using a mesh of 16×16 rectangular elements. The results for plates

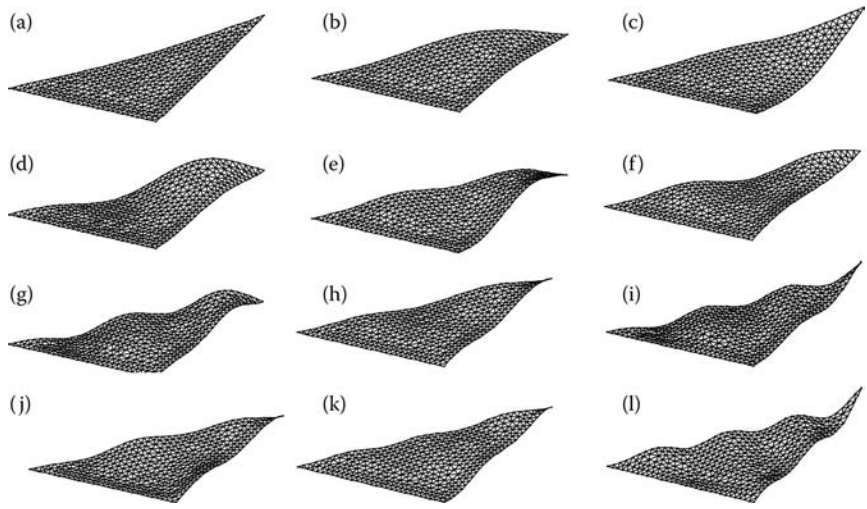

FIGURE 12.18 The first 12 shape modes of a square triangular plate with $t/a = 0.001$. (a)–(l) 1 to 12 shape modes.

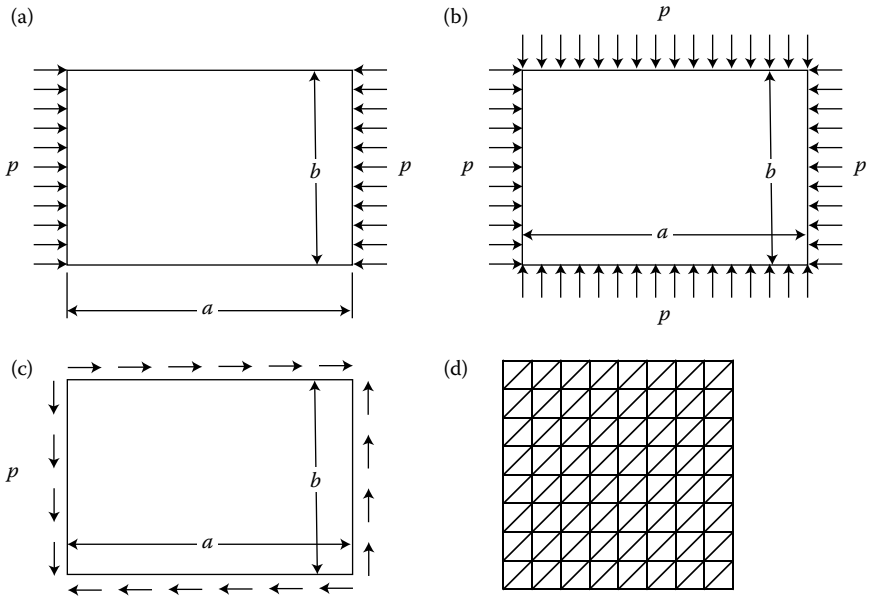

FIGURE 12.19 Rectangular plates: (a) axial compression, (b) biaxial compression, (c) shear in-plane, and (d) a regular mesh using three-node triangular elements.

TABLE 12.10

The Factors K of Axial Buckling Loads along the x-Axis of Rectangular Plates with Length-to-Width Ratios $a/b = 1$ and Thickness-to-Width Ratios $t/b = 0.01$

Plates Type	Elements	4 × 4	8 × 8	12 × 12	16 × 16	20 × 20
SSSS	DSG3	7.5891	4.8013	4.3200	4.1590	4.0889
	ES-FEM-DSG3	4.7023	4.1060	4.0368	4.0170	4.0089
CCCC	DSG3	31.8770	14.7592	11.9823	11.0446	10.6282
	ES-FEM-DSG3	14.7104	11.0428	10.3881	10.2106	10.1410

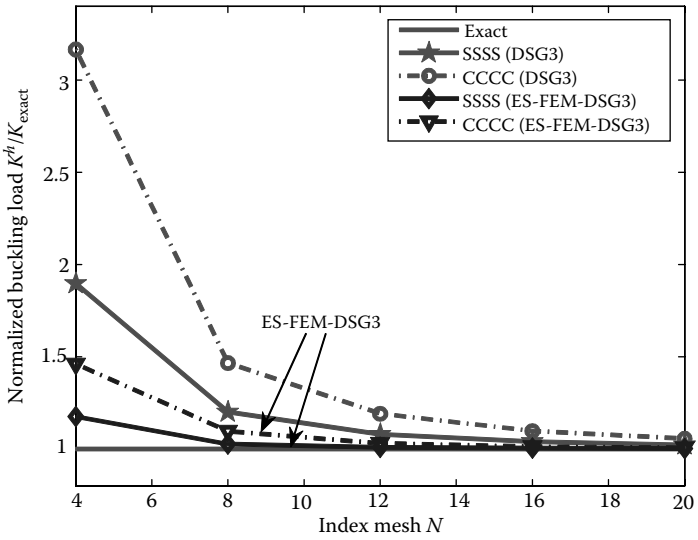

FIGURE 12.20 Normalized buckling load K^h/K_{exact} obtained using ES-FEM-DSG3 and DSG3 for square plates with $t/b = 0.01$.

TABLE 12.11

The Factor K_b of Axial Buckling Loads along the x-Axis of Square Plates with Thickness-to-Width Ratios $t/b = 0.01$

BC Types	DSG3	ES-FEM-DSG3	Liew [35]	Ansys [35]	Timoshenko [49]	Tham [50]	Vrcelj [51]
SSSS	4.1590	4.0170	3.9700	4.0634	4.00	4.00	4.0006
	(3.97%)	(0.4%)	(−0.75%)	(1.85%)	(0.0%)	(0.0%)	(0.02%)
CCCC	11.0446	10.2106	10.1501	10.1889	10.07	10.08	10.0871
	(9.68%)	(1.4%)	(0.8%)	(1.18%)	(0.0%)	(0.1%)	(0.17%)

TABLE 12.12

The Factor K_b of Axial Buckling Loads along the x-Axis of a Square Plate with Various Thickness-to-Width Ratios

t/b	BC Types	DSG3	ES-FEM-DSG3	RPIM [35]	Pb-2 Ritz [52]
0.05	SSSS	3.9786	3.9412	3.9464	3.9444
	CCCC	9.8284	9.5426	9.5819	9.5586
	FCFC	3.8365	3.7654	3.8187	3.8005
0.1	SSSS	3.7692	3.7702	3.7853	3.7873
	CCCC	8.2670	8.2674	8.2931	8.2921
	FCFC	3.4594	3.4966	3.5138	3.5077

TABLE 12.13

The Factor K_b of Axial Buckling Loads along the x-Axis of Rectangular Plates with Various Length-to-Width Ratios and Various Thickness-to-Width Ratios

a/b	t/b	DSG3	ES-FEM-DSG3	Mesh Free [53]	Pb-2 Ritz [52]
0.5	0.05	6.0478	5.9873	6.0405	6.0372
	0.1	5.3555	5.3064	5.3116	5.4777
	0.2	3.7524	3.7200	3.7157	3.9963
1.0	0.05	3.9786	3.9412	3.9293	3.9444
	0.1	3.7692	3.7402	3.7270	3.7865
	0.2	3.1493	3.1263	3.1471	3.2637
1.5	0.05	4.3930	4.2852	4.2116	4.2570
	0.1	4.0604	3.9844	3.8982	4.0250
	0.2	3.2014	3.1461	3.1032	3.3048
2.0	0.05	4.1070	3.9811	3.8657	3.9444
	0.1	3.8539	3.7711	3.6797	3.7865
	0.2	3.2023	3.1415	3.0783	3.2637
2.5	0.05	4.3577	4.1691	3.9600	4.0645
	0.1	4.0644	3.8924	3.7311	3.8683
	0.2	3.2393	3.1234	3.0306	3.2421

with the thickness-to-width ratio $t/b = 0.001$ and length-to-width ratios $a/b = 1.0,\ 2.0,\ 3.0$, and 4.0 are listed in Table 12.15. The ES-FEM-DSG3 results are compared to the exact solutions in Ref. [54] and the mesh-free solution [53]. It can be found that the ES-FEM-DSG3 method agrees well with the exact solution. The results of the shear buckling load for the simply supported plate are illustrated in Figure 12.23. Figure 12.24 plots the shear buckling modes of simply supported rectangular plates with the thickness-to-width ratio $t/b = 0.01$ and various length-to-width ratios $a/b = 1.0,\ 2.0,\ 3.0$, and 4.0. No spurious buckling modes are found.

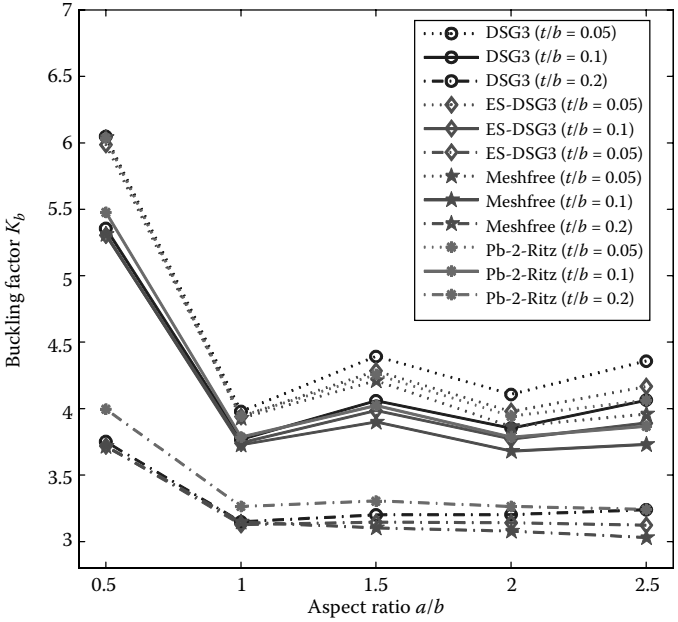

FIGURE 12.21 Convergence of axial buckling load K_b of an SSSS plate with various length-to-width ratios and various thickness-to-width ratios.

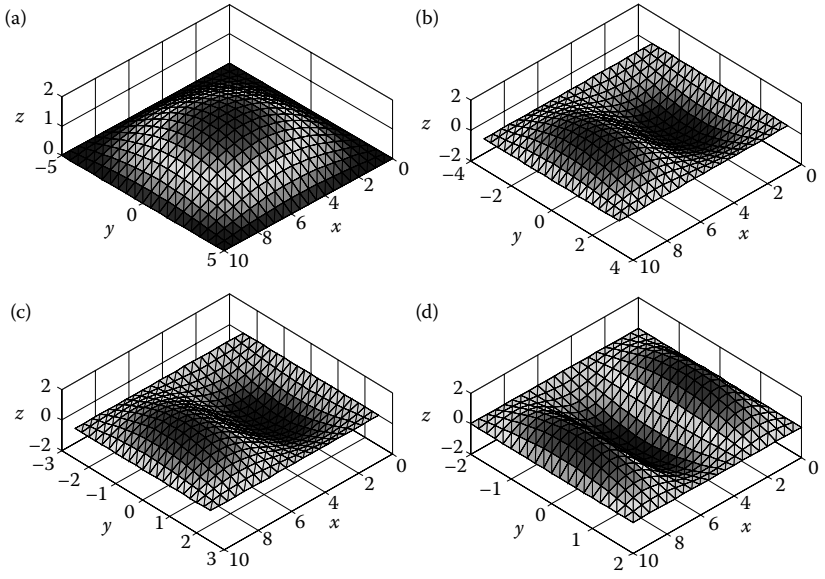

FIGURE 12.22 Axial buckling modes of simply supported rectangular plates with thickness-to-width ratios $t/b = 0.01$ and various length-to-width ratios: (a) $a/b = 1.0$; (b) $a/b = 1.5$; (c) $a/b = 2.0$; and (d) $a/b = 2.5$.

TABLE 12.14

The Factors K of Biaxial Buckling Loads of a Square Plate with Thickness-to-Width Ratios $t/b = 0.01$ and Various Boundary Conditions

Plates Type	DSG3	ES-FEM-DSG3	Timoshenko [49]	Tham [50]	Vrcelj [51]
SSSS	2.0549	2.0023	2.00	2.00	2.0008
CCCC	5.6419	5.3200	5.31	5.61	5.3260
SCSC	4.0108	3.8332	3.83	3.83	3.8419

TABLE 12.15

The Factors K of Shear Buckling Loads of Simply Supported Rectangular Plates with Various Length-to-Width Ratios, Choose $t/b = 0.01$

a/b	DSG3	ES-FEM-DSG3	Mesh Free [53]	Exact [54]
1.0	9.5195	9.2830	9.3962	9.34
2.0	6.7523	6.4455	6.3741	6.34
3.0	6.5129	5.8830	5.7232	5.784
4.0	6.3093	5.6732	5.4367	5.59

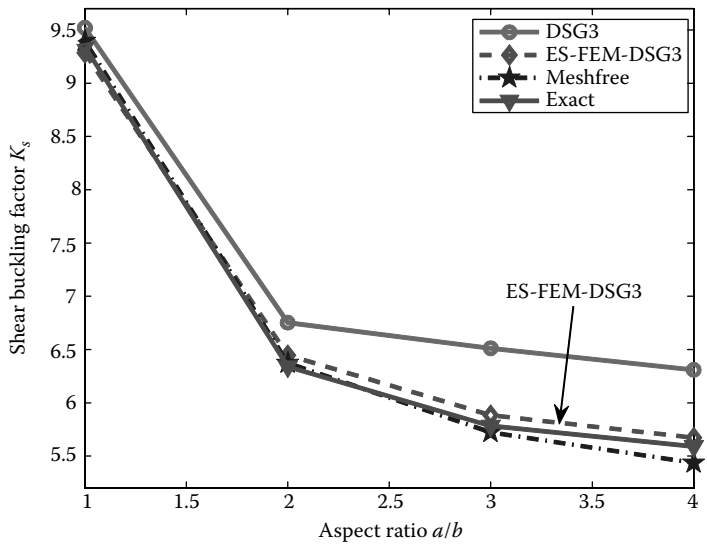

FIGURE 12.23 Shear buckling load for simply supported rectangular plates with various length-to-width ratios.

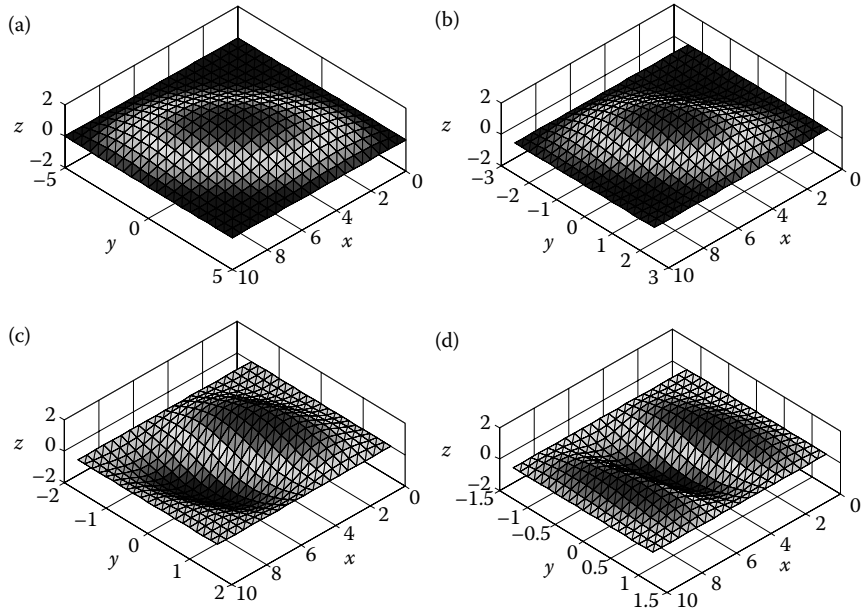

FIGURE 12.24 Shear buckling mode of simply supported rectangular plates using the ES-FEM-DSG3 with various length-to-width ratios: (a) $a/b = 1.0$; (b) $a/b = 2.0$; (c) $a/b = 3.0$; and (d) $a/b = 4.0$.

TABLE 12.16

The Factors K of Shear Buckling Loads of Rectangular Plates with Length-to-Width Ratios $a/b = 1$, Thickness-to-Width Ratios $t/b = 0.01$, and Various Boundary Condition

Plates Type	DSG3	ES-FEM-DSG3	Timoshenko [49]	Tham [50]	Vrcelj [51]
SSSS	9.5195	9.2830	9.33	9.40	9.3847
CCCC	15.6397	14.6591	14.66	14.58	14.6601
SCSC	13.1652	12.5533	12.58	12.58	12.5997

We finally consider a square plate subjected to in-plane shear with three boundary conditions: SSSS, CCCC, and SCSC. The ES-FEM-DSG3 result is given in Table 12.16, together with those obtained using other methods. It can again be seen that the ES-FEM-DSG3 method is very good in comparison to the analytical solution [49] and the spline finite strip methods [50,51].

12.9 Remarks

The ES-FEM using triangular elements is extended in this chapter for static, free vibration, and buckling analyses of the Reissner–Mindlin plates, with a stabilized DSG for overcoming the shear locking problem. In the ES-FEM-DSG3 method, the approximations for the displacements and rotations are the same as in the standard FEM. The bending, geometrical, and shear strains are, however, smoothed over the smoothing domain associated with the edges of the triangles. As a result, the stiffness matrices based on these smoothed fields are obtained by simple summations. More importantly, the ES-FEM uses only three-node triangular meshes and no additional DOFs are required. Through the formulations and numerical examples, we note the following:

- The ES-FEM-DSG3 method can improve significantly the performance of the original FEM-DSG3 method.
- The ES-FEM-DSG3 method outperforms other existing models using triangular elements and often even those using quadrilateral elements.
- For the free vibration analysis, the ES-FEM-DSG3 method often produces more accurate results and does not have spurious modes.
- For the buckling analysis, the ES-FEM-DSG3 method is found to be superior to the FEM-DSG3 method, and no spurious buckling modes were found.
- The ES-FEM-DSG3 method works well with triangular elements and, hence, is applicable to plates with complicated geometries.
- The ES-FEM-DSG3 method is free of shear locking and works well for both thin and thick plates.

In summary, the ES-FEM-DSG3 is a simple, effective, and robust numerical tool for the analysis of various problems of both thin and thick plates. It remains still a "star."

References

1. Liu GR and Quek SS. 2002. *The Finite Element Method: A Practical Course*. Butterworth Heinemann, Oxford.
2. Liu GR. 2009. *Meshfree Methods: Moving Beyond the Finite Element Method*, 2nd edition. Taylor & Francis/CRC Press, Boca Raton, FL.

3. Hughes TJR, Taylor RL, and Kanoknukulchai W. 1977. Simple and efficient element for plate bending. *International Journal for Numerical Methods in Engineering*; 11: 1529–1543.
4. Hughes TJR, Cohen M, and Haroun M. 1978. Reduced and selective integration techniques in finite element method of plates. *Nuclear Engineering and Design*; 46: 203–222.
5. Malkus DS and Hughes TJR. 1978. Mixed finite element methods—reduced and selective integration techniques: A unification of concepts. *Computer Methods in Applied Mechanics and Engineering*; 46: 203–222.
6. Zienkiewicz OC, Taylor RL, and JM Too. 1971. Reduced integration technique in general analysis of plates ans shells. *International Journal for Numerical Methods in Engineering*; 3: 275–290.
7. Auricchio F and Taylor RL. 1994. A shear deformable plate element with an exact thin limit. *Computer Methods in Applied Mechanics and Engineering*; 118: 393–412.
8. Auricchio F and Taylor RL. 1995. A triangular thick plate finite element with an exact thin limit. *Finite Elements in Analysis and Design*; 19: 57–68.
9. Ayad R, Dhatt G, and Batoz JL. 1998. A new hybrid-mixed variational approach for Reissner–Mindlin plate, the MiSP model. *International Journal for Numerical Methods in Engineering*; 42: 1149–1179.
10. Brasile S. 2008. An isostatic assumed stress triangular element for the Reissner–Mindlin plate-bending problem. *International Journal for Numerical Methods in Engineering*; 74: 971–995.
11. De Miranda S and Ubertini F. 2006. A simple hybrid stress element for shear deformable plates. *International Journal for Numerical Methods in Engineering*; 65: 808–833.
12. Lee SW and Pian THH. 1978. Finite elements based upon Mindlin plate theory with particular reference to the four-node isoparametric element. *AIAA Journal*; 16: 29–34.
13. Lee SW and Wong C. 1982. Mixed formulation finite elements for Mindlin theory plate bending. *International Journal for Numerical Methods in Engineering*; 18:1297–1311.
14. Lovadina C. 1998. Analysis of a mixed finite element method for the Reissner–Mindlin plate problems. *Computer Methods in Applied Mechanics and Engineering*; 163: 71–85.
15. Taylor RL and Auricchio F. 1993. Linked interpolation for Reissner–Mindlin plate element: Part II—a simple triangle. *International Journal for Numerical Methods in Engineering*; 36: 3043–3056.
16. Zienkiewicz OC and Lefebvre D. 1988. A robust triangular plate bending element of the Reissner–Mindlin type. *International Journal for Numerical Methods in Engineering*; 26: 1169–1184.
17. Zienkiewicz OC, Xu Z, Zeng LF, Samuelsson A, and Wiberg NE. 1993. Linked interpolation for Reissner–Mindlin plate element: Part I—a simple quadrilateral. *International Journal for Numerical Methods in Engineering*; 36: 3043–3056.
18. Simo JC and Rifai MS. 1990. A class of mixed assumed strain methods and the method of incompatible modes. *International Journal for Numerical Methods in Engineering*; 29: 1595–1638.

19. Cardoso RPR, Yoon JW, Mahardika M, Choudhry S, Alves de Sousa RJ, and Fontes Valente RA. 2008. Enhanced assumed strain (EAS) and assumed natural strain (ANS) methods for one-point quadrature solid-shell elements. *International Journal for Numerical Methods in Engineering*; 75: 156–187.
20. Simo JC, Fox DD, and Rifai MS. 1989. On a stress resultant geometrically exact shell model. Part II: The linear theory, computational aspects. *Computer Methods in Applied Mechanics and Engineering*; 73: 53–92.
21. César de Sá JMA and Natal Jorge RM. 1999. New enhanced strain elements for incompatible problems. *International Journal for Numerical Methods in Engineering*; 44: 229–248.
22. César de Sá JMA, Natal Jorge RM, Fontes Valente RA, and Areias PMA. 2002. Development of shear locking-free shell elements using an enhanced assumed strain formulation. *International Journal for Numerical Methods in Engineering*; 53: 1721–1750.
23. Bathe KJ and Dvorkin EN. 1985. A four-node plate bending element based on Mindlin/Reissener plate theory and a mixed interpolation. *International Journal for Numerical Methods in Engineering*; 21: 367–383.
24. Bathe KJ and Dvorkin EN. 1986. A formulation of general shell elements. The use of mixed interpolation of tensorial components. *International Journal for Numerical Methods in Engineering*; 22: 697–722.
25. Batoz JL and Lardeur P. 1989. A discrete shear triangular nine d.o.f. element for the analysis of thick to very thin plates. *International Journal for Numerical Methods in Engineering*; 29: 533–560.
26. Batoz JL and Katili I. 1992. On a simple triangular Reissner/Mindlin plate element based on incompatible modes and discrete constraints. *International Journal for Numerical Methods in Engineering*; 35: 1603–1632.
27. Dvorkin EN and Bathe KJ. 1984. A continuum mechanics based four-node shell element for general nonlinear analysis. *Engineering with Computers*; 1: 77–88.
28. Hughes TJR and Taylor RL. 1982. The linear triangular plate bending element. In *The Mathematics of Finite Elements and Applications IV*, JR Whiteman, Ed. MAFELAP 1981, Academic Press, New York, pp. 127–142.
29. Hughes TJR and Tezduyar T. 1981. Finite elements based upon Mindlin plate theory with particular reference to the four-node isoparametric element. *Journal of Applied Mechanics*; 48: 587–596.
30. MacNeal RH. 1982. Derivation of element stiffness matrices by assumed strain distribution. *Nuclear Engineering and Design*; 70: 3–12.
31. Tessler A and Hughes TJR. 1985. A three-node Mindlin plate element with improved transverse shear. *Computer Methods in Applied Mechanics and Engineering*; 50: 71–101.
32. Zienkiewicz OC, Taylor RL, Papadopoulos P, and Õnate E. 1990. Plate bending elements with discrete constraints: New triangular elements. *Computers and Structures*; 35: 505–522.
33. Bletzinger KU, Bischoff M, and Ramm E. 2000. A unified approach for shear-locking free triangular and rectangular shell finite elements. *Computers and Structures*; 75: 321–334.
34. Lyly M, Stenberg R, and Vihinen T. 1993. A stable bilinear element for the Reissner–Mindlin plate model. *Computer Methods in Applied Mechanics and Engineering*; 110: 343–357.

35. Liew KM and Chen XL. 2004. Buckling of rectangular Mindlin plates subjected to partial in-plane edge loads using the radial point interpolation method. *International Journal of Solids and Structures*; 41: 1677–1695.
36. Nguyen-Xuan H, Liu GR, Thai-Hoang C, and Nguyen-Thoi T (2009) An edge-based smoothed finite element method with stabilized discrete shear gap technique for analysis of Reissner–Mindlin plates. *Computer Methods in Applied Mechanics and Engineering*; 199: 471–489.
37. Liu GR, Nguyen-Thoi T, and Lam KY. 2009. An edge-based smoothed finite element method (ES-FEM) for static and dynamic problems of solid mechanics. *Journal of Sound and Vibration*; 320: 1100–1130.
38. Bischoff M and Bletzinger KU. 2001. Stabilized DSG plate and shell elements. In *Trends in Computational Structural Mechanics*. CIMNE, Barcelona, Spain.
39. Morley LSD. 1963. *Skew Plates and Structures*. Pergamon Press, Oxford.
40. Cen S, Long YQ, Yao ZH, and Chiew SP. 2006. Application of the quadrilateral area co-ordinate method: A new element for Mindlin–Reissner plate. *International Journal for Numerical Methods in Engineering*; 66: 1–45.
41. Abbassian F, Dawswell DJ, and Knowles NC. 1987. *Free Vibration Benchmarks Softback*. Atkins Engineering Sciences, Glasgow, 40pp.
42. Leissa AW. 1969. *Vibration of Plates*. NASA, SP-160, Washington, DC.
43. Karunasena W, Liew KM, and Al-Bermani FGA. 1996. Natural frequencies of thick arbitrary quadrilateral plates using the pb-2 Ritz method. *Journal of Sound and Vibration*; 196: 371–385.
44. Irie T, Yamada G, and Aomura S. 1980. Natural frequencies of Mindlin circular plates. *Journal of Applied Mechanics*; 47: 652–655.
45. Lee SJ. 2004. Free vibration analysis of plates by using a four-node finite element formulated with assumed natural transverse shear strain. *Journal of Sound and Vibration*; 278: 657–684.
46. Lee SJ and Han SE. 2001. Free-vibration analysis of plates and shells with a nine-node assumed natural degenerated shell element. *Journal of Sound and Vibration*; 241: 605–633.
47. McGee OG, Leissa AW, and Huang CS. 1992. Vibrations of cantilevered skewed trapezodial and triangular plates with corner stress singularities. *International Journal of Mechanical Sciences*; 34: 63–84.
48. Karunasena W, Kitipornchai S, and Al-bermani FGA. 1996. Free vibration of cantilevered arbitrary triangular Mindlin plates. *International Journal of Mechanical Sciences*; 38: 431–442.
49. Timoshenko SP and Gere JM. 1970. *Theory of Elastic Stability*, 3rd edition. McGraw-Hill, New York.
50. Tham LG and Szeto HY. 1990. Buckling analysis of arbitrary shaped plates by spline finite strip method. *Computers and Structures*; 36: 729–735.
51. Vrcelj Z and Bradford MA. 2008. A simple method for the inclusion of external and internal supports in the spline finite strip method (SFSM) of buckling analysis. *Computers and Structures*; 86: 529–544.
52. Kitipornchai S, Xiang Y, Wang CM, and Liew KM. 1993. Buckling of thick skew plates. *International Journal for Numerical Methods in Engineering*; 36: 1299–1310.
53. Liew KM, Wang J, Ng TY, and Tan MJ. 2004. Free vibration and buckling analyses of shear-deformable plates based on FSDT meshfree method. *Journal of Sound and Vibration*; 276: 997–1017.

54. Azhari M, Hoshdar S, and Bradford MA. 2000. On the use of bubble functions in the local buckling analysis of plate structures by the spline finite strip method. *International Journal for Numerical Methods in Engineering*; 48: 583–593.
55. Robert DB. 1979. *Formulas for Natural Frequency and Mode Shape*. Van Nostrand Reinhold, New York.
56. Gustafson PN, Stokey WF, and Zorowski CF. 1953. An experimental study of natural vibrations of cantilevered triangular plate. *Journal of the Aeronautical Sciences*; 20: 331–337.
57. McGee OG and Butalia TS. 1992. Natural vibrations of shear deformable cantilevered skewed trapezodial and triangular thick plates. *Computers and Structures*; 45: 1033–1059.

13

S-FEM for Piezoelectric Structures

13.1 Introduction

One of the essential features of piezoelectric materials is the capability of converting the energy between mechanical energy and electric energy. Due to this attractive feature, piezoelectric materials are currently widely used in various applications such as sensors, actuators, transducers, and active damping devices for various engineering systems [1–4]. These materials are also used to design "smart" structures in industrial, medical, military, and communication areas (e.g., [2,5]). Because of the outstanding adaptation to complicated geometry, the FEM is currently the most popular numerical tool for analyzing and designing piezoelectric structures [5–12]. Since the work of Ref. [7] for piezoelectric analysis using the FEM, most of the finite element models use displacement and electric potential as primary functions of field variable, and both the functions and their derivatives satisfy fully the compatibility conditions. These elements are, however, often found to be less accurate and sensitive to mesh distortion due to the overestimation or over stiffness of the stiffness matrix. Many techniques have been proposed to improve the standard finite elements such as the bubble/incompatible displacement method, mixed and hybrid formulations [13–18], and formulation of the piezoelectric finite element with drilling DOFs [19–21]. Special types of elements have also been proposed for the analysis of piezoelectric plates [22,23]. Several mesh-free methods [24] have also been used to analyze piezoelectric structures such as the point collocation method (PCM) [25], the PIM [26], and the radial point interpolation method (RPIM) [27,28].

This chapter extends the S-FEM formulation to solids of piezoelectric materials. We start from the derivation of the standard Galerkin weak form from the general formulation of Hamilton's principle for dynamic problems. The standard FEM formulation is then provided. Following the procedure and principles given in Chapter 4 and the standard Galerkin weak form, the smoothed Galerkin weak form is then presented, followed by a general formulation of S-FEM models.

Due to the known excellent property of the "star" performer ES-FEM, it is chosen to conduct a number of static and frequency analyses of piezoelectric structures [29], using three-node triangular elements and hence

the linear shape functions. On top of the triangular mesh, the problem domain is subdivided into a set of smoothing domains associated with edges of triangles. Both the smoothed strains and smoothed electric fields are then obtained by applying the gradient smoothing technique over these edge-based smoothing domains. Because the ES-FEM uses the linear shape functions and the constant smoothed gradient fields, the computation of the stiffness matrix becomes a simple summation over these edge-based smoothing domains. A number of numerical examples are presented to demonstrate the accuracy, stability, and effectiveness of the ES-FEM, and comparisons are made between the ES-FEM results and those of the standard FEM, analytical solutions as well as experimental ones [29].

13.2 Galerkin Weak Form for Piezoelectrics

In this section, a finite element formulation for piezoelectricity is first established based on the standard variational formulation [7,30]. Consider a piezoelectric solid occupying a 2D space with domain Ω bounded by Γ. The following Lagrangian energy functional L is defined as a summation of kinetic energy, strain energy, dielectric energy, and external work within the piezoelectric solid:

$$L = \int_{\Omega} \left[\frac{1}{2}\rho \dot{\mathbf{u}}^T \dot{\mathbf{u}} - \frac{1}{2}\boldsymbol{\varepsilon}^T \boldsymbol{\sigma} + \frac{1}{2}\mathbf{W}^T \mathbf{E} + \mathbf{u}^T \mathbf{b} - \boldsymbol{\varphi}^T \mathbf{q}_s \right] d\Omega + \sum \mathbf{u}^T \mathbf{F}_p - \sum \boldsymbol{\varphi}^T \mathbf{Q}_p, \tag{13.1}$$

where $\mathbf{u}$ and $\dot{\mathbf{u}}$ are the vectors of mechanical displacement and velocity; $\boldsymbol{\varphi}$ denotes the vector of the electric potential field ϕ at points; $\boldsymbol{\sigma}$ and $\boldsymbol{\varepsilon}$ are the vectors of mechanical stress and strain; $\mathbf{W}$ and $\mathbf{E}$ are the vectors of dielectric displacement and electric field; $\mathbf{b}$ and $\mathbf{F}_p$ denote the vectors of the mechanical surface and point loads; and $\mathbf{q}_s$ and $\mathbf{Q}_p$ denote the vectors of surface charges and point charges.

For the linear electroelastic problems, the constitutive equations can be expressed in the following matrix form:

$$\begin{bmatrix} \boldsymbol{\sigma} \\ \mathbf{W} \end{bmatrix} = \begin{bmatrix} \mathbf{c}_{\mathbf{E}} & -\mathbf{e}^T \\ \mathbf{e} & \boldsymbol{\theta}_{\boldsymbol{\varepsilon}} \end{bmatrix} \begin{bmatrix} \boldsymbol{\varepsilon} \\ \mathbf{E} \end{bmatrix}, \tag{13.2}$$

where $\mathbf{c}_{\mathbf{E}}$ denotes the matrix of elastic constants measured at constant electric field; $\boldsymbol{\theta}_{\boldsymbol{\varepsilon}}$ is the matrix of dielectric constants measured at constant mechanical strain; and $\mathbf{e}$ is the piezoelectric matrix.

The strain–displacement relationships are expressed using the usual *compatibility equations*:

$$\boldsymbol{\varepsilon} = \mathbf{L}_d \mathbf{u}. \tag{13.3}$$

The electric field–potential relationships (compatibility equations) for the electrostatic state (compared to the mechanical fields) electric potential field are expressed using

$$\mathbf{E} = -\text{grad}\phi. \tag{13.4}$$

Applying now Hamilton's variational principle, we have

$$\delta \int_{t_1}^{t_2} L \, \mathrm{d}t = 0. \tag{13.5}$$

Using a similar procedure as that given in Ref. [31], performing variational operations, and a little lengthy but simple manipulations, we arrive at the following standard Galerkin weak form for general dynamic problems:

$$\int_{\Omega} \left[\rho \delta \mathbf{u}^T \ddot{\mathbf{u}} + \begin{Bmatrix} \delta\boldsymbol{\varepsilon}^T & \delta\mathbf{E}^T \end{Bmatrix} \begin{bmatrix} \mathbf{c}_\mathbf{E} & -\mathbf{e}^T \\ -\mathbf{e} & -\boldsymbol{\theta}_\boldsymbol{\varepsilon} \end{bmatrix} \begin{Bmatrix} \boldsymbol{\varepsilon} \\ \mathbf{E} \end{Bmatrix} - \delta \mathbf{u}^T \mathbf{b} + \delta \boldsymbol{\varphi}^T \mathbf{q}_s \right] \mathrm{d}\Omega$$
$$- \sum \delta \mathbf{u}^T \mathbf{F}_p + \sum \delta \boldsymbol{\varphi}^T \mathbf{Q}_p = 0. \tag{13.6}$$

When the mechanical field can also be treated as static, we can then drop the mechanical inertial term, which leads to the standard Galerkin weak form for static problems for piezoelectric solids.

$$\int_{\Omega} \left[\begin{Bmatrix} \delta\boldsymbol{\varepsilon}^T & \delta\mathbf{E}^T \end{Bmatrix} \begin{bmatrix} \mathbf{c}_\mathbf{E} & -\mathbf{e}^T \\ -\mathbf{e} & -\boldsymbol{\theta}_\boldsymbol{\varepsilon} \end{bmatrix} \begin{Bmatrix} \boldsymbol{\varepsilon} \\ \mathbf{E} \end{Bmatrix} - \delta \mathbf{u}^T \mathbf{b} + \delta \boldsymbol{\varphi}^T \mathbf{q}_s \right] \mathrm{d}\Omega$$
$$- \sum \delta \mathbf{u}^T \mathbf{F}_p + \sum \delta \boldsymbol{\varphi}^T \mathbf{Q}_p = 0. \tag{13.7}$$

For stability reasons, we require, of course, the SPD property of the material constant matrix $\begin{bmatrix} \mathbf{c}_\mathbf{E} & -\mathbf{e}^T \\ -\mathbf{e} & -\boldsymbol{\theta}_\boldsymbol{\varepsilon} \end{bmatrix}$: the piezoelectric material must be "stable" (see Remark 2.1).

13.3 Finite Element Formulation for the Piezoelectric Problem

In an FEM setting, the problem domain is divided into various types of elements as discussed in Chapter 3. In this chapter, we consider 2D problems,

and the problem domain Ω is discretized into N_e three-node triangular finite elements such that $\Omega = \bigcup_{i=1}^{N_e} \Omega_i^e$ and $\Omega_i^e \cap \Omega_j^e \neq \emptyset$, $i \neq j$. The finite element approximations for the variables of mechanical displacements $\tilde{\mathbf{u}}(\mathbf{x})$ and electric potential $\tilde{\phi}(\mathbf{x})$ can be expressed as

$$\tilde{\mathbf{u}}(\mathbf{x}) = \sum_{I=1}^{N_n} \begin{bmatrix} N_I(\mathbf{x}) & 0 \\ 0 & N_I(\mathbf{x}) \end{bmatrix} \tilde{\mathbf{d}}_I, \quad \tilde{\phi}(\mathbf{x}) = \sum_{I=1}^{N_n} N_I(\mathbf{x}) \tilde{\phi}_I, \tag{13.8}$$

where N_n is the total number of nodes in the problem domains, $\tilde{\mathbf{d}}_I = [\tilde{u}_I \quad \tilde{v}_I]^T$ is the nodal DOFs of $\tilde{\mathbf{u}} = [\tilde{u} \quad \tilde{v}]^T$ associated with node I, and $N_I(\mathbf{x})$ is the linear shape function for node I of a triangular element. Substituting the approximations (Equation 13.8) into Equations 13.3 and 13.4, we obtain the compatible strain field

$$\tilde{\boldsymbol{\varepsilon}} = \mathbf{L}_d \tilde{\mathbf{u}} = \sum_{I=1}^{N_n} \tilde{\mathbf{B}}_I^u \tilde{\mathbf{d}}_I, \tag{13.9}$$

where

$$\tilde{\mathbf{B}}_I^u = \begin{bmatrix} \partial N_I/\partial x & 0 \\ 0 & \partial N_I/\partial y \\ \partial N_I/\partial y & \partial N_I/\partial x \end{bmatrix}. \tag{13.10}$$

The (compatible) electric field becomes

$$\tilde{\mathbf{E}} = -\text{grad}\tilde{\phi} = -\sum_{I=1}^{N_n} \tilde{\mathbf{B}}_I^{\phi} \tilde{\phi}_I, \tag{13.11}$$

where

$$\tilde{\mathbf{B}}_I^{\phi} = \begin{bmatrix} \partial N_I/\partial x \\ \partial N_I/\partial y \end{bmatrix}. \tag{13.12}$$

Using Equations 13.8 and the Galerkin weak form (Equation 13.6), and after a little lengthy but trivial manipulation, we arrive at a system of piezoelectric dynamic equations:

$$\begin{bmatrix} \mathbf{m} & \mathbf{0} \\ \mathbf{0} & \mathbf{0} \end{bmatrix} \begin{Bmatrix} \ddot{\tilde{\mathbf{d}}} \\ \ddot{\tilde{\boldsymbol{\Phi}}} \end{Bmatrix} + \begin{bmatrix} \tilde{\mathbf{k}}^{uu} & \tilde{\mathbf{k}}^{u\phi} \\ \left(\tilde{\mathbf{k}}^{u\phi}\right)^T & -\tilde{\mathbf{k}}^{\phi\phi} \end{bmatrix} \begin{Bmatrix} \tilde{\mathbf{d}} \\ \tilde{\boldsymbol{\Phi}} \end{Bmatrix} = \begin{Bmatrix} \mathbf{F} \\ \mathbf{Q} \end{Bmatrix}, \tag{13.13}$$

where

$$\mathbf{m} = \sum_{i=1}^{N_e} \int_{\Omega_i^e} \rho \left(\mathbf{N}^u\right)^T \mathbf{N}^u \, \mathrm{d}\Omega, \tag{13.14}$$

$$\tilde{\mathbf{k}}^{uu} = \sum_{i=1}^{N_e} \int_{\Omega_i^e} (\tilde{\mathbf{B}}^u)^T \mathbf{c}_E \tilde{\mathbf{B}}^u \, \mathrm{d}\Omega, \tag{13.15}$$

$$\tilde{\mathbf{k}}^{u\phi} = \sum_{i=1}^{N_e} \int_{\Omega_i^e} (\tilde{\mathbf{B}}^u)^T \mathbf{e}^T \tilde{\mathbf{B}}^\phi \, \mathrm{d}\Omega, \tag{13.16}$$

$$\tilde{\mathbf{k}}^{\phi\phi} = \sum_{i=1}^{N_e} \int_{\Omega_i^e} (\tilde{\mathbf{B}}^\phi)^T \boldsymbol{\theta}_{\boldsymbol{\varepsilon}} \tilde{\mathbf{B}}^\phi \, \mathrm{d}\Omega, \tag{13.17}$$

$$\mathbf{F} = \sum_{i=1}^{N_e} \int_{\Omega_i^e} \left(\mathbf{N}^u\right)^T \mathbf{b} \, \mathrm{d}\Omega + \sum_{I \in S_{\mathbf{F}_p}} \mathbf{N}_I^u \mathbf{F}_{pI}, \tag{13.18}$$

$$\mathbf{Q} = -\sum_{i=1}^{N_e} \int_{\Omega_i^e} \left(\mathbf{N}^\phi\right)^T \mathbf{q}_s \, \mathrm{d}\Omega - \sum_{I \in S_{\mathbf{Q}_p}} N_I Q_{pI}. \tag{13.19}$$

In Equation 13.18, $S_{\mathbf{F}_p} = \left\{I, \mathbf{F}_{pI} \neq 0\right\}$ is the set containing nodes in which the mechanical point load $\mathbf{F}_{pI} \neq 0$. In Equation 13.19, $S_{\mathbf{Q}_p} = \left\{I, Q_{pI} \neq 0\right\}$ is the set containing nodes in which the point charge $Q_{pI} \neq 0$. These matrices of shape functions have the following form:

$$\mathbf{N}^u = \begin{bmatrix} N_1 & 0 & N_2 & 0 & N_3 & 0 \\ 0 & N_1 & 0 & N_2 & 0 & N_3 \end{bmatrix}, \quad \mathbf{N}^\phi = [N_1 \quad N_2 \quad N_3],$$
$$\mathbf{N}_I^u = \begin{bmatrix} N_I & 0 \\ 0 & N_I \end{bmatrix}. \tag{13.20}$$

The strain–displacement matrix for 2D plane stress/strain problems is given by

$$\tilde{\mathbf{B}}^u = \begin{bmatrix} \partial N_1/\partial x & 0 & \partial N_2/\partial x & 0 & \partial N_3/\partial x & 0 \\ 0 & \partial N_1/\partial y & 0 & \partial N_2/\partial y & 0 & \partial N_3/\partial y \\ \partial N_1/\partial y & \partial N_1/\partial x & \partial N_2/\partial y & \partial N_2/\partial x & \partial N_3/\partial y & \partial N_3/\partial x \end{bmatrix}. \tag{13.21}$$

The electric–potential matrix for 2D plane stress/strain problems has the form of

$$\tilde{\mathbf{B}}^{\phi} = \begin{bmatrix} \partial N_1/\partial x & \partial N_2/\partial x & \partial N_3/\partial x \\ \partial N_1/\partial y & \partial N_2/\partial y & \partial N_3/\partial y \end{bmatrix}. \tag{13.22}$$

For axisymmetric problems, we use

$$\tilde{\mathbf{B}}^{u} = \begin{bmatrix} \dfrac{\partial N_1}{\partial r} & 0 & \dfrac{\partial N_2}{\partial r} & 0 & \dfrac{\partial N_3}{\partial r} & 0 \\ \dfrac{N_1}{r} & 0 & \dfrac{N_2}{r} & 0 & \dfrac{N_3}{r} & 0 \\ 0 & \dfrac{\partial N_1}{\partial z} & 0 & \dfrac{\partial N_2}{\partial z} & 0 & \dfrac{\partial N_3}{\partial z} \\ \frac{\partial N_1}{\partial z} & \dfrac{\partial N_1}{\partial r} & \dfrac{\partial N_2}{\partial z} & \dfrac{\partial N_2}{\partial r} & \dfrac{\partial N_3}{\partial z} & \dfrac{\partial N_3}{\partial r} \end{bmatrix}, \quad \tilde{\mathbf{B}}^{\phi} = \begin{bmatrix} \dfrac{\partial N_1}{\partial r} & \dfrac{\partial N_2}{\partial r} & \dfrac{\partial N_3}{\partial r} \\ \dfrac{N_1}{r} & \dfrac{N_2}{r} & \dfrac{N_3}{r} \\ \dfrac{\partial N_1}{\partial z} & \dfrac{\partial N_2}{\partial z} & \dfrac{\partial N_3}{\partial z} \end{bmatrix}. \tag{13.23}$$

For convenience (not very rigorous), matrices $\tilde{\mathbf{B}}^{u}$ and $\tilde{\mathbf{B}}^{\phi}$ are called the "gradient matrix." For static problems, we have

$$\begin{bmatrix} \tilde{\mathbf{k}}^{uu} & \tilde{\mathbf{k}}^{u\phi} \\ \left(\tilde{\mathbf{k}}^{u\phi}\right)^{T} & -\tilde{\mathbf{k}}^{\phi\phi} \end{bmatrix} \begin{Bmatrix} \tilde{\mathbf{d}} \\ \tilde{\mathbf{\Phi}} \end{Bmatrix} = \begin{Bmatrix} \mathbf{F} \\ \mathbf{Q} \end{Bmatrix}. \tag{13.24}$$

13.4 S-FEM for the Piezoelectric Problem

The above equations are the basic formulae for the analyses of piezoelectric solids using the standard FEM, which offer a base for our formulation of the S-FEM models. An S-FEM model uses also a mesh of elements, but with its unique way of evaluating the potential energy in the piezoelectric solid. When three-node triangular elements are used, the shape functions used in the S-FEM are identical to those used in the FEM. Therefore, the mechanical displacement field and the electric potential field in the S-FEM are also piecewise linear and continuous over the whole problem domain. The differences will be the gradient (strain and electric) fields used in evaluating the energy potentials: in the FEM we use the compatible strain and electric fields, but in the S-FEM we use the smoothed strain and electric fields. In addition, we use the smoothed Galerkin weak form.

13.4.1 Smoothed Galerkin Weak Form for Piezoelectrics

Following the procedure discussed in Chapter 4, and using the standard Galerkin weak form given in Equation 13.6, the smoothed Galerkin weak form for piezoelectric solids can be simply written as

$$\sum_{i=1}^{N_s} A_i^s \begin{Bmatrix} \delta\bar{\boldsymbol{\varepsilon}}_i^T & \delta\bar{\mathbf{E}}_i^T \end{Bmatrix} \begin{bmatrix} \mathbf{c_E} & -\mathbf{e}^T \\ -\mathbf{e} & -\boldsymbol{\theta}_{\boldsymbol{\varepsilon}} \end{bmatrix} \begin{Bmatrix} \bar{\boldsymbol{\varepsilon}}_i \\ \bar{\mathbf{E}}_i \end{Bmatrix} + \int_{\Omega} \left[\rho \delta \mathbf{u}^T \ddot{\mathbf{u}} - \delta \mathbf{u}^T \mathbf{b} + \delta \boldsymbol{\varphi}^T \mathbf{q}_s \right] \mathrm{d}\Omega$$
$$- \sum \delta \mathbf{u}^T \mathbf{F}_p + \sum \delta \boldsymbol{\varphi}^T \mathbf{Q}_p = 0. \tag{13.25}$$

The smoothed strains and smoothed electric fields used in the foregoing equation must be obtained by following the same principles as given in Chapter 4 with at least the minimum number of linear independent smoothing domains to ensure the stability and convergence of the smoothed Galerkin weak formulation. Therefore, we can have various S-FEM models such as CS-FEM, NS-FEM, ES-FEM, and even αFEM, as discussed in earlier chapters. For mechanically static problems, we simply drop the inertial term and have the following smoothed Galerkin weak form for piezoelectric solids.

$$\sum_{i=1}^{N_s} A_i^s \begin{Bmatrix} \delta\bar{\boldsymbol{\varepsilon}}_i^T & \delta\bar{\mathbf{E}}_i^T \end{Bmatrix} \begin{bmatrix} \mathbf{c_E} & -\mathbf{e}^T \\ -\mathbf{e} & -\boldsymbol{\theta}_{\boldsymbol{\varepsilon}} \end{bmatrix} \begin{Bmatrix} \bar{\boldsymbol{\varepsilon}}_i \\ \bar{\mathbf{E}}_i \end{Bmatrix} + \int_{\Omega} \left[-\delta \mathbf{u}^T \mathbf{b} + \delta \boldsymbol{\varphi}^T \mathbf{q}_s \right] \mathrm{d}\Omega$$
$$- \sum \delta \mathbf{u}^T \mathbf{F}_p + \sum \delta \boldsymbol{\varphi}^T \mathbf{Q}_p = 0. \tag{13.26}$$

13.4.2 Smoothed Mechanical Strain and Electric Fields

Using a set of properly formed smoothing domains, the smoothed strains and smoothed electric fields over the kth smoothing domain Ω_k^s are assumed to be constants and are evaluated using, respectively, the following equations (for 2D plane stress/strain problems):

$$\bar{\boldsymbol{\varepsilon}}_k = \frac{1}{A_k^s} \int_{\Omega_k^s} \tilde{\boldsymbol{\varepsilon}}(\mathbf{x})\, \mathrm{d}\Omega = \frac{1}{A_k^s} \int_{\Omega_k^s} \mathbf{L}_d \tilde{\mathbf{u}}(\mathbf{x})\, \mathrm{d}\Omega = \frac{1}{A_k^s} \int_{\Gamma_k^s} \mathbf{n}_k^u(\mathbf{x}) \tilde{\mathbf{u}}(\mathbf{x})\, \mathrm{d}\Gamma, \tag{13.27}$$

$$\bar{\mathbf{E}}_k = \frac{1}{A_k^s} \int_{\Omega_k^s} \tilde{\mathbf{E}}(\mathbf{x})\, \mathrm{d}\Omega = -\frac{1}{A_k^s} \int_{\Omega_k^s} \mathrm{grad}\tilde{\phi}(\mathbf{x})\, \mathrm{d}\Omega = -\frac{1}{A_k^s} \int_{\Gamma_k^s} \mathbf{n}_k^{\phi}(\mathbf{x}) \tilde{\phi}(\mathbf{x})\, \mathrm{d}\Gamma, \tag{13.28}$$

where A_k^s is the area of the smoothing domain Ω_k^s; Γ_k^s is the boundary of the smoothing domain Ω_k^s; and $\mathbf{n}_k^u$ and $\mathbf{n}_k^{\phi}$ are the matrices of outward normal

components on the boundary Γ_k^s defined by

$$\mathbf{n}_k^u(\mathbf{x}) = \begin{bmatrix} n_{kx}^s & 0 \\ 0 & n_{ky}^s \\ n_{ky}^s & n_{kx}^s \end{bmatrix}, \quad \mathbf{n}_k^\phi(\mathbf{x}) = \begin{bmatrix} n_{kx}^s & n_{ky}^s \end{bmatrix}^T, \tag{13.29}$$

in which n_{kx}^s and n_{ky}^s are two components in the x- and y-directions of the outward normal vector on the boundary Γ_k^s.

Using the smoothed strains, the vectors of the smoothed mechanical stresses $\bar{\boldsymbol{\sigma}}$ and the smoothed dielectric displacements $\bar{\mathbf{W}}$ for the S-FEM can be expressed as

$$\begin{bmatrix} \bar{\boldsymbol{\sigma}} \\ \bar{\mathbf{W}} \end{bmatrix} = \begin{bmatrix} \mathbf{c}_E & -\mathbf{e}^T \\ \mathbf{e} & \boldsymbol{\theta}_{\boldsymbol{\varepsilon}} \end{bmatrix} \begin{bmatrix} \bar{\boldsymbol{\varepsilon}} \\ \bar{\mathbf{E}} \end{bmatrix}. \tag{13.30}$$

13.4.3 Smoothed Stiffness Matrices Using the S-FEM

The smoothed strain (Equation 13.27) and the smoothed electric field (Equation 13.28) in the smoothing domain Ω_k^s can be written in terms of the "smoothed gradient matrices" and vectors of discrete nodal variables:

$$\bar{\boldsymbol{\varepsilon}}_k = \frac{1}{A_k^s} \int_{\Gamma_k^s} \mathbf{n}_k^u \, \tilde{\mathbf{u}}(\mathbf{x}) \, \mathrm{d}\Gamma = \sum_{I \in S_k^s} \bar{\mathbf{B}}_I^u(\mathbf{x}_k) \bar{\mathbf{d}}_I, \tag{13.31}$$

$$\bar{\mathbf{E}}_k = -\frac{1}{A_k^s} \int_{\Gamma_k^s} \mathbf{n}_k^\phi(\mathbf{x}) \tilde{\phi}(\mathbf{x}) \, \mathrm{d}\Gamma = -\sum_{I \in S_k^s} \bar{\mathbf{B}}_I^\phi(\mathbf{x}_k) \bar{\phi}_I, \tag{13.32}$$

where S_k^s is the set of nodes in all the elements associated with the smoothing domain Ω_k^s; $\bar{\mathbf{B}}_I^u(\mathbf{x}_k)$ and $\bar{\mathbf{B}}_I^\phi(\mathbf{x}_k)$ are termed the smoothed strain–displacement and electric gradient–potential matrices for the smoothing domain Ω_k^s. For convenience (not very rigorous), matrices $\bar{\mathbf{B}}^u$ and $\bar{\mathbf{B}}^\phi$ are called "smoothed gradient matrix."

As presented in earlier chapters, there are two ways of computing smoothed gradient matrices for the S-FEM using three-node triangular elements. In the first and *general* way, the integration along the boundary of smoothing domains and the values of shape functions is directly used, which works for general n-sided polygonal elements including linear triangular elements. In this case, we do not need to evaluate the compatible strain–displacement and electric gradient–potential matrices. In the second *particular* way, the smoothed gradient matrices are the area-weighted average of the compatible strain–displacement and electric gradient–potential

matrices of elements sharing the smoothing domain. In this case, we need to evaluate the compatible strain–displacement and electric gradient–potential matrices, and hence it only works for elements such as the linear triangular elements whose compatible strain–displacement and electric gradient–potential matrices are readily and cheaply available. Here, we summarize the two ways.

In the first way, the smoothed gradient matrices $\bar{\mathbf{B}}_I^u(\mathbf{x}_k)$ and $\bar{\mathbf{B}}_I^\phi(\mathbf{x}_k)$ for 2D plane stress/strain problems are computed by

$$\bar{\mathbf{B}}_I^u(\mathbf{x}_k) = \frac{1}{A_k^s}\begin{bmatrix} \int_{\Gamma_k^s} N_I(\mathbf{x}) n_{kx}^s \, \mathrm{d}\Gamma & 0 \\ 0 & \int_{\Gamma_k^s} N_I(\mathbf{x}) n_{ky}^s \, \mathrm{d}\Gamma \\ \int_{\Gamma_k^s} N_I(\mathbf{x}) n_{ky}^s \, \mathrm{d}\Gamma & \int_{\Gamma_k^s} N_I(\mathbf{x}) n_{kx}^s \, \mathrm{d}\Gamma \end{bmatrix}, \tag{13.33}$$

$$\bar{\mathbf{B}}_I^\phi(\mathbf{x}_k) = \frac{1}{A_k^s}\begin{bmatrix} \int_{\Gamma_k^s} N_I(\mathbf{x}) n_{kx}^s \, \mathrm{d}\Gamma \\ \int_{\Gamma_k^s} N_I(\mathbf{x}) n_{ky}^s \, \mathrm{d}\Gamma \end{bmatrix}. \tag{13.34}$$

Using the linear shape function of triangles as in the FEM, the displacement field in the S-FEM is linearly compatible along the boundary Γ_k^s. Therefore, one Gaussian point is sufficient for the accurate line integration along each segment of boundary $\Gamma_{k,p}^s \in \Gamma_k^s$. Hence Equations 13.33 and 13.34 can be further simplified to summation forms

$$\bar{\mathbf{B}}_I^u(\mathbf{x}_k) = \frac{1}{A_k^s}\sum_{p=1}^{n_\Gamma^s}\begin{bmatrix} N_I(\mathbf{x}_p^G) n_{kx,p}^s(\mathbf{x}_p^G) & 0 \\ 0 & N_I(\mathbf{x}_p^G) n_{ky,p}^s(\mathbf{x}_p^G) \\ N_I(\mathbf{x}_p^G) n_{ky,p}^s(\mathbf{x}_p^G) & N_I(\mathbf{x}_p^G) n_{kx,p}^s(\mathbf{x}_p^G) \end{bmatrix} l_{k,p}^s, \tag{13.35}$$

$$\bar{\mathbf{B}}_I^\phi(\mathbf{x}_k) = \frac{1}{A_k^s}\sum_{p=1}^{n_\Gamma^s}\begin{bmatrix} N_I(\mathbf{x}_p^G) n_{kx,p}^s(\mathbf{x}_p^G) \\ N_I(\mathbf{x}_p^G) n_{ky,p}^s(\mathbf{x}_p^G) \end{bmatrix} l_{k,p}^s, \tag{13.36}$$

where $\mathbf{x}_p^G$ and $l_{k,p}^s$ are the midpoint (Gauss point) and the length of the smoothing domain boundary segment $\Gamma_{k,p}^s \in \Gamma_k^s$, respectively; n_Γ^s is the total number of boundary segments of Γ_k^s (e.g., $n_\Gamma^s = 3$(*AB*, *BI*, *IA*) for boundary edge *m* and $n_\Gamma^s = 4$(*FO*, *OD*, *DH*, *HF*) for inner edge *k* as shown in Figure 7.2).

Equations 13.35 and 13.36 show clearly that no derivative of shape functions is used in computing the gradients and only the shape function values at some particular points along segments of the smoothing domain boundary are required.

For axisymmetric problems, the smoothed strain–displacement and electric gradient–potential matrices are computed, respectively, using

$$\bar{\mathbf{B}}_I^u(\mathbf{x}_k) = \begin{bmatrix} \dfrac{1}{A_k^s}\displaystyle\sum_{p=1}^{n_\Gamma^s} N_I(\mathbf{x}_p^G) n_{kr,p}^s(\mathbf{x}_p^G) l_{k,p}^s & 0 \\ \dfrac{1}{r_k^s}\dfrac{\sum_{p=1}^{n_\Gamma^s} N_I(\mathbf{x}_p^G)}{n_\Gamma^s} & 0 \\ 0 & \dfrac{1}{A_k^s}\displaystyle\sum_{p=1}^{n_\Gamma^s} N_I(\mathbf{x}_p^G) n_{kz,p}^s(\mathbf{x}_p^G) l_{k,p}^s \\ \dfrac{1}{A_k^s}\displaystyle\sum_{p=1}^{n_\Gamma^s} N_I(\mathbf{x}_p^G) n_{kz,p}^s(\mathbf{x}_p^G) l_{k,p}^s & \dfrac{1}{A_k^s}\displaystyle\sum_{p=1}^{n_\Gamma^s} N_I(\mathbf{x}_p^G) n_{kr,p}^s(\mathbf{x}_p^G) l_{k,p}^s \end{bmatrix}, \tag{13.37}$$

$$\bar{\mathbf{B}}_I^\phi(\mathbf{x}_k) = \begin{bmatrix} \dfrac{1}{A_k^s}\displaystyle\sum_{p=1}^{n_\Gamma^s} N_I(\mathbf{x}_p^G) n_{kr,p}^s(\mathbf{x}_p^G) l_{k,p}^s \\ \dfrac{1}{r_k^s}\dfrac{\sum_{p=1}^{n_\Gamma^s} N_I(\mathbf{x}_p^G)}{n_\Gamma^s} \\ \dfrac{1}{A_k^s}\displaystyle\sum_{p=1}^{n_\Gamma^s} N_I(\mathbf{x}_p^G) n_{kz,p}^s(\mathbf{x}_p^G) l_{k,p}^s \end{bmatrix}, \tag{13.38}$$

where r_k^s is determined at the central point of the kth smoothing domain (which can be the kth node in NS-FEM, the center of the kth cell in CS-FEM, and the midpoint of the kth edge in ES-FEM).

In the second way of area-weighted average, $\bar{\mathbf{B}}_I^u(\mathbf{x}_k)$ and $\bar{\mathbf{B}}_I^\phi(\mathbf{x}_k)$ are calculated simply by an assembly process similarly to the case of FEM:

$$\bar{\mathbf{B}}_I^u(\mathbf{x}_k) = \frac{1}{A_k^s}\sum_{j=1}^{n_k^e}\frac{1}{3}A_j^e\tilde{\mathbf{B}}_j^u, \quad \bar{\mathbf{B}}_I^\phi(\mathbf{x}_k) = \frac{1}{A_k^s}\sum_{j=1}^{n_k^e}\frac{1}{3}A_j^e\tilde{\mathbf{B}}_j^\phi, \tag{13.39}$$

where n_k^e is the number of elements sharing the smoothing domain Ω_k^s (e.g., in an ES-FEM setting, $n_k^e = 1$ for the boundary edges, and $n_k^e = 2$ for inner edges as shown in Figure 7.2); $\tilde{\mathbf{B}}_j^u$ and $\tilde{\mathbf{B}}_j^\phi$ are constant gradient matrices of the jth element sharing the smoothing domain Ω_k^s. Note that the matrices in Equation 13.39 are directly constructed from the area and the

usual "compatible" gradient matrices of the standard FEM using triangular elements.

Once the smoothed gradient matrices $\bar{\mathbf{B}}_I^u(\mathbf{x}_k)$ and $\bar{\mathbf{B}}_I^\phi(\mathbf{x}_k)$ are computed, the discrete system of equations for S-FEM is obtained using the smoothed Galerkin weak form (Equation 13.25):

$$\begin{bmatrix} \mathbf{m} & \mathbf{0} \\ \mathbf{0} & \mathbf{0} \end{bmatrix} \begin{Bmatrix} \ddot{\mathbf{d}} \\ \ddot{\boldsymbol{\Phi}} \end{Bmatrix} + \begin{bmatrix} \bar{\mathbf{k}}^{uu} & \bar{\mathbf{k}}^{u\phi} \\ (\bar{\mathbf{k}}^{u\phi})^T & -\bar{\mathbf{k}}^{\phi\phi} \end{bmatrix} \begin{Bmatrix} \bar{\mathbf{d}} \\ \bar{\boldsymbol{\Phi}} \end{Bmatrix} = \begin{Bmatrix} \mathbf{F} \\ \mathbf{Q} \end{Bmatrix}, \tag{13.40}$$

where

$$\bar{\mathbf{k}}^{uu} = \sum_{k=1}^{N_{eg}} \int_{\Omega_k^s} \left(\bar{\mathbf{B}}_k^u\right)^T \mathbf{c}_E \bar{\mathbf{B}}_k^u \, \mathrm{d}\Omega = \sum_{k=1}^{N_{ed}} \left(\bar{\mathbf{B}}_k^u\right)^T \mathbf{c}_E \bar{\mathbf{B}}_k^u A_k^s, \tag{13.41}$$

$$\bar{\mathbf{k}}^{u\phi} = \sum_{k=1}^{N_{eg}} \int_{\Omega_k^s} \left(\bar{\mathbf{B}}_k^u\right)^T \mathbf{e}^T \bar{\mathbf{B}}_k^\phi \, \mathrm{d}\Omega = \sum_{k=1}^{N_{ed}} \left(\bar{\mathbf{B}}_k^u\right)^T \mathbf{e}^T \bar{\mathbf{B}}_k^\phi A_k^s, \tag{13.42}$$

$$\bar{\mathbf{k}}^{\phi\phi} = \sum_{k=1}^{N_{eg}} \int_{\Omega_k^s} \left(\bar{\mathbf{B}}_k^\phi\right)^T \boldsymbol{\theta}_{\boldsymbol{\varepsilon}} \bar{\mathbf{B}}_k^\phi \, \mathrm{d}\Omega = \sum_{k=1}^{N_{ed}} \left(\bar{\mathbf{B}}_k^\phi\right)^T \boldsymbol{\theta}_{\boldsymbol{\varepsilon}} \bar{\mathbf{B}}_k^\phi A_k^s. \tag{13.43}$$

Equations 13.41 through 13.43 provide a simple way of computing the stiffness matrices for the smoothing domains. Finally, we note that the trial functions $\tilde{\mathbf{u}}(\mathbf{x})$, $\tilde{\phi}(\mathbf{x})$ are the same as those given in Equation 13.8, and thus force vectors $\mathbf{F}$, $\mathbf{Q}$, and mass matrix $\mathbf{m}$ in the S-FEM are also computed in the same way as in the FEM. In other words, S-FEM changes only the stiffness matrices. For static problems, we shall have

$$\begin{bmatrix} \bar{\mathbf{k}}^{uu} & \bar{\mathbf{k}}^{u\phi} \\ \left(\bar{\mathbf{k}}^{u\phi}\right)^T & -\bar{\mathbf{k}}^{\phi\phi} \end{bmatrix} \begin{Bmatrix} \bar{\mathbf{d}} \\ \bar{\boldsymbol{\Phi}} \end{Bmatrix} = \begin{Bmatrix} \mathbf{F} \\ \mathbf{Q} \end{Bmatrix}. \tag{13.44}$$

13.5 Numerical Results

A 2D code has been developed based on the above-derived equations. In this section, benchmark problems are examined for piezoelectrics using the ES-FEM models that are established using the formulation given in

Section 13.4, but with smoothing domains created based on the edges of meshes of triangular elements (ES-FEM-T3). The ES-FEM is chosen because of its excellent stability (both spatially and temporally) and accuracy for various problems tested in earlier chapters. For comparison, other available elements are also used in the examination. All these elements used are denoted as follows:

- FEM-Q4—the standard four-node quadrilateral element of bilinear shape function using 2×2 Gauss points
- FEM-T3—the standard three-node element with linear shape function
- ES-FEM-T3—the ES-FEM [32] using linear triangular elements

PVDF, PZT4, and PZT5 materials are used and their features are referred to by

- PZT4 [15]

$c_{11} = 139 \times 10^3$, c_{33}= 113×10^3, c_{13}= 74.3×10^3, c_{55}= $25.6 \times 10^3 (\mathrm{N/mm^2})$,

$e_{15} = 13.44 \times 10^6$, $e_{31} = -6.98 \times 10^6$, $e_{33} = 13.84 \times 10^6 (\mathrm{pC/mm^2})$,

$\theta_{11} = 6.00 \times 10^9$, θ_{33}= $5.47 \times 10^9 (\mathrm{pC/GVmm})$.

- PVDF [25]

$$c_{11} = 2.18 \times 10^{-3},\ c_{13} = 6.33 \times 10^{-4},\ c_{33} = 2.18 \times 10^{-3},$$
$$c_{55} = 7.75 \times 10^{-4} (\mathrm{N/\mu m^2}),$$
$$e_{31} = e_{33} = 4.6 \times 10^{-8} (\mathrm{N/V\mu m}),$$
$$\theta_{11} = \theta_{33} = 1.062 \times 10^{-10} (\mathrm{N/V^2}).$$

- PZT5 [25]

$$s_{11} = 16.4 \times 10^{-6},\ s_{13} = -7.22 \times 10^{-6},\ s_{33} = 18.8 \times 10^{-6},$$
$$s_{55} = 47.5 \times 10^{-6} (\mathrm{mm^2}/N),$$
$$d_{31} = -172 \times 10^{-9},\ d_{33} = 374 \times 10^{-9},\ d_{15} = 584 \times 10^{-9} (\mathrm{mm/V}),$$
$$\psi_{11} = 1.53105 \times 10^{-8},\ \psi_{33} = 1.505 \times 10^{-7} (\mathrm{N/V^2}).$$

The constant matrices $\mathbf{c}_E$, $\mathbf{e}$, and $\boldsymbol{\theta}_{\boldsymbol{\varepsilon}}$ are used for the following cases:
Plane problems:

$$\begin{bmatrix} \mathbf{c}_E & -\mathbf{e}^T \\ \mathbf{e} & \boldsymbol{\theta}_{\boldsymbol{\varepsilon}} \end{bmatrix} = \begin{bmatrix} c_{11} & c_{13} & 0 & 0 & -e_{31} \\ c_{13} & c_{33} & 0 & 0 & -e_{33} \\ 0 & 0 & c_{55} & -e_{15} & 0 \\ 0 & 0 & e_{15} & \theta_{11} & 0 \\ e_{31} & e_{33} & 0 & 0 & \theta_{33} \end{bmatrix}. \tag{13.45}$$

Axisymmetric problems:

$$\begin{bmatrix} \mathbf{c}_E & -\mathbf{e}^T \\ \mathbf{e} & \boldsymbol{\theta}_{\boldsymbol{\varepsilon}} \end{bmatrix} = \begin{bmatrix} c_{11} & c_{12} & c_{13} & 0 & 0 & -e_{31} \\ c_{12} & c_{11} & c_{13} & 0 & 0 & -e_{31} \\ c_{13} & c_{13} & c_{33} & 0 & 0 & -e_{33} \\ 0 & 0 & 0 & c_{44} & -e_{24} & 0 \\ 0 & 0 & 0 & e_{24} & \theta_{22} & 0 \\ e_{31} & e_{31} & e_{33} & 0 & 0 & \theta_{33} \end{bmatrix}. \tag{13.46}$$

The following relations [15] are more convenient to use:

$$\begin{bmatrix} s_{11} & s_{13} & g_{31} \\ s_{13} & s_{33} & g_{33} \\ g_{31} & g_{33} & -f_{33} \end{bmatrix} = \begin{bmatrix} c_{11} & c_{13} & e_{31} \\ c_{13} & c_{33} & e_{33} \\ e_{31} & e_{33} & -\theta_{33} \end{bmatrix}^{-1} \tag{13.47}$$

and

$$\mathbf{d} = \mathbf{e}\mathbf{c}_E^{-1}, \quad \boldsymbol{\theta}_{\boldsymbol{\sigma}} = \begin{bmatrix} \psi_{11} & 0 \\ 0 & \psi_{33} \end{bmatrix}, \quad \boldsymbol{\theta}_{\boldsymbol{\varepsilon}} = \boldsymbol{\theta}_{\boldsymbol{\sigma}} - \mathbf{e}\mathbf{c}_E^{-1}\mathbf{e}^T. \tag{13.48}$$

Example 13.5.1: Eigenvalues and Rank of the Stiffness Matrix

Using the 2D code, it is easy to verify that the ES-FEM-T3 model contains only four zero eigenvalues including the three rigid body modes corresponding to the mechanical movements and one zero eigenvalue of the constant potential field. Hence an ES-FEM-T3 model always has a sufficient rank and no spurious zero-energy modes, as long as a set of proper essential boundary conditions is imposed for the piezoelectric solid. This implies that the ES-FEM-T3 model is at least spatially stable (see Remark 1.2).

Example 13.5.2: Patch Test

The standard patch test considers a patch with linear primary field variables (both mechanical and electric displacements) specified along all the edges of the patch of the piezoelectric solid. Passing the patch test requires that a

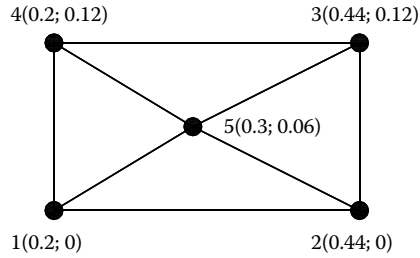

FIGURE 13.1 Standard patch for piezoelectrics.

constant distribution of all quantities for the derivatives of the primary field variables is reproduced for a mesh with arbitrary internal nodes. For this test, we use the rectangular patch [15] with geometry and mesh shown in Figure 13.1. The PZT4 material is used for this patch test.

The boundary conditions for mechanical displacement and electric potential are assumed to be

$$u = s_{11}\sigma_0 x, \quad v = s_{13}\sigma_0 y, \quad \phi = g_{31}\sigma_0 y, \tag{13.49}$$

where σ_0 is an arbitrary stress parameter. Hence, the exact results in terms of mechanical stresses and the dielectric displacements should be

$$\sigma_{xx} = \sigma_0, \quad \sigma_{xy} = \sigma_{yy} = W_x = W_y = 0. \tag{13.50}$$

It is found from Table 13.1 that all the results produced by ES-FEM-T3 are exactly to machine precision. This implies that ES-FEM-T3 has second-order accuracy, and the errors will be on the terms of second order and above. Together with stability, we know that the ES-FEM-T3 solution will converge to the exact solution when the mesh is refined.

TABLE 13.1

Results of the Standard Patch Test

	Results	
Variable	**Exact**	**ES-FEM-T3**
u	2.3765e−06	2.3765e−06
v	−1.8188e−07	−1.8188e−07
ϕ	−1.0667e−09	−1.0667e−09
σ_{xx}	1.0	1.0
σ_{yy}	0	−3.7609e−15
σ_{xy}	0	−1.2924e−16
W_x	0	−6.0396e−14
W_y	0	3.6593e−13

Example 13.5.3: Singer-Player Piezoelectric Strip

This example examines the accuracy of ES-FEM-T3 under both mechanical loading and electric potential boundary conditions. This problem was studied previously in Ref. [25] for the performance of a so-called meshless PCM. We consider here the shear deformation of a 1×1 mm piezoelectric strip under the compressive stress $\sigma_0 = 5N/mm^2$ and an applied voltage $V_0 = 1000$ V, as shown in Figure 13.2. The material PZT-5 is used for this problem. The electric field is applied on the left and right edges in order to create the polarization of the material resulting in shear strain. The mechanical and electrical boundary conditions are prescribed to the edges of the strip as follows:

$$\begin{aligned}
&\frac{\partial \phi}{\partial y}(x, y = \pm h) = 0, \quad \sigma_{yy}(x, y = \pm h) = \sigma_0, \quad \sigma_{xy}(x = L, y) = 0,\\
&\sigma_{xy}(x, y = \pm h) = 0, \quad \phi(x = L, y) = -V_0, \quad \sigma_{xx}(x = L, y) = 0,\\
&\phi(x = 0, y) = +V_0, \quad u(x = 0, y) = 0, \quad v(x = 0, y = 0) = 0.
\end{aligned} \tag{13.51}$$

The analytical solution for this simple problem can be found easily and has been given in Ref. [25]:

$$u = s_{13}\sigma_0 x, \quad v = \frac{d_{15}V_0 x}{h} + s_{33}\sigma_0 y, \quad \phi = V_0\left(1 - 2\frac{x}{L}\right). \tag{13.52}$$

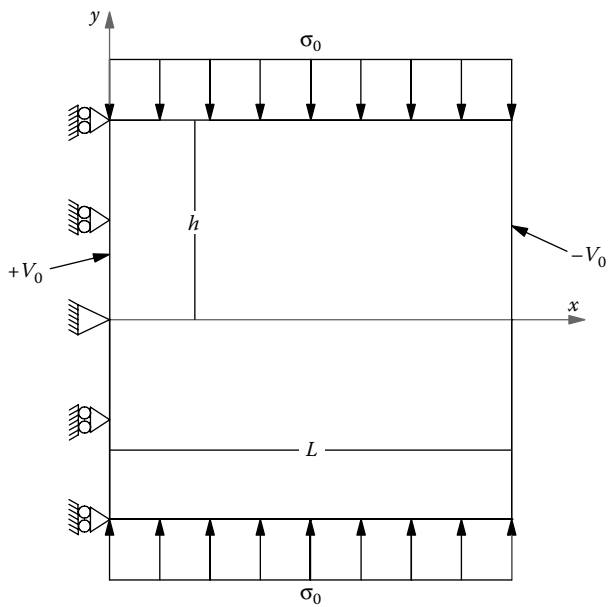

FIGURE 13.2 Piezostrip subjected to a uniform mechanical loading and electric voltage.

Using ES-FEM-T3, the computed results of the horizontal displacement u, the vertical displacement v, and the electric potential ϕ at the central line ($y = 0$) are plotted in Figure 13.3. It is seen that the results of ES-FEM-T3 agree well with the exact solutions. This confirms again that ES-FEM-T3 can reproduce linear fields and hence is of second-order accuracy.

Example 13.5.4: Cook's Membrane

This benchmark problem, shown in Figure 13.4, refers to a clamped tapered panel subjected to a distributed load on the tip edge of the panel, resulting in a deformation dominated by bending. The PZT4 material is used in this case. The mechanical boundary conditions are similar to the popular Cook's membrane [33]. The boundary condition of the lower surface is prescribed with zero voltage. The analytical solution of the problem is unknown, and hence the reference solutions of the vertical displacement and the electric potential at the center tip (A), 2.109×10^{-4} mm and 1.732×10^{-8} GV [21], are used for comparison.

The convergences of the vertical displacement and electric potential at point A are illustrated in Figure 13.5. It is shown that the results of ES-FEM-T3 are much more accurate than those of FEM-T3 and FEM-Q4.

On the computational efficiency of the present method (computational time for the same accuracy measured in displacement or electric potential errors), a study is carried out in comparison with the FEM models. The code is run on a PC with Intel® Core™ 2 Duo (CPU—2 GHz and RAM—2 GB), using the full matrix solver. The computational cost consists of two items: overhead CPU time for setting up the global stiffness matrix and the CPU time to solve the algebraic system of equations. Figure 13.6 illustrates the errors in vertical displacement and electric potential at point A against the total CPU time (seconds) for Cook's membrane problem. It is observed that the "overhead" computation time (observed from a very small model and hence small CPU time) of ES-FEM-T3 is a little longer than those of FEM-Q4 and FEM-T3, due to the additional time to compute the global stiffness matrix. However, for larger models where the solver time dominates, ES-FEM-T3 is more effective. More details of the computational efficiency of ES-FEM-T3 can be found in Chapter 7. More thorough studies using bandwidth solvers for solid mechanics problems can be found in Ref. [24].

Example 13.5.5: Light Reflector: An MEMs Device

The purpose of this problem is to simulate the tilt angle of the reflected light by a mirror of an MEM device. The device consists of two parallel bimorphs made of the same PVDF material and connected by a mirror, as shown in Figure 13.7. Each bimorph is of length $L = 10\,\mu$m and height $H = 1\,\mu$m. The bimorph beam is divided into the top and bottom layers as shown in Figure 13.8.

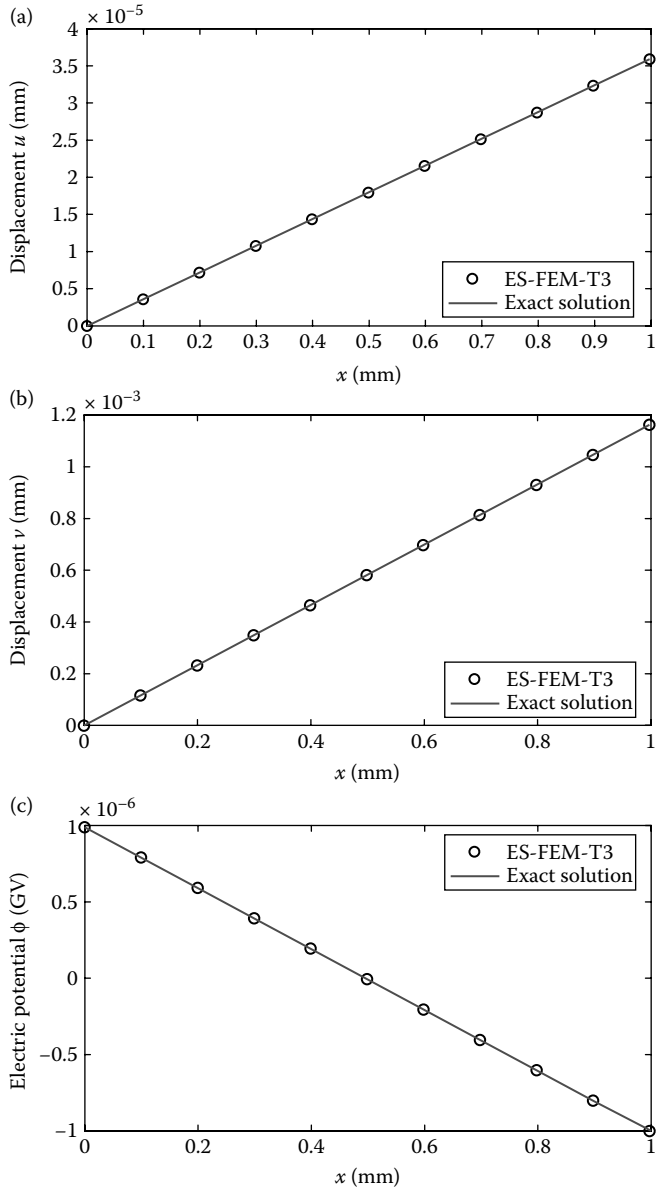

FIGURE 13.3 Results at the central line ($y = 0$) using ES-FEM-T3 for the singer-player piezoelectric strip: (a) horizontal displacement u; (b) vertical displacement v; and (c) electric potential ϕ.

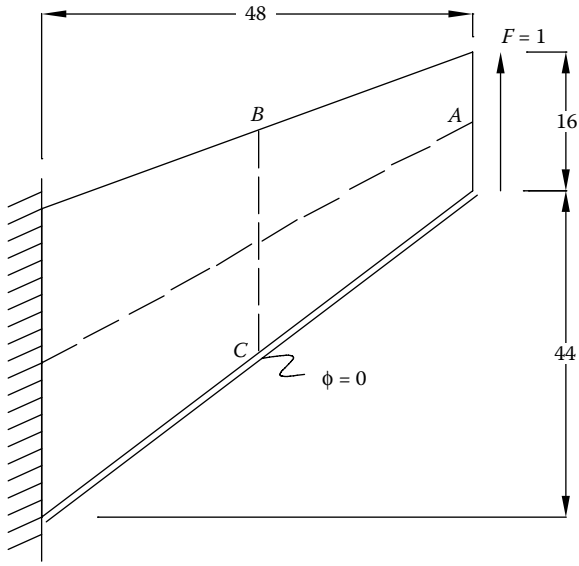

FIGURE 13.4 The setting for Cook's membrane problem.

The following boundary conditions are applied to layer 1 of the bimorph beam:

$$
\begin{aligned}
&\phi^{(1)}(x, y=0) = V, \quad \sigma_{yy}^{(1)}(x, y=0) = 0, \quad \sigma_{xy}^{(1)}(x, y=0) = 0,\\
&\phi^{(1)}(x, y=h) = 0, \quad \sigma_{yy}^{(1)}(x, y=h) = \sigma_{yy}^{(2)}(x, y=h),\\
&\sigma_{xy}^{(1)}(x, y=h) = \sigma_{xy}^{(2)}(x, y=h),\\
&\frac{\partial \phi^{(1)}}{\partial x}(x=0, y) = 0, \quad u^{(1)}(x=0, y) = 0, \quad v^{(1)}(x=0, y) = 0,\\
&\frac{\partial \phi^{(1)}}{\partial x}(x=L, y) = 0, \quad \sigma_{xx}^{(1)}(x=L, y) = 0, \quad \sigma_{xy}^{(1)}(x=L, y) = 0.
\end{aligned}
\tag{13.53}
$$

Boundary conditions for layer 2 are

$$
\begin{aligned}
&\phi^{(2)}(x, y=h) = \phi^{(1)}(x, y=h), \quad u^{(2)}(x, y=h) = u^{(1)}(x, y=h),\\
&v^{(2)}(x, y=h) = v^{(1)}(x, y=h), \qquad \phi^{(2)}(x, y=2h) = V,\\
&\sigma_{yy}^{(2)}(x, y=2h) = 0, \qquad \sigma_{xy}^{(2)}(x, y=2h) = 0,\\
&\frac{\partial \phi^{(2)}}{\partial x}(x=0, y) = 0, \quad u^{(2)}(x=0, y) = 0, \quad v^{(2)}(x=0, y) = 0,\\
&\frac{\partial \phi^{(2)}}{\partial x}(x=L, y) = 0, \quad \sigma_{xx}^{(2)}(x=L, y) = 0, \quad \sigma_{xy}^{(2)}(x=L, y) = 0.
\end{aligned}
\tag{13.54}
$$

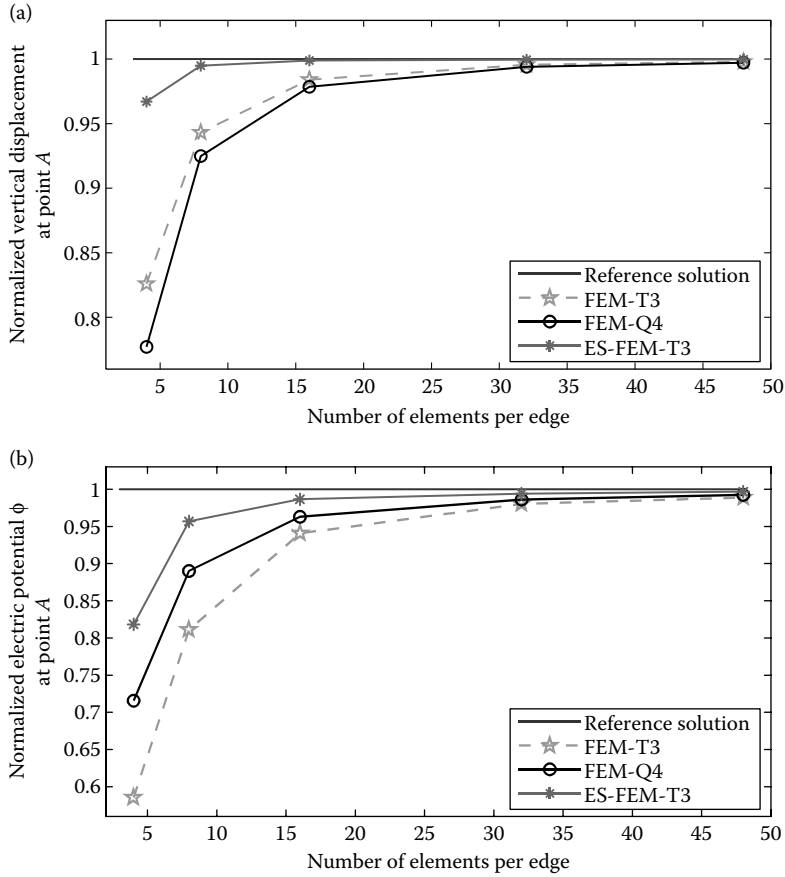

FIGURE 13.5 Convergence of results obtained using ES-FEM-T3 in comparison with other methods for Cook's membrane: (a) vertical displacement and (b) electric potential.

The centers of bimorphs are connected by a 1-μm-long mirror. Linear elastic is assumed for the mirror material. When a voltage is applied, the bimorphs displace vertically in opposite directions and rotate the mirror to achieve a desired tilt angle. As a result, the direction of the reflected light can be changed as desired when a proper voltage is applied.

Note that the analytical solution of this problem is not available; hence the comparison is made with published data. Similarly to the analysis given in Ref. [25], a mesh (80 × 20) of 1701 nodes is used. The tip displacements of the bimorphs using FEM and ES-FEM are computed for several voltages. From the tip displacement, the tilt angle of the mirror is found and compared to the reference result in Ref. [25]. The tilt angle of the mirror could be calculated by normal deflection of the beam at the point connection between the mirror

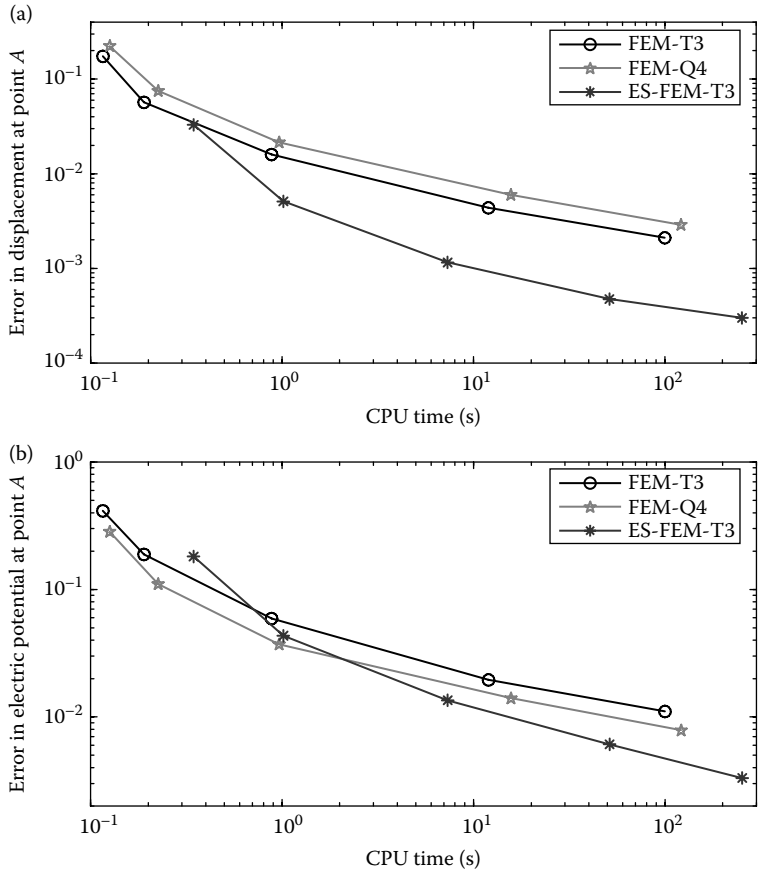

FIGURE 13.6 Computational efficiency of ES-FEM-T3 in comparison with other methods for Cook's membrane: (a) displacement error and (b) electric potential error.

and beam in which the horizontal displacement of this point is supposed to be zero.

The results of FEM-T3, FEM-Q4, and ES-FEM-T3 are given in Table 13.2. The tilt angle is plotted in Figure 13.9. Similarly to the PCM [25], it is

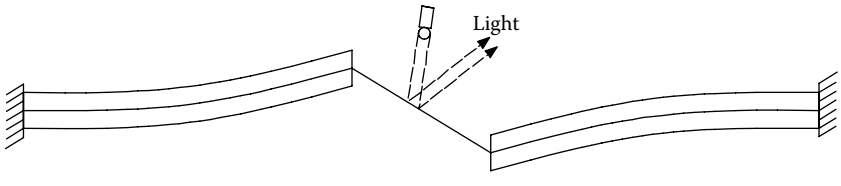

FIGURE 13.7 Bimorph MEM device.

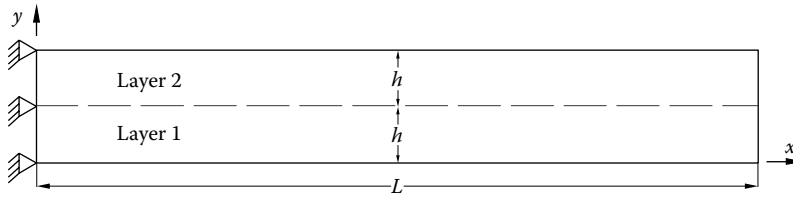

FIGURE 13.8 Geometry of a parallel bimorph.

TABLE 13.2

Results of the Tip Deflections (μm) on the Mirror

Applied Voltage (V)	FEM-T3	FEM-Q4	ES-FEM-T3	Reference [25]
1.00	0.004794	0.004866	0.004808	0.004936
2.00	0.009588	0.009731	0.009614	0.009872
5.00	0.023971	0.024328	0.024034	0.024681
10.00	0.047942	0.048655	0.048068	0.049362
15.00	0.071913	0.072983	0.072102	0.074043
20.00	0.095884	0.097310	0.096136	0.098724
25.00	0.119855	0.121638	0.120169	0.123405
50.00	0.239710	0.243276	0.241339	0.246811

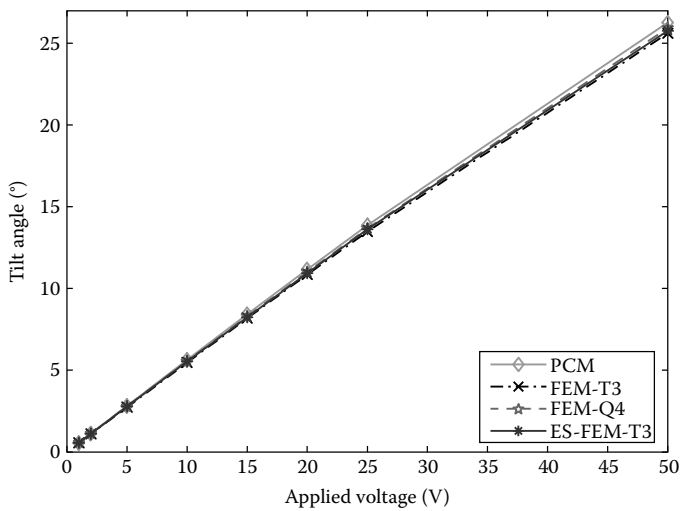

FIGURE 13.9 Results of the tilt angle of the mirror obtained using ES-FEM-T3 in comparison with other methods for the bimorph MEM device.

also found that the tip displacements of the bimorphs and the tilt angle of the mirror for FEM-T3, FEM-Q4, and ES-FEM-T3 models vary almost linearly with applied voltages.

Note that the displacement of ES-FEM-T3 is larger than that of FEM-T3, because the ES-FEM-T3 model is softer than the FEM-T3 model. For this problem, ES-FEM-T3 solutions are slightly "stiffer" than those of FEM-Q4 and PCM, but "softer" than that of FEM-T3.

Example 13.5.6: Eigenvalue Analysis of a Piezoelectric Transducer

This example performs an eigenvalue analysis of a cylindrical transducer using a piezoelectric wall made of PZT4 material with brass end caps, as shown in Figure 13.10. On the inner and outer surfaces, the electrodes are attached. This is the example problem given in Section 6.1.1 of the ABAQUS

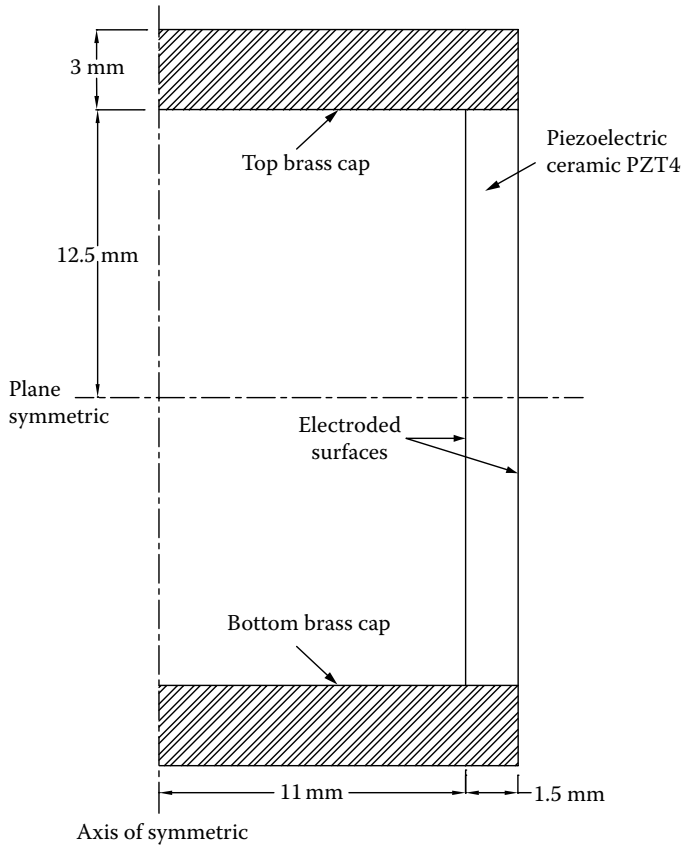

FIGURE 13.10 Configuration of a transducer.

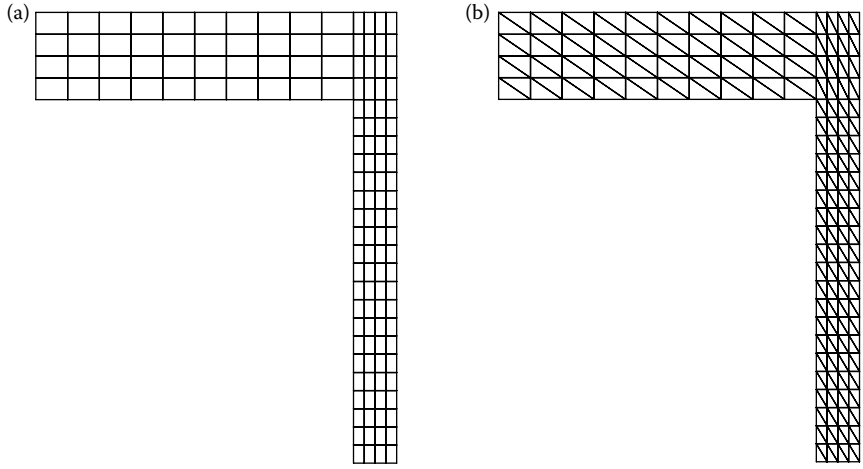

FIGURE 13.11 Domain discretization of the transducer: (a) using 136 rectangular elements and (b) using 272 triangular elements.

manual [6]. This problem is also identical to the one that studied experimentally in Ref. [34]. The transducer is modeled as an axisymmetric problem and meshes with 136 rectangular elements and 272 triangular elements are used, as shown in Figure 13.11. Homogeneous constraints of the potentials on the inside surface are imposed. The frequencies correspond to those for antiresonance. The ES-FEM-T3 is applied to analyze the eigenvalues of this transducer. We note first that no spurious non-zero-energy modes were found. This shows that ES-FEM-T3 is also temporally stable at least for this problem (see Remark 1.3).

Table 13.3 shows the first five frequencies, and the relative error percentages compared with experimental results are given in parentheses. Their corresponding eigenmode shapes are plotted in Figure 13.12. It can be seen that these eigenmode shapes are almost identical to those described in the ABAQUS manual [6].

From Table 13.3, it is observed that the results of ES-FEM-T3 agree well with the experimental results given in Ref. [34]. The relative error percentage corresponding to each mode of ES-FEM-T3 is smaller than those of FEM-T3 and FEM-Q4. This means that the eigenvalues of ES-FEM-T3 are better than those of standard FEM using the same mesh.

TABLE 13.3

Eigenvalues (kHz) Obtained Using Different Methods with the Same Number of 175 Nodes

Element Type	Mode 1	Mode 2	Mode 3	Mode 4	Mode 5
FEM-T3	19.98 (7.42%)	43.31 (24.01%)	62.78 (15.83%)	67.78 (7.08%)	94.23 (6.12%)
FEM-Q4	19.7 (5.91%)	42.9 (21.19%)	61.1 (12.73%)	66.7 (5.37%)	92.2 (3.83%)
ES-FEM-T3	18.74 (0.75%)	41.74 (17.91%)	59.21 (9.24%)	65.23 (3.05%)	89.85 (1.18%)
Experimental [34]	18.6	35.4	54.2	63.3	88.8

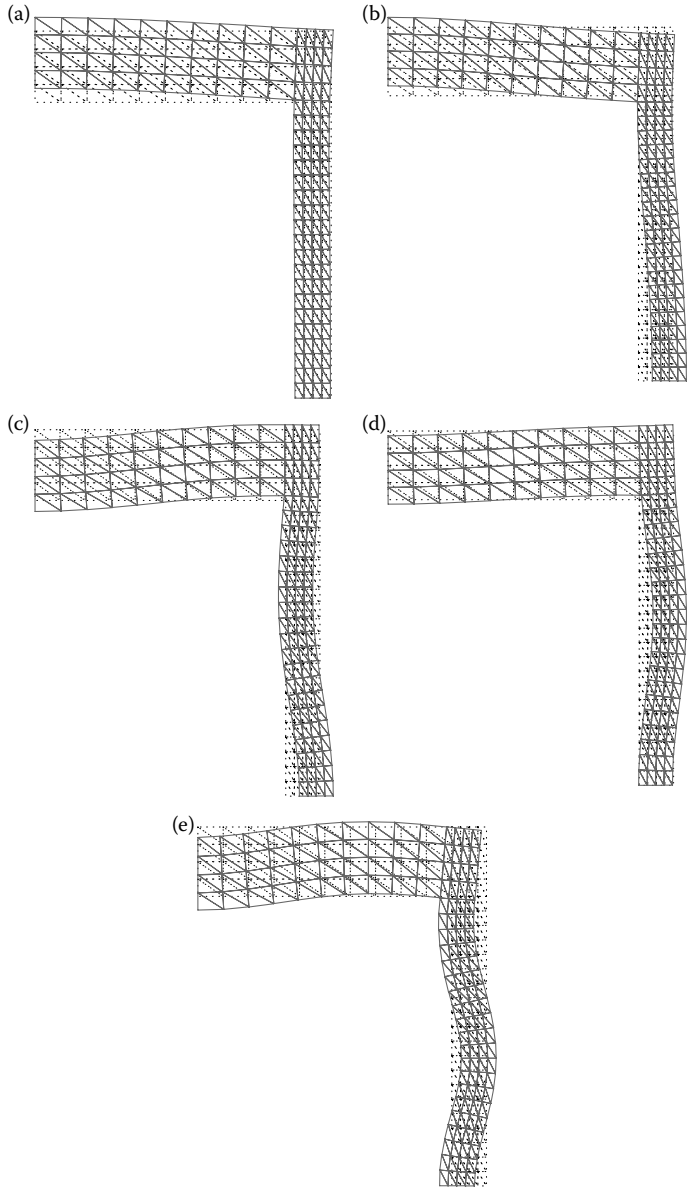

FIGURE 13.12 The first five eigenmodes for the piezoelectric transducer obtained using ES-FEM-T3. (a) 1st eigenmode; (b) 2nd eigenmode; (c) 3rd eigenmode; (d) 4th eigenmode; and (e) 5th eigenmode.

13.6 Remarks

This chapter presents a general formulation for S-FEM models for solids of piezoelectric materials. The standard Galerkin weak form is first derived from the general formulation of Hamilton's principle for dynamic problems. The smoothed Galerkin weak form is then presented, followed by a general formulation of S-FEM models.

In particular, the ES-FEM using a triangular mesh (ES-FEM-T3) is coded and applied to analyze various 2D piezoelectric structures. Using ES-FEM-T3, displacements and electric potentials are approximated in the same manner as in the standard FEM, but mechanical strains and electric field are smoothed over the set of smoothing domains associated with the edges of the mesh. We now note the following.

- The ES-FEM-T3 works well with triangular meshes with only unknown DOFs at the nodes and no additional DOFs are required.
- The ES-FEM-T3 passes the standard patch test for plane piezoelectric problems and hence is of second-order accuracy.
- The results of ES-FEM-T3 obtained agree well with analytical solution as well as experimental results found in the published literature.
- The ES-FEM-T3 results are found more accurate than those of FEM-T3, and are often found to be even more accurate than FEM-Q4 for static and eigenvalue analyses of the transducers.
- The ES-FEM-T3 is very easy to implement into a standard finite element program using triangular meshes that can be generated with ease for problems with complicated geometry.

In summary, the ES-FEM-T3 may still keep its "star" performer title also for piezoelectrics. We finally note that other S-FEM models can also be used to simulate the piezoelectric structures for solutions of desired solutions. For example, the NS-FEM can be used for upper bound solutions to static and dynamic (with proper stabilization techniques) problems.

References

1. Tzou HS and Tseng CI. 1990. Distributed piezoelectric sensor/actuator design for dynamic measurement/control of distributed parameter systems: A finite element approach. *Journal of Sound and Vibration*; 138: 17–34.
2. Liu GR and Xi ZC. 2001. *Elastic Waves in Anisotropic Laminates*. CRC Press LLC, Boca Raton, FL.

3. Liu GR, Peng XQ, Lam KY, and Tani J. 1999. Vibration control simulation of laminated composite plates with integrated piezoelectrics. *Journal of Sound and Vibration*; 220(5): 827–846.
4. Xu YG and Liu GR. 2002. A modified electro-mechanical impedance model of piezoelectric actuator-sensors for debonding detection of composite patches. *Journal of Intelligent Material Systems and Structures*; 13(6): 327–396.
5. Cai C, Liu GR, and Lam KY. 2001. A technique for modeling multiple piezoelectric layers. *Smart Materials and Structure*; 10: 689–694.
6. ABAQUS/Standard Example Problems Manual Version 6.6 2006 (Hibbitt: Karlsson and Sorensen Inc.) Section 6.1.1.
7. Allik H and Hughes TJR. 1970. Finite element method for piezo-electric vibration. *International Journal for Numerical Methods in Engineering*; 2: 151–157.
8. Benjeddou A. 2000. Advances in piezoelectric finite element modeling of adaptive structural elements: A survey. *Computers and Structures*; 76: 347–363.
9. Lam KY, Peng XQ, Liu GR, and Reddy JN. 1997. Finite element model for piezoelectric composite laminates. *Smart Materials and Structures*; 6: 583–591.
10. Han X and Liu GR. 2003. Elastic waves propagating in a functionally graded piezoelectric cylinder. *Smart Materials and Structures*; 12(6): 962–971.
11. Liu GR and Tani J. 1992. SH surface waves in functionally gradient piezoelectric material plates. *Transactions of the Japan Society of Mechanical Engineers*; 58(A): 504–507.
12. Liu GR and Tani J. 1994. Surface waves in functionally gradient piezoelectric material plates. *ASME Journal of Vibration and Acoustics, U.S.A.*; 116: 440–448.
13. Cannarozzi AA and Ubertini F. 2001. Some hybrid variational methods for linear electroelasticity problems. *International Journal of Solids and Structures*; 38: 2573–2596.
14. Sze KY and Pan YS. 1999. Hybrid finite element models for piezoelectric materials. *Journal of Sound and Vibration*; 226: 519–547.
15. Sze KY, Yang XM, and Yao LQ. 2004. Stabilized plane and axisymmetric piezoelectric finite element models. *Finite Elements in Analysis and Design*; 40: 1105–1122.
16. Sze KY and Yao LQ. 2000. Modeling smart structures with segmented piezoelectric sensors and actuators. *Journal of Sound and Vibration*; 235: 495–520.
17. Sze KY, Yao LQ, and Yi S. 2000. A hybrid stress ANS solid-shell element and its generalization for smart structure modeling. Part II—smart structure modeling. *International Journal for Numerical Methods in Engineering*; 48: 565–582.
18. Wu CC, Sze KY, and Huang YQ. 2001. Numerical solutions on fracture of piezoelectric materials by hybrid element. *International Journal of Solids and Structures*; 38: 4315–4329.
19. Bergan PG and Felippa CA. 1985. A triangular membrane element with rotational degrees of freedom. *Computer Methods in Applied Mechanics and Engineering*; 50: 25–69.
20. Groenwold AA and Stander N. 1998. A 24 d.o.f. 4-node flat shell finite element for general unsymmetric orthotropic layered composites. *Engineering with Computers*; 15: 518–543.
21. Long CS, Loveday PW, and Groenwold AA. 2006. Planar four node piezoelectric with drilling degrees of freedom. *International Journal for Numerical Methods in Engineering*; 65: 1802–1830.

22. Liu GR, Dai KY, Han X, and Ohyoshi T. 2003. Dispersion of waves and characteristic wave surfaces in functionally graded piezoelectric plates. *Journal of Sound and Vibration*; 268(1): 131–147.
23. Liu GR, Dai KY, and Nguyen-Thoi T. 2007. A smoothed finite element method for mechanics problems; *Computational Mechanics*; 39: 859–877.
24. Liu GR. 2009. *Meshfree Methods: Moving Beyond the Finite Element Method*, 2nd edition. Taylor & Francis/CRC Press, Boca Raton, FL.
25. Ohs RR and Aluru NR. 2001. Meshless analysis of piezoelectric devices. *Computational Mechanics*; 27: 23–36.
26. Liu GR, Dai KY, Lim KM, and Gu YT. 2002. A point interpolation mesh free method for static and frequency analysis of two-dimensional piezoelectric structures. *Computational Mechanics*; 29: 510–519.
27. Liu GR, Dai KY, and Lim KM. 2004. Static and vibration control of composite laminates integrated with piezoelectric sensors and actuators using the radial point interpolation method. *Smart Materials and Structures*; 13(6): 1438–1447.
28. Liu GR, Dai KY, Lim KM, and Gu YT. 2003. A radial point interpolation method for simulation of two-dimensional piezoelectric structures. *Smart Materials and Structures*; 12: 171–180.
29. Nguyen-Xuan H, Liu GR, Nguyen-Thoi T, and Nguyen-Tran C. 2009. An edge-based smoothed finite element method (ES-FEM) for analysis of two-dimensional piezoelectric structures. *Smart Materials and Structures*; 18: 065015.
30. Peng XQ, Lam KY, and Liu GR. 1998. Active vibration control of composite beams with piezoelectrics: A finite element model with third-order theory. *Journal of Sound and Vibration*; 209(4): 635–650.
31. Liu GR and Quek SS. 2002. *The Finite Element Method: A Practical Course*. Butterworth Heinemann, Oxford.
32. Liu GR, Nguyen-Thoi T, and Lam KY. 2009. An edge-based smoothed finite element method (ES-FEM) for static, free and force vibration analyses of solids. *Journal of Sound and Vibration*; 320: 1100–1130.
33. Cook R. 1974. Improved two-dimensional finite element. *Journal of Structural Division (ASCE)*; 100(ST6): 1851–1863.
34. Mercer CD, Reddy BD, and Eve RA. 1987. Finite element method for piezoelectric media. Applied Mechanics Research Unit, Technical Report No. 92, University of Cape Town/CSIR.

14

S-FEM for Heat Transfer Problems

14.1 Introduction

In previous chapters, we have introduced a number of S-FEM models and demonstrated the excellent properties and performance of these models for mechanics problems of solids and structures. This chapter aims to extend the formulations and applications of these S-FEM models for heat transfer problems.

Heat transfer is a very important physical phenomenon in most of the practical systems in engineering and science [1]. It is in fact one of the most fundamental and common topics in the analyses and design of mechanical, civil, electrical, chemical, and biological systems. We will start from the general mathematical model for heat transfer problems in engineering, and then provide simple models for bioheat transfer problems related to hyperthermia treatments for cancer tumor.

In terms of numerical modeling, FEM [2,3] has been the major tool for heat transfer problems in the past decades. This chapter provides a detailed formulation for the standard FEM and the recent S-FEM models for general heat transfer problems. We first introduce some weak forms for the heat transfer problems that can be used for establishing the standard FEM models. We next present the weak forms for S-FEM models. The discretized system of equations for both FEM and S-FEM models is then derived. We apply the NS-FEM for 1D, 2D, and 3D heat transfer problems to show the upper bound property of NS-FEM models for heat transfer problems. Finally, we will apply a 3D FS-FEM to solve a bioheat transfer problem simulating the hyperthermia treatments of breast cancer.

Compared to the solid mechanics problems, the heat transfer problems are easier to deal with, because the *primary* field variables (displacements) for solid mechanics problems are vector fields, while that for heat transfer problems is temperature, which is a scalar field. There are, of course, essential differences in the physics of these two types of problems. For experienced readers with both solid mechanics and heat transfer problems, these weak forms, the FEM and S-FEM equations, for heat transfer problems can be written out easily based on the equations for solid mechanics problems, without going through again the derivation process. For others, this could be quite difficult to comprehend. We therefore choose to provide

a complete but easy-to-understand derivation process for all these equations for heat transfer problems. Proper linkages between the formulations given in this chapter and those in Chapter 3 (for FEM) and Chapter 4 (for S-FEM) will also be provided, so that readers can have a better understanding of the physics as well as the mathematical formulation for both solid mechanics and heat transfer problems. For readers who are interested only in heat transfer problems, this chapter can be read and followed through quite easily and independently from the other chapters.

14.2 Strong-Form Equations for Heat Transfer Problems

Based on the physics of heat in a continuous solid or medium, the governing equation for general dynamic heat transfer problems can be written in the form of [1,3]

$$\underbrace{\rho c \frac{\partial T}{\partial t}}_{\text{heat change in time}} = \underbrace{\mathbf{L}_d^T \mathbf{c} \mathbf{L}_d T}_{\text{heat conduction}} - \underbrace{h_T T}_{\text{heat convection}} + \underbrace{Q}_{\text{heat source}} \quad \text{in } \Omega, \tag{14.1}$$

where T is the unknown temperature field in the medium, c is the specific heat capacity, ρ is the density of the medium, and k is the thermal conductivity of the medium, h_T is the heat convection coefficient, $\mathbf{L}_d$ is a differential operator (for the heat transfer problems, it is simply the well-known gradient operator often denoted as ∇) given by

$$\mathbf{L}_d = \nabla = \begin{cases} \dfrac{\partial}{\partial x} & \text{for 1D,} \\ \left\{ \dfrac{\partial}{\partial x} \quad \dfrac{\partial}{\partial y} \right\}^T & \text{for 2D,} \\ \left\{ \dfrac{\partial}{\partial x} \quad \dfrac{\partial}{\partial y} \quad \dfrac{\partial}{\partial z} \right\}^T & \text{for 3D,} \end{cases} \tag{14.2}$$

and $\mathbf{c}$ is the matrix of heat conductive coefficients of the medium given by

$$\mathbf{c} = \begin{cases} k_x & \text{for 1D,} \\ \begin{bmatrix} k_x & 0 \\ 0 & k_y \end{bmatrix} & \text{for 2D,} \\ \begin{bmatrix} k_x & 0 & 0 \\ 0 & k_y & 0 \\ 0 & 0 & k_z \end{bmatrix} & \text{for 3D,} \end{cases} \tag{14.3}$$

where k_i $(i = x, y, z)$ is the heat conductivity coefficient in the i-direction.

In Equation 14.1, Q is the heat source (or sink, when negative) provided externally to the medium. It is therefore very clear that the terms in Equation 14.1 count for the balance of the possible terms in an idealized general heat transfer situation at any point in the problem domain (medium) [1–3].

For static heat transfer problems, we simply drop the dynamic term and obtain the strong-form governing equation as follows:

$$\mathbf{L}_d^T \mathbf{c} \mathbf{L}_d T - h_T T + Q = 0. \tag{14.4}$$

We note that Equation 14.1 or 14.4 resembles Equation 2.20, but (1) T is now a scalar and (2) we have one term containing T. We choose these matrix-form equations so that we can accommodate easily a medium that is generally anisotropic, meaning for example that the heat conductivities can depend on the direction of heat conduction. We note also that the spatial operators in Equation 14.1 or 14.4 are still *symmetric*, and hence the Galerkin formulations will work most efficiently, because the symmetry will be preserved. Of course, Equation 14.1 or 14.4 can only be solved in a meaningful manner with properly defined boundary conditions, so that the original heat transfer problem is well posed (see Remark 1.1).

14.3 Boundary Conditions

For general heat transfer problems, the boundary Γ can in general consist of three parts: $\Gamma = \Gamma_{\mathrm{D}} \cup \Gamma_{\mathrm{N}} \cup \Gamma_{\mathrm{R}}$, and the boundary conditions can be Dirichlet, Neumann, and Robin, respectively, for each of these parts, and can be expressed in detail as follows [1–3]:

$$T = T_\Gamma \quad \text{on Dirichlet boundary } \Gamma_{\mathrm{D}}, \tag{14.5}$$

$$-\mathbf{L}_n^T \mathbf{c} \mathbf{L}_d T = q_\Gamma \quad \text{on Neumann boundary } \Gamma_{\mathrm{N}}, \tag{14.6}$$

$$-\mathbf{L}_n^T \mathbf{c} \mathbf{L}_d T = h_T (T - T_{\mathrm{a}}) \quad \text{on Robin boundary } \Gamma_{\mathrm{R}}, \tag{14.7}$$

where T_Γ is the fixed temperature on the Dirichlet boundary, q_Γ is the given heat supply on the Neumann boundary Γ_{N}, and T_{a} is the known temperature in the ambient fluid on the Robin boundary Γ_{R}. Therefore, T_Γ, q_Γ, and T_{a} are all given for the well-posed heat transfer problem before it is to be solved. When $q_\Gamma = 0$ for parts of the Neumann boundary, it is sometimes also called adiabatic boundary. In Equations 14.6 and 14.7, the

matrix $\mathbf{L}_n^T$ is in fact the vector of the outwards normal given by

$$\mathbf{L}_n = \mathbf{n} = \begin{cases} n_x & \text{for 1D,} \\ \{n_x \quad n_y\}^T & \text{for 2D,} \\ \{n_x \quad n_y \quad n_z\}^T & \text{for 3D,} \end{cases} \tag{14.8}$$

where n_i $(i = x, y, z)$ is the i-direction components of unit outward normal on the boundary. Equations 14.6 and 14.7 can be written explicitly for 3D problems as

$$-n_x k_x \frac{\partial T}{\partial x} - n_y k_y \frac{\partial T}{\partial y} - n_z k_z \frac{\partial T}{\partial z} = q_\Gamma \quad \text{on Neumann boundary } \Gamma_{\mathrm{N}}, \tag{14.9}$$

$$-n_x k_x \frac{\partial T}{\partial x} - n_y k_y \frac{\partial T}{\partial y} - n_z k_z \frac{\partial T}{\partial z} = h(T - T_{\mathrm{a}}) \quad \text{on Robin boundary } \Gamma_{\mathrm{R}}, \tag{14.10}$$

which may be more familiar to many.

The statement of the strong formulation for heat transfer problems becomes "to search for the temperature field function T that satisfies Equations 14.1 at any point in the problem domains and Equations 14.5 through 14.7 on the boundary."

14.4 Weak Forms for Heat Transfer Problems

Obtaining the exact solution that satisfies the strong form of governing equation 14.1 with boundary conditions given in Equations 14.5 through 14.7, is in general not possible, and can only be done for extremely simple cases. We therefore seek approximate solutions, and want to do it in as effective as possible ways. For this purpose, we often resort to various weak formulations that are detailed in Ref. [4]. The weighted residual weak form is a very general weak form and hence is a good starting point, as we have done for the FEM for solid mechanics problems (see Chapter 3).

14.4.1 Weighted Residual Weak Form for Heat Transfer Problems

The weighted residual equation can be obtained by multiplying the governing equation 14.1 with a weight (or test) function w that is sufficiently

smooth, and integrating the weighted equation over the entire problem domain [2–3]:

$$\int_{\Omega} w \cdot \rho c \frac{\partial T}{\partial t} \, \mathrm{d}\Omega = \int_{\Omega} w \cdot \left(\mathbf{L}_d^T \mathbf{c} \mathbf{L}_d T \right) \mathrm{d}\Omega - \int_{\Omega} w \cdot h_T T \, \mathrm{d}\Omega + \int_{\Omega} w \cdot Q \, \mathrm{d}\Omega. \quad (14.11)$$

Performing the integration by parts and using the boundary conditions given in Equations 14.6 and 14.7, the first term in Equation 14.11 becomes

$$\begin{aligned} \int_{\Omega} w \cdot \left(\mathbf{L}_d^T \mathbf{c} \mathbf{L}_d T \right) \mathrm{d}\Omega = & \int_{\Gamma_N} w \cdot \underbrace{\left(\mathbf{L}_n^T \mathbf{c} \mathbf{L}_d T \right)}_{-q_\Gamma} \mathrm{d}\Gamma + \int_{\Gamma_R} w \cdot \underbrace{\left(\mathbf{L}_n^T \mathbf{c} \mathbf{L}_d T \right)}_{-h_T (T - T_a)} \mathrm{d}\Gamma \\ & + \int_{\Gamma_D} w \cdot \underbrace{\left(\mathbf{L}_n^T \mathbf{c} \mathbf{L}_d T \right)}_{-q_D} \mathrm{d}\Gamma - \int_{\Omega} (\mathbf{L}_d w)^T \mathbf{c} \, (\mathbf{L}_d T) \, \mathrm{d}\Omega, \end{aligned} \quad (14.12)$$

where q_D is the unknown heat flux on Γ_D. Substituting the foregoing equation into Equation 14.11, we obtain

$$\begin{aligned} & \int_{\Omega} \rho c \, w \frac{\partial T}{\partial t} \, \mathrm{d}\Omega + \int_{\Omega} (\mathbf{L}_d w)^T \, \mathbf{c} \, (\mathbf{L}_d T) \, \mathrm{d}\Omega + \int_{\Omega} h_T w T \, \mathrm{d}\Omega \\ & - \int_{\Omega} w Q \, \mathrm{d}\Omega + \int_{\Gamma_N} w q_\Gamma \, \mathrm{d}\Gamma + \int_{\Gamma_R} w h (T - T_a) \, \mathrm{d}\Gamma + \int_{\Gamma_D} w \cdot q_D \, \mathrm{d}\Gamma = 0. \end{aligned} \quad (14.13)$$

Equation 14.13 is the weighted residual weak form for our heat transfer problems. The reason for calling Equation 14.13 weak is the fact that the order of derivatives on the field variable function T is reduced to one, from the original two required in Equation 14.1. We note that in deriving the weak-form equation 14.13, we used Equations 14.1, 14.6, and 14.7. Therefore, our original problem stated in Equations 14.1 and 14.5 through 14.7 is now stated as "To search for the temperature field function T that satisfies Equation 14.5 and the weak-form equation 14.13, for a *set* of *properly* chosen weight functions w."

Here, we have not yet decided how the weight function w should be chosen. We, of course, require any chosen w from the "proper set," and all these terms in Equation 14.13 must be "bounded" so that it can be evaluated. Hence, Equation 14.13 is quite general. Different choices of the w set will lead to different types of numerical methods with different properties (both good and bad, stable and unstable). In other words, the weak-form equation 14.13 offers a general means to obtain a T, but without any promise on

the quality of the T or whether a T can really be obtained. More discussions in this direction can be found in Ref. [4] in the general context of mesh-free methods. We now discuss a special choice of the w set, which leads to the so-called *Galerkin weak form* that is with some "promises" and is used in the FEM formulation.

14.4.2 Galerkin Weak Form for Heat Transfer Problems: Continuous Form

For our heat transfer problems, the temperature field that we want to obtain from Equation 14.13 is a function defined in the problem domain Ω. In fact, it must be the exact solution that satisfies Equations 14.1 and 14.5 through 14.7. To ensure this, we now choose an "arbitrary" variation of T as the weight function:

$$w(\mathbf{x}) = \delta T(\mathbf{x}), \tag{14.14}$$

where $\delta T(\mathbf{x})$ satisfies also the Dirichlet boundary condition on Γ_D, which is said to be "admissible." Equation 14.13 now becomes

$$\int_\Omega \rho c(\delta T)\cdot\frac{\partial T}{\partial t}\,\mathrm{d}\Omega + \int_\Omega (\delta \mathbf{L}_d T)^T\,\mathbf{c}\,(\mathbf{L}_d T)\;\mathrm{d}\Omega + \int_\Omega h_T\,(\delta T)\cdot T\,\mathrm{d}\Omega$$
$$-\int_\Omega \delta T Q\,\mathrm{d}\Omega + \int_{\Gamma_\mathrm{N}} (\delta T)\,q_\Gamma\,\mathrm{d}\Gamma + \int_{\Gamma_\mathrm{R}} (\delta T)\,h_T(T-T_\mathrm{a})\,\mathrm{d}\Gamma + \int_{\Gamma_\mathrm{D}} \underbrace{\delta T}_{=0}\cdot q_\mathrm{D}\,\mathrm{d}\Gamma = 0. \tag{14.15}$$

In the foregoing equation, we used the simple fact that the variational operator and the spatial differential operator can swap orders, because they operate with respect to different variables. The spatial differential operator operates with respect to the coordinates, x, y, or z, while the variational operator operates on parameters that control the shape of function T. Note also that the last term in Equation 14.15 will vanish because on Γ_D, T is given by boundary condition 14.5 and thus the variation of a given quantity becomes zero (a given quantity cannot be "varied" any more). We then finally have

$$\int_\Omega \rho c(\delta T)\cdot\frac{\partial T}{\partial t}\,\mathrm{d}\Omega + \int_\Omega \delta\,(\mathbf{L}_d T)^T\,\mathbf{c}\,(\mathbf{L}_d T)\,\mathrm{d}\Omega + \int_\Omega h_T(\delta T)\cdot T\,\mathrm{d}\Omega$$
$$-\int_\Omega \delta T Q\,\mathrm{d}\Omega + \int_{\Gamma_\mathrm{N}} (\delta T)\,q_\Gamma\;\mathrm{d}\Gamma + \int_{\Gamma_\mathrm{R}} (\delta T)\,h_T(T-T_\mathrm{a})\,\mathrm{d}\Gamma = 0. \tag{14.16}$$

Equation 14.16 is the well-known Galerkin weak form for heat transfer problems, which promises that the exact solution that satisfies the original

problem stated in Equations 14.1 and 14.5 through 14.7 satisfies Equation 14.16. We can also go backwards: A T that satisfies Equations 14.5 and 14.16 will satisfy Equations 14.1 and 14.5 through 14.7 as long as T has sufficient smoothness for the differential operations in Equations 14.1 and 14.5 through 14.7. In fact, the weak statement (Equation 14.16) is more general in terms of admission of data: it allows us to find solutions for some less "regular" heat source (in domain or on the boundary) that cannot be expressed in the strong statements.

The admissible conditions for T in Equation 14.16 need some further elaborations. Heuristically, we require that (1) T has to satisfy Equation 14.5, because it has been used as one of the conditions in deriving the Galerkin weak form given in Equation 14.16, and (2) using such a T, all the terms in Equation 14.16 have to be bounded. Mathematically, we simply require $T \in \mathbb{H}_0^1(\Omega; \mathrm{R}^1)$(see Chapter 3). This admissible condition essentially ensures that Equation 14.16 has a unique solution as long as the original problem is well posed with "stable" medium [e.g., the material constant matrix $\mathbf{c}$ is SPD or strictly positive k_i $(i = x, y, z)$].

Note that the continuous form of the Galerkin weak form given in Equation 14.16 is still difficult to solve for the exact solution: we did not make much progress in this regard. However, it provides a convenient platform for us to now seek an approximate solution. The idea is to discretize the problem domain for easy approximations of T in a finite dimension and try to find an approximated T that satisfies Equations 14.5 and 14.16 and converges to the exact solution when the discretization is refined.

14.4.3 Galerkin Weak Form: Discrete Form

We now discretize the problem domain Ω using elements (for FEM settings) or nodes (in mesh-free settings). We then somehow create an approximation of T denoted as $\breve{T}$ such that it satisfies the admissible condition of $\breve{T} \in \mathbb{H}_{0,h}^1(\Omega; \mathrm{R}^1)$ as well as the following equation:

$$\int_\Omega \rho c\left(\delta\breve{T}\right) \cdot \frac{\partial \breve{T}}{\partial t}\, \mathrm{d}\Omega + \int_\Omega \delta\left(\mathbf{L}_d\breve{T}\right)^T \mathbf{c}\left(\mathbf{L}_d\breve{T}\right) \mathrm{d}\Omega + \int_\Omega h_T\left(\delta\breve{T}\right) \cdot \breve{T}\, \mathrm{d}\Omega$$
$$- \int_\Omega \delta\breve{T} Q\, \mathrm{d}\Omega + \int_{\Gamma_\mathrm{N}} \left(\delta\breve{T}\right) q_\Gamma\, \mathrm{d}\Gamma + \int_{\Gamma_\mathrm{R}} \left(\delta\breve{T}\right) h_T(\breve{T} - T_\mathrm{a})\, \mathrm{d}\Gamma = 0. \quad (14.17)$$

Such a $\breve{T}$ is then regarded as *an* approximate solution. Equation 14.17 is the Galerkin weak form in discrete form for heat transfer problems, which promises a unique approximate solution that converges to the exact solution of the original well-posed problem stated in Equations 14.1

and 14.5 through 14.7 when the discretization is refined, and hence $\mathbb{H}^1_{0,h}(\Omega;\mathrm{R}^1) \to \mathbb{H}^1_0(\Omega;\mathrm{R}^1)$.

14.4.4 Smoothed Galerkin Weak Form: Discrete Form

We are now ready to establish the smoothed Galerkin for heat transfer problems. We first discretize the problem domain Ω using elements (for FEM settings) or nodes with background cells (in mesh-free settings). On top of the mesh of elements/cells, we then further divide the problem domain into smoothing cells, as detailed in Section 4.5.1. Next, we somehow create an approximation of T denoted as $\overline{T}$ such that it satisfies the admissible condition of $\overline{T} \in \mathbb{H}^1_{0,h}(\Omega;\mathrm{R}^1)$ as well as the following equation:

$$\int_\Omega \rho c\left(\delta\overline{T}\right)\cdot\frac{\partial\overline{T}}{\partial t}\,\mathrm{d}\Omega + \int_\Omega \delta\left(\overline{\mathbf{L}_d T}\right)^T \mathbf{c}\left(\overline{\mathbf{L}_d T}\right)\mathrm{d}\Omega + \int_\Omega h_T\left(\delta\overline{T}\right)\cdot\overline{T}\,\mathrm{d}\Omega$$
$$-\int_\Omega \delta\overline{T}Q\,\mathrm{d}\Omega + \int_{\Gamma_\mathrm{N}}\left(\delta\overline{T}\right)q_\Gamma\,\mathrm{d}\Gamma + \int_{\Gamma_\mathrm{R}}\left(\delta\overline{T}\right)h_T(\overline{T}-T_\mathrm{a})\,\mathrm{d}\Gamma = 0. \quad (14.18)$$

It is clear that the temperature gradient $(\mathbf{L}_d T)$ is now replaced by the "smoothed temperature gradient" $\left(\overline{\mathbf{L}_d T}\right)$ over the smoothing domains. These smoothing domains can be cell-based (Chapter 5), node-based (Chapter 6), edge-based (Chapter 7), face-based (Chapter 8), and partially node-based (αFEM, Chapter 9). In any such set of smoothed domains, the smoothed temperature gradient becomes constant in each of the smoothing domains. Therefore, the "smoothed" Galerkin weak form for the heat transfer equation can be rewritten as

$$\int_\Omega \rho c\left(\delta\overline{T}\right)\cdot\frac{\partial\overline{T}}{\partial t}\,\mathrm{d}\Omega + \sum_{i=1}^{N_s} A_i^s\delta\left(\overline{\mathbf{L}_d T}\right)^T \mathbf{c}\left(\overline{\mathbf{L}_d T}\right) + \int_\Omega h_T\left(\delta\overline{T}\right)\cdot\overline{T}\,\mathrm{d}\Omega$$
$$-\int_\Omega \delta\overline{T}Q\,\mathrm{d}\Omega + \int_{\Gamma_\mathrm{N}}\left(\delta\overline{T}\right)q_\Gamma\,\mathrm{d}\Gamma + \int_{\Gamma_\mathrm{R}}\left(\delta\overline{T}\right)h_T(\overline{T}-T_\mathrm{a})\,\mathrm{d}\Gamma = 0, \quad (14.19)$$

where A_i^s is the area of the ith smoothing domain and N_s is the number of smoothing domains. A $\overline{T} \in \mathbb{H}^1_{0,h}(\Omega;\mathrm{R}^1)$ that satisfies Equation 14.19 is then regarded as an approximate solution. Equation 14.19 is the smoothed Galerkin weak form in discrete form for heat transfer problems, which promises a unique approximate solution that converges to the exact solution of the original well-posed problem stated in Equations 14.1 through 14.7 when the discretization is refined, and hence $\mathbb{H}^1_{0,h}(\Omega;\mathrm{R}^1) \to \mathbb{H}^1_0(\Omega;\mathrm{R}^1)$,

and the smoothing domains satisfy the conditions listed in Table 4.2. The proof of this can be generated in a similar way to that given in Ref. [4] or in Chapter 4.

We note that in the smoothed Galerkin weak form, we do not necessarily require $\overline{T} \in \mathbb{H}^1_{0,h}(\Omega; \mathrm{R}^1)$. We can have much more relaxed admissible conditions: $\overline{T} \in \mathbb{G}^1_{0,h}(\Omega; \mathrm{R}^1)$, meaning that the assumed temperature functions can be in proper $\mathbb{G}$ space [4–8]. Such a relaxation is very useful in establishing models in much more general mesh-free settings [4,5]. In this book, however, our S-FEM models are all based on the finite element settings, and hence we have the stronger (hence sufficient) requirement of $\overline{T} \in \mathbb{H}^1_{0,h}(\Omega; \mathrm{R}^1)$.

14.5 FEM Equations

In an FEM setting, we divide the problem domain into elements. Based on these elements we create nodal shape functions, as in the FEM (see Chapter 3). Using these nodal shape functions, the FEM solution for the temperature at any point $\mathbf{x} \in \Omega$ can be approximated in the following form:

$$\tilde{T}(\mathbf{x}) = \sum_{i=1}^{N_n} N_i(\mathbf{x}) \tilde{T}_i = \mathbf{N}(\mathbf{x}) \tilde{\mathbf{T}}, \tag{14.20}$$

where $\tilde{\mathbf{T}}$ is the vector of unknown nodal temperatures at all the nodes in the problem domain:

$$\tilde{\mathbf{T}} = \begin{bmatrix} \tilde{T}_1 & \tilde{T}_2 & \cdots & \tilde{T}_{N_n} \end{bmatrix}^T, \tag{14.21}$$

in which $\tilde{T}_i$ is the FEM solution for the nodal temperature at the ith node. The matrix $\mathbf{N}$ contains nodal shape functions for all the nodes in the problem domain:

$$\mathbf{N}(\mathbf{x}) = \begin{bmatrix} N_1(\mathbf{x}) & N_2(\mathbf{x}) & \cdots & N_{N_n}(\mathbf{x}) \end{bmatrix}, \tag{14.22}$$

where N_i is the shape function for the ith node. Note that because the nodal shape function N_i is locally supported only by the elements connected to the node, it is zero in all the other elements. Therefore, $\mathbf{N}(\mathbf{x})$ is very sparse for any given $\mathbf{x} \in \Omega$.

The variation of $\tilde{\mathbf{T}}(\mathbf{x})$ is given by

$$\delta\tilde{T}(\mathbf{x}) = \sum_{i=1}^{N_n} N_i(\mathbf{x}) \delta\tilde{T}_i = \mathbf{N}(\mathbf{x}) \delta\tilde{\mathbf{T}}. \tag{14.23}$$

Substituting Equations 14.20 and 14.23 into Equation 14.16, we obtain

$$\int_\Omega \rho c\left(\mathbf{N}\delta\tilde{\mathbf{T}}\right)^T \mathbf{N}\frac{\partial\tilde{\mathbf{T}}}{\partial t}\,\mathrm{d}\Omega + \int_\Omega \delta\left(\mathbf{L}_d\mathbf{N}\tilde{\mathbf{T}}\right)^T \mathbf{c}(\mathbf{L}_d\mathbf{N})\,\tilde{\mathbf{T}}\,\mathrm{d}\Omega + \int_\Omega h_T\left(\mathbf{N}\delta\tilde{\mathbf{T}}\right)^T \mathbf{N}\tilde{\mathbf{T}}\,\mathrm{d}\Omega - \int_\Omega \left(\mathbf{N}\delta\tilde{\mathbf{T}}\right)^T Q\,\mathrm{d}\Omega + \int_{\Gamma_N}\left(\mathbf{N}\delta\tilde{\mathbf{T}}\right)^T q_\Gamma\,\mathrm{d}\Gamma + \int_{\Gamma_R}\left(\mathbf{N}\delta\tilde{\mathbf{T}}\right)^T h_T\left(\left(\mathbf{N}\tilde{\mathbf{T}}\right)^T - T_\mathrm{a}\right)\mathrm{d}\Gamma = 0 \tag{14.24}$$

or

$$\left(\delta\tilde{\mathbf{T}}\right)^T\left[\begin{array}{l}\displaystyle\int_\Omega \rho c\mathbf{N}^T\mathbf{N}\frac{\partial\tilde{\mathbf{T}}}{\partial t}\,\mathrm{d}\Omega + \int_\Omega (\mathbf{L}_d\mathbf{N})^T\mathbf{c}\,(\mathbf{L}_d\mathbf{N})\,\tilde{\mathbf{T}}\,\mathrm{d}\Omega + \int_\Omega h_T\mathbf{N}^T\mathbf{N}\tilde{\mathbf{T}}\,\mathrm{d}\Omega \\ \displaystyle -\int_\Omega \mathbf{N}^T Q\,\mathrm{d}\Omega + \int_{\Gamma_N}\mathbf{N}^T q_\Gamma\,\mathrm{d}\Gamma + \int_{\Gamma_R}\mathbf{N}^T h_T\left(\mathbf{N}\tilde{\mathbf{T}} - T_\mathrm{a}\right)\mathrm{d}\Gamma\end{array}\right] = 0. \tag{14.25}$$

Due to the *arbitrary* nature of the variation of the nodal temperature $\delta\tilde{\mathbf{T}}$, the only way to have Equation 14.25 to be *always* satisfied is to have

$$\int_\Omega \rho c\mathbf{N}^T\mathbf{N}\frac{\partial\tilde{\mathbf{T}}}{\partial t}\,\mathrm{d}\Omega + \int_\Omega (\mathbf{L}_d\mathbf{N})^T\mathbf{c}\,(\mathbf{L}_d\mathbf{N})\,\tilde{\mathbf{T}}\,\mathrm{d}\Omega + \int_\Omega h_T\mathbf{N}^T\mathbf{N}\tilde{\mathbf{T}}\,\mathrm{d}\Omega - \int_\Omega \mathbf{N}^T Q\,\mathrm{d}\Omega + \int_{\Gamma_N}\mathbf{N}^T q_\Gamma\,\mathrm{d}\Gamma + \int_{\Gamma_R}\mathbf{N}^T h_T\left(\mathbf{N}\tilde{\mathbf{T}} - T_\mathrm{a}\right)\mathrm{d}\Gamma = 0. \tag{14.26}$$

Because $\tilde{\mathbf{T}}$ is the nodal temperature that is not a function of coordinates, we will now further have

$$\underbrace{\int_\Omega \mathbf{N}^T\rho c\mathbf{N}\,\mathrm{d}\Omega}_{\tilde{\mathbf{M}}}\frac{\partial\tilde{\mathbf{T}}}{\partial t} + \underbrace{\int_\Omega (\mathbf{L}_d\mathbf{N})^T\mathbf{c}(\mathbf{L}_d\mathbf{N})\,\mathrm{d}\Omega}_{\tilde{\mathbf{K}}}\tilde{\mathbf{T}} + \underbrace{\left(\int_\Omega \mathbf{N}^T h_T\mathbf{N}\,\mathrm{d}\Omega + \int_{\Gamma_R}\mathbf{N}^T h_T\mathbf{N}\,\mathrm{d}\Gamma\right)}_{\tilde{\mathbf{C}}}\tilde{\mathbf{T}} - \underbrace{\left(\int_\Omega \mathbf{N}^T Q\,\mathrm{d}\Omega - \int_{\Gamma_N}\mathbf{N}^T q_\Gamma\,\mathrm{d}\Gamma + \int_{\Gamma_R}\mathbf{N}^T h_T T_\mathrm{a}\,\mathrm{d}\Gamma\right)}_{\tilde{\mathbf{F}}} = 0 \tag{14.27}$$

or simply

$$\tilde{\mathbf{M}}\frac{\partial \tilde{\mathbf{T}}}{\partial t} + \tilde{\mathbf{K}}\tilde{\mathbf{T}} + \tilde{\mathbf{C}}\tilde{\mathbf{T}} = \tilde{\mathbf{F}}, \tag{14.28}$$

which is the FEM equation for dynamic heat transfer problems. The matrix $\tilde{\mathbf{M}}$ is the global thermal mass (heat capacity) matrix given by

$$\tilde{\mathbf{M}} = \int_{\Omega} \rho c \mathbf{N}^T \mathbf{N} \, \mathrm{d}\Omega. \tag{14.29}$$

The matrix $\tilde{\mathbf{C}}$ is the "heat damping" matrix induced by heat convection evaluated using

$$\tilde{\mathbf{C}} = \int_{\Omega} h_T \mathbf{N}^T \mathbf{N} \, \mathrm{d}\Omega + \int_{\Gamma_R} h_T \mathbf{N}^T \mathbf{N} \, \mathrm{d}\Gamma, \tag{14.30}$$

and

$$\tilde{\mathbf{F}} = \int_{\Omega} \mathbf{N}^T Q \, \mathrm{d}\Omega + \int_{\Gamma_R} h_T \mathbf{N}^T T_a \, \mathrm{d}\Gamma - \int_{\Gamma_N} \mathbf{N}^T q_\Gamma \, \mathrm{d}\Gamma \tag{14.31}$$

is the heat flux vector for all the nodes in the problem domain.

In Equation 14.28, the global thermal stiffness (heat conduction) matrix $\tilde{\mathbf{K}}$ is computed using

$$\tilde{\mathbf{K}} = \int_{\Omega} \underbrace{(\mathbf{L}_d \mathbf{N})^T}_{\tilde{\mathbf{B}}^T} \mathbf{c} \underbrace{(\mathbf{L}_d \mathbf{N})}_{\tilde{\mathbf{B}}} \, \mathrm{d}\Omega = \int_{\Omega} \tilde{\mathbf{B}}^T \mathbf{c} \tilde{\mathbf{B}} \, \mathrm{d}\Omega, \tag{14.32}$$

where $\tilde{\mathbf{B}}$ is the gradient-temperature matrix (an analogue of the strain–displacement matrix defined in Equation 3.68). Because $\mathbf{N}$ is very sparse, $\tilde{\mathbf{B}}$ must also be very sparse and, hence, so too is the $\tilde{\mathbf{K}}$ matrix. In addition, $\tilde{\mathbf{K}}$ will also be banded if the nodes in the problem domain are properly numbered. Making use of the sparseness in actual computations, we will not actually form the "global" matrices $\mathbf{N}$ and $\tilde{\mathbf{B}}$ for the entire problem domain, because they contain mostly zero for large models. Rather, we form those for each element and compute the element stiffness matrix $\tilde{\mathbf{K}}^e_{IJ}$:

$$\tilde{\mathbf{K}}^e_{IJ,i} = \int_{\Omega^e_i} \tilde{\mathbf{B}}^T_I \mathbf{c} \tilde{\mathbf{B}}_J \, \mathrm{d}\Omega, \tag{14.33}$$

where Ω_i^e is the domain of the element. The global stiffness matrix $\tilde{\mathbf{K}}$ can then be formed easily by assembling the entries given in Equation 14.33. The integration in Equation 14.33 is performed using the Gauss integration scheme based on elements (see Section 3.15).

Note that the evaluation of the matrices $\tilde{\mathbf{M}}$ and $\tilde{\mathbf{C}}$ and the vector $\tilde{\mathbf{F}}$ is similar to the case of $\tilde{\mathbf{K}}$: by an assembly using elemental matrix and vectors. It can be easily seen from Equations 14.32, 14.29, and 14.30 that the matrices $\tilde{\mathbf{K}}$, $\tilde{\mathbf{M}}$, and $\tilde{\mathbf{C}}$ are all symmetric and banded if the nodes in the problem domain are properly numbered, which implies that Equation 14.28 can be solved very efficiently using standard routines for a set of first-order differential equations with respect to time.

14.6 S-FEM Equations

In an S-FEM model, we divide the problem domain into elements, and based on these elements we create nodal shape functions, as in the FEM (see Chapter 3). Using these nodal shape functions, the S-FEM solution for the temperature at any point $\mathbf{x} \in \Omega$ can be approximated in the following form:

$$\overline{T}(\mathbf{x}) = \sum_{i=1}^{N_n} N_i(\mathbf{x})\overline{T}_i = \mathbf{N}(\mathbf{x})\overline{\mathbf{T}}, \tag{14.34}$$

where $\overline{\mathbf{T}}$ is the vector of the nodal temperatures at all the nodes in the problem domain:

$$\overline{\mathbf{T}} = \begin{bmatrix} \overline{T}_1 & \overline{T}_2 & \cdots & \overline{T}_{N_n} \end{bmatrix}^T, \tag{14.35}$$

in which $\overline{T}_i$ is the S-FEM solution for the nodal temperature at the ith node. The matrix $\mathbf{N}$ contains nodal shape functions and has the same form of Equation 14.22 and hence has the same sparseness.

The variation of the $\overline{\mathbf{T}}(\mathbf{x})$ is given by

$$\delta\overline{T}(\mathbf{x}) = \sum_{i=1}^{N_n} N_i(\mathbf{x})\delta\overline{T}_i = \mathbf{N}(\mathbf{x})\delta\overline{\mathbf{T}}. \tag{14.36}$$

Substituting Equations 14.34 and 14.36 into Equation 14.19, we obtain

$$\int_{\Omega} \rho c\left(\mathbf{N}\delta\overline{\mathbf{T}}\right)^{T}\mathbf{N}\frac{\partial\overline{\mathbf{T}}}{\partial t}\,\mathrm{d}\Omega + \sum_{i=1}^{N_s} kA_i^s\left(\delta\overline{\mathbf{T}}\right)^{T}\left(\overline{\mathbf{L}_d\mathbf{N}}\right)^{T}\cdot\left(\overline{\mathbf{L}_d\mathbf{N}}\right)\overline{\mathbf{T}}$$
$$+\int_{\Omega} h_T\left(\mathbf{N}\delta\overline{\mathbf{T}}\right)^{T}\mathbf{N}\overline{\mathbf{T}}\,\mathrm{d}\Omega - \int_{\Omega}\left(\mathbf{N}\delta\overline{\mathbf{T}}\right)^{T}Q\,\mathrm{d}\Omega + \int_{\Gamma_{\mathrm{N}}}\left(\mathbf{N}\delta\overline{\mathbf{T}}\right)^{T}q_{\Gamma}\,\mathrm{d}\Gamma$$
$$+\int_{\Gamma_{\mathrm{R}}}\left(\mathbf{N}\delta\overline{\mathbf{T}}\right)^{T}h_T\left(\left(\mathbf{N}\overline{\mathbf{T}}\right)^{T}-T_{\mathrm{a}}\right)\mathrm{d}\Gamma = 0 \tag{14.37}$$

or

$$\left(\delta\overline{\mathbf{T}}\right)^{T}\left[\begin{array}{l}\displaystyle\int_{\Omega}\rho c\mathbf{N}^{T}\mathbf{N}\frac{\partial\overline{\mathbf{T}}}{\partial t}\,\mathrm{d}\Omega + \sum_{i=1}^{N_s} kA_i^s\left(\overline{\mathbf{L}_d\mathbf{N}}\right)^{T}\left(\overline{\mathbf{L}_d\mathbf{N}}\right)\overline{\mathbf{T}} + \int_{\Omega} h_T\mathbf{N}^{T}\mathbf{N}\overline{\mathbf{T}}\,\mathrm{d}\Omega \\ \displaystyle -\int_{\Omega}\mathbf{N}^{T}Q\,\mathrm{d}\Omega + \int_{\Gamma_{\mathrm{N}}}\mathbf{N}^{T}q_{\Gamma}\,\mathrm{d}\Gamma + \int_{\Gamma_{\mathrm{R}}}\mathbf{N}^{T}h_T\left(\mathbf{N}\overline{\mathbf{T}}-T_{\mathrm{a}}\right)\mathrm{d}\Gamma\end{array}\right] = 0. \tag{14.38}$$

Due to the arbitrary nature of $\delta\overline{\mathbf{T}}$, the only way to have Equation 14.25 to be always satisfied for *any* $\delta\overline{\mathbf{T}}$ is to have

$$\int_{\Omega}\rho c\mathbf{N}^{T}\mathbf{N}\frac{\partial\overline{\mathbf{T}}}{\partial t}\,\mathrm{d}\Omega + \sum_{i=1}^{N_s} kA_i^s\left(\overline{\mathbf{L}_d\mathbf{N}}\right)^{T}\left(\overline{\mathbf{L}_d\mathbf{N}}\right)\overline{\mathbf{T}} + \int_{\Omega} h_T\mathbf{N}^{T}\mathbf{N}\overline{\mathbf{T}}\,\mathrm{d}\Omega$$
$$-\int_{\Omega}\mathbf{N}^{T}Q\,\mathrm{d}\Omega + \int_{\Gamma_{\mathrm{N}}}\mathbf{N}^{T}q_{\Gamma}\,\mathrm{d}\Gamma + \int_{\Gamma_{\mathrm{R}}}\mathbf{N}^{T}h_T\left(\mathbf{N}\overline{\mathbf{T}}-T_{\mathrm{a}}\right)\mathrm{d}\Gamma = 0. \tag{14.39}$$

Because $\overline{\mathbf{T}}$ is the nodal temperature vector that is not a function of coordinates, we will now further have

$$\underbrace{\int_{\Omega}\mathbf{N}^{T}\rho c\mathbf{N}\,\mathrm{d}\Omega}_{\tilde{\mathbf{M}}}\frac{\partial\overline{\mathbf{T}}}{\partial t} + \underbrace{\sum_{i=1}^{N_s} A_i^s\left(\overline{\mathbf{L}_d\mathbf{N}}\right)^{T}\mathbf{c}\left(\overline{\mathbf{L}_d\mathbf{N}}\right)}_{\overline{\mathbf{K}}}\overline{\mathbf{T}} + \underbrace{\left(\int_{\Omega}\mathbf{N}^{T}h_T\mathbf{N}\,\mathrm{d}\Omega + \int_{\Gamma_{\mathrm{R}}}\mathbf{N}^{T}h_T\mathbf{N}\,\mathrm{d}\Gamma\right)}_{\tilde{\mathbf{C}}}\overline{\mathbf{T}}$$
$$-\underbrace{\left(\int_{\Omega}\mathbf{N}^{T}Q\,\mathrm{d}\Omega - \int_{\Gamma_{\mathrm{N}}}\mathbf{N}^{T}q_{\Gamma}\,\mathrm{d}\Gamma + \int_{\Gamma_{\mathrm{R}}}\mathbf{N}^{T}h_T T_{\mathrm{a}}\,\mathrm{d}\Gamma\right)}_{\tilde{\mathbf{F}}} = 0 \tag{14.40}$$

or

$$\tilde{\mathbf{M}}\frac{\partial \overline{\mathbf{T}}}{\partial t} + \overline{\mathbf{K}\mathbf{T}} + \tilde{\mathbf{C}}\overline{\mathbf{T}} = \tilde{\mathbf{F}}, \tag{14.41}$$

which is the set of discretized equations for the S-FEM models. The matrices $\tilde{\mathbf{M}}$, $\tilde{\mathbf{C}}$, and $\tilde{\mathbf{F}}$ are exactly the same as those in Equations 14.29 through 14.31. The global "smoothed" thermal stiffness (heat conduction) matrix $\overline{\mathbf{K}}$ is defined as

$$\overline{\mathbf{K}} = \sum_{i=1}^{N_s} A_i^s \underbrace{\left(\overline{\mathbf{L}_d \mathbf{N}}\right)^T}_{\overline{\mathbf{B}}^T} \mathbf{c} \underbrace{\left(\overline{\mathbf{L}_d \mathbf{N}}\right)}_{\overline{\mathbf{B}}}. \tag{14.42}$$

For the same sparseness argument given for the FEM model, we know that $\overline{\mathbf{B}}_I$ will be very sparse, and hence we will not perform the above summation in the actual computations. Instead, we perform an assembly, similar to what we do in the FEM, using the entries computed based on smoothing domains:

$$\overline{\mathbf{K}}_{IJ,k}^s = A_k^s \overline{\mathbf{B}}_I^T \mathbf{c} \overline{\mathbf{B}}_J, \tag{14.43}$$

where A_k^s is the area of the kth smoothing domain. The evaluation of the smoothed gradient matrix $\overline{\mathbf{B}}_I$ used in Equation 14.43 is performed using a given type of smoothed domains, and will be discussed in more detail in Section 14.7. Compared to Equation 14.33, the S-FEM model uses (1) assembly over all the smoothing domains rather than elements, and (2) a smoothed gradient-temperature matrix instead of the (compatible) gradient-temperature matrix.

We observe that the S-FEM model changes only the stiffness matrix, and all the other matrices and vector are the same as the FEM counterparts using the same mesh. We note also that in computing the smoothed stiffness matrix, no numerical integration is needed, and only a summation over the smoothing domains is required. If cell-based smoothing domains are used, we have the CS-FEM model (see Chapter 5). Likewise, we can have the NS-FEM model (see Chapter 6), the ES-FEM model (see Chapter 7), and the FS-FEM model (see Chapter 8). If partially node-based smoothing domains are used, we have an αFEM model (see Chapter 9). Equation 14.41 is a unified S-FEM equation of all these models for heat transfer problems.

For steady-state heat transfer problems, we simply drop the dynamic term and have the following discrete system of equations:

$$\left[\overline{\mathbf{K}} + \tilde{\mathbf{C}}\right]\overline{\mathbf{T}} = \tilde{\mathbf{F}}, \tag{14.44}$$

which is a set of simple algebraic equations with $[\overline{\mathbf{K}} + \tilde{\mathbf{C}}]$ being SPD that can be solved easily using standard routines for the linear algebraic system of equations.

For dynamic problems, we need to solve Equation 14.41 that is a set of first-order differential equations with respect to time. Such a differential equation has been well studied and can be solved in a number of well-established methods, such as the forward difference method, the backward difference method, the Crank–Nicholson method, and so on. In this chapter, we use the simple backward difference method, where the temperature gradient with respect to time is given by

$$\frac{\partial T}{\partial t} = \frac{T^m - T^{m-1}}{\Delta t}, \tag{14.45}$$

where the superscript "m" stands for the mth time step. Substituting Equation 14.45 into Equation 14.41 results in

$$\left[\tilde{\mathbf{M}} + \Delta t(\overline{\mathbf{K}} + \tilde{\mathbf{C}})\right]\overline{\mathbf{T}}^m = \Delta t\tilde{\mathbf{F}}^m + \tilde{\mathbf{M}}\mathbf{T}^{m-1}. \tag{14.46}$$

The history of the nodal temperature can then be computed by solving Equation 14.46 with the time marching forward.

The FEM solution can be obtained by solving Equation 14.44 for the static problem or Equation 14.46 for the dynamic problems in the same manner but with $\overline{\mathbf{K}}$ being replaced by $\tilde{\mathbf{K}}$.

14.7 Evaluation of the Smoothed Gradient Matrix

We now evaluate the smoothed gradient matrix $\overline{\mathbf{B}}_I$ needed in Equation 14.43:

$$\overline{\mathbf{B}}_I = \left(\overline{\mathbf{L}_d\mathbf{N}}\right) = \begin{cases} \overline{\dfrac{\partial N_I}{\partial x}} & \text{for 1D,} \\ \left\{\overline{\dfrac{\partial N_I}{\partial x}} \quad \overline{\dfrac{\partial N_I}{\partial y}}\right\}^T & \text{for 2D,} \\ \left\{\overline{\dfrac{\partial N_I}{\partial x}} \quad \overline{\dfrac{\partial N_I}{\partial y}} \quad \overline{\dfrac{\partial N_I}{\partial z}}\right\}^T & \text{for 3D,} \end{cases} \tag{14.47}$$

where $N_I(\mathbf{x})$ is the shape function for node I. Because the smoothing is performed over a smoothing domain Ω_k^s bounded by Γ_k^s, we will have

$$\overline{b}_{Ip} = \overline{\frac{\partial N_I}{\partial p}} = \frac{1}{A_k^s}\int_{\Gamma_k^s} N_I(\mathbf{x})n_p(\mathbf{x})\,\mathrm{d}\Gamma, \tag{14.48}$$

where $p = x$ for 1D problems, $p = \{x, y\}$ for 2D problems, and $p = \{x, y, z\}$ for 3D problems.

Using the Gauss integration (see Section 3.15) along each segment of boundary $\Gamma_k^s$of the smoothing domain Ω_k^s that may be node-, edge-, face-, or cell-based, the above equations can be rewritten in the following summation forms:

$$\bar{b}_{Ip} = \frac{1}{A_k^s} \sum_{q=1}^{N_{\text{sg}}} \left[\sum_{r=1}^{n^{\text{G}}} w_r N_I(\mathbf{x}_{qr}) n_p(\mathbf{x}_{qr}) \right], \tag{14.49}$$

where N_{sg} is the number of segments of the boundary Γ_k^s, n^G is the number of Gauss points distributed in each segment, $\mathbf{x}_{qr}$ is the rth Gauss point on the qth segment of the boundary Γ_k^s, and w_r is the corresponding weight for the Gauss point.

Note that when linear triangular or tetrahedral elements are used, the smoothed gradient matrix for NS- and ES-FEM models can be evaluated in a simple way as discussed in Chapters 6 and 7.

14.8 Numerical Example

In this section, we present a number of 1D, 2D, and 3D examples solved using NS-FEM and FS-FEM methods, together with FEM using the same mesh. To examine quantitatively the properties of S-FEM models for heat transfer problems, the error indicator in temperature norms is defined as

$$e_T = \sqrt{\frac{\sum_{i=1}^{N_n} \left(T_i^{\text{exact}} - \overline{T}_i^{\text{nume}} \right)^2}{\sum_{i=1}^{N_n} (T_i^{\text{exact}})^2}}, \tag{14.50}$$

where the subscript "i" denotes the ith node, superscript "exact" denotes the exact or analytical solutions, and superscript "nume" denotes a numerical solution obtained using a numerical method that can be an FEM or an S-FEM model. When the *exact* solution is not available, a *reference* solution computed using the FEM with a very fine mesh is used instead. To study the bound property, the equivalent thermal energy of the whole system for heat transfer problem [9] is defined as follows:

$$\mathrm{U}_e = \sum_{k=1}^{N_s} A_k^s \left(\overline{\mathbf{L}_d T} \right)^T \mathbf{c} \left(\overline{\mathbf{L}_d T} \right). \tag{14.51}$$

The examples presented in this section are similar to some of those presented in Refs. [10–12].

14.8.1 1D Thermal Fin

The first example studied here is a simple 1D thermal fin with length L and a uniform cross-sectional area subjected to a uniformly distributed heat source Q, as shown in Figure 14.1. We consider the adiabatic condition over the circumference of the fin, and there is no heat convection on the surface of the fin. Therefore, h_T is set to zero. The temperature on the left end of the fin is fixed at T_Γ and heat flux q_Γ is provided at the right end. In the computation, the related parameters are set as $L = 1.0\,\text{m}$, $k = 5.0\,\text{W/m}\,^\circ\text{C}$, $q_\Gamma = 200\,\text{W/m}^2$, $Q = 100\,\text{W/m}^3$, $T_\Gamma = 0^\circ$, and $h_T = 0$.

The *exact* solution for the temperature distribution along the 1D thermal fin can be given analytically as

$$T(x) = -\frac{Q}{2k}x^2 + \frac{q_\Gamma + Q}{k}x + T_\Gamma. \tag{14.52}$$

Using the foregoing equation, the *exact* solution in equivalent energy can be calculated easily and given as

$$\mathrm{U}_e = \sum_{i=1}^{N_s} A_i^s \left(\overline{\mathbf{L}_d T}\right)^T \mathbf{c} \left(\overline{\mathbf{L}_d T}\right) = 12,666.6666\ (\text{J m}^{-3}\,^\circ\text{C}). \tag{14.53}$$

The solution convergence in energy is examined using the NS-FEM models with different numbers of uniformly distributed nodes, and the results of the equivalent energy computed using Equation 14.51 are plotted in Figure 14.2. For comparison, the results obtained using the FEM with the same meshes are also plotted. It can be clearly seen that as long as more than three nodes (two elements) are used, the equivalent energy solution of NS-FEM is always larger than that of the *exact* solution, while the FEM's solution is always a lower bound. This echoes the finding in Chapter 6 for solid mechanics problems. This important upper bound property of

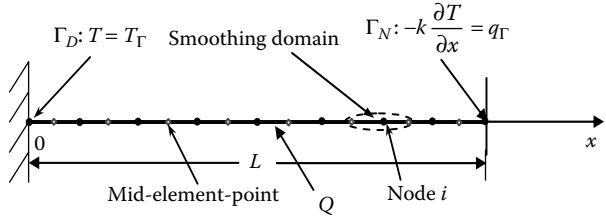

FIGURE 14.1 A 1D thermal fin subjected to a uniformly distributed heat source. The circumference of the fin is adiabatic.

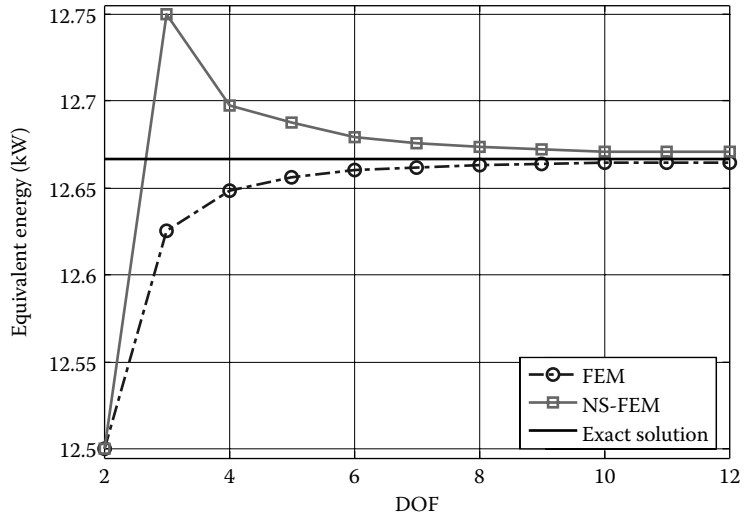

FIGURE 14.2 A 1D thermal fin subjected to a uniformly distributed heat source. The circumference of the fin is adiabatic.

the NS-FEM for heat transfer problems is an important complement to the standard FEM. We can now easily bound the exact solution for both sides using NS-FEM together with FEM using the same mesh.

14.8.2 Heat Transfer in a 2D Solid

A 2D heat transfer problem of a rectangular plate shown in Figure 14.3 is now studied. The parameters used in the computation are length $L = 0.05\,\text{m}$, height $H = 0.01\,\text{m}$, $h = 1500\,\text{W/m}^2\,^\circ\text{C}$, $T_\text{a} = 200^\circ\text{C}$, $T_\Gamma = 0^\circ\text{C}$, $k_x = 15\,\text{W/m}\,^\circ\text{C}$, $k_y = 10\,\text{W/m}\,^\circ\text{C}$, and $q_\Gamma = -4000\,\text{W/m}^2$. As no *exact* solution is available for this problem, a *reference* solution is obtained

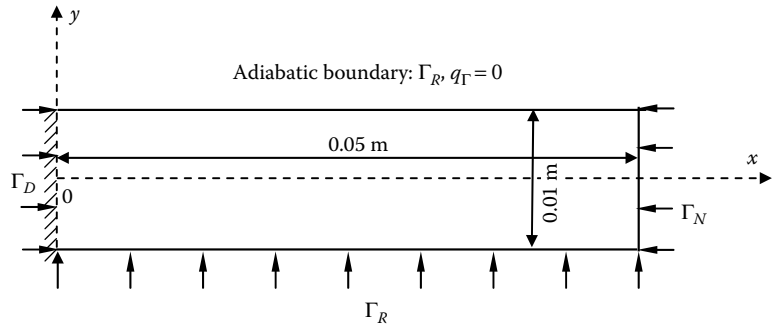

FIGURE 14.3 Heat transfer in a 2D solid.

using ABAQUS© with a very fine mesh of 329,217 nodes for comparison purposes.

14.8.2.1 Temperature and Its Gradients

Figure 14.4 presents temperature distributions along the bottom edge obtained using NS-FEM and FEM with linear triangular elements, together with the reference solution. It can be seen that the NS-FEM solutions are in much better agreement with the reference solution, compared to the FEM.

Figure 14.5 plots the contour of the temperature gradients in the y-direction computed using NS-FEM and FEM using the same mesh of linear triangular elements, together with the reference solution. It shows clearly that the distribution of the temperature gradient computed using NS-FEM agrees well with the reference solution, and is more accurate than the FEM solution.

14.8.2.2 Bound Property of Solutions

As discussed in Chapter 6, the NS-FEM can provide an upper bound and the compatible FEM gives a lower bound in energy norm for the exact solution to elasticity problems of multiple dimensions. To show the bound

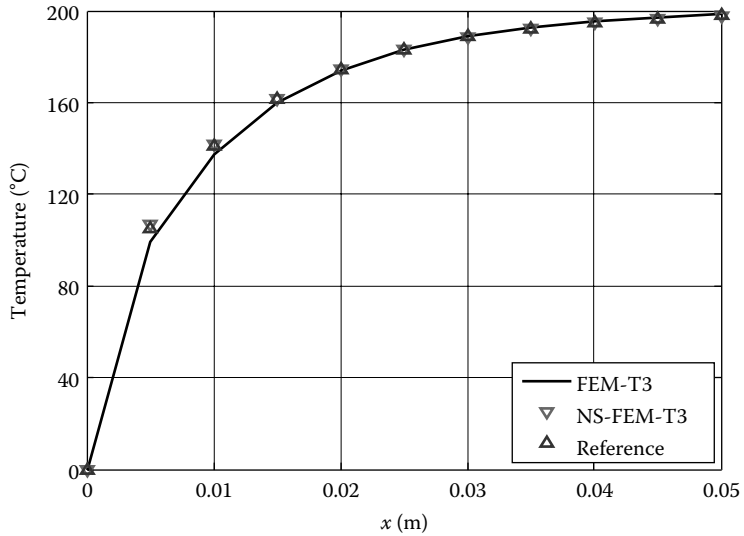

FIGURE 14.4 Temperature distributions along the bottom edge of the 2D solid obtained using NS-FEM-T3 and FEM-T3 with linear triangular elements, together with the reference solution.

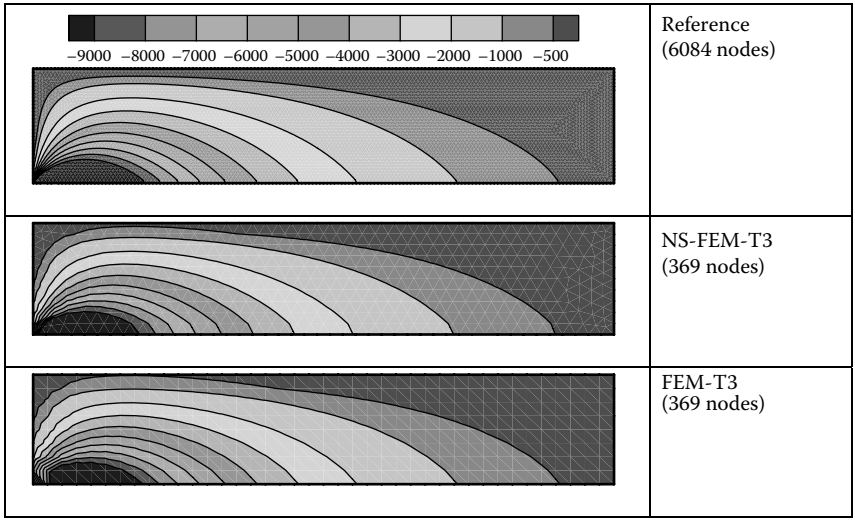

FIGURE 14.5 Contour of the temperature gradients in the y-direction computed using NS-FEM-T3 and FEM-T3 with linear triangular elements, together with the reference solution obtained using a fine mesh.

property of the NS-FEM for 2D heat transfer problems, four models with regularly distributed 33, 105, 369, and 1377 nodes are created to analyze the heat transfer in the 2D medium shown in Figure 14.3. In this analysis, we compute first the temperature distribution and then evaluate the equivalent thermal energy in the whole domain.

Figure 14.6 shows the equivalent thermal energy defined in Equation 14.51 computed using NS-FEM and FEM using the same meshes, together with the reference solution. It is clearly shown that NS-FEM gives the upper bound and FEM gives the lower bound solutions for this 2D heat transfer problem with homogeneous essential boundary conditions ($T_\Gamma = 0$). It is also observed that with the increase of DOFs, the equivalent energy of the NS-FEM model and the FEM model converges to the reference solution, respectively, from above and below.

14.8.2.3 Accuracy and Convergence Rate

We now further examine the accuracy and convergence rate of NS-FEM in comparison with FEM using the four models created in Section 14.8.2.2. Figure 14.7 plots the convergence curves of error in the temperature solution obtained using NS-FEM and linear FEM when the average nodal spacing h is reduced. The convergence rate, R, is estimated via linear regression. It is seen that the NS-FEM achieves better accuracy, compared to the linear FEM. It is also found that the NS-FEM achieves a higher convergence rate with $R = 1.93$ than that of the linear FEM with $R = 1.78$.

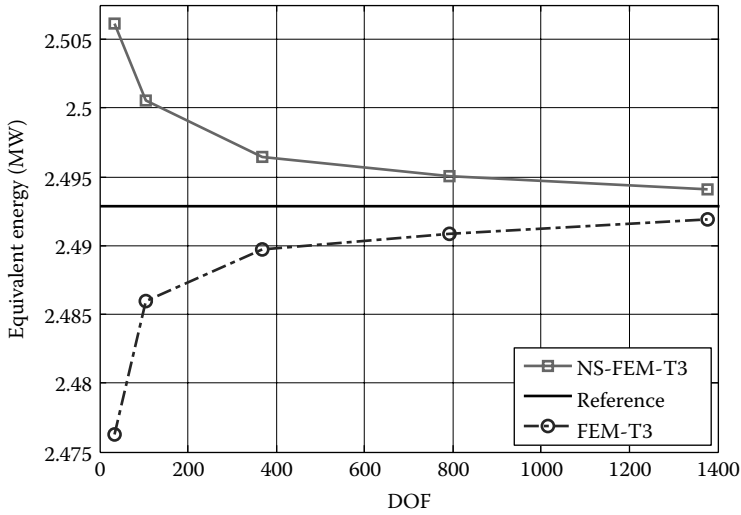

FIGURE 14.6 Convergence of the equivalent energy defined in Equation 14.51 computed using NS-FEM-T3 and FEM-T3 using the same meshes.

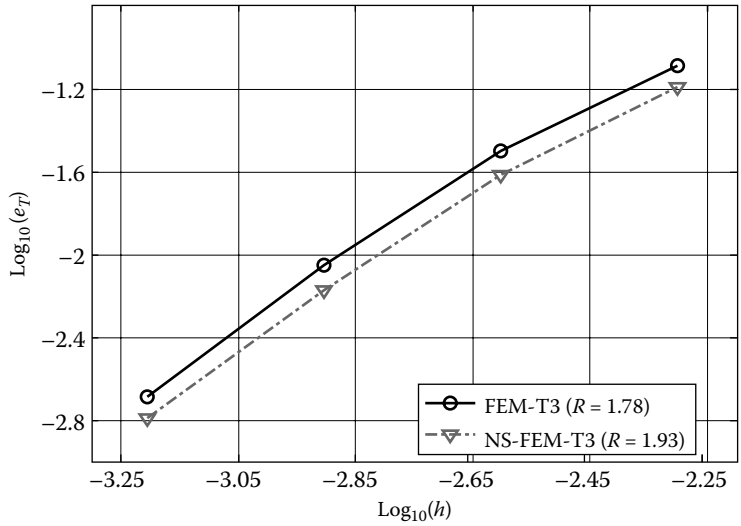

FIGURE 14.7 Convergence curves for the solution error in the temperature field obtained using NS-FEM-T3 and linear FEM-T3 when the average nodal spacing h is reduced.

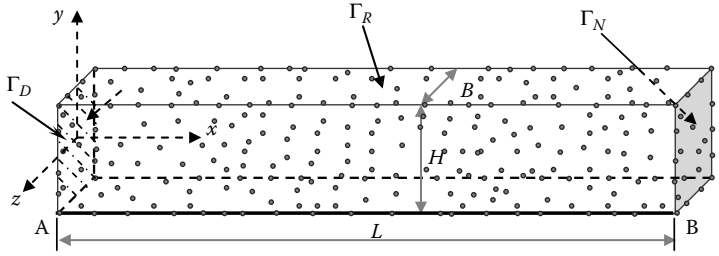

FIGURE 14.8 3D heat conduction in a beam.

14.8.3 A 3D Heat Conduction Beam

We now consider 3D problems. The first example considered here is a simple 3D heat conduction beam as shown in Figure 14.8. The room temperature T_Γ is prescribed onto the left surface of the beam, heat flux q_Γ is given on the right surface, and heat convection occurs between the top surface and the ambience with a convection coefficient h. The parameters used in the computation are

Geometry: $L = 0.1\,\text{m}$, $H = 0.01\,\text{m}$, and $B = 0.01\,\text{m}$
Heat conductivity: $Q = 0$, $k_x = 15\,\text{W/m}\,^\circ\text{C}$, $k_y = 10\,\text{W/m}\,^\circ\text{C}$, and $k_z = 5\,\text{W/m}\,^\circ\text{C}$
Heat convection coefficient: $h = 1500\,\text{W/m}^2\,^\circ\text{C}$
Heat source: $Q = 0$
Boundary conditions: $T_\Gamma = 0$, $T_\text{a} = 400\,^\circ\text{C}$, and $q_\Gamma = -2000\,\text{W/m}^2$

The beam is meshed with 508 nodes using the four-node tetrahedral (T4) elements. The same mesh is used for both NS-FEM and FEM models. The reference solution is obtained using a very fine mesh with 14,843 nodes that has about 30 times more nodes compared with the coarse model.

14.8.3.1 Temperature Distribution

The temperatures at the nodes on the bottom edge (AB edge in Figure 14.8) are computed using NS-FEM and FEM and the results are listed in Table 14.1, together with linear FEM and reference solutions. It can be found that

TABLE 14.1

Comparison of the Solutions of Temperature (°C) along the AB Edge

x (m)	0.01	0.02	0.03	0.04	0.05	0.06	0.07	0.08	0.09	0.10
Reference	286.30	371.77	393.03	398.28	399.58	399.91	400.02	400.20	400.81	403.16
NS-FEM-T4	287.84	372.16	392.88	398.26	399.57	399.90	400.02	400.20	400.80	403.21
FEM-T4	283.47	371.43	392.91	398.25	399.57	399.91	400.02	400.20	400.80	403.11

NS-FEM and FEM solutions are in very good agreement with those of the reference ones. This shows that the NS-FEM model works well also for this 3D heat transfer problem. This finding is consistent with those in the previous chapters: NS-FEM gives at least a similar accuracy for the results of the primary variables that is temperature in this case. For the gradient of the primary variables, the S-FEM solution will be much better, as will be shown in the following.

14.8.3.2 Distribution of Temperature Gradients

In the design of many engineering systems with thermal effects, the temperature gradient is a very important consideration. Because such information is difficult to obtain via physical experiments, it is often much more preferred to predict the gradient distribution using numerical means. Figure 14.9 plots the distribution of the y-component of the temperature gradient (°C/m) in the 3D beam obtained using NS-FEM and FEM, together with the reference solution. It can be clearly observed that the result obtained

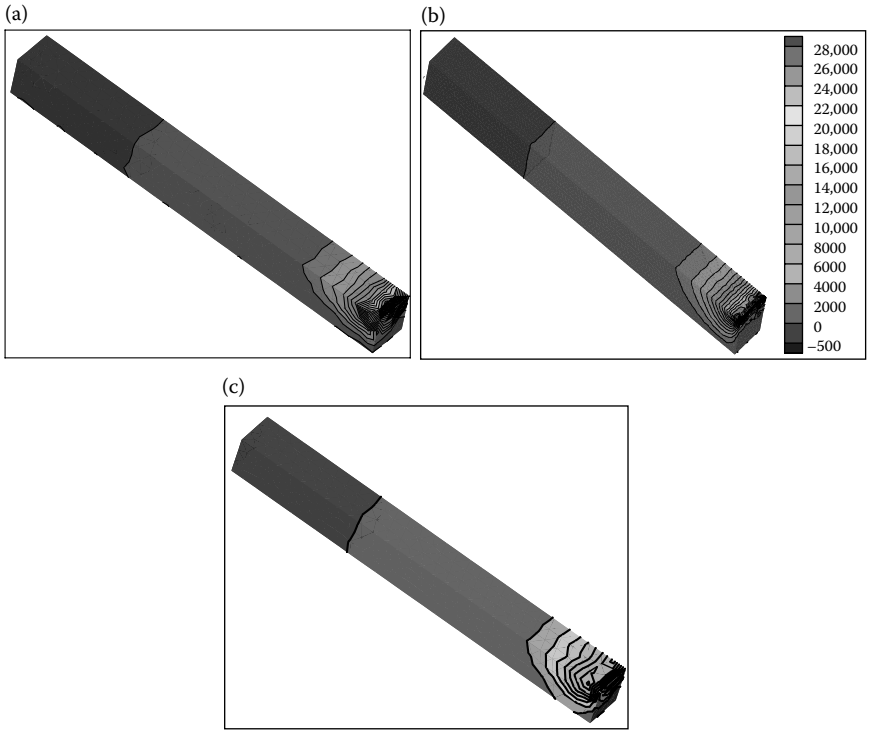

FIGURE 14.9 Distribution of the y-component of the temperature gradient (°C/m) in the 3D beam. (a) NS-FEM using 508 nodes; (b) reference solution using 14,843 nodes; and (c) FEM using 508 nodes.

using NS-FEM is in very good agreement with the reference one. On the overall distribution, the NS-FEM solution is much more accurate than the FEM solution, compared to the reference solution, especially in the high gradient zone. Figure 14.10 shows the distribution of the z-component of the temperature gradient (°C/m) in the 3D beam, and similar observations can be made. This is because of the well-known fact that the FEM using tetrahedral elements is overly stiff and produces a constant gradient field within the elements, which can lead to inaccurate results, especially in the high gradient zone. To examine this quantitatively, the minimum and maximum of the temperature gradients in the 3D beam are computed using NS-FEM-T4 and FEM-T4 with the same mesh, and the computed results in Figure 14.11 in comparison with the reference solution. It reveals that the NS-FEM can obtain a significantly better accuracy than the linear FEM for the maximum gradients. This is because the NS-FEM uses the gradient smoothed operations. Hence the model behaves much "softer" compared with the FEM model and hence produces a much more accurate solution in terms of temperature gradient. A similar phenomenon has also been observed in Chapter 6 for solid mechanics problems.

14.8.3.3 Solution Bound

As seen in the 1D and 2D examples, the NS-FEM can produce upper bound solutions for "flux driving" heat transfer (or force driving for solid

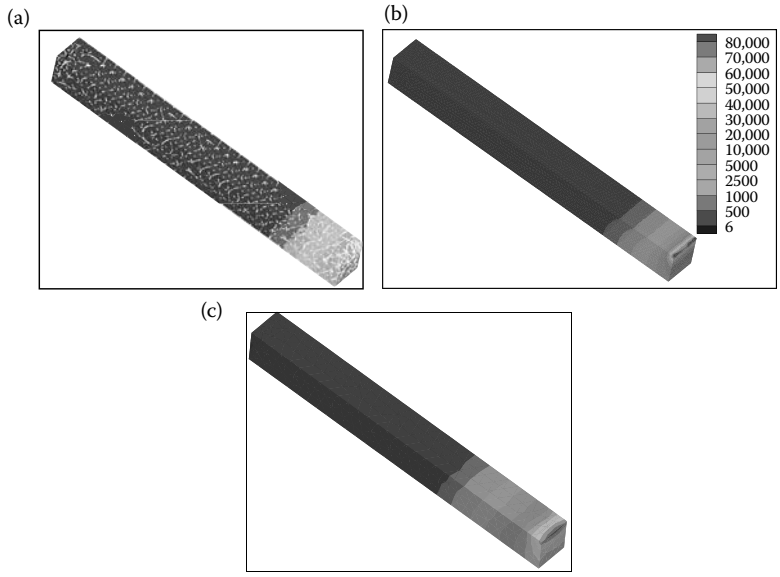

FIGURE 14.10 Distribution of the z-component of the temperature gradient (°C/m) in the 3D beam. (a) NS-FEM using 508 nodes; (b) reference (FEM) solution using 14,843 nodes; and (c) FEM using 508 nodes.

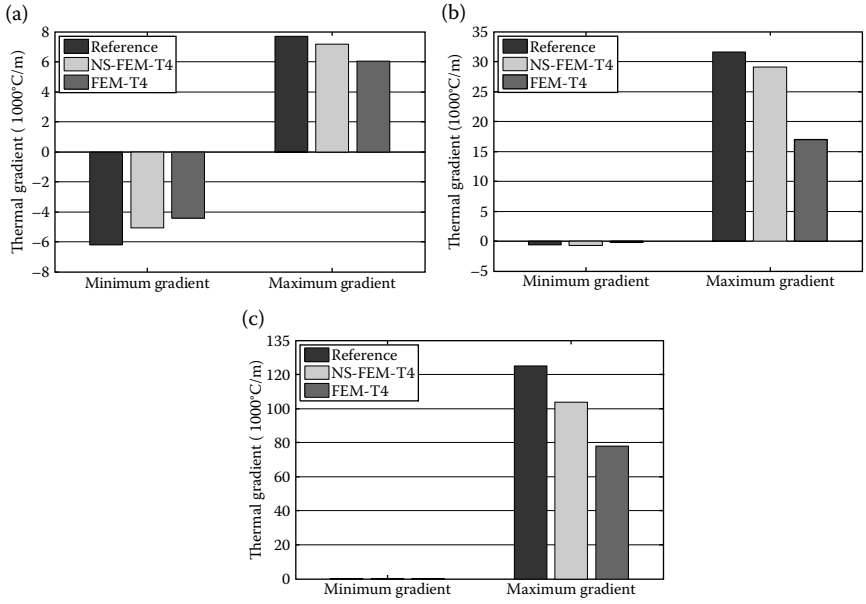

FIGURE 14.11 The minimum and maximum of the temperature gradients in the 3D beam obtained using NS-FEM-T3 and FEM-T3 in comparison with the reference solution. (a) x-direction; (b) y-direction; and (c) z-direction.

mechanics) problems. To examine the same important property for 3D problems, four 3D models of the heat conduction beam are built with irregularly distributed nodes (163, 508, 1147, and 2605), and both NS-FEM and FEM are used to compute the results using all these four models. Figure 14.12 shows the convergence process of the solution in terms of the equivalent energy with the increase of DOFs, where the reference solution is obtained using ABAQUS® with a very fine mesh of second-order elements with 14,843 nodes. It can be clearly observed that the equivalent thermal energy solution of NS-FEM is larger than that of the reference solution. On the contrary, the FEM solution is smaller than the reference one. This finding confirms that NS-FEM can also provide upper bound solutions for 3D heat transfer problems [13], NS-FEM is an important complement to the fully compatible FEM.

14.8.4 An Engine Pedestal

We now apply the NS-FEM to a more practical 3D problem: a real engine pedestal with complex geometries. The pedestal part is made of a superalloy material, and detailed dimensions and processing parameters can be found in Ref. [14]. Using our in-house 3D NS-FEM and FEM codes, the

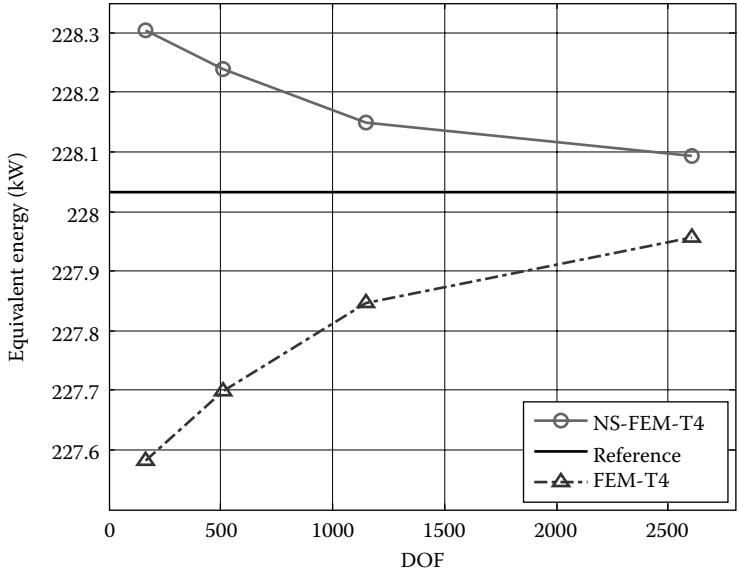

FIGURE 14.12 Convergence process of the solution in terms of the equivalent energy for the 3D heat conduction beam problem.

heat transfer analysis is conducted. Figure 14.13 shows the geometry of the engine pedestal and the setting of the problem. The boundary conditions are defined in Equations 14.5 through 14.7. The parameters and conditions used are the same as the 3D conduction beam studied in Section 14.8.3. The problem domain is divided into a mesh of tetrahedral elements with

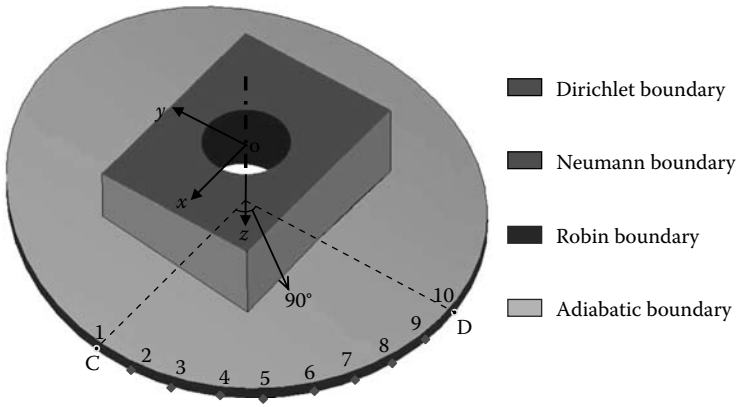

FIGURE 14.13 The geometry of the engine pedestal and the setting of the problem. The boundary conditions are defined in Equations 14.5 through 14.7.

TABLE 14.2

Comparison of the Solutions of Temperature (°C) along the CD Arc Line

Node ID	1	2	3	4	5	6	7	8	9	10
Reference	266.62	277.35	282.46	288.12	293.94	299.55	304.53	308.81	314.54	316.47
NS-FEM-T4	269.89	281.34	285.66	290.89	296.68	302.20	307.16	311.06	316.22	318.74
FEM-T4	262.93	273.46	278.50	284.36	290.31	296.36	301.42	306.23	311.94	313.79

754 nodes. Both NS-FEM-T4 and FEM-T4 are used in the computation for this 3D problem, and the results will be output at 10 evenly distributed points along the CD arc edge (see Figure 14.13). For comparison purposes, a reference solution is obtained using the FEM with a very fine mesh of 30,222 nodes.

14.8.4.1 Temperature Distribution

Table 14.2 shows the temperature solution obtained at the nodes located on the CD arc edge, together with the reference solution. It can be observed that the temperature results obtained using NS-FEM-T4 are always larger than those of the linear FEM-T4 and reference ones, and linear FEM solutions are the smallest, showing again the upper bound property of the NS-FEM and the lower bound property of the FEM. Note that, for this particular problem, the temperatures obtained are all positive, and hence the bound property (which is usually observed in the energy norm) can also be observed even for the temperature solution. This may not be true in general.

14.8.4.2 Temperature Gradients

Figure 14.14 plots the contour of temperature gradients (°C/m) in the x-direction obtained using the NS-FEM-T4 and the linear FEM-T4, together with the reference solution. It can be clearly seen for this 3D problem that temperature gradients obtained using the NS-FEM agree well with the reference ones, and the results are more accurate than those of the FEM, especially in the high gradient regions. Figure 14.15 shows the results of temperature gradients in the z-direction. It can be observed again that the NS-FEM-T4 result is more accurate than the result of the linear FEM-T4, in comparison with the reference one, especially in the high temperature gradient regions. For quantitative analysis, Figure 14.16 shows the minimum and maximum of the temperature gradients in the 3D engine pedestal obtained using NS-FEM-T4 and FEM-T4, in comparison with the reference solution. It can be clearly seen that the NS-FEM-T4 results of temperature

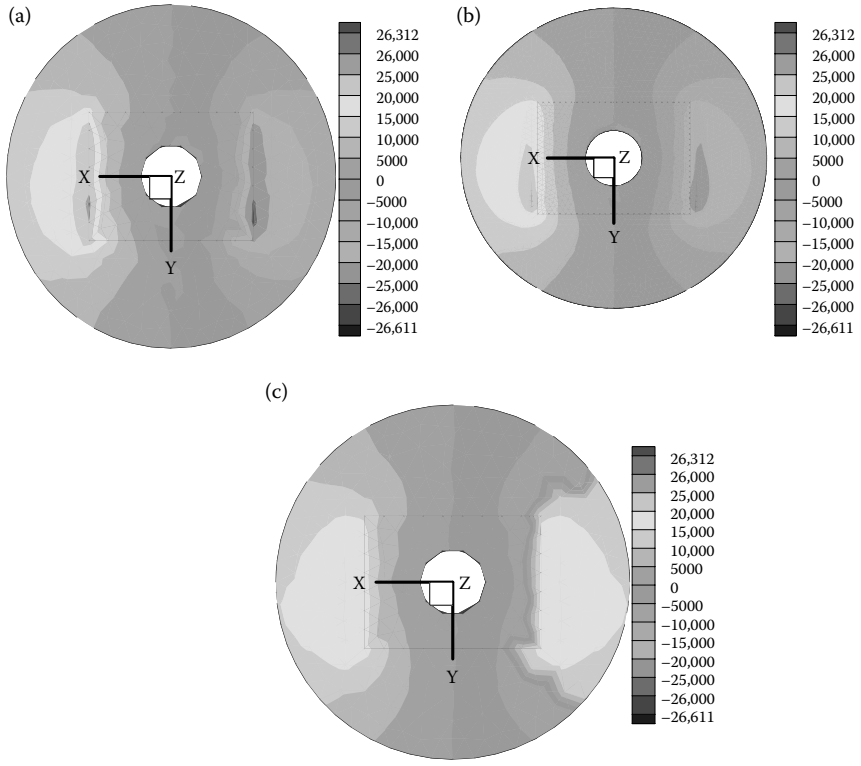

FIGURE 14.14 Contour of temperature gradients in the x-direction. (a) NS-FEM solution using 754 nodes; (b) reference (FEM) solution using 30,222 nodes; and (c) FEM solution using 754 nodes.

gradients are very close to the reference results, and are much more accurate than those of the FEM-T4.

14.8.4.3 Solution Bound

To further confirm the upper bound property for 3D problems with complicated geometry, four models for this complex problem are generated with irregularly scattered 754, 1389, 2447, and 3287 nodes. Figure 14.17 plots the convergence of the numerical solutions in terms of equivalent energy obtained using NS-FEM-T4 and FEM-T4, where the reference one is obtained using a very fine mesh of 30,222 nodes. It can be observed that for this complicated 3D engine pedestal, the NS-FEM-T4 produces again an upper bound solution in equivalent energy norm with homogeneous essential boundary conditions ($T_\Gamma = 0$), and the solution converges from above to the reference solution with the increase in DOFs. On the contrary, the FEM solution approaches the reference solution from below. Note that

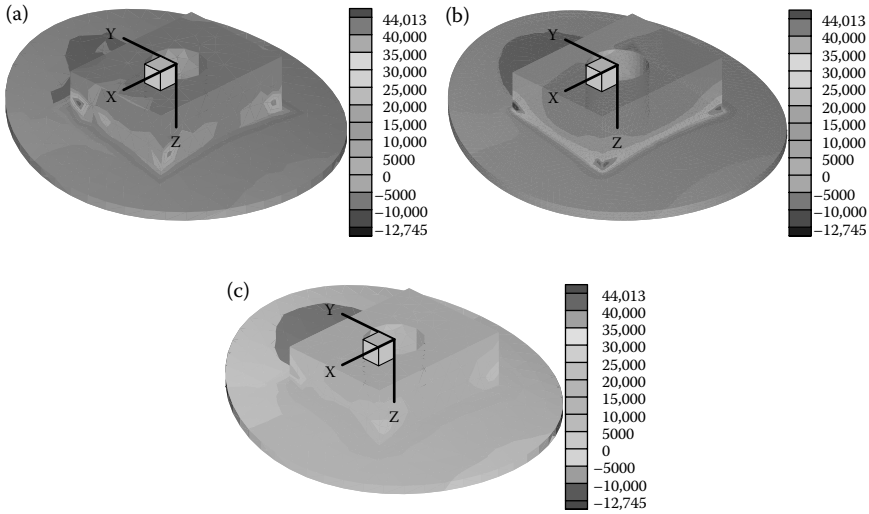

FIGURE 14.15 Distribution of temperature gradients in the z-direction. (a) NS-FEM solution using 754 nodes; (b) reference (FEM) solution using 30,222 nodes; and (c) FEM solution using 754 nodes.

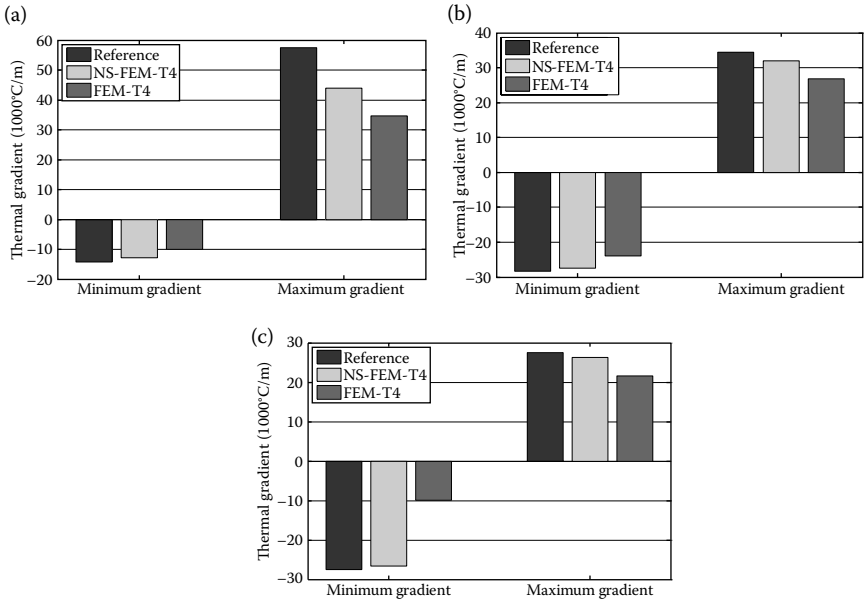

FIGURE 14.16 The minimum and maximum of the temperature gradients in the 3D engine pedestal obtained using NS-FEM-T4 and FEM-T4, in comparison with the reference solution. (a) x-direction; (b) y-direction; and (c) z-direction.

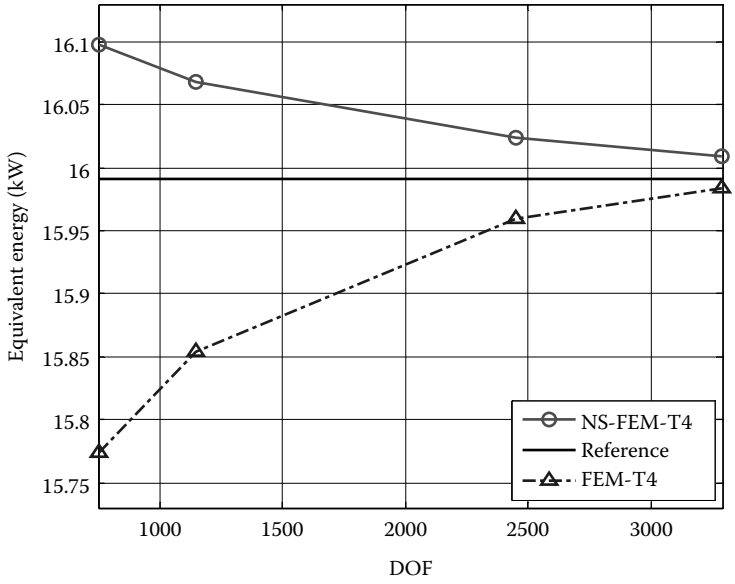

FIGURE 14.17 Convergence of the equivalent energy obtained using NS-PIM-T4 and FEM-T4. The reference one obtained using FEM with a very fine mesh of 30,222 nodes.

because the reference solution is obtained using the FEM, by itself it is an underestimation of the exact solution. Therefore, the true exact solution should be higher than the reference solution shown in Figure 14.17, and hence is closer to the NS-FEM-T4 solution.

Figures 14.2 (1D), 14.6 (2D), 14.12 (3D), and 14.17 (3D) have all shown that with the increase of DOFs, the equivalent thermal energy of the FEM model and the present NS-FEM model converges to the reference solution, with FEM from below and NS-FEM from above. This finding is very similar to what we have found in Chapter 6 for solid mechanics problems. Therefore, it is also possible to develop an αFEM for heat transfer problems for nearly exact solutions, as we have done in Chapter 9 for the solid mechanics problems.

14.9 Bioheat Transfer Problems

The modeling of bioheat transfer in the human body is very important in many aspects, including the development of medical technology in treating diseases such as tumor. The hyperthermia treatment has been found effective with little side effects in some cancer treatments. It uses the thermal energy to kill cancer cells without causing much damage to the

surrounding tissues [15–17]. In a hyperthermia treatment, the temperature needs to be increased to above 42°C on the tumor, but without much change in the healthy tissue [9,18,19]. Therefore, the major challenge in such a hyperthermia treatment is to properly control the temperature distribution to maximize the treatment effects and minimize the damage. The FEM has been often used in the simulation of hyperthermia treatments to predict the temperature distribution. However, because of the overly stiff feature of the FEM model, we can have accuracy problems in the FEM predicted solution.

In this subsection we first derive the strong-form equation for bioheat transfer problems and then apply the FS-FEM-T4 to study one particular 3D bioheat transfer example of hyperthermia treatment for a breast cancer.

14.9.1 The Pennes' Bioheat Transfer Model

Bioheat transfer in the living tissue is, in reality, quite complicated, compared to the heat transfer problems in engineering systems, owing mainly to the complicity of the living tissues. There are a number of models available to analyze the bioheat transfer in the living tissue [13]. Pennes' bio-heat model is one of the simplest models that consider various heat source terms in idealized situations. It considers two major biology-related mechanisms: blood perfusion and metabolism that regulate the temperature distribution in the living tissues. As suggested by Pennes [20–24], the thermal energy balance for a perfused tissue can be written in matrix form as

$$\rho c \frac{\partial T}{\partial t} = \mathbf{L}_d^T \mathbf{c} \mathbf{L}_d T + Q_\mathrm{b} + Q_\mathrm{r} + Q_\mathrm{m} \quad \text{in } \Omega. \tag{14.54}$$

In Equation 14.1, Q_b is the heat exchanged between the blood and tissue. In Pennes' model, it is assumed that the net rate of heat exchange between blood and tissue is proportional to the product of the volumetric perfusion rate and the difference between the arterial blood temperature and the local tissue temperature [20]. Based on this assumption, the term Q_b can be expressed simply as follows:

$$Q_\mathrm{b} = c_\mathrm{b} \omega_\mathrm{b} (T_\mathrm{b} - T), \tag{14.55}$$

where c_b is the specific heat of blood, ω_b is the blood perfusion rate, and T_b is the body core temperature that is set as a constant of 37°C. Therefore, blood is regarded as a local heat "regulator" by a "heat convection-like" mechanism. When Q_b is positive, the blood acts like a heat source to the tissue, and when Q_b is negative, the blood becomes a heat sink.

In Equation 14.1, Q_m is the volumetric heat source provided to the tissue via metabolism, and Q_r stands for the externally supplied heat source that represents the heat applied during the hyperthermia treatment.

Substituting Equation 14.55 into Equation 14.1, the bioheat transfer equation can be written as

$$\begin{aligned}\rho c\frac{\partial T}{\partial t} &= \mathbf{L}_d^T\mathbf{c}\mathbf{L}_d T + \omega_{\mathrm{b}}c_{\mathrm{b}}(T_{\mathrm{b}} - T) + Q_{\mathrm{r}} + Q_{\mathrm{m}} \\ &= \mathbf{L}_d^T\mathbf{c}\mathbf{L}_d T - \underbrace{\omega_{\mathrm{b}}c_{\mathrm{b}}}_{h_T} T + \underbrace{\omega_{\mathrm{b}}c_{\mathrm{b}}T_{\mathrm{b}} + Q_{\mathrm{r}} + Q_{\mathrm{m}}}_{Q},\end{aligned} \tag{14.56}$$

which is Equation 14.1 for the general dynamic heat transfer problems with

$$h_T = \omega_{\mathrm{b}}c_{\mathrm{b}}, \tag{14.57}$$

$$Q = \omega_{\mathrm{b}}c_{\mathrm{b}}T_{\mathrm{b}} + Q_{\mathrm{r}} + Q_{\mathrm{m}}. \tag{14.58}$$

For static heat transfer problems, we have Equation 14.4. The boundary conditions have the same form of Equations 14.5 through 14.7.

We have successfully converted the bioheat transfer problem into a standard heat transfer problem that we have dealt with in Sections 14.2 through 14.7. All these equations that developed in these sections can be now simply applied directly to solve bioheat transfer problems.

14.9.2 Hyperthermia Treatment: A 3D Bioheat Transfer Case Study

We finally present a 3D model simulating the hyperthermia treatment of a cancer in a female breast. The geometry of the 3D breast is simplified as a half-sphere with a diameter of 180 mm, as shown in Figure 14.18. On the base of the sphere, we assume that the temperature is kept by the human body at 37°C; hence a Dirichlet boundary condition is applied there with $T_\Gamma = 37°\mathrm{C}$. On the surface of the sphere, a heat convection boundary condition is applied. All the parameters used in the computation are summarized in Table 14.3.

TABLE 14.3

Details of Parameters used in the Hyperthermia Treatment Problem

c	Specific heat of tissue 4200 J/kg °C	ρ	Density of tissue 1000 kg/m^3
k_i ($i = x, y, z$)	Thermal conductivity of tissue $k_i = 0.5$ W/m °C	ω_{b}	Blood perfusion rate 0.5 kg/m^3
c_{b}	Specific heat of blood 4200 J/kg °C	Q_{m}	Volumetric heat 33,800 W/m^3
T_{b}	Body core temperature 37°C	T_Γ	Temperature of the human body 37°C
T_{a}	Known ambient temperature 10°C	h_T	Ambient heat transfer coefficient 100 W/m^2

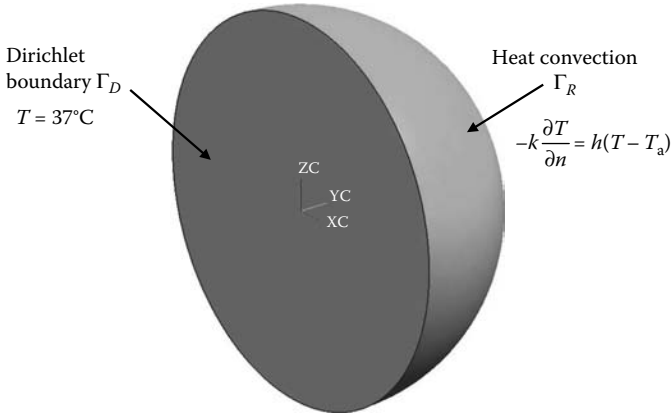

FIGURE 14.18 Geometry of the 3D breast is simplified as a half-sphere of diameter 180 mm.

The breast cancer is also simplified as a small sphere of radius $r = 7.1$ mm, and it is located at ($x_0 = -23$ mm, $y_0 = 30$ mm, $z_0 = 0$), as shown in Figure 14.19. Therefore the heat source is also applied over the region of the cancer:

$$Q_{\mathrm{r}}(x, y, z, t) = \begin{cases} T_{\mathrm{C}}(t) & \text{in the cancel region,} \\ 0 & \text{elsewhere,} \end{cases} \tag{14.59}$$

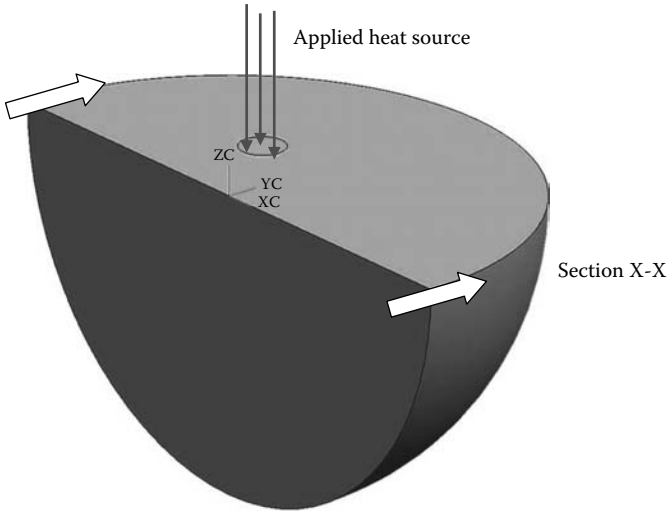

FIGURE 14.19 Location of the heat source distributed in a small sphere of $r = 7.1$ mm. The center of the heat source is ($x_0 = -23$ mm, $y_0 = 30$ mm, $z_0 = 0$).

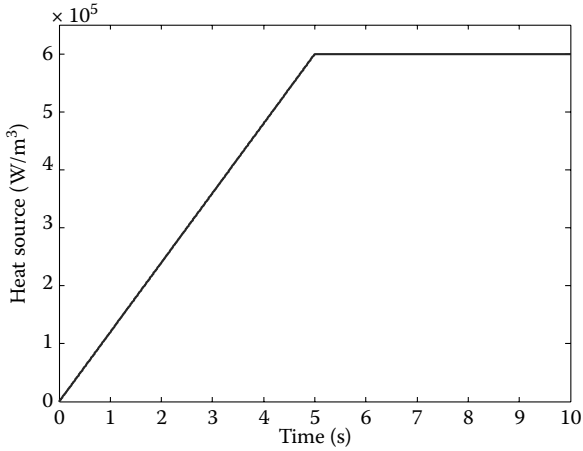

FIGURE 14.20 Time history $P(t)$ of the applied heat source over the cancer region.

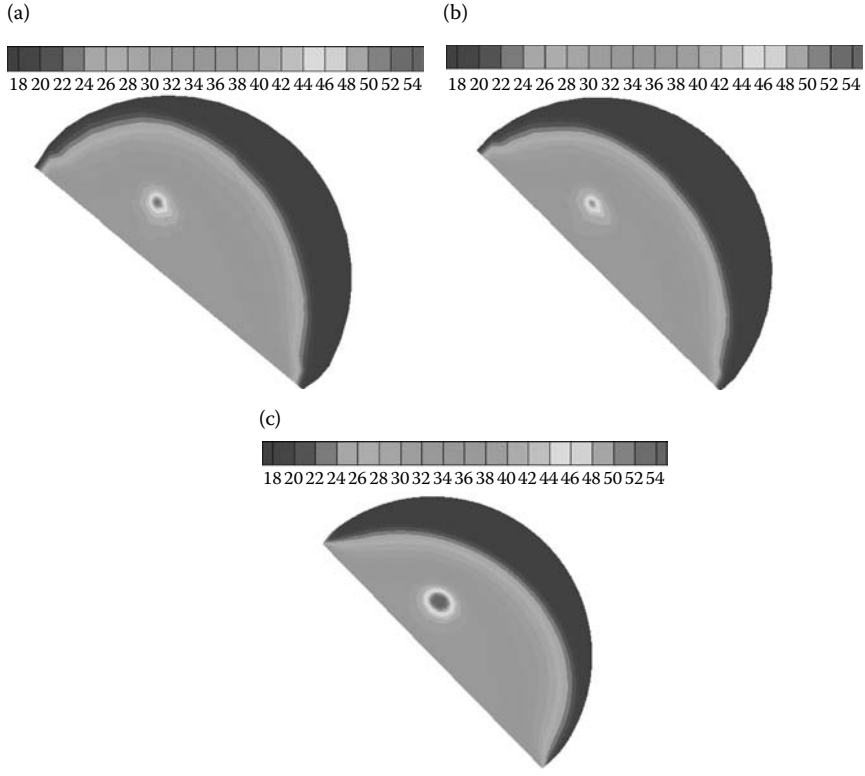

FIGURE 14.21 Transient temperature distribution at $t = 10$ s. (a) FS-FEM model using 1692 nodes; (b) FEM model using 1692 nodes; and (c) reference (FEM) solution using 14,900 nodes.

where $T_C(t)$ is the time history of the applied heat source that is plotted in Figure 14.20. Both FS-FEM-T4 and FEM-T4 are used in the simulation of the dynamic heat transfer problem with a time step $\Delta t = 0.01$ s.

Figure 14.21 shows the contours of the temperature distribution obtained using FS-FEM and FEM using the same mesh of tetrahedral elements with a total of 1692 nodes. Because the exact solution for this problem is not available, a very fine FEM model with 14,900 nodes is used to obtain the reference solution for comparison. It is shown that the overall solution obtained using the FS-FEM is much closer to the reference solution.

To examine the difference quantitatively, the time history of the maximum temperature (found at the center of the tumor) is also computed using FS-FEM and FEM using the same mesh with 668 nodes, and the results are plotted in Figure 14.22, together with the reference solution. Figure 14.22 shows clearly that the temperature of the FEM solution rises much more slowly than that of the reference solution. The FS-FEM solution, however, respond much better. At the steady state, the FS-FEM solution has about 2.5°C error in temperature; the FEM has about 5.5°C. The difference between FS-FEM and FEM using the same mesh is about 3.0°C, which is very significant for the hyperthermia treatment. In conclusion, the FS-FEM is much more reliable for the modeling of bioheat transfer problems.

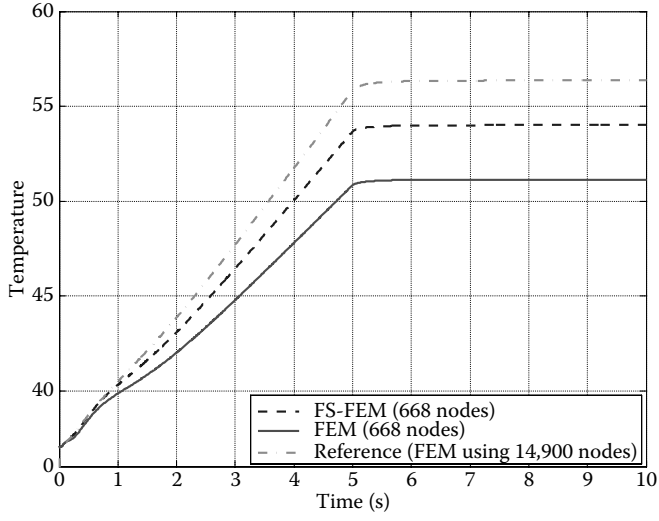

FIGURE 14.22 Time history of the maximum temperature (registered at the center of the cancer tumor) obtained using different FS-FEM and FEM models with time step $t = 0.01$ s.

14.10 Remarks

In this chapter, we presented formulations for the S-FEM models for heat transfer problems. We then used some of the S-FEM models to solve heat transfer problems in engineering and biosystems. We now close the chapter by stating the following remarks.

1. The S-FEM model changes only the stiffness (conductivity) matrix of the discrete model.
2. The NS-FEM model can provide upper bound to the exact solution in terms of equivalent energy of the system for a flux driving the heat transfer problem of all dimensions, as long as the mesh is sufficiently fine to provide sufficient softening effects. For other types of problems, the NS-FEM and FEM should bound the solution in a norm from both sides of the exact solution.
3. The FS-FEM can produce a much more accurate solution compared to the FEM counterpart using the same mesh. Hence it is much more reliable for problems requiring high precision in temperature prediction, such as the simulation of hyperthermia treatments. More detailed studies for ES-FEM and FS-FEM for heat transfer problems can be found in Ref. [21], where the outstanding performances of ES-FEM and FS-FEM have been reported.
4. The S-FEM models work very well with a linear triangular mesh, and have been found to be less sensitive to the mesh distortion.
5. The S-FEM models have been applied also to thermoelastic problems with very important findings [10–12]. The strain energy of the thermoelastic problems can also be properly bounded using NS-FEM together with FEM models of the same mesh.

References

1. Thomas LC. 1992. *Heat Transfer*, international edition. Prentice-Hall, NJ.
2. Segerlind LJ. 1984. *Applied Finite Element Analysis*. Wiley, NY.
3. Liu GR and Quek SS. 2002. *The Finite Element Method: A Practical Course*. Butterworth Heinemann, Oxford.
4. Liu GR. 2009. *Mesh Free Methods: Moving Beyond the Finite Element Method*, 2nd edition. CRC Press, Boca Raton, FL.
5. Liu GR. 2009. A G space theory and weakened weak (W^2) form for a unified formulation of compatible and incompatible methods, Part I: Theory and Part II: Applications to solid mechanics problems. *International Journal for Numerical Methods in Engineering*; 81: 1093–1156.

6. Liu GR. 2009. On a G space theory. *International Journal of Computational Methods*; 6(2): 257–289.
7. Liu GR and Zhang GZ. 2009. A normed G space and weakened weak (W^2) formulation of a cell-based smoothed point interpolation method. *International Journal of Computational Methods*; 6(1): 147–179.
8. Liu GR. 2008. A generalized gradient smoothing technique and the smoothed bilinear form for Galerkin formulation of a wide class of computational methods. *International Journal of Computational Methods*; 5(2): 199–236.
9. Arora D, Skliar M, and Roemer RB. 2002. Model-predictive control of hyperthermia treatments. *IEEE Transactions on Biomedical Engineering*; 49: 629–639.
10. Wu SC, Liu GR, Zhang HO, and Zhang GY. 2009. A node-based smoothed point interpolation method (NS-PIM) for thermoelastic problems with solution bounds. *International Journal of Heat and Mass Transfer*; 52(5–6): 1464–1471.
11. Wu SC, Liu GR, Zhang HO, and Zhang GY. 2008. A node-based smoothed point interpolation method (NS-PIM) for three-dimensional thermoelastic problems. *Numerical Heat Transfer, Part A: Applications*; 54(12): 1121–1147.
12. Wu SC, Liu GR, Zhang HO, Xu X, and Li ZR. 2009. A node-based smoothed point interpolation method (NS-PIM) for three-dimensional heat transfer problems. *International Journal of Thermal Sciences*; 48(7): 1367–1376.
13. Arkin H, Xu LX, and Holmes KR. 1994. Recent developments in modeling heat transfer in blood perfused tissues. *IEEE Transactions on Biomedical Engineering*; 41: 97–110.
14. Wang GL, Wu SC, and Zhang HO. 2007. Numerical simulation of temperature field on complicated parts during plasma deposition dieless manufacturing. *Transactions of the China Welding Institution*; 28(5): 49–52.
15. Stauffer PR and Goldberg SN. 2004. Introduction: Thermal ablation therapy, *International Journal of Hyperthermia*; 20: 671–677.
16. Stauffer PR. 2005. Evolving technology for thermal therapy of cancer. *International Journal of Hyperthermia*; 21: 731–744.
17. Ambrosio VD, Dughiero F, and Forzan M. 2007. Numerical models of RF-thermal ablation treatments. *International Journal of Applied Electromagnetics and Mechanics*; 25: 429–433.
18. Field SB and Hand JW. 1990. *An Introduction to the Practical Aspects of Hyperthermia*. Taylor & Francis, New York.
19. Diederich CJ. 2005. Thermal ablation and high-temperature thermal therapy: Overview of technology and clinical implementation. *International Journal of Hyperthermia*; 21: 745–753.
20. Wissler EH. 1998. Pennes' 1948 paper revisited. *Journal of Applied Physiology*; 85: 35–41.
21. Li E., Liu GR, and Tan VBC. 2009. ES-FEM on heat transfer problems (submitted).
22. Shen W, Zhang J, and Yang F. 2004. Modelling and numerical simulation of bio-heat transfer and biomechanics in soft tissue. Technical Report No. 391-04, Department of Computer Science, University of Kentucky, Lexington, KY.

23. Torvi DA and Dale JD. 1994. A finite element model of skin subjected to a flash fire. *ASME Journal of Biomechanical Engineering*; 116: 250–255.
24. Zhao JJ, Zhang J, Kang N, and Yang F. 2005. A two level finite difference scheme for one dimensional Pennes's bio-heat equation. *Applied Mathematics and Computation*; 171: 320–331.

15

S-FEM for Acoustics Problems

15.1 Introduction

In previous chapters, we have introduced a number of S-FEM models and demonstrated the excellent properties and outstanding performance of these models for problems of solid and structural mechanics, fracture mechanics, and heat transfer. This chapter aims to extend further the applications of these S-FEM models for acoustics problems.

Acoustics is one of the most relevant topics that are very close to our daily life. We communicate verbally, we play and listen to music, and we are bothered every minute by the noise. All these activities related to directly the *sound* transmitting in the form of *acoustic waves*. Acoustics is a classic research topic that studies various aspects of the acoustic waves since ancient times from at least 3000 BC, when the Chinese invented the Guqin to produce desired music by design. Mathematical models for acoustics problems have been already well established, and the strong-form governing equations, such as the well-known Helmholtz equation, represent the physics of all linear acoustics problems. Various analytical methods for solving the acoustic equations with simple settings have also been developed. During the past several decades, many powerful computational methods have been developed for solving very complicated acoustic, aero-acoustic, and structural-acoustics problems [1–10]. The standard FEM and the boundary element method (BEM) are currently the most well-developed and widely-used methods in solving these acoustics problems, and some software packages are now commercially available.

When a numerical method such as the FEM is used, one of the well-known issues of solving acoustics problems governed by the Helmholtz equation is the so-called numerical "pollution" that is caused by the discretization errors in the phase (dispersion error) and the amplitude (dissipation error) [11–13]. In using a discrete numerical method to solve acoustics problems, the dispersion error is much more difficult to deal with compared to the dissipation error. Many numerical methods can often provide acceptable results for problems in a lower frequency range. In the higher frequency range, however, the dispersion error can grow significantly and the numerical results can deviate substantially from the exact

solution even to a well-posed acoustic problem. Often, an extremely fine mesh beyond the usual "rule of thumb" must be used. On the other hand, using such a very fine mesh will lead to a dramatic increase of the computational cost, especially for large-scale 3D acoustics problems, and hence it is not always a viable option.

Instead of using a fine mesh (hence more elements), using a higher order of elements seems to be more effective, and it has been reported that using high-order elements can reduce the dispersion error [6,14]. Another approach is the Galerkin/least-squares FEM [10,15] with a stabilization term. In recent years, mesh-free methods have been developed and applied to many engineering problems, including the acoustics problems [16]. The element-free Galerkin (EFG) method [17] has been used to solve acoustics problems; it has been found that the EFG is also affected by the dispersion error, but these effects are relatively lower compared to FEM [18]. The discontinuous FEM [19] has also been used for acoustics problems and is found to give significant improvement in accuracy, but at a higher computational cost. More effective ways include the use of semiexact models [3–5]. However, these types of semiexact models have limitations for different types of problems.

Acoustics problems governed by the Helmholtz equation are typical wave propagation problems with characteristics controlled by frequency or wave number. The root of the dispersion error in a numerical method for a wave propagation problem is the error in approximating the "acoustic stiffness" of the system and hence the natural frequencies of the acoustic media. If a fully compatible displacement method, such as the FEM, is used, the model behaves always very "stiff," as we have seen in the previous chapters for solid mechanics problems, resulting in shifting of the eigenvalues of the system, which can be observed as the phase shifts for wave propagation problems. Therefore, a numerical model that provides a good approximation for the stiffness of the system is crucial in effectively reducing the dispersion errors mentioned above. In the past, this is achieved by increasing either the number of elements or the order of elements in FEM settings, which works to a certain extent but is not treating the root of the dispersion error problem.

In this chapter, we first derive both the standard Galerkin and the smoothed Galerkin weak forms for acoustics problems. We then provide the general formulations for both FEM and S-FEM models for acoustics problems. The "star" performers ES-FEM and FS-FEM are next chosen for analyzing a number of 2D and 3D acoustics problems, respectively. Because it has been found that the ES-FEM and FS-FEM can provide a very "close-to-exact" stiffness for solid mechanics and heat transfer problems, it can tackle right to the root of the dispersion error problem. Therefore, it is natural to expect that the ES-FEM and FS-FEM can overcome the dispersion error in the numerical solutions for acoustics problems.

Note that the formulations given in this chapter have some similarities to those for heat transfer problems presented in Chapter 14. The difference is that the field variable for the acoustics problem is acoustic pressure, while that for heat transfer problems is temperature. In addition, the acoustics problems focus more on wave propagation phenomena, in which the wave number becomes a major player in the "game," and the "culprit" of the dispersion error. For wave propagation problems, such a dispersion error can "pollute" very far. In the heat transfer problem, however, our concern is more on the distribution of the temperature field that may change with time.

This chapter is written rather independently of other chapters, and hence readers who are only interested in acoustics problems can read directly this chapter. Proper cross-references will be provided for necessary additional materials.

15.2 Mathematical Model of Acoustics Problems

Consider an acoustic (fluid) media defined in domain Ω with boundary Γ. The boundary is decomposed into three portions such that $\Gamma = \Gamma_D \cup \Gamma_N \cup \Gamma_R$, where Γ_D, Γ_N, and Γ_R denote, respectively, boundary segments with the Dirichlet, Neumann, and Robin (admittance) boundary conditions. These boundary conditions are quite similar to those for heat transfer problems discussed in Chapter 14. The acoustic wave equation can be written as follows:

$$\Delta p - \frac{1}{c^2}\frac{\partial^2 p}{\partial t^2} = 0 \quad \text{in } \Omega, \tag{15.1}$$

where p denotes the unknown field variable of (acoustic) pressure in the media, c is the speed of an acoustic wave traveling in the media that is known for a given media, and t is the time. The notation Δ denotes the Laplace operator with respect to coordinates given by

$$\Delta = \mathbf{L}_d^T \mathbf{L}_d, \tag{15.2}$$

where $\mathbf{L}_d$ is a differential operator (for the acoustics problem, it is the gradient operator often denoted as ∇) given by

$$\mathbf{L}_d = \nabla = \begin{cases} \dfrac{\partial}{\partial x} & \text{for 1D,} \\ \left\{ \dfrac{\partial}{\partial x} \quad \dfrac{\partial}{\partial y} \right\}^T & \text{for 2D,} \\ \left\{ \dfrac{\partial}{\partial x} \quad \dfrac{\partial}{\partial y} \quad \dfrac{\partial}{\partial z} \right\}^T & \text{for 3D.} \end{cases} \tag{15.3}$$

Using Equation 15.2, Equation 15.1 can be rewritten as

$$\mathbf{L}_d^T \mathbf{L}_d p - \frac{1}{c^2} \frac{\partial^2 p}{\partial t^2} = 0 \quad \text{in } \Omega, \tag{15.4}$$

which is the time-domain governing equation for acoustics problems that is quite similar to Equation 14.1 for heat transfer problems.

In the acoustics problem, we are often concerned with the characteristics of the acoustic fields in the design of an acoustic system. We thus study acoustics problems frequently in the so-called frequency domain, and we shall convert Equation 15.4 to the frequency domain. To that end, we assume that the acoustic pressure p is a small harmonic perturbation around a steady state in the media expressed by

$$p = P e^{j\omega t} \tag{15.5}$$

where $j = \sqrt{-1}$, ω is the angular frequency, and P is the amplitude of the acoustic pressure. Substituting Equation 15.5 into Equation 15.4, we obtain the well-known Helmholtz equation:

$$\Delta P + k_{\mathrm{w}}^2 P = 0, \tag{15.6}$$

where k_{w} is the wave number that relates to the frequency and wave speed in the form of

$$k_{\mathrm{w}} = \frac{\omega}{c}. \tag{15.7}$$

Since c is a material (media) constant, controlling the wave number is effectively the same as controlling the frequency. Equation 15.6 is the well-known governing equation for acoustics problems in the frequency (or wave-number) domain.

In general, the acoustic pressure P is complex-valued in the frequency domain, and the real and imaginary parts relate to the amplitude and the phase of the pressure wave field. The Dirichlet, Neumann, and Robin boundary conditions can be described as follows:

$$P = P_{\mathrm{D}} \quad \text{on } \Gamma_{\mathrm{D}}, \tag{15.8}$$

$$\nabla P \cdot \mathbf{n} = -j\rho\omega v_{\mathrm{n}} \quad \text{on } \Gamma_{\mathrm{N}}, \tag{15.9}$$

$$\nabla P \cdot \mathbf{n} = -j\rho\omega A_{\mathrm{n}} P \quad \text{on } \Gamma_{\mathrm{R}}, \tag{15.10}$$

where v_n, ρ, A_n, and $\mathbf{n}$ represent, respectively, the normal velocity on the boundary Γ_N, the density of the medium, the admittance coefficient on

boundary Γ_R, and the unit vector of the outwards normal on the boundary. The unit normal vector $\mathbf{n}$ is given by

$$\mathbf{L}_{\mathrm{n}} = \mathbf{n} = \begin{cases} n_x & \text{for 1D,} \\ \{n_x \quad n_y\}^T & \text{for 2D,} \\ \{n_x \quad n_y \quad n_z\}^T & \text{for 3D,} \end{cases} \tag{15.11}$$

with n_i $(i = x, y, z)$ being the i-direction components of the unit outwards normal on the boundary.

The acoustic particle velocity (amplitude) $\mathbf{v}$ in an ideal fluid media relates to the gradient of acoustic pressure p by

$$\nabla P + j\rho\omega\mathbf{v} = 0. \tag{15.12}$$

15.3 Weak Forms for Acoustics Problems

Quite similar to the heat transfer problems described in Chapter 14, the Galerkin weak form for our acoustics problems can be derived easily as follows. Our formulation here is for the acoustics equation in the frequency domain, and starts with the weighted residual weak form.

15.3.1 Weighted Residual Weak Form for Acoustics Problems

The weighted residual equation is first obtained by multiplying the strong-form equation 15.6 in the frequency domain with a weight or test function w in the entire domain addressed by

$$-\int_{\Omega} w\left(\Delta P + k_{\mathrm{w}}^2 P\right) \mathrm{d}\Omega = 0, \tag{15.13}$$

where we deliberately add in a minus sign that does not affect balance of the equation, but helps us later to derive a "nicer looking" form of equations. Integrating by part or using Green's theorem, we have

$$\int_{\Omega} \nabla w \cdot \nabla P \, \mathrm{d}\Omega - k_{\mathrm{w}}^2 \int_{\Omega} w \cdot P \, \mathrm{d}\Omega - \int_{\Gamma} w \left(\nabla P \cdot \mathbf{n}\right) \mathrm{d}\Gamma = 0. \tag{15.14}$$

Applying the boundary conditions shown in Equations 15.8 and 15.10, we obtain

$$\int_{\Omega} \nabla w \cdot \nabla P \, \mathrm{d}\Omega - k_{\mathrm{w}}^2 \int_{\Omega} w \cdot P \, \mathrm{d}\Omega + j\rho\omega \int_{\Gamma_{\mathrm{n}}} w \cdot v_{\mathrm{n}} \, \mathrm{d}\Gamma + j\rho\omega A_{\mathrm{n}} \int_{\Gamma_{\mathrm{R}}} w \cdot P \, \mathrm{d}\Gamma = 0. \tag{15.15}$$

This is the weighted residual weak form for acoustics problems in the frequency domain. Here, we have not yet decided how the weight function w should be chosen. Different choices of w will lead to different numerical methods with different properties. More discussions in this direction can be found in Ref. [16]. We now discuss a special choice of w that leads to the so-called Galerkin weak form.

15.3.2 Galerkin Weak Form for Acoustics Problems

For our acoustics problem, the pressure is a function defined in the problem domain Ω. In the continuous form, it is in fact the exact solution that satisfies Equation 15.6 and the Dirichlet boundary condition on Γ_{D}. We now choose an "admissible" variation of P as the weight function:

$$w(\mathbf{x}) = \delta P(\mathbf{x}), \tag{15.16}$$

where $\delta P(\mathbf{x})$ satisfies also the Dirichlet boundary condition on Γ_{D}. Equation 15.15 now becomes

$$\int_{\Omega} (\delta \nabla P) \cdot \nabla P \, \mathrm{d}\Omega - k_{\mathrm{w}}^2 \int_{\Omega} \delta P \cdot p \, \mathrm{d}\Omega + j\rho\omega \int_{\Gamma_{\mathrm{n}}} \delta P \cdot v_{\mathrm{n}} \, \mathrm{d}\Gamma + j\rho\omega A_{\mathrm{n}} \int_{\Gamma_{\mathrm{R}}} \delta P \cdot P \, \mathrm{d}\Gamma = 0. \tag{15.17}$$

This is the well-known Galerkin weak form for the acoustics problem in the frequency domain. Equation 15.17 is equivalent to (and more general than) Equations 15.6, 15.9, and 15.10, provided P and $\delta P(\mathbf{x})$ are admissible, by which we mean that they are continuous and satisfy the Dirichlet boundary condition. Mathematically, we require $P, \delta P \in \mathbb{H}_0^1(\Omega)$ (see Chapter 3, but the space is for complex-valued functions) for the standard Galerkin weak form given in Equation 15.17.

Note that solving Equation 15.17 is as difficult as solving the original strong-form equations. However, Equation 15.17 provides a good platform to establish a discrete FEM model for an approximate solution that converges to the exact solution of the original strong form when the discretization is refined.

15.3.3 Galerkin Weak Form: Discrete Form

We now discretize the problem domain Ω using elements for FEM settings. We then somehow create an approximation of P denoted as $\breve{P}$ such that it satisfies the admissible condition of $\breve{P} \in \mathbb{H}^1_{0,h}(\Omega)$, as well as the following equation:

$$\int_{\Omega} \left(\delta \nabla \breve{P}\right) \cdot \nabla \breve{P} \, \mathrm{d}\Omega - k_{\mathrm{w}}^2 \int_{\Omega} \delta \breve{P} \cdot \breve{P} \, \mathrm{d}\Omega + j\rho\omega \int_{\Gamma_{\mathrm{n}}} \delta \breve{P} \cdot v_{\mathrm{n}} \, \mathrm{d}\Gamma + j\rho\omega A_{\mathrm{n}} \int_{\Gamma_{\mathrm{R}}} \delta \breve{P} \cdot \breve{P} \, \mathrm{d}\Gamma = 0. \tag{15.18}$$

Such a $\breve{P}$ is then regarded as *any* approximate solution. Equation 15.18 is the Galerkin weak form in discrete form for acoustics problems, which promises a unique approximate solution that converges to the exact solution of the original well-posed problem stated in Equations 15.6, 15.8, and 15.10, when the discretization is refined so that $\mathbb{H}^1_{0,h}(\Omega) \to \mathbb{H}^1_0(\Omega)$.

15.3.4 Smoothed Galerkin Weak Form: Discrete Form

In creating a smoothed Galerkin model, we first discretize the problem domain Ω using elements (for FEM settings) or nodes with background cells (in mesh-free settings). On top of the mesh of elements, we then further divide the problem domain into smoothing domains, as detailed in Section 4.5.1. We next somehow create an approximation of P denoted as $\bar{P}$ such that it satisfies the admissible condition of $\bar{P} \in \mathbb{H}^1_{0,h}(\Omega)$, as well as the following equation:

$$\int_{\Omega} \left(\delta \overline{\nabla P}\right) \cdot \overline{\nabla P} \, \mathrm{d}\Omega - k_{\mathrm{w}}^2 \int_{\Omega} \delta \bar{P} \cdot \bar{P} \, \mathrm{d}\Omega + j\rho\omega \int_{\Gamma_{\mathrm{n}}} \delta \bar{P} \cdot v_{\mathrm{n}} \, \mathrm{d}\Gamma + j\rho\omega A_{\mathrm{n}} \int_{\Gamma_{\mathrm{R}}} \delta \bar{P} \cdot \bar{P} \, \mathrm{d}\Gamma = 0. \tag{15.19}$$

It is clear that the pressure gradient ∇P is now replaced by the "smoothed pressure gradient" $\overline{\nabla P}$ over the smoothing domains. These smoothing domains can be cell-based (Chapter 5), node-based (Chapter 6), edge-based (Chapter 7), face-based (Chapter 8), and partially node-based (αFEM, Chapter 9). In any such set of smoothed domains, the smoothed pressure gradient becomes constant in each of the smoothing domains. Therefore,

the "smoothed" Galerkin weak form for the acoustics problems can be rewritten as

$$\sum_{k=1}^{N_s} A_k^s \left(\delta\overline{\nabla P}\right) \cdot \overline{\nabla P} - k_{\mathrm{w}}^2 \int_{\Omega} \delta\bar{P} \cdot \bar{P}\, \mathrm{d}\Omega + j\rho\omega \int_{\Gamma_{\mathrm{n}}} \delta\bar{P} \cdot v_{\mathrm{n}}\, \mathrm{d}\Gamma + j\rho\omega A_{\mathrm{n}} \int_{\Gamma_{\mathrm{R}}} \delta\bar{P} \cdot \bar{P}\, \mathrm{d}\Gamma = 0, \tag{15.20}$$

where A_k^s is the area of the kth smoothing domain and N_s is the number of smoothing domains. A $\bar{P} \in \mathbb{H}^1_{0,h}(\Omega)$ that satisfies Equation 15.20 is then regarded as an approximate solution of an S-FEM model. Equation 15.20 is the smoothed Galerkin weak form in discrete form for acoustics problems, which promises a unique approximate solution that converges to the exact solution of the original well-posed problem stated in Equations 15.6, 15.8, and 15.10, when the discretization is refined so that $\mathbb{H}^1_{0,h}(\Omega) \to \mathbb{H}^1_0(\Omega)$, and the smoothing domains satisfy the conditions listed in Table 4.2. The proof of this can be generated in a similar way to that given in Refs. [16,20].

We note that in the smoothed Galerkin weak form, we do not necessarily require $\bar{P} \in \mathbb{H}^1_{0,h}(\Omega)$. We can have much more relaxed admissible conditions: $\bar{P} \in \mathbb{G}^1_{0,h}(\Omega)$, meaning that the assumed pressure functions can be in proper G space [20–23]. Such a relaxation is very useful in establishing models in much more general mesh-free settings [19,20]. In this book, however, our S-FEM models are all based on the FEM settings, and hence we have the stronger (hence sufficient) requirement of $\bar{P} \in \mathbb{H}^1_{0,h}(\Omega)$.

15.4 FEM Equations

We now discretize the problem domain into N_e elements with N_n nodes as in the FEM (see Chapter 3). Using these elements, a set of nodal shape functions can be created using the standard FEM procedure. For our acoustics problem, the pressure P is the field variable and it is a scalar field. At any point $\mathbf{x} \in \Omega$, it can be approximated using the FEM shape functions in the following general form:

$$\tilde{P}(\mathbf{x}) = \sum_{i=1}^{N_n} N_i(\mathbf{x})\tilde{P}_i = \mathbf{N}(\mathbf{x})\tilde{\mathbf{P}}, \tag{15.21}$$

where $\tilde{\mathbf{P}}$ is the vector of unknown nodal pressures at all the nodes in the problem domain arranged as

$$\tilde{\mathbf{P}} = \begin{bmatrix} \tilde{P}_1 & \tilde{P}_2 & \cdots & \tilde{P}_{N_n} \end{bmatrix}^T, \tag{15.22}$$

in which $\tilde{P}_i$ ($i = 1, \ldots, N_n$) is the pressure (amplitude) at the ith node. The matrix $\mathbf{N}$ contains nodal shape functions for all the nodes in the problem domain:

$$\mathbf{N}(\mathbf{x}) = \begin{bmatrix} N_1(\mathbf{x}) & N_2(\mathbf{x}) & \cdots & N_{N_n}(\mathbf{x}) \end{bmatrix}, \tag{15.23}$$

where N_i ($i = 1, \ldots, N_n$) is the shape function for the ith node. Because the nodal shape function N_i is locally supported, only by the elements connected to the node, it is zero at any point in all the other elements. Therefore, $\mathbf{N}(\mathbf{x})$ is very sparse for any given $\mathbf{x} \in \Omega$.

Using Equation 15.21, we should have

$$\delta\tilde{P}(\mathbf{x}) = \sum_{i=1}^{N_n} N_i(\mathbf{x})\delta\tilde{P}_i = \mathbf{N}(\mathbf{x})\delta\tilde{\mathbf{P}}. \tag{15.24}$$

Substituting Equations 15.21 and 15.24 into the standard Galerkin weak-form equation 15.18, we obtain

$$\delta\tilde{\mathbf{P}} \left\{ \int_\Omega (\nabla\mathbf{N})^T \cdot \nabla\mathbf{N} \; \mathrm{d}\Omega\tilde{\mathbf{P}} - k_\mathrm{w}^2 \int_\Omega \mathbf{N}^T \cdot \mathbf{N} \, \mathrm{d}\Omega \, \tilde{\mathbf{P}} \right.$$

$$\left. + j\rho\omega \int_{\Gamma_\mathrm{n}} \mathbf{N}^T \cdot v_\mathrm{n} \, \mathrm{d}\Gamma + j\rho\omega \int_{\Gamma_\mathrm{R}} A_\mathrm{n}\mathbf{N}^T \cdot \mathbf{N} \, \mathrm{d}\Gamma \, \tilde{\mathbf{P}} = 0 \right\}. \tag{15.25}$$

Owing to the arbitrary nature of the variation of the nodal pressure $\delta\mathbf{P}$, the only way to ensure that Equation 15.25 is *always* satisfied is to have

$$\underbrace{\int_\Omega (\nabla\mathbf{N})^T \cdot \nabla\mathbf{N} \, \mathrm{d}\Omega \, \tilde{\mathbf{P}}}_{\tilde{\mathbf{K}}} - k_\mathrm{w}^2 \underbrace{\int_\Omega \mathbf{N}^T \cdot \mathbf{N} \, \mathrm{d}\Omega \, \tilde{\mathbf{P}}}_{\tilde{\mathbf{M}}} + j\rho\omega \underbrace{\int_{\Gamma_\mathrm{R}} A_\mathrm{n}\mathbf{N}^T \cdot \mathbf{N} \, \mathrm{d}\Gamma \, \tilde{\mathbf{P}}}_{\tilde{\mathbf{C}}}$$

$$= -j\rho\omega \underbrace{\int_{\Gamma_\mathrm{n}} \mathbf{N}^T \cdot v_\mathrm{n} \, \mathrm{d}\Gamma}_{\tilde{\mathbf{F}}} \tag{15.26}$$

or

$$[\tilde{\mathbf{K}} - k_{\mathrm{w}}^2\tilde{\mathbf{M}} + j\rho\omega\tilde{\mathbf{C}}]\tilde{\mathbf{P}} = -j\rho\omega\tilde{\mathbf{F}}, \tag{15.27}$$

where

$$\tilde{\mathbf{K}} = \int_{\Omega} \underbrace{(\nabla\mathbf{N})^T}_{\tilde{\mathbf{B}}^T}\underbrace{(\nabla\mathbf{N})}_{\tilde{\mathbf{B}}}\,\mathrm{d}\Omega = \int_{\Omega} \tilde{\mathbf{B}}^T\tilde{\mathbf{B}}\,\mathrm{d}\Omega \quad \text{(acoustical stiffness matrix)}, \tag{15.28}$$

$$\tilde{\mathbf{M}} = \int_{\Omega} \mathbf{N}^T\cdot\mathbf{N}\,\mathrm{d}\Omega \quad \text{(acoustical mass matrix)}, \tag{15.29}$$

$$\tilde{\mathbf{C}} = \int_{\Gamma_{\mathrm{R}}} \mathbf{N}^T\cdot\mathbf{N}A_{\mathrm{n}}\,\mathrm{d}\Gamma \quad \text{(acoustical damping matrix caused by boundary admittance)}, \tag{15.30}$$

$$\tilde{\mathbf{F}} = \int_{\Gamma_{\mathrm{n}}} \mathbf{N}^T\cdot v_{\mathrm{n}}\,\mathrm{d}\Gamma \quad \text{(nodal acoustic force vector)}. \tag{15.31}$$

In Equation 15.28, $\tilde{\mathbf{B}}$ is the gradient-pressure matrix (an analogue of the strain–displacement matrix defined in Equation 3.68) or simply the gradient matrix. Because $\mathbf{N}$ is very sparse, $\tilde{\mathbf{B}}$ will also be very sparse and so is the $\tilde{\mathbf{K}}$ matrix. In addition, $\tilde{\mathbf{K}}$ will also be banded if the nodes in the problem domain are properly numbered. Making use of the sparseness in actual computations, we will not actually form the "global" matrices $\mathbf{N}$ and $\tilde{\mathbf{B}}$ for the entire problem domain, because they contain mostly zero for large models. Rather, we form those for each element and compute the element stiffness matrix $\tilde{\mathbf{K}}_{IJ}^e$:

$$\tilde{\mathbf{K}}_{IJ,i}^e = \int_{\Omega_i^e} \tilde{\mathbf{B}}_I^T\tilde{\mathbf{B}}_J\,\mathrm{d}\Omega, \tag{15.32}$$

where Ω_i^e is the domain of the element. The global stiffness matrix $\tilde{\mathbf{K}}$ can then be formed easily by assembling the entries given in Equation 15.32. The integration in Equation 15.32 is performed using the Gauss integration scheme based on elements (see Section 3.15).

Note that the evaluation of matrices $\tilde{\mathbf{M}}$ and $\tilde{\mathbf{C}}$ and the vector $\tilde{\mathbf{F}}$ are similar to $\tilde{\mathbf{K}}$: by an assembly using elemental matrix and vectors. It can be easily seen from Equations 15.28, 15.29, and 15.30 that the matrices $\tilde{\mathbf{K}}$, $\tilde{\mathbf{M}}$, and $\tilde{\mathbf{C}}$ will all be symmetric and banded if the nodes in the problem domain are properly numbered, which implies that Equation 15.27 can be solved very efficiently using standard routines of the linear equation solver.

15.5 S-FEM Equations

In an S-FEM model, we divide the problem domain into elements, and based on these elements we create nodal shape functions, as in the FEM (see Chapter 3). Using these nodal shape functions, the S-FEM solution for the pressure at any point $\mathbf{x} \in \Omega$ can be approximated in the following form:

$$\bar{P}(\mathbf{x}) = \sum_{i=1}^{N_n} N_i(\mathbf{x})\bar{P}_i = \mathbf{N}(\mathbf{x})\bar{\mathbf{P}}, \tag{15.33}$$

where $\bar{\mathbf{P}}$ is the solution of the nodal pressure at all the nodes in the problem domain:

$$\bar{\mathbf{P}} = \begin{Bmatrix} \bar{P}_1 & \bar{P}_2 & \cdots & \bar{P}_{N_n} \end{Bmatrix}^T, \tag{15.34}$$

in which $\bar{P}_i$ $(i = 1, \ldots, N_n)$ is the S-FEM solution for the nodal pressure (amplitude) at the ith node. The matrix $\mathbf{N}$ contains nodal shape functions and has the same form of Equation 15.23 and hence has the same sparseness.

The variation of the $\bar{\mathbf{P}}(\mathbf{x})$ is given by

$$\delta\bar{P}(\mathbf{x}) = \sum_{i=1}^{N_n} N_i(\mathbf{x})\delta\bar{P}_i = \mathbf{N}(\mathbf{x})\delta\bar{\mathbf{P}}. \tag{15.35}$$

Substituting Equations 15.33 and 15.35 into Equation 15.20, using the arbitrary nature of the variation of the nodal pressure $\delta\bar{\mathbf{P}}$, we obtain

$$\underbrace{\sum_{k=1}^{N_s} A_k^s \overline{\nabla\mathbf{N}}^T \cdot \overline{\nabla\mathbf{N}}\,\bar{\mathbf{P}}}_{\tilde{\mathbf{K}}} - k_w^2 \underbrace{\int_\Omega \mathbf{N}^T \cdot \mathbf{N}\,\mathrm{d}\Omega\,\bar{\mathbf{P}}}_{\tilde{\mathbf{M}}} + j\rho\omega \underbrace{\int_{\Gamma_R} A_n \mathbf{N}^T \cdot \mathbf{N}\,\mathrm{d}\Gamma\,\bar{\mathbf{P}}}_{\tilde{\mathbf{C}}}$$

$$= \underbrace{-j\rho\omega \int_{\Gamma_n} \mathbf{N}^T \cdot v_n\,\mathrm{d}\Gamma}_{\tilde{\mathbf{F}}} \tag{15.36}$$

or

$$[\overline{\mathbf{K}} - k_w^2\tilde{\mathbf{M}} + j\rho\omega\tilde{\mathbf{C}}]\bar{\mathbf{P}} = -j\rho\omega\bar{\mathbf{F}}, \tag{15.37}$$

which is the set of discretized equations for the S-FEM models. The matrices $\tilde{\mathbf{M}}$, $\tilde{\mathbf{C}}$, and $\tilde{\mathbf{F}}$ are exactly the same as those in Equations 15.29, 15.30, and 15.31. The global "smoothed" acoustic stiffness matrix $\overline{\mathbf{K}}$ is defined as

$$\bar{\mathbf{K}} = \sum_{k=1}^{N_s} A_k^s \underbrace{\left(\overline{\nabla \mathbf{N}}\right)^T}_{\bar{\mathbf{B}}^T} \underbrace{\left(\overline{\nabla \mathbf{N}}\right)}_{\bar{\mathbf{B}}} = \sum_{k=1}^{N_s} A_k^s \bar{\mathbf{B}}^T \bar{\mathbf{B}}, \tag{15.38}$$

where $\bar{\mathbf{B}}$ is the "smoothed" gradient-pressure matrix or simply smoothed gradient matrix. For the same sparseness argument given for the FEM model, we know that $\bar{\mathbf{B}}_I$ will be very sparse, and hence we will not perform the above summation in the actual computations. Instead, we perform an assembly, similar to what we do in the FEM, but using the entries computed based on smoothing domains:

$$\overline{\mathbf{K}}_{IJ,k}^s = A_k^s \bar{\mathbf{B}}_I^T \bar{\mathbf{B}}_J, \tag{15.39}$$

where A_k^s is the area of the kth smoothing domain. The evaluation of the smoothed gradient matrix $\bar{\mathbf{B}}_I$ used in Equation 15.39 is performed exactly in the same way as in Section 14.7. Compared to Equation 15.32, the S-FEM model uses (1) assembly over all the smoothing domains rather than elements; (2) a smoothed gradient matrix instead of the (compatible) gradient matrix.

We observe that the S-FEM model changes only the stiffness matrix, and all the other matrices and vectors are the same as the FEM counterparts using the same mesh. We note also that, in computing the smoothed stiffness matrix, no numerical integration is needed, and only a summation over the smoothing domains is required. If cell-based smoothing domains are used, we have the CS-FEM model (see Chapter 5). Similarly, we shall have the NS-FEM model (see Chapter 6), the ES-FEM model (see Chapter 7), and the FS-FEM model (see Chapter 8). If partially node-based smoothing domains are used, we have an αFEM model (see Chapter 9). Equation 15.37 is a unified S-FEM equation of all these models for acoustics problems.

In the S-FEM models, we can compute the smoothed velocity. This can be done with the help of Equation 15.12:

$$\bar{\mathbf{v}}(\mathbf{x}_k) = \frac{1}{A_k^s} \int_{\Omega_k^s} \mathbf{v}(\mathbf{x})\, \mathrm{d}\Omega = -\frac{1}{j\rho\omega A_k^s} \int_{\Omega_k^s} \nabla P\, \mathrm{d}\Omega = -\frac{1}{j\rho\omega A_k^s} \int_{\Gamma_k^s} P \cdot \mathbf{n}\, \mathrm{d}\Gamma. \tag{15.40}$$

Using the FEM shape function for field variable interpolation in the form of Equations 15.33, the smoothed velocity (or the smoothed pressure

gradient) for edge k can be obtained using

$$\bar{\mathbf{v}}(\mathbf{x}_k) = -\frac{1}{j\rho\omega} \sum_{I \in n_k^s} \bar{\mathbf{B}}_I(\mathbf{x}_k) \bar{P}_I, \tag{15.41}$$

where n_k^s is the total number of nodes contributing to the smoothing domain.

15.6 Error in a Numerical Model

It is well known that the major concern of computing acoustics (or other wave propagation) problems using an FEM model is the control of the error caused in the discretized model. For wave propagation problems, controlling errors in a discretized model is much more involved, and controlling the so-called *interpolation error* is not sufficient. This is because the simulated waves are "dispersive," that is, the wave number of the numerical solution is bound to be different from the exact wave number [14]. Such a numerical dispersive error reduces with the refinement of the mesh. There is a so-called rule of thumb that states that a "minimum" number of elements are needed per wavelength to obtain a stable solution to the Helmholtz equation. However, such a rule is more for the interpolation error, because such an error can effectively be controlled by refining the mesh. However, increasing the number of elements is not always productive in reducing the dispersive error, especially for higher dimensional problems at high frequency. Below is the detailed argument on this important issue.

For the convenience in the argument, we need to first quantify the error in a precise manner. We use the gradient field of acoustic pressure P (or the velocity) as the *global error* indicator for the numerical solutions. The numerical error indicator can be defined in the form of the L^2 norm of the velocity error:

$$\begin{aligned} e_n &= \sqrt{\int_\Omega \left(\mathbf{v}_i^{*\text{exact}} - \mathbf{v}_i^{*h}\right)^T \left(\mathbf{v}_i^{\text{exact}} - \mathbf{v}_i^{h}\right) \mathrm{d}\Omega} \\ &\doteq \sqrt{\sum_{i=1}^{N_\mathrm{Q}} A_i^{\mathrm{Q}} \left(\mathbf{v}_i^{*\text{exact}} - \mathbf{v}_i^{*h}\right)^T \left(\mathbf{v}_i^{\text{exact}} - \mathbf{v}_i^{h}\right)}, \end{aligned} \tag{15.42}$$

where $\mathbf{v}^*$ is the complex conjugate of velocity $\mathbf{v}$, the superscript *exact* denotes the exact solution, h denotes the numerical solution obtained from

a numerical method that can be S-FEM or FEM, A_i^{Q} is the area/volume of the quadrature domain that is defined by

$$A_i^{\mathrm{Q}} = \begin{cases} \text{area/volume of the element, } A_i^e, & \text{for FEM,} \\ \text{area/volume of the smoothing domain, } A_k^s, & \text{for S-FEM,} \end{cases} \tag{15.43}$$

and N_{Q} is the number of quadrature domains that is defined by

$$N_{\mathrm{Q}} = \begin{cases} \text{Number of the elements, } N_e, & \text{for FEM,} \\ \text{Number of the smoothing domains, } N_s, & \text{for S-FEM.} \end{cases} \tag{15.44}$$

It can be shown that the *relative velocity error* is bounded by [17]

$$\gamma_e = \frac{e_n}{e_e} = \frac{\sqrt{\int_\Omega \left(\mathbf{v}^{*\mathrm{exact}} - \mathbf{v}^{*h}\right)^T \left(\mathbf{v}^{\mathrm{exact}} - \mathbf{v}^h\right) \mathrm{d}\Omega}}{\sqrt{\int_\Omega \mathbf{v}^T \mathbf{v} \, \mathrm{d}\Omega}} \leq C_1' \left(\frac{k_{\mathrm{w}} h}{p_n}\right) + C_2' \phi \left(\frac{k_{\mathrm{w}} h}{p_n}\right)^2, \tag{15.45}$$

where p_n is the order of the interpolation used in the elements, C_1' and C_2' are constants independent of the wave number k_{w} and the characteristic length of mesh size h. Note that in our numerical analysis, the integration in Equation 15.45 is performed in the same way as in Equation 15.42.

It is clearly shown that the relative error is bounded by two terms: the first term is the *interpolation error*, which defines the difference between the interpolation and the exact solution; the second term is generally known as the *dispersive error*, which relates to the numerical error in approximating the phase of the wave. It is shown in Refs. [13,18] that if $k_{\mathrm{w}} h < 1$, the relative error for acoustics problems can be expressed by

$$\gamma_e \leq C_1 k_{\mathrm{w}} h + C_2 k_{\mathrm{w}}^3 h^2. \tag{15.46}$$

It is clearly seen that the error bound in the second terms depends heavily on the wave number k_{w} and mesh size h. The interpolation error (relates to $k_{\mathrm{w}} h$) is called the preasymptotic estimate, and the dispersive error (relates to $k_{\mathrm{w}}^3 h^2$) is called asymptotic estimate [24]. The *interpolation error* can be controlled by keeping k_{w}^h constant. This is in fact the usual "rule of thumb" that prescribes the relation between the wave number and mesh size. Because of the presence of the second term in Equation 15.46, following the rule of thumb and keeping $k_{\mathrm{w}} h$ constant alone are not sufficient to control the error, because the *dispersive error* will increase proportionally with the increase

of k_w. Therefore, following the usual "rule of thumb" is necessary for a numerical model, but is not sufficient. In this chapter, we rely mainly on the "right-stiffness" behavior of ES-FEM/FS-FEM to suppress the dispersive error and hence to improve the solution accuracy. It will be shown in the next section that the accuracy of acoustics problem is improved significantly as compared with the standard FEM using the same mesh.

15.7 Numerical Examples

We choose now ES-FEM and FS-FEM for solving 2D and 3D acoustics problems, respectively. This is because the ES-FEM/FS-FEM models have been found in previous chapters to have "close-to-exact" stiffness [25,26], which is essential to reduce the dispersive error. In this section, a number of acoustic examples problems will be used to examine the effectiveness of ES-FEM/FS-FEM. Two examples with analytical solutions will be used first to validate and to investigate in great detail the accuracy and convergence of the ES-FEM solution. ES-FEM/FS-FEM is then used to solve two practical problems: one is the 2D problem of acoustic fields in a car passenger compartment (ES-FEM), and the other is the 3D problem of noise in an engine chamber (FS-FEM). The examples presented in this section are similar to those reported in Ref. [27].

In our analysis, we often use nondimensional quantities. Suppose that l is the length of the problem domain (or media), and the Cartesian 2D coordinates are nondimensionalized by

$$\xi = x/l, \qquad \eta = y/l. \tag{15.47}$$

Similarly, the wave number k_w is also nondimensionalized by

$$\kappa = k_w l, \tag{15.48}$$

where κ is the dimensionless wave number. Note that as per usual convention in FEM or S-FEM, the mesh size h is already relative to the dimension of the problem l, by default.

15.7.1 Problem with the Dirichlet Boundary Condition

Consider that a time-harmonic wave propagates in a 1D domain $\Omega = (0, 1)$. The governing Helmholtz equation has the form of

$$\frac{d^2P}{d\xi^2} + \kappa^2 P = 0 \quad \text{in } \Omega \ (0 \le \xi \le 1). \tag{15.49}$$

The Dirichlet boundary condition for the field variable pressure is given for the left end of the domain as

$$P(0) = 1, \tag{15.50}$$

and the Neumann boundary condition for the pressure gradient is given for the right end of the domain and is described as follows:

$$\frac{\mathrm{d}P}{\mathrm{d}\xi}(1) = 0. \tag{15.51}$$

Because this 1D problem is very simple, we can easily obtain the analytical solution that is given as follows:

$$P(\xi) = \cos(\kappa\xi) + \tan\kappa \sin(\kappa\xi). \tag{15.52}$$

It is very easy to verify that Equation 15.52 satisfies Equations 15.49 and 15.51. In our numerical analysis, we model the 1D problem as a 2D problem with a very elongated domain meshed with triangular elements, as shown in Figure 15.1. The boundary conditions 15.50 will be applied on the whole left edge of the elongated 2D domain, and the boundary conditions 15.51 will be applied on the whole right edge. Because the original problem is 1D, the pressure field is independent of the y-coordinate. To simulate this, we apply

$$\frac{\mathrm{d}P}{\mathrm{d}\eta} = 0 \text{ on both the upper and lower edges of the 2D domain.} \tag{15.53}$$

In the computation, the following parameters are used: the density of fluid is 0.004 kg/m^3, the speed of sound in the media is 340 m/s, and the mesh is uniform with a nodal spacing controlled at 0.03. A typical 2D mesh for solving this 1D problem is given in Figure 15.1. In this study, we will keep the aspect ratio of the elements unchanged, meaning that when we increase the mesh density in the ξ-direction, we will do the same in the η-direction. Solutions at three different frequency values [400 Hz ($\kappa = 7.39$), 800 Hz ($\kappa = 14.78$), and 1200 Hz ($\kappa = 22.18$)] will be computed using ES-FEM-T3. For the purpose of comparison, linear FEM-T3 solutions are also computed using the same mesh and settings. When plotting the solution, we use those along the bottom edge of the elongated 2D domain.

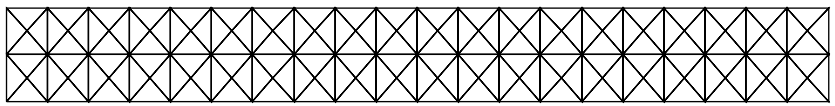

FIGURE 15.1 A typical 2D mesh for solving the 1D example problems.

The numerical results of acoustic pressure using ES-FEM and FEM at different frequency values are plotted in Figure 15.2, together with the exact solutions. It can be found that (1) for the problem of low frequency at 400 Hz (low wave number), ES-FEM and FEM give similar results, both of which are in very good agreement with the exact solution as shown in Figure 15.2a; (2) with the increase of frequency, the numerical solutions of ES-FEM and FEM depart from the exact solution. Compared to FEM, ES-FEM produces much more accurate results, owing to the very "close-to-exact" stiffness of the ES-FEM model, as shown in Figure 15.2b and c.

The convergence and accuracy of the ES-FEM are next examined using four models with different numbers of uniformly distributed nodes (103, 365, 1369, and 5297 nodes). The frequencies are set at 400 Hz ($\kappa = 7.39$) and 800 Hz ($\kappa = 14.78$). The results obtained from both ES-FEM and FEM in terms of the global error defined in Equation 15.42 are plotted together in Figure 15.3. From Figure 15.3 it can be found that at low frequency (400 Hz), ES-FEM achieves greater accuracy and a similar convergence rate compared with FEM; with the increase of frequency, ES-FEM can achieve much better accuracy and a higher convergence rate. These results also show that the error of the ES-FEM solution is less sensitive to the increase of frequency compared with FEM, which is in line with our predictions based on the error analysis and the theorem for ES-FEM.

Figure 15.4 plots the relative error of the numerical results against nondimensional wave number (with a fixed mesh size), obtained using both

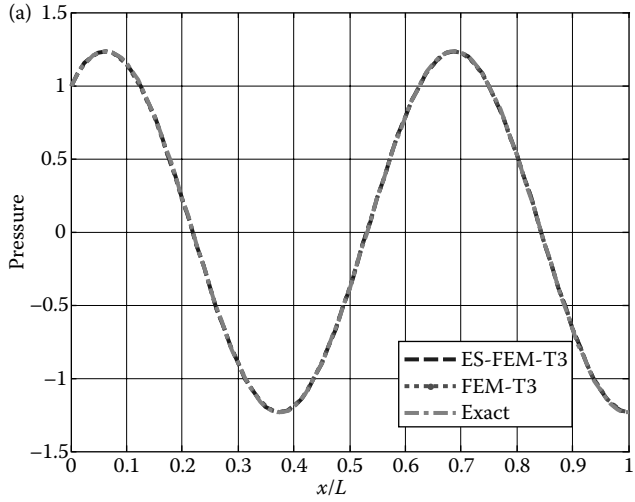

FIGURE 15.2 Exact and numerical solutions for the acoustic pressure at different excitation frequencies for the time-harmonic 1D problem. (a) 400 Hz; (b) 800 Hz; and (c) 1200 Hz.

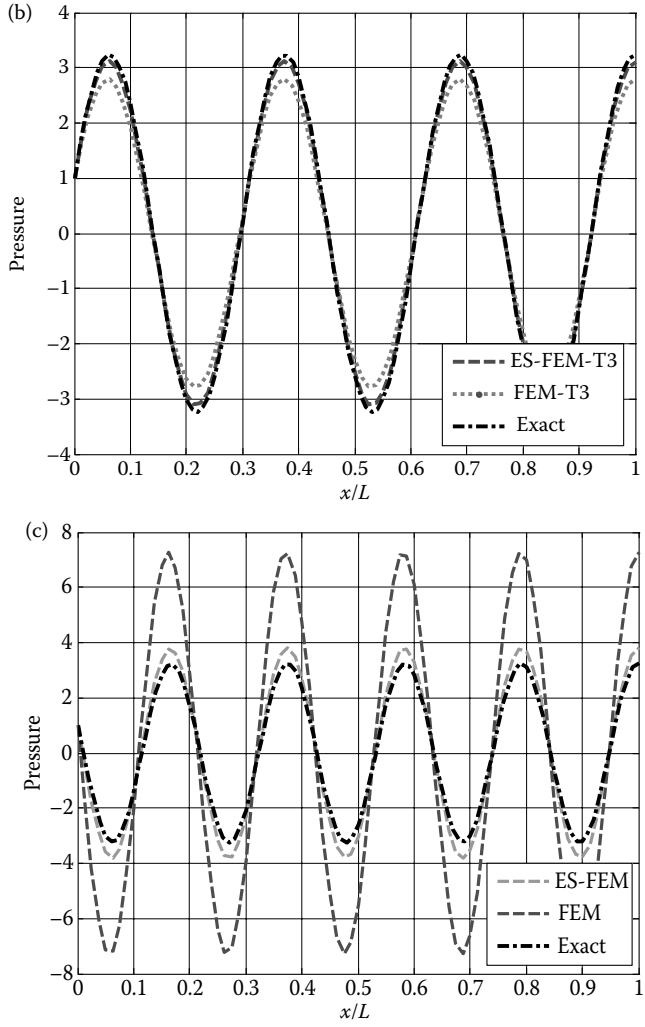

FIGURE 15.2 (*Continued*)

ES-FEM and FEM with exactly the same settings. The cases of $\kappa h = 1$ and $\kappa^3 h^2 = 1$ are also indicated in Figure 15.4. It can be observed that the relative errors at low wave numbers obtained from FEM and ES-FEM are all small. With the increase of wave number, the relative errors increase dramatically for the FEM solution, but the relative error for the ES-FEM solution is much smaller than that of FEM, although it also increases a little. These findings again show clearly that ES-FEM is much less sensitive to the wave number (or frequency), compared to FEM.

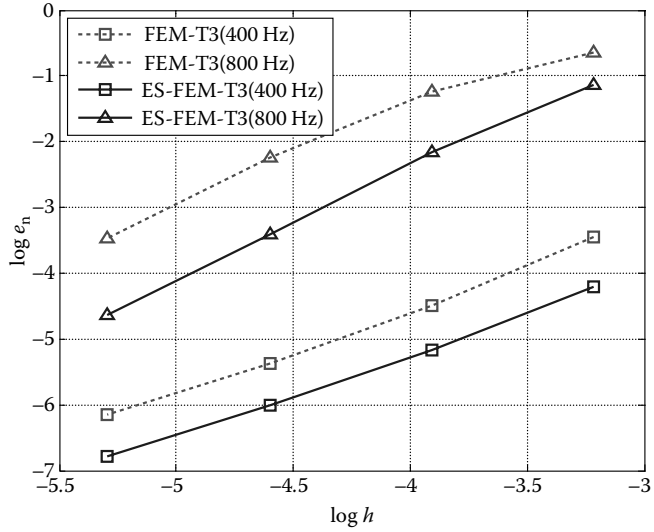

FIGURE 15.3 Comparison of accuracy and convergence of the velocity field at different frequencies between ES-FEM and FEM.

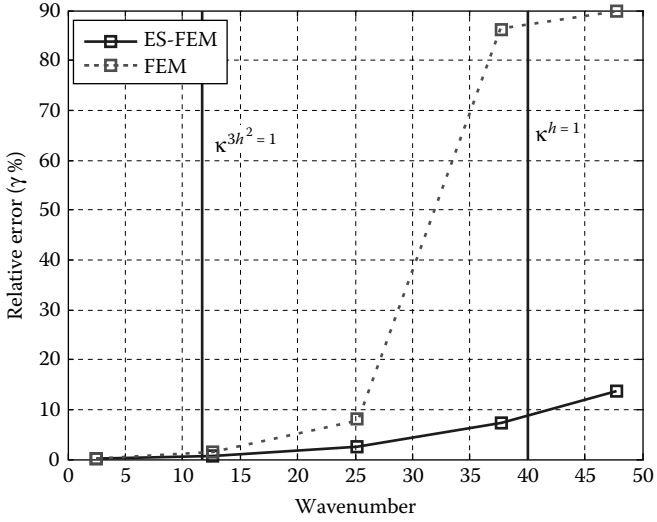

FIGURE 15.4 Relative error in numerical solutions in relation to nondimensional wave numbers obtained using ES-FEM and FEM based on the same T3 mesh.

15.7.2 Problem with the Neumann Boundary Condition

We next consider the problem of a rectangular chamber filled with water as shown in Figure 15.5. The dimensions of this chamber are length $l = 1$ m

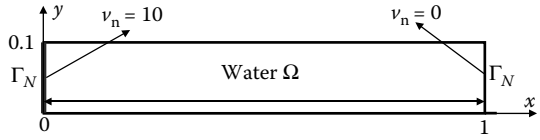

FIGURE 15.5 A thin acoustic chamber filled with water with the Neumann boundary conditions at two ends.

and width $b = 0.1$ m. The left edge of the chamber is excited by a harmonic motion with a given normal velocity of $v_n = 10$ m/s (amplitude). The right edge of the chamber is a rigid wall, and the normal velocity of the media (water) there is set as $v_n = 0$. The density of water ρ is 1000 kg/m^3 and the speed of sound in water is 1500 m/s. Since the chamber is very elongated, the exact solution for the 1D problem is an excellent reference. The 1D analytical solution for this problem can be obtained very easily, and the pressure and velocity fields are given as follows:

$$P = -j\rho c v_{\mathrm{n}} \frac{\cos[\kappa(1-\xi)]}{\sin(\kappa)}, \tag{15.54}$$

$$v = v_x = \frac{v_{\mathrm{n}} \sin[\kappa(1-\xi)]}{\sin(\kappa)}. \tag{15.55}$$

At free status, the 1D chamber has natural frequencies of

$$f = \frac{c}{2}\sqrt{\left(\frac{m}{l}\right)^2 + \left(\frac{n}{b}\right)^2}, \quad m = 0, 1, 2, \ldots \quad n = 0, 1, 2, \ldots \tag{15.56}$$

where f denotes the natural frequencies of this chamber, and m and n are integers but cannot be zero simultaneously. Note that in the vicinity of the above natural frequency values, the problem becomes ill-conditioned. Therefore, significant increases in solution error in a numerical method are expected, which serves as a good test for numerical models.

15.7.3 Convergence Study

Four models with 103, 365, 1369, and 5297 uniformly distributed nodes are also created for this problem to examine the convergence of the solution. Figure 15.6 plots the convergence curves for the global relative error in the velocity solution defined in Equation 15.42 for both ES-FEM and FEM. The excitation frequencies are 2000 and 4000 Hz. It can be found that the solutions of both models converge, and the ES-FEM gives more accurate results than the FEM.

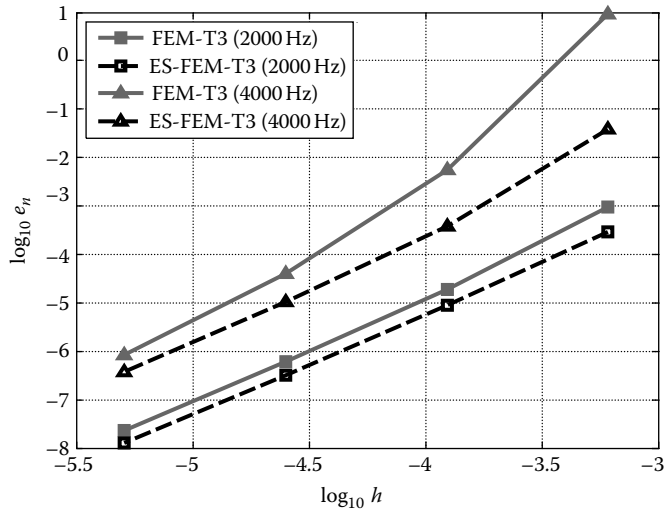

FIGURE 15.6 Comparison of convergence of the solutions obtained using FEM and ES-FEM.

15.7.4 Accuracy of the Acoustic Pressure Field

The numerical solutions of acoustic pressure along the x-axis computed using ES-FEM and FEM and the same mesh are listed in Table 15.1 (for 2000 Hz or $\kappa = 8.38$) and Table 15.2 (for 4000 Hz or $\kappa = 16.76$). In Tables 15.1 and 15.2, the local relative error in acoustic pressure e_p is defined as

$$e_p = \frac{\left|p^{\text{exact}} - p^{\text{num}}\right|}{p^{\text{exact}}} \times 100\%, \tag{15.57}$$

TABLE 15.1

Comparison of the Solutions of Acoustic Pressure along the ξ-Axis (at 2000 Hz)

Coordinates $[x_1, x_2]$ (m)	ES-FEM ($\times 10^7$)	FEM ($\times 10^7$)	Exact Solution ($\times 10^7$)	Local Error e_p (%)		
				ES-FEM	FEM	FEM/ES-FEM
(0.1, 0.0)	−0.56109	−0.60532	−0.53523	4.83157	13.09530	2.71036
(0.2, 0.0)	−1.58860	−1.56680	−1.58230	0.39815	0.97959	2.46032
(0.3, 0.0)	−1.56910	−1.50540	−1.58230	0.83423	4.86001	5.82576
(0.4, 0.0)	−0.51549	−0.46131	−0.53523	3.68813	13.81089	3.74468
(0.5, 0.0)	0.87790	0.88393	0.86603	1.37062	2.06690	1.50800
(0.6, 0.0)	1.69270	1.65210	1.69420	0.08854	2.48495	28.06667
(0.7, 0.0)	1.39190	1.34180	1.40130	0.67081	4.24606	6.32979
(0.8, 0.0)	0.17373	0.15555	0.18105	4.04308	14.08451	3.48361
(0.9, 0.0)	−1.15890	−1.13230	−1.15900	0.00863	2.30371	267.00000
(1.0, 0.0)	−1.72110	−1.68090	−1.73210	0.63507	2.95595	4.65455

TABLE 15.2

Comparison of the Solutions of Acoustic Pressure along the ξ-Axis (at 4000 Hz)

Coordinates	ES-FEM	FEM	Exact Solution	Local Error e_p (%)		
$[x_1, x_2]$ (m)	($\times 10^7$)	($\times 10^7$)	($\times 10^7$)	ES-FEM	FEM	FEM/ES-FEM
(0.1, 0.0)	−1.43650	−1.37890	−1.40130	2.51195	1.59852	0.63636
(0.2, 0.0)	1.48190	2.43840	1.15900	27.86022	110.38827	3.96222
(0.3, 0.0)	1.16790	1.09270	1.15900	0.76790	5.72045	7.44944
(0.4, 0.0)	−1.69360	−2.56670	−1.40130	20.85920	83.16563	3.98700
(0.5, 0.0)	−0.86094	−0.79144	−0.86603	0.58774	8.61287	14.65422
(0.6, 0.0)	1.84960	2.65960	1.58230	16.89313	68.08443	4.03030
(0.7, 0.0)	0.52565	0.47927	0.53523	1.78988	10.45532	5.84134
(0.8, 0.0)	−1.94490	−2.71580	−1.69420	14.79754	60.29985	4.07499
(0.9, 0.0)	−0.17319	−0.16049	−0.18105	4.34134	11.35598	2.61578
(1.0, 0.0)	1.94790	2.73470	1.73210	12.45886	57.88349	4.64597

where P^{exact} is the exact (or reference) pressure solution and P^{num} is the numerical solution. From Tables 15.1 and 15.2, it can be clearly observed that the ES-FEM solutions are much (around 2–30 times) more accurate that those of the FEM model.

Figure 15.7a plots the relative error in pressure defined in Equation 15.57 along the x-axis obtained using both ES-FEM and FEM, at a frequency of 2000 Hz ($\kappa = 8.38$). Figure 15.7b plots the acoustic particle velocity representing the gradient of acoustic pressure. It is clearly shown that at the maximum velocities where the gradient of pressure is highest, large errors in pressure solution are registered. For this problem, the excitation point is at the left end with a normal velocity (or pressure gradient) given as $v_n = 10$. At the right end, the velocity (or pressure gradient) is set to zero. Therefore, the error in the pressure solution is generally large near the left end and smaller at the right end. These findings are true for both ES-FEM and FEM. However, the relative errors in pressure for ES-FEM are much smaller than that for FEM. Figure 15.8 gives the same plots as Figure 15.7, but with a higher excitation frequency of 4000 Hz ($\kappa = 16.76$). Similar observations can be made, except that the errors in pressure are larger, and it is clearer that the ES-FEM is much more accurate than the FEM. This is because the edge-based gradient smoothing operation used in the ES-FEM made the model "softer," leading to more accurate solutions.

15.7.5 Natural Frequency Analysis

Natural frequency analysis for acoustic systems is routinely performed in the design of engineering structures, such as music halls, car passenger compartments, aircraft cabins, etc., because sound quality design has

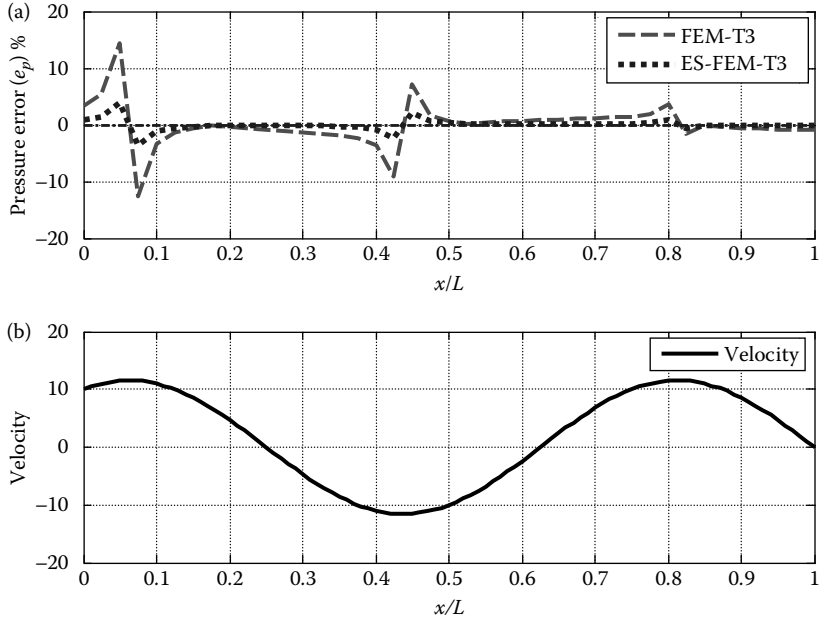

FIGURE 15.7 (a) Distribution of the relative error in acoustic pressure obtained using ES-FEM and FEM and (b) velocity distribution along the ξ-axis (2000 Hz).

become more and more important. Natural frequency analysis provides the inherent acoustic characteristics for such systems or products, in the form of natural frequencies (or natural frequencies) and acoustic modes (or eigenmodes). The eigen or natural frequencies are the essential indicators of the "stiffness" of acoustic systems. It is known that the FEM model behaviors are "overly stiff," which can be clearly observed from the higher values of the predicted natural frequencies. We therefore conduct an acoustic natural frequency analysis using ES-FEM, in comparison with the FEM using the same mesh.

We consider again the same 2D acoustic chamber. It is now discretized with linear elements of an average mesh size of 0.025 m that satisfies the usual "rule of thumb" for the frequency limit at 9554 Hz. Table 15.3 lists the first 20 natural frequencies obtained from ES-FEM and FEM with the same mesh. The analytical solutions obtained using Equation 15.56 are also listed in Table 15.3. It can be found from Table 15.3 that the error in natural frequencies obtained using ES-FEM is largely less than 1%, but those obtained using FEM can be more than 6%. The ES-FEM solution is about 4–60 times more accurate than the FEM solution. This example is a very convincing indication that the ES-FEM model has a very close-to-exact stiffness for acoustic systems. These findings echo those given in Section 7.7 for structural vibration problems.

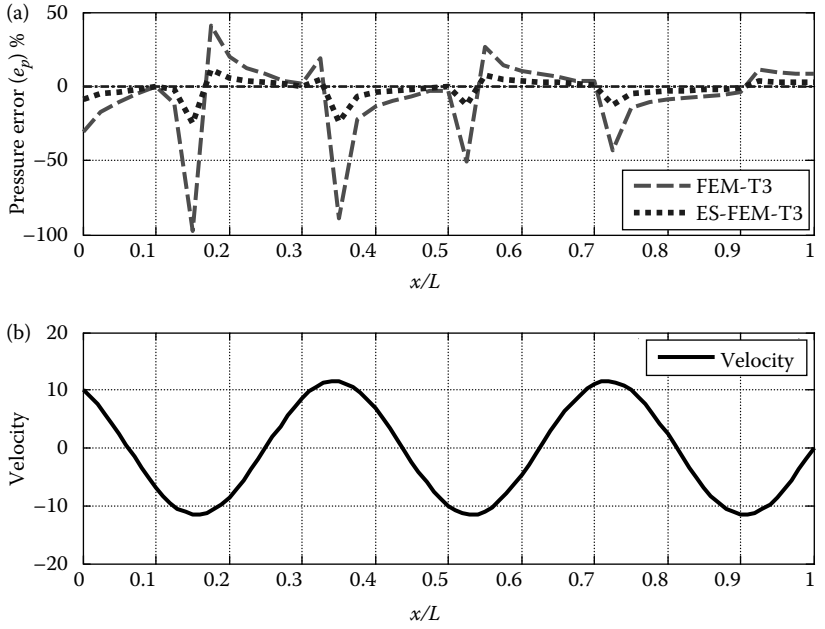

FIGURE 15.8 (a) Distribution of the relative error in acoustic pressure obtained using ES-FEM and FEM and (b) velocity distribution along the ξ-axis (4000 Hz).

15.7.6 Error Control for ES-FEM Models

To properly control the error in an ES-FEM model, a more detailed study on the relative error in the velocity field defined in Equation 15.45 is conducted. Four models with different numbers of uniformly distributed (103, 365, 1369, and 5297) nodes are employed in this study. The results for the relative error obtained for different excitation frequencies using the ES-FEM are plotted in Figure 15.9. It is found that at lower frequencies, the relative error is smaller, and a larger mesh size can be used. With the increase of frequency, the relative error increases, but the level of error can be controlled using more nodes for the ES-FEM according to the excitation frequency.

To devise an effective means for such an error control, the relation between the frequency (or nondimensional wave number κ) and mesh size needs to be studied in more detail. Based on Equation 15.46, the numerical error is related to two nondimensional terms: κh and $\kappa^3 h^2$. Keeping $\kappa h < 1$ and constant while varying the wave number and mesh size, the relative error will increase linearly with wave number κ due to the presence of the term $\kappa^3 h^2$. On the other hand, keeping $\kappa^3 h^2$ constant while varying the wave number and mesh size, the relative error shall depend

TABLE 15.3

Natural Frequencies in a 2D Chamber Calculated using FEM and ES-FEM with the Same Mesh

Mode	Exact (Hz)	FEM (Hz)	Error of FEM (%)	ES-FEM (Hz)	Error of ES-FEM (%)	Error of FEM / Error of ES-FEM
1	750.0	750.2	0.02933	750.0	0.00000	—
2	1500.0	1501.8	0.12000	1500.0	0.00000	—
3	2250.0	2256.1	0.27111	2250.1	0.00444	61.0
4	3000.0	3014.5	0.48333	3000.3	0.01000	48.3
5	3750.0	3778.3	0.75467	3750.6	0.01600	47.2
6	4500.0	4549.2	1.09333	4501.0	0.02222	49.2
7	5250.0	5328.5	1.49524	5251.6	0.03048	49.1
8	6000.0	6117.8	1.96333	6002.3	0.03833	51.2
9	6750.0	6918.8	2.50074	6753.3	0.04889	51.2
10	7500.0	7733.2	3.10933	7504.6	0.06133	50.7
11	7500.0	7836.2	4.48267	7582.0	1.09333	4.1
12	7537.4	7878.3	4.52278	7618.4	1.07464	4.2
13	7648.5	8004.3	4.65189	7726.9	1.02504	4.5
14	7830.2	8211.0	4.86322	7904.5	0.94889	5.1
15	8077.7	8494.0	5.15370	8147.0	0.85792	6.0
16	8250.0	8562.9	3.79273	8256.1	0.07394	51.3
17	8385.3	8848.0	5.51799	8448.8	0.75728	7.3
18	8746.4	9267.3	5.95559	8804.2	0.66084	9.0
19	9000.0	9409.7	4.55222	9007.9	0.08778	51.9
20	9154.9	9746.6	6.46321	9207.3	0.57237	11.3

only on the term κh and, hence, can be well controlled. Based on these simple analyses, a numerical examination is conducted to reveal the relation between the relative error and κh and $\kappa^3 h^2$, using both ES-FEM and FEM. Figure 15.10 plots the relative errors obtained by keeping, respectively, κh and $\kappa^3 h^2$ constant. It is clearly seen that when $\kappa^3 h^2$ is kept constant, the relative errors for both ES-FEM and FEM are quite small. Especially, the error in the ES-FEM solution is very small and well under control. When κh is kept constant, the relative errors of both ES-FEM and FEM increase noticeably. It can be concluded that keeping $\kappa^3 h^2$ constant is a much more efficient way to obtain accurate results for both ES-FEM and FEM models. We also observed that keeping κh constant in ES-FEM achieves a similar accuracy as keeping $\kappa^3 h^2$ constant in FEM. In other words, the dispersive error in the ES-FEM solution is quite negligible compared to the FEM solution.

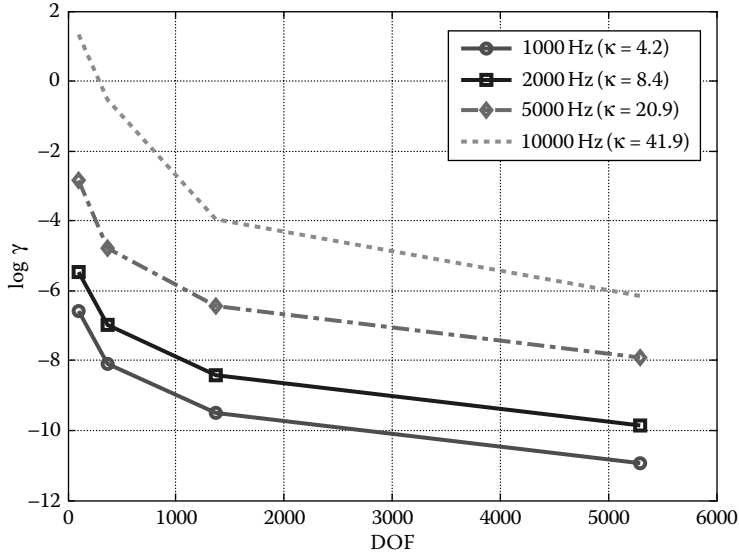

FIGURE 15.9 The relative error in the velocity field at different frequency values is obtained using ES-FEM.

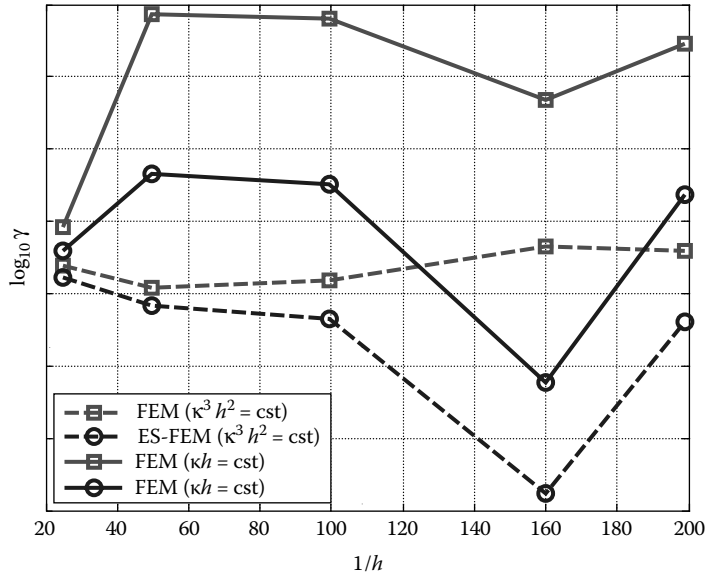

FIGURE 15.10 Comparison of relative error obtained using ES-FEM-T3 and FEM-T3 by keeping κh and $\kappa^3 h^2$ constant.

15.7.7 Sensitivity to Nodal Irregularity

To evaluate the influence of the mesh irregularities on the solution accuracy, a test is conducted to compute the numerical results using both a regular mesh and an irregular mesh. The irregularly distributed nodes are generated based on the regularity with random alternations to the nodal coordinates. The coordinates of the irregular nodes are computed using the following expression:

$$x' = x + \Delta x \cdot r_c \cdot \beta_{ir},$$
$$y' = y + \Delta y \cdot r_c \cdot \beta_{ir},$$

where x' and y' are the coordinates of the irregular nodes; x and y are original regular coordinates; Δx and Δy are the initial regular nodal spacing in the x- and y-directions; r_c is a computer-generated random number between -1.0 and 1.0, and β_{ir} is a prescribed irregularity degree whose value is varied between 0.0 and 0.5. A bigger value of β_{ir} leads to a more irregular node distribution. Figure 15.11 presents the result of two mesh models of different nodal irregularity.

This nodal sensitivity study is performed at a frequency of 4000 Hz. The acoustic pressure distributions along the x-axis (bottom edge) are computed using both ES-FEM and FEM with different types of meshes. The results are plotted in Figure 15.12a and b, together with the *exact* solution. The results show that the accuracy of the FEM results significantly deteriorates when the irregular mesh is used. When the ES-FEM is used, the accuracy of acoustic pressure for irregular nodes changes only a little as compared with regular nodes. These findings imply that the present ES-FEM works well even with the distorted elements. The FEM, however, is well known and is confirmed here to be sensitive to mesh distortions.

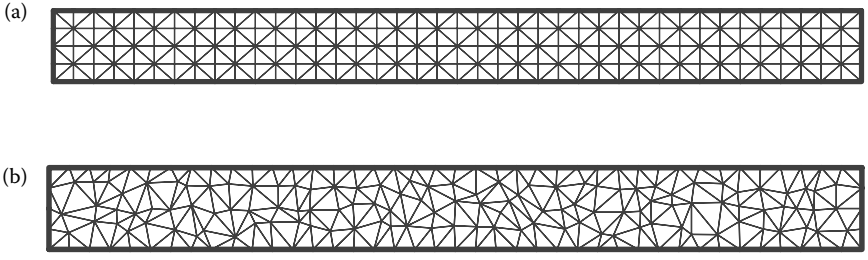

FIGURE 15.11 Two mesh models of different nodal irregularity; (a) regular mesh ($\beta ir = 0.0$) and (b) irregular mesh with $\beta ir = 0.4$.

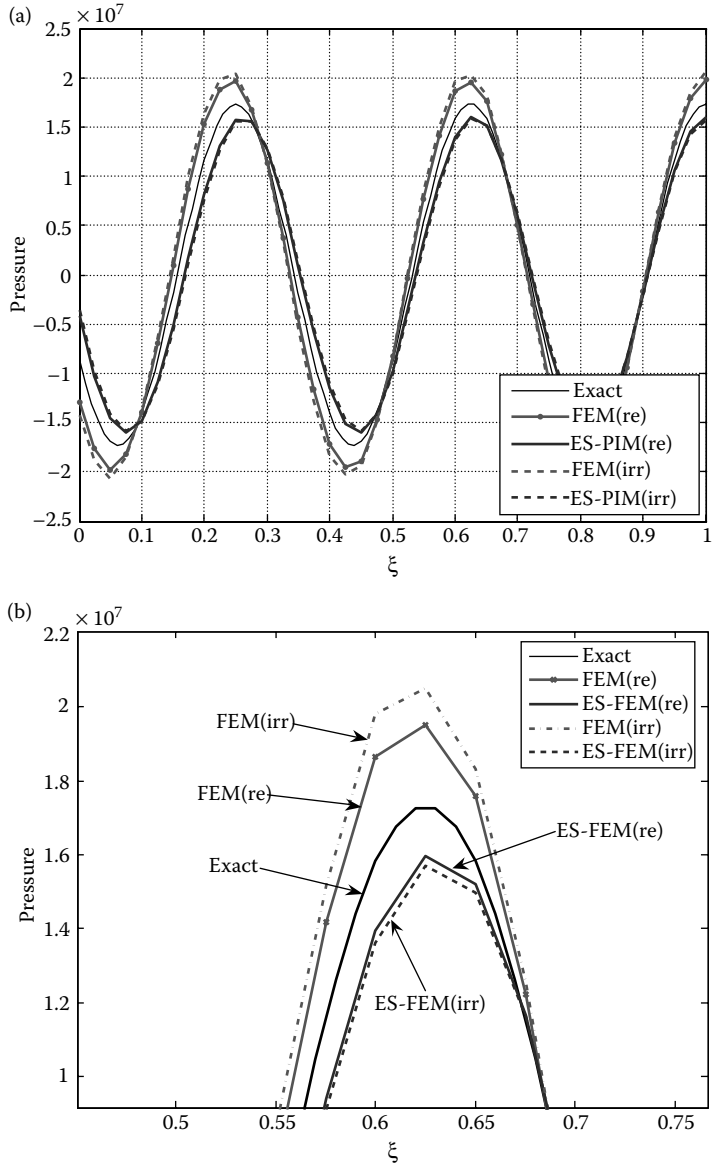

FIGURE 15.12 Acoustic pressure distribution obtained using ES-FEM and FEM along the ξ-axis (bottom edge) of the elongated 2D chamber (4000 Hz); (a) full range distribution and (b) zoomed-in distribution.

15.7.8 The 2D Car Acoustic Problem

We now consider a practical problem of acoustic pressure distribution in a car passenger compartment [7]. The compartment is excited by the

vibrating engine. The geometry of the passenger compartment is 3D and can be approximately considered as prismatic. For simplicity, it is simplified as a 2D problem. Figure 15.13a illustrates the 2D geometry of the problem domain, and the setting of the problem. The front panel of the passenger compartment is subjected to a given velocity of 0.01 m/s, simulating the vibration coming from the engine. The roof of the passenger compartment is attached with absorbing material with an admittance of 0.00144 $m^3/(Pa\ s)$. The citation frequencies are 200 and 400 Hz. Figure 15.13b shows the mesh used in this study with 305 nodes and an average spacing of 0.1 m that satisfies the usual "rule of thumb" for the considered frequency values.

Figure 15.14 plots the contour of the acoustic pressure within the passenger compartment for an excitation frequency of 200 Hz. Contour Figure 15.14a is obtained using ES-FEM, while contour Figure 15.14b is obtained using FEM. Because the analytical solution is unavailable for this problem, a reference solution obtained using FEM with a very fine mesh (22,524 nodes) is plotted in Figure 15.14c for comparison. Figure 15.15 plots the same set of results but for the excitation frequency of 400 Hz. From Figures 15.14 and 15.15, it is found that the pressure contours obtained using ES-FEM are much closer to those using FEM for both the cases of 200 and 400 Hz.

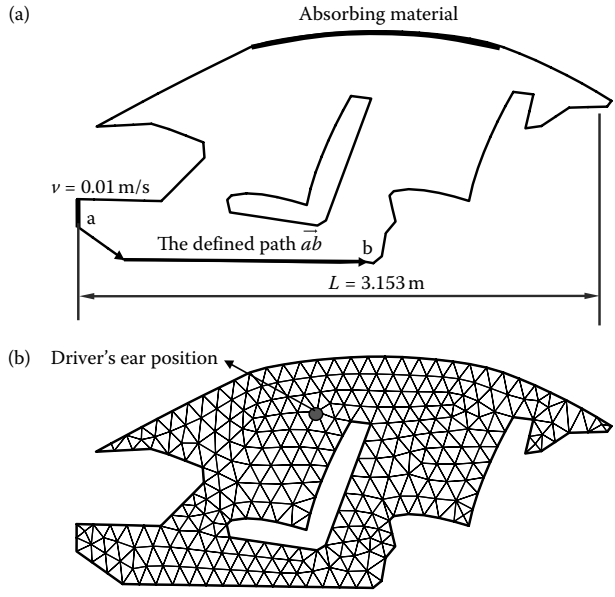

FIGURE 15.13 A 2D car passenger compartment model: (a) geometry, boundary conditions; the results on the $\vec{ab}$ path will be examined and (b) triangular mesh used in the simulation.

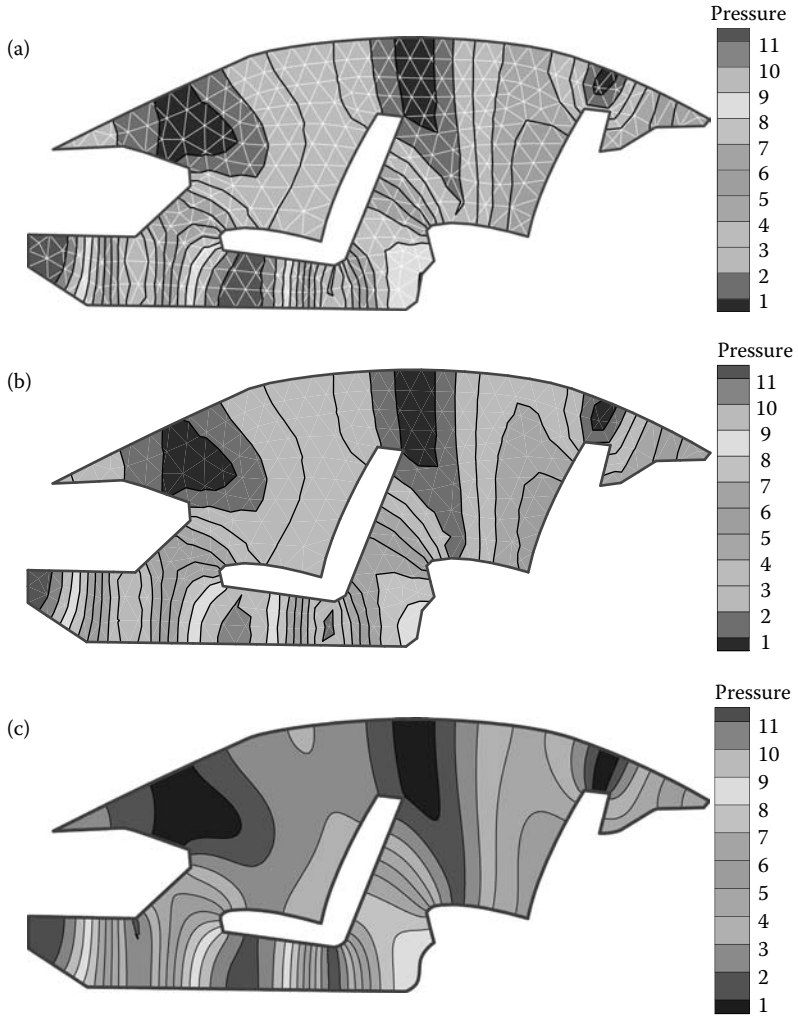

FIGURE 15.14 Acoustic pressure distribution (200 Hz): (a) EF-FEM (305 nodes); (b) FEM (305 nodes); and (c) reference solution obtained using FEM with 22,524 nodes.

To examine the results quantitatively, the real part of pressure distributed along the defined path $\vec{ab}$ are computed using both ES-FEM and FEM. The results are plotted in Figure 15.16. It is shown clearly in Figure 15.16a that the errors of the real part of the pressure obtained from ES-FEM and FEM are all quite close to the reference result, at the frequency of 200 Hz. For the frequency of 400 Hz, the results obtained from the ES-FEM are still very close to the reference result. In contrast, the FEM solution is very far from

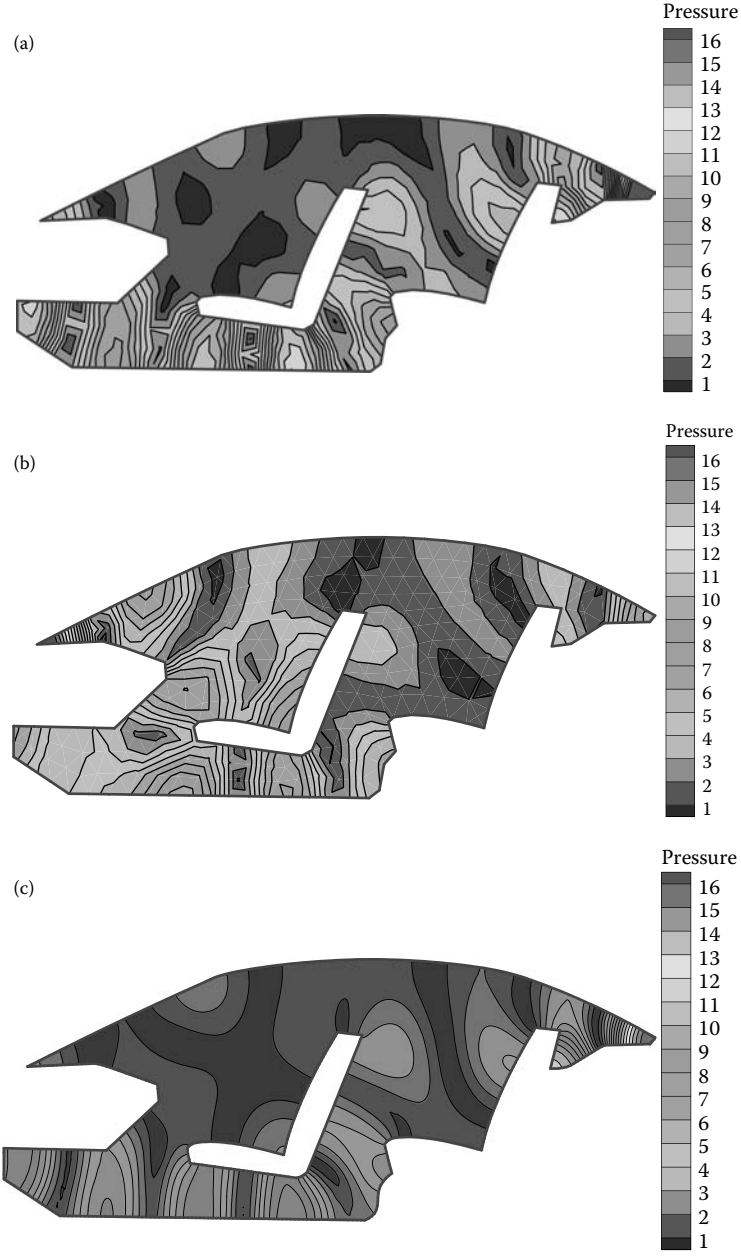

FIGURE 15.15 Acoustic pressure distribution (400 Hz): (a) EF-FEM (305 nodes); (b) FEM (305 nodes); (c) reference solution obtained using FEM with 22,524 nodes.

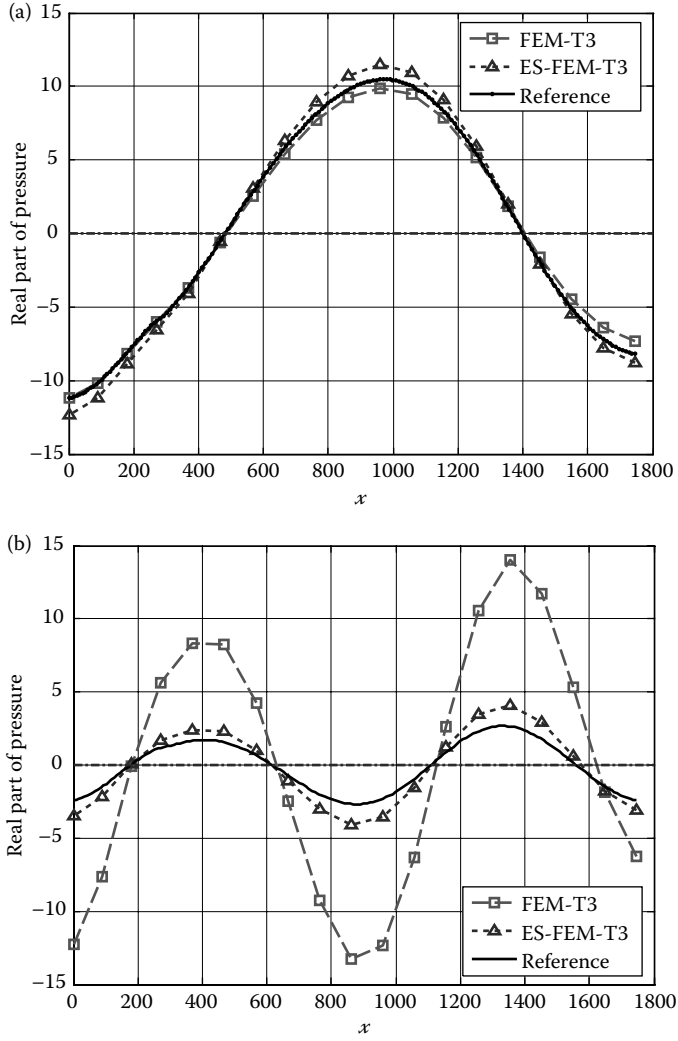

FIGURE 15.16 Distribution of the real part of acoustic pressure along the path $\overrightarrow{ab}$ marked in (a) 200 Hz and (b) 400 Hz.

the reference solution. This 2D practical problem demonstrates also that the ES-FEM is much more accurate than FEM, using the same mesh.

Frequency response is now computed over a full frequency range from 1 to 800 Hz with intervals of 1.0 Hz. In this case, we examine the response (sound pressure level) at the driver's ear point (see Figure 15.13b). The boundary conditions for this 2D car problem are the same as the previous one including the Neumann and admittance boundary conditions.

The average mesh size is now 0.1 m, which gives the frequency limit of 541 Hz (based on the usual "rule-of-thumb"). The computed results are plotted in Figure 15.17 for both ES-FEM and FEM using the same mesh. As the analytical solution is unavailable, the reference solution using FEM with 22,524 nodes is obtained for comparison. As shown in Figure 15.17, the ES-FEM produces much more accurate results compared to FEM over the full frequency range. We also note that when the frequency exceeds 400 Hz, which is a little smaller than the 541 Hz that is the limit for the FEM to produce acceptable results based on the rule of thumb, the FEM solution deviates clearly away from the reference solution. The ES-FEM is good up to 550 Hz, which is slightly beyond the limit of 541 Hz. This finding shows that when ES-FEM is used, the rule of thumb can still be used as a reasonably good gauge on mesh density needed for solutions at the desired frequency. In other words, the error in the ES-FEM solution is newly controlled by the interpolation error, and hence the "usual" rules apply.

15.7.9 The 3D Engine Chamber Problem

In this final example, we apply FS-FEM to a practical 3D problem using a 3D in-house code developed by Liu's group [27]. In this 3D example, we consider the acoustical pressure distribution in a car engine chamber, with the vibration of the engine being the major noise source. The geometry of the 3D car engine chamber and the settings of the problem are shown in Figure 15.18a. The engine is located at the center of the chamber floor, and a velocity excitation of 0.01 m/s on the surface of the engine is applied to

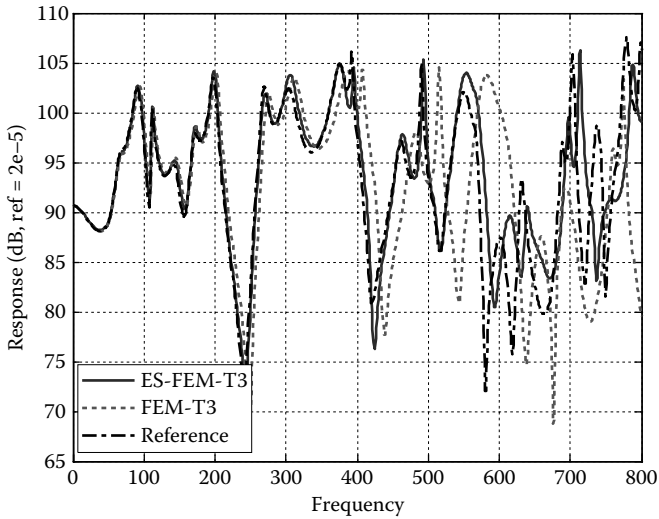

FIGURE 15.17 Acoustic frequency response registered at the driver's ear for the 2D car problem obtained using ES-FEM and FEM with the same mesh.

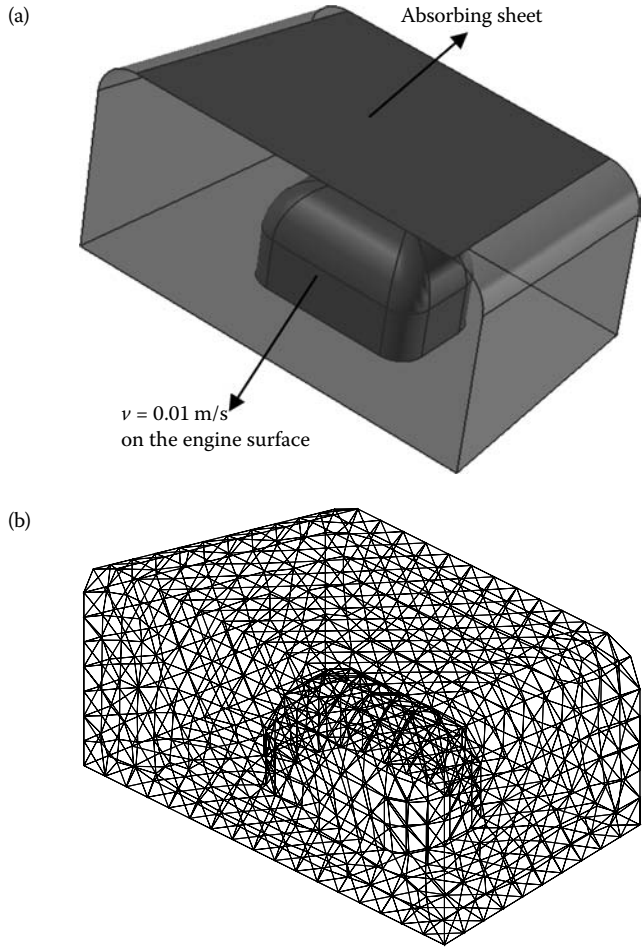

FIGURE 15.18 Acoustics in a 3D engine chamber: (a) geometry and problem setting and (b) mesh of tetrahedral elements.

simulate the vibration on the engine surface. A sheet of absorbing material with an admittance of 0.00144 $m^3/(Pa\ s)$ is attached to the engine hood. The 3D model is discretized using tetrahedral elements with 1211 nodes. The mesh is relatively "regular" and the average nodal spacing is controlled at 0.05 m. The analyses are performed using both FEM and FS-FEM at a frequency of 400 Hz. A similar example has also been studied in Ref. [8] using a meshless method.

Figure 15.19 plots the distribution of the real part of the acoustic pressure obtained using FS-FEM (Figure 15.19a) and FEM (Figure 15.19b), all using 1211 nodes. The reference results are obtained using the FEM with a very

fine mesh of 21,197 nodes, and the results are plotted in Figure 15.19c. Figure 15.19 reveals that for this 3D case, the overall contour lines of the FS-FEM solution are much closer to the reference solutions, compared to those of FEM results, especially in the high pressure gradient regions.

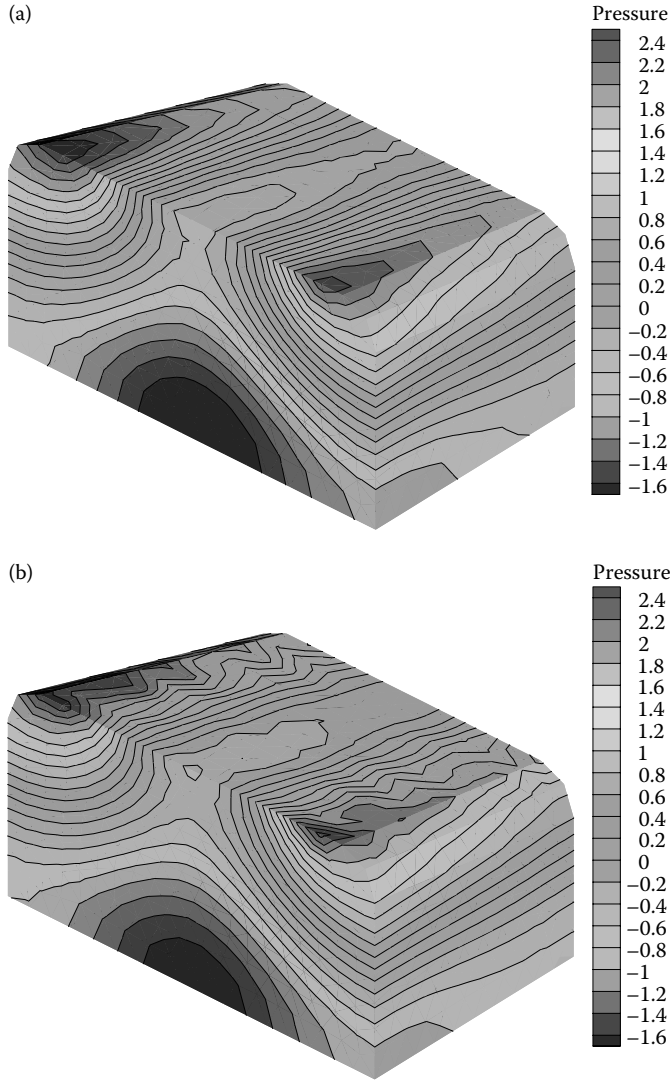

FIGURE 15.19 Distribution of the real part of acoustic pressure computed using different models (frequency=400 Hz): (a) FS-FEM using 1211 nodes; (b) FEM using 1211 nodes; and (c) reference solution using 21,197 nodes.

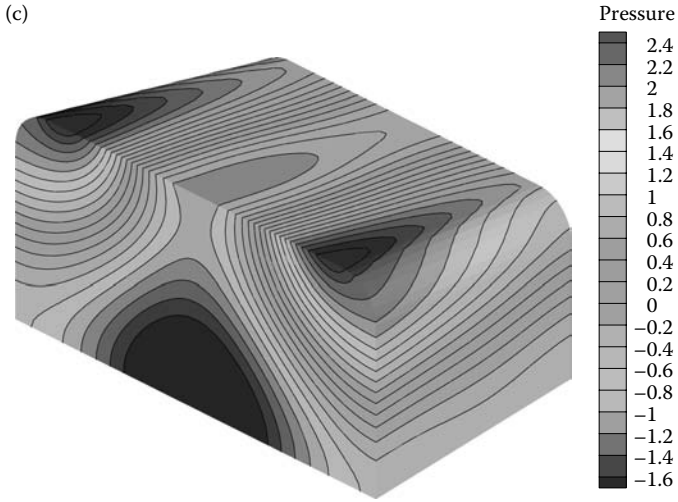

FIGURE 15.19 (*Continued*)

15.8 Remarks

In this chapter, both the standard and smoothed Galerkin weak forms for Helmholtz equations are first presented, and the S-FEM models are then formulated for acoustics problems. Aiming to solve the dispersive error, the "star" performers ES-FEM and FS-FEM are chosen to solve a number of acoustics problems. The accuracy, convergence, and error control in ES-FEM and FS-FEM are examined in detail. The following remarks may be made from our study:

a. The S-FEM models use triangular types (triangular for 2D and tetrahedral for 3D) of elements and can be effectively applied for acoustics problems as long as the softening effects of S-FEM can be well made use of.
b. ES-FEM and FS-FEM have a lot of similarity to the FEM model, and can be implemented in a straightforward way with little change to the FEM code for acoustics problems.
c. ES-FEM and FS-FEM are much less sensitive to the wave number, compared with FEM, and hence *can effectively suppress the dispersive error*. Hence, they can achieve higher accuracy than the FEM, especially for larger wave number.
d. ES-FEM and FS-FEM can also provide a much better solution in frequency response and natural frequencies for acoustics problems. This is because the edge-based and face-based gradient smoothing

techniques used in ES-FEM and FS-FEM produce a close-to-exact stiffness in the model.

e. The usual rule of thumb cannot be applied to the FEM model for high-frequency excitations, but it is still applicable to the ES-FEM and FS-FEM models. This means that the error in the ES-FEM and FS-FEM models is still largely controlled by the interpolation error for the problem governed by Helmholtz equations such as the acoustics problems.

f. ES-FEM is found to be less sensitive to distortion of element, compared to FEM.

g. For the practical acoustics problems, ES-FEM and FS-FEM are much more accurate than FEM with the same nodes. We have also shown that the ES-FEM can be applied to problems of complicated geometry due to the use of triangular mesh.

The S-FEMs have been applied to many other more complicated acoustics problems. A coupled ES/FS-FEM has been recently developed for structural-acoustics problems [28]. The ES-FEM is also coupled with the BEM method for fluid–structure interaction problems [29]. In addition, a coupled FS-FEM and FEM model has also been developed for the analysis of 3D structural-acoustics problems [30].

Using the upper bound property of NS-FEM [31], further studies on using NS-FEM for obtaining the lower bound for natural frequencies of structures or acoustic media and upper bound for transient dynamics problems have also been conducted recently [32]. Following Ref. [33], an αFEM has also been formulated for acoustics problems, and it is found that the α FEM can control very well both the interpolation and the dispersion errors [34].

Finally, we may note that because of the features of ES-FEM-T3 and FS-FEM-T4 for acoustics problems, these models are "star" performers and may be the best linear model for complicated acoustics problems, in terms of (1) adaptation to complicated geometry; (2) suitability for automatically meshing [35]; (3) stability; (4) solution accuracy; (5) computational efficiency; and (6) suppression of dispersion errors. We can also quite safely expect that they should work well for other types of wave propagation problems.

References

1. Liu GR and Xi ZC. 2001. *Elastic Waves in Anisotropic Laminates*. CRC Press, Boca Raton, FL.

2. Liu GR, Achenbach JD, Kim JO, and Li ZL. 1992. A combined finite element method/boundary element method for $V(z)$ curves of anisotropic-layer/substrate configurations. *Journal of the Acoustical Society of America, USA*; 92(5): 2734–2740.
3. Liu GR, Tani J, Ohyoshi T, and Watanabe K. 1991. Transient waves in anisotropic laminated plates, Part 1: Theory, Part 2: Application. *ASME Journal of Vibration and Acoustics, USA*; 113: 230–239.
4. Liu GR, Tani J, Watanabe K, and Ohyoshi T. 1990. A semi-exact method for the propagation of harmonic waves in anisotropic laminated bars of rectangular cross section. *Wave Motion, USA*; 12: 361–371.
5. Liu GR, Tani J, Watanabe K, and Ohyoshi T(1991) Characteristics of surface wave propagation along the edge of an anisotropic laminated semi-infinite plate. *Wave Motion, USA*; 13: 243–251.
6. Petersen S, Dreyer D, and Estorff OV. 2006. Assessment of finite and spectral element shape functions or efficient iterative simulations of interior acoustics. *Computer Methods in Applied Mechanics and Engineering*; 195: 6463–6478.
7. Nefske DJ, Wolf JA, and Howell LJ. 1982. Structural-acoustic finite element analysis of the automobile passenger compartment: A review of current practice. *Journal of Sound and Vibration*; 80(2): 247–266.
8. Bouillard PH, Lacroix V, and De Bel E. 2004. A wave-oriented meshless formulation for acoustical and vibro-acoustical applications. *Wave Motion, USA*; 39: 295–305.
9. Deu JF, Larbi W, and Ohayon R. 2008. Piezoelectric structural acoustics problems; symmetric variational formulation and finite elements. *Computer Methods in Applied Mechanics and Engineering*; 197: 1715–1724.
10. Guasch Codina R. 2007. An algebraic subgrid scale FEM for the convected Helmholtz equation in two dimension with applications in aeroacoustics. *Computer Methods in Applied Mechanics and Engineering*; 196: 4672–4689.
11. Suleau S, Deraemaeker A, and Bouillard Ph. 2000. Dispersion and pollution of meshless solution for the Helmholtz equation. *Computer Methods in Applied Mechanics and Engineering*; 190: 639–657.
12. Harari I and Magoulès F. 1994. Numerical investigations of stabilized finite element computations for acoustics. *Wave Motion, USA*; 39: 339–349.
13. Ihlenburg F and Babuška I. 1997. Reliability of finite element methods for the numerical computation of waves. *Advances in Engineering Software*; 28: 417–424.
14. Deraemaeker A, Babuska I, and Bouillard Ph. 1999. Dispersion and pollution of the FEM solution for the Helmholtz equation in one, two and three dimension. *International Journal for Numerical Methods in Engineering*; 46: 471–499.
15. Thompson L and Pinsky P. 1995. A Galerkin least-squares finite element method for the two-dimensional Helmholtz equation. *International Journal for Numerical Methods in Engineering*; 38: 371–397.
16. Liu GR. 2009. *Meshfree Methods: Moving Beyond the Finite Element Method*, 2nd edition. Taylor & Francis/CRC Press, Boca Raton, FL.
17. Belytschko T, Lu YY, and Gu L. 1994. Element-free Galerkin methods. *International Journal for Numerical Methods in Engineering*; 37: 229–256.
18. Bouillard Ph and Suleau S. 1998. Element-free Garlekin solutions for Helmholtz problems: Formulation and numerical assessment of the pollution effect. *Computer Methods in Applied Mechanics and Engineering*; 162: 317–335.

19. Alvarez GB, Loula AFD, Carmo EGDd, and Rochinha FA. 2006. A discontinuous finite element formulation for Helmholtz equation. *Computer Methods in Applied Mechanics and Engineering*; 195: 4018–4035.
20. Liu GR. 2009. A G space theory and weakened weak (W^2) form for a unified formulation of compatible and incompatible methods, Part I: Theory and Part II: Applications to solid mechanics problems. *International Journal for Numerical Methods in Engineering*; 81: 1093–1156.
21. Liu GR. 2009. On a G space theory. *International Journal of Computational Methods*; 6(2): 257–289.
22. Liu GR and Zhang GR. 2009. A normed G space and weakened weak (W^2) formulation of a cell-based smoothed point interpolation method. *International Journal of Computational Methods*; 6(1): 147–179.
23. Liu GR. 2008. A generalized gradient smoothing technique and the smoothed bilinear form for Galerkin formulation of a wide class of computational methods. *International Journal of Computational Methods*; 5(2): 199–236.
24. Irimie S and Bouillard Ph. 2001. A residual a posteriori error estimator for the finite element solution of the Helmholtz equation. *Computer Methods in Applied Mechanics and Engineering*; 190: 2027–2042.
25. Liu GR, Nguyen-Thoi T, and Lam KY. 2009. An edge-based smoothed finite element method (ES-FEM) for static, free and forced vibration analysis. *Journal of Sound and Vibration*; 320: 1100–1130.
26. Nguyen-Thoi T, Liu GR, Lam KY, and Zhang GY. 2009. A face-based smoothed finite element method (FS-FEM) for 3D linear and nonlinear solid mechanics problems using 4-node tetrahedral elements. *International Journal for Numerical Methods in Engineering*; 78: 324–353. .
27. He ZC, Liu GR, Zhong ZH, Wu SC, Zhang GY, and Cheng AG. 2009. An edge-based smoothed finite element method (ES-FEM) for analyzing three-dimensional acoustic problems. *Computer Methods in Applied Mechanics and Engineering*; 199: 20–33.
28. He ZC, Liu GR, Zhong ZH, Cui XY, and Zhang GY. 2009. A coupled edge-based/face-based smoothed finite element method for structural-acoustic problems. *Applied Acoustics*; (revised).
29. He ZC, Liu GR, Zhong ZH, and Zhang GY. 2009. A coupled ES-FEM/BEM method for fluid–structure interaction problems. *Engineering Analysis with Boundary Elements*; (submitted).
30. He ZC, Liu GR, Zhong ZH, and Zhang GY. 2009. Coupled analysis of 3D structural-acoustic problems using edge-based smoothed finite element method/finite element method. *Finite Elements in Analysis and Design*; (submitted).
31. Liu GR and Zhang GY. 2008. Upper bound solution to elasticity problems: A unique property of the linearly conforming point interpolation method (LC-PIM). *International Journal for Numerical Methods in Engineering*; 74: 1128–1161.
32. Zhang ZQ and Liu GR . 2009. Temporal stabilization of node-based smoothed finite element method (NS-FEM) and solution bound of linear elastostatics and vibration problems, *Computational Mechanics*; (submitted).
33. Liu GR, Nguyen-Thoi T, and Lam KY. 2008. A novel alpha finite element method (αFEM) for exact solution to mechanics problems using triangular and

tetrahedral elements. *Computer Methods in Applied Mechanics and Engineering*; 197: 3883–3897.
34. He ZC, Liu GR, Zhong ZH, and Zhang GY. 2009. An alpha finite element method (α-FEM) for analyzing acoustic problems large wave numbers, *Computer Methods in Applied Mechanics and Engineering*; (revised).
35. Tang Q, Liu GR, and He ZC, Adaptive analysis of acoustic problems (submitted).

Index

G

H

M

N

W

Mechanical Engineering

Smoothed Finite Element Methods

G.R. Liu and Nguyen Thoi Trung

Developed by the authors and their colleagues, the smoothed finite element method (S-FEM) requires only a triangular/tetrahedral mesh to achieve accurate results, a generally high convergence rate in energy without increasing computational cost, and easy auto-meshing of the problem domain. Drawing on the authors' extensive research results, ***Smoothed Finite Element Methods*** presents the theoretical framework and development of various S-FEM models.

After introducing background material, basic equations, and an abstracted version of the FEM, the book discusses the overall modeling procedure, fundamental theories, error assessment matters, and necessary building blocks to construct useful S-FEM models. It then focuses on several specific S-FEM models, including cell-based (CS-FEM), node-based (NS-FEM), edge-based (ES-FEM), face-based (FS-FEM), and a combination of FEM and NS-FEM (αFEM). These models are then applied to a wide range of physical problems in solid mechanics, fracture mechanics, viscoelastoplasticity, plates, piezoelectric structures, heat transfer, and structural acoustics.

Requiring no previous knowledge of FEM, this book shows how computational methods and numerical techniques like S-FEM help in the design and analysis of advanced engineering systems in rapid and cost-effective ways. Readers can easily apply the methods presented in the text to their own engineering problems for reliable and certified solutions.

Features

- Describes newly developed S-FEM models that combine FEM and mesh-free techniques
- Presents techniques for computing certified solutions with both lower and upper bounds
- Covers methods that produce super-convergent and nearly exact solutions for displacement and energy error measures
- Explains the basic theories, principles, formulation, techniques, and procedures of S-FEM models
- Addresses key issues related to future computational methods
- Provides a large number of practical engineering examples, along with illustrations and tables

CRC Press
Taylor & Francis Group
an informa business
www.crcpress.com

6000 Broken Sound Parkway, NW
Suite 300, Boca Raton, FL 33487
270 Madison Avenue
New York, NY 10016
2 Park Square, Milton Park
Abingdon, Oxon OX14 4RN, UK

K11070

ISBN: 978-1-4398-2027-8
90000
9 781439 820278

www.crcpress.com